LBL-12000
UC-13

36110

MASTER

MATERIALS AND MOLECULAR RESEARCH DIVISION

Annual Report 1980

June 1981

DISTRIBUTION OF THIS DOCUMENT IS UNLIMITED

Lawrence Berkeley Laboratory
University of California

LBL-12000

Prepared for the U.S. Department of Energy under Contract W-7405-ENG-48

LBL-12000

MATERIALS AND MOLECULAR RESEARCH DIVISION

Annual Report 1980

June 1981

DISCLAIMER

[illegible]

Lawrence Berkeley Laboratory
University of California
Berkeley, California 94720

DISTRIBUTION OF THIS DOCUMENT IS UNLIMITED

CONTENTS

GENERAL INTRODUCTION xxi
Alan W. Searcy

I. MATERIALS SCIENCES
A. Metallurgy and Ceramics
1. Structure of Materials

a. Atomic Resolution in Microscopy
Ronald Gronsky and Gareth Thomas, Investigators

1. High Resolution Transmission Electron Microscopy 3
2. Grain Boundary Structure and Segregation in Al Alloys 4
3. High Resolution Studies of High-Rank Coals 5
4. Lattice Imaging of Glassy Carbon 6
5. Tem/Stem Study of Grain Boundary Structure and Segregation in CVD Thin-Film Silicon 8
6. Characterization of the Defect Structure of Si-SiO_2 Interfaces 8

Research Plans for Calendar Year 1981 9
1980 Publications and Reports 10

b. Microstructure, Properties, and Alloy Design: Inorganic Materials
Gareth Thomas, Investigator

Alloy Design: Steels

1. An Investigation of Correlations for Predicting Mechanical Properties of "Quatough" Steels 11
2. Sliding Wear, Toughness, and Microstructural Relationships in High Strength Fe/Cr/C Experimental Steels 12

Dual Phase Steels

3. Impact Properties of Fe/1.5Mn/0.6C Dual Phase Steel 13
4. Effect of Vanadium on Structure-Property Relations of Dual Phase Fe/Mn/Si/C Steels 14
5. The Effect of the Processing Variables on the Mechanical Properties of Dual Phase Steels 16
6. Mechanical Properties and Microstructures of Fe/1.0Al/0.06C Steel 16
7. The Effect of Martensite Morphology on Fatigue Crack Propagation in Duplex Ferrite Martensite 18
8. The Ferrite Structure and Partitioning of Alloying Elements in Dual Phase Steels 18

Phase Transitions

9. Morphology and Crystallography of Lath Martensite in Steels 19
10. The Stabilization Mechanisms of Retained Austenite in Steels 19
11. High Resolution Studies in Martensite 20
12. In-Situ Observation of the Decomposition of Retained Austenite in Fe/Cr/Mn/C Alloys by HVEM 21

Magnetic Materials

13. Step-Aged Rare Earth-Cobalt Alloy Magnets 22
14. Zero-Magnetostrictive Fe/Co/B/Si Amorphous Alloys 23
15. Microstructure-Domain Wall Interaction in (Mn-Zn)Fe_2O_4 and $LiFe_5O_8$ 23

Ferroelectric Materials

16. Grain Boundary Phase and Poling of PZT 24
17. Structure of Domains and Domain Walls in PZT 24

Refractory Ceramics

18. Silicon Nitrides 25
19. Silicon Nitride Alloys: Sialons 25
20. Nitride Glasses 25

Research Plans for Calendar Year 1981 26
1980 Publications and Reports 26

c. 1.5 MeV Electron Microscope
Kenneth H. Westmacott, Investigator

1. Progress Report on Facility Development 29
2. The Role of Vacancies in Precipitation of Interstitial Phases 29
3. The Origin of Orientation Relationships 32

Research Plans for Calendar Year 1981 33
1980 Publications and Reports 34

2. Mechanical Properties

a. Theoretical Problems in Alloy Design
J. W. Morris, Jr., Investigator

Theoretical Studies

1. Study of Precipitate Morphology by Consideration of Elastic Strain Energy 35

Experimental Research

2. Observations of the Morphology of Plate Precipitates 36
3. Mössbauer Effect Metallography 36

Structural Alloy Development

4. Investigation of Intergranular Embrittlement in Fe-Mn Steels by High Resolution Scanning Auger Microscopy 37

Welding Research

5. Developing a Welding Research Laboratory 38
6. Characterization of Ferritic G.M.A. Weld Deposits in 9%Ni Steel for Cryogenic Application 39
7. Research in Support of Materials Selection for the Cases of Forced-Cooled Superconductors 39

Superconductivity Research

8. Microstructure and Properties of A15 Superconductors Formed by Direct Precipitation 40
9. The Effects of Third Element Addition on the Mechanical Properties of the V-Ga Alloys 41
10. Nb-Al and Nb-Al Based A15 Superconductors by Solid-Liquid Reaction 42
11. Metallurgical Failure Analysis with a Large Superconducting Solenoid Magnet 42

Research Plans for Calendar Year 1981 42
1980 Publications and Reports 43

b. Structure-Property Relationships in Semiconductor Materials
Jack Washburn, Investigator

1. Structure of Cu_2S in CdS-Cu_xS Solar Cells 45
2. Segregation of Phosphorus at Dislocation Loops in Silicon-Effect on Electrical Properties 45
3. Laser Annealing of Phosphorus Implanted Si 46
4. High Power Pulsed Electron Beam Annealer 47

5. Structural Damage-Dopant Atom Interaction in Gallium Arsenide 47
6. Comparison of Channeled Backscattering from Subsurface Defects and Cross Section Electron Microscope Observations of the Same Specimens 48
7. The Effect of Microtwins on the Migration of a {111} Amorphous-Crystalline Interface in Silicon 49
8. Atomic Distribution of Arsenic in MOS Test Devices Measured by Rutherford Backscattering 50

Research Plans for Calendar Year 1981 51
1980 Publications and Reports 52

c. Mechanical Properties of Ceramics
Anthony G. Evans, Investigator

High Temperature Deformation and Failure

1. Cavitational Effects During Creep in Polycrystalline Alumina 54
2. Creep Cavitation Effects in Polycrystalline Alumina 55
3. Creep Fracture in Ceramic Polycrystals 56
4. The High Temperature Internal Friction Background in Polycrystals 59
5. The Influence of Cavities on Grain Boundary Sliding 61

Toughening Mechanisms

6. Transformation Toughening in Ceramics 63
7. The Toughness of Zirconia Composites 65

Indentation Processes

8. The Response of Solids to Elastic/Plastic Indentation 66

Ceramic Processing

9. Final Stage Sintering Models 69

Research Plans for Calendar Year 1981 70
1980 Publications and Reports 71

3. Physical Properties

a. Superconductivity Effects - High Field Superconductivity
Moshe Rosen, Investigator

1. Experimental Program - Final Phase 73

1980 Publications and Reports 74

b. Interfaces and Ceramic Microstructures
Joseph Pask, Investigator

1. Wetting and Reactions in Glass/Non-Precious Metal Systems 75
2. Wetting and Reactions in Glass/Titanium Systems 76
3. Wetting and Adherence of Glasses to Noble Metals 78
4. Reactions and Spreading in the Cu-Ag System 79
5. Sintering of Mullite-Containing Compositions 80
6. Effect of Silica Impurities on Electrophoretic Properties and Sintering of Alumina 80
7. Thermodynamics of Sintering 81
8. High Temperature Solid State Reactions in Kaolinite 82
9. Processing of PZT and Effect on Coupling Coefficient 83

Research Plans for Calendar Year 1981 86
1980 Publications and Reports 86

c. High-Temperature Reactions
Alan W. Searcy, Investigator

1. In-Situ Studies of $MgCa(CO_3)_2$ Decomposition by TEM 87
2. The Kinetics of Reaction of Porous CaO Aggregates with Water Vapor 88
3. Strain-Induced Phenomena in $Ca(OH)_2$ Made by Reaction of CaO With Water Vapor 88
4. Collision Distributions in Porous Catalyst Pellets 89
5. Rate Limiting Processes in $MgSO_4$ Decomposition 90
6. Electronic Ceramics in High Temperature Environments 91

Research Plans for Calendar Year 1981 91
1980 Publications and Reports 91

d. Chemical Properties of Ceramic Alloys
Lutgard De Jonghe, Investigator

1. Gaseous Reduction of an Alloy Oxide 93
2. In Situ Observations of Gas/Solid Reactions: Cobalt Ferrite Reduction 95
3. Reduction Kinetics and Microstructures of Al^{3+} Containing Cobalt Ferrites 97

Research Plans for Calendar Year 1981 99
1980 Publications and Reports 99

e. Structure and Electrical Properties of Composite Materials
Robert H. Bragg, Investigator

1. Density Changes in Heat Treated Glass-Like Carbon (GC) 100
2. Experimental Determination of Compton Scattering from Pyrolytic Graphite and Glassy Carbon 102
3. Hall Coefficient, Magnetoresistance and Electrical Conductivity in Glassy Carbon 104

Research Plans for Calendar Year 1981 105
1980 Publications and Reports 106

f. High-Temperature Oxidation and Corrosion of Materials
David P. Whittle, Investigator

1. Mechanism of Sulfur-Induced Accelerated Corrosion at Low Oxygen Potentials 107
2. Simultaneous Internal Oxidation and Sulfidation 109
3. Thermodynamics of Low Temperature (700-850°C) Hot Corrosion 110
4. Aluminum Diffusion During the Aluminizing of Iron 112
5. Diffusion and Multiphase Systems 112
6. Al_2O_3 Adherence on CoCrAl Alloys 114
7. Oxidation Behavior of Overlay Coatings 115
8. Motion of Defects During Growth of Solid Solution Oxides 116

Research Plans for Calendar Year 1981 118
1980 Publications and Reports 119

4. Engineering Materials

a. Erosion-Corrosion Wear Program
Alan V. Levy, Investigator

1. The Effect of Surface Doping on the Oxidation of Chromia Former Alloys 121
2. Metal Erosion by Spherical Particles at Normal Incidence 123
3. Erosion of Thin Corrosion Scales 124
4. Erosion of Oxide Scales on CoCrAl Coatings 125
5. Modeling the Erosion of Brittle Materials 126
6. A Numerical Solution to Dilute Gas Particle Flows at High Velocity 127
7. Particle Rebound Phenomena in Two Phase Flow 128

8. Boundary Layer Gas Composition Control in Piping 129
9. Turbulent Modeling in Two Phase Boundary Layer Flow 130
10. Laser Doppler Velocimeter Measurements of the Two-Phase Flows in Curved Ducts 131
11. Modeling of Turbulent Two Phase Flow in a Curved Channel 133

Research Plans for Calendar Year 1981 133
1980 Publications and Reports 134

b. In-Situ Investigation of Gas-Solid Reactions by Electron Microscopy
James W. Evans, Investigator

1. Ex-Situ Studies of the Reduction of NiO Crystals 136
2. In-Situ Studies 137

Research Plans for Calendar Year 1981 137
1980 Publications and Reports 137

B. Solid State Physics
1. Experimental Solid-State Physics

a. Far-Infrared Spectroscopy
Paul L. Richards, Investigator

1. Infrared Spectra of $NbSe_3$ in the Charge Density Wave State 139
2. Electrons on the Surface of Liquid Helium 140
3. Infrared Emission Spectroscopy of Surfaces 141
4. New Types of Near-Millimeter Wave Filters 142

Research Plans for Calendar Year 1981 143
1980 Publications and Reports 144

b. Experimental Solid-State Physics and Quantum Electronics
Y. Ron Shen, Investigator

1. Surface Enhanced Second Harmonic Generation 146
2. Local Refractive Index Measurement on a Cholesteric Liquid Crystal Using the Surface Plasmon Technique 147
3. Surface Nonlinear Optics 149
4. Two-Phonon Coherent Anti-Stokes Raman Scattering 152
5. Nonlinear Spectroscopy by Multiresonant Four-Wave Mixing 152
6. Experiment on Multi-Resonant Four-Wave Mixing 153
7. Laser Interaction with Molecular Beams 155

Research Plans for Calendar Year 1981 155
1980 Publications and Reports 156

c. Excited Quantum Fluids in Solids
Carson D. Jeffries, Investigator

1. Free Excitons in Ge: A New Outlook 158
2. Enhancement Factor for the Strain-Confined Electron Hole Liquid 160
3. Studies of Defects in Ge by Ultra-Sensitive Spin Resonance Techniques 162
4. Development of an Ultrasensitive IR Detector 163

Research Plans for Calendar Year 1981 163
1980 Publications and Reports 163

d. Superconductivity, Superconductivity Devices, and 1/f Noise
John Clarke, Investigator

1. Quantum Noise in Josephson Junctions and DC Squids: Theory 165
2. Quantum Noise in Josephson Junctions and DC Squids: Experiment 166
3. Measurement of the Charge-Imbalance Relaxation Rate in the Presence of a Pair-Breaking Super-Current in Dirty, Superconducting Al Films 168

4. A New Method for Determining Regional Strike in Magnetotellurics 170

Research Plans for Calendar Year 1981 171
1980 Publications and Reports 172

2. Theoretical Solid-State Physics

a. Theoretical Studies of the Electronic Properties of Solid Surfaces
Leo Falicov, Investigator

1. Electronic Properties of Complex Impurities in Ultrapure Germanium 174
2. Theoretical Study of Lithium Intercalation in Transition-Metal Dichalcogenides 175
3. Photoemission Properties at the Surface of Transition Metals 175

Research Plans for Calendar Year 1981 176
1980 Publications and Reports 176

b. Theoretical Solid-State Physics
Marvin L. Cohen, Investigator

1. Pseudopotential Techniques 178
2. Solid Surfaces and Interfaces 178
3. Electronic Structure 179
4. Total Energy Calculations 179
5. Demons and Superconductivity 180

Research Plans for Calendar Year 1981 181
1980 Publications and Reports 181

C. Materials Chemistry
1. Chemical Structure

a. Low-Temperature Properties of Materials
Norman E. Phillips, Investigator

1. Calorimetric Investigation of Spin-Glass Ordering in Cu Mn 183
2. Heat Capacity of Cu Mn Spin Glasses in High Magnetic Fields 184

Research Plans for Calendar Year 1981 186

b. Electrochemical Processes
Charles W. Tobias, Investigator

1. Gas-Electrode-Electrolyte Interfaces; Resistance of Bubble Layers 187
2. High Rate Electrolysis Processes - The Effect of Suspended Inert Particles on Limiting Currents to a Rotating Disk 188

Research Plans for Calendar Year 1981 190
1980 Publications and Reports 191

2. High Temperature and Surface Chemistry

a. High-Temperature Thermodynamics
Leo Brewer, Investigator

1. Unusual High-Temperature Properties of Transition Metals 192
2. Phase Boundaries of the Hexagonal, Close-Packed Phases of the Co-Mo System 193
3. Use of Nitride Dissociation Pressures to Characterize Stability of Acid-Base Intermetallic Phases 193

Research Plans for Calendar Year 1981 194
1980 Publications and Reports 194

b. Chemistry and Materials Problems in Energy Production Technologies
Donald R. Olander, Investigator

1. Thermal-Gradient Migration of Brine Inclusions in Salt 195
2. Tracer Surface Diffusion on UO_2 196
3. Point Defects in Uranium Dioxide 197
4. Stress Corrosion Cracking of Zircaloy by Metal Iodides and Cadmium 198
5. Release of Water Vapor from Uranium Dioxide 200

Research Plans for Calendar Year 1981 202
1980 Publications and Reports 202

c. Plasma-Enhanced Deposition of Thin Films
Dennis W. Hess, Investigator

1. Plasma Enhanced Deposition of Iron/Iron Oxide Films 203

Research Plans for Calendar Year 1981 204
1980 Publications and Reports 204

d. Electrochemical Phase Boundaries
Rolf H. Muller, Investigator

1. Expanding Capabilities of the Automatic Ellipsometer 205
2. Laser Velocimetry for Boundary Layer Measurements 205
3. Optimum Angle of Incidence for Monochromatic Interface in Transparent Films on Absorbing Substrates 206

Research Plans for Calendar Year 1981 207
1980 Publications and Reports 207

e. Solid-State and Surface Reactions
Gabor A. Somorjai, Investigator

Surface Structure and Chemisorption by Low Energy Electron Diffraction

1. The Surface Structure of Ethylene and Acetylene on the Rh(111) Crystal Face 208
2. Leed Studies of Hydrocarbons Adsorbed on Platinum 208
3. Leed, AES, and TDS Studies of CO and K on Pt(111) Surfaces 208
4. Ag Monolayers on Pt Single Crystal Surfaces: A Study of Their Growth and Their Influence on the Chemisorptive Properties of Pt Single Crystals 209
5. Digital Leed Project 209
6. Reliability Factors in Surface Crystallography by Leed 209

Electron Spectroscopy Studies of Solid Surfaces and Adsorbates

7. Evidence for an Oxygen Intermediate in the Catalytic Reduction of NO by CO on Rhodium Surfaces 209
8. The Chemisorption of Propylene on Pt(111) Studied by High Resolution Electron Energy Loss Spectroscopy 210
9. Auger Electron Spectroscopy Studies of the Surface Composition of the Iron/Iron-Oxide/Oxygen System 210

Molecular Beam-Surface Interactions

10. The Velocity Distributions of NO and NH_3 Scattered from Pt(111) 210
11. Modulated Molecular Beam Scattering of CO and NO from Pt(111) and Pt(557) Surfaces 211

Studies of Catalyzed Surface Reactions

12. The Structure Sensitivity of n-Heptane Dehydrocyclization and Hydrogenolysis Catalyzed by Platinum Single Crystals at Atmospheric Pressure 211

13. Deuterium Isotope Effect and Exchange Reaction Studies During Hydrocarbon Conversion Over Platinum Single Crystal Surfaces 211
14. A New Radiotracer Technique for General Surface Studies: Application to ^{14}C-Benzene Chemisorption on Pt(111) 212
15. Transient Response Techniques for Studying the Chemistry of Carbon Deposits on Metal Catalyst Surfaces 212
16. The Enhanced Reactivity of Ordered Metal Layers on Single Crystal Surfaces of Other Metals: Au On Pt(100), and Pt on Au(100) 212

Research Plans for Calendar Year 1981 213
1980 Publications and Reports 213

f. Nuclear Magnetic Resonance
Alexander Pines, Investigator

1. Effects of Temperature, Viscosity and Solvent on the Magnetic Isotope Effect 217
2. Theory of Selective Excitation on N-Quantum Transitions 217
3. Statistical Theory of Multiple Quantum Transitions 218
4. Molecular Conformation in Liquid Crystals 218
5. Correlated Motion of Methyl Groups 219
6. Aliphatic Chain Configuration in Oriented Molecules 219
7. Relaxation of Multiple Quantum Transitions by Paramagnetic Impurities 220
8. High Resolution NMR in Inhomogeneous Fields 220
9. Noise in Two-Dimensional Spectroscopy 221
10. Analysis of Dipolar Couplings by Separated Local Fields 221
11. Computer Simulations of Multiple Quantum NMR 222
12. Molecular Motion in Hexamethylbenzene 222
13. Spin Diffusion in Deuteron Spin Lattice Relaxation 223

Research Plans for Calendar Year 1981 224
1980 Publications and Reports 224

II. CHEMICAL SCIENCES
A. Fundamental Interactions
1. Photochemical and Radiation Sciences

a. Photon-Assisted Surface Reactions, Materials and Mechanisms
Gabor A. Somorjai, Investigator

1. The Photocatalyzed Dissociation of H_2O at High Temperatures and Pressures Over $SrTiO_3$ Crystal 229
2. Photoelectron Spectroscopy Studies of the Mechanism of Photon-Assisted Dissociation of Water Over $SrTiO_3$ Surfaces 229
3. Isotope Exchange Studies of the Oxidation and Reduction of $SrTiO_3$ Single Crystal Surfaces by Water and Hydrogen 229
4. UPS Study of the Adsorption of Oxygen on Reduced $SrTiO_3$ Surfaces 229

Research Plans for Calendar Year 1981 230
1980 Publications and Reports 230

b. Photochemistry of Materials in the Stratosphere
H. S. Johnston, Investigator

1. Kinetics of the Reaction of HO and $HOONO_2$ 231
2. The Kinetics and Product Yield of the Reaction of HO With HNO_3 233
3. Reaction Rates of Atomic Chlorine With ClNO and $ClNO_2$ 235
4. The Rate of Reaction of Atomic Chlorine with Nitric Acid 236

Research Plans for Calendar Year 1981 236
1980 Publications and Reports 237

2. Chemical Physics

a. Energy Transfer and Structural Studies of Molecules on Surfaces
Charlee B. Harris, Investigator

1. Electronic Energy Transfer to Metal Surfaces: A Test of Image Dipole Theory at Short Distances . . . 238
2. Optical Properties of Molecules Chemisorbed on the Ni(111) Surface . . . 239
3. Inhomogeneous Broadening of Liquid Vibrational Linewidths Revealed by Selective, Coherent Pico-Second Stokes Scattering . . . 240
4. The Origin of Homogeneous Broadening of Molecular Vibrations in Liquids and Solids . . . 242

Research Plans for Calendar Year 1981 . . . 242
1980 Publications and Reports . . . 242

b. Molecular Beam Spectroscopy
John S. Winn, Investigator

1. Bonding Trends in Weakly-Bound Molecules . . . 244
2. Laser-Assisted Penning Ionization . . . 245
3. Production of Thin Metal Films From Metal Carbonyl Dissociation . . . 245
4. Implications of the Virial Theorem on the Description of Weak Bonding . . . 246

Research Plans for Calendar Year 1981 . . . 247
1980 Publications and Reports . . . 247

c. Selective Photochemistry
C. Bradley Moore, Investigator

1. Overtone Spectra of Gaseous Alkanes and Alkenes . . . 248
2. Vibrational Relaxation Dynamics of HCl in Rare Gas Matrices . . . 249
3. Vibrational Relaxation of D_2O (ν_2) . . . 250
4. Kinetics of Formation of DNA Crosslinks by 4'-Aminomethyl-4,5', 8-Trimethylpsoralen . . . 252

Research Plans for Calendar Year 1981 . . . 253
1980 Publications and Reports . . . 253

d. Physical Chemistry with Emphasis on Thermodynamic Properties
Kenneth S. Pitzer, Investigator

1. Relativistic Effects on covalent Bonding for Heavy Atoms as Exemplified in TlH . . . 255
2. Electronic Structure and Dissociation Curves for the Ground States of Tl_2 and Tl_2^+ from Relativistic Effective Potential Calculations . . . 256
3. Phase Equilibria for Highly Unsymmetrical Plasmas and Electrolytes . . . 258
4. Dissociation Energies of Molecules with Very Heavy Atoms from Mass Spectrometry . . . 260

Research Plans for Calendar Year 1981 . . . 261
1980 Publications and Reports . . . 261

e. Chemical Dynamics Studies
Bruce H. Mahan, Yuan T. Lee, and John S. Winn, Investigators

1. Optical Spectrum and Radiative Lifetime of Singlet CH^+ . . . 262
2. Internal State Distribution of Electron Impact Ionized CO^+ . . . 263
3. Collisional Heating of Rotational States of N_2^+ . . . 263
4. Electronic State Composition of Ion Beams . . . 264

Research Plans for Calendar Year 1981 . . . 266
1980 Publications and Reports . . . 266

f. Theory of Low-Energy Atomic and Molecular Collision Processes
William H. Miller, Investigator

1. Collision Induced Absorption Spectra for Gas Phase Chemical Reactions in a High Power IR Laser Field 267
2. Classical Model for Laser-Induced Electronically Non-Adiabatic Collision Processes 267
3. Reaction Path Model for Tunneling in the NHC → HCN Unimolecular Isomerization 268
4. Model Studies of Mode-Specificity in Unimolecular Reaction Dynamics 268
5. Further Development of the Reaction Path Formulation of Polyatomic Reaction Dynamics 269

Research Plans for Calendar Year 1981 269
1980 Publications and Reports 269

g. Photoelectron Spectroscopy
David A. Shirley, Investigator

Overview of Surface Science Research

1. Fourier-Transform Analysis of Normal Photoelectron Diffraction Data for Surface-Structure Determination 271
2. Normal Photoelectron Diffraction of c(2x2)O(1s)-Ni(001) and c(2x2)S(2p)-Ni(001), with Fourier Transform Analysis 273
3. Temperature Dependence of Normal Emission Photoelectron Diffraction and Analogies with EXAFS 274
4. Structural Determination of Molecular Overlayer Systems with Normal Emission Photoelectron Diffraction: c(2x2)CO-Ni(001) and $(\sqrt{3} \times \sqrt{3})R30^{\circ}$ CO-Ni(111) 276
5. Substrate-Dependent C(1s) Shape Resonance in CO Overlayers on Ni(111) and Ni(001) 278
6. K-Edge Structure and EXAFS on Sulfur in Various Coals 280
7. Particle Size Induced Valence Changes in Samarium Clusters 283
8. Development of a Monochromatic Light Source in the 800-1500 eV Range 285

Overview of Gas-Phase Research

9. Photoelectron and Auger Electron Angular Distributions: Alignment of $Xe^{+}(^{2}D_{5/2})$ 285
10. Photoionization Mass Spectrometry of Ne_2 and of He Clusters 287
11. New High Resolution Photoelectron Spectrometer 289
12. Photoelectron Angular Distributions of Small Molecules 291

Research Plans for Calendar Year 1981 293
1980 Publications and Reports 293

h. Crossed Molecular Beams
Y. T. Lee, Investigator

1. Primary Product Identification and Dynamics of $O + C_2H_4$ 295
2. Reaction Dynamics of) + Acetylene 296
3. Vibrational Effects in Proton and Charge Transfer in the H_2^{+} + Ar System 297
4. Comparison of Vibrational Energy Effects on the Reactions of D_2^{+} with H_2 and H_2^{+} with D_2 299
5. Interaction Potentials for $Br(^{2}p$ + Ar, Kr, $Xe(^{1}S)$ 300
6. On the Photodissociation of Nitromethane at 266 nm 301
7. Measurement of Singlet-Triplet Splitting of CH_2 303
8. Dynamics of Endothermic Reactions X + YR → XY + R 304
9. State Distribution of Photodissociation Products of O_3 304
10. Molecular Beam Studies of the F + HD Reaction 306

Research Plans for Calendar Year 1981 307
1980 Publications and Reports 307

i. Potential Energy Surfaces for Chemical Reactions
Henry F. Schaefer III, Investigator

1. The Prototype Aluminum-Carbon Single, Double and Triple Bonds: $Al\text{-}CH_3$, $Al{=}CH_2$, and $Al{\equiv}CH$ 310
2. A Possible Role for Triplet H_2CN^+ Isomers in the Formation of HCN and HNC in Interstellar Clouds 311
3. Electronic Structure of the N_4^+ Molecular Ion 312
4. Geometry and Electronic Structure of $(CO)_3\ NiCH_2$, a Model Transition Metal Carbene 313
5. Mechanism of the $H + O_3$ Reaction 314
6. Large Multiconfiguration Self-Consistent-Field Wavefunctions for the Ozone Molecule 316
7. Theoretical Challenge to the Experimentally Determined Geometrical Structure of Dimethylsilaethylene 316

Research Plans for Calendar Year 1981 318
1980 Publications and Reports 318

j. Picosecond Laser Excitation of Chemical Reactions
John H. Clark, Investigator

1. A Systematic Study of Excited-State Proton Transfer in Naphthols and Sulfonated Naphthols 321
2. The Kinetics of Quenching of Electronically Excited States by Solvated Protons 324

Research Plans for Calendar Year 1981 325
1980 Publications and Reports 325

3. Atomic Physics

a. Atomic Physics
Richard Marrus, Investigator

1. Electron Capture by Trapped Ne^{10+} at Very Low Energies 326
2. New Observation of Parity Nonconservation in Atomic Thallium 328
3. Vacuum Spark Source for Trapped Metal Ions 330
4. Initial Tests of Possible Second Born-Induced Asymmetry in Forward Electron Ejection by Fast Bare Nuclei 331

Research Plans for Calendar Year 1981 333
1980 Publications and Reports 333

B. Processes and Techniques
1. Chemical Energy

a. Formation of Oxides of Sulfur from SO_2
Robert E. Connick, Investigator

1. Oxidation of Bisulfite Ion by Oxygen 334
2. The Oxidation of Bisulfite Ion by Oxygen 334

Research Plans for Calendar Year 1981 335
1980 Publications and Reports 335

b. Conversion of Coal to Clean Liquid and Gaseous Fuels
Gabor A. Somorjai and Alexis T. Bell, Investigators

1. Hydrogenation of CO Over Rhodium Oxide Catalysts 336
2. The Construction of a High Pressure Wheels Apparatus for Studies of Reaction Intermediates 336
3. Effects of Metal-Support Interactions on the Synthesis of Methanol Over Palladium 336
4. The Mechanism and Kinetics of Hydrocarbon Synthesis Over Ruthenium 337
5. The Influence of Potassium Promotion on Fischer-Tropsch Synthesis Over Iron 338

6. Participation of Molecular H_2 in the Hydrogenolysis of Coal-Related Model Compounds by Zinc Chloride 338
7. Effects of Lewis Acid Catalysts on the Hydrogenation and Cracking of Aromatic and Hydroaromatic Structures Related to Coal† 340

Research Plans for Calendar Year 1981 340
1980 Publications and Reports 340

c. Organometallic Chemistry of Coal Conversion
K. Peter Vollhardt, Investigator

1. Biscarbyne Cobalt Clusters as Homogeneous Analogs of Fischer-Tropsch Intermediates on Surfaces 343
2. Synthesis and Reactivity of Homogeneous Analogs of Polystyrene-Bound Cyclopentadienyl cobalt dicarbonyl† 343

Research Plans for Calendar Year 1981 344
1980 Publications and Reports 344

d. Synthetic and Physical Chemistry
William L. Jolly, Investigator

1. On Correlating Phosphorus Core Binding Energies, Phosphorus Lone Pair Ionization Potentials, and Proton Affinities of Tervalent Phosphorus Compounds 347
2. Electronic Interaction of Ligands with Carbonyl Groups in Transition-Metal Complexes of the Types $LMn(CO)_5$ and $LMo(CO)_5$ 348
3. A Table of Absolute Core-Electron Binding-Energies for Gaseous Atoms and Molecules 348

Research Plans for Calendar Year 1981 349
1980 Publications and Reports 349

e. Chemistry and Morphology of Coal Liquefaction
Alexis T. Bell, Robert G. Bergman, James W. Evans, Heinz Heinemann, Alan V. Levy, Gabor A. Somorjai, and K. Peter Vollhardt, Investigators
(See Fossil Energy section)

f. Electrochemical Systems
John Newman, Investigator

1. Mass Transfer to Rotating Disks and Rotating Rings in Laminar, Transition, and Fully Developed Turbulent Flow 350
2. Theoretical Analysis of Liquid-Junction Photovoltaic Cells 352

Research Plans for Calendar Year 1981 352
1980 Publications and Reports 352

g. Metal-Cluster, Metal-Surface Analogy
Earl L. Muetterties, Investigator

1. Chemical and Structural Features of Chemisorbed Species on Metallic Surfaces 353

Research Plans for Calendar Year 1981 353
1980 Publications and Reports 354

h. High-Energy Oxidizers and Delocalized-Electron Solids
Neil Bartlett, Investigator

1. The Electrical Conductance of Graphite-AsF_5 Intercalation Compounds and Their Relationship to Other Graphite-MF_6 Salt Conductances 355
2. Thermodynamic and Structural Studies of $(GeF_5)_n^{n-}$ and GeF_6^{2-} Salts 358

3. The Relationship of Graphite Fluorosulfates to Relatives Containing Flourosulfuric Acid 360
4. Work in Progress 361

Research Plans for Calendar Year 1981 362
1980 Publications and Reports 362

i. Analysis of Transplutonium Elements in Dilute Solution
Steven D. Brown, Investigator

1. Separation of Overlapped Voltammetric Peaks by Recursive Digital Filtering 364
2. Noise Processes in Electrochemistry 364
3. Work in Progress 365

Research Plans for Calendar Year 1981 365
1980 Publications and Reports 365

j. Transition Metal Catalyzed Conversion of CO, NO, H_2, and Organic Molecules to Fuels and Petrochemicals
Robert G. Bergman, Investigator

1. The Mechanism of Aldehyde Formation in the Reaction of a Molybdenum Alkyls 366
2. Observation of Chemically Induced Dynamic Nuclear Polarization During Hydrogenolysis of a Cobalt Alkylidyne Cluster Complex 367
3. Phosphine Substitution in η^5-Cyclopentadienyl-Bis-Triphenylphosphinecobalt. Evidence for a Dissociative Mechanism 368
4. Mechanism of Hydrogenolysis of Dialkylcobalt Complexes: Evidence for an Autocatalytic Mechanism Involving a Metal Hydride/Metal Alkyl Reaction as a Critical Step 369
5. Intermolecular Cyclopentadienyl Ligand Exchange Between Metal Atoms in Organocobalt Complexes 371

Research Plans for Calendar Year 1981 372
1980 Publications and Reports 372

2. Chemical Engineering Sciences

a. High-Pressure Phase Equilibria in Hydrocarbon-Water (Brine) Systems
John M. Prausnitz, Investigator

1. High-Pressure Phase Equilibria for Methane-Water (Brine) 375
2. Modifications of Generalized Van Der Waals Theory for Mixtures 376
3. Calculation of Fluid-Phase Equilibria from Equations of State 377

Research Plans for Calendar Year 1981 378
1980 Publications and Reports 378

III. NUCLEAR SCIENCES
A. Low-Energy Nuclear Sciences
1. Heavy Element Chemistry

a. Actinide Chemistry
Norman M. Edelstein, Richard A. Andersen, Neil Bartlett, John G. Conway, Kenneth N. Raymond, Glenn T. Seaborg, Andrew Streitwieser, Jr., David H. Templeton, and Alan Zalkin, Investigators

Specific Sequestering Agents for the Actinides

1. Synthesis of and ^{238}Pu(IV) Removal from Mice by Carboxylate Catechoyl Amides 381
2. The Oxidation of Uranium(IV) by N-Phenylbenzo-Hydroxamic Acid and the Structure of the Reaction Product: Chlorodioxo-N-Phenylbenzo-Hydroxamato-Bis(Tetrahydrofuran) Uranium(IV) 386
3. Sulfonated Catecholamide Analogues of Enterobactin 387

Synthetic and Structural Studies of Actinides and Other Compounds

4. Pentamethylcyclopentadienyl Derivatives of the Trivalent Lanthanide Elements (Neodymium, Samarium, and Ytterbium) 389
5. Alkyl and Hydride Bis(Trimethylsilyl)Amido Derivatives of the Actinide Elements; Preparation and Hydrogen-Deuterium Exchange 389
6. Actinide-Carbon Bonds: Insertion Reactions of Carbon Monoxide, Tert-Butylisocyanide, and Tert-Butylcyanide into $[(Me_3Si)_2N]_2\overline{MCH_2Si(Me)_2NSiMe_3}$ 390
7. Divalent Lanthanide Chemistry; Bis(Penta-Methylcyclopentadienyl) Europium(II) and Ytterbium(II) Derivatives: Crystal Structure of Bis(Pentamethylcyclopentadienyl)Ytterbium(II) Tetrahydrofuran Hemi (Toluene) at 176 K 391
8. Crystal and Molecular Structure of Hydridotris[Bis(Trimethylsilyl) Amido]Uranium(IV) 392
9. Divalent Lanthanide Chemistry; Preparation of Some Four and Six Coordinate Bis(Trimethylsilyl-Amido) Complexes of Europium(II). The Crystal Structure of Bis[Di(Trimethylsilyl)Amido]Bis(1,2-Dimethoxyethane)Europium(II) 393
10. Preparation and Crystal Structure of the 1,2-Dimethoxyethane Complex of Bis[Di(Trimethylsilyl)Amido]Dichlorouranium(IV) 395
11. Bonding in Metal-Borohydride Complexes 395
12. 1,4- and 1,6-Di-Tert-Butylcyclooctatetraenes 397
13. Bis-π-(Cyclobutenocyclooctatetraene) Uranium(IV) 398

Physical and Spectroscopic Studies

14. Optical Spectra and Zeeman Effect for Er^{3+} in $LuPO_4$ and $HfSiO_4$ 400
15. Vibrational Spectra and Normal Coordinate Analysis of Neptunium (IV) Borohydride and Neptunium (IV) Borodeuteride 401
16. Electronic Solution Spectra for Uranium and Neptunium in Oxidation States (III) to (VI) in Anhydrous Hydrogen Fluoride 403
17. Electron Paramagnetic Resonance Spectra of Er(III), Dy(III), and Gd(III) in Yttrium and Lanthanum Hydrides 404
18. Spectrum and Energy Levels of Pr^{3+} in $ThBr_4$ 406

Research Plans for Calendar Year 1981 406
1980 Publications and Reports 407

IV. FOSSIL ENERGY

a. Electrode Surface Chemistry
Philip N. Ross, Investigator

1. Oxygen Adsorption on Pt Intermetallic Surfaces 413
2. The Kinetics of the O_2/CO_2 Reaction in Molten Carbonate: Reaction Orders for O_2 and CO_2 on NiO 413

Research Plans for Calendar Year 1981 414
1980 Publications and Reports 414

b. Deuterium Analysis of Coal by NMR
Alexander Pines, Investigator

1. Cylindrical Sample Turbine for Magic Angle NMR 415
2. Deuterium Spin-Lattice Relaxation in Magic Angle Spinning 415
3. Proton-Deuterium Cross Polarization in Rotating Solids 416
4. Double Quantum NMR in Solids 417
5. Carbon-13 NMR of Whole and Processed Coals 417
6. Synthesis of Isotopically Labeled Molecules and Liquid and Solid Crystals . . . 418
7. Symmetry of Motional Molecular Jumps in Solids 418

Research Plans for Calendar Year 1981 419
1980 Publications and Reports 419

c. Oil Shale Retort Components
Alan V. Levy, Investigator

1. Corrosion in Simulated In-Situ Oil Shale Retorts 421
2. Corrosion in Laboratory Crucible Tests 422
3. Aluminide Coatings for Ferrous Alloys 423
4. Laser Modification of Coatings and Alloys 424

Research Plans for Calendar Year 1981 425
1980 Publications and Reports 425

d. Chemistry and Morphology of Coal Liquefaction
Alexis T. Bell, Robert G. Bergman, James W. Evans, Heinz Heineman, Alan V. Levy, Gabor A. Somorjai, and K. Peter Vollhardt, Investigators

1. Selective Synthesis of Gasoline Range Components from CO and H_2 427
2. Electron Microscope Studies of Coal During Hydrogenation 428
3. Catalyzed Low Temperature Hydrogenation of Coal 430
4. Selective Hydrogenation, Hydrogenolysis, and Alkylation of Coal and Coal Derived Liquids by Organometallic Systems 430
5. Chemistry of Coal Solubilization and Liquefaction Pyrolysis Studies 432

Research Plans for Calendar Year 1981 435
1980 Publications and Reports 436

e. Coal Liquefaction Alloys Test Program
Alan V. Levy, Investigator

1. Erosion Behavior of Alloys in Coal Slurry Pot Tests 438
2. Jet Impingement Tester 439

Research Plans for Calendar Year 1981 440
1980 Publications and Reports 440

f. Materials Characterization in Fossil Fuel Combustion Products
David P. Whittle, Donald H. Boone and Alan V. Levy, Investigators

1. Substrate Effects on Coating Protection 441
2. Characterization of Thermal Barrier Ceramic Coatings 442
3. Effect of Coating Processing and Structure on Oxide Formation and Protectiveness 443
4. Raman and IR Spectroscopy Characterization of Oxide Coatings 445

Research Plans for Calendar Year 1981 446
1980 Publications and Reports 446

g. Solution Thermodynamics of Sulfites and Sulfite Oxidation Mechanisms
Leo Brewer and Robert E. Connick, Investigators

1. Thermodynamic Data for Flue-Gas Desulfurization Processes 447
2. The Oxidation of Bisulfite Ion by Oxygen 447

Research Plans for Calendar Year 1981 448
1980 Publications and Reports 448

h. Process Chemical Parameters in Aqueous Sulfur Dioxide Removal by Lime/Limestone Scrubbers
Robert E. Connick, Investigator

1. Raman Spectroscopic Determination of Aqueous Sulfur Oxyanions 450
2. The Decomposition of Ammonia-Sulfur Dioxide Solutions 450
3. Thermal Decomposition of Sulfite 450
4. Thermal Decomposition of Thiosulfate 451
5. The Reaction of Sulfite with Formaldehyde 451
6. Chemistry of Waste Sulfur Utilization 451

Research Plans for Calendar Year 1981 451
1980 Publications and Reports 451

i. Coal Liquefaction Research
Heinz Heinemann, Investigator

1. Fixed Bed and Suspension Bed Fischer-Tropsch Reaction 453

Research Plans for Calendar Year 1981 453
1980 Publications and Reports 453

V. ADVANCED ISOTOPE SEPARATION TECHNOLOGY

a. Isotope Separation by Laser Photochemistry
C. Bradley Moore, Investigator

1. Laser Pyrolysis of Tetralin 457
2. Quenching, Electronic Energy Transfer and Rotational Relaxation of S_1 Formaldehyde 458

Research Plans for Calendar Year 1981 460
1980 Publications and Reports 461

b. Molecular Beam Laser Isotope Separation
Yuan T. Lee and Y. Ron Shen, Investigators

1. Photofragmentation Translational Spectroscopy of Br_2 462
2. Photodissociation of Bromine Dimers 463
3. Vibrational Predissociation Spectra of Molecular Dimers 463
4. Reactive Scattering of CF_3I + Br, Vibrational Effects 465
5. Dynamics of Vibrational Predissociation of Van der Waals Molecules 465

Research Plans for Calendar Year 1981 467
1980 Publications and Reports 467

VI. ENERGY STORAGE

a. Development of Electrochemical Synthesis and Energy Storage
James W. Evans, Rolf H. Muller, John Newman, Philip N. Ross, and Charles W. Tobias, Investigators

1. Ellipsometric Studies of Lithium in Propylene Carbonate Solutions 471
2. Transient Electrochemical Measurements on Lithium in Propylene Carbonate Solutions 472
3. Microstructural Development During Mass Transfer Controlled Deposition 473
4. Effects of Hydrodynamic Flow on the Electrocrystallization of Zinc from Acid Electrolytes 475
5. Dynamic Modeling of Surface Profiles in Electrodeposition and Dissolution 475

Bifunctional Air Electrodes for Metal-Air Batteries

6. Oxygen Reduction with Carbon-Supported Metallic Cluster Catalysts in Alkaline Electrolyte 478
7. Rotating Ring-Disc Studies of Oxygen Reduction on Pt and Ag in Alkaline Electrolyte 479

Improvements in Efficiency of Aluminum Reduction Cells

8. Current Inefficiencies in Aluminum Reduction Cells 481

Electrochemical Properties of NASICON

9. Properties of NASICON 483

Analysis and Simulation of Electrochemical Systems

10. Mathematical Modeling of the Lithium-Aluminum, Iron Sulfide Battery 483
11. Metal Couples in Non-Aqueous Solvents 485

Research Plans for Calendar Year 1981 486
1980 Publications and Reports 486

b. Engineering Analysis of Gas Evolution in Electrolysis
Charles W. Tobias, Investigator

1. Gas Evolution in Forced Flow 489
2. Mass Transfer Studies with a Microsegmented Electrode 491

Research Plans for Calendar Year 1981 492
1980 Publications and Reports 492

VII. MAGNETIC FUSION ENERGY

a. Materials and Weldments for High Field Superconducting Magnets
John W. Morris, Jr., Investigator

1. Alloying Element Effect on the Cryogenic Mechanical Properties of 12Ni-0.25Ti Steel 497
2. Microstructural Refinement Mechanisms During the 2B Treatment of Fe-12Ni-0.25Ti Steel 497
3. A Study on the Weldability of Grain-Refined Fe-12Ni-0.25Ti Steel with Matching Ferritic Filler Metal 499

Research Plans for Calendar Year 1981 499
1980 Publications and Reports 500

VIII. NUCLEAR WASTE MANAGEMENT

a. Thermodynamic Properties of Chemical Species in Nuclear Waste
Norman M. Edelstein, Investigator

1. Determination of Trace Metal Complexation by Convolution Voltammetry 503
2. Studies of Copper and Neodymium Hydrolysis 504
3. Separation of Overlapped Peaks by Semidifferential Electroanalysis 504
4. Solubility of Americium Hydroxide in Neutral and Basic Solutions 505

Research Plans for Calendar Year 1981 507
1980 Publications and Reports 507

IX. OTHER PROJECTS

a. Solubilities of Heavy Hydrocarbons in Water
John M. Prausnitz, Investigator

1. Liquid-Liquid Phase Equilibria for Heavy Hydrocarbon-Water System 511

Research Plans for Calendar Year 1981 511
1980 Publications and Reports 511

b. High Strength Austenitic Alloys for Generator Retaining Rings
John W. Morris, Jr., Investigator

1. Ultra High Strength Precipitation-Hardened Austenitic Steels 513

1980 Publications and Reports 514

c. Investigation of New Fuel Cell Electrolyte and Electrode Concepts
Philip N. Ross, Investigator

1. Oxygen Reduction on Carbon-Supported Pt and Pd Intermetallic Cluster Catalysts in Acid Electrolyte 515
2. Oxygen Reduction Kinetics on Pt in Perfluoroalkyl Acid Electrolytes 517

Research Plans for Calendar Year 1981 518
1980 Publications and Reports 518

d. Improved Beta-Alumina Electrolytes for Advanced Storage Batteries
Lutgard C. De Jonghe, Investigator

1. Local Electrode Current Density and Flaw Decoration of Sodium-Beta" Alumina 519
2. Slow Degradation and Electron Conduction in Sodium-β Aluminas 520
3. Initiation of Degradation in Polycrystalline Sodium-Beta Alumina Electrolytes 522

Research Plans for Calendar Year 1981 523
1980 Publications and Reports 523

X. APPENDICES

Appendix A. Personnel

Scientific Staff 527
Support Staff 535

Appendix B. Materials and Molecular Research Division Committees 536

Appendix C. List of Seminars 537

Appendix D. Index of Investigators 541

* * *

General Introduction

In the MMRD annual report of last year Dave Shirley noted his intention to resign as Division Head. His long-standing plan was to spend a year in full-time research as a Miller Research Professor and then to return to his duties as a faculty member in the Chemistry Department and Investigator in MMRD. Things did not go according to plan. Andrew Sessler, having served seven and a half years as Director of the Lawrence Berkeley Laboratory, asked to be relieved of his duties. After a national search for a new director, Dave Shirley was appointed, effective April 1, 1981. I became Division Head April 15, 1981.

Dr. Shirley sacrificed considerable time from his formidable new job in order to inform and advise me on problems of managing MMRD. For this I am grateful, and I am particularly pleased that despite his heavy responsibilities as Director he has maintained his amazingly productive career as an Investigator in this Division. Conway Peterson, the Division Administrator, Rolf Muller, the Assistant Division Head, and the Division Administrative Staff have continued to discharge their responsibilities effectively and efficiently and have, in addition, been tactful teachers for me.

At the end of 1980 there were affiliated with MMRD 8 staff senior scientists; 53 faculty as faculty senior scientists or associated faculty, 83 staff scientists; 84 postdoctorals and other scientific personnel; 353 graduate students; and 91 technical, administrative, or clerical support staff--for a total of 672. During calender year 1980, 351 journal articles and LBL reports were published by members of MMRD, and 37 Ph.D. and 9 M.S. degrees were awarded to MMRD students.

In 1980 MMRD staff again garnered an impressive number of honors. A selected list appears below:

Neil Bartlett was awarded the medal of the Josef Stefan Institute of Ljubljiana, Yugoslavia.

Marvin Cohen was elected to the National Academy of Sciences.

Yuan Lee was asked to serve as the Falk-Plaut Lecturer at Columbia University; was made an Honorary Professor of the Institute of Chemistry of the Chinese Academy of Sciences, Beijing, China, and an Honorary Professor at Fudon University, Shanghai, China; and he was elected member of the Academia Sinica, Taipei, Taiwan, China.

John W. Morris, Jr. was judged by program managers for the Materials Sciences Programs at DOE national laboratories and in Washington DC to have completed materials science research at a national laboratory with the most significant implications for energy during the previous year.

Joseph Pask was awarded the Berkeley Citation by the University of California, Berkeley, for distinguished achievement and for notable service to the University. He was also given a medal of the Spanish Ceramic Society Foundation and membership in the Founders' Group of the Spanish Society for Ceramics and Glass, Madrid, Spain. In addition, he was awarded the 1979 Gold Medal and Certificate of the Societe de'Encouragement pour la Recherche et l'Invention, Paris, France.

John Prausnitz was chosen as faculty research lecturer for 1980-81 by his academic colleagues of the Berkeley faculty.

Kenneth Raymond was awarded a Guggenheim Fellowship.

Glenn Seaborg was made one of the University of California System's 12 University Professors--a title reserved for scholars of international distinction who are recognized and respected as teachers with exceptional ability.

Steve Shaffer was awarded first prize for his poster in the student category at the International Metallographic Exhibition in England.

Y. Ron Shen was made an honorary professor of the Institute of Physics, The Academy of Sciences, Beijing, China.

David A. Shirley was elected to the Academy of Arts and Sciences.

Gabor Somorjai was an invited scholar and received an Outstanding Scientist Award from the German Federal Republic. He was announced to be the 1981 recipient of the ACS award in Colloid or Surface Chemistry.

Gareth Thomas was awarded a Humboldt Fellowship for research in the German Federal Republic.

David Whittle was awarded a Doctor of Science from the University of Manchester.

The year 1980 brought many new scientific accomplishments. The partial list below gives some idea of the diversity of research at MMRD.

John Clarke and his associates made further progress on theoretical understanding and experimental development of superconducting quantum interference devices for use as supersensitive magnetometers and voltmeters. By reducing the areas of electrical junctions to less than 10^{-5} mm^2 they have achieved a sensitivity that lies within a factor of 2 of the theoretical limit set by the quantum mechanical uncertainty principle.

Marvin Cohen and his associates have used

pseudopotential theory to predict, with only the atomic number as an input parameter, the energy-volume phase diagrams for silicon and germanium. Predicted properties such as interatomic distances and cohesive energies differ from experimental values by little more than the uncertainty in experimental measurements.

Richard Marrus and his colleagues of the atomic physics group have been able to measure electron capture cross-sections as a function of ion velocity for Ne^{10+} ions (i.e., the ions produced by removing all the valence electrons from a neon atom) as a function of ion-kinetic energy. These data are of value to understanding energy loss mechanisms in fusion devices and astrophysical plasmas.

Several years ago, John W. Morris, Jr. and his coworkers showed that it was possible to achieve an outstanding combination of strength and toughness at 4 K in ferritic cryogenic steels. Now they have developed successful techniques for producing tough weldments of these steels that also remain ductile at 4 K. This opens the way to practical application of these cryogenic materials in superconducting magnet cases.

David Shirley and associates discovered and applied a new technique of normal photoelectron diffraction to study selenium and sulfur adsorbate structures on nickel surfaces. The ordered structures of Se on Ni showed photoelectron diffraction at low coverage for which no LEED pattern was obtained.

Gabor Somorjai and coworkers demonstrated that a monolayer of gold, which itself is not a catalyst for the dehydrogenation of cyclohexene, when present as a monolayer on a platinum surface increased the cyclohexane dehydrogenation rate by as much as a factor of 5 over the rate on a pure platinum surface.

MMRD suffered a serious setback in 1980 when we learned that some of the funds already allocated for the Chemical and Materials Sciences Laboratory (CMSL) in FY 1980 were withdrawn. As things stand in early 1981, the Atomic Resolution Microscope portion of the CMSL project will proceed, but the laboratory building appears unlikely to be funded before FY 1983. This delay constitutes a sad loss. We have made good progress in studies of surface science and related studies in coal chemistry and morphology and catalysis, but a centralized laboratory is badly needed to provide space to focus on these and other programs. On a brighter note, the National Electron Microscopy Center (NEMC) took tangible form as a new component of MMRD in 1980. Installation of the High Voltage (1.5 MeV) Electron Microscope was completed and its testing was well underway at the end of the year. Gareth Thomas, who has been the principal driving force in bringing the project to fruition, will serve as the Center Chairman; Kenneth Westmacott will be Manager of the High Voltage Electron Microscope (HVEM) facility; and Ronald Gronsky will be Manager of the Atomic Resolution Microscope (ARM) facility. The HVEM and ARM, which should become operational in 1982, will be made available free of charge upon approval of the scientific merits of a project by the Committee. Companies who wish to retain proprietary rights in processes studied with these instruments may do so upon arrangements to pay the full costs of the study.

Nine scientists--W. L. Bell (GE Vallecitos), D. G. Howitt (UC Davis), J. C. Spence (Arizona State), A. Taylor (ANL, Argonne), M. Simnad (General Atomic Company, San Diego), and R. M. Glaeser, R. Gronsky, G. Thomas, and K. H. Westmacott of LBL--have accepted my invitation to serve as members of the NEMC Steering Committee, with Dr. Simnad as Committee Chairman. The Committee had its first meeting in December 1980. They have approved approximately 27 proposals for studies with the HVEM. About half of the proposals are from LBL or the Berkeley campus, and the remainder from elsewhere.

Two new principal investigators joined MMRD in 1980. They are Professor Didier de Fontaine of the UC Berkeley Department of Materials Science and Mineral Engineering, and Professor Peter Yu of the Physics Department. Professor de Fontaine is a theoretical metallurgist; he will participate with the electron microscopists in coordinated theoretical and experimental studies of ordering and clustering phenomena. Professor Yu will use tunable dye lasers to study the behavior of semiconductors and superconductors. Professor Joseph Pask has reached retirement age at the University, but we hope to have him continue his association with MMRD. In fact, since his formal retirement he, together with Professor A. G. Evans, presided over one of three very successful conferences sponsored by MMRD in 1980, "Surfaces and Interfaces in Ceramic and Ceramic-Metal Systems," held July 28-30, 1980. The other conferences were the "First Berkeley Catalysis and Surface Science Conference," hosted by Dr. Heinz Heinemann and Professor Gabor Somorjai, held July 16-18, 1980, and the "Semi-Annual Bay Area High-Temperature Meeting," hosted by Professor Leo Brewer, held October 21, 1980.

The Annual Review of our 1980 programs was held on February 9-10, 1981. Professor M. E. Fine of Northwestern University served as Chairman of the Review Committee. Other members were: Professor R. L. Coble, Massachusetts Institute of Technology; Professor S. Liu, Iowa State University; Professor M. Boudart, Stanford University; Professor R. B. Bernstein, Columbia University; and Dr. H. W. Paxton of United States Steel. They reviewed approximately half of the programs of the Division. It is our intention to review each Division program approximately every other year.

MMRD is a remarkably vital and productive research organization. My predecessors--Kenneth Pitzer, Leo Brewer, and David Shirley--encouraged research studies that were not only individually strong but mutually interacting and stimulating. I will work to maintain the Division's momentum along the sound path that they laid out for us.

Alan W. Searcy
Division Head

A. Metallurgy and Ceramics

1. Structure of Materials

a. Atomic Resolution in Microscopy*

Ronald Gronsky and Gareth Thomas, Investigators

Introduction. Atomic resolution microscopy received funding as a line item this year at a level that established it as the largest project in transmission electron microscopy ever to be undertaken in the United States. Its objective is to study the structure and properties of materials directly at the atomic level by electron-optical imaging of individual atoms. To this end, a set of design specifications was issued by LBL earlier this year (see Fig. 1) for the Atomic Resolution Microscope (ARM), an instrument that will be capable of resolving atomic positions in close-packed structures with the further provision for variable voltage operation so as not to exclude imaging of radiation-sensitive materials. On July 24, 1980 the contract for the ARM was awarded to JEOL, USA, Inc., with shipment expected during August of 1982. When installed near MMRD Building 72, this instrument will become a shareable resource in LBL's National Facility for Electron Microscopy.

The first of the feeder instruments associated with the ARM, a JEM 200 CX, was installed in December 1980. Initial resolution tests have been highly successful (Fig. 2) and this instrument is currently being calibrated for high resolution operation to initiate the research programs in atomic resolution microscopy.

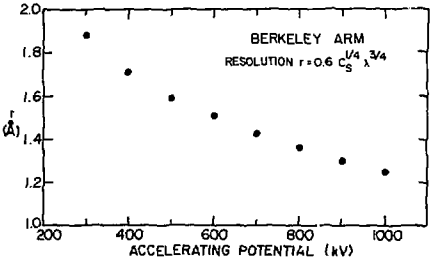

Fig. 1. Plot of theoretical resolution (r) as a function of accelerating potential for the atomic resolution microscope. Values are determined by maintaining a constant product of spherical aberration coefficient (C_s) and illumination wavelength (λ). (XBL 803-4822)

Fig. 2. First run resolution test from the JEM 200 CX. The image was taken in an axial illumination mode at 200 kV with a standard hairpin filament. The imaged periodicity represents the (004) spatial frequency (1.018 Å) in the evaporated Au specimen. (XBB 811-627)

To date, these programs include the study of coherent transformations with emphasis on incipient interfacial structure, the relationship between grain boundary structure and properties in metallic, ceramic and semiconductor materials, structural analysis of glass-like materials, and the theoretical analysis of the imaging capabilities of modern electron-optical systems.

Progress during the past year in a number of these areas is reported below.

1. HIGH RESOLUTION TRANSMISSION ELECTRON MICROSCOPY†

Ronald Gronsky

It has by now been well established that the spatial periodicities recorded in a high resolution transmission electron microscope are not always uniquely representative of the atomic structure of a specimen. This effect is due to the resolution limitations imposed by lens aberrations in the electron-optical case (as compared to illumination wavelength in the light-optical case). The purpose of this on-going program is to develop the necessary theoretical reference frame for accurate interpretation of atomic resolution images.

Computations have been performed to determine the form of the envelope functions describing the detrimental effects of partial coherence[1] in the electron course (E_α) which arise from a finite illumination aperture, α, and the effects (E_c) of chromatic aberration[2] due to fluctuations in voltage supply (ΔV), fluctuations in objective

* This work was supported by the Director, Office of Energy Research, Office of Basic Energy Sciences, Materials Sciences Division of the U. S. Department of Energy under Contract No. W-7405-ENG-48.

less current (ΔI) and energy spread (ΔE) or temporal coherence of the electron beam.

Using accepted forms[1,2] of these functions,

$$E_\alpha = \frac{2J_1(P)}{P}$$

$$E_c = \exp\left[-\frac{\pi^2\lambda^2}{2}\cdot C_c\, Q^2\mu^4\right]$$

where

$$P = \frac{2\pi}{\lambda}\,[C_s\lambda^3\mu^3 + \Delta Z\lambda\mu]$$

and

$$Q^2 = \left[\frac{\Delta V}{V}\right]^2 + \left[\frac{2\Delta I}{I}\right]^2 + \left[\frac{\Delta E}{E}\right]^2$$

typical plots of the envelope functions were generated as a function of the reciprocal space parameter μ, the electron wavelength λ, and the defocus (ΔZ) and aberration coefficients C_s, C_c of the objective lens (see Figs. 3 and 4). Comparisons with experimental results show some discrepancy with the form of E_α for pointed cathodes, using optical diffractogram analysis, but the agreement with E_c is very good.

* * *

†Excerpted in part from LBL-11243.

1. K.-J. Hanszen and R. Trepte, Optik 33, 166 (1971).
2. P. L. Fejes, *Acta Cryst* A33, 109 (1977).

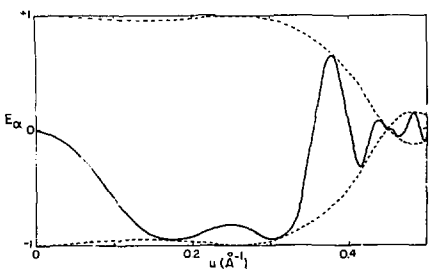

Fig. 3. Plot of the effect of the envelope function (dotted line) on the Scherzer defocus coherent transfer function (solid line) for a 100 kV electron microscope with C_s = 0.7 mm and $\alpha = 10^{-3}$ rad. (XBL 807-5500)

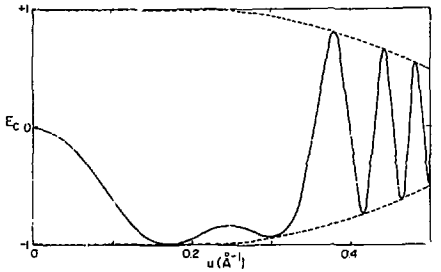

Fig. 4. Plot of the effect of the envelope function (dotted line) on the Scherzer defocus coherent transfer function (solid line) for 100 kV electron microscope with C_s = 0.7 mm and C_cQ = 50 Å. (XBL 807-5499)

2. GRAIN BOUNDARY STRUCTURE AND SEGREGATION IN Al ALLOYS†

Jose Briceño-Valero and Ronald Gronsky

Studies of grain boundary segregation in metallurgical systems are traditionally based upon the premise that grain boundaries are more likely sites for solute atoms than their surrounding grains. This idea is manifested in experimental studies which distinguish the solute concentration at boundaries from that of grain interiors using various spectroscopic techniques, including more recently, energy dispersive spectroscopy (EDS) of x rays in TEM/STEM instruments. The present program is concerned with an alternative study of grain boundary segregation where the distribution of solute atoms along the boundary plane (as opposed to that across the boundary plane) is sought. The interest here is to establish whether or not a relationship exists between the structural defect configuration of the boundary plane and the site preference for solute segregation.

Aluminum bicrystal specimens with controlled amounts of Zn dopant were prepared according to Fig. 5 and examined in a Philips EM 400 TEM/STEM equipped with LaB_6 gun. The electron probe size was 50 A at the specimen surface and spot readings were taken at intervals of a few hundred angstroms along boundaries of constant thickness.

Results of the study for a particular bicrystal are presented in Fig. 6, which shows the Zn/Al count rate ratio as a function of distance along the boundary plane. A relative change in Zn concentration of approximately 20% is evident at periodic intervals of approximately 4000 angstroms. Diffraction analysis of the bicrystals confirms that the adjacent grains are misoriented by a 58.73°

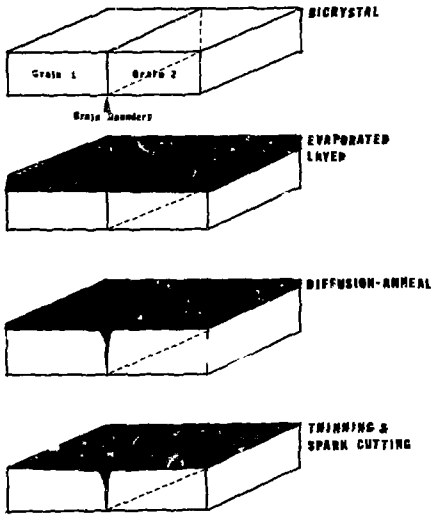

Fig. 5. Schematic of specimen preparation method. The Al bicrystal is first coated with an evaporated layer of solute, then subjected to a diffusion anneal. Foils are prepared from the edge-on doped boundary region after surface residue is removed. (XBL 802-8370)

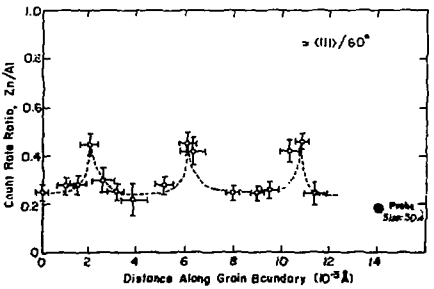

Fig. 6. Plot of composition variation (count rate ratio of Zn to Al) as a function of distance along a ⟨111⟩/60° coherent twin boundary. The periodicity of the segregation events is ~ 4000 Å. (XBL 802-8369)

rotation about the direction [-1.0 -1.28 1.11]. This is very close to a ⟨111⟩/60° CSL boundary which characterizes a coherent twin. It would not be unusual therefore to observe a 4000 Å periodicity in the defect structure for this highly ordered boundary. Subsequent results confirm however that even secondary relaxations in the boundary plane can be significant solute sites.

* * *

†Brief version of LBL-10683.

3. HIGH RESOLUTION STUDIES OF HIGH-RANK COALS†

John A. Little‡ and Ronald Gronsky

A study has been undertaken to characterize the microscopic constituents of coals at high levels of spatial resolution, not only for the purpose of identifying these constituents but also to determine their effects on various conversion (gasification or liquefaction) reactions. Particular attention has been paid to the maceral content of the coal, and even its basic carbon skeleton with associated functional groups, as well as the submicron sized mineral particles which are known to profoundly influence the rate of gasification reactions. For this phase of the research, higher-rank anthracites have been chosen, primarily to concentrate on the crystalline carbon regions of the microstructure.

Specimens were prepared by careful hand-grinding using diamond paste down to a thickness of approximately 5 to 10 μm, followed by ion beam milling to final perforation. Microscopy was performed in the axial illumination mode on a Siemens Elmiskop 102 equipped with high-angle-tilt goniometer stage.

As anticipated, the meta-anthracite specimens contained a large number of highly ordered regions similar to those shown in Fig. 7. At this level of resolution the true morphology of these regions was revealed however, and there were a number of interesting effects. Figure 7 clearly shows an undulation in the parallel lattice planes of carbon which are found to possess an average local spacing of 3.4 Å, corresponding to the (0002) basal planes in graphite. In some regions these graphitic planes were arranged in circular fashion at very small (10-15 Å) radii of curvature. It is thought that such structures may correspond to the carbon chains in the original plant materials which have now sufficiently metamorphosed so that most of the hetero-atoms and aromatic groupings have become part of the pure carbon meta-anthracite skeleton. To date there has been no high resolution evidence of either long or short range carbon ordering in anthracite specimens, which agrees with earlier observations.[1]

At the same level of resolution, the small mineral particles present in the anthracite specimens were found to have a very characteristic

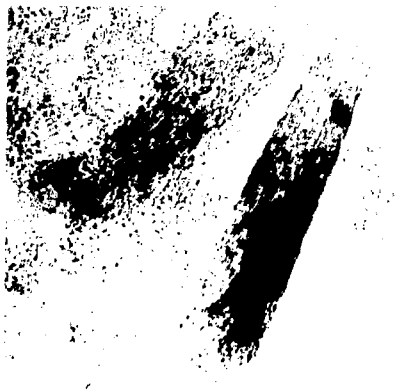

Fig. 7. High resolution image of ordered regions of the carbon skeleton in meta-anthracite. Lattice planes are spaced at 3.4 Å, corresponding to the (0002) planes of graphite. (XBB 805-5616)

morphology. A detailed version in Fig. 8 illustrates that the surfaces of the particle are highly crystallographic, with broad faces parallel to the imaged set of lattice planes. The truncated corner however, has a high density of ledges, most only one or two atom layers in height (arrowed), which maximize the surface area of the same imaged lattice planes. This finding indicates a possible microscopic origin for the catalytic activity of such particles in coal conversion reactions.

* * *

†Brief version of LBL-11612.
‡Now at Department of Metallurgy, University of Cambridge, Cambridge, England.

1. E. L. Evans, J. M. Jenkins and J. M. Thomas, Carbon 10, 637 (1972).

4. LATTICE IMAGING OF GLASSY CARBON

Ronald Gronsky, A. S. Rao,† and Robert H. Bragg

The morphology of glassy carbon as a function of heat treatment temperature has been closely examined in this research program by phase contrast lattice imaging using the transmission electron microscope. Specimens were ion milled from samples treated at 1800°C, 1900°C, 2200°C, 2500°C and 2700°C and viewed in a Siemens Elmiskop 102 operated at 100 kV. Images were recorded using axial illumination with no objective aperature, and subsequently examined by optical diffraction for their resolution content. Comparisons were then made between images recorded at identical camera lengths and objective lens focal settings (to ± 0.1 mA), with astigmatism corrected to within 60 Å.

The deficiencies of conventional imaging are revealed in Fig. 9, which is an axial dark field representation of a specimen treated at 2500°C. Bright regions in the micrograph (a) represent those areas scattering strongly at the aperture position circled in (b), and obviously reveal only a severely restricted sampling of the actual structure. The ring-like diffraction pattern indicates the isotropic character of this carbon specimen, and explains the origin of the designation "glassy."

Fig. 8. High resolution image of a mineral particle in anthracite. Two sets of lattice planes are revealed at ~ 3.6 Å spacing, but the exact composition of the particle is unknown. (XBB 811-628)

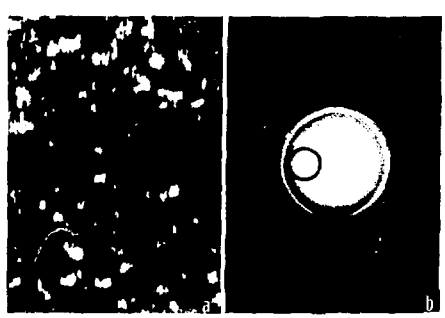

Fig. 9. Dark field (a) and selected area diffraction pattern (b) of glassy carbon treated at 2500°C. (XBB 800-12200)

By comparison, the through-focus high resolution images in Fig. 10 show that there is in fact a high degree of crystallinity in this specimen (2500°C) where the carbon atoms are arranged in interpenetrating fibrils. The change in focus between images (220 Å) is sufficient to reveal "optimum" imaging conditions (b).

A higher magnification version of the 2700°C specimen is shown in Fig. 11 at the same focal increments, with the optimum image in (b). Here the graphitic ribbons are clearly shown in a number of confluence configurations. At the center of each image is a 2π rotation disclination for example, with a very large degree of adjacent bending.

The results of this study demonstrate directly that the character and gross morphology of the stabilized polymer chains in glassy carbon are identical throughout the heat treatment range. The principal differences between these specimens are the density of fibrils and consequently, their local morphology, i.e., the nature of disclination atmospheres. A continuation of this study at higher resolution is planned for the purpose of modeling a three-dimensional reconstruction of the fibril stacking sequences.

* * *

+Now at Argonne National Laboratory, Materials Science Division, Argonne, Illinois 60439.

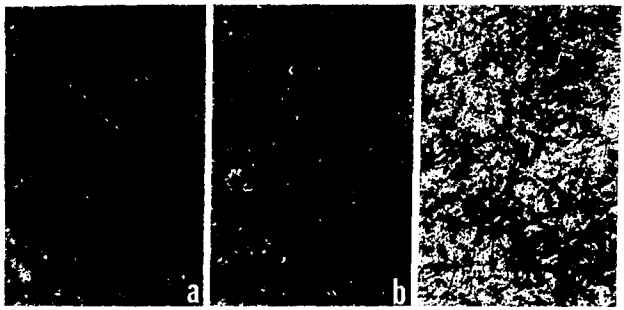

Fig. 10. High resolution images of the 2500°C specimen at 220 Å focus increments. Optimum image is shown in (b). (XBB 800-12197)

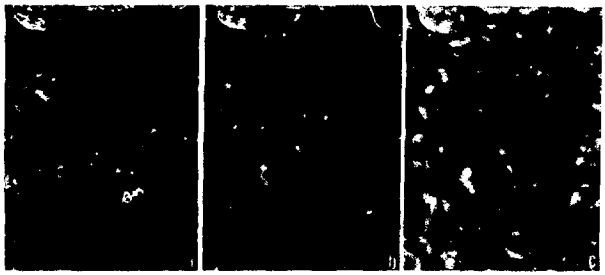

Fig. 11. High resolution images of the 2700°C specimen at 220 Å focus increments. Optimum image is shown in (b), where lattice fringes are spaced by 3.4 Å. (XBB 800-12193)

5. TEM/STEM STUDY OF GRAIN BOUNDARY STRUCTURE AND SEGREGATION IN CVD THIN-FILM SILICON

Jamie H. Rose and Ronald Gronsky

With the relatively recent advent of thin-film polycrystalline silicon in integrated circuit devices, the influence of grain boundaries on electrical properties (e.g., resistivity, mobility) is of urgent concern. It is anticipated that these boundaries exert two types of effect: first, dopant segregation to grain boundaries may reduce majority carrier concentration in the matrix;[1] and second, the segregate species may induce defect states in the band gap, trapping free carriers and producing a space charge region about the boundary plane.[2] In this program, attention is being paid to both effects, and the structure and segregation of dopant species at grain boundaries are being monitored at high spatial resolution.

Specimens have been prepared by low pressure chemical vapor deposition (LPCVD) of silicon films, and characterized in the Philips EM 400 TEM/STEM. Undoped material deposited on native oxide was observed to be heavily faulted, but had attractively large grain size (~ 1 μm) after annealing. This is clearly an advantage both in terms of electrical properties and the potential for accurate assessment of the extent of boundary segregation.

A subset of specimens was then heavily doped with phosphorus by annealing at 950°C in PH_3 for 40 minutes, yielding a substantial P peak in the EDS spectra (Fig. 12) which did not vary substantially between grain interior and grain boundary at this high concentration level.

It was also observed that subsequent anneals of the doped material resulted in a rapid loss of P to the specimen surfaces. This prompted an additional surface coating treatment by SiO_2 sputtering, and comparisons with the Stanford University computer program for device modeling (SUPREM) of solute concentration profiles for both coated and uncoated specimens are currently underway.

Fig. 12. EDS spectra from grain interior (dotted line) and grain boundary (solid curve) in heavily doped LPCVD polysilicon. (CBB 811-631)

TEM images of these specimens reveal highly structured boundary regions, even after substantial annealing treatments. It is believed that these high energy configurations are responsible for much of the resistivity observed even in undoped specimens.

* * *

1. M. E. Cowher and T. O. Sedgwick, J. Electrochem. Soc. 119, 1565 (1972).
2. T. I. Kamins, J. Appl. Phys. 42, 4357 (1971).

6. CHARACTERIZATION OF THE DEFECT STRUCTURE OF Si-SiO_2 INTERFACES

Jerzy Mazur and Ronald Gronsky

Thermally grown silica layers on silicon are of considerable importance because of their applications in modern integrated circuit technology. They are used as a gate dielectric in MOS devices, as masks against dopant diffusion and as passivating agents in active device regions and junctions. The nature of the oxide is therefore often critical to device performance, particularly in VLSI circuits and tunneling devices, e.g., MOS solar cells.[1] This study seeks to characterize the morphology and interfacial structure of silica on silicon by high resolution electron microscopy and diffraction.

MOS specimens were prepared from n^+-type Sb-doped (111) silicon wafers, wet oxidized at 850°C and evaporation coated with < 1000 Å of Al at ~ 10^{-6} torr. The specimens were then annealed at 400°C in forming gas (90%N, 10%H) atmosphere for 10 minutes. After ion milling, cross-sectional specimens were examined in a Siemens Elmiskop 102 at 100 kV. In each instance the electron beam was oriented along a [100] Si direction in the interface plane. Images were obtained at ~ 1000 Å defocus from Gaussian.

Figure 13 shows a high resolution micrograph of a specimen with a 70 Å oxide layer. The Si-SiO_2 interface is irregular at a 5 Å level but with no well-defined periodicity to the interfacial undulations. By comparison the 100 Å oxide layer in Fig. 14 is irregular to ~ 10 Å in ledge height with similar random ledge distribution along the interface.

These thicker oxides differ from previously studied[2] oxides (~ 30 Å thickness) in their image contrast features. It is thought that the layered appearance may be due to the formation of a new oxide phase which may create further electronic effects to compete with those due to greater surface irregularity.

Fig. 13. High resolution image of an MOS cross section with 70 Å oxide layer. The interface is comprised of an irregular array of 5 Å ledges. (XBB 811-630)

Grain boundary precipitation. A comprehensive study of the grain boundary nucleation event in dilute Al base alloys is in progress and will continue through next year. These studies are being conducted at atomic resolution on the JEM 200 CX and will be complemented with a full image-simulation routine for accurate interpretation of the favored structural sites for precipitate nucleation. Data will be gathered on the nature of all interfaces, the extent and character of faceting and the effects on local boundary structure attributed to nucleation.

Accommodation of deformation at grain boundaries. A study is underway to determine the mechanisms by which crystal dislocations dissociate at, and slip through, the grain boundary plane in bcc metals. Visibility conditions have been established for both weak beam and lattice resolution images using Fe, Nb and Mo bicrystal and polycrystalline specimens, and imaging will be performed and compared with computed structural unit models.

Fig. 14. High resolution image of an MOS cross section with 1000 Å oxide layer. The interface is comprised of an irregular array of 10 Å ledges. (XBB 811-629)

* * *

1. R. G. Godfrey and M. A. Green, Appl. Phys. Lett. 34, 913 (1979).
2. O. L. Krivanek and J. Mazur, Appl. Phys. Lett. 37, 392 (1980).

RESEARCH PLANS FOR CALENDAR YEAR 1981

Grain boundary segregation. Data has been collected on the temperature variation of Zn segregation in Al for a wide range of boundary structures. Correlations will be sought with the actual defect distribution observed by high resolution TEM and local activation energies computed for defect-modified grain boundary segregation, enrichment factors, and phase stability limits.

Similar studies will be carried out for P in Si and As in Si to correlate with measured electrical properties in polysilicon specimens.

Amorphous materials. A new program in rapidly quenched materials has begun with emphasis on the relaxation phenomena induced by annealing. Attention will be given to the characterization of topological and compositional short range order by high resolution imaging and spectroscopic analysis.

These techniques are also currently being applied to characterize the defect structures both before and after laser annealing in hydrogenated amorphous silicon for correlation with spectral response data.

Image simulation and processing. Work will continue on the computer simulation of atomic resolution images with careful attention devoted to the sampling of elastic diffuse scattering.

A comparison of computer codes is underway and will be catalogued for efficient simulation on the LBL mainframe. Studies will also be conducted to determine the optimum organization of the computing effort for the atomic resolution microscopy facility.

1980 PUBLICATIONS AND REPORTS

Refereed Journals

1. R. Gronsky, "The U.S. Atom-Resolving Microscope Project," in 38th Annual Proc. Electron Microscopy Soc. Amer., Reno, Nevada, G. W. Bailey (ed.), p.2, (1980), LBL-10682.

2. J. Briceño-Valero and R. Gronsky, "Detection of Solute Segregation in Grain Boundaries," in 38th. Annual Proc. Electron Microscopy Soc. Amer., Reno, Nevada, G. W. Bailey (ed.) p. 360, (1980), LBL-10683.

3. R. Gronsky and P. Furrer, "Grain Boundary Precipitation in Aluminum Alloys: Effect of Boundary Structure," Met. Trans. 12A, 121 (1981), LBL-9737.

4. D. J. H. Cockayne and R. Gronsky, "Lattice Fringe Imaging of Modulated Structures," Phil. Mag. (in press), LBL-10158.

Other Publications

1. R. Gronsky, "High Resolution Transmission Electron Microscopy," in Treatise on Materials Science and Technology: Experimental Techniques, H. Herman (ed.), Academic Press, (in press), LBL-11243.

2. R. Gronsky, "Direct Imaging of Grain Boundaries," in Grain Boundary Structure and Kinetics, R. W. Balluffi (ed.), American Society for Metals 45, (1980), LBL-9779.

LBL Reports

1. R. Gronsky, G. Thomas, O. L. Krivanek and R. K. Mishra, "Physical and Chemical Characterization of Interfaces by Electron Optical Methods," proceedings of the 7th LBL/MMRD International Materials Symposium on "Surface and Interfaces in Ceramic and Ceramic/Metal Systems, July 28/30 - August 1, 1980, LBL-11413.

2. R. Gronsky and J. A. Little, "High Resolution Studies of High-Rank Coal Microstructures," LBL-11612.

Invited Talks

1. R. Gronsky, "Atomic Resolution Microscopy," Basic Research, Physics Division Seminar, U.S. Steel Corporation, Monroeville, Pennsylvania, February 19, 1980.

2. R. Gronsky, "Atomic Resolution Microscopy in Materials Science," Staff Seminars in Metallurgy and Materials Science, Carnegie-Mellon University, Pittsburgh, Pennsylvania, February 21, 1980.

3. J. Briceño-Valero, R. H. Hoel and R. Gronsky, "Grain Boundary Structure and Segregation in Al Alloys," TMS/AIME Annual Meeting, Las Vegas, Nevada, February 25, 1980.

4. R. Gronsky, "Interfaces at Atomic Resolution," U.S. Department of Energy BES/DMS Meeting on Coal Structure and Properties, Gatlinburg, Tennessee, April 8-10, 1980.

5. R. Gronsky, "Teaching Electron Microscopy: Formal Courses," Electron Microscopy Society of America Physical Sciences Tutorial, 38th Annual Meeting, Reno, Nevada, August 4-8, 1980.

6. R. Gronsky, "High Resolution Imaging of Spinodals," in Symposium on "Modulated Structures: Properties and Microstructure," Fall Meeting of TMS/AIME, Pittsburgh, Pennsylvania, October 5-8, 1980.

7. R. Gronsky, "High Resolution Studies of Grain Boundary Reactions," Department of Metallurgy and Materials Science, Carnegie-Mellon University, Pittsburgh, Pennsylvania, October 1, 1980.

8. R. Gronsky, "Grain Boundary Structure and Transformations," Department of Metallurgy, Lehigh University, Bethlehem, Pennsylvania, October 9, 1980.

9. R. Gronsky and R. H. Bragg, "Lattice Images in Glassy Carbon," 33rd. Pacific Coast Regional Meeting, American Ceramics Society, San Francisco, California, October 26, 1980.

b. Microstructure, Properties, and Alloy Design: Inorganic Materials*

Gareth Thomas, Investigator

Alloy Design: Steels

Introduction. This research program is a fundamental program involving detailed studies of microstructure-composition-property relations to optimize the properties of medium and low carbon steels utilizing duplex structures, viz., martensite-austenite (~ 25%) or martensite-ferrite (60-80%) or other ferrite-composites. The program on medium carbon steels has shifted toward improving fatigue and wear resistance, as interest from the mining and agricultural areas has increased. That of low carbon steels has shifted to broader applications than originally investigated (weight savings, automotive), especially with the aim of improving low temperature toughness. These alloy design programs are all directed toward improved energy savings and material conservation.

In addition, fundamental studies of martensite and bainite are being continued, including in-situ studies in the HVEM. Specific examples of research projects follow.

1. AN INVESTIGATION OF CORRELATIONS FOR PREDICTING MECHANICAL PROPERTIES OF "QUATOUGH" STEELS

Chung-Yuan Kung and Gareth Thomas

The low-alloy Fe/Cr/Mn/C system (called quatough steels) has been developed over the last decade at Berkeley, to yield an excellent combination of high strength and good toughness. From this development, a detailed investigation has grown of the role of microstructure in the area of mechanical properties and of the mechanisms by which high strength and high toughness are obtained.

The present objective has been to correlate the microstructural and mechanical data obtained to date. For simplicity of analysis, the alloys chosen for this study have equivalent yield strength, ($\sigma_y \approx 180$-200 ksi), hardness ($R_c \approx 48 \pm 3$), and a similar microstructure. Using this approach, a correlation of plane strain fracture toughness, K_{IC}, with Charpy v-notch toughness, E_{CV} has been obtained (Fig. 1). The data points fit the following relationship

$$K_{IC}/\sigma_y = 0.008\left(E_{CV}/\sigma_y \cdot A\right)^2 + 0.3 ,$$

where A is the cross-sectional area of Charpy bar from the lower bound of data. As an alternative to costly and difficult testing, the K_{IC} values

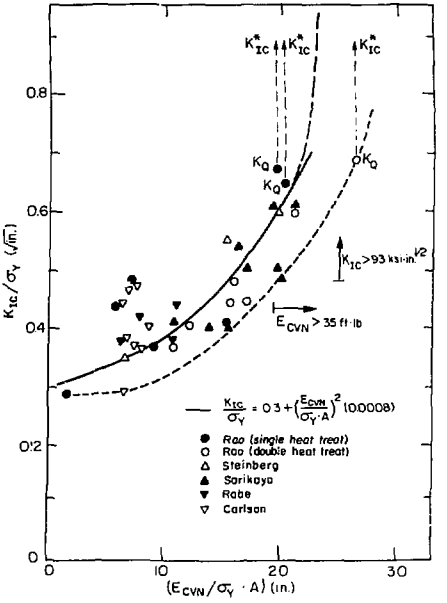

Fig. 1. Correlation between K_{IC} and E_{CV} for quatough steels. (XBL 8010-6195)

can be conservatively estimated from the existing E_{CV} values. For the quaternary steels investigated in this program, a specimen with an E_{CV} value of ~ 35 ft-lb will have a K_{IC} value of at least 93 ksi in.$^{1/2}$.

The correlation between elongation and toughness was found to be poor, whereas an interesting result was obtained for the relationship between reduction of area and E_{CV}. The E_{CV} data are almost completely independent of reduction of area at low and median ranges of ductility. However, at the high range of ductility, E_{CV} increases rapidly (Fig. 2). This result would seem to suggest that other factors than just ductility determine the Charpy v-notch toughness. A factor is the notch sensitivity, which in the present study was found to exhibit a correlation with Charpy v-notch toughness. The notch sensitivity (q_V) for a Charpy v-notch is defined here as the ratio between impact energy and tensile fracture energy, and is different from the conventional definition. The relationship between q_V, E_{CV} and ductility is shown in Fig. 3. The lines of equal q_V are approximately parallel to each other, with q_V decreasing with decreasing

*This work was supported by the Director, Office of Energy Research, Office of Basic Energy Sciences, Materials Sciences Division of the U.S. Department of Energy under Contract No. W-7405-ENG-48.

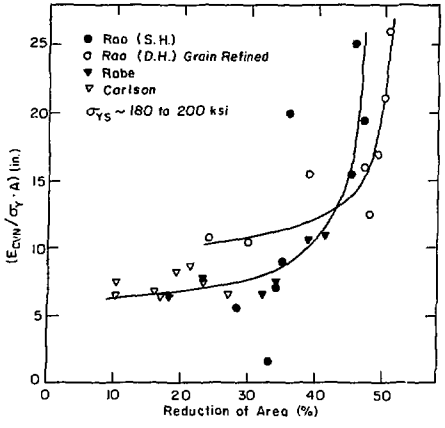

Fig. 2. Correlation between E_{CV} and reduction of area (%) for quatough steels. (XBL 8010-6197)

toughness for the same ductility, and decreasing with increasing ductility for the same toughness. Figure 2 shows that both notch sensitivity (q_V) and ductility (reduction of area) contribute to the Charpy v-notch toughness of Fe/Cr/Mn/C steels.

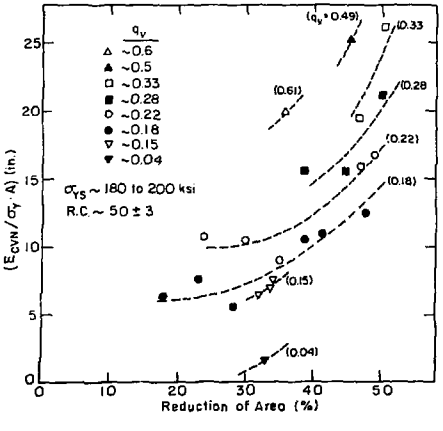

Fig. 3. The relationship between E_{CV} and reduction of area as a function of q_V (notch sensitivity). (XBL 8010-6198)

2. SLIDING WEAR, TOUGHNESS, AND MICROSTRUCTURAL RELATIONSHIPS IN HIGH STRENGTH Fe/Cr/C EXPERIMENTAL STEELS

William J. Salesky† and Gareth Thomas

The development of strong, tough martensitic medium carbon steels in this laboratory[1] has stimulated interest from several industries including the mining industry. As a result, a wear program has been initiated to try to understand some of the fundamental structure and property parameters that may be of significance.

Traditionally, hardness has been believed to be the major parameter influencing wear resistance of materials, but in this work combinations of high strength and toughness appear to be beneficial to optimum wear resistance. In fact, as shown in Fig. 4, there is not a good correlation between wear and hardness; however, small additions of Mn or Ni to the Fe/4Cr/0.3C martensitic alloys (designated "quatough") have been previously shown to increase toughness while maintaining high strength through increased volume fraction of retained austenite.

Experimental results of sliding wear resistance (pin-on-disk experiments) for these experimental steels are shown in Fig. 5. These results show

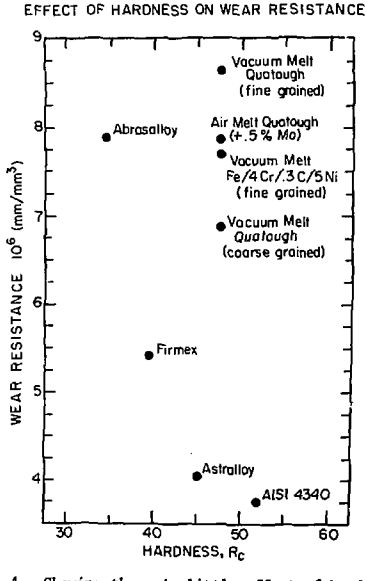

Fig. 4. Showing there is little effect of hardness on sliding wear of a range of steels including "quatough." (XBL 801-4564)

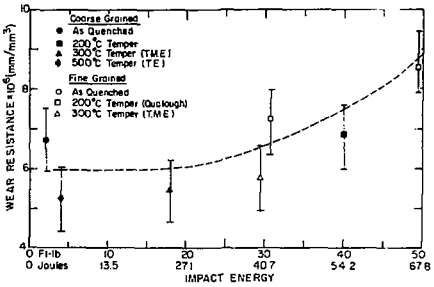

Fig. 5. Showing good correlation between Charpy impact toughness and sliding wear resistance of Fe/Cr/C/Mn Steels. (XBL 801-4563)

that the microduplex Fe/4Cr/0.3C/2Mn have superior wear characteristics over the commercial alloys examined. Even more significant is the correlation shown in Fig. 6 between the wear resistance and % retained austenite which, in previous work, was

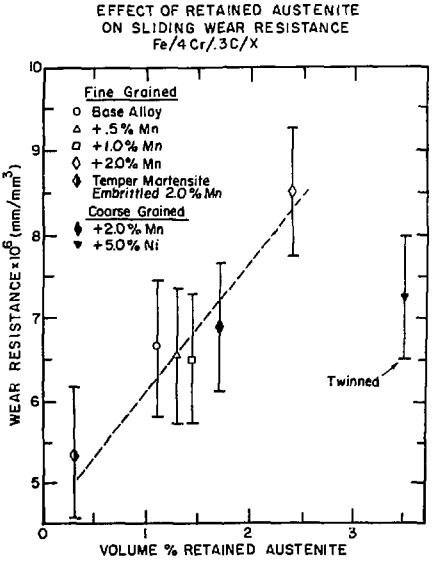

Fig. 6. Showing the correlation between % retained austenite and sliding wear resistance of quatough steels. (XBL 801-4565)

correlated with toughness. These results show that Charpy data are more meaningful than hardness data for evaluating friction wear resistance.

* * *

†M.S. thesis, LBL-10994.

1. B. V. N. Rao and G. Thomas, Met. Trans. 11A, 441 (1980).

Dual Phase Steels

3. IMPACT PROPERTIES OF FE/1.5Mn/0.6C DUAL PHASE STEEL

Nack-Joon Kim and Gareth Thomas

Since the development of dual phase steels, there have been numerous studies of microstructure-mechanical property correlations[1,2] and the main emphasis has been placed on the improvement in formability. However, more general applications of these dual phase steels for structural components such as bridges, pipelines, pressure vessels, etc., require high resistance to brittle fracture and low transition temperature (DBTT). Thus, the main objectives of this investigation are to characterize the impact properties of dual phase steels and to develop a dual phase steel for possible application at low temperature by precise hot rolling processes[3] for grain refinement.

When Fe/1.5Mn/0.06C alloys are controlled rolled, followed by quenching, nonconventional dual phase structures that consist of ferrite and upper bainite are developed (Fig. 7). As the finish rolling temperature is decreased, the ferrite grain size becomes finer, which in turn increases the strength and decreases the DBTT (Fig. 8). When these as-hot rolled structures are intercritically annealed, there are changes in the microstructures and the resulting mechanical properties. In these cases, the structures mainly consist of ferrite and martensite. As the two phase annealing temperature is increased, both strength and DBTT increase (Fig. 9). These changes in mechanical properties can be explained by the increase in the volume fraction of martensite with increase of the two phase annealing temperature. It is interesting to note that ferritic-bainitic dual phase structures have lower DBTT than ferritic-martensitic dual phase structures at the same strength level. Thus, these as-hot rolled ferritic-bainitic dual phase steels have high potential for low temperature applications, e.g., pipeline.

* * *

1. R. A. Kot and J. W. Morris, eds., Structure and Properties of Dual Phase Steels, AIME, New York, N.Y. (1979).
2. A. T. Davenport, ed., Formable HSLA and Dual Phase Steels, AIME, New York, N.Y. (1979).
3. J. Crane, ed., Microalloying 75, Union Carbide Corporation, New York, N.Y. (1977).

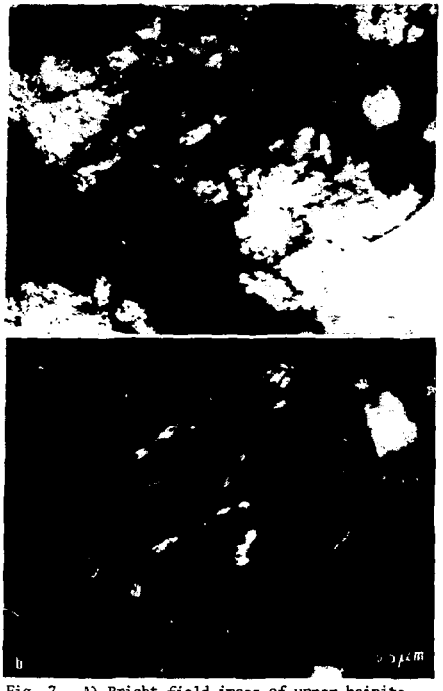

Fig. 7. A) Bright field image of upper bainite region developed in the as-hot rolled condition; B) Dark field image of interlath carbides.
(XBB 809-11371)

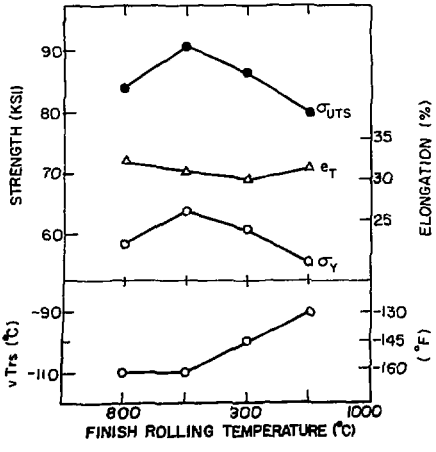

Fig. 8. Plot of strength, elongation, DBTT variation with finish rolling temperature.
(XBL 809-5980)

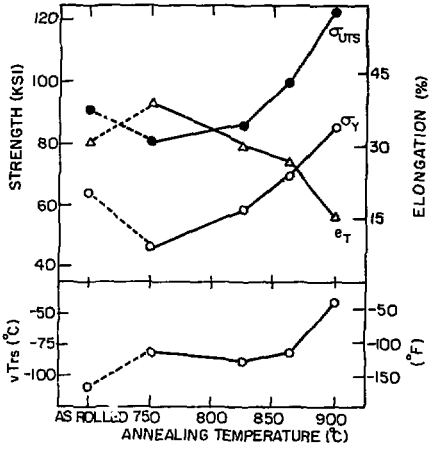

Fig. 9. Plot of strength, elongation, DBTT variation with two phase annealing temperature.
(XBL 809-5982)

4. EFFECT OF VANADIUM ON STRUCTURE-PROPERTY RELATIONS OF DUAL PHASE Fe/Mn/Si/C STEELS

Alvin Nakagawa,† Ja-Yung Koo,† and Gareth Thomas

This investigation is concerned with the effect of 0.12% vanadium addition on an Fe/1.2Mn/0.6Si/0.1C dual phase steel. A comparison of the structure and mechanical properties is being made between two vacuum melted alloys, one with vanadium and an identical one without. Besides the fundamental research reasons for studying the effect of vanadium as a carbide former on the structure and mechanical properties, there are economic and resource conservation reasons for determining whether or not vanadium is a necessary alloying addition in dual phase steels.

Two-phase ($\alpha + \gamma$) and single (γ) annealing treatments in a vertical tube furnace were followed by several different cooling rates. The results of the tensile tests of 1 in. gauge length flat tensile specimens appear in Table 1. Overall, the vanadium containing alloy does not show superior properties over the alloy without vanadium. The lower strength of the vanadium containing alloy probably results because the carbide strengthening was not sufficient to counteract the lower strength of the martensite because of the loss of carbon to the precipitates. In the treatment that produces the best results, 900°C and oil quench, the mechanical properties of the two alloys are almost identical.

Table 1. Tensile property summary of dual phase Fe/Mn/Si/C steels.

Heat Treatment	Alloy	Yield Strength (MPa)	Ultimate Tensile (MPa)	Uniform Elongation (%)	Total Elongation (%)
800°C IBQ	MB[1]	448	785	13	19
	MV[2]	400	723	13	19
800°C OIL	MB	324	589	23	30
	MV	369	661	17	25
900°C OIL	MB	531	813	12	28
	MV	544	795	12	31
800°C AC	MB	345	531	17	29
	MV	396	517	17	29
900°C AC	MB	370	517	21	35
	MV	341	520	21	34

There are, however, differences in the microstructures. The optical micrographs of the 900°C and air cool specimen (Fig. 10) is a typical example of the smaller grain size of the vanadium containing specimens. Figure 11 shows the vanadium carbide precipitates found in the 800°C and iced brine quench specimen. This microstructure is similar to the interphase type of carbide found during isothermal aging.

* * *

[†]M.S. thesis, LBL-12044.
[‡]Exxon Research and Engineering Corporation, Linden, N.J.

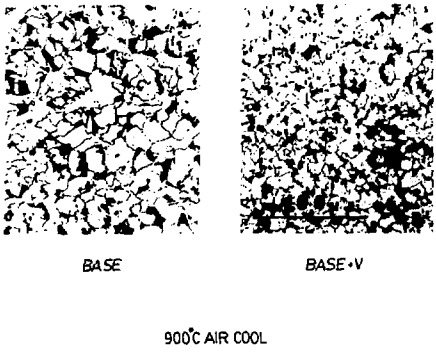

Fig. 10. Optical microstructures of dual phase alloys without (A) and with 0.12% V (B). (XBB 800-12383)

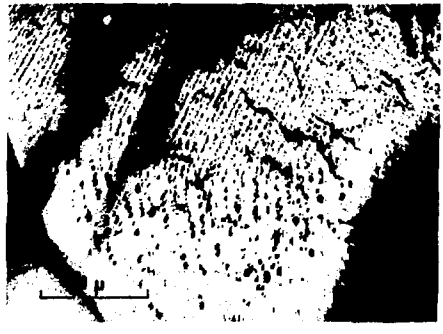

Fig. 11. Transmission electron micrograph showing arrays of carbide precipitates. (XBB 800-12393)

5. THE EFFECT OF THE PROCESSING VARIABLES ON THE MECHANICAL PROPERTIES OF DUAL PHASE STEELS

Jing-sheng Gau and Gareth Thomas

The effect of some processing variables such as the annealing temperature, cooling rate and the transformation path on the mechanical properties has been examined for 0.1 carbon dual phase steels with Nb and Mo.

The results show that both the strength and the U.T.S./Y.S. ratio increase with increasing cooling rate. All air cooling and forced air cooling processes result in a microstructure comprised predominantly of ferrite and pearlite with a corresponding tendency for undesirable discontinuous yielding. The ultimate tensile strength, following direct intercritical annealing has no significant dependence upon the volume fraction of martensite (Fig. 12).

As expected, the precipitation of alloy carbides with the strong carbide forming elements, Nb and Mo, is a strong strengthening mechanism. The plate-like precipitates lie on {100} planes of the matrix and a precipitate free zone adjacent to the grain boundary was observed (see Fig. 13).

By changing the transformation path, variations in the final mechanical properties reflect the differences in the morphology of the martensite product. The highest strength (115 ksi) is produced by continuous intercritical annealing that results in a microstructure of large irregular-shaped martensite regions in the ferrite matrix. However, higher ductility is obtained from the fibrous morphology of martensite obtained by the intermediate intercritical annealing process. This is because of the more efficient load transfer from the soft ferrite to martensite in such structures.

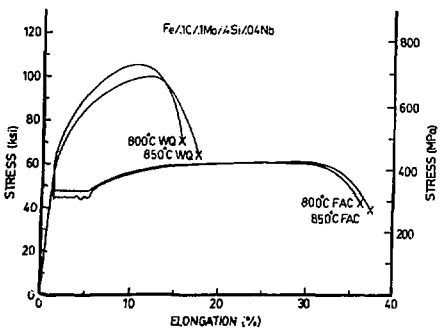

Fig. 12. The engineering stress-strain curves of the steel after various heat treatments.
(XBL 8010-12573)

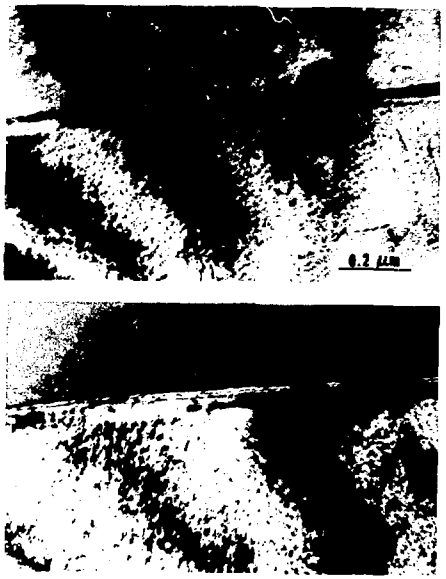

Fig. 13. TEM micrographs showing extensive precipitation in the ferrite matrix. Alloy heat treated at 850°C followed by water quenching.
(XBB 800-11952)

6. MECHANICAL PROPERTIES AND MICROSTRUCTURES OF Fe/1.0Al/0.06C STEEL

Xing-Fang Wu[†] and Gareth Thomas

An investigation concerning the effect of heat treatment on the microstructure and mechanical properties of air melted Fe/1.0Al/0.06C steel is being carried out. Relationships between the microstructure, tensile and impact properties in this steel have been established. This project follows on an earlier investigation by O'Neill.[1]

The intermediate quench steels containing ferrite-martensite dual phase structures have strength and lower toughness than the nearly 100% martensitic alloy. All the mechanical property data are shown in Table 2. The mechanical properties were also found to be independent of the volume fraction of martensite after dual phase treatment confirming O'Neill's results.[1]

The mechanical properties of the air cooled specimens are much poorer (~ 20%) than those of the two-phase specimen. This is due to the presence of pearlite. Even in the quenched alloys, a small amount of pearlite structure was detected by electron microscopy.

Table 2. Mechanical properties of Fe/1.0Al/0.06C steel at different heat treatments

Heat Treatment	Volume of M (%)	Yield		UTS		Uniform Elongation (%)	Total Elongation (%)	Uniform Reduction of Area (%)	Reduction of Area (%)	Impact Property Ft. b
		Ksi	Mpa	Ksi	Mpa					
Quench[a]	~100	64.9	447.4	83.4	575	7.7	26.8	4.7	77.4	>120
Quench + 1045°C 20'	40	70.0	482.9	92.3	636	6.4	28.0	6.3	74.3	~ 36
Quench + 960°C 20'	20	68.0	470.0	92.8	640	7.2	26.4	7.1	74.5	~ 40
Quench + 1010°C 20' air cooling	describe pearlite	60.6	417.9	71.8	495	8.7	23.2	2.4	78.0	> 20
Quench + natural tempering	M and carbide	70.0	482.9	88.5	610		29.8			

[a]"Quench" 1085°C, 1 hour to ice water.

The strain hardening coefficient of the dual phase alloy is higher than that of 100% martensite alloy (~ 8%). This result is expected if the ferrite phase is capable of multiple cross slip. Evidence for this can be seen in the fracture surface shown in Fig. 14.

TEM observations showed mainly dislocated martensite with some microtwinned martensite.[2] Lattice imaging studies showed both coherent and incoherent boundaries in these microtwinned regions (Fig. 15). The dislocations at the boundary appear to be (111) type screw dislocations. These microtwins may be found as a mechanism for stress relaxation. They also indicate a locally high carbon concentration.

* * *

[1]Visiting Scientist, Beijing, University of Iron and Steel Technology.

1. T. O'Neill, "Mechanical Properties and Microstructures of Dual Phase Steels Containing Silicon, Aluminum, and Molybdenum," M.S. thesis, LBL-9047 (1979).
2. J. Y. Koo, "Design of Duplex Low Carbon Steels for Improved Strength: Weight Applications," Ph.D. thesis, LBL-6657 (1977).

Fig. 14. Fractograph showing fine cross slip in the fracture surface of Fe-Al-C dual phase steel (20% martensite). (XBB 812-2042)

Fig. 15. Lattice image of martensite in 100% martensite condition. (XBB 812-2043)

7. THE EFFECT OF MARTENSITE MORPHOLOGY ON FATIGUE CRACK PROPAGATION IN DUPLEX FERRITE MARTENSITE (DFM) STEELS

James Wasynczuk and Gareth Thomas

The effect of martensite morphology and volume fraction on fatigue crack propagation in AISI 1018 DFM steel is being determined by comparing DFM steels of similar yield strengths, but different martensite morphologies. The different martensite morphologies are obtained through two DFM heat treatments: (1) intercritical annealing and (2) intermediate quench.

At approximately equivalent volume fractions of martensite, the coarse globular DFM microstructure resulting from (1) gives higher yield and ultimate tensile strengths, but less elongation, than the fine fibrous DFM microstructure resulting from (2). Initial fatigue tests show that at approximately equal volume fractions of martensite, the value of threshold alternating stress intensity (ΔK_{TH}) of the coarse DFM structure is 21% lower than that of the fine structure. Above threshold, the increase in crack propagation rate with ΔK is steeper for the coarse DFM microstructure.

8. THE FERRITE STRUCTURE AND PARTITIONING OF ALLOYING ELEMENTS IN DUAL PHASE STEELS

Rune H. Hoel[1] and Gareth Thomas

The ferrite phase of Fe/1.5Si/0.15C base duplex steels containing 0.03 wt% Nb or 0.38 wt% Mo has been found to contain fine plate precipitates (Fig. 16).[1] By weak beam imaging the plates are found to be less than 25 Å thick and with a mean diameter of 135 (± 20) Å. These plates are oriented within 12° of the {100} planes. Foil thicknesses are measured by convergent beam microdiffraction and the precipitate density in the base + Nb steel was found to vary with martensitic volume fraction, V_m. As V_m is increased from 25 to 40% there is an increase in the average interparticle spacing from 500 (± 35) Å to 640 (± 35) Å. The corresponding drop in the precipitation strengthening level is 10.4 (± 4) ksi [71.8 (± 27) MPa]. This results in unexpected behavior; the yield strength of the duplex martensite-ferrite aggregate decreases with increasing martensite volume fraction.[2,3] Both σ_α and σ_m in the law of mixtures are inverse functions of V_m. Ultrafine plate precipitates are also always observed in the ferrite phase of dual phase steels of compositions Fe/2Si/0.1C, Fe/0.5Mn/0.1C and Fe/0.6Si/0.1C/1.2Mn/0.1V.[4]

Mo and Nb are known as strong carbide formers. As well as forming fine plate alloy precipitates, they also form spherical inclusions in the dual phase steels. These spherical inclusions are typically a few μm in diameter. Figure 17 shows an energy dispersive x-ray spectrum from the ferrite matrix (white spots) superimposed on a spectrum acquired from the inclusion in a base + Nb duplex steel. The presence of the Nb, L and K peaks clearly show that the inclusions are Nb rich. Similar inclusions are found in the base + Mo

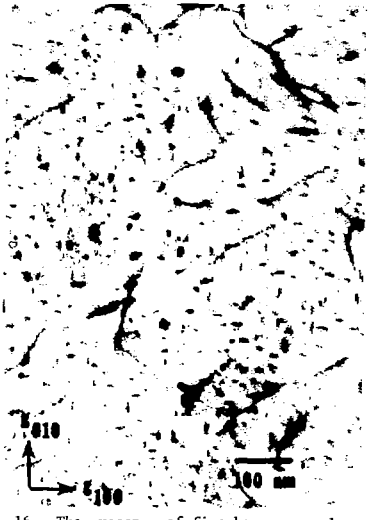

Fig. 16. The presence of fine homogeneously nucleated precipitates in the ferrite phase of the base + Nb alloy. (XBB 806-7299)

(a)

(b)

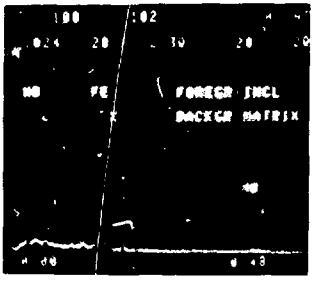

Fig. 17. EDX spectra from the ferrite matrix (white spots) and Nb rich inclusion in the base + Nb alloy. (XBB 8012-14734)

(Mo rich inclusions) and the Fe/0.5Mn/0.1C (Mn rich inclusions) dual phase steels.

* * *

†Work supported by NSF.

1. R. H. Hoel and G. Thomas, "Ferrite Structure and Mechanical Properties of Low Alloy Steels," submitted to Acta Met , (1980).
2. P. K. Costello, "Design of Duplex Low Carbon Steels with Carbide Forming Elements," M.S. thesis, LBL-8628 (1979).
3. G. Thomas and J. Y. Koo, "Developments in Strong, Ductile, Duplex Ferrite-Martensitic Steels," in Symposium on Structure and Property of Dual Phase Steels, TMS-AIME, New Orleans, Louisiana, F. A. Kot and J. W. Morris, eds., (1979), p. 183.
4. R. H. Hoel and A. Nakagawa, "Effect of Vanadium on Dual Phase Fe/Mn/Si/0/0.1C Steels," M.S. thesis, in progress.

Phase Transitions

9. MORPHOLOGY AND CRYSTALLOGRAPHY OF LATH MARTENSITE IN STEELS

Mehmet Sarikaya and Gareth Thomas

The common orientations in lath martensite-retained austenite determined by electron microscopy are $(111)_\alpha//(110)_\gamma//(110)_\alpha$. In this investigation, by using a very small electron (100 Å) probe size, it was possible to obtain diffraction information within an accuracy of 0.5° which is sufficient to identify uniquely the exact orientation relationships (O.R.) in this material. The results show that the O.R.'s are actually clustered around the Gr. inger and Toroiano one,[1] with some variation. Furthermore, this range of O.R.'s may develop between the individual laths in a group and retained-γ in a single packet with up to 5° variability.

An earlier hypothesis,[2] concerning the relative orientations of adjacent laths in packet martensite, was that the strain energy created during the martensitic transformation is minimized by the successive nucleation of laths with consecutive changes in their relative orientation around a common $(110)_\alpha$ direction. However, it is clear from this research that the change in O.R.'s between the laths and the retained austenite shows that successive laths rotate around either of the close packed directions, i.e., (110)M or (111)A, (Fig. 18). Assuming $(110)_{\alpha'}$ is the common axis, a rotation takes place in such a way that every other lath obeys a different O.R. However, it still remains to be explained why occasionally diffraction patterns from adjacent laths obey the same O.R.

* * *

1. B. V. N. Rao, Met. Trans. 10A, 645 (1979).
2. B. V. N. Rao, "Morphology, Crystallography and Formation of Dislocated 'Lath' Martensites in Steels," in ICOMAT Conference Proceedings, Boston, Massachusetts, MIT Press, (1979), p.12.

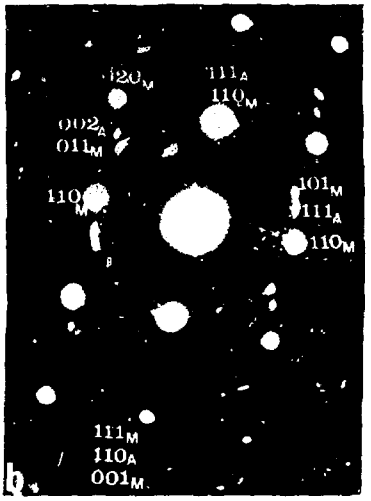

Fig. 18. An SAD pattern showing frequently observed (111)M//(110)A//(100)M triple pattern from Fe/3Cr/2Mn/0.5Mo/0.3C steel (alloy #5). (XBB 8012-14348)

10. THE STABILIZATION MECHANISMS OF RETAINED AUSTENITE IN STEELS

Mehmet Sarikaya and Gareth Thomas

Basically, three types of mechanisms have been suggested for carbon-induced stabilization of austenite at low temperatures: (1) During the austenite to martensite transformation, C diffuses into surrounding austenite, which lowers the local Ms temperature so that austenite becomes chemically stable.[1] This should be effective in the case of steels with a high Ms temperature.[2] Carbon diffuses, together with interstitial N, to form dislocation atmospheres, preventing stress relaxation, and inhibiting the motion of the α'/γ interface. This is called thermal stabilization.[3] Austenite is mechanically stabilized by plastic deformation to accommodate the stresses created during the $\gamma \rightarrow \alpha$ (martensitic) transformation that involve higher dilatational stresses for high C concentrations. Thus, it seems that in the Fe/Cr/C structural steels of interest, C is necessary for stabilizing austenite, but the amount is determined by other alloying elements through their interaction with carbon.

Results with a field ion microscope Atom Probe Analyser (APA), in conjunction with Oxford University, show that there is indeed considerable partitioning of C to the austenite and to the α'/γ interface (Fig. 19). This method involves precise

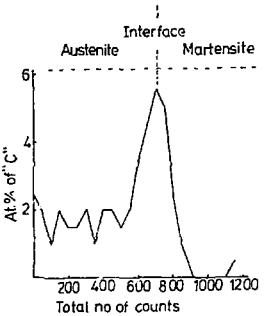

Fig. 19. Atom Probe Analysis showing C profile across the interface. (Data courtesy of Dr. G. Smith, Oxford University, U.K.). (XBL 8012-13502)

chemical analysis with high spatial resolution (<20 Å). As shown in Fig. 19 there is about 2 wt% C at the interface, and almost none in martensite in a foil from as-quenched Fe/3Cr/0.3C/2Mn/0.5Mo and 200°C tempered steel. It is significant to note that in a very low C steel (0.07 wt%) even with a fast (water) quench there was still a considerable amount of retained austenite.

* * *

1. B. V. N. Rao and G. Thomas, Met. Trans. 11A, 441 (1980).

11. HIGH RESOLUTION STUDIES IN MARTENSITE†

Mehmet Sarikaya, Kenneth Easterling,‡ and Gareth Thomas

Detailed microstructural studies have been performed in steels containing 0.1 and 0.3 wt% by lattice fringe imaging. This method provided considerable information on the substructural details of dislocated lath martensite. In such steels, very thin films (≈ 200 Å) of retained austenite have been found to decorate the lath boundaries. At lower of C concentrations, e.g., 0.1 wt%, since the dilatational component of the shear strain is small, no retained austenite is needed for the accommodations of strains. Hence, occasionally, adjacent laths show varying degrees of shear strain of angles ranging between 4° and 11°. In order to relieve the strain either dislocations (s) or long-range strain fields form (Fig. 20).

At the tip of the laths the lattice planes at the leading edge are continuous into adjacent laths (Fig. 21). However, there are numerous dislocations present at the curved interface on the sides. This suggests that the laths grow in transverse direction by the creation of dislocations at the boundary, well behind the tip, and their movement to and disappearance at the tip, as was theoretically predicted.

* * *

†Work partially supported by NSF.
‡University of Lulea, Lulea, Sweden.

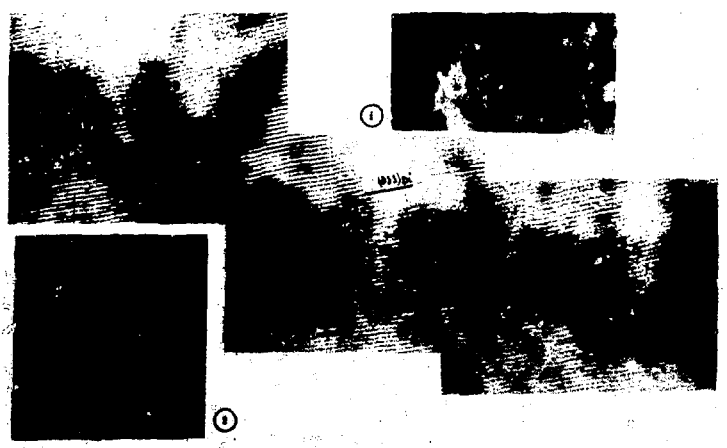

Fig. 20. Accommodations of transformation strains by dislocation (d) and strain fields near and at the boundary. Inset (1) Location of boundary; Inset (2) Low Mag DF micrograph showing the characteristic appearance of continuous films or retained at the lath boundaries (0.1 wt% C steel). (XBB 802-2540)

Fig. 21. LI photograph of a "tip" of a martensite showing continuous lattice fringes. (XBB 802-2535)

12. IN-SITU OBSERVATION OF THE DECOMPOSITION OF RETAINED AUSTENITE IN Fe/Cr/Mn/C ALLOYS BY HVEM

Mehmet Sarikaya, Ashok Jhingan, Hiroyuki Tokushige, and Gareth Thomas

Thin film retained austenite at the martensite lath boundaries is known to decompose upon tempering at 300-400°C regime in Fe/Cr/C structural steels, a phenomenon known as Tempered Martensite Embrittlement.[1] The nature of decomposition, as well as its effect on the mechanical properties, is very significant. In-situ experiments were performed on a set of steels, by using the high voltage HU-650 microscope equipped with a hot-stage, to investigate the decomposition reaction. Foils in the as-quenched conditions were heated to the critical temperature regions and held there for the reaction to take place. The decomposition process was recorded either by a high speed movie camera or by a set of sequential photographs. An example is shown in Fig. 22 where the reflection $00\bar{2}_\gamma$ was used to record the dark field images. Initially, continuous configuration of retained-γ films breaks down as the temperature is increased. Cementite particles nucleate, probably at the interface, but on the austenite side, and subsequently start growing by absorbing carbon, especially from austenite. They grow further as the temperature is increased (or if the holding time is extended), and form islands of carbides of larger thicknesses than the original retained-γ

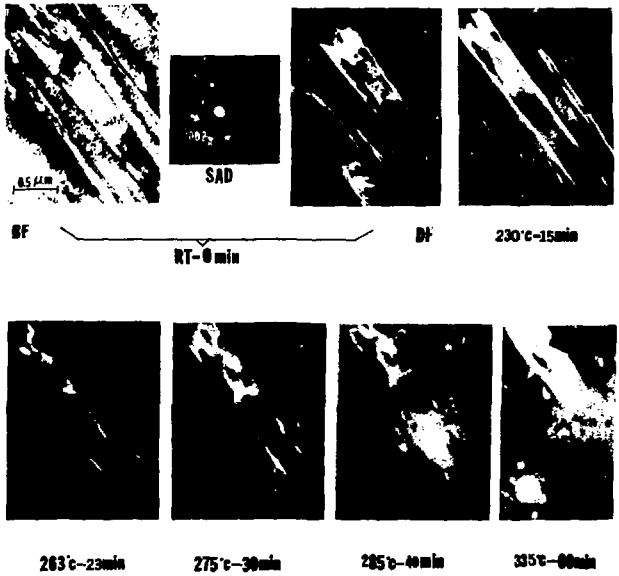

Fig. 22. Sequence of heating Fe/3Cr/0.3C steel in-situ at 500 kV. (XBB 8012-14345)

films along the lath boundaries. The final structure, highly recovered tempered martensite and discontinuous carbides along the boundaries, closely resemble the so-called "upper bainitic" structure.[2,3]

* * *

1. G. Thomas, Met. Trans. 9A, 439 (1978).
2. R. F. Heheman, K. R. Kinsman, and H. I. Aaronson, Met. Trans. 3, 1077 (1972).
3. G. Thomas, Iron-Steel Int. 46, 451 (1973).

Magnetic Materials

Introduction. The main research theme in this program is the design of magnetic and electronic materials through microstructure and composition control. Electron microscopy and chemical microanalysis are used in conjunction with various physical property measurement techniques to establish the desirable and undesirable microstructural features in ferroelectric and ferromagnetic materials. This, in turn, leads to designing new compositions and new processes for preparing superior materials. Current research on magnetic materials and ferroelectric materials are discussed separately below.

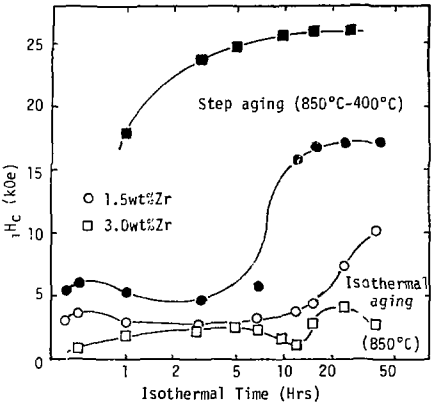

Fig. 23. Variation of the iHc with isothermal aging time for 1.5 wt% and 3 wt% Zr alloys with and without step aging. (XBL 8011-7418)

13. STEP-AGED RARE EARTH-COBALT ALLOY MAGNETS

Raja K. Mishra

Alloys with compositions Co-25.5wt/o Sm-8w/o Cu-15 w/o Fe-3w/o Zr and Co-Sm-Cu-Fe1.5 w/o Zr have been step aged to produce magnets with coercive force (iHc) in the range of 10-25KOe, much higher than those reported so far in the literature for the Zr alloys. The high coercive force magnets are typically aged at 800-850°C for 10-30 hr following solution treatment at 1150°C. Subsequently, these are step aged to produce materials with high coercivity (Fig. 23). The microstructure in all these alloys has a two-phase cellular morphology with a 2:17 phase surrounded by a 1:15 boundary phase (Fig. 24). The long aging treatments at 800-850°C lead to coarsening of the two phase structure. The subsequent step aging does not change the morphology, but only changes the chemical composition of the two phases.

Best properties are obtained in materials with a coherent microstructure of optimum boundary phase thickness and optimum chemical composition. The highest values of iHc obtained so far are ~ 26kOe and ~ 16kOe for the 3% Zr and 1.5% Zr alloys, respectively. The best hard magnetic properties of $(BH)_{max}$ = 33 MGOe and iHc = 13kOe are for a 25% Sm-20% Fe-4 Cu-2%Zr alloy.

Fig. 24. Two phase cellular microstructure of 1.5 wt% Zr alloy, isothermally aged at 850°C for 1 hr showing coherent and continuous 1:5 boundary phase. (XBB 8012-14344)

14. ZERO-MAGNETOSTRICTIVE Fe/Co/B/Si AMORPHOUS ALLOYS

Llewellyn Rabenberg and Raja K. Mishra

The effects of low temperature annealing on the magnetic properties of the amorphous alloy $Co_{71.4}Fe_{4.6}Si_{9.6}B_{14.4}$ have been investigated. Annealing this alloy below 400°C results in magnetic hardening; annealing above 400°C but below the crystallization temperature results in magnetic softening. Above the crystallization temperature, the alloy hardens drastically and irreversibly (Fig. 25). Conventional and high resolution transmission electron microscopy show that the magnetic property changes at low temperature occur, whilst the alloy is truly amorphous. By imaging the magnetic microstructure, using Lorentz microscopy, it has been possible to detect the presence of microscopic inhomogenieties in this alloy, causing the induced anisotropy to fluctuate on a much finer scale (Fig. 26). For annealing above 400°C and below T_{cry}, thermal energy tends to disrupt the local anisotropies and the material magnetically softens. To obtain the softest possible ferromagnetic material, the localized anisotropies must be removed either by post-fabrication anneals or during fabrication.

Fig. 26. Lorentz image of a typical crosstie wall showing Bloch walls (A-A), Neil segments (B), Bloch lines (C), and magnetic ripples. (XBB 804-4578)

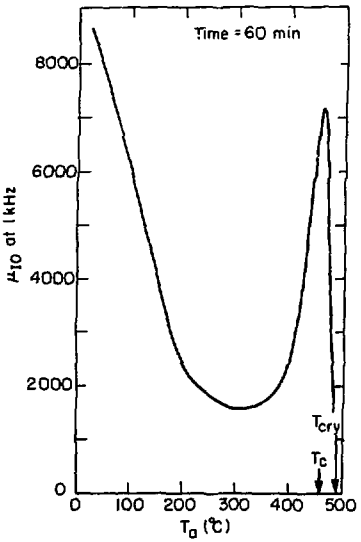

Fig. 25. Variation of initial permeability with annealing temperature (1 hr anneals). (XBL 802-4641)

15. MICROSTRUCTURE-DOMAIN WALL INTERACTION IN $(Mn\text{-}Zn)Fe_2O_4$ AND $LiFe_5O_8$

I-Nan Lin and Raja K. Mishra

The interaction of microstructural features with moving magnetic domain walls in $(Mn\text{-}Zn)Fe_2O_4$ and $LiFe_5O_8$ has been studied in situ by Lorentz microscopy. In $(Mn\text{-}Zn)Fe_2O_4$, it is seen that domain walls are pinned by pores and cracks. The interaction of the domain walls with grain boundaries is more complex. The domain wall can pass through the boundary if it makes a large angle with the boundary. Otherwise, the grain boundary acts as an obstacle. Besides, any chemical segregation such as CaO, SiO_2, etc., along grain boundaries results in local microstress concentrations near the boundary area. The resulting induced anisotropy is such that the domain wall motion stops at some distance from the grain boundary, and in such a case, reverse domain nucleation can occur. In $LiFe_5O_8$, the $LiFeO_2$ precipitates pin the domain walls completely, resulting in high coercive force. At semicoherent interfaces, however, reverse domains can nucleate more easily as shown in Fig. 27.

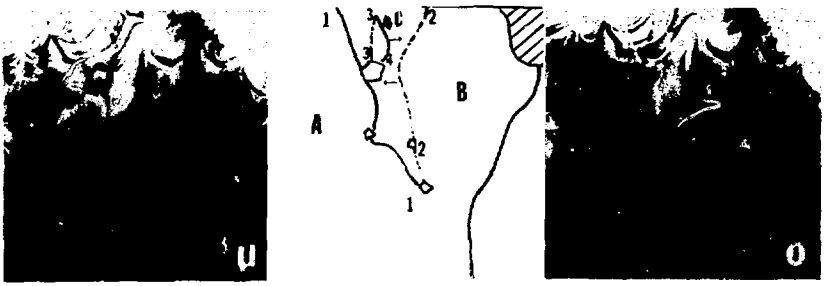

Fig. 27. The domain wall 11 is pinned by the precipitates. The reverse domain C has nucleated on a semicoherent precipitate. (XBB 8010-11968)

Ferroelectric Materials

16. GRAIN BOUNDARY PHASE AND POLING OF PZT

Edward K. Goo and Raja K. Mishra

Transmission electron microscopy and chemical microanalysis have been used for the physical and chemical characterization of the thin, amorphous grain boundary phase in sintered PZT ceramics. Samples sintered with 3 wt% PbO contain a Pb-rich amorphous phase which extends through the boundaries, and is $\lesssim$ 100 Å in thickness (Fig. 28). It is thus suggested, that the excess PbO, which is added for rapid sinterability, forms a liquid phase and aids in sintering. However, upon cooling, this liquid phase solidifies without any crystallization. The thin intergranular phase can significantly affect the poling. For a grain boundary phase of thickness 100 Å in a 3 μm diameter PZT grain, more than half the DC voltage drop can occur at the boundary and the high dielectric constant of the ceramic can be due to the high capacitance of the boundary phase.

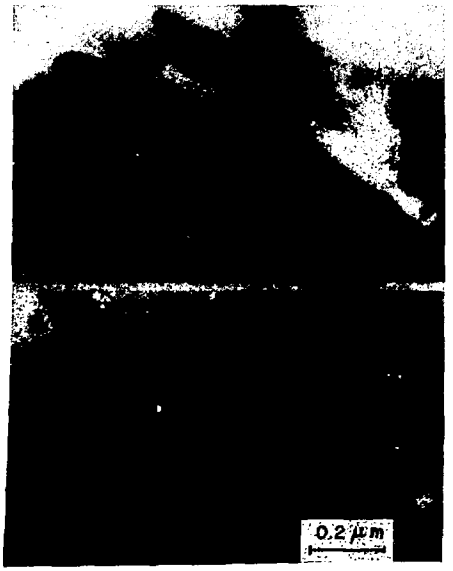

Fig. 28. (a) Bright field and (b) Diffuse dark field images taken from PZT sample showing the presence of a thin intergranular amorphous phase. (XBB 803-3458)

17. STRUCTURE OF DOMAINS AND DOMAIN WALLS IN PZT

Edward K. Goo and Raja K. Mishra

Ferroelectric domains are twins that are formed when PZT undergoes a phase transformation from a nonferroelectric cubic phase to a ferroelectric tetragonal phase upon cooling below 375°C. The tetragonal phase is spontaneously polarized in the direction of the c-axis, making each twin a ferroelectric domain. Figure 29(a) shows the typical domain configuration inside a grain. The 90° domains are the predominant ones and the domain walls lie on {110} planes. The domain walls have a finite thickness to minimize the total wall energy. The postulated wall structure is a distorted crystal in the wall region and the dark field image in Fig. 29(b) shows alternating light and dark contrast from the distortions at the walls. The widths of the alternating bright and dark regions are 100 Å, which is the projected width of the domain wall and hence an upper limit of the domain wall thickness.

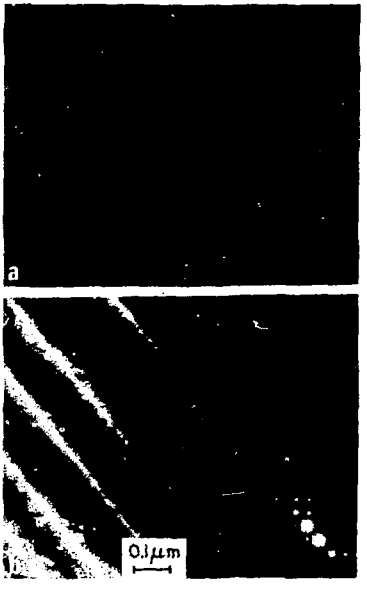

Fig. 29. (a) Bright field and (b) dark field images of 90° domain walls taken with g = 110. There is an alternating light and dark contrast at 90° domain walls. (XBB 803-3452)

Refractory Ceramics†

18. SILICON NITRIDES

Ondrej L. Krivanek and Channing Ahn

It is found that all nitrogen ceramics studied so far,[1] whether hot-pressed or sintered with additives such as MgO, Al_2O_3, Y_2O_3, etc., contain glassy phases at all grain boundaries. Current research on Toshiba manufactured "grain boundary crystallized" Si_3N_4 with Y_2O_3 confirmed even in this material (and contrary to the claims of the manufacturer) that 20 Å films of glassy phase persist at boundaries and at the crystalline yttrium rich phases present at most grain corner junctions.

* * *

†Work supported by NSF.

1. O. L. Krivanek, T. M. Shaw and G. Thomas, J. Am. Ceram. Soc. 62, 585 (1979).

19. SILICON NITRIDE ALLOYS: SIALONS†

Thomas M. Shaw and Gareth Thomas

High resolution imaging has been successful in understanding the complexities of some of the "alloyed" silicon nitride, for example, the block structure of the "15R" Beryllium sialons. Information has also been obtained on the tie lines which describe the phase relationships in these alloys.

* * *

†Brief abstract of J. Solid State Chem. 33, 63 (1980).

20. NITRIDE GLASSES

Thomas M. Shaw†

Crystallization behavior of glasses in the SiO_2-MgO-Si_3N_4 system has been examined. Glasses for the investigation were prepared in collaboration with Dr. R. Loehman from Stanford Research Institute, who is currently studying glass formation in this and other systems. The glasses examined have compositions close to the eutectic between $MgSiO_3$ and SiO_2 in the binary MgO-SiO_2 system, but contain ~ 10 wt% Si_3N_4.

Microstructural and microchemical analysis of as-cooled melts show that they separate into two glassy phases on cooling and that phase separation in the glasses arises from extension of the miscibility gap on the MgO-SiO_2 binary into this system.

In characterization of the crystallization behavior of glasses in the SiO_2-MgO-Si_3N_4 system, differential thermal analysis was used to determine temperature ranges in which reactions occurred. The products of crystallization reactions were identified using x-ray diffraction and the development of the microstructure was followed using both optical and transmission electron microscopy. The general crystallization behavior of Mg-Si-O-N glasses can be summarized as follows:[1]

a. Below the glass transition temperature (~ 800°C), no crystallization occurs.

b. At temperatures below 1000°C, but above the glass transition temperature, crystal growth is slow, but nucleation can readily occur.

c. At intermediate temperatures (1000 - 1300°C) rapid crystallization of the MgO-rich matrix glass to clinoenstatite ($MgSiO_3$) occurs and optical microscopy shows that spherulites ≈ 50 μm in diameter have grown from internal nuclei in the glass.

d. After heating at temperatures greater than 1300°C, several microstructural differences are observed including dissolution of SiO_2-rich phase, recrystallization of the clinoenstatite grains to faceted crystals and formation of fan-like arrangements of clinoenstatite plates.

* * *

†Ph.D. thesis, LBL-11759.

1. T. M. Shaw and G. Thomas, "Spherulitic Crystal Growth from an Oxynitride Glass," Proceedings of the 7th European Congress on Electron Microscopy, The Hague, Holland, Electron Microscopy 1, 438 (1980).

RESEARCH PLANS FOR CALENDAR YEAR 1981

Alloy Design: Steels. Gareth Thomas will be at the Max-Planck-Institut in Stuttgart, West Germany, to conduct in-situ plastic deformation studies on a 1 MeV microscope. He plans to use this equipment for (a) in-situ studies of the mechanical stability of retained austenite in the medium carbon steels; (b) studies of the slip distribution in dual phase ferrite-martensite steels. These projects are fundamental to the understanding of the mechanical behavior of these steels.

The wear program will concentrate on abrasive wear testing with some tests to be done under industrial conditions, e.g., ball mill grinding, cutting blades (for agriculture). The design work on bainitic steels is aimed at producing tough microstructures by isothermal annealing or continuous cooling (for thick wall applications). This involves TTT diagrams and detailed TEM analysis.

It is anticipated that the crystallographic studies of dislocated martensite and bainite will be completed. Dual phase ferrite steels continue to be promising for structural applications (beyond automotive). Research will be done on micro-alloying and controlled rolling so as to achieve higher toughness properties, especially at low temperatures (pipeline applications). The cooperative program with Sandia will continue with corrosion tests to be done at Hawaii. This program is related to applications of dual phase steels for geothermal and other energy sources.

Fatigue Studies. Although, theoretically, the quatough steels are anticipated to have excellent fatigue properties, the following test data are to be compiled:

1. Document the fatigue behavior of these newly developed high strength-high toughness steels in comparison with other commercial alloys.

2. Fatigue crack propagation studies must be done at a very low ΔK range and compared with data from commercial steels.

3. Studies are to be done on low cycle fatigue behavior and fatigue crack initiation, including the role of retained austenite.

Magnetic Materials. The changes in the microstructure of the Sm/Co/Cu/Fe/Zr alloys with varying amounts of Sm, Co, Cu, Fe, Zr will be studied with special emphasis on the chemical microanalysis of the cellular microstructure. Efforts will be made to combine the high $(BH)_{max}$ with high iHc.

Work on the local magnetic fluctuations in Fe/Co/B/Si has been concluded. Future research will focus on the study of atomistic clustering in the pre-crystallized alloys by using high resolution microscopy.

In ceramic magnets, rapid sintering and hot deformation of $(MnZn)Fe_2O_4$ will be investigated with a view to manipulate the microstructure so as to produce segregate-free grain boundaries. Efforts to control Zn loss and Fe^{+2} concentration will be made by manipulating processing.

In a collaborative program with Professor D. de Fontaine, a theoretical and experimental study of the origin of growth induced anisotropy in epitaxial garnet films will be carried out.

Ferroelectric Materials. Having established the role of excess PbO in PZT, work will now be concentrated to study the role of other additives such as Mn, Cr, etc., on the processing and poling of PZT. The effects of point defects and the grain boundary segregates on the properties will be studied by theoretical modeling.

Nitrogen Ceramics (NSF Sponsored). The program on characterizing hot-pressed and sintered Si_3N_4 has been continued; detailed microchemical analyses of the intergranular glassy phases, especially ELS work on nitrogen and oxygen, remain to be done but the problem is very difficult because of resolution limitations (the glassy phases are usually ~ 20 Å wide). It is anticipated that the proposed research on oxynitride glass ceramics with especial emphasis on Y-Al-Si-N-O systems will be supported.

1980 PUBLICATIONS AND REPORTS

Refereed Journals

†1. T. M. Shaw and G. Thomas, "An Electron Microscopy Study of Crystallographic and Phase Relationships in the Be_3N_2-$BeSiN_2$ System," J. of Sol. State Chem. 33 (1), 63 (1980).

†2. T. M. Shaw and G. Thomas, "Spherulitic Crystal Growth from an Oxynitride Glass," Proceedings of the 7th European Congress on Electron Microscopy, The Hague, Holland, Electron Microscopy 1, 438 (1980).

3. M. Sarikaya, K. Easterling, and G. Thomas, "High Resolution Studies in Martensite," Proceedings of the 7th European Congress on Electron Microscopy, The Hague, Holland, Electron Microscopy 1, 176 (1980), LBL-10575.

4. G. Thomas, R. K. Mishra, and K. H. Westmacott, "Impact of HVEM in Materials Science," 6th International Conference on HVEM, Antwerp, Belgium, Electron Microscopy 4, 392 (1980), LBL-11622.

†5. O. L. Krivanek and P. Rez, "Imaging of Atomic in [110] Silicon," EMSA Pacific Regional Conference Proceedings, Reno, NV, edited by G. W. Bailey, pp. 170-173 (1980), LBL-10927.

†6. O. L. Krivanek, "Applications of Energy Loss Spectroscopy in Materials Science," EMSA Pacific Regional Conference Proceedings, Reno, NV, edited by G. W. Bailey, pp. 86-89 (1980).

7. M. Sarikaya, B. V. N. Rao, and G. Thomas, "Identification of Some Crystallographic Features of Martensite in Steels by Microdiffraction," EMSA Pacific Regional Conference Proceedings, Reno, NV, edited by G. W. Bailey, pp. 392-393 (1980), LBL-10808.

8. L. Rabenberg, "Lorentz Electron Microscopy Study of Co/Fe/Si/B Amorphous Alloys," EMSA Pacific Regional Conference Proceedings, Reno, NV, edited by G. W. Bailey, pp. 160-161 (1980), LBL-10831.

9. E. K. Goo and R. K. Mishra, "Ferroelectric Domain Structure of $Pb(Zr_{.52}Ti_{.48})O_3$," EMSA Pacific Regional Conference Proceedings, Reno, NV, edited by G. W. Bailey, pp. 214-215 (1980), LBL-11939.

10. R. K. Mishra, "Applications of Chemical Analysis to the Study of Ferromagnetic and Ferroelectric Ceramics," EMSA Pacific Regional Conference Proceedings, Reno, NV, edited by G. W. Bailey, pp. 106-109 (1980), LBL-10687.

†11. C. K. Wu, A. F. Marshall, G. Thomas, and R. Sinclair, EMSA Pacific Regional Conference Proceedings, Reno, NV, edited by G. W. Bailey, pp. 176-177 (1980).

12. L. Rabenberg, R. K. Mishra, G. Thomas, O. Kohmoto, and T. Ojima, "Electron Microscopy Study of Co/Fe/B/Si Amorphous Alloys," IEEE Transactions on Magnetics MAG-16, 1135 (1980), LBL-10831.

13. T. F. Roth, R. K. Mishra, and G. Thomas, "Segregation in Czochralski Grown Calcium Gallium Germanium Garnet Single Crystals," J. Appl. Phys. 33 (1980), LBL-10832.

†14. O. L. Krivanek, "High Resolution Studies of Glass-Crystal Interfaces," J. of Microscopy 119, 81 (1980).

†15. O. L. Krivanek and J. Mazur, "The Structure of Ultra-Thin Oxide on Silicon," Appl. Phys. Letts. 37, 392 (1980).

16. M. H. Harmer, R. K. Mishra, and G. Thomas, "EM Study of Annealed $(Ni,Zr,Co)Fe_2O_4$," J. Am. Ceram. Soc., 13 (1980), LBL-11223.

17. B. V. N. Rao and G. Thomas, "Structure-Property Relations and the Design of Fe-4Cr-C Base Structural Steels for High Strength and Toughness," Met. Trans. 11A, 441 (1980).

18. J. Y. Koo, M. J. Young, and G. Thomas, "On the Law of Mixtures in Duel Phase Steels," Met. Trans. 11A, 852 (1980).

19. J. Y. Koo, M. Raghavan, and G. Thomas, "Compositional Analysis of Dual Phase Steels by Transmission Electron Microscopy," Met. Trans. 11A, 351 (1980).

20. N. J. Kim and G. Thomas, "Effects of Morphology on the Mechanical Behavior of Dual Phase Fe/Si/C Steels," submitted to Met. Trans. (1980), LBL-10457.

†21. O. L. Krivanek, "The Structure of the Si-SiO_2 Interface," Proceedings of Surfaces and Interfaces in Ceramic and Ceramic-Metal Systems Conference, Berkeley, CA, in press.

22. G. Thomas, R. Gronsky, O. L. Krivanek, and R. K. Mishra, "Physical and Chemical Characterization of Interfaces by Electron Optical Methods," Proceedings of Surfaces and Interfaces in Ceramic and Ceramic-Metal Systems Conference, Berkeley, CA, in press, LBL-11941.

23. R. K. Mishra and G. Thomas, "Amorphous Grain Boundary Phases in Ferrimagnetic $(Mn,Zn)Fe_2O_4$ and Ferroelectric PZT Ceramics," Proceedings of Surfaces and Interfaces in Ceramic and Ceramic-Metal Systems Conference, Berkeley, CA, in press, LBL-11511.

24. R. K. Mishra, E. K. Goo, and G. Thomas, "Grain Boundary Phases in Ferromagnetic $(Mn,Zn)Fe_2O_4$ and Ferroelectric PZT," Proceedings of Surfaces and Interfaces in Ceramic and Ceramic-Metal Systems Conference, Berkeley, CA in press, LBL-11621.

25. E. K. Goo, R. K. Mishra, and G. Thomas, "Electron Microscopy Study of the Ferroelectric Domain and Domain Wall Structure in $Pb(Zr_{.52}Ti_{.48})O_3$," J. of Appl. Phys., in press, LBL-11256.

26. G. Thomas, E. K. Goo, and R. K. Mishra, "Transmission Electron Microscopy of $Pb(Zr_{.52}Ti_{.48})O_3$," submitted to J. Am. Ceram. Soc. (1980), LBL-11369.

27. R. K. Mishra and G. Thomas, "Recent Progress in Electron Microscopy Studies in Ferrites," Proceedings of the Third International Conference in Ferrites, Kyoto, Japan, in press, LBL-11529.

28. A. Nakata, T. Kamijo, N. Kaihara, K. Okutani, R. Mishra, and G. Thomas, "Microstructure of Commercial Grade Manganese Zinc Ferrites," Proceedings of the Third International Conference on Ferrites, Kyoto, Japan, in press.

29. Y. Belli, K. Kubarych, M. Okada, and R. Mishra, "The Effect of V and Ti on the Magnetic and Mechanical Properties of Fe/Cr/Co Hard Magnets," Mat. Sci. Eng., in press, LBL-8384.

30. R. K. Mishra, G. Thomas, T. Yoneyama, A. Fukono, and T. Ojima, "Microstructure and Properties of Step Aged Rare Earth Alloy Magnets," J. Appl. Phys., in press, LBL-11680.

Other Publications

1. B. V. N. Rao, J. Y. Koo, and G. Thomas, "Mechanical Behavior of Dual Phase Steels Containing Strong Phase Martensite," in Proceedings of the Joint U.S.-Japan Seminar on Mechanical Behavior of Metals and Alloys Associated with Displacive Phase Transformations, R.P.I. Press, p. 41 (1980), LBL-9508.

LBL Reports

1. W. J. Salesky, "Sliding Wear, Toughness, and Microstructural Relationships in High Strength Fe/Cr/C Experimental Steels," M.S. thesis, LBL-10994.

2. L. Rabenberg, "Annealing Behavior of High Permeability Amorphous Alloys," M.S. thesis, LBL-10995.

3. E. Goo, "Microstructure and Domain Structure of PZT," M.S. thesis, LBL-10651.

4. M.I. Perez, "Secondary Defects in Quenched Platinum," M.S. thesis, LBL-10178.

5. T. Shaw, "The Crystallization of Glasses in the Mg-Si-O-N System," Ph.D. thesis, LBL-11759.

Invited Talks

1. G. Thomas, R. Gronsky, O. L. Krivanek, and R. K. Mishra, (presented by G. Thomas) "Physical and Chemical Characterization of Interfaces by Electron Optical Methods," Surfaces and Interfaces in Ceramic and Ceramic-Metal Systems Conference, Berkeley, CA, July 28-30, 1980.

2. T. M. Shaw and G. Thomas, (presented by G. Thomas), "Spherulitic Crystal Growth From an Oxynitride Glass," 7th European Congress on Electron Microscopy EUREM 80, The Hague, Holland, August 24-30, 1980.

3. G. Thomas, R. K. Mishra, and K. H. Westmacott, (presented by G. Thomas), "Impact of HVEM in Materials Science," Antwerp, Belgium, September 1-3, 1980.

4. G. Thomas, "Twenty-five Years of Electron Microscopy in Materials Science" (Distinguished Award Address), EMSA Pacific Regional Conference, Reno, NV, August 2-9, 1980.

5. R. K. Mishra and G. Thomas, (presented by G. Thomas), "Microstructure and Properties of Step-Aged Rare Earth Alloy Magnets," 26th Annual Materials Research Society Symposium, Boston, MA, November 16-21, 1981.

6. R. K. Mishra and G. Thomas, (presented by G. Thomas), "Recent Progress in Electron Microscopy Studies of Ferrites," 3rd International Conference on Ferrites" (Keynote Address), Kyoto, Japan, September 30-October 2, 1980.

7. G. Thomas, Series of Lectures on Electron Microscopy, Materials Science, and Alloy Design at Shanghai Tong University, Northwestern Polytechnic University, and Beijing University of Iron and Technology, The People's Republic of China, October through November 1980.

8. G. Thomas, "Transmission Electron Microscopy in the 1980's," First Congress of the Chinese Society for Electron Microscopy (Keynote Address), Chengdu, The People's Republic of China, November 1980.

9. L. Rabenberg, R. K. Mishra, G. Thomas, O. Kohmoto, and T. Ojima, (presented by R. K. Mishra) "Electron Microscopy Study of Co/Fe/B/Si Amorphous Alloys," INTERMAG Conference, Boston, MA, April 21-24, 1980, LBL-10831.

10. R. K. Mishra, "Applications of Chemical Analysis to the Study of Ferromagnetic and Ferroelectric Ceramics," EMSA Pacific Regional Conference, Reno, NV, August 2-9, 1980.

11. O. L. Krivanek, "Applications of Energy Loss Spectroscopy in Materials Science," EMSA Pacific Regional Conference, Reno, NV, August 2-9, 1980.

* * *

†Work supported by NSF.

c. 1.5 MeV Electron Microscope*

Kenneth H. Westmacott, Investigator

Introduction. The overall goal of this program is to obtain a better understanding of the effects of interstitial elements on the structure and properties of metals. The research area is broad since it encompasses solid state reactions and gas-solid reactions including oxidation, reduction, carbonization and nitriding, etc. All such studies are greatly facilitated by the application of high voltage electron microscope (HVEM) techniques that allow direct in-situ dynamic observations of the structural transformations resulting from gas-solid reactions. During the year, significant progress has been made toward reaching a unified understanding of the diverse elements involved in phase transformations in interstitial alloys, such as nucleation, habit, morphology and orientation relationship.

1. PROGRESS REPORT ON FACILITY DEVELOPMENT

Kenneth H. Westmacott

During 1980 the new Kratos 1.5 MeV HVEM was installed in Building 72, but the final system and acceptance tests have not yet been completed. Some teething problems with the accelerator have been experienced but the overall impression of the HT stability and beam at 1.5 MeV is that it will be excellent. The vibration isolation system is fully operational and the seismic restraints are in position. If the present schedule can be maintained, full acceptance of the instrument will be made early in 1981. An HVEM Steering Committee has been constituted, and all the proposals for using the HVEM are being reviewed.

2. THE ROLE OF VACANCIES IN PRECIPITATION OF INTERSTITIAL PHASES

Ulrich Dahmen, Alan Pelton, Mike J. Witcomb and Kenneth H. Westmacott

Background. In spite of many similarities in the precipitation behavior of different interstitial alloys, no single model has been proposed to date that can account for the conflicting experimentally observed features. Some results indicate interstitial diffusion is the rate-controlling process while others suggest vacancies. It is now clear that vacancies influence precipitation not only in fcc interstitial alloys such as Pt(C)[1] but also in bcc alloys as for example Ta(C).[2] It appears that as a result of the binding to interstitial atoms, vacancies can be retained in a concentration sufficient to make "heterogeneous" nucleation, i.e., the formation of a precipitate nucleus with the aid of vacancies, the dominant mode of precipitation.

The present work is a systematic attempt to elucidate the role of vacancies in interstitial phase precipitation. Three different aspects of vacancies may be distinguished, 1) their influence on kinetics, as postulated in the vacancy pump model,[3] 2) their thermodynamic role, as in Khachaturyan's[4] and Russell's[5] theories, and 3) their structural aspect, as in Westmacott and Pèrez's[1] model of co-precipitation. In view of the high mobility of interstitial solute atoms, the kinetic influence was considered to be minor. However, the question of a structural versus a purely thermodynamic aspect is important because it affects both the degree and the quality of vacancy involvement. The fundamental distinction appears to be in the conservation of lattice sites. If all lattice sites are preserved, a precipitate is truly coherent and the process of precipitation can be described as a homogeneous transformation. In this case the influence is mainly through the excess volume. A collapse of vacancies, on the other hand, destroys lattice sites and there is no longer a one-to-one correspondence between lattice sites in the matrix and the precipitate. Such a particle is no longer fully coherent and the transformation is in part heterogeneous, i.e., it is accompanied by a lattice-variant shear in the form of a matrix dislocation. This is the structural role of vacancies. It has recently been pointed out by Olson and Cohen[6] that the homogeneous part of the transformation may be represented by "coherency dislocations," the lattice-variant shear by "anticoherency" or misfit dislocations. These concepts are extremely useful because they show that the combined use of conventional and high resolution transmission electron microscopy can experimentally distinguish between a purely thermodynamic and a structural role of vacancies. This has been demonstrated for the Pt(C) system.

Pt(C) alloys. The unusual defects on {100} planes of Pt have been analyzed as 1/3 ⟨100⟩ stacking faults stabilized by a single layer of carbon atoms.[1] Since the faulted loops, or single layer precipitates, result from the collapse of a sheet of vacancies, lattice sites are not conserved and the transformation is heterogeneous. However, the same local atomic arrangement can be achieved by a homogeneous transformation involving a shear vector of 1/6 ⟨130⟩. The situation is completely analogous to the more familiar case of partial dislocations in fcc materials where a fault created by a 1/3 ⟨111⟩ Frank loop is identical to one generated by a 1/6 ⟨112⟩ Shockley partial. In one case (the Shockley partial) the lattice sites are conserved, while in the other (the Frank loop) they are eliminated. The fault made by either partial constitutes a thin layer of hexagonal stacking and originates from a homogeneous transformation and a heterogeneous transformation, respectively. One can be described as a thin coherent hcp precipitate, the other one as a semi-coherent precipitate which has lost coherency through a reaction with a 1/2 ⟨110⟩ "anticoherency dislocation," namely

*This work was supported by the Director, Office of Energy Research, Office of Basic Energy Sciences, Materials Sciences Division of the U. S. Department of Energy under Contract No. W-7405-ENG-48.

$$1/6\ \langle \bar{1}\bar{1}2 \rangle + 1/2\ \langle 110 \rangle = 1/3\ \langle 111 \rangle\ .$$

By analogy with this familiar dislocation reaction the corresponding reaction for the faulted precipitates in Pt(C) can be written

$$1/6\ \langle \bar{3}\bar{1}0 \rangle + 1/2\ \langle 110 \rangle = 1/3\ \langle 010 \rangle\ .$$

Figure 1 shows a contrast analysis of a more complex precipitate (arrow) obtained after prolonged aging of quenched Pt. The dislocation segment which is invisible in (d) and visible in (c) is consistent with 1/6 ⟨310⟩ ; the segment which is out of contrast in (c) has a Burgers vector normal to the plane of the precipitate consistent with 1/3 ⟨010⟩, and the short segment visible in (a), (c) and (d) is a 1/2 ⟨110⟩ dislocation. This observation supports the hypothesis of two different mechanisms generating the same structure. It also suggests that multiple layer defects could be formed by either one of both mechanisms. The technique of high resolution lattice fringe imaging was employed to make this distinction. Being sensitive to the conservation or elimination of lattice sites, it can decide whether a precipitate has thickened by a homogeneous (site-conserving) transformation or by the addition of more vacancy-carbon complexes (site-eliminating). Figure 2 shows an example of a lattice fringe image taken of a multilayer precipitate. As most such precipitates, it is seven layers thick, and a Burgers circuit reveals that one layer is missing. Thus the mechanism of formation involves only a single layer of vacancies followed by subsequent shear.

Ta(C) alloys. The appearance of carbide precipitates in Ta is similar to that encountered in the Pt(C) system. Precipitates exhibit contrast similar to dislocation loops, and a detailed contrast analysis[2] has shown them to be plate like with a {310} habit plane and a displacement vector of roughly 1/3 ⟨310⟩ . Even more so than in the Pt(C) system, the loop analogy fails when the precipitates grow in thickness. At this stage of the precipitation process, the concept of "coherency" and "anti-coherency" dislocations suggested by Olson and Cohen bridges the gap between the description as dislocation loops and as precipitates. A homogeneous transformation may be described by a series of "coherency dislocations" distorting the matrix into the precipitate structure. If countered by "anticoherency" dislocations, the coherency stresses are partially relieved and the precipitate becomes semi-coherent. Figure 3 shows a lattice fringe image of a carbide precipitate in Ta. The coherency distortion has effected a 10° shear of close-packed planes when crossing from the matrix into the precipitate. Since all the lattice fringes are continuous, there is no indication of the presence of "anticoherency" dislocations. A complete analysis would require another high resolution image of fringes parallel to the habit plane. Even though at present, the small spacing of {310} planes is beyond the limit

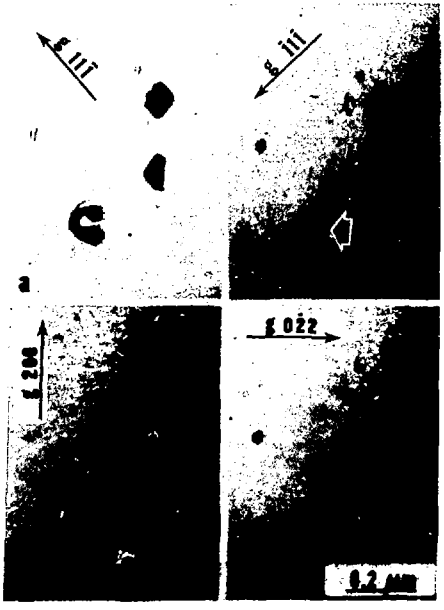

Fig. 1. Contrast analysis of multiple layer carbides on {100} planes of Pt. (Courtesy of M. Pèrez). (XBB 8012-14621A)

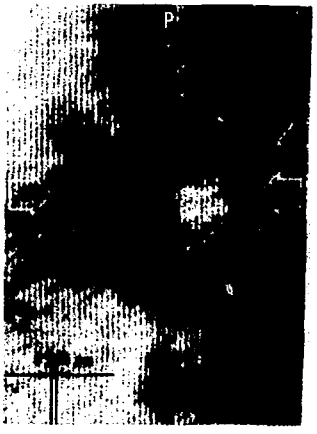

Fig. 2. Lattice image of 7-layer {100} carbide precipitate in Pt showing missing fringe due to vacancy collapse. (XBB 8012-14620)

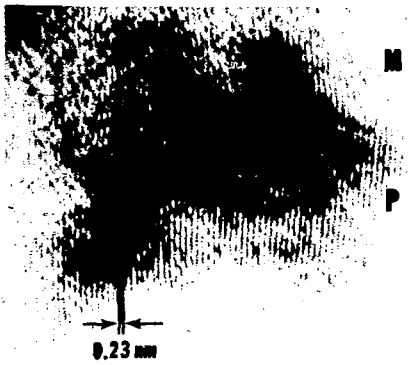

Fig. 3. Lattice fringe image of {310} carbide precipitate in Ta illustrating the shear component of the transformation. (XBB 807-8737)

of resolution of the available microscopes, there is evidence to suggest that, at this stage, the precipitates are fully coherent. Hence no vacancy collapse similar to the Pt(C) system is involved. Yet it is conceivable that at some earlier stage of the precipitation, the particles are semi-coherent.

The local collapse of vacancies on {310} matrix planes accompanied by the simultaneous precipitation of carbon could constitute a nucleus with the carbide structure and a net strain field of vacancy type. As a consequence of such a mechanism, the precipitation sequence would pass through several stages due to the reversal of the net strain field during precipitate growth, and multi-stage hardening has indeed been found in V-C and Nb-C.

If vacancies retain their identity throughout the process of precipitation, they have no structural role as described above. Their significance in this case lies mainly in the partial accommodation of coherency stresses. The precipitates would be fully coherent during the entire sequence, and no explanation could be given for the reported age-hardening behavior. Both modes of vacancy-assisted nucleation are consistent with all of the other experimental observations and it seems clear that vacancies play a critical role in the formation of the carbide precipitates.

Fe(C) alloys. The technological importance of iron-based alloys has inspired numerous investigations of precipitation reactions. However, the sequence of events leading to the formation of these interstitial phases has eluded understanding, even in binary Fe(C) alloys. Since carbides can drastically alter a steel's physical properties (e.g., tensile strength, ductility and formability), a clarification of the phase transformations is imperative. In view of the successful interpretation of carbide precipitation via vacancy-carbon interactions in both Pt(C) and Ta(C) systems, an analogous approach was taken to illuminate the precipitation reaction in an Fe - 2 wt% Si - 0.15 wt% C alloy. Samples of this material were quenched from the two phase ($\alpha+\gamma$) region into ice water and subsequently aged between 25 and 100°C for various times.

Aging for 168 hours at 25°C produced a high density of coherent particles homogeneously dispersed in the ferrite grains. Analysis of these precipitates shows that they lie on $\{100\}\alpha$ planes with a displacement vector normal to their habit planes. These plate-like precipitates are approximately 300 Å in diameter and are in the range of 10-50 Å thick.

The effect of a combination of aging at 25 and 100°C is shown in Fig. 4. These treatments enable a direct comparison to be made between precipitates which nucleated and grew at 100°C and at 25°C (Fig. 4(b)) and those which nucleated at 25°C with subsequent growth at 100°C (Fig. 4(a)). Analysis of these micrographs shows that: (1) all of the precipitates have a $\{100\}\alpha$ habit plane; (2) the size of the precipitates formed at 100°C (~ 600 Å in diameter) is independent of prior heat treatment; and (3) "preaging" at 25°C produces a higher density of the larger precipitates.

Although these microstructural observations may be interpreted solely in terms of the precipitation of supersaturated carbon atoms, other evidence indicates a vacancy-assisted transformation. For example, precipitate-free-zones are found around vacancy sinks. The precipitate density in Fig. 4 is estimated to be approximately $10^{16}/cm^3$ and the corresponding vacancy concentration at the quench temperature (850°C) is $\sim 4 \times 10^{16}/cm^3$. This suggests that the nucleus of the precipitates could consist of a vacancy/carbon complex. It is interesting to note that a precipitous drop in vacancy concentration (observed by positron annihilation experiments) with a concomitant decrease in the concentration of carbon in solid solution (by internal friction measurements) between 25 and 100°C has been found in neutron-irradiated Fe(C).

Thus, it appears that the nucleation event in dilute bcc Fe(C) alloys is analogous to that observed in Ta(C) systems.

* * *

1. K. H. Westmacott, M. I. Pèrez, J. Nucl. Mat. 83, 231 (1979).
2. U. Dahmen, K. H. Westmacott and G. Thomas, Acta Met. (in press).
3. L. A. Girifalco and H. Herman, Acta Met. 13, 583 (1965).
4. A. G. Khachaturyan, Sov. Phys.-Solid State 13, 2024 (1972).
5. K. C. Russell, Scripta. Met. 3, 313 (1969).
6. G. B. Olson and M. Cohen, Acta Met. 27, 1907 (1979).

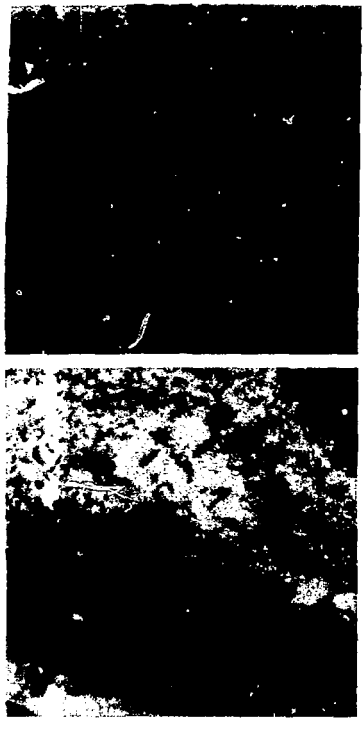

Fig. 4. (a) A comparison of precipitates produced by preaging at 25°C for 168 hr followed by 100°C for 0.5 hr, and an additional 336 hr at 25°C; and (b) aging at 100°C for 0.5 hr and 25°C for 336 hr. (XBB 812-2109)

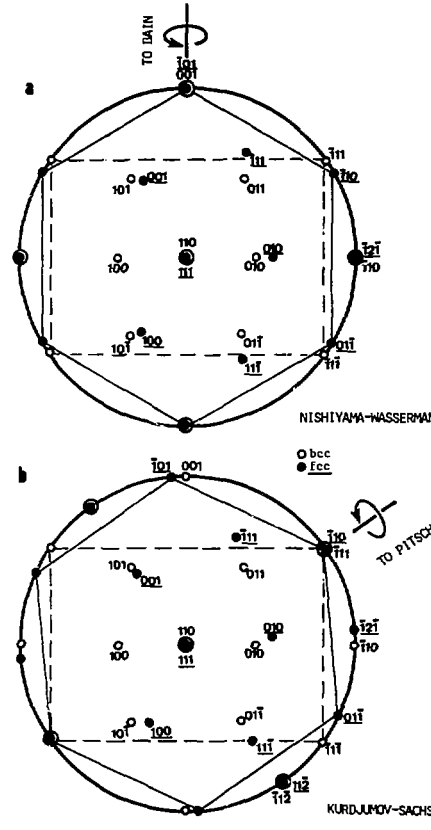

Fig. 5. Sterograms of bcc/fcc orientation relationship (a) Nishiyama-Wassermann; (b) Kurdjumov-Sachs. (XBL 8012-13554)

3. THE ORIGIN OF ORIENTATION RELATIONSHIPS

Ulrich Dahmen

The orientation relationship (OR) between two phases of different crystal structure is of great importance because it has a strong bearing on the microstructures and properties of multiphase materials. There is increasing evidence that deviations from exact OR's are common.[1] The present work seeks to explain and predict such deviations through a systematic examination of the features inherent in all OR's.

Figures 5 and 6 illustrate the most frequently found OR's of bcc/fcc and bcc/hcp systems in stereograms projected along common poles of close-packed planes. The symmetries of the lattices within these close-packed planes are symbolized by a rectangle for {100} bcc and a hexagon for both {111} fcc and {0001} hcp.

It is evident from Figs. 5 and 6 that all the well-known OR's are much closer to each other than commonly recognized. They can be derived from each other by continuous rotations whose exact angle depends on lattice symmetries irrespective of lattice parameters. However, many systems deviate from the ideal OR's determined by lattice symmetries and atomic match demands a dependence on lattice parameters. It is possible to maximize atomic matching in one direction by adding a rigid body rotation to the pure deformation that relates two lattices to each other. The angle of rotation

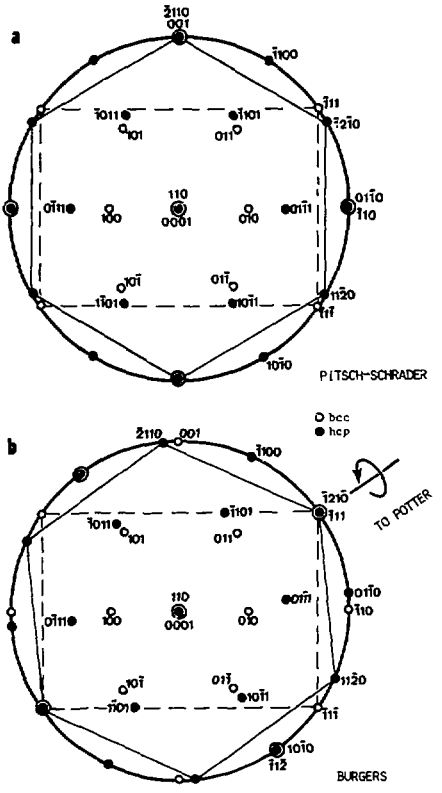

Fig. 6. Stereograms of bcc/hcp relationships (a) Pitsch-Schrader; (b) Burgers. (XBL 8012-13555)

Θ is a continuous function of a dimensionless parameter R, the ratio of the lattice constants of the two phases. For the specific case of an OR between bcc and hcp lattices ($R = a_{hcp}/a_{bcc}$) and for their lattice correspondence of maximum symmetry, Θ can be calculated as

$$\Theta = \cos^{-1}\left[\frac{1 + \sqrt{1.5}\,R^2}{(1 + \sqrt{1.5})R}\right] . \qquad (1)$$

Θ varies rapidly between zero degrees for $R < 0.82$ and $R \geq 1$ and a flat maximum of 5.8° at $R \approx 0.9$.

A comparison with published experimental results on twelve different bcc/hcp precipitation systems shows a good agreement with the OR's calculated on the basis of an invariant line strain. This agreement is illustrated particularly well using the example of hexagonal Mo_2C precipitates; when formed in ferrite (R = 1.05), no rotation is experimentally observed,[2] but when precipitated in molybdenum (R = 0.95), a 5.36° rotation is reported.[3] A survey of experimental observations on 15 different bcc/fcc systems shows the same tendencies; for example, Fe deposited on a {111} Ni substrate follows mainly the KS OR (Fig. 5(b)) while it only forms in the NW OR (Fig. 5(a)) when deposited on Au or Ag as predicted by the theory.

The theory has also been successful in predicting simple morphologies on the basis of directional matching. It was shown that the planar matching criterion commonly applied is in error and predicts particle axes normal to those given by directional matching. Further development of the theory is expected to permit the prediction of more complex morphologies of coherent and semicoherent precipitates in materials of any crystal structure.

* * *

1. U. Dahmen, Ph.D. thesis, January (1979), LBL-8661.
2. D. J. Dyson, S. R. Keown, D. Raynor and J. A. Whiteman, Acta Met. 14, 867 (1966).
3. P. Burck, Ph.D. thesis, Freiberg, Germany (1977).

RESEARCH PLANS FOR CALENDAR YEAR 1981

The fundamental connection between vacancy condensation and the growth of a new precipitate phase, which has now been established for a number of diverse systems, e.g., carbon solutions in Ta, Pt and Fe-Si, will be studied using in-situ HVEM techniques. This may allow us to follow the entire sequence of events during precipitate nucleation, growth, loss of coherency, formation of equilibrium phase, and eventual dissolution, to test and assess the relative importance of several possible growth mechanisms. Specifically, the thickening of carbide plates in Pt(C) will be studied, the structural changes accompanying the morphological and habit plane changes in Ta(C), precipitate reactions in Fe-base alloys, as well as other systems yet to be decided.

In-situ studies of the initial stages of oxidation in Al-base alloys will be continued in order to elucidate the role of stress build-up, and if successful will be extended to other systems.

"O"-lattice theory is being used to describe the dislocation networks formed between phases of disparate lattice parameters or structures. The predictions of the theory will be tested experimentally using several systems.

1980 PUBLICATIONS AND REPORTS

Refereed Journals

1. K. H. Westmacott, "Life Beyond 1 MeV," 38th Annual Proceedings of the Electron Microscopy Society of America Conference, Reno, Nevada, 1980, G. W. Bailey (ed.), p. 30, (1980), LBL-10666.

2. J. A. Little, J. W. Evans and K. H. Westmacott, "The Characterization of Coal Structures for Coal Gasification Reactions Using TEM/STEM Techniques," 38th Annual Proceedings of the Electron Microscopy Society of America, Reno, Nevada, 1980, G. W. Bailey (ed.), p. 220, (1980).

Other Publications

1. J-Y. Laval and K. H. Westmacott, "Electron Beam Sensitivity and Structure of the Glassy Phase of Ceramics," Inst. Phys. Conf. Ser. No. 52 C, 1980, Chapter 5, 295, LBL-10476.

2. J-Y. Laval and K. H. Westmacott, "Characterization of Intercalation Compounds by Electron Inelastic Scattering Analysis," American Institute Conference Proceedings, No. 53, 72, (1979).

3. G. Thomas, R. K. Mishra and K. H. Westmacott, "Impact of HVEM in Materials Science," Electron Microscopy 4, 392 (1980).

4. J-Y. Laval, "Pretransition Phenomena and Long-Range Ordering in Non-Stoichiometric Oxides," Proceedings of the Mod. Structures Meeting, Kailua Kona, Hawaii, March 22-25, 1979, AIP Conference Proceedings No. 53, 379, (1979).

LBL Reports

1. J-Y. Laval and K. H. Westmacott, "The Mechanism of Ionization Damage in Glassy Ceramics," Journal American Ceramic Society, in press, LBL-9008.

2. J. A. Little, M. Rühle, H. Schmid and K. H. Westmacott, "The Origin of Unusual Dislocation Structures Observed in Ion-Thinned Nickel Oxide," Phys. Stat. Sol. (a), in press, LBL-10591.

3. U. Dahmen, G. Thomas and K. H. Westmacott, "A Study of Precipitation in Interstitial Alloys, I. Precipitation Sequence in TaC Alloys," Acta Met., in press, LBL-11244.

4. U. Dahmen, K. H. Westmacott and G. Thomas, "An Electron Microscopy Analysis of a Simple Metal/Ceramic Interface," presented at the LBL/MMRD International Materials Symposium on "Surfaces and Interfaces in Ceramic and Ceramic-Metal Systems," Lawrence Berkeley Laboratory, Berkeley, CA, 1980, in press, LBL-11405.

5. U. Dahmen, "Further Discussion of Orientation Relationships, Surface Reliefs and FCC-BCC Transformations in Steels," Scripta Met., in press, LBL-11803.

6. U. Dahmen, "The Role of the Invariant Line in the Search for an Optimum Boundary by O-Lattice Theory," Scripta Met., in press, LBL-11804.

7. M. I. Pérez, "Secondary Defects in Quenched Platinum," M.S. thesis, LBL-10178.

2. Mechanical Properties

a. Theoretical Problems in Alloy Design*

J. W. Morris, Jr., Investigator

Introduction. The research program described below is a multi-faceted one of research oriented toward the development of new materials to meet advanced energy needs. The overall program includes fundamental research supporting new materials development and applied research in the development of new structural alloys, weldments and welding procedures, and high field superconducting materials.

Theoretical Studies

1. STUDY OF PRECIPITATE MORPHOLOGY BY CONSIDERATION OF ELASTIC STRAIN ENERGY

D. E. Wedge

The equilibrium shape of a coherent second phase inclusion is determined by minimizing the sum of the elastic strain energy induced by the particle and of the interface energy of its boundary with the surrounding matrix. Five different shape models are used to calculate the elastic strain energy of α'' ($Fe_{16}N_2$) particles in the Fe-N system. Four of the models are based on the elastic energy of A. G. Khatchaturyan for a coherent inclusion of arbitrary shape in an anisotropic medium, with the restriction that the elastic constants have the same values in both phases. Of these models, three represent numerical computations for different plate-like shapes--disk, lens, and ellipsoid. The fourth, the "loop" model, is derived from an analytical approximation by Khatchaturyan treating the particle as a dislocation loop around its edge. The last model, "B and Ng," is derived by Boyd and Nichlson from the work of J. D. Eshelby for an ellipsoid particle in an elastically isotropic medium. For each model, the elastic energy is calculated as a function of the aspect ratio (diameter/thickness) of the particle. Combining this with the interface energy (γ), we can predict the aspect ratio of the particle as it grows, by minimizing this energy sum.

Alternatively, the result can be expressed by solving for γ as a function of observed particle dimensions. By plotting aspect ratio versus particle size and by fitting the calculated relation to the data points, a value for γ is extracted. Three reports of experimental observations of α'' particles for a wide range of particle size are used to compute values for γ, first assuming the interface energy to be isotropic. The results of the curve fitting are illustrated in of Fig. 1(a), showing the computed γ value as a solid bar for each of the three data sets and for each of the five elastic energy models. Also shown for each model is the γ value obtained by the three data sets into a single set of experimental points,

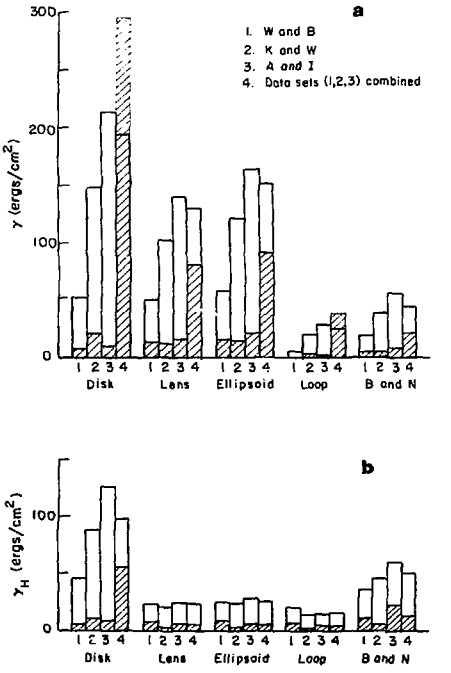

Fig. 1. Inferred surface energy of the $Fe_{16}N_2$ precipitate using various models for precipitate shape (XBL 811-7527)

*This work was supported by the Director, Office of Energy Research, Office of Basic Energy Science, Materials Science Division of the U.S. Department of Energy, and funds for the welding equipment was supplied by the Division of Magnetic Fusion Energy, Office of Fusion Energy, U.S. Department of Energy under Contract No. W-740S-ENG-48.

representing a much wider range of particle size than any one set taken alone. The hatched bars indicate the magnitude of the average error in each curve fit. The curve fit is reasonably good for each data set but not for the combined set.

A second interface energy model takes into account some anisotropy by considering the habit plane interface energy (γ_H) separately from that of the particle periphery (γ_p). γ_p is fixed at 300 erg/cm^2, as determined by coarsening theory, and the curve fitting is repeated to obtain a value for γ_H (see Fig. 1(b)). The curve fits are seen to give much smaller errors for the combined data set with the anisotropic surface energy model than with the isotropic model, indicating the improved applicability of the anisotropic model over a wide range of particle sizes.

Fig. 2. ($Fe_{16}N_2$) α" precipitate morphology aged at 75° for 10 min. from Fe-0.011 wt% N alloy. The beam direction is near [139] and $g = 23\bar{1}$. (XBB 812-1779)

Experimental Research

2. OBSERVATIONS OF THE MORPHOLOGY OF PLATE PRECIPITATES

Yih-Cheng Shih

The equilibrium shape of a coherent precipitate particle is determined by the minimum of the sum of the elastic strain energy and the surface energy associated with the particle. From the elastic strain energy formula developed by A. G. Khatchaturyan, we can express the elastic strain energy in a very simple form as a function of the aspect ratio (= diameter/thickness) for thin plate precipitates. If the precipitates have equilibrium shapes, we also can calculate the surface energy from observations of the aspect ratio of precipitates. The calculated surface energy of coherent precipitates should be constant as the particles grow and this can be used as a test of the strain energy theory.

In this work, the thin plate nitride precipitate α" ($Fe_{16}N_2$) was observed under TEM. By setting the concentration of nitrogen in iron very low (0.011 wt%), a relatively low density of α" precipitate was established in order to determine the detailed precipitate shape. Figure 2 shows that the morphology of α" precipitates is a rosette on (001) habit plane. The growth branches stretch out in [100], [010], [110] and [110] directions.

It is planned to observe the dimension of α" precipitate particles systematically over a large range of particle size up to the maximum size of coherent precipitates, with weak beam dark field technique (and/or lattice image) to obtain aspect ratio data as accurately as possible.

3. MÖSSBAUER EFFECT METALLOGRAPHY

Brent Fultz

Substantial alloy element segregation to precipitating austenite occurs during two-phase tempering of martensitic Fe-Ni steels. Such temper-induced chemistry difference between the austenite and martensite phases can have an important influence on the microstructural stability and hence mechanical properties of these steels. There is therefore a need for rapid quantitative techniques to monitor this segregation. We have been investigating the possibility that Mössbauer spectroscopy may be useful for this purpose.

This year we completed a systematic study of effects of Ni and Mn, Cr, Si, or C (denoted "X") on the Fe-Ni-X martensite Mössbauer spectra, and we are now able to quantify changes smaller than 0.1 at% in the chemical composition of the martensite by using a difference spectrum procedure. For example, difference spectra showing the intensity changes of four martensite lines after tempering are shown in Fig. 3. From these data we have determined a reduction of 0.5%Ni and 0.2%Mn in the martensite after the precipitation of 6% austenite (austenite peak not shown). This technique for chemical analysis of the martensite has sufficient sensitivity to follow the global kinetics of alloy element segregation simultaneously with the kinetics of austenite precipitation. We will be pursuing such a study over the next year.

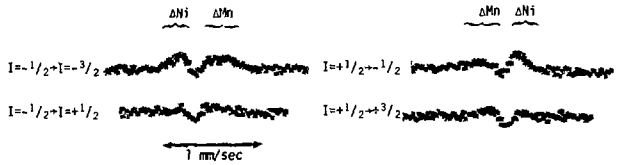

Fig. 3. Difference of Mössbauer peaks from Fe-9Ni-0.7Mn martensite after tempering minus before tempering. ΔNi effect is due to a peak broadening and shifting. ΔMn effect is due to an intensity change in a satellite peak from Fe^{57} nuclei with one Mn neighbor. (XBL 812-8256)

Structural Alloy Development

4. INVESTIGATION OF INTERGRANULAR EMBRITTLEMENT IN Fe-Mn STEELS BY HIGH RESOLUTION SCANNING AUGER MICROSCOPY

Hyung Jai Lee

For several years we have been developing iron-manganese alloys as an alternative to Fe-Ni steels for cryogenic use. Ferritic Fe-Mn grades within the composition range 5-12%Mn were successfully designed, using appropriate chemical modification together with thermal and thermomechanical treatment to establish good low-temperature properties. A particularly relevant question during this research has been the source of low temperature embrittlement of Fe-12Mn steels since the fracture mode below the DBTT dramatically changes from quasi-cleavage to a catastrophic intergranular fracture mode with changing composition from 8%Mn to 12%Mn. Previous research suggested that the source of this intergranular fracture was due not to the segregation of chemical impurities but to the inherent properties of prior austenite boundaries in the 12%Mn steel.

Employing high resolution scanning Auger microscopy, the intergranular fracture surfaces of Fe-12Mn steel in the as-austenitized condition were carefully investigated in an effort to find any possible segregation of the deleterious impurities such as P, S, and Sb. As shown in Fig. 4, high resolution chemical analysis of the intergranular fracture surfaces revealed no consistent segregation of P, S, or O but did show a slight segregation of C. The occasional appearance of S or O on the fracture surface was also studied and found to be associated with MnS or MnO_2 precipitates along the prior austenite grain boundaries (Fig. 5).

Using the Ar^+ ion gun, sputter profiles of the Mn composition near grain boundaries were made. These showed no enrichment of manganese along the prior austenite grain boundaries. Further studies showed that carbon atoms, not carbides, are on the grain boundaries and carbon atoms were segregated along the grain boundaries to about 50 Å depth. Since carbon is believed not to promote intergranular fracture unless it is in the form of carbides, it is most likely that carbon segregation does not affect the intergranular embrittlement.

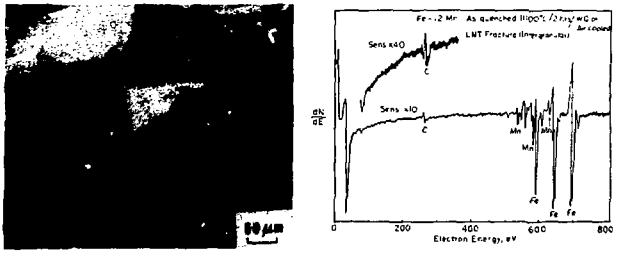

Fig. 4. SEM of Fe-12Mn steels in the as-austenitized condition and high resolution Auger electron spectrum of the intergranular fracture surface. (XBB 812-1600)

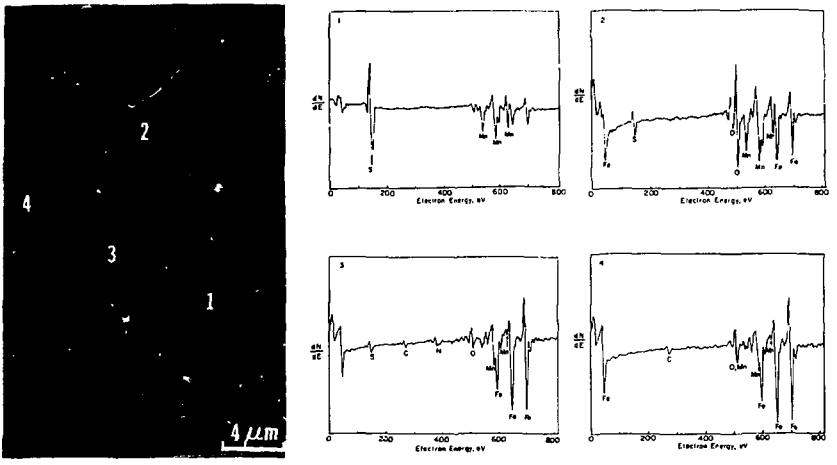

Fig. 5. High resolution chemical analysis of four different regions on the intergranular fracture surface shows (1) MnS, (2) MnO_2, (3) surface of the crater separated by precipitate, (4) grain boundary.
(XBB 800-13508)

Welding Research

5. DEVELOPING A WELDING RESEARCH LABORATORY

Leonard T. Summers

Recently there has been growing interest in developing processes to produce sound weldments in a variety of steels, such as low alloy steels, precipitation hardening stainless steels, and nitrogen-strengthened stainless steels. This research necessitates facilities capable of generating quantitative data or welding parameters and reproducibility of research weldments under a wide range of operating conditions.

To meet these needs, a research welding laboratory has been developed. To allow researchers to tackle a wide variety of problem areas, a high degree of flexibility and versatility were incorporated into the laboratory's design. Utilization of a Miller 300 power supply allows production of gas tungsten arc welds (GTAW) with a power output ranging from 15-300 A, GTAW weldments can be produced in both the conventional dc mode or ac mode for aluminum-based metals. Current output can be adjusted from the conventional flat mode to the pulsed arc mode, with background to peak ratio, percent peak on time, and pulse frequency under the operator's control. Addition of filler metals can be achieved by manual hand feed, or by automatic wire feed methods.

Shielded metal arc welds (SMAW) and gas metal arc welds (GMAW) can both be produced by two power supplies, a Synchrowave 400 and an Airco PA-3A. Output currents can be adjusted from 75-400 A, which allows the deposition rate to be varied from relatively low to significantly high values. Similar to GTAW, GMAW welds can be produced in both flat current and pulsed arc modes; the pulsed mode being capable of welding thin sections where spray transfer is desired but where low average input current is required.

Fully automatic welding concepts have been employed to achieve exact reproducibility of welding. All welding equipment has been interfaced with "pack rat" automatic welding guides and Cobra automatic wire feeders. Therefore the operator can select a constant travel speed, stickout length, and heat input. Furthermore, all equipment can be interfaced with high speed recorders giving a permanent record of amperage/voltage characteristics during experimental weld passes.

Future work includes the interfacing of work pieces with multichannel temperature recorders to obtain data in both the longitudinal and transverse directions to the weld pass. This will give researchers precise control not only of welding modes but of heat input preheat, postheat, and interpass temperatures as well.

6. CHARACTERIZATION OF FERRITIC G.M.A. WELD DEPOSITS IN 9%Ni STEEL FOR CRYOGENIC APPLICATION

Kim W. Mahin†

Four ferritic multipass gas metal arc (GMA) weldments were evaluated for the development of matching ferritic weld consumables suitable for the gas metal arc welding of Fe-9Ni steel. Toughness testing of the weldments, as shown in Table 1, indicated that each of the weld deposits at the centerline and the fusion zone has a lower 77 K (-196°C) absorbed impact energy than its corresponding base plate. The possible factors influencing this behavior were determined to include the large columnar grain size, the high level of interstitials (oxygen, hydrogen, and nitrogen in the weld puddle), the density of inclusions and second phase particles, and the absence of retained austenite.

Correlations between chemistry and mechanical properties indicated that as the solute (interstitial and substitutional) level in the weld deposit increased (in the absence of beneficial grain refinement), the level of impact energy absorbed by the weld at 77 K (-196°C) decreased.

Correlations between microstructure and mechanical properties indicated that the 77 K (-196°C) notch toughness of the weld deposit depended on the recovery potential of the matrix and the volume, size, and morphology of second phase particles (inclusions and "M-A" phase) within the matrix. The highest impact toughness values corresponded to maximum amounts of polygonal ferrite structure and minimal amounts of inclusions and "M-A" phase, i.e., minimum solute levels. However, these minimum solute levels also promoted maximum porosity levels.

Thus, optimization of both weld toughness (at 77 K) and weld soundness in ferritic G.M.A. weldments, as evidenced in this study, requires acceptance of a nominal solute, i.e., inclusion, level in the weld deposit, and of a reduction in the critical cleavage stress in the weld matrix. Minimizing cleavage failure and maximizing the amount of impact energy absorbed at 77 K under these conditions corresponds to minimizing the size of the polyhedral carbides or carbonitrides and reducing the volume of "M-A" phase or strain-induced carbides formed.

* * *

†Present address: Lawrence Livermore Laboratory.

7. RESEARCH IN SUPPORT OF MATERIALS SELECTION FOR THE CASES OF FORCED-COOLED SUPERCONDUCTORS

Michael J. Strum

In a number of advanced superconducting magnets, it is desirable to employ a "forced-cooled" superconductor configuration. In this configuration the superconductor is made as a loose cable and is wrapped with a non-magnetic alloy that serves to contain helium used to cool the conductor. Strength considerations dictate that the non-magnetic conduit case be some kind of non-magnetic steel. Assembly constraints require that the steel be wrapped around the superconductor cable and continuously seam welded in order to close it. If the superconductor is an A15, such as Nb_3Sn, then the combined superconductor and conduit, must be given a prolonged treatment at elevated

Table I. Charpy V notch and 3-point bend fracture toughness test results for the four weldments at 77 K (-196°C).

WELDMENT	NOTCH LOCATION	C_v ft-lb (J)	LAT. EXP. mils (mm)	$K_{IC}^{E.E.}$ ksi-$\sqrt{in}$ (MPa-$\sqrt{m}$)	K_{IC}^{J} ksi-$\sqrt{in}$ (MPa-$\sqrt{m}$)	C.O.D. mils (mm)
778-5	W.M.*	122 (165)	63 (1.6)	---	---	---
	F.Z.**	99 (134)	55 (1.4)	---	---	---
778-6	W.M.	22 (30)	14.7 (.4)	---	---	---
	F.Z.	38 (52)	23 (.6)	---	---	---
7B6-1	W.M.	40 (54)	25 (.6)	199 (217)	152 (166)	3.1 (.08)
	(with porosity)	--	--	127 (138)	99 (108)	2.8 (.07)
	F.Z.	63.4 (86)	34 (.9)	194 (211)	156 (170)	4.2 (.11)
LCMM-1	W.M.	25 (34)	19.5 (.5)	---	---	---
	Stress-Relieved W.M.	29 (39)	18 (.45)	---	---	---

* W.M.: Weld Metal
** F.Z.: Fusion Zone

temperature after assembly to react the A15 superconductor. Since there were uncertainties regarding the selection of conduit case materials, particularly for the specific case of the Nb_3Sn conductor to be used in the Westinghouse contribution to the MFE large coil program, we were asked to conduct research to assist in materials selection.

The first research task involved the investigation of the properties of the alloy Nitronic 40, which had been suggested as a candidate for the forced-cooled conductor case. Mechanical properties research on this alloy revealed that it became extremely brittle in the fully reacted condition. Subsequent metallurgical studies showed that the source of the brittleness lay in a sensitization reaction which took place in the steel during the prolonged heat treatment required to form the superconducting phase. The brittleness was particularly pronounced in the autogenous seam weldment. In this case the brittleness was compounded by the transformation of a continuous matrix of ferrite within the weldment into the brittle sigma phase. For these reasons it was decided that Nitronic 40 is not a suitable material for the forced-cooled conductor case.

The search for an alternative material was conducted under the constraint that the material be one which could be purchased in sheet form on a reasonable procurement schedule. We participated in this research as one member of a committee of representatives of several national laboratories assembled by the Office of Magnetic Fusion Energy to address the problem. In collaboration with the Lawrence Livermore Laboratory we selected the material JBK-75, which is a modified iron-based superalloy recently developed at the Sandia Laboratories. This alloy seemed attractive because of its natural heat treatment range for precipitation hardening lay in the same range of temperatures employed for reaction of the A15 compound. Mechanical property tests on this alloy after autogenous GTA welding seem to indicate its suitability for the forced-cooled conductor application. After additional testing at Westinghouse and other laboratories, it was tentatively selected for use in the forced-cooled superconductor case of the Westinghouse magnet for the Large Coil Program.

Superconductivity Research

8. MICROSTRUCTURE AND PROPERTIES OF A15 SUPERCONDUCTORS FORMED BY DIRECT PRECIPITATION

Minghwei Hong, I.-Wei Wu, and Daniel R. Dietderich

In this work the "direct precipitation process," previously developed in this laboratory was employed to create the A15 superconductors from the V-Ga and Nb-Al systems. The critical current characteristics of the resulting materials were good but not better than those obtainable in the best multifilamentary wires. Microstructural investigations were hence undertaken to characterize the precipitation process and to provide guidelines for property improvement.

The direct precipitation process yields a superconducting material in which discrete crystallites of the A15 phase are distributed through a matrix of residual solution. The critical current characteristic of the material at 4.2 K is expected to be a function of at least four parameters: the stoichiometry of the A15 phase, the grain size of the A15 precipitates, the continuity of the precipitate network, and the aggregate volume fracture of A15. The first parameter is related to the composition of the A15 phase; the latter three concern its microstructural characteristics.

The composition of the A15 phase should determine inherent superconducting properties such as its critical temperature (T_c) and upper critical field (H_{c2}). In V-Ga aged at 700°C both the critical temperature and critical field increases with the Ga content of the starting alloy. Both tend to reach a maximum, then decrease after long aging times, a behavior pattern which suggests an eventual decrease in the Ga content of the A15 phase. The maximum T_c and H_{c2} (4.2 K) of V-18 Ga, 15 K and 210 kG, correspond to a nearly stoichiometric A15 phase. In the Nb-Al material the critical temperature and the critical field increase with the starting content of Al and also monotonically with aging time. The data suggest a gradual increase in the Al content of the A15 phase, which, however, remains lean in Al since the maximum values of T_c and H_{c2} are significantly below their values for stoichiometric Nb_3Al.

Example microstructures of deformed and aged V-Ga and Nb-Al samples are presented in Figs. 6 and 7. The morphological characteristics of the two precipitates are different; V_3Ga precipitates as a set of discrete particles which grow in a lenticular shape away from the boundaries into the interior of the grains. The precipitates tend to be surrounded by matrix phase, suggesting a preferential wetting by the matrix material. Alternatively, Nb_3Al precipitates as small, more nearly equiaxed particles that densely coat the dislocation subcell boundaries at an early stage of the reaction.

Fig. 6. TEM micrograph of V-15.6 at% Ga aged at 700°C for 108 hr. Regions A and B are A15 and BCC, respectively. (XBB 809-11069)

Fig. 7. TEM micrograph of Nb-18.0 at% Al aged at 750°C for 1.5 hr. Regions A and B are A15 and BCC, respectively. (XBB 802-2119)

From the perspective of establishing a microstructure conducive to good current-carrying properties, the Nb_3Al precipitation pattern revealed in these studies is clearly preferable to that of V_3Ga. On the other hand, the inherent superconducting properties of V_3Ga are better. The two materials we have produced to date hence include one having a basically good A15 phase in an undesirable morphology and one having a less attractive A15 in a very promising morphology. These features are reflected in their overall critical current characteristics, as shown in Figs. 8 and 9.

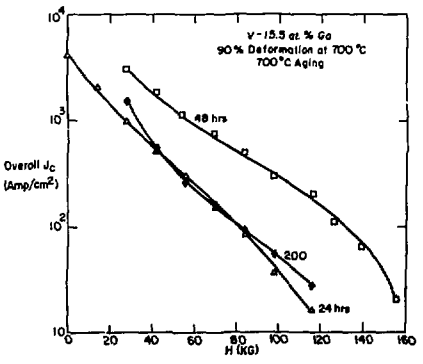

Fig. 8. Overall critical current density versus applied field for V-Ga samples with different aging times. (XBL 805-5104)

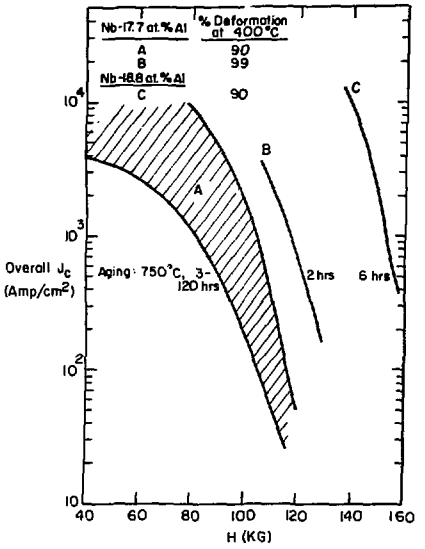

Fig. 9. Overall critical current density versus applied field for Nb-Al samples with different compositions (curves A and C) and different amounts of deformation (curves A and B). (XBL 806-5275)

9. THE EFFECTS OF THIRD ELEMENT ADDITION ON THE MECHANICAL PROPERTIES OF THE V-Ga ALLOYS

Daniel R. Dietderich, Minghwei Hong, and Joseph C. Barrett

High interstitial contents of oxygen and nitrogen after arc-casting had often been encountered in the early stages of this program when only vanadium and gallium were melted together. The samples with high oxygen and nitrogen contents could be reduced less than 75% in thickness. However, for the samples containing low oxygen and nitrogen, the thickness-reduction could be 90% or more.

In order to consistently obtain samples with low interstitial impurities using the arc-melting method a third element addition was used to remove oxygen and nitrogen from the cast sample. Among the third elements added to the V-Ga melt, small amounts of cerium, ~ 0.5 at%, were found to be very effective in reducing the oxygen and the nitrogen content. During the melting cerium, which has a stronger affinity for oxygen than vanadium, reacted with the oxygen in the sample and formed cerium oxides. Since the melting point of cerium oxide is higher than that of the V-Ga alloys, the oxides are in a solid form during the melting; the

solid oxides float on the surface of the melt and can be easily peeled off after cooling. The strong contrast between the cerium-refined and noncerium-refined samples is indicated in Fig. 10. It should be noted that small amounts of cerium have not affected the superconducting properties of the tested samples.

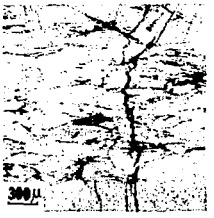

NOT CERIUM REFINED

OXYGEN 3000 ppm

NITROGEN 2000 ppm

DEFORMABILITY <75 %

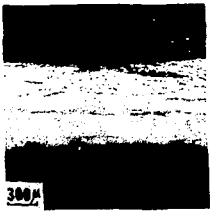

CERIUM REFINED

OXYGEN 1000 ppm

NITROGEN 200 ppm

DEFORMABILITY >95 %

Fig. 10. Highly deformable V-Ga alloys (for 12-18 at% Ga). (XBB 803-3351)

10. Nb-Al AND Nb-Al BASED A15 SUPERCONDUCTORS BY SOLID-LIQUID REACTION

Minghwei Hong, John T. Holthuis, and J. W. Morris, Jr.

Solid state diffusion methods which have reached the stage of commercial fabrication are only applicable to a limited number of A15 superconducting compounds, such as Nb_3Sn and V_3Ga. Fabrication of multifilamentary superconductors of the even more promising A15 compounds including Nb_3Al, $Nb_3(Al,Ge)$ can, however, be achieved by another mechanism, nonequilibrium solid-liquid reaction. Fine wires (diam = 0.15 mm) containing sub-micron sized filaments of Nb and X (X-Al, Al-Si, or Al-Ge) are made by a conventional powder metallurgy approach and a liquid infiltration method. The A15 phase can then be formed by an appropriate interfacial solid (Nb) and liquid (X) reaction. Heat treatments of one temperature aging resulted in a sharp transition with an inductive T_c onset of ~ 15.5 K, H_{c2} (4.2 K) ≥ 21 T and compatible overall J_c's of ≥ 10^4 A/cm^2 at 10 T and 4.2 K. Furthermore, a double aging treatment increased the inductive T_c onset to 16.3 K; the overall current density and the upper critical field are also expected to be higher. Research on processing, including kinetic studies, microstructure characterization and relevant thermodynamics are now in progress.

11. METALLURGICAL FAILURE ANALYSIS WITH A LARGE SUPERCONDUCTING SOLENOID MAGNET

J. W. Morris, Jr., Jung-Ihl Kim, Brent Fultz, and Minghwei Hong

During the past year a large solenoid Nb-Ti superconducting magnet was constructed at LBL for use in the time projection chamber at SLAC. This magnet failed during its testing phase through formation of a serious and damaging short. Our research group was asked to undertake a metallurgical failure analysis of the remains of the magnet in collaboration with the analyses being performed by other groups at LBL to determine the source of the failure. This analysis included an overall investigation of the pattern of damage to the magnet, specific chemical and metallurgical analyses of suspect regions within the damaged coil and corollary experiments to determine the degradation properties of the insulation material. Investigation revealed a suspicious contamination of iron on the aluminum inner bore tube of the magnet and which appeared to originate from a small mechanical gauge in the bore tube. This evidence, taken together with results of other investigations of specific items of damage in the failed magnet, strongly suggested that the failure was due to a small iron chip present on the bore tube at the time the magnet was wrapped, which caused a short between the bore tube and an aluminum wire circuit separated from the bore tube by a thin layer of insulation. This interpretation of the failure is consistent with the analysis of other aspects of magnet performance conducted by other divisions of the laboratory.

RESEARCH PLANS FOR CALENDAR YEAR 1981

Research plans for this project include the following:

1. We plan to complete our combined theoretical-experimental investigation of the shape and coarsening behavior of nitride precipitates in iron and the interpretation of precipitation characteristics through the elastic theory.

2. We plan to continue investigation of the influence of low temperature structural anomalies on the flow characteristics of dislocations in solids, in the hope of gaining further insight

into the fundamental sources of low temperature mechanical behavior.

3. We will continue the development of Mössbauer spectroscopy as a technique for following chemical alterations during decomposition reactions in steel and will utilize the technique to monitor chemical changes during the precipitation of austenite.

4. We plan to continue research on the inherent intergranular fracture in Fe-Mn cryogenic steels, using Auger electron spectroscopy to gain further insight into the role of boron as "grain boundary glue."

5. We plan to conduct alloy development research on the high temperature properties of iron superalloys, with the objective of developing alloys which retain exceptional strength in high temperature applications.

6. We plan to research on the welding of austenitic steels, which will focus on the aging kinetics of superalloys aged after autogenous welding, and on the role of δ-ferrite in the weldments of conventional austenitic steels.

7. We plan to continue research with new high field superconducting materials, with that research focusing on Nb-Al superconductors manufactured either through "direct precipitation" or powder metallurgical techniques.

1980 PUBLICATIONS AND REPORTS

Refereed Journals

1. K. W. Mahin, K. Hanson and J. W. Morris, Jr., "Comparative Analysis of the Cellular and Johnson-Mehl Microstructures through Computer Simulation," Acta Met. 28, 443 (1980), LBL-8752.

2. M. Hong, D. Dietderich and J. W. Morris, Jr., "Development of A15 (V_3Ga) Superconducting Material through Controlled Precipitation," J. of Appl. Phys. 51, 5 (1980), LBL-9797.

3. S. K. Hwang and J. W. Morris, Jr., "The Use of a Boron Addition to Prevent Intergranular Embrittlement in Fe-12Mn," Met. Trans. 11A, 1197 (1980), LBL-9583.

4. J. I. Kim and J. W. Morris, Jr., "On the Scavenging Effect of the Retained Austenite in a Low Carbon Fe-5.5Ni Alloy," Met. Trans. 11A, 1401 (1980), LBL-9835.

5. M. Niikura and J. W. Morris, Jr., "Thermal Processing of Ferritic 5Mn Steels for Toughness at Cryogenic Temperatures," Met. Trans. 11A, 1531 (1980), LBL-9798.

6. M. Hong and J. W. Morris, Jr., "Superconductors through Direct 'Solid-State Precipitation'," Appl. Phys. Letts. 37, 1044 (1980), LBL-11190.

Other Publications

1. R. A. Kot and J. W. Morris, Jr., eds., "The Structure and Properties of Dual Phase Steels, The Metallurgical Society, Pittsburgh, (1980).

2. J. W. Morris, Jr., "Heat," edited by R. G. Lewis and G. L. Trigg, Addison Wesley, New York (1980).

3. S. Chen, A. G. Khatchaturyan, and J. W. Morris, Jr., "Computer Simulation of the "Tweed" and Modulated Structures in Decomposition Reactions," Proceedings of the Kona Conference on Modulated Structures, AIP 53, 168 (1979), LBL-9098.

LBL Reports

1. D. E. Williams, "The Weldability of Thermally Grain-Refined Fe-12Ni-0.25Ti for Cryogenic Structural Applications," LBL-10259.

2. S. H. Wen, E. Kostlan, M. Hong, A. G. Khatchaturyan, and J. W. Morris, Kr., "The Habit of a Tetragonal Precipitate in a Cubic Matrix: Analytical Results," LBL-10262.

3. Kim W. Mahin, "Characterization of Ferritic GMA Weld Deposits in 9%Ni Steel for Cryogenic Applications," LBL-10922.

4. Brent Fultz and J. W. Morris, Jr., "The Thickness Distortion of Fe^{57} Backscatter Mössbauer Spectra, LBL-11022.

5. S. Wen, A. G. Khatchaturyan, and J. W. Morris, Jr., "Computer Simulation of a 'Tweed Transformation' in an Idealized Elastic Crystal," LBL-11238.

6. K. M. Chang and J. W. Morris, Jr., "Development of High Strength Hydrogen Resistant Austenitic Alloys," LBL-11023.

7. Minghwei Hong, "A15 Superconductors through Direct 'Solid-State' Precipitation: V_3Ga and Nb_3Al," LBL-11021.

8. M. Hong, D. R. Dietderich, I. W. Wu, and J. W. Morris, Jr., "Microstructure and properties of A15 Superconductors formed by Direct Precipitation," LBL-11605.

Invited Talks

1. J. W. Morris, Jr., "Materials Research for High Field Accelerator Magnets," High Energy Physics Advisory Panel (HEPAP), Stanford University, January 1980.

2. J. I. Kim, "The Formation of Precipitated Austenite by ($\alpha+\gamma$) Two-Phase Annealing," TMS/AIME Annual Meeting, Las Vegas, NV, February 24-28, 1980.

3. Peiching Ling, "Evolution of the Metallurgical Microstructure with Controlled Precipitation Process in V-Ga System, TMS/AIME Annual Meeting, Las Vegas, NV, February 24-28, 1980.

4. Chol K. Syn, "Fracture Path in 9Ni Steel," TMS/AIME Annual Meeting, Las Vegas, NV, February 24-28, 1980.

5. Minghwei Hong, "Progress with Controlled-Precipitation Process A15 Superconducting Materials," TMS/AIME Annual Meeting, February 24-28, 1980.

6. D. R. Dietderich, "The Effects of Third Element Addition on the Metallurgical and Superconducting Properties of Wires or Tapes in the V-Ga System, TMS/AIME Annual Meeting, Las Vegas, NV, February 24-28, 1980.

7. J. L. Wang, "The Influence of Temperature on the Fabrication of Nb_3Sn Multifilamentary Superconducting via the Infiltration Process," TMS/AIME Annual Meeting, Las Vegas, NV, February 24-28, 1980.

8. J. W. Morris, Jr., "Materials Research Needs for High Field Superconducting Accelerator Magnets," DOE/HEP Workshop on Superconducting Magnet Technology, Brookhaven National Laboratory, March 1980 (Executive Session).

9. J. W. Morris, Jr., "The Habit of a Tetragonal Precipitate in a Cubic Matrix," American Physical Society, New York, March 1980.

10. J. W. Morris, Jr., "Computer Simulation of the Martensite Transformation," American Physical Society, New York, March 1980.

11. J. W. Morris, Jr., "The Role of Dislocation Theory in the Design of Engineering Alloys," Acta Met/Scripta Metallurgical International Conference on Dislocation Modeling, Gainesville, Florida, (Keynote address), June 1980.

12. J. W. Morris, Jr., "Alloy Design," Bell Telephone Laboratories, Murray Hill, July 1980.

13. Minghwei Hong, "Microstructure and Properties of A15 Superconductors Formed by Direct Precipitation," Applied Superconductivity Conference, Santa Fe, NM, September 1980.

14. J. W. Morris, Jr., "The Influence of Precipitated Austenite on the Ductile-Brittle Transition in Cryogenic Steels," TMS/AIME Fall Meeting, Pittsburgh, October 1980 (invited paper).

15. Jung-Ihl Kim, "Effects of the Phases in a 3-Step Heat-Cycled Fe-6Ni Alloy," TMS/AIME Fall Meeting, Pittsburgh, October 1980.

16. Hee Jin Kim, "Mechanical Properties of Weldments in Grain-refined Fe-12Ni-0.25Ti," TMS/AIME Fall Meeting, Pittsburgh, October 1980.

17. Brent Fultz, "A Mössbauer Study of Microstructural and Chemistry Changes in Fe-9%Ni Steel During Two-Phase Tempering," Materials Research Society, Boston, MA, November 1980.

18. J. W. Morris, Jr., "Steel Below Zero," University of California Science Editor, CBS Radio Network, October 1980.

b. Structure-Property Relationships in Semiconductor Materials*

Jack Washburn, Investigator

Introduction. This program is aimed at a more complete fundamental understanding of the ways in which point defects, dislocations, and more complex clusters of point defects affect the electrical properties of semiconductor materials after various processing steps including ion implantation and laser and electron beam annealing. This type of information is important to improvement of the reliability, life time and performance of solid state devices including solar cells. A combination of experimental techniques including high resolution transmission electron microscopy and diffraction, channeled Rutherford back scattering, secondary ion mass spectroscopy and electrical measurements are being utilized.

1. STRUCTURE OF Cu_2S IN CdS-Cu_xS SOLAR CELLS

U. Dahmen, R. Chin, and J. Washburn

A critical factor in the efficiency of low-cost CdS/Cu_xS photovoltaic cells is the composition of the Cu_xS layer. Theoretical studies have predicted that the heterojunction is optimized when the Cu_xS layer has the composition of chalcocite, Cu_2S. Experimental results have generally agreed with this prediction, but compositional measurements were averaged over large areas. In this study, the local phase distribution has been investigated with high spatial resolution using transmission electron microscopy. To eliminate complicating factors, highly perfect single crystals of melt-grown CdS were transformed to Cu_xS by an ion exchange reaction in both the wet and the dry process.

In contrast to previous beliefs, it was found that the composition was far from homogeneous. A multitude of phases occurred in localized areas, often too small to be identified by selected area diffraction. The use of high resolution structural imaging has allowed the identification of "grains" of different structure only a few tens of nanometers in size. An example is given in Fig. 1 which shows the boundary between two apparently unrelated regions of Cu_xS. However, the optical diffractograms displayed below each "grain" had a common sulphur sublattice (shown in the center). hence, the only difference between the two regions was the arrangement of Cu atoms, e.g., the simplest "superlattice" consistent with the left spot pattern would be a single Cu vacancy in every 64 unit cells of the stoichiometric chalcocite, corresponding to the composition $Cu_{.97}S$.

This study has further shown that in the dry process the growth front proceeds by forming plate-like precipitates and ends up in a phase mixture similar to the wet-processed Cu_xS.

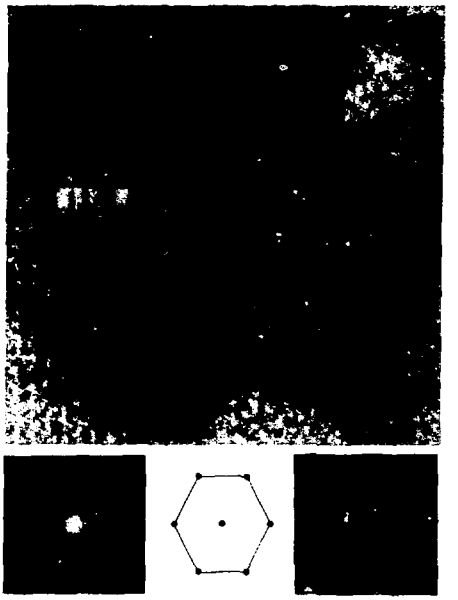

Fig. 1. High resolution transmission electron micrograph of ordered Cu_xS showing two domains of different structures with continuous sulphur sublattice (above) as evident from the optical diffractograms (below). (XBB 804-4873)

As evident from this work, a better understanding of the fine-scale microstructure of real cells is essential to the development of more efficient CdS/Cu_xS photovoltaic devices with improved stability.

2. SEGREGATION OF PHOSPHORUS AT DISLOCATION LOOPS IN SILICON--EFFECT ON ELECTRICAL PROPERTIES†

D. K. Sadana and J. Washburn

The aim of this work was to study the furnace annealing behavior of buried amorphous layers formed due to P^+ implantation into (111) Si and to investigate the effects of annealing on the electrical properties of the implanted layer. For this purpose, P^+ was implanted at room temperatur into (111) Si in a non-channeling direction at 120 keV to a dose of $3 \times 10^{14}/cm^2$. The implanted samples were subsequently annealed at 750°C. Ninety degree cross-sectional transmission electron

*This work was supported by the Director, Office of Energy Research, Office of Basic Energy Sciences, Materials Sciences Division of the U.S. Department of Energy under Contract No. W-7405-ENG-48.

microscopy (TEM), MeV He^+ channeling, secondary-ion mass spectrometry (SIMS), and electrical results were obtained from the same specimen.

The TEM cross section micrograph of a 750°C-annealed specimen showed two well-defined damage layers S and T at mean depths of 600 Å and 1100 Å (Fig. 2(a)). Both of these layers contained dislocation loop defects. The analysis of these

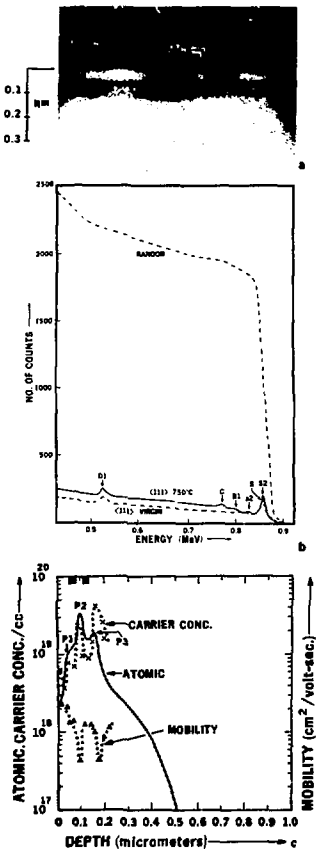

Fig. 2. $P^+ \rightarrow$ (111) Si, 120 keV, $3\times10^{14}/cm^2$, 750°C annealed for 20 min. (a) TEM cross-section micrograph showing two discrete layers of dislocation loops; (b) Channeling spectrum (1.56 MeV He^+) from the same specimen (continuous line). (c) Phosphorus (SIMS) (continuous line), carrier concentration (broken line x) and Hall mobility (broken line ▲ distribution curves from the same specimen.
(XBB 806-7152)

defects indicated that the Burgers vectors of the loops were of two types, 1/2a⟨110⟩ and 1/3a⟨111⟩. The mean diameter of the loops was 150 Å. The channeling spectrum from the same specimen showed that the material was a single crystal but there were three damage regions at depths of 600 Å, 950 Å, and 1700 Å, respectively, as indicated by three peaks, namely, A2, B1, and C in Fig. 2(b). The peaks A2 and B1 corresponded to the layers S and T of dislocation loops seen in the TEM cross section micrograph (Fig. 2(a)). Peak C at a depth of 1700 Å corresponding to the damage region beyond layer T in Fig. 2(a) is thought to arise because of interstitial point defects or their clusters at that depth. The phosphorus atomic profile obtained by the SIMS measurements showed two pronounced peaks P2 and P3 at depths of 950 Å and 1520 Å, respectively. There was also a shoulder P1 at a depth of 600 Å in the atomic profile. Shoulder P1 and the first peak P2 in Fig. 2(c) corresponded the two damage layers S and T, respectively, the TEM micrograph (Fig. 2(b)). However, peak P3 in Fig. 2(c) corresponded to peak C in Fig. 2(b), but there was no detectable coarse damage in the TEM micrograph at this depth. The electrical profile, namely carrier concentration versus depth, and mobility versus depth taken from another part of the same specimen, showed that the carrier distribution very closely followed the atomic distribution as obtained by the SIMS measurements. The carrier-concentration profile showed three peaks at 600, 1000, and 1700 Å corresponding to peaks P1, P2, and P3, respectively, in Fig. 2(c). However, the mobility profiles showed two pronounced dips at depths of 900 and 1700 Å, respectively, corresponding to the deeper-lying damage layers.

Although the segregation of impurities at the damage regions has been suspected for the last several years, we believe this is the first study of its kind that gives direct experimental evidence. From the practical point of view these findings are important because a significant fraction of the implanted ions become concentrated in the damage regions.

* * *

†Brief version of LBL-11319.

3. LASER ANNEALING OF PHOSPHORUS IMPLANTED Si

D. K. Sadana and J. Washburn

The work described in this section demonstrates how seemingly minor variations in the initial implantation conditions can cause dramatically different damage structures on subsequent pulsed laser annealing.

For this experiment phosphorus was implanted into (111)Si at 120 keV to a dose of $10^{16}/cm^2$ at room temperature in two different modes. In the first mode, Si wafer A was scanned in front of a stationary ion beam (Lintott implanter). In the second mode, the ion beam was scanned on a stationary wafer B (Extrion implanter). The rates

of scanning were vastly different in the two cases, being nearly two orders of magnitude higher in the latter case. The dose rates used in the two cases were 3 $\mu A/cm^2$ and 1.5 $\mu A/cm^2$, respectively. The resulting As-implanted damage structures in both cases contained amorphous material in the implanted region extending to the surface of the wafers. Both types of wafers were zapped at energies of 0.7 J/cm^2 and 1.5 J/cm^2, respectively, with a Q-switched ruby laser (0.695 μm) of pulse length 50 nsec and the output was transmitted through a specially designed bent quartz rod homogenizer.[1] The microstructures in the laser zapped wafers A and B, as obtained by transmission electron microscopy (TEM) on the plan-view specimens from these wafers are shown in Fig. 3. Figure 3(a) (0.6 J/cm^2) shows that the initial amorphous material was converted into polycrystalline material indicating that melting occurred during the annealing. Figure 3(b) (1.5 J/cm^2) shows a high density of stacking faults. In this case, the molten layer extended close to the initial amorphous/crystalline interface and the damage clusters at the interface probably acted as nucleating centers for the stacking faults observed. Similar damage structures were expected to occur for wafer B. However, Figs. 3(c) and 3(d) show neither polycrystalline material for a 0.7 J/cm^2 zapping nor any dislocations or stacking faults for a 1.5 J/cm^2 zapping, respectively.

To further investigate the effect of amorphous layer structure on laser melting a Q-switched ruby laser facility is being set up at MMRD to permit further work of this type under more carefully controlled conditions.

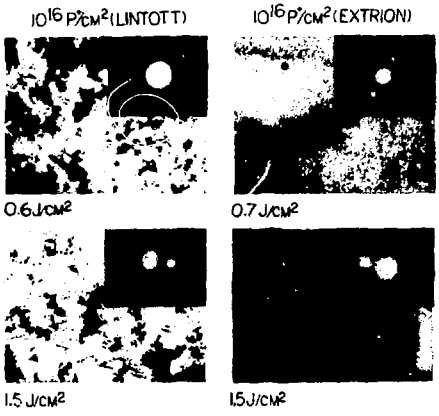

Fig. 3. TEM planar views from laser annealed P^+ implanted Si, $10^{16}/cm^2$, 120 keV, RT implant. (a) 0.6 J/cm^2 and (b) 1.5 J/cm^2 (Lintott); (c) 0.7 J/cm^2 and (d) 1.5 J/cm^2 (Extrion). (XBB 8010-12316)

* * *

1. A. G. Cullis, H. C. Webber and P. Bailey, J. Phys. E. Sci. Instrum. 12, 688 (1979).

4. HIGH POWER PULSED ELECTRON BEAM ANNEALER

M. Strathman,[1] D. K. Sadana, and R. True[‡]

An electron beam annealer capable of providing a short 100 ns pulse of high energy has been designed and is under construction. The instrument will be used in a similar manner to a pulsed high power laser for rapid melting and resolidification of the surface layers of semiconductors and metals to achieve desired electrical, mechanical, or corrosion resistant properties of various materials.

The instrument consists of a hot cathode, a grid, a focusing ring, an annular Faraday shield, a drift tube terminated by a second Faraday shield, and a target holder. The electrons are accelerated by a 90 kV potential difference between the cathode and the Faraday shield at the entrance to the drift tube. A magnetic field focuses the beam and directs it toward the target. The target is at ground potential and the cathode is at -20 kV. Penetration of the electrons into the target is minimized by deceleration to 20 kV and by the spiral path produced by the magnetic field which results in their striking the target at a small angle. In this way, most of the energy of the beam is delivered to the near-surface layers of the target. The specimen is introduced into the target position through a vacuum interlock chamber.

All the major pieces of this equipment have been fabricated and are currently being assembled.

* * *

[1]Department of Instrumentation and Techniques, Lawrence Berkeley Laboratory, University of California, Berkeley.
[‡]Litton Industries, San Carlos, California.

5. STRUCTURAL DAMAGE-DOPANT ATOM INTERACTION IN GALLIUM ARSENIDE

D. K. Sadana and J. Washburn

The depth profiles of visible defects as obtained by cross-sectional transmission electron microscopy (XTEM) and electrical profiles obtained by Hall measurements in conjunction with layer stripping has demonstrated that in Si there is strong correlation between the structural and electrical properties. A significant number of impurity atoms were found to segregate near the defects visible by TEM causing a pronounced distortion in the distribution of the implanted impurity. This distortion was also reflected in the electrical profiles.[1,2] Similar correlations for ion-implanted GaAs are not available at present. The aim of this work was therefore to

understand the structural-electrical properties correlation in Se^+-implanted GaAs. For this purpose, semi-insulating Cr-doped (100) GaAs was implanted in a nonchanneling direction with Se^+ ions at 450 keV to a dose of $5 \times 10^{14}/cm^2$. The substrate temperature was kept at 200°C during the implantation. The resulting specimen was encapsulated with a 5000 Å thick Al layer and annealed at temperatures in the range 400-800°C. Cross-sectional transmission electron microscopy (XTEM), MeV He^+ channeling, secondary ion mass spectrometry (SIMS) and electrical measurements were performed on the same sample.

The XTEM micrograph from this sample showed a 2400 Å wide band of damage clusters (Fig. 4(a)) that was located at a mean depth of 3000 Å. The 1.6 MeV He^+ channeling method gave complementary results (Fig. 4(b)). The atomic distribution of ^{78}Se obtained from the same specimen is shown in Fig. 4(c). Significant diffusion in the vicinity of visible defects was observed (note the position of the damage band shown as the shaded region in Fig. 4(c)). The carrier concentration profile also exhibited a pronounced asymmetry, including a minimum over-the-depth range of 1000 to 3000 Å. The portion of the profile showing asymmetry corresponded approximately to the position of the damage band (Fig. 4(a)). The mobility profile showed a dip corresponding to the upper edge of the damage band in Fig. 4(a), followed by a progressive increase over the depth range 1000 to 3000 Å. The overall increase in the mobility in the deeper parts was by a factor of 5. The hypothetical Gaussian shaped profile (dotted lines over the carrier concentration profiles in Fig. 4(c) that might have arisen if there were no asymmetry in the carrier concentration profiles indicated an overall background compensation of ~ 50.

It has been deduced from the present study that (1) Deep diffusion of Se occurs in the as-implanted GaAs sample at the implantation temperature of 200°C. (2) Formation of secondary defects at and beyond R_p, significant amounts of Se diffusion beyond R_p and compensation of electrical carriers are associated with the mobile point defects present in the hot implanted GaAs.

* * *

1. D. K. Sadana et al., J. Appl. Phys. 37, 615 (1980), LBL-11319.
2. D. K. Sadana, J. Fletcher and G. R. Booker, Electronics Lett. 13, 632 (1979).

6. COMPARISON OF CHANNELED BACKSCATTERING FROM SUBSURFACE DEFECTS AND CROSS SECTION ELECTRON MICROSCOPE OBSERVATIONS OF THE SAME SPECIMENS

D. K. Sadana and J. Washburn

In this article damage detection by two techniques, namely cross-sectional electron microscopy (XTEM) and channeled Rutherford backscattering (RBS), are compared. XTEM gives a direct view of the damage-depth distribution while RBS gives an estimate of the disorder and its depth distribution indirectly. However, the RBS method is non-destructive and less time consuming as compared to XTEM. Therefore, the present work was aimed at improving the interpretation of channeled RBS for various kinds of defects and their depth distributions.

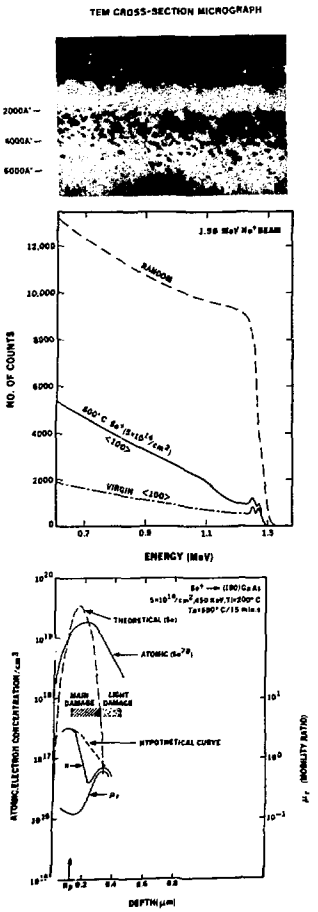

Fig. 4. $Se^+ \rightarrow$ (100) GaAs, Ti = 200°C, 450 keV, 5×10^{14} cm^2 annealed at 600°C for 15 min with Al encapsulant. (a) TEM cross-section micrograph showing a single buried band of damage clusters. (b) 1.6 MeV He^+ channeling spectrum from the same specimen. (c) Atomic Se (SIMS), carrier concentration and Hall mobility profiles from the same specimen. (XBB 8011-12894)

The damage structures compared were as follows: a buried amorphous layer, a continuous amorphous layer extending to the surface, double discrete buried amorphous layers, double discrete buried layers of dislocation loops, a single dislocation network, a single layer of damage clusters, a polycrystalline layer on top of a single crystal substrate, etc.[1] For this report, the example chosen is shown in Fig. 5. The XTEM micrograph in Fig. 5 (inset) shows a high density of stacking faults that are in direct contact with a high density of damage clusters. The channeling spectrum from the same specimen is also shown in Fig. 5. The dotted curves in the figure are for virgin single crystal Si in the channeled and random direction, respectively.

The two techniques gave complementary results in that the discrete damage layers in the XTEM appeared as peaks in the channeling spectrum. However, the widths and depths from the channeled RBS required a correction factor due to the dechanneling of the He^+ particles. The correction factor obtained by our empirical method published earlier gives a good quantitative correlation between the two methods. The width of the damage band in this case was obtained by subtracting the dechanneling background starting at kink K.

Further analysis of the spectrum indicated the following.

(1) The specimen surface was heavily damaged.
(2) The extended defects were present in the region between the surface and a depth (kink K) of 1775 Å.
(3) A dense band of damage 500 Å wide was present at a mean depth of 2025 Å. The band contains a higher density of damage near the upper edge (peak D) followed by a lightly damaged region (peak D').

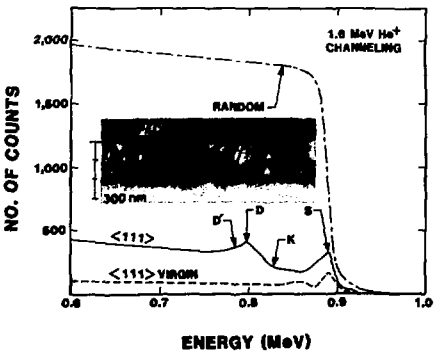

Fig. 5. Cross-sectional TEM micrograph (inset) showing a band of stacking faults extending to the surface in direct contact with a layer of damage clusters and 1.56 MeV He^+ channeled spectrum from the same specimen. Note the change in the slope at K and peaks D and D'; these correspond to stacking fault/damage cluster interfaces, and a band of damage with varying density of damage clusters, respectively. (XBB 8012-14675)

* * *

1. D. K. Sadana et al., J. Appl. Phys. 51, 5718 (1980), LBL-10725.

7. THE EFFECT OF MICROTWINS ON THE MIGRATION OF A {111} AMORPHOUS-CRYSTALLINE INTERFACE IN SILICON

R. Drosd and J. Washburn

Microtwins on $(\bar{1}11)$, $(1\bar{1}1)$ or $(11\bar{1})$ accelerate crystal growth at a (111) amorphous-crystalline interface. The rate-controlling step for growth of the silicon crystal at an atomically flat (111) interface is thought to be nucleation of growth ledges. This requires rearrangement of a group of atoms in the amorphous material adjacent to the crystal so that three new atoms are simultaneously on crystal lattice sites. The line of interaction of a twin boundary with the growing α/C interface can act as an easy nucleation site for growth steps. At this line only two atoms are required instead of three, and once the line of intersection has been decorated with two atom pairs the resulting growth step can move away from the twin boundary by addition of single atoms to the growing crystal.

One of the two twin boundaries associated with a microtwin will be much more effective in promoting growth than the other. This is because a growth step in a ⟨110⟩ direction on a {111} face has a fast and a slow direction of migration. In the fast direction single atoms may attach at the steps, but in the slow direction a two atom nucleus is required to form a pair of kinks that can then move along the step until a single row is completed by addition of single atoms. Each new row requires a new double kink. Because of this anisotropy the twin boundary on one side nucleates a fast step for the matrix and also for the twin while at the other boundary it is a slow step. The expected result is faster growth on one side of a twin than on the other as illustrated schematically in the growth sequence of Fig. 6. As shown in the figure, it is expected that only one side surface of the twin will ever become exposed to the amorphous material. Therefore, thickening of the twin should occur only from one side. The transmission electron micrograph in Fig. 7 confirms this expected growth morphology.

Csepregi et al.[1] have presented a mechanism by which microtwins may increase {111} α/c interface migration rate during annealing. They proposed that since the exposed surface of the twin is initially (511) it will be able to grow much faster than the surrounding (111) matrix interface. The (511) surface is close to (100) and hence should achieve a high growth rate initially. However, a protruding twin should soon become bounded by its slowest growing {111} faces.

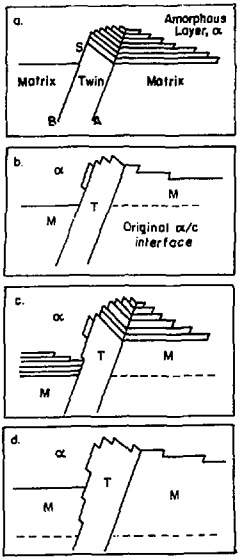

Fig. 6. Schematic drawing of a growth sequence showing effect of a microtwin that nucleates fast moving growth steps at the right hand twin--matrix --amorphous material line of intersection.
(XBL 803-4849)

Fig. 7. *Transmission electron micrograph showing* effect of microtwins on the advancement of a (111) α/c interface into amorphous silicon.
(XBB 7911-15623)

Once this has occurred the twin can not continue to grow faster than the matrix. Any continued acceleration of growth rate would then have to be explained in some other way such as by the growth step nucleation effect described above.

* * *

1. L. Csepregi et al., J. Appl. Phys. 49, 3906 (1978).

8. ATOMIC DISTRIBUTION OF ARSENIC IN MOS TEST DEVICES MEASURED BY RUTHERFORD BACKSCATTERING.

D. K. Sadana, N. R. Wu, J. Washburn, M. Strathman,† and M. Current‡

The aim of this study was to examine the structure and location of ion-implantation damage, oxygen recoil during the implantation, and As atomic distribution for As implants through various thicknesses of screen oxides (30-1000 Å) in the dose range 10^{15}-10^{16}/cm^2. This information will be used to understand the effects of processing variables on metal-oxide-semiconductor (MOS) device performance. In this article, results from only a 7.5×10^{15}/cm^2 As implant through an SiO_2 layer of 775 Å that was subsequently annealed at 1000°C in N_2 ambient are described. The thickness of the oxide layer (775 Å) was almost equal to the projected range of As in SiO_2 (750 Å). The damage was examined both by weak-beam transmission electron microscopy (TEM) and backscattering spectrometry. The TEM micrograph (Fig. 8) shows the presence of dislocation loops of mean diameter ~ 600 Å with a density of 2.5×10^9/cm^2 and a high density of background fine damage (≤ 20 Å across).

Fig. 8. *Weak beam TEM micrograph showing the* dislocation loops and fine damage in the As implanted (through SiO_2) and annealed sample.
(XBB 8012-14676)

The atomic concentration profiles for implanted As and recoiled O, and lattice location of As were obtained from the channeled and random backscattering spectra of He^+ particles of 1.56 MeV incident energy. The backscattered particles were detected by a high resolution Si surface barrier detector (6 kV FWHM) cooled to -20°C at 170° with respect to the incident beam. Figures 9 and 10 show such spectra taken from regions with and without SiO_2 layer at the surface, respectively. The analysis of the spectra showed the following:

(1) Oxygen recoil during the implantation formed a layer of composition SiO_x immediately below the original SiO_2/Si interface on subsequent annealing. The composition of the top SiO_x layer was $SiO_{1.5}$. The oxygen was found to be present to a depth of ~ 400 Å below the SiO_x/Si interface.

(2) Only 40% of implanted As was present in substitutional sites, the remaining 60% was present in interstitial sites.

(3) A damage band was present at a mean depth of ~ 825 Å from the Si surface. This band is believed to correspond to the position of the dislocation loops observed in the TEM micrograph.

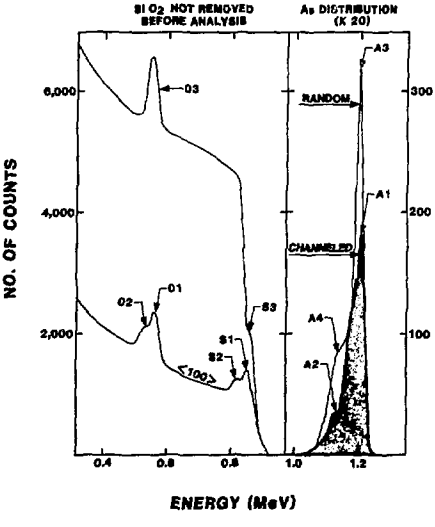

Fig. 9. Channeled and random backscattering spectra of 1.56 MeV He^+ beam from the same sample as Fig. 8. The oxide layer was not removed during the analysis. Note the changes in the As distribution (A2 and A4) and kinks (S2 and O2) at the SiO_2/Si interface in the channeling spectrum. (XBL 8012-13577)

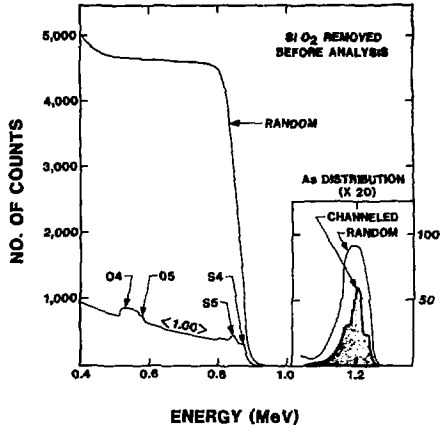

Fig. 10. Same as Fig. 9 except that the oxide layer was removed before the backscattering analysis. (XBL 8012-13578)

* * *

†Department of Instrumentation Techniques, Lawrence Berkeley Laboratory.

‡Signetics Corporation, Sunnyvale, CA 94086.

RESEARCH PLANS FOR CALENDAR YEAR 1981

The formation and perfection of Cu_2S formed by the replacement reaction between copper and CdS will be investigated in detail. The preliminary results described in this report revealed non-uniformity in the Cu_xS composition on a very fine scale. High resolution electron microscopy and diffraction and lattice image techniques will be applied to Cu_xS layers grown under different conditions and after aging treatments. The research is aimed at improving the reliability, yield and lifetime of CdS-Cu_xS solar cells.

The electron microscope technique for study of defect formation and rates for the amorphous to crystalline transformation in silicon will be applied to a study of the effect of phosphorous, boron, and arsenic concentrations on the perfection and growth rate of the crystalline phase. A modification of the model developed to explain the effect of crystallographic orientation of the growing face on the amorphous to crystalline transformation rate may be able to explain impurity effects.

The effect on the formation of secondary defects and on the electrical properties of the implanted layers for arsenic implants into silicon through

500 to 750 Å thickness of SiO_2 will be studied in a cooperative research program with Signetics Corporation. Injection of oxygen during implantation is known to have deleterious effects on carrier concentration and mobility. The aim of this research will be to understand the reasons for the observed effects. Both Rutherford backscattering and cross-sectional electron microscopy techniques will be applied to the problem at our laboratories while specimen preparation, implantations, and electrical measurements will be carried out at Signetics Corporation.

Research on the properties of polycrystalline silicon will focus attention on the effect of impurities or dopant atoms on the mobility of grain boundaries during grain growth and on the electrical properties of polycrystalline silicon produced by laser and electron beam pulse annealing of amorphous silicon. Microanalytical techniques utilizing the Philips 400 microscope operating in the STEM mode and microdiffraction information will be used to obtain information concerning segregation of impurities to grain boundaries.

A 100 ns pulsed electron beam annealer and Q-switched ruby laser annealing facilities will become operational during calendar year 1981. These will be applied to a study of surface layer melting and the resulting epitaxial-solidification of silicon and gallium arsenide. Channeled Rutherford backscattering and electron microscope techniques will be used to study the effects that occur both in the regrown crystal layers and in the layers immediately below the melted region. These observations will be correlated with electrical measurements and determination of the depth distribution of solutes made by secondary ion mass spectroscopy techniques.

Finally, a fundamental study of channeled Rutherford backscattering spectra from buried layers of different types, such as amorphous layers, small dislocation loops, and damage clusters produced by low dose implants, will use the cross-section transmission electron microscopy technique to independently monitor the depth of the scattering defects. This work should improve understanding of RBS spectra from complex surface layers.

1980 PUBLICATIONS AND REPORTS

Refereed Journals

1. R. Drosd and J. Washburn, "A New Technique for Observing the Amorphous to Crystalline Transformation in Thin Surface Layers on Silicon Wafers," J. App. Phys. 51, 4106 (1980), LBL-10311.

2. D. K. Sadana, M. Strathman, J. Washburn and G. R. Booker, "Transmission Electron Microscopy and Rutherford Backscattering Studies of Single and Double Discrete Buried Damage Layers in P^+ Implanted Si on Subsequent Laser Annealing," J. App. Phys. 51, (1980), LBL-10625.

3. D. K. Sadana, M. Strathman, J. Washburn, and G. R. Booker, "Transmission Electron Microscopy and Rutherford Backscattering Studies of Different Damage Structures," J. Appl. Phys. 51, 5718 (1980), LBL-10725.

4. D. K. Sadana, M. Strathman, J. Washburn, C. W. Magee, M. Maenpaa, and G. R. Booker, "Effect on Electrical Properties of Segregation of Implanted P^+ at Defect Sites in Si," Appl. Phys. Lett. 37, 615 (1980), LBL-11319.

5. D. K. Sadana, M. Strathman, J. Washburn, and G. R. Booker, "On the Comparison of Transmission Electron Microscopy and Channeled Rutherford Backscattering Techniques to Evaluate the Multilayer P Subsurface Damage Structures," Appl. Phys. Lett. 37, 234 (1980), LBL-10725.

6. D. K. Sadana, M. C. Wilson, G. R. Booker and J. Washburn, "Regrowth Behavior of Three Different Damage Structures in P^+ Implanted and Subsequently Laser Annealed Si," J. Electrochem. Soc. 127, 1589 (1980), LBL-10008.

7. A. Masuyama, M. A. Nicolet, I. Golecki, J. L. Tandom, D. K. Sadana, and J. Washburn, "Solid State Thermally Annealed GaAs with Room Temperature Implanted Si," Appl. Phys. Lett. 36, 749 (1980).

8. D. K. Sadana, M. C. Wilson and G. R. Booker, "Electron Microscope Studies of Ion Implanted Si and GaAs after Laser and Furnace Annealing," J. Microscopy 118, 51 (1980).

9. D. K. Sadana, G. R. Booker, B. J. Sealy, K. G. Stephens and M. M. Badawmi, "Correlation Between Structural and Electrical Profiles in Ion-Implanted GaAs," Radiation Effects 49, 183 (1980).

10. J. L. Tandom, I. Golecki, M. A. Nicolet, D. K. Sadana and J. Washburn, "Pulsed Electron Beam Induced Recrystallization and Damage in GaAs," Appl. Phys. Lett. 35, 867 (1979).

11. C. Lampert, "Metallurgical Analysis and High Temperature Degradation of the Black Chrome Solar Selective Absorber," Thin Solid Films 72, 75 (1980), LBL-10293.

12. C. Lampert, "Selective Absorber Coated Foils for Solar Collectors," Plating and Surface Finishing 20 (1980), LBL-10249.

Other Publications

1. C. L. Lampert and J. Washburn, "Chemical and Structural Characterization of Thermally Degraded Black Chrome, Proc. of 1980 Mtg. ISES, American Section, p. 1126, LBL-10689.

Invited Talks

1. J. Washburn, "Formation and Effects of Secondary Defects in Ion Implanted Si," Materials Research Society Mtg., Boston, MA, November 1980.

2. D. K. Sadana, "TEM, RBS, SIMS, and Electrical Measurements on P^+ Implanted Si," National Bureau of Standards, Washington, D.C., June 1980.

3. D. K. Sadana, "Ion Implanted Si and GaAs: Structural-Electrical Correlation," Hewlett-Packard, Santa Rosa, CA, June 1980.

c. Mechanical Properties of Ceramics*

Anthony G. Evans, Investigator

Introduction. The research reported herein is an interdisciplinary study of the response of ceramics to stress. The generalized scope of the study is outlined in Fig. 1. The principal foci of the current research projects are problems that demand scientific attention by virtue of their considerable technological significance in the energy sphere. The research areas are (1) high temperature deformation and failure, (2) microstructure and toughness relations, and (3) microstructure development during sintering.

The three research areas are new topics that are anticipated to continue for several years. The high temperature deformation and failure issue concerns the response of refractory materials to stress. A scientific basis for predicting high temperature failure and for relating the deformation and failure to microstructure does not presently exist. Research in this area is therefore devoted to the generation of a self-consistent scientific comprehension of the mechanisms of deformation and failure, leading eventually to a predictive capability. The enhancement of toughness in ceramics is pertinent primarily to the minimization of damage when a ceramic component is subject to impact, thermal shock, machining, etc. Toughness is thus a principal property involved in the structural integrity of ceramic components. Improved toughness can be induced by certain stress activated microstructural changes occurring in the vicinity of a crack tip, particularly martensitic transformation. The study is devoted to a theoretical understanding of the microstructural conditions that afford optimum toughness, coupled with the experimental development of optimum microstructures. The development of microstructure during sintering has a direct influence upon the defect structure in the material and hence, upon the mechanical strength (Fig. 1). Much of the microstructure evolution occurs during the final stage of sintering. A study has thus been initiated to examine microstructural changes during this stage. Again, a combination of theoretical and experimental work has been embarked upon in order to identify and quantify the critical issues. Particular emphasis is being devoted to the pore grain boundary separation phenomenon, which is known to presage exaggerated grain growth and to terminate densification.

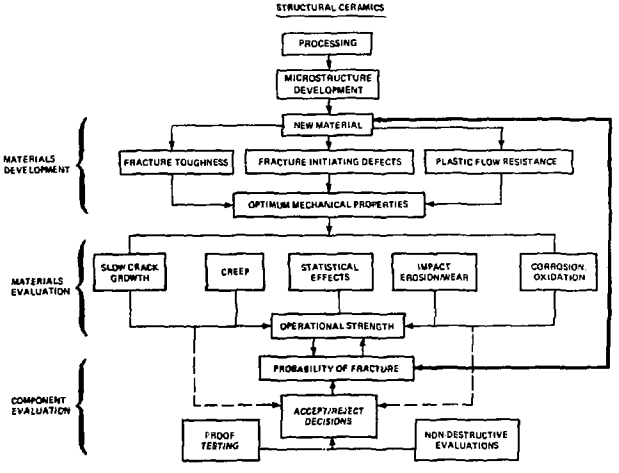

Fig. 1. A scheme for obtaining the information pertinent to structural design with brittle materials. (XBL 802-267A)

*This work was supported by the Director, Office of Energy Research, Office of Basic Energy Sciences, Materials Sciences Division of the U.S. Department of Energy under Contract No. W-7405-ENG-48.

High Temperature Deformation and Failure

1. CAVITATIONAL EFFECTS DURING CREEP IN POLYCRYSTALLINE ALUMINA‡

William R. Blumenthal

Metal and ceramic materials subject to creep have frequently been observed to develop cavities along grain boundaries. These cavities have been cited as the probable source of creep rupture.[1,2] A study was initiated to provide observations of cavity evolution in high strength alumina under controlled strain rate and temperature conditions.[3] Hot-pressed, fully dense, single phase Al_2O_3 + 1/4% MgO with an average grain size of 2 μm was studied. Creep data were obtained using three-point flexure in the temperature range 1550 to 1750 K. The macroscopic creep behavior shown in Fig. 2 can be characterized by a stress exponent of 1.8 and activation energy of 480 kJ/mole.

Microstructural examination with the SEM provided many important observations. Firstly, three distinct cavity shapes were found to evolve, depending upon the applied strain rate, temperature and cavity volume. Initially, "equilibrium" symmetrically shaped cavities were noted (Fig. 3(a)) These cavities typically form at three grain junctions and maintain their shape up to relatively large cavity volumes, when the strain-rate and temperature are low. Such conditions encourage the observed cavity symmetry by virtue of relatively rapid surface diffusion rates (vis-a-vis grain boundary diffusion). Subsequently, the cavities extend along boundaries nearly perpendicular to the applied stress (Fig. 3(b)). These, "crack-like" cavities are encouraged by high strain-rates and high temperatures. The crack-like configuration is a consequence of relatively low surface diffusivities, which limit the ability of cavities to maintain constant surface curvatures. Finally, full-facet cavities form (Fig. 3(b)). This type of cavity develops when a crack-like cavity extends fully across a grain facet. Subsequent growth of these cavities occurs by increases in cavity width, at essentially constant length.

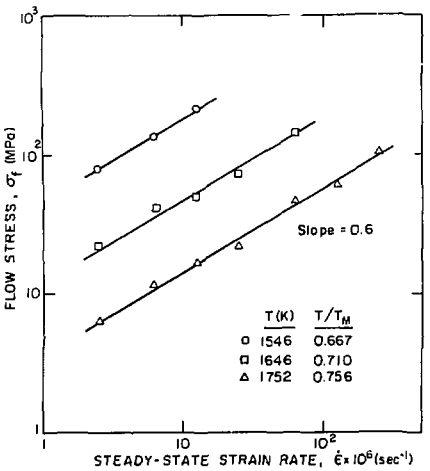

Fig. 2. Flow stress versus strain rate behavior of 2 μm Al_2O_3 + 1/4% MgO. The strain rate exponent is 0.6 with an activation energy of 480 kJ/mole. (XBL 805-5198)

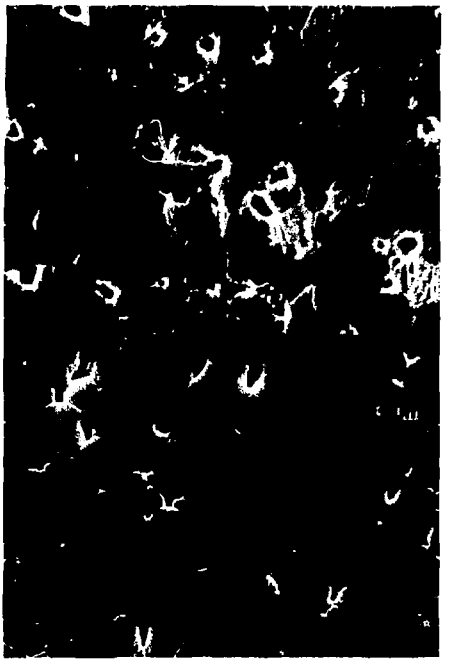

Fig. 3. (a) Micrograph of a sample deformed at 2×10^{-6}sec^{-1} and 1752 K. Equilibrium cavitation is prominent, but inhomogeneity distributed. (b) Micrograph of a sample deformed at 1×10^{-4}sec^{-1} and 1752 K. Crack-like and full-facet cavitation is prominent and very inhomogeneous. (XBB 8012-14671)

The inhomogeneity of the cavitation process is also illustrated by Fig. 3. The non-uniform cavity distribution leads to premature creep rupture. The origin of the inhomogeneity thus provides vital information about the incidence of high temperature failure. These origins are presently under experimental and theoretical investigation. The creep rupture culminates in the lateral spreading of cavitation zones and in cavity coalescence (Fig. 4). The cavity coalescence generates macroscopic cracks that finally extend to failure.

Fig. 4. Micrograph of full-facet cavities coalescing in extended arrays due to their inhomogeneous distribution. Coalescence ultimately produces macrocracks. (XBB 8012-1467J)

* * *

†Brief version of LBL-11830.

1. R. C. Folweiler, J. Appl. Phys. 32, 773 (1961).
2. A. G. Evans and A. Rana, Acta Met. 28, 129 (1980).
3. W. R. Blumenthal, M. S. thesis, University of California, Berkeley (1980).

2. CREEP CAVITATION EFFECTS IN POLYCRYSTALLINE ALUMINA

John R. Porter and Anthony G. Evans

The high temperature deformation of ceramics is frequently accompanied by the nucleation and growth of cavities at grain boundaries.[1] The presence of the cavities is evidently detrimental to the creep performance, since the cavities are both the ultimate origin of creep rupture[2] and a potential source of enhanced deformation. Creep experiments are described that include measurements of the deformation behavior and observations of the dominant cavity morphologies. The material selected for the study is a fine grained alumina, devoid of amorphous phases.

Appreciable cavity formation was invariably observed at the larger strain levels and, in all instances, the cavity distributions are inhomogeneous: an observation of major significance to the interpretation of creep rupture. At low stress the dominant morphology consists of equiaxed cavities at triple points. These cavities are of essentially constant surface curvature and can thus be regarded as the equilibrium-shaped analogy of the lenticular diffusion-created cavities frequently observed in metals on two grain junctions. At the higher stresses, a substantial portion of the cavities exhibit elongated morphologies. Closer examination indicates two characteristic elongated cavities; cavities that occupy an entire grain facet and cavities that extend partially across a grain facet, commencing from a triple point. The latter exhibit a tip morphology typical of crack-like cavities; cavities predicted to exist for conditions wherein relatively slow rates of surface diffusion limit the formation of an equilibrium shape.[3]

The grain boundaries were examined before and after deformation by TEM and STEM techniques. Amorphous phases were not detected (either at two grain or three grain junctions) and no significant segregation of MgO at the grain boundaries could be identified within the STEM resolution capabilities. Most grain boundaries were featureless, but a small fraction (~ 0.1) exhibited periodic structures.

The cavity observations indicate several important effects. The first significant observation is the inhomogeneous nature of the cavity distribution. This nonuniformity derives from the influence of material inhomogeneity in the nucleation and initial growth of the cavities. Probable sources of inhomogeneity are local variability in the dihedral angle or the diffusivity along the cavity surfaces. Boundaries with periodic structures are, for example, likely to exhibit larger dihedral angles than the general boundary and it is, perhaps, significant that such boundaries have not been observed to contain cavities.

The near-tip shape of crack-like cavities created by diffusion is dictated primarily by the surface diffusivity of the material and the cavity velocity.[3] The specific shapes of observed crack-like cavities (Fig. 5) are thus examined in detail in order to determine the level of conformance with the predictions of the diffusive cavity growth model. An explicit prediction of the model is an expression for the cavity width.[3] For each case examined, the measured width was always less than the upper bound value and within a factor of 3. Considering the uncertainty in the diffusion parameter, these correspondences are considered to be sufficiently close to confirm that the observed crack-like cavities had indeed formed by a diffusive mechanism, with surface diffusion as the rate limiting step.

The transition from the equilibrium to crack-like cavity morphology has been predicted to depend upon the stress level, the relative cavity size and the ratio Δ of the surface to boundary diffusivities.[4] The location of this transition is plotted in Fig. 6 for a temperature of 1550 K ($0.15 < \Delta < 0.5$), $\Delta = D_b\delta_s/D_b\delta_b$. The experimentally observed cavities can be placed on the transition diagram to examine conformance with the prediction. This is achieved by adopting the following procedure. Colinear arrays of crack-like and equilibrium cavities nearly normal to the strain axis are identified. The cavity size ratio within the array is determined by direct measurement and the position on the transition diagram is located and plotted. Figure 6 shows results obtained at 1550 K; open circles represent arrays

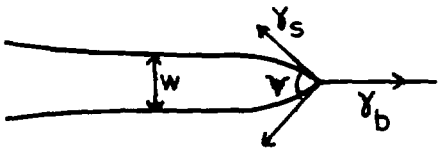

b

Fig. 5. A crack-like cavity. (a) TEM image, σ = 100 MPa, T = 1750 K; (b) schematic. (XBB 809-11136)

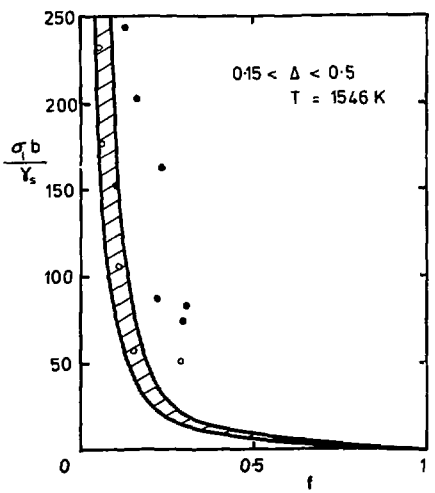

Fig. 6. Cavity transition diagram. Crack-like cavities are predicted above the shaded region, equilibrium cavities below. • represents observation of crack-like cavities. o represents observations of equilibrium cavities. (XBL 808-11538)

of equilibrium-shaped cavities and closed circles refer to crack-like arrays. At this temperature, the predicted transition line adequately separates the experimental observations of the two cavity types.

The reasonable correlations of both the predicted crack-like cavity shapes and the transition condition with the present observations lend credence to the diffusive model as a quantitative description of the cavitation process in fine-grained Al_2O_3.

* * *

1. R. C. Folweiler, J. Appl. Phys. 32, 773 (1961).
2. A. G. Evans and A. Rana, Acta Met. 28, 129 (1980).
3. T-J Chuang and J. R. Rice, Acta Met. 21, 1625 (1973).
4. T-J Chuang et al., Acta Met. 27, 265 (1979).

3. CREEP FRACTURE IN CERAMIC POLYCRYSTALS

Chun Hway Hsueh and Anthony G. Evans

High temperature failure in ceramics often occurs through the gradual growth and coalescence of cavities by diffusive processes, until a macro-crack is formed that subsequently propagates to failure.[1] The process is inhomogeneous, involving preferential cavitation in certain regions of the polycrystalline array.[2] The intent of this article is to examine the role of cavitation inhomogeneity upon the cavity evolution process and hence, upon the time to failure.

The principal sources of inhomogeneity are assumed to derive from local variations in the grain boundary or surface diffusivity (attributed to grain orientation effects, augmented by impurity distributions)[2] or in the dihedral angle (i.e., the ratio of the boundary to the surface energy). The inhomogeneity is needed to provide preferred sites for initial cavitation.

Differences in matter transport rates associated with local variations in grain boundary diffusion, and/or inhomogeneous cavitation result in local stresses. These stresses are induced by the constraint of the surrounding material, and tend to suppress the original differences in matter transport.[3] The constraint thus provides some stability to the inhomogeneous cavity arrays and thereby contributes importantly to determining the rupture time. Determination of these local stresses is central to the analysis of creep rupture. The stress distributions in polycrystalline aggregate are complex. But, an approximate solution to the problem, suggested by Rice,[4] can be used to simulate the principal features of the stress field. This solution is derived from the related problem of a crack in a viscoelastic solid. The solution requires matter to be deposited in a zone of length, d (Fig. 7), at a rate which differs from the average mass transport rate in the surrounding material, due to differences in diffusivity and/or to localized cavity growth. This

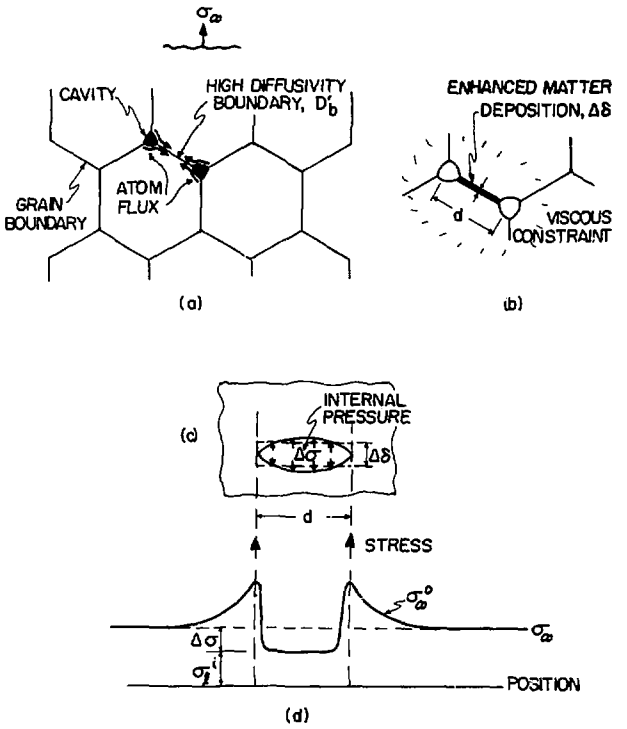

Fig. 7. Schematic indicating localized diffusive flow from cavities and the resultant development of constraint (a) the cavity configuration and atom flux, (b) the thickening displacement between cavities, (c) a crack under internal pressure, and (d) the resultant stress field in a viscous solid. (XBL 8010-6152)

additional matter deposition $\Delta\delta$ exerts normal stresses $\Delta\sigma$ on the region d, similar in magnitude to the stresses created by a crack subject to internal pressure (Fig. 7). The average magnitude of this stress for a circular zone under steady-state conditions is given by

$$\Delta\sigma = -\frac{3\pi\Delta\dot{\delta}\tau_\infty}{2\dot{\gamma}_\infty d}, \qquad (1)$$

where τ_∞ and $\dot{\gamma}_\infty$ are the remote shear stress and shear strain-rate, respectively. The local normal stress, σ_ℓ^i, acting over this region is thus

$$\sigma_\ell^i = \sigma_\infty + \Delta\sigma . \qquad (2)$$

Stresses of opposite sign are created outside region d (Fig. 7). Cavitation rates subject to these local stresses can be deduced for both equilibrium and crack-like cavities. Some typical velocities predicted from the equations derived are plotted in Fig. 8, illustrating the effects of the constraint, the applied stress, the dihedral angle and the surface diffusivity.

The time taken for cavities to extend across grain facets is of principal importance for the creep rupture process. If cavity nucleation occurs soon after steady state is established, the time t_p needed to create a cavity of relative length f can be determined directly from the cavity velocity. Some typical propagation times are plotted in Fig. 9. When the dihedral angle or the local surface diffusivity are small and/or the stress is relatively large, most of the time required to develop a full facet length cavity is dictated by the growth in the crack-like mode (as might be anticipated from the velocity diagrams). The

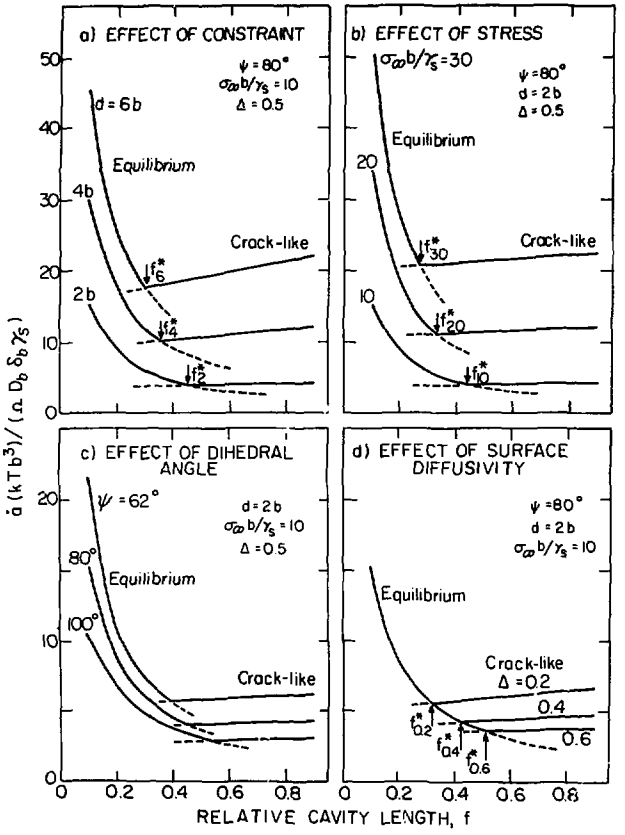

Fig. 8. Plots of cavity velocity for several choices of the important variables, (a) the effect of constraint, (b) the influence of the applied stress, (c) the effect of the dihedral angle, and (d) the effect of small changes in the surface diffusivity. (XBL 8010-6166)

initial cavitation that occurs in local regions of a creeping polycrystal (due to small local values of Ψ or D_s) can thus be approximately characterized by a constant velocity relation; whereupon the propagation time t_f becomes

$$t_f\dot{\varepsilon}_\infty \approx 4\pi(g/d)^{3/2}\,(\gamma_s/\sigma_\infty b)^{1/2}\,\sin(\Psi/4)^{3/2}\,(D_s\delta_s/D_b\,b)^{1/2}, \quad (3)$$

where $\dot{\varepsilon}_\infty$ is the steady-state strain rate, $D_b\delta_b$ and $D_s\delta_s$ are the boundary and surface diffusion parameters, respectively, Ψ is the dihedral angle, γ_s is the surface energy, g is the grain diameter, and b is the grain facet length.

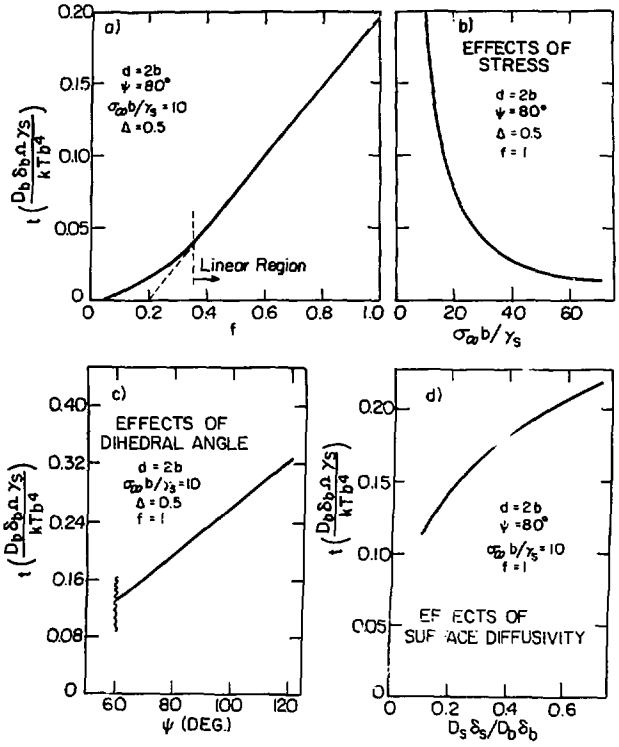

Fig. 9. The cavity propagation time characteristics (a) the variation of time with cavity length, (b) the effect of stress on the time taken to reach f = 1.0, (c) the effect of dihedral angle, and (d) the influence of surface diffusivity. (XBL 8010-6159)

The analysis thus anticipates a strong interdependence of the failure time and the steady-state creep rate, as generally observed (the Monkman-Grant Relationship), although an additional dependence of the failure time on the stress $(\gamma_s/\sigma_\infty b)^{1/2}$ emerges from the present analysis. Important effects of the local dihedral angle and of the diffusivity ratio are also predicted, in the sense that small values of these parameters encourage failure.

* * *

1. R. C. Folweiler, J. Appl. Phys. 32, 773 (1961).
2. J. R. Porter, W. Blumenthal, and A. G. Evans, to be published.
3. B. F. Dyson and D. McClean, Metal Sci. J. 6, 200 (1972).
4. J. R. Rice, to be published.

4. THE HIGH TEMPERATURE INTERNAL FRICTION BACKGROUND IN POLYCRYSTALS

Amar P. S. Kana, Anthony G. Evans, and Roland M. Cannon

Internal friction measurements performed on polycrystals are usually characterized by a peak, superimposed on a background that increases in intensity with increase in temperature or decrease in frequency[1] (Fig. 10). Both the peak and the background[2] is not well understood, but is presumed to relate to the plastic flow or diffusion that occurs in response to the elastic

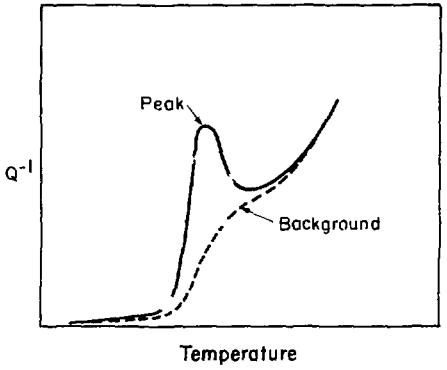

Fig. 10. Internal friction (Q^{-1}) vs. temperature. (XBL 8010-6059A)

stresses, causing these displacements to redistribute with time. The intent of the present article is to examine the internal friction background in ceramic polycrystals and to establish its dependence on grain boundary diffusion.

Examination of internal friction data for ceramic polycrystals[3] indicates that the background usually exhibits rapid development at temperatures above the peak, as illustrated in Fig. 10. Such behavior is indicative of a background that can be enhanced by the same mechanism that provides the peak itself: presumably, grain boundary sliding. In this case, the background intensity is considered to be dictated primarily by the diffusion that occurs in response to the sliding induced local displacements.

Grain boundaries are considered capable of sliding with a negligible viscosity, as appropriate for temperatures in excess of the sliding peak. Elastic singularities can thus develop at the grain corners. For cyclic conditions the periodic displacement of the freely sliding grain boundaries leads to a cyclic singularity. The stresses that result from diffusive redistribution of the cyclic singularity (Fig. 11) are not in-phase with the applied displacement; the out-of-phase component of the stress is the source of the internal friction given by

$$Q^{-1} = \frac{\int_0^{Sp^*} [p^{1/6}/(1+p^2)]dp}{\int_0^{Sp^*} [p^{7/6}/(1+p^2)]dp}, \qquad (1)$$

where $p^* = \omega\ell^3(1-\nu^2)kT/ED_b\delta_b\Omega$, ℓ is the grain facet length, ω is the frequency, $D_b\delta_b$ is the grain boundary diffusion parameter and Ω is the atomic volume. This result is plotted in Fig. 12. The

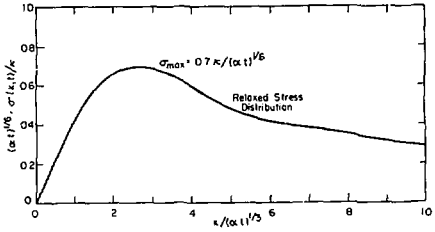

Fig. 11. Relaxed stress distributions plotted using normalized coordinates as suggested by the analysis. (XBL 8010-6063)

low frequency limit is analogous to steady-state cyclic creep controlled by grain boundary sliding and grain boundary diffusion and has the form of the Coble creep resul . The high frequency limit exhibits an exponent of 1/6, typical of sliding dominated relaxation effects. This exponent arises because the relaxed stress field is characterized by the product of a relaxation distance that varies as $t^{-1/3}$ and an elastic singularity that varies as $x^{-1/2}$.

Exclusion of grain boundary sliding leads to an internal friction at the high frequency limit given by;

$$Q_b^{-1} = 2(1+\nu)\left[\frac{ED_b\delta_b\Omega}{\omega\ell^3(1-\nu^2)kT}\right]^{1/2} \qquad (2)$$

This solution is plotted on Fig. 12, where it is compared it is compared with the grain boundary sliding solution. The principal distinction is the 1/2 exponent, which causes Q_b^{-1} to exceed the grain boundary sliding result Q_s^{-1} at intermediate frequencies.

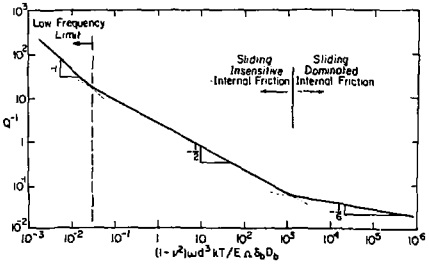

Fig. 12. The predicted internal friction, (Q^{-1}), versus $(1-\nu^2)\omega d^3kT/E\Omega\delta_b D_b$ showing the low, intermediate and high frequency regions. (XBL 8010-6065)

The available internal friction data suitable for correlation with Fig. 12 are sparse. Predictions of grain boundary diffusivities for Al_2O_3 obtained from internal friction results are summarized in Fig. 13. The predicted boundary diffusivities locate within the range of values determined by other methods.[3] Grain boundary viscosity predictions for Si_3N_4 are summarized in Table 1, where they are compared with viscosities obtained by extrapolating the viscosity levels inferred from the sliding peak.[4] The correlation is reasonable.

The internal friction background provides a very sensitive measure of effects of microstructure on the grain boundary diffusivity or viscosity. The method is also relatively simple and non-destructive: advantages that permit trends in the diffusivity/viscosity with microstructure to be studied in a single specimen. The accuracy of the diffusivity measurements, based on the present interpretation of the background, remains to be established. However, the preliminary correlations are encouraging.

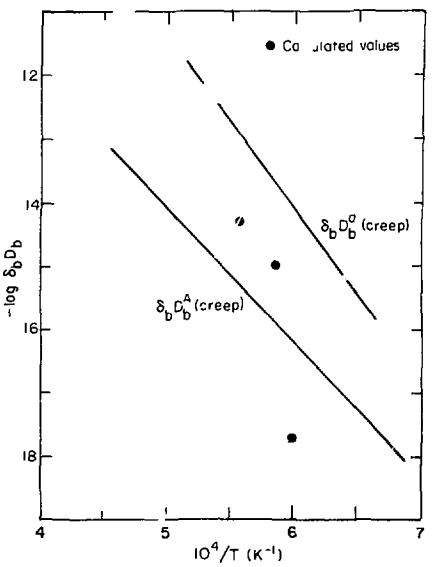

Fig. 13. The grain boundary diffusivity of Al_2O_3. The values calculated from the internal friction background are shown for comparison. (XBL 010-6058)

Table 1. Comparison of viscosity per unit thickness for Si_3N_4 (grain boundary thickness ~ 20 Å) predicted from the background and the internal friction peak.

	(η/δ) Poise/cm	
T(K)	Background	Peak (extrapolated)
1338	1.9×10^{12}	1.6×10^{12}
1398	1.2×10^{12}	2.0×10^{11}
1458	4.6×10^{11}	4.0×10^{10}

* * *

1. A. S. Nowick and B. S. Berry, "An Elastic Relaxation in Crystalline Solids," Academic Press, New York, 1972.
2. B. Escaig, Acta Met. 10, 829 (1962).
3. J. M. Dynys, R. L. Coble, and W. S. Coblenz, "Mechanisms of Atom Transport During Initial Stage Sintering of Al_2O_3" in Sintering Processes, C. C. Kuczynski, ed., Plenum Publishing Co., 1980.
4. D. R. Mosher and R. Raj, J. Mat. Sci. 11, 49 (1976).

5. THE INFLUENCE OF CAVITIES ON GRAIN BOUNDARY SLIDING

Amar P. S. Rana and Anthony G. Evans

High temperature failure in ceramics frequently involves the nucleation, growth and coalescence of grain boundary located microcracks or cavities, accompanied by grain boundary sliding.[1] The intent of the present study was to examine grain boundary sliding in the presence of pre-existing cavities (using an internal friction technique) in order to establish its role in the cavitation process. The study recognizes that high temperature failure in ceramics is strongly microstructure dependent.[1] Two types of microstructure, and the concommitant modes of grain boundary sliding, have been distinguished. The first is a single phase material; the second consists of grains encompassed by an amorphous second phase. Models of grain boundary sliding have been developed for both microstructures, with cavities located at three grain junctions. The models suggest a minimum influence of cavities on the sliding amplitude and thus, upon the internal friction peak. Experimental studies of the internal friction peak have confirmed the minor role of cavities, for both classes of microstructure. Consequently, grain boundary sliding is shown to be incidental to the cavitation process.

The sliding that occurs in the presence of cavities can be deduced from a wedge crack analysis conducted during the previous year.[2] In this analysis, the elastic displacements of sliding boundaries were derived for situations in which small wedge cracks were located at three grain junctions. The compliance of a cavity is precisely the same as that of a wedge crack and hence, the sliding solutions for a wedge crack can be directly transferred to the present problem. The average elastic sliding displacement $\langle u \rangle_{tpc}$ relative to the sliding displacement that occurs without cavities $\langle u \rangle$ is plotted in Fig. 14. It is noted that, for small values of a/ℓ (typical of the present internal friction experiments) the contribution to the sliding from triple point cavities is small.

The relaxation time for grain boundary sliding (the quantity evaluated experimentally from the internal friction peak) can be determined directly from the elastic sliding displacement. The relaxation time τ is given by:

$$\frac{\tau \cos\theta}{d \cos 2\theta} = (\eta/\delta)\,\frac{3(1-\nu^2)}{16E}\left[1 + \frac{2\pi F \cos\theta \operatorname{cosec} 2\theta}{d} \times \left(\kappa(3d/8\cos\theta)^{1/2} - \sin 4\theta\,(\pi a/2)^{1/2}\right)\right], \quad (1)$$

where F is the fraction of triple points containing cavities, δ is the grain boundary thickness, d is the grain size, η is the viscosity of the grain boundary, θ is the boundary inclination and κ is the function plotted in Fig. 15.

Experimentally determined relaxation times for various tests are plotted logarithmically against reciprocal absolute temperature in Fig. 16. The activation energy for the single phase microstructure is 160 ± 20 kcal/mole and 95 ± 5 kcal/mole for the microstructure containing the continuous glassy film at the grain boundaries. Both values correlate quite well with values that exist in the literature.[3] Also shown on the figures are the relaxation times predicted from Eq. (1). The predictions were conducted by obtaining values for the boundary viscosity from internal friction measurements performed on similar polycrystals, sintered to full density. Within the uncertainties associated with this procedure, the correlations are considered to be satisfactory in both cases. The minor role of cavities upon the sliding process is thus validated.

Complementary studies indicate that the relatively small increases in sliding displacement in the

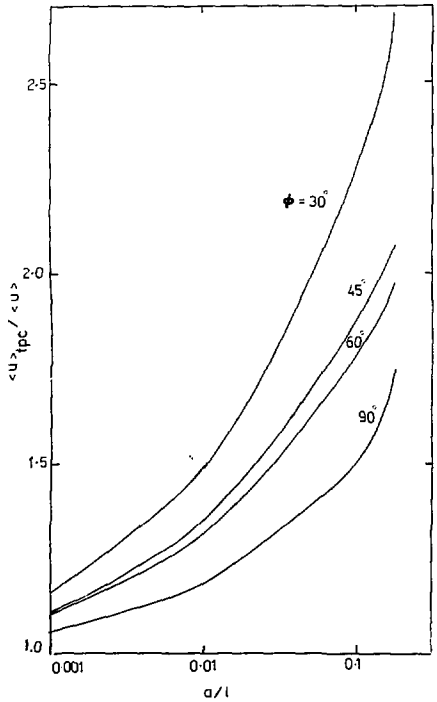

Fig. 14. Variation of the ratio of the elastic displacements with and without triple point cavities as a function of cavity size and angle. (XBL 809-11787)

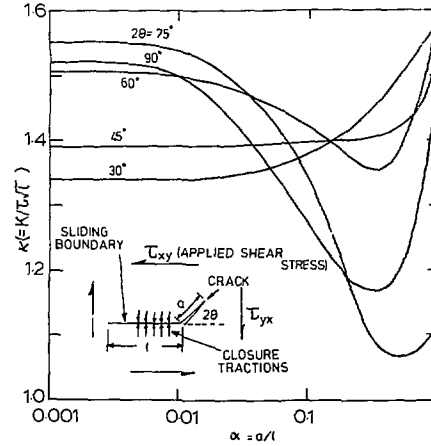

Fig. 15. The variations of stress intensity factor with crack length and angle, for a kinked crack subject to in-plane shear and small closure tractions. (XBL 806-10227)

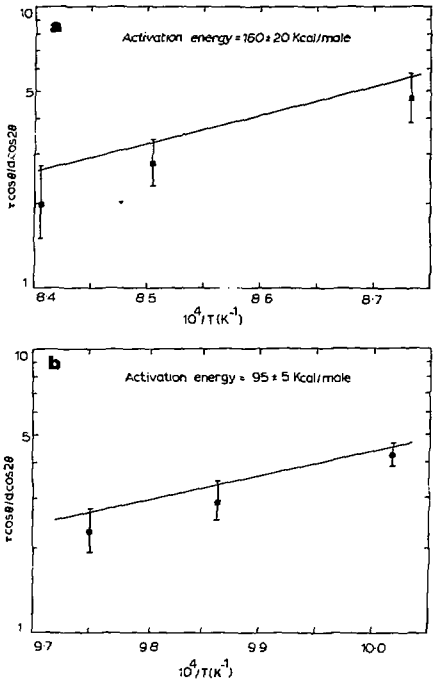

Fig. 16. Normalized relaxation time plotted as a function of reciprocal absolute temperature for (a) mullite (75 wt% Al_2O_3), and (b) mullite (71.8 wt% Al_2O_3).
[(a) XBL 8019-12366; (b) XBL 8010-12367]

presence of cavities are insufficient to appreciably enhance the cavitation rate compared with a system in which sliding is prohibited. Specifically, an upper bound increase in cavitation rate by a factor of 2 obtains due to the transfer of normal stress from the sliding boundaries to the cavitating boundaries.

* * *

1. A. G. Evans and A. S. Rana, Acta. Met. 28, 129 (1980).
2. A. G. Evans, Acta. Met. 28, 1155 (19[illegible]).
3. R. A. Penty and D. P. H. Hasselman, [illegible]. Res. Bull. 7, (10), 1117 (1972).

6. TRANSFORMATION TOUGHENING IN CERAMICS

David B. Marshall and Anthony G. Evans

The toughness of ceramic materials can be considerably enhanced by designing microstructures with second phase particles which transform martensitically in the vicinity of a crack tip.[1] Major research efforts are currently devoted to the use of the tetragonal to monoclinic transformation in ZrO_2 with various matrix materials (e.g., stabilized cubic ZrO_2, Al_2O_3, ZnO). The development of optimum toughness requires strict control of composition and microstructure. An ability to predict optimum conditions is thus of considerable importance.

Theoretical analyses of martensite toughening are subject to some controversy. For instance, previous analyses (all based on thermodynamic arguments) involve assumptions concerning the critical conditions for transformation, whether the transformation is reversible, whether microcracking occurs, and which energy terms are significant. There are even conflicting predictions of the sign of the toughness change resulting from a given energy term. Therefore the toughening models have been reevaluated with the aim of comparing the toughening calculated by two independent approaches: one using mechanics procedures and other using a thermodynamic treatment. The influence of various transformation zone geometries has been evaluated, with particular attention being directed to comparison of the toughening resulting from a zone contained entirely ahead of the crack tip, and zones extending over the crack surface (Fig. 17). The agreement obtained from the two models is encouraging, and in particular the prediction, by both models, of previously unexpected R-curve behavior (Fig. 17) tends to substantiate some of the assumptions of the analyses.

In the mechanics approach, the toughening is calculated directly in terms of the change in local crack tip stress intensity induced by the transformation zone. A procedure similar in principle to that developed by Eshelby for calculating stress fields around transformed particles and inclusions is adopted: the prospective transformation zone is removed from the matrix and allowed to transform, a stress σ_{ij} is applied to the zone surface to restore its original dimensions, the zone is reinserted into the matrix, and equal and opposite tractions T_{ij} are applied to the zone boundary to achieve stress continuity (Fig. 17). These tractions induce a change in stress intensity factor.[2] The change in stress intensity factor was evaluated for a series of zone profiles; first a zone defined by a contour of the dilational component of the crack tip stress field, then profiles obtained by allowing the crack to advance a distance Δa so that the zone maintains the dilation field contour ahead of the crack, but traces out a wake of uniform width r_0 extending over the

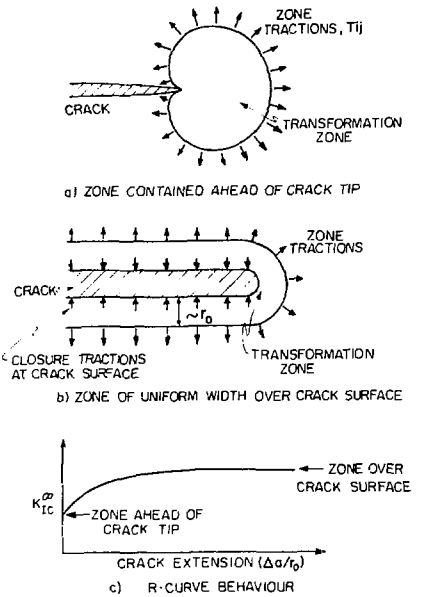

Fig. 17. (a) A process zone contained ahead of the crack tip, with the hydrostatic contour. ΔK for this zone is zero. (b) A process zone contained over the crack surface. This zone provides crack tip shielding. (c) A schematic of R-curve behavior for transformation toughening in an annealed material. (XBL 809-5932A)

crack surfaces. The initial configuration gives $\Delta K_I = 0$, hence no toughening is experienced. Then, ΔK_I increases continuously with X and approaches a saturation level for $\Delta a \gtrsim 3r_o$ (Fig. 17(c)) given by

$$\Delta K_{IC} = 0.34\ V_f\ E\ \Delta V\ \sqrt{r_o}\ ,$$

where V_f is the volume fraction of tetragonal particles, E is Young's modulus and ΔV is the unconstrained volume transformation strain of an individual particle. *This expression is based on* the assumption that the transformation volume strain is the major source of toughening. The expression gives reasonable agreement with measured toughness increases, thus providing some support to the assumption. However, more reliable experimental measurements of zone dimensions are required for a more definitive distinction.

In the thermodynamic analysis, the energy changes that accompany a crack increment dc relate to the critical strain energy release rate G_{IC}: $G_{IC} = G_{IC}^{o} + \Delta G_{IC}$, where $G_{IC}^{o}\, d\alpha = 2\,\Gamma\, d\alpha$ is the surface energy increase and $\Delta G_{IC}\, d\alpha$ is the increase in energy associated with the transformed particles. The criterion selected to define the zone boundary requires that the change in potential following transformation be zero. Then, ΔG_{IC} can be expressed as a function of $\Delta\phi_{int}^{o}$ and $\Delta\phi_{int}^{A}$, the interaction energies at the front and rear of the zone boundary (Fig. 18). By computing the stress on the rear boundary ΔG was evaluated for the zone configurations already described. For the initial dilational zone, $\Delta\phi_{int}^{o} = \Delta\phi_{int}^{A}$, and there is no toughness increase. Then, ΔG increases as the zone extends behind the crack tip and approaches a saturation value for $\Delta\alpha > 3r_o$ (Fig. 18) given by

$$\Delta G/G_{IC}^{o} = 0.07\ V_f\ \Delta V^2\ E/(1-\nu^2)\ \Delta\varepsilon\ , \qquad (1)$$

where $\Delta\varepsilon$ is the transformation energy change in the absence of an external field.

Defining r_o in the mechanics description by the same thermodynamic criterion gives

$$\Delta K_{IC}/K_{IC}^{o} = 0.09\ V_f\ \Delta V^2\ E/\Delta\varepsilon\ . \qquad (2)$$

This is remarkably similar to the expression derived from the thermodynamics analysis.

The prediction of identical R-curve behavior by these two independent derivations adds further credence to the models. The increase of toughness with crack extension, for a crack which initially has no transformation zone, should be observable with carefully designed experiments. The practical implications of the effect are expected to be most important for small cracks where the zone size is a significant fraction of the crack length. The implications for optimum toughness concern the criticality of the temperature, the chemical composition of the martensite, the toughness of the matrix and the particle size distribution.[3]

* * *

1. R. C. Garvie, R. H. Hanninck and R. T. Pascoe, *Nature* 258, 703 (1975).
2. P. C. Paris, R. McMeeking, and S. Tada, ASTM STP 601 (1978).
3. A. G. Evans, N. Burlingame, M. Drory, and W. M. Kriven, Acta Met., in press.

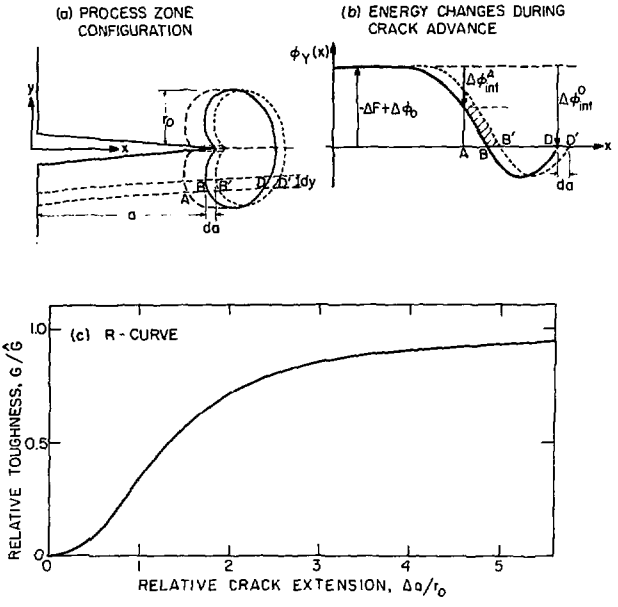

Fig. 18. The R-curve determined by employing a thermodynamic treatment. (a) The zone characteristics. (b) The potential change during a crack increment. (c) The relative toughening during a crack advance.
(XBL 809-5895)

7. THE TOUGHNESS OF ZIRCONIA COMPOSITES

Nicholas H. Burlingame and Anthony G. Evans

Toughness data have been obtained on a range of ZrO_2 containing materials, selected to encompass the variables that exert a primary influence upon martensitic toughening: solute content, matrix material, particle size distribution, volume fraction and temperature.[1,2] Two principal matrices were selected for study, Al_2O_3 and mullite. The solutes chosen were Y_2O_3, MgO and CaO. The relative contents of the tetragonal and monoclinic ZrO_2 phases and the fracture toughness were determined in each experiment. The toughness can be uniquely related to the phase ratio through the influence of the particle size distribution upon the transformation.[2] The materials were fabricated by a sol-gel process (Al_2O_3-ZrO_2) or by in-situ reaction (mullite-ZrO_2).

The expected increase in the fracture toughness K_{IC} with V_f is exhibited. However, the initial increase in toughness also coincides with an increase in the monoclinic phase content. This effect presumably relates to a coarsening of the ZrO_2 particles and, thus, a decrease in their stability, as V_f is increased. At large V_f the toughness diminishes rapidly. This decrease is presumed to coincide with the onset of microcracking. Supporting this assumption are the trends in hardness, which indicate a sharp decline in hardness beyond the maximum toughness. The concomitant changes in particle size and volume fraction introduce some ambiguity into interpretation of size effects. Two mullite-ZrO_2 materials with similar volume fractions and different size distributions have thus been compared (Fig. 19). These results clearly demonstrate that the toughness is a strong function of the particle size.

Matrix effects on toughness can be isolated by altering the matrix toughness without changing the composition. This was accomplished by studying a mullite-ZrO_2 system before and after annealing. The annealing increased the matrix toughness, by modifying the grain aspect ratio (cf. Si_3N_4). The material with the higher matrix toughness exhibited a substantially greater toughness enhancement, in conformance with predictions.[1,2]

The effect of solute additives is illustrated in Fig. 20. A peak in toughness occurs, coincident with a significant proportion of monoclinic phase.

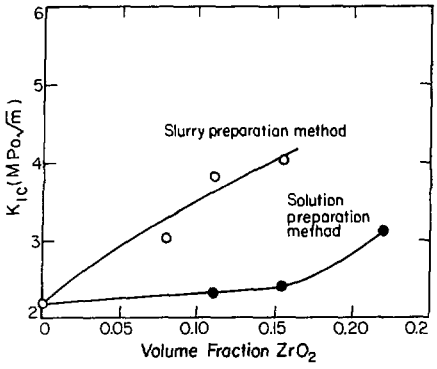

Fig. 19. The variation of fracture toughness with the volume fraction of ZrO_2 for mullite/ZrO_2. (XBL 812-359)

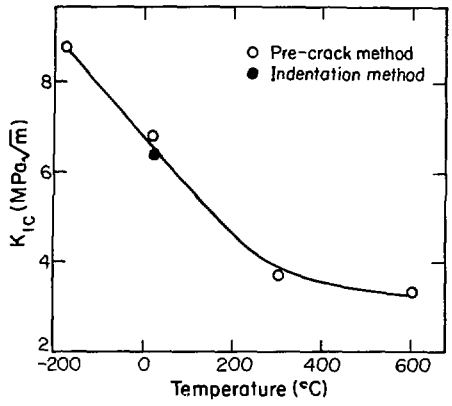

Fig. 21. Fracture toughness as a function of temperature for a Al_2O_3 material with 0.4 volume fraction ZrO_2. (XBL 812-538)

This coincidence is qualitatively consistent with theoretical expectations. However, quantitative discrepancies with the existent theory are evident upon detailed scrutiny. These discrepancies remain to be solved.

A change in temperature has an effect similar to the addition of a solute. For a material with a high content of tetragonal phase, it is demonstrated (Fig. 21) that the toughness will decrease as the temperature increases. However, it is important to note than an extremely high value of toughness (K_{IC} = 8.8 MPa√m) obtains at liquid nitrogen temperature. It is assumed that this value could be achieved at room temperature by optimizing the solute content or the particle size distribution.

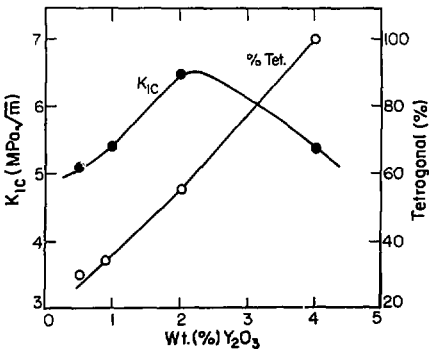

Fig. 20. Fracture toughness and percent tetragonal plotted as a function of the weight percent Y_2O_3 for a Al_2O_3/ZrO_2 material with 0.3 volume fraction ZrO_2 (hot pressed at 1550°C). (XBL 812-360)

An indirect method of toughening is also possible in ZrO_2 composites, due to the formation of a compressive region at the surface. This layer will form as a consequence of transformation during abrasion. The effective toughness (K_{eff}) is given by

$$K_{eff} = \frac{2}{\sqrt{\pi}} \sigma_o \sqrt{c} + K_{IC} , \qquad (1)$$

where σ_o is the stress at the surface. Rather large increases in the effective toughness are possible. The effect is strongly related to the depth of the transformed layer.

* * *

1. A. G. Evans and A. H. Heuer, J. Am. Ceram. Soc. 63, 241 (1980).
2. A. G. Evans, N. H. Burlingame, M. Drory and W. M. Kriven, Acta Met., in press.

Indentation Processes

8. THE RESPONSE OF SOLIDS TO ELASTIC/PLASTIC INDENTATION

Shu Sheng Chiang, David B. Marshall, and Anthony G. Evans

A new approach for analyzing indentation plasticity and indentation fracture has been devised. The analysis devises relations between material

properties (notably hardness, yield strength and elastic modulus) and the dimensions of the indentation and of the plastic zone. Calculations of the indentation stress fields have been conducted and used to generate predictions of indentation fracture thresholds for the three dominant crack types: radial, median and lateral. The approach uses new concepts for extending the existent spherical cavity model to a generalized indentation.

The observed shape invariance of the indentation pressure[1] (hardness, H) and plastic zone dimension permit experimental indentation results to be referred to a common indentation geometry. A convenient reference geometry is the hemispherical indentation with hemispherical pastic zone. Transferring the indentation pressure directly to the reference geometry permits experimental results to be readily compared with hemispherical indentation analyses.

The analysis of the hemispherical indentation commences with the elastic/plastic solution for a spherical cavity which provides an initially symmetric elastic/plastic field (Fig. 22), and then creates a free surface by eliminating the tangential

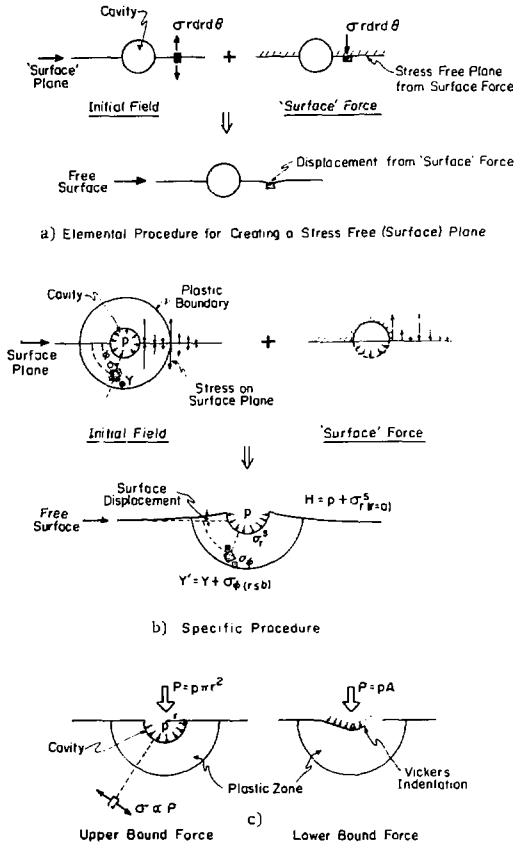

Fig. 22. A schematic showing the analytic procedure for creating a stress free surface and hence, for deforming the residual stress distribution (a) the general procedure, (b) the specific procedure for the hemispherical indentation, and (c) the upper and lower bound conditions used for calculating the stress at peak load. (XBL 806-5376)

stress field acting over a plane through the cavity center (Fig. 22). This elimination is achieved by using the elastic point force solutions pertinent to the half-space problem. The stresses that result from these forces superimpose onto the initial, symmetric stresses to generate the indentation stress field.

The radial and tangential stresses induced within the plastic zone result in a pressure modification. The modified pressure can be used to evaluate the relationship between the indentation characteristics and the elastic and plastic properties of the material. These resultant curves (e.g., Fig. 23) indicate a good correlation with the experimental results.

The stress field can also be used to predict the fracture initiation threshold, by deducing stress intensity factors, K. A peak in the stress intensity factor is encountered. A minimum threshold occurs when this peak attains K_c. The minimum threshold load for a Vickers pyramidal indenter is given by

$$P_{min} = 2H[K_{IC}/H]^4/(0.45)^2 \quad . \qquad (1)$$

The trends in the threshold are summarized in Fig. 24. Minimum threshold loads for the three crack types predicted for materials with a range of plastic zone radii indicate that radial cracks exhibit the lowest thresholds and lateral cracks the largest.

Observed radial crack threshold conditions are compared with predictions in Table 2. Good agreement is shown for Ge, Si, Al_2O_3 and ZnS. The observed threshold for NaCl appears to be lower than predicted. However, as noted by Lankford and

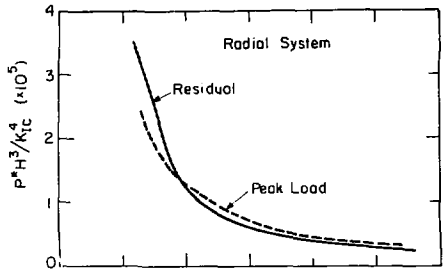

Fig. 24. Trends in the radial fracture threshold predicted by the present analysis. (XBL 8010-6057)

Table 2. Radial crack initiation threshold.

Material	β	Prediction c* (μm)	Prediction p* (N)	Experimental observations c* (μm)	Experimental observations p* (N)
Glass	2.2	1.1	0.6	17	5
Ge	2.5	0.16	0.014	0.25	0.02
Si	2.65	0.36	0.05	0.65	0.03
Al_2O_3	2.5	0.6	0.4	3	0.25-0.5
NaCl	6.3	340	120	100	15-60
ZnS	4.0	17	8	70	6

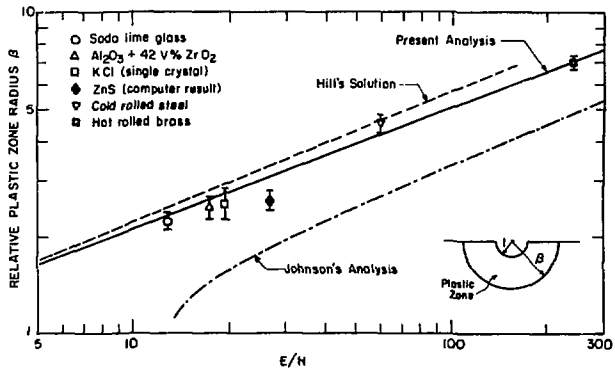

Fig. 23. The effect of the ratio of the modulus to the hardness, E/H, on the relative plastic zone size β (b/a) for a range of materials. Also shown are the theoretical predictions from the Hill solution, the Johnson analysis, and the present analysis. (XBL 806-5362A)

Davidson,[2] the NaCl threshold is sensitive to crystallographic orientation; the experimental value listed in Table 2 corresponds to cracks parallel to (110). Radial cracks could not be nucleated in other orientations, within the available load range (~ 60 N). The (110) cracks in NaCl are coincident with the primary slip bands that occur outside the generalized plastic zone. The cracks result from an enchancement of the local stress by the stress field of the dislocations, and a threshold appreciably smaller than that associated with the generalized deformation is to be anticipated.

The observed thresholds for glass are an order of magnitude higher than predicted. This observation suggests that the precursor flaw density is too small to permit an appreciable sampling of flaws of the requisite size, at the minimum threshold load. The excess threshold load can be quantified (in terms of the availability of preexistent nucleating flaws) by adapting some existing statistical data for surface flaws in glass.[3] At the observed threshold load (5 N) the expected number of flaws of the required size (0.5 μm) in the tensile zone (at initiation) is calculated to be ~ 0.1. This is sufficiently close to the required value of unity (considering the approximate nature of the flaw statistics) that the statistical description is considered to provide a reasonable interpretive description of the excess threshold load.

* * *

1. L. E. Samuels, T. O. Mulhearn, J. Mech. Phys. Solids 5, 125 (1957).
2. J. Lankford and D. L. Davidson, J. Mat. Sci. 14, 1662 (1979).
3. J. R. Matthews, W. Shack, and F. A. McClintock, J. Am. Ceram. Soc. 59, 304 (1976).

Ceramic Processing

9. FINAL STAGE SINTERING MODELS

Marlene Spears, Chun Hway Hsueh, and Anthony G. Evans

The major impediment to the development of a fine grained pore free microstructure (with good mechanical properties) is the pore, grain boundary separation phenomenon. The separation event presages exaggerated grain growth and a termination of the densification process. The event is only qualitatively understood in terms of a phenomenological model.[1,2] A quantitative, physical model is needed in order to design sintering schedules that avert separation. The preliminary development of such a model, and its experimental validation, is the purpose of the present study. Specifically, pore shapes have been calculated as a function of their velocity, and grain boundary shapes during the breakaway process have been evaluated. These quantities are used to identify conditions wherein the boundary velocity exceeds the pore velocity.

The existent model[1] assumes a pore that remains spherical throughout its motion (i.e., a dihedral angle $\Psi = \pi$) and allows the grain boundary intersection line to move freely over the pore surface. Once the boundary has sufficient driving force to achieve an inclination of 45° to the direction of pore motion, a maximum force condition pertains and breakaway is assumed to ensue. When more realistic choices of the dihedral angle are made, however, the pore/grain boundary behavior is found to be different.

Initial calculations of the pore shape have been performed. These calculations involve considerations of the atom flux over the pore surface, as dictated by the curvature of the surface.[2] The solutions specify the inclination of the pore surfaces at the grain intersections points (Fig. 25) as functions of the velocity v and dihedral angle (a result that will be used later):

$$\Psi_1 = \frac{\Psi}{2} - \frac{vkTa^3}{3D_s\delta_s\gamma_s\Omega} \qquad (1a)$$

$$\Psi_2 = \frac{\Psi}{2} + \frac{vkTa^3}{3D_s\delta_s\gamma_s\Omega}, \qquad (1b)$$

where a is the spacing between opposite grain intersection points, $D_s\delta_s$ is the surface diffusion parameter, γ_s is the surface energy and Ω is the atomic volume. Also, the detailed shapes of the pore surfaces can be deduced. Some typical shapes are plotted in Fig. 26.

By also noting that the pore volume is velocity independent (no shrinkage has been allowed in this analysis), integration over the pore shape leads to the conclusion that the pore width, a, is velocity independent. The constancy of the pore width implies that there is no force maximum at 45° boundary inclination (in contrast to the spherical pore analysis), and hence, no upper bound pore velocity.

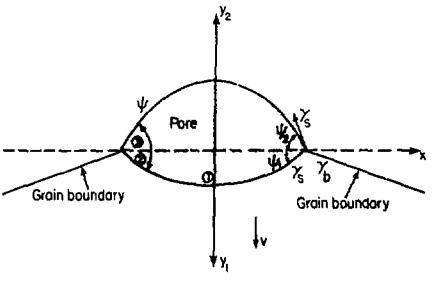

Fig. 25. Two-grain boundary interaction with a "lenticular" pore ($\Psi < \pi$). (XBL 812-361)

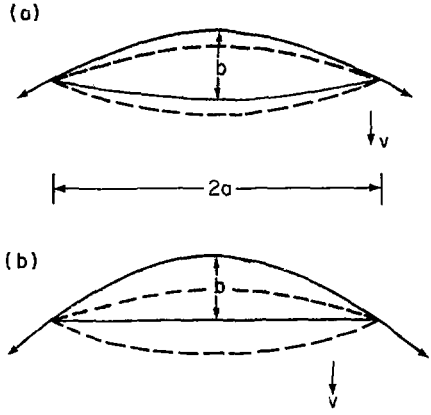

Fig. 26. Pore shape variation with velocity. (a) low velocity. (b) "intermediate" velocity.
(XBL 812-357)

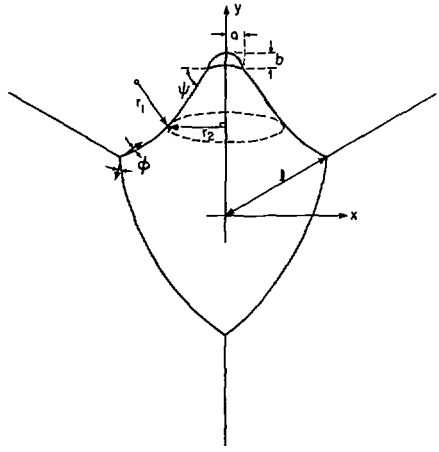

Fig. 27. Pore drag of a moving grain boundary.
(XBL 812-362)

The absence of a maximum pore velocity requires that the breakaway criterion be re-examined. This is best achieved by noting the pore, grain boundary morphology expected prior to a breakaway sequence (Fig. 27). A determination of the shape of the grain boundary containing the pore can be conducted presuming that the chemical potential along the boundary is uniform. The inclination of the boundary at the pore ($x = a$) can thereby be deduced for any grain dimension, ℓ. This inclination, ψ, (Fig. 25) defined the velocity v_p that the pore must exhibit in order that equilibrium be satisfied. The velocity v_b of the other two boundaries can also be directly expressed in terms of ℓ and the boundary mobility, M_b. A comparison of the two velocities, v_b and v_p, permits a breakaway condition to be identified. This comparison shows that pore separation occurs whenever the pore size, a, exceeds a critical value, independent of the grain size,

$$a_c^2 = \frac{D_s \delta_s \gamma_s \Omega}{3kT\gamma_b M_b} \quad . \qquad (2)$$

This critical pore size has a similar functional form to the pore size at the "knee" of the separation region in the spherical pore theory. The qualitative implications are thus essentially the same; notably, the need to decrease the boundary mobility vis-a-vis the surface diffusivity. However, significant quantitative differences exist; differences that are presently subject to experimental evaluation. Finally, it is noted that, since the pore size typically scales with the grain size in the final stages of sintering, Eq. (2) has obvious implications for the control of grain coarsening as a means of limiting pore separation.

* * *

1. F. M. A. Carpay, "The Effect of Pore Drag on Ceramic Microstructures," Ceramic Microstructures '76, R. M. Fulrath and J. A. Pask, eds., 1977.
2. R. J. Brook, "Pore-Grain Boundary Interactions and Grain Growth," J. Am. Ceram. Soc. 52 (1), 56 (1969).
3. Tze-Jer Chuang, "Models of Intergranular Creep Crack Growth by Coupled Crack Surface and Grain Boundary Diffusion," Ph.D. thesis, Department of Engineering, Brown University, November 1974.

RESEARCH PLANS FOR CALENDAR YEAR 1981

High Temperature Deformation and Failure in Ceramics

High temperature failure studies conducted with a variety of ceramic polycrystals indicate a diversity of failure processes. Each process will require study in order to provide a comprehensive framework for failure prediction and microstructural design--the ultimate objective of studies conducted in this area. Studies initiated on several characteristic microstructural groupings will be continued during 1981. These include: single phase materials (e.g., sintered SiC, Al_2O_3) in both the fine-grained and coarse-grained regimes, and materials with a continuous grain boundary phase (e.g., sintered Si_3N_4). Ultimately, it is hoped to develop failure maps that relate these failure processes.

Single Phase Materials

Fine Grained Polycrystals. Theoretical analysis of cavity evolution coupled with experimental observations on a fine grained Al_2O_3 have established a preliminary framework for the prediction of creep rupture in fine-grained, single phase ceramics. A validation of the model developed during 1980 will be conducted by performing creep rupture experiments on Al_2O_3, and by extending the present calculations of the cavity zone spreading process to include statistical accumulations of cavitation prone regions (using the statistical procedures identified in the preceding year). Attempts at identifying the origin of these regions will also be continued using TEM and STEM techniques. Particular emphasis will be placed upon distinguishing the relative roles of a low local dihedral angle, vis-a-vis a low surface diffusivity (the important variables identified in the theoretical study), as influenced by crystal anisotropy and/or solute distributions. Large grained zones have also been identified in recent studies as preferred sites for high temperature failure. Theoretical and experimental studies have been initiated on this problem, with the objective of elucidating the failure propensity from such regions. The relative importance of coarse grained regions to the creep rupture tendencies of ceramic components can then be ascertained.

Coarse Grained Polycrystals. Experiments have been initiated to examine creep rupture processes in coarse grained (more creep resistant) polycrystals of single phase materials, particularly Al_2O_3. Different modes of cavity formation have already been noted; notably, cavities more generally form on two grain junctions, rather than at three grain junctions. Experiments, coupled with theoretical analysis, will be conducted in order to comprehend the new failure mechanisms that exist in coarse grained materials.

Continuous Grain Boundary Phase. Experiments on Si_3N_4 have been embarked upon in order to study the failure evolution process in materials that contain a continuous second phase at the grain boundaries: viz., liquid phase sintered materials. Particular emphasis will be placed on the role of the second phase as a viscous cavitating medium vis-a-vis cavity growth by solution/reprecipitation. Again, the development of models that can be used for failure prediction is the ultimate objective.

Sintering

A recently developed model of final stage sintering suggests the existence of some important effects that should be amenable to experimental study. In particular, pore and grain boundary shapes during a breakaway sequence have been predicted and a critical pore size at breakaway has been anticipated. Studies of the pore and grain boundary morphologies (and critical pore sizes) during final stage sintering in Al_2O_3 and MgO have been initiated in order to examine these issues. Correlations with the theoretical expectations will be made in all possible cases, particularly during imminent breakaway situations. Theoretical studies will continue, by examining symmetric pore configurations (and by including simultaneous pore shrinkage due to grain boundary diffusion). A clear definition of the breakaway condition is the ultimate objective. Such a definition will then provide a clear focus for processing procedures, in the final stage, that avert the highly detrimental breakaway situation.

Martensitic Toughening

An important influence of the shape of the transformation zone (R-curve behavior) on the magnitude of martensitic toughening was identified in a theoretical study conducted during the current year. Notably, high toughness is only expected when the zone extends over a portion of the crack surface. This shape effect has possible implications for the temperature dependence of the fracture toughness. Specifically, the prior formation of a transformation zone at the temperature which provides the largest transformation zone should provide high levels of toughness at higher temperatures provided that slow crack growth can be excluded. However, once stable crack growth initiates, failure would be catastrophic. The opportunities that exist for high temperature martensitic toughening, by exploitation of the theoretical expectations of R-curve behavior, will be the primary research emphasis during the coming year. The initial studies will be conducted on partially stabilized ZrO_2, because of the good microstructural control possible in the system. Additional work will encompass the Al_2O_3/ZrO_2 and mullite/ZrO_2 systems.

1980 PUBLICATIONS AND REPORTS

Refereed Journals

1. A. G. Evans, J. R. Rice and J. P. Hirth, J. Am. Ceram. Soc. 63, 368 (1980), LBL-8336.

2. A. G. Evans and A. H. Heuer, J. Am. Ceram. Soc. 63, 241 (1980), LBL-8442.

3. A. G. Evans and A. S. Rana, Acta Met. 28, 129 (1980), LBL-8692.

4. A. G. Evans, Acta Met. 28, 1155 (1980), LBL-10342.

Other Publications

1. A. G. Evans, Fundamentals of Acoustic Emission (K. Uno, ed.), UCLA Publication (1980), p. 209.

2. J. Porter, W. Blumenthal and A. G. Evans, Surfaces and Interfaces in Ceramics (J. A. Pask and A. G. Evans, eds.), Plenum (1980).

LBL Reports

1. S. S. Chiang, D. B. Marshall and A. G. Evans, "The Response of Solids to Elastic/Plastic Indentation," LBL-11842.

2. J. Porter, W. Blumenthal and A. G. Evans, "Creep Fracture in Ceramic Polycrystals I. Creep Cavitation Effects in Polycrystalline Alumina," LBL-11560 1/2.

3. C. H. Hseuh and A. G. Evans, "Creep Fracture in Ceramic Polycrystals II. Effects of Inhomogeneity on Creep Rupture," LBL-11560 2/2.

4. A. S. P. Rana and A. G. Evans, "Internal Friction in Ceramic Polycrystals: The High Temperature Background," LBL-11547.

5. A. G. Evans, D. B. Marshall and N. H. Burlingame, "Transformation Toughening in Ceramics," LBL-11598.

6. M. Spears, C. H. Hseuh and A. G. Evans, "Pore Breakaway in Final Stage Sintering," LBL-11954.

7. N. H. Burlingame (M.S. thesis), "Toughening of Zirconia Composition," LBL-10787.

8. A. S. P. Rana (Ph.D. thesis), "High Temperature Creep in Al_2O_3-SiO_2 Ceramics," LBL-10602.

9. W. Blumenthal (M.S. thesis), "Cavitational Effects During Creep in Polycrystalline Alumina," LBL-11830.

10. S. S. Chiang, (Ph.D. thesis), "The Response of Solids to Elastic/Plastic Indentation and its Application to Adhesion Measurements," LBL 11841.

Invited Talks

1. A. G. Evans, "Toughening Mechanisms in Ceramics," Gordon Conference, Meriden, New Hampshire, August 1980.

2. A. G. Evans, "Plasticity in Polycrystalline Ceramics," International Workshop on Oxides, Lyon, France, September 1980.

3. A. G. Evans, "Transformation Toughening," Max-Planck Institut, Stuttgart, Germany, September 1980.

4. A. G. Evans, "High Temperature Failure," MRC Meeting, La Jolla, CA, July 1980.

5. A. G. Evans, "Toughening in Ceramics," American Ceramic Society Meeting, Chicago, IL, May 1980.

6. A. G. Evans, "Failure Processes in Ceramics," Japanese Ceramic Society Meeting," Tokyo, Japan, January 1980.

7. M. D. Huang, "Strain Energy of Martensite," American Ceramic Society Meeting, San Francisco, CA, October 1980.

8. M. Spears, "Final Stage Sintering," American Ceramic Society Meeting, San Francisco, CA, October 1980.

9. S. S. Chiang, "Indentation in Brittle Solids," American Ceramic Society Meeting, San Francisco, CA, October 1980.

10. A. S. P. Rana, "Internal Friction Background in Polycrystal," American Ceramic Society Meeting, San Francisco, CA, October 1980.

11. C. H. Hseuh, "High Temperature Failure in Ceramic Polycrystals," American Ceramic Society Meeting, San Francisco, CA, October 1980.

12. W. Blumenthal, "Creep in Polycrystalline Alumina," American Ceramic Society Meeting, San Francisco, CA, October 1980.

13. W. Blumenthal, A. G. Evans, J. R. Porter, "High Temperature Deformation Mechanisms in Ceramics," American Ceramic Society Meeting, Chicago, IL, May 1980.

14. J. R. Porter and A. G. Evans, "Microstructural Changes During Creep in Alumina," American Ceramic Society Meeting, San Francisco, CA October 1980.

15. J. R. Porter, "Cavitation and Non-linear Creep in Hot-Pressed Alumina," Cornell University, Department of Materials Science and Engineering, Ithaca, NY, June 1980.

16. J. R. Porter, "Cavitation and Non-linear Creep in Hot-Pressed Alumina," Case Western Reserve University, Department of Metallurgy, Cleveland, OH, June 1980.

17. J. R. Porter, W. Blumenthal and A. G. Evans, "Creep Cavitation Effects in Polycrystalline Alumina," Surfaces and Interfaces in Ceramic and Ceramic-Metal Systems, 7th LBL/MMRD International Materials Symposium, Berkeley, CA, July 1980.

3. Physical Properties

a. Superconductivity Effects—High Field Superconductivity*

Moshe Rosen, Investigator

Introduction. A specific mandate defined the scope of this work during the past year. It was to bring all activities to an orderly close by the end of FY 1980, and to achieve this objective within a limited budget. Responsibility for implementation and for a final report summarizing the research performed on multifilamentary superconducting composites was given to Dr. Moshe Rosen, a visiting scientist from Israel's University of the Negev, now with Johns Hopkins University in Baltimore, Maryland.

In point of fact, two reports were prepared and submitted by M. Rosen, J. T. Holthuis and M. R. Pickus, the latter two authors having been associated with the superconductivity program since its inception. Since M. R. Pickus had been invited to present a paper on the Infiltration Process, an LBL development, at the ICMC Topical Conference on Filamentary A15 Superconductors, Brookhaven National Laboratory, Upton, New York, May 28-29, 1980, it was decided to prepare two reports as follows. One, entitled, "Binary and Ternary Niobium-Base Superconductors by the Infiltration Process,"[1] is a comprehensive and detailed account of the work performed in the course of this program and is intended to serve as the requested final report. In contrast, the second entitled "A15 Multifilamentary Superconductors by the Infiltration Process,"[2] is a condensed version in a format appropriate for scheduled publication in the ICMC Conference Proceedings.

* * *

1. M. Rosen, J. T. Holthuis, and M. R. Pickus, LBL-11222 (1980).
2. M. Rosen, J. T. Holthuis, and M. R. Pickus, LBL-10761 (1980).

1. EXPERIMENTAL PROGRAM — FINAL PHASE

Moshe Rosen, John T. Holthuis, and Milton R. Pickus

In order to establish the reproducibility of superconducting data obtained on Nb—Nb_3Sn wires made by the infiltration process, the entire procedure was repeated many times during the past year. Plots of current carrying capacity versus applied magnetic field for wires reduced from the different infiltrated compacts resulted in a smooth curve with very little spread of data points. To further elucidate the current carrying capacity at very high fields, steady field tests were made recently at the Francis Bitter National Magnet Laboratory (MIT) over the range from 15 to 22 tesla. The data points fell smoothly along the previously established curve. The critical current density was 6×10^4 A/cm^2 at 15 tesla and 1×10^4 A/cm^2 at 20 tesla. Wires made by the infiltration process appear to be especially suitable for applications requiring fields of the order of 15 tesla. In another series of tests, it was found that the critical current density increases with decreasing filament size down [illegible] about 1 micron, below which there appears to [illegible] diminishing effect. The minimum diameter [illegible] h the reacted wires can be bent with no deg[illegible] n of the critical current density is 2 cm. [illegible], too, there is an effect of filament size [illegible] it is anticipated that with finer filaments [illegible] maller bend diameters can be tolerated.

An ongoing cooperative program between MMRD and Teledyne Wah Chang Albany (Mr. C. Craig Wojcik's Research Group) has disclosed the existence of a detrimental size effect with respect to ductility. The 3/16 inch diameter infiltrated compacts prepared at MMRD could be reduced to fine wire with little difficulty, whereas the 1-1/2 inch diameter compacts made by Wah Chang were too brittle for successful reduction. Vacuum fusion analyses showed a steep oxygen concentration gradient from the surface to the center of the bars. Hardness profiles showed a corresponding gradient. From this work it was concluded that the necessary oxygen level reduction can not be achieved in large diameter bars by vacuum sintering alone. It was therefore decided that Wah Chang would prepare coarser niobium powder (-60 + 100 mesh in contrast to the -270 mesh powder previously used), with an anticipated reduction in the initial oxygen concentration. Indeed the coarser powder had an oxygen content of ~ 200 ppm compared to ~ 2000 ppm for the finer powder. Indicative of the dramatic improvement in ductility that resulted is the fact that 1/2 inch diameter compacts can now be subjected consistently to a reduction in area ratio of 4-5000:1. Wah Chang is also planning to investigate a spherical niobium powder produced by a rapid solidification technique which is expected to have a very low oxygen content.

Figures 1 to 3 illustrate the key stages of the infiltration process for preparing multifilamentary Nb-Nb_3Sn superconducting wire: the preparation of a ductile niobium matrix containing a network of interconnected pores; infiltration of the pore system with tin; mechanical reduction of the infiltrated composite to the desired wire size and subjecting the wire to a thermally controlled diffusion reaction.

*This work was supported by the Director, Office of Energy Research, Office of Basic Energy Sciences, Materials Sciences Division of the U. S. Department of Energy under Contract No. W-7405-ENG-48.

Fig. 1. Scanning electron micrograph of porous niobium sintered for 30 min at 2250°C. (XBB 768-7563)

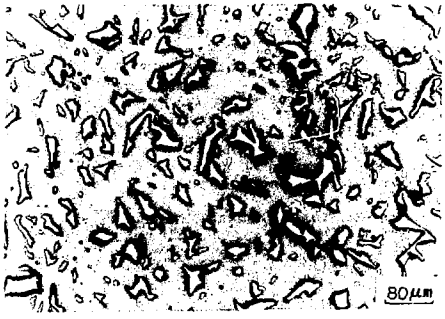

Fig. 2. Optical micrograph of porous niobium infiltrated with tin (white areas). (XBB 755-3884)

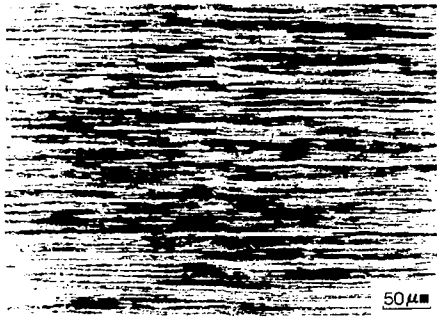

Fig. 3. Longitudinal section of heat treated wire. Dark filaments are Nb_3Sn; light matrix is niobium. (XBB 755-3885)

In regard to the ternary niobium-aluminum-silicon system, a systematic investigation of the influence of heat treatment on the critical temperature (T_c) of wires prepared by the infiltration process was carried out. The highest value of T_c obtained in this study is 18.1 K. A report covering the essential findings of this investigation has been submitted for publication in Scripta Metallurgica.

1980 PUBLICATIONS AND REPORTS

Refereed Journal

1. M. Malekzadeh and M. R. Pickus, "Magnetostrictive Properties of Rare Earth-Iron Laves Phase Materials Prepared by Powder Metallurgy Techniques," IEEE Trans. Magn., MAG-16, 536, 1980, LBL-8092.

Patent

1. M. Malekzadeh and M. R. Pickus, "Sintered Rare Earth-Iron Laves Phase Magnetostrictive Alloy Product and Preparation Thereof," Patent No. 4, 152, 178, 1979.

LBL Report

1. M. R. Pickus, J. T. Holthuis and M. Rosen, "Binary and Ternary Niobium-Base Superconductors by the Infiltration Process," LBL-11222.

Invited Talks

1. M. R. Pickus, J. T. Holthuis, and M. Rosen, (presented by M. R. Pickus), "A15 Multifilamentary Superconductors by the Infiltration Process," Filamentary A15 Superconductors, edited by Masaki Suenaga and Alan F. Clark, Plenum Press, N.Y. 1980, pgs. 331-353. ICMC Topical Conference on Filamentary A15 Superconductors, Brookhaven National Laboratory, Upton, New York, May 28-29, 1980, LBL-10761.

b. Interfaces and Ceramic Microstructures*

Joseph Pask, Investigator

1. WETTING AND REACTIONS IN GLASS/NON-PRECIOUS METAL SYSTEMS†

Antoni P. Tomsia, Zhang Feipeng, and Joseph A. Pask

The current theory of glass to metal bonding based on studies in this laboratory states that chemical bonding occurs between metal and glass when the interfacial zone is saturated with the oxide of the substrate metal, i.e., the activity of the oxide is one in the interfacial zone. During limited previous studies with the binary alloys of Ni-Fe and Ni-Co, it was found that adherence developed if the glass was saturated with the oxide of either of the alloy components. The main objective of this investigation is to determine the applicability of the bonding theory to the two component alloy systems of nickel and chromium.

A series of Ni-Cr alloys were prepared from high purity metal powders (99.999+%) of the following compositions: Ni95Cr5, Ni90Cr10, Ni80Cr20, Ni70Cr30, Ni60Cr40 (in wt%). Together with these alloys, pure nickel and chromium were included as end members of the series. Sessile drop experiments combined with weight loss measurements were made at an ambient pressure of 2×10^{-9} atm in two furnaces: "alumina furnace" with a pO_2 of $\sim 10^{-10}$ atm and a "graphite furnace" with a pO_2 of $\sim 10^{-20}$ atm.

Time and temperature dependence studies of sodium disilicate on Ni, Ni-Cr alloys and Cr were made at 900 to 1100°C. The data for weight loss and contact angle vs. composition at 1000°C for 120 min are shown in Fig. 1. The average reaction rate was first measurable at 950°C for all systems except pure nickel (1000°C) and increased both with temperature and time. The highest reaction rate, as was expected, was found for chromium, the lowest for nickel with an essentially linear increase for Ni-Cr alloys with increasing amounts of Cr. Chromium silicide formation was evident at the periphery of the glass drop and at the interface for all Ni-Cr alloys. Nickel participated by reduction of sodium ions in the glass. In all cases, the overall reactions were faster in the graphite furnace for comparable experimental conditions. Smaller contact angles were usually associated with higher weight losses.

In all experiments with the alloys, the sodium disilicate separated into two immiscible glasses. The glass zone near the interface developed a green color, and the upper part of the drop had a brown color, with a distinct interface between the two zones. The thickness of the green zone (~ 10 to 50 microns) was related to the Cr content

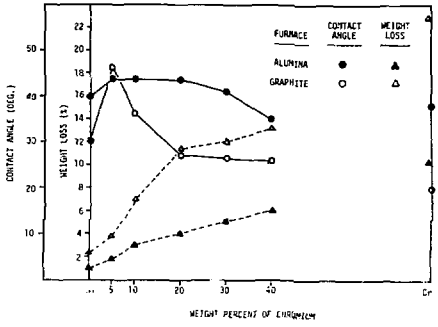

Fig. 1. Contact angles and weight loss of sodium disilicate glass on nickel, nickel-chromium alloys and chromium after 2 hr at 1000°C in 2×10^{-6} torr vacuum. (XBL 813-8659)

in the alloy. In adherence measurements based on slowly bending the plates of the respective alloys, fracture always occurred at the green-brown glass interface, indicating that the adherence of the green interfacial glass zone to the metal substrate was stronger. The adherence was found to be better for specimens tested in the alumina furnace than in the graphite furnace because of a higher oxidation rate of the alloys in the former furnace leading to faster saturation of the interface with Cr_2O_3. AES studies and depth profiles revealed that the amount of Cr_2O_3 on the surface was always about five times greater in the alumina furnace. In the alumina furnace all alloys always had a Cr_2O_3 layer whose thickness increased with the Cr content in the alloy (from 5000 Å for Ni95Cr5 to ~ 2 micron in case of the alloy Ni80Cr40).

SEM and AES studies showed that brown glass was richer in NiO with only a small amount of chromium (< 1 wt%), and the green glass was richer in Cr_2O_3 with a small amount of NiO. These results suggest at least qualitatively that the diffusion of the chromium into the glass is much slower than diffusion of nickel.

These results led to a study of the effect of saturating NS_2 with NiO and Cr_2O_3 on adherence, wetting and reactivity of Ni-Cr alloys. Sodium disilicate saturated with NiO (8.0 wt%) on Ni and Ni-Cr alloys showed greater reactivity than NS_2 alone. The smallest contact angle, lowest weight loss, and excellent adherence were obtained on pure nickel. Increasing amounts of Cr in the alloys did not produce a linear effect on these properties. In contrast to NS_2, weight loss and contact angle increased under similar conditions in both furnaces, reaching a maximum value for Ni80Cr20 and Ni70Cr30 alloys. The next alloy in the series

*This work was supported by the Director, Office of Energy Research, Office of Basic Energy Sciences, Materials Sciences Division of the U.S. Department of Energy under Contract No. W-7405-ENG-48.

showed markedly lower weight loss during one- and two-hour experiments. The adherence decreased with increase of Cr, becoming poor in the center of the sessile drops on alloys with more than 30 wt% Cr.

Sodium disilicate saturated with Cr_2O_3 showed the highest reactivity of all the glasses studied. The contact angles were smaller than 8 degrees in all of the experiments, and spreading occurred on all alloys with 20 wt% Cr and higher in about 20 minutes after the occurrence of a violent reaction associated with bubbling. The adherence was very good in all cases.

All of the results indicate that the redox reactions at glass-alloy interface are sensitive to the O/Si ratio in the glasses and the pO_2 in the ambient atmosphere. Redox reactions introduce substrate metal oxides into the glass which are favorable for development of adherence. Chromium also participates in redox reactions leading to the formation of silicides which apparently are not favorable for development of adherence.

* * *

†This work was partially supported by the National Institute of Dental Research of the National Institutes of Health.

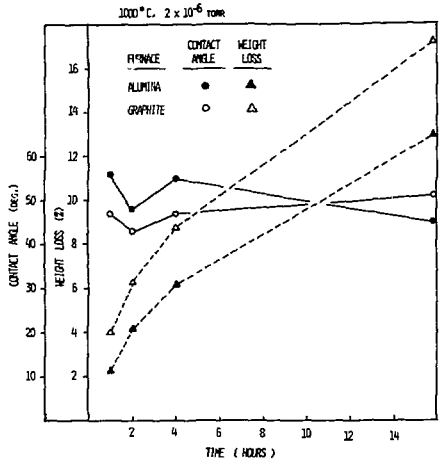

Fig. 2. Contact angles and weight loss from sodium disilicate glass on titanium vs. time from 1 to 16 hr at 1000°C and 2 × 10^{-6} torr. (XBL 8010-12599)

2. WETTING AND REACTIONS IN GLASS/TITANIUM SYSTEMS

Zhang Feipeng, Antoni P. Tomsia, and Joseph A. Pask

Interfacial reactions and wetting of sodium disilicate (NS_2) and sodium borosilicate glass (NBS) on high purity titanium were studied using the sessile drop technique combined with weight loss measurements and SEM observations. Two vacuum furnaces were used: one with a graphite core and heating element and an estimated P_{O_2} of 10^{-20} atm, and a second with an alumina core and an estimated P_{O_2} of 10^{-10} atm. A survey of the literature on the wetting behavior of NS_2 glass on Ti[1,2] revealed observed contact angles from 48 to 80 degrees and little information about the reaction mechanisms.

The first series of experiments with sodium disilicate were made at 1000°C for times from 1 to 16 hr. The reaction rate determined by weight losses increased, both with time and temperature as seen in Figs. 2 and 3, but the associated change in contact angles was small. In all experiments the glass drop had a very regular shape and changed in color to brown or brown-violet.

Figure 4 shows the edge of the NS_2 glass drop on Ti after 2 hr at 1000°C in the alumina furnace. Titanium is at the botom of the photo, with a characteristic kink surface structure, and the glass drop is on top. The phase formed at the interface, which separates Ti and glass, was identified by x-ray diffraction analysis as titanium silicide - Ti_5Si_3. The thickness was time and temperature dependent and was always greater in the graphite furnace than in the alumina furnace under similar conditions. After 16 hr in the graphite furnace at 1000°C, the average thickness of Ti_5Si_3 in the center of the glass drop was 8 microns and in the alumina furnace, 4 microns.

The formation of the Ti_5Si_3 phase provides an explanation for the essentially constant values of contact angle under all experimental conditions. Redox reactions at the interface between NS_2 and Ti were always faster at the periphery of the glass drop because of the short diffusion paths. The formation of the new phase froze the position of

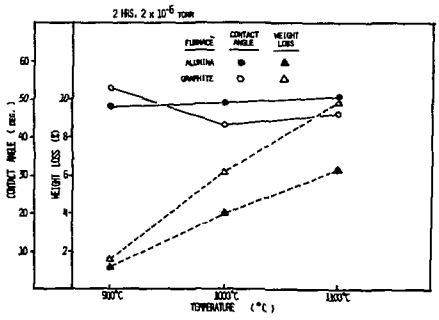

Fig. 3. Contact angles and weight loss of sodium disilicate glass on titanium at 900 to 1100°C after 2 hr at 2 × 10^{-6} torr. (XBL 8010-12598)

Fig. 4. Top view of the edge of the sodium disilicate glass drop on titanium in alumina furnace after 2 hr at 1000°C and 2×10^{-6} torr. Titanium substrate at the bottom. (5000x) (XBB 813-2390)

Fig. 5. Area on titanium just outside the periphery of the sodium borosilicate drop in graphite furnace after 2 hr at 1000°C and 2×10^{-6} torr. Reaction resulted in the formation of black tarnish layer. Open area in the center was sputter-etched for Auger Electron Spectroscopy (AES). (XBB 813-2391)

the drop edge. It was further found that the formation of this phase occurs rapidly and is thus sensitive to the heating rate. With a very fast heating rate to the experimental temperature, it was possible to obtain an 80° contact angle as reported in the literature. In this case, the position of the drop edge was frozen before it had time to flow to the smaller angle.

The adherence of the Ti_5Si_3 layer to the titanium was always very good, but separation occurred at the Ti_5Si_3-glass interface. The net result was poor adherence from an engineering viewpoint.

With sodium borosilicate glass, obtuse contact angles in the range of 110-120° were obtained on Ti in vacuum at temperatures from 900 to 1200°C. Examination of the samples after an experiment showed that the glass drop had a distorted and irregular surface. Cross sections showed that the glass is in contact with Ti only at the periphery and that the remainder of the interface had extensive gaseous cavities.

This unusual appearance, together with weight losses of less than 2 wt%, suggested decomposition of the glass drop surface, causing the flow to be arrested and freezing the shape of the drop.

Using simultaneous Auger electron spectroscopy and ion sputter-etching, the glass surface, the area under the glass and the black deposit were analyzed. Figure 5 shows a surface view of the black (seen here as grey) deposit near the glass drop. The open area in the center was caused by sputter-etching and analysis. The thickness of the layer deposit is 1 micron. Figure 6 shows several Auger spectra: the upper was taken from the surface of the black layer and the lower after

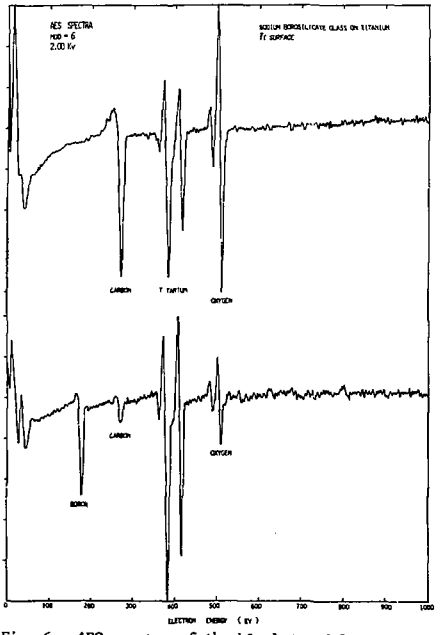

Fig. 6. AES spectra of the black tarnish layer surface (top) and of the titanium surface beneath the layer, after 5 min of sputtering (bottom). (XBL 8010-12600)

sputtering. The spectra indicate that the surface of the layer contains carbon, Ti and oxygen. A depth profile showed that the carbon concentration rapidly diminished from the surface. Underneath the black layer, Auger spectra showed the appearance of boron. Boride was formed by reaction of the Ti with B_2O_3 evolved during glass decomposition. The area under the glass drop contained titanium boride and titanium silicide.

Glass itself, as was found from surface analysis, decomposed rapidly from 900°C by evolving B_2O_3. A silica rich shell formed on its surface. The high viscosity of the silica rich layer prevented the glass from flowing to form an acute contact angle which would normally be expected since $\gamma_{sv} > \gamma_{lv}$.

* * *

1. A. Passerone, G. Valbusa, and E. Biagini, J. Mat. Sci. 12, 2465 (1977).
2. I. J. McColm and C. Dimbylow, J. Mat. Sci. 9, 1320 (1974).

3. WETTING AND ADHERENCE OF GLASSES TO NOBLE METALS

V. K. Nagesh,† Antoni P. Tomsia, and Joseph A. Pask

Wetting studies between different glasses and precious metals are very important to the glass and the electronic industries. Bushing nozzles for glass fibers and hollow fiber production parts are usually made from precious metal alloys. For fiber drawing, it is desirable that the glass does not react with and spread over the bushing. Most of the thick film conductor systems use lead borosilicate glass as a binder between the metals Ag, Au, and Pt and the alumina ceramic substrate. Here, good adhesion and associated low contact angles of the glass are essential.

Sessile drop experiments with lead borosilicate, sodium borate, sodium borosilicate, and sodium disilicate glasses were conducted on Ag, Au and Pt under four different atmospheric conditions, namely, air, 1 atm helium, and 2×10^{-9} atm vacuum with $\sim 10^{-10}$ atm P_{O_2} and $\sim 10^{-20}$ atm P_{O_2}.

In an air atmosphere, the LBS and SB glasses spread on silver into a uniform extended circle. In case of LBS, glass crystallization was evident at the periphery of the glass extension. NS_2 and NBS glasses formed contact angles of $\sim 30°$ and became transparent yellow. All four glasses had very good adherence because of solution of silver oxide by the glasses resulting in saturation of the interface. SEM-EDAX analysis indicated that the solubility of Ag_2O in NS_2 and NBS glasses is about 4 times lower than in LBS and SB glasses. Some of the silver precipitated from these glasses during cooling and formed spheres of 0.2-0.3 micron diameter without complete loss of transparency of the glass.

Under low oxygen partial pressure in vacuum all glasses showed slightly weaker adhesion than in air; the LBS glass, however, showed the strongest adhesion. LBS glass drifted on the silver plate and showed 2.8% weight loss after the sessile drop experiment. Bubbling was also evident, which indicated a reaction at the interface. No weight loss occurred for the other glasses and no indication of any reaction was noticed from the examination of the cross-sections. Those observations and the low contact angle of LBS glass (4°) compared to all other glasses (> 30°) indicate the possibility of a redox reaction between Ag and lead oxide in the glass. The possible overall reaction under these low oxygen partial pressure conditions is:

$$2\,Ag_{(s)} + PbO_{(glass)} = Ag_2O_{(glass)} + Pb_{(g)}\ .$$

The standard free energy for this reaction at 700°C is positive. Reaction could be achieved if lead is formed in the vapor state and is immediately removed from the reaction site. At 700°C, the vapor pressure of Pb is $\sim 10^{-5}$ atm which is higher than the total ambient pressure of 2×10^{-9} atm.

In the presence of gettered helium at 1 atm, the adherence of all glasses was poor. All glass drops could be easily removed from the surface of the metal. No reactions were observed with any of the glasses, not even LBS. These factors are reflected in the high contact angles (> 50°) for all glasses.

All glass drops on gold had finite contact angles under all atmospheric conditions. Good adherence was observed for all glasses in air. In vacuum, however, the adherence was poor, even though the contact angle was lower than in the air atmosphere for the LBS and SB glass. The strong adhesion of glasses in the presence of oxygen is due to the dissolution of the surface oxide by the glass which approaches saturation and the formation of a chemical bond at the interface. Adherence was always stronger at the edges of the glass drops than the center. Auger electron spectroscopy (AES) showed a higher Au concentration in the glass at the interface close to the periphery than at the center.

The adherence was poor under vacuum and in helium, indicating the absence of any reaction between glass and the gold. This premise was supported by AES of several glasses which did not detect any traces of Au at the glass surface removed from the gold. LBS and SB glasses showed lower contact angles in vacuum than in air, which can be explained by a higher driving force for wetting represented by $(\gamma_{sv}-\gamma_{sl})$. Even though γ_{sl} in air is lower than in vacuum, γ_{sv} is sufficiently larger in vacuum than in air to give a larger overall value for $(\gamma_{sv}-\gamma_{sl})$.

All glasses showed strong adhesion to platinum when fired in air. SB glass spread on Pt while the other three glasses showed low but finite contact angles. As for Ag and Au, the low contact angle and strong adherence in air are due to the saturation of glass by the metal oxide at the interface. Because of the solution of the surface oxide of platinum in glass, the interfacial energy is greatly reduced resulting in a large driving

force for wetting (γ_{SV}-γ_{SL}) and a low contact angle.

Under vacuum, only sodium disilicate showed a low contact angle (15°) and fair adherence. All other glasses had high contact angles (> 50°) and poor adherence. Because of carbon contamination of the Pt surface in a graphite core furnace, which reduces the Pt surface energy, contact angles for all glasses are larger than those obtained in an alumina core furnace.

In summary, the results for Ag, Au, and Pt indicate that heating in air always results in good adherence because of saturation of the interface with the respective metal oxide which forms on the metal surface at high partial pressures of oxygen. Although the amount is small, it is adequate because of the low solubility of the oxides in the glasses. The absence of redox or solution reactions at the interface and/or oxygen leads to an increased contact angle caused primarily by a decreased (γ_{SV}-γ_{SL}). Changes in contact angles with time and associated weight losses always indicate reaction at the interface and improved adherence. In all cases, the values of contact angles correlate well with adhesion, i.e., the lower the contact angle, the better the adhesion.

* * *

†Now at Hewlett-Packard Co., Palo Alto, California.

Fig. 7. Liquid of eutectic composition at eutectic temperature (~ 782°C) on (a) Cu and (b) Cu-solidus. (XBB 807-8509)

4. REACTIONS AND SPREADING IN THE Cu-Ag SYSTEM

Paul R. Sharps,† Antoni P. Tomsia, and Joseph A. Pask

Sessile drop experiments were performed on substrates in the Cu-Ag system at the eutectic temperature of 780°C and at 900°C at partial pressures of oxygen below the dissociation pressures of the metallic oxides. The experiments support the generalization that the use of solids and liquids in chemical equilibrium in binary metal systems results in wetting or an acute contact angle but not spreading, i.e., the surface energy of the solid is greater than that of the liquid, but the energetic driving force for wetting does not exceed the surface energy of the liquid. Specifically, the driving force for wetting of the Cu-solidus by the eutectic liquid at 782°C is greater (smaller contact angle) than that for wetting of the Ag-solidus. Another experimental observation is that no mass transport occurs across the interface as indicated in Fig. 7 when chemical equilibrium exists, i.e., the interfaces remain flat and are continuous with the free surfaces of the substrates.

When the sessile drops are not in chemical equilibrium with the substrate, solution reactions occur. If the substrate is undersaturated relative to a component in the liquid, the specific free energy of the solution reaction contributes enough to the driving force for wetting in most cases to cause spreading, i.e., it exceeds the specific surface energy of the liquid. If only the liquid is undersaturated relative to a component in the substrate, the solution reaction does not increase the driving force for wetting and no spreading occurs. In both cases, however, a mass redistribution occurs and the interface does not remain flat and continuous with the substrate surface. For example, the eutectic liquid on Cu-solidus at 900°C causes a lenticular depression by dissolving sufficient substrate to reach the equilibrium Cu-liquidus composition (Fig. 8).

Development of nonhomogeneity in the Cu-solidus with grain boundaries attaining continuous non-equilibrium compositions results in some movement of liquid along the grain boundaries ahead of the liquid drop, which contributes to the driving force for wetting. This appearance can be misinterpreted as primarily capillary movement of liquid along thermally grooved grain boundaries.

This study indicates the importance of controlling the conditions of the sessile drop experiment and of careful preparation of specimens. Cross sections should be made and analyzed to determine the details of any reactions that may have been occurring during the experiment. That is, careful characterization must be applied to the specimen assemblies, especially in the possible presence of inhomogeneities, in order to fully understand and avoid misinterpretations of "simple" sessile drop experiments.

* * *

†Now at Purdue University, Lafayette, Indiana.

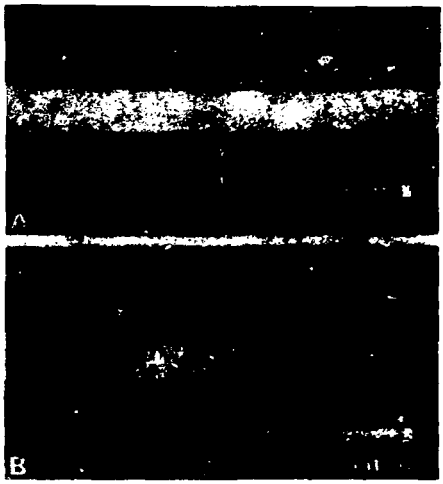

Fig. 8. Liquid of eutectic composition at 900°C on (a) Cu and (b) Cu-solidus. (XBB 807-8510)

5. SINTERING OF MULLITE-CONTAINING COMPOSITIONS†

Michael D. Sacks† and Joseph A. Pask

Al_2O_3 and SiO_2 raw materials were processed by "powder" and "gel" processes to form mullite-containing materials for sintering studies. The effects of phase composition, particle packing in the green compact, powder surface area, and sintering atmosphere on microstructural evolution and sintering kinetics (densification and grain growth) were investigated.

Rapid densification was observed when large amounts of liquid were present during sintering. Even trace amounts of glassy phase, which can only be resolved by transmission electron microscopy, can cause notable increases in densification rate. However, it is important to be cognizant of trade-offs between increased densification rate and possible adverse affects on properties (such as high temperature strength).

In "powder" process materials with compositions near or within the mullite solid solution range, a proportionality was observed between % theoretical density and the logarithm of time for the various sintering temperatures. This observation is consistent with the predictions of several intermediate stage sintering models. The non-uniformity in packing and in size of particles led to the rapid formation of dense microregions (in which pores in closely packed regions were quickly eliminated), while large pores "opened up" in regions which were initially packed with a low density. This development requires the use of an "effective grain size" as a measure of the diffusion path length during sintering. This parameter is experimentally determined by measuring the spacing between pores. Pore spacing measurements are also used to show that inhomogeneity affects the rate of approach to theoretical density.

In "gel" materials, enhanced densification rates with increasing grinding times of the calcined powders is observed because of increasing surface area (decreasing particle size). Particle packing was important in determining the final density. Although the initial pore volume was kept nearly constant, lower final densities were observed when large pores were present in the green microstructure. Packing arrangements also caused the occurrance of densification substages during the intermediate stage of sintering. A detailed microstructural analysis is required in order to assess whether a sintering model is physically realistic.

Sintering atmosphere, in which the total pressure and the partial pressure of oxygen were the important variables, affected the microstructural development and the rates of grain growth and densification. The partial pressure of oxygen can affect the diffusion coefficients and the interfacial energies. The total pressure is an important factor in determining the amount of gas that is entrapped in pores.

* * *

†This work was partially supported by the National Science Foundation.

‡Now in Department of Materials Science and Engineering, University of Florida, Gainesville, Florida.

6. EFFECT OF SILICA IMPURITIES ON ELECTROPHORETIC PROPERTIES AND SINTERING OF ALUMINA

Jose S. Moya,† Jorge R. Rubio,‡ and Joseph A. Pask

When an oxide powder is immersed in water, an electric double layer is formed at the oxide/water interface. The zeta potential that forms is dependent on the pH of the liquid. At the isoelectric point (i.e.p.) the charge is zero, and the dispersed particles tend to aggregate or flocculate. This behavior affects the packing of the particles and resulting microstructure after high temperature sintering, which in turn affects the properties.

When silica is present as an impurity (0.03 wt% in the Al_2O_3 specimen studied), the electrokinetic properties are modified. Figure 9 shows that the variations of the zeta potential with pH is dependent on the pretreatment of the alumina sample.

An i.e.p. of pH 8.9 was obtained after removal of the silica impurity with a 0.1N solution of HF, washing and storing the powder in polyethylene bottles at a pH 6.9 for 10 days. Subsequent contamination with Na_2SiO_3 changed the i.e.p. to

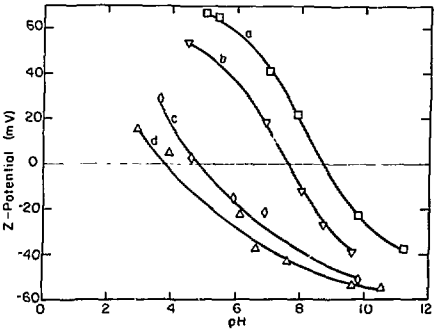

Fig. 9. Zeta potential vs pH curves for Al_2O_3 suspensions with different pretreatments: *a) equilibration at ~ pH 4.5 in pyrex glass con*trainers, b) aging for 24 hr at each of the pH values of measurement, c) leaching with concentrated HCl for 4 hr, washing and aging at pH 6.7, and d) aging for 24 days at pH 6.7. (XBL 794-6077)

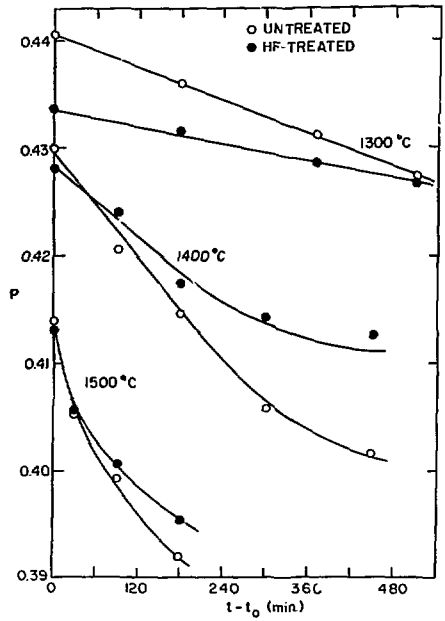

Fig. 10. Porosity vs time for HF-treated and untreated Al_2O_3 compacts sintered isothermally in air at indicated temperatures. (XBL 7[illegible]-7031)

pH 6.1. These experiments, as well as others, indicate that surface contamination by soluble species from sources such as sample impurities or containers on aging lead to variable i.e.p. values. Uncontrolled variations of this type will cause variations in agglomeration of the particles which will affect rheological behavior of such slurries and cause non-reproducibility.

Further experiments on Al_2O_3 powder, as received and treated as above to remove the silica impurity, indicated that the silica plays a significant role both in processing of the powders and in sintering and microstructure development of alumina compacts. When the silica is removed, compactibility of the powder is affected adversely. Silica improves densification during the initial stage of sintering (Fig. 10); it also decreases the activation energy of sintering and moderately inhibits grain growth.

* * *

†Now at Instituto de Ceramic y Vidrio, Arganda del Rey (Madrid), Spain.

‡Now at Universidad Federal Do Rio Grande Do Sal, Departmento de Metalurgia, Porto Alegre, Brasil.

7. THERMODYNAMICS OF SINTERING

Boon Wong[†] and Joseph A. Pask

Single phase materials at chemical equilibrium are generally densified by sintering at high temperatures, and the process is normally studied kinetically. The objective of this study is to develop a better understanding of the mechanisms of the sintering process through a thermodynamic approach. Since the sintering system ideally is under chemical equilibrium and the driving force for sintering is a reduction of the free energy of the system by reduction of surface area, an understanding of sintering requires an understanding of the thermodynamics of interfaces.

Densification of a compact requires movement of mass from particle contacts to adjoining surfaces resulting in an increase of grain boundary area and decrease of surface area. This process is thermodynamically possible because the specific grain boundary free energy γ_{ss} is less than twice the specific surface free energy γ_{sf}. This inbalance provides the driving force for mass transport or sintering which continues until the increase of total grain boundary free energy at a given time becomes equal to the decrease of total surface free energy. At this point the dihedral angle, obtained in a model two sphere system by passing a plane through the centers of the spheres, is at equilibrium as shown in Fig. 11. The two-sphere system then is in metastable equilibrium. In most compacts complete densification, or closure of pores, occurs before the increasing dihedral angles reach their metastable equilibrium value. Therefore, the γ_{ss}/γ_{sf} ratio should be small for favorable sintering; more open or less dense powder compacts require smaller ratios.

The overall mass transport process consists of two steps: movement of material from a contact boundary area being formed between two phases to the "neck" between them and movement from the neck to the adjoining free surfaces. In the previous case the second step was faster than the first resulting in no neck formation and an increasing dihedral angle between the spheres until the equilibrium angle was reached. Another extreme case occurs when the first step is much faster than the second step resulting in the formation of a neck with an equilibrium dihedral angle. The driving force for sintering then is the reverse curvature of the neck surfaces. Most sintering experiments indicate that a neck is formed; with this type of mechanism, complete densification occurs before the reverse curvature is eliminated. The same requirement for a small γ_{ss}/γ_{sf} also holds in this case.

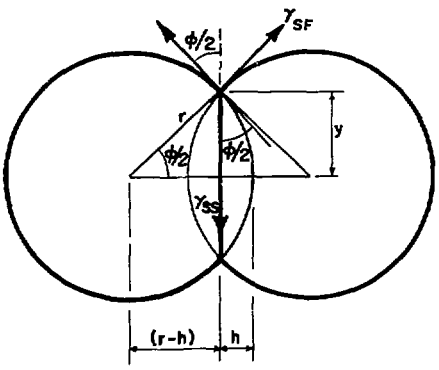

Fig. 11. Two sphere model after densification showing grain boundary with formation of dihedral angle, ϕ. The displaced mass is distributed uniformly on the free surface with an appropriate increase of radius, r. When $\gamma_{ss}dA_{ss} = \gamma_{sf}dA_{sf}$, the dihedral angle is at metastable equilibrium and is represented by $\gamma_{ss} = 2\gamma_{sf} \cos \phi/2$.
(XBL 798-6757)

* * *

†Now at ARCO Solar, Inc., Chatsworth, California.

8. HIGH TEMPERATURE SOLID STATE REACTIONS IN KAOLINITE†

S. M. Johnson, J. S. Moya,‡ and J. A. Pask

Kaolinite is the mineral name for a hydrous alumino silicate ($Al_2Si_2O_5(OH)_4$ or $Al_2O_3 \cdot 2SiO_2 \cdot 2H_2O$) which is the principal constituent of fire clays and white-firing clays. These clays are the principal raw or starting materials for refractories which are the principal candidates for lining of furnaces in coal gasification processes; they also are the principal raw materials for many traditional ceramic products. Consequently, the solid state reaction sequence on heating kaolinite has been widely studied. One of the principal research tools has been differential thermal analysis (DTA); several thermograms are shown in Fig. 12. Most of the work reported in the literature has been centered on the nature of the endothermic reaction (peak temperature about 625°C) and the first exothermic reaction (peak temperature about 980°C). This study was concerned with the nature of the second and third exothermic reactions that occur and the effect of small additions of K_2O and CaO, since such impurities very strongly affect the refractoriness of the clay.

Kaolinite, which becomes metakaolinite after dehydroxylation corresponding to the main endothermic peak in DTA, undergoes several successive reactions (represented by three exothermic peaks in a DTA run) in attaining the equilibrium phases of mullite ($3Al_2O_3 \cdot 2SiO_2$) and cristobalite (SiO_2). It has been postulated that the first exothermic peak represents the formation of mullite nuclei. This study indicates that the second exothermic peak is the result of rapid growth of mullite by a solution-precipitation process prompted by the formation of an amorphous or liquid-like silica-rich phase, and that the third exothermic peak is the result of the crystallization and growth of cristobalite.

When additions of K_2O are made, a solid state side reaction occurs at the "metakaolinite" grain contacts independently to form compounds which react with the precursor amorphous phase in the grain to form the modified liquid associated with the second exothermic peak. The modified SiO_2-rich phase causes an acceleration of the mullite growth with a shift of the second exothermic reaction peak to a lower temperature. Additions of CaO have a similar effect as observed in Fig. 13,

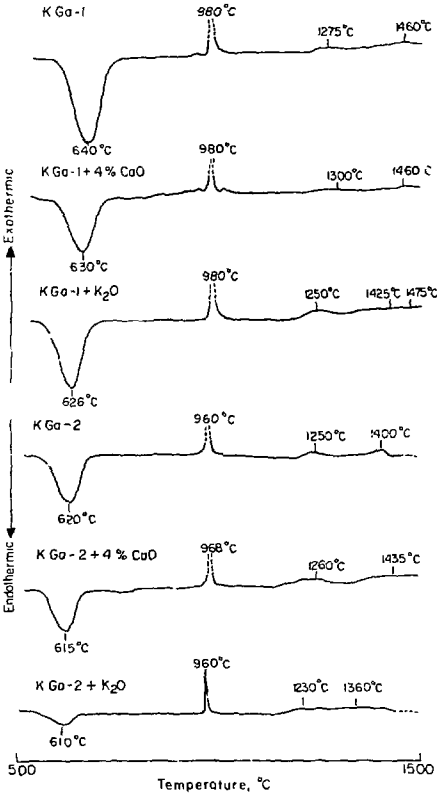

Fig. 12. DTAs of two kaolinites with 4% CaO, 1.5% K_2O, and no additives. (XBL 8010-6021)

except that the peak temperature of the second exothermic reaction in the DTA (Fig. 12) is shifted to a higher temperature. The crystallization and growth of cristobalite, and the equilibrium amount of cristobalite are affected by the modified liquid phase with a corresponding effect on the third exothermic peak.

This reaction is an excellent example of a complex solid state reaction. The kinetic and metastability aspects have a strong bearing on the microstructure development which, in turn, determines the properties of the material. Therefore, it is important to understand the various mechanisms and step reactions of the overall solid state reaction.

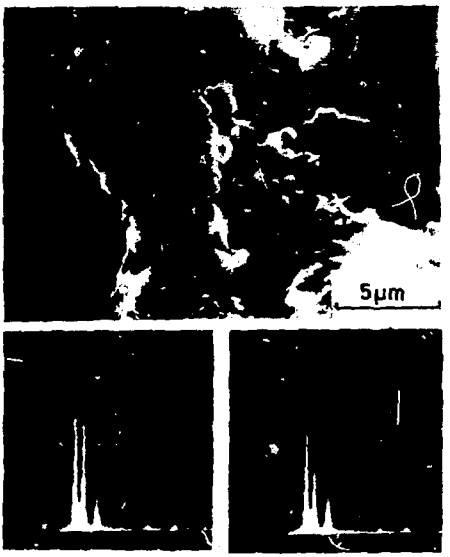

Fig. 13. SEM photomicrograph of HF-etched specimen of a kaolinite with 4% CaO after DTA run up to 1310°C, and EDAX analysis of original grain (a) and grain in liquid phase (b). (XBB 800-11985)

* * *

+This work was partially supported by the National Science Foundation.

+Now at the Instituto de Ceramic y Vidrio, Arganda del Rey (Madrid), Spain.

9. PROCESSING OF PZT AND EFFECT ON COUPLING COEFFICIENT

Shu Sheng Chiang, Michihiro Nishioka,+ and Joseph A. Pask

The microstructure and properties of lead zirconate titanate (PZT) are sensitive to the various steps in the fabrication process. The first part of this study investigated the influence of the mixing medium, distilled water or isopropyl alcohol, used with polyvinyl alcohol (PVA) binder on the sintering behavior and coupling coefficient (K_p) of fired $Pb(Zr_{0.5}Ti_{0.5})O_3$. The second part investigated the effect of excess PbO (0-5 wt%) additions to calcined $Pb(Zr_{0.5}Ti_{0.5})O_3$ powder on its density, shrinkage, grain size, dielectric constant, remnant polarization, and K_p after firing at 1200°C.

In order to study the effect of the mixing medium, powders were prepared for four compactions using water (designated as H) and alcohol (designated as A) separately for mixing unfired starting powders for calcination and the calcined powders for compaction, i.e., H-H, H-A, A-H and A-A. The green density of each pellet was essentially the same, ~ 51.7% theoretical, but differences occurred in the individual powder characteristics. The first difference appeared during granulation of the dried mixtures containing calcined powders: the calcines that were milled with alcohol (i.e., H-A and A-A) crushed easily. The resulting powders were more bulky, as indicated by an ~ 20% volume increase compared with the H-H and A-H powders. A scanning electron microscope examination (Fig. 14) showed that H-A and A-A powders dispersed uniformly and that H-H and A-H powders agglomerated extensively.

Another difference appeared in the preparation of the cold pressed specimens. Pressing of A-H and H-H powders was more difficult since a crack frequently appeared on the surface of the specimen, which caused it to break during subsequent handling. An SEM examination of the surface of uncracked specimens showed nonuniform packing behavior in comparison with the H-A and A-A specimens which appeared to be homogeneous. This difference was attributed to the agglomeration of the A-H and H-H powders. The effect of this difference in homogeneity appears in the sintered specimens. Microstructures of fired A-A and H-H specimens are shown in Fig. 15; the H-H specimen shows large pores. Bulk density, shrinkage and grain size values are higher when alcohol instead of water is used for mixing the sintering batch; it appears, however, that the medium used for mixing the powder for calcining, i.e., A-H or H-H, is not critical. The behavior difference on using water or alcohol for mixing the powders can be related to the behavior observed on dilution of the starting water solution PVA (4 wt% PVA) itself: with water the solution remained clear, whereas with alcohol

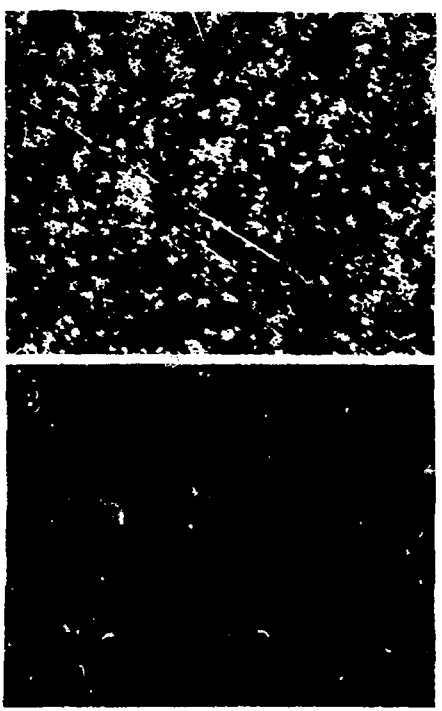

Fig. 14. SEM photographs of dried calcined powders mixed with (a) polyvinyl alcohol (A-A) and (b) distilled water (H-H). (XBB 806-7750)

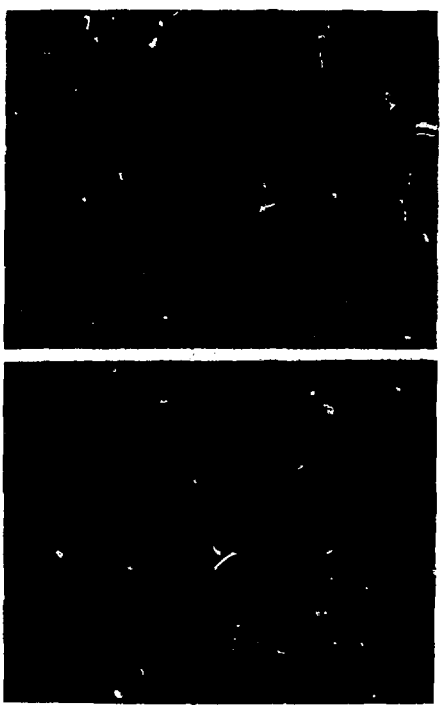

Fig. 15. SEM photographs of fired microstructure of compacts prepared with calcined powders mixed with (a) polyvinyl alcohol (A-A) and (b) distilled water (H-H). (XBB 806-7751)

the solution became murky. It was thus concluded that the water diluted solution became gelatinous on drying and the alcohol diluted solution became essentially granulated.

No strong trends in K_p values were evident even though large pores appeared in the specimens whose sintering batch was mixed with water. However, it is expected that these specimens will have lower K_p values under more severe poling conditions.

In the second part, experiments were made on the effect of excess PbO (0-5 wt%), used to compensate the PbO loss from the specimen at sintering temperature and to provide a liquid phase sintering mechanism, added to calcined powder $Pg(Zr_{0.5}Ti_{0.5})O_3$. The density, linear shrinkage, and grain size increased with an increase of excess PbO after sintering at 1200°C for 1 and 8 hr, as seen in Fig. 16. Relationships between remnant polarization (P_r), saturation polarization (P_s), coercive field (E_s), dielectric constant (E_r), and coupling coefficient (K_p) obtained under poling conditions are shown in Fig. 17. It can be seen that K_p values are significantly higher after 8 hr of sintering and that K_p also increased with increasing amounts of excess PbO in both the 1 and 8 hr sintering series. It appears that a homogeneous distribution of PbO, and perhaps saturation of the grains with PbO associated with the higher densities (Fig. 3), are the most critical factors for increasing K_p values.

* * *

†Now at Mitsubishi Mining and Cement Co., Yokoze, Japan.

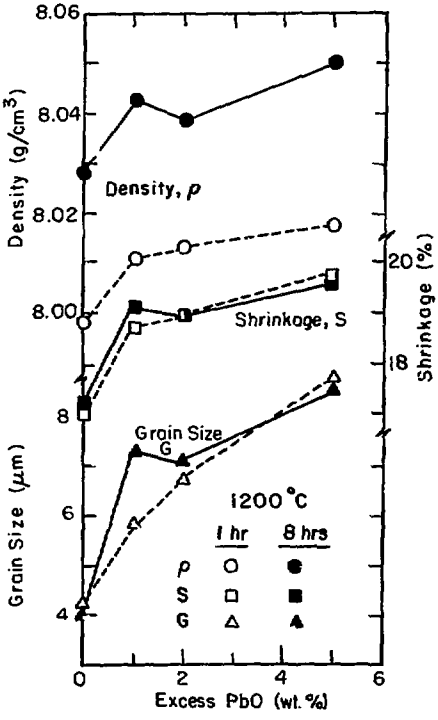

Fig. 16. Density, shrinkage, and grain size vs. excess PbO for $Pb(Zr_{0.5}Ti_{0.5})O_3$ specimens sintered for 1 and 8 hr at 1200°C. (XBL 793-5844)

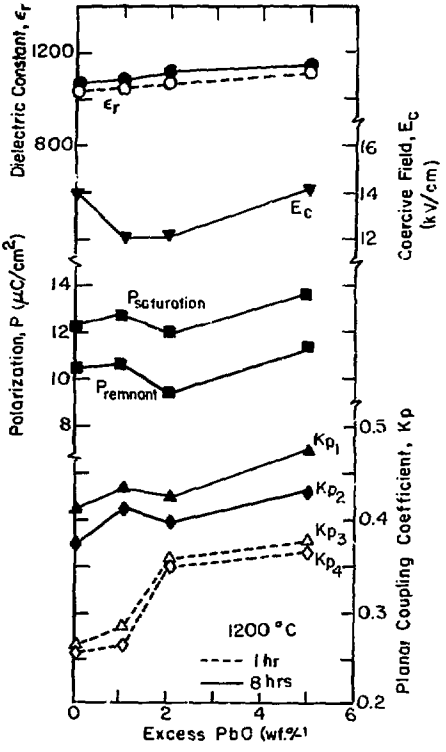

Fig. 17. Dielectric constant (ϵ_r), coercive field (E_c), permanent polarization (P_s), remnant polarization (P_r) and planar coupling coefficient (K_p) vs. the amount of excess PbO for $Pb(Zr_{0.5}Ti_{0.5})O_3$ specimens sintered for 1 and 8 hr at 1200°C. Specimens were poled for 30 min with a field of 3.5 kV/mm at a poling temperature of 100°C for K_{p_1} and K_{p_3} and 90°C for K_{p_2} and K_{p_4}. (XBL 793-5845)

RESEARCH PLANS FOR CALENDAR YEAR 1981

Studies are continuing on spreading, wetting and reactions at interfaces at elevated temperatures between liquid glasses and metals. Factors being explored are the effects of bulk impurities and adsorbed species Metals of primary interest are iron, nickel, cobalt, titanium, and chromium. Current concepts based on single element metals are being applied to binary and ternary alloys. Of particular interest is a study to develop an understanding of the solid state redox chemical reactions that occur extensively between metal/ceramic components of a system that is not at chemical thermodynamic equilibrium.

Studies are continuing on liquid phase sintering of alumina with calcium alumino silicate liquids. The hot stage scanning electron microscope is being used as a major tool for dynamic experiments. SEM observations are correlated with sessile drop and dihedral angle data and with interfacial reactions. The liquid composition selected for correlations include a liquid in equilibrium with alumina, a liquid undersaturated relative to alumina, and a liquid reactive with alumina to form a compound at the temperature of the experiment. These factors will be evaluated on the basis of microstructure development and kinetics of sintering.

1980 PUBLICATIONS AND REPORTS

Refereed Journals

1. Joseph A. Pask, "Ceramic Processing--A Ceramic Science," Bull. Am. Ceram. Soc. 58(12), 1163 (December 1979), LBL-9179.

2. Dipak R. Biswas and Richard M. Fulrath, "Strength and Porous Polycrystalline Ceramics," Trans. and J. of British Cer. Soc. 79(1), 1 (January 1980), LBL-8630.

3. Dipak R. Biswas and Richard M. Fulrath, "Effect of Surface Treatments on Strength of PZT Polycrystalline Ceramics," J. Mat. Sci. 14 2721 (1979), LBL-8647.

Other Publications

1. Helmut Riegger, H. E. Exner, and Joseph A. Pask, "Direct Observation of Densification and Grain Growth in a W-Ni Alloy," in Sintering Processes--Materials Science Research, Vol. 13, edited by G. C. Kuczynski, Plenum Press, New York, pp. 219-233 (1980).

LBL Reports

1. Michael D. Sacks, "Sintering Behavior of Mullite-Containing Materials," Ph.D. thesis, December 1979, LBL-10372.

2. S. S. Chiang, R. M. Fulrath, and J. A. Pask, "Influence of Microcracking and Slow Crack Growth on Planar Coupling Ciefficient in PZT," May 1979, LBL-9205.

3. Jose S. Moya, Jorge Rubio, and Joseph A. Pask, "The Electrophoretical Behavior of Silica-Bearing Alumina Surfaces," January 1980, LBL-9206.

4. Boon Wong and Joseph A. Pask, "A Thermodynamic Derivation of the Dihedral Angle Equation for a Two Phase System," January 1980, LBL-9670.

5. Jose S. Moya and Joseph A. Pask, "Influence of Surface Silica Impurities on the Sintering Behavior of Alumina Powders," January 1980, LBL-10392.

6. Paul R. Sharps, Antoni P. Tomsia, and Joseph A. Pask, "Wetting and Spreading in the Cu-Ag System, October 1980, LBL-11119.

7. I. A. Aksay, Joseph A. Pask, and R. F. Davis, "Chemical Interdiffusion in Mullite," October 1980, LBL-11334.

8. S. S. Chiang, M. Nishioka, R. M. Fulrath, and Joseph A. Pask, "Effect of Processing on Microstructure and Properties of PZT Ceramics," November 1980, LBL-8868.

9. M. Nishioka, R. M. Fulrath, and J. A. Pask, "Influence of Mixing Medium on Sintering and Coupling Coefficient of PZT Ceramics," November 1980. LBL-8869.

10. Joseph A. Pask and Antoni P. Tomsia, "Wetting, Spreading and Reactions at Liquid/Solid Interfaces," November 1980, LBL-11335.

11. Jose S. Moya and Joseph A. Pask, "Strength and Fracture Toughness of Aluminum Silicate Materials," December 1980, LBL-

c. High-Temperature Reactions*

Alan W. Searcy, Investigator

Introduction. Five articles in this report bear on various aspects of the complex dependence of decomposition reaction kinetics and product properties on reaction variables: TEM studies show that $MgCa(CO_3)_2$ in vacuum decomposes to a metastable MgO-CaO solid solution, which separates at longer times to the stable MgO and CaO phases. Very rapid reactions of porous CaO aggregates with water vapor have been measured and are shown to depend on accessibility of inner surfaces of < 100 Å pores. Room temperature reactions of three forms of CaO which differ in surface areas and porosities are shown to yield three physically distinguishable forms of $Ca(OH)_2$, all of which undergo an exothermic, strain relieving process when heated to ~ 300°C. The fourth article provides a theoretical means for evaluating the average number of collisions that gas molecules experience with capillary walls. Such information is important to understanding, for example, the conversion of SO_3 from sulfate decomposition to SO_2 and O_2. The fifth article shows that SO_3 gas is not an intermediate in SO_2 formation from $MgSO_4$ decomposition, as had been concluded by others.

1. IN-SITU STUDIES OF $MgCa(CO_3)_2$ DECOMPOSITION BY TEM

Tien Tien Dai, W. Kriven, and Alan W. Searcy

Characterization of the properties of the porous oxide products of carbonate decompositions by SEM, x-ray diffraction, and BET methods provided information on their surface morphology, crystallinity, and porosity. However, the vacuum decomposed products react with H_2O or CO_2 in the atmosphere readily, and the particle sizes of the product oxides often are below the resolution limit of the SEM technique. Therefore, in-situ hot stage TEM work was initiated on $MgCO_3$, $CaCO_3$ (calcite form), $MgCa(CO_3)_2$, dolomite, and $SrCO_3$ to make direct observations of the decomposition reaction and properties of the oxide product. Dolomite results are reported here.

Single crystal specimens were prepared from naturally formed minerals. A simple spot-diffraction pattern was usually chosen so that it represented one of the low-index planes. Decomposition was followed continuously by recording the changing images and diffraction patterns.

The diffraction pattern (Fig. 1) of a partially decomposed sample gave a ring pattern with continuous intensities between CaO (200) and MgO (200) rings and between CaO (220) and MgO (220) rings.

Fig. 1. Diffuse rings of the product of partially decomposed dolomite. (XBB 812-1516)

The continuity in intensities implies the formation of a solid solution of CaO and MgO. As the decomposition progressed, the rings became less diffuse and a discrete ring pattern (Fig. 2) developed that indicated the growth of separate oxides. From the image the dimension of the oxide crystallites can be estimated to be less than 100 Å. Evidently decomposition proceeds by a two-step process in which CO_2 escapes to leave a metastable solid solution of MgO and CaO, which then separates into the stable solid products, MgO and CaO. The intensity distribution around the circumference of the diffraction rings remained inhomogeneous

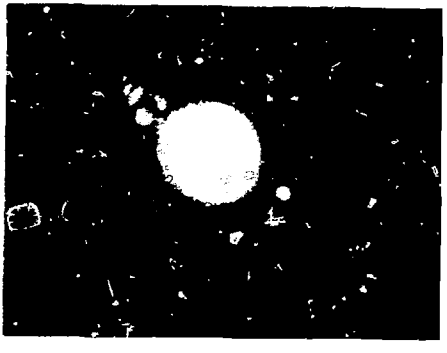

Fig. 2. Separate MgO and CaO rings for fully decomposed dolomite. (XBB 812-1515)

*This work was supported by the Director, Office of Energy Research, Office of Basic Energy Sciences, Materials Sciences Division of the U.S. Department of Energy under Contract No. W-7405-ENG-48.

throughout the decomposition process. The spatial relationships between segments of the ring which show strong intensities and the spot diffraction pattern of dolomite showed that ⟨001⟩ directions of oxides preferentially nucleate along ⟨010⟩ directions of dolomite, and {110} planes of oxides preferentially grow on {101} planes of dolomite.

2. THE KINETICS OF REACTION OF POROUS CaO AGGREGATES WITH WATER VAPOR

Dario Beruto,[†‡] L. Barco,[*] and Alan W. Searcy[†]

Aggregates of crystals of CaO that are traversed by pores of < 100 Å are produced by decomposing $CaCO_3$ or $Ca(OH)_2$ in vacuum. The rate of reaction with water vapor of ~ 27 mg quantities of these porous CaO aggregates (formed by decomposition of $CaCO_3$ powder to produce sr-CaO, of $CaCO_3$ single crystals to form sc-CaO, and of $Ca(OH)_2$ to form h-CaO) have been measured at 25°C. For sr-CaO the rates were measured as a function of H_2O gas pressure. The morphological and porosity changes that accompany these reactions have already been reported.[1]

Figure 3 shows rates of reaction of sr-CaO, h-CaO, and sc-CaO with water vapor at 4 torr pressure. Several conclusions and inferences can be drawn: 1) Samples of either sr-CaO, or h-CaO are largely converted to a poorly crystalline form of $Ca(OH)_2$ (see following article) within 2 minutes by room temperature exposure to water vapor at a relative humidity of ~ 20 to 30%. 2) Rates of reaction are not limited by solid state diffusion, at least until 70% or more conversion to $Ca(OH)_2$. (Such a process would cause a parabolic time dependence.) Some process such as H_2O gas diffusion over a constant diffusion distance or a surface reaction must be rate limiting. SEM and porosity measurements show that reaction proceeds at all the inner surfaces of the porous aggregates. The sc-CaO, which has a higher internal surface than does sr-CaO, may hydrate more slowly than the powders because the water vapor must diffuse through longer pores to complete the reaction. 3) In later stages of the reaction, rates become nearly constant but are much slower than initial rates. This fact and the fact that the transition to the regime of slower reaction occurs at similar percent hydration for sr-CaO and sc-CaO, which have similar porosities, and earlier for h-CaO, which has a smaller porosity, suggest that the rates slow when smaller pores become blocked by $Ca(OH)_2$ formation.

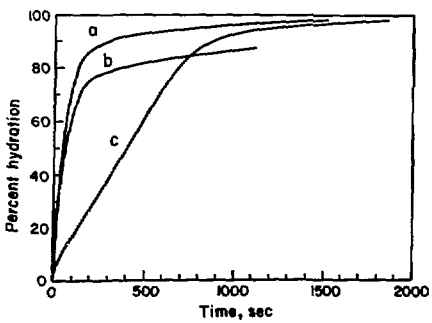

Fig. 3. Hydration rate for sr-CaO (from $CaCO_3$ powder decomposition), curve a; for h-CaO (from $Ca(OH)_2$ powder decomposition), curve b; and for sc-CaO (from $CaCO_3$ single crystal decomposition), curve c. (XBL 976-10232)

Rates of reaction of sr-CaO were measured at five partial pressures of H_2O. From 20 to > 50% hydration the rates R fit an expression of the form $R = K(P_{H_2O}/P^o_{H_2O})^n$, where $K = (7.5 \pm 1) \times 10^{-10}$, $P^o_{H_2O}$ is one atm, and $n = 0.74 \pm 0.01$. As reaction approaches completion, K decreases, as expected from Fig. 3, but n remains unchanged at least to > 80% completion of reaction.

Acknowledgment

Support was provided by the Italy-U.S. Exchange Program of the Consiglio Nazionale delle Ricerche and the National Science Foundation and by the Division of Materials Sciences, Office of Basic Energy Sciences, U.S. Department of Energy under Contract No. W-7405-ENG-48.

* * *

[†]Materials and Molecular Research Division, Lawrence Berkeley Laboratory and Department of Materials Science and Mineral Engineering, University of California, Berkeley (U.S.A.).
[‡]Laboratorio di Chimica Facolta di Ingegneria, Universita di Genova, Italy.

1. D. Beruto, L. Barco, G. Belleri, and A. W. Searcy, J. Am. Ceram. Soc., in press.

3. STRAIN-INDUCED PHENOMENA IN $Ca(OH)_2$ MADE BY REACTION OF CaO WITH WATER VAPOR

Dario Beruto,[†‡] Alan W. Searcy,[†] Luigi Barco,[‡] and Gabriele Belleri[‡]

Three physically distinguishable, poorly crystalline forms of $Ca(OH)_2$ were made by reactions of water vapor at 25°C with CaO powders. One form (sr-$Ca(OH)_2$) was made by the sequence

$$CaCO_3(s) \xrightarrow[Vac]{\Delta} CaO(s) \xrightarrow{H_2O(g)} Ca(OH)_2(s);^1$$

a second was made (h-$Ca(OH)_2$) by the sequence

$$Ca(OH)_2 \xrightarrow[Vac]{\Delta} CaO(s) \xrightarrow{H_2O(g)} Ca(OH)_2;$$

and a third (is-$Ca(OH)_2$), by reacting nonporous CaO powders of ~ 1 μm cross sections with water vapor. This study examined the nature of the exothermic transformations that all three forms are found to undergo when heated to 300°C.

For each, the exothermic process is accompanied by decreases in XRD integral line breadths. The decreases (in radians × 10^3) are for sr-$Ca(OH)_2$ from 22.5 to 13.5, for h-$Ca(OH)_2$ from 23.4 to 17, and for is-$Ca(OH)_2$ from 16.6 to 2.9.

For is-$Ca(OH)_2$, the integral line breadth after heating is smaller than that measured for ~ 1 μm crystals of $Ca(OH)_2$ grown from aqueous solutions. The surface area of is-$Ca(OH)_2$ is low, ~ 3 m^2/g, and is not measurably changed by the heat treatment. The exothermic process for is-$Ca(OH)_2$ probably is recrystallization of highly strained $Ca(OH)_2$ to form essentially strain-free crystals.

For sr- and h-$Ca(OH)_2$, not only reductions in internal strain but also reductions in surface areas and internal porosities are produced by the heat treatment. The porosity of sr-$Ca(OH)_2$ decreases from 9.8 to 6.5 mm^2/g and the surface area decreases from 35 to 18 m^2/g. For h-$Ca(OH)_2$, the corresponding decreases are from 5.9 to 4.6 mm^2/g and from 16.5 to 11.5 m^2/g.

Figure 4 shows the effect on the surface area of sr-$Ca(OH)_2$ of being heated to various temperatures for 40-minute periods. The fact that heating beyond 320°C causes no further reduction in surface area implies that the driving force for reduction in surface area is low after the exothermic strain-relieving process.

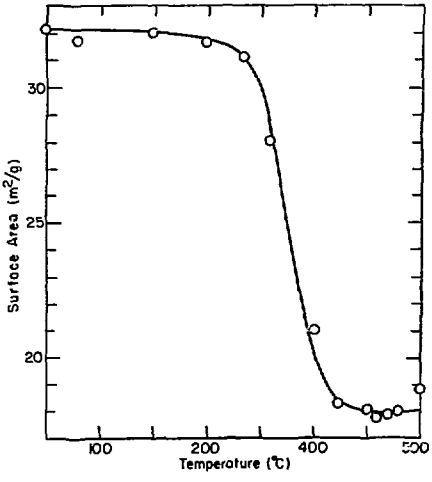

Fig. 4. Effect of heating on surface area of sr-$Ca(OH)_2$. (XBL 801-4533)

Acknowledgment

Research supported by the Division of Materials Science, Office of Basic Sciences, U.S. Department of Energy under Contract No. W-7405-ENG-48 and by the Italy-U.S. Exchange Program of the Consiglio Nazionale delle Ricerche and the National Science foundation.

* * *

†Materials and Molecular Research Division, Lawrence Berkeley Laboratory and Department of Materials Science and Mineral Engineering, University of California, Berkeley (U.S.A.).

‡Laboratorio di Chimica, Facolta di Ingenerai, Universita di Genova, Italy.

1. D. Beruto, A. W. Searcy, L. Barco, and G. Belleri, *J. Am. Ceram. Soc.*, in press.

4. COLLISION DISTRIBUTIONS IN POROUS CATALYST PELLETS

Nathan S. Jacobson, David J. Meschi, and Alan W. Searcy

Industrial catalysts are typically precious metals deposited on the interior of an inert porous material. A reactant molecule diffuses into a pore, strikes the walls of the pore, reacts, and the product diffuses out. One important question is the location of the precious metal--whether it should be evenly distributed along the pore or concentrated at the entrance. We have developed a computer model to answer this question. The same basic model can also be used to extract reaction probabilities from experimental determinations of the fraction of molecules that react when a gas passes through a porous barrier.

Because pore dimensions are small, diffusion in these processes is typically by Knudsen flow. A number of investigators have modeled Knudsen flow on computers by a Monte Carlo technique. We have adapted this approach to obtain the reactive collision probability as a function of distance into a porous catalyst pellet. The pores are assumed to be straight with closed ends, and the catalyst is assumed to be uniformly distributed along the pores.

Figures 5 and 6 are the results for a pore with a length to radius ratio of 100 and reaction probabilities of 1 and 0.001, respectively. For a reaction probability of 1, most of the reactive collisions occur at the entrance to the pore, suggesting that this is the optimum location for the precious metal. For a reaction probability of 0.001, the precious metal should be deposited more uniformly along the pore.

We are currently fitting a function to the data so that, given a reaction probability, we can predict the optimum pore dimensions and optimizing distribution of the precious metal. We also plan to extend the model to deal with reactions for which back reactions are significant.

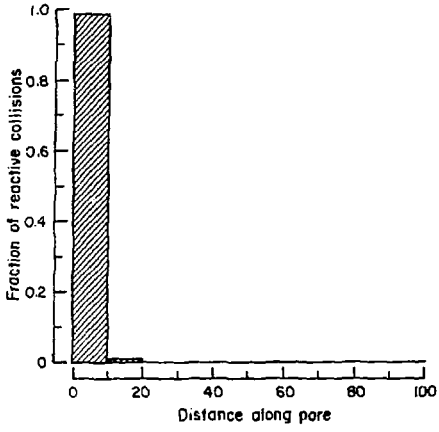

Fig. 5. Distribution of reaction collisions along a pore with a length-to-radius ratio of 100 when each collision of an unreacted molecule causes a reaction. (XBB 811-5101)

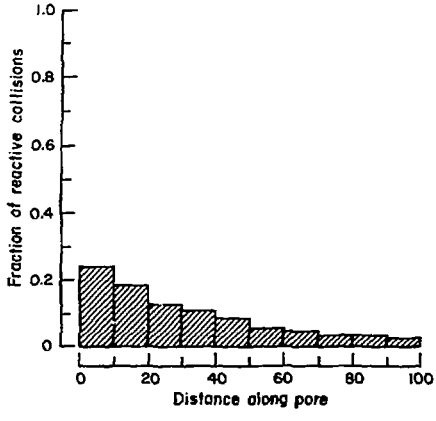

Fig. 6. Distribution of reactive collisions along a pore with a length-to-radius ratio of 100 when each collision of an unreacted molecule has a reaction probability of 10^{-3}. (XBB 811-5102)

5. RATE LIMITING PROCESSES IN $MgSO_4$ DECOMPOSITION

D. J. Meschi and Alan W. Searcy

Magnesium sulfate decomposes primarily by means of the reactions[1,2,3]

$$MgSO_4(s) = MgO(s) + SO_3(g), \quad (1)$$

$$MgSO_4(s) = MgO(s) + SO_2(g) + 1/2\ O_2(g). \quad (2)$$

Lau, Cubicciotti, and Hildenbrand[3] have found that, for some conditions, at 1000 K the decomposition proceeds chiefly according to reaction (1), even though the SO_2 equilibrium pressure at that temperature was about 10^{-4} atm, which is almost 100 times greater than the equilibrium pressure of SO_3.[2,3] The pressures they measured by means of a torsion-effusion method were consistent with this interpretation, except for very small orific areas for which pressure and molecular weights approached values expected from reaction.[2] The addition to the magnesium sulfate of a few mole percent of Fe_2O_3 as a catalyst produced pressures consistent with reaction (2) even for large orifices.

Lau, Cubicciotti, and Hildenbrand believed that the decomposition reaction in all cases was essentially reaction (1), and that the SO_2 was formed as a result of the reaction

$$SO_3(g) = SO_2(g) + 1/2\ O_2(g). \quad (3)$$

This last reaction was, in their opinion, the rate limiting one and the one which was catalyzed by the Fe_2O_3.

It seemed more likely to us that their observations must result from catalysis of reactions (1) or (2) by Fe_2O_3. To determine if this were the case, we carried out a series of calculations assuming various values for the rate constants of the forward and backward processes corresponding to reactions (1), (2), and (3). Because of the experimental uncertainties and the complexity of the series of rate equations, it was not possible to find a unique set of rate constants which fit the experimental data exactly, but it was possible to confirm our expectation that catalysis of reaction (3) alone could not yield the observed behavior and to set limits on possible influences of the catalysts on the three reactions.

If the catalyst affected reactions (1) and (3) only, it would have to increase the rate of reaction (1) by a factor of about 10, and it would concurrently have to increase the rate of reaction (3) by a factor of at least 10^{10}. If, on the other hand, it affected reaction (2) only, it would suffice to increase the rate of this reaction by a factor of 4000. Another less likely possibility would be an increase by a factor of 3000 in the rate of reaction (2), coupled with an increase in the rate of reaction (3) by a factor of 10^{10}.

In our opinion, the most likely hypothesis is that the major effect of the catalyst is on reaction (2). The rate limiting step for reaction (2) may be conversion of adsorbed SO_3 to $SO_2(g)$ + $1/2\ O_2(g)$; the concentration of adsorbed SO_3 on the $MgSO_4$ surface can be primarily determined by the rate of a reaction such as $MgSO_4(s) = MgO(s) + SO_3(ads)$, and may be little affected by the $SO_3(g)$ pressure.

* * *

1. H. H. Kellogg, Trans. Metall. Soc. AIME 230, 1622 (1964).
2. V. V. Pechkovsky, J. Appl. Chem. USSR 29, 1229 (1956).
3. K. H. Lau, D. Cubicciotti, and D. L. Hildenbrand, J. Chem. Phys. 66, 4532 (1977).

6. ELECTRONIC CERAMICS IN HIGH TEMPERATURE ENVIRONMENTS†

Alan W. Searcy and David J. Meschi

Using information from the authors' experience and from the literature, the article abstracted here uses principles of thermodynamics to show how high temperatures or temperature gradients may influence compositions and properties of semiconductors: Discussed are the effect of temperature on intrinsic and extrinsic carrier concentrations, the influence of temperature on the composition for congruent vaporization of a binary semiconductor (using Ga_2S_3 as an example), the effect of temperature on the solubility of a second solid in a solid of nominally constant composition (using solubility of CaO in $CaCO_3$ as an example), and the effect of a temperature gradient on the composition and physical properties of a two-phase solid mixture of initially uniform composition (using the Zr-H system as an example).

As these examples show, increased temperatures may alter the state of thermodynamic equilibrium of a ceramic in ways that are sometimes quite subtle but that nevertheless have a significant effect on its performance as an electronic device.

* * *

†Submitted to the Bulletin of the American Ceramic Society.

RESEARCH PLANS FOR CALENDAR YEAR 1981

During calendar year 1980 we obtained evidence that several vapors pass through ~ 1 mm thick alumina disks that are traversed by pores with cross sections of the order of 1 μm predominantly by surface diffusion rather than by Knudsen flow. This finding opens the way to measurements of surface diffusion coefficients of high temperature vapors on solids, and their temperature dependence, which are quantities of great importance at a wide range of high temperature processes, including sintering and heterogeneous catalysis of decomposition of one solid by particles of a second solid (see article 5 above). Experimental study of surface diffusion of gases and high temperature vapors on high temperature surfaces, and work on a Monte Carlo model for surface diffusion, will be important components of the program in the coming year.

SEM will be used to study the rearrangements that occur apparently by cooperative movements of submicron particles of CaO subsequent to their formation from $CaCO_3$ decomposition, and of porous $Ca(OH)_2$ aggregates formed by vapor phase hydration when those particles are heated to 300°C (see article 2 above). TEM studies similar to that described in the first article above will be completed for $CaCO_3$, $MgCO_3$, and $SrCO_3$.

An effort to correlate the influence of catalysts such as Fe_2O_3 on rates of $SrSO_4$ decomposition, which was initiated last year, will be completed instead for $MgSO_4$ because catalysis was slight for $SrSO_4$. A related study of heterogeneous catalysis of SO_3 decomposition, which was delayed in order to concentrate effort on the study of transport of vapors by surface diffusion, will be resumed.

A solution calorimeter study of the thermodynamic stabilities of CaO formed by $CaCO_3$ decomposition and of MgO formed by $Mg(OH)_2$ decomposition in vacuum is expected to be completed. These studies should establish whether large discrepancies between apparent stabilities measured by Knudsen effusion methods and known stabilities of the bulk oxides result because (a) vacuum decomposition produces the oxides in highly metastable states, or (b) a previously unrecognized kind of partial equilibrium fixes the measured decomposition pressures. Further efforts to clarify decomposition kinetics and the dependence of properties of the solid oxide products of decomposition reactions on processing conditions probably will include (a) hot-pressing experiments for $CaCO_3$ and high surface area CaO with LiCl, (b) measurement of the influence of particle size and powder bed depth on rates of calcite decomposition, and (c) participation in studies with Dario Beruto's group at the University of Genoa of the dependence of surface areas of CaO from large calcite crystals on the extent of reaction. There is reason to believe that large calcite crystals may decompose by a significantly different process than do powders.

1980 PUBLICATIONS AND REPORTS

Refereed Journals

1. E. K. Powell and A. W. Searcy, "The Rate and Activation Enthalpy of Decomposition of $CaCO_3$," Metall. Trans. 11B, 427 (1980).

†2. D. Beruto, L. Barco, A. W. Searcy, and G. Spinolo, "Characterization of the Porous CaO Particles Formed by Decomposition of $CaCO_3$ and $Ca(OH)_2$ in Vacuum," J. Am. Ceram. Soc. 63(7), 439 (1980).

Other Publications

†1. D. Beruto, A. W. Searcy, L. Barco, and G. Belleri, "Strain Induced Phenomena in $Ca(OH)_2$ Made by Reaction of CaO with Water Vapor," Proceedings of the 9th International Symposium on the Reactivity of Solids, Cracow, Poland, September 1980, LBL-11128.

LBL Reports

1. Taghi Darroudi, "The Effect of CO_2 Pressure on the Rate of Decomposition of Calcite," M.S. thesis, January 1980, LBL-10309.

2. Gary F. Knutsen, "The Thermodynamics and Kinetics of the Reaction: $CaCO_3 = CaO + CO_2$," Ph.D. thesis, September 1980, LBL-11459.

†3. D. Beruto, A. W. Searcy, L. Barco, and G. Belleri, "Vapor Phase Hydration of Submicron Particles of CaO," submitted to J. Am. Ceram. Soc., June 1980, LBL-9443.

4. Alan W. Searcy and David J. Meschi, "Electronic Ceramics in High Temperature Environments," LBL-9713.

5. E. K. Powell and A. W. Searcy, "Effects of Temperature and Annealing Time on the Surface Area of CaO Produced by Decomposition of Large $CaCO_3$ Crystals," LBL-11207.

Invited Talks

1. Alan W. Searcy, "Changing Concepts of Decomposition Reactions," Bay Area Conference on High Temperature Science and Technology, SRI International, Menlo Park, April 1980.

2. Alan W. Searcy, "Inner Surfaces: Manipulating the Dimensions of Submicron Pores in CaO," Banquet Lecture, 7th LBL/MMRD International Materials Symposium on "Surfaces and Interfaces in Ceramic and Ceramic-Metal Systems," July 1980.

†3. D. Beruto, A. W. Searcy, and L. Barco, "Strain Induced Phenomena in $Ca(OH)_2$ Made by Reaction of CaO With Water Vapor," 9th International Symposium on the Reactivity of Solids, Cracow, Poland, September 1-6, 1980.

4. Tien Tien Dai and Alan W. Searcy, "Decomposition of Group II Carbonate Single Crystals: An Investigation by Transmission Electron Microscopy," *Pacific Coast Regional Meeting, American Ceramic Society*, October 28, 1980.

5. Alan W. Searcy and David J. Meschi, "Electronic Ceramics in High Temperature Environments," Invited introductory lecture for the Symposium on Electronic Ceramics in Severe Environments, Pacific Coast Regional Meeting, American Ceramics Society, San Francisco, October 27, 1980.

* * *

†Research performed partly in Italy under the U.S.-Italy exchange program of CNR and NSF, and partly in the U.S. under the Division of Materials Sciences, DOE.

d. Chemical Properties of Ceramic Alloys*

Lutgard De Jonghe, Investigator

Introduction. When a dense oxide alloy reacts with a strongly reducing gas such as hydrogen, a porous metal product layer can develop at its surface. If the gas flow is sufficient to eliminate the external mass transfer resistance, the pore structure of the metal layer and the nature of the metal/oxide interface reaction will determine the overall reduction rate kinetics. When the reduction is directly from dense unreduced oxide to metal alloy and the reaction is topochemical, a fairly simple reduction model can be applied.[1,2] This model leads to layer growth kinetics described by

$$\dot{\xi} = \frac{P^{o}_{H_2}}{RTC_o}\left(\frac{\xi}{D_{eff}} + \frac{1}{k_r}\right)^{-1}, \qquad (1)$$

where ξ = porous product layer thickness

$\dot{\xi}$ = $d\xi/dt$

$P^{o}_{H_2}$ = hydrogen pressure in the gas stream

C_o = oxygen concentration in the solid oxide

D_{eff} = effective gas diffusivity in the porous product layer

k_r = interface reaction rate parameter

The details of the assumptions involved in this model have been discussed by Porter and De Jonghe.[2]

Analysis of the layer growth data with Eq. (1) will thus permit a separation of the contributions to the overall reaction resistance of gas diffusion in the scale and of the interface reaction. This *analysis was used recently to study the reduction* reaction of cobalt ferrite.[2]

1. GASEOUS REDUCTION OF AN ALLOY OXIDE†

Jeffrey Allender and Lutgard C. De Jonghe

We report here on the reduction kinetics and product phase morphologies of $NiFe_2O_4$ and $Ni(Al,Fe)_2O_4$ ceramic alloys. Although Ni and Co are fairly similar elements, some interesting differences exist in the Ni-Fe-O and the Co-Fe-O phase relationships that should affect the kinetics and micromorphology of the reduction: Ni ion diffusion is not significantly slower than that of Co ions in their respective ferrite spinels at all oxygen activities.

The alloy oxides used in this study were dense polycrystalline $NiFe_2O_4$, $NiAl_{0.02}Fe_{1.98}O_4$, and $NiAl_{0.1}Fe_{1.9}O_4$. Grain sizes were between 4 and 8 microns. Porosities were about 2.5%.

Some results of optical layer growth measurements are shown in Fig. 1. The product layer thicknesses after a reaction time of 3000 sec are compared in Fig. 2. For $NiFe_2O_4$ and $NiAl_{0.02}Fe_{1.98}O_4$, the increase of the interface advance rate diminishes in a temperature range between 500°C and 700°C. This slowdown is, however, not comparable to the pronounced reaction rate minimum that was observed for cobalt ferrites in this temperature range.[2] For $NiAl_{0.1}Fe_{1.9}O_4$ alloys, a reaction rate slowdown is not observed. These results clearly demonstrate the pronounced effect of Al^{3+} on the reduction behavior of the Ni-Al-Fe oxide alloys.

Analysis that begins with Eq. (1) leads to the identification of reaction regimes and the determination of D_{eff} and k_r. Thus, when

$$\xi = \xi_c \approx b/2a , \qquad (2)$$

where $a = C_0RT/2D_{eff}\, P^{o}_{H_2}$ and $b = C_0RT/kr\, P^{o}_{H_2}$, the gas diffusion resistance and the interface reaction resistance contribute equally to the control of the overall reduction kinetics. Thus, the reaction

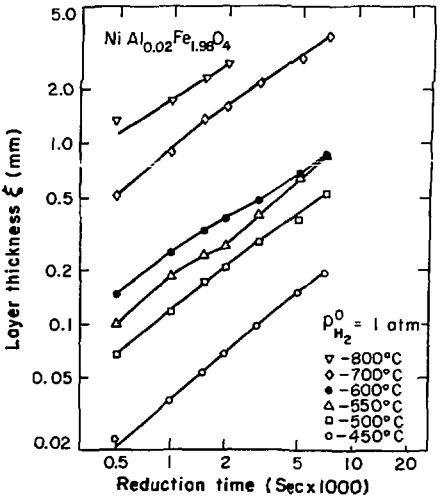

Fig. 1. Total product layer thickness, ξ, as a function of time and temperature for hydrogen reduction of $NiAl_{0.02}Fe_{1.98}O_4$. (XBL 807-1521)

*This work was supported by the Director, Office of Energy Research, Office of Basic Energy Sciences, Materials Sciences Division of the U.S. Department of Energy under Contract No. W-7405-ENG-48.

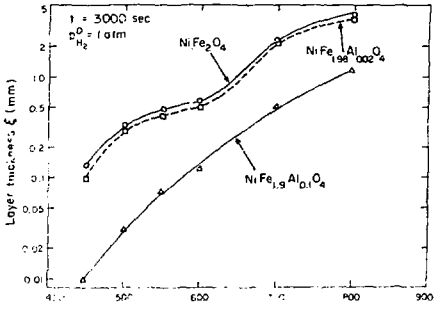

Fig. 2. Total product layer thickness, ξ, after 300 sec as a function of temperature, T (°C), for reduction with hydrogen. (XBL 807-1527)

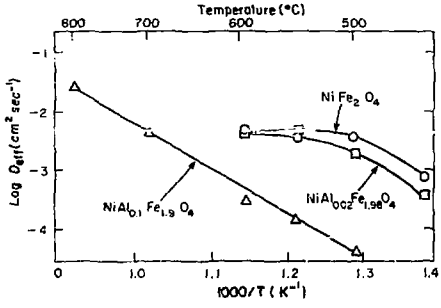

Fig. 3. The effective gas diffusion coefficient, D_{eff}, for transport through the porous product layer. Above 600°C the values of D_{eff} for $NiFe_2O_4$ and $NiAl_{0.02}Fe_{1.98}O_4$ could not be calculated since the scales were no longer single phase. (XBL 807-1522)

will be mainly under interface reaction control when $\xi \ll b/2a = \xi_C$, and will be under gas transport control when $\xi \gg \xi_C$.

Application of this analysis to the data obtained for the reduction of nickel ferrites yielded the results shown in Table 1.

The values of ξ_C the kinetic data clearly indicate that the reactions are under mixed control in the temperature and time intervals of the measurements. In addition, for the measurement interval reported here, the importance of the gas transport resistance through the porous scale increases with increasing temperatures.

Calculated values of D_{eff} are shown in Fig. 3. D_{eff} for $NiFe_2O_4$ and $NiAl_{0.002}Fe_{1.98}O_4$ does not vary simply with temperature. The values for D_{eff} for $NiAl_{0.02}Fe_{1.98}O_4$ were generally lower than those for $NiFe_2O_4$ indicating higher scale tortuosities when Al^{3+} is present.

The activation enthalpy for k_r for $NiFe_2O_4$ and for $NiAl_{0.02}Fe_{1.98}O_4$ and 10 kcal/mole, while for $NiAl_{0.1}Fe_{1.98}O_4$ it is 12 kcal/mole (Fig. 4). The main action of Al^{3+} alloying additions thus appears to be the depression of the pre-exponential factor of the interface reaction-rate parameter.

In general, at the lower reaction temperatures all scales consisted simply of a porous metal alloy. At temperature above 600°C, the scales that formed on $NiFe_2O_4$ and on $NiAl_{0.02}Fe_{1.98}O_4$ were more complex and proved to be two-phase.

The microstructure of the scales formed on $NiAl_{0.02}Fe_{1.9}O_4$ were comparable to those on $NiFe_2O_4$. Up to 600°C, a single porous metal product layer is formed. Above 600°C, the microstructural sequence is spinel/spinel + metal/wustite + metal/metal. There are some differences, however, from the simple $NiFe_2O_4$ behavior: even after 7000 sec reduction at 600°C the interface structure is still spinel/metal. At 700°C the presence of Al^{3+} appears to have promoted preferential grain boundary attack (Fig. 5).

Table 1. Product layer thickness, ξ_C, at which the gas diffusion and the interface reaction contribute equally to the total reaction resistance.

	ξ_C (mm)					
Material	450°C	500°C	550°C	600°C	700°C	800°C
$NiFe_2O_4$	0.4	0.45	0.19	0.13	-	-
$NiAl_{0.02}Fe_{1.98}O_4$	0.21	0.36	0.25	0.17	-	-
$NiAl_{0.1}Fe_{1.9}O_4$	-	0.06	0.07	0.04	0.13	0.24

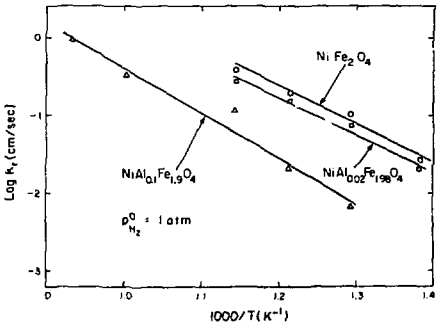

Fig. 4. The interface reaction rate parameter, k_r, as a function of temperature for nickel aluminum ferrite by hydrogen. (XBL 807-1528)

Preferential grain boundary reaction will then depend on the ratio of the grain boundary diffusivity to the grain bulk diffusivity, as well as on ratio of the reaction rate to the grain boundary transport rate of the less reducible cations that build up at the reaction interface. We can therefore expect alloy oxides to have a limited range of reaction conditions where grain boundary attack is pronounced.

* * *

†Brief version of LBL-11125.

Fig. 5. Preferential intergranular reduction in $NiAl_{0.02}Fe_{1.98}O_4$ after 7000 sec of reduction at 600°C. M is porous metal alloy, S is spinel. (XBB 808-9667)

2. IN SITU OBSERVATIONS OF GAS/SOLID REACTIONS: COBALT FERRITE REDUCTION†

Lutgard C. De Jonghe

One of the most significant advantages of high voltage transmission electron microscopy is that it permits in situ observation of phase transformations in thick foils. One class of transformations of technological importance involves gas/solid reactions in which a metal oxide is reduced to metal. Examples of such reactions can be found in ore reduction, and in hydrogen production by the steam/iron process.

The rates of reduction reactions depend on a number of parameters, including the composition of the ceramic alloy and the environmental conditions. The early stages of reduction are not easily accessible by conventional methods such as thermogravimetric analysis. High voltage transmission electron microscopy with environmental control can fruitfully be used to clarify these early reaction stages. The reactions that can be studied are necessarily limited to those that proceed fairly slowly, in order to permit the recording of the transformation events. For cobalt ferrite, this restricts the reaction condition to a temperature range of 400 to 650°C and a pressure range of the reducing gases at 10^{-5} to 10^{-6} torr. In our reduction experiments with H_2/H_2O, the gas composition and processes were monitored with a partial pressure gage.

When ceramic alloy oxides are reduced, the element having the least stable oxide will be preferentially removed. For cobalt ferrite at 500°C, and at low driving forces, nearly pure cobalt is produced on the foil surface. The chemical reaction is roughly:

$$CoFe_2O_4 + 4H_2(g) \rightarrow Co(m) + 2Fe^{2+}\ 4H_2O(g)$$

The continued growth of the metal phase thus consumes the matrix oxide. The divalent iron that is produced at the reaction surface is mainly injected into the matrix oxide, thus establishing an oxygen chemical potential gradient. The divalent iron preferentially occupies octahedral interstices, thus leading to the formation of small, coherent (Fe,Co)O clusters, as can be seen in Fig. 6. The appearance of the strain contrast is very rapid, indicating that the excess divalent iron cannot be accommodated by the spinel in solid solution. The nucleation appears to be quasi-homogeneous. At a somewhat later time, competitative growth and strain interactions lead to the appearance of coherent precipitates of the wüstite type phase nearly regularly spaced in ⟨440⟩ directions, Fig. 6(c).

The metal phase is initially oriented with respect to the matrix oxide, especially on near {111} planes. The orientation relationship for the hexagonal cobalt metal phase is $(0001)_{Co}//(111)_{ox}$, and $(2\bar{1}\bar{1}0)_{Co}//(\bar{1}10)_{ox}$. The metal particles tend to facet along ⟨2110⟩ directions in their basal plane, thus providing a reference direction. Comparison of Fig. 7(a) and 7(b) shows that the

Fig. 6. Time sequence of an in situ reduction of cobalt ferrite at 500°C, with a total pressure of 10^{-5} torr, H_2/H_2O = 1/10. Fe^{2+} is immediately injected into the bulk leading to strong stain contrast from coherent precipitates, as shown in b. After long times, c, competitive growth and strain interactions lead to quasi periodic precipitate arrangements (a = 0 min; b = 4 min; c = 75 min).
(XBB 803-3227)

cobalt does not maintain its orientation relationship upon continued growth. A rotation of about 6° can be observed in the two successive micrographs. Fig. 7(a) and 7(b) also show that the cobalt particles move along with the receding metal/oxide interface. This mode of morphological development implies that oxygen is readily removed from the metal/oxide interface, probably by an interface diffusion process.

In a gas/solid reaction of the type described here, the entire reaction zone is observed at once. The finite foil thickness makes it a limited sink for the excess cations that are being injected. As a result, the appearance of the phase changes may depend on the foil thickness. Furthermore, the surface oxygen chemical potential can depend on local reaction conditions. These local conditions involve the interrelation of gas phase mass transfer processes, surface reaction rates, and solid state transport rates. At sufficiently low pressures, gas phase mass transfer is unlikely to be rate limiting. Then the surface reaction rate and the solid state diffusion rate will determine the surface oxygen chemical potential. Due to the finite foil thickness, this oxygen potential will be time dependent. In the thinner part of the foil a quasi equilibrium may have been reached, while thicker parts of the foil are still reacting and show different phase relationships. This condition is illustrated in Fig. 8. The thin section of the foil has reached the spinel-metal quasi equilibrium, while the thicker parts of the foil still show the presence of the coherent (Co,Fe)O phase.

Only reactions at low driving forces can be fruitfully studied. The observations are not readily extended to the higher reaction rates that are common in processes of technological significance. Indeed, in recent observations,[1] it was found that no wüstite could be detected ahead of the advancing metal/oxide interface up to about 700°C. Then the wüstite started to form as a continuous subscale with an associated drop in reaction rates.

* * *

+Brief version of LBL-10729.

1. M. C. Rey and L. C. DeJonghe, J. Mat. Sci. 15, 2241 (1980).

Fig. 7. Cobalt ferrite reacting with hydrogen at 520°C. The H_2/H_2O = 1/20, and the total pressure was 5×10^{-6} torr. The reaction product particles are nearly pure cobalt and tend to facet. These facets can be used as reference directions. The particles C and D, marked with an arrow, can be used as a reference line for the matrix, since they did not displace. Comparison of subfigures a and b show how the metal particles (A and B) translate and rotate upon continued reaction. The rotation leads to a gradual loss of the initial orientation relationships.
(XBB 803-3226)

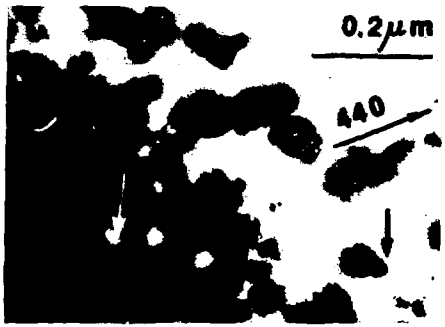

Fig. 8. The foil thickness affects the phase relationships that are observed in this cobalt ferrite reduced under the same conditions as in Fig. 7. In the thin part of the foil a condition has been reached where a cobalt rich metal phase is in near equilibrium with an iron rich spinel (black arrow). In the thick part of the foil, the wüstite type phase is still present (white arrow). (XBB 803-3225)

3. REDUCTION KINETICS AND MICROSTRUCTURES OF Al^{3+} CONTAINING COBALT FERRITES†

Michael C. Rey and Lutgard C. De Jonghe

The reduction of cobalt ferrite and of cobalt ferrite with aluminum added in solid solution was studied. The purpose was to investigate the reduction behavior of multi-cation oxides and the effects of hard-to-reduce interactive dopant on the reduction behavior. Since the reduction kinetic studies alone do not give sufficient information about the process, efforts were made to determine the microstructural characteristics of the reduction products as well.

The experiments were done on dense polycrystalline specimens of cobalt ferrite and alumina doped cobalt ferrites. Compositions were 99.4% dense $CoFe_2O_4$, 99.5% dense $CoAl_{0.02}Fe_{1.98}O_4$, and 98.9% dense $CoAl_{0.1}Fe_{1.9}O_4$. Layer growth measurements, micromorphological characterization of the reduction product layers, and weight loss kinetics by means of thermogravimetry were carried out. Samples with edge lengths of about 0.5 cm were reacted in flowing hydrogen containing 0.01% of water at a total pressure of 1 atmosphere at fixed temperatures between 500 to 800°C, for times between 5 minutes and 1 hour.

The growth kinetics were determined from optical microscope measurements on sectioned layers. Identification of the reaction product was made by x-ray diffraction or chemical etching.

Kinetics were determined by thermogravimetric methods. Figure 9 shows a log-log plot of layer thickness versus time for undoped samples reacted

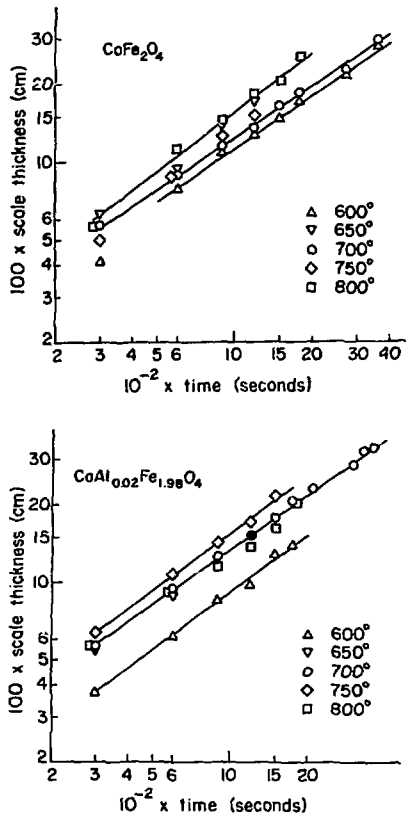

Fig. 9. Log-log plot of layer growth data for $CoFe_2O_4$ and $CoAl_{0.02}Fe_{1.98}O_4$. Note that for $CoFe_2O_4$ the reaction kinetics are slower at 700°C than at 650°C. Each data point represents the simple average of 3 to 6 different reduction runs. The slopes of the lines through the data points indicate approximate time dependences of $t^{0.75}$ for the 800°C reductions and at $t^{0.67}$ for the 600 and 700°C reductions. This indicates a mixed reaction control. (XBL 791-8165)

between 600 and 800°C. Time dependences were sublinear, between $t^{0.75}$ and $t^{0.65}$. Such sublinear kinetics usually indicate mixed reaction control. A reaction rate anomaly occurs between 650°C and 700°C for this undoped cobalt ferrite and for lightly doped cobalt ferrites (Fig. 9).

The product layer thicknesses after 20 minutes of reduction are compared for undoped and lightly doped ferrites as a function of temperature in Fig. 10. Below 650°C, Al^{3+} lowers the rate of

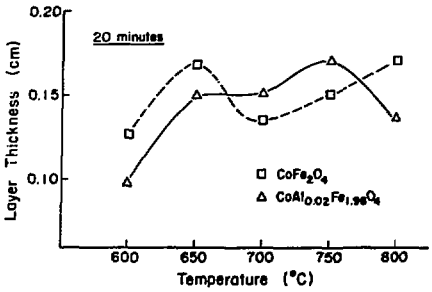

Fig. 10. Comparison of undoped and lightly doped layer growth data for specimens reacted under one atmosphere (1013 mbar) of hydrogen for 20 minutes. (XBL 791-8163)

reduction. Above 650°C the reaction rate of the undoped material decreases while that of the lightly alloyed material continues to increase. Between about 675°C and 775°C the lightly alloyed material actually reacts faster than the undoped material.

Little densification of the metal product scale occurred even at reaction temperatures as high as 800°C. Nonetheless, the pore structure coarsened as a function of time (except for the heavily doped ferrites). Possibly, surface diffusion is the dominant metal transport mode, or the initial layer density is too low to permit significant scale densification.

For $NiFe_2O_4$ 500°C and 600°C significant grain boundary attack is observed in the undoped ferrite. Etching with hydrochloric acid showed that the cores of the individually shrinking grains were unreduced spinel. The degree to which this mode of interface advance took place became more pronounced with lower reaction temperatures and with increased Al^{3+} content (Fig. 11). When the individual grains have been completely reduced, loosely connected relics of the original spinel grains constitute the metal product layer. The interface instability must arise from rapid grain boundary reaction and slow bulk reaction. The extent to which the interface is distributed thus depends on the grain bulk/grain boundary cation transport rates.

At about 650°C the product scale morphology changes. Extensive grain boundary attack is not observed while pore coarsening occurs to some extent in the scale. At 700°C, grain boundary attack is absent and the interface is clearly defined.

The pore structures of the scale could best be observed on samples that had been RF sputter etched after mechanical polishing (Fig. 12). Below 650°C the scale has a clearly dual pore structure. Pores

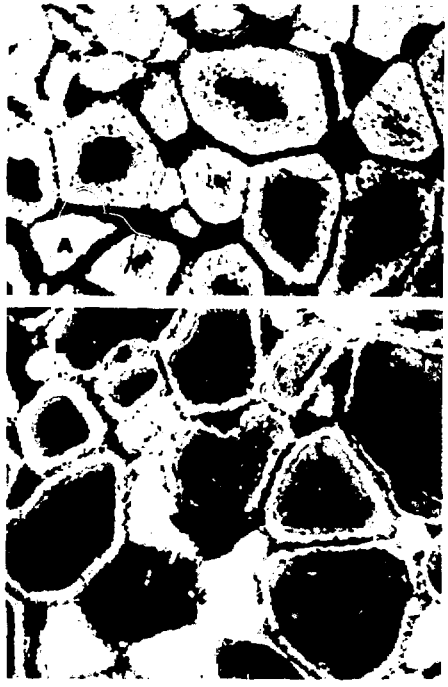

Fig. 11. Distributed reaction interface of heavily doped specimen reacted at 600°C. The width of the total reaction interface is on the order of 100 micrometers. (A) is toward the outside of the reaction zone while (B) is toward the inner region of the reaction zone. The individual grains now behave as particles for which the shrinking core model could be applied again. (XBB 794-5002)

have formed along the original ferrite grain boundaries leaving very finely porous metal grains that are relics of the original ferrite grains. The pore structure becomes coarser and more homogeneous as the temperature is increased above 650°C. It follows that the reaction rate anomaly is associated with the interface behavior rather than with the scale structure. This supports the earlier conclusion[1] that the rate anomaly is the result of formation of a wüstite type sub-scale.

* * *

†Brief version of J. Mat. Sci. 15, 2241 (1980).

1. J. Porter and L. C. De Jonghe, Lawrence Berkeley Laboratory Report LBL-9801, June 1979.

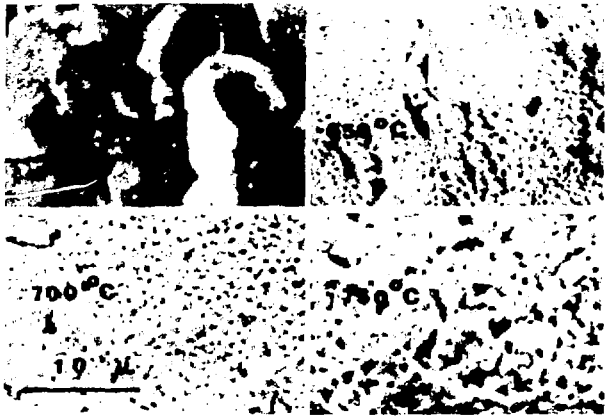

Fig. 12. Pore network morphologies in the metal scales of undoped specimens at the temperature indicated. The major morphological changes are not correlated with the reaction rate anomaly. (XBB 794-5001)

RESEARCH PLANS FOR CALENDAR YEAR 1981

The role of the interface reaction during the gaseous reduction of an alloy oxide will be studied in more detail. In particular, the relative contribution of the interface transport step will be compared to the gas/solid reaction step.

The effect of gas composition on scale morphology will be examined: it has been observed that reduction by CO/CO_2 mixtures leads to significantly swelled scales whereas reduction by H_2/H_2O mixtures does not. The role of the interface and transport reaction step and the nucleation step of the initial product phase will be studied. Thermogravimetric methods, as well as electronic microscope methods will be used in the analysis.

1980 PUBLICATIONS AND REPORTS

Refereed Journals

1. M. C. Rey and L. C. De Jonghe, "Reduction Kinetics and Microstructures of Al^{3+}-Containing Cobalt Ferrites," J. Mat. Sci. 15, 2241 (1980).

LBL Reports

1. J. Allender and L. C. De Jonghe, "Gaseous Reduction of an Alloy Oxide," LBL-11125.

2. L. De Jonghe, "In Situ Observations of Gas/Solid Reactions," LBL-10729.

3. Mei Chang and L. C. De Jonghe, "The Reaction Interface in Reduction," LBL-11392.

4. Mei Chang, "Gas-Solid Interface Reaction," M.S. thesis, LBL-11124.

Invited Talks

1. L. De Jonghe, "Microcharacterization by Electron-Optical Methods," Am. Ceram. Soc. Meeting, Chicago, April 1980.

e. Structure and Electrical Properties of Composite Materials*

Robert H. Bragg, Investigator

Introduction. The objective of this research on carbon materials is to delineate the relationship between their structure and physical properties, with emphasis on how galvomagnetic properties are related to structure. Carbon materials find such uses as mineral fuels, re-entry thermal protection structures, coatings on nuclear fuels, and medical prosthetic devices. This wide range of applications is obtained by combining in appropriate proportions two broad classes of materials, hard carbons and soft carbons, whose properties differ markedly, into composite materials. The hard carbons are derived from pyrolysis and subsequent carbonization of thermosetting carbonaceous substances, whereas the soft carbons are prepared either by thermal degradation of thermoplastic carbonaceous substances that liquify upon heating or by chemical vapor deposition of hydrocarbons such as methane on a hot polycrystalline graphite substrate at temperatures above about 2000°C. Our approach is to induce structural changes by chemical treatments or heating in inert atmospheres at temperatures up to 3000°C and to characterize the structure using wide range x-ray diffraction (XRD), small angle x-ray scattering (SAXS), electron microscopy and electron diffraction.

There is a considerable body of scientific literature on the structure and properties of soft carbons, for which commercially obtainable pyrocarbon or pyrolytic graphite (PG) is a convenient model material. Much less is known about the hard carbons for which glassy carbon (GC), so-called because it is a black shiny material which fractures conchoidally, has been chosen as a model material. GC is also obtainable commercially in chemically pure monolithic form convenient for a wide range of measurements of physical properties. The term glassy is a misnomer since GC does not melt, but in other respects such as compressive strength, chemical inertness, and impermeability, the analogy is close.

The work at LBL has shown that contrary to popular belief GC "graphitizes," i.e., the interlayer spacing d_{002} decreases from 0.344 nm toward the 0.335 nm of ideal graphite, when heated above about 2000°C. The activation energy of 225 ± 30 kcal/mole obtained from kinetic studies of the broadening of x-ray diffraction line profiles of GC is close to the generally accepted 260 kcal/mole value found for soft carbons. It can fairly be claimed that this work has also pioneered the use of SAXS to study the specific surface area (S/V) and characterize reaction kinetics.

The thrust of the research in 1980 was in areas concerned with redetermination of the activation energies for graphitization and vacancy migration, verification that the latter mechanism has been correctly identified, identification of the mechanism of graphitization and why it seems to occur only for temperatures above about 2000°C, identification of the mechanism of the nonkinetic density decrease, extension of the electrical measurements to lower temperatures and obtaining more data on the temperature dependence of R_H.

Work was initiated to adapt the techniques developed for analysis of diffraction patterns of GC to the characterization of coals of various ranks. One cannot but be struck by the remarkable similarities of the XRD patterns of these substances, and thus optimistic that the considerable work (in press) done on amorphous carbons will shed new light on the structure of coals. Work was also initiated on the preparation of graphite intercalation compounds.

1. DENSITY CHANGES IN HEAT TREATED GLASS-LIKE CARBON (GC)†

Bhola N. Mehrotra and Robert H. Bragg

Rose[1] observed that when GC is heated above its process temperature (typically 1000°C), the density decrease is nonkinetic. This led Bose and Bragg[2] to the hypothesis that the instantaneous density decrease was caused by lattice thermal expansion. The initial support for this came from the observation that because of the large anisotropy, thermal stresses of the order of 2.2×10^4 MPa (3.2×10^6 psi) would be generated, comparable to the failure stress of graphite in the presence of Griffith flaws of length about 1.0 mm. This size is consistent with the scale of heterogeneities in the microstructure seen in lattice image photographs of GC. Furthermore, if the observed volume change is ascribed to thermal expansion of the crystal lattice, then a rough calculation shows that the order of magnitude of the volume change is predicted correctly provided that somehow the expansion is not reversible.

In this work, measurements were made of dimensions, mass and density of the samples before and after heat treatments. As received plates of GC[3] were cut into specimens of 5 cm × 2.5 cm × 0.25 cm and heated for 3 hr in the range 1000-2700°C. Heating rates of 15-75°C/min were employed. Densities, pycnometric, weight, and linear dimensions were measured to an accuracy of ± 0.001 g/cm^3, ± 0.001 g and ± 0.00025 cm, respectively.

Figure 1 shows the results of isochronal heat treatments. There is no appreciable weight change for HTT > 2000°C, but the volume continues to increase up to the highest HTT. The figure also shows that the dimensional change can be taken as isotropic. The average linear expansion calculated from Fig. 1 is shown in Fig. 2 as a function of heat treatment temperature.

*This work was supported by the Director, Office of Energy Research, Office of Basic Energy Sciences, Materials Sciences Division of the U.S. Department of Energy under Contract No. W-7405-ENG-48.

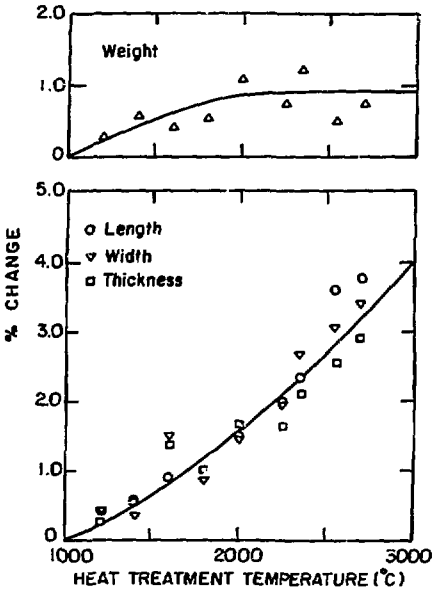

Fig. 1. Effect of HTT on dimensions and weight of GC. (XBL 8012-13465)

Density measurements obtained from several experiments in the present work are shown in Fig. 3. The three sets of LBL data in Fig. 3 were obtained from different batches prepared by the same vendor and agree fairly closely, but differ from those reported by Fischbach and Rorabaugh.[4] Variation of heating rates ranging from 15°C/min to 75°C/min had little effect on the resulting densities. If the density decreases are attributed to volume expansion and mass loss then one can calculate the average dimensional change from density decrease by correcting it for mass loss at each HTT. Figure 4 shows a comparison of the average dilation obtained in this way from the LBL data in Fig. 3, with the measured data shown in Fig. 2. The close correlation verifies that the pycnometric measurements are not affected by ingestion of fluid (water or kerosene).

The strain at temperature T should be quadratic in T. However, an experiment involves first preparation of the materials by heating to 1000°C and cooling to room temperature. The experimental data points are obtained by heating to temperatures above 1000°C and cooling to room temperature for measurements. Since the dimensional changes are irreversible, a ratchet mechanism which prevents shrinkage back to the initial values must be operating. The resistance of the "ratchet" must be extremely strong. Experiments were done wherein samples previously heated to various temperatures were subjected to hydrostatic pressures in a bomb, which employed 20 wt% turbine oil as the working fluid. The data in Fig. 5 shows that GC once expanded because of the anisotropy in thermal expansion coefficients will undergo very little reversible contraction. Consequently the net expansion for ΔT above 1000°C should be given by

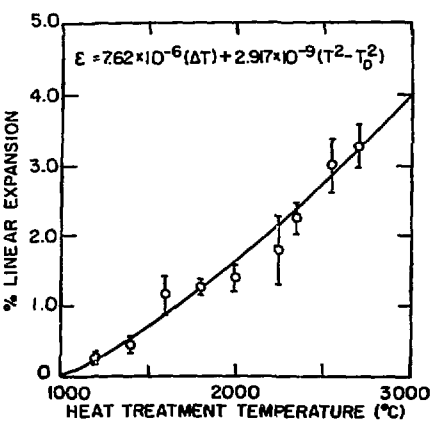

Fig. 2. Average linear expansion of GC versus HTT. (XBL 8012-13466)

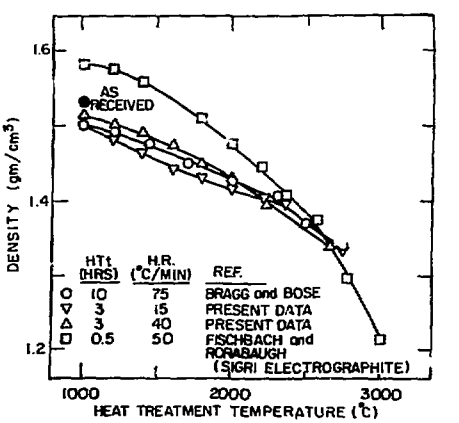

Fig. 3. Effect of HTT on the density of GC. (XBL 8010-6147)

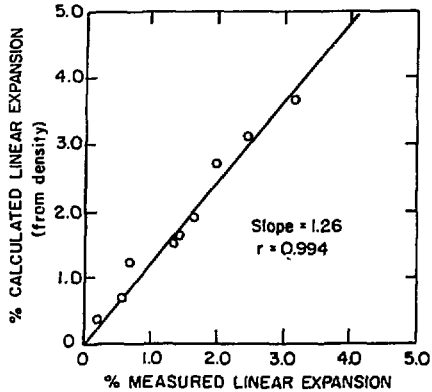

Fig. 4. Relationship between linear and volumetric expansion of GC. (XBL 8012-13464)

$$\epsilon_T = \left(\frac{1}{3}\alpha_1 + \frac{2}{3}\alpha_a - \bar{\alpha}\right)(T-T_o) + \frac{1}{3}\alpha_2(T^2-T_o^2) \quad , \qquad (1)$$

where $\alpha_1 + \alpha_2 T$ = the coefficient of thermal expansion in the c-direction and α_a is the coefficient in the a-direction.

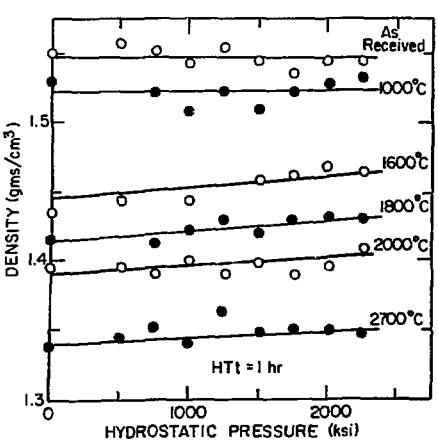

Fig. 5. Effect of hydrostatic pressure on the density of GC for various HTT. (XBL 8012-13463)

The data of Fig. 2 have been least squares fitted to Eq. (1).

Fischbach and Rorabaugh[4] have argued that most of the volume expansion is caused by gas pressure of volatile pyrolysis products trapped in GC during processing which cannot escape at high heating rates. There is some evidence in their results that greater volume expansions accompany higher treating rates. In their experiments and in ours, thick specimens invariably fractured when higher heating rates were employed. However, our results indicate that for the range of heating rates employed, which are comparable to theirs, there is no clear indication of an effect of heating rate.

The irreversible thermal expansion hypothesis not only provides a plausible explanation for the density decrease, it also provides a simple exlanation of a puzzling feature of the magnetoresistance. The magnetoresistance is negative and becomes stronger as HTT increases. It can be shown that $\Delta\rho/\rho$ will be negative for a paramagnetic or ferromagnetic material and proportional to the square of the net magnetic moment. A net moment can arise from unpaired electron spins in a magnetic field and since bonds are broken when the sample expands, the increase in $\Delta\rho/\rho$ should correspond to an increase in HTT. Furthermore, the impermeability of the material prevents the saturation of these dangling bonds, e.g., by diffusion of atmospheric gases into the samples.

* * *

†Brief version of LBL-10623 Rev.

1. S. Bose, "Pore Structure and Growth Kinetics in Carbon Materials," Ph.D. thesis, LBL-7638.
2. R. H. Bragg and S. Bose, "Thermally Induced Density Changes in Glassy Carbon," 14th Biennial Carbon Conference, University Park, PA, June 1979, p. 189.
3. Polycarbon, Inc., North Hollywood, CA. Processing temperature is said to be 1000°C.
4. D. B. Fischbach and Rorabaugh, High Temperature and High Pressure 9, 199 (1977).
5. B. T. Kelly and R. Taylor, Chemistry and Physics of Carbon, P. L. Walker Jr. and P. A. Thrower, eds., Mercel Dekker, Inc., New York, Vol. 8, (1973), p.31.

2. EXPERIMENTAL DETERMINATION OF COMPTON SCATTERING FROM PYROLYTIC GRAPHITE AND GLASSY CARBON†

Leo G. Henry and Robert H. Bragg

In the LBL report here abbreviated, a procedure for correcting wide range x-ray diffraction patterns of GC was presented. The procedure involved correcting the observed data for Compton scattering, for distortion caused by low specimen absorption and for SAXS prior to making the usual corrections for the angular variation of the atomic scattering factor and Lorentz polarization factors. In that report an indirect method for correcting for the

Compton intensity was employed. Here is reported a method for determining the Compton intensity directly. While repeating some experiments it was found that a considerable error is made in using the low angle data obtained in reflection measurements to estimate the power law to be used in correcting for the SAXS. The error was detected when it was seen that data taken in transmission had the expected h^{-3} asymptotic behavior ($h = 4\pi/\lambda \sin\theta$), whereas the data taken in reflection decreased more like h^{-2}.

A thorough analysis of the x-ray optics showed that for the length L of specimen employed, specimen to detector distance R, and for a fixed angular divergence of the x-ray beam 2α, the beam no longer fully irradiates the sample when 2α is given by $L \sin(\theta-\alpha) = 2R \sin \alpha$. At lower angles the observed data must be multiplied by a correction factor $2R\alpha/L \sin \theta$. This correction restores the expected h^{-3} asymptotic dependence except for HTT < 2000°C. The difficulty was finally resolved when it was realized that for HTT < 2000°C the scattering is expected to decrease as h^{-2} because of the diffuseness in the electron density in the "solid" phase in GC.[1]

For the direct measurements, the Compton fraction of the total intensity was determined using the balanced (Co-Ni) filter method described by Short[2] and applied to samples of carbon materials whose wide range patterns are shown in Fig. 6.

A strong (006) graphite reflection is evident in the PG pattern, whereas only a weak (11) hk band is evident for the GC samples. Pryolytic graphite has a strong basal texture so that in regions far from (00ℓ) reflections the observed intensity should be due entirely to Compton scattering. In Fig. 7 the total intensity and the Compton intensities measured at several points are shown. It can be seen that in PG the background intensity far from a Bragg reflection is essentially all Compton. Thus by appropriate scaling using direct measurements of linear absorption coefficients μ, thickness T, and densities ρ, measurements of background intensities can be made at appropriate angles, e.g., at $2\theta = 100°$, on PG and used to calculate the Compton contribution to the total intensity in GC. Table 1 compares direct determinations and data calculated from measurements on PG. The agreement is generally good. Table 1 also shows that the original proposal to use the background of the GC sample itself would be surprisingly accurate for $\sin\theta/\lambda \approx 0.61\ A^{-1}$.

* * *

†Brief version of LBL-10225.

1. S. Bose and R. H. Bragg, "Small Angle Scattering by Diffuse Interfaces," LBL-6656.
2. M. A. Short, Acta Cryst. 14, 486 (1961).

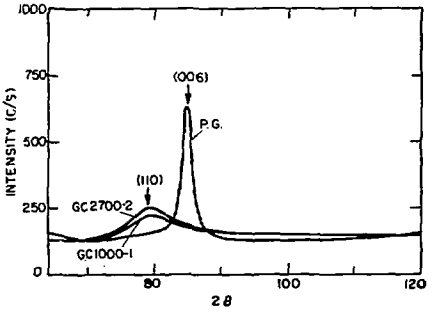

Fig. 6. X-ray line profiles of PG and GC (CuK_α radiation. (XBL 8012-13460)

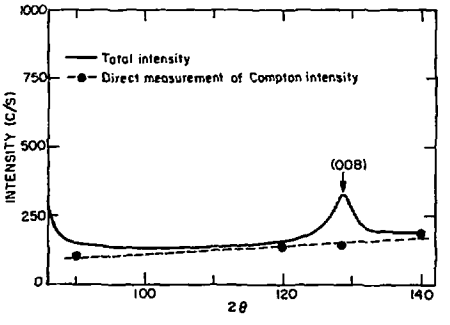

Fig. 7. X-ray line profile of PG near 008 reflection (CuK_α radiation). (XBL 8012-13461)

Table 1. Compton intensity determinations.

Material	2θ deg	$\frac{I_{inc}}{I_{TOT}}$	I_{TOT}	I_{inc}(meas.)	I_{inc}(calc'd)
Pyrolytic Graphite					
$\mu T = 1.16$	140	0.995	190	189	-
$\mu = 8.91\ cm^{-1}$	128.5	0.396	320	127	-
$T = 0.125\ cm$	120	0.857	160	137	-
$\rho = 2.11\ gm/cm^3$	90	0.748	140	105	-
$(\mu/\rho) = 4.22\ cm^2/gm$					
GC 1000 - 1					
$\mu T = 1.06$	140	0.945	180	170	188
$\mu = 6.43\ cm^{-1}$	128.5	0.829	160	123	125
$T = 0.165\ cm$	120	0.817	150	137	135
$\rho = 1.52\ gm/cm^3$	90	-	160	-	104
$(\mu/\rho) = 4.22\ cm^2/gm$					
GC 2700 - 2					
$\mu T = 1.00$	140	0.980	180	176.4	183.8
$\mu = 5.58\ cm^{-1}$	128.5	0.778	160	124.5	123.4
$T = 0.180$	120	0.569	150	85.4	133.8
$\rho = 1.32\ gm/cm^3$	90	-	160	-	103
$(\mu/\rho) = 4.22\ cm^2/gm$					

3. HALL COEFFICIENT, MAGNETORESISTANCE AND ELECTRICAL CONDUCTIVITY IN GLASSY CARBON

Dennis F. Baker and Robert H. Bragg

In the first known systematic investigation of the galvanomagnetic properties of GC, measurements were made on samples heated in the range 1000-2750°C.[1] However, the cryostat used then did not attain temperatures below 10 K and very few measurements of the Hall coefficient, R_H, were made on any samples.

With the rebuilt low-temperature apparatus, measurements have been made down to 2.8 K in magnetic fields H to 5.0 tesla. As found by previous workers, the magnetoresistance $\Delta\rho/\rho$ was found to be negative for HTT > 1000°C and is more negative the greater is HTT (Fig. 8). Despite

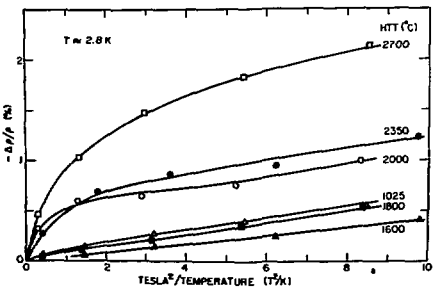

Fig. 8. Negative magnetoresistance in GC.
(XBL 8012-13459)

the fact that kT has been reduced by more than a factor of 3, the data do not show convincingly that $\Delta\rho/\rho$ saturates as H increases or T decreases.

Figure 9 shows that the $[A\ln T/T_0]$ term reported earlier does not appear to be required to describe the electrical conductivity σ. Instead it appears that the σ_0 term is also temperature dependent. This becomes evident at the lower T values obtained with the rebuilt cryostat insert. The Hall mobility μ_H shown in Fig. 10 was plotted vs. $T^{-1/2}$ to afford easy recognition of a $T^{-1/2}$ dependence of μ_H. It can be seen that μ_H is not a strong function of T, and if anything decreases as T decreases.

Measurements were made of the ac conductivity of GC up to 100 kHz and no ac component was found. Giuntini et al.[2] found no ac conductivity of anthracence chars heated to 1000°C. Since the properties of these chars are similar to those of GC it is now possible to draw the conclusion that the hopping distance for dc conduction in GC must be much shorter than for ac conduction.

The data in Fig. 10 do not lead strong support to the hypothesis[1] of a $T^{-1/2}$ dependence of μ_H upon T. It must be borne in mind that μ_H and μ, the drift mobility, may not be synonymous. Furthermore in the more recent experiments at lower T the data do not present a clear case for $|\Delta\rho/\rho|^{1/2}$ to be a single valued function of the $H/T^{1/2}$ variable. An alternative argument, based upon a spin-flip mechanism, predicts that $\Delta\rho/\rho$ is proportional to $-m^2$. That it is proportional accounts for the negative sign in a natural way and suggests a means of relating $\Delta\rho/\rho$ to magnetic susceptibility.

* * *

1. R. Saxena, "The Structure and Electrical Properties of Glassy Carbon," Ph.D. thesis, LBL-5129 (1975).
2. J. C. Giuntini et al., J. Non-Crystalline Solids 30, 87 (1978).

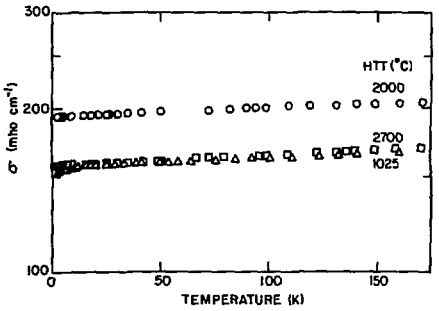

Fig. 9. Conductivity of GC vs T. (XBL 8012-13456)

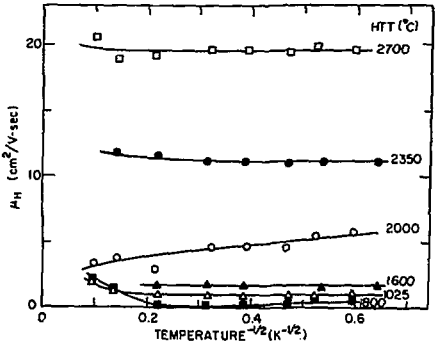

Fig. 10. Hall mobility of GC vs $T^{-1/2}$. (XBL 8012-13458)

RESEARCH PLANS FOR CALENDAR YEAR 1981

The rebuilt cryostat insert and 5.0 tesla superconducting magnet are working well, and apart from some difficulties with rapid burnout of graphite heating elements the general condition of our apparatus is good. It is intended to investigate the feasibility of a hookup of one or two of our XRD 5 diffractometers to a PDP 11 computer on the 3rd floor of Building 8 to eliminate time-consuming steps currently required in retrieval and subsequent use of x-ray data now being collected on a teletype. We plan to do the following in 1981:

Electrical Properties. It is necessary to obtain isochronal data for about five additional HTT, and kinetic runs will be made at a temperature above and below 2000°C to determine if the changes in σ, R_H or $\Delta\rho/$ are kinetic.

Graphitization. The activation energies for graphitization and S/V decrease will be redetermined. The analysis of the graphitization data should be complete by June 1981 but the identification of the mechanism of S/V decrease will require parallel data on PG, and hence an extensive set of heat treatments and SAXS measurements. Since the SAXS by GC is isotropic these data can be obtained at Berkeley. However, it will probably be necessary to go to ORNL to the National SAXS/SANS Facility for the data for Pyrolitic graphite (PG) because previous work has shown the the scattering is anisotropic. A target date for this work at ORNL is summer 1981.

Intercalation Compounds. An extensive series of heat treatments will be completed and graphite-$FeCl_3$-$AlCl_3$ compounds will be prepared and characterized. Initial efforts will involve producing improved, i.e., highly graphitized PG from ordinary PG by oxidation with Cl_2 or HNO_3-H_2SO_4 mixtures followed by heating at high temperatures. It is expected that intercalation experiments will begin in Summer 1981.

Amorphous Material Characterization. Radial distribution analyses will be determined for GC heated at 1000, 2000, and 3000°C. It should be possible to make far better analyses than were possible heretofore because of our advances in making quantitative corrections for SAXS and Compton scattering. The possibility of using NMR to determine the structural configuration of residual H_2 in GC will be investigated. Standard samples of coals of various ranks will be collected for analysis of coal structures before and after charring.

Annealing of Graphite. The annealing of carbons by laser radiation will be studied. The objective is to obtain highly oriented graphite for intercalation experiments by combining high pressure with laser heating of ordinary PG. The interpretation of R_g data will also be investigated. Our previous results suggest that R_g grows as $t^{1/3}$ and it may be possible to do kinetic analysis of the R_g data from SAXS on GC and other carbons. A third task is to make a careful assessment of requirements for setting up a magnetic susceptibility apparatus using a 1.0 tesla magnet.

1980 PUBLICATIONS AND REPORTS

Refereed Journals

1. R. H. Bragg, "Small Angle X-Ray Scattering: A Resurgence and an Opportunity," NTA Journal, April-June 1980.

2. D. F. Baker and R. H. Bragg, "The Thermal Expansion of Directionally Solidified Al-$CuAl_2$ Eutectic," Met. Trans. A (in press), LBL-10640.

LBL Reports

1. S. Bose and R. H. Bragg, "Kinetics of Pore Coarsening in Glassy Carbon," submitted to Carbon, LBL-7659.

2. S. Bose and R. H. Bragg, "Small Angle X-Ray Scattering by Diffuse Interfaces," submitted to J. Appl. Cryst., LBL-6656.

3. D. F. Baker, R. H. Bragg, and A. S. Rao, "Effect of Grinding on the Structure of Glassy Carbon," Submitted to J. Am. Ceram. Soc., LBL-10224.

Invited Talks

1. R. Gronsky and R. H. Bragg, "Lattice Images in Glassy Carbon," 33rd Pacific Coast Regional Meeting, American Ceramic Society, San Francisco, CA, October 1980.

2. D. F. Baker and R. H. Bragg, "Electrical Properties of Glassy Carbon," 33rd Pacific Coast Regional Meeting, American Ceramic Society, San Francisco, CA, October 1980.

3. L. G. Henry and R. H. Bragg, "Graphitization Kinetics in Glassy Carbon," 33rd Pacific Coast Regional Meeting, American Ceramic Society, San Francisco, CA, October 1980.

4. B. N. Mehrotra and R. H. Bragg, "Irreversible Thermal Expansion in Glassy Carbon," 33rd Pacific Coast Regional Meeting, American Ceramic Society, San Francisco, CA, October 1980.

5. R. H. Bragg, "Negative Magnetoresistance in Glassy Carbon," Annual Meeting, Society of Black Physicists, Stanford, CA, April 1980.

6. R. H. Bragg, "Electrical Properties of Glassy Carbon," Joint Seminar, Ceramics and Materials Science Departments, Rutgers University, New Brunswick, NJ, November 1980.

7. R. H. Bragg, "Kinetics of Void Growth in Glassy Carbon," Materials Research Department, Power Systems Division, United Technologies, East Hartford, CT, November 1980.

1. High-Temperature Oxidation and Corrosion of Materials*

David P. Whittle, Investigator

Introduction. This is a multi-faceted program which attempts to gain an understanding of the corrosion chemistry and materials behavior in high temperature environments. Of particular interest are the mechanisms of attack in environments containing more than one oxidant, such as sulfur and oxygen. Sulfur is a critical impurity in almost all energy sources. It can appear in a number of forms: in gaseous environments, it can appear as H_2S when the oxidizing potential of the atmosphere is low, such as in energy conversion systems, or as SO_2/SO_3 at higher oxygen potentials as in fuel combustion. It may also appear in deposits. Work during the past year has continued to investigate the various forms of sulfur-induced accelerated attack, and a number of common mechanisms have been identified. One of the methods of achieving adequate protection lies in forming and maintaining protective oxide scales, especially Al_2O_3. Continued study of the formation and adherence of Al_2O_3 on typical alloys and coatings has identified the potential importance of alloy or coating structure: this has important ramifications in the design of coatings. Finally, continued development of definitive quantitative models of alloy oxidation has involved a more detailed consideration of the defect chemistry of oxide solutions and the inter-relationships between transport and thermodynamic properties.

1. MECHANISM OF SULFUR-INDUCED ACCELERATED CORROSION AT LOW OXYGEN POTENTIALS†

Haroun Hindam and David P. Whittle

Cr_2O_3 is considered to be among the best protective barriers for oxidation resistance. It is thermodynamically very stable and grows slowly due to its low concentration of native defects. However, in environments where the oxidation potentials are relatively low, typically 10^{-20} - 10^{-14} atm, and in which sulfur is present, primarily as H_2S and at fugacities around 10^{-4} atm, the protective behavior of the Cr_2O_3 scale is apt to breakdown. This has been investigated by exposing Fe-, Ni and Co-Cr alloys, containing 25 wt% Cr which is sufficient to form and maintain a Cr_2O_3 scale, to H_2-H_2O-H_2S mixtures in which the P_{O_2} and P_{S_2} are controlled at the values indicated in Fig. 1. Figure 1 also shows that thermodynamic considerations indicate that the sulfides, not the oxides, of Fe, Ni or Co could be formed under these conditions.

At 1200 and 1300 K, the general pattern of behavior of Fe, Ni, and Co-Cr alloys was similar.

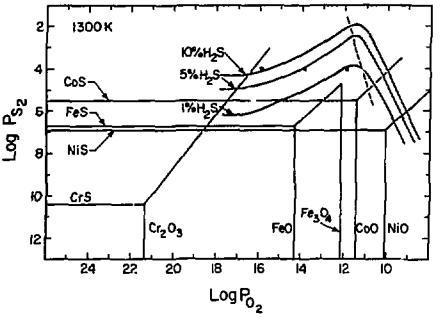

Fig. 1. M-O-S phase diagrams at 1200 and 1300 K. (XBL 8012-12919A)

Initially a continuous Cr_2O_3 scale was formed and remained intact for a period which depended slightly on P_{O_2}, varying typically from 1 hr to 10 hr for a $P_{O_2} = 10^{-16}$ and 10^{-12} atm, repectively, for Ni-25 Cr at 1300 K. Subsequently, a few sulfide agglomerates were formed, and the density of these nodules increased rapidly. This sequence is shown in Fig. 2. A more developed localized sulfide growth tended to initiate at sample corners, Fig. 2(d), but was not confined to these locations. Indeed, where the localized growth occurred near the specimen edges, different nodules showed different stages of development, as opposed to locations away from sample edges where the sizes of the nodular growths were all comparable, Fig. 2(c), suggesting that they all started to grow at about the same time. Cross sections through the regions of localized growth show that the sulfides formed outside the original Cr_2O_3 layer are primarily Ni-(~ Co-) rich sulfides, molten at the reaction temperature, while inside the sulfides are rich in Cr. The original Cr_2O_3 film still separates the two regions, and analysis indicates it contains almost undetectable amounts of sulfur or the base metal Ni, Co, or Fe. Cr_2O_3 is often precipitated out in the outer molten sulfide and sometimes is present as a faceted skin on the surface giving rise to the filament-like protrusions. Pre-oxidation of the alloys in a sulfur-free, H_2-H_2O environment prolonged the pre-breakaway stage, but not by much (Fig. 3).

Most of our observations point to sulfur transport through the oxide layer as the operative mechanism for accelerated corrosion. Solid state transport of sulfur through the oxide may be involved, but the evidence indicates that it is at least supplemented by molecular transport of the H_2S through pre-existing physical defects in the oxide. Similar mechanisms are invoked to explain the accelerated and breakaway type of corrosion

*This work was supported by the Director, Office of Energy Research, Office of Basic Energy Sciences, Materials Sciences Division of the U.S. Department of Energy under Contract No. W-7405-ENG-48.

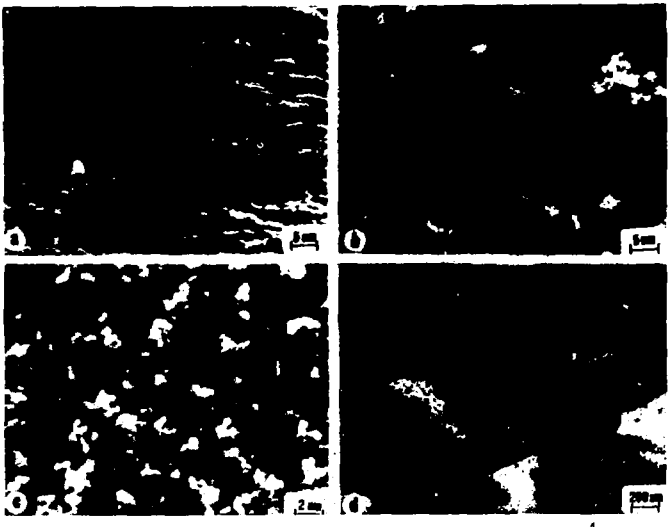

Fig. 2. Top views of Ni-25 wt% Cr oxidized at 1300 K and $p_{S_2} = 10^{-4}$ atm, $p_{O_2} = 10^{-16}$ atm, illustrating the development Ni-S protrusions through Cr_2O_3 film. (a) 1 hr, (b) 2 hr, (c) and (d) 3 hr. (XBB 800-14104)

Fig. 3. Top views of Ni-25 wt% Cr pre-oxidized at 1300 K in H_2/H_2O ($p_{O_2} = 10^{-14}$ atm) for 5 hr and subsequently exposed to $H_2/H_2O/H_2S$ ($p_{S_2} = 10^{-4}$ atm, $p_{O_2} = 10^{-14}$ atm) for 17 hr. (a) and (b) outward flow of liquid Ni-S through Cr_2O_3 film, (c) long filaments emanating from Ni-S nodules, (d) unattacked Cr_2O_3 film exhibiting whisker formation. (XBB 800-14106)

observed in combustion-type (SO_2-containing) environments and CO_2 atmospheres. For example, the sulfur potential in the bulk gas is too low to produce sulfides. If, however, SO_2 transport through physical defects in the oxide, the oxygen potential effectively decreases, causing a rise in the sulfur potential to an extent that sulfides can be formed. In the present system, a decrease in the oxygen potential, by removal of H_2O through reaction to form oxide, also causes the sulfur potential to decrease, but not sufficiently to render the sulfides unstable, as shown in Fig. 1. The growth of the sulfide from that point reflects the behavior of these alloys in oxygen-free environments.

In addition, gross cracking and mechanical loss of the protective oxide near specimen edges and corners can also occur. This phenomenon must, however, be related to a Cr-depletion produced at the alloy surface during the initial Cr_2O_3-formation, otherwise there is no reason to suppose that Cr_2O_3 could not reform, as it did on initial exposure. As a consequence, by raising the Cr content of the alloy to a high enough value, there would still be sufficient Cr to reform the oxide at the interface even if scale cracking occurred. However, this would not eliminate the problem of scale breakdown via gaseous sulfur transport through the minute physical defects in the Cr_2O_3 scale. To achieve this, there is a need to examine the factors that affect the "porosity" (or permeability) of the Cr_2O_3. It is interesting to speculate that, if the so called pores were wider or the path length of the gas through the oxide shorter (thinner oxide), there might be less oxygen removal on passing through the scale and hence less propensity to form sulfides at the alloy/scale interface.

* * *

†Brief version of LBL-12052, to be presented at N.A.C.E. Corrosion '81, Toronto, Canada.

2. SIMULTANEOUS INTERNAL OXIDATION AND SULFIDATION

Peter J. Risse and David P. Whittle

A significant feature of the corrosion of high temperature alloys is the formation of internal oxides and sulfides behind the surface scale. This can have two effects: (1) it can degrade the materials properties of the material to much greater extents than can be accounted for by superficial scale formation, and (2) it can tie up elements such as Cr or Al, preventing them from forming protective external scales. The internal oxidation or sulfidation occurs by partial dissociation of the surface scale at the scale/alloy interface, dissolution of the oxygen or sulfur in the alloy, and diffusion inwards where they react with the dissolved Cr or Al to form internal precipitates. The solubility and diffusivity of the oxidant in the base metal are the important parameters. One of the most appropriate methods of measuring the premeability (solubility × diffusivity product) is to measure the progress of internal sulfidation or oxidation under idealized conditions. Thus, iron-base alloys containing small concentrations of Al or Cr have been exposed to H_2/H_2S or H_2/H_2O atmospheres in which the P_{S_2} or P_{O_2} were such that the Fe would behave as a noble metal. Providing, $D_X N_X \gg D_B N_B^o$, where D_X and D_B are the diffusion coefficients of the oxidant and the alloying element in the alloy and N_X and N_B^o are the solubility of the oxidant at the surface and bulk atomic fraction of alloying element respectively, then

$$N_X D_X(\text{permeability}) = \frac{1}{2}\left[\frac{\xi^2}{t}\ N_B^o\right] ,$$

where ξ is the depth of internal precipitation at time t, and advance of the precipitation front has been assumed to be under exclusive diffusion control.

Figure 4 shows typical internal sulfide penetration as a function of $t^{1/2}$ for Fe-1 and 5 Cr and Fe-1Al alloys at 927°C at a $P_{S_2} = 10^{-8}$ atm. In all three cases, a parabolic rate law is followed. Unfortunately, there is little scope for varying the sulfur potential. At potentials of 10^{-11} atm., both the 1% Al and 5% Cr alloys are within the transition region for continuous scale formation. As a result the depth of internal precipitation tends to be irregular around the sample. Fe-1% Cr still sulfidizes internally. An alloy of Fe-5% Al formed a continuous sulfide layer even at the higher potential. The internal precipitates appear to show some tendency to be formed preferentially at grain boundaries. However, with experiments in which the alloy grain size varied, there were no detectable differences in the depths of internal sulfidation. Preferential sulfur diffusion along alloy grain boundaries does not seem to be involved. However, preferential precipitation in grain boundaries is prevalent, particularly at distances well away from the alloy surface. At these locations the degree of supersaturation is low and nucleation occurs heterogeneously on grain boundaries. Near

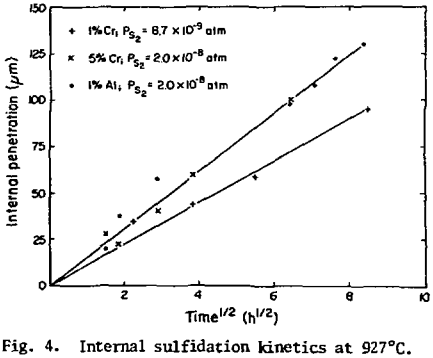

Fig. 4. Internal sulfidation kinetics at 927°C. (XBL 813-454)

the surface, the alloy before precipitation is highly supersaturated, and random homogeneous nucleation occurs. Nevertheless, the precipitate grows preferentially along the {100} faces of the fcc crystal. Coarsening of the precipitates appears to continue after precipitation. This is in part related to the relatively low stability of the sulfides, in comparison, for example, to corresponding oxides.

Now that baseline determinations of sulfur permeability have been established, simultaneous internal oxidation and sulfidation experiments will be continued, along with more detailed examination of the precipitate morphologies.

A regular solution model was used, when it became obvious that the calculated value of the interaction parameter W_L of the liquid solution was insensitive to the value W_S of the solid solution, which could be taken as zero, ideal solid solution behavior. Table 1 gives the calculated interaction parameters for the liquid solutions. Calculated data show satisfactory agreement with the limited solubility data available.[1] Figure 5 shows the minimum P_{SO_3} necessary for liquid formation in the CoO-Na_2SO_4 system. The P_{SO_3} level for liquid formation from a Na_2SO_4-NiO mixture is higher than in the Co-based systems, which is primarily responsible for the greater corrosion resistance of Ni-based alloys in this temperature

3. THERMODYNAMIC OF LOW TEMPERATURE (700-850°C) HOT CORROSION†

Ajaya Misra, David P. Whittle and Wayne L. Worrell†

Hot corrosion of first stage blades and guide vanes of gas turbines exposed to marine and industrial environments is due primarily to a deposit of Na_2SO_4 on the component surface. The sulfur comes from impurities in the fuel. At 900°C and above, where Na_2SO_4 is molten, the corrosion proceeds by interaction of metal oxides with the Na_2SO_4 melt. In contrast, the mechanism at 650-850°C, where Na_2SO_4 is solid, seems to involve the formation of mixed sulfates, Na_2SO_4-MSO_4 (M = Co or Ni) or Na_2SO_4-$M_2(SO_4)_3$ (M = Fe, Al or Cr), by the reaction of metal oxides with SO_2/SO_3 in the gas turbine atmosphere. The sulfur again comes from impurities in the fuel. The formation of a molten sulfate can be described by

$$MO + SO_3 = MSO_4 \text{ (dissolved in } Na_2SO_4\text{)},$$

$$K_1 = \frac{a_{MSO_4}\text{ (melt)}}{P_{SO_3}} . \qquad (1)$$

Thus the P_{SO_3} required for mixed sulfate formation will depend on the activity of the MSO_4 in the melt. Existing phase diagrams in the systems Na_2SO_4-MSO_4 (M = Ni, Co) and Na_2SO_4-$M_2(SO_4)_3$ (M = Al, Cr, Fe) have been used to calculate the thermodynamic properties.

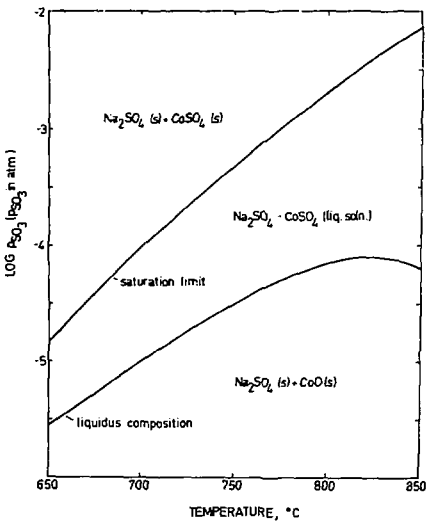

Fig. 5. Minimum p_{SO_3} required for liquid formation as a function of temperature in the Na_2SO_4 - CoO - SO_3 system. (XBL 809-11572)

Table 1. Interaction parameters, W_L, for regular solution models of molten Na_2SO_4 - MSO_4 or $M_2(SO_4)_3$ systems.

	$NiSO_4$	$CoSO_4$	$Fe_2(SO_4)_3$	$Al_2(SO_4)_3$	$Cr_2(SO_4)_3$
W_L (kcal/mole)	-65±1	-7±1	-35.4	-55.2	-14.3
Temp. Range(°C)	700-800	600-850	650-800	700-800	700-800

range. The activity of $Al_2(SO_4)_3$, $Cr_2(SO_4)_3$, and $Fe_2(SO)_4)_3$ in sulfate melts can be lowered to such an extent that liquid sulfate solutions can be formed at p_{SO_3} levels that are prevalent in marine gas turbine operations; this can be explained on the basis of complex formation in the melt.

In this lower temperature range of 650-800°C, the oxidation behavior of resistant alloys, which at high temperatures normally rely for their protection on the formation of a continuous layer of Al_2O_3 or Cr_2O_3, has not been well-characterized. However, it is anticipated that formation of a continuous layer of the protective oxide will be difficult at least in the early stages of oxidation. Thus formation of the base metal oxides NiO or CoO will continue for some appreciable time. As a consequence, the early stages of the low-temperature hot-corrosion process is considered to be the formation of Na_2SO_4 - MSO_4(M = Co, Ni) melts, while the subsequent propagation process depends on the interaction of this melt with the protective oxides Al_2O_3 and Cr_2O_3 themselves. The possible reactions between the mixed sulfate melt and Cr_2O_3 or Al_2O_3 can be expressed as

$$NiSO_4 + M_2O_3 = NiM_2O_4 + SO_3 \qquad (M = Cr \text{ or } Al) \quad (2)$$

$$3MSO_4 + 4M_2O_3 = M_2(SO_4)_3 + 3NiM_2O_4 \qquad (M = Cr \text{ or } Al) \quad (3)$$

$$Na_2SO_4 + M_2O_3 = 2NaMO_2 + SO_3 \qquad (M = Cr \text{ or } Al) \quad (4)$$

or similar reactions with Co replacing Ni. Reaction (4) is not expected at the SO_3 levels prevalent in gas turbine operation, and is not considered further. For reaction (2), upon fixing the p_{SO_3}, the a_{NiSO_4} (or a_{CoSO_4}) in the melt saturated with the spinels is automatically fixed. If instead of a spinel, the Al_2O_3 and Cr_2O_3 from their respective sulfates in the melt by reaction (3), the activity of MSO_4 in the melt will depend upon the activity of $Al_2(SO_4)_3$ or $Cr_2(SO_4)_3$ in the melt. At a given p_{SO_3}, the activity of $Al_2(SO_4)_3$ or $Cr_2(SO_4)_3$ in the melt will be governed respectively by the following equilibrium:

$$M_2O_3 + 3SO_3 = M_2(SO_4)_3 \ . \qquad (7)$$

Thus, the a_{NiSO_4} (or a_{CoSO_4}) in the melt can be predicted for different p_{SO_3} levels at each temperature. Figure 6 shows the equilibrium relationships in the Na_2SO_4 - $CoSO_4$ - Al_2O_3 - SO_3 system; corresponding equilibria in the Na_2SO_4 - $CoSO_4$ - Cr_2O_3 - SO_3, Na_2SO_4 - $NiSO_4$ - Al_2O_3 - SO_3 and Na_2SO_4 - $NiSO_4$ - Cr_2O_3 - SO_3 systems have also been calculated.

The thermodynamic calculations have shown that the activity of $Al_2(SO_4)_3$ and $Fe_2(SO_4)_3$ in the molten sulfates can be lowered to such an extent that Na_2SO_4 - $Al_2(SO_4)_3$ and Na_2SO_4 - $Fe_2(SO_4)_3$ liquids can be formed at p_{SO_3} levels that can be attained in the marine gas turbine operations. This has been explained on the basis of complex formation in the melt. Thermodynamic analysis of the interaction of the Na_2SO_4 - MSO_4 (M = Co or Ni) melt with protective oxides Al_2O_3 and Cr_2O_3

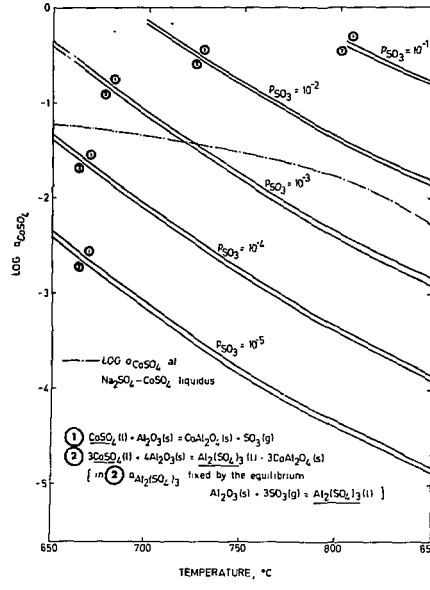

Fig. 6. Equilibrium relationships in the Na_2SO_4 - $CoSO_4$ - Al_2O_3 - SO_3 systems. (XBL 809-11580)

has demonstrated the vulnerability of aluminum-containing alloys to hot-corrosion attack. It appears that the development of a continuous layer of Cr_2O_3 or a $NiCr_2O_4$ spinel layer from the onset of oxidation would improve the hot-corrosion resistance considerably.

Although thermodynamic analysis has shown that Na_2SO_4 - $Al_2(SO_4)_3$ and Na_2SO_4 - $Fe_2(SO_4)_3$ melts can be formed at p_{SO_3} level and at temperatures of concern to low-temperature hot-corrosion process, the kinetics of both the formation of mixed sulfates and the reaction of mixed sulfates with the oxides of the alloying elements will eventually be the determining factor in developing alloys for improved hot-corrosion resistance. Unfortunately, practically no information currently exists on the kinetics of these important reactions in the hot-corrosion process, and this is an area where further work is required.

* * *

†Brief version of LBL-11495, submitted to J. Electrochem. Soc.

‡Department of Metallurgy, University of Pennsylvania, Philadelphia, PA.

4. ALUMINUM DIFFUSION DURING THE ALUMINIZING OF IRON

Hilary C. Akeuzue and David P. Whittle

Aluminizing of Fe-based alloys recently has received revived impetus as a means to improve the high temperature corrosion resistance of materials likely to be considered in many energy related applications. A pack cementation process is widely used. A mixture of either pure Al or an Fe-Al alloy powder, Al_2O_3 used as an anti-sintering agent, and a halide salt, is used to provide a vapor phase around the component to be coated. The vapor phase is an Al halide gas, whose type and activity depend on the activity of Al, the halide salt, and the temperature of operation. During the process, the effective concentration of Al at the surface remains essentially independent of time. Thus, solid state diffusion is the rate-controlling step both during the coating process and during subsequent degradation of the coating during service by continued interdiffusion with the substrate or to the surface to form the protective Al_2O_3 scale. For adequate prediction and control of the aluminizing process and coating behavior, the diffusion coefficient matrix in the relevant systems is an absolute prerequisite.

To this end, pure iron samples ground to 600 grit finished were aluminized at temperatures in the range 850-1050°C, using a pack consisting of Fe-50 at.% Al powder (300 mesh), NH_4Cl and Al_2O_3 (300 mesh) in the ratio 49:49:2. A covered cylindrical, recrystallized Al_2O_3 crucible was used as the pack container. Prior to aluminizing, the blended pack was pre-heated to 850°C for 25 hours. Temperatures were controlled to within ± 0.2°C and samples were aluminized for different periods of time. Weight changes followed a parabolic rate law with time, as might be expected: the rate constants were 3.11×10^{-10}, 2.02×10^{-9}, and $1.3 \times 10^{-8} g^2\ cm^{-4} s^{-1}$ at 850, 950 and 1050°C, respectively. Layer thickness measurements were also made after etching the samples. Layer thickness is somewhat of a misnomer. According to the Fe-Al phase diagram, at the diffusion (aluminizing) temperature, only the α solid solution phase is stable in the composition range up to about 50 at.% Al, except for a very small region of γ-solid solution at less than about 1 at.% Al above 900°C. The observed ordered phases β_1 (Fe_3Al) and β_2 (FeAl) are probably formed on cooling. The outer β_2 layer consists of relatively large columnar grains, whole the inner β_1 and α layer is equiaxed. In part, this is related to the growth direction of the layers. Analogous to the Ni-Al system, the ratio of intrinsic diffusivities D_{Ni}/D_{Al} is expected to be a strong function of composition.

The growth rates of the layers show the expected parabolic behavior: apparent rate constants are 61.3 (β_2), 192 (α), 540 (β_2) and 1473 (α) μm^2/hr at 840 and 950°C, respectively. These layer growth rates are, of course, related to the diffusivities; however, the relationship is complex since the diffusivity is a strong function of composition, as shown below. Once this dependence has been established, layer growth rates can be calculated under other experimental conditions.

Samples aluminized at 850°C were analyzed by EPMA and from the resulting Al concentration profiles. Values of the Fe-Al interdiffusion coefficients, as a function of composition, were obtained using the Boltzmann-Matano equation for $\tilde{D}$. Figure 7 shows the variation of $\tilde{D}$ with Al content. The values compare well with available literature data. $\tilde{D}$ rises with Al content, reaching a maximum at about 34 at.% Al, which corresponds with the appearance of the ordered FeAl phase.

Because of the very strong dependence of $\tilde{D}$ on composition, it is not possible to use a simple error function solution of the diffusion equation. Instead, an iterative solution procedure of a transformed equation is used. This technique has proved satisfactory in reproducing experimentally measured Al concentration profiles, and therefore can be used to predict the progress of the aluminizing process under a variety of conditions.

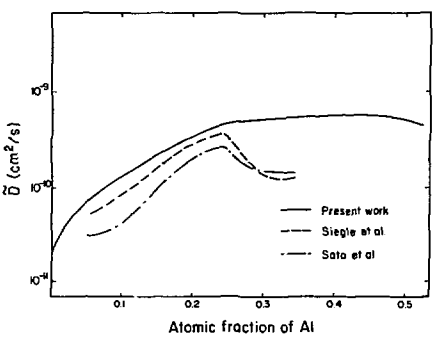

Fig. 7. Interdiffusion coefficients in Fe-Al alloys at 850°C as a function of composition.
(XBL 813-456)

5. DIFFUSION AND MULTIPHASE SYSTEMS†

Glyn W. Roper‡ and David P. Whittle

Because many of the practical situations where diffusion is important involve systems of more than one phase, an understanding of the diffusion path (defined as the locus of compositions across the diffusion zone) in such systems is important. Phase boundaries move as the diffusion process takes place, and this compounds the difficulties of modeling such a system. It is possible to cope with phase boundary movements in a binary system because the Phase Rule prohibits the development of composition gradients parallel to the reaction front through two phase regions. This causes the phase boundaries to remain stable and planar. Since

phase boundary movements are diffusion controlled, changes of position of a planar boundary are confined to the dimension of diffusion and to a parabolic rate that can be simply defined.

In ternary systems, on the other hand, the additional component gives an additional degree of freedom. This means that α and β phases, for example, can co-exist at equilibrium over a range of compositions, even when pressure and temperature are fixed; and non-planar interfaces and/or internal precipitates can arise. Thus, concentration gradients in the vicinity of the interface are no longer necessarily restricted to the single dimension of the macrogradient of composition, which destroys the conditions for parabolic behavior of the phase interface. An approximate approach to the problem in ternary diffusion couples between two different single phases is to treat the system as a pseudo-binary by assuming that interphase boundaries remain planar. It is then possible to match solutions to the diffusion equation on either side of the phase boundary by means of flux continuity relations. By plotting this diffusion path on the appropriate isotherm of the ternary phase diagram, it is possible determine if the path runs through any two phase regions. If the only incursion to a two-phase region is straight across a tie-line, as for example at the assumed planar junction between α and β phases, the calculated diffusion path is a stable solution, i.e., the assumption of planar interfaces is valid. If, however, the calculated diffusion path loops into two-phase regions, cutting across tie-lines to create a finite region of supersaturation, the solution is unstable because supersaturation is not usually tolerated in a real system. The diffusion path is then a virtual path, although in many instances it is broadly similar to the composite path which would describe the real behavior. It has been shown that where a portion of a (composite) diffusion path passes into a two-phase region from a single phase region at an angle to the tie-lines, the morphology of the resulting two-phase zone is dependent on the way in which that path exits from the two-phase region of the phase diagram. Exit to the same single-phase region describes a zone of isolated precipitation in the diffusion couple, while exit into another phase represents a non-planar interface (possibly with associated isolated precipitation). Composite diffusion paths have been derived from first principles for two diffusion couples in which the pseudo-binary approach is inadequate: each comprises a single phase (α) alloy annealed in contact with a two-phase (α + β) alloy. This model system approximates the behavior in the Co-Cr-Al ternary system.[1]

The reason for interest in diffusion couples, whose two terminal alloys lie in the same single phase field but whose diffusion path loops into adjacent two-phase and even single-phase regions, lies in a problem that besets coating development for high temperature superalloys: coating deterioration in service as a result of (among other things) interdiffusion with the substrate. Up to the present, attempts to suppress this deterioration by interposition of a physical diffusion barrier between the coating and the alloy substrate have proven largely unsuccessful.

A possible answer considered was manipulation of the metal chemistry of the superalloy surface to maintain a protective aluminide by the mechanism described above, i.e., growing a region of protective β phase by harnessing diffusional interaction in an otherwise single phase α system. However, it soon became apparent that, in the case of the Co-Cr-Al system, at least, this would not be feasible because of the low value of the cross diffusion coefficient D^{Co}_{AlCr} coupled with the fact that the α phase boundary is almost parallel to the chromium axis. These two features are probable manifestations of a single characteristic of the system.

The reason why diffusion path looping out of the single phase α region is not possible is that the Co-Cr-Al system closely approximates to the model system ABC in Fig. 8, where D^{A}_{CB} is zero and the α phase boundary is parallel to the B axis. For any β phase to be formed in a couple between W and X, the diffusion path must loop into a region of higher C concentration than that of alloy W. However, this is impossible if D_{CB} is zero because, under these circumstances, the B concentration gradient has no influence on the diffusion of C; and C is bound to diffuse down its own concentration gradient. This argument applies even in the case of a diffusion couple between alloy compositions W and Y, whose diffusion path is simply a vertical line between the two terminal compositions. Attempts to find other systems which might be able to utilize this phenomenon are continuing.

* * *

[+]Brief version of LBL-11689, submitted to Metal Science Journal.

[‡]Shell Research Center, Thornton, Nr. Chester, England.

1. G. W. Roper and D. P. Whittle, Metal Sci. J. 14 (Jan. 1980).

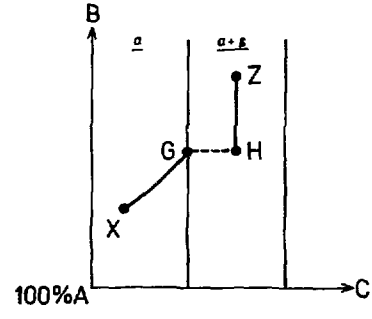

Fig. 8. Schematic isothermal section of ABC phase diagram with composite diffusion path of diffusion couple XZ superimposed. (XBL 809-11791)

6. Al_2O_3 ADHERENCE ON CoCrAl ALLOYS

Lori M. Kingley and David P. Whittle

Although additions of active elements, such as Y, Hf, etc., or of dispersed oxide phases are known, and used to improve the adhesion of Al_2O_3 protective scales on MCrAl (M = Ni or Co) type coatings, the mechanism of improved adhesion is still unclear. Although it must be realized that the mechanisms proposed are not mutually exclusive, the most important are:

(a) enhanced scale plasticity, either by a chemical change of the defect concentration or (more likely) by included particles of oxide acting as dislocation sources in the scale;

(b) formation of compound oxide between metal and scale which has a coefficient of thermal expansion intermediate between that of metal and scale and thus acts in the same way as a "graded seal" in the joining of glass;

(c) modification to the growth process, thereby reducing the growth stresses;

(d) improved chemical bounding across the interface due to the presence of highly oxygen-affine elements in the alloy;

(e) the reactive metal atoms or (more probably) the particles of the stable oxide acting as sites for the condensation of vacancies injected by the oxidation process, preventing their condensation at the scale-metal interface as voids;

(f) mechanical keying ("pegging") of the scale to the alloy by inward growth of Al_2O_3 around the dispersed oxide particles.

Although our earlier results have always favored the last three models, it has not been possible to differentiate between the chemical bonding and mechanical bonding models. Our earlier work also showed that greater improvements were achieved in scale/metal adhesion if the metallic Hf addition were converted into an oxide dispersion by pre-internal oxidation treatment. The procedure used for the latter was virtually identical to that used during aluminizing, and the two processes could perhaps be combined. Thus, the major objectives were: (a) to determine whether a fine dispersion of Al_2O_3 particles in a CoCrAl type alloy would be as efficient in improving the adhesion of the Al_2O_3 scale, which forms on subsequent high temperature exposure as an active element (Y, Hf, etc.) or active element oxide dispersion (HfO_2, ThO_2, etc.), thereby eliminating the "chemical" effect from the proposed mechanisms; and (b) to determine whether CoCrAl alloys containing metallic Hf additions could be converted to HfO_2-dispersion containing materials during an aluminizing pre-treatment.

To achieve the first objective an internal oxidation step, separate from the aluminizing treatment was required. Therefore, a Co-10Cr-1Al alloy was internally oxidized in a "Rhines pack." Co-10Cr, used as a base, was the level of Cr used in our previous studies. After the internal oxidation pretreatment, it was necessary to aluminize the Co-10Cr-1Al alloy, or it would not form an Al_2O_3 scale on subsequent exposure. Figure 9 shows weight change/time curves during 20-hour cycles at 1200°C. The aluminized Co-10Cr-1Al alloy, with no internal oxidation pre-treatment, completely deteriorated in the first cycle. Aluminized alloys with originally 5% Al also oxidized rapidly after the first few cycles when the supply of Al to replenish spalled Al_2O_3 ran out. The time at which this occurs depends on the duration of the aluminizing treatment. The Co-10Cr-1Al alloy, internally oxidized and aluminized, showed minimal spallation of the protective Al_2O_3. Its oxidation resistance is not as good as those containing Hf (see below), but compares very well with that of similar alloys containing other additions studied earlier. The presence of the internal oxide dispersion increased the rate of aluminizing of the alloy: depths were about 100 μm in comparison to 60 μm in the same alloy without an internal oxidation treatment. The internal Al_2O_3 particles were present throughout the CoAl layer which forms on the surface, indicating an inward growth of the aluminide layer. The underside of the Al_2O_3 layer formed in the internally oxidized and aluminized Co-10Cr-1Al alloy, revealed after dissolving away the substrate, showed extensive peg development, characteristic of the improved adhesion as shown in our earlier work. Thus, inward growth of the Al_2O_3 surface scale along the incoherent interface between the dispersed oxide particles and the matrix again appears responsible; the chemical nature of the dispersed phase is not critical.

In relation to the second objective, a CoCrAl alloy, again containing 10% Cr but now with 11% Al, and various levels of Hf was used. This also permitted comparison with previous work. Normally, it would not be necessary to aluminize this alloy to ensure formation of an Al_2O_3 scale; however,

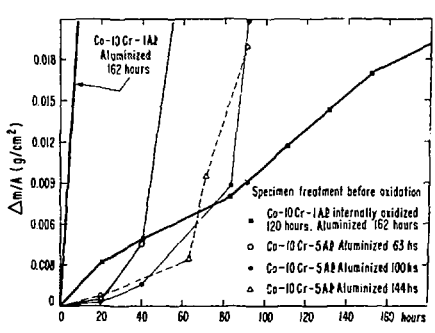

Fig. 9. Cyclic oxidation kinetics at 1200°C and 20-hour cycles of Co-10Cr-1Al and 5Al after various pre-treatments. (XBL 805-1087)

simultaneous enrichment of the surface layers of the alloy with Al during internal oxidation was not anticipated to have a detrimental effect unless the surface became too brittle. To partially counteract this, Co-10Cr-5Al-Hf alloys were also subjected to similar treatments. Figure 10 shows the results of cyclic oxidation experiments, again at 1200°C. The aluminizing, and hence internal oxidation, treatment produces significant increases in oxidation resistance, the improvements being similar to a solely internal oxidation pre-treatment of this alloy in earlier work. Again, internal oxide particles, in this instance of HfO_2, are formed within alloy and aluminide layer during aluminizing, and these give rise to peg formation beneath the surface scale during subsequent exposure. The distribution of the internal oxide particles depends on the internal oxidation (or aluminizing) pre-treatment and the Hf content of the alloy, and this determines the ultimate peg distribution and hence the improvement in adhesion. An additional feature was also noted which relates to the observations reported in the following article. The enrichment of Al in the surface layers during aluminizing also increases the β-CoAl content at the surface. Pegs never develop in the β-phase and thus too high a surface Al content is actually detrimental to the oxidation resistance.

* * *

†Brief version of LBL-10952.

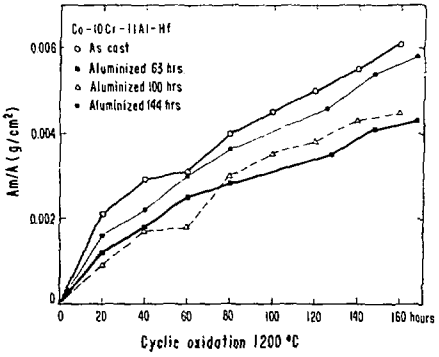

Fig. 10. Cyclic oxidation kinetics at 1200°C and 20-hour cycles of Co-10Cr-11Al-Hf alloys after various pre-treatments. (XBL 805-1090)

7. OXIDATION BEHAVIOR OF OVERLAY COATINGS†

Steve Shaffer and David P. Whittle

The most important group of alloys, other than the conventional heater alloys, to which active elements are added is the MCrAlY group of overlay cladding alloys where M is Fe, Ni, or Co. These alloys are widely used to protect gas turbine blades exposed to severe environments. When exposed to high temperature oxidizing environments, the coating develops an Al_2O_3 surface oxide which grows isothermally at a slow rate. The coating is eventually degraded, principally by the progressive loss of oxide as a result of thermal cycling; the principal role of yttrium is therefore to improve the adhesion. However, Y may not be the optimum active element for improving the overall oxidation resistance. Our earlier work[1] indicated that Hf was a much more efficient active element addition than Y, in cast CoCrAl alloys, and this difference was related to the distribution of Hf and Y in the alloys. Hf was in complete solution; as a result, internal oxidation of the Hf produced a fine, random distribution of HfO_2 particles in the alloy. The Y on the other hand, tended to segregate to alloy grain boundaries as an intermetallic yttride. Thus, the Y-rich internal oxide produced on exposure were rather coarsely distributed throughout the alloy. Distribution of the internal oxides is important because the inwardly growing "pegs" of Al_2O_3 grow along the incoherent interface between alloy matrix and internal oxide particles. These pegs, keying the surface scale to the alloy, are the main, although not necessarily the only, factor promoting the improved scale adhesion.[2]

In considering actual coatings, particularly those produced by electron beam physical vapor deposition, differences between various additions were anticipated to be less marked, because segregation of either Hf or Y within the coating would not be expected. A number of Co-20Cr-10Al (a composition similar to the earlier cast alloys) coatings containing different active elements were prepared by Airco Temescal under DOE contract No. ET-78-C-03-2156. These were oxidized at 1000°C for various times and the coating/surface scale interface examined in detail. Initially, a stripping technique was used as in earlier work, where all the underlying metal was dissolved away using a Br-MeOh solution. This permitted the underside of the oxide to be examined in the SEM. Subsequently, a much improved technique was adopted, involving deep etching of the metallographically prepared samples in the same Br-MeOH solution, but only removing sufficient metal to enable the underside of the oxide to be examined. This technique has considerable advantage over the complete stripping of the oxide, because the detailed oxide morphology can be related to the coating (or alloy) microstructure.

Figure 11(A) shows a typical metallographic section through the coating after the 240 hour

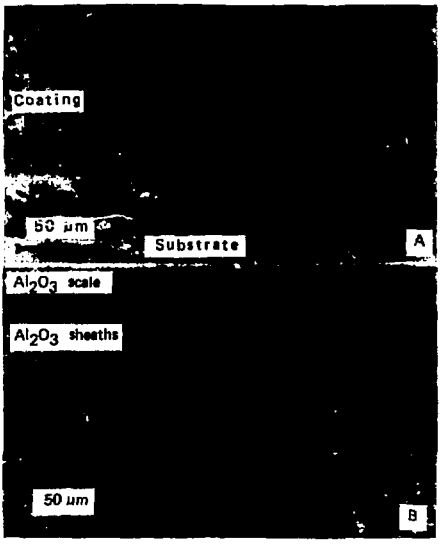

Fig. 11. Al_2O_3 peg formation - The "key" to scale adherence. (XBB 814-3089)

exposure at 1000°C. This particular micrograph shows CoCrAl coating containing no addition elements. The coating consists of a dark, dendritic β-CoAl phase in a lighter α-Co-rich matrix. The β-phase is orientated normal to the growth direction of the coating. In addition, there is also a band at the surface of the coating, which is devoid of the β-phase. This is formed as a result of the loss of Al from the surface to form the Al_2O_3 scale during oxidation. The Al_2O_3 scale is not visible in the optical micrograph, because of its poor contrast with the other phases. It can, however, be revealed by adjusting the lighting conditions.

An additional feature of the coating is that the β-phase in the outer half of the coating is a slightly darker color than that in the inner half of the coating. The reason for this only became apparent when the sample was deep etched, as shown in Fig. 11(B). The β-phase in the outer half of the coating is sheathed with Al_2O_3. Presumably this sheath is very thin, because there is no indication of its presence in the optical micrograph. The surface Al_2O_3 scale is also visible, and it is clear that this is not attached to the Al_2O_3 sheaths or the pegs penetrating into the alloy. The Al_2O_3 pegs do not cross the β-depleted zone. These observations throw quite a different light on the mechanism of peg formation. It appears to be related to preferential diffusion of oxygen inwards along the α/β phase boundaries, although there is an important difference between this and the CoCrAl coating because the pegs or Al_2O_3 sheaths are now attached to the surface scale. With the Hf-containing coating, a profuse distribution of pegs is attached to the surface scale; and these do not seem to penetrate down the α/β boundaries of the coating. Indeed, there is a β-free region immediately below the pegged scale. These inwardly growing pegs presumably grew around internal oxide particles of HfO_2, as observed with the as-cast alloys.

It appears, therefore, that the oxide pegs form by preferential oxygen diffusion into the alloy or coating along incoherent interfaces. These interfaces may be either between the α and β phases in the metallic structure or between an oxide dispersion and the matrix, the oxide dispersion being added intentionally during the processing or as a result of internal oxidation of an active element addition during high temperature exposure. This means that the coating or alloy structure plays a more important role than previously suspected. Some of the critical diferences between different methods of applying coatings -- such as by pack cementation, plasma spraying, or sputtering -- may be associated with the structure. This and other factors are currently being examined.

* * *

†Brief version of LBL-10607 to appear in Thin Solid Films, and a paper to appear in Proc. Int. Conf. on Surfaces and Interfaces in Ceramics and Ceramic-Metal Systems.

1. I. M. Allam, D. P. Whittle and J. Stringer, Oxid. of Metals 13, 381 (1978).
2. D. P. Whittle and J. Stringer, Phil. Trans. Roy. Soc. (London) A295, 309 (1980).

8. MOTION OF DEFECTS DURING GROWTH OF SOLID SOLUTION OXIDES†

David P. Whittle, Francesco Gesmundo‡ and Fulvio Viani‡

Real advance in understanding alloy oxidation can be achieved only if the interrelationship between transport and thermodynamic properties are developed quantitatively. Recently,[1] the growth of solid solution scales containing ions of the same valence on binary monophase alloys has been examined. The equations developed describe the simultaneous transport of two cations through a growing surface scale; and, although these equations are quite general, their application to a particular system requires a knowledge of the dependence of the self-diffusion coefficients of the two cations on both oxygen activity and oxide composition. Thus, a detailed knowledge, or model, of the defect structure of the oxide solution is required. The model used in our earlier analysis,[1] and by others, was formulated on the basis of a simple approximation that only a single type of cation vacancy prevailed. However, it is becoming increasingly evident that this simple model is no longer adequate, and a more complete model for the defect structure of the oxide solution is

necessary. Indeed, the growth of the solid solution oxide via the transport of the defect species, rather than the diffusion of ions, may be considered as an alternative approach.

In the ideal oxide solid solution formed from isotypic oxides AO and BO of known defect structures, assuming that electron transport is much more rapid than ionic transport (semiconducting oxides), that the presence of defects in the oxygen sublattice and interstitial cations can be neglected, and that interactions between the different types of defects can be ignored, the quasi-chemical equations for the formation of cation vacancies may be written in the general form

$$\frac{1}{2} O_2 = O^x + V^x;\ V^x = V' + h^{\cdot};\ V' = V'' + h^{\cdot}\ . \quad (1)$$

These equations give rise to corresponding equilibrium constants which are related to the standard free energies of formation of the various defects, $(\Delta G^\circ)_i$, $(i = V^x, V', V'')$, which are functions of the composition in the oxide solution. For ideal solution behavior, it is appropriate to approximate these free energies of defect formation to a composition weighted average. Thus, the concentrations of the various defects vary exponentially with oxide composition; and, using the local neutrality condition, they can be calculated, providing that the free energies of defect formation in the two pure oxides and their intrinsic ionization constants are known.

The flux of defects through the oxide solution can be related to the parabolic rate constant, eventually leading to the expression

$$\frac{1}{2} K_x y = \int_{a_o'}^{a_o''} D_V \left([V^x] + [V'] + [V'']\right) d\ln a_0, \quad (2)$$

where y is the fractional distance through the scale; K_x is the parabolic rate constant in terms of scale thickness; a_o' and a_o'' are the oxygen activities at alloy/scale and scale/gas interfaces, respectively; and D_V is the diffusion coefficient of the defects assumed to be independent of their effective charge. To evaluate the integral in Eq. (2) and hence calculate the oxygen activity profile through the scale and the parabolic rate constant K_x, the function $\Sigma[v]$ must be known. In the present case where the oxide contains two types of cation, this function depends on both a_o and ξ, the oxide composition. As a consequence, the dependence of ξ on the local position in the scale (or on a_o, although ξ is not a single-valued function of a_o) is also required. The present approach has used experimentally determined[2] cation concentration profiles, i.e., $\xi = F(y)$, as input data, so that the calculations can be completed. However, the analysis is being continued to include considerations of the differences in the rates of exchange of the different cations with neighboring defects (jump frequencies) and correlation effects which allow calculation of the cation concentration profiles from the defect transport equations.

Figure 12 shows the defect concentration profiles through the (NiCo)O scale growing on a Ni-10% Co oxidized at 1000°C. These have been calculated using Eq. (2), experimentally determined Co concentration profiles, and free energies of defect formation in pure NiO and CoO. There is good agreement between calculated and measured scale growth constants. Similar calculations have been made for other alloys for which experimental data are available. It is clear that:

(a) Singly charged vacancies, V', predominate, especially at higher oxygen potentials for all the alloys,

(b) As the cobalt content of the alloy and hence the Co concentration in the oxide increases, the concentrations of V^x and V'' become increasingly significant,

(c) As the cobalt content of the oxide increases, the total concentration of all types of defect increases.

Previous analysis of the growth of solid solution scales assumed an oxide defect model in which only one kind of vacancy predominates. Although this is certainly an oversimplification, it is interesting to make a comparison of the two approaches to the problem: Using these defect transport equations and ionic transport equations

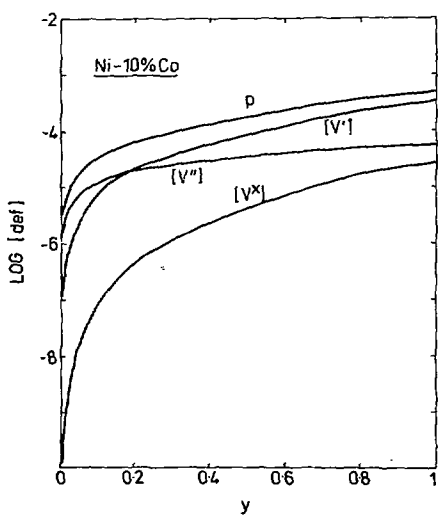

Fig. 12. Calculated concentrations of defects across the NiO scale formed on Ni 10.9% Co at 1000°C. (XBL 809-11699)

as in earlier work. Under the assumption of a single type of vacancy, the pseudo-chemical equation for formation of a vacancy of effective charge z is:

$$\frac{1}{2} O_2 = O^x + V^{z'} + zh^{\cdot}; \quad [V^{z'}] = K^{AO}_{V^{z'}} (k^{BO}_{V^{z'}} / K^{AO}_{V^{z'}})^{\xi} O_o / p^z, \tag{6}$$

where $K^{AO}_{V^{z'}}$ and $K^{BO}_{V^{z'}}$ are the equilibrium constants relating to the formation of a defect of effective charge z', relative to the perfect lattice, for pure oxides AO and BO, respectively.

This expression is consistent with that used to express ionic diffusivities in the scale as functions of composition and oxygen potential. Using appropriate data from the literature, both ionic and defect transport equations were solved, under the assumption of a single type of vacancy. Figure 13 compares the variation of [V''] and [V'] through the scale calculated according to the two approaches. Agreement between the two approaches is excellent; and agreement with available experimental data, for example the growth of the scale, is also good. However, the intention of this analysis was not to obtain better agreement with already acceptable experimental data for the Ni-Co system, derived using the ionic transport equations, but to more fully describe the true defect properties of the oxide solid solution, in particular the dependence on composition and oxygen activity because further analyses should use a combination of the two approaches.

* * *

†Brief version of LBL-11735, accepted by Oxidation of Metals.

‡Centro Studi di Chimica Fisica Applicata alle Caratteristiche d'Impiego del Materiali del C.N.R., Genova, Italy.

1. B. D. Bastow, D. P. Whittle and G. C. Wood, Proc. Roy. Soc., London A356, 177 (1977).
2. B. D. Bastow, D. P. Whittle and G. C. Wood, Corros. Sci. 16, 57 (1976).

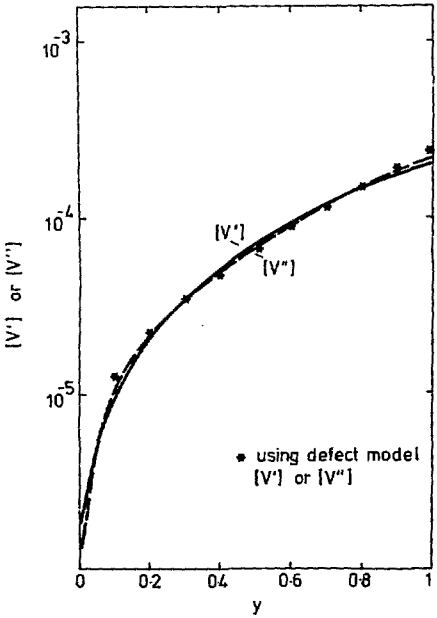

Fig. 13. A comparison of the calculated variation of defect concentrations across the scale formed on Ni 10.9% Co oxidized at 1000°C using defect diffusion and ionic diffusion equations.
(XBL 809-11693)

RESEARCH PLANS FOR CALENDAR YEAR 1981

Studies of high temperature corrosion by gaseous environments containing both sulfur and oxygen will continue. Cr_2O_3 appears to have limited capabilities as a protective oxide when sulfur is present in the atmosphere and breaks down either mechanically, by transport of sulfur through the oxides via a lattice transport mechanism, or through physical defects. Attempts to distinguish between these two mechanisms will be intensified. Thermogravimetric measurements of the influence of sulfur on the defect properties of Cr_2O_3 have been initiated and will continue. Transport via physical defects has proved difficult to identify; oxide grain boundaries may be important, and more detailed examinations of the oxide grain size and means of modifying it will be pursued. An adequate safety system enabling the use of CO-rich mixtures has now been installed. This will permit evaluation of the importance of the rate of change of sulfur potential with removal of oxygen as the gas mixture permeates the oxide. Work currently in progress on sulfide growth indicates a dependence on the overall composition, and not on the sulfur potential alone.

The thermodynamic calculations have shown that only very low SO_3 contents in the gas are necessary for stabilization of mixed liquid sulfate melt in the presence of Na_2SO_4 and that these mixed sulfates are potentially capable of reacting with protective oxides Al_2O_3 and, to a lesser extent, Cr_2O_3. This project is now concentrating on the kinetics of formation of the liquid sulfates. The extent of NiO formation in the early stages of oxidation of Ni-Cr alloys in the 650-800°C temperature regime is also being investigated.

The work on Al_2O_3-forming alloys and coatings and, in particular, scale adherence, has taken

on a new emphasis with the indication that the α/β phase boundaries are as important as the presence of active elements. A more detailed examination of the diffusion along these interfaces and of the partition of the active elements between the two phases is planned. Possible use of in-situ oxidation in the SEM to follow the early stages of growth is being considered.

Measurements of interdiffusion coefficients in Al-containing systems will be extended to ternary alloys with continued exploration of ways of manipulating the alloy chemistry to minimize coating degradation by harnessing the diffusional interactions. Theoretical studies will concentrate on the defect chemistry and transport in oxides containing more than one cation. A collabration with Dr. Gesmundo in Italy is extending the analysis developed earlier to include oxide solutions in which the cations have different valencies. In addition, defect clustering models are being examined in order to rationalize variations in ratio of cation jump frequencies with composition.

1980 PUBLICATIONS AND REPORTS

Refereed Journals

1. D. P. Whittle and J. Stringer, "Improvements in Properties: Additives in Oxidation Resistance," Phil. Trans. Roy. Soc., London A295, 309 (1980).

2. T. Hodgekeiss, G. C. Wood, D. P. Whittle, and B. D. Bastow, "Oxidation of Ni-70% Cr in Oxygen at 1073-1473 K," Oxid. of Metals 14, 263 (1980).

3. G. W. Roper and D. P. Whittle, "Interdiffusion in Ternary Co-Cr-Al Alloys," Met. Sci. J. 21-28 (Jan. 1980).

4. D. N. H. Trafford and D. P. Whittle, "Salt-Induced Corrosion of Fe-Cr Alloys. I: Dilute Alloys," Corrn. Sci. 20, 497 (1980).

5. D. N. H. Trafford and D. P. Whittle, "Salt-Induced Corrosion of Fe-Cr Alloys. II: Alloys Rich in Chromium," Corrn. Sci. 20, 509 (1980).

6. F. Gesmundo, P. Nanni, and D. P. Whittle, "Oxidation Behavior of a Two Phase Fe-Cu Alloy," J. Electrochem. Soc. 127, 1773 (1980).

7. G. W. Roper and D. P. Whittle, "Theoretical Diffusion Profiles in Single Phase Ternary Systems," Met. Sci. J. 541 (Nov. 1980). LBL-10469.

8. D. P. Whittle, D. H. Boone, and I. M. Allam, "Morphology of Al_2O_3 Scales on Doped CoCrAl Coatings," Thin Solid Films 73, 359 (1980).

9. I. M. Allam, H. C. Akuezue, and D. P. Whittle, "Influence of Small Pt Additions on Al_2O_3 Scale Adherence," Oxid. of Metals 14, 517 (1980).

10. H. Hindam and W. W. Smeltzer, "Growth and Microstructure of α-Al_2O_3 on Ni-Al Alloys: Internal Precipitation and Transition to External Scale," J. Electrochem. Soc. 127, 1622 (1980).

11. H. Hindam and W. W. Smeltzer, "Growth and Microstructure of α-Al_2O_3 on β-NiAl," J. Electrochem. Soc. 127, 1630 (1980).

12. H. Hindam and W. W. Smeltzer, "Application of Auger Electron Spectroscopy and Inert Metal Marker Techniques to Determine Metal and Oxygen Transport in Oxide Films on Metals," Oxid. of Metals 14, 337 (1980).

Other Publications

1. D. P. Whittle, "Kinetic and Morphological Relationships in High Temperature Corrosion," in Environmental Degradation of High Temperature Materials," Series 3, No. 13 vol. 1, (March 1980).

2. K. N. Strafford, D. P. Whittle, P. J. Hunt, and A. K. Misra, "The Corrosion of MCrAlY-type Alloys: Evaluation Studies," Proc. of 4th Conference on Gas Turbine Materials in a Marine Environment, U.S. Naval Sea Systems Command, 221 (1980).

3. I. M. Allam, D. P. Whittle, and J. Stringer, "The Role of Active Elements and Oxide Dispersions in The Development of Oxidation-Resistant Alloys and Coatings," in Corrosion and Erosion Behavior of Materials, edited by K. Natesan, Met. Soc., AIME, p. 103 (1980).

LBL Reports

1. D. P. Whittle, F. Gesmundo, B. D. Bastow, and G. C. Wood, "Formation of Subscales of Varying Composition," LBL-10067.

2. H. C. Akuezue, "Calcium Sulfate Induced Accelerated Corrosion" (M.S. thesis), LBL-10286.

3. L. M. Kingley, "Morphology of Al_2O_3 Scales on Doped CoCrAl," (M.S. thesis) LBL-10952.

4. A. K. Misra, D. P. Whittle, and W. Worrell, "Thermodynamics of Low Temperature (700-850°C) Hot Corrosion," LBL-11495.

5. D. P. Whittle, F. Gesmundo, B. D. Bastow, and G. C. Wood, "Formation of Solid Solution Oxides During Internal Oxidation," LBL-11496.

6. G. W. Roper and D. P. Whittle, "Interdiffusion in Two Phase Ternary Systems," LBL-11689.

7. D. P. Whittle, F. Gesmundo, and F. Viani, "Parabolic Growth of Oxide Solid Solutions on Binary Alloys," LBL-11735.

Invited Talks

1. D. P. Whittle, "Kinetic and Morphological Relationships in High Temperature Corrosion," Int. Meeting on Environmental Degradation of High Temperature Materials, Isle of Man, March 1980.

2. D. P. Whittle, D. H. Boone, and I. M. Allam, "Morphology of Al_2O_3 Scales on Doped CoCrAl Coatings," Int. Conf. on Metallic Coatings, San Diego, April 1980.

3. D. P. Whittle and D. H. Boone, "Al_2O_3 Scale Adherence to CoCrAl Alloys and Coatings," Int. Conf. on Surfaces and Interfaces in Ceramic and Ceramic Metal Systems, Berkeley, CA., July 1980.

4. B. D. Bastow, D. P. Whittle, and G. C. Wood, "The Diffusion-Controlled Growth of Solid Solution Scales on Binary Alloys," 9th Int. Symp. on the Reactivity of Solids, Cracow, Poland, Sept. 1980.

5. M. Landkof, A. V. Levy, D. H. Boone, and D. P. Whittle, "Modification of Protective Oxide Scales in Stainless Steel," TMS-AIME Fall Meeting, Pittsburgh, PA., Oct. 1980.

4. Engineering Materials

a. Erosion-Corrosion Wear Program*

Alan V. Levy, Investigator

Introduction. Continuing studies of erosion and corrosion behavior of ductile metals and brittle ceramics have broadened the base for gaining a detailed understanding of the behavior of structural materials that will be utilized in synthetic fuels production processes. The improvement in corrosion resistance of chromia barrier scale forming alloys by internal alloying with small amounts of active element (Y, La, Hf, Ce) was extended to surface alloying by the application and reaction of active element nitrate salts to alloy surfaces. Marked improvement in scale adhesion in cyclic oxidation tests was observed. Periodic reapplication of the salts further extended cyclic oxidation life. It was determined that the erosion behavior of thin scales on both chromia and alumina former alloys was caused by a cracking and chipping mechanism. The stronger the scale-metal interface, the more the scale resisted erosion.

The platelet mechanism of erosion of ductile metals defined in the past year was used to develop an analytical model for erosion by spherical particles at a 90° impingement angle. Further numerical analysis of two phase flow resulted in the definition of the rebound behavior of particles. This behavior causes many of particles to re-enter the gas-particle flow after an initial rebound and re-strike the target surface, often several times, in the same manner that a stone restrikes a water surface while skipping along it. Further fluid mechanics studies of surface gas composition control by steam injection into a boundary layer region have indicated that such a method of overcoming sulfide corrosion attack in coal gasifier piping components, such as heat exchangers, may be possible.

The laser doppler velocimeter (LDV) instrumented two phase flow system, both liquid and gas, has been completed and checked out. It is now generating flow system data that will be used to determine the validity of analytical models of two phase flow developed in this program in past years. It is capable of gathering and analyzing 400 readings per sec and represents one of the few state-of-the-art systems available in the country to study low speed, two phase flow.

The projects that have been carried out in 1980 are summarized below in the order: corrosion, erosion, two phase gas flow, and two phase liquid flow studies.

*This work was supported by the Director, Office of Energy Research, Office of Basic Energy Sciences, Materials Sciences Division of the U.S. Department of Energy under Contract No. W-7405-ENG-48.

1. THE EFFECT OF SURFACE DOPING ON THE OXIDATION OF CHROMIA FORMER ALLOYS†

Maria Landkoff

The influence of the surface application of active elements (doping) on the composition, morphology, adherence, and the growth rate of the oxide scales formed on chromia former alloys during high temperature oxidation has been investigated. The active elements were applied as an aqueous solution of the nitrate salts, which were subsequently thermally decomposed to oxide. Y, Ce, La, Hf, Ca and Zr were used as the active elements on 304 and 310 stainless steels and a nickel base superalloy, Inconel 738.

The doping procedure employed consisted of heating the sample at 500°C in air for five minutes and then hot dipping it into a 10% aqueous nitrate solution of the active elements. After drying, the sample was heated for an additional 30 minutes at 500°C to decompose the nitrate. The specimens were oxidized in air, either isothermally at 1000°C for 50 hr or by thermally cycling them for 20 hr cycles at 1000°C, cooling the specimens to room temperature between each cycle.

The samples after isothermal oxidation are shown in Fig. 1. Y, Ce, and La doping prevented spalling of the oxide scale. The oxides on the Zr, Hf, and Ca doped samples spalled off to about the same degree as oxide on the undoped 304SS sample.

The undoped scale on 304SS, in an area where it remained adherent, measured 25 μm thick and was primarily iron oxide with some spinel, $FeCr_2O_4$. The Y doped scale on 304SS was about one fifth the thickness of the scale on the undoped specimen and consisted primarily of Cr_2O_3 with a small amount of manganese; no iron could be detected using EDAX.

On the under surface of the Y doped scale (Fig. 2), SiO_2 webs can be seen in areas conforming to the underlying alloy grain boundaries. No indication of oxide pegs were found in the doped scale to account for the increased scale adherence, as occurs in some alloys with internally- rather than surface-added active elements.

The most pronounced effect of surface active element doping with yttrium was observed on 304SS alloy. The doping affected the adherence, thickness, composition and morphology of the oxide scale formed. The doped scale did not undergo any spallation after eight cycles (20 hr at 1000°C for each cycle), while the scale on the undoped specimen spalled on the first cycle. Although the enhanced protection from a single application of an active element salt occurred for only eight thermal cycles

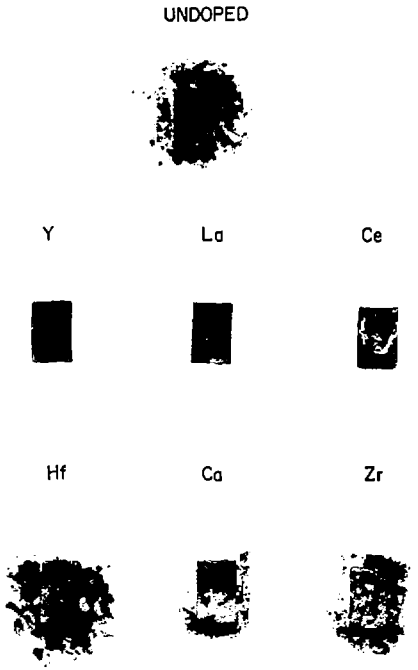

Fig. 1. Test alloys after one thermal cycle. (XBC 803-3113)

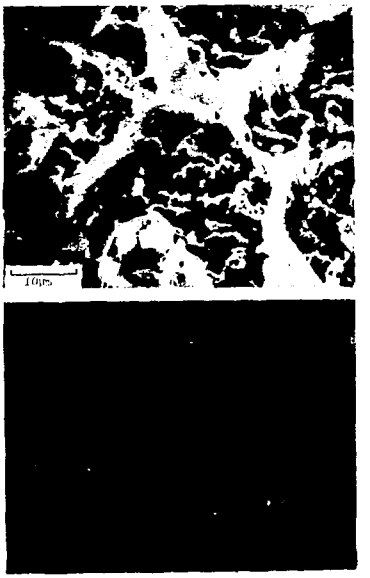

Fig. 2. Undersurface of oxide scale formed on yttrium doped 304SS. (XBB 805-6205A)

maximum, it appears that the effect may be prolonged by additional applications of the doping element. It was found that, by reapplying the yttrium nitrate after the third thermal cycle, only very slight spallation appeared after 13 thermal cycles.

The scanning Auger microscope (SAM) was used to determine the location of the dopant yttrium during the various stages of nitrate decomposition and oxidation of 304SS. After the decomposition stage (30 minutes at 500°C), yttrium could be readily detected in the surface film. The thin film (800 Å) was mostly Y_2O_3 with some chromium and iron oxide formed near the scale-metal interface. After a short oxidation period at high temperature (15 min at 1000°C), the yttrium could barely be detected in the Cr_2O_3 scale which formed.

The probable explanation for the beneficial effect of yttrium, cerium, and lanthanum on the performance of the oxide barrier scales is that they act as nucleation sites which decrease the distance between the more stable chromia forming nuclei during the early stages of oxidation and, thereby, the oxide grain size. The surface was completely covered by the protective chromia layer at an earlier time. The smaller grain size may also improve the adherence of the scale, making the scale more deformable during the growing reaction and during thermal cycling (easier deformation by sliding along grain boundaries).

The poor behavior of hafnium and zirconium externally doped scales was quite surprising. The absence of an active element effect may be explained by anisotropy of the oxides, which can be more important for external than for internal doping, expecially for the initial stages of oxidation. The thermal expansion along one of their crystallographic axes is extremely low. Also, the total polycrystalline thermal expansion of ZrO_2 and HfO_2 in the monoclinic form is somewhat lower than that of the Y, Ce, and La oxides, making them more incompatible with the higher thermal expansion base metals.

The enhancement of the behavior of chromia protective barrier scales on stainless steels by external doping with active element aqueous salts holds considerable promise to economically extend the life of components in coal conversion systems.

* * *

†Brief version of LBL-11127.

2. METAL EROSION BY SPHERICAL PARTICLES AT NORMAL INCIDENCE†

Ian Hutchings

A theoretical analysis was developed for the erosion of metals by spheres at normal incidence. The model employs a criterion of critical plastic strain to determine when material will be removed and predicts velocity exponents of 3 for erosion. The mechanical properties of the metal are described by two quantities: its dynamic hardness and its ductility under erosion conditions.

The model developed was based upon the platelet formation mechanism of erosive wear wherein repeated impacts of the surface of a ductile metal result in the extrusion of highly distressed, thin platelets of metal that are knocked off the surface by subsequent particles. Since the erosion process involves an accumulation of plastic deformation in the surface layers of the target, a critical strain, ε_c, was selected as a suitable criterion for the amount of plastic strain that a particle must achieve before it could be removed. The critical strain is a property of the metal that is a measure of its ductility under erosion conditions.

From the criterion of critical strain, a value for the mean number of plastic strain cycles needed to remove a wear fragment can be deduced. Consider the target to be struck by a large number of spherical projectiles distributed at random over the surface, each traveling at the same velocity and, therefore, causing the same pattern of plastic deformation in the target on impact. As will be shown below, an average strain $\Delta\varepsilon_p$ can be associated with each impact. For simplicity, we assume that the whole volume plastically deformed by each impacting sphere is subjected to a plastic strain increment of the same magnitude, $\Delta\varepsilon_p$, and that the strains are directed with circular symmetry about the line of impact of the sphere. Material at any point on the surface will, therefore, be subjected to successive increments of strain of magnitude, $\Delta\varepsilon_p$, randomly oriented in the plane of the surface. After N impacts the expectation value of the resultant strain at the point may be shown from random walk theory to be $\Delta\varepsilon_p N^{1/2}$. If N_f is the mean number of impacts (i.e., strain increments) needed to cause detachment of material, then application of the failure criterion gives

$$\Delta\varepsilon_p N_f^{1/2} = \varepsilon_c \ . \qquad (1)$$

The volume of material, which is plastically strained by each impact, is $\alpha mv^2/2P$ where α is volume of indentation, m is mass of eroding sphere, v is impact velocity and P is dynamic hardness; this volume will be called the "elementary volume." Under steady state erosion conditions, one elementary volume will be removed after N_f impacts, according to the failure criterion defined above. The volume loss per impact is therefore $\alpha mv^2/2PN_f$. If the target material has density ρ, the erosion E defined as the mass loss from the target per unit mass of impinging particles is given by:

$$E = \alpha\rho V^2/2PN_f \ . \qquad (2)$$

Tabor has shown empirically that, for quasi-static indentation by a rigid sphere of radius r, the average strain introduced into a metal is given by

$$\varepsilon \approx 0.2\ a/r \ , \qquad (3)$$

where a is the final chordal radius of the indentation and ε is the strain in an equivalent uniaxial compression test.

By equating the initial kinetic energy of the impinging sphere with the work done in forming the indentation, it may be shown that

$$a = 2^{1/2}\ r\ v^{1/2}\ (2\rho/3P)^{1/4} \qquad (4)$$

and combining Eqs. (1), (2), (3), and (4), the erosion is given by

$$E = 0.033\ \frac{\alpha\rho\sigma^{1/2}v^3}{\varepsilon_c^2 P^{3/2}} \ . \qquad (5)$$

In this equation, the properties of the target material are described by three quantities: density, dynamic hardness, and ε_c, which may be called "erosion ductility".

Erosion rates for 6061-T6 aluminum alloy were calculated from Eq. (5) for steel shot (density 7.85 mg^{-3}) and glass beads (density 2.48 mg^{-3}). The dynamic hardness, P, was taken as 1.15 GPA, as measured in the single impact experiments. The straight lines of slope 3.0 plotted in Fig. 3 represent the theoretical prediction for α/ε_c^2 = 0.7, a value chosen to give the best fit to the data. Agreement between theory and experiment is fair, although it is evident that the dependence of erosion on spherical particle density is stronger than that predicted by the theory and that particle size also influences erosion rate. Possible explanations for these discrepancies lie with strain-rate effects and work-hardening.

* * *

†Brief version of LBL-12014.

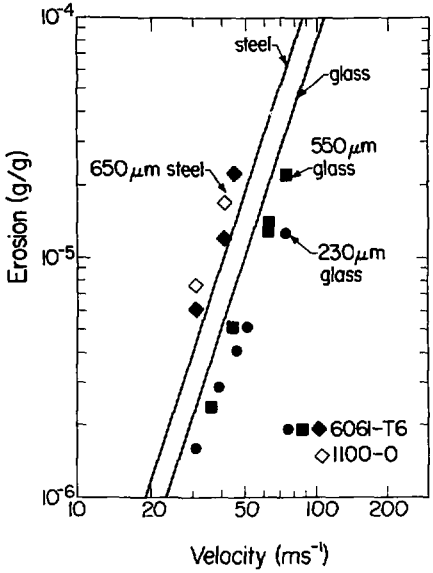

Fig. 3. Erosion rate vs velocity for 6061-T6 Al eroded by glass beads and steel shot. (XBL 811-126)

3. EROSION OF THIN CORROSION SCALES[+]

J. Maasberg

The erosion behavior of thin corrosion scales formed on metals at high temperatures is important in designing metallic components for use in energy conversion systems. The susceptibility of various corrosion scales to erosion was studied on two alloys: an alumina forming Fe-18Cr-5Al-1Hf, and a chromia forming 310 stainless steel. Both as-received and burnished surfaces on the specimens were present prior to their corrosive exposure to 900° and 1000°C for 100 hours. Air, low P_{O_2}, and combined low P_{O_2} and P_{S_2} gas mixtures were used in the corrosive exposure. The corrosion product scales were subsequently eroded using an air-particle stream containing 50 μm SiC traveling at 200 fps. Erosion rates of the scales were compared to determine the effect of the various corrosion parameters on the susceptibility to erosion.

Specimens exposed to air at 1,000°C formed thicker, friable oxide layers that were much more susceptible to erosion than scales formed at low P_{O_2}. There was no difference in the amount of erosion between 900° and 1000°C for the low P_{O_2} specimens, see (Table 1). The scale was about 4 μm thick and appeared continuous. The thickness of the oxidized, sulfidized scale was the same as that of the low P_{O_2} oxidized scale. Only two of the specimens exposed to combined low P_{O_2} and P_{S_2} appeared to form sulfides which exhibited high erosion rates. Among other specimens, it appeared that the presence of sulfur degraded the scale,

Table 1. Low P_{O_2} oxidation of 310SS.

	°C	Log P_{O_2}	Log P_{S_2}	Scale thickness (μm)	90° weight loss (mg) after 0.3g SiC	90° weight loss (mg) after 1.2g SiC	30° weight loss (mg) after 0.3g SiC	30° weight loss (mg) after 1.2g SiC
Surface:								
	900	-15	---		0.4	0.7		
As-received	900	-15	---	4	0.3	0.6	0.1	0.3
	900	-16.5	---		0.4	0.7		
	1000	-16.5	---		0.4	0.7		
Simultaneous Sulfidation-Oxidation of 310SS:								
	1000	-15	-6	5	0.8	1.3	0.8	1.2
As-received	1000	-15.2	-8.5		0.7	1.35		
	1000	-16.9	-6		1.1	1.8		
	1000	-17.4	-7	2.5	1.0	1.6	0.7	1.2
	1000	-15	-6		0.9	1.7		
Burnished	1000	-15.2	-8.5		0.7	1.2		
	1000	-16.9	-6		0.9	1.6		
	1000	-17.4	-7		0.9	1.6		

even though no sulfur could be detected in the scale. These non-sulfur containing oxidized-sulfidized scales had a higher erosion rate than those exposed to oxygen only, (Table 1). The surface condition prior to corrosion, as-received or burnished, had little effect on the susceptibility to erosion.

Figure 4 shows a typical chromia scale after being impacted with a few particles of SiC. The small crystallites are undisturbed oxide scale surface. There are a few areas where erosion of the scale is beginning. The scale appears to have been removed by a chipping mechanism; particles of SiC hit the surface and fracture the brittle scale. From sequential erosion tests in which the erosion process was interrupted every few particles and the surface studied under a scanning electron microscope, it appeared that the scale was fractured by the initial impacting particles and that subsequent particles removed small chips of scale. This loss mechanism is typical for brittle materials.

The greater erosion at 90° compared to that at 30° also indicates that the thin oxide layers on a metal substrate have erosion behavior similar to that of brittle ceramic materials. No weight loss was found when the erosion conditions used in this test were applied against an unoxidized ductile metal substrate; thus the erosion loss recorded was that of the scale, not the substrate.

Fig. 4. Scale on 310SS at early stage of erosion. (XBB 808-10079)

* * *

†Brief version of LBL-12015.

4. EROSION OF OXIDE SCALES ON CoCrAl COATINGS†

J. Maasberg

Erosion of barrier oxide scales formed on CoCrAl high temperature corrosion protection coatings was investigated. The effect of active element additions to the CoCrAl coatings on erosion behavior was determined. Their effects on enhancing corrosion protection is well known. The purpose of the active element additions is to modify the alumina scale which forms on the oxidized CoCrAl coating to make the oxide more adherent.

Coatings of CoCrAl containing small amounts of either Hf, Ti, Si, Y, or Zr were vapor deposited (ebpvd) on Inco 738 substrates and oxidized in air at 1000°C for 100 hr. The coatings were then eroded in a gas-particle stream of 50 μm SiC in air moving at 200 fps at room temperature. Erosion was measured as the weight loss of scale by a 3.0 g weight of SiC impacting particles.

The erosion behavior of the scales on the various coatings is shown in Fig. 5. The impingement angle dependence of the erosion was similar to that of brittle materials; the highest erosion rate occurred at a 90° angle. The scale was observed to be removed by a chipping action. Erosion tests on an unoxidized CoCrAl coating showed that the measured weight loss was due to scale erosion and not unreacted coating erosion.

Microstructural examinations showed that the active element additions had a profound effect on the nature of the oxide scale-coating interface (Fig. 5). The Y- and Hf-containing specimens formed fingers of scale which deeply penetrated into the unreacted coating, pinning the scale to the metal and enhancing erosion resistance. The Zr-containing specimen also formed deep fingers but the oxide was quite porous and friable, thus accounting for its very low erosion resistance. Specimens containing Ti and Si formed thin oxides similar to the Hf and Y specimens but without the pinning fingers. Their increase in erosion susceptibility is due to the absence of pins.

Control of scale morphologies through the use of active element additions shows promise in the development of erosion-corrosion resistant materials.

* * *

†Brief version of LBL-12016.

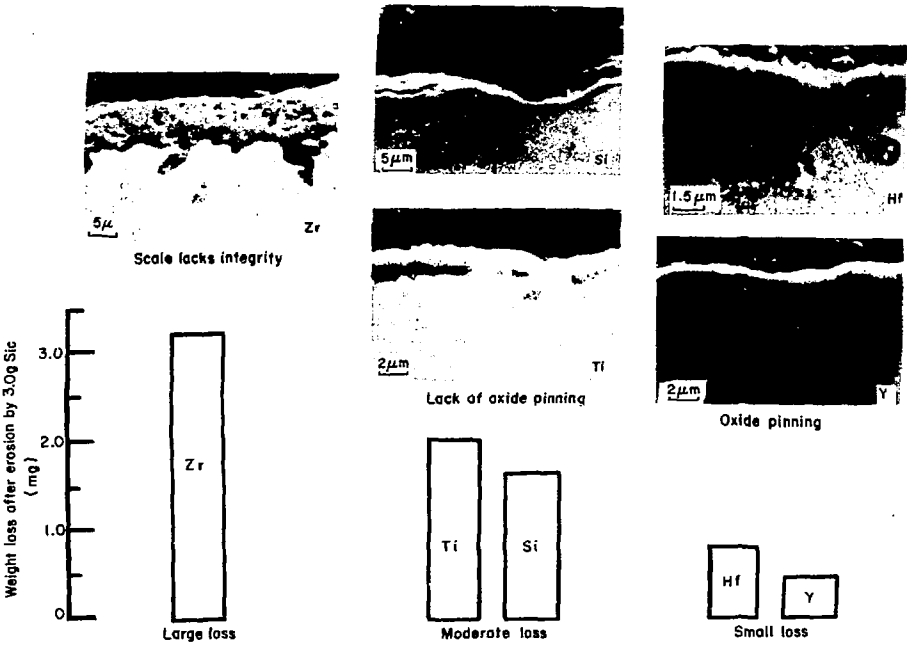

Fig. 5. Oxide microstructures and weight loss measurements of Zr, Si and Y doped *CoCrAl coatings*. (XBB 809-10348)

5. MODELING THE EROSION OF BRITTLE MATERIALS†

Mohsen Khatibloo

The factors involved in the indentation and erosion of brittle materials by solid particles have been analyzed. It was found that brittleness is only a state rather than a property. Brittle behavior in a ceramic material is observed when a surface is impacted with large blunt particles, while ductile behavior is observed when very small or much sharper particles are used. For spherical particles the critical radius, Rc, at which this transition occurs is given by the following equation:

$$Rc = \frac{4100\ K_{Ic}}{\lambda \pi^3 H^3} \qquad (1)$$

$$\lambda = \frac{3}{4}\left[\frac{1-\nu_p^2}{E_p} + \frac{1-\nu_s^2}{E_s}\right],$$

where K_{Ic} is surface fracture toughness, H is surface hardness, and ν and E are Poisson's ratio and elastic modulus, respectively. P and S subscripts refer to particle and surface, respectively. The combined effect of surface hardness and particle size on transition from brittle to ductile behavior is shown in Fig. 6. Figure 6(A) presents experimental data for two particle sizes and a number of different target materials. Figure 6(B) shows a family of calculated curves showing the trend for changing particle radius, R.

The Hertz solution has been used for the analysis of erosion when blunt particles are used. However, it has been consistently found that the application of the Hertz theory to the elastic contact problem, which occurs where the particle and brittle surface contact, leads to an incorrect prediction of the fracture load and its location. In this study, a new method was developed to analyze the Hertzian contact stress problem, and the validity of the procedures used was proven by the agreement between the calculated and experiment results as shown in

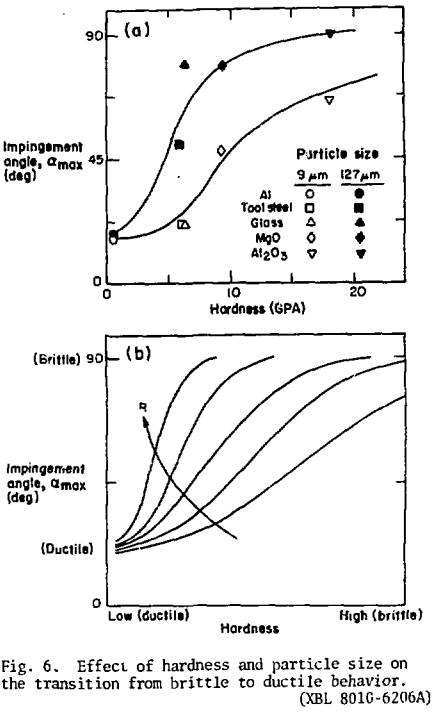

Fig. 6. Effect of hardness and particle size on the transition from brittle to ductile behavior. (XBL 8010-6206A)

Fig. 6. This new method resolves the problems that previously existed in this type of stress analysis and also enables one to determine many important surface properties that can be used as a basis for predicting the resistance of brittle materials to damage by particle impact. In environments where the erosive particles can be controlled by keeping the particle velocity below Vc, given by the following equation, erosion can probably be prevented at 90° impact.

$$Vc \approx 450 \left(\frac{\lambda}{\rho}\right)^{1/2} \left(\frac{K_{Ic}}{R}\right)^{5/6} , \qquad (2)$$

where ρ is the particle density.

The general conclusion to be drawn from this study on the effect of material properties on erosion resistance of brittle materials is that the fracture toughness plays the most important role. Hardness has a lesser effect on erosion, primarily when the surface plastically deforms prior to fracture. The elastic properties of the surface material have only a second order effect on erosion behavior.

* * *

†Brief version of LBL-11883.

6. A NUMERICAL SOLUTION TO DILUTE GAS PARTICLE FLOWS AT HIGH VELOCITY†

Jonathan A. Laitone

Prediction of the fluid mechanical characteristics of a gas-solid particle flow is necessary for the most efficient design of coal gasification systems. The difficulties associated with the analysis of gas-particle flows have precluded general solutions, with most research applied to simple geometries and often to flow conditions that are not particularily useful. In this work a general numerical solution, suitable for modeling dilute suspension flows over a wide range of velocities and flow geometries, is presented.

Conventional finite difference schemes are "blind" to the small eddy structures in the flow. Because of the high velocity found in most industrial systems, the influence of viscosity is confined to narrow regions of high fluid shear. These small regions, which are initially invisible to a finite difference grid, grow larger. Qualitatively, the effects of these small regions are quite pronounced. The flow may reverse direction and recirculate, giving rise to large scale mixing and downstream turbulance. Finite difference schemes cannot store enough grid points in these small areas of high shear to predict backflow with sufficient accuracy.

The Discrete Vortex Method (DVM) numerical solution circumvents these difficulties. The scheme is grid free because the vorticity within the fluid is partitioned into vortex "blobs" which are moved according to two components. One component is a random displacement; in this way the effect of viscous momentum diffusion is modeled. The other component is a deterministic displacement found by moving the blobs according to their mutual interaction effects. This interaction is similar to the way point vorticies in an inviscid fluid interact according to the Biot Savart Law.

In this work, the method has been applied to model gas and particles flowing around a cylinder. The technique produces the periodic vortex structure in the wake known as the Karman Vortex Street. Figure 7, a computer generated drawing of particle flow around the obstacle, illustrates the influence of the wake on particles. The particles have velocity vectors indicating their speed and direction. The small dots are computational vorticies which are essentially gas flow markers and can be thought of as smoke generated on the cylinder's surface. There is a strong focusing of particles behind the cylinder. Furthermore, in the wake, particles that passed under the cylinder tend to mix with particles that passed over the cylinder.

The unsteady wake has a surprisingly strong upstream influence on particles of less than 20

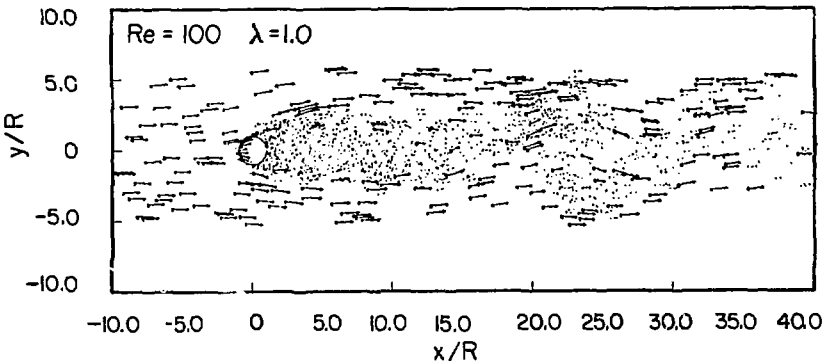

Fig. 7. Flow of one micron particles around a cylinder at a Reynolds number of 100. (XBL 804-9462)

microns diameter. The trajectories of small particles initially on the dividing streamline are deflected above or below the leading stagnation point. The direction of deflection depends upon the rotational trailing edge. Good agreement is obtained between the numerical solution and experimental drag coefficients at Reynolds numbers from 10^2 to 10^5. The results indicate the important role of unsteady flow analysis in erosion prediction.

* * *

†Brief version of LBL-9996.

7. PARTICLE REBOUND PHENOMENA IN TWO PHASE FLOW†

Jonathan Laitone

This investigation considered flow around a circular cylinder having all the attributes of a blunt leading edge, similar to a turbine blade, while exhibiting a large separate region in the rear, typical of flow around box bends. Computer generated movies that visually depicted particle trajectories showed three characteristic types of particle behavior:

- Imbedment,
- Single impact and rebound and
- Multiple impact.

Particle imbedment occurs when a particle strikes the surface and dissipates all of its kinetic energy. Single impacts occur when a particle strikes the surface and dissipates some kinetic energy but still leaves the surface with modified kinetic energy. In the third case, particles impact the surface two or more times before rebounding free of the surface. These particles tend to bounce across the surface similar to the way a stone skips across the smooth surface of a lake.

These three types of behavior are qualitatively evident for particles ranging in size from 20 to 500 microns, although the computed rebound conditions are quantitatively accurate for a particle size of 200 microns and a Reynolds number of 100,000 (assuming a 2 cm diameter cylinder, this corresponds to a flow velocity of 74.3 m/sec).

There is a strong focusing of particles behind the cylinder due to eddy shedding. In Fig. 8, an eddy is shed from the upper shoulder of the cylinder. This eddy has a very strong clockwise rotational motion and creates a force on the particles, deflecting their paths downward past the cylinder. An inviscid solution is inadequate in this prediction. Some particles impact more than once on the cylinder's leading surface, as predicted by the computer.

In Fig. 9, a velocity histogram is plotted for a single particle with an inertia number of unity. This means that the particle has a history of past events as well as being significantly influenced by present conditions. This particular example is chosen to illustrate a typical multiple impact experienced by a particle. The particle impacts and rebounds three times before clearing the top of the cylinder. The non-dimensional particle speed is presented historically at each impact point. The difference in impact speed and rebound speed is proportional to the momentum lost by the particle while eroding the surface.

At the first impact with the cylinder (slightly above the forward stagnation point), the particle's speed is already reduced to about 70% of its free

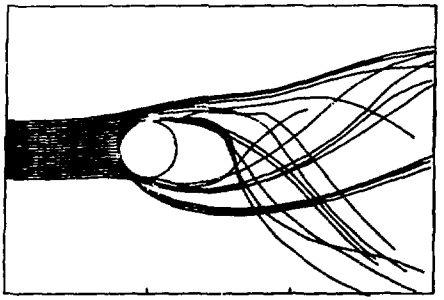

5 MICRONS, RE = 10^5

Fig. 8. Particle paths for 5 micron particles flowing around a cylinder at a Reynolds number of 100,000. (XBL 806-10523A)

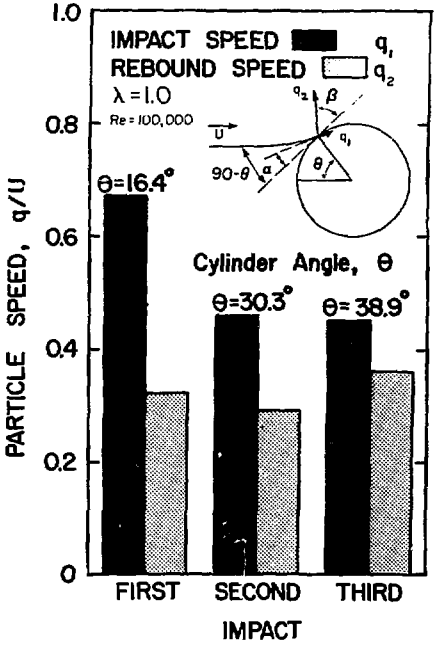

Fig. 9. Particle velocity histogram for a triple impact and rebound with the cylinder's surface. (XBL 806-10525)

stream value. This is caused by gas deflecting around the cylinder; consequently, the particle "sees" gas nearly at rest relative to its motion, and experiences a retarding force. The impact impingement angle local to the cylinder's surface is 64 degrees, and the rebound angle is 35 degrees.

A surprising result is found at the second impact point, which occurs at 30.3 degrees on the cylinder's front shoulder. The impact speed has increased over the rebound speed from the first impact. Evidently the gas flow has had sufficient time to work on the particle. An acceleration is expected in this case due to the gas accelerating away from the stagnation point and reaching a maximum of approximately twice the free stream speed at the top of the cylinder.

This observation is significant in erosion prediction; it means that in flow around blunt objects, particles can obtain a large fraction of their original kinetic energy prior to a secondary impact. Tilly[1] has found secondary erosion obtaining significant fractions of primary erosion. In Tilly's experiments, particles larger than 30 microns fragmented on impact. This analysis indicates that secondary erosion is also highly dependent upon the aerodynamic forces acting on the particle and does not require fragmenting. The model can be extended to account for fragmentation of particles on impact.

The actual work done on the surface is proportional to the change in momentum of the particle before and after impact. In Fig. 9, the trend is toward a decreasing value of the momentum change after each impact. This implies that the absolute value of erosion in secondary and subsequent impacts will always decrease monotonically. However, the secondary erosion may obtain significant fractional levels of the primary erosion for the reasons described above.

* * *

†Brief version of LBL-12017.

1. G. P. Tilly, Wear 23, 87 (1973).

8. BOUNDARY LAYER GAS COMPOSITION CONTROL IN PIPING†

William Chou-Chun Yeung

In coal gasification processes, oxidation and sulfidation can cause serious corrosion of the piping materials. Sometimes the corrosion rate is so high that the pipes need to be changed after a few weeks of operation. The purpose of this investigation was to analytically determine the feasibility of reduction of corrosion of the pipes by injection of steam into a boundary layer at the entry to the pipes. The injection will form a thin, less corroding gas boundary layer along the pipes, protecting the wall from contact with the highly corrosive coal gasification mixture. The key to this means of inhibiting high temperature corrosion is to maintain the protective mixture

far enough down the pipe before the reactive gas will diffuse through the injectant layer.

The first step was the calculation of the interaction between the pipe flow and the jet, treated on an inviscid basis. Steam is injected as a jet of small, finite width at the entry to the pipe. The shape of the streamline separating the pipe stream from the jet was calculated. This dividing streamline influences the main stream in a manner similar to that of a solid boundary, and its effect can be represented by a line of sources along the jet entry section. The jet changes the inviscid pipe flow in two ways. First, the pipe stream is displaced towards the center line of the pipe so that corrosive elements are no longer adjacent to the pipe wall. Second, a favorable pressure gradient is introduced along the dividing streamline.

Once the inviscid flow has been determined, the viscous mixing of pipe flow and the injected jet is calculated numerically using the Method of Integral Relations. Both velocity and concentration profiles across the layer are found, together with the growth rate of the mixing layer. The present analysis assumes laminar mixing (valid for sufficiently low Reynolds numbers) and shows that jet injection is an effective means of reducing the surface corrosion potential of the total gas flow due to H_2S or other undesirable species. The flow configuration for normal injection is shown in Fig. 10. The mass concentration variation is shown in Fig. 11.

* * *

Brief version of LBL-12018.

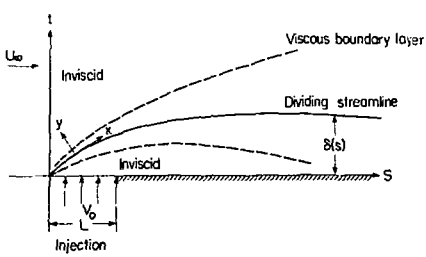

Fig. 10. Flow configuration for normal injection of a boundary layer gas. (XBL 813-460)

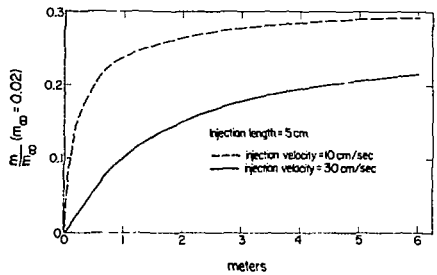

Fig. 11. Mass concentration variation of H_2S along a pipe. (XBL 813-462)

9. TURBULENT MODELING IN TWO PHASE BOUNDARY LAYER FLOW[†]

W. S. Yeung and R. J. Yang

The fluid flows which occur in coal gasification systems are incompressible at moderate or high values of Reynolds numbers. Such flows are best treated as interactions between inviscid flows in the main, central part of the gas stream and viscous flows in boundary layers, wakes, and separated regions. In calculating such flows numerically, it is necessary to solve the governing partial differential equations for the inviscid and viscous flows simultaneously as a coupled set. Finite difference methods are unwieldy for coupled systems since these must be matched across an inviscid-viscous boundary, the shape of which is one of the unknowns in the problem.

A technique was developed for such systems based on the Method of Lines for inviscid flows and the Method of Integral Relations for boundary layers. This technique was applied to the calculation of gas-particle flow at the entry section of a curved pipe. The analysis developed is for laminar flow in the boundary layer. It is obviously desirable to extend the Method of Integral Relations to apply to turbulent flow; this is the object of the present investigation. The method requires that the shear stress in the boundary layer be expressed as a polynomial in the streamwise velocity component. The difficulties in achieving this in turbulent flow are twofold: first, the turbulent boundary layer velocity profile is highly inflected compared with the laminar profile; and second, the eddy viscosity model must be given in analytical form.

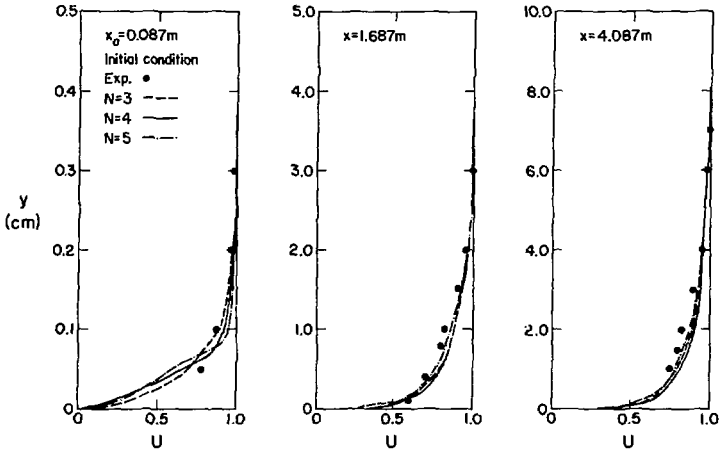

Fig. 12. Initial velocity profile and its development. (XBL 813-452)

A satisfactory model in the turbulent flow regime has been developed for two cases: first, when there is no external pressure gradient and, second, when the pressure gradient is accelerating. Typical velocity profiles in these two cases are shown in Fig. 12. Extension to retarded flow profiles is now under development.

* * *

†Brief version of LBL-12027.

10. LASER DOPPLER VELOCIMETER MEASUREMENTS OF THE TWO-PHASE FLOWS IN CURVED DUCTS

A. Modavi and J. Humphrey

The experimental apparatus designed for the investigation of fluid/solid flow in conduits is now operational and is actively engaged in the acquisition of data relevant to the erosion/corrosion problems in coal liquefaction and coal gasification, 2-phase, turbulent and laminar flow models.

The data acquisition system developed for measurement of the velocity fields in various flow configurations utilizes the latest "state of the art" in flow and instrumentation systems. It is capable of fully automatic positioning of sensors and acquiring, reducing and plotting data under programmed instructions. Special software developed for this system allows the user to adapt the system to new test configurations in much shorter time than was previously possible. The data acquisition rate is several orders of magnitude faster than manual operation; this makes possible the required accumulation of large amounts of data in any investigation.

The primary data acquisition system is based on a two component laser doppler velocimeter (LDV) with frequency enhancing data quality in low velocity regions of the flows. The LDV system is linked to a minicomputer (PDP 11/34 unit) which commands the process of acquiring velocity data. The minicomputer also places the LDV light probe at desired positions of the flow under study via general purpose program packages which process and plot the acquired data instantaneously.

The flow models currently under study are a water system in a 180 degree duct of square cross section, 43 × 43 mm^2, with a radius of curvature of 150 mm, and an air/solid-particle system flow in a 90 degree duct of 2 × 2 $in.^2$ cross section and 4 inch radius of curvature. The square cross section geometry makes optical probing of the flow relatively easy. The water flow system was constructed with support from the National Science Foundation and the Office of Naval Research, primarily for investigation of developing curved duct turbulent flow, and has been used to calibrate and test the data acquisition system. Data obtained in the 180 degree curved duct provides a base to compare the turbulent gas/solid flow data in the 90 degree curved duct.

The tangential mean velocity and turbulence intensity of the water flow has been determined in the 180 degree curved duct at a bulk flow rate of 1 m/sec and 1.5 m/sec (Reynolds no. 40,000, and 60,000), with particles of mean diameters 15 (polyvinyl chloride) and 12 (corn starch) microns,

respectively. The quality of the data obtained in the above mentioned configuration has been excellent. Both the optics and electronics associated with the computerized data acquisition system are functioning properly.

Figure 13 shows the mean tangential velocity and the turbulence intensity of the fully developed turbulent flow upstream of the curved duct section. These profiles are in good agreement with the results obtained by A. Melling[1] and J. A. C. Humphrey[2] in the square duct flows and confirms the validity and the accuracy of the data acquisition system. Figure 14 shows the development of the secondary motion of the water flow at 90 and 135 degree stations from the inlet. The curvature-induced secondary motion generates two symmetrical regions of circulation in the curved section which affects the impact angles of particles on solid boundaries and therefore should alter the erosion rate of the conduits at various locations. The profiles show where regions of high velocity and stress are likely to arise in the flow. This and similar information will help explain the heat transfer and erosive wear processes arising in curved duct flows. The water flow apparatus will subsequently be modified to accommodate the presence of larger particles.

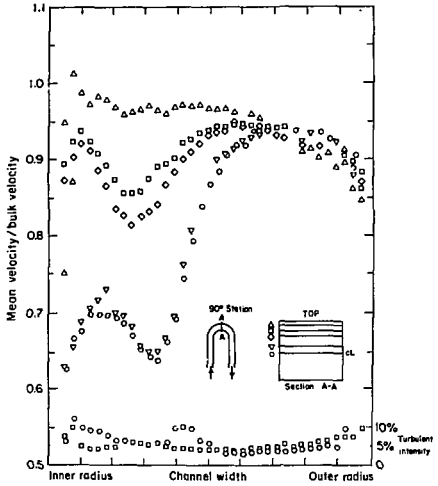

Fig. 14. Development of secondary motion of water flow at 90° and 135° stations from the inlet. (XBL 814-701)

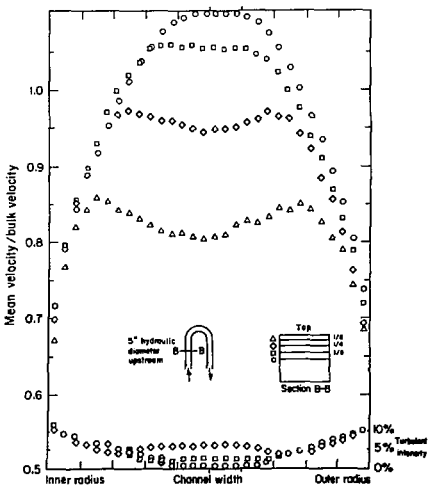

Fig. 13. Mean tangential velocity and turbulence intensity of fully developed turbulent flow upstream of curved duct section. (XBL 814-9448)

Measurements are now being made in the air/solid-particle flow for a 90 degree curved duct. The test schedule includes measurements of the air velocity profiles by introducing micron size particles in the flow at mean velocities of 5 to 30 m/sec. Subsequently, slip velocity measurements of larger solid particles of irregular geometry (e.g., 50-200 microns) will be made. Emphasis will be placed on the plane of symmetry of the flow field for sake of comparison with the numerical prediction of the flows in the cross-sectional curved pipes of W. S. Yeung and M. Holt.[3]

* * *

1. A. Melling, "Investigation of Flow in Non-Circular Ducts and Other Configurations by Laser-Doppler Anemometry," Ph.D. thesis, Department of Mechanical Engineering, Imperial College of Science and Technology, London, 1975.
2. J. A. C. Humphrey, "Flow in Ducts with Curvature and Roughness," Ph.D. thesis, Department of Mechanical Engineering, Imperial College of Science of Technology, London, June 1977.
3. W. S. Yeung and M. Holt, "Perturbation Solution for the Particle Trajectories of a Gas-Solid Mixture Entering a Curved Duct," LBL-8521, December 1978.

11. MODELING OF TURBULENT TWO PHASE FLOW IN A CURVED CHANNEL†

F. Pouramahdi and J. Humphrey

The purpose of this research is to develop and apply numerical calculation procedures capable of predicting two-phase fluid motion in a turbulent-flow curved channel configuration. With an appropriate treatment of the erosive wear processes occurring at the solid-liquid interfaces, the procedure can be applied to predict wear in various simple industrial flow components and extended to encompass more complex configurations in solid particle, liquid two-phase flows.

The first step, which has been completed, was to establish numerically the fluid mechanics of turbulent curved channel flow. Based on the established fluid mechanics, a model appropriate for predicting dilute two-phase solid particle liquid flow systems is being developed and tested. Subsequently, it will be incorporated into the prediction procedure to establish its validity for a variety of experimentally documented flows.

Current flow tests utilizing water in a curved rectangular channel with laser doppler velocimeter (LDV) instrumentation are yielding reasonable results compared to the model. Typical calculations produced to date are shown in Figs. 15 and 16 for mean velocity and turbulence kinetic energy, respectively. The predictions are in relatively good agreement with experimental data in the literature. It is important to note that earlier attempts to predict this flow with simpler models of turbulence were unsuccessful. Further and very rigorous testing is still required to validate the model.

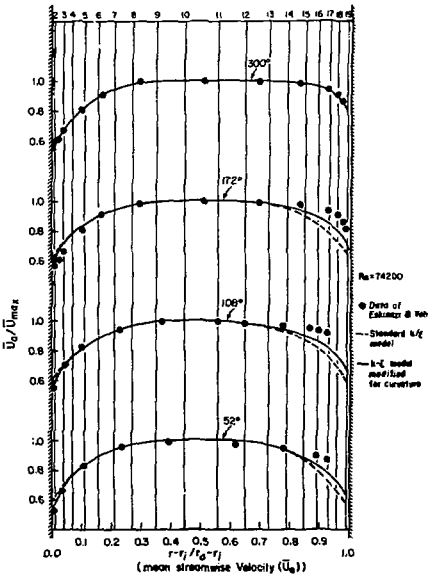

Fig. 15. Mean velocity profiles in turbulent channel flow. (XBL 814-4543)

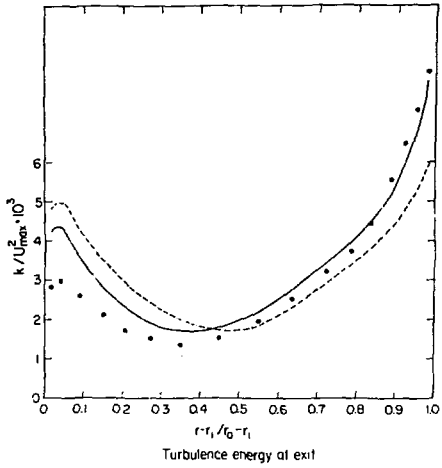

Fig. 16. Turbulence kinetic energy at exit station in a curved channel flow. (XBL 814-4544)

* * *

†Brief version of LBL-12009.

RESEARCH PLANS FOR CALENDAR YEAR 1981

The platelet mechanism of erosion will be further investigated by sequential erosion of a variety of alloys with different crystallographic structures and morphologies over a range of testing conditions. Protective coating systems on metal substrates to enhance either or both erosion and corrosion resistance of structural alloys will be investigated. Elevated temperature erosion behavior for a number of metals and ceramics will be determined. Further modeling of erosion processes in ductile metals and brittle ceramics will be carried out. Combined erosion-corrosion testing will be conducted in oxidizing atmospheres. The potential of surface doping of stainless steels with active element salts to promote scale retention will be further defined, particularly the ability of reapplications of the salts to continue the enhancement.

The fluid mechanics work will concentrate on relating experimental results in both liquid and gas-solid particle flows to predicted particle behavior from previously developed models. Further modeling of boundary layer gas composition control will be carried out in the turbulent regime. The liquid-particle flow model in curved channels will be completed in the two-phase flow regime.

1980 PUBLICATIONS AND REPORTS

Refereed Journals

1. W. S. Yeung, "Laminar Boundary Layer Flow Near the Entry of a Curved Annular Pipe," J. of Appl. Mechanics 102, (December 1980).

2. W. S. Yeung, "Perturbation Solutions for the Particle Trajectories of a Gas-Solid Mixture Entering a Curved Duct," ZAMM 60, 241 (1980).

3. J. Johanmir, "The Mechanics of Subsurface Damage in Solid Particle Erosion," WEAR 61, 309 (1980).

4. L. Lapides and A. Levy, "The Halo Effect in Jet Impingement Solid Particle Erosion Testing of Ductile Metals," WEAR 58, 308 (1980).

Other Publications

1. D. Boone, "Overlay Coatings for Gas Turbine Airfoils," presented in the AGARD Lecture Series No. 106 on Materials Coating Techniques, March 1980, Lisbon, Portugal and Athens, Greece; in April, Ankara, Turkey and published in the proceedings March, 1980.

2. D. P. Whittle and D. Boone, "Alumina Scale Adherence to CoCrAl Alloys and Coatings," presented at the Conference on Surfaces and Interfaces in Ceramic and Ceramic-Metal Systems, July 28-August 1, 1980, Berkeley, California and published in the proceedings.

3. A. Levy, R. Bellman, Jr., and J. Maasberg, "Mechanisms of Erosion/Corrosion of Metals and Their Oxide Scales," in Proceedings of Conference on the Properties and Performance of Materials in the Coal Gasification Environment, ASM-MPC, Pittsburgh, Pennsylvania, September 1980.

4. I. Hutchings, "A Model for the Erosion of Metal by Spherical Particles at Normal Incidence," to be published by Wear Journal.

5. D. Boone, D. P. Whittle, and I. M. Allam, "Adherence of Al_2O_3 to CoCrAl Coatings," to be published in Thin Solid Films and presented at the International Conference on Metallurgical Coatings, San Diego, April 21-25, 1980.

6. D. Boone, E. P. Eppinger and W. K. Halnan, "Hot Corrosion of CoCrAl Coatings," presented at the International Conference on Metallurgical Coatings, San Diego, April 21-25, 1980 and accepted for publication as extended abstract in Thin Solid Films.

7. J. Laitone, "A Numerical Solution for Gas-Particle Flows at High Reynolds Numbers," to be published by the Journal of Applied Mechanics.

LBL Reports

1. G. Zambelli and A. Levy, "Particulate Erosion of NiO Scales," accepted by Wear Journal, LBL-8524.

2. A. Levy, "The Erosion Behavior of Steel as a Function of Microstructure in Solid Particle Erosion," accepted by Wear Journal, (LBL-10798).

3. R. Bellman, Jr. and A. Levy, "Erosion Mechanism in Ductile Metals," accepted by Wear Journal, (LBL-10289).

4. M. Landkof, D. H. Boone, D. P. Whittle, and A. V. Levy, "The Effect of Surface Doping on the Oxidation of Chromia Former Alloys," LBL-11127.

5. J. Maasberg and A. Levy, "Erosion of Thin Oxide Scales," LBL-12015.

6. J. Maasberg, D. H. Boone, D. P. Whittle, A. V. Levy, "Erosion Resistance of CoCrAl Coatings Containing Active Element Additions," LBL-12016.

7. M. Khatibloo, "On the Indentation and Erosion of Brittle Materials," LBL-11883.

8. J. Laitone, "Characterization of Particle Rebound Phenomena in the Erosion Turbomachinery," LBL-12017.

9. W. C. Yeung and M. Holt, "Boundary Layer Gas Composition Control in Piping," LBL-12018.

10. W. S. Yeung and R. J. Yang, "Application of the Method of Integral Relations to the Calculation of Two-Dimensional Incompressible Turbulent Boundary Layer," LBL-12027.

11. J. A. C. Humphrey and F. Pouramahdi, "A Generalized Algebraic Relation for Predicting Developing Curved Channel Flow with a K/E Model of Turbulence," LBL-12009.

12. A. Levy, R. Bellman, Jr., and J. Maasberg, "Mechanisms of Erosion/Corrosion of Metals and Their Oxide Scales," LBL-12023.

Invited Talks

1. A. Levy, "Abrasion, Erosion and Wear," Materials Science Problems in Synthetic Fuel Technology Conference, Argonne National Laboratory, Argonne, Illinois, June 1980.

2. A. Levy, "Erosion in Gas-Solid Particle and Liquid Slurry Streams," Seminar, Exxon Research and Engineering Company, Florham Park, New Jersey, June 1980.

3. A. Levy, "Erosion in Gas-Solid Particle and Liquid Slurry Systems," Seminar, Ingersoll Rand Corp. Research Center, Princeton, New Jersey, June 1980.

4. D. Boone, "High Temperature Coatings," invited lecturer and participant in Deposition Technologies and Applications, UCLA Short Course, June 16-20, 1980.

5. A. Levy, "Erosion in Gas-Solid Particle Streams," Seminar, Shell Oil Company Westhollow Research Center, Houston, Texas, July 1980.

6. A. Levy, "Erosion in Gas-Solid Particle and Liquid Slurry Streams," Seminar, Exxon Corporation Research Laboratory, Linden, New Jersey, October 1980.

7. D. Boone, "High Temperature Component Protection," presentation and panel member, Large Scale Processing Workshop, AVS 27th National Symposium, Detroit, Michigan, October 16, 1980.

8. A. Levy, "Catalyst Corrosion and Gas-Solid Particle Erosion," Seminar, Mobil Research Laboratory, Paulsboro, New Jersey, October 1980.

9. A. Levy, "Platelet Mechanism of Erosion," Seminar, National Bureau of Standards, Gaithersburg, Maryland, October 1980.

10. R. Bellman, Jr. and A. Levy, "Erosion of Ductile Metals by Platelet Formation," AIME-TMS Annual Meeting, Pittsburgh, Pennsylvaniz, October 1980.

11. J. Maasberg and A. Levy, "Erosion of Elevated Temperature Corrosion Scales on Metals," AIME-TMS Annual Meeting, Pittsburgh, Pennsylvania, October 1980.

12. M. Landkof, A. Levy, D. Boone, and D. Whittle, "Modification of Protective Oxide Scales on Stainless Steel," AIME-TMS Annual Meeting, Pittsburgh, Pennsylvania, October 1980.

13. J. Laitone, A. Levy, "Effect of Particle Aerodynamics on Erosion of Metals," ASM Materials and Processes Show and Congress, Cleveland, Ohio, October 1980.

14. A. Levy, "The Materials Side of Synfuels Production and Utilization in the 1980s"; LBL Colloquium, November 1980.

b. In-Situ Investigation of Gas-Solid Reactions by Electron Microscopy*

James W. Evans, Investigator

Introduction. Reactions between gases and solids have been the object of considerable research activity for several years because of their importance in many technologies (e.g., the combustion of gaseous fuels and the reduction of iron ores to metal).[1] Recently, interest has developed in the relationship between microstructure and solid reactivity; it has become clear that many macroscopically observable phenomena, such as catalysis and the effect of mechanical stress on solid reactivity, must be dependent on the microstructure of the solid. The transmission electron microscope is one of the most powerful instruments for examining microstructure and is being used at Berkeley in a study which, although presently concerned with microstructure/reactivity effects in oxide reduction reactions, will eventually embrace other reactions, such as sulfidation and oxidation of metals.

This report describes some initial studies using ex-situ and in-situ techniques, of the reduction of nickel oxide by hydrogen. The ex-situ technique is to be contrasted with the more advanced in-situ technique, presently being employed at Berkeley, wherein the reaction is carried out in an environmental cell located in the microscope. The literature on nickel oxide reduction is extensive,[2] but nearly all prior work is concerned with macroscopically observable phenomena; an exception is the work of Rao[3] who used an optical microscope to study the development of the second (nickel) phase during reduction.

1. EX-SITU STUDIES OF THE REDUCTION OF NiO CRYSTALS

John A. Little,[†] James W. Evans, and Kenneth H. Westmacott

Nickel oxide single crystal, in the form of a boule, was sectioned using a diamond saw and the sections ground to 3 mm diameter disks, 1 mm thick. After annealing in air at 1350°C for 24 hours, the disks were further ground to a 50-80 μm thickness and then thinned by ion milling. Reduction was carried out in α-alumina high purity crucibles placed in a tubular furnace. The samples were brought up to temperature under helium, and reduction was then initiated under a flow of hydrogen at pressures slightly above atmospheric. Reaction was stopped by evacuation of the hydrogen and cooling carried out under vacuum. The specimens were examined at 100 kV in a Philips 301 electron microscope.

In work reported earlier, it was shown that during the early stages of reduction, most, but not all, of the nickel nuclei form epitaxially on the nickel oxide surface. After more prolonged exposure to hydrogen, the surfaces become nearly completely covered with nickel islands, many of which have coalesced. At this stage, the majority of the nickel nuclei are non-epitaxial, as revealed by the diffraction pattern (Fig. 1) where only the spots of the remaining nickel oxide lattice and the powder rings of the non-epitaxial nuclei are evident. A topic of interest is whether or not microstructural features play a role in the nucleation of the second phase. Figure 2 shows that cracks in the nickel oxide are indeed preferred nucleation sites. However, the sites where grown-in matrix dislocations intersected the surfaces do not appear to act in a similar manner.

This investigation is the first in which a shift from epitaxy to non-epitaxy of the reaction product, as reaction proceeds, has been observed in the reduction of a metal oxide. A connection has been shown between nickel nucleation and one microstructural feature, cracks. A fuller account of the ex-situ studies may be found in a recent publication.[4]

* * *

[†]Present address: Department of Metallurgy, University of Cambridge, Cambridge, England.

1. J. Szekeley, J. W. Evans, and H. Y. Sohn, "Gas-Solid Reactions," Academic Press, New York, 1976.
2. J. W. Evans, S. Song and C. E. Leon-Sucre, Met. Trans. 7B, 51, (1976).
3. Y. K. Rao, Met. Trans. 10B, 243, (1979).
4. J. A. Little, J. W. Evans and K. H. Westmacott, Met. Trans. 11B, 519 (1980).

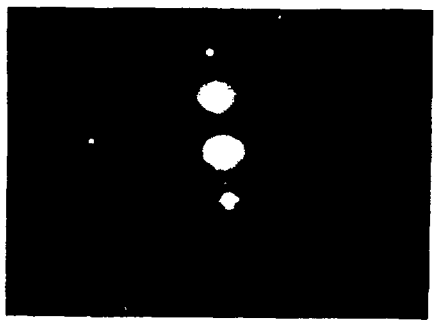

Fig. 1. Diffraction pattern from nickel oxide in final stages of reduction. Powder rings from non-epitaxial nickel are pronounced. (XBB 7911-15325)

*This work was supported by the Director, Office of Energy Research, Office of Basic Energy Sciences, Materials Sciences Division of the U. S. Department of Energy under Contract No. W-7405-ENG-48.

Fig. 2. Nucleation of the nickel at a crack in the nickel oxide. (XBB 7911-15330)

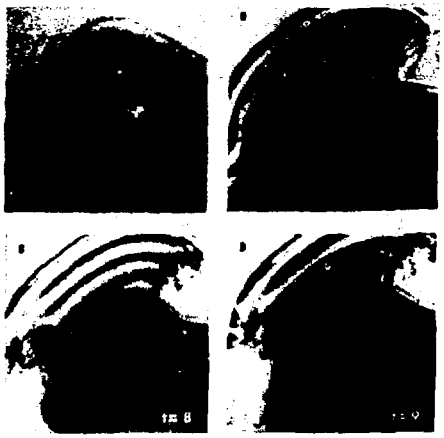

Fig. 3. Sequence of micrographs showing heterogeneous nucleation and growth of nickel colonies during in-situ reduction of nickel oxide. (XBB 807-8728)

2. IN-SITU STUDIES

In-situ observations have been made in the Hitachi HU65D fitted with the environmental cell, using samples from the same NiO boule. Runs at several different temperatures were made in a flowing gas of 10% H_2 in He at a pressure of ~ 40 torr.

At a temperature of about 250°C, the reduction process proceeded in a manner rather similar to that observed in the ex-situ studies. Islands of nickel nucleated, grew, and coalesced until the entire area was covered. It was noticeable, however, that certain areas remained unreduced for long periods. This difference in behavior could not be related to a visible structural feature. After reduction times of the order of 1 hour, the observed structures were indistinguishable from those found after ex-situ reduction.

With an increase in temperature to ~ 275°C, a different behavior was observed. At this temperature, as seen in Fig. 3, colonies of Ni islands nucleated and grew rapidly while the surrounding surfaces remained unchanged. Again, the nucleation sites for the colonies could not be related to any microstructural features.

Further experiments in progress are being conducted to study the temperature and pressure dependence of the reduction process in greater detail.

RESEARCH PLANS FOR CALENDAR YEAR 1981

In-situ investigations of nickel oxide reduction will determine the relationship between nickel nucleation and microstructural features such as grain boundaries or dislocations. A recently acquired mass spectrometer, attached to the gas outlet from the environmental cell, will enable a simultaneous observation of the reacting solid and measurement of its reaction rate. Research will be initiated on other reactions of interest in energy technologies.

1980 PUBLICATIONS AND REPORTS

Refereed Journals

1. J. A. Little, J. W. Evans, and K. H. Westmacott, "Early Stages of the Reduction of Nickel Oxide Single Crystals: An Investigation by Transmission Electron Microscopy," Met. Trans., 11B, 519 (1980), LBL-10176.

†2. M. Ranade and J. W. Evans, "The Reaction Between a Gas and a Solid in a Non-isothermal Packed Bed: Simulation and Experiments," I. and E. C. Process Design and Development 19, 118 (1980).

†3. A. Malazgirt and J. W. Evans, "Production of Aluminum and Aluminum Coatings by Thermal Decomposition of Aluminum Alkyls," Met. Trans. 11B, 225 (1980).

†4. J. W. Evans and M. Ranade, "The Grain Model for Reaction Between a Gas and a Porous Solid—A Refined Approximate Solution to the Equations," Chem. Eng. Sci. 35, 1261 (1980).

†5. J. W. Evans, M. H. Abbasi, and A. Sarin, "A Monte Carlo Simulation of the Diffusion of Gases in Porous Solids," J. Chem. Phys. 72, 2967 (1980).

LBL Reports

1. J. A. Little, M. I. Perez, and J. W. Evans, "Transmission Electron Microscopy Studies of Coals," LBL-11473.

2. J. W. Evans, Y. Zundelevich, and D. Sharma, "A Mathematical Model for Prediction of Currents, Magnetic Fields, Melt Velocities, Melt Topography, and Current Efficiency in Hall-Héroult Cells," LBL-11675.

Invited Talks

§1. D. Ziegler, M. Dubrovsky, and J. W. Evans, (presented by D. Ziegler), "The Use of Novel Anodes in the Electrowinning of Metals of Fluidized Bed Cathodes," Annual Meeting of the American Institute of Metallurgical Engineers, Las Vegas, NV, February 24-28, 1980.

†2. I. Masterson, M. Dubrovsky and J. W. Evans, (presented by J. W. Evans), "Fluidized Bed Electrowinning of Cobalt from Sulfite Solutions," Annual Meeting of the American Institute of Metallurgical Engineers. Las Vegas, NV, February 24-28, 1980.

3. J. A. Little, J. W. Evans and K. Westmacott, (presented by J. A. Little), "Ex-situ and In-situ Studies of the Reduction of Nickel Oxide Single Crystals Using Transmission Electron Microscopy," Annual Meeting of the American Institute of Metallurgical Engineers, Las Vegas, NV, February 24-28, 1980.

†4. M. Abbasi and J. W. Evans, (presented by J. W. Evans), "A Monte Carlo Simulation of the Diffusion of Gases in Porous Solids," Annual Meeting of the American Institute of Metallurgical Engineers. Las Vegas, NV, February 24-28, 1980.

* * *

†Partially supported by NSF.
‡Partially supported by Office of Surface Mining, Department of Interior.
§Partially supported by intramural funding.

B. Solid-State Physics

1. Experimental Solid-State Physics

a. Far-Infrared Spectroscopy*

Paul L. Richards, Investigator

Introduction. The objective of our research is to use the infrared and near-millimeter wavelength range of the electromagnetic spectrum as a probe to do experiments which are selected for their technical novelty and potential for revealing new physics. Our work includes development of new measurement techniques, such as new spectrometers, detectors, etc. In recent years, considerable effort has been devoted to sensitive infrared detectors for use in experiments in which the background photon level is low. The Ge:Ga photoconductors, the uniaxially stressed Ge:Ga photoconductors, the composite bolometers, and the superconducting diode photon detectors developed in this project are now the most sensitive infrared and near-millimeter detectors ever produced over the wavelength range from 50 μm to 8 mm. The superconducting diode devices are also the most sensitive available heterodyne receivers at mm wavelengths.

Experimental projects, which will not be described in detail in this report, include a recently completed balloon measurement of the spectrum of the cosmic (blackbody) background radiation comprising 90% of the radiant energy in the universe. This experiment was the first to show that the spectrum of the microwave background falls at frequencies above the peak at 6 cm^{-1}. It also showed deviations from a blackbody spectrum at the confidence level of 3 standard deviations. A new experiment is being prepared to check these deviations. It will be different in most respects, to reduce the possibility of common systematic errors. If the deviations are confirmed by new experiments, they will be a matter of highest importance for cosmology.

Other investigations, in progress but not described in detail here, include: a balloon experiment, which had its first flight in the spring of 1979, to survey the sky at far infrared wavelengths; a project to improve the performance of photoconductive infrared detectors and to test fundamental noise theory; a project to use adiabatic demagnetization to cool bolometric infrared detectors below 0.3 K; and a project to use modern ion-implantation techniques to eliminate the current dependent inverse frequency noise that now limits the performance of composite bolometric detectors when operated at high background flux levels. These studies will be described in future annual reports as the investigations are completed.

*This work was supported by the Director, Office of Energy Research, Office of Basic Energy Sciences, Materials Sciences Division of the U.S. Department of Energy under Contract No. W-7405-ENG-48.

1. INFRARED SPECTRA OF $NbSe_3$ IN THE CHARGE DENSITY WAVE STATE

William A. Challener, Pierre Monceau,† and Paul L. Richards

$NbSe_3$ is an extremely interesting member of the class of quasi-one-dimensional metals. It undergoes two charge density wave (CDW) transitions, at 59 K and 145 K, which are both accompanied by large anomalies in electrical resistivity. The CDW's are generally believed to be pinned to the lattice by impurities, but small electric fields are able to free them to conduct electrical current.

Mean field theory[1] predicts a BCS-type gap equation for such materials relating the size of an energy gap at the Fermi surface at absolute zero to the CDW transition temperature. The energy gap decreases continuously to zero at the transition temperature in the same manner as the superconducting energy gap in the BCS theory.[2] The 59 K transition in $NbSe_3$ thus corresponds to an energy gap at absolute zero of about 140 cm^{-1}, in the far infrared. The initial motivation for studying the infrared properties of $NbSe_3$ was to look for evidence of this energy gap.

$NbSe_3$ crystallizes into long, narrow fibers. Typical dimensions are $10 \times 0.02 \times 0.01$ mm^3. These dimensions create difficult problems for measuring optical properties in a frequency region where the wavelength of light is ten times larger than the smallest dimension of the crystal. To overcome this problem, we have made samples by placing large numbers of fibers on a Mylar tape substrate with all orientations approximately parallel to each other. An attempt is made to make the layer of fibers homogeneous and to have the fiber separation small compared to one wavelength. In this way, we have been able to measure reflectance and transmittance spectra on the same sample from 10 to 350 cm^{-1}. Transmittance measurements have been made over a temperature range of 1.5 K to 90 K, while all reflectance measurements were made at 1.5 K. The spectra were measured with both polarized and unpolarized light. Examples of both types of spectra are shown in Fig. 1.

Our measurements show no evidence of an energy gap in this frequency interval. The absence of dramatic energy gap effects may be related to the fact that the energy gap covers only a part of the Fermi surface. Our spectra do, however, reveal very dramatic structure when the sample is cooled below the 59 K transition temperature. At this temperature, the intensity of the structure continuously decreases to zero, demonstrating that it is associated with this transition. Because the structure has no temperature-dependent frequency

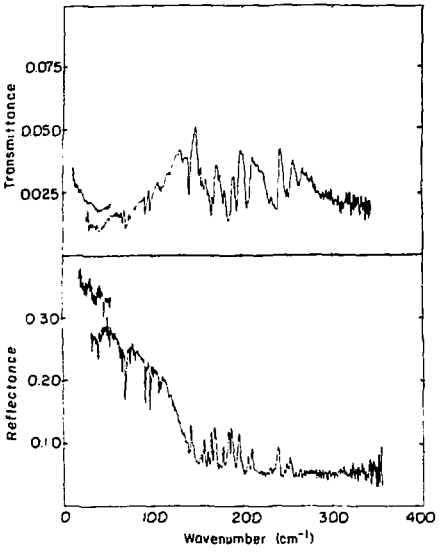

Fig. 1. Transmittance and reflectance of $NbSe_3$ at 1.5 K using unpolarized light. (XBL 8011-13309)

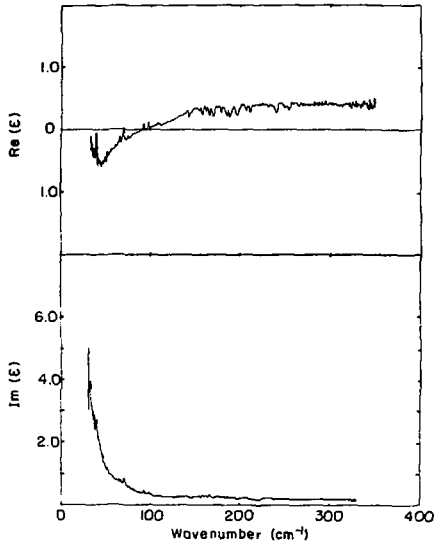

Fig. 2. Complex dielectric function calculated from the data in Fig. 1. (XBL 8011-13311)

shifts, we do not associate it with an energy gap. Instead, we believe that it is caused by the excitation of new optical phonon modes created by folding of the Brillouin zone at the CDW transition. The structure is present in spectra measured with the incident light polarized parallel to the fiber axis as well as perpendicular to the fiber axis. This is not surprising in that the k-vector of the 59 K CDW has components along all crystal lattice vectors.

Using the reflectance and transmittance measurements shown in Fig. 1, we have calculated appropriate values for the complex dielectric function of $NbSe_3$ in the infrared range. The calculations are based on a homogeneous sheet model with various estimates for the effective thickness. One example is shown in Fig. 2.

Although our calculated curve for the imaginary part of the dielectric constant is much smaller than what is expected from the low frequency measurements of the conductivity, our results do suggest a possible explanation for the unusual shape of the phonon structure. The structure can be understood as the results of "dielectric anomalies," i.e., zero-crossings in the real part of the dielectric function. In this way relatively weak modes can have dramatic effects on the transmittance and reflectance of a sample.

* * *

†Permanent Address: CRTBT, CNRS, F-38042, Grenoble, France.

1. H. Frohlich, Proc. R. Soc. London Ser. A 223, 296 (1954).
2. C. G. Kuper, Proc. R. Soc. London Ser. A 227, 214 (1955).
3. G. Grüner, et al., Phys. Rev. Lett. 45, 935 (1980).

2. ELECTRONS ON THE SURFACE OF LIQUID HELIUM†

David K. Lambert‡ and Paul L. Richards

Electrons pressed onto the surface of superfluid liquid helium from the gas by an external electric field can populate image-potential-induced surface states. Electrons in such states have large mobility along the surface and, to a good approximation, can be described as a two-dimensional electron gas. We have used a far infrared molecular laser to study transitions from the ground state to various excited states of this gas. The transition frequencies are a function of both the applied electric field and the surface charge density.

The measured values of the field at resonance for low surface charge densities (Fig. 3) are in excellent agreement with curves calculated from a one-dimensional Schrödinger equation. The Hamiltonian included an inverse square-law image field, an infinite abrupt barrier at the liquid surface and the applied electric field.

The coverage of surface electrons was indirectly obtained by measuring the capacitance between electrodes placed above and below the surface of the helium. A self-consistent electrostatic shielding calculation was used to interpret these measurements and to obtain values for the surface charge density which were accurate to 1%. A dependence of the value of the applied field required for resonance on the surface charge density arises because of the electric dipole field from the surface electrons (and their image charges) surrounding the electron undergoing the transition. Although this surface charge density effect is small, it can be measured. It can also be calculated if a model for the radial distribution function of the surface electrons is available. In previous work, we showed that the measurements are in good agreement with published calculations of the radial distribution function.[1]

We have used the experimental determination of the charge density dependence of the resonance field to extrapolate the measurements to zero surface charge density. The resulting values for the resonance frequencies shown in Fig. 4 are about 7 GHz above the values calculated from the model of an abrupt liquid-gas interface. This small ($\lesssim$1%) effect can be interpreted as a lowering of the ground state energy due to the finite width of the liquid gas interface. Fits to calculations in the literature[2] give an effective width for the surface of ~3 Å.

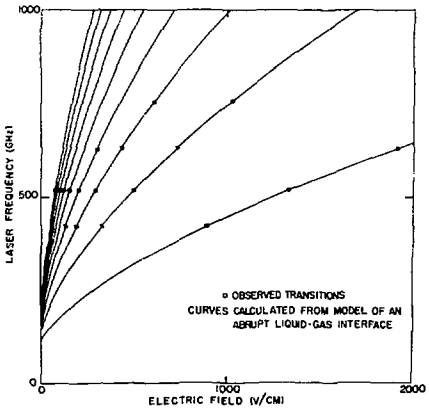

Fig. 3. Plot of the laser frequency versus the electric field at which transitions are observed. (XBL 798-6725)

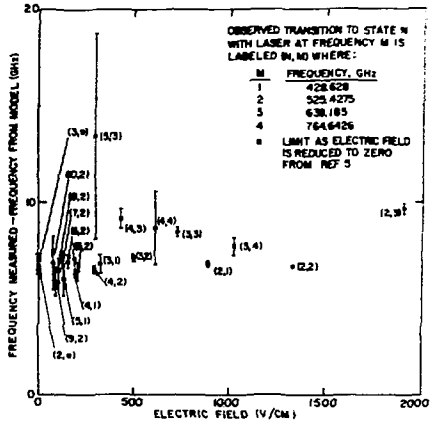

Fig. 4. The laser frequency for resonance minus the frequency calculated from the abrupt surface model. (XBL 798-6722)

* * *

†A brief version of LBL-10343.

‡Permanent address: Research Laboratories, General Motors Corporation, Warren, Michigan 48090.

1. D. K. Lambert and P. L. Richards, Phys. Rev. Lett. 44, 1427 (1980).
2. F. Stern, Phys. Rev. B 17, 5009 (1978).

3. INFRARED EMISSION SPECTROSCOPY OF SURFACES

Shirley Chiang, Roger G. Tobin and Paul L. Richards

We are developing a technique for measuring the infrared emission from vibrational modes of molecules adsorbed on a clean, single crystal metal surface. We have constructed a high sensitivity, cooled infrared grating spectrometer which is coupled to an ultra-high vacuum sample chamber equipped for the deposition and characterization of sub-monolayer layers of various gases on clean surfaces. This apparatus is shown in Fig. 5.

Thermal emission from the sample at room temperature is substantial for wavelengths longer than 3 μm and provides the infrared signal which is focused onto the entrance slit of the cold spectrometer. For improved performance at shorter wavelengths, it is possible to adapt the system for polarization-modulated infrared reflection spectroscopy.[1]

High infrared sensitivity has been achieved by cooling the compact infrared spectrometer to liquid

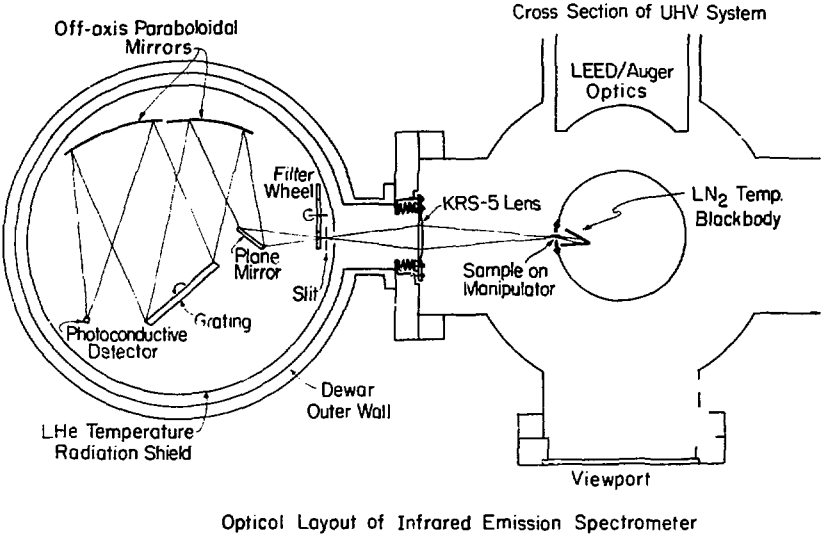

Fig. 5. Horizontal cross section of the cooled infrared spectrometer attached to the UHV surface apparatus. (XBL 8012-13382)

helium temperature and using an extremely low noise photoconductive detector. The detector, developed for use in satellite astronomy, is noise limited by random fluctuations in the photon arrival rate, even with the very low background provided by the cold spectrometer. The ~ 5 cm^{-1} resolution of the spectrometer is sufficient, not only for the identification of vibrational frequencies corresponding to molecules adsorbed at different sites on a single crystal surface, but also for the study of the lineshapes of these modes. Lineshape information has been inaccessible to electron energy loss spectroscopy with its poorer resolution.[2]

The sample is mounted in an ultra-high vacuum chamber where it can be cleaned by ion bombardment, annealed by heating, exposed to a calibrated flux of gas molecules, and characterized by LEED and Auger spectroscopy. The combination of these conventional surface analysis tools with infrared vibrational spectroscopy, which can provide information regarding the identity, location, and bonding characteristics of adsorbed molecules, will afford valuable insight into the properties of the surface and its interactions with adsorbed molecules.

* * *

1. F. M. Hoffman and A. M. Bradshaw, Proceedings of the Seventh International Vacuum Congress and Third International Conference on Solid Surfaces, 1167 (1977).

2. H. Ibach, H. Hopster and B. Sexton, Applications of Surface Science 1, 1 (1977).

4. NEW TYPES OF NEAR-MILLIMETER WAVE FILTERS†

Thomas T. Timusk‡ and Paul L. Richards

The development of ultrasensitive far infrared detectors has placed heavy demands on our ability to make band-pass filters to reduce background loading on the detector. We have developed new types of band-pass filters for broad band photometry in the frequency range from 3 to 12 cm^{-1}. The transmittance bands of these filters are shown in Fig. 6. These filters were developed for use in a new measurement of the spectrum of the cosmic microwave background radiation. The novel techniques used in the manufacture of these filters, however, are applicable to a wide variety of experiments.

The primary band limiting element in these filters is a Fabry-Perot interferometer. The interferometer is made by evaporating a square array of metallic squares (a capacitive mesh[1]) on each side of a Mylar polyester substrate. The transmittance of such an interferometer has a broad zero-order peak, a first order peak of moderate width, and narrow higher order response peaks.

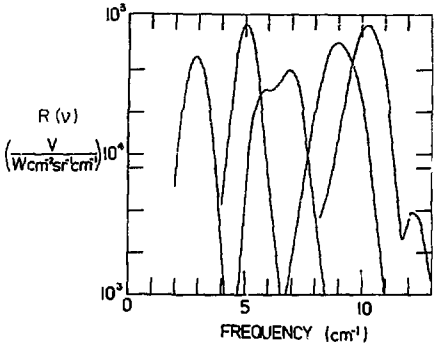

Fig. 6. Overall responsivity of a system of filters designed to measure the cosmic microwave background radiation. (XBL 8012-12955)

There is also broad-band leakage at much higher frequencies. Two interferometers in series are used in first order to define the primary pass-band of the filter. The higher order peaks and the broad band leakage are blocked with black polyethylene and soda-lime glass low-pass filters. The Beer's law extinction coefficient for soda-lime glass varies as frequency cubed, so the filter onset frequency can be adjusted by varying the thickness of the glass.

A new type of infrared high frequency pass filter was invented to eliminate the zero-order response. This is the thick grill filter shown in Fig. 7. It consists of a hexagonal close-packed array of holes of diameter d drilled in a metal plate whose thickness is about two hole diameters. Since each hole acts as a waveguide cut-off filter, there is an extremely rapid decrease in transmittance for frequencies below that of the lowest frequency propagating mode in a circular waveguide $\nu_c = 0.586/d$. It is expected that the techniques of optical lithography will permit such filters to be made with cut-off frequencies anywhere in the infrared.

* * *

†A brief version of LBL-11931.

‡Permanent Address: Department of Physics, McMaster University, Hamilton, Ontario, Canada L8S 4M1

1. R. Ulrich, Infrared Phys. 7, 37 (1967); Infrared Phys. 7, 65 (1967): Applied Optics 7, 1987 (1968).

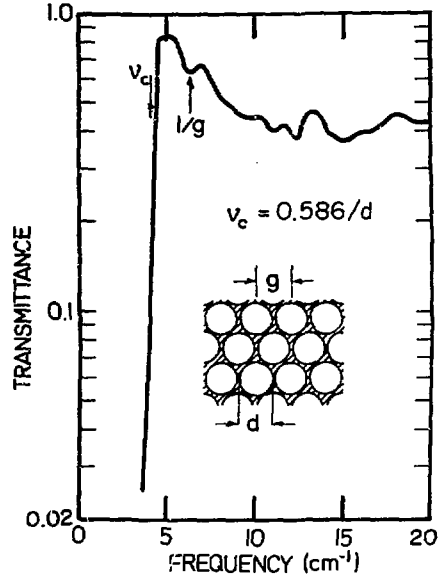

Fig. 7. Transmission of a thick grill filter. This high-pass filter consists of a pattern of 1.4 mm diameter holes on a 1.6 mm spacing in a 3 mm thick metal plate. (XBL 8012-12954)

RESEARCH PLANS FOR CALENDAR YEAR 1981

Surface Spectroscopy. The infrared emission apparatus described above for measuring the vibrational spectra of molecules on metal surfaces will be completed during the coming year. The first experiment will be to search for the infrared absorptions caused by metal-molecule vibrations in simple systems. It is anticipated that a newly arrived postdoctoral physicist will use an existing infrared thermal detection technique described in previous annual reports to search for low frequency surface modes.

One-dimensional Conductors. Our infrared data on the one-dimensional conductor $NbSe_3$ will be extended to higher and lower frequency ranges and will be subjected to a more sophisticated analysis. It is anticipated that we will complete work on this project during the coming year.

Experimental Cosmology. The conclusion from our previous measurement of the cosmic background radiation was that the spectrum was close to that of a blackbody, but with significant deviations. A new balloon experiment, being developed for flight in 1981, will provide an independent test of these apparent deviations. This new experiment is also well adapted to measure the anisotropy of the cosmic microwave background radiation.

Our one-meter aperture balloon telescope is being readied for a second flight. This experiment is designed to survey the northern sky in seven far infrared wavelength bands. The primary scientific goal is to measure the temperature, density, and distribution of dust in our galaxy.

Technology Development. A portable adiabatic demagnetization system has been constructed to cool a new generation of ultra-high sensitive far infrared bolometric detectors to temperatures in the neighborhood of 100 mk. These more sensitive detectors will have application in both surface spectroscopy and cosmology. The demagnetization apparatus has been successfully operated and will be completely characterized in the coming year.

Current-dependent inverse frequency noise has been a long-standing limitation in the application of bolometric far infrared detectors to laboratory measurements which have significant photon flux background. Preliminary measurements have shown that ion-implanted contact techniques can eliminate this noise in the semiconducting chip used to measure the temperature of the bolometer. Our careful evaluation of bolometer performance has recently revealed that the thermal impedance between the semiconducting chip and the remainder of a composite bolometer seriously limits optical response in high backgrounds. Several solutions to this problem will be explored during the coming year.

We are continuing to explore the detailed performance of photoconductive infrared detectors. Our present approach is to use Ge:Ga detectors produced with low compensation levels from ultra-pure germanium starting material. These detectors show a dramatic increase in photoconductive gain compared with more highly compensated detectors. We are exploring the noise and responsivity of both low compensation and high compensation detectors as a function of background photon flux in order to understand deviations from ideal performance which reduce the practical utility of these detectors. Any resulting improvement in detector performance will directly impact our surface emission spectroscopy experiments. When detector performance is understood sufficiently, it should be possible to test experimentally some aspects of the theory of photon noise from thermal sources which were originally proposed by Einstein, but not yet tested in detail.

1980 PUBLICATIONS AND REPORTS

Refereed Journals

†1. Paul L. Richards and Tek-Ming Shen, "Superconductive Devices for Millimeter Wave Detection Mixing and Amplification," IEEE Trans. Electron Devices, Vol. ED-27, 10, 1909 (1980).

†2. Paul L. Richards and Tek-Ming Shen, "Conversion Gain in Millimeter Wave Heterodyne Mixers," Appl. Phys. Lett. 36, 777 (1980).

3. Paul L. Richards, "Direct Measurements of the Spectrum of the Near-Millimeter Cosmic Background," Physica Scripta, Vol. 21, 610 (1980).

†4. Tek-Ming Shen, Paul L. Richards, R. E. Harris, and F. L. Lloyd, "SIS Quasiparticle Junctions as Microwave Photon Detectors," Appl. Phys. Lett. 36, 480 (1980).

5. Paul L. Richards and David K. Lambert, "Measurement of Local Disorder in a Two-dimensional Electron Fluid," Phys. Rev. Lett. 44, 1427 (1980), LBL-10048.

6. William A. Challener, Paul L. Richards, S. Carlos Zilio, and H. L. Garvin, "Grid Polarizers for Infrared Fourier Spectrometers," Infrared Physics 20, #4, 215 (1980), LBL-8944.

Other Publications

1. Paul L. Richards and David P. Woody, "The Spectrum of the Microwave Background," in IAU Symposium 92, Objects at Large Redshift, G. O. Abell and P. J. E. Peebles (eds.), D. Reidel, Boston (1980), LBL-9843.

2. Paul L. Richards, Tek-Ming Shen, R. E. Harris, and F. L. Lloyd, "SIS Quasiparticle Junctions as Microwave Photon Detectors, and Mixers with Conversion Gain," American Physical Society, New York, March 24-28, 1980. Bull. Am. Phys. Soc. 25, 198 (1980).

LBL Reports

‡1. Paul L. Richards and Larry T. Greenberg, "Infrared Detectors for Low Background Astronomy Incoherent and Coherent Devices from one Micrometer to one Millimeter," Infrared and Millimeter Waves, Vol. 5 (to be published).

2. Robert B. Bailey, Takeo Iri, and Paul L. Richards, "Infrared Spectra of Carbon Monoxide on Evaporated Nickel Films: A Low Temperature Thermal Detection Technique," submitted to Surface Science, LBL-10159.

3. David K. Lambert and Paul L. Richards, "Far Infrared and Capacitance Measurements of Electrons on Liquid Helium," submitted to Phys. Rev., LBL-10343.

4. David P. Woody and Paul L. Richards, "Near-Millimeter Spectrum of the Microwave Background," submitted to Astrophysical Journal, LBL-10343.

5. Thomas T. Timusk and Paul L. Richards, "Near-Millimeter Wave Bandpass Filters," submitted to Applied Optics, LBL-11931.

Invited Talks

1. Paul L. Richards, "Infrared Spectra of Molecules on Metal Surfaces - A New Direct Detection Tech-

nique," 1980 Mid-winter Solid State Research Conference - Concepts in Surface Science, Laguna Beach, California, January 14-18, 1980.

2. Paul L. Richards and Tek-Ming Shen, "Superconducting Millimeter-Wave Devices," Millimeter-Wave Techniques and Their Applications, Epping, New South Wales, Australia, February 13-15, 1980.

3. Paul L. Richards and David P. Woody, "The Microwave Background Radiation," Millimeter-Wave Techniques and Their Applications, Epping, New South Wales, Australia, February 13-15, 1980.

4. Paul L. Richards, "The Spectrum of the Cosmic Microwave Background Radiation," Physics Colloquium, UC Irvine, March 7, 1980.

5. Paul L. Richards, "Microwave Devices Using Quasiparticle Tunneling in SIS Junctions," American Physical Society, New York, March 24-48, 1980, Bull. Am. Phys. Soc. 25, 197, (1980).

6. Paul L. Richards, "The Spectrum of the Cosmic Background Radiation - Superconducting Quasiparticle Heterodyne Mixers," Physics Seminar, Sao Carlos Campus, University of Sao Paulo, Brazil, July 9, 1980.

7. Paul L. Richards, "Infrared Measurements of Molecules on Metal Surfaces and Electrons on the Surface of Liquid Helium," Physics Seminar, Sao Carlos Campus, University of Sao Paulo, Brazil, July 10, 1980.

8. Paul L. Richards, "Infrared Measurements of the Spectrum of the Cosmic Microwave Background Radiation," Physics Seminar, University of Sao Paulo, Brazil, July 14, 1980.

9. Paul L. Richards, "Superconducting Quasiparticle Tunnel Junctions as Microwave Heterdyne Mixers," Physics Seminar, Pontifica Universidade Catolica de Rio, Rio de Janeiro, Brazil, July 17, 1980.

10. Paul L. Richards, "Infrared Spectra of Molecules Adsorbed on Metal Surfaces," Physics Seminar, University of Campinas, Campinas, Brazil, July 15, 1980.

11. Paul L. Richards, "Superconducting Receivers of Microwave Radiation," U.S. Naval Postgraduate School, Monterey, California, September 12, 1980.

12. Paul L. Richards, Tek-Ming Shen, R. E. Harris, and F. L. Lloyd, "SIS Quasiparticle Junctions as Microwave Photon Detectors, and Mixers with Conversion Gain," 1980 Applied Superconductivity Conference, Santa Fe, New Mexico, September 29 - October 2, 1980.

13. Paul L. Richards, "SIS Quasiparticle Tunnel Junctions as Detectors and Mixers at Millimeter Wavelengths," Fifth International Conference on Infrared and Millimeter Waves, Wurzburg, Germany, October 8, 1980.

14. Paul L. Richards, "Superconducting Millimeter Wave Receivers Reach Fundamental Sensitivity Limits," Physics Colloquium, UC Berkeley, October 15, 1980.

15. Paul L. Richards, "Superconducting Millimeter Wave Receivers Reach Fundamental Sensitivity Limits," Physics Colloquium, UC San Diego, October 29, 1980.

* * *

†Work supported by the U.S. Office of Naval Research.
‡Work supported by NASA.

b. Experimental Solid-State Physics and Quantum Electronics*

Y. Ron Shen, Investigator

1. SURFACE ENHANCED SECOND HARMONIC GENERATION†

Chenson K. Chen, A. Rubens B. de Castro, and Y. Ron Shen

Surface enhanced Raman scattering (SERS) has recently caused a great deal of excitement.[1] It was found experimentally that the effective Raman cross-sections of some molecules on a roughened silver surface can be 10^5 to 10^6 times larger than those of the same molecules in solution.[2] Various mechanisms have been suggested to explain the enhancement. Some involve molecular interaction between the molecules and the metal (known as the chemical effect).[1] Others rely on the electromagnetic interaction between molecules and metal (the electromagnetic effect).[1] The chemical effect is often the main issue of discussion on SERS, evidenced by the observation that only selective molecules on metal surfaces exhibit Raman enhancement.[2] However, there is difficulty in understanding how an allowed Raman transition of the molecules can have its strength increased by 10^6 through metal-molecule interaction but have its corresponding Raman shift nearly unchanged. The electromagnetic effect, on the other hand, can lead to an enhancement of ~ 10^4, with controlled surface preparation under ultrahigh vacuum. The local field created by local surface plasmon excitation on the rough surface structure is presumably responsible for the enhancement. Most likely, however, it is the combined force of the chemical effect and the electromagnetic effect that gives rise to the total enhancement of ~ 10^6.

One would like to separate the chemical effect from the electromagnetic effect. This is, unfortunately, not easy with the molecules adsorbed on the metal surface. We realize, however, that if the local field enhancement picture is correct, the surface enhanced phenomenon should also be present for all nonlinear optical processes. If the metal surface alone has a detectable nonlinearity, the enhancement on the nonlinear optical effect should be observable on a metal-air interface. Here, our recent measurements on second harmonic (SH) reflection (2ω at 0.53 μm) from smooth and rough surfaces of evaporated films and bulk samples of silver, copper, and gold are presented. Large enhancements due to surface roughness were actually observed.

With the 1.06 μm TM input, the second harmonic signal from the smooth film was a well collimated beam in the direction of specular reflection and was polarized in the TM mode. The signal from an electrolytically roughened surface, however, was highly diffuse, nearly isotropic in angular distribution, and independent of both input and output polarizations. In both cases, the SH was generated at a metal-air interface, with the input laser at a 45° angle of incidence.

The spectra of the output signals are shown in Fig. 1 for silver. The second harmonic generation was evidenced by the sharp peak at 0.53 μm. In addition, a broad spectral background, highly diffuse and extending from ~ 3500 Å to the infrared (limited to ~ 6000 Å by our detection system), also appeared. For the smooth film, the background was weak; but, for the rough surface, it was exceptionally strong.

The second harmonic signal from the electrolytically roughened surface of bulk silver (total charge transfer ~ 65 mCoul/cm^2), integrated over the 2π emission solid angle, was found to be 1 x 10^4 times larger than the collimated SH from the smooth film. Note that a similarly prepared surface produced a surface Raman enhancement of ~ 10^6 for pyridine. With less electrolytic cycling, both the

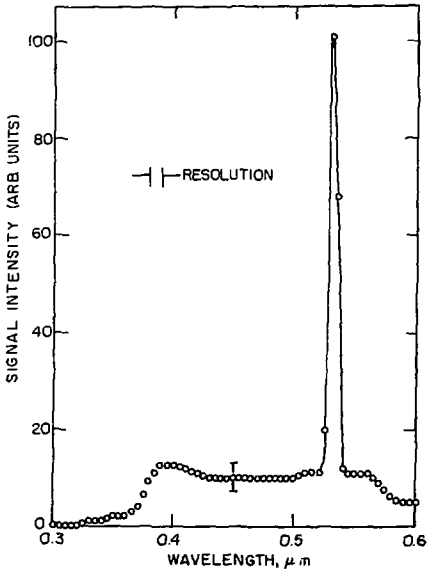

Fig. 1. Spectral distribution of the nonlinear signal from a rough bulk silver sample.
(XBL-809-5840)

*This work was supported by the Director, Office of Energy Research, Office of Basic Energy Sciences, Materials Sciences Division of the U. S. Department of Energy under Contract No. W-7405-ENG-48.

second harmonic and the background output became weaker, indicating that roughness was essential for the observed background and signal enhancement.

The laser power dependency of the second harmonic signals from the smooth and rough surfaces were also measured. In all cases, the SH signal was quadratic in laser power, as shown in Fig. 2. For the electrolytically cycled bulk silver samples, the power dependency of the broadband background was found to be ~ $I(\omega)^3$ on the anti-Stokes side and between $I(\omega)^2$ and $I(\omega)^3$ on the Stokes side, and the pulse shape closely resembled the pump laser pulse. However, for the electrolytically cycled silver films (charge transportation < 25 mC/cm^2), the power dependency of the broadband background was found to be ~ $I(\omega)^6$ on the anti-Stokes side and ~ $I(\omega)^3$ on the Stokes side.

Similar results were obtained for gold, although both the second harmonic signal and the luminescence background from the rough surface was much weaker. The observed enhancement for second harmonic generation at the electrolytically cycled surface was ~ 10^3. For copper, the broadband luminescence from the rough surface was several times stronger than in silver, and masked off the narrowband second harmonic signal. Consequently, we were only able to say that the surface enhancement for SH on copper, if any, was less than 5 x 10^3.

Using the theory of local field correction due to plasmon resonance on rough structure, we estimated from our experimental result a local field enhancement factor of ~ 20. This value of local field correction is very reasonable considering that on a smooth silver-air interface, the field enhancement due to surface plasmon excitation can already be as high as ~ 20. Copper and gold are expected to have smaller $L(\omega)$ because of the larger values in their $Im(\varepsilon(\omega))$. Measurement of the frequency dependence of enhanced second harmonic generation on rough surfaces is currently in progress.

* * *

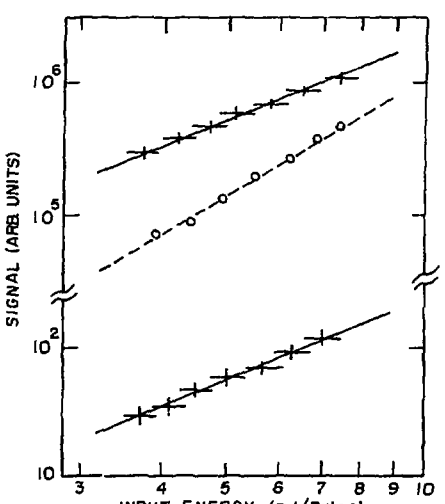

Fig. 2. Power dependencies of the nonlinear signal on silver. The upper and lower solid curves show the quadratic dependency of the diffuse SH signal from the rough bulk sample and of the collimated SH signal from the smooth film, respectively; the dashed curve shows the cubic dependency of the diffuse anti-Stokes signal from the rough bulk sample. (XBL-809-5841)

†Brief version of LBL-11596.

1. See, for example, the latest review by T. E. Furtak and J. Reyes, Surf. Sci. 93, 351 (1980), and references therein.
2. D. L. Jeanmaire and R. P. Van Dyne, J. Elec. Chem. 84, 1 (1977);
M. Fleischmann, P. J. Hendra, and A. J. McQuillan, Chem. Phys. Lett. 26, 163 (1974).

2. LOCAL REFRACTIVE INDEX MEASUREMENT ON A CHOLESTERIC LIQUID CRYSTAL USING THE SURFACE PLASMON TECHNIQUE†

Nan-Ming Chao,‡ Kung-Chao Chu,§ and Y. Ron Shen

Reports on refractive index and optical birefringence measurements of liquid crystals have appeared frequently in recent literature,[1] but few deal with materials in the cholesteric phase. This is presumably because of the difficulty in extracting the "local" refractive indices from the measured quantities, owing to the helical structure of the cholesterics. The information of the local refractive indices in a plane perpendicular to the helical axis is nevertheless very important, since the corresponding linear birefringence reflects the orientational ordering of molecules in that plane.

Several methods are commonly used to determine refractive indices (or birefringence) of cholesteric liquid crystals, including the Abbe refractometer method, the optical rotatory dispersion (ORD) method, and the circular dichroism (CD) method. These methods, however, are rather inaccurate. We propose a surface plasmon technique which allows us to determine the local refractive indices of a cholesteric to an accuracy of $\lesssim 10^{-4}$, clearly better than the other techniques.

A surface plasmon is a transverse magnetic electromagnetic wave traveling along the interface between a metal and a dielectric. It decays exponentially in directions normal to the interface with decay lengths of the order of λ/π, where λ is the wavelength in the boundary media, so that its propagation characteristics are quite sensitive to the property of the dielectric medium. In our experiment, we used Kretschmann's scheme[2] to excite the surface plasmon on an interface between the

metal and the cholesteric, as shown in Fig. 3. The reflected TM wave was monitored as a function of the incident angle. The resulting reflectivity curve was then fit by the theory of linear reflection using the refractive indices as adjustable parameters, and the refractive indices were deduced.

The sample, arbitrarily chosen, was a 1.75:1.00 mixture of cholesteryl chloride and cholesteryl myristate. This was inserted in a two-stage temperature controlled oven that was in turn mounted on a rotating stage driven by a stepping motor. The temperature stability could be better than 1 mK.

Typical reflectivity curves at $T < T_c$ and $T > T_c$, obtained with a CW He-Ne laser, are shown in Fig. 4, where T_c is the isotropic-cholesteric transition temperature. The theoretical fit is shown as solid lines in the figure. The local refractive indices $n_{\parallel} - n_{\perp}$ in the quasi-nematic layer of the cholesteric liquid crystal deduced are shown in Fig. 5. The accuracy of these n values, ~ 10^{-4}, was limited by the angular resolution of our apparatus (0.01°).

The orientational order parameter is one of the most important quantities of a liquid crystal. It is commonly believed that the cholesteric structure can be regarded as a twisted nematic or that a nematic is a special case of cholesterics with an infinite pitch. Thus, the molecular orientational ordering of a cholesteric in the planes perpendicular to the helical axis should resemble that of a nematic in the bulk, and the theory of molecular ordering for a nematic should apply equally well to the molecular ordering in the quasi-nematic layers of a cholesteric. The local birefringence $\Delta n = n_{\parallel} - n_{\perp}$ can be used as the orientational order parameter for molecules in the quasi-nematic layers. We can therefore compare the experimental values of Δn with the theoretical models for nematic ordering, as shown in Fig. 6. Here, the solid curve was obtained from the Maier-Saupe mean field theory[3] and the dashed curve from the improved theory of Humphries, James and Luckhurst (HJL).[4] The latter is in excellent agreement with our results. As a comparison between cholesterics and nematics, we have also plotted in Fig. 6 the order parameter results of anisaldazine

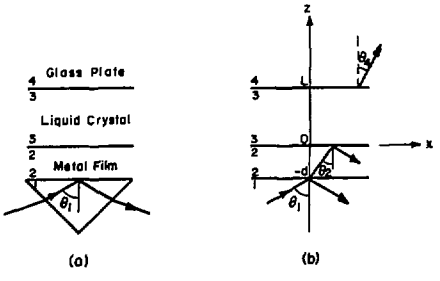

Fig. 3. Schematic of the sample assembly. (XBL 804-5003)

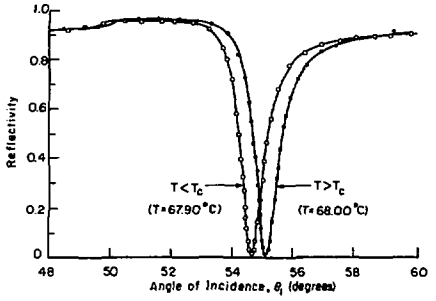

Fig. 4. Reflectivity curves versus the angle of incidence θ_1 at $T < T_c$ and $T > T_c$. The solid curves are theoretical curves obtained by nonlinear least square fitting. (XBL 804-5004)

from the optical anisotropy measurements and MBBA from the Raman scattering measurements. The good agreement of these different sets of data with the theoretical curve of HJL indicate first, that the HJL theory is a valid description of the nematic ordering, and second, that the molecular ordering in the planes perpendicular to the helical axis of a cholesteric is indeed nematic.

* * *

†Brief version of a paper of the same title submitted to Mol. Cryst. Liq. Cryst. This work was supported by the National Science Foundation under Grant No. DMR78-18826.

‡On leave from Tsinghua University, Beijing, People's Republic of China.

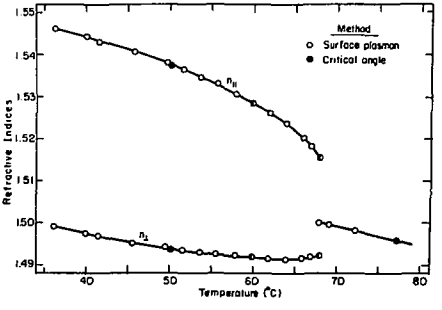

Fig. 5. Refractive indices of the mixture of 1.75 cholesteryl chloride and 1 cholesteryl myristate versus temperature. (XBL 804-5006)

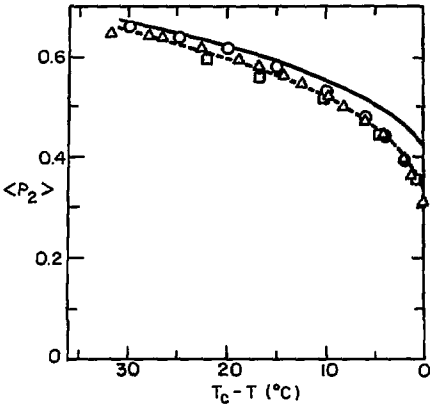

Fig. 6. Theoretical and experimental order parameters $\langle P_2 \rangle$ versus temperature: the solid line is obtained from the Maier-Saupe theory and the dashed line from the Humphries-James-Luckhurst theory with parameters $\lambda = -0.55$ and $\gamma = 10$. Squares are values deduced from measurements of optical anisotropy of anisaldazine in the nematic phase. Circles are results from Raman scattering in MBBA. Triangles are normalized Δn values for the cholesteric mixture. (XBL 804-5008)

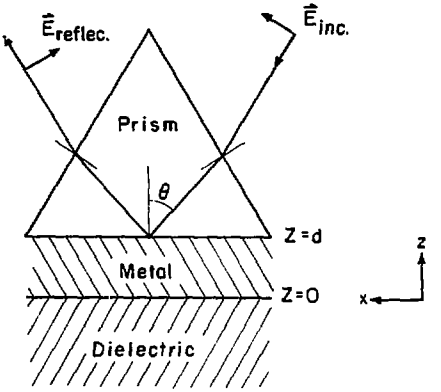

Fig. 7. Kretschmann geometry for exciting surface plasmons. The fields incident on the prism excite surface plasmons at the metal-dielectric interface. (XBL 8011-6281)

§Permanent address: Bell Laboratories, Murray Hill, New Jersey.

1. I. Haller, Progress in Solid State Chemistry 10, 103 (1975), and references therein.
2. K. Kretschmann, Zeit. Phys. 241, 313 (1971).
3. W. Maier and A. Saupe, Z. Naturforsch. 13a, 564 (1958); 14a, 882 (1959); 15a, 287 (1960).
4. R. L. Humphries, P. G. James, and G. R. Luckhurst, J. Chem. Soc. Faraday Trans. II, 68, 1031 (1972).

3. SURFACE NONLINEAR OPTICS†

Chenson K. Chen, A. Rubens B. de Castro, and Y. Ron Shen

Surface plasmons (SP) are electromagnetic waves propagating along a metal-dielectric interface with field amplitudes confined to the interface. Although their existence was predicted as early as 1909, it was not until the attenuated total reflection (ATR) technique[1] was developed in 1968 by Otto and improved in 1971 by Kretschmann (see Fig. 7) that surface plasmons have become a useful surface probe. In recent years, surface plasmons have had interesting applications in the study of overlayers and molecular adsorption on surfaces, in the probing of phase transitions, and in the measurement of refractive indices. In our laboratory, we have been interested in the nonlinear interaction of surface plasmons for two reasons: first, although nonlinear optics in the bulk is a well-developed field, surface nonlinear optics has been relatively unexplored; and second, we would like to study the possibility of using surface nonlinear optics for material studies.

The theory of nonlinear interaction of surface plasmons is governed by the nonlinear Maxwell equations,

$$\nabla \times (\nabla \times \vec{E}(\omega)) - c\frac{\omega^2}{c^2}\vec{E}(\omega) = \frac{4\pi\omega^2}{c^2}\vec{P}^{NL}(\omega)$$
$$\nabla \cdot (\vec{D} + 4\pi\vec{P}^{NL}) = 0 \qquad (1)$$

with the nonlinear driving term

$$\vec{P}^{NL}(\omega) = \overleftrightarrow{\chi}^{NL}:\vec{E}_1(\omega_1) \ldots \vec{E}_n(\omega_n) \qquad (2)$$

where $\vec{E}_1(\omega_1) \ldots \vec{E}_n(\omega_n)$ are the input surface plasmon fields. Equation (1) can then be solved in a straightforward manner using appropriate boundary conditions.

Harmonic Generation by Surface Plasmons. The simplest nonlinear optical process is optical second harmonic generation. Second harmonic generation by SP is, in fact, readily observable even at an air-metal interface, as first demonstrated by Simon and coworkers.[2] In this case, metal is the nonlinear medium. However, its second-order nonlinearity is small because of the existence of inversion symmetry. The induced second-order nonlinear polarization arises from electric-quadrupole and magnetic-dipole contribution and can be written in the form

$$\vec{P}^{(2)}(2\omega) = \alpha(\vec{E}\cdot\nabla)\vec{E} + \beta(\nabla\cdot\vec{E})\vec{E} + \gamma\vec{E}\times\beta. \quad (3)$$

From the wavevector matching condition, it is easily seen that two counter-propagating fundamental SP should generate a bulk second harmonic output propagating along the surface normal.[3] However, the corresponding nonlinear polarization obtained from Eq. (3) has a vanishing component parallel to the surface. Consequently, no second harmonic generation along the surface normal should be observed. We have verified experimentally that this is indeed the case. By varying the angle between the two fundamental SP, we should be able to determine the coefficients α, β, and γ in Eq. (3) separately. Such work is still in progress. Harmonic generation by SP is actually a viable method for studying optical nonlinearity of metals.

The second harmonic generation can be greatly enhanced if, in the above case, air is replaced by a nonlinear dielectric medium, for example, quartz or KDP. The process is now dominated by the nonlinearity of the nonlinear dielectric. Symmetry of the medium generally allows the existence of a nonlinear polarization component parallel to the surface, even for counter-propagating SP. Thus, second harmonic generation along the surface normal becomes easily observable.[3] The one-to-one correspondence between the propagation direction of the second harmonic beam in the three-dimensional space and the interaction geometry of the two SP in the two-dimensional plane may find applications in information processing.

We have also observed third harmonic generation by surface plasmons at a metal-methanol interface. The nonlinearity was dominated by the liquid as the signal was reduced beyond detectibility when the methanol was replaced by air. The experimental setup is shown in Fig. 8, with the fundamental surface plasmon at 1.06 μm excited in the Kretschmann configuration, and with the third harmonic signal detected on the prism side. The results are shown in Fig. 9. As expected, the third harmonic signal is maximum when the surface plasmon is optimally excited, and in addition, was monochromatic at 0.35 μm and TM polarized with ~ 1 mrad beam divergence. From the observed signal and using the solution of the nonlinear Maxwell equations, we estimated that for methanol $\chi^{(3)}_{1111}(3\omega = \omega+\omega+\omega)$ $\sim 3\times10^{-14}$ esu.

Surface CARS. Coherent anti-Stokes Raman spectroscopy (CARS) has recently become a useful nonlinear spectroscopic technique. Recently, we demonstrated the feasibility of surface CARS at a silver-benzene interface, using the setup shown in Fig. 10.[4] Physically, two input surface plasmons at frequencies ω_1 and ω_2 beat with one another in the benzene, creating a nonlinear polarization at $2\omega_1 - \omega_2$. This in turn excites a surface plasmon at the anti-Stokes frequency. The surface CARS signal is maximized when the input surface plasmons are optimally excited, the frequency difference $\omega_1 - \omega_2$ is adjusted to a Raman resonance of the benzene, and the phase matching condition is satisfied. Here, additional surface CARS results in pyridine and absorbing media are presented. For surface CARS at a silver-pyridine interface, the experimental resonant spectrum of the anti-Stokes output

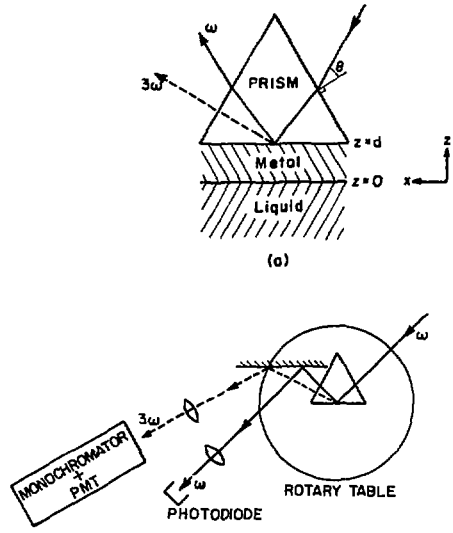

Fig. 8. (a) The sample assembly. (b) Schematic of the experimental setup. (XBL 8011-6283)

was obtained by scanning $\omega_1 - \omega_2$ as shown in Figs. 11-12, in good agreement with the theoretical prediction. For an input of 2.8 mJ/cm^2 at ω_1 and 32 mJ/cm^2 at ω_2 with a pulsewidth of 30 ns and a beam cross section of 0.25 cm^2, the measured signal at the resonance 991 cm^{-1} peak is 1.5×10^4 photons/pulse, while the theoretical prediction is 3.3×10^4 photons/pulse. Other characteristic features of the observed anti-Stokes output also agree well with the surface CARS prediction.

Surface plasmons actually have rather short attenuation lengths ℓ because of the large loss in the metal. Typically, $\ell = 1/K'' \sim 10$ μm on silver in the visible. This means that the interaction length in surface CARS is only of the order of 10 μm. Even if the dielectric medium is strongly absorbing, the anti-Stokes is not expected to be appreciably reduced by the absorption. We have tested this expectation with a 1:2 acetone-benzene mixture on silver. When 1.1 mM of oxazine 725 is dissolved in the solution so that it has an absorption coefficient of $\alpha \sim 400$ cm^{-1} at the anti-Stokes frequency, the anti-Stokes output remains essentially unchanged.

In summary, surface CARS has the characteristics of large induced nonlinear polarization, small field penetration depth into the medium at the surface, short nonlinear interaction length, a highly

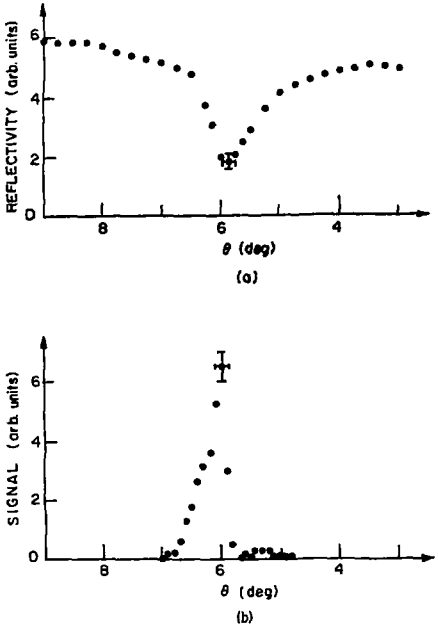

Fig. 9. (a) Reflectivity of the incident laser beam versus θ; θ is defined in Fig. 8(a). (b) Third harmonic intensity versus θ. (XBL 8011-6284)

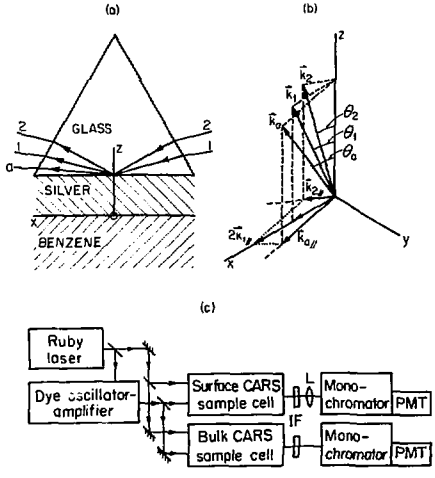

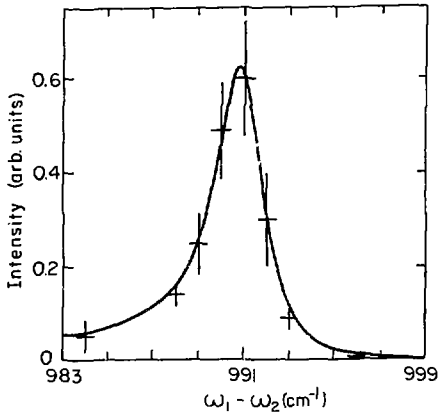

Fig. 11. Surface CARS signal versus $\omega_1 - \omega_2$ near the 991 cm^{-1} Raman resonance of pyridine. (XBL 807-5505)

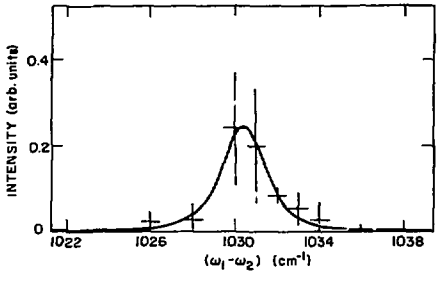

Fig. 12. Surface CARS signal versus $\omega_1 - \omega_2$ near the 1030 cm^{-1} Raman resonance of pyridine. (XBL 8011-6285)

Fig. 10. (a) Prism-metal-liquid assembly for the surface CARS measurement. Beam 1 is in the x-z plane, but beam 2 and the output are not. (b) Wave vectors in the glass prism, with components in the x-y plane phase matched. (c) Diagram of the apparatus: IF is an interference filter and L is a lens. (XBL 796-3540)

directional coherent output, and the possibility of an effective reduction of luminescence background. Surface CARS can therefore be used to study materials with strong absorption and luminescence, thin films, molecular overlayers, and adsorbed molecules, and other surface specific problems. Surface CARS output increases with the input laser intensities as $I^2(\omega_1)I(\omega_2)$. Ultimate sensitivity is limited by optical damage on the surface. Since the damage usually has a fluence threshold rather than an intensity threshold, the ultimate sensitivity of surface CARS can be greatly improved by using picosecond pump pulses. From our experimental results with Q-switched pulses, we can estimate an output of ~ 10^{11} photons/pulse for benzene on silver from an input of 10 μJ/pulse with a pulse width of 10 ps and a focal spot of 0.15 mm^2. The signal will reduce by a factor of 10^4 to 10^5 if there is only a monolayer of benzene molecules on silver. Thus, with picosecond pulses, surface CARS should be sensitive enough to detect a submonolayer of adsorbed molecules.

* * *

†Brief version of LBL-11252.

1. A. Otto, Z. Phys. 216, 398 (1968); E. Kretschmann, Z. Phys. 241, 313 (1971).
2. H. J. Simon, D. E. Mitchell, and J. G. Watson, Phys. Rev. Lett. 33, 1531 (1974).
3. C. K. Chen, A. R. B. de Castro, and Y. R. Shen, Opt. Lett. 4, 393 (1979).
4. C. K. Chen, et al. Phys. Rev. Lett. 43, 946 (1979).

4. TWO-PHONON COHERENT ANTI-STOKES RAMAN SCATTERING†

Y. Ron Shen

Laser Raman spectroscopy has been most valuable for study of two-phonon Raman scattering. The high sensitivity of the technique allows the probing of details in the two-phonon spectra. Recently, coherent anti-Stokes Raman scattering (CARS) (or coherent Raman spectroscopy in general) has been developed. It has been suggested that the latter technique can yield as much or more information than the conventional Raman scattering technique. This expectation follows from the general conviction that the third-order nonlinear susceptibility governing CARS should be proportional to the product of two Raman matrix elements (or in the off-resonance case, proportional or nearly proportional to the Raman cross section). The classical description of one-phonon CARS is as follows: The incoming laser waves at ω_1 and ω_2 beat in the crystal to create a coherent phonon wave at $\omega_1 - \omega_2 \simeq \omega_{phonon}$, which in turn coherently scatters the laser beam at ω_1 to generate an anti-Stokes wave at $\omega_a = 2\omega_1 - \omega_2$. Questions now arise on how the two-phonon CARS should be described. Does the beating of the pump waves at ω_1 and ω_2 create simultaneously two coherent phonon waves, these two waves then interacting simultaneously with the wave at ω_1 to generate the anti-Stokes output? Or is the phonon wave generated actually a coherent two-phonon bound-state wave? Which phonon relaxation time would the time-delayed CARS measure? If the existence of two-phonon bound states and the simultaneous creation of two coherent phonon waves are not likely, does the correspondence between spontaneous Raman scattering and CARS break down in the two-phonon or multiphonon cases? Would the two-phonon CARS then be observable? Although CARS has been well developed in recent years, no experimental observation of two-phonon CARS has ever been reported.

By treating phonons as waves and coherent Raman scattering as the result of photon-phonon wave coupling, we can show that two-phonon CARS should yield a third-order nonlinear susceptibility that is proportional to the two-phonon Raman cross-section, if the phonon occupation number is nearly zero. This is usually the case since high-frequency phonons are always highly damped. However, if the incoming pump fields at ω_1 and ω_2 are very strong, the two phonon waves can be generated by a parametric amplification process with a resultant exponential growth. Then the two-phonon CARS will yield a spectrum very different from a normal CARS spectrum, although the resonance still occurs at the frequency $\omega_1 - \omega_2 = 2\omega_{phonon}$. No two-phonon bound state is needed for the observation of two-phonon CARS. Two-phonon Raman lines can be as sharp and strong as one-phonon Raman lines, and should therefore be observable. Our derivation here also shows that the time-delayed CARS signal should decay exponentially with a time constant given by the inverse of the sum of the damping constants of the two phonons.

* * *

†Brief version of LBL-10715.

5. NONLINEAR SPECTROSCOPY BY MULTIRESONANT FOUR-WAVE MIXING†

Jean-Louis Oudar‡ and Y. R. Shen

Four-wave mixing is a well-known nonlinear optical effect. It describes a mixing process in which three propagating light waves interact nonlinearly in a medium and generate a fourth wave. The third-order nonlinear susceptibility that governs the process should exhibit resonances characteristic of the medium. They can be probed through the resonant enhancement of the four-wave mixing output. Thus, the process can be used as a tool for spectroscopic studies. With the recent advances of tunable lasers, it is being rapidly developed into an important practical spectroscopic technique for many applications, including chemical analysis, combustion research, studies of material properties, etc. The most important advantages of this technique are its capability for high-resolution spectroscopic study, elimination of strong fluorescence background, and time-resolving measurements of ultrafast dynamic properties.

In most four-wave mixing experiments reported in the literature, single resonances of the third-order nonlinear susceptibility are usually probed and studied. Singly resonant four-wave mixing has

the merit that the experimental arrangement is relatively simple and interpretation of the results is often straightforward. It generally yields the kind of spectroscopic information one would obtain from one-photon or two-photon transition measurements. In comparison to ordinary Raman scattering, four-wave mixing with double or triple resonances, like resonant Raman scattering, should be able to yield more selective spectroscopic information. In addition to the resonant frequencies, the dipole matrix elements between selective states can, in principle, be deduced. Extremely strong resonant enhancement is of course also expected in doubly or triply resonant four-wave mixing, as has been demonstrated in recent experiments. Druet et al.[1] have recently shown that it is also possible to obtain Doppler-free spectra with doubly and triply resonant four-wave mixing.

We give here a thorough discussion on the various problems involved in doubly and triply resonant four-wave mixing processes. We have derived expressions for third-order nonlinear susceptibilities under different resonant conditions. Both one-photon and two-photon resonances are explicitly displayed, including a predicted two-photon resonance between two excited states. Since real absorption occurs in resonant four-wave mixing, the nonlinear susceptibilities may consist of a part involving only transverse relaxation and a part involving also longitudinal relaxation. The latter often dominates if the longitudinal relaxation time is much longer than the transverse relaxation time.

The resonant spectrum of a singly resonant third-order susceptibility is usually dominated by inhomogeneous broadening. This is not the case with double and triple resonances. Whenever there is a product of two resonant denominators with damping constants of opposite signs, the inhomogeneous broadening of the corresponding resonant line of the nonlinear susceptibility can be greatly reduced. This can be considered as a generalization of the saturation spectroscopy. We show theoretically how the Doppler-free spectrum can be obtained by doubly or triply resonant four-wave mixing, and extend the consideration to ions or molecules in solids.

The output of four-wave mixing in doubly and triply resonant cases is often complicated by absorption at the pump frequencies and/or the output frequency. Absorption reduces the active length of interaction, limits the pump intensity, and broadens the phase-matching peak. Moreover, the dispersion of absorption near resonance distorts the resonant structure of four-wave mixing and makes the four-wave spectrum difficult to interpret. We have studied how the output depends on resonances, absorptions, and polarizations of the four waves, and show that it is possible to eliminate the dispersion effect of absorption by polarization measurements.

Resonant four-wave mixing can provide detailed spectroscopic information about various transitions. We have considered a number of physical problems in which the application of resonant four-wave mixing spectroscopy is most attractive. From the resonant four-wave mixing spectra, both the transition frequencies and the transition matrix elements can be deduced. In some cases, spectra with reduced inhomogeneous broadening can be obtained. This is most interesting for studies of Raman transitions between excited states because they cannot be studied by other techniques. Doubly or triply resonant mixing with an induced population change also leads to a measurement of the longitudinal relaxation times for various states. Then, by observing the difference between different but related resonant four-wave mixing spectra, one should be able to distinguish resonant Raman scattering and resonant flourescence, which has been a controversy in recent years.

Finally, we give some consideration to the practical experimental problems. The incoherent scattering and luminescence background can be minimized by spatial and frequency filtering, and in some cases, by time discrimination. The nonresonant background of the resonant mixing spectrum is most effectively suppressed by induced gain or loss spectroscopy or by polarization arrangement. The signal-to-noise ratio of four-wave mixing is studied. In most cases with pulsed laser sources, the noise arises mainly from laser intensity fluctuations. With the polarization-sensitive four-wave mixing, however, this type of noise is practically eliminated.

* * *

†Brief version of LBL-10200.

‡Permanent address: CNET, Department RPM, 196 rue de Paris, 92220 Bagneux, France.

1. S. A. J. Druet, J-P. E. Taran, and Ch. J. Bordé, J. de Physique 40, 841 (1979).

6. EXPERIMENT ON MULTI-RESONANT FOUR-WAVE MIXING†

Robert W. Smith and Y. R. Shen

The theory of multi-resonant four-wave mixing indicates several interesting features to be examined experimentally. Most notable among these are the lineshapes of the processes which should show the narrowing well below the inhomogeneous width if the homogeneous width is much smaller. Also, it should be possible to determine dipole matrix elements and Raman polarizabilities between various levels of the material system using these nonlinear techniques. Because ions in condensed matter can provide sharp electronic transitions that show inhomogeneous strain broadening, they are nearly ideal to demonstrate the features of the multi-resonant susceptibilities. Furthermore, the four-wave mixing techniques can be used to study the physical parameters of the ions, which to date have been studied mostly by absorption and fluorescence techniques.

We used in our experiment a sample of LaF_3:1% Pr, and studied the triply resonant RIKE (Raman induced Kerr effect) process involving resonant transitions $^3H_4 \rightarrow {}^3P_0 \rightarrow {}^3H_6$. From the linear absorption and laser emission threshold measurements of the

sample, we could derive the oscillator strengths for the $^3H_4 \rightarrow {}^3P_0 \rightarrow {}^3H_6$ transitions from which we estimated the third-order nonlinear susceptibility for the triply resonant RIKE process to be

$$(\chi_R^{(3)})_{max} \sim 2 \times 10^{-8} \text{ esu.}$$

This indicated that the RIKE signal could be easily detected, and indeed even with flash-pumped dye lasers, we could measure the RIKE spectrum as shown in Fig. 13 and found

$$(\chi_R)_{max} \approx 4.8 \times 10^{-8} \text{ esu}$$

with an estimated error of about ± 30% due to the errors in measuring the intensity at ω_1 and the only approximate plane wave beam profiles. From this value of $|(\chi_R)_{max}|$, we obtained a more accurate value for the electric dipole matrix element $\langle {}^3P_0|\mu|{}^3H_6\rangle \approx 9.7 \times 10^{-21}$ esu.

Of interest also in this triple resonance case is the predicted lineshape of the susceptibility--both as a function of ω_1 and ω_2. According to the theory, the resonant RIKE spectrum as a function of ω_2 should show a line narrowing from the inhomogeneous broadening (the expected narrow linewidth in the absence of accidental degeneracy is the sum of the homogeneous linewidths of the two transitions), while the spectrum as a function of ω_1 should resemble the linear absorption spectrum. We found that this is indeed the case as shown in Figs. 13 and 14.

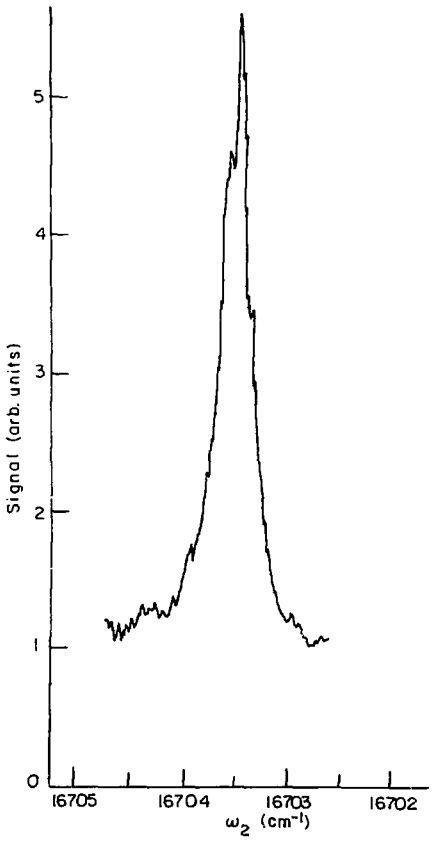

Fig. 13. RIKE spectrum with ω_1 exactly on resonance. Plot of output signal through crossed polarizer as ω_2 is scanned. (LBL-807-5549)

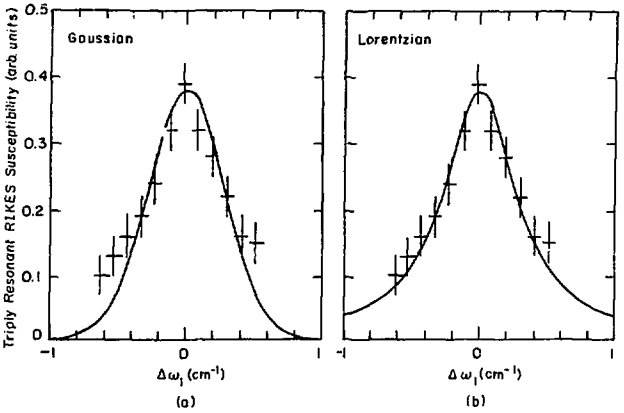

Fig. 14. Peak RIKE susceptibility as ω_1 is scanned across the one-photon resonance. (a) Gaussian fit to data; (b) Lorentzian fit to same data. (XBL 807-5550)

* * *

†Brief version of LBL-11518.

7. LASER INTERACTION WITH MOLECULAR BEAMS

Y. Ron Shen, *in collaboration with* Yuan T. Lee's group.

See Section on Molecular Beam Laser Isotope Separation.

RESEARCH PLANS FOR CALENDAR YEAR 1981

Second harmonic generation from an interface between media with inversion symmetry should be sensitive enough to detect a single monolayer of adsorbed molecules at the interface. Experiments will be performed to test the idea. Different adsorbed molecules on different surfaces will be tried. In particular, molecules adsorbed on metal and semiconductor surfaces in an electrolytic process will be studied in more detail. Experiments on molecular monolayers on surfaces in high vacuum will also be considered. The results may find important applications in the study of liquid-solid and gas-solid interfaces.

Sum-frequency generation of adsorbed molecules should also be observable. With a tunable laser, it is then possible to record the spectrum of the adsorbed molecules. This experiment will be performed with a Nd:YAG laser together with an optical parametric oscillator. The resolution is expected to be less than 1 cm^{-1}, far better than for electron loss spectroscopy. The technique, if successful, is unique for study of adsorbed molecules at liquid-solid interfaces.

A rough silver surface can enhance a nonlinear optical process at the surface by many orders of magnitude. It is therefore expected that coherent anti-Stokes Raman scattering (CARS) from adsorbed molecules on the rough surface may be observable. The experiment will be carried out on CN or pyridine adsorbed on electrolytically roughened silver surface. The CARS spectrum of CN or pyridine will be measured.

Surface-enhanced Raman scattering (SERS) will be studied by surface plasmon excitation in an effort to determine the relative contribution of the surface field to the enhancement. Weakly cycled silver film in electrolytic solution with adsorbed pyridine will be used in the experiment. Aside from the macroscopic surface plasmon enhancement, further enhancement from local field effects due to surface roughness and molecule-metal interaction is expected.

Optical nonlinearities of metals have rarely been studied. This is because metals are opaque to light. It is, however, possible to study the nonlinearities by surface plasmon excitation or by nonlinear reflection. Second harmonic generation and third-harmonic generation from metal surfaces will be performed. The relative magnitudes of electric-quadrupole and magnetic-dipole contribution may be deduced from the angular distribution of the output.

In second harmonic generation from metal surfaces, a broad luminescence background has been simultaneously observed. The physical mechanism

giving rise to this luminescence background is not yet understood. Measurements of the spectrum as a function of laser intensity, angular position, temperature, etc., may help in unraveling the mystery. Multiphoton excitation and phonon-assisted emission may be responsible for the luminescence.

A mode-locked picosecond laser system will be in its final construction stage. It will be used to pump an optical parametric oscillator to yield a tunable infrared source. The system will be tried out on a surface nonlinear optics problem. The high peak intensity with limited energy per pulse will greatly improve the signal-to-noise ratio of the output without reaching the surface damage threshold.

Resonant four-wave mixing as a spectroscopy technique will be tested on magnons in magnetic crystals. The inhomogeneous broadening of the two-magnon lines may be suppressed by the wave mixing technique. Transient resonant four-wave mixing with picosecond pulses will also be considered. Emphasis will be on measurements of lifetimes and energy transfer.

A theoretical study will be made on the relation between anharmonicity and phonon localization. Neither local modes nor extended phonons can correctly describe the excitation of anharmonic solids. Transition from the local oscillator picture to the extended phonon picture should occur if one could continuously increase the phonon dispersion. This appears as a phonon analog to the metal-insulator transition.

1980 PUBLICATIONS AND REPORTS

Refereed Journals

1. J-L. Oudar and Y. R. Shen, "Nonlinear Spectroscopy by Multi-Resonant Four-Wave Mixing," Phys. Rev. A 22, 1141 1980, LBL-10220.

2. P. A. Schulz, Aa. S. Sudbø, E. R. Grant, Y. R. Chen, and Y. T. Lee, "Multiphoton Dissociation of SF_6 by a Molecular Beam," J. Chem. Phys. 72, 4985 (1980), LBL-9702.

3. C. K. Chen, A. R. B. de Castro, and Y. R. Shen, "Coherent Second Harmonic Generation by Counter-Propagating Surface Plasmons," Opt. Lett. 4, 393 (1979), LBL-9542.

4. K. C. Chu, C. K. Chen, and Y. R. Shen, "Measurement of Refractive Indices and Study of Isotropic-Nematic Phase Transition by the Surface Plasmon Technique," Mol. Cryst. Liq. Cryst. 59, 97 (1980), LBL-9398.

5. P. A. Schulz, Aa. S. Sudbø, D. J. Krajnovich, H. S. Kwok, Y. R. Shen, and Y. T. Lee, "Multiphoton Dissociation of Polyatomic Molecules," Annual Rev. Phys. Chem. 30, 379 (1979), LBL-8751.

Other Publications

1. Y. R. Shen, "Nonlinear Optics with Surface Electromagnetic Waves," in Proceedings of the First International School on Laser Application in Atomic, Molecular, and Nuclear Physics, Nauka, Moscow, 1979, p. 213, LBL-8223.

2. Aa. S. Sudbø, P. A. Schulz, Y. T. Lee, and Y. R. Shen, "Molecular Beam Studies of Infrared Multiphoton Unimolecular Dissociation," Proceedings of the First International School on Laser Application in Atomic, Molecular, and Nuclear Physics, Nauka, Moscow, 1979, p. 338, LBL-8224.

+3. K. C. Chu, C. K. Chen, and Y. R. Shen, "Measurement of Refractive Indices and Study of Isotropic-Nematic Phase Transition by the Surface Plasmon Technique," Bull. Am. Phys. Soc. 25, 214 (1980), LBL-9398 Abs.

4. P. Motisuke, S. Durbin, V. I. Safarov, and Y. R. Shen, "Electron Spin Orientation by Two-Photon Optical Pumping in p-Type GaAs," Bull. Am. Phys. Soc. 25, 361 (1980), LBL-10261 Abs.

5. S. Durbin, P. Motisuke, V. I. Safarov, and Y. R. Shen, "Linear-Circular Dichroism in Two-Photon Absorption in p-Type GaAs," Bull. Am. Phys. Soc. 25, 361 (1980), LBL-10260 Abs.

6. Y. R. Shen, C. K. Chen, and A. R. B. de Castro, "Coherent Raman Spectroscopy via Surface Plasmons," in Proceedings of the VIIth International Conference on Raman Spectroscopy, Aug. 4-9, 1980, Ottawa, Canada, p. 659, LBL-10554.

‡7. N-M. Chao, K. C. Chu, and Y. R. Shen, "Local Refractive Index Measurement on a Cholesteric Liquid Crystal Using the Surface Plasmon Technique." NSF preprint (1980).

‡8. P. Ye and Y. R. Shen, "Four-Wave Mixing and Optical-Field-Induced Helical Structure in Liquid Crystalline Materials." NSF preprint (1980).

LBL Reports

1. C. K. Chen, A. R. B. de Castro, and Y. R. Shen, "Surface Enhanced Second Harmonic Generation," LBL-11596.

2. R. W. Smith, "Wave Mixing Spectroscopy," (Ph.D. thesis), LBL-11518.

3. Y. R. Shen and F. DeMartini, "Nonlinear Wave Interaction Involving Surface Polaritons," LBL-11358.

4. Y. T. Lee and Y. R. Shen, "Molecular Beam Studies of IR Laser Induced Multiphoton Dissociation and Vibrational Predissociation," LBL-11105.

5. M. W. Sigrist, D. J. Krajnovich, F. Huisken, Z. J. Zhang, Y. T. Lee, and Y. R. Shen, "Laser-Induced Dissociation of Monomers and Dimers of Bromine," LBL-10991.

6. Y. R. Shen, "A Note on Two-Phonon Coherent Anti-Stokes Raman Scattering," LBL-10715.

7. Y. R. Shen, C. K. Chen, and A. R. B. de Castro, "Surface Nonlinear Optics," LBL-11252.

Papers Presented at Meetings

1. F. Huisken, D. J. Krajnovich, Z. Zhang, Y. R. Shen, and Y. T. Lee, "Two-Channel Multiphoton Dissociation of CF_2CL_2 and Ethyl Vinyl Ether," Third European Study Conference on Low Energy Molecular Collisions, (MOLEC III), Oxford, England, Sept. 2-6, 1980.

2. D. J. Krajnovich, F. Huisken, Z. Zhang, Y. R. Shen, and Y. T. Lee, "Competing Dissociation Channels in Multiphoton Dissociation of Polyatomic Molecules," Photochemistry Conference, Newport Beach, CA, March 30-April 3, 1980.

3. D. J. Krajnovich, F. Huisken, Z. Zhang, Y. T. Lee, and Y. R. Shen, "Two-Channel Multiphoton Dissociation of Polyatomic Molecules," XI International Quantum Electronics Conference 1980, Boston, Mass. June 23-26, 1980.

4. C. K. Chen, A. R. B. de Castro, and Y. R. Shen, "Nonlinear Interaction of Surface Electromagnetic Waves," XI International Quantum Electronics Conference 1980, Boston, Mass., June 23-26, 1980.

‡5. S. Durbin and Y. R. Shen, "Measurements of Orientational Statistics of a Liquid Crystal by Optical Absorption and Photoluminescence," VIIIth International Liquid Crystal Conference, Kyoto, Japan, June 30-July 4, 1980.

†6. N-M. Chao, K. C. Chu, and Y. R. Shen, "Refractive Index Measurements on a Cholesteric Liquid Crystal Using the Surface Plasmon Technique," VIIIth International Liquid Crystal Conference, Kyoto, Japan, June 30-July 4, 1980.

Invited Talks

1. H. S. Kwok, D. J. Krajnovich, M. Verson, Y. R. Shen, and Y. T. Lee, "Vibrational Predissociation Spectra of Small Clusters of H_2O, HF, NH_3, CH_3OH, C_6H_6 and C_6H_{12}," XI International Quantum Electronics Conference, Boston, Mass., June 23-26, 1980.

2. Y. R. Shen, "That Horse Has Given Us a Great Ride," XI International Quantum Electronics Conference, Boston, Mass., June 23-26, 1980.

3. Y. R. Shen, "Laser-Molecular Beam Study of Vibrational Spectra of Molecular Clusters," U.S.-Japan Bilateral Seminar on Nonlinear Laser Spectroscopy, Kauai, Hawaii, Sept. 8-12, 1980.

4. Y. R. Shen, "Infrared Multiphoton Dissociation of Molecules," Colloquium, National Bureau of Standards, Washington, D. C., May 14, 1980.

5. Y. R. Shen, "Surface Plasmons and Surface Physics," Colloquium, Physics Dept. Univ. of Calif. at Santa Barbara, Oct. 21, 1980.

6. Y. R. Shen, "Surface Nonlinear Optics," Sergio Porto Memorial Symposium on Lasers and Applications, Rio de Janiero, Brazil, June 29-July 3, 1980.

7. Y. R. Shen, "Coherent Raman Spectroscopy via Surface Plasmons," VIIth International Conference on Raman Spectroscopy, Ottawa, Canada, Aug. 4-9, 1980.

8. Y. R. Shen, "Four-Wave Mixing," Shanghai Institute of Optics and Fine Mechanics, Academia Sinica, Shanghai, China, Aug. 26, 1980.

9. Y. R. Shen, "Lasers and Surface Science," Fudan University, Shanghai, China, Aug. 27, 1980.

10. Y. R. Shen, "Nonlinear Optical Effects in Liquid Crystals," Institute of Physics, Academia Sinica, Beijing, China, Aug. 29, 1980.

11. Y. R. Shen, "Laser Applications in Sciences," Bureau of Science and Technology, Hupei, China, Aug. 31, 1980.

12. Y. R. Shen, "Spectroscopy by Four-Wave Mixing," Sun-Yat-see University, Canton, China, Sept. 4, 1980.

---

†Partially supported by the National Science Foundation, Grant DMR78-18826.

‡Supported by the National Science Foundation, Grant DMR78-18826.

c. Excited Quantum Fluids in Solids*

Carson D. Jeffries, Investigator

Introduction. When light strikes a cold semiconductor, Ge or Si for example, the excited electrons and holes quickly combine to form free mobile excitons (FE) and even multiexciton complexes, such as the free biexciton in Si. Pokrovskii discovered that the exciton gas makes a first-order condensation into a Fermi liquid, electron-hole droplets (EHD) which are metallic and mobile. This transition has many of the classical aspects of the water vapor-fog droplet condensation. However, the EHD constitute a novel state of matter. In pure Ge, it is a cold, dense, multicomponent, anisotropic, compensated plasma of constant density (2×10^{17} electrons and holes per cm^3). This liquid is a collective excited state of the crystal lattice with a lifetime of 10^{-4} sec and is the first example of a Fermi liquid in a periodic lattice. We have studied in detail many of its properties, including the nucleation process; motion and diffusion of droplets; confinement of sizeable volumes of the liquid in potential wells of crystal strain; magneto-oscillatory phenomena; unusual magnetic properties; Alfvén wave dimensional resonances; lifetimes, decay mechanisms and phonon interactions in stressed and unstressed crystals; optical hysteresis and memory; droplet surface tension; and compressibility of the liquid. We are also studying novel properties of free excitons in Ge in a strain well, where long lifetimes and novel decay mechanisms have been found. Crystals of Ge are being used as self-resonators in an ultra-high sensitivity study of spin resonance, and a novel emissive magnetic dipole transition has been discovered which is probably due to defect states.

1. FREE EXCITONS IN Ge: A NEW OUTLOOK

James C. Culbertson, John E. Furneaux, and Carson D. Jeffries

The decay of free excitons (FE) in Ge at liquid helium temperatures has been poorly understood. In unstressed Ge, the FE radiative lifetime (τ_{rx}) is estimated (see Article 2) to be about 600 μs. Actual measurements of the FE lifetime (τ_x) vary from 1 to 30 μs. The large nonradiative recombination rate [$(1/\tau_{nrx})$] is not yet understood. Impurities, dislocations, and surfaces may all act as recombination sites. Since it is estimated $\tau_{rx} \gg \tau_x$, the FE lifetime is predominantly due to nonradiative mechanisms $\tau_x \approx \tau_{nrx}$. In stressed Ge where the conduction and valence band degeneracies are removed, the FE radiative lifetime is estimated (Article 2) to be 2.8 ms. By confining free excitons in a strain induced potential well, we have measured FE decay curves as a function of temperature and stress. These experiments have lead to the following new results: the FE lifetime is enhanced by a factor of 50 to at least 1.6 ms, a novel temperature-dependent decay mechanism is observed, and a characterization of nonradiative and radiative decay rates is obtained.

A stress along a [1,1,1] crystal direction reduces crystal symmetry, which also reduces the band structure symmetry. The indirect band gap along the [1,1,1] direction applied stress is lowered relative to the other three [1,1,1] directions; and the valence band degeneracy is removed such that, for stresses $\sigma \gtrsim 5$ kgf/mm^2, we can model excitons at $T \approx 4$ K as a thermal distribution of bound states of electrons in the lowered conduction valley and holes in the upper valence band. Once this high stress limit is reached, increasing the stress does not affect the FE binding energy because the electron and hole mass are insensitive to further changes in stress. When this stress is applied inhomogeneously by means of a rounded plunger,[1] a shear strain maximum is created inside the crystal. Locally the indirect gap shifts in accordance with the local shear strain. Where strain is maximum, the indirect gap is smallest, and we have a strain induced potential energy well for electrons, excitons, and EHD.

The density distribution of FE at temperture T in the parabolic strain well is found by requiring the chemical potential for this classical gas to be independent of position. The resultant distribution is a Gaussian:

$$n(\vec{r}) = n_0 \exp(-\alpha r^2/kT)$$

where αr^2 is the strain potential energy as a function of radial distance r from the potential minimum. We have verified this density distribution experimentally by studying the spatial extent of the confined excitons.[2]

The basic experimental setup is shown in Fig.1. Scanning position, wavelength, time, and excitation power are automated by allowing a microcomputer to control the output lens position, the spectrometer wavelength drive, the transient recorder, and the light source feedback control. The transient recorder reduces the time required to record a decay curve from 100 minutes to 1 minute.

Typical luminescence decays (Fig. 2) clearly show nonexponential character. Care is taken to keep excitation power below the threshold for EHD formation. The decay rate becomes faster as the FE density decreases, contrary to the predictions of an exciton-exciton decay mechanism. Lifetimes corresponding to the initial decay rate have been measured to be up to 1.6 ms. The basic trends observed in the FE decay data are:

*This work was supported by the Director, Office of Energy Research, Office of Basic Energy Sciences, Materials Sciences Division of the U. S. Department of Energy under Contract No. W-7405-ENG-48.

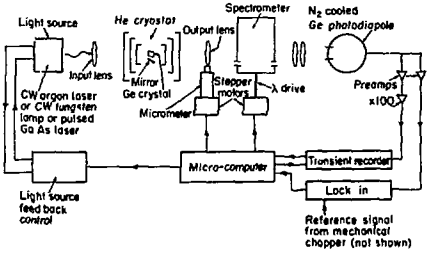

Fig. 1. Schematic of microcomputer-controlled experimental setup. (XBL 813-551)

- as FE density decreases, decay rate increases;
- as temperature increases, decay rate increases;
- as stress decreases, decay rate increases.

In an effort to put restrictions on possible FE decay models, the data are fitted to:

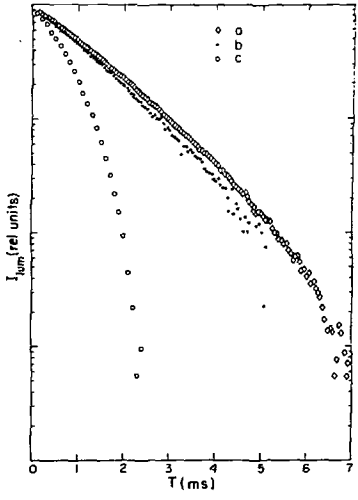

Fig. 2. Decay curves for a strain-confined free exciton (FE) gas. The FE decay faster as their numbers decrease. Temperature and well-depth measurements for the curves are: (a) 3.2 K, 9.5 meV; (b) 3.2 K, 7 meV; and (c) 4.7K, 7 meV. (XBL 813-552)

$$\frac{dN}{dt} = -\frac{N}{\tau_x} - aN^{\xi}$$

where N = number of FE in well. If a = 0, this is exponential decay with lifetime τ_x. The second term with $0 < \xi < 1$ allows for the nonexponential nature of the decay. Unfortunately, even though we have data over more than three orders of magnitude in N, values of ξ from 0.3 to 0.7 fit almost equally well. This difficulty motivates a study of the differential equation directly, using steady state excitation measurements of total FE luminescence intensity from the well versus excitation power (G):

$$\frac{dN}{dt} = 0 = -\frac{N}{\tau_x} - aN^{\xi} + G .$$

This is done by mechanically chopping the luminescence and using lock-in detection. Preliminary results indicate ξ is in the range $0.5 < \xi < 0.7$.

Several decay mechanisms may be important. We consider the following models, keeping in mind the basic trends in the observed data:

(1) Entropy ionization of FE to free carriers would show the general features of FE decay and would agree numerically with our data, provided $(N_c/\tau_c > N_x/\tau_x)$ where N_c and N_x are the number of excitons and electrons and τ_c is the lifetime of electrons. In this model the law of mass action leads to $N_x \propto N_c^2$.

The above equation combined with the loss equation:

$$\frac{d}{dt}(N_x + N_c) = -\frac{N_x}{\tau_x} - \frac{N_c}{\tau_c}$$

satisfies all the basic trends the decay data show except the dependence on stress, unless τ_x or τ_c are stress dependent.

(2) Free excitons or carriers may be thermally excited out of the well to recombine at a crystal surface or may reach a region of low stress where they have a short lifetime. The temperature and stress dependences of this mechanism are qualitatively correct, but the exponential decay it leads to for exciton loss is not.

(3) Saturation of recombination sites by FE would show a decay rate increase with decreasing exciton density. The stress and temperature dependences of this mechanism would depend on the details of the model.

To date, the qualitative features of the decay of a strain-confined FE gas have been investigated, and a quantitative understanding is on the horizon. Experimentally, we know the radiative FE lifetime is at least 1.6 ms as compared to the theoretically estimated 2.8 ms lifetime.

* * *

1. R. S. Markiewicz, J. P. Wolfe, C. D. Jeffries, Phys. Rev. B 15, 1988 (1977).
2. J. P. Wolfe, R. S. Markiewicz, S. M. Kelso, J. E. Furneaux, and C. D. Jeffries, Phys. Rev. B 18, 1479 (1978).

2. ENHANCEMENT FACTOR FOR THE STRAIN-CONFINED ELECTRON HOLE LIQUID

James C. Culbertson, John E. Furneaux, and Carson D. Jeffries

By suitably stressing a dislocation-free Ge crystal as discussed in the previous section, one can create a strain-induced potential energy minimum inside the crystal for photo-excited species such as free excitons (FE), electron hole liquids (EHL), and free carriers (ionized excitons). This fact permits the study of well-defined distributions of these excited species. Measurements of the steady state FE and EHL luminescence intensity versus the number of exciting photons show the EHL radiative efficiency ($\xi_{r\ell}$) is 1.6 times the exciton radiative efficiency (ξ_{rx}). By measuring the FE and EHL lifetimes (τ_x and τ_ℓ) at the same stress (9 kgf/mm^2) and temperature (2.8 K), and making an additional spectroscopic measurement to determine the EHL density (N_0), the EHL enhancement factor [$g_{eh}(o)$] is found. The enhancement factor is a measure of the enhancement of the probability of finding an electron hole correlation in the EHL. Since g_{eh} is a direct measure of correlations, it is a valuable test for the predictions of many-body theory calculations.

From equivalent expressions for the ratio of the radiative decay rates for FE and EHL, it can be shown that:

$$g_{eh}(o) = \left(\frac{\xi_{r\ell}}{\xi_{rx}}\right)\left(\frac{\tau_x}{\tau_\ell}\right)\left(\frac{|\psi(o)|^2{}_x}{N_o}\right).$$

The EH[illegible]y is measured spectroscopically. The FE lifet[illegible] lifetime are measured in a pulsed experiment, [illegible] the previous section. The ratio of the radia[illegible]ve efficiencies of FE and EHL is measured by putting large slits in the spectrometer, replacing the grating with a mirror, and measuring total luminescence from the well both above and below the EHL formation threshold as shown in Fig. 3. The ratio of the slopes above and below threshold, corrected for the different collection efficiencies for FE and EHL, is the ratio of the radiative efficiencies for FE and EHL. Using the values found in this work, shown in Table 1, gives $g_{eh}(o) = 4$ for a strain-confined EHL at $\sim$ 9 kgf/mm^2.

The radiative lifetime for the strain-confined FE gas at temperature T = 2.8 K and stress $\sigma \simeq 9$ kgf/mm^2 can be found from the measurements made in this work and elsewhere in two different ways, and the results can be compared to check the consistency of the parameters describing the stressed and unstressed FE and EHL. To clarify which quantities are for stressed and which for unstressed GE, a superscript asterisk (*) will denote unstressed while a superscript dagger (†) will denote stressed. Using the measured $\tau_x{}^\dagger$, the ratio of radiative efficiencies for FE and EHL and a previous measurement of $\xi_{r\ell}{}^\dagger$, we find for FE in stressed Ge

$$\tau_{rx}{}^\dagger = \frac{\tau_x{}^\dagger}{\xi_{rx}{}^\dagger} = \tau_x{}^\dagger \frac{\dfrac{\xi_{r\ell}{}^\dagger}{\xi_{rx}{}^\dagger}}{\xi_{r\ell}{}^\dagger} = 3.3 \text{ ms}.$$

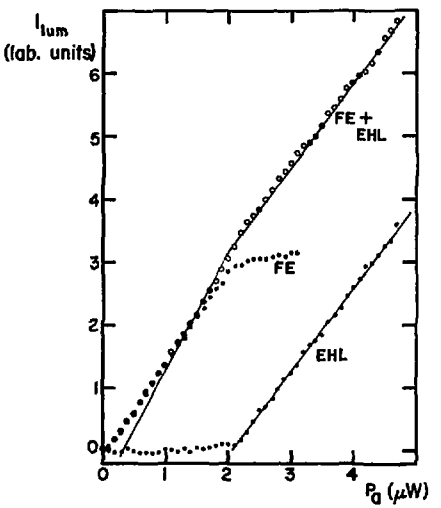

Fig. 3. Luminescence intensity from the strain well plotted as a function of absorbed excitation power, allowing a measurement of the relative radiative efficiencies of strain-confined FE and EHL at 2.8 K and 9 kgf/mm^2 stress. The FE curve shows only FE luminescence intensity. The EHL curve shows predominantly the EHL luminescence intensity. The FE+EHL curve shows the total FE and EHL luminescence intensity. The break in slope for all three curves occurs at the same excitation power, the power threshold for EHL formation.
(XBL 811-7641)

The second way to find $\tau_x{}^\dagger$ starts by using $\tau_\ell{}^*$, $\xi_{r\ell}{}^*$ and $\tau_{rx}{}^*/\tau_{r\ell}{}^*$ from Table 1 to give $\tau_{rx}{}^* = 607$ μs. To get $\tau_{rx}{}^\dagger$ from this, one uses the relation

$$\frac{1/\tau_{rx}{}^*}{1/\tau_{rx}{}^\dagger} = \frac{|\psi(o)|^2{}_x{}^*}{|\psi(o)|^2{}_x{}^\dagger}.$$

When solved for $\tau_{rx}{}^\dagger$, this yields a radiative FE lifetime $\tau_{rx}{}^\dagger = 2.8$ ms for the stress on $\sigma \simeq 9$ kgf/mm^2. Therefore, the parameters describing the stressed and unstressed FE and EHL appear internally consistent. This also shows that the marked increase in the strain-confined exciton lifetime is due not to some anomaly in radiative recombination but to a suppression of the non-radiative mechanism.

Table 1. Measured and derived FE and EHL parameters in stressed(†) and unstressed(*) germanium.

	Unstressed(*)	Stressed(†)
	EHL	
N_o	2.3×10^{17} cm^{-3}(m)	3.6×10^{16} cm^{-3}(w)
τ_ℓ	40 μs(m)	930 μs(w)
$\xi_{r\ell} = \frac{\tau_\ell}{\tau_{r\ell}}$	0.25(m,1)	0.75(m,2)
$\tau_{r\ell}$	160 μs	1280 μs
$g_{eh}(o)$	4.37(m)	See equation for $g_{eh}(o)^\dagger$, below
	FE	
$\lvert\psi(o)\rvert^2_x$	$\frac{18.46}{4\pi a_o^3} = 2.649 \times 10^{17}$ cm^{-3}(t,4)	$\frac{1}{\pi a_o^3} = 5.7 \times 10^{16}$ cm^{-3}(t)
τ_x	30 μs(m)	1.56 μs(t)
τ_{rx}	$\left(\tau_{r\ell}\left(\frac{\tau_{rx}}{\tau_{r\ell}}\right)\right) = 607$ μs	$\tau^*_{rx}\frac{\lvert\psi(o)\rvert^{2\,*}_x}{\lvert\psi(o)\rvert^{2\,\dagger}_x} = 2.8$ ms
$\xi_{rx} = \frac{\tau_x}{\tau_{rx}}$	0.05	0.47
	FE and EHL	
$\frac{\tau_{rx}}{\tau_{r\ell}}$	3.8(3)	----------
$\frac{\xi_{r\ell}}{\xi_{rx}}$	5.06	1.52

$$g_{eh}(o)^\dagger = \left(\frac{\xi_{r\ell}}{\xi_{rx}}\right)^\dagger \left(\frac{\tau_x}{\tau_\ell}\right)^\dagger \left(\frac{\lvert\psi(o)\rvert^2_x}{N_o}\right)^\dagger = 4.1$$

$$(\tau_{rx})^\dagger = (\tau_x)^\dagger \left(\frac{(\xi_{r\ell}/\xi_{rx})}{\xi_{r\ell}}\right) = 3.3 \text{ ms}$$

(m)Values from previous measurements.
(w)Values measured in this work.
(t)Theoretical values.
a_o = Bohr radius.

1. F. Betzler et al., Sol. State Comm. 17, 577 (1975).
2. S. M. Kelso, J. E. Furneaux, Solid State Electron. 21, 1377 (1978).
3. R. M. Westervelt, Proc. of 13th Int. Conf. of Semiconductors, 902 (1976).
4. M. Altarelli, N. O. Lipari, Phys. Rev. Lett. 36, 619 (1976).

3. STUDIES OF DEFECTS IN Ge BY ULTRA-SENSITIVE SPIN RESONANCE TECHNIQUES

Elga J. Pakulis and Carson D. Jeffries

A high sensitivity superheterodyne EPR spectrometer, coupled with a large microwave resonant Ge crystal, has revealed the existence of photo-induced emissive spin resonance in Ge. The observed lines were centered at g = 1.6, when the magnetic field was along the [1,0,0] crystal direction, and exhibited a large anisotropy in g. The samples were large n-type Ge crystals, with net donor concentrations 10^{12}-10^{14} cm^{-3}, which serve as their own microwave cavity having a quality factor $Q \approx 10^5$. This provides an incredibly sensitive probe for paramagnetic centers.

The resonances (Fig. 4) were observed only when the sample was pumped with sub-band gap radiation. A set of interference filters was used to narrow the wavelengths most effective for inducing the resonances. Preliminary results showed that maximum enhancement was for wavelengths in the range $1.87 \leq \lambda \leq 2.05$ microns.

Where do these emissive spin resonances originate? The challenge is to track down the impurity or defect center responsible. The overall symmetry and g anisotropy of the lines (Fig. 5) bear some resemblance to EPR absorption observed in Sb-doped Ge.[1,2]

The emissive spin resonances also resemble EPR absorption by the lithium oxygen donor in Ge.[3] The crystals are known to contain hydrogen in excess of 10^{12} cm^{-3}.[4] In fact, both donor (oxygen-hydrogen)[5] and acceptor (Si-hydrogen, C-hydrogen)[6] complexes involving hydrogen have been studied and may be candidates for EPR behavior with the same symmetry as the LiO complex. As a check for this possibility, one sample was cut from a crystal grown from a melt contained in graphite (rather than quartz). Here one expects a high concentration of C impurity, low concentration of Si and oxygen. The resonances in this crystal were the same as for quartz-grown samples. Hydrogen may also form complexes with the shallow donor (P, As, etc.); however, no difference was measured between phosphorous and arsenic doped crystals.

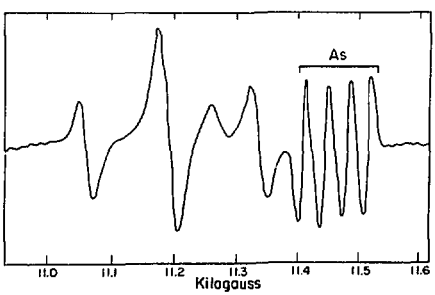

Fig. 4. Derivative curves of photo-induced emissive spin resonance in arsenic-doped Ge(N_D-N_A ≈ 10^{14} cm^{-3}). Note reversal of lines as compared to arsenic hyperfine structure (As). Magnetic field is approximately along the [1,0,0] direction. T = 2 K. Frequency = 25.16 GHz. (XBL 813-549)

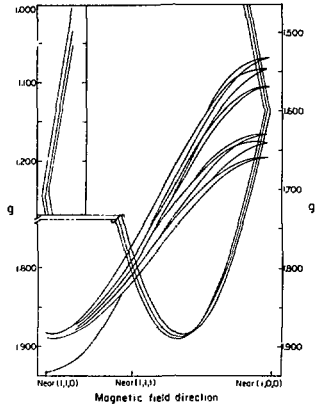

Fig. 5. Angular dependence of g-factor of resonances, for a sample of phosphorous-doped Ge (N_D-N_A ≈ 10^{12} cm^{-3}), as the magnetic field is rotated in a plane somewhat tilted from the [1,1,0] plane. No data were taken for g < 1, corresponding to 19 kG, the limit of the magnet used. Insert shows continuation of the lines for low values of g. Frequency = 26.06 GHz. (XBL 813-550)

Besides impurity complexes, paramagnetic defects and/or defect-impurity complexes can also have highly anisotropic g values. Two obvious types of defects to consider are vacancies and dislocations. Because all the samples studied had been cut from dislocated crystals, a dislocation-free crystal was tried next. No trace of the emissive spin resonances was seen. Evidently, dislocations may harbor centers that become paramagnetic when the crystal is pumped optically. On the other hand, dislocation-free crystals grown in a hydrogen atmosphere have a high density of hydrogen precipitates,[4] and these may be responsible for the absence of the lines. Two additional pieces of information favor the first interpretation. First, the range of wavelengths found to be most effective for inducing the resonances is also sufficient to induce dislocation band to impurity conduction band transitions. Second, comparison of the dislocation densities for nine crystals revealed at least a qualitative correlation between the number of dislocations and the size of the emissive resonance signals.

Some interesting characteristics of the lines can be seen in Fig. 5. The symmetry axis of the

center is actually about a degree off the [1,1,1] crystal axis. (If the center was located at a dislocation, some distortion would be expected.) Each of the [1,1,1] axes contributes six lines, but the lines are paired for two of the axes, and the two lines in each pair are too close to show individually in the figure. The average position of the lines is well described by a g tensor with $g_\perp = 1.89$ and $g_\parallel = 0.73$. In addition to these 24 lines, each about 15 gauss peak to peak, there are four very asymmetric lines, each about 50 gauss peak to peak. The position of one pair of the broad lines is indicated in the lower left-hand corner of the figure. Data from a different sample yielded $g_\perp = 1.94$ and $g_\parallel = 0.34$ for the broad liner.

Even without a microscopic model for the paramagnetic center, one can picture what may be happening. When dislocations are formed within a crystal, centers are created which act as acceptors. In an n-type crystal, these centers will be completely filled with electrons, leaving some number of shallow donors ionized. An even number of electrons per center is indicated because the ground state is not paramagnetic. When the crystal is pumped optically, however, an acceptor-donor transition can occur, leaving the center with an odd electron. The fact that the shallow donor hyperfine structure is substantially enhanced by optical pumping supports this view. The ionized donors which have been neutralized in the process provide a long-lived haven for the excited electrons. While there, the electrons acquire a net polarization from the applied magnetic field. If they then undergo a $\Delta m_s = \pm 1$ transition in recombining the odd electron at an acceptor center and if recombination occurs preferentially for two electrons of opposite spin, a population inversion will result for the remaining paramagnetic acceptor centers. Such an inversion would give an emissive spin resonance signal.

* * *

1. R. E. Pontinen and T. M. Sanders, Jr., Phys. Rev. 152, 850 (1966).
2. E. B. Hale, J. R. Dennis, and Shih-Hua Pan, Phys. Rev. B 12, 2553 (1975).
3. E. E. Haller and L. M. Falicov, Phys. Rev. Letters 41, 1192 (1978).
4. E. E. Haller, W. L. Hansen, and F. S. Goulding, Advances in Physics, in press.
5. B. Joós, E. E. Haller, and L. M. Falicov, Phys. Rev. B 22, 832 (1980).
6. E. E. Haller, B. Joós, and L. M. Falicov, Phys. Rev. B 21, 4729 (1980).

4. DEVELOPMENT OF AN ULTRASENSITIVE IR DETECTOR

Jose Perez and Carson D. Jeffries

Considerable progress has been made in our development of a new ultrasensitive IR detector. We have been able to achieve a noise equivalent power (NEP) of 1×10^{-14} W/√Hz at 1.75 μm with a 4.2 K Ge photoresistor which is comparable to the NEP for the photodiodes cooled to ~ 100 K we currently use. The photoresistor is made sensitive to the 1.75 μm 709 meV light, which is less energetic than the normal Ge indirect gap at 4.2 K, by stressing the crystal with 90 kgf/mm^2. This stress lowers the indirect gap from 744 meV to 655 meV. Since noise reduction is currently limited by the preamplifier, we are developing a cooled preamplifier which should allow us to achieve an NEP of 2×10^{-16} W/√Hz, or 50 times as good as our present detector.

RESEARCH PLANS FOR CALENDAR YEAR 1981

Stress dependence of the EHL enhancement factor. Conflicting many-body theories predict a markedly different enhancement factor for the EHL as a function of stress. By making careful measurements of the enhancement factor for the strain-confined EHL, we will be able to make a definitive test of these theories.

Study of recombination centers. Because the lifetime of the strain-confined excitons is very long, it is possible to study the recombination rates various centers sensitively. We propose to study various Ge samples doped with shallow and deep impurities in order to determine the impurity recombination rates. This information could be invaluable in designing possible future state-of-the-art detectors and other devices such as solar cells.

Ultrasensitive microwave paramagnetic resonance studies in Ge and Si. The fruitful ultrasensitive microwave paramagnetic resonance studies of defects and impurities in Ge will be continued and extended. We plan to look at a greater variety of samples and extend our technique to time-resolved studies in Ge. Further, since these techniques have proven so useful in Ge, they will be extended to Si. This work promises to give very detailed information about defects in these semiconductors and, therefore, will be important in the design of devices such as γ-ray detectors and solar cells.

Ultrasensitive luminescence spectroscopy in Ge. The new ultrasensitive IR detector will be used to search for phenomena previously unobservable due to their extremely weak luminescence. Prime candidates for this search in Ge are: biexcitons; multiexciton complexes; band to band recombination; and the onset of nucleation of individual small EHD in unstressed Ge. These experiments will test the validity of nucleation theory and provide more detailed information about excited states of the important semiconductor Ge.

1980 PUBLICATIONS AND REPORTS

Other Publications

1. Carson D. Jeffries, "Dynamically Polarized Targets: An Outgrowth of Magnetic Resonance," Chapter 4 of Felix Bloch and 20th Century Physics," Rice University Press, 1980.

2. J. C. Culbertson and J. E. Furneaux, "Strain-Confined Free Exciton Lifetime in Ge," Bull. Amer. Phys. Soc. 25, 268 (1980), LBL-10266.

3. J. E. Furneaux, "Buildup of the Strain-Confined Electron-Hole Liquid in Ge," Bull. Amer. Phys. Soc. 25, 268 (1980), LBL-10267.

4. R. M. Westervelt and J. C. Culbertson, "Experimental Limit on the Net Charge of Electron-Hole Drops in Ge," Bull. Amer. Phys. Soc. 25, 267 (1980), LBL-10474.

Invited Talks

1. J. E. Furneaux, "Strain-Confined Excitons in Ge," Colloquium, Physics Department, University of Illinois, Urbana, Illinois, March 21, 1980; General Electric Research Center, Schenectady, New York, April 2, 1980; and Bell Telephone Laboratories, Murray Hill, New York, April 3, 1980.

2. J. E. Furneaux, "Strange New Results on Excitons in Ge," Physics Department Solid State Seminar, University of California, Berkeley, California, June 4, 1980.

3. J. E. Furneaux, "Strain-Confined Excitons: a New Probe of Recombination Mechanisms in Ge," General Electric Research Center, Schenectady, New York, November 19, 1980; Naval Research Laboratory, Washington, D. C., November 20, 1980; and Xerox Research Center, Palo Alto, California, December 12, 1980.

d. Superconductivity, Superconducting Devices, and 1/f Noise*

John Clarke, Investigator

1. QUANTUM NOISE IN JOSEPHSON JUNCTIONS AND DC SQUIDS: THEORY†

Roger H. Koch, Dale J. Van Harlingen, and John Clarke

The theory of thermal noise in Josephson junctions and SQUIDs is well understood and is in good accord with experimental data. However, until recently, there has been little work on noise in junctions in the limit where quantum corrections are important. Such effects are not only of considerable intrinsic interest, but also set the ultimate sensitivity of devices such as SQUIDs and mixers. We briefly present results on calculations of quantum noise in both single junctions and SQUIDs.

Single junctions. We consider a Josephson tunnel junction with critical current I_0 and capacitance C, shunted with resistance R. We assume that the only significant source of noise is the equilibrium current noise in the shunt resistor, $I_N(t)$, which has a spectral density, including zero point fluctuations,

$$S_I(\omega) = (\hbar\omega/\pi R)\ \coth(\hbar\omega/2k_BT) \qquad (1)$$

at angular frequency ω. The phase difference across the junction, δ, evolves according to the Langevin equation

$$\beta_c \frac{\ddot{\delta}}{I_0}\left(\frac{\Phi_0}{2\pi R}\right)^2 + \dot{\delta}\left(\frac{\Phi_0}{2\pi R}\right) + I_0 \sin\delta = I + I_N, \qquad (2)$$

where $\beta_c = 2\pi I_0 R^2 C/\Phi_0$, and I is the bias current. In the limit in which the $\ddot{\delta}$ term is very small, we have solved Eq. (2) analytically to find the spectral density of the voltage noise across the junction at a frequency much less than the Josephson frequency:

$$S_V(0) = R_D^2\left[\frac{2k_BT}{\pi R} + \frac{eV}{\pi R}\left(\frac{I_0}{I}\right)^2 \coth\left(\frac{eV}{k_BT}\right)\right], \qquad (3)$$

where R_D is the dynamic resistance. The first term is the noise generated at the measurement frequency; the second is the noise mixed down from frequencies near the Josephson frequency. To observe quantum effects, we require $eV \gg k_BT$ and $eV \gg k_BT(I/I_0)^2$; these limits necessarily imply $\kappa = eI_0R/k_BT \gg 1$. Figure 1 shows $S_V(0)/4k_BTR$ vs. $i = I/I_0$ for five values of κ. For $\kappa = 0.1$, the noise is essentially in the classical limit. As κ is increased, for example, by lowering the temperature, the noise at intermediate bias currents increases above the classical value. In the limits $V \to 0$ and $V \to \infty$, the noise tends asymptotically to the classical limit. The insert of Fig. 1 shows the voltage spectral density vs. temperature for a junction with $I_0 = 1$ mA, $I = 1.41$ mA, and $R = 0.86\ \Omega$; the dashed line shows the classical results. The flattening out of the noise as T is reduced is clearly evident.

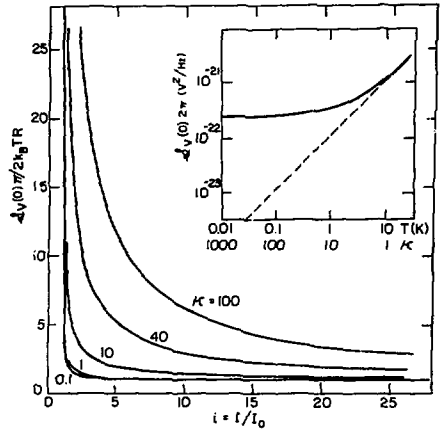

Fig. 1. Low frequency spectral density $S_V(0)$ of the voltage noise vs. current for 5 values of $\kappa \equiv eI_0R/k_BT$ with $\beta_c \ll 1$. Inset shows $S_V(0)$ vs. T for $I_0 = 1$ mA, $I = 1.41$ mA, and $R = 0.86\ \Omega$ (chosen to give $V = I_0R$ and $\kappa = 10$ at 1 K). Dashed line shows the classical result.

(XBL 804-5062A)

We have extended our calculations over the range $\beta_c \le 1$ using a computer, and find qualitatively similar results to the case $0 < \beta_c \ll 1$. Thus, our theory predicts that the limiting voltage noise in a Josephson junction with $\beta_c \le 1$ is set by zero point fluctuations in the shunt resistor.

dc SQUID. We have extended out theory to the dc SQUID, which consists of two identical shunted junctions on a superconducting ring of inductance L. The SQUID is described by the equations

$$J/I_0 = (\delta_1 - \delta_2 - 2\pi\Phi/\Phi_0)/\pi\beta, \qquad (4)$$

$$V = (\dot{\delta}_1 + \dot{\delta}_2)\Phi_0/4\pi, \qquad (5)$$

*This work was supported by the Director, Office of Energy Research, Office of Basic Energy Sciences, Materials Sciences Division of the U. S. Department of Energy under Contract No. W-7405-ENG-48.

$$\beta_c \frac{\ddot{\delta}_1}{I_0}\left(\frac{\Phi_0}{2\pi R}\right)^2 + \dot{\delta}_1\left(\frac{\Phi_0}{2\pi R}\right) = \frac{I}{2} - J - I_0 \sin\delta_1 + I_{N1} \tag{6}$$

and

$$\beta_c \frac{\ddot{\delta}_2}{I_0}\left(\frac{\Phi_0}{2\pi R}\right)^2 + \dot{\delta}_2\left(\frac{\Phi_0}{2\pi R}\right) = \frac{I}{2} + J - I_0 \sin\delta_2 + I_{N2}, \tag{7}$$

where J is the current in the SQUID loop, Φ is the applied flux, $\beta = 2LI_0/\Phi_0$, and the subscripts 1 and 2 refer to the two junctions. We have solved Eqs. (4)-(7) numerically for $T = 0$, where the spectral densities of the current noise reduce to $2h\nu/R$ (ν is the frequency). Figure 2(a) shows the time-averaged voltage V, the transfer function $\partial V/\partial\Phi$, the voltage noises spectral density S_V, and $\varepsilon/1\text{Hz}$ vs. Φ for three values of β_c. Here, $\varepsilon/1\text{Hz} = S_\Phi/2L$, where $S_\Phi = S_V/(\partial V/\partial\Phi)^2$. The minima in $\varepsilon/1\text{Hz}$ are all close to h, which thus represents the ultimate sensitivity of the SQUID.

The calculations have also been extended to the experimentally realistic case $T > 0$. We find that an optimized SQUID at 4.2 K should have $\varepsilon/1\text{Hz} \approx 3h$, while if this SQUID is cooled to 0.9 K, $\varepsilon/1\text{Hz} \approx 1.1\,h$. Thus, it appears feasible to operate a SQUID in the liquid He^4 temperature range with a performance approaching the limit set by zero point fluctuations in the shunt resistors.

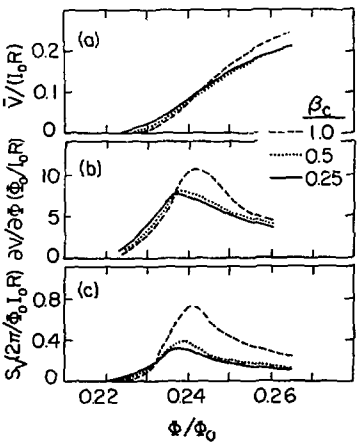

Fig. 2. Computed values of V, $\partial V/\partial\Phi$, S_V, and $\varepsilon/1\text{Hz}$ vs. Φ/Φ_0 for a dc SQUID at $T = 0$ with $R \approx 40\Omega$, $2LI_0 = \Phi_0$, $I = 1.63I_0$, and for $\beta_c = 0.25$, 0.5, and 1. (XBL 8010-6149A)

We conclude by noting that the essential condition that must be satisfied to observe quantum effects is $\kappa = eI_0R/k_BT = (e/k_BT) \times (\beta_c\Phi_0 j_1/2\pi c)^{1/2} \gg 1$, where j_1 is the critical current density, and c is the capacitance per unit area of the tunnel junction. Thus, one requires a low temperature and/or a high current density. In practice, one may have to take account of both heating effects and flicker (1/f) noise, which have been neglected in our calculations.

* * *

†Brief version of LBL-11414 and LBL-11729.

2. QUANTUM NOISE IN JOSEPHSON JUNCTIONS AND DC SQUIDS: EXPERIMENT†

Dale J. Van Harlingen, Roger H. Koch, and John Clarke

Single junction experiments. We have measured the current-voltage (I-V) characteristics and the voltage noise spectral density $S_V(\nu)$ of Josephson tunnel junctions designed to exhibit significant quantum corrections. To remove intrinsic hysteresis, the junctions are externally shunted with resistance R such that $\beta_c \equiv 2\pi I_0R^2C/\Phi_0 < 1$, where I_0 is the critical current and C is the capacitance.

The design of the junctions is shown in Fig. 3(a). The resistive shunt, 10 μm wide by 40-100 nm thick, is composed of Cu or a CuAl alloy (typically 3% Al) deposited through an aperture mask onto a glass substrate. The lower electrode is a 250 nm thick PbIn alloy (20% In) film patterned into a 10 μm wide cross-strip using a photolithographic liftoff procedure. The alloy is

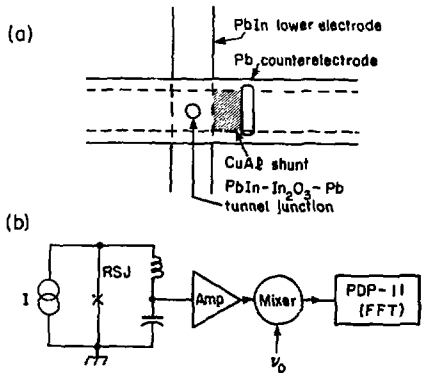

Fig. 3. (a) Layout of the resistively-shunted Josephson tunnel junctions fabricated by thin film photolithography; (b) Noise measurement system: voltage fluctuations near the tank circuit resonant frequency ν_0 are amplified, demodulated to low frequencies, and fast Fourier transformed to obtain noise power spectra. (XBL 813-545)

evaporated to completion from a single boat; the In evaporates at a lower rate than the Pb to give an indium-rich surface. The junction is defined by opening a 2.5 μm diam window in a SiO insulator layer by liftoff; a second window sets the shunt length at 5 μm. After patterning the photoresist for the upper electrode, the surfaces of the lower electrode and shunt films inside the windows are cleaned by rf sputter-etching in argon. The oxide barrier, In_2O_3, is grown by thermal oxidation for 10 minutes at room temperature in an oxygen pressure of 100 to 2000 μmHg, depending on the critical current desired. Without breaking vacuum, the counterelectrode, 400 nm of pure lead, is deposited to form the junction and contact the shunt. This upper electrode also forms a groundplane for the resistive shunt, reducing its inductance. The range of critical currents is 0.1 to 15 mA, corresponding to a current density of 2×10^3 to 3×10^5 A cm^{-2}. The junction capacitance is estimated to be 0.5 pF. The junctions have been found to recycle well and are electrically durable, although we do find a decrease of the critical current if the junctions are allowed to remain at room temperature for more than a few hours.

We measure the noise by connecting the junction to a tank circuit, as shown in Fig. 3(b). The tank circuit with Q ≈ 40-200 amplifies the voltage fluctuations at the resonant frequency, maching the low resistance junction (typically 0.05-1.0 Ω) to a low-noise pre-amplifier. The amplified signal is demodulated at the resonant frequency, and the resulting low frequency fluctuations are fast Fourier transformed by a PDP-11 computer to yield the voltage spectral density at the tank circuit frequency to an accuracy of ± 5%. In most cases, we simultaneously measure the noise at 100 kHz and 30 kHz using two tank circuits so that we can estimate and subtract any 1/f noise.

In Fig. 4, we show the voltage spectral density at 100 kHz vs. the bias current for a junction in the classical limit $\kappa \ll 1$, with $I_0 = 0.3$ mA and $R = 0.08\ \Omega$, yielding $\kappa = 0.07$ at 4.2 K. The dashed line represents the prediction of the thermal limit, $S_V = (4k_BTR_D^2/R)\,(1 + 1/2\,(I_0/I)^2)$. The increase in S_V as $I \to I_0$ reflects the increase of R_D; for $I < I_0$, noise-rounding reduces R_D and rolls off the noise. The agreement is excellent.

As we increase the critical current density and hence κ, the measurements are complicated by heating in the shunt resistors, structure in the I-V characteristic, and increased 1/f noise, causing deviations from the simple model. For example, Fig. 5 shows the spectral density of the noise for a junction with $I_0 = 1.5$ mA, $R = 0.09\ \Omega$, and $\kappa = 1.1$ at 1.4 K. The measured noise is everywhere substantially greater than our prediction [Eq. (3) in article 1] and exhibits oscillatory structure. We attribute the peaks in the noise to LC resonances involving the junction capacitance and shunt inductance. The strong nonlinearities in the I-V characteristic near the resonances result in noise mixing down from higher harmonics of the Josephson frequency than are included in the simple model. However, preliminary computer computations of the mixing coefficients have verified the dominance of zero-point fluctuations in the mixed down noise. Thus, we believe this noise represents a direct observation of zero point fluctuations.

dc SQUID experiments. We have also fabricated and tested dc SQUIDs with high κ junctions. To optimize the performance of a SQUID, it is necessary to select the critical current of each junction such that $\beta \equiv 2I_0L/\Phi_0 \approx 1$, where L is the SQUID loop inductance. Our SQUID design is shown in Fig. 6(a) and is schematically depicted in Fig. 6(b). The fabrication follows closely that of the single junction except that we make two shunted junctions, each 2.5 μm diam and separated by 30 μm. The SQUID loop, formed by the parallel

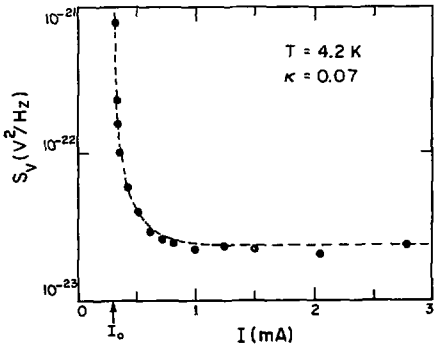

Fig. 4. Voltage noise spectra density of an RSJ with κ = 0.07 plotted vs. the bias current I. The dashed line is the theoretical prediction of Likharev and Semenov for thermal noise. (XBL 813-547)

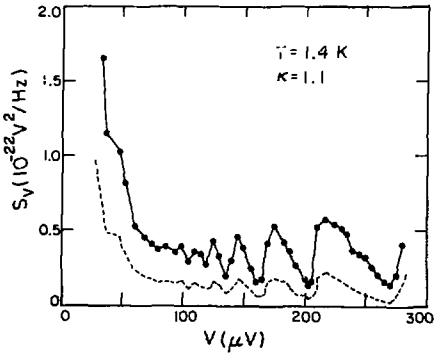

Fig. 5. Measured (-) and computed (---) values of spectra density of voltage noise in resistively shunted junctions vs. voltage. (XBL 813-546)

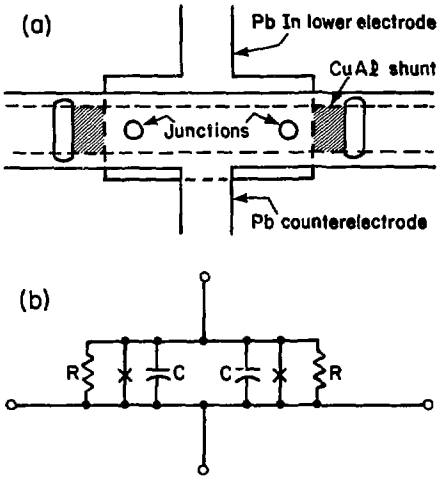

Fig. 6. (a) Layout of the dc SQUID designed to exhibit quantum noise; (b) Schematic representation of the SQUID, depicting junction capacitance C and shunt resistance R. (XBL 813-548)

PbIn and Pb films separated by the SiO layer, has a self-inductance of ≈ 1.8 pH. The flux in the SQUID may be modulated by passing current along one side of the loop.

We characterize the performance of the SQUID by $\varepsilon/1\text{Hz} \equiv S_\Phi/2L$, where $S_\Phi = S_V/(\partial V/\partial\Phi)^2$. The voltage noise across the SQUID, S_V, is measured as described above, while the transfer function $(\partial V/\partial\Phi)$ is measured by modulating the flux in the SQUID and detecting the voltage with a lock-in amplifier. For example, for a SQUID with $I_0 = 1.5$ mA and $R = 4.0\ \Omega$, for which $\kappa = 2.7$, $\beta_C = 0.4$, and $\kappa = 1.7$ at 4.2 K, we have obtained a maximum $\partial V/\partial\Phi$ of 5.0 mV/Φ_0. At 100 kHz, the noise energy obtained is 1.2 h while at 30 kHz we measure 2.0 h. From this we determine the white noise level to be 0.8 h ≈ 5 h and attribute the rest to 1/f noise. This yields a 1/f crossover frequency of ~ 70 kHz. The values obtained are in excellent agreement with computer calculations of the noise for the parameters used. At lower temperatures, the noise decreases, reaching a minimum total noise energy of 5.5 h at 2.8 K for a transfer function of 7.3 mV/Φ_0. If the 1/f noise contribution is assumed to be the same as at 4.2 K, this yields a white noise level of ~ 3 h. Decreasing the temperature further increases the critical current so that the SQUID becomes hysteretic. Further work is underway to optimize the parameters in an attempt to approach the predicted quantum limit of h.

* * *

†Brief version of LBL-12134.

3. MEASUREMENT OF THE CHARGE-IMBALANCE RELAXATION RATE IN THE PRESENCE OF A PAIR-BREAKING SUPERCURRENT IN DIRTY, SUPERCONDUCTING Al FILMS†

Thomas R. Lemberger and John Clarke

The rate at which the charge imbalance, Q^*, in a superconductor relaxes can yield valuable information on electron scattering processes. As an example, in the 1979 Annual Report,[1] we described measurements of the charge-imbalance relaxation rate, $1/F^*\tau_{Q^*}$, in AlEr films, in which the Er is a pair-breaking magnetic impurity. These measurements were made for $0.1 \le \Delta/k_BT_c \le 1.4$ and for $3 \le \tau_E/\tau_S \le 250$, where Δ is the superconducting order parameter, T_c is the transition temperature, τ_E^{-1} is a characteristic electron-phonon scattering rate, and τ_S^{-1} is the pair-breaking rate associated with magnetic impurities, the exchange scattering rate. The experimental results were compared with a numerical calculation based on the Boltzmann equation. Large discrepancies between the data and the numerical results were found. Specifically, we found experimentally that

$$1/F^*\tau_{Q^*} \propto (1 + 2\tau_E/\tau_S)^{1/2} \qquad (1)$$

for any fixed temperature. This result was first obtained theoretically by Schmid and Schön (SS), but only for $\Delta/k_BT_c \ll 1$. The numerical calculation reproduces this result for $\Delta/k_BT_c \ll 1$, but deviates significantly for all other values of Δ/k_BT_c.

To determine whether the disagreement concerned the effect of magnetic impurities in particular or pair-breaking in general, we measured $1/F^*\tau_{Q^*}$ in dirty Al films in which the pair-breaking was caused by an applied supercurrent. The experimental techniques were essentially the same as for the AlEr experiment; Fig. 7 shows the sample. A current, I_i, flowing through the tunnel barrier between the Al base electrode and the second Al film injects charge into the latter. The induced shift in the condensate chemical potential is detected by a Cu film making a tunneling contact to the Al film. The measurement of V_d is made with a null-balancing SQUID voltmeter and enables one to deduce $1/F^*\tau_{Q^*}$. At a given temperature and for fixed injection current I_i, we measured this voltage as a function of the supercurrent, I_s, in the second Al film. Typical experimental curves are shown in Fig. 8.

Predictions for the shape of these curves can be made based on the experimental and numerical results for AlEr in the following way. Bulyzhenkov and Ivlev have shown that the Boltzmann equation for charge relaxation in the presence of a supercurrent is the same as for magnetic impurities, provided one replaces the pair-breaking rate for magnetic impurities with the appropirate rate for a supercurrent,

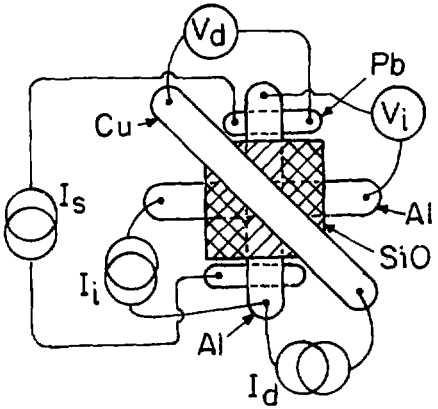

Fig. 7. Sample configuration. (XBL 813-8364)

$$\frac{1}{\tau_s} = \frac{1}{2} D \left(\frac{p_s}{\hbar}\right)^2 . \qquad (2)$$

Here, D is the electron diffusion constant and p_s is the momentum of a Cooper pair. Since $F^*\tau_{Q^*} \propto V_d$, by combining Eqs. (1) and (2) and using the familiar relations: $p_s = 2mv_s$, $j_s = n_s e v_s$, $n_s = mc^2/4\pi\lambda^2 e^2$, and $\lambda^2(0) = \lambda^2_L(0)\xi_0/\ell$, we find

$$V_d(I_s) = V_d(0)/(1 + b^{ss} I_s^{\,2})^{1/2} . \qquad (3)$$

Here,

$$b^{ss} = \left(\frac{8\pi e}{\hbar c^2}\right)^2 \frac{\tau_E v_F \xi_0^{\,2} \lambda_L^{\,4}(0)}{3d^2 w^2 \ell} \; \frac{\lambda^4(T/T_c)}{\lambda^4(0)} , \qquad (4)$$

v_s is the superfluid velocity, n_s is the superelectron density, $\lambda(T/T_c)/\lambda(0)$ is the electromagnetic penetration depth normalized to its value at zero temperature, $\lambda_L(0)$ is the zero-temperature value of the London penetration depth, $\xi_0 = \hbar v_F/\pi\Delta(0)$ is the zero-temperature coherence length, ℓ is the electron mean free path, and d and w are the thickness and width of the sample film. Similarly, an examination of the dependence of the numerically calculated values of $1/F^*\tau_{Q^*}$ on τ_E/τ_S yields the same functional form as Eq. (3), with b^{ss} replaced by b^{num}.

As illustrated in Fig. 8, the experimental value of b is determined by fitting a function of the form of Eq. (3) to the data. For each temperature and value of V_i of interest, four values of b are determined, corresponding to $\pm I_s$

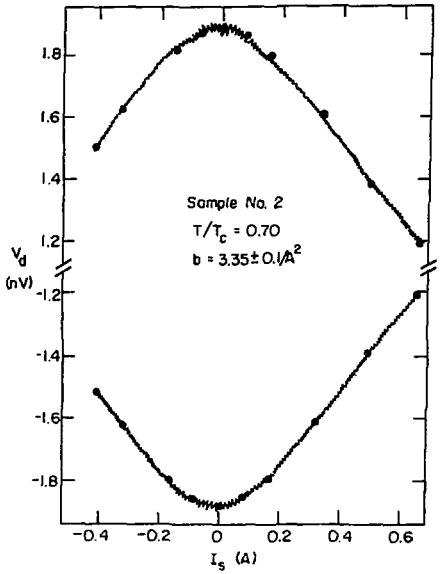

Fig. 8. Solid line represents measured values of V_d vs. I_s. Points are calculated from $V_d(I_s) = V_d(0)/(1 + bI_s^2)^{1/2}$, with b chosen to fit the data for each combination of $\pm V_d$ and $\pm I_s$. (XBL 808-5669)

and $\pm V_d$. These average values of b are plotted in Fig. 9, with error bars indicating the spread in the four values. The solid and dashed curves represent b^{ss} and b^{num}, respectively, normalized to fit the data at $T/T_c \approx 0.9$. Clearly, b^{ss} provides an excellent fit to the data over the entire temperature range studied for both samples, whereas b^{num} is a very poor fit. Quantitatively, the measured magnitude of b was 2.4 ± 0.4 times larger than the value of b^{ss} expected from Eq. (4). However, given the uncertainties in the values of ξ_0, $\lambda_L(0)$, v_F, and ℓ, this is well within experimental uncertainty. Therefore, the measurements of $1/F^*\tau_{Q^*}$, with pair-breaking caused by magnetic impurities and by an applied supercurrent, are in agreement with each other, but not with the results of the numerical calculation.

From these results, we conclude that either the currently accepted formulation of the Boltzmann equation for charge relaxation is incorrect, or the Boltzmann equation is inadequate to describe charge relaxation.

* * *

†Brief version of LBL-11406.

1. MMRD Annual Report 1979, LBL-10000, pg. 199.

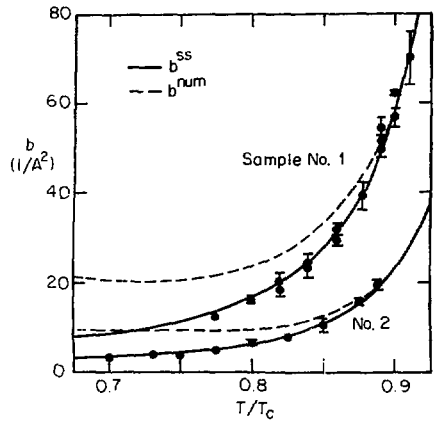

Fig. 9. Plot of the measured values of b (points with error bars), b^{ss} (solid line), and b^{num} (dashed line) vs. T/T_c for two samples.
(XBL 808-5666)

4. A NEW METHOD FOR DETERMINING REGIONAL STRIKE IN MAGNETOTELLURICS†

Wolfgang M. Goubau, Thomas D. Gamble, Robert F. Miracky, and John Clarke

Magnetotellurics is a powerful tool in the search for geothermal and mineral sources, and is of growing importance in surveying for oil reserves. The introduction of the remote reference technique[1] has greatly improved the accuracy with which the impedance tensor of the ground can be determined. The next major goal in the development of the magnetotelluric technique is to find a simple method of deducing the conductivity of the ground as a function of position from the impedance tensor.

A magnetotelluric survey determines the spatial and frequency dependence of the impedance tensor $\underline{Z}(\vec{r},\omega)$ that relates the horizontal components of the naturally occurring fluctuating electric and magnetic fields $\vec{E}(\vec{r},\omega)$ and $\vec{H}(\vec{r},\omega)$ at the surface of the earth via the relation $\vec{E}(\vec{r},\omega) = \underline{Z}(\vec{r},\omega)\,\vec{H}(\vec{r},\omega)$. The determination of the conductivity of the ground as a function of position from $\underline{Z}$ is a formidable problem that requires lengthy computer calculations. The interpretation is greatly simplified if there exists a direction in which the conductivity is translationally invariant; such a direction is called the strike. If a strike exists, the coordinate axes with respect to which $\underline{Z}$ was originally measured can be rotated so that in the new frame $Z_{xx} = Z_{yy} = 0$. The components of the electric field are then decoupled with $E_x = Z_{xy}H_y$ and $E_y = Z_{yx}H_x$. Often, there exists a long range regional strike direction defined by a mountain range or a fault line, but this regional strike may be obscured in measurements of $\underline{Z}$ at a single site because of a complex local geology. One therefore requires a method for combining the impedance estimates from a number of sites to produce an estimate of the regional strike direction.

We have devised and tested two simple schemes for determining regional strikes. In the first, we find the angle, θ, between the original coordinate system and the rotated coordinate system that minimizes $|Z_{xx}|^2 + |Z_{yy}|^2$ in a least squares sense. Our procedure is to define a quantity

$$B(\theta) = \sum_i (|Z_{xx}|^2 + |Z_{yy}|^2)W_i \qquad (1)$$

where the summation is over all frequencies and all magnetotelluric sites in the region of interest. The frequency-dependent function W_i weights the relative significance of each term. We then find the angle θ such that $\partial B/\partial\theta = 0$:

$$\theta_Z = \frac{1}{2}\tan^{-1}\left[\frac{2\sum_i \mathrm{Real}(Z_{xyi} + Z_{yxi})(Z^*_{yyi} - Z^*_{xxi})W_i}{\sum_i (|Z_{xyi} + Z_{yxi}|^2 - |Z_{yyi} - Z_{xxi}|^2)W_i}\right]. \qquad (2)$$

The second method involves the tipper $\vec{T}(\vec{r},\omega) = [T_x(\omega), T_y(\omega)]$ that relates the vertical component of the magnetic field, $H_z(\vec{r},\omega)$, to the horizontal field via the relation

$$H_z(\vec{r},\omega) = \vec{T}(\vec{r},\omega)\cdot H(\vec{r},\omega). \qquad (3)$$

T_x is zero when the x-axis is parallel to the strike. We define the quantity

$$A(\theta) = \sum_i W_i |T_{xi}(\theta)|^2, \qquad (4)$$

where the summation is again over all frequencies and magnetotelluric sites, and W_i is a weighting function. We then find the angle θ such that $\partial A/\partial\theta = 0$:

$$\theta_T = \frac{1}{2}\tan^{-1}\left[\frac{\sum_i \mathrm{Real}(T_{xi}T^*_{yi})W_i}{\sum_i (|T_{xi}|^2 - |T_{yi}|^2)W_i}\right]. \qquad (5)$$

To test the method, we analyzed data obtained at the geothermal field at Cerro Prieto, Mexico. Figure 10 shows the location of the magnetotelluric sites surveyed in 1978 and 1979. In Table 1, we we list the angles with respect to magnetic north obtained along the line DD' using weighting functions t^0, $t^{1/2}$, t, and $t^{3/2}$, where t is the period. We see that the angles are essentially independent of the form of the W_i. In Table 2, we list the directions obtained on the lines DD', EE', and FF' with the weighting function t. We see that the

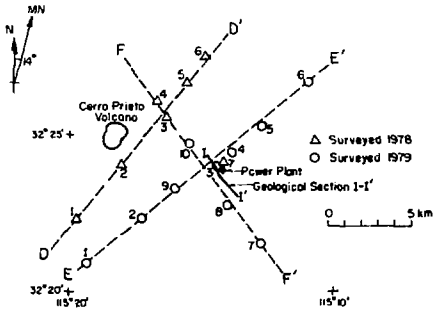

Fig. 10. Configuration of MT stations at Cerro Pricto, Mexico. (XBL 7911-12866)

angles obtained from the two methods agree well on DD' and on FF', but differ significantly on EE'. On the other hand, the directions obtained from the impedance tensor are in reasonably good agreement for all three lines. These results confirm our impression that there is a relatively well-defined regional strike, but also show that a two-dimensional model is definitely inapplicable for the line EE'.

It is our strong feeling that techniques such as these should be used to define a single coordinate system appropirate for the region surveyed and that the results for all sites and all frequencies should be referred to this frame. If the coordinate system rotates from station to station and from frequency to frequency, it is very difficult to interpret the data in a useful way.

* * *

†Brief version of LBL-10846.

1. MMRD Annual Report 1978, LBL-8580, pgs. 165-168; 1979, LBL-10000, pgs. 191-193.

Table 1. Regional strike on line DD' estimated with different weighting functions

Function of Period	Strike from Z	Strike from T
t^0	-32.3°	-30.6°
$t^{1/2}$	-30.0°	-30.1°
t	-28.4°	-29.8°
$t^{3/2}$	-27.8°	-30.2°

Table 2. Regional strikes on different lines with weighting function t

Line	Z strike	T strike
DD'	-28.4°	-29.8°
EE'	-27.9°	-17.3°
FF'	-25.5°	-22.3°

RESEARCH PLANS FOR CALENDAR YEAR 1981

Superconducting devices. It is hoped that the experiments to attain the quantum noise limit of dc SQUIDs will be completed. New electronic circuitry will be developed to enable these devices to be used in a flux-locked loop and also as small signal amplifiers. The use of these devices as amplifiers at frequencies of 100 MHz and above will be investigated. A project will be initiated to study the low-frequency (1/f) noise in SQUIDs. The noise current circulating around a SQUID is to be measured, and compared with our theoretical calculations. Finally, we hope to fabricate and test a new planar SQUID with a very fast slewing rate for use in geophysical measurements.

Non-equilibrium superconductivity. Experiments to study the enhancement of the superconducting energy gap by means of photon or phonon irradiation should be completed during the coming year. In each of the two experiments, it is hoped to measure the enhancement of the energy gap and the enhancement of the critical current simultaneously. Present theories suggest that in the non-equilibrium state the critical current will exceed the value predicted from the energy gap by equilibrium BCS theory. An experiment will be initiated to investigate the relaxation rate of charge imbalance under pulsed conditions rather than in the steady state situation that has always been studied previously. It is expected that near T_c the relaxation rate under pulsed conditions will be considerably faster than in the steady state. An experiment to measure the charge imbalance generated near the boundary of a superconductor in the presence of a thermal gradient is being assembled. It is hoped that this measurement will shed some light on the magnitude of the supercurrent established by the thermal gradient. This magnitude is believed to be well understood theoretically, but present experimental results are in considerable conflict with each other and with the theory.

Geophysics. We plan to perform several experiments to investigate the earth's magnetic field gradient fluctuations. We propose to set up three 3-axis SQUID magnetometers, with one as a remote reference. The separation between the remaining two magnetometers will be varied. This technique will enable us to make accurate measurements of

the difference in the magnetic field fluctuations at spatially separated sites. At the same time, these measurements are likely to yield valuable information on the magnetic noise observed in our magnetotelluric measurements, thereby providing a means for choosing the optimum separation between the magnetotelluric site and the remote reference.

1980 PUBLICATIONS AND REPORTS

Referred Journals

1. John Chi and John Clarke, "Addendum to 'Quasiparticle Branch Mixing Rates in Superconducting Aluminum'," Phys. Rev. B1, 21, 333 (1980), LBL-9695.

2. Thomas Y. Hsiang and John Clarke, "Boundary Resistance of the Superconducting-Normal Interface," Phys. Rev. B1, 21, 945 (1980), LBL-9577.

3. John Clarke and Michael Tinkham, "Theory of Quasiparticle Charge Imbalance Induced in a Superconductor by a Supercurrent in the Presence of a Thermal Gradient," Phys. Rev. Lett. 44, 106 (1980), LBL-9559.

4. John Clarke, "Advances in SQUID Magnetometers," IEEE Trans. Electron Devices, Vol. ED-27 10, 1896 (1980) LBL-10845.

5. Richard F. Voss, Robert Laibowitz, Stanley Raider, and J. Clarke, "All-Nb Low Noise dc SQUID with 1 μm Tunnel Junctions," J. Appl. Phys. 51, 2306 (1980), LBL-9893.

6. Roger H. Koch, Dale J. Van Harlingen, and John Clarke, "Quantum Noise Theory for the Resistively Shunted Josephson Junction," Phys. Rev. Lett., 45, 2132 (1980), LBL-11414.

Other Publications

1. Richard Dalven, Introduction to Applied Solid State Physics, Plenum Press, New York (1980).

2. John Clarke, Superconductive Devices in Encyclopedia of Physics, R. G. Lerner and G. L. Trigg (eds.), Addison-Wesley, Massachusetts (1980).

LBL Reports

1. Thomas D. Gamble, Wolfgang M. Goubau, Robert Miracky and John Clarke, "Magnetotelluric Regional Strike," submitted to Geophysics, LBL-10846.

2. Thomas R. Lemberger and John Clarke, "Charge-imbalance Relaxation in the Presence of a Pair-breaking Supercurrent in Dirty, Superconducting Al Films," submitted to Phys. Rev. B., LBL-11406.

3. Thomas R. Lemberger and John Clarke, "Charge-imbalance Relaxation in the Presence of a Pair-breaking Interaction in Superconducting AlEr Films," submitted to Phys. Rev. B., LBL-11201.

4. Roger H. Koch, Dale J. Van Harlingen, and John Clarke, "Quantum Noise Theory for the dc SQUID," submitted to Appl. Phys. Lett., LBL-11729.

Invited Talks

1. John Clarke, "Present Status and Future Development of SQUIDs," Workshop on Research in Magnetotellurics: Implications of Electrical Investigation for Geothermal Exploration, Christian Brothers Retreat House, Napa Valley, California, 20-22 February 1980.

2. Thomas D. Gamble, "Field Analysis of MT Data," Workshop on Research in Magnetotellurics: Implications of Electrical Investigation for Geothermal Exploration, Christian Brothers Retreat House, Napa Valley, California, 20-22 February 1980.

3. Wolfgang M. Goubau, "Remote Reference Magnetotellurics," Workshop on Research in Magnetotellurics: Implications of Electrical Investigation for Geothermal Exploration, Christian Brothers Retreat House, Napa Valley, California, 20-22 February 1980.

4. John Clarke, "SQUIDs and Geophysics," colloquium at the University of Vancouver, Vancouver, B. C., 28 February 1980.

5. Roger H. Koch, Dale J. Van Harlingen, John Clarke, and Claudia Tesche, "Quantum Limited Josephson Junction Noise," American Physical Society March meeting, New York, 24 March 1980.

6. John Clarke, "Fluctuations Analysis," Second International Conference on SQUIDs, Berlin, Germany, 5-9 May 1980.

7. John Clarke, "Summary and Conclusions," Second International Conference on SQUIDs, Berlin, Germany, 5-9 May 1980.

8. Wolfgang M. Goubau, "Geophysical Applications of SQUIDs," Second International Conference on SQUIDs, Berlin, Germany, 5-9 May 1980.

9. John Clarke, "Remote Reference Magnetotellurics with SQUIDs," SQUID-Geophysics Workshop, Los Alamos, New Mexico, 2-4 June 1980.

10. Thomas R. Lemberger, "Pair-breaking and Branch Imbalance in Non-equilibrium Superconductors," Solid State Physics Seminar, University of California, Berkeley, California, May 1980.

11. John Clarke, "Charge Imbalance," NATO Advanced Institute on Non-equilibrium Superconductivity, Phonons and Kapitza Boundaries, Acqufredda di Maratea, Italy, 25 August - 5 September 1980. (4 lectures).

12. Wolfgang M. Goubau, "Remote Reference Magnetotellurics with SQUIDs," Workshop on Magnetotellurics, University of Utah, Salt Lake City, Utah, 12 September 1980.

13. Thomas R. Lemberger, "Charge-imbalance Relaxation in Superconductors Containing Paramagnetic Impurities," Solid State Physics Seminar, Institut fur Theorie der Kondensierten Materie, Universität Karlsruhe, West Germany, September 1980.

14. Roger H. Koch, Dale J. Van Harlingen, and John Clarke, "Quantum Noise in the dc SQUID,"

Applied Superconductivity Conference, Santa Fe, New Mexico, 30 September 1980.

15. Thomas R. Lemberger and Dale J. Van Harlingen, "Superconductivity, Phonons, and Kapitza Boundaries," Solid State Physics Seminar, University of California, Berkeley, California, October 1980.

16. Thomas R. Lemberger, "Charge-imbalance in Superconductors," Solid State Physics Seminar, Xerox Corp., Palo Alto, California, November 1980.

17. John Clarke, "Progress in the Physics of Josephson Junctions," Second International Conference on Superconducting Tunnel Junctions, Chengdu, China, 3 November 1980.

18. John Clarke, "Junctions and Circuit Fabrication-Computers," Second International Conference on Superconducting Tunnel Junctions, Chengdu, China, 4 November 1980.

19. John Clarke, "SQUIDs and Their Noise Limitations," Second International Conference on Superconducting Tunnel Junctions, Chengdu, China, 4 November 1980.

20. John Clarke, "Charge-imbalance in Superconductors," Second International Conference on Superconducting Tunnel Junctions, Chengdu, China, 5 November 1980.

21. John Clarke, "SQUIDs in Measurement and Computers," Seminar at the Bureau of Metrology, Shanghai, China, 7 November 1980.

22. John Clarke, "Superconducting Electronics," New Horizons in Science, the 18th Annual Briefing of the Council for the Advancement of Science Writers, Durham, North Carolina, 1 December 1980.

23. John Clarke, "Charge-imbalance in Superconductors," Bariloche 80, Centro Atomico Bariloche, Bariloche, Argentina, 15 December 1980.

2. Theoretical Solid-State Physics*

a. Theoretical Studies of the Electronic Properties of Solid Surfaces*

Leo Falicov, Investigator

This program is concerned mostly with the study of the electronic structure of solid surfaces and interfaces as well as its consequences for structural, magnetic and chemical properties. The general modus operandi of the principal investigator and his collaborators in the projects is the formulation of theories and models and the performance of calculations which are either prototypes of important real situations or "realistic" calculations of specific properties. In all parts of this program, there is a constant and fruitful interaction with experimental groups at LBL, both within MMRD (Profs. Somorjai and Shirley) and in other Divisions (Prof. E. E. Haller, Engineering and Technical Services Division) as well as in other laboratories (e.g., Prof. Y. Pétroff, at L.U.R.E., Orsay, France). These experimental-theoretical collaborations result, in some cases, in publications of mixed character in which a given problem is presented both as an experimental result and as an exposition of its underlying theory.

1. ELECTRONIC PROPERTIES OF COMPLEX IMPURITIES IN ULTRAPURE GERMANIUM

L. M. Falicov, Bela Joós and Eugen E. Haller

In the extremely pure germanium samples obtained at LBL by Prof. E. E. Haller, it is possible to identify by optical and resonance means complex impurity centers which, under normal conditions, would remain undetected. In particular, by means of photothermal ionization spectroscopy (PTIS), and with the help of exhaustive theoretical analysis, we have been able to identify two types of new and very interesting complex impurity centers:

(1) Acceptors A (H,Si) and A (H,C), which consist of a group IV (Si or C) isoelectronic substitutional impurity and an attached hydrogen;

(2) a donor D (H,O) formed by an oxygen atom, probably also substitutional, which also has an attached hydrogen.

These impurities, because of the presence of the very light hydrogen atom, present a dynamic "nucleus" in which the light atom tunnels among four equilibrium positions about the heavier substitutional atom. They are shown schematically in Figs. 1 and 2. A germanium conduction-band electron (for the donor) or a valence-band hole (for the acceptor) orbit in the impurity 1s level about the complex dynamic "nucleus."

The electronic-complex-nucleus system is thus essentially a three-body problem, with a Coulomb interaction between the "nucleus" and the band carrier, and a slow tunneling interaction between the hydrogen and the heavier atom. The diamond-type structure of Ge and its well known but complex conduction and valence electronic band structures play a very important role.

This three-body problem has been solved on a restricted basis, which involves the diagonalization in each case of a 16×16 matrix for the total energy of the impurity center. The matrix elements are energy parameters which, in most cases, can be determined by an analysis of the experimental spectroscopic data as a function of photon frequency, temperature, and direction and strength of applied uniaxial stresses. An overall consistent picture of the electronic properties, in agreement with the chemical history of each particular sample, has been obtained.[1,2]

* * *

1. E. E. Haller, B. Joós and L. M. Falicov, Phys. Rev. B 21, 4729 (1980).
2. B. Joós, E. E. Haller and L. M. Falicov, Phys. Rev. B 22, 832 (1980).

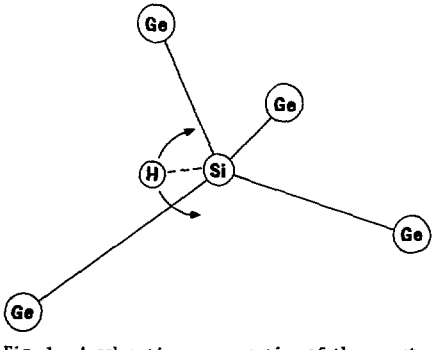

Fig. 1. A schematic representation of the acceptor A (H,Si) impurity in germanium, with the Si atom in a substitutional position. (XBL 798-11028)

*This work was supported by the Director, Office of Energy Research, Office of Basic Energy Sciences, Materials Sciences Division of the U.S. Department of Energy under Contract No. W-7405-ENG-48.

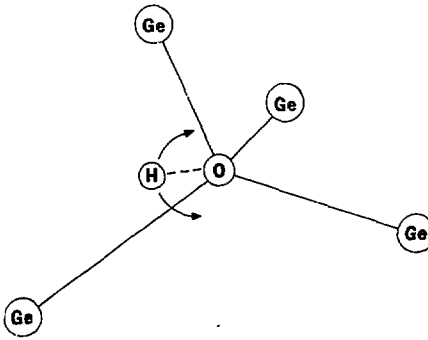

Fig. 2. A schematic representation of the donor D (H,O). (XBL 802-7970)

2. THEORETICAL STUDY OF LITHIUM INTERCALATION IN TRANSITION-METAL DICHALCOGENIDES

L. M. Falicov and Roberto Osório

Transition metal dichalcogenides are layered compounds of formula MX_2 (TiS_2 is a typical example) in which strongly bound X-M-X sandwiches are only weakly (van der Waals) bound to each other in varying layer stacks. Intercalation of Li^+ between the layers has resulted in a useful cathode for commercially viable batteries.[1-7] Electrochemical measurements on Li_xTiS_2 cells have permitted a detailed study of the thermodynamics of the Li intercalation, and the determination of the characteristics of what is in practice a strongly interacting two-dimensional lattice gas: the Li^+ ions distribute themselves on sites between the layers; these sites form a two-dimensional triangular lattice. We have examined this situation in several model calculations:

- A relatively simple three-sublattice Bragg-Williams calculation[8] illustrates the meaning of the features in the incremental capacity versus concentration curves: (a) minima are associated with ordered structures, (b) sharp maxima (divergences) are caused by the coexistence of ordered and disordered phases over concentration intervals, and (c) smooth maxima can be found at concentrations of no direct relevance to ordering.
- A more sophisticated three-sublattice triangle approximation[9] with nearest-neighbor repulsion and three-particle attractions was also examined. Order-disorder phase diagrams and thermodynamic functions were computed. Peaks in the incremental capacity as function of concentration reproduce the experimental data of Thompson,[1,2] in particular the maxima and minima.

We have thus confirmed the validity of the lattice gas model as a first approximation for the problem of ordering of Li^+ ions in systems like Li_xTiS_2. Better results could almost certainly be achieved by introducing longer-range interactions. The improvements, however, are limited mainly by the inaccurate description of the guest-host interaction and the electronic contributions due to the filling of the TiS_2 conduction band.

* * *

1. A. H. Thompson, Phys. Rev. Letters 40, 1511 (1978).
2. A. H. Thompson, J. Electrochem. Soc. 126, 608 (1979).
3. D. W. Murphy and R. A. Trumbore, J. Crystal Growth 39, 185 (1977).
4. M. S. Whittingham, Science 192, 1126 (1976).
5. M. S. Whittingham, J. Electrochem. Soc. 123, 315 (1976).
6. B. G. Silbernagel and M. S. Whittingham, J. Chem. Phys. 64, 3670 (1976).
7. B. G. Silbernagel, Mat. Sci. and Eng. 31, 281 (1977).
8. R. Osório and L. M. Falicov, submitted to Phys. Rev. B., LBL-11474.
9. R. Osório and L. M. Falicov, submitted to Phys. Rev. B, LBL-11475.

3. PHOTOEMISSION PROPERTIES AT THE SURFACE OF TRANSITION METALS

L. M. Falicov and Jerry Tersoff

X-ray photoemission spectroscopy has become an invaluable tool for the study of electron-electron interactions in transition metals. The spectra show rich structures, which differ considerably from the naive picture to be expected from simple one-electron theory. Nickel has been the subject of several experimental[1-3] and theoretical[1-4] studies; these studies have been correlated with others involving Auger electron spectroscopy.[5,6]

The general characteristic of the experimental data is the existence of satellite lines, attached to the main core and conduction band peaks, which in general are located approximately 3-6 eV below the corresponding main feature. These satellites have been unequivocally assigned to a localized many-electron excitation of the transition metal.

We have developed[7] a theory of the satellite structure of the core-level photoemission spectrum of transition metals. It was applied to the $2p_{3/2}$ level of metallic nickel. The calculation was carried out for both the paramagnetic and ferromagnetic states and was based on two scattering parameters, one intraband and one interband. Agreement with experiment is very good.

* * *

1. C. Guillot, Y. Ballu, J. Paigne, J. Lecante, K. P. Jain, P. Thiry, R. Pinchaux, Y. Pétroff, and L. M. Falicov, Phys. Rev. Lett. 39, 1632 (1977).

2. G. G. Tibbets and W. F. Egelhoff, Jr., Phys. Rev. Lett. 41, 188 (1978).
3. S. P. Kowalczyk, Ph.D. thesis, University of California, Berkeley, 1976.
4. D. R. Penn, Phys. Rev. Lett. 42, 921 (1979).
5. A. M. Bard, M. Salmerón and J. M. Rofo, J. Phys. F 5, 826 (1979).
6. G. A. Sawatsky, Phys. Rev. Lett. 39, 504 (1977).
7. E. Antonides and G. A. Sawatsky in Transition Metals 1977, M. J. G. Lee, J. M. Parz and E. Fawcett, eds., Institute of Physics, Bristol and London, 1978, p. 134.
8. J. Tersoff, L. M. Falicov and D. R. Penn, Solid State Commun. 32, 1045 (1979).

RESEARCH PLANS FOR CALENDAR YEAR 1981

Work nearing completion will analyze the contributions of the various atomic configurations and the interconfiguration fluctuations to both the photoemission spectra and the chemical activity of (a) clean, smooth surfaces of Ni, (b) clean, smooth surfaces of Cu (c) stepped surfaces of both Ni and Cu, (d) smooth overlayers of Cu on Ni and Ni on Cu, (e) irregular, stepped overlayers of Cu on Ni and Ni on Cu, and (f) isolated attached impurities (kinks) of both Ni and Cu on either Ni or Cu metal.

The following projects will be also conducted during 1981:

1. Study of the spectral properties of hydrogen in ultrapure germanium and in germanium with substitutional impurities.

2. Analysis of the electronic and chemical properties of transition and noble metal surfaces; the surfaces will be ideal, stepped or with other defects.

3. Analysis of the many-electron effects in the surface photoemission of transition metals.

1980 PUBLICATIONS AND REPORTS

Refereed Journals

†1. L. M. Falicov and M. E. Foglio, "Theory of Intermediate Valence. III. Electronic Specific Heat," Phys. Rev. B 21, 4154 (1980).

†2. L. M. Falicov and J. L. Morán-López, "Spin Waves at the Surface of Ferromagnetic Alloys: A Cluster-Bethe-Lattice Approach," J. of Magnetism and Magnetic Materials 15-18, 1077 (1980).

3. L. M. Falicov, E. E. Haller and B. Joós, Acceptor Complexes in Germanium: Systems with Tunneling Hydrogen," Phys. Rev. B 21, 4729 (1980).

4. L. M. Falicov, B. Joós and E. E. Haller, "Donor Complex with Tunneling Hydrogen in Pure Germanium," Phys. Rev. B 22, 832 (1980), LBL-10499.

†5. L. M. Falicov and T. H. Lin, "Diatomic-Molecule Model for a Mixed-Valence System," Phys. Rev. B 22, 857 (1980).

†6. L. M. Falicov and C. A. Balseiro, "Phonon Raman Scattering in Superconductors," Phys. Rev. Letters 45, 662 (1980).

†7. L. M. Falicov and P. Thalmeier, "Broken-Symmetry States in Solids with Multiple Bands," Phys. Rev. B. 22, 2456 (1980).

†8. L. M. Falicov and R. E. McMurray, Jr., "Theory of Electric Breakdown in Solids with General Two-band Crossings," Phys. Rev. B 22, 4047 (1980).

Other Publications

1. L. M. Falicov and R. C. Kittler, "Band Theory for Order-Disorder Phase-Transformation: CuAu, Cu_3Au and $CuAu_3$," in Theory of Alloy Phase Formation, edited by L. H. Bennett, The Metallurgical Soceity of AIME, New York (1980).

2. L. M. Falicov and C. A. Balseiro, "Superconductivity and Charge-Density Waves," in Superconductivity in d- and f-Band Metals, edited by H. Suhl and M. B. Maple, Academic Press, Inc., New York (1980).

LBL Reports

1. L. M. Falicov and R. Osório, "Three-Sublattice Model for a Triangular Lattice Gas," LBL-10685.

2. L. M. Falicov and R. Osório, "Cluster-Variation Method for the Triangular Lattice Gas I. Three-Sublattice Point Approximation," LBL-11474.

3. L. M. Falicov and R. Osório, "Cluster-Variation Method for the Triangular Lattice Gas II. Triangle Approximation," LBL-11475.

Invited Talks

1. L. M. Falicov, "Propiedades de las Superficies de Aleaciones Binarias," Symposium on the Physics of Condensed Matter, in celebration of the 10th anniversary of the foundation of University Simon Bolivar, Caracas, Venezuela, 20 February 1980.

2. L. M. Falicov, "The Theory of Electron Photoemission," Symposium on Trends in Studies of Electronic Properties of Metals by Photoemission, Centre de Physique des Houches, Ecole de Physique Theorique, France, 3-14 March 1980.

3. L. M. Falicov, Annual Conference of the Condensed Matter Division of the European Physical Society, Antwerp, Belgium, 9-11 April 1980. (Invitation declined)

4. L. M. Falicov, "Electron Correlation Effects in Photoemission," Meeting on Major Problems in the Theory of Surfaces, Institute for Theoretical Physics, University of California, Sants Barbara, 11-12 August 1980.

5. L. M. Falicov, "Band Theory for Order-Disorder Phase-Transformations," 28th Midwest Solid State Physics Conference, Michigan State University, 24-25 October 1980.

6. L. M. Falicov, "Intraatomic Correlation in Canonical d-Bands," 1980 March meeting of the American Physical Society, New York, NY, March 24-28, 1980 (presented by P. Thalmeier).

7. L. M. Falicov, "Surface Spin Density Wave in the Cr-Re Alloys," 1980 March meeting of the American Physical Society, New York, NY, March 24-28, 1980 (presented by G. J. Mata).

8. L. M. Falicov, "Acceptor Complexes in Germanium with Tunneling Hydrogen," 1980 March meeting of the American Physical Society, New York, NY March 24-28, 1980 (presented by B. Joós).

9. L. M. Falicov, "Surface Properties of Binary Alloys," James Franck Institute, University of Chicago, IL, October 23, 1979.

10. L. M. Falicov, "Surface Properties of Binary Alloys," Oregon State University, Corvallis, Oregon, January 28, 1980.

11. L. M. Falicov, "Electronic Hamiltonians," Institute for Theoretical Physics, University of California, Santa Barbara, July 14, 1980.

12. L. M. Falicov, "Electronic Hamiltonians," Institute for Theoretical Physics, University of California, Santa Barbara, July 17, 1980.

13. L. M. Falicov, "Surface Properties of Binary Alloys," National Bureau of Standards, Washington, D.C., September 15, 1980.

14. L. M. Falicov, "Intermediate Valence Solids: An Overview," National Science Foundation, Washington, D.C., September 16, 1980.

15. L. M. Falicov, "Theory of Intermediate Valence for Systems (a) with One and (b) with Two Magnetic Configurations," Institute for Theoretical Physics, University of California, Santa Barbara, October 6, 1980.

†Supported by NSF Grant DMR78-03408.

b. Theoretical Solid-State Physics*

Marvin L. Cohen, Investigator

1. PSEUDOPOTENTIAL TECHNIQUES

The relative ease in doing calculations associated with pseudopotentials is usually attributed to the fact that core electrons are not examined. Only valence electron energy levels and wavefunctions are computed. These calculations are normally done in a momentum or k-space representation, and Fourier components of the charge density of the electrons and the form factors for the potentials are the usual outputs. Most formalisms for total energy calculations are based on a real space representation, and these approaches are often too cumbersome to implement. We have, therefore, developed a momentum-space formalism[1] to deal with total energy calculations. This approach allows accurate total energy computations using the ordinary outputs from electronic energy band calculations. The ease and flexibility of this new method have enabled us to do accurate calculations having important consequences. These are discussed in article 4 below.

The first-principles pseudopotential approach, which we developed previously, was used to compute properties of solids.[2] The scheme enables a determination of a pseudopotential starting with only atomic properties. The potentials have been used in a number of applications on atoms, molecules, and solids. They are usually generated in numerical form, but we have recently devised a simple analytical form[3] to model the main physical properties of the potentials. Fitting parameters for the first three ions of the periodic table have been found, and these reflect the chemical trends of the elements. We found that a minimum of three parameters is required to reproduce the regularities of the periodic table.

* * *

1. J. Ihm, A. Zunger, and M. L. Cohen, J. Phys. C12, 4409 (1979).
2. A. Zunger and M. L. Cohen, Phys. Rev. B20, 4082 (1979).
3. P. K. Lam, M. L. Cohen, and A. Zunger, Phys. Rev. B22, 1698 (1980).

2. SOLID SURFACES AND INTERFACES

We continued our studies of solid surfaces. These included: calculations of the electronic structure of Mo(001) with a hydrogen monolayer,[1,2] the clean (110) surface of GaAS[3,4] and GaAs(110) with an Al overlayer,[5] and the Si(001) 2 × 1 surface.[6] The latter calculation tested dimer models for the two dangling bonds on the Si(001) surface. Most surface structure models assume that the dangling bonds form symmetric dimers, that is, both bonds reconstruct in the same way. Chadi recently proposed an asymmetric dimer structure using the tight-binding method. Our calculation supports Chadi's model. The energetics of the asymmetric dimer are favorable, and the electronic properties are in better agreement with experiment than the results for the symmetric dimer model.

Interface work concentrated on metal-semiconductor interfaces (Schottky barriers)[5,7-10] and semiconductor-semiconductor interfaces (heterojunctions).[8,10,11,12-14] One recent study[13,14] concentrated on the question of symmetry-induced localization. In previous calculations, we demonstrated that an interface between two semiconductors could localize electrons if the semiconductors had different ionicities. Examples are Ge-GaAs and GaAs-ZnSe interfaces. In these cases, the symmetry remains the same on both sides of the interface, but the ionicity does not. For systems like GaAs-AlAs, both the symmetry and the ionicity are approximately unchanged, and no localized interface states are found.

The question remained as to whether a symmetry change alone could localize interface states. To test this case, a zincblende-wurtzite interface between these two crystalline modifications for ZnS and for ZnSe were assumed in the model calculations. At the interface, the bonds do not change, that is, no change in ionicity occurs; but the symmetry changes over a distance corresponding to three nearest neighbors. The calculational results reveal that electronic states or resonances are localized near the interface. The region of localization is approximately three nearest neighbor lengths. This corresponds to the distance that an electron state "knows" that there is a symmetry change.

A similar calculation was done for a rotation twin stacking fault in β-ZnS.[14] This calculation also revealed localization caused by the symmetry change associated with the stacking fault.

* * *

1. G. P. Kerker, M. T. Yin, and M. L. Cohen, Solid State Comm. 32, 433 (1979).
2. G. P. Kerker, M. T. Yin, and M. L. Cohen, Phys. Rev. B20, 4940 (1979).
3. J. R. Chelikowsky and M. L. Cohen, Phys. Rev. B20, 4150 (1979).

*This work was supported in part by the Director, Office of Energy Research, Materials Sciences Division of the U. S. Department of Energy under Contract No. 7405-ENG-48 and by the National Science Foundation.

4. J. R. Chelikowsky and M. L. Cohen, J. Vac. Sci. Technol. 16, 1307 (1979).
5. J. R. Chelikowsky, D. J. Chadi, and M. L. Cohen, "Electronic Structure of the GaAs(110)-Al Chemisorption System," UCS Physics Dept. preprint. Submitted to Phys. Rev. B.
6. J. Ihm, M. L. Cohen, and D. J. Chadi, Phys. Rev. B21, 4592 (1980).
7. M. L. Cohen, J. Vac. Sci. Technol. 16, 1135 (1979).
8. M. L. Cohen, "Electrons at Interfaces," in Advances in Electronics and Electron Physics, Vol. 51, edited by L. Marton and C. Marton, Academic Press, New York (1980).
9. J. Ihm, M. L. Cohen, and J. R. Chelikowsky, "Electronic Structure of a Pd Monolayer on a Si(111) Surface," UCB Physics Dept. preprint. Submitted to Phys. Rev. B.
10. M. L. Cohen, "Pseudopotential Calculations for Ideal Surfaces," in Proceedings of the Seventh LBL/MMRD International Materials Symposium on Surfaces and Interfaces in Ceramics and Ceramic-Metal Systems.
11. J. Ihm, P. K. Lam, and M. L. Cohen, Phys. Rev. B20, 4120 (1979).
12. J. Ihm, P. K. Lam, and M. L. Cohen, J. Vac. Sci. Technol. 16, 1512 (1979).
13. J. E. Northrup, J. Ihm, and M. L. Cohen, Phys. Rev. B22, 2060 (1980).
14. J. Northrup and M. L. Cohen, "Electronic Structure of the Rotation Twin Stacking Fault in β-ZnS," UCB Physics Dept. preprint. Submitted to Phys. Rev. B.

3. ELECTRONIC STRUCTURE

The pseudopotential approach was used to explore the electronic structure of an O_2 molecule,[1] H in Ge,[2] semiconductors,[3] and an A15 metal.[4,5] It was also used to explore the valence charge distribution and electric field gradients in GaAs-AlAs mixed crystals[6] and the mechanisms causing the temperature dependence of semiconductor energy gaps.[7]

The calculation for the A15 metal concentrated on V_3SI.[4,5] The electronic charge density had been determined using x-ray measurements. One of the main purposes of the electronic calculation was to compare the computed electron charge density with the measured results and to explore the bonding nature of this high temperature superconductor. To investigate the V-V, Si-Si, and V-Si interactions, charge density calculations were done for V_3 (chain only) and Si (bcc) model structures. By comparing the results for these model calculations, it was possible to conclude that the bonding between V atoms is covalent-like along the chains, and it is metallic in nature between the V and Si atoms. The agreement between experiment and theory was good for the total charge density and for that part of the electronic band structure which had been measured using photoemission.

* * *

1. G. P. Kerker, A. Zunger, M. L. Cohen, and M. Schlüter, Solid State Comm. 32, 309 (1979).
2. W. E. Pickett, M. L. Cohen, and C. Kittel, Phys. Rev. B20, 5050 (1979). Erratum: Phys. Rev. B22, 3135 (1980).
3. M. L. Cohen and J. R. Chelikowsky, "Pseudopotentials for Semiconductors," in Handbook on Semiconductors, Vol. 1, edited by W. Paul, North-Holland, Amsterdam.
4. P. K. Lam and M. L. Cohen, "Electronic Charge Density and Bonding in V_3Si," UCB Physics Dept., preprint. Submitted to Phys. Rev. B.
5. P. K. Lam and M. L. Cohen "Effective Atomic Volumes for Elements in A15 Compounds," UCB Physics Dept. preprint, submitted to Physics Letters.
6. J. Ihm, M. L. Cohen, and V. I. Safarov, Solid State Comm. 34, 325 (1980).
7. M. L. Cohen and D. J. Chadi, "Temperature Dependence of Semiconductor Band State," in Handbook on Semiconductors, Vol. 2, edited by M. Balkanski, North-Holland, Amsterdam (1980).

4. TOTAL ENERGY CALCULATIONS

Using the total energy approach in momentum space discussed in article 1 above a number of new calculations have become possible.[1,2,3,4,5,6,7] These calculations require very accurate pseudopotentials which give reliable energy levels and wavefunctions for both atomic and solid state limits. Several approaches have yielded pseudopotentials of the desired accuracy (Starkloff and Joannopoulos; Zunger and Cohen; Hamann, Schlüter, and Chiang; and Kerker). In our calculations, we have used the potentials of Hamann, Schlüter, and Chiang.

The method has been applied to Si and Ge. We will focus on Si here, but comparable results are obtained for Ge. Minimization of the total energy gives the Si lattice constant, 5.451 Å (5.429, 0.4%); cohesive energy, 4.67 eV/atom (4.63, 0.9%); and bulk modulus, 0.98×10^{12} erg/cm^3 (0.99×10^{12}, -1.0%). The experimental values and deviations are given in parenthesis. Lattice vibrational frequencies are also calculated by distorting the crystal according to phonon displacements (frozen phonon model) and computing force constants. The calculated (measured, deviation) frequencies for the Γ, X, and L points of the Brillouin zone, 10^{12} Hz, are: LTO(Γ), 15.16 (15.53, -2.4%); TA(X), 4.45 (4.49, - 0.9%); TO(X), 13.48 (13.90, -3.0%); LOA(X), 12.16 (12.32, - 1.3%); LA(L), 10.81 (11.35, -4.8%); LO(L), 12.58 (12.60, -0.2%): TA(L), 3.35 (3.43, -2.3%); TO(L), 14.06 (14.68, -4.2%). The agreement is remarkable considering that only the atomic number and crystal structure are used for input. In addition, this is the first truly ab initio phonon calculation.

Another calculation which has previously been difficult to do accurately is structural stability.

The case considered for Si was a comparison of the diamond, hexagonal diamond, β-tin, hcp, bcc, and fcc structures. Using calculations of the total energies, minimum volumes, and minimum energies, the differences in the minimum energy for each of the above crystal structures and of the diamond structure can be evaluated. These are (in eV): hexagonal diamond (0.016); β-tin (0.27); hcp (0.55); bcc (0.53); and fcc (0.57). These results are shown in Fig. 1. The cubic diamond structure is clearly lowest in energy at atmospheric pressure.

Using similar techniques, the pressure-induced diamond-β-tin phase transition can be computed. The microscopic explanation of a solid-solid phase transition is at least a 60 year old problem in materials science. The results are shown in Fig. 1. The fcc, bcc, and hcp structures are high in energy compared to the β-tin, hexagonal, and cubic diamond structures for the volumes of interest. With increasing hydrostatic pressure, the system follows the path 1→2→3→4 illustrated in Fig. 1. The phase transition occurs along 2→3 which is the common tangent of the energy versus volume curves. This region represents the mixed states of the diamond and β-tin phases. The tangent points determine the transition volumes for the diamond, V_t^d, and β-tin, V_t^β, phases, and the slope of the tangent gives the transition pressure, P_t, which is less precisely determined theoretically. The calculated (measured, deviation) values are: V_t^d, 0.928 (0.918, 1.1%); V_t^β, 0.718 (0.710, 1.1%), V_t^β/V_t^d, 0.774 (0.773, 0.1%); and P_t, 99 (125, 20%). The volumes are normalized to the measured zero-pressure volume, and the pressure is given in kbar. The only input to this calculation is the atomic number and the consideration of a limited number of structural types.

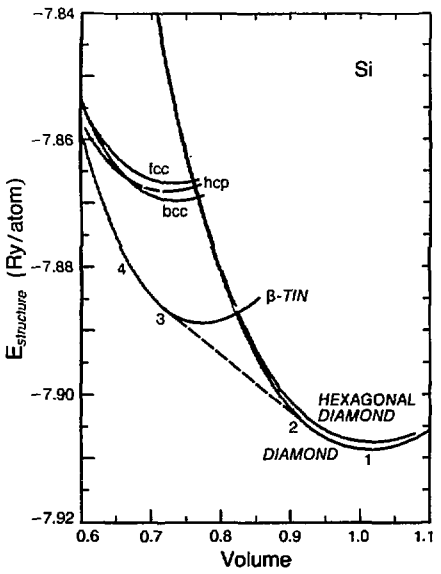

Fig. 1. The diamond, hexagonal diamond, β-tin, hcp, bcc, and fcc structural energies (in units of Ry/atom) as a function of the atomic volume (normalized to the measured free volume) for Si. The dashed line is the common tangent of the energy curves for the diamond and the β-tin structures. (XBL 814-9170)

The excellent results for static, vibrational, and structural properties represent a breakthrough in solid state physics calculations. These results give support to the theoretical constructs, which are primarily the pseudopotential and density-functional approaches.

* * *

1. J. Ihm and M. L. Cohen, Phys. Rev. B21, 3754 (1980).
2. M. T. Yin and M. L. Cohen, Phys. Rev. Lett. 45, 1004 (1980).
3. M. L. Cohen, "Pseudopotentials and Crystal Structure," in Structure and Bonding in Crystals, Vol. 1, edited by M. O'Keeffe and A. Navrotsky, Academic Press, New York.
4. J. Ihm, M. T. Yin, and M. L. Cohen, "Quantum Mechanical Force Calculations in Solids: The Phonon Spectrum of Si," UCB Physic Dept. preprint. Submitted to Solid State Communications.
5. J. Ihm and M. L. Cohen, "Equilibrium Properties and the Phase Transition of Grey and White Tin," UCB Physics Dept. reprint. Submitted to Phys. Rev. B.
6. M. L. Cohen, Pseudopotential Theory of Surface and Bulk Properties of Semiconductors," in Proceedings of the 15th International Conference on the Physics of Semiconductors, to be published by Physical Society of Japan.
7. M. T. Yin and M. L. Cohen, "Microscopic Theory of the Static Structural Properties and Phase Transformation of Ge," UCB Physics Dept. preprint. Submitted to Solid State Communications.

5. DEMONS AND SUPERCONDUCTIVITY

Various electronic mechanisms have been proposed for superconductivity, but there is no compelling experimental evidence to support the view that existing superconductors owe their loss of resistance to any mechanism other than conventional electron-phonon interactions. However, the appeal of electronic mechanisms remains because of the potential high transition temperatures possible using electron-electron Coulomb interactions. We have investigated some of these suggestions[1,2] with emphasis on the demon mechanism.

In a two component plasma in a gas or solid, the lighter mass component can screen interactions between the heavier mass particles, and an acoustic plasma mode can result. For a solid,

it is the screening of the ion-ion interactions by the lighter electrons which gives rise to acoustic phonon modes. For transition metals, the heavier d-electron interactions can be screened by the light s-electrons, and an acoustic plasmon results. This acoustic plasmon or demon mode has not be observed experimentally, but it is a natural consequence of the theory of solid state plasmas.

One suggestion for electronic-interaction-induced superconductivity is based on s-electrons exchanging demons much like conventional superconductors involve electrons, electrons exchanging phonons. The demon problem has previously been formulated primarily in this way; however, this approach is not reliable for accurate estimates of the pairing interactions.

We have, therefore, used a total dielectric functional approach based on model band structures. The results show that the demon mechanism generally reduces the repulsive Coulomb interaction between electrons. Under suitable conditions, the model calculations indicate that the electron-electron interaction via demons can be attractive, but the results also suggest that this mechanism is probably not dominant in transition metals and transition metal compounds. An attractive interband contribution is also found, and it is proposed that this effect may lead to electron pairing in suitable systems.

* * *

1. M. L. Cohen, "Theoretical Overview--Emphasis on New Mechanisms," in Superconductivity in d- and f-Band Metals, edited by H. Suhl and M. B. Maple, Academic Press, New York (1980).
2. J. Ihm, M. L. Cohen, and S. F. Tuan, "Demons and Superconductivity," UCB Physics Dept. preprint. Submitted to Phys. Rev. B.

RESEARCH PLANS FOR CALENDAR YEAR 1981

The successes with the total energy calculations described in article 4 above have motivated us to concentrate in this area. Further calculations on phonons, phase transitions, and static properties of bulk crystals will be done. In addition, an attempt to determine surface reconstruction will be made using total energy calculations.

A promising method for calculating electronic structure has been developed by our collegue, Professor Steven Louie. This approach involves localized orbitals and is much simpler and cheaper than computer time, but not as accurate to use as the self-consistent pseudopotential approach. We hope to apply these results to more complex crystal types and deferts. One calculation in progress is on the electronic properties of a line defect. We also hope to explore the properties of H in Si using this method.

1980 PUBLICATIONS AND REPORTS

Refereed Journals

1. J. Ihm, A. Zunger, and M. L. Cohen, "Momentum-Space Formalism for the Total Energy of Solids," J. Phys. C 12, 4409 (1979).

2. G. P. Kerker, A. Zunger, M. L. Cohen, and M. Schlüter, "A Solid State Approach to the Electronic Structure of Molecules: Self-Consistent Pseudopotential Calculation of O_2," Solid State Comm. 32, 309 (1979).

3. G. P. Kerker, M. T. Yin, and M. L. Cohen, "Self-Consistent Electronic Structure for a Mo(001) Surface with Saturated H Adsorption," Solid State Comm. 32, 433 (1979).

4. A. Zunger and M. L. Cohen, "First-Principles Nonlocal-Pseudopotential Approach in the Density Functional Formalism. II. Application to Electronic and Structural Properties of Solids," Phys. Rev. B20, 4082 (1979).

5. J. Ihm, P. K. Lam, and M. L. Cohen, "Electronic Structure of the (001) InAs-GaSb Superlattice," Phys. Rev. B20, 4120 (1979).

6. J. R. Chelikowsky and M. L. Cohen, "Self-Consistent Pseudopotential Calculation for the Relaxed (110) Surface of GaAs," Phys. Rev. B20, 4150 (1979).

7. M. L. Cohen, "Schottky and Bardeen Limits for Schottky Barriers," J. Vac. Sci. Technol. 16, 1135 (1979).

8. J. R. Chelikowsky and M. L. Cohen, "The (110) Surface of GaAs," J. Vac. Sci. Technol. 16, 1307 (1979).

9. J. Ihm, P. K. Lam, and M. L. Cohen, "Electronic Structure of the (100) InAs-GaSb Superlattice," J. Vac. Sci. Technol. 16, 1512 (1979).

10. G. P. Kerker, M. T. Yin, and M. L. Cohen, "Self-Consistent Electronic Structure of a Transition Metal Surface with an Adsorbate: H on Mo(001)," Phys. Rev. B20, 4940 (1979).

11. W. E. Pickett, M. L. Cohen, and C. Kittel, "Theory of the Hydrogen Interstitial Impurity in Germanium," Phys. Rev. B20, 505 (1979). Erratum: Phys. Rev. B22, 3135 (1980).

12. M. L. Cohen, Science Citation Classic: M. L. Cohen and T. K. Bergstresser, Phys. Rev. 141, 789 (1966); Current Contents 11, 14 (1980).

13. M. L. Cohen and D. J. Chadi, "Temperature Dependence of Semiconductor Band State," in Handbook on Semiconductors, Vol. 2, edited by M. Balkanski, North-Holland, Amsterdam (1980).

14. J. Ihm and M. L. Cohen, "Calculation of Structurally Related Properties of Bulk and Surface Si," Phys. Rev. B21, 1527 (1980). Erratum: *Phys. Rev. B22, 2135 (1980)*.

15. J. Ihm and M. L. Cohen, "Comment on 'Correction to Fuchs' Calculation of the Electrostatic Energy of a Wigner Solid'," Phys. Rev. B21, 3754 (1980).

16. J. Ihm, M. L. Cohen, and V. I. Safarov, "Valence Charge Distribution and Electric Field Gradients in GaAs-AlAs Mixed Crystal," Solid State Comm. 34, 325 (1980).

17. M. L. Cohen, "Theoretical Overview--Emphasis on New Mechanisms," in Superconductivity in d- and f-Band Metals, edited by H. Suhl and M. B. Maple, Academic Press, New York (1980).

18. J. Ihm, M. L. Cohen, and D. J. Chadi, "(2 × 1) Reconstructed Si(001) Surface: Self-consistent Calculations of Dimer Models," Phys. Rev. B21, 4592 (1980).

19. M. L. Cohen, "Electrons at Interfaces," in Advances in Electronics and Electron Physics, Vol. 51, edited by L. Marton and C. Marton, Academic Press, New York (1980).

20. M. L. Cohen, "Comment on 'Quantum Photoyield of Diamond (111)--A Stable Negative-Affinity Emitter'," Phys. Rev. B22, 1095 (1980).

21. M. T. Yin and M. L. Cohen, "Microscopic Theory of the Phase Transformation and Lattice Dynamics of Si," Phys. Rev. Lett. 45, 1004 (1980).

22. P. K. Lam, M. L. Cohen, and A. Zunger, "Analytic Representation for First-Principles Pseudopotentials," Phys. Rev. B22, 1698 (1980).

23. J. E. Northrup, J. Ihm, and M. L. Cohen, "Electronic Structure of Zincblende-Wurtzite Interfaces: ZnS-ZnS (111-0001) and ZnSe-ZnSe(111-0001)," Phys. Rev. B22, 2060 (1980).

Reports

1. M. L. Cohen and J. T. Chelikowsky, "Pseudopotentials for Semiconductors," in Handbook on Semiconductors, Vol. 1, edited by W. Paul, North-Holland, Amsterdam.

2. J. R. Chelikowsky, D. J. Chadi, and M. L. Cohen, "Electronic Structure of the GaAs(110)-Al Chemisorption System," UCB Physics Dept. preprint. Submitted to Phys. Rev. B.

3. J. Ihm, M. L. Cohen, and J. R. Chelikowsky, "Electronic Structure of a Pd Monolayer on a Si(111) Surface," UCB Physics Dept. preprint. Submitted to Phys. Rev. B.

4. J. Ihm, M. L. Cohen, and S. F. Tuan, "Demons and Superconductivity," UCB Physics Dept. preprint. Submitted to Phys. Rev. B.

5. M. L. Cohen, "Pseudopotentials and Crystal Structure," in Structure and Bonding in Crystals, Vol. 1, edited by M. O'Keeffe and A. Navrotsky, Academic Press, New York.

6. M. L. Cohen, "Pseudopotential Calculations for Ideal Surfaces," in Proceedings of the Seventh LBL/MMRD International Materials Symposium on Surfaces and Interfaces in Ceramics and Ceramic-Metal Systems, Plenum Publishing Co., New York (1981).

7. J. Ihm, M. T. Yin, and M. L. Cohen, "Quantum Mechanical Force Calculations in Solids: The Phonon Spectrum of Si," UCB Physics Dept. reprint. Submitted to Solid State Communications.

8. J. Ihm and M. L. Cohen, "Equilibrium Properties and the Phase Transition of Grey and White Tin," UCB Physics Dept. preprint. Submitted to Phys. Rev. B.

9. J. Northrup and M. L. Cohen, "Electronic Structure of the Rotation Twin Stacking Fault in β-ZnS," UCB Physics Dept. preprint. Submitted to Phys. Rev. B.

10. P. K. Lam and M. L. Cohen, "Electronic Charge Density and Bonding in V_3Si," UCB Physics Dept. preprint. Submitted to Phys. Rev. B.

11. M. L. Cohen, "Pseudopotential Theory of Surface and Bulk Properties of Semiconductors," in Proceedings of the 1st International Conference on the Physics of Semiconductors, to be published by Physical Society of Japan.

12. P. K. Lam and M. L. Cohen, "Effective Atomic Volumes for Elements in A15 Compounds," UCB Physics Dept. preprint. Submitted to Phys. Lett. A.

13. M. T. Yin and M. L. Cohen, "Microscopic Theory of the Static Structural Properties and Phase Transformation of Ge," UCB Physics Dept. preprint. Submitted to Solid State Communications.

C. Materials Chemistry

1. Chemical Structure

a. Low-Temperature Properties of Materials*

Norman E. Phillips, Investigator

1. CALORIMETRIC INVESTIGATION OF SPIN-GLASS ORDERING IN Cu Mn

William E. Fogle, James D. Boyer, Norman E. Phillips, and John Van Curen

There is currently a high level of interest in the properties of disordered systems and the nature of the phase transitions that they can display. Metallic spin glasses, of which Cu Mn is a prototypical example, constitute an important class of disordered systems, and the discovery of a sharp cusp in the low-field ac susceptibility[1] prompted serious consideration of the possibility of a thermodynamic phase transition at a characteristic temperature T_{sg}. Edwards and Anderson[2] proposed a model for a spin glass in which the long-range RKKY interaction between randomly distributed spins was replaced by a Gaussian distribution of bond strengths coupling spins on a regular lattice. Mean field solutions for this model and for extensions of it do produce a cusp in the susceptibility, χ, but they also predict a cusp in the magnetic specific heat, C. Although a broad anomaly in C extending from (presumably) T = 0 to well above T_{sg} was well known, no sharp feature of the type predicted had been reported. More recent measurements of C specifically directed to finding such a feature and with a precision of the order of 1% have generally produced negative results, but in one case[3] a "knee," or discontinuity in slope of C/T vs. T, was reported. By making several refinements in our measuring techniques we have obtained a precision of approximately 0.02% in C for a 2790 at. ppm sample of Cu Mn near T_{sg}, which is approximately 3.9 K. New zero-field data have been obtained, and C has also been measured as a function of magnetic field. The results show clearly, for the first time, the nature of the thermal effects associated with spin-glass ordering. There are no discontinuities in C or its temperature derivative to within the precision of the data. A broad anomaly in the temperature derivative does exist and extends over several K, from well below to well above T_{sg} but with no sharp structure associated with T_{sg}. A relatively sharp dip in the low-field field derivative of C is centered at T_{sg} and is the only feature that is clearly correlated with T_{sg}. The most striking feature of the field derivative, however, is that it is thermodynamically inconsistent with χ data. The apparent explanation is that even though χ and C measurements show no observable relaxation effects when made following cooling in constant field, they do not give true equilibrium properties. There are obvious and serious implications for the comparison of theory with experiment.

Figure 1 shows the derivative of C/T with respect to T as obtained by taking point-to-point differences of the raw capacity data. The smooth curve represents an interpolation between higher- and lower-temperature data for which the differences vary smoothly. A distinct s-shaped wiggle in the differences is readily apparent, independently of the somewhat arbitrary position of the interpolated reference curve. Figure 2 shows typical low-field data on the field dependence of C and least-squares fits of the form $C/T = A + BH^2$. Figure 3 shows the temperature dependence of B in the vicinity of T_{sg}. The field dependence of C and the temperature dependence of χ are thermodynamically related by $(\partial^2\chi/\partial T^2)_H = H^{-1}[\partial(C/T)/\partial H]_T$. In Fig. 4 the temperature dependence of χ obtained by double integration of this relation is compared with 5 Hz χ_{ac} data on the same sample and with χ_{dc} estimated for Cu Mn of this composition from data on other samples. The constants of integration were obtained from the 5 Hz data near 4.5 K. It is well known that below T_{sg}, χ_{dc} and χ_{ac} differ and that dc measurements made by application of a field after cooling in zero field exhibit time dependence.[4] However, χ_{dc} data obtained by cooling in constant field do not show a time dependence and have been taken as representing the infinite-time limit of data obtained by changing the field. One would therefore have expected the χ_{dc} data to correspond to thermodynamic equilibrium and to be related to the C data, which were obtained under the same conditions, by the standard thermodynamic relations. Figure 4 shows that this is not the case. The discrepancy suggests that, even though no time effects are observed when samples are cooled in constant field, the full range of microscopic states that contribute to the thermodynamic properties are not being sampled by the system.

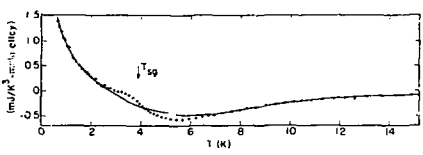

Fig. 1. Derivative of C/T with respect to T. (XBL 8012-13567)

*This work was supported by the Director, Office of Energy Research, Office of Basic Energy Sciences, Materials Sciences Division of the U. S. Department of Energy under Contract No. W-7405-ENG-48.

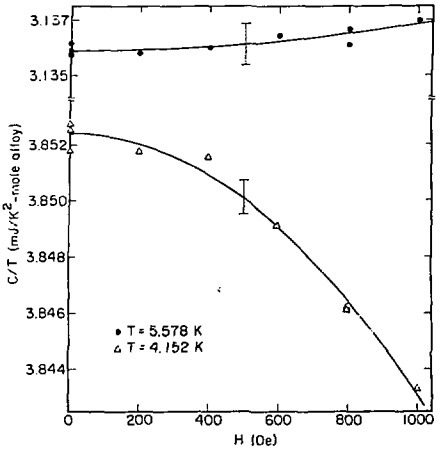

Fig. 2. The low-field field dependence of C/T just above (4.152 K) and well above (5.578 K) T_{sg}. The error bars indicate the effect of ±0.01% errors in total measured heat capacity. (XBL 813-8399)

In summary, the upper limit to possible discontinuities in C and its temperature derivative has been lowered by almost 2 orders of magnitude. Evidence for a more subtle heat capacity anomaly associated with spin glass ordering has been obtained. Perhaps most important, however, is the implication that meaningful comparison of theory and experiment below T_{sg} may have to be based on consideration of dynamics rather than equilibrium properties alone.

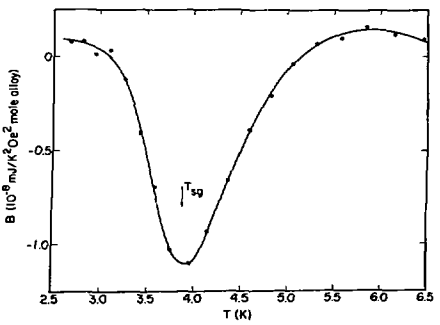

Fig. 3. Effect of temperature on the coefficient B (see text). (XBL 8012-13573)

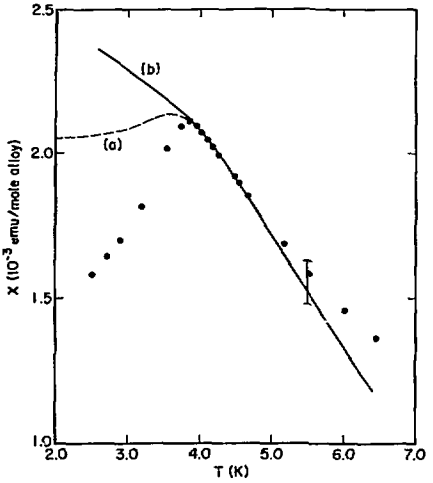

Fig. 4. The temperature dependence of χ as obtained from various sources. The points represent experimental 5 Hz χ_{ac} data. The solid curve (b) represents χ thermodynamically derived from C as described in the text. The slow departure from χ_{ac} above 5 K is associated with eddy current effects. The dashed curve (a) represents an estimate of χ_{dc} based on data on other samples. (XBL 8012-13569)

* * *

1. V. Cannella and J. A. Mydosh, Phys. Rev. B 6, 4220 (1972); V. Cannella, Amorphous Magnetism, H. O. Hooper and A. M. de Graaf, eds., Plenum Press, New York, 1973, p. 195.
2. S. F. Edwards and P. W. Anderson, J. Phys. F 5, 965 (1975).
3. D. L. Martin, Phys. Rev. B 20, 368 (1979); 21, 1902 (1980).
4. C. N. Guy, J. Phys. F 5, L242 (1975); S. Nagata, P. H. Keesom, H. R. Harrison, Phys. Rev. B 19, 1633 (1979).

2. HEAT CAPACITY OF Cu Mn SPIN GLASSES IN HIGH MAGNETIC FIELDS

William E. Fogle, Konrad Matho[+] and Norman E. Phillips

Although there has been little theoretical work on the properties of spin glasses in magnetic fields to date, it has been frequently recognized that measurements in magnetic fields would provide an additional opportunity to test qualitative

models of spin glasses and, as the theory is developed, quantitative calculations. Motivated by these general considerations, the almost total lack of in-field heat capacity data, and an extension of pair approximation calculations to a point at which comparison with experiment is of interest, we have undertaken a collaboration involving both theory and experiment to investigate the magnetic heat capacity, C, of spin glasses in magnetic fields.

We have made extensive measurements of C for a 2790 at. ppm sample of Cu Mn between 0.25 and 25 K and in fields to 75 kOe. These data are shown in Fig. 5. Less complete measurements have also been made on several more dilute Cu Mn samples, and a comparison of data for a 235 at. ppm sample in several fields with a pair approximation calculation is shown in Figs. 6 and 7. There are no adjustable parameters in the calculation--both the spin and the strength of the RKKY interaction are determined by other measurements--but the agreement in the vicinity of the maximum in C is remarkably good. Similar agreement is obtained for a 94 at. ppm sample (not shown) but not for the 2790 at. ppm sample. This and the trend in the maximum values of C with H for the latter sample (see Fig. 5), which is also in disagreement with theory, may constitute evidence for the importance of clusters in more concentrated samples. For all samples, the low-temperature C is substantially greater than

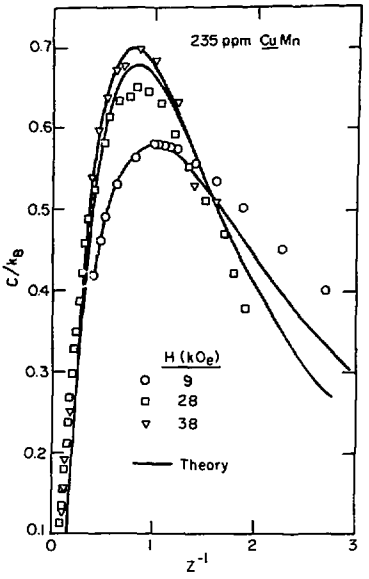

Fig. 6. Comparison of C with theory for 235 at. ppm Cu Mn. $Z \equiv g\mu_B H/kT$. (XBL 8012-13446)

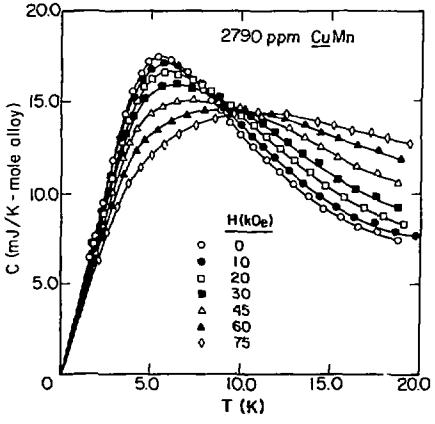

Fig. 5. Magnetic heat capacity as a function of H and T for 2790 at. ppm Cu Mn. (XBL 8012-13448)

calculated, as illustrated in Figs. 6 and 7, for 235 at. ppm (but the values of H and T involved for the 2790 sample are outside the ranges for which the approximation is valid). In this respect, the in-field pair approximation calculation is reminiscent of a number of other zero-field calculations in that it underestimates the number of low-energy excited states. It is thus more apparent than ever that there are important low-energy modes that have not yet been recognized or taken into account in theoretical calculations.

* * *

†On leave from the Centre de Recherches sur les Très Basses Temperatures, Centre National de la Recherche Scientifique, Grenoble, France.

1. Konrad Matho, J. Low Temp. Phys. 35, 165 (1979); M. D. Núñez-Regueiro and Konrad Matho, to be published.

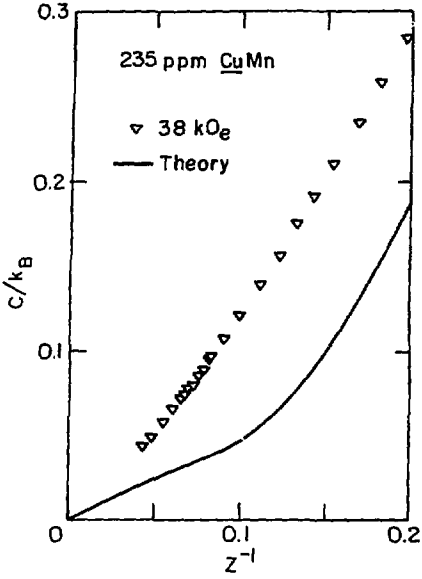

Fig. 7. Low-temperature detail from Fig. 2.
(XBL 8102-13447)

RESEARCH PLANS FOR CALENDAR YEAR 1981

Apparatus for the intercomparison of a number of very low temperature thermometers (diluted CMN, nuclear orientation, nuclear susceptibility, and an NBS "fixed point" device) and a preliminary version of apparatus for heat capacity measurements on ^{3}He is nearly complete. The first experimental results with it should be obtained early in 1981.

Measurements on the heat capacity of cerium under pressure have been further delayed by problems with pressure-transmitting media, but these have now been resolved and the measurements on cerium will be made.

New apparatus, for heat capacity measurements in the 30 mK to 25 K region, using a dilution refrigerator, is also nearing completion. It will be used for studies on several systems, including intercalated graphites, spin-glasses, and possibly potassium.

b. Electrochemical Processes*

Charles W. Tobias, Investigator

Introduction. The purpose of this program is to advance scientific methods for the analysis of scale-dependent cell processes and to provide means by which the design and operation of such processes may be optimized with respect to energy efficiency and capital cost. Physical description and quantitative characterization of transport of charged and uncharged specie to and from electrode surfaces by convective diffusion represent a core interest in this program. The analysis of high rate processes, such as electromachining and electroforming, is undertaken to point the way to new applications in electrometallurgy. A smaller part of this program is devoted to the exploration of novel electrochemical processes. Emphasis is placed on investigations in aprotic solvent systems which may be of potential use in galvanic cells, or in electrowinning or refining of reactive metals.

1. GAS-ELECTRODE-ELECTROLYTE INTERFACES; RESISTANCE OF BUBBLE LAYERS

Paul J. Sides and Charles W. Tobias

The analytical evaluation of the current distribution around a single bubble on an electrode surface[1] and the increase in resistance caused by its presence cannot be extended to dense arrays of spheres. The minimum resistance of such an array can be obtained by considering the constriction of flux between two closely spaced spheres. To assess the usefulness of various theoretical approximations for the representation of the resistance of an ordered array of bubbles, audio-frequency resistance measurements were carried out on precisely defined, large scale models.

A lucite tube 40 cm long with a hexagonal cross section limited at both ends by planar gold-plated copper electrodes, was built to serve as a model of a unit cell of a hexagonal array of bubbles on an electrode. The cell accommodates a 10.16 cm diameter sphere, at the maximum, which represents close packing. The spheres rest on the bottom electrode while the upper electrode is attached to a piston so that the distance between the two electrodes can be changed. The cell, containing the largest sphere and surrounded by others 9.65, 9.14, 8.64, 7.11, and 5.84 cm in diameter, appears in Fig. 1. The different-sized spheres, simulating a range of void fractions in the bubble layer, were placed in the cell one at a time and the resistance between the hexagonal electrodes. 1M KCl served as electrolyte.

In some experiments the 120° wedges, appearing in the foreground and in the cell in Fig. 2, were

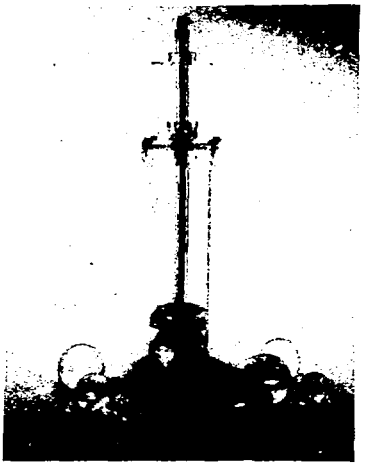

Fig. 1. Hexagonal cell with lucite spheres and wedges in the foreground. Note assembly with large sphere in cell and wedges placed in the corners. (CBB 801-242)

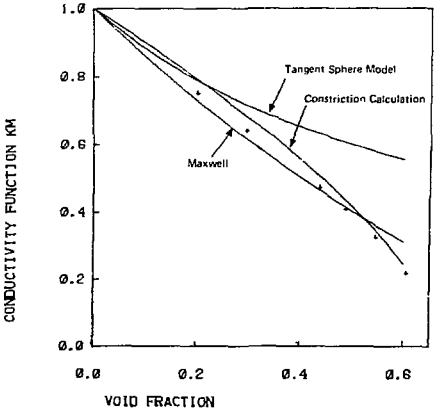

Fig. 2. Data of hexagonal cell for single spheres compared to calculated values. (XBL 8011-7574)

*This work was supported by the Director, Office of Energy Research, Office of Basic Energy Sciences, Materials Sciences Division of the U. S. Department of Energy under Contract No. W-7405-ENG-48.

placed in the cell corners. Cut from spheres of various diameters, the wedges served to model a second layer of bubbles underneath the larger ones.

Assuming that the gas is confined to a layer of thickness xL close to the electrode, where x is the fraction of the interelectrode gas, L, occupied by a bubble layer, we used the following form to describe the total electrode resistance, R_T, for a parallel plate configuration:

$$R_T = (1 - x) \frac{L}{\kappa S} + \frac{xL}{\kappa S K_m} \qquad (1)$$

in which κ is the electrolyte conductivity, S is the electrode area, and K_m is the ratio of the conductivity with gas present to that with gas absent. Knowing the cell and sphere dimensions and the electrolyte conductivity, and measuring the resistance, R_T, we calculated K_m. All theoretical and experimental results were expressed as the function K_m for convenient comparison of data with various theoretical models.

The results of the hexagonal cell experiments on uniform spheres, the tangent sphere prediction, the constriction calculation, and Maxwell's equation for Ref. 2 appear in Fig. 2. As predicted by the tangent sphere calculation,[1] the experimental resistance values are greater than those predicted by the Maxwell relation at small void fractions; the electrode plane on one side of the bubble terminates the electrical activity and hence limits the resistance presented by a tangent sphere to 90% of that of a similar sphere in the bulk electrolyte. At close packing, the conductivity of the bubble layer is reduced by a factor of nearly 5. This means that a close-packed bubble layer occupying 5% of the interelectrode gap causes a 20% increase of the overall cell resistance expressed in Eq. (1).

The tangent sphere calculation grossly overestimates the conductivity except at the low bubble layer occupancies for which it was derived. The opposite is true of the constriction calculation. It does not agree with the data at dilute bubble occupancies because the curved surfaces of the sphere force the current to take longer paths through the electrolyte to get around them and hence offers higher resistance to the current than the constriction calculation permits. However, at void fractions near close packing the calculation provides a rather satisfactory representation of measured resistances.

The results of the two-layer experiments, in which the wedges shown in Fig. 1 were inserted in the cell corners, appear in Fig. 3. At the lowest void fractions, the new conductivities are lower than the single sphere line alone would predict, while at the high bubble occupancies the new conductivities are higher than the single sphere data alone would predict. The transition from one tendency to the other occurs near a bubble coverage of 0.4. This trend indicates that, as the small spheres are added, the system behaves more like a three-dimensional homogeneous dispersion rather than a two-dimensional array.

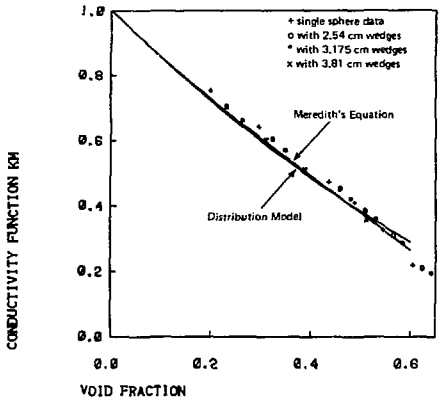

Fig. 3. The hexagonal cell results compared to the Distribution Model and Meredith's equation.
(XBL 8011-7585)

When spheres of two different diameters (e.g., 5:1 diameter ratio) are added, the Distribution Model[3] best predicts the conductivity of the layer. In Fig. 3, plots of the Distribution Model, and Meredith's equation,[4] which were derived for disordered and ordered three dimensional dispersions of spheres in the bulk electrolyte, respectively, are compared to the hexagonal cell data. At low void fractions, the experiment confirms the theoretical prediction that the conductivity of the bubble layer exceeds that predicted by these equations. At high void fractions, where the constriction between bubbles dominates whether in bulk solution or on the electrode surface, the data and equations are in close agreement.

* * *

1. P. Sides and C. W. Tobias, MMRD Annual Report for 1979, LBL-10000, p. 211.
2. J. C. Maxwell, A Treatise on Electricity and Magnetism, 2nd ed. V. 1, Clarendon Press, p. 435, 1981.
3. R. E. Meredith and C. W. Tobias, J. Electrochem. Soc. 108, 286, 1961.
4. R. E. Meredith and C. W. Tobias, J. Appl. Phys. 31, 1270, 1960.

2. HIGH RATE ELECTROLYSIS PROCESSES - THE EFFECT OF SUSPENDED INERT PARTICLES ON LIMITING CURRENTS TO A ROTATING DISK

David Roha, Rolf H. Muller, and Charles W. Tobias

Although high surface area electrodes, such as those in packed and fluidized beds, have high mass transfer coefficients, there are situations, such

as in electroplating, where these techniques cannot be applied. In such cases, a method for increasing the rate of mass transfer to more or less flat surfaces is needed. Simply pumping the solution faster over the electrode surface to reduce the boundary layer thickness is limited by the sharply increasing pumping power requirement.

Introducing small inert solid particles in the flow stream has been reported to be very effective in reducing the boundary layer thickness. Our investigation was undertaken with the purpose of establishing quantitative criteria for the use of suspended inert solids in electrochemical practice. For our experimental vehicle, we have chosen a rotating disk electrode at which ferricyanide ion was reduced, $(Fe(CN)_6^{3-} + e^- \rightarrow Fe(CN)_6^{4-})$, in the presence of large excesses of NaOH. A large surface area foil around the periphery of the cell served as anode, where the ferrocyanide ion was oxidized to ferricyanide. Weighed amounts of glass beads were added to the electrolyte; the limiting currents were determined by plotting cathodic overvoltage versus current.

From a data base of 1152 valid limiting current measurements involving two disks with active electrode areas of 1 cm^2 and 6.26 cm^2, eight rotation speeds from 387 to 2870 rpm and six particle sizes from 4 to 75 microns, the following conclusions were obtained:

a. Little or no increase in limiting current occurs until the volume of glass beads is above 5-10% (cf. Fig. 4).

b. Beyond 5 to 10 vol% the limiting current increases sharply and reaches a maximum at about 35%.

c. At the higher rotation speeds, the 8.4 micron glass beads gave the highest increases in limiting current; at lower speeds, the maximum shifted towards the larger particle sizes.

d. In the presence of inert solids, the larger diameter disk electrode always yielded much higher limiting current densities than the smaller one.

e. The relative percentage increase in limiting current in the presence of beads was highest at the greatest rotation speeds, up to more than 3 times higher than that without particles.

f. The limiting current versus disk rotation speed curve changes, with increasing particle concentration, from a parabolic $\Omega^{1/2}$ dependence (where Ω is rotation speed) to an almost linear dependence on Ω (Fig. 5).

In an attempt to explain the behavior of this system, a mathematical model based on surface renewal theory was developed. This model envisions the particles as traveling across the disk electrode surface and replacing the depleted solution of the boundary layer with fresh solution from the bulk liquid. Points in the wake of a moving particle experience a sharp jump in limiting current which then decays to the steady state value as concentration profiles reestablish themselves. This model best fits the data when a particle is considered

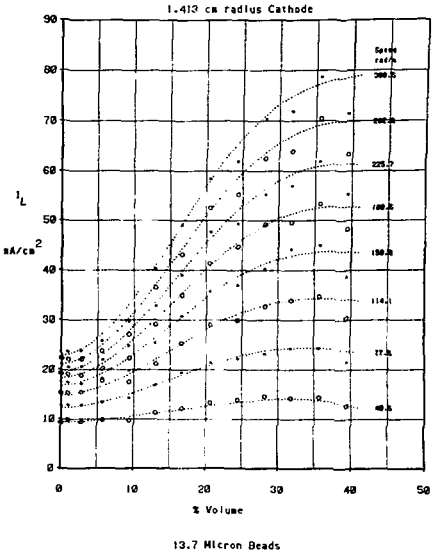

Fig. 4. Limiting current versus vol% of 13.7 micron diameter glass beads. Active part of the rotating disk cathode had a radius of 1.41 cm. Curves for the eight different disk rotation speeds are shown. (XBL 8011-7530)

to approach the surface to within 1/45 d of the particle diameter. This finding points to the possible existence of a thin fluid layer which the spherical glass bead carries as it rotates in the velocity gradient near the surface, bringing fresh reactant to the electrode surface.

The measure for any type of agitation used to increase the rate of mass transfer is the increase one gets for each unit of energy dissipated in the agitation process. Figure 6 compares the calculated power consumption for increasing the limiting current of a rotating disk electrode by rotating it faster to the power consumption for adding glass beads to the solution. Increased viscosity of the suspension due to particle loading is taken into consideration. In Fig. 7, the ratio of power consumption to limiting current (a theoretical measure of energy loss due to agitation which might then be compared to IR drop, surface overvoltage, etc.) is plotted against the volume fraction of glass beads. The specific energy consumption actually decreases at the higher rotation speeds while the limiting current goes up. It is hoped this energy savings realized for the rotating disk might also apply to industrial cells of different design when suspended particulates are introduced.

* * *

1. D. Roha, R. H. Muller, C. W. Tobias, LBL-10000, p. 212.

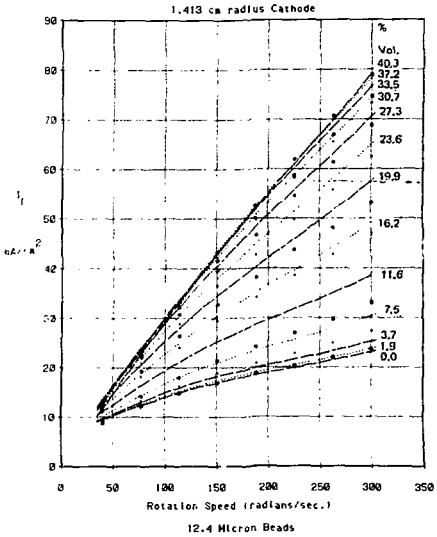

Fig. 5. Limiting current versus disk rotation speed. Each line represents a different particle volume fraction. Bead diameter: 12.4 micron. The disk radius is 1.41 cm. (XBL 8011-7534)

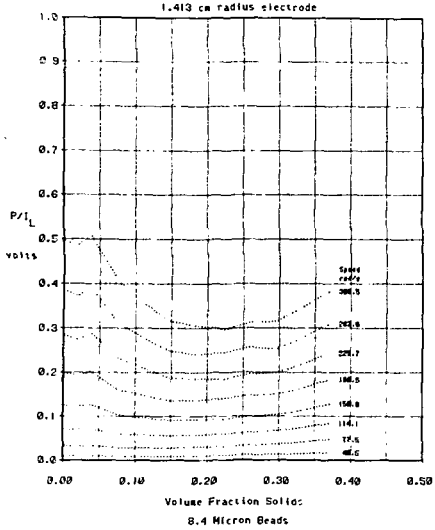

Fig. 7. Power consumption divided by limiting current density as a function volume fraction of 8.4 micron beads, at various disk rotational speeds. (XBL 8011-12766)

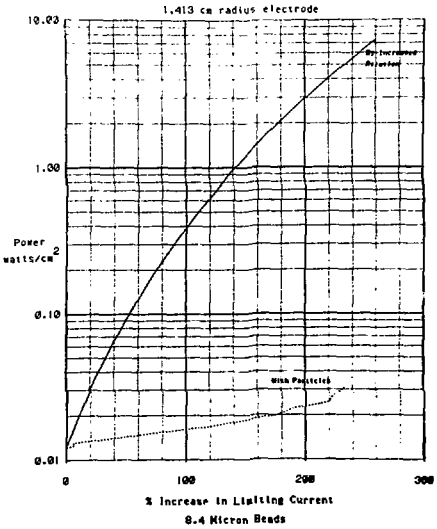

Fig. 6: Power required for increasing limiting current by spinning the disk faster, or by adding increasing volume fractions of 8.4 micron diameter glass beads to the electrolyte. Base case: 300 radians per sec, 0 vol% beads. For a 200% increase of limiting current the rpm has to be raised to 2700 radians/sec. Instead, addition of 27 vol% of glass beads achieves the same improvement in mass transfer. (XBL 8012-12936)

RESEARCH PLANS FOR CALENDAR YEAR 1981

Gas-Electrode-Electrolyte Interfaces. High speed motion picture sequences will be taken of nucleation distribution and bubble coalescence, both in light reflected from metal electrodes and using transparent antimony doped tin oxide electrodes. Attempts will be made to detect surface charge on bubbles and to evaluate what effect such a charge may have on bubble behavior.

High Rate Electrolysis Processes.† The dependence of valence of dissolution (cutting efficiency) and of surface finish of refractory carbides on the various metal binders used in their manufacture, will be evaluated using our electrochemical machining apparatus.

The influence of mass transport conditions in the electropolishing of low-alloy carbon steels will be evaluated using a rotating disk electrode.

To enhance the usefulness of the method of boundary layer thinning in electrolysis by suspended inert solids, the roles of particle-shape, -size, and -volume fraction and the type of electrode and/or electrolyte movement will be characterized.

Anodic Processes in Propylene Carbonate. The use of bromine discharge as an anodic reaction will be reevaluated, with emphasis on resolving conflicting claims on solvent stability. The need for identifying half reactions suitable for positive electrodes is obvious; this is one of the main roadblocks to future application of organic solvents in extractive metallurgical processes.

* * *

†Jointly directed with Rolf H. Muller.

1980 PUBLICATIONS AND REPORTS

Refereed Journals

1. Paul J. Sides and Charles W. Tobias, "Primary Potential and Current Distribution Around a Bubble on an Electrode," J. Electrochem. Soc. 127, 288-291 (1979). (LBL-8745)

2. John F. Cooper, Rolf H. Muller, and Charles W. Tobias, "Periodic Phenomena during Anodic Dissolution of Cooper at High Current Densities," J. Electrochem. Soc. 127, 1733-1744 (1980). (LBL-9404)

Other Publications

See listing of Extended Abstracts under category IV, (items 1, 2, 4, 5, 6, 7, 8, 10).

LBL Reports

†1. Wing Cheong Hui with Charles W. Tobias, "Electrolytic Gas Evolution in Forced Flow," M.S. thesis, University of California, Berkeley, 1980. (LBL-11945)

(See also items 7, 8, and 10 under Invited Talks.)

Invited Talks

1. Karrie J. Hanson, Rolf H. Muller, and Charles W. Tobias, "Mass Transfer Enhancement by Turbulence Promoters," Extended Abstracts, vol. 80-1, no. 388, pp. 963-965 (based on LBL-9038), paper presented at 157th Meeting of the Electrochemical Society, St. Louis, MO, May 11-16, 1980.

2. Paul J. Sides and Charles W. Tobias, "Resistance of a Planar Array of Bubbles at an Electrode," paper presented at the 157th Meeting of the Electrochemical Society, St. Louis, MO, May 11-16, 1980. Extended Abstracts, vol. 80-1, no. 386, pp. 958-960.

3. Charles W. Tobias, "The Coming of Age of Electrochemical Engineering," opening address at the Symposium on Energy Savings in the Electrolytic Industries," 89th National Meeting of the American Institute of Chemical Engineers, Portland, OR, August 17-20, 1980.

†4. Milan M. Jaksic, and Charles W. Tobias, "Hydrodynamic Flow Visualization by the Electrochemical Method," paper presented at the International Symposium on Flow Visualization, Ruhr-University Bochum, Germany, September 9-12, 1980.

†5. Radoslav T. Atanasoski, Henry H. Law, and Charles W. Tobias, "Electrochemical Reduction of Potassium from Potassium Chloride in Propylene Carbonate with Aluminum Anodes," paper presented at the 31st meeting of the International Society of Electrochemistry, Venice, Italy, September 22-26, 1980. Extended Abstracts, vol. 12, F1, pp. 729-731.

‡6. Peter C. Foller, and Charles W. Tobias, "The Generation of Ozone by the Anodic Oxidation of Water," paper presented at the 158th meeting of the Electrochemical Society, Hollywood, FL, October 5-10, 1980. Extended Abstracts, vol. 80-2, no. 628, p. 1567-68, 1980.

†7. Henry H. Law, and Charles W. Tobias, "The Kinetic Stability of Potassium in Propylene Carbonate Electrolytes," paper presented at the 158th meeting of The Electrochemical Society Hollywood, FL, October 5-10, 1980. Extended Abstracts, vol. 80-2, no. 39, pp. 106-108, 1980. Based on LBL-11487.

†8. Henry H. Law, and Charles W. Tobias, "The Morphology of Potassium Deposited from Propylene Carbonate Electrolyte," paper presented at the 158th meeting of The Electrochemical Society, Hollywood, FL, October 5-10, 1980. Extended Abstracts, vol. 2, no. 392, p. 991-92. Based on LBL-11253.

9. Charles W. Tobias, "Prospects and Problems in Electrochemical Engineering," invited address delivered in the frame of the International Symposium on Electrochemistry in Industry - New Directions, celebrating the centennial of Case Institute of Technology, Cleveland, OH, October 20-22, 1980.

†10. Geoffrey A. Prentice, and Charles W. Tobias. "Finite Difference Calculations of Current Distributions at Polarized Electrodes," paper presented at the 73rd Annual Meeting of the American Institute of Chemical Engineers, Chicago, IL, November 16-20, 1980. Based on LBL-11058.

* * *

†Supported by the Division of Electrochemical Systems Research, Office of Conservation and Solar Energy, U.S. Department of Energy.

‡Supported entirely from University funds.

2. High Temperature and Surface Chemistry

a. High-Temperature Thermodynamics*

Leo Brewer, Investigator

1. UNUSUAL HIGH-TEMPERATURE PROPERTIES OF TRANSITION METALS

John Gibson

The Engel theory has been very productive in providing thermodynamic data and equilibrium phase boundaries for transition metal systems. The predictions of the effect of pressure or solute addition upon the relative stability of the bcc, hcp, and ccp phases have been confirmed with an accuracy of almost 100%. Thus, it is of interest to extend the theory to a wider range of properties. The consequences of the partial delocalization of the inner shell valence electrons have been considered for properties such as high temperature heat capacity, entropy of fusion, coefficient of expansion, compressibility, and the related bulk modulus.

The basis of the prediction is the distinction between the bonding behavior of the outer shell s and p electrons which range far beyond the core of closed shells of an atom and can be considered as an electron gas in metals and the somewhat localized distribution in real space of the inner shell d and f electrons. Thus, the bonding due to these inner shell electrons will be mainly to nearest neighbors. Since good overlap in real space of the bonding orbitals is required for effective bonding, the bonding due to d electrons, for example, will be caused predominately by overlap with d orbitals of neighboring atoms. The repulsion of the closed shell cores prevents a good overlap, and bonding due to inner shell d electrons is not as effective as that due to outer shell s and p electrons. At the far left side of the periodic table where the d orbitals are first occupied, they have not contracted much. Thus their bonding is almost as effective as that of the outer shell electrons and the distinctions between the d and s,p electrons is not a large factor. However, as the nuclear charge increases upon moving to the right in the periodic table, the inner shell d orbitals contract and become more localized.

Because of crystal field splitting, some of the orbitals require different promotion energies and differ in their degree of localization. In the center of the transition metal portion of the periodic table, all of the d orbitals are used in bonding, and the bonding energy per d electron averaged over the d orbitals of varying degrees of localization is rather poor. At the edges of the transition metal region, only the most effective orbitals are used in bonding, and the least effective are filled with non-bonding electrons on the right side of the transition metal region or are vacant on the left side. It is the central region in which the distinction between the inner and outer shell electrons will be most pronounced. Because of the poor overlap of inner shell orbitals between neighboring atoms, the bonding varies significantly with internuclear distance. If the metal is compressed, the bonding due to the improved overlap of the inner shell d orbitals is markedly improved. Thus, we see the anomaly of increased pressure stabilizing bcc d^3s Zr with a coordination number of 8 over hcp d^2sp Zr with a close-packed coordination number of 12.

The recognition of the rapid change in bonding capability of inter shell d or f valence electrons with change in internuclear distance provides the means of predicting unusual behavior for transition metals. For normal metals which use outer shell s,p electrons, heat capacities for the solid and the liquid are somewhat higher than the Dulong and Petit value of 3R due to anharmonic and electronic contributions but usually by not more than 20 to 30%. The entropies of fusion are close to the value of R. For the transition metals, the expansion that results normally upon heating will reduce the effectiveness of the d bonding, and the heat capacity represents not only the usual lattice vibrational contributions but also a substantial reduction in cohesion. Thus, metals with substantial inner shell d electron bonding should show abnormally high heat capacities as the molal volume increases upon heating. Because of the reduction of cohesion upon heating, the expansion will be expected to be even more rapid than for normal metals and will enhance the heat capacity even more. The expansion upon melting will greatly reduce the d electron bonding, thus resulting in a considerably increased enthalpy and entropy of fusion. Because compression will bring the nuclei closer together and improve the d electron bonding, the transition metals will have abnormally high compressibilities.

In summary, transition metals with extensive d bonding and actinides with 5f electron and d electron bonding will be expected to have abnormally large high-temperature heat capacities, entropies of fusion, coefficients of expansion, and compressibilities. High-temperature data, particularily for the very refractory transition metals with extensive d bonding, are scanty; but available data do confirm the expected abnormal behavior for transition metals. Shaner, Gathers,

*This work was supported by the Director, Office of Energy Research, Office of Basic Energy Sciences, Materials Sciences Division of the U.S. Department of Energy under Contract No. W-7405-ENG-48.

and Minichino[1] have recently applied new dynamic measurements to tantalum and molybdenum and have obtained abnormally high entropies of fusion and liquid heat capacities. Their values have generally been disregarded because they are so much higher than earlier measurements and are so abnormally high compared to normal metals. Analysis of previous measurements indicate systematic errors, and it is believed that the new results, which are consistent with the Engel theory, are reliable. Available data will be analyzed to establish quantitatively the parameters for the theory, which will be used for predicting the large group of yet unmeasured values.

* * *

1. J. W. Shaner, C. R. Gathers, and C. Minichino, "High Temperatures-High Pressure," 9, 331-43 (1977).

2. PHASE BOUNDARIES OF THE HEXAGONAL, CLOSE-PACKED PHASES OF THE Co-Mo SYSTEM

D. Davis

The Engel correlation between the bcc, hcp, and ccp crystal structures and the electronic configuration $d^{n-1}s$, $d^{n-2}sp$, and $d^{n-3}sp^2$, together with the distinction between the bonding characteristics of outer shell s,p electrons and inner shell d or f electrons, provides a direct prediction of phase diagram behavior for transition metal alloys. As a simple example, one can immediately predict the effect of pressure upon a phase transition. The d electrons from an inner shell do not overlap well with neighboring d orbitals. Increasing pressure will enhance the effectiveness of d bonding and will stabilize the structure using the most d electrons in bonding. Thus, pressure will stabilize bcc d^3s Ti over hcp d^2sp Ti or the bcc structure of any of the fourth to sixth group transition metals for which the bcc structure has more bonding d electrons than the hcp structure, and the d orbitals are somewhat localized. For transition metals to the right of the six group, the bcc structure will have more d electrons but fewer unpaired d electrons in the valence state available for bonding. Thus, pressure favors hcp d^6sp Fe with four possible bonding d electrons over bcc d^7s Fe with only three possible bonding d electrons. Similarly, the effect of various solutes upon the relative stability of two structures is readily predicted. Data have become available to test most of these predictions. The predictions have been verified with an accuracy of 95 to 98%.

The addition of molybdenum with vacant p orbitals to cobalt is predicted to stabilize hcp d^7sp Co over fcc d^6sp^2 Co by draining off p electrons. For pure cobalt, the hcp phase becomes unstable above 400 to 450°C, but the range of stability should be increased by at least 400°C by addition of molybdenum. The 1973 Metals Handbook[1] shows only an isolated hcp phase at Co_9Mo_2 between 1018°C and 1200°C with no extension of the hcp-fcc transition. To check whether the Co-Mo system represented a contradiction of the theoretical prediction, cobalt samples with around 15 at.% Mo were heated in a special furnace with a temperature gradient between 500 and 1100°C for over 1000 hours. X-ray examination of the samples indicated stabilization of hcp Co to above 800°C, thus confirming the predictions of the Engel theory. It was established that the extension of the hcp phase to higher temperatures does not join the Co_9Mo_2 phase.

* * *

1. Metals Handbook, 8th Ed., Vol. 8, Ed. T. Lyman, Am. Soc. for Metals, Metals Park, Ohio (1973).

3. USE OF NITRIDE DISSOCIATION PRESSURES TO CHARACTERIZE STABILITY OF ACID-BASE INTERMETALLIC PHASES

John Gibson, Dave Goodman, and Bea-Jane Lin

The Engel theory of metals predicts extraordinary stability for intermetallic phases of transition metals on the left-hand side of the Periodic Table, which have vacant d orbitals, combined with transition metals with non-bonding d electron pairs such as the platinum group metals. Previous studies[1] of the ternary systems of Zr and C with Ru, Rh, Pd, Ag, Re, Os, Ir, Pt, and Au have confirmed the qualitative features of the theory. EMF cells have been used[2] for the platinum-rich portion of the Zr-Pt diagram to obtain partial molal Gibbs energies. It is desirable to obtain data over a wider range of compositions to obtain a more complete picture of the generalized-Lewis-acid-base interaction between zirconium and platinum. It would be desirable to obtain data corresponding to a complete titration curve between an acid such as a fourth or fifth group transition metal with a platinum metal base. Cell measurements using thoria electrolytes doped with yttria are in progress, but they are limited to a rather narrow temperature range because of difficulty of equilibration at temperatures below about 900°C and short-circuiting diffusive reactions.

The general type of reaction illustrated by $ZrN + xPt = ZrPt_x + 1/2\ N_2(g)$ offers the possibility of determining the partial molal Gibbs energy of zirconium as a function of concentration by variation of the nitrogen pressures. Measurements have been carried out[3] in the range 1900 to 2300°C, yielding, for the platinum-rich boundary of the Zr_9Pt_{11} phase, an activity of zirconium relative to pure zirconium of 2.4×10^{-4} at 1985°C. At the temperature available for carrying out this type of reaction, equilibration is readily reached, and data will be obtained for a variety of generalized-Lewis-acid-base systems.

* * *

1. L. Brewer, P. Wengert, Met. Trans. 4, 83 (1973).
2. P. J. Meschter, W. L. Worrell, Met. Trans. 8A, 503 (1977).
3. D. A. Goodman, LBL-10633, May 1980.

RESEARCH PLANS FOR CALENDAR YEAR 1981

The research program will be directed toward improving our ability to quantitatively predict the thermodynamic properties and temperature-composition ranges of the various phases of transition metal systems. The experimental studies will continue along the three lines of research presently underway: (1) use of the gradient furnace to establish the equilibrium range of phase of limited stability; (2) measurements of thermodynamic activity around 900-1300 K over a composition range using solid electrolyte EMF cells; and (3) measurements of gaseous equilibria involving nitrides and oxides at temperatures of 2000-2500 K to fix thermodynamic properties. The theoretical work will involve extending the Engel theory of transition-metal bonding to a variety of properties. A subsidiary activity will be critical evaluation of thermodynamic properties of oxides and their vaporization processes; this will relate to our use of gaseous equilibria involving oxides mentioned above, and will also be carried out on a broader basis in cooperation with Stanford Research Institute and the National Bureau of Standards.

1980 PUBLICATIONS AND REPORTS

Refereed Journals

1. J. Winn and L. Brewer, "Models for Calculation of Dissociation Energies of Homonuclear Diatomic Molecules," Faraday Symposium 14, 126-135 (1980).

Other Publications

1. Leo Brewer, "Bibliography on the High-Temperature Chemistry and Physics of Materials, Vol. 24, Part 2, Gases: (A) Spectroscopy of Interest to High-Temperature Chemistry, and (B) Reactions Between Gases and Condensed Phases," published by IUPAC Commission on High Temperatures and Refractory Materials, edited by M. G. Hocking and V. Vasantasree, London, 1980.

2. Leo Brewer, Editor, "Atomic Energy Review Special Issue No. 7, Molybdenum: Physico-Chemical Properties of Its Compounds and Alloys," International Atomic Energy Agency, Vienna, 714 pp., 1980.

3. Leo Brewer and R. H. Lamoreaux, "Thermochemical Properties of Molybdenum and Its Compounds and Alloys," Atomic Energy Review Special Issue No. 7, International Atomic Energy Agency, Vienna, pp. 7-192, 1980.

4. Leo Brewer and R. H. Lamoreaux, "Phase Diagrams of Molybdenum Binary Systems," Atomic Energy Agency, Vienna, pp. 193-356, 1980.

5. Leo Brewer, G. M. Rosenblatt, J. B. Berkowitz, H. Kent Brown, H. G. Drickamer, J. W. Hastie, M. Lapp, T. A. Milne, and W. Weltner, Jr., "High Temperature Science: Future Needs and Anticipated Developments," 139 pgs., National Academy of Sciences, 1979.

LBL Reports

1. David Alan Goodman (Ph.D. thesis). "High-Temperature Activities of Zirconium in Platinum Alloys Determined by Nitrogen-Nitride Equilibria LBL-10633.

2. Leo Brewer, "The Role and Significance of Empirical and Semiempirical Correlations," LBL-10736.

Papers Presented

1. J. Winn and L. Brewer, "Models for Calculation of Dissociated Energies of Homonuclear Diatomic Molecules," Faraday Society Meeting, January 8-9, 1980, Manchester, England, presented by J. Winn.

2. L. Brewer, "The Role and Significance of Empirical and Semiempirical Correlation," Conference on Chemistry of Complex Solids, Castle Hot Springs, Arizona, January 25, 1980.

3. L. Brewer, "Future Directions in High Temperature Science and Technology," Gordon Research Conference on High Temperature Chemistry, August 4-8, 1980, Plymouth State College, North Plymouth, New Hampshire.

4. L. Brewer, "Thermodynamic Data for Flue-Gas Desulfurization Processes," DOE Symposium on Desulfurization Processes, November 6-7, 1980, Morgantown, West Virginia.

b. Chemistry and Materials Problems in Energy Production Technologies*

Donald R. Olander, Investigator

1. THERMAL-GRADIENT MIGRATION OF BRINE INCLUSIONS IN SALT

A. J. Machiels,† S. Yagnik and D. R. Olander

Bedded salt has been proposed as a storage medium for nuclear wastes. Radioactive decay heating of the waste produces temperature gradients in the surrounding salt, which contains ~ 0.5% water in the form of small cubical brine inclusions. In a thermal gradient, the inclusions migrate towards the heat source. The mechanism of migration is based on the increase of the solubility of salt in water with temperature; in the presence of a temperature gradient across the inclusion, salt dissolves into the inclusion at the hot surface and crystallizes out at the cold surface. Transport by thermal and molecular diffusion of salt within the liquid from the hot to the cold faces causes the inclusion to move in the opposite direction. The velocity depends on the temperature coefficient of solubility and interfacial kinetic resistances to dissolution and crystallization.

Experiments have demonstrated that the inclusion speed is controlled principally by the rate of solid dissolution at the hot face of the inclusion. This process, in turn, depends upon the presence of dislocations intersecting the surface which provide the imperfections needed to permit dissolution to occur at small undersaturation of the adjacent liquid. If the hot face of the inclusion were flat on an atomic scale, removal of solid atoms from the perfect surface would be so energetically unfavorable that very large undersaturation would be needed to produce the required dissolution rates. A dislocation, which intersects the dissolving surface, provides sites at which the atoms of the solid are less tightly bound than in a perfect atomic plane; and hence their removal to the liquid phase is correspondingly easier. A number of experiments support this interpretation:

a. When the mechanical load on the crystal is increased, additional dislocations are created; these interact with the inclusions, causing them to speed up. The effect is not elastic in nature, because the high migration speeds persist when the crystal is unloaded.

b. Experiments were performed in which selected inclusions were subjected to various temperature gradients, but the average temperature was not changed. In a liquid diffusion-controlled process or one with linear interface kinetics (e.g., Anthony and Cline's model[1]), the velocity should be proportional to the temperature gradient. However, we found that the velocity varied as the temperature gradient rose to a power > 2. A theoretical model that explains this observation is the Burton, Cabrerra, and Frank theory of crystal growth[2] which, when taken in reverse (to model dissolution), predicts a dependence of the velocity on the square of the temperature gradient.

c. If a single inclusion is followed for a long period of time, variations in its velocity by a factor of 4 are observed (Fig. 1). This variation is attributed to the loss and gain of dislocations at the hot face. In the low dislocation density synthetic crystals used in the experiments, each inclusion face is on the average intersected by less than three dislocations. Consequently, loss or gain of one dislocation (for example) can alter the velocity by a substantial fraction.

The pattern shown on Fig. 1 can be rationalized in the manner shown schematically in Fig. 2. At time zero, the hot face of the inclusion is intersected by a single dislocation (No. 1) close to the center of the face of the inclusion. In general, the dislocation does not intersect the surface at 90° so that as the inclusion moves, the intersection point moves further off-axis. At off-axis positions, the temperature of the surface, and hence the undersaturation of the liquid, is less than it is close to the axis; hence, the inclusion slows down. Somewhere between 8 and 20 hours, the inclusion picks up another dislocation, designated as No. 2 in Fig. 2. The three dislocation intersections with the dissolving face result in a several-fold increase in the inclusion velocity. As the intersections of the No. 2 dislocation with the hot face move off-axis, the inclusion again begins to slow down.

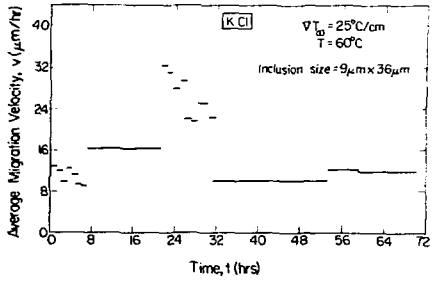

Fig. 1. Variation of the migration velocity of an inclusion in KCl. (XBL 813-509)

*This work was supported by the Director, Office of Energy Research, Office of Basic Energy Sciences, Materials Sciences Division of the U.S. Department of Energy under Contract No. W-7405-ENG-48.

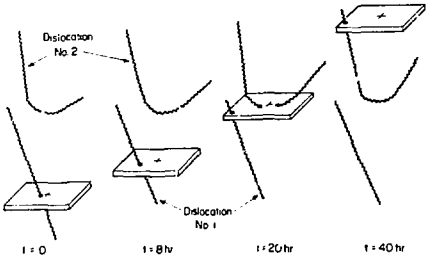

Fig. 2. Schematic explanation of the mechanism of the effect of dislocation intersections on the velocity of inclusions in solids. (XBL 813-510)

The dislocation-controlled migration process is qualitatively consistent with all experiments designed to test the hypothesis. It also explains the very large scatter of the measured velocities of small inclusions in crystals of high perfection. Larger inclusions in natural crystals on the other hand are not limited by the number of dislocation intersections at the dissolving face, and these inclusions appear to move at the rate predicted by liquid diffusion control.

* * *

*Present address: University of Illinois, Champaign, IL.

1. T. R. Anthony and H. E. Cline, J. Appl. Phys. 42, 3380 (1971).
2. P. Bennema and G. H. Gilmer, in Crystal Growth: an Introduction, P. Hartman, Ed., North-Holland (1973).

2. TRACER SURFACE DIFFUSION ON UO_2*

D. R. Olander

The coefficient of surface self-diffusion on UO_2 is a key parameter in the processes affecting the behavior of oxide nuclear fuels. Although small fission gas bubbles may not be mobile under normal operating conditions, it is widely believed that in rapid transients, gas release is controlled by the motion of these bubbles in the grains. Moreover, their velocity in a temperature gradient is assumed to be governed by the mechanism of surface diffusion; therefore, the surface diffusivity is an important material property in fuel modeling codes.[1-3] This quantity can be measured either by tracer techniques or by mass transfer methods (grain boundary grooving or scratch decay). Maiya's experiments using the latter technique[4] indicated that the grain boundary grooving method is totally evaporation controlled in UO_2 for temperatures above 1700°C.

The only tracer study of surface diffusion on UO_2 is that of Marlowe and Kaznoff.[5] This technique for measuring surface diffusivity is shown in Fig. 3. A needle of 93% enriched UO_2 with a flattened point contacted a polished surface of a pellet of depleted UO_2 (0.2% U-235). After a known contact time at a fixed temperature, the radial distribution of tracer was determined by counting the U-234 alpha activity. The experiment was conducted in flowing hydrogen. No transfer of activity from the needle to the pellet was observed when the two were slightly separated. The needle was not sintered to the pellet after the anneal. The tracer spreading data were interpreted in terms of surface diffusion alone; volume diffusion and gas phase transport were claimed to be unimportant. Robertson,[6] using a method proposed by Shewmon,[7] corrected the tracer results at 1915°C (the only temperature at which the original data were available) and concluded that the correct value of D_s implied by these data is 300 times larger than the value deduced by Marlowe and Kaznoff, or more than three orders of magnitude larger than the values from the Maiya correlation. Consequently, either there is a real physical difference between the mass transfer and tracer methods or the mathematical interpretation of the tracer spreading data is incorrect. In this study, the latter possibility is examined.

An analysis of surface spreading data which utilizes both the magnitude and the radial variation of the tracer count rate has been developed and implemented numerically. Depletion of the tracer source as well as enrichment of the tracer sink are treated by the model. Parasitic effects such as a contact resistance and evaporation are taken into account. Volume diffusion of tracer is an integral part of the process because it alone permits detection of the tracer transported by surface diffusion. However, volume diffusion does not contribute to radial spreading per se.

Application of the analysis method to the only set of surface spreading data on UO_2 in the literature produces a surface diffusion coefficient (D_s)

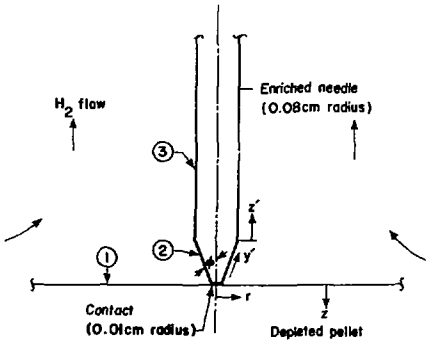

Fig. 3. Diffusion couple for measurement of surface diffusion on UO_2 by the tracer method. (XBL 813-511)

at 1915°C which is ~ 3000 times larger than that obtained from the same data by the original experimenters and 4 orders of magnitude larger than that obtained by extrapolation of surface diffusivities inferred from mass transfer methods at lower temperatures. The present analysis yields a surface diffusivity between 0.1 and 0.2 cm^2/s at 1915°C. This extreme mobility suggests that UO_2 molecules move on their own surface more like particles in an ideal gas than by a conventional hopping mechanism. This value of D_s is also very much larger than those used in current fuel modeling codes whose predictions of fission gas release are very sensitive to the value of the surface diffusivity employed.

* * *

*Brief version of article to be published in J. Nucl. Mater.

1. J. R. Matthews and M. H. Wood, J. Nucl. Mater. 84, 125 (1979).
2. J. Rest and S. M. Gehl, 5th Intern. Conf. on Structural Mechanics in Reactor Technology, Berlin, Germany (1979).
3. E. E. Gruber, Nucl. Technol. 35, 617 (1977).
4. P. S. Maiya, J. Nucl. Mater. 40, 57 (1971).
5. M. O. Marlowe and A. I. Kaznoff, J. Nucl. Mater. 25, 328 (1968).
6. W. M. Robertson, J. Nucl. Mater. 30, 36 (1969).
7. P. G. Shewmon, J. Appl. Phys. 34, 755 (1963).

3. POINT DEFECTS IN URANIUM DIOXIDE

K. C. Kim and D. R. Olander

The tracer diffusion coefficient of oxygen in UO_{2-x} has been measured using a diffusion couple consisting of two matched hypostoichiometric wafers, one enriched with oxygen-18 and the other normal, which were pressed together with a layer of liquid uranium. The uranium metal bond has a sufficiently high oxygen permeability to transport oxygen from one wafer to the other quite efficiently, thus eliminating an interface resistance in the diffusion couple.

In order not to perturb the stoichiometries of the wafers by the presence of liquid uranium, the experiments were performed only in the $U(\ell) + UO_{2-x}$ two-phase region. The stoichiometries were fixed automatically by the temperature; and, therefore, the diffusion measurements apply only to oxide O/U ratios along the lower phase boundary.

Following a diffusion anneal, the $^{18}O/(^{18}O + {}^{16}O)$ profiles were determined by ion microprobe mass analysis. Details of the experimental methods are given in Ref. 1.

In hypostoichiometric urania, oxygen self-diffusion occurs solely by the vacancy mechanism for which D is given by

$$D = D_o^v \theta_v (1 - \theta_v) \exp(-\Delta H_v/RT) \qquad (1)$$

where θ_v is vacancy concentration ($x/2$ in UO_{2-x}), ΔH_v is the activation energy of vacancy migration, and D_o^v is a constant. Our diffusion measurements were well correlated by Eq. (1) (see Fig. 4), from which $D_o^v = 4.4 \times 10^{-4}$ cm^2/sec and $\Delta H_v = 11.7$ kcal/mole were obtained. The activation energy is in good agreement with those of other oxides of fluorite structure (CeO_{2-x} and PuO_{2-x}).

Assuming that oxygen diffusion in UO_{2+x} proceeds simultaneously and independently by both vacancy and interstitial migration, the total oxygen diffusion coefficient can be expressed as the sum:

$$D = D_{(v)} + D_{(i)} \ . \qquad (2)$$

In substantially hypostoichiometric UO_{2-x}, $D_{(i)} \cong 0$ and the diffusivity is that given by Eq. (1). Similarly, in highly hyperstoichiometric UO_{2+x}, $D_{(v)} \cong 0$ and the observed oxygen diffusivity reduces to:

$$D \cong D_{(i)} = D_o^i \theta_i (1-\theta_i) \exp(-\Delta H_i/RT) \qquad (3)$$

where θ_i is the interstitial concentration. Values of $D_o^i = 4.7 \times 10^{-3}$ cm^2/s and $\Delta H_i = 21.8$ kcal/mole were obtained by re-analyzing the existing oxygen diffusion data on UO_{2+x}.[2,3] From the above equations, the oxygen diffusivity for all O/U ratios is given by:

$$D = 4.4 \times 10^{-4}\, \theta_v (1-\theta_v) \exp(-11700/RT) + 4.7 \times 10^{-3}\, \theta_i (1-\theta_i) \exp(-21800/RT) \ . \qquad (4)$$

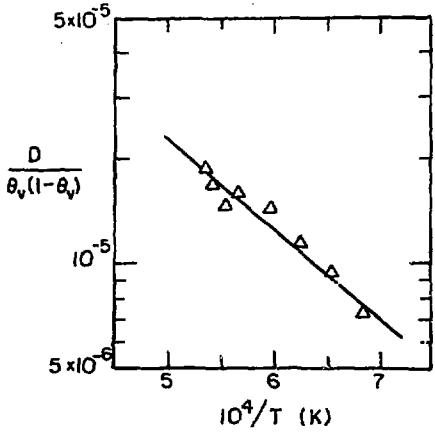

Fig. 4. Stoichiometry and temperature dependence of the oxygen tracer diffusivity in UO_{2-x}.
(XBL 3010-6088)

In oxides far removed from stoichiometry, the point defect concentrations θ_V and θ_i are simply related to the nonstoichiometry parameter x in $UO_{2\pm x}$. However, in stoichiometric UO_2, the point defect concentration is determined by the thermodynamics of anion Frenkel disorder. The law of mass action for this defect reaction is

$$K_F = \frac{\theta_V}{1-\theta_V} \cdot \frac{\theta_i}{1-\theta_i} = \exp(\Delta S_F/R)\exp(-\Delta H_F/RT), \quad (5)$$

which, with the condition of electroneutrality, $\theta_i = 2\theta_V$, determines θ_i and θ_V. Thus D can be expressed in terms of the Frenkel entropy and enthalpy (ΔS_F and ΔH_F) by using Eq. (5) in Eq. (4). Oxygen diffusion data for stoichiometric UO_2[4] were fitted in this manner to obtain $\Delta S_F = 18.2 \pm 7.3$ e.u. and $\Delta H_F = 85.6 \pm 9.2$ kcal/mole. With these values of ΔS_F and ΔH_F, contributions of vacancies ($D_{(V)}$) and interstitials ($D_{(i)}$) to the oxygen diffusion coefficient in stoichiometric UO_2 were calculated. At very low temperatures, vacancies are the primary species that contribute to oxygen mobility. In the temperature range 800-1800°C, neither of the species is completely predominant, and at 1400°C the contributions of the two species are approximately equal.

It is well known that the enthalpy of UO_2 displays an unusually rapid increase from 1500°K to 3100 K which cannot be explained by lattice vibrations. Szwarc[5] attributed all of this excess enthalpy to Frenkel disorder, from which he deduced the Frenkel entropy and energy of $\Delta S_F = 14.8 \pm 0.8$ e.u. and $\Delta H_F = 71.3 \pm 2.2$ kcal/mole, respectively. Recently, however, a series of attempts have been made to re-interpret the excess enthalpy of UO_2 in terms of electronic excitation.[6-8] Although quantitative results could not be obtained because the electronic structure of UO_2 is not well established, it was demonstrated that the electronic contribution to the enthalpy could be significant; in this case the component of the Frenkel disorder is less than determined by Szwarc.[5] Our values of the Frenkel energy and entropy are in line with this theory because they yield a lower population of Frenkel defects than predicted by Szwarc's model;[5] therefore, their contribution to the enthalpy is also smaller. After removing the lattice contribution from the measured excess enthalpies and applying the two-band model of the electronic contribution,[6] a band gap of 2.0 eV and an effective mass of 7.6 m_e were obtained. The former figure is in good agreement with the values obtained from electrical conductivity data.[9]

* * *

1. K. Kim and D. R. Olander, MMRD Annual Report, LBL-10000, p. 222 (1979).
2. P. Contamin, J. J. Backmann, and J. F. Marin, J. Nucl. Mater. 42, 54 (1972).
3. G. E. Murch, D. H. Bradhurst, and H. J. deBruin, Phil. Mag. 32, 1141 (1975).
4. J. F. Marin and P. Contamin, J. Nucl. Mater. 30, 16 (1969).
5. R. Szwarc, J. Phys. Chem. Solids, 30, 705 (1969).
6. D. A. MacInnes, J. Nucl. Mater. 78, 225 (1978).
7. R. J. Thorn, G. H. Winslow and J. S. Ziomek, J. Nucl. Mater. 87, 416 (1979).
8. D. A. MacInnes and C. R. A. Catlow, J. Nucl. Mater. 89, 354 (1980).
9. J. L. Bates, C. A. Hinman, and T. Kawada, J. Am. Ceram. Soc. 50, 652 (1967).

4. STRESS CORROSION CRACKING OF ZIRCALOY BY METAL IODIDES AND CADMIUM

Shih-Hsiung Shann and D. R. Olander

Even at low pressures, molecular iodine is an effective stress corrosion cracking (SCC) agent for zircaloy.[1] However, inside a reactor fuel pin, iodine is present mainly as cesium iodide. Also, metal iodides such as FeI_2 and AlI_3 could attain partial pressures in the mtorr range. Cadmium is a fission product which thermodynamics suggests should exist inside a fuel pin in the metallic state. Liquid cadmium is known to cause severe embrittlement of zircaloy. In an inpile situation, however, the cladding is in contact with the vapor phase with low metal partial pressure rather than with a condensed phase. Therefore, a study of the stress rupture behavior of zircaloy in the presence of $AlI_3(g)$, $FeI_2(g)$, $CsI(g)$, and $Cd(g)$ was undertaken.

Tube specimens are internally pressurized with argon in order to produce a biaxial tensile stress. Rupture lifetimes are measured as a function of stress, temperature, and partial pressure of the active chemical agent, which impinges as a molecular beam on a spot ~ 1 cm diameter. The fracture mode is also observed by SEM.

Failure times are greatly reduced by the presence of iron and aluminum iodides. For both iodine[1] and these iodides, there exists a stress (376 MPa), beyond which "burst-type' failure occurs. Lower stresses produce "pinhole-type" failures. However, fractography of both types of failure shows cleavage characteristics very different from the ductile-dimple fracture surface found in the absence of a corrosive agent. These three types of stress-rupture failures are shown in Fig. 5.

All specimens tested under cadmium exhibited burst-type failure and the fracture surface showed brittle-type cleavage features. For cadmium, the rupture times were shorter than those of the control specimens but exhibited more scatter than those in iodine or the metal iodides. Fracture occurred randomly inside the cadmium-affected region on the zircaloy specimen, unlike iodine and the iodides where failure always took place at the center of the molecular beam spot. There may be some unknown surface inhomogenity controlling the cadmium embrittlement process which is not present in SCC by iodine or metal iodides. Specimens cut from different tubes gave widely varying rupture times in cadmium, but tests using the same zircaloy tubes gave consistent results.

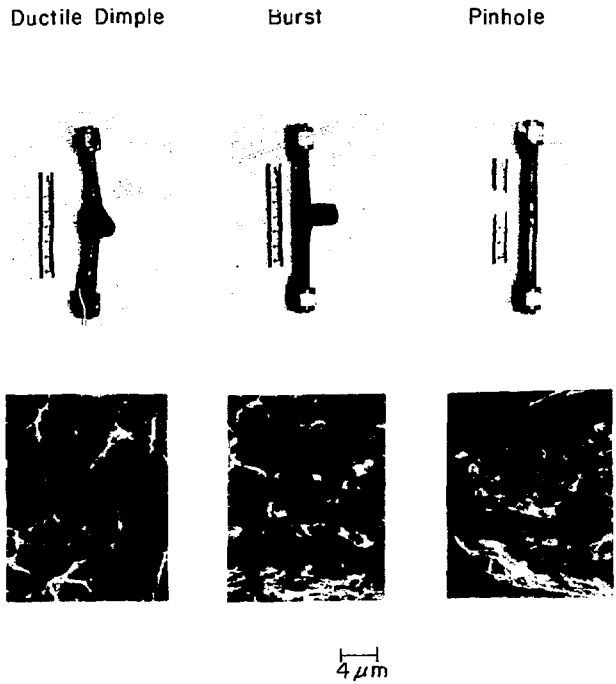

Fig. 5. Comparison of three types of fractography. (XBB 8010-14059A)

In cesium iodide tests, plots of time-to-failure versus stress did not show any decrease in comparison with control specimens. SEM fractography revealed completely ductile behavior, the same behavior as without a corrosive agent.

Greatly reduced failure times and brittle fractography are the two main features of stress corrosion cracking. On both counts, iodine, iron iodide, and aluminum iodide are stress corrosion cracking agents for zircaloy; however, cesium iodide is not. This behavior is consistent with the structural free energies of the reactions[2] to form $ZrI_{1.1}$, which are negative for reaction of Zr(s) with I_2(y), AlI_3(g) or FeI_2(g), but positive for reaction with CsI.

The rupture time data are correlated in terms of the crack growth model:[3]

$$\frac{da}{dt} = A\, p^n \exp(-E/RT) \exp(BK/T) \qquad (5)$$

where a is the crack length, p is the partial pressure of the SCC agent, K is the stress intensity factor, and T is the temperature. A and B are constants. When integrated from initial length a_0 to final length a_f, at which the net section stress reaches the ultimate tensile stress, Eq. (5) gives the rupture time. The chemical or corrosion aspect of SCC is related to the reaction order n and activation energy E. These parameters are shown in Table 1.

The reaction orders for I_2 and FeI_2 are both unity, whereas that of AlI_3 is 2/3. These values reflect a rate-limiting surface chemical step with kinetics associated with the number of iodine atoms per molecule of SCC agent. Since it is unlikely that a nonlinear chemical reaction is involved in cadmium embrittlement (only alloying with the substrate metal is possible), the order for this species should be unity.

This crack growth model also predicts SCC experiments with variable loading and surface roughness.[4]

* * *

1. S.-H. Shann and D. R. Olander, Trans. Am. Nucl. Soc. 32, 268 (1979).

Table 1. Chemical Parameters of Stress Corrosion Cracking of Zircaloy

SCC Agent	Minimum partial pressure for SCC (torr)	order (n)	Activation energy, E (kcal/mole)
I_2	1.4×10^{-3}	1.0 ± 0.1	7 ± 1
FeI_2	3.0×10^{-3}	0.9 ± 0.1	131 ± 5
AlI_3	1.4×10^{-3}	0.7 ± 0.1	-
Cd	7×10^{-3}	0.8 ± 0.1	54 ± 2

2. D. Cubicciotti, R. L. Jones, and B. C. Syrett, "Chemical Aspects of Iodine-Induced Stress Corrosion Cracking of Zircaloy," ASTM Fifth Conference on "Zirconium in Industry," 1980.
3. A. G. Evans and T. G. London, Progress in Materials Science 21, 307 (1976).
4. S.-H. Shann and D. R. Olander, "Correlation of Failure Times for Iodine SCC of Zircaloy," Nucl. Technol., to be published.

5. RELEASE OF WATER VAPOR FROM URANIUM DIOXIDE

Douglas Sherman and D. R. Olander

Uranium dioxide is known to adsorb water vapor rapidly from the air. When the UO_2 is subsequently heated, the water is released. This water is a potential source of the hydrogen that can cause hydriding of zircaloy cladding. Another source of water in UO_2 fuel pellets is the gaseous atmosphere used during sintering. In order to control the stoichiometry during sintering, either cracked ammonia or wet hydrogen is used, so hydrogen-bearing gases may be retained by the solid during densification at high temperature (~ 1750°C).

Uranium dioxide samples of differing porosities and microstructures were exposed to D_2O instead of H_2O in order to avoid measurement difficulties due to the large H_2O background in the vacuum system. To simulate the retention of water during sintering, other UO_2 samples were fabricated in a D_2/D_2O atmosphere. The characteristics of the specimens are shown in Table 2. The type-A and B pellets were used to simulate physical adsorption of water vapor; type-C pellets studied hydrogen/water vapor retention during sintering; and the type-D pellets served as blanks. The sintering conditions of the type-A pellets resulted in high open and closed porosities and a measurable BET surface area. The type B and D pellets were prepared under standard commercial fuel sintering conditions and resulted in low closed and essentially no open porosity. Their surface area was less than the limit of detection of the BET method. The type-A and B pellets were immersed in liquid D_2O after being outgassed in vacuum in order to physically adsorb water on their surfaces. The type-C and D pellets were not treated after sintering.

The pellets are heated in a tungsten crucible suspended in a vacuum furnace. The outgassed D_2O effuses from the exit capillary of the furnace and is chopped to produce a modulated molecular beam which is detected by a mass spectrometer in the vacuum. The mass spectrometer is calibrated with a known flow rate of neon. There was a large release of physically adsorbed water for the high porosity type-A pellets and a negligible release for the low porosity type-B pellets. The 5 anneals of type-C pellets (Fig. 6) -- at 910 to 1860°C -- show abrupt release rate increases upon changing temperature followed by a roughly exponential decay.

The model used to describe the release process is desorption-limited. The water contained in the UO_2 is assumed to be located on multiple binding sites with a distribution of binding energies. Each site has a characteristic desorption rate constant, B, which is related to the binding energy E and pre-exponential factor A by:

$$B = Ae^{-E/KT} .$$

Table 2. UO_2 Specimens used in Outgassing Experiments.

Type	Sintering Conditions	Porosity (%) Open	Porosity (%) Closed	BET surface area (m^2/g)	D_2O loading method
A	1450°C, in H_2O/H_2, 2 hr.	5.1	15	0.14	immersion in boiling D_2O liquid
B	1750°C, in H_2O/H_2, 6 hr.	< 0.1	7	< 0.01	immersion in boiling D_2O liquid
B	1750°C, in D_2O/D_2, 6 hr.	< 0.1	7	< 0.01	D_2 sintering gas saturated with D_2O at 30 - 40°C
D	1750°C, in H_2O/H_2, 6 hr.	< 0.1	7	< 0.01	none

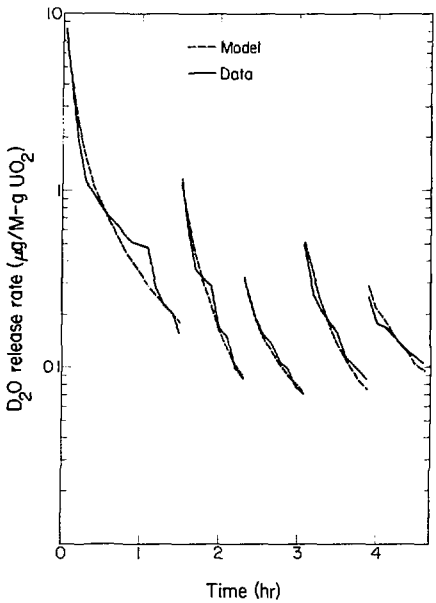

Fig. 6. Comparison of experimental D_2O release rates with predictions of the multiple binding site model. (XBL 813-513)

The sites that bind water in UO_2 are characterized by the distributions of the parameters A and E. In order to simplify the analysis, the site distribution is assumed to have a constant pre-exponential factor A and the binding energies are distributed according to the function:

$n_s(E)dE$ = number of binding sites/g UO_2 with binding energies between E and E + dE.

To analyze the constant-temperature anneals, this distribution is converted to a distribution of desorption rate constants, which is defined by:

$N_s(B)$ = number of sites/g UO_2 with desorption constants between B and B + dB at temperature T.

The distribution of desorption rate constants, $N_s(B)$, is determined from the binding energy distribution $n_s(E)$ and the anneal temperature.

A binding energy distribution is assumed. For each constant temperature anneal, this $n_s(E)$ guess gives a corresponding rate constant distribution $N_s(B)$, which in turn yields a release rate prediction. Figure 7 shows the binding site distribution that produced the best fit to the release data. The dashed curves in Fig. 6 show the computer fit to the data. The release rate data suggest that water retained by UO_2 during the sintering process contains a major component bound with ~ 25 kcal/mole, and smaller components with binding energies of ~ 40 and ~ 53 kcal/mole.

* * *

1. A. Srivastava and D. R. Olander, Trans. Am. Nucl. Soc. 28, 216 (1978).

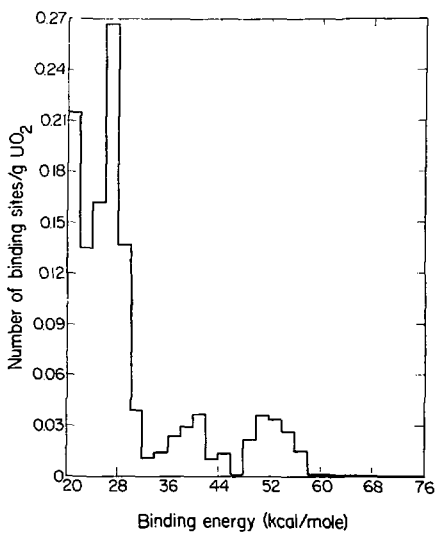

Fig. 7. Normalized distribution of binding sites for water in polycrystalline uranium dioxide (type-C). (XBL 813-512)

RESEARCH PLANS FOR CALENDAR YEAR 1981

The vapor pressures of refractory nuclear fuels, UO_2 and UC, at temperatures well above their melting points will be measured using a pulsed laser as a surface heat source and in-situ mass spectrometry as a method of detecting the vaporized species. The behavior of ruthenium inclusions in UO_2 in a thermal gradient will be investigated using a temperature gradient furnace. The surface diffusion coefficient on UO_2 will be measured using a tracer spreading technique. The effect of irradiation on the stress corrosion cracking of zircaloy by cesium iodide will be studied using a Van de Graaff accelerator as a radiation source. The dependence of the rate of reduction of urania by atomic hydrogen will be measured as a function of oxide stoichiometry. The role of dislocations in the thermal gradient migration of brine inclusion in synthetic alkali halide single crystals will be quantified, and tests on natural rock salt will be conducted. Molecular beam experiments on the thermal decomposition of silane on single crystal silicon substrates will be completed and a model of the process developed.

1980 PUBLICATIONS AND REPORTS

Refereed Journals

1. D. R. Olander, "The Materials of Fast Breeder Reactor," Naturwissenschaften 67, 61 (1980).

2. D. R. Olander, A. J. Machiels, M. Balooch, E. Muchowski and S. K. Yagnik, "Thermomigration of Brine Inclusions in Sodium Chloride Single Crystals," Trans. Am. Nucl. Soc. 34, 352 (1980).

3. D. R. Olander, "Interaction of Stresses with Inclusions in Solids," J. Nucl. Mater. 92, 163, (1980).

LBL Reports

1. D. R. Olander, A. J. Machiels and E. Muchowski, "Migration of Gas-Liquid Inclusions in KCl and NaCl Single Crystals," LBL-11815.

2. S. Shann and D. R. Olander, "Correlation of Failure Times for Iodine Stress Corrosion Cracking of Zircaloy," LBL-11813.

3. D. R. Olander, "Interpretation of Tracer Surface Diffusion Experiments on UO_2," LBL-11817.

4. R. L. Yang, "The High Temperature Behavior of Metallic Inclusions in Uranium Dioxide," (Ph.D. thesis), LBL-11117.

5. R. L. Yang and D. R. Olander, "Behavior of Metallic Inclusions in Uranium Dioxide," LBL-11816.

6. D. R. Olander, "Nuclear Materials Research Progress Reports for 1979," LBL-11030.

Invited Talks

1. D. R. Olander, "Molecular Beam Studies of Surface Reactions," Institute of Inorganic Chemistry, University of Zurich, February 1, 1980.

2. D. R. Olander, "The Gas Centrifuge for Uranium Isotope Separation," Chemistry Division, Isotope Separation Department, CEA-Saclay, 6 Seminars, February-March 1980.

3. D. R. Olander, "Basic Studies of Nuclear Materials," European Institute for Transuranium Elements, Karlsruhe, April 28, 1980.

4. D. R. Olander, "Uranium Enrichment by Laser," Chemistry Division, CEA-Pierralatte, May 7, 1980.

5. D. R. Olander, "Nuclear Waste Management," Chemistry Division, CEA-Marcoule, May 8, 1980.

6. D. R. Olander, "Nuclear Materials Research," Metallurgy Division, Department of Plutonium-Based Fuels, CEA-Fontenay Aux Roses, May 17, 1980.

7. D. R. Olander, "Thermal Migration of Brine Inclusions in Salt," Dept. of Chem. and Nucl. Engin., University of California Santa Barbara, Nov. 6, 1980.

c. Plasma-Enhanced Deposition of Thin Films*

Dennis W. Hess, Investigator

1. PLASMA ENHANCED DEPOSITION OF IRON/IRON OXIDE FILMS

C. S. Blair, A. Wakita, and D. W. Hess

Thin films are used in a variety of applications, ranging from optical and electronic devices to passivation coatings. The specific application depends upon the optical, electronic, and chemical properties of the film. Such properties are ultimately linked to deposition or formation techniques which establish chemical composition and film structure.

Thin films (~ 1 μm) of iron/iron oxide are deposited by igniting an rf discharge in iron pentacarbonyl vapor in the pressure range of 0.1 - 0.5 torr.[1] Deposition rates increase with increasing rf power and with decreasing substrate temperature. In addition, film densities increase with increasing substrate temperature and with decreasing rf power. These changes are such that the overall mass deposition rate (mg/cm^2 min) remains relatively constant with rf power and substrate temperature. The observed trends are consistent with an increase in the relative amount of iron oxides in the film as the temperature decreases and as the power increases.[1]

Resistivity of the films, as measured by the four-point-probe method, is shown in Fig. 1 as a function of rf power and substrate temperature. The increase in resistivity with increasing power and decreasing substrate temperature is consistent with the concomitant increase in iron oxide content and the decrease in α-iron crystallite concentration observed via chemical analysis and x-ray diffraction studies.[1] Further, such results agree with preliminary transmission electron microscopy studies on the iron/iron-oxide films.

In order to utilize plasma-deposited (PD) iron/iron-oxide films in electronic or optical devices, patterning techniques are needed. The simplest method of forming patterns is to use acid etch baths such as hydrochloric acid solutions. These solutions often utilize dissolved salts to increase the chloride ion concentration.

The PD films were deposited at 250°C and 50 W rf power, and contained 68 mole % iron, 20 mole % oxygen, and 12 mole % carbon. The pH of the etchant solution was determined by the HCl concentration, and the chloride ion concentration was fixed at 0.25 M by addition of either NaCl, KCl, or CsCl. Typical etch rate data for HCl and various HCl/alkali salt solutions are shown in Fig. 2. These

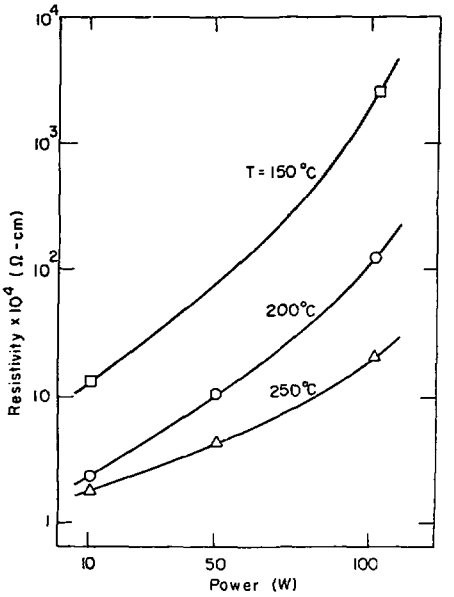

Fig. 1. Resistivity of iron/iron-oxide films as a function of rf power and substrate temperature. (XBL 8011-13302)

The above effects can be explained by analogy to a model proposed for the inhibition of corrosion in acidic solutions by organic cation addition.[2] The ionic radii of the cations increase from sodium to potassium, to cesium. Since hydrogen ions must adsorb onto the iron surface for etching to occur, the hydrogen ions compete with other cations for adsorption sites. As the cation size increases, its ability to adsorb onto the surface diminishes. Thus, hydrogen ions can more easily displace the cation as the cation size increases; and, therefore, the film etch rate increases. This results in a lower etch rate for the NaCl solution than for the KCl or CsCl solution.

* * *

* This work was supported by the Director, Office of Energy Research, Office of Basic Energy Sciences, Materials Sciences Division of the U.S. Department of Energy under Contract No. W-7405-ENG-48.

1. D. M. Wroge and D. W. Hess, "The Plasma Enhanced Deposition of Iron and Iron Oxide Thin Films," LBL-9879.
2. N. Hackerman, J. Electrochem. Soc. 113, 7 (1966).

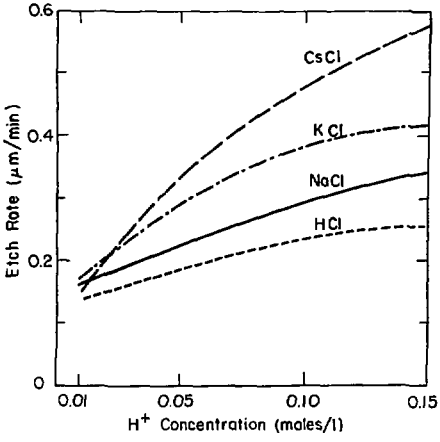

Fig. 2. Iron/iron-oxide etch rates as a function of hydrogen ion concentration for various HCl/chloride salt solutions. The chloride ion concentration is 0.25 M, and the etch bath temperature is 25°C. (XBL 8011-13303)

data indicate significant etch rate increases with salt additions. Chloride ions adsorbed to the iron surface assist in attracting hydrogen ions to the surface. However, the relative increase in etch rate depends upon the size of the cation in the salt.

RESEARCH PLANS FOR CALENDAR YEAR 1981

Capacitance-voltage and current-voltage studies will be performed on the iron/iron-oxide films so that electronic conduction mechanisms can be ascertained. More extensive transmission electron microscopy investigations will allow the relationships between conductivity and film structure (i.e., α-iron particle size distribution) to be determined.

Since iron oxides (particularly Fe_2O_3) may be useful as photoelectrochemical cell (PEC) materials, the chemical, physical, and electronic effects of oxygen addition during deposition of iron/iron-oxide films will be studied. In addition, the quantum efficiences and thermodynamic stabilities of these materials will be investigated in various electrolyte solutions.

1980 PUBLICATIONS AND REPORTS

Refereed Journals

1. K. Tokunaga and D. W. Hess, "Aluminum Etching in Carbon Tetrachloride Plasmas," J. Electrochem. Soc. 127, 928 (1980).

Invited Talks

1. D. W. Hess, "Aluminum Etching in CCl_4 and BCl_3 Plasmas," Southern California Chapter, American Vacuum Society, Anaheim, California, March 1980.

2. D. W. Hess, "The Si-SiO_2 Interface: Current Understanding of Chemical and Electronic Defects," Conference on Surfaces and Interfaces in Ceramic and Ceramic-Metal Systems, Berkeley, California, July 1980.

Papers Presented

1. D. M. Wroge and D. W. Hess, "Plasma Enhanced Deposition of Iron/Iron Oxide Films," The Electrochemical Society Meeting, St. Louis, Missouri, May, 1980 (LBL-9879).

2. D. W. Hess, "Comparison of Aluminum Etch Rates in CCl_4 and BCl_3 Plasmas," Gordon Research Conference on Plasma Chemistry, Andover, New Hampshire, August 1980.

d. Electrochemical Phase Boundaries*

Rolf H. Muller, Investigator

Introduction. The purpose of this work is to advance the understanding of boundary layers and thin films at electrochemical interfaces. Boundary layers control the chemical environment in which electrode processes take place and are often responsible for limiting the specific rate at which reactions can be conducted. Localized properties of boundary layers are determined, and new means to accelerate electrochemical mass transport are investigated in order to increase space-time yield and material and energy efficiency. Thin films at electrodes control the chemical properties of most materials in liquid environments and often represent the controlling resistance in metal deposition and dissolution reactions. Energy conversion in many batteries and corrosion reactions involve the transformation of solid surface layers. Formation and properties of thin films are determined to find means for their control and for the prediction of their many effects such as surface finish and electrode shape in deposition and dissolution processes. New optical techniques for the observation of electrode surfaces in liquid media are developed and used. They include ellipsometry combined with Auger spectroscopy, interferometry, thin film interference, and Doppler velocimetry.

Work on high-rate electrodeposition and dissolution, conducted jointly with C. W. Tobias, is described in the section "Electrochemical Processes." Applied research, "Anodic Surface Layers on Battery Materials," is described under "Electrochemical Synthesis and Energy Storage."

1. EXPANDING CAPABILITIES OF THE AUTOMATIC ELLIPSOMETER

Joseph C. Farmer, Felix Schwager and R. H. Muller

The laboratory-built self-compensating ellipsometer[1] that has been used successfully since 1973 is still the fastest and most sensitive instrument of its type with the widest dynamic range. In order to take full advantage of its capabilities and to further broaden its utility, several modifications have been made to the instrument.

A new digital data acquisition and control system makes it possible to efficiently collect ellipsometer and electrochemical measurements from eight channels with high speed (10 ms) and resolution (10^{-5}) over extended periods of time (minutes to weeks). The digital system consists of an LSI-11 computer with associated memory, dual floppy disk, and graphics terminal. A FORTRAN compiler and extensive specially-developed software are used for data acquisition reduction, storage, and limited interpretation.

A 1 W argon ion laser source has been added in order to extend observations to rough films or other poorly reflecting surfaces that have produced low signal-to-noise ratios or loss of signal with the short-arc light source. A shroud with suitable interlocks has been installed for the protection of the operator.

Facilities for fast spectroscopic ellipsometry over the visible range have been added for use in adsorption and microporosity determinations. The spectral scan is accomplished with a rotating filter disc. The large amount of time-dependent spectral data is sorted out by the computer.

To extend the present dynamic range of compensation of 55° for polarizer and analyzer azimuths, electromechanical analyzer and polarizer rotation has been introduced. This computer-controlled rotation is initiated when the limit of the rotation range of the Faraday cells is approached and will greatly reduce the loss of data encountered during the slower manual re-adjustment.

* * *

1. H. J. Mathieu, D. E. McClure and R. H. Muller, Rev. Sci. Instrum. 45, 789 (1974).

2. LASER VELOCIMETRY FOR BOUNDARY LAYER MEASUREMENTS

Joseph C. Farmer and R. H. Muller

A feasibility study has been conducted on the use of laser Doppler velocimetry for the investigation of unusual electrolyte flow patterns near electrodes which result in greatly increased rates of mass transfer. Of immediate interest are the combination of forced and natural convection and the effect of turbulence-inducing flow obstacles.

Velocimetry measurements in electrochemical boundary layers are complicated by the small size of the probe volume that must be examined, the proximity of the solid electrode, and light deflection in the refractive-index field of the boundary layer. It was concluded that backscattered light had to be used for the measurement. Low signal intensity is a well-known problem with the backscatter mode of operation. In addition, light scattered from the electrode (flare) results in a large DC signal that may overload the detector; the electrode also restricts the solid angle available for illumination and light collection.

A dual-beam velocimeter with a 30 mW He-Ne laser and a Tektronix spectrum analyzer has been built and bench-tested. A typical spectrum obtained

*This work was supported by the Director, Office of Energy Research, Office of Basic Energy Sciences, Materials Sciences Division of the U.S. Department of Energy under Contract No. W-7405-ENG-48.

from a rotating disk with backscatter operation is shown in Fig. 1. The measured center frequency agrees with that expected on the basis of rotation rate. The width of the frequency distribution is attributed to vibration of the disk. Bulk velocities of water in channel flow have been measured with forward scatter operation. Acceptable results could be obtained for the velocity component parallel to the surface, but the normal component could not be measured. With backscatter operation, only poor signal-to-noise ratios could be obtained. Since spectrum analyzers work in the frequency domain, the flow must be stationary over extended periods of time (minutes).

A commercially available (TSI) laser Doppler velocimeter has also been tested with an electrochemical flow channel. This equipment used a digital frequency counter coupled to a minicomputer that also performed a data validation routine. This signal processing scheme results in a better signal-to-noise ratio, extends the measurements to lower beat frequencies, and operates in the time domain. The equipment also used the dual-beam principle and a 30 mW He-Ne laser. The tests showed that velocity components in boundary layers parallel to the interface could be measured in the backscatter mode, but the normal velocity component could not be determined because of surface flare. Single-beam operation to derive the third velocity component was not possible.

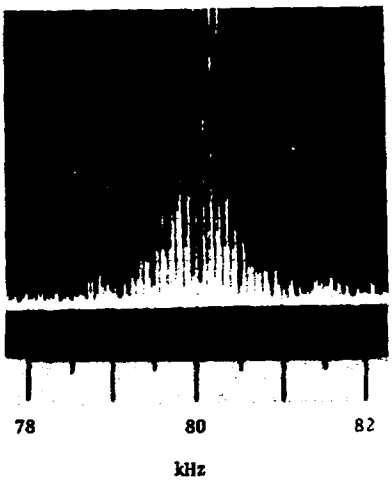

Fig. 1. Beat-frequency spectrum of dual-beam laser velocimeter signal obtained with backscattering from a rotating disk. (XBB 800-14174)

It was concluded that for a viable velocimetry system, a rather expensive ($30 K) digital data acquisition system and a more powerful (2 W) laser would be essential. The laboratory-built optical train appeared superior to commercially available equipment. Even with the addition of single-beam operation, only two velocity components parallel to the interface could be measured. Determination of the third (normal) velocity component close to the interface awaits a solution to the surface flare problem.

3. OPTIMUM ANGLE OF INCIDENCE FOR MONOCHROMATIC INTERFERENCE IN TRANSPARENT FILMS ON ABSORBING SUBSTRATES†

Rolf H. Muller and Michael L. Sand

Thin-film interference is a convenient technique for the determination of transient local film thickness over extended surface areas. For the practical utility of the technique, the interference phenomenon has to result in high fringe contrast. While good fringe contrast is usually obtained near normal incidence with unsupported transparent films, good contrast is often not obtained for films on metal substrates which are of electrochemical interest. Here, the unequal amplitudes of light waves reflected from the two film surfaces generally result in only partial extinction under conditions of destructive interference.

An analysis of optical interference in transparent films on metallic substrates has quantitatively defined conditions which result in the best attainable monochromatic fringe contrast. To establish well-defined phase relations, pure s- or p-polarized light must be used because the phase change due to reflection, as well as film thickness, affects the interference. For both states of polarization, the dependence of fringe visibility on angle of incidence has been computed and confirmed experimentally (Fig. 2); optimum angles of incidence for which a fringe visibility of one is obtained have been determined for different optical constants of film and substrate materials. The examination of model tapered cryolite films on aluminum substrates, where interference is not detectable near normal incidence, has shown well-defined interference fringes under the predicted optimum angles of incidence.

* * *

†Brief version of LBL-7662, Rev.

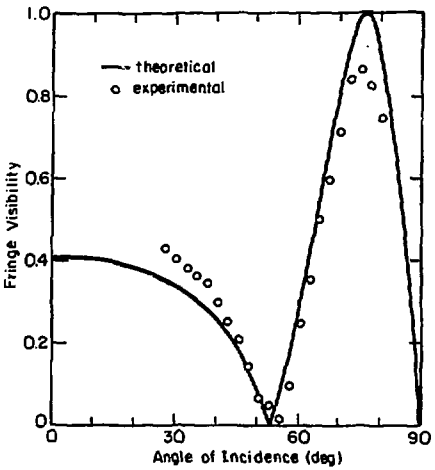

Fig. 2. Computed and photometrically determined fringe visibility for interference in a tapered cryolite film (n = 1.34) on a silicon substrate (n = 4.14-0.03 i). p-polarization, wavelength 546 nm. (XBL 754-6067)

RESEARCH PLANS FOR CALENDAR YEAR 1981

The spectral scanning capabilities of the ellipsometer will be used for investigating the adsorption of surface-active materials at electrodes during electrodeposition. Of particular interest is the potential-dependence of the adsorption of leveling agents and their effect on the microtopography of electrodeposited metals. The electromechanical rotation of ellipsometer components will be extended to the compensating element in order to program automatic four-zone and reflectance measurements.

The optical capabilities of the dual-beam laser velocimeter will be tested with an electrochemical flow channel, using the present laser and spectrum analyzer. Of particular interest for the utility of the technique is a determination of the closest approach of the probe volume to the electrode surface that can be used.

An analysis of surface forces responsible for the formation of electrolyte films on gas electrodes will be initiated. The effects of particulate impurities and finite surface roughness are to be considered.

With C. W. Tobias, conditions for the electrochemical machining of cemented transition metal carbides which avoid the preferential dissolution of the binder will be established.

Research supported by the Division of Electrochemical Systems Research, Office of Conservation and Solar Energy, DOE, are reported in the section "Electrochemical Synthesis and Energy Storage."

1980 PUBLICATIONS AND REPORTS

Refereed Journals

1. Rolf H. Muller and Craig G. Smith, "Use of Film Formation Models for the Interpretation of Ellipsometer Measurements," Surf. Sci. 96, 325 (1980), LBL-9428.

2. P. S. Hauge, R. H. Muller and C. G. Smith, "Conventions and Formulas for Using the Mueller-Stokes Calculus in Ellipsometry," Surf. Sci. 96, 81 (1980), LBL-10172.

3. Rolf H. Muller and Michael L. Sand, "Optimum Angle of Incidence for Monochromatic Interference in Transparent Films on Absorbing Substrates," J. Opt. Soc. Am. 70, 93 (1980), LBL-7662 Rev.

4. John F. Cooper, Rolf H. Muller and Charles W. Tobias, "Periodic Phenomena During Anodic Dissolution of Copper at High Current Densities," J. Electrochem. Soc. 127, 1733 (1980), LBL-9404.

Other Publications

1. R. H. Muller, R. M. A. Azzam and D. E. Aspnes, editors, "Proceedings of the Fourth International Conference on Ellipsometry, Berkeley, Calif., August 20-22, 1979," North Holland, Amsterdam, 1980, also Surface Sci. 96, June 1980.

Papers Presented

1. R. H. Muller and C. G. Smith, "Ellipsometry of Supersaturation and Adsorption in Dissolution-Precipitation Reactions," Electrochem. Soc., Hollywood, Florida, Oct. 5-10, 1980, Ext. Abst. No. 125, vol. 80-2.

2. Karrie J. Hanson, Rolf H. Muller and Charles W. Tobias, "Mass Transfer Enhancement by Turbulence Promoters," Electrochem. Soc., St. Louis, MO., May 11-16, 1980, Ext. Abst. No. 388, vol. 80-1, LBL-10120.

e. Solid-State and Surface Reactions*

Gabor A. Somorjai, Investigator

Surface Structure and Chemisorption by Low Energy Electron Diffraction

1. THE SURFACE STRUCTURE OF ETHYLENE AND ACETYLENE ON THE Rh(111) CRYSTAL FACE

R. J. Koestner, M. Van Hove, and G. A. Somorjai

Low energy electron diffraction (LEED) intensity versus incident electron energy (I(hk)-eV) curves have been collected for several molecules adsorbed on the Rh(111) crystal face, forming ordered surface structures. These structures are due to the metastable as well as the stable configurations of propylene, the stable acetylene, and the unstable as well as the stable ethylene species. The curves are presently being analyzed using multiple scattering calculations to obtain the precise atomic arrangement of these molecules on the Rh(111) surface. Some conclusions about the structures of these small hydrocarbons can already be drawn. First, the I-eV profiles obtained from the surface structures of adsorbed monolayers of the stable acetylene and ethylene are identical. This indicates that the adsorption of either molecule results in the same surface structure. It should be noted that hydrogen must be added to the acetylene overlayer for conversion into the stable structure. Second, preliminary results obtained during the structure analysis of the metastable ethylene indicate the presence of an ethylidyne species bonded perpendicular to the surface at a threefold hollow site. This agrees with the findings of recent vibrational spectroscopy experiments and is the same species that was found for ethylene adsorbed on the Pt(111) face. Third, the ordered surface structures of propylene and methyl acetylene show remarkably similar I-eV profiles on Rh(111), indicating that they form identical surface structures by suitable chemical rearrangement upon adsorption.

2. LEED STUDIES OF HYDROCARBONS ADSORBED ON PLATINUM

J. Frost and G. A. Somorjai

Using an apparatus explicitly adapted for and dedicated to the collection of low energy electron diffraction(LEED) data, the ordered adsorption of several hydrocarbons on the Pt(111) crystal face have been studied. I-V profiles have been obtained for the ordered over-layers of propylene, methyl-acetylene, cis-2-butene, and trans-2-butene at angles of incidence near to and far from the surface normal. The method used was to photograph the phosphor display screen, scan the negatives with a microdensitometer, and reduce the data using a computer. To this end, a new and nearly automatic set of algorithms have been coded and tested which allow for the tracing and measurement of the diffraction spots. The propylene and methyl-acetylene form (2 × 2) over-layers at low exposures (~ 1 L). The cis- and trans-butenes display an exposure-dependent morphology culminating in a $(2\sqrt{3} \times 2\sqrt{3})$ R30° structure at an exposure of ~ 1000 Langmuirs. The marked similarity in the I-V profiles for propylene and ethylene, even at high polar angles, suggests that the ethylidyne model proposed for ethylene holds for propylene but that the third carbon atom is disordered about the ethylidyne C-C bond axis. The cis- and trans-2-butene I-V profiles are identical at all angles, showing that they rearrange on the surface to form the same chemical species. The exposure-dependent morphology (including an (8 × 8) structure and short range $(2\sqrt{3}, 2\sqrt{3})$R30°. fluctuations on a basic (2 × 2) structure) together with a detailed comparison of the I-V profiles suggests that these have essentially the same bonding to the substrate as ethylene and propylene; but that, unlike propylene, the carbon chains order at high coverage due to adsorbate-adsorbate interactions.

3. LEED, AES, AND TDS STUDIES OF CO AND K ON Pt(111) SURFACES

E. Garfunkel and G. A. Somorjai

The role of alkali metal promoters in catalysis is being studied by standard UHV techniques. Potassium was adsorbed on the Pt(111) surface and examined by low energy electron diffraction (LEED), Auger electron spectroscopy (AES), and thermal desorption spectroscopy (TDS) for determination of structures, composition, and heats of adsorption. Thermal desorption data display two broad peaks centered at 700 and 900 K. From the known heat of sublimation of K, it can be inferred that the low energy peak is due to K desorption from a multilayer of potassium, and that the high energy peak is the result of K desorption from Pt. Ordered LEED patterns of the potassium overlayer appear in the coverage (θ) range of $0.5 < \theta_K < 1$ if the surface is heated for several seconds to ~ 300°C then cooled to below 50°C. A series of at least three patterns has been discerned, changing from a c(2 × 2) => (2 × 10) => (4 × 4) with increasing coverage. The thermal desorption of CO from the Pt(111) and Pt(111)/K surfaces has been studied. The binding energy of CO to the Pt substrate was found to increase from 27 kcal/mole at $\theta_K = 0$ to 33 kcal/mole at $\theta_K = 0.3$. A new high binding energy site at ~ 40 kcal/mole appeared which is due to a K-CO complex on the Pt surface.

*This work was supported by the Director, Office of Energy Research, Office of Basic Energy Sciences, Materials Sciences Division of the U. S. Department of Energy under Contract No. W-7405-ENG-48.

4. Ag MONOLAYERS ON Pt SINGLE CRYSTAL SURFACES: A STUDY OF THEIR GROWTH AND THEIR INFLUENCE ON THE CHEMISORPTIVE PROPERTIES OF Pt SINGLE CRYSTALS

P. W. Davies and G. A. Somorjai

AES, thermal desorption, and LEED techniques have been used to determine the growth mechanisms and influence on the chemisorptive properties of Ag monolayers on the Pt(111) and stepped Pt(553) single crystal surfaces. Ag was generated from an effusive source which produced a flux of 0.1 A/minute at the crystal surfaces. The exact amount of Ag present on the surfaces was determined by several different techniques: a. By directly measuring the Ag flux with a quartz crystal oscillator. b. By finding that Ag desorbed completely from the Pt surface on heating to ~ 800 K. A measure of the Ag content of the surface could, therefore, be obtained from the integrated thermal desorption yield. c. From measuring the ratio of the Ag to the Pt transitions in the AES spectra of the surfaces. This method was used after calibration using methods 1 and 2 above.

The growth mechanisms were determined by plotting the Ag and Pt Auger peak heights against the amount of Ag deposited. In the case of Pt(111), distinct breaks were found in these plots which indicated a layer-by-layer growth mechanism. The corresponding plot for growth on the Pt(553) showed no breaks, indicating that Ag growth was occurring as 3-dimensional crystallites. These conclusions were supported by the Ag thermal desorption from both surfaces. Two distinct peaks were found for Pt(111), corresponding to the growth of the first and subsequent Ag layers; whereas only a single, rather broad, Ag peak was observed during thermal desorption from the Pt(553) surface.

A study of the chemisorption of small molecular species (CO, H_2, C_2H_4) on these Ag-dosed Pt surfaces have revealed several interesting phenomena. In the presence of Ag, the single CO desorption peak observed from a Pt(111) surface is merely attenuated; however, the CO desorption from a stepped Pt surface exhibits two peaks centered at 300 K and 410 K. The lower temperature peak is associated with adsorption on terrace sites and the higher temperature peak with adsorption at step sites. In the presence of Ag the lower temperature peak was selectively attenuated, indicating that Ag adsorption was preferential at terrace sites. Similar behavior is observed for H_2 adsorption, except that preliminary results indicate that the presence of Ag induces a tightly bound adsorption state in addition to those normally observed on Pt surfaces.

5. DIGITAL LEED PROJECT

J. Frost and G. A. Somorjai

The design of a new LEED system is in an advanced state. The system features single electron counting using a microchannel plate (MCP) electron multiplier and digital determination of the multiplier output to 8 × 8 bit accuracy. The position determination is done by algebraic operations on the currents from four charge-sensitive amplifiers at the edges of a resistive anode plate at the rear of the MCP. The system calls for a 64 K × 16 bit buffer memory and an oscilloscope display of both the incoming counts and the events stored in the buffer. A CSI 11/23 with 128 K of memory will read and process the information in the buffer. Permanent storage is provided by two 5-megabyte hard disks. Interactive facilities include a teletype and a hard copy printer. The computer will also control the electron gun voltage. The MCP allows extremely sensitive Auger spectroscopy even in RFA mode. At the first stage, mostly commercially available parts will be used. Even at this stage, the very low incident beam current (10^{-12} A) will remove the possibility of electron beam damage to the sample; and, when insulators are used, sample charging effects. The automatic digital data collection makes the measurements rapid (5 sec per energy) and simple. A suite of Fortran IV programs has been written and tested (using the CDC-7600 and microdensitometered photographs of diffraction patterns). They provide automatic tracking and measurement of diffraction spot shapes and intensities, and were written with a minicomputer environment in mind. At the second stage of development, the spatial resolution of the detector system will be improved together with a redesign of the electron gun. The aim is an order of magnitude improvement in the reciprocal space resolution (R) together with a reduction in the incident beam diameter (D), such that $D \leq 10/R$.

6. RELIABILITY FACTORS IN SURFACE CRYSTALLOGRAPHY BY LEED

M. A. Van Hove, R. J. Koestner, and G. A. Somorjai

The use of so-called reliability factors (or R-factors) in surface structural determination by low energy electron diffraction has been studied. In particular, 10 different R-factors, several of them already in use by various workers to assess the quality of agreement between theory and experiment, were compared. Their differences were shown to be both significant and useful for discriminating between the correct surface structure and those incorrect surface structures that also produce local minima in the R-factors. Furthermore, the difference between R-factors calculated for different emergence directions of the electrons were shown to be even more capable of such discrimination between correct and incorrect structures. This capability is of obvious importance in surface crystallography based on a structural search. Our studies, therefore, also addressed the question of automation of the structural search with the help of R-factors, pointing out the usefulness of such approaches as "projection improvement," least squares fit, steepest descent, and functional fit.

Electron Spectroscopy Studies of Solid Surfaces and Adsorbates

7. EVIDENCE FOR AN OXYGEN INTERMEDIATE IN THE CATALYTIC REDUCTION OF NO by CO ON RHODIUM SURFACES

L. H. Dubois, P. K. Hansma, and G. A. Somorjai

Evidence for an oxygen intermediate in the reaction of NO and CO to form N_2 and CO_2 over rhodium

surfaces has been presented. High resolution electron energy loss spectroscopy (ELS) measurements indicate that both NO and CO molecules associatively adsorb on the Rh(331) single crystal surface at 300 K. Chemisorbed NO readily dissociates on this surface upon heating to 450 K. At 700 K, high-resolution ELS and Auger electron spectroscopy both indicate that only oxygen is present on the catalyst surface. N_2 desorption below this temperature is easily detected by mass spectroscopy. The addition of CO to this surface oxygen at 700 K results in the formation of gaseous CO_2 and the removal of the surface oxygen species. Similar results were obtained when O_2 was substituted for NO as a control, indicating that oxygen is indeed a surface intermediate under our experimental conditions. The reaction mechanism to reduce NO to N_2 by CO over rhodium surfaces may then be expressed as:

$$2NO_{(g)} \rightarrow N_{2(g)} + 2O_{(ad)} \text{ and } 2O_{(ad)} + 2CO \rightarrow 2CO_{2(g)}.$$

8. THE CHEMISORPTION OF PROPYLENE ON Pt(111) STUDIED BY HIGH RESOLUTION ELECTRON ENERGY LOSS SPECTROSCOPY

J. Crowell and G. A. Somorjai

The chemisorption of simple hydrocarbons and their subsequent reactions on well-characterized transition metal surfaces can provide information on the initial stages of hydrocarbon catalysis. Acetylene and ethylene have been shown to form stable (2 × 2) surface structures, and ELS data have been interpreted in terms of the formation of a stable ethylidyne ($\rightarrow$ C-CH_3) surface species. The The addition of a methyl group to these species should provide additional insight into the structure of these species on transition metals. LEED investigations have shown that propylene forms a similar stable (2 × 2) surface structure on Pt(111) at room temperature. Thermal desorption measurements show that below 270 K propylene remains intact, but dissociates to evolve hydrogen at 285 K and 425 K. Experiments are currently underway to examine the vibrational spectra of propylene as a function of temperature and coverage using electron energy loss spectroscopy. Preliminary results show that propylene spectra are more complicated than that of ethylene and acetylene.

9. AUGER ELECTRON SPECTROSCOPY STUDIES OF THE SURFACE COMPOSITION OF THE IRON/IRON-OXIDE/OXYGEN SYSTEM

N. Langell and G. A. Somorjai

Iron oxidation and the subsequent oxide surface properties are being investigated by LEED (low energy electron diffraction) and Auger electron spectroscopic techniques. The experimental apparatus is also equipped with a high-pressure isolation cell. The surface composition of thin oxide films grown on polycrystalline foil, and electrophoretically deposited Fe_2O_3 samples have been determined as a function of surface treatment and oxide formation conditions. Clean iron foil, when allowed to reach thermodynamic equilibrium under oxygen at room temperature, inevitably forms Fe_2O_3 surfaces. If subjected to reducing conditions (heating in UHV under H_2, etc.), a surface layer of Fe_3O_4 can be formed on the bulk Fe_2O_3. Similar results are obtained when Fe_2O_3 powders are studied. When first introduced into UHV, the Fe_2O_3 powder surface is covered with an H_2O surface species. The hydroxylated layer is tenacious and tends to protect the surface from reduction under UHV. The layer can be removed by argon ion bombardment or extended heating at temperatures of about 400°C. Once removed, the species can only be regenerated by high pressures (~ 18 torr) of water vapor. Studies of H_2O adsorption are also under way. In addition to the tenacious species mentioned above, a less strongly adsorbed H_2O surface species has been observed. This species desorbs at temperatures above 350°C and can easily be regenerated by exposure to H_2O at pressures as low as 2×10^{-8} torr. Structural studies focus on Fe_2O_3 and Fe(110) single crystals. The effect of oxygen and water vapor partial pressure on the two-dimensional surface symmetry is currently under investigation. With use of the isolation cell, oxygen pressures to one atmosphere and H_2O to saturation vapor pressures can be employed without exposure to atmospheric conditions.

Molecular Beam—Surface Interactions

10. THE VELOCITY DISTRIBUTIONS OF NO AND NH_3 SCATTERED FROM Pt(111)

W. Guthrie, T. H. Lin, and G. A. Somorjai

The velocity distributions of NO and NH_3 scattered from the (111) face of a platinum crystal are being measured over a range of crystal temperatures of 400 K to 1200 K. These molecules adsorb associatively with adsorption probabilities near unity and interact strongly with the platinum with chemisorption energies of 15 kcal/mole and 29 kcal/mole for NH_3 and NO respectively. NO molecules scattered into the direction of the surface normal are trapped and then inelastically scattered. At lower temperatures (400-900 K) there is substantial energy exchange between the adsorbate and substrate, and the NO velocity distributions accurately match the Maxwell-Boltzmann distribution for the crystal temperature. At higher crystal temperatures (900 - 1200 K) the velocity distributions begin to deviate from the Maxwell-Boltzmann distribution due to an incomplete energy transfer. NO molecules scattered into the direction of the specular reflection have velocity distributions that indicate significant trapping followed by inelastic scattering. The velocity data for NH_3 shows behavior similar to NO for scattering into the angle of the surface normal. These studies are being conducted to determine the extent of energy transfer between the metal surface and the gas molecules. It appears that the energy transfer is less complete as the crystal temperature increases and the surface residence time of the molecules decreases.

11. MODULATED MOLECULAR BEAM SCATTERING OF CO AND NO FROM Pt(111) AND Pt(557) SURFACES

Te-Hua Lin and G. A. Somorjai

The modulated molecular beam scattering of CO and NO from Pt(111) and Pt(557) has been studied. For CO scattered from Pt(111), an adsorption-desorption model with constant sticking coefficient fits those data above 500 K well. The best fitting parameters are the preexponential factor for desorption, $\nu = 2.9 \times 10^{13}$, activation energy for desorption, E = 29.9 kcal/mole, and sticking coefficient, S = 0.74. For CO scattered from Pt(557), the same model fits those data above 550 K well, and the best-fitting parameters are: $\nu = 7.9 \times 10^{13}$, E = 33.6 kcal/mole, and S = 0.74. The higher activation energy for Pt(557) than that for Pt(111) suggests that the incident molecule can be adsorbed at the step as well as at the terrace but desorbs only at the step after it arrives there by surface diffusion. An adsorption-desorption model with coverage-dependent sticking coefficient can fit all the data well for both surfaces without changing the desorption kinetic parameters much. For NO scattered from Pt(111), the adsorption-desorption model with constant sticking coefficient fits those data above 525 K well with $\nu = 6.2 \times 10^{13}$, E = 28.6 kcal/mole, and S = 0.65. For NO scattered from Pt(557), the same model fits those data above 525 K well with $\nu = 1.2 \times 10^{14}$, E = 32.3 kcal/mole, and S = 0.71. The higher activation energy suggests again that NO can be adsorbed at the terrace and rapidly diffuse to the step site before desorbing from the surface. Below 525 K, the NO results are quite different from those of CO and can not be simulated with the simple models that were tried. The data can be used, however, to rule out several models of surface interactions. NO does not dissociate detectably between 400 K and 1200 K under our experimental conditions. The sticking coefficient decreases with increasing coverage.

Studies of Catalyzed Surface Reactions

12. THE STRUCTURE SENSITIVITY OF *n*-HEPTANE DEHYDROCYCLIZATION AND HYDROGENOLYSIS CATALYZED BY PLATINUM SINGLE CRYSTALS AT ATMOSPHERIC PRESSURE

W. D. Gillespie, R. K. Herz, E. E. Petersen, and G. A. Somorjai

The dehydrocyclization and hydrogenolysis of n-heptane, catalyzed by platinum single crystal surfaces, have been investigated at temperatures from 533 to 603 K in the range of one atmosphere total pressure. The flat (111), stepped (557), and kinked [(19,8,7) and (25,10,7)] surfaces used in this study were characterized in ultrahigh vacuum by low energy electron diffraction and Auger electron spectroscopy before and after reaction experiments. The rate of dehydrocyclization to toluene on the four surfaces increased in the order (111) < (25,10,7) < (557) < (10,8,7). Hydrogenolysis, however, increased in the order (557) < (10,8,7) < (111) < (25,10,7). As a result, the selectivity of toluene production versus hydrogenolysis increased by an order of magnitude in the order (25,10,7) < (111) < (10,8,7) < (557). The sum of the rates of hydrogenolysis and toluene production remains relatively constant. The effect of preoxidation of the single crystal catalysts was to increase the rate of hydrogenolysis and decrease the rate of dehydrocyclization. In general, the reaction rates decreased with increasing reaction time. This decrease was shown to be the result of the deposition of irreversibly adsorbed carbonaceous species.

13. DEUTERIUM ISOTOPE EFFECT AND EXCHANGE REACTION STUDIES DURING HYDROCARBON CONVERSION OVER PLATINUM SINGLE CRYSTAL SURFACES

S. M. Davis and G. A. Somorjai

Inverse deuterium isotope effects have been measured for a variety of hydrocarbon reactions that are catalyzed near atmospheric pressure over initially clean platinum single crystal surfaces. Hydrogenolysis, isomerization, cyclization, and dehydrogenation reactions for n-hexane, neopentane, isobutane, and cyclohexane catalyzed in the presence of deuterium gas at 40-360°C display reaction rates that are two to four times higher than the rates of the same reactions carried out in hydrogen under identical experimental conditions. The magnitude of these isotope effects depends little on surface structure and decreases with increasing temperatures. These thermodynamic isotope effects exist because deuterium exchange is fast compared with catalyzed hydrocarbon conversion, and deuterated reaction intermediates are thermodynamically more stable than hydrogenated intermediates. Thus, their surface concentration is larger. Because parallel reactions often display deuterium isotope effects of different magnitude, the selectivity of the hydrocarbon conversion can be altered appreciably when the reactions are carried out in deuterium.

The exchange reactions of n-hexane and n-heptane with deuterium gas have also been investigated in the temperature range 235-380°C over the flat (111) and kinked (10,8,7) crystal faces [illegible] inum. Exchange rates and product distributions [illegible] influenced appreciably by the presence of [illegible] nd kinks on the platinum surface. Exchange [illegible] low conversion display zero activation ene[illegible] strong, positive order dependence on D_2 pr[illegible] and a strong negative order dependence on [illegible] face coverage by carbonaceous species. The [illegible] rate of deuterium chemisorption on uncovered metal active sites appears to control the exchange kinetics. Exchange product distributions vary markedly with temperature, D_2 pressure, and surface composition. Single or complete exchange is favored at low temperatures (≤ 300°C) and on surfaces that are precovered with carbonaceous deposits. At higher temperatures, both surfaces display a high specificity for the production of n-hexane-d_{10} and n-heptane-d_{12}; i.e., four of 14 or 16 hydrogen atoms do not exchange. By comparing deuterium exchange rates (fast) with hydrocarbon conversion rates (slow) that were measured simultaneously, it was possible to determine for the first time absolute exchange reaction probabilities for hydrocarbon molecules that become chemically bonded on the catalyst surface. These reaction probabilities increase from 0.01-0.04 at 240°C to 0.2-0.4 at 380°C.

14. A NEW RADIOTRACER TECHNIQUE FOR GENERAL SURFACE STUDIES: APPLICATION TO ^{14}C-BENZENE CHEMISORPTION ON Pt(111)

S. M. Davis, B. E. Gordon, G. A. Somorjai

A sensitive counting system has been developed that enables ^{14}C-radiotracer studies to be carried out in ultrahigh vacuum systems in connection with hydrocarbon adsorption and catalysis studies on small area surfaces. In our investigations, a compact surface barrier detector, mounted on a rotatable feedthru and interfaced to charge-sensitive counting electronics, is used to detect beta radiation emitted by ^{14}C-labeled hydrocarbons chemisorbed on platinum single crystal surfaces. With this system, the absolute surface coverage by adsorbed species can be accurately and non-destructively determined at coverages well below 1% of a monolayer. Dynamic experiments can also be performed easily at both high and low pressures to determine the kinetics of important surface phenomena ranging from isothermal desorption, bulk dissolution, and surface diffusion to hydrogen transfer and rehydrogenation reactions for adsorbed species. The great usefulness of this radiotracer technique was demonstrated in studies of ^{14}C-benzene chemisorption, hydrogen transfer, and rehydrogenation reactions on the (111) crystal face of platinum at temperatures ranging from 50 to 350°C. Combined investigations using radiotracer analysis with quantitative hydrogen thermal desorption spectroscopy revealed that dissociative chemisorption and sequential dehydrogenation proceed over this temperature range with an activation energy of 1.5 - 2.5 kcal/mole that increases with increasing coverage. Carbon surface coverages determined from the radiotracer analysis were correlated with C_{273}/Pt_{237} Auger peak-to-peak height ratios, providing a convenient absolute Auger calibration for carbon coverage on platinum. Rehydrogenation of benzene chemisorbed at 50 - 100°C was found to proceed readily at low temperatures (50 - 100°C) in one atmosphere of hydrogen. Rehydrogenation of ^{14}C-benzene deposited at 300 - 350°C occurred much more slowly even at temperatures as high as 400°C. Removal of the strongly adsorbed ^{14}C-deposit by hydrogen transfer reactions from unlabeled hydrocarbons was found to proceed at least as easily as direct rehydrogenation with H_2. The rate of rehydrogenation at 350°C was slow compared with the steady state rates of simple hydrogenolysis reactions that were carried out over the same carbon-covered surface (viz. isobutane, neopentane, n-hexane). Extensive studies are in progress to determine if these hydrocarbon conversion reactions take place in exchange with or on top of the preadsorbed ^{14}C-deposit.

15. TRANSIENT RESPONSE TECHNIQUES FOR STUDYING THE CHEMISTRY OF CARBON DEPOSITS ON METAL CATALYST SURFACES

S. M. Davis and G. A. Somorjai

Several transient response techniques were developed in our laboratory during the past year to investigate the reaction chemistry of carbon deposits that form during hydrocarbon synthesis and reforming over metal catalysts. Reactant pulse methods, reaction rate studies over preadsorbed carbon layers, and consecutive and competitive reaction rate studies were devised for this purpose. Presently, these techniques are being applied to understand how carbon deposits participate in reforming catalysis over small-area platinum single crystal surfaces. The catalysts are investigated in an apparatus that combines surface analysis studies in UHV, using LEED and Auger spectroscopy, with reaction rate studies that are performed near atmospheric pressure in a retractable isolation cell. Reaction rate studies over preadsorbed carbonaceous overlayers have provided relative rehydrogenation rates for carbon deposits that form as a function of temperature and hydrogen pressure from n-hexane, neopentane, and isobutane. Competitive reaction rate studies have been used to measure relative adsorption equilibrium constants for the same hydrocarbons. These studies have shown that adsorption equilibrium constants and residence times for strongly adsorbed species increase with increasing molecular weight and decreasing degree of substitution, i.e., n-hexane > neopentane ≈ isobutane. Pulse and consecutive reaction experiments have been used to measure differences in catalytic activity and selectivity that exist between clean and carbon-covered platinum. While carbon-covered surfaces are always less active than clean platinum, these catalysts are still highly active and often display higher selectivity for non-destructive reforming reactions. Aromatization of n-hexane to benzene and dehydrogenation of isobutane to isobutene, for example, are two important reactions which display enhanced selectivity over carbon covered platinum catalysts. Quantitative hydrogen thermal desorption spectroscopy has also been used to measure the hydrogen content of carbon deposits as a function of their formation temperature.

16. THE ENHANCED REACTIVITY OF ORDERED METAL LAYERS ON SINGLE CRYSTAL SURFACES OF OTHER METALS: Au ON Pt(100), AND Pt ON Au(100)

J. W. A. Sachtler and G. A. Somorjai

Catalysts consisting of alloys of an active group VIII transition metal and an inactive group Ib metal are of great importance for the catalysis of hydrocarbon reactions. It has been found that such alloys can show higher selectivities and better resistance against deactivation than the group VIII metals alone. These studies have been performed using dispersed alloy particles, often supported on high surface area oxides where it is difficult to control the surface structure and composition independently. It appears that the separation of these important experimental variables is necessary to understand the reason for the altered chemical behavior of these alloys. We have approached this problem by choosing as a substrate a single-crystal metal that can be prepared with a controlled surface structure (geometry, concentrations of step, and kink atoms). The other metal is deposited in amounts ranging from a fraction of a monolayer to several layers onto this substrate under appropriate conditions. In particular, we have studied the Au on Pt(100) and Pt on Au(100)

systems. The surface structures at various coverages have been investigated using low energy electron diffraction (LEED) and Auger electron spectroscopy (AES). The metal adsorbate coverages themselves were independently determined with a quarter-crystal thickness monitor. It appears that multilayers of platinum on a Au(100) surface and up to two layers of gold on a Pt(100) single-crystal surface form (1 ×1) structures with the lattice constant of the substrate. In the case of gold on a Pt(100), (5 × 1) and (7 × 1) LEED patterns were observed at high coverages after annealing. Using AES, it has been determined that the gold film grows on a Pt(100) surface through the completion of successive monolayers. Platinum on Au(100) forms small three-dimensional crystallites without a monolayer stage. The chemical reactivity of these surfaces was tested using low-pressure cyclohexene dehydrogenation to benzene (6×10^{-8} torr cyclohexene in 1×10^{-6} torr hydrogen, 373 K). We have found that the deposition of gold, not active for this reaction, onto a Pt(100) single crystal surface actually enhances the reactivity until a maximum is reached at one monolayer of gold. At this point, the surface is four times more active than the pure Pt(100) crystal face. When the gold monolayer coverage is exceeded, the reactivity decreases rapidly. When platinum is deposited onto a Au(100) single crystal surface, the reactivity for cyclohexene dehydrogenation increases with coverage until a maximum value is reached at about 1.5 platinum layers. This maximum value is retained up to about 3.5 to 4 layers. Again, this maximum reactivity is about four times that of the (100) surface of a bulk platinum single crystal. When the platinum coverage is increased further, the reactivity decreases slowly. Eight platinum layers on Au(100), the highest coverage achieved in our experiments, are still more active than a pure Pt(100) surface.

The addition of a high-pressure sample isolation cell to the UHV system used for these studies has been completed. This device permits the running of reactions at near atmospheric pressures over a surface that is prepared and characterized before and after the reaction under UHV conditions. The effect of gold on the reactivity of a Pt(100) single crystal surface under these conditions will be studied not only for the cyclohexene reaction, but also for isomerization, hydrogenolysis, and dehydrocyclization reactions. Also, the variation of the substrate geometry and adsorbate metal will be investigated by using different platinum crystal faces and copper or silver instead of gold.

RESEARCH PLANS FOR CALENDAR YEAR 1981

We shall solve the surface structures of several small hydrocarbon molecules (from propylene to butenes) on the platinum and rhodium (111) crystal faces by LEED and determine their chemical bonding behavior by electron spectroscopy. Vibrational spectroscopy (HREELS) will be used to study the structure of hydrocarbon fragments that deposit during catalytic reactions on platinum surfaces. The structure and reactivity of metal monolayers of Au, Ag, and Cu deposited on other transition metal surfaces will be investigated in an attempt to build new metal catalyst systems. ^{14}C-labeled organic molecules will be used to explore the catalytic role of carbonaceous deposits in hydrocarbon conversion reactions on platinum surfaces. The role of catalyst additives, alkali metals, and chlorine, in controlling reaction selectivity, will be explored. Energy transfer during H and D atom recombination on various surfaces will be studied by molecular beam-surface scattering.

1980 PUBLICATIONS AND REPORTS

Refereed Journals

1. S. M. Davis and G. A. Somorjai, "The Effect of Surface Oxygen on Hydrocarbon Reactions Catalyzed by Platinum Crystal Surfaces with Variable Kink Concentrations," Surface Sci. 91, 73 (1980).

2. M. Salmerón and G. A. Somorjai, "A LEED-AES Study of the Reconstructed Pt(110) Surface and the Effect of Oxygen Treatment," Surface Sci. 91, 373 (1980).

3. L. H. Dubois and G. A. Somorjai, "The Dissociative Chemisorption of CO_2 on Rhodium Surfaces," Surface Sci. 88, L13 (1979).

4. L. E. Firment and G. A. Somorjai, "Low Energy Electron Diffraction (LEED) Study of the Adsorption of Acetic Acid and Propanoic Acid on Ag(111) and Pt(111)," J. Vac. Sci. & Technol. 17, 574 (1980).

5. L. H. Dubois and G. A. Somorjai, "The Chemisorption of CO and CO_2 on Rh(111) Studied by High Resolution Electron Energy Loss Spectroscopy," Surface Sci. 91, 514 (1980).

6. G. A. Somorjai, "Catalysis and Surface Science," 2nd European Conf. on Surface Science, Plenary Lecture, Cambridge, England, March 19-23, 1979 Surface Sci. 89, 496 (1979).

7. M. A. Van Hove and G. A. Somorjai, "Adsorbed Monolayers on Solid Surfaces," in Structure and Bonding, Vol. 38, Springer-Verlag 1979.

8. J. P. Bibérian and G. A. Somorjai, "Surface Structures of Metallic Monolayers on Metal Crystal Surfaces," J. Vac. Sci. & Technol. 16, 2073 (1979).

9. M. A. Van Hove and G. A. Somorjai, "A New Microfacet Notation for High Miller Index Surfaces of Cubic Materials with Terrace, Step, and Kink Structures," Surface Sci. 92, 489 (1980).

10. H. Ibach and G. A. Somorjai, "Evidence for the Weakening of the C≡O Bond Upon Coadsorption with Hydrocarbons," Appl. of Surface Sci. 3, 293 (1979).

11. S. M. Davis and G. A. Somorjai, "Correlation of Cyclohexene Reactions on Platinum Crystal Surfaces over Ten Orders of Magnitude Pressure Range: Variations of Structure Sensitivity, Rates, and Reaction Probabilities," J. Catal. 65, 78 (1980).

12. L. H. Dubois, D. G. Castner, and G. A. Somorjai, "The Chemisorption of Acetylene and Ethylene on Rh(111): A Low Energy Electron Diffraction (LEED), High Resolution Electron Energy Loss (ELS), and Thermal Desorption Mass Spectrometry (TDS) Study," J. Chem. Phys. 72, 5234 (1980).

13. C.-M. Chan, W. H. Weinberg, E. D. Williams, and M. A. Van Hove, "An R-factor Analysis of Several Models of the Reconstructed Ir(100)-(1 × 2) Surface," Surface Science 91, 440 (1980).

14. R. J. Behm, K. Christmann, G. Ertl, and M. A. Van Hove, "Adsorption of CO on Pd(100)," J. Chem. Phys. 73, 2984 (1980).

15. S. Y. Tong, A. Moldonado, C. H. Li, and M. A. Van Hove, "The Structure of c(2 × 2)-CO on Ni(001) by LEED; Self-Consistent Scattering Potentials for Adsorbed CO," Surface Sci. 94, 73 (1980).

LBL Reports

1. D. G. Castner, R. L. Blackadar, and G. A. Somorjai, "CO Hydrogenation over Clean and Oxidized Rhodium Foil and Single Crystal Catalysts. Correlations of Catalyst Activity, Selectivity, and Surface Composition," LBL-10018.

2. D. G. Castner and G. A. Somorjai, "LEED, AES, and Thermal Desorption Studies of the Oxidation of the Rh(111) Surface," LBL-9288.

3. L. H. Dubois, P. K. Hansma, and G. A. Somorjai, "Evidence for an Oxygen Intermediate in the Catalytic Reduction of NO by CO on Rhodium Surfaces," LBL-10061.

4. L. H. Dubois and G. A. Somorjai, "The Application of High Resolution Electron Energy Loss Spectroscopy to the Characterization of Adsorbed Molecules on Rh Single Crystal Surfaces," LBL-10340.

5. M. A. Van Hove, R. J. Koestner, P. C. Stair, J. P. Bibérian, L. L. Kesmodel, and G. A. Somorjai, "The Surface Reconstructions of the (100) Crystal Faces of Iridium, Platinum, and Gold: I. Experimental Observations and Possible Structural Models," LBL-10340.

6. M. A. Van Hove, R. J. Koestner, P. C. Stair, J. P. Bibérian, L. L. Kesmodel, and G. A. Somorjai, "The Surface Reconstructions of the (100) Crystal Faces of Iridium, Platinum, and Gold: II. Structural Determination by LEED Intensity Analysis," LBL-10340.

7. W. Guthrie, J. Sokol, and G. A. Somorjai, "The Decomposition of Ammonia on the Flat (111) and Stepped (557) Platinum Crystal Surfaces," LBL-10536.

8. L. H. Dubois, P. K. Hansma, and G. A. Somorjai, "The Application of High Resolution Electron Energy Loss Spectroscopy to the Study of Model Supported Metal Catalysts," LBL-10733.

9. W. D. Gillespie, R. K. Herz, and G. A. Somorjai, "Cyclohexane Dehydrogenation and Hydrogenolysis Catalyzed by Platinum Single Crystals at Atmospheric Pressure," LBL-10576.

10. J. W. A. Sachtler, M. A. Van Hove, J. P. Bibérian, and G. A. Somorjai, "The Variable Bond Length and Enhanced Reactivity of Ordered Monolayers of Gold on Pt(100) and Platinum on Au(100) Single Crystal Surfaces," LBL-10840.

11. S. M. Davis and G. A. Somorjai, "Hydrocarbon Conversion over Metal Catalysts," LBL-11103.

12. D. G. Castner, L. H. Dubois, B. A. Sexton, and G. A. Somorjai, "Evidence for CO Dissociation on Rhodium Surfaces," LBL-11205.

13. R. J. Koestner, M. A. Van Hove, and G. A. Somorjai, "A Surface Crystallography Study by Dynamical LEED of the CO-($\sqrt{3} \times \sqrt{3}$)R30° Structure on the Rh(111) Crystal Surface," LBL-11263.

14. G. A. Somorjai, "The Catalytic Hydrogenation of CO. The Formation of C_1 Hydrocarbons," LBL-11354.

15. G. A. Somorjai, "LEED: A 50 Year Perspective," LBL-11536.

16. S. T. Ceyer, W. J. Siekhaus, and G. A. Somorjai, "Design of a Molecular Beam Surface Scattering Apparatus for Velocity and Angular Distribution Measurements," LBL-11553.

17. L. H. Dubois and G. A. Somorjai, "The Application of High Resolution Electron Energy Loss Spectroscopy to the Characterization of Adsorbed Molecules on Rh Single Crystal Surfaces," LBL-10188.

18. G. A. Somorjai, "Surface Science and Heterogeneous Catalysis," LBL-11690.

19. W. D. Gillespie, R. K. Herz, E. E. Petersen, and G. A. Somorjai, "The Structure Sensitivity of n-Heptane Dehydrocyclization and Hydrogenolysis Catalyzed by Platinum Single Crystals at Atmospheric Pressures," LBL-11704.

20. G. A. Somorjai, "Auger Electron Spectroscopy," LBL-11720.

21. T. H. Lin and G. A. Somorjai, "Modulated Molecular Beam Scattering of CO and NO from Pt(111) and the Stepped Pt(557) Crystal Surfaces," LBL-11787.

22. P. R. Watson and G. A. Somorjai, "On the Formation of Oxygenated Products during the Hydrogenation of CO over Rhodium Catalysts," LBL-11791.

Invited Talks

1. G. A. Somorjai, "High Resolution Electron Loss Spectroscopy and Low Energy Electron Diffraction Studies of CO, H_2, and Organic Adsorbates on Pt and Rh Surfaces," Oblad Symposium, Salt Lake City, Utah, October 3, 1979.

2. G. A. Somorjai, "Catalytic Hydrogenation of CO." Physical Chemistry Seminar, University of California, Berkeley, October 9, 1979.

3. G. A. Somorjai, "Photocatalytic Dissociation of H_2O," MMRD Seminar, LBL, October 10, 1979.

4. G. A. Somorjai, "The Application of High Resolution Electron Energy Loss Spectroscopy to the Characterization of Adsorbed Molecules on Rh Single Crystal Surfaces," *1979 Conference on Chemistry* and Spectroscopy, Pasadena, October 10, 1979.

5. G. A. Somorjai, "Surface Science of Heterogeneous Catalysis by Metal Surfaces," Waite Philip Fishel Lecture, Vanderbilt University, Nashville, November 9, 1979.

6. G. A. Somorjai, "The Atomic Scale Characteristics of Catalytically Active Metal Surfaces. Search for Correlations with Cluster Chemistry," U.S.-France Cooperative Scientific Seminar, Asilomar, California, November 19, 1979.

7. G. A. Somorjai, "New Horizons in Hydrocarbon Chemistry," International Symposium at the University of Southern California, Los Angeles, December 10, 1979.

8. W. D. Gillespie, "Reforming Reactions of Heptane and Cyclohexane on Pt Crystals at Atmospheric Pressures," National Meeting of Chemical Engineering Institute, San Francisco, December 2, 1979.

9. G. A. Somorjai, "The Surface Chemical Bond," University of Texas (Robert A. Welch Foundation Lecture), Arlington, Texas, February 1, 1980.

10. G. A. Somorjai, "The Surface Chemical Bond," University of Texas, El Paso, Texas, February 5, 1980.

11. G. A. Somorjai, "The Surface Chemical Bond," University of Texas, Prairie View, Texas, February 6, 1980.

12. G. A. Somorjai, "The Importance of Surface Structure and Additives to the Selective HC Catalysis by Pt," AIME 109th Annual Meeting, Las Vegas, February 26, 1980.

13. J. W. A. Sachtler, "The Reactivity of Ordered Metal Layers on Single Crystal Surfaces of Other Metals: Au on Pt(100) and Pt on Au(100)," North American Catalysis Society, Berkeley, California, March 13, 1980.

14. G. A. Somorjai, "The Reactivity of Organic and Metal Monolayers on Transition Metal Surfaces," Catalysis Institute of Spain, Madrid, March 26, 1980.

15. G. A. Somorjai, "Introduction to Surface Science: Principles," Uppsala University, Uppsala, Sweden, April 14, 1980.

16. G. A. Somorjai, "Sample Preparation. Surface Composition." Uppsala University, Uppsala, Sweden, April 15, 1980.

17. G. A. Somorjai, "Structure of Clean Surfaces," Uppsala University, Uppsala, Sweden, April 16, 1980.

18. G. A. Somorjai, "The Structure and Bonding of Adsorbed Monolayers on Solid Surfaces," Swedish Institute of Surface Chemistry, Stockholm, Sweden, April 17, 1980.

19. G. A. Somorjai, "Structure of Adsorbed Monolayers," Uppsala University, Uppsala, Sweden, April 18, 1980.

20. G. A. Somorjai, "The Surface Science of Heterogeneous Catalysis," American Chemical Society, Princeton, April 23, 1980.

21. G. A. Somorjai, "The Structure and Reactivity of Organic and Metal Monolayers on Transition Metal Surfaces," Mobil Research Laboratories, Paulsboro, New Jersey, April 24, 1980.

22. G. A. Somorjai, The Bickerman Lecture, "The Chemical Bonding and Catalytic Conversion of Hydrocarbons on Metal Surfaces," Case Western Reserve University, Cleveland, April 25, 1980.

23. G. A. Somorjai, "Surface Chemical Bond," Uppsala University, Uppsala, Sweden, April 28, 1980.

24. G. A. Somorjai, "The Structure and Chemical Activity of Ordered Surface Defects and Surface Compounds," University of Stockhom, Stockholm, Sweden, April 28, 1980.

25. G. A. Somorjai, "Surface Dynamics," Uppsala University, Uppsala, Sweden, April 29, 1980.

26. G. A. Somorjai, "XPS Studies of Oxygen, CO, and CO_2 on Thorium," American Vacuum Society, 16th Annual Symposium, Santa Fe, May 6, 1980.

27. G. A. Somorjai, "The Catalyzed Hydrogenation of CO over Transition Metal Surfaces," ETH, Zurich, Switzerland, May 12, 1980.

28. G. A. Somorjai, "Surface Science of Heterogeneous Catalysis," Swiss Chemical Society, Plenary Lecture, University of Zurich, Zurich, Switzerland, May 14, 1980.

29. G. A. Somorjai, "Applications of Modern Surface Science to Build New Technologies," IBM Research Laboratory, Zurich, Switzerland, May 16, 1980.

30. G. A. Somorjai, "Surface Phases and Surface Compounds of Metals, Oxides, and Sulfides: Their Structure and Reactivity," Technische Hochschule, Aachen, Germany.

31. G. A. Somorjai, "The Reactivity of Organic and Metal Monolayers on Transition Metal Crystal Surfaces," University of Munich, Munich, Germany, June 11, 1980.

32. G. A. Somorjai, "Heterogeneous Catalysis on the Molecular Scale," Austrian Chemical Society Lecture, Vienna, Austria, June 17, 1980.

33. G. A. Somorjai, "Heterogeneous Catalysis on the Molecular Scale," University of Florence, Florence, Italy, June 24, 1980.

34. G. A. Somorjai, "The Structure and Reactivity of Hydrocarbons on Platinum: The Reasons for Selectivity and the Building of Platinum Catalysts," Fritz-Haber -Institute, Berlin, Germany, June 26, 1980.

35. G. A. Somorjai, "The Reactivity of Platinum for Hydrocarbon Reactions, Studies on the Atomic Scale," University of Strasbourg, Strasbourg, France, July 1, 1980.

36. G. A. Somorjai, "Structure and Reactivity of Hydrocarbons on Platinum: Reasons for Selectivity and the Building of New Catalysts," Université Louis Pasteur, Strasbourg, France, July 2, 1980.

37. G. A. Somorjai, "The Catalyzed Hydrogenation of CO on Transition Metal Surfaces," Université Louis Pasteur, Strasbourg, France, July 3, 1980.

38. G. A. Somorjai, (a) "Surface Bonding, (b) Electronic Effects of Noble Metals Adsorbed on Transition Metals," Institute for Theoretical Physics, University of California, Santa Barbara, August 12, 1980.

39. R. J. Koestner, "A LEED Structural Analysis of the Rh(111)-($\sqrt{3} \times \sqrt{3}$)R30° CO and CO_2 Surfaces, ACS Meeting, Las Vegas, August 25, 1980.

40. W. Guthrie, "Molecular Beam Study of the Velocities of Small Molecules Desorbed from Single Crystal Surfaces of Platinum," ACS Meeting Las Vegas, August 26, 1980.

41. S. M. Davis, "Reactant Pulse and ^{14}C-Radiotracer Techniques for Model Catalytic Studies over Single Crystal Surfaces," ACS Meeting, Las Vegas, August 27, 1980.

42. G. A. Somorjai, "Catalytic Hydrocarbon Conversion and CO Hydrogenation Reactions in Heterogeneous and Homogeneous Media," ACS Meeting, Las Vegas August 28, 1980.

43. S. M. Davis, "Deuterium Isotope Effect and Exchange Reaction Studies During Hydrocarbon Conversion over Pt Single Crystal Surfaces," California Catalysis Society, University of California, Irvine, October 24, 1980.

4. P. R. Watson, "Rh Oxide as a Fischer-Tropsch Catalyst--Catalytic and Surface Science Measurements," California Catalysis Society, University of California, Irvine, October 25, 1980.

45. M. A. Van Hove, "The Structure of CO, CO_2, C_2H_2, and C_2H_4 Adsorbed on Rh(111)," American Physical Society, New York, March 24, 1980.

46. M. A. Van Hove, "Molecular Surface Phenomena," California State University, Hayward, California, April 17, 1980.

47. M. A. Van Hove, "Computation Procedure of the Combined Space Method," Conference on LEED, IBM, Yorktown Heights, New York, June 19, 1980.

48. M. A. Van Hove, "A New Use of R-factors and LEED Calculations for Large Molecules," Conference on LEED, IBM, Yorktown Heights, New York, June 20, 1980.

49. M. A. Van Hove, "Structure Determination of Adsorbed Species on Metal Surfaces by Low Energy Electron Diffraction," ACS Symposium Las Vegas, August 25, 1980.

50. M. A. Van Hove, "The Structures of CO, CO_2, and Small Hydrocarbon Molecules (Acetylene, Ethylene, Propylene, Methylacetylene) Adsorbed on Rh(111) Studied by LEED and HREELS," 4th Intl. Conf. and 3rd ECCOS, Cannes, France, September 22, 1980.

51. M. A. Van Hove, "Atomic Positions at Surfaces by Low Energy Electron Diffraction: Surface Reconstructions and Molecular Adsorption," University of British Columbia, Vancouver, October 6, 1980.

52. M. A. Van Hove, "Atomic Positions at Surfaces by Low Energy Electron Diffraction: Surface Reconstruction and Molecular Adsorption," University of Washington, Seattle, October 7, 1980.

53. M. A. Van Hove, "Surface Crystallography by LEED: A Progress Report," American Vacuum Society, Detroit, October 14, 1980.

54. M. A. Van Hove, "Surface Structure of Adsorbed Layers of Atoms and Molecules on Metals by Low Energy Electron Diffraction," 24th Industrial Affiliates Symposium, Stanford, October 20, 1980.

1. Nuclear Magnetic Resonance*

Alexander Pines, Investigator

1. EFFECTS OF TEMPERATURE, VISCOSITY AND SOLVENT ON THE MAGNETIC ISOTOPE EFFECT†

L. Sterna, D. Ronis, S. Wolfe and A. Pines

A very important feature of free radical chemistry is the effect of electron spin on chemical bonding. In general, two radicals can bond only if the two unpaired electrons have singlet (S = 0) correlation. The triplet state (S = 1) has repulsive potential. The electron-nuclear hyperfine coupling causes interconversion of the electron spin states. This can be used to separate nuclear isotopes of different hyperfine coupling into different chemical products (magnetic isotope effect). We, as well as other groups, have demonstrated this experimentally and have obtained large ^{13}C enrichments in the cyclic photochemical reaction of dibenzylketone (1,3-diphenyl-2-propanone). A crucial factor in the operation of the magnetic isotope effect in a cyclic reaction is that the two radicals of the prepared triplet must stay in the vicinity of one another on a time scale comparable to the inverse hyperfine couplings. In previous reports we have shown that the ^{13}C enrichment in the dibenzylketone reaction exhibits a strong viscosity dependence and goes through a maximum at ~ 10 poise. Work by Turro et al. has shown that the radicals may also be constrained in micelles which act as small reflecting spheres. We have developed a theory which characterizes the viscosity, temperature, and micelle size dependence of the enrichment and extended it also to layered solvents. Representative results are shown in Fig. 1. Thus, the magnetic isotope effect, which is very interesting in itself as a novel method of isotope separation, also provides a new means of probing the microscopic diffusive behavior of radicals.

* * *

†Based in part on J. Chem. Phys. 73, 5493 (1980)

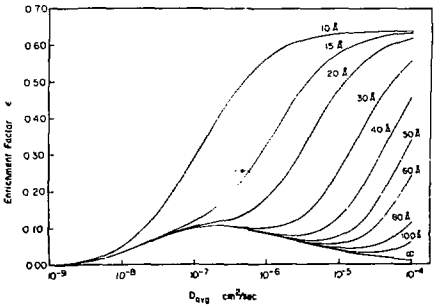

Fig. 1. Enrichment factor for photolysis of dibenzylketone within a sphere with a reflecting wall (e.g. a micelle). The curves are labeled by the radius of the sphere in angstroms. The ordinate is the average diffusion coefficient of the radicals in the micelle. The sole datum is taken from the work of Turro et al. for photolysis in the hexadecyltrimethylammonium chloride micelle with diffusion coefficient taken from data for a similar micelle. Our own data corroborate the bottom curve (radius = ∞) for normal unbounded 3-dimensional diffusion. (XBL 805-9681A)

2. THEORY OF SELECTIVE EXCITATION ON N-QUANTUM TRANSITIONS+

W. S. Warren, D. P. Weitekamp and A. Pines

The question of whether a molecule can be used to absorb and emit photons only in groups of n has been treated. Pulse sequences have been introduced which in effect induce excitation by only resonant groups of n photons. This caused only n-quantum transitions even when many other transitions might be resonant. The theory explains how this is done by using repeated phase shifts of $2\pi/n$ in the radiation to build up the selected coherences with all other coherences interfering destructively. Coherent averaging theory was extended to describe selective sequences and, together with time reversal excitation, produces efficient n-quantum pumping which is selective to arbitrarily high order in the average Hamiltonian. The selectivity produces an enormous enhancement of the high n-quantum coherences (or populations) which are normally very weak when governed by an incoherent statistical process. For example, the 10-quantum transition in a 10-spin system can be enhanced by four to five orders of magnitude. An example of wideband nonselective versus 4-quantum selective excitation in the NMR of oriented bromobutane appears in Fig. 2.

* * *

+Based in part on LBL-10817, J. Chem. Phys. 73, 2084 (1980).

*This work was supported by the Director, Office of Energy Research, Office of Basic Energy Sciences, Materials Sciences Division of the U. S. Department of Energy under Contract No. W-7405-ENG-48.

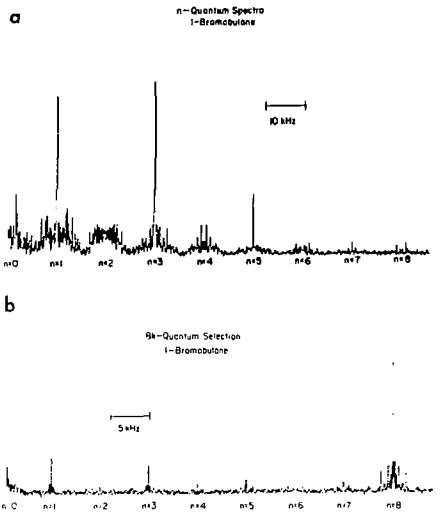

Fig. 2. a. Multiple-quantum NMR spectra by wideband non-selective excitation in a liquid crystal solvent. The number of allowed transitions decreases dramatically as ΔM increases, and the intensity above n = 5 makes these transitions essentially unobservable. b. Multiple-quantum spectra with selective 8-quantum excitation. Only the 0- and 8-quantum coherences are produced with appreciable intensity. (XBL 808-11260 and XBL 808-11262)

3. STATISTICAL THEORY OF MULTIPLE QUANTUM TRANSITIONS†

R. D. Levine, S. Mukamel, W. S. Warren and A. Pines

In wideband *non*-selective excitation, multiple quantum spectra typically have fewer lines and lower intensities than single quantum spectra as expected from an energy-level diagram (Fig. 3). The ensemble average of many multiple quantum spectra reveals a roughly Gaussian dependence of multiple quantum intensities on the number of quanta. A statistical approach to the intensity dependence, using information theory, has been made in order to learn about the conditions and values of parameters which favor high intensity for high multiple quantum transitions. This leads to a "dynamic random-phase approximation" in which the single quantum pumping matrix elements yield intensity patterns for the n-quantum spectra. The effects of pumping time on temperature are also accounted for by the theory.

* * *

†Based in part on LBL-11885, W. S. Warren, Ph.D. thesis (1980).

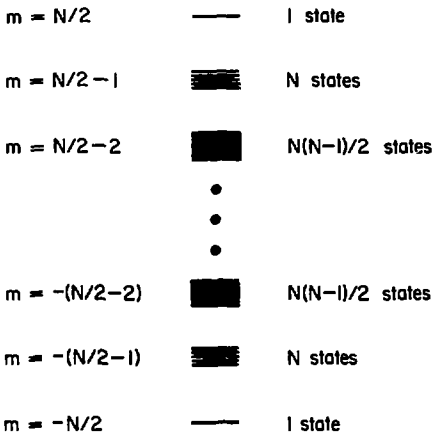

Fig. 3. Energy level diagram for N coupled spin $\frac{1}{2}$ nuclei. There are many single quantum ($\Delta m = 1$) transitions but only one N-quantum ($\Delta m = N$) transition. A statistical theory of the n-quantum intensities has been developed. (XBL 805-9725)

4. MOLECULAR CONFORMATION IN LIQUID CRYSTALS†

S. Sinton and A. Pines

The study of the conformation of aromatic units in liquid crystal molecules is important in understanding the physics and chemistry of their various fascinating phases. This can usually be accomplished only with deuterium isotope substitution and complex analysis of the NMR spectra. However, multiple quantum transitions are extremely sensitive to both static and dynamic correlations between the protons of a molecule and are usually resolvable and simple to analyze. We have used this to study the conformations of a number of liquid crystal systems and the relationship of these conformations to the macroscopic phases. For example, in the nematic phase of cyanobiphenyl systems, the conformation of the biphenyl group could be analyzed by fitting the 6- and 7-quantum spectra (the normal 1-quantum spectrum has ~ 1000 lines and can hardly be analyzed) to theoretical models of the order parameters and biphenyl dihedral angle. Fig. 4 shows the relevant geometry and the 6- and 7- quantum regions of the multiple quantum spectrum with theoretical fits.

* * *

†Based in part on LBL-11344, Chem. Phys. Lett. 76, 263 (1980).

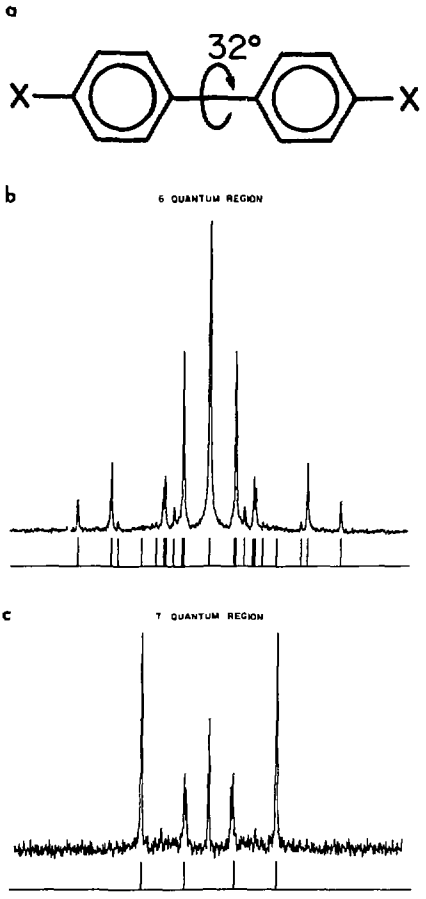

Fig. 4. (a) Biphenyl region of liquid crystal molecule showing dihedral angle with best fit value of 32° for a particular nematic phase. (b) and (c) 6- and 7-quantum regions of multiple quantum NMR spectrum with theoretical line positions.
[(a) XBL 811-7660; (b,c) XBL 808-10943]

5. CORRELATED MOTION OF METHYL GROUPS†

J. Tang, Y. S. Yen, L. Sterna and A. Pines

Two approaches have been taken to study the degree of correlated motion of two proximate methyl groups in a molecule e.g., Fig. 5.1: (a) shape and relaxation of single and multiple quantum NMR

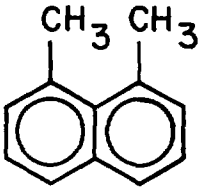

Fig. 5. Molecule with coupled methyl groups. The correlated motion of such groups is being studied by NMR lineshapes and exchange of rotational polarization. (XBL 811-7661)

spectra, and (b) behavior and exchange of rotational polarization. Lineshapes and rotational polarization angular dependences have been calculated for the cases of completely correlated and uncorrelated methyl group rotations and predict easy distinction between these cases. Several examples have been observed in which the correlation time for correlated motion is less than 1 msec. Studies are under way to observe the onset of longer correlation times at low temperatures and their dependence on molecular and crystal parameters.

* * *

†Based in part on LBL-11014, J. Chem. Phys. 73, 2512 (1980).

6. ALIPHATIC CHAIN CONFIGURATION IN ORIENTED MOLECULES†

D. P. Weitekamp, G. Drobny and A. Pines

We are continuing our study of aliphatic chain configuration by NMR of molecules oriented in lyotropic bilayers or thermotropic solvents. The quantities of interest are the chain order parameters and the probabilities of single bond conformations shown in Fig. 6. Previous work has

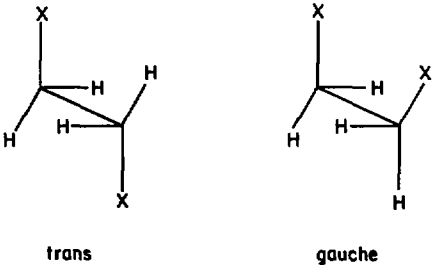

Fig. 6. Trans and gauche configuration of an aliphatic chain. Such chain configurations along an oriented chain are being studied.
(XBL 811-7662)

employed measurements of motionally averaged nuclear quadrupole interactions or resolved direct dipolar interactions in specifically deuterated molecules. From current work employing proton NMR, multiple quantum NMR, and relaxation studies, resolution of one part per thousand is possible, yielding an analysis of the chain configurations and gauche-trans-gauche kink probabilities.

* * *

†Based in part on LBL-11157, Proc. Roy. Soc. (in press).

7. RELAXATION OF MULTIPLE QUANTUM TRANSITIONS BY PARAMAGNETIC IMPURITIES†

J. Tang, Y. S. Yen, J. F. Wang and A. Pines

We have demonstrated one particular application of multiple quantum NMR in the study of the relaxation mechanism of the system of partially oriented acetonitrile molecules with paramagnetic impurities. This shows that the fluctuating magnetic field produced by the electron spin at each methyl proton site is completely correlated due to the fast reorientation of the methyl group and the low concentration of the impurity. Another important example is a molecule with two mobile groups, e.g., methyl groups as in Fig. 7. Because of the fast reorientation of the methyl group, each proton in the same methyl group will experience the same fluctuating field produced by the electron. However, the fluctuations at each site of the two methyl groups may not be completely correlated. The molecule 2,3 dimethylmaleic anhydride, dissolved with various concentrations of paramagnetic impurity DTBN, has been studied. The spectral density of the fluctuations, the degree of correlation, and the correlation times can be determined by the measurement of the linewidths of the 4-, 5-, and 6-quantum spectra of the molecule.

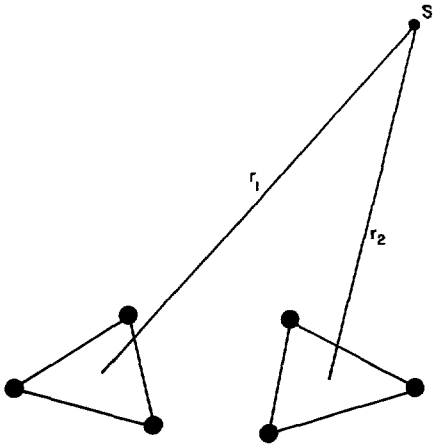

Fig. 7. Geometry of molecule with two methyl groups interacting with the electrons of a dissolved paramagnetic impurity. The electron spin S produces fluctuating magnetic fields at each methyl site. (XBL 811-7663)

* * *

†Based in part on LBL-9853, J. Chem. Phys. 72, 3290 (1980).

8. HIGH RESOLUTION NMR IN INHOMOGENEOUS FIELDS†

J. R. Garbow, D. P. Weitekamp and A. Pines

The most common limitation to high resolution in NMR is the inhomogeneity of the external field, which is caused by the requirement of finite sample size and available magnet technology. It has been considered impossible to remove this inhomogneity by spin echoes without affecting the chemical shifts (resonance frequency differences) in the spectrum. To appreciate this, consider that the nuclear spin cannot "tell" the difference between a change in resonance frequency caused by a chemical shift and that caused by a slighly different magnetic field in the same profile. We have overcome this problem for the first time by capitalizing on one parameter, common to all the spins in the sample over the whole inhomogeneous field profile, which is independent of chemical shifts and spin-spin couplings: the total spin coherence. By transferring coherence from this transition to the normal allowed transitions in an echo experiment, a spectrum can be obtained which is totally devoid of inhomogeneous broadening. An example is depicted from our preliminary work in Fig. 8. Since echo refocusing is sensitive to molecular translational diffusion, this approach makes it possible to measure with great sensitivity the anisotropic diffusion of molecules in oriented and viscous phases for the first time.

* * *

†Based in part on LBL-12085, submitted to J. Am. Chem. Soc.

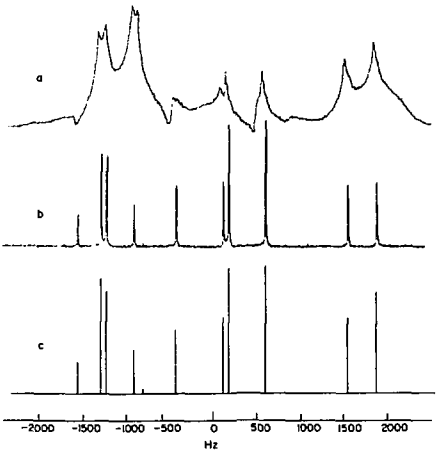

Fig. 8. Removal of inhomogeneous broadening by total spin coherence transfer echo spectroscopy: (a) the single quantum Fourier transform proton spectrum of acetaldehyde in a nematic liquid crystal was taken in an inhomogeneous field and then (b) with a coherence transfer pulse sequence yielding lines with widths limited only by homogeneous broadening. The simulation of this AB_3 system is shown in (c) demonstrating that there are no distortions in line positions. The lines of E symmetry are absent because they do not correlate with the total spin transition. (XBL 811-7538)

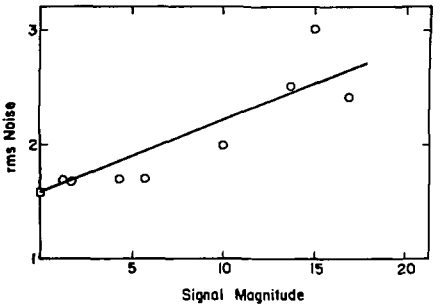

Fig. 9. Dependence of t_1 noise in a two-dimensional experiment on signal amplitude showing positive correlation. (XBL 811-7664)

9. NOISE IN TWO-DIMENSIONAL SPECTROSCOPY

D. P. Weitekamp and A. Pines

In two-dimensional NMR spectroscopy, a recently developed technique of enormous value, the observable magnetic dipole radiation is recorded in a period t_2 as a function of variable evolution times t_1. Fourier transformation of the resulting signal $g(t_1,t_2)$ yields a two-dimensional spectrum $g(\omega_1, \omega_2)$.[1] It has long been observed that such experiments are subject to noise contributions which play no role in the traditional one-dimensional experiments. Its existence has been attributed arbitrarily to instrumental instability, but no theory of its statistical nature or methods for its elimination or minimization have been previously proposed. Experience in our laboratory shows this "t_1 noise" to be the dominant contribution limiting the sensitivity and applicability of two-dimensional experiments. We have developed a simple model of t_1 noise as resulting from random fluctuations in the transfer function characteristic of the measurement process. The model predicts a positive dependence of the observed noise on signal amplitude which has been confirmed in several ways, an example of which appears in Fig. 9. The model and experiments demonstrate that t_1 noise is multiplicative, in contrast to usual thermal mechanisms which produce additive noise. This understanding provided us an approach to minimization of t_1 noise and enhancement of two-dimensional sensitivity by the use of pulsed field gradients, coherence transfer echoes, and selective excitation sequences.

* * *

1. W. P. Aue, E. Bartholdi and R. R. Ernst, J. Chem. Phys. 64, 2229 (1976).

10. ANALYSIS OF DIPOLAR COUPLINGS BY SEPARATED LOCAL FIELDS

J. R. Garbow, D. P. Weitekamp and A. Pines

Consider a carbon-13 nuclear spin coupled to a number of protons, a rather common situation in organic molecules, depicted in Fig. 10. Contained in the dipolar couplings of the ^{13}C to the protons (the local fields) is the geometry of the internuclear vectors and their averaged motional behavior. However, this information is normally impossible to extract with high resolution in normal two-dimensional NMR since, as shown in Fig. 10a, each of the proton local fields can be up or down, giving too many lines for any but the smallest molecules. We have overcome this problem using heteronuclear multiple quantum NMR, which involves the simultaneous non-linear irradiation of both species. This permits separation of the proton local fields by total magnetic quantum number and produces resolved sets of spectra. An example in which all protons but one are ordered, yielding only a number of lines equal to twice the number of protons, is shown in Fig. 10b. This directly determined all the ^{13}C-^{1}H dipolar couplings for the first time and is being used to study molecular conformational motion.

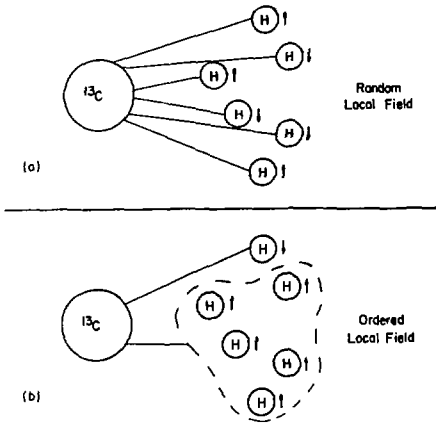

Fig. 10. The ^{13}C-^{1}H dipolar couplings contain information about the internuclear vectors and their motional averages. However, the spectrum is normally too complex due to the many proton configurations in 10a. In 10b, the separation of proton local fields by heteronuclear multiple quantum NMR permits direct determination of ^{13}C-^{1}H couplings. (XBL 8012-12934)

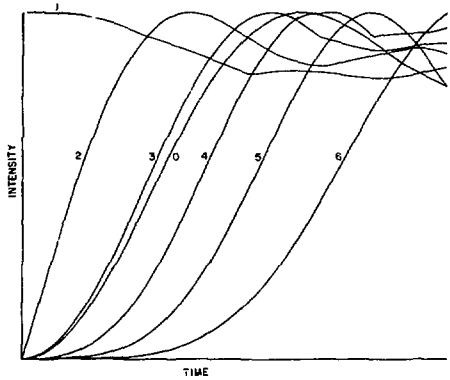

Fig. 11. Computer simulation of average n-quantum coherences (n = 0, 1, ...6) as a function of pumping time for benzene dissolved in a liquid crystal. The high order coherences show the expected non-linear onset of coherence. (XBL 806-9838)

11. COMPUTER SIMULATIONS OF MULTIPLE QUANTUM NMR†

J. B. Murdoch, W. A. Warren and A. Pines

A multiple quantum FT-NMR experiment consists of three stages: the multiple quantum coherences of interest must first be prepared, then allowed to evolve at their characteristic frequencies, and finally must be converted back to single quantum coherences in order to be detected. The intensity of the resulting spectral lines depends greatly on the actual rf pulses and delays used during preparation and detection. Because an N-coupled-spin-1/2 systems has 2^N states, a computer is necessary in all but the simplest cases to solve for the exact time evolution of the system, using the matrix equation (Fig. 11)

$$\rho(t) = e^{-i\mathcal{H}t}\rho(o)e^{i\mathcal{H}t}.$$

Computer programs developed in the past year for the analysis of non-selective multiple quantum pulse sequences have allowed us to (a) accurately simulate the intensity patterns of experimental spectra; (b) predict the build-up of the average n-quantum coherence magnitude as a function of preparation time; (c) quickly calculate the intensity of multiple quantum transitions averaged over all values of the preparation time; (d) relate the relative magnitudes of these "ultimate" averages to similarities in the dipolar couplings between spins; and (e) determine that an optimal overall signal is obtained when the preparation and detection times are equal. An important application is the study of kinetics in chemically exchanging systems, e.g., bond pseudo-rotation in cyclooctatetraene.

* * *

†Based in part on LBL-11885, W. S. Warren, Ph.D. Thesis (1980).

12. MOLECULAR MOTION IN HEXAMETHYLBENZENE†

J. Tang, L. Sterna and A. Pines

Molecules in solids may exhibit various kinds of symmetric motion. Hexamethylbenzene (HMB) is a good example. The methyl groups of the molecule reorient about their C_3-symmetry axes rapidly while the whole molecule may reorient about its C_6-axis at a slower rate. Spin-lattice relaxation and lineshape measurements provide a great deal of information about the nature and rates of these restricted motions. In deuterated hexamethylbenzene (HMB - d_{18}), the relaxation and lineshape are dominated by the deuterium quadrupole coupling. We have observed the anisotropic relaxation of HMB-D_{18} in the range -36 to +70°C and shown that it is consistent with a model of C_6 molecular motion modulating a deuterium quadrupole coupling of 39.1 kHz. The C_3 motion of the methyl groups is too fast to contribute. Lineshape measurements over the range -167 to +11°C show the onset of the C_6 motion by a reduction of one-half in the measureable quadrupole coupling. The data of Fig. 12 show that the

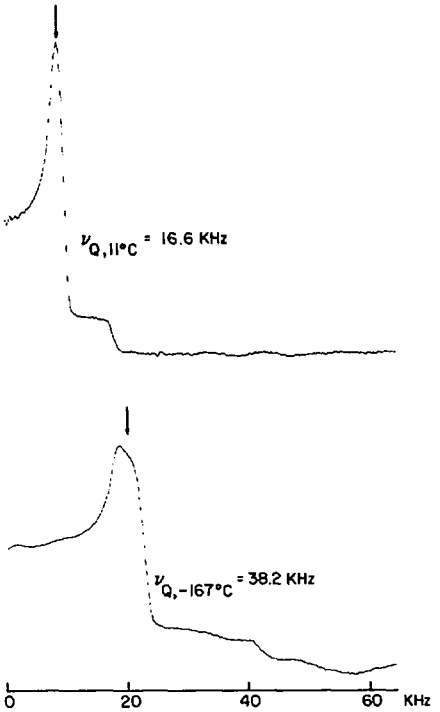

Fig. 12. Quadrupole powder pattern for hexamethylbenzene-d_{18}. The quadrupole coupling ν_Q equals twice the frequence of the large peak. In going from -167 to 11°C, ν_Q is expected to decrease by one-half due to the onset of C_6-molecular motion. The measured reduction indicates the presence of another motion in addition to C_6. (XBL 8011-12737)

reduction is ~15% greater than expected, thereby indicating the onset of an additional type of motion besides in-plane reorientation. This third type of motion is being studied and additional experiments are under way to elucidate its exact nature.

* * *

†Based in part on LBL-10734, J. Mag. Res. 41, 389 (1980).

13. SPIN DIFFUSION IN DEUTERON SPIN LATTICE RELAXATION

D. P. Weitekamp and A. Pines

In recent years, a number of spin labeling techniques have been developed which use deuterium nuclear magnetic resonance as a local probe[1] of molecular ordering, electronic structure, and molecular motion in solids and liquid crystals. The role of spin diffusion is obviously significant; and, in our recent studies, we have concluded that the static dipolar coupling can act as an efficient mechanism for magnetization transfer or spin diffusion between transitions which, in the lowest order theory, appear to be uncoupled (Fig. 13). This effect is of particular importance in solids, both because of the larger dipolar couplings relative to liquid crystals and because of the small fluctuations in electric field gradient at rigid deuterons, which leave spin diffusion as the only significant mechanism for their relaxation. An operator formalism has been derived which demonstrates that the magnetizations of two dipolar coupled deuterons are not independent relaxation modes even when a large difference in their time averaged electric field gradients separates their single quantum resonances. Thus, the relaxation of these resolved lines is not indicative of the single particle rate

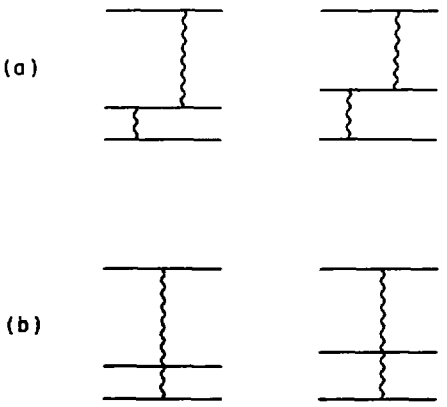

Fig. 13. (a) The coupling of inequivalent deuterons (spin-1 3-level systems) appears to make spin diffusion impossible due to energy mismatch in the allowed $\Delta m = 1$ transitions. (b) Spin diffusion can occur slowly by "forbidden" $\Delta m = 2$ energy mismatch. A theory of spin energy diffusion by this mechanism has been developed. (XBL 811-7665)

even though the dominant mechanism is the single particle electric field gradient fluctuations. An advantage of the operator formalism is its general applicability to many spin systems, such as occur in solids; it also allows the incorporation of sample spinning, which is used to obtain high resolution chemical shift spectra and is expected to effect the spin diffusion dynamics.

* * *

1. S. Hsi, H. Zimmerman and Z. Luz, J. Chem. Phys. 69, 4126 (1978).

RESEARCH PLANS FOR CALENDAR YEAR 1981

1. Extension of selective n-quantum NMR excitation to systems where time reversal interactions are not possible. This will be approached by high order phase cycling.

2. Study of conformation of liquid crystal molecules and hydrocarbon chain configuration and determination of correlated motion by multiple quantum relaxation.

3. Measurement of methyl group coupling in crystals by time dependence and exchange of rotational polarization.

4. Orientational order and diffusion of molecules in bilayers. This will be used to study how molecular orientation changes at a liquid-liquid interface. Diffusion studies with field gradients are needed to some of our magnetic isotope work.

5. New work attempting NMR decoupling of strongly scalar coupled spins. We believe this can now be done using selective double quantum pulses to break the rotational symmetry of the scalar coupling which should permit analysis of large molecules with normally intractable spectra.

6. Two-dimensional spectroscopy to be implemented with a new computer hook-up to allow phased projections of spectral lines.

7. Continuation of the study of the magnetic isotope effect. Investigations of the effect of dimensionality by extending photochemistry to bilayers and studying conditions for optimal enhancement of the isotope selectivity.

1980 PUBLICATIONS AND REPORTS

Refereed Journals

1. J. Tang and A. Pines, "Multiple Quantum NMR and Relaxation of an Oriented CH_3 Group," J. Chem. Phys. 72, 3290 (1980), LBL-9853.

2. J. Tang, A. Pines and S. Emid, "Spin-Lattice Relaxation of Reorienting or Tunneling Deuterated Methyl Groups," J. Chem. Phys. 73, 172 (1980) LBL-10162.

3. W. S. Warren, D. P. Weitekamp and A. Pines, "Theory of Selective Excitation of Multiple-Quantum Transitions," J. Chem. Phys. 73, 2084 (1980), LBL-10817.

4. S. Vega, T. W. Shattuck and A. Pines, "Double-Quantum Cross-Polarization NMR in Solids," Phys. Rev. A 22, 638 (1980), LBL-10338.

5. L. Sterna, D. Ronis, S. Wolfe and A. Pines, "Viscosity and Temperature Dependence of the Magnetic Isotope Effect," J. Chem. Phys. 73, 5493 (1980).

6. J. Tang and A. Pines, "Multiple Quantum NMR Study of Correlation of Two Methyl Groups," J. Chem. Phys. 73, 2512 (1980) LBL-11014.

7. S. Emid, J. Smidt and A. Pines, "Selective Double-Quantum NMR in Solids," Chem. Phys. Lett. 73, 496 (1980) LBL-11016.

8. L. Müller, R. Eckman and A. Pines, "Proton-Enhanced Deuterium NMR in Rotating Solids," Chem. Phys. Lett. 76, 149 (1980) LBL-11156.

9. S. Emid, J. Konijnendijk, J. Smidt and A. Pines, "On the Short Time Behavior of the Dipolar Signal," Physica 100B, 215 (1980) LBL-9261.

10. W. S. Warren, D. P. Weitekamp and A. Pines, "High Order Selective Sequences in Multiple Quantum Spectroscopy," J. Mag. Res. 40, 581 (1980) LBL-10161.

11. S. Sinton and A. Pines, "Study of Liquid Crystal Conformation by Multiple Quantum NMR: n-Pentyl Cyanobiphenyl," Chem. Phys. Lett. 76, 263 (1980) LBL-11344.

Reports

1. D. Wemmer, R. J. Ruben and A. Pines, "NMR Study of Details of Molecular Reorientation in Solid Permethylferrocene," LBL-10563. In press: J. Am. Chem. Soc.

2. D. E. Wemmer and A. Pines, "Carbon-13 Chemical Shifts in Solid Metal Sandwich Compounds," LBL-10864. In press: J. Am. Chem. Soc.

3. G. Drobny, A. Pines, S. Sinton, W. S. Warren and D. P. Weitekamp, "Selectivity in Multiple-Quantum Spectroscopy," LBL-11157. In press: Proc. Roy. Soc.

4. A. Pines, "Principles of Nuclear Magnetic Double Resonance in Solids," LBL-12168. In press: Proc. Roy. Soc.

5. W. S. Warren and A. Pines, "Analogy of Multiple-Quantum NMR to Isotopic Spin Labeling," LBL-11345. In press: J. Am. Chem. Soc.

6. W. S. Warren and A. Pines, "Experiments on Selective Excitation of Multiple Quantum Transitions in NMR Spectroscopy," LBL-11916. In press: J. Chem. Phys.

7. W. S. Warren, "Selectivity in Multiple Quantum Nuclear Magnetic Resonance," Ph.D. Thesis, November 1980, LBL-11885.

8. D. P. Weitekamp, J. R. Garbow, J. B. Murdoch and A. Pines, "High Resolution NMR in Inhomogeneous Magnetic Fields: Application of Total Spin Coherence Transfer Echoes," LBL-12085. Submitted to: J. Amer. Chem. Soc.

Invited Talks

1. A. Pines, Symposium on Chemistry and Physics of Coal, American Physics Society, New York, March 1980.

2. A. Pines, Chemistry Department, University of California, Riverside, California, April 1980, Seminar.

3. A. Pines, Royal Society Discussion Meeting on New Coal Chemistry, London, England, May 1980.

4. A. Pines, Royal Society Discussion Meeting on NMR in Solids, London, England, June 1980.

5. A. Pines, Shell Research Laboratories, Amsterdam, The Netherlands, June 1980.

6. A. Pines, Physics Department, University of Delft, The Netherlands, Seminar.

7. A. Pines, "Selectivity in Multiple Quantum Spectroscopy," Rocky Mountain Conference on Analytical Chemistry of Spectroscopy, Denver, Colorado, August 1980, Plenary Lecture.

8. A. Pines, "Selective Absorption of Groups of Photons in Spectroscopy," 12th International Meeting on Spectroscopy, Sydney, Australia, August 1980, Plenary Lecture.

9. A. Pines, Chemistry Department, University of Sydney, Sydney, Australia, August 1980, Seminar.

10. A. Pines, Advanced NATO Workshop on High Resolution NMR in Solids, Sardinia, Italy, September 1980.

11. A. Pines, "New Vistas in Chemical Instrumentation," Dedication of New Facility, California Institute of Technology, October 1980.

12. A. Pines, Chemistry Department, University of Brisbane, Brisbane, Australia, August 1980, Seminar.

13. A. Pines, University of Pennsylvania, Physics Department, Philadelphia, March 1980, Seminar.

14. A. Pines, Purdue University, Lafayette, Indiana, March 1980, Seminar.

15. A. Pines, Department of Chemistry, UCLA, Los Angeles, February 1980, Seminar.

16. A. Pines, Physics Department, University of California, Berkeley, February 1980, Seminar.

II Chemical Sciences

A. Fundamental Interactions

1. Photochemical and Radiation Sciences

a. Photon-Assisted Surface Reactions, Materials and Mechanisms*

Gabor A. Somorjai, Investigator

1. THE PHOTOCATALYZED DISSOCIATION OF H_2O AT HIGH TEMPERATURES AND PRESSURES OVER $SrTiO_3$ CRYSTAL SURFACES

R. G. Carr and G. A. Somorjai

Photodissociation of high pressure (1-8 atm) water vapor adsorbed onto the partially platinized surface of single crystal $SrTiO_3$ has been observed. The reaction is catalytic; several thousands of monolayers of hydrogen have been produced. The reaction requires light of greater than bandgap (3.1 eV) energy and proceeds vigorously only if elevated temperatures (375-450 K) and high pressures are used. Recombination of products and poisoning of the metal appears to diminish the reaction rate after several hours. This reaction differs from the photolysis of water in the analogous short-circuit electrochemical cell because we use no electrolyte and are able to use non-conducting, stoichiometric $SrTiO_3$ because bulk electrical conductivity has little influence on localized surface reactions.

2. PHOTOELECTRON SPECTROSCOPY STUDIES OF THE MECHANISM OF PHOTON-ASSISTED DISSOCIATION OF WATER OVER $SrTiO_3$ SURFACES

S. Ferrer, F. T. Wagner, and G. A. Somorjai

About one monolayer of Ti^{3+} species is detectable at the surface of reduced $SrTiO_3(111)$ single crystals by XPS and UPS. In dark adsorption experiments, H_2 and O_2 cause a decrease in initial Ti^{3+} concentration, while H_2O does not. The Ti^{3+} photogeneration on the oxygen covered surface is associated with oxygen photodesorption as indicated by XPS and UPS. UPS measurements give evidence for surface hydroxylation resulting from water and hydrogen adsorption. The activity of the stoichiometric $SrTiO_3(111)$ crystal face for O_2 and H_2 adsorption is very low when compared with the reduced $SrTiO_3$ samples.

3. ISOTOPE EXCHANGE STUDIES OF THE OXIDATION AND REDUCTION OF $SrTiO_3$ SINGLE CRYSTAL SURFACES BY WATER AND HYDROGEN

S. Ferrer and G. A. Somorjai

Thermal desorption studies of chemisorbed D_2 and D_2O on a reduced $SrTiO_3(111)$ surface reveal that D_2 causes the reduction of the crystal whereas D_2O causes its oxidation. Thermal desorption of $H_2^{18}O$ indicates that there is a 15% exchange between the oxygen in the adsorbed water molecules and the lattice oxygen. After chemisorptions of D_2 or D_2O on the clean and reduced $SrTiO_3(111)$ surface, the thermally desorbed molecules that could be detected were D_2 and D_2O. The relatively high temperature of the peak maximum is indicative of the presence of hydroxyl species on the surface that forms during D_2O adsorption in agreement with previous reports on $SrTiO_3$ and TiO_2. The presence of desorbed D_2O after a D_2 exposure indicates that oxygen is removed from the crystal. We can represent this reaction as $D_2(ads) + O_{crystal} = D_2O(g)$. Similar analysis for the D_2O adsorption experiment reveals the presence of a reaction $D_2O(ads) = (1-x)D_2O(g) + xD_2(g) + O_{crystal}$, where (1-x) indicates the fraction of D_2O that does not react and x is the fraction that reacts giving D_2 in the gas phase and leads to oxygen incorporation in the crystal lattice. The reaction leading to an oxidation of the crystal by adsorbed D_2O is about five times more probable than the reduction of the crystal by adsorbed deuterium. After pure $H_2^{18}O$ adsorption, the thermally desorbed water in the gas phase will consist of $H_2^{18}O$ and $H_2^{16}O$. This indicates that after water adsorption on the clean and reduced $SrTiO_3(111)$ surface, 15% of the water molecules that desorb during the thermal desorption experiment originate from the interaction of lattice oxygen with hydrogen.

4. UPS STUDY OF THE ADSORPTION OF OXYGEN ON REDUCED $SrTiO_3$ SURFACES

S. Ferrer and G. A. Somorjai

The adsorption of oxygen on a reduced $SrTiO_3(111)$ surface occurs in two distinct phases. At low exposures (less than 1 langmuir[1] (L)), the adsorption leads to the incorporation of O^{2-} ions into vacant lattice oxygen sites. At higher exposures a second different oxygen species adsorbs. At low exposures (less than 1 L), there is a very rapid oxygen uptake that results in oxidation of Ti^{3+} to Ti^{4+} and an increasing work function. At higher exposures, there are smaller rates of Ti^{3+} oxidation and work function increase, indicating a smaller sticking coefficient for oxygen. The intensity of the oxygen-induced 10 eV emission is very small at low oxygen exposures, but it increases continuously during exposures greater than 1 L. This different behavior between the O2p and 10 eV emissions indicates that the increase in the intensity of the O2p and 10 eV emission corresponds to two different oxygen species. The similarity in the line shapes of the O2p emissions from the clean surface and that from adsorbed oxygen obtained

*This work was supported by the Director, Office of Energy Research, Office of Basic Energy Sciences, Chemical Sciences Division of the U.S. Department of Energy under Contract No. W-7405-ENG-48.

after 1 L exposure strongly suggest that the species responsible for the increase in the O2p intensity are adsorbed O^{2-} ions. The oxygen species responsible for the 10 eV emission is also capable of charge transfer, but of smaller magnitude, as indicated by the slower oxidation rate of Ti^{3+} at higher oxygen exposures. Therefore, this species is also negatively charged. ESR studies indicate that superoxide ions are common adsorbed oxygen species for many oxides, including TiO_2. As a consequence, O_2^- is a good candidate to account for the UPS emission at 10 eV.

* * *

1. 1 langmuir ≡ 10^{-6} torr/sec.

RESEARCH PLANS FOR CALENDAR YEAR 1981

The electronic structure and composition of $SrTiO_3$ surfaces that underwent photochemical reaction at high pressures will be studied by XPS and UPS with a high pressure-low pressure apparatus that was built for this purpose. The photochemical activity of iron silicates for water dissociation will be explored.

1980 PUBLICATIONS AND REPORTS

Refereed Journals

1. J. C. Hemminger, R. Carr, J. W. Lo, and G. A. Somorjai, "Photochemical Processes at the Solid-Gas Interface: The Adsorption and Reactions of Gaseous CO_2 and H_2O on Pt-$SrTiO_3$ Single Crystal Sandwiches," Adv. in Chem. Series 184, 233 (1980).

2. S. Ferrer and G. A. Somorjai, "UPS and XPS Studies of the Chemisorption of O_2, H_2, and H_2O on Reduced and Stoichiometric $SrTiO_2$(111) Surfaces," Surface Sci. 94, 41 (1980).

3. F. T. Wagner and G. A. Somorjai, "The Photocatalyzed Production of Hydrogen from Water on Pt-Free $SrTiO_3$ Single Crystals in the Presence of Alkali Hydroxides," Nature 285, 559 (1980).

4. S. Ferrer and G. A. Somorjai, "Isotope Exchange Studies of the Oxidation and Reaction of $SrTiO_3$ Single Crystal Surfaces by Water and Hydrogen," Surface Sci. 97, L304 (1980).

5. F. T. Wagner and G. A. Somorjai, "Photocatalytic and Photoelectrochemical Hydrogen Production on Strontium Titanate Single Crystals," J.A.C.S. 102, 5494 (1980).

LBL Reports

1. F. T. Wagner, S. Ferrer, and G. A. Somorjai, "Photocatalytic Hydrogen Production from Water over $SrTiO_3$ Crystal Surfaces, Electron Spectroscopy Studies of Adsorbed H_2, O_2, and H_2O," LBL-9942.

2. F. T. Wagner and G. A. Somorjai, "Photocatalytic and Photoelectrochemical Hydrogen Production on Strontium Titanate Single Crystals," LBL-10020.

3. F. T. Wagner, S. Ferrer, and G. A. Somorjai, "Surface Aspects of Hydrogen Photogeneration on Titanium Oxides," LBL-11456.

4. S. Ferrer and G. A. Somorjai, "UPS Study of the Adsorption of Oxygen on Reduced $SrTiO_3$ Surfaces," LBL-11614.

5. S. Ferrer and G. A. Somorjai, "Evidence for Photodissociation of Water Vapor on Reduced $SrTiO_3$(111) Surfaces in a High Vacuum Environment. Relationship between the Rate of Hydrogen Evolution and the Surface Concentration of Ti^{3+} Species," LBL-11661.

6. R. Carr and G. A. Somorjai, "Hydrogen Production from Photolysis of Steam Adsorbed onto Platinized $SrTiO_2$," LBL-11872.

Invited Talks

1. G. A. Somorjai, "Photocatalytic Dissociation of Water," Solar Energy Research Institute, Golden, Colorado, January 31, 1980.

2. G. A. Somorjai, "The Photochemical Dissociation of Water Vapor over $SrTiO_3$ and TiO_2 Crystal Surfaces," 109th AIME Annual Meeting, Las Vegas, NV.

3. F. T. Wagner and G. A. Somorjai, "Photocatalytic Dissociation of Water over $SrTiO_3$ Crystal Faces," North American Catalysis Society, Berkeley, CA, March 13, 1980.

4. G. A. Somorjai, "Photocatalyzed Dissociation of Water over Oxide Surfaces," ETH Laboratorium fur Festkorperphysik, Zurich, Switzerland, May 7, 1980.

5. G. A. Somorjai, "Photocatalyzed Dissociation of Water over Oxide Surfaces," Technische Hochschule, Aachen, Germany, May 29, 1980.

6. G. A. Somorjai, "Photocatalytic and Photoelectrochemical Hydrogen Production on $SrTiO_3$," University of Notre Dame, South Bend, IN, June 3, 1980.

7. G. A. Somorjai, "Photocatalytic Dissociation of Water," University of Innsbruck, Innsbruck, Austria, June 12, 1980.

8. G. A. Somorjai, "Kinetics and Mechanism of H_2O Dissociation over $SrTiO_3$ Surfaces," Fritz-Haber-Institut, Berlin, Germany, June 27, 1980.

9. G. A. Somorjai, "Kinetics and Mechanism of Photocatalyzed Dissociation of Water on Oxide Surfaces," Universite Louis Pasteur, Strasbourg, France, July 2, 1980.

b. Photochemistry of Materials in the Stratosphere*

H. S. Johnston, Investigator

1. KINETICS OF THE REACTION OF HO AND $HOONO_2$

David Littlejohn and Harold S. Johnston

Numerical models of photochemistry and atmospheric dynamics are used to predict the future effect of increased chlorine (chlorofluorocarbons, other organic chlorides) and increased nitrogen oxides (stratospheric aircraft, nitrous oxide from fertilizer, etc.) on stratospheric ozone. The predicted effects are strongly dependent on the chemical species included in the model and on the values of rate coefficients used in the model. In recent years, it has been noted that situations that favor high concentrations of hydroxyl radicals, HO, lead to predictions of large ozone decreases from chlorine and small ozone decreases or even to small ozone increases from added nitrogen oxides. Also, it has been noticed that the models used since about 1977 appear to over-estimate the amount of hydroxyl radicals in the lower half of the stratosphere, that is, below 30 km altitude. When these two statements are considered together, the implication is that the models since 1977 probably overpredict the effect of chlorine on ozone and underpredict the effect of nitrogen oxides on ozone. In this laboratory, reactions that might affect hydroxyl radicals in the lower stratosphere have been investigated or reinvestigated.

Until recently peroxynitric acid has been largely neglected in models of the stratosphere. The atmospheric importance of the reaction of hydroxyl radicals with peroxynitric acid is the following cycle,

$$\begin{array}{lll} & HOO + NO_2 \xrightarrow{M} HOONO_2 & \\ & HO + HOONO_2 \longrightarrow H_2O + O_2 + NO_2 & (1) \\ \hline \text{net:} & HO + HOO \longrightarrow H_2O + O_2 & \end{array}$$

which gives catalytic destruction of HO_x free radicals by the oxides of nitrogen. Because of the role of total gas pressure, M, the effect is altitude dependent. If the rate constant exceeds 10^{-12} cm^3 s^{-1}, then this catalytic process becomes one of the major paths for destruction of odd hydrogen (H, HO, HOO) at altitudes below 30 km, but it is unimportant at altitudes well above 30 km. To date, no definite values have been obtained for the rate constant for the reaction of hydroxyl radicals with peroxynitric acid. The objective of this study was to obtain a value.

It is difficult to prepare, purify, and use peroxynitric acid. A special method of preparation was developed as a part of this study. Peroxynitric acid used in these experiments was generated by reacting N_2O_5 with H_2O_2 in a flowing stream of nitrogen and with catalysis by a short section of stainless steel turbing. The major impurity was HNO_3 with some NO_2, H_2O_2, and N_2O_5 also present. These gases were flowed into the apparatus shown in Fig. 1. The apparatus consists of a 63 liter cylindrical quartz cell in a temperature-controlled enclosure. Infrared analyses were made for gases (N_2O_5, H_2O_2, NO_2, $HOONO_2$, $HONO_2$) in the cell. The reactants reached a steady state with respect to flow and slow (4 minutes on, 4 minutes off) periodic photolysis of NO_2.

In these experiments hydroxyl radicals were generated in an indirect manner by way of photolysis of nitrogen dioxide in the presence of peroxynitric acid. These hydroxyl radicals reacted competitively with nitrogen dioxide and peroxynitric acid

$$HO + NO_2 \xrightarrow{M} HNO_3$$

$$HO + HOONO_2 \longrightarrow H_2O + O_2 + NO_2$$

If the reaction proceeds by way of the first reaction, nitrogen dioxide remains constant when the other reactions are considered. If the reaction proceeds by way of the second reaction, nitrogen dioxide increases even though it is being destroyed by direct photolysis.

Typical concentration profiles in light and in dark for $HOONO_2$, NO_2, H_2O_2, and N_2O_5 are shown by Fig. 2. It can be seen that the concentration of nitrogen dioxide increases when the light that destroys it is turned on, which indicates that the rate of the unknown reaction of HO with $HOONO_2$ is faster than the rate of the known reaction of HO with NO_2. From the magnitude of these concentrations and rate constants, one can say on simple grounds that k (HO + $HOONO_2$) is greater than 1×10^{-12} cm^3 s^{-1} under conditions of these experiments. Graham et al.[2] found the rate constant to be less than 3×10^{-12} s^{-1}, and thus the rate constant is bracketed by these two simple observations.

In an effort to get a closer estimate of the rate constant, the observed rates were compared with computer simulations for the complex system as a whole. The mechanism included the species: $HOONO_2$, NO_2, N_2O_5, H_2O_2, $HONO_2$, H_2O, O_2, O, HOO, HO, NO_3, NO. There were 19 chemical reactions, and the calculation included flow in and flow out of all long-lived species. All rate constants and photolysis constants were obtained from the recent literature,[1] except for that for HO + $HOONO_2$. Values of k (HO + $HOONO_2$) were varied from 2×10^{-13} to 2×10^{-11} cm^3 s^{-1}. For the photolysis phase,

*This work was supported by the Director, Office of Energy Research, Office of Basic Energy Sciences, Chemical Sciences Division of the U. S. Department of Energy under Contract No. W-7405-ENG-48.

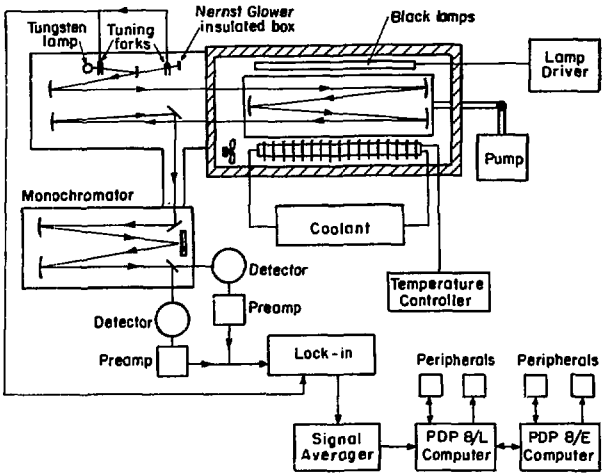

Fig. 1. Schematic diagram of apparatus used in the experiments. (XBL 806-5352)

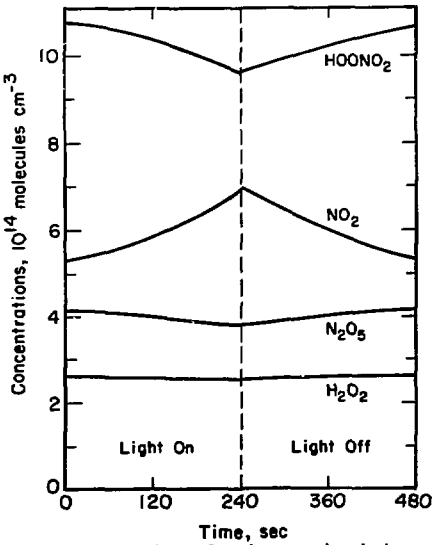

Fig. 2. Concentrations of various species during the long-term steady-state experiments while photolysis lamps are on and off. These curves are the average of numerous superimposed cycles. (XBL 813-8363)

the slopes of $HOONO_2$ obtained from the simulations were plotted as a function of rate constants, for example, Fig. 3. For each experiment (compare Fig. 2), the slope of observed concentrations vs time during photolysis was fit by least squares to the data to give an observed rate and its standard

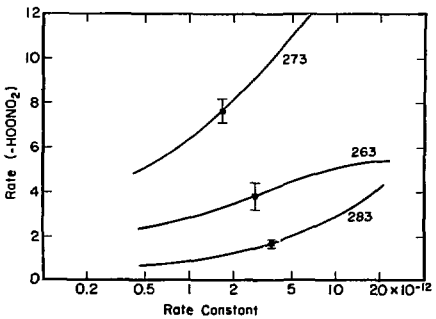

Fig. 3. The average reaction rate (molecules cm^{-3} s^{-1} × 10^{-11}) with respect to $HOONO_2$ while the photolysis lamps are on. The smooth curves are calculated for a range of assumed values for the rate constant, k ($HO + HOONO_2$), and the experimental data are given by point and error bar. These three runs are examples of data at 263, 273, and 283 K. (XBL 813-8362)

error. These experimentally derived slopes were plotted on the lines drawn through the calculated slopes, Fig. 3, and uncertainty in the observed slopes were translated into uncertainties in the rate constant. The average rate constant ($\pm 2\sigma$) based on $HOONO_2$ for all runs was $1.9 \pm 0.6 \times 10^{-12}$ $cm^3\ s^{-1}$. The average rate constant based on NO_2 was $5.0 \pm 0.6 \times 10^{-12}$ $cm^3\ s^{-1}$. From the combined data, we suggest for the rate constant k (HO + $HOONO_2$) a value of $2^{+2}_{-1}) \times 10^{-12}$ $cm^3\ s^{-1}$.

* * *

1. D. L. Baulch, R. A. Cox, R. F. Hampson, Jr., J. A. Kerr, J. Troe, and R. T. Watson, J. Phys. Chem. Ref. Data 9, 295 (1980).

2. R. A. Graham, A. M. Winer, and J. N. Pitts, Geophys. Res. Lett. 5, 909 (1978).

2. THE KINETICS AND PRODUCT YIELD OF THE REACTION OF HO WITH HNO_3

Herbert H. Nelson, William J. Marinelli and Harold S. Johnston

The rate constant for the reaction of hydroxyl radicals with nitric acid

$$HO + HNO_3 \rightarrow H_2O + NO_3 \qquad (1)$$

was recently remeasured by Wine et al.[1] and found in their study to be faster than previously accepted at room temperature and to have a negative temperature dependence. The unusually low A factor that was measured has led to speculation about a long-lived intermediate complex which may not decompose to NO_3 and H_2O. Because of the potential importance of these recent results to an understanding of atmospheric chemistry, we have studied this reaction in both the reactant and product channels. The techniques of flash photolysis/resonance fluorescence (FP/RF) and flash photolysis/laser absorption (PF/LA) were used to obtain kinetic information by following the time evolution of HO and NO_3 respectively.

The flash photolysis/resonance fluorescence studies were conducted in an apparatus of conventional design.[2] Hydroxyl radicals were produced by photodissociation of HNO_3 with the output of a Lumonics 860-01 excimer laser operating at 249 nm (KrF). Repetition rates were typically 30 Hz and the output energy was 10 - 20 mJ. Fluorescence from the hydroxyl radical was excited by the output of a microwave-driven resonance lamp operating on a 3% H_2O/Ar mixture at a total pressure of 1 torr. The fluorescence signal was monitored at right angles to the laser beam and resonance lamp with a PMT (RCA C31034) operated in photon counting mode. The time evolution of the fluorescence signal was obtained by recording the photon counting output with an instrument computer operating in the multichannel scaling mode. Typically, the decay following 4096 laser flashes was averaged to obtain a pseudo-first order rate constant.

The flash photolysis/laser absorption experiments were conducted in a single-pass, jacketed, 1.9 m absorption cell. Nitric acid, entrained in a slow flow ($\sim$ 280 standard $cm^3\ min^{-1}$) of N_2 passed through a saturator at 250 K, flowed through the cell at 10 torr total pressure, and was photolyzed by output of the excimer laser[3] operating at 249 nm. Approximately 0.04% of the HNO_3 in the beam was photolyzed per 10-20 mJ shot at repetition rates of 1-2 Hz. The energy of each photolysis pulse was measured using an energy meter located at the cell exit, and a suitable model of photolysis-laser-beam divergence was used to calculate an averaged fluence. The NO_3 produced from the reaction of HO with HNO_3 was monitored by observing the absorption of the CW output from a Spectra-Physics Model 375 dye laser propagated coaxially to the photolysis beam and operating on R6G dye at 623.5 nm. The dye laser output was monitored by a silicon photodiode and was interfaced to a multichannel scaler. A typical experiment was the sum of 256 shots.

All experiments in the flash photolysis/resonance fluorescence study were performed under pseudo-first-order conditions with [HNO_3] > 1000 [HO]. A typical semilogarithmic HO decay plot is shown in Fig. 4. The decay is linear over 2 to 3 1/e times.

The bimolecular rate constant was determined at 3 total pressures and for a 21 fold range of HNO_3 concentration. These data are shown plotted vs HNO_3 concentration in Fig. 5. The rate constants calculated are $8.0 \pm 0.3 \times 10^{-14}$, $9.2 \pm 0.56 \times 10^{-14}$, and $7.5 \pm 0.89 \times 10^{-14}$ cm^3 $molecule^{-1}\ s^{-1}$ at 10, 25, and 50 torr total pressure respectively. The uncertainties are twice the standard deviation and do not include systematic errors. The non-zero intercepts are a result of HO diffusion from the product-viewing zone and reaction with impurities in the Ar carrier gas. This method was calibrated by studying the similar system ($H_2O_2 + h\nu \rightarrow 2$ HO, HO + $H_2O_2 \rightarrow H_2O$ + HOO), and the second order rate constant was found to be $1.57 \pm 0.1 \times 10^{-12}$ cm^3 $molecule^{-1}\ s^{-1}$, which is in good agreement with recent determinations of this rate constant, 1.65×10^{-12}.

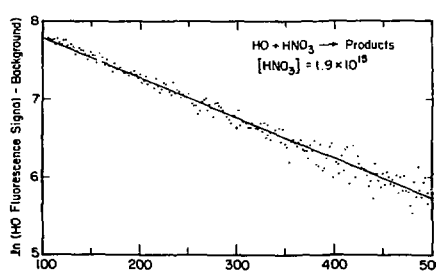

Fig. 4. A typical semilogarithmic HO decay plot from the flash photolysis/resonance fluorescence experiments with the line fit to the data by linear least-squares methods. (XBL 8010-12314)

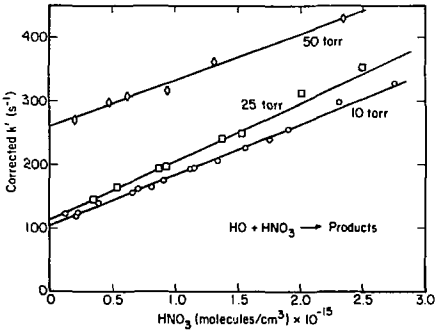

Fig. 5. Pseudo-first-order rate constant k' plotted against the concentration of nitric acid obtained in the flash photolysis/resonance fluorescence experiments at 10, 25, and 50 torr total pressure. A linear least-squares fit to each data set results in the lines shown. (XBL 8010-12316)

The data in the NO_3 absorption experiments were recorded in transmission mode (Fig. 6a) and converted to optical density [$D = \ln(I_0/I)$] by using the transmission during the pretrigger period as I_0 (Fig. 6b). The time evolution of the NO_3 optical density was analyzed by fitting it to the expression

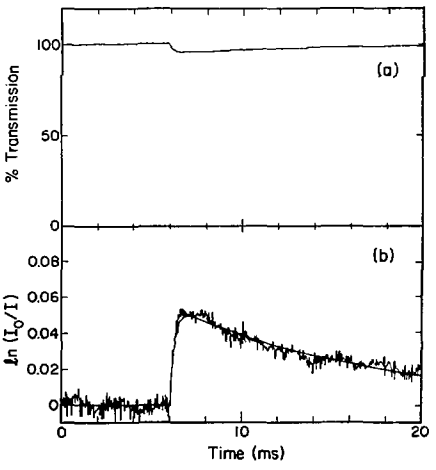

Fig. 6. (a) Data as recorded in transmission mode for NO_3 laser absorption. (b) Data converted to optical density ($\ln I_0/I$) and computer fit to expression (3). (XBL 8011-3990)

$$D(t) = D_A\left(e^{-k_r t} - e^{-k' t}\right) \qquad (2)$$

where k' is the pseudo-first-order rate constant for reaction (1), k_r is the first-order rate constant for removal of NO_3 (diffusion from the viewing area, reaction with trace amounts of NO_2, NO, or other species) and D_A would be the asymptotic optical density of NO_3 if the removal processes k_r had negligible rates. A non-linear, least squares, iteration method was used to fit D_A, k_r, and k' to the experimental data and that fit is included in Fig. 6b. For each experiment i the second-order rate constant k_1 for reaction (1) is related to the pseudo-first-order rate constant by $k_{1i} = k_i'/[HNO_3]_i$. The average of the second order rate constants ($\pm 2\sigma$) is $10.6 \pm 3.4 \times 10^{-14}$ cm^3 $molecule^{-1}$ s^{-1}.

The NO_3 product yield (ϕ) from reaction (1) relative to the number of photons absorbed by nitric acid depends on the value of the optical absorption cross section for the nitrate radical, NO_3, and this quantity is not well known. For 15 determinations the apparent average product yield ($\pm 2\sigma$) is 0.92 ± 0.12 (Ref. 5), or 1.34 ± 0.18 (Ref. 6), or 1.53 ± 0.21 (Ref. 7), depending on which value one uses for the optical absorption cross section. While the NO_3 product yield cannot be precisely determined from these results, it is clear that NO_3 was produced at a rate comparable to that of HO loss ($10.6 \pm 3.4 \times 10^{-14}$ relative to $8.2 \pm 1.8 \times 10^{-14}$) and with a product quantum yield comparable to one. Thus the major product channel of reaction (1) is confirmed to be formation of H_2O and NO_3.

The room temperature rate constants for the reaction of HO with HNO_3 determined in this work are $8.2 \pm 1.8 \times 10^{-14}$ cm^3 $molecule^{-1}$ s^{-1} (FP/RF) and $10.6 \pm 3.4 \times 10^{-14}$ cm^3 $molecule^{-1}$ s^{-1} (FP/LA). The rate constant measured in the FP/RF experiments disagrees with the results of Wine et al.[1] (12.5×10^{-14}). However the value of k_1 determined by Wine et al. does fall within the upper error limit of the FP/LA result. Measurement of the temperature dependence of this reaction is currently being carried out in this laboratory.

* * *

1. P. H. Wine, A. R. Ravishankara, N. M. Kreuter, R. C. Shah, J. M. Nicovich, and R. L. Thompson, In press: J. Geophys. Rev.
2. F. Magnotta and H. S. Johnston, Geophys. Rev. Lett. 7, 769 (1980).
3. The excimer laser was obtained as a loan from the San Francisco Laser Center, which is supported by the National Science Foundation under Grant No. CHE 78-16250 awarded to the University of California at Berkeley in collaboration with Stanford University.
4. L. F. Keyser, J. Phys. Chem. 84, 1659 (1980).
5. F. Magnotta, Ph.D. Thesis, University of California, Berkeley, 1979.
6. R. A. Graham and H. S. Johnston, J. Phys. Chem. 82, 254 (1978).
7. D. N. Mitchell, R. P. Wayne, P. J. Allen, R. P. Harrison, and R. J. Twin, J.C.S. Daraday II 76, 785 (1980).

3. REACTION RATES OF ATOMIC CHLORINE WITH ClNO AND $ClNO_2$

Herbert H. Nelson and Harold S. Johnston

The reactions studied here were 1) the photolysis of nitrosyl chloride

$$ClNO + h\nu\ (350\ nm) \rightarrow Cl + NO \qquad (1)$$

$$Cl + ClNO \rightarrow Cl_2 + NO$$

and 2) the photolysis of nitryl chloride

$$ClNO_2 + h\nu\ (350\ nm) \rightarrow Cl + NO_2 \qquad (2)$$

$$Cl + ClNO_2 \rightarrow Cl_2 + NO_2$$

ClNO of 97% minimum purity was obtained from Matheson Company and purified by vacuum distillation. $ClNO_2$ was prepared using the method of Volpe and Johnston.[1]

Photolyses at 350 nm were by a Lumonics 860-01 excimer laser, 10 to 20 mJ per flash, and typically 30 flashes per second. The atomic chlorine produced by the laser pulse was followed as a function of time by resonance fluorescence at 138.0 and 139.0 nm, which was excited by a microwave driven resonance lamp operating on 0.1% Cl_2 in He at 1 torr. The chlorine atom fluorescence was observed at right angles to both photolysis and excitation beams and was monitored by a Nicolet 1074 instrument-computer operating in the multichannel scaling model. In each experiment 4096 laser flashes were averaged to obtain a pseudo-first-order rate constant.

In the experiments with nitryl chloride, the carrier gas was Ar or N_2, the total pressure was 10 torr or 25 torr, and the range of $ClNO_2$ concentrations was 0.5 to 8 $\times 10^{14}$ molecules cm^{-3}, as determined by UV absorption in a one-meter cell and 210 nm radiation. The results of a typical experiment are shown in Fig. 7, where the natural logarithm of fluorescence intensity (corrected for background) is plotted against time with a 20 μs channel width. The first five channels show strong fluorescence of the reaction cell, and the signal becomes weak at long times. Pseudo-first-order rate constants were obtained as the slope of the points between the two arrows. The second-order rate constant, k ($Cl + ClNO_2$), was found by plotting the pseudo-first-order rate constants against the concentration of $ClNO_2$ (Fig. 8). The value ($\pm 2\sigma$) is $5.50 \pm 0.24 \times 10^{-12}$ cm^3 $molecule^{-1}$ s^{-1}. No other investigation of this rate constant appears to have been published.

In the experiments with nitrosyl chloride, the carrier gas was N_2 at 10 torr or at 30 torr. Pseudo-first-order rate constants k' were found by a semi-logarithmic plot of corrected fluorescence signal against time, and the second-order rate constant was found by plotting k' against the concentration of ClNO (Fig. 9). The rate constant ($\pm 2\sigma$) calculated from all the data is $1.65 \pm 0.12 \times 10^{-11}$ cm^3 $molecule^{-1}$ s^{-1}. This value does not agree with either of two recent, direct determinations of this rate constant: 3.0×10^{-11} (Ref. 2), 0.54×10^{-11} (Ref. 3).

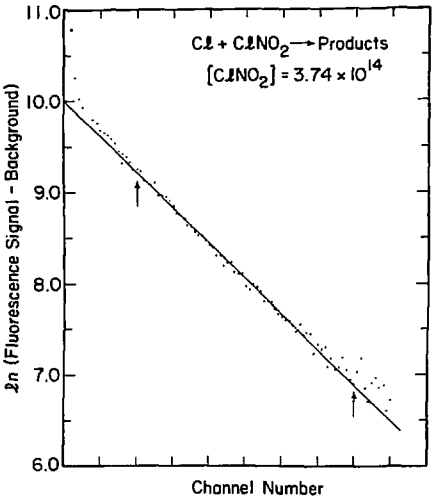

Fig. 7. ℓn (signal-background) vs time for the reaction of Cl + $ClNO_2$ with the limits of the computer fit denoted by arrows. (XBL 8010-12323)

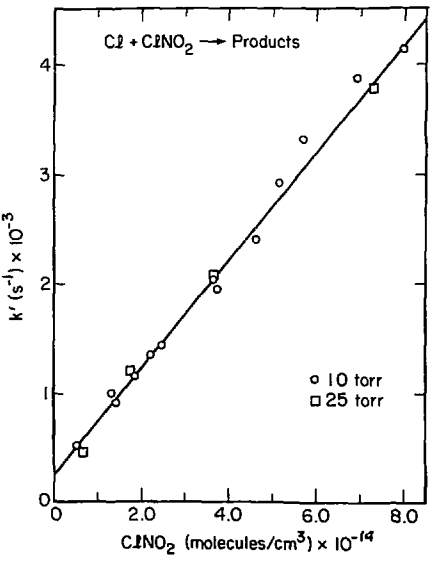

Fig. 8. Plot of k' vs $ClNO_2$ concentration for the reaction Cl + $ClNO_2$. (XBL 8010-12322)

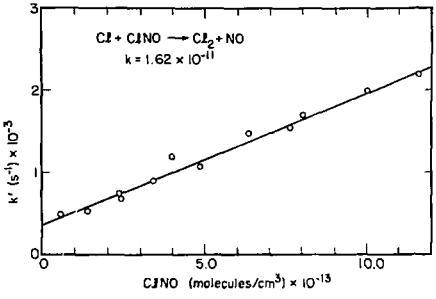

Fig. 9. Data for the Cl + ClNO reaction. (XBL 8010-12321)

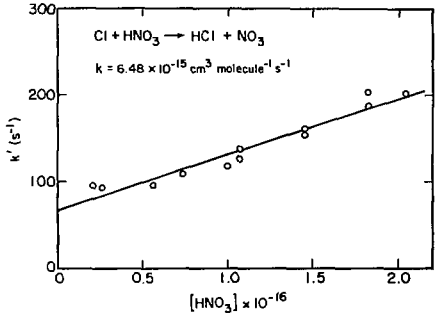

Fig. 10. Plot of pseudo-first-order rate constant against HNO_3 concentration for the reaction $Cl + HNO_3 \rightarrow HCl + NO_3$. (XBL 8012-12918)

* * *

1. M. Volpe and H. S. Johnston, J. Am. Chem. Soc. 78, 3903 (1956).
2. M. A. A. Clyne and H. W. Cruse, J. Chem. Soc., Faraday Trans. II 68, 1281 (1972).
3. A. J. Grimley and P. L. Houston, J. Chem. Phys. 72, 1471 (1980).

4. THE RATE OF REACTION OF ATOMIC CHLORINE WITH NITRIC ACID

William J. Marinelli and Harold S. Johnston

The technique of flash photolysis and resonance fluorescence (described above) was used to obtain the rate of reaction of Cl atoms with HNO_3 by use of the sequence

$$Cl_2 + h\nu \ (350\ nm) \rightarrow Cl + Cl$$

$$Cl + HNO_3 \rightarrow HCl + NO_3$$

Molecular chlorine was introduced into the photolysis cell from a mixture of 7×10^{-4} Cl_2/Ar in a 5 liter glass bulb through a metering valve and monitored by pressure. The molecular chlorine was photolyzed by 10 ns pulses, 10-20 mJ per flash, and about 30 flashes per second. The concentration of HNO_3 in the flowing stream was measured by absorption of UV at 215 nm in an optical cell in series with the photolysis cell. The concentration of atomic chlorine was followed by resonance fluorescence. The d.c. radiation from the atomic chlorine resonance lamp dissociated Cl_2 and produced a large background signal; which limited the range of conditions that could be covered and limited the signal-to-noise ratio that could be attained. The decay of Cl could be followed for only one half-time of the reaction. All experiments were conducted with a 10^4 or greater excess of HNO_3 over Cl, so that pseudo-first-order kinetics are to be expected. The pseudo-first-order rate constants k' obtained over a factor of ten range in nitric acid concentration are shown in Fig. 10, and the slope of this figure gives the second-order rate constant $6.5 \pm 1.2 \times 10^{-15}$ cm^3 $molecule^{-1}$ s^{-1}. This result is in agreement with the other published study of this reaction at room temperature by Leu and DeMore,[1] $6.8 \pm 3.4 \times 10^{-15}$.

The excimer laser was obtained as a loan from the San Francisco Laser Center, which is supported by the National Science Foundation under Grant No. CHE 78-16250 awarded to the University of California at Berkeley in collaboration with Stanford University.

* * *

1. M. Leu and W. B. DeMore, Chem. Phys. Lett. 41, 121 (1976).

RESEARCH PLANS FOR CALENDAR YEAR 1981

The rate of the reaction $HO + HNO_3$ will be studied at low temperature to check the recent report by others (Ref. 1, Article 2 above) that this reaction is much faster at low temperature than at room temperature. The rate of the reaction $HO + HOONO_2$ will be followed by the method of laser flash photolysis and resonance fluorescence. The infrared absorption spectrum of the HOO and HO free radicals will be studied by a diode laser. At high resolution (scanning dye laser excited by argon ion laser), the visible spectrum of the nitrate free radical will be measured, and the infrared emission spectrum of NO_3 will be sought. Laser flash photolysis studies in the vacuum ultraviolet will be initiated. One underlying theme of these investigations is to identify the source of the discrepancy between model calculated hydroxyl radicals and observed hydroxyl radicals in the lower stratosphere.

1980 PUBLICATIONS AND REPORTS

Refereed Journals

1. S. Solomon, H. S. Johnston, M. Kowalczyk and I. Wilson, "Instantaneous Global Ozone Balance Including Observed Nitrogen Dioxide," Pageoph 118, 58 (1980), LBL-9607.

2. F. Magnotta and H. S. Johnston, "Photodissociation Quantum Yields for the NO_3 Free Radical," Geophys. Res. Lett. 7, 769 (1980), LBL-10425.

LBL Reports

1. F. Magnotta and H. S. Johnston, "Rate Constant for the Reaction $NO_2 + O \rightarrow NO + O_2$," LBL-10424 (1980).

2. H. S. Johnston, "Odd Nitrogen Processes," LBL-10585 (1980).

3. G. S. Selwyn and H. S. Johnston, "Ultraviolet Absorption Spectrum of Nitrous Oxide as Function of Temperature and Isotopic Substitution," LBL-11234 (1980).

4. D. Littlejohn, "The Chemistry of HO_2NO_2 and the Photochemistry of the HO_x-NO_x-CO_x System", Ph. D. Thesis, University of California, Berkeley, August, LBL-11480 (1980).

5. H. H. Nelson, "The Photochemistry and Kinetics of Gas Phase Reactions Involving HO and Cl Radicals," Ph. D. Thesis, University of California, Berkeley, November 1980, LBL-11666 (1980).

Invited Talks

1. W. J. Marinelli, "Kinetics and Product Yield of the Reaction $HO + HNO_3 \rightarrow H_2O + NO_3$," American Geophysical Union 1980 Fall Meeting, December 8-12, 1980, San Francisco, California.

2. D. Littlejohn, "Rate Constant for the Reaction of Hydroxyl Radicals and Peroxynitric Acid," American Geophysical Union 1980 Fall Meeting, December 8-12, 1980, San Francisco, California.

2. Chemical Physics

a. Energy Transfer and Structural Studies of Molecules on Surfaces*

Charles B. Harris, Investigator

Introduction. Our laboratory is engaged in developing new methods for investigating energy transfer processes in condensed phases on metal surfaces and for studying a variety of questions associated with the electronic and molecular structure of molecules on single crystal metal surfaces. In the past year, electronic energy transfer from molecules to metal surfaces at distances < 50 Å has been measured. A cubic distance dependence was observed to distances as small as 7 Å from the metal surface. In addition, a comprehensive study was made of the role of chemisorption in inducing changes in the d-band structure associated with the Ni(111) surface, as observed in the visible and UV regions of the spectra. We have also been developing nonlinear optical laser techniques for studying energy transfer and relaxation in condensed phases. Using these techniques, the dynamics and structure of polyatomic liquids have been directly studied on the picosecond timescale.

1. ELECTRONIC ENERGY TRANSFER TO METAL SURFACES: A TEST OF IMAGE DIPOLE THEORY AT SHORT DISTANCES

C. B. Harris, A. Campion, H. J. Robota, and P. M. Whitmore

Considerable interest has developed in the response of metal surfaces to electromagnetic fields as well as in the properties of molecules adsorbed on these surfaces. Interpretation of photoemission experiments on metal surfaces and adsorbate-surface systems depends critically on the microscopic behavior of the local fields. Measurements of optical properties of similar systems have largely employed macroscopic geometrical boundary conditions for data interpretation. Advances in theoretical modeling of such systems have underscored the need to obtain detailed information about the microscopic behavior of metal surface-adsorbate interactions.[1] An excellent method for detecting the deviations of metal surface response from predictions of macroscopic theory is the measurement of energy transfer from excited molecules to metal surfaces. Electrodynamic descriptions of the behavior of excited molecules near metal surfaces have thus far been within the framework of classical theory.[2] However, quantum mechanical predictions regarding the behavior of excited molecules near metal surfaces show deviations from classical behavior in the region of greatest scientific interest, namely in the layers of adsorbate molecules very near the surface.

In an effort to discover nonclassical behavior we have made careful measurements of the rate at which molecules transfer energy to the substrate metal as a function of excited molecule-surface separation. In the regime of small separation, classical theory predicts that the decay of the excited molecules is dominated by energy transfer from the near field components of the oscillating dipole field to surface plasmon polariton modes of the metal interface.[3] Far from the surface, experiments have shown oscillations of the apparent excited state lifetime with increasing distance due to interference of directly emitted photons with those reflected from the surface. However, none of these experiments was able to explore the region of greatest interest, distances very near the metal surface.

In our experimental approach we have deviated from previous methods in a number of significant ways. Use of a single crystal surface in an UHV environment ensures a well ordered, flat surface free from atomic impurities, a critical factor when separation distances approach atomic dimensions. The spacing layer consists of argon atoms deposited onto the crystal surface at 10 K. This allows distance variation of much smaller steps as well as precluding interference from thermally activated relaxation channels. Although the lifetimes were not specifically measured, the related quantity, phosphorescence yield will exhibit the same distance dependence.

The UHV chamber used in these experiments had a base pressure about 2×10^{-10} torr. A nickel(111) single crystal was mounted on a variable cold tip where argon atoms were deposited at 10 K. The thickness of the argon spacer layer was monitored with an automated ellipsometer at 6328 Å wavelength. The cleanliness and order of the crystal was assured with Auger electron spectroscopy and LEED measurements. A 5 Å thick layer of pyrazine was deposited on top of the spacer layer. Pyrazine phosphorescence was excited using a filtered medium pressure Hg arc at 60° to the surface normal. The phosphorescence was collected normal to the surface using f/1.5 collection optics. The phosphorescence was isolated using colored glass filters. The intensity was determined by counting photons and averaging for a period of time.

Figure 1 shows the distance dependence of the emission intensity. The data, plotted on a log-log scale, yield a least squares slope of 3.07 ± 0.05 in excellent agreement with the $1/d^3$

*This work was supported by the Director, Office of Energy Research, Office of Basic Energy Sciences, Chemical Sciences Division of the U. S. Department of Energy under Contract No. W-7405-ENG-48.

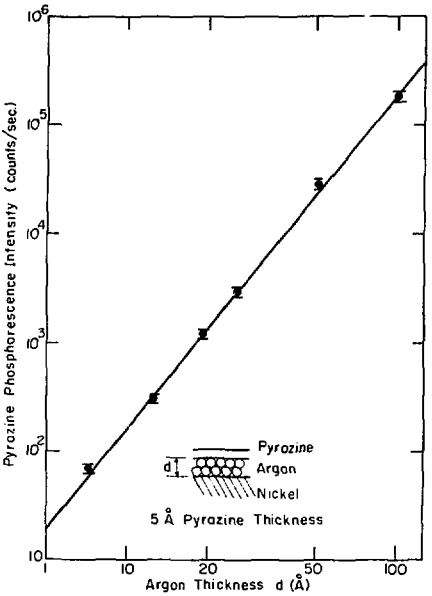

Fig. 1. Pyrazine phosphorescence intensity as a function of argon spacer thickness for a fixed pyrazine overlayer thickness of 5 A. The ordinate shows the average count rate although longer counting times were used to improve the statistics. The error bars reflect the uncertainty in the thickness of the pyrazine overlayer, which, in a series of separate experiments, we determined to be reproducible to ± 10%. The line shown is a least squares fit to a power law with an exponent of 3.07 ± 0.05. (XBL 7912-5468)

prediction. Complications due to scattered radiation at the shortest distances made the final measurements more difficult than those where a high intensity is detected. This constant contribution of the background radiation precluded measurements at smaller separation in these experiments. However, the validity of classical predictions is seen to hold for distances as close as 7 Å.

We conclude that in order to detect nonclassical behavior for radiating molecule-metal surface systems the separation distance must approach intimate contact between adsorbate and metal in this particular system. The possibility for other systems to exhibit more pronounced deviations is also being explored. Finally, future experiments will measure the radiating lifetime directly in order to develop a more complete dynamical description of the interaction and decay process.

* * *

1. S. Mukhopadhyay and S. Lundquist, Phys. Scr. 17, 69 (1978).
2. R. R. Chance, A. Prock and R. Silbey, in Advances in Chemical Physics Vol. 37, I. Prigogine and S. A. Rice Eds., Wiley Interscience, New York, p. 543.
3. Resulting in a $1/d^3$ distance dependence for the non-radiative energy transfer rate.

2. OPTICAL PROPERTIES OF MOLECULES CHEMISORBED ON THE Ni(111) SURFACE

C. B. Harris, H. J. Robota, and P. M. Whitmore

To understand the nature of the surface chemical bond one must ultimately examine the changes in the electronic structure of the metal surface and adsorbate upon chemisorption. Photoelectron spectroscopy has been used to study adsorption-induced changes in filled adsorbate and metal electronic states, and some qualitative pictures of bonding mechanisms have emerged. Electron energy loss spectroscopy has also added information about unfilled levels which lie above the Fermi level, but the details of the bonding interaction, particularly the role played by the metal electronic states near the surface, are still unknown.

Even more information in principle can be obtained by the use of surface optical spectroscopy, which is a very sensitive probe of changes in the dielectric response of the metal surface upon adsorption of a molecule. Perturbations in the metal states, particularly in the valence band near the Fermi energy, and electronic transitions in the adsorbate layer provide insights into the bonding shifts and interactions of both filled and unfilled electronic states.

We have studied the adsorption of several small molecules on a Ni(111) surface in UHV using a scanning rotating analyzer ellipsometer. Briefly, the ellipsometer is used to measure the optical constants of the clean nickel surface as a function of wavelength. A gas is adsorbed and another spectrum is taken, and, by using a three-layer model for the reflecting system, the dielectric response of an effective "overlayer" can be calculated. This overlayer can be considered to be the adsorbate layer plus the perturbed metal layer adjacent to it.

Figure 2 shows the absorption spectrum of a layer of pyrazine chemisorbed on Ni(111) at 230 K. The dominant feature of the spectrum in this region is a broad, structureless absorption at 2800 Å. There is no evidence of the molecular transitions which characterize the spectrum of pyrazine physisorbed on Ni(111) which has been reported previously.[1] This striking absorption peak also dominates the spectrum of chemisorbed O_2, CO, benzene, pyridine, and naphthalene, with little shift in position or width.

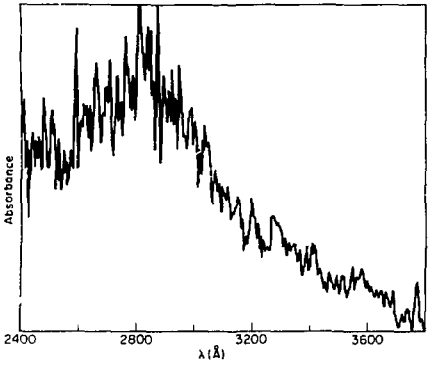

Fig. 2. Spectrum of chemisorbed pyrazine on Ni(111) at 230 K. (XBL 811-3973)

This peak is not related to molecular transitions or charge transfer transitions, because it is essentially identical for such a wide variety of adsorbates. Rather, the appearance of this absorption peak must reflect changes in the electronic configuration of the metal surface. This region of the nickel spectrum is dominated by interband transitions out of the d-band to empty states above the Fermi level, and photoemission studies show that a general decrease in d-band emission is observed upon adsorption of a wide variety of molecules. This optical spectrum is a reflection of these changes in the d-band, and much more theoretical work must be done before a detailed description of how the bonding process affects the d-bands can be offered.

* * *

1. C. B. Harris, D. A. Zwemer, A. R. Gallo and H. J. Robota, Surface Science, 85, 1 (1979).

3. INHOMOGENEOUS BROADENING OF LIQUID VIBRATIONAL LINEWIDTHS REVEALED BY SELECTIVE, COHERENT PICOSECOND STOKES SCATTERING†

C. B. Harris, S. M. George, H. Auweter, and A. L. Harris

Using the combined results of isotropic spontaneous Raman studies and coherent picosecond probing experiments,[1] we have determined that symmetric CH_3-stretching vibrational linewidths in non-hydrogen-bonded liquids are inhomogeneously broadened to various degrees.[2,3] These results jeopardize some of the conclusions of isotropic Raman line shape investigations that have tacitly assumed that vibrational linewidths are only homogeneously broadened in order to extract dynamical information.[4]

Figure 3 shows the picosecond Stokes scattering results for the symmetric CH_3-stretching vibration in acetone and methyl sulfide as well as the isotropic Raman line shapes for the same vibrations. The picosecond results enable us to calculate the corresponding homogeneous Lorentzian line shapes which are also drawn in Fig. 3. From the superimposed line shapes the inhomogeneous broadening in these non-hydrogen-bonded liquids is vividly illustrated. The picosecond results, calculated homogeneous linewidths, isotropic Raman spontaneous linewidths and inhomogeneous broadening linewidths are listed in Table 1.

Because our results demonstrate that symmetric CH_3-stretching vibrational linewidths are inhomogeneously broadened, attempts were made to correlate the inhomogeneous broadening linewidths to various liquid parameters. A correlation between the inhomogeneous broadening linewidths and the liquid's local number density distribution width was established. This correlation is shown in Fig. 4.

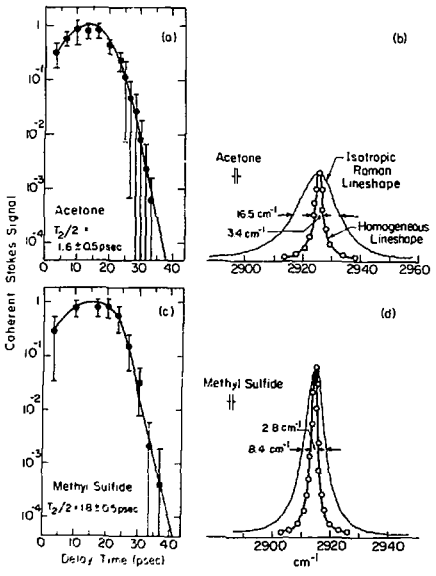

Fig. 3. Experimental data for the symmetric CH_3-stretching vibration in acetone and methyl sulfide. Coherently scattered Stokes signal as a function of probe pulse delay in (a) acetone and (c) methyl sulfide. Isotropic Raman line shapes and homogeneous Lorentzian line shapes calculated from the measured dephasing times in (b) acetone and (d) methyl sulfide. (XBL 804-5014)

Table 1. Experimental dephasing times, calculated homogeneous linewidths, isotropic Raman linewidths, and inhomogeneous broadening linewidths for the symmetric CH_3-stretching vibrations in the various liquids studied.

Molecule	$\omega(cm^{-1})$	Average *experimental* T_2 (psec)	*Calculated* homogeneous $\Delta\omega(cm^{-1})$	Isotropic *spontaneous* Raman $\Delta\omega(cm^{-1})$	*Gaussian* inhomogeneous $\Delta\omega(cm^{-1})$
(1) 1,1,1-Trichloroethane	2938.5	2.6	4.1	4.3	0.9
(2) Methyl Iodide	2948	2.4	4.4	5.0	1.7
(3) Acetonitrile	2945	5.4	2.0	6.6	5.5
(4) Methyl Sulfide	2913.5	3.8	2.8	8.4	6.8
(5) Dimethyl Sulfoxide	2914.5	1.4	7.6	11.8	6.9
(6) Acetic Anhydride	2942.5	2.2	4.8	16.8	14.1
(7) Acetone	2925	3.0	3.5	16.5	14.6
(8) Methyl Formate	2961	2.2	4.8	17.5	14.8
(9) Pentane	2877	2.7	3.9	~ 17	~ 14.8
(10) Ethanol	2929	2.5	4.2	18.0	15.6
(11) Methanol	2836	2.4	4.4	18.0	16.3

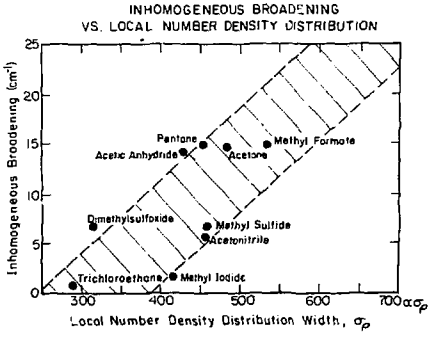

Fig. 4. Graph of the inhomogeneous broadening linewidth versus the liquid's local number density distribution width. (XBL 803-8518)

Based on this correlation, we have constructed a theoretical model for inhomogeneous broadening of vibrational linewidths in liquids.[2] Moreover, we have developed a stochastic line shape theory in which homogeneous and inhomogeneous broadening are treated simultaneously in terms of one vibrational correlation function. This treatment unifies the fast and slow modulation approaches to vibrational dephasing and demonstrates how isotropic spontaneous Raman scattering studies and picosecond coherent probing experiments can be used in conjunction to study the inhomogeneous broadening of vibrational linewidths.

* * *

†This work was partially supported by the National Science Foundation.

1. A. Laubereau and W. Kaiser, Rev. Mod. Phys. 50, 607 (1978).
2. S. M. George, H. Auweter and C. B. Harris, J. Chem. Phys. 73, 5573 (1980).
3. C. B. Harris, H. Auweter and S. M. George in Picosecond Phenomena II, ed. by R. Hochstrasser, W. Kaiser and C. V. Shank (Springer-Verlag, New York, 1980) p. 151.
4. D. W. Oxtoby, Adv. Chem. Phys. 40, 1 (1979).

4. THE ORIGIN OF HOMOGENEOUS BROADENING OF MOLECULAR VIBRATIONS IN LIQUIDS AND SOLIDS†

C. B. Harris, S. Marks, S. M. George, M. A. Berg, and P. A. Cornelius

Vibrational dynamics in liquids and solids occur on the picosecond timescale.[1] The experimental determination of vibrational dynamics usually involves line shape analysis or a direct measurement in the picosecond time domain. The investigations of the past year[2-4] have provided experimental tests of various vibrational dephasing theories proposed by ourselves and others[5,6] and have given strong evidence in support of a theory based on intermolecular energy exchange.[6]

We have successfully applied exchange theory to the C-H (D) stretches in solid h_{14} (d_{14}) durene. Important corroborative evidence in durene for the extracted parameters' validity was obtained in the spectra of the low frequency modes and the combination region. One major result from these experiments is to rule out as significant effects the dephasing mechanisms of Abbot and Oxtoby[5] and the additional mechanisms of Wertheimer.[5] In addition, the dephasing time of the symmetric methyl stretch of various liquids was determined by direct picosecond measurements. As in the case of solids, many mechanisms have been proposed for the dephasing channels. The most critical evaluation of the theories at a single temperature is to examine the dephasing times for isotopically substituted molecules. The reason is that in polyatomic molecules substitution of D for H barely changes the frequency of collision but severely affects the reduced mass of the C-H (or D) stretch and in turn the frequency of the stretch. Intermolecular forces and molecular densities are also essentially constant. The effect of isotopic substitution on the homogeneous dephasing time of the symmetric CH_3-stretching vibration in methanol and acetone was negligible. Both the binary collision model[7] and the hydrodynamic model[8] for dephasing predict substantial differences in the rate of dephasing upon isotopic substitution based on mass and frequency changes. The absence of an isotope effect is inconsistent with the predictions of both the binary collision and hydrodynamic models, but is in approximate agreement with exchange theory.

* * *

†This work was partially supported by the National Science Foundation.

1. A. Laubereau and W. Kaiser, Rev. Mod. Phys. 50, 607 (1978).
2. C. B. Harris, H. Auweter and S. M. George, Phys. Rev. Lett. 44, 737 (1980).
3. C. B. Harris, H. Auweter and S. M. George in Picosecond Phenomena II, ed. by R. Hochstrasser, W. Kaiser and C. V. Shank (Springer-Verlag, New York, 1980) p. 151.
4. S. Marks, P. A. Cornelius and C. B. Harris, J. Chem. Phys. 73, 3069 (1980).
5. D. W. Oxtoby, Adv. Chem. Phys. 40, 1 (1979).
6. C. B. Harris, R. M. Shelby and P. A. Cornelius, Phys. Rev. Lett. 38, 1415 (1977); Chem. Phys. Lett. 57, 8 (1978); J. Chem. Phys. 70, 34 (1979).
7. S. F. Fischer and A. Laubereau, Chem. Phys. Lett. 35, 6 (1975).
8. D. W. Oxtoby, J. Chem. Phys. 70, 2605 (1979).

RESEARCH PLANS FOR CALENDAR YEAR 1981

In the calendar year 1981, the experiments started in 1980 to understand the nature of chemisorbed molecules on metal surfaces in its relationship to the optical spectrum will be continued. Studies on metal surfaces less reactive than Ni(111) will be initiated to separate adsorbate induced changes of the metal states from changes in the molecular and electronic structure of the chemisorbed molecule. In addition, the frequency dependence of the energy transfer rate from molecules near or on the silver 111 and silver 110 surfaces in the region of the surface plasmon resonance will be investigated. The results obtained will be used to test the various theories currently being proposed for energy transfer processes from molecules to metal surfaces.

Finally, the initial studies of laser induced Raman scattering from single crystal silver surfaces (not reported in this Annual Report due to the preliminary nature of the results) will be continued in order to determine the relative importance of surface plasmon states, plasmon localization, and surface roughness on the "giant Raman enhancement" effect.

1980 PUBLICATIONS AND REPORTS

Refereed Journals

1. A. Campion, A. R. Gallo, C. B. Harris, H. J. Robota and P. M. Whitmore, "Electronic Energy Transfer to Metal Surfaces: A Test of Classical Image Dipole Theory at Short Distances," Chemical Phys. Lett. 73, 447 (1980), LBL-10134.

†2. C. B. Harris, H. Auweter and S. M. George, "A Critical Test of Vibrational Dephasing Theories in Liquids Using Selective Coherent Picosecond Stokes Scattering", Phys. Rev. Lett. 44, 737 (1980), LBL-10142.

†3. S. Marks, P. A. Cornelius and C. B. Harris, "A Critical Test of Vibrational Dephasing Theories in Solids Using Spontaneous Raman Scattering in Isotopically Mixed Crystals," Journal of Chemical Physics, 73, 3069 (1980), LBL-10181.

4. A. R. Burns and C. B. Harris, "Heat Pulses in Molecular Solids: Phonon-Induced Delocalization of Trapped Excited Triplet States," Molecular Crystal and Liquid Crystal, special issue, 58, 1, (1980), LBL-9127.

†5. S. M. George, H. Auweter and C. B. Harris, "Inhomogeneous Broadening of Vibrational Linewidths in Polyatomic Liquids," J. Chem. Phys. 73, 5573 (1980), LBL-10141.

6. P. A. Cornelius and C. B. Harris, "The Role of Self-Phase Modulation in Stimulated Raman Scattering from More than One Mode," Optics Letters, in press (1980), LBL-10143.

7. J. L. Chao, "Applications of the Optical Multichannel Analyzer for (1) Low Light Level Signal Averaging and (2) 2-D Mode Detection of Picosecond Laser Generated Raman Spectra," submitted to Applied Spectroscopy, (1980), LBL-11391.

LBL Reports

1. Paul A. Cornelius, "Spontaneous and Stimulated Raman Studies of Vibrational Dephasing in Condensed Phases," Ph. D. Thesis, (1980), LBL-10966.

2. James L. Chao, "Optical Multichannel Analyzer Techniques for High Resolution Optical Spectroscopy," Ph. D. Thesis (1980), LBL-10992.

3. H. J. Robota, P. M. Whitmore and C. B. Harris, "Optical Properties of Molecules Chemisorbed on the Ni(111) Surface," (1980), LBL-11837.

4. J. J. Chao, and C. B. Harris, "LSI-11 Microcomputer Based Data Acquisition System for an Optical Multichannel Analyzer," (1980), LBL-10782.

Invited Talks

1. C. B. Harris, "The Structure and Dynamics of Liquids on a Picosecond Timescale," IBM, San Jose, January 1980.

2. C. B. Harris, University of California, Los Angeles, February 1980.

3. C. B. Harris, Stanford University Chemistry Colloquium, Palo Alto, March 1980.

4. C. B. Harris, Bell Laboratories, Physics Colloquium, April 1980.

5. C. B. Harris, Harvard-Massachusetts Institute of Technology Chemistry Colloquium, April 1980.

6. C. B. Harris, "The Structure of Liquids on a Picosecond Timescale as Determined by Coherent Stokes Scattering," Electrical Engineering Seminar, University of California, Berkeley, April 1980.

7. C. B. Harris, "The Effect of Liquid Structure on Coherent Stokes Scattering," Chemistry Colloquium, Technische Universität München, July, 1980.

8. C. B. Harris, "The Use of Non-linear Optics to Study Liquid Structure on the Picosecond Timescale," Physics Colloquium, Physikalisches Institute 3, Universität Stuttgart, August 1980.

9. C. B. Harris, "The Structure and Dynamics of Liquids on a Picosecond Timescale," Columbia University, October 1980.

10. C. B. Harris, Physical Chemistry Seminar, University of California, Berkeley, October 1980.

11. C. B. Harris, "The Structure and Dynamics of Liquids on a Picosecond Timescale," Conference on Picosecond Phenomena, Hyannis, Cape Cod, Massachusetts, June, 1980.

12. C. B. Harris, "The Use of Optical Techniques for Studying Aromatic Hydrocarbons on Single Crystal Metal Surfaces," 9th Molecular Crystal Symposium, Austria, Sept.-Oct. 1980.

13. C. B. Harris, "The Use of Optical Techniques for Studying Aromatic Hydrocarbons on Single Crystal Metal Surfaces," Abstract presented at the 9th Molecular Crystal Symposium, Austria, (1980).

†14. C. B. Harris, H. Auweter, and S. M. George, "The Dynamics and Structure of Liquids Revealed by the Homogeneous and Inhomogeneous Broadening of Liquid Vibrational Transitions," Abstract presented at the Picosecond Phenomena Conference Proceedings, Cape Cod, Massachusetts, June (1980), LBL-11169.

* * *

†Partially supported by the National Science Foundation.

b. Molecular Beam Spectroscopy*

John S. Winn, Investigator

1. BONDING TRENDS IN WEAKLY-BOUND MOLECULES‡

J. H. Goble and J. S. Winn

We have used an analytic potential function inversion method, described in previous annual reports, to examine the equilibrium bonding trends in many weakly bound diatomics. This method of analysis[1] permits one to ascertain the extent to which long-range interactions persist near the equilibrium position in the potential. The potential function we use is the Thakkar function,

$$V(R) = e_0\lambda^2[1 + \Sigma e_n\lambda^n]$$

where $\lambda = 1 - (R_e/R)^p$ and p is a positive parameter. At large R, this potential varies as R^{-p}; thus, the parameter p indicates the way in which long-range behavior is, or is not, modified near R_e. It is important to note that p is not fit to the long-range part of the potential. It is purely a property of the equilibrium position of the potential function.

In Table 1, a number of p values for many types of weakly bound diatomics is given along with values for D_e, the well depth, R_e, the bond length, and κ, the reduced curvature or dimensionless force constant for the potential. Note that diatomic families fall into categories based on p and κ rather more easily than categories based on bond energies. For instance, the alkaline earth dimers[2] show p values considerably smaller than rare gas dimers but larger than the typical values (0.5 to 2.5) observed in chemically bound molecules. From this observation (and others), one can not only deduce incipient covalent bonding in these dimers, but one also can make such trends quantitative.

Similarly, the series Ne_2 - NeXe shows an interesting saturation in bond energies which is contrary to expectations, given the increasing polarizabilities of the rare gases Ne through Xe. The p and κ values are seen to increase, however, demonstrating the effect of a more rapid onset of repulsion as one moves through this series.

Much of chemical thought is organized around an understanding of strong chemical forces among atoms, radical fragments, and reactive molecules Terms such as covalent character, charge delocalization, hydrogen bonding, and the like conjure specific models of bonding interactions with a host of well-understood consequences associated with each. Systematic analyses of weak interactions of the type described here should indicate the nature of the terms needed to understand such interactions at the same level as one now understands chemical bonding.

Table 1. Potential well parameters for weakly bound diatomics. Energies in cm^{-1}, R_e in Å.

Molecule	D_e	R_e	κ	p	Method[a]
He_2	7.65	2.96	77	5.2	E
Ne_2	29.7	3.03	80	5.6	E
Ar_2	100.	3.76	88.4	5.62	ESB
Kr_2	140.	4.01	81.4	6.33	ESB
	138.	4.11	(72-87)[b]	(5-5.6)	E
Xe_2	196.	4.36	78.3	6.69	ESB
	192.	4.45	(88-84)	(5.6-5.5)	E
HeNe	9.9	3.21	43	3.64	E
HeAr	16.8	3.54	59	4.43	E
HeKr	17.2	3.75	57	4.34	E
HeXe	17.5	4.15	56	4.29	E
NeAr	50.	3.43	87	5.60	E
NeKr	52.	3.58	98	6.00	E
NeXe	52.	3.75	125	6.91	E
Be_2	800.	2.49	59.5	4.94	A
Mg_2	430.	3.89	32.7	3.59	S
Ca_2	1095.	4.28	41.9	3.56	S
Sr_2	1100.	4.50	38	3.35	S
NaNe	8.1	5.29	--	----	S
NaAr	41.	4.99	51	4.31	S
LiHg	871.	3.00	33.5	2.54	E
NaHg	444.	4.72	40.9	3.10	E
KHg	420.	4.91	40.0	3.00	E
CsHg	403.	5.09	46.2	3.40	E
NeF	42.	2.85	(110-92)	(6.4-5.8)	E
ArF	98.	2.95	37.0	3.30	E
KrF	108.	3.00	37.0	3.30	E
XeF	1175.	2.32	(144-92)	(7.5-5.8)	E
	1175.	2.32	116.6	5.53	S
XeCl	280.	3.23	(54-22)	(4.2-2.3)	E
$HeNe^+$	6200.	1.33	48.9	4.30	S
$BeAr^+$	4536.	2.09	27.5	3.16	S
$BeKr^+$	5511.	2.22	29.1	2.84	S
$CaAr^+$	1000.	2.80	36.3	3.93	S

[a]Methods E, elastic scattering; S, optical spectroscopy; B, bulk data used in fit; A, ab initio calculation.

[b]When the model potential had two Morse functions joined at R_e, κ and p are not well defined. Data in parenthesis list values for the inner Morse function and the outer Morse function, respectively.

*This work was supported by the Director, Office of Energy Research, Office of Basic Energy Sciences, Chemical Sciences Division of the U. S. Department of Energy under Contract No. W-7405-ENG-48.

* * *

†This work was supported in part by the National Science Foundation.

1. J. S. Winn, submitted to Accts. Chem. Research.
2. J. H. Goble and J. S. Winn, In press: Chem. Phys. Lett. LBL-11708.

2. LASER-ASSISTED PENNING IONIZATION

J. H. Goble, W. E. Hollingsworth, and J. S. Winn

The idea of coupling an intense radiation field to a molecular collision is a relatively new concept. The main point is that the field need not be resonant with any transition among isolated reactant or product molecules but rather with a transition between a reactant pair state and a product pair state. We have looked into this effect as applied to chemi-ionization.

We have a good understanding[1] of the ionization processes in the unilluminated reactions:

$$Ar^*(^3P) + Ca \rightarrow Ar + Ca^+ + e^-$$

$$\rightarrow CaAr^+ + e^-.$$

The first is direct Penning ionization; the second is associative ionization; and either can lead to ions in excited states. One endothermic process is

$$Ar^*(^3P) + Ca \rightarrow Ar + Ca^+(5p\ ^2P) + e^-.$$

The energy of this excited state of Ca^+ is above the energy of Ar^* by an amount which translates into a photon of wavelength 596 nm. Note that this photon cannot be absorbed by any reactant or product atom along; but, when absorbed by the collision pair, it can lead to an energy input great enough to surmount the endothermicity of the reaction.

We have investigated[2] this process by irradiating a flowing afterglow flame of Ar^* and Ca with the high intensity light from a focused, pulsed Nd:YAG pumped dye laser. The reaction is followed by a time-synchronized detection of the fluorescent cascade

$$Ca^+(5p\ ^2P) \rightarrow Ca^+(5s\ ^2S) \rightarrow Ca^+(4p\ ^2P)$$

detecting the final step at a wavelength of 373 nm.

As the laser is tuned through the resonance region, a broad (~ 15 cm^{-1}) peak is seen (one at each of the fine-structure levels of the 5p ^2P state) but with very low intensity. The effect appears to occur but with diminished probability, due to several possible competing processes. One such process is anti-Stokes scattering from Ar^* itself. This process would have a very weak wavelength dependence, however. The second, and more likely, competing process has the excess photon energy carried away by the Penning electron. We cannot ascertain the likelihood of this process in our experiment.

With increased metastable concentrations (which can be obtained from a pulsed microwave discharge, for example), one should be able to increase the signal in these types of experiments by several orders of magnitude and thereby raise the sensitivity of the technique to the point where quantitative measurements of the reaction cross-section and branching ratios can be made.

* * *

1. D. C. Hartman and J. S. Winn, In press, J. Chem. Phys., LBL-10168; D. C. Hartman, Ph. D. Thesis, LBL-9819.
2. J. H. Goble, Ph.D. thesis, University of California (1980).

3. PRODUCTION OF THIN METAL FILMS FROM METAL CARBONYL DISSOCIATION

B. C. Hale, W. E. Hollingsworth, D. V. Horak, and J. S. Winn

The possibility that volatile metal carbonyl compounds or metal alkyls can be used to generate transition metal atoms, clusters, and thin films has been under investigation in our group for some time. We have been investigating various processes by which metal-ligand bonds can be broken selectively, freeing the metal atom. We have shown[1] that electronic energy transfer from metastable rare gas atoms to the metal carbonyl breaks all metal-ligand bonds in a single elementary process. Our results were described in the last annual report.

Our current efforts have centered on photochemical means of dissociation. The possibility that metal clusters can be formed from discharge or photochemical methods has been pursued[2] using mass-spectrometric sampling methods. The rate of production of atoms and clusters by discharge methods appears to be too slow to be of practical use.

We are now investigating several types of direct photochemical methods. The first was vacuum UV radiation in the same energy region as that carried by metastable rare gases, 9 to 15 eV. We monitor dissociation by following the atomic Fe fluorescence (in the case of $Fe(CO)_5$ dissociation) distribution as a function of VUV wavelength. These distributions are qualitatively different from those observed in the collision excitation flames, and we anticipate a full analysis of them will lead to a more detailed understanding of photochemical dissociation.

A second process involves UV illumination of a substrate immersed in the vapor of a low pressure carbonyl. A thin metal film is found to grow on the substrate, and the mechanism is thought to involve photoemission of electrons

from the substrate followed by dissociative attachment to the carbonyl followed by recombination of the negative carbonyl fragment ion onto the surface. Wavelength dependent studies indicate the role played by the work function of the substrate in initializing the reaction and the work function of the thin film in promoting further film growth.

More work will be needed to ascertain more clearly the film composition and structure and to ascertain the size limits of the features one can deposit by this method, but there are potentially many types of technological processes which could benefit by this type of photochemically controlled metal film deposition.

* * *

1. D. C. Hartman, W. E. Hollingsworth, and J. S. Winn, J. Chem. Phys. 72, 833 (1980).
2. J. S. Winn, Faraday Diss., Faraday Symp. 14, 256 (1980).

4. IMPLICATIONS OF THE VIRIAL THEOREM ON THE DESCRIPTION OF WEAK BONDING†

John W. Winn

Application of the virial theorem to the total energy of a diatomic molecule within the Born-Oppenheimer approximation yields an instructive description of the physical origin of bonding between two atoms.[1] If W(R) is the Born-Oppenheimer total energy of the atoms, then the virial theorem relates the average kinetic energy of the electrons <T(R)> and the average Coulombic potential energy of the diatomic <V(R)> to W(R) via the relations

$$\langle T(R)\rangle = -W(R) - R\, dW(R)/dR$$

and

$$\langle V(R)\rangle = 2W(R) + R\, dW(R)/dR.$$

These three functions for the ground state of H_2 are shown in Fig. 1. The distance scale is measured in multiples of the H_2 equilibrium bond length, and the energy scale is measured in multiples of the H_2 bond energy. Note that bonding occurs over a relatively large distance; the potential energy slowly falls, and repulsion is due to a gradual increase in electron kinetic energy. Only at $R/R_e < 0.5$ does nuclear repulsion contribute to a rise in <V>.

This behavior should be contrasted to that observed in weakly bound diatomics. Using Ar_2 as an example, the same three functions, W, T, and V, are plotted in Fig. 2 to the same scale used in Fig. 1. One immediately notices that bonding in Ar_2 occurs over a relatively shorter distance and that repulsive interactions arise much more abruptly for Ar_2 than for H_2. This abrupt increase in repulsive interactions is typical of the behavior found for weakly bound diatomics in general.

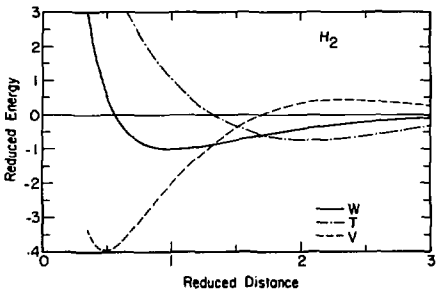

Fig. 1. Total energy (W), potential energy (V), and electron kinetic energy (T) curves for the ground state of H_2. (XBL 811-7881)

If one has an analytic form for the total energy function, this qualitative analysis can be made quantitative and can be related to Born-Oppenheimer wavefunctions. If one defines k_e to be the quadratic force constant and ℓ_e to be the cubic force constant, the quantity p which appears in the Thakkar analytic potential function (described earlier in this annual report) can be written

$$p = -\ell_e R_e/3k_e - 1.$$

One can show that

$$(d\langle V\rangle/dR)_{R_e} = -(d\langle T\rangle/dR)_{R_e} = k_e R_e,$$

$$(d^2\langle T\rangle/dR^2)_{R_e} = 3pk_e,$$

and

$$(d^2\langle V\rangle/dR^2)_{R_e} = (1-3p)k_e.$$

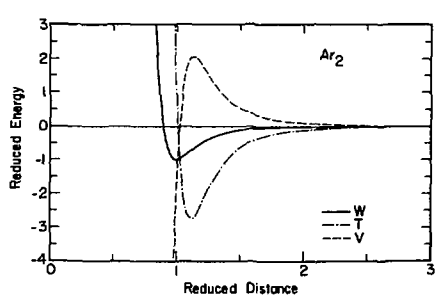

Fig. 2. As Fig. 1, but for the ground state of Ar_2. (XBL 811-7882)

Each of these terms may be written as functions of the Born-Oppenheimer wavefunction. Also, since p may be expressed in terms of equilibrium spectroscopic constants as

$$p = \alpha_e \omega_e / 6B_e^2$$

One can, in principle, relate spectroscopic observables to the detailed behavior of the Born-Oppenheimer wavefunction near R_e.

* * *

†Supported in part by the National Science Foundation.

1. J. S. Winn, In press: J. Chem. Phys. (1981).

RESEARCH PLANS FOR CALENDAR YEAR 1981

Work in the area of laser induced fluorescence of trapped molecular ions is described under Bruce Mahan's research program and will be conducted as a joint effort.

The program on metal carbonyl dissociation and thin metal film formation will continue in several directions. Atomic fluorescence from multiphoton dissociation will be studied as a function of laser frequency and laser pulse length. Pulse lengths of 10 nsec are available from a Nd:YAG dye laser system and pulse lengths of 1 μsec are available from a flashlamp pumped dye laser. These fluorescence spectra will be compared to those obtained by VUV single photon dissociation and by metastable rare gas collisional dissociation.

The program on weakly bound molecules will continue with studies using molecular beam electric resonance spectroscopy to probe the structures of weakly bound molecules such as HeClF and other rare gas-ClF or rare gas-halogen molecules.

1980 PUBLICATIONS AND REPORTS

Refereed Journals

1. K. V. Chance, K. H. Bowen, J. S. Winn, and W. Klemperer, "Electric Deflection Studies of Halogen and Interhalogen Polymers," J. Chem. Phys. 72, 791 (1980).

2. D. C. Hartman, W. E. Hollingsworth, and J. S. Winn, "Dissociation of Metal Carbonyls by Metastable Rare Gases: Fe and Ni Emission Analysis," J. Chem. Phys. 72, 833 (1980).

3. L. Brewer and J. S. Winn, "Models for Calculations of Dissociation Energies of Homonuclear Diatomic Molecules," Faraday Discussions #14, p. 126 (1980).

4. J. S. Winn, "Gas Phase Production and Chemistry of Transition Metal Atoms and Clusters from Polynuclear Metal Carbonyls," Faraday Discussion #14, p. 102 (1980).

LBL Reports

1. F. J. Grieman, B. H. Mahan, A. O'Keefe, and J. S. Winn, "Laser Induced Fluorescence of Trapped Molecular Ions: The CH^+ $A^1\Pi \leftarrow X^1\Sigma^+$ System," LBL-11534.

c. Selective Photochemistry*

C. Bradley Moore, Investigator

Introduction. The major emphasis of this program is on the study of high vibrational overtone excitations to understand coupling among vibrational modes at high internal energies and to explore the photochemistry following excitation. The techniques of optoacoustic spectroscopy and intracavity dye laser spectroscopy are used for these studies. Results are described in the following sections. In addition, dye laser absorption spectroscopy has been developed for studying the dynamics and chemistry of HCO. HCO reaction rate measurements have begun. Other work includes vibrational relaxation, chemistry and spectroscopy in condensed phases.

1. OVERTONE SPECTRA OF GASEOUS ALKANES AND ALKENES

James S. Wong

The search for bond selective vibrational photochemistry has proven to be an elusive goal to photochemists.[1] Single photon excitation of high vibrational overtones seems to hold the most promise.[2] Accurate assignments of the excited C-H oscillators are crucial in the search for photochemical unimolecular reactions in which the reaction coordinate involves C-H stretching motion. The concept of local modes in which the oscillator strength derives from the stretching of a single C-H bond has been useful in interpreting these spectra.[3] However, only a few overtone spectra of gaseous molecules have been reported. Splittings and shifts obscured in the liquid phase spectra yield important information on vibrational modes and their couplings. In this work, the $\nu_{CH} = 6$ spectra of 14 gaseous alkanes and alkenes have been recorded using laser optoacoustic spectroscopy and means for assigning the spectra have been developed.

By selectively deuterating all C-H bonds except one in various organic molecules, McKean et al.[4] were able to resolve these same splittings in the infrared fundamental spectra. The remaining C-H stretch is decoupled from the rest of the vibrations at much lower frequency. Thus the infrared spectrum obtained is essentially a "local mode" spectrum in the fundamental region. By moving the remaining hydrogen atom around the molecule, they obtained isolated C-H stretching frequencies for each bond in the molecule. It was found that the microwave spectroscopic and ab initio bond lengths decreased linearly with the local mode fundamental frequency. Thus armed with these frequencies or accurate C-H bond lengths, it should be possible to assign the observed high overtone spectra since the anharmonicities vary little.

The spectrum corresponding to the fifth overtone of the C-H stretching vibrations of propene is shown in Fig. 1. Also shown in Fig. 1 is the equilibrium geometry of the molecule. Note the distinction between the in-plane and out-of-plane methyl group C-H bonds, $C\text{-}H_s$ and $C\text{-}H_a$, respectively. Although the methyl group undergoes a hindered internal rotation, the two types of hydrogen atoms are inequivalent on the time-scale of the optical transition. This inequivalence is clearly evident in the high overtone spectrum. The lowest energy peak at 15690 cm^{-1} corresponds to absorption by the $C\text{-}H_a$ oscillators while the peak at 15900 cm^{-1} corresponds to absorption by the $C\text{-}H_s$ bond. The higher energy peaks correspond to absorptions by the olefinic C-H bonds, and they are easily assigned by referring to the selectively deuterated infrared spectra or the ab initio bond lengths. These assignments are illustrated in Fig. 1. Splitting of the C-H stretching peaks is observed in all cases studied when the hydrogens are not required to be equivalent by symmetry.

When the C-H bond length determined by microwave or infrared spectroscopy is plotted vs overtone transition frequency, the data can be fit by the linear equation

$$r^{0}_{CH}\ (\text{spec}) = (1.333 \pm 0.057\ \text{Å})$$

$$- [(1.499 \pm 0.355) \times 10^{-5}\ \frac{\text{Å}}{\text{cm}^{-1}}]\ \nu_{\nu_{CH} = 6(\text{cm}^{-1})}$$

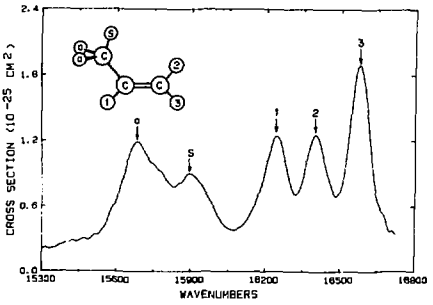

Fig. 1. Fifth overtone spectrum of propene recorded using laser optoacoustic spectroscopy. Peak assignments of the local mode transitions are given. (XBL 8012-13629)

*This work was supported by the Director, Office of Energy Research, Office of Basic Energy Sciences, Chemical Sciences Division of the U. S. Department of Energy under Contract No. W-7405-ENG-48.

However, there is considerable scatter in the data, mainly because of difficulties in precisely locating the hydrogen atoms using microwave spectroscopy. If one uses the bond lengths calculated using a 4-31G basis set,[5] the scatter is much smaller as shown in Fig. 2 and the resultant linear fit is given by

$$r^{o}_{CH}\ (\text{calc}) = (1.320 \pm 0.021\ \text{Å})$$

$$- [(1.429 \pm 0.133) \times 10^{-5}\ \frac{\text{Å}}{\text{cm}^{-1}}]\ \nu_{CH} = 6(\text{cm}^{-1})$$

Thus, with accurate C-H bond lenths, it should be possible to assign the various spectroscopic peaks observed in the overtone spectra of molecules of spectroscopic and photochemical interest.

* * *

1. J. S. Wong and C. B. Moore, Proceedings of the Sergio Porto Memorial Symposium on Lasers and Applications, June 29 - July 3, 1980, Rio de Janeiro, Brazil.
2. C. B. Moore and I. W. M. Smith, Faraday Disc. Chem. Soc. 67, 146 (1979).
3. B. R. Henry, Acc. Chem. Res. 10, 207 (1977).
4. D. C. McKean, Chem. Soc. Rev. 7, 399 (1980).
5. C. E. Blom, P. J. Slingerland, and C. Altona, Mol. Phys. 31, 1359 (1976).

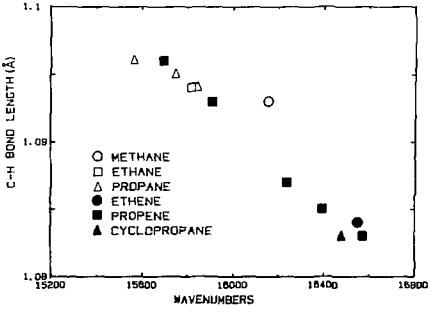

Fig. 2. Ab initio (4-31G basis set, Ref. 5) C-H bond lengths vs observed fifth overtone transition frequency. (XBL 8012-13630)

2. VIBRATIONAL RELAXATION DYNAMICS OF HCl IN RARE GAS MATRICES†

Linda Young

Investigation of diatomic molecules isolated in inert gas matrices shows the rates of vibrational relaxation to be very slow,[1,2] in some cases (e.g., CO in Ar and Ne) actually reaching the radiative limit. The long vibrational lifetimes of matrix isolated diatomics suggest the possibility of using such systems as energy storage devices.

Qualitative prediction of energy transfer mechanisms for matrix isolated diatomics is beginning to be possible. Molecules with large vibrational frequencies and large moments of inertia relax much more slowly than those with small moments of inertia where energetic local modes, i.e., guest rotation and translation, actively participate in the relaxation process. A quantitative model is sought for vibrational energy relaxation involving guest-host interaction in addition to host and guest properties. It should be possible to establish such a model for vibrational energy transfer to local modes of translation and rotation for the HCl/rare gas system, where the forces causing the spectral perturbations of the v = 1 states are well understood.[3,4] (See Figure 3).

We have measured the lifetimes of HCl (v = 1, 2, 3) as a function of host lattice and temperature using infrared laser induced vibrational fluorescence. The variation of intensity with time is studied for wavelength-resolved fluorescence. In addition, the first and second overtone regions were investigated using Fourier transform infrared absorption spectroscopy and fluorescence excitation spectroscopy, respectively.

The spectroscopy of these levels has allowed the determination of the pure vibrational frequencies of the $v = 0 \rightarrow 1$, $1 \rightarrow 2$, and $2 \rightarrow 3$ transitions and, hence, their perturbation from the gas phase values. It is shown that the gas phase constants $\omega_e x_e$ and $\omega_e y_e$ combined with a matrix shift $\Delta\nu_{matrix}$ are insufficient to determine the pure vibrational transition frequencies for the HCl/Ar, Kr, Xe system, in contrast to the CO/Ne, Ar system where good fits up to v = 8 are obtained.[1] (See Table 1.) The anharmonicity is seen to increase relative to the gas phase value with host size and polarizability. These effects are predictable by both cage size and polarizability arguments. For a given pair of vibrational levels (v', v''), the difference in attractive energies will be greater in the more polarizable matrices, and the repulsive interaction will play a smaller role in the larger cages. Both effects lead to a decrease in the HCl bond strength and, hence, the vibrational frequency. The trend with increasing quantum number is for shifts to increase

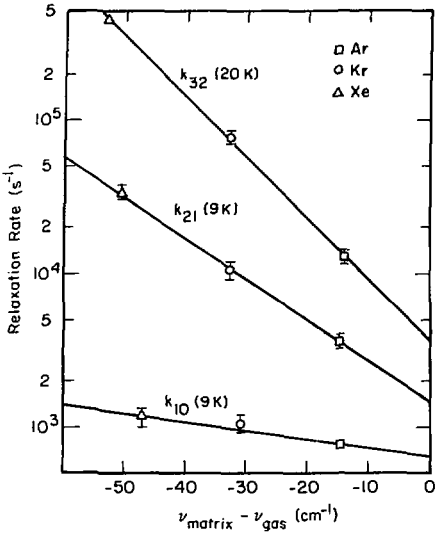

Fig. 3. Relaxation rate $k_{v'v''}$ as a function of matrix-gas frequency shift. (XBL 813-8416)

until the bond length is long enough for the cage to become tight. Repulsive forces then cause the shift to decrease with increasing v. The overall shift from gas phase values is not monoatomic for increasing v within a specific guest/host system.

The dynamical behavior of the HCl/Ar, Kr, and Xe systems reflect the complexity of the host/guest interaction. Two features are again apparent: (a) For a given vibrational state, the relaxation rate increases in the series $k_{Ar} < k_{Kr} < k_{Xe}$, i.e., in the order of the spectral shifts, and (b) As the host size increases, the deviation from the harmonic approximation, $k_v = vk_0$, also increases, such that the relaxation rate for v = 3 → 2 in

Table 1. Gas-Matrix shift for pure vibrational transitions of HCl.[a]

v'	v''	gas	Ar observed	Ar Δ	Kr observed	Kr Δ	Xe observed	Xe Δ
1	0	2885.82	2871.3	-14.5	2855.1	-30.8	2838.8	-47.0
2	1	2782.23	2767.4	-14.8	2749.6	-32.6	2731.6	-50.6
3	2	2678.97	2666.2	-13.0	2647.0	-32.0	2624.7	-54.3

[a] Uncertainties are ± 0.1 cm^{-1} for (1,0), ± .0.2 cm^{-1} for (2,1), and ± 0.6 cm^{-1} for (3,2).

Xe is two orders of magnitude larger than in Ar, whereas the v = 1 → 0 rates are comparable at 9 K. The fact that the relaxation rates mimic the spectral shifts is evidence that those forces which perturb the spectrum are also responsible for inducing relaxation.

These data, combined with earlier data on the DCl(v = 2) lifetimes in Ar[4], suggest that the rate limiting step for relaxation is the transfer of vibrational energy to a local mode (e.g. guest rotation or translation). Direct transfer of vibrational energy via a multiphonon process is unimportant in these systems. Such a process would exhibit an energy gap law and would be expected to be slower in the heavier rare gases where the Debye frequency is smaller. The energy gap law is violated as DCl(v = 2) is found to relax an order of magnitude more slowly than HCl(v = 2). The relaxation rates are also found to be faster in heavier rare gases. Work is currently underway to model the relaxation from these states to a combination of local translational and rotational modes in order to fit the observed T and v dependence.

* * *

†This work was partially supported by the U. S. Army Research Office, Triangle Park, NC.

1. H. Dubost, R. Charneau, Chem. Phys. 12, 407 (1976).
2. J. M. Wiesenfeld and C. B. Moore, J. Chem. Phys. 70, 930 (1979).
3. H. Friedmann and S. Kimel, J. Chem. Phys. 47, 3589 (1967).
4. H. Friedmann and S. Kimel, J. Chem. Phys. 43, 3925 (1965).

3. VIBRATIONAL RELAXATION OF D_2O (ν_2)†

Scepan S. Miljanić

The rate of vibration-to-translation and rotation (V→T,R) energy transfer for the lowest fundamental of $D_2O(\nu_2)$ is expected to be fast since it is known that the V → T, R relaxation of H_2O and other hydrogen bonding systems, such as NH_3 and HF, is also very fast.[1] The strong hydrogen bonding interaction and the small moments of inertia are believed to be responsible for such very rapid relaxation in those systems. Data for D_2O should be especially valuable for developing models of vibrational relaxation in such systems. Recently ir-ir double resonance experiments have given a relaxation probability of 0.16 for self deactivation of D_2O and much lower rates for V - T, R relaxation of D_2O by buffer gases.[2] A model calculation[3] showed strong negative temperature dependence for the relaxation of $H_2O(\nu_2)$ in the 200 - 400 K range. Such behavior has been observed experimentally for several hydrogen bonding systems and may be expected for D_2O.[1]

Laser-excited vibrational fluorescence was used to measure rates of relaxation of D_2O in collisions with different buffer gases at room temperature

and of pure D_2O as a function of temperature. The results serve as an independent check on earlier D_2O data, as a test of theoretical treatments, and as a calibration for semiempirical estimates of rates for hydrogen-bonded systems.

The rate constants for $D_2O(\nu_2)$ relaxation are summarized in Table 2. The data for pure D_2O and D_2O-D_2 agree well with those of Ref. 2. The $V \rightarrow T$, R relaxation probability for pure D_2O, Table 2, is very large, 0.16, but only about half that for H_2O, 0.28 - 0.47.[1] The probability increases as temperature decreases. Other systems with strong hydrogen bonding, such as ammonia and hydrogen halides, also have very fast relaxation times and negative temperature dependences near room temperature. The importance of hydrogen bonding in D_2O is further demonstrated by the large decrease in probabilities from D_2O - D_2O to D_2O - He and D_2O - Ar. The ratios are about 600, while the analogous ratios for CH_4, a system without hydrogen bonding, are 1.2.[4]

That D_2O relaxes about a factor of two less rapidly than H_2O in spite of its lower frequency indicates the importance of rotational velocities for vibrational relaxation. The average thermal velocity ratios are the inverse square roots of the moment of inertia ratios. The latter are 1.8, 2.0, and 1.9 for I_A, I_B and I_C respectively. Relaxation probability ratios for other hydride/deuteride combinations are $P_{HF}/P_{DF} = 2.5$, $P_{HCl}/P_{DCl} = 4$, $P_{NH_3}/P_{ND_3} = 7$, and $P_{CH_4}/P_{CD_4} = 2$.[1] For DCl deactivated by HCl the probability is 2.3 times greater than for DCl deactivated by DCl. For D_2O, relaxation by HDO or H_2O does not seem to be much faster. The much stronger hydrogen bonding (compared to HCl) of the D of the vibrationally excited molecule to the O of the collision partner may leave the H (or D) of the collision partner out of the region of strongest intermolecular forces.

Table 2. Measured rate constants for vibrational relaxation of $D_2O(\nu_2)$ by M at 295 K.

M	$k(sec^{-1}\ torr^{-1})$	$k(cm^3\ molecule^{-1}\ sec^{-1})$	$d^a(nm)$	P^b
D_2O	$(1.03 \pm 0.05)\cdot 10^6$	$3.2\cdot 10^{-11}$	0.280	0.162
D_2	$(1.18 \pm 0.08)\cdot 10^4$	$3.6\cdot 10^{-13}$	0.247	$1.20\cdot 10^{-3}$
HD	$(3.9 \pm 0.4)\cdot 10^4$	$1.2\cdot 10^{-12}$	0.247	$3.5\cdot 10^{-3}$
H_2	$(1.08 \pm 0.05)\cdot 10^5$	$3.3\cdot 10^{-12}$	0.247	$8.2\cdot 10^{-3}$
He	$(2.3 \pm 0.3)\cdot 10^3$	$7.1\cdot 10^{-14}$	0.224	$2.6\cdot 10^{-4}$
Ar	$(1.0 \pm 0.4)\cdot 10^3$	$3.0\cdot 10^{-14}$	0.286	$1.8\cdot 10^{-4}$

[a] Average values obtained from gas viscosities and Van der Waals b.

[b] $P = k/k_{gk}$ where k_{gk} is calculated from:

$$k_{gk} = d^2_{AB}\left(\frac{8\pi RT}{\mu}\right)^{1/2},\ \mu = \text{reduced mass.}$$

The decreasing probabilities for D_2O relaxed by H_2, HD, and D_2 reflect the decreasing velocities of both translation and rotation. The 4.7-fold decrease in probability comparing D_2 to He indicates the D_2 rotation, and presumably HD or H_2 rotation, significantly enhances D_2O relaxation. The two rare gases, He and Ar, exhibit probabilities of the same order of magnitude. Comparable values are found for $P_{O_2} = 3.6\cdot 10^{-4}$ and $P_{N_2} = 3.4\cdot 10^{-4}$ in Ref. 2.

Quantitative theoretical treatments of vibrational relaxation for hydrogen bonding polyatomics with energy transfer cross sections approaching gas kinetic are not likely to be available soon. Useful information comes from detailed treatment of HF, from simple closed-form models,[3] and from empirical correlations. These works provide some qualitative understanding of the collision dynamics in the presence of strong attractive forces which result in negative temperature dependences. For D_2O the data of Table 3 exhibit a negative temperature dependence which fits the empirical equation[5]

$$P(T) = C \exp(\varepsilon/kT)$$

where $\varepsilon = (778 \pm 34)$ K and $C = 1.1\cdot 10^{-2}$ (Fig. 4). This value of ε fits well with those correlated by Gordon.[5]

Work in progress deals with relaxation probabilities for D_2S and H_2Se along with a more complete consideration of the role of hydrogen bonding in vibrational relaxation.

* * *

†This work was partially supported by the U. S. Army Research Office, Triangle Park, NC.

1. F. E. Hovis and C. B. Moore, J. Chem. Phys. 72, 2397 (1980).
2. R. L. Sheffield, K. Boyer, and A. Javan, Opt. Lett. 5, 10 (1980).
3. H. K. Shin, J. Chem. Phys. 69, 1240 (1978).
4. P. Hess and C. B. Moore, J. Chem. Phys. 65, 2339 (1976).
5. R. J. Gordon, J. Chem. Phys. 72, 779 (1980).

Table 3. Temperature dependence of $D_2O(\nu_2)$ deactivation probabilities.

T(K)	$k(sec^{-1}\ torr^{-1})$	$k(cm^3\ molecule^{-1}\ sec^{-1})$	P
260	$(1.5 \pm 0.1)\cdot 10^6$	$4.0\cdot 10^{-11}$	0.22
295	$(1.03 \pm 0.05)\cdot 10^6$	$3.2\cdot 10^{-11}$	0.162
350	$(5.8 \pm 0.3)\cdot 10^5$	$2.1\cdot 10^{-11}$	0.100
400	$(4.3 \pm 0.2)\cdot 10^5$	$1.80\cdot 10^{-11}$	0.079

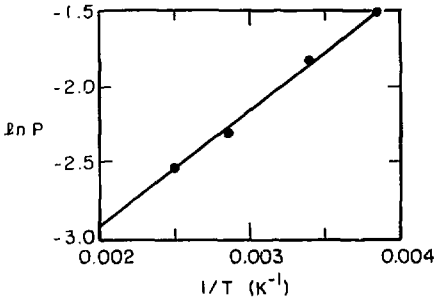

Fig. 4. Plot of ln P vs 1/T for D_2O. Slope = (778 ± 34) K. (XBL 801-7702)

4. KINETICS OF FORMATION OF DNA CROSSLINKS BY 4'-AMINOMETHYL-4,5', 8-TRIMETHYLPSORALEN[2]

John F. Hearst, Brian H. Johnston, and A. H. Kung

This is a joint project between this research group and John Hearst and Brian H. Johnston of the Melvin Calvin Laboratory of Chemical Biodynamics. The primary objective is to assess the possibilities for selective photochemical manipulation of very large molecules of major biochemical interest. The reaction which results in cross-linking of DNA by psoralen was chosen for this study. Psoralens are widely used to treat psoriasis and vitiligo. They have also been used to locate nuclease-protected regions of DNA in chromatin and regions of secondary structure in single-stranded DNA and RNA, to study DNA repair mechanisms, and in other applications. It is thus important to characterize the psoralen-DNA photoreaction as a clinical and biochemical tool and to explore the use of pulsed radiation for manipulation of the reaction.

Psoralen is a planar dye molecule which slips between the base-pair planes of double-stranded DNA. Upon absorption of uv light, a double bond is opened; and the dye attaches to a DNA base forming a "monoadduct." When this molecule subsequently absorbs a photon, it can attach to a base on the complementary strand. The two DNA strands are thus permanently tied by strong chemical bonds. The molecules cannot replicate and cell growth is stopped.

Earlier, Johnston et al.[1] described the use of single, 15 ns pulses of uv light from a frequency-doubled ruby laser to generate psoralen-DNA monoadducts in a mixture of T4 DNA and 4'-aminomethyl-4,5', 8-trimethylpsoralen (AMT) without significant production of cross-links. The latter are formed only with additional pulses of light. This result was interpreted in terms of a model in which crosslinks can only be formed via the absorption of a photon by an appropriate monoadduct. Such a monoadduct appears only after a delay (long compared to the laser pulse-width) following the initial absorption of a photon by AMT; and the delay represents the time required for the excited AMT to form a monoadduct capable of further photoreacting. This time delay has now been measured and a mechanism for cross-linking is proposed.[2]

To measure the time delay, samples containing T4 DNA and AMT are subjected to two laser pulses separated by a variable time interval. Cross-linking is monitored as a function of the time between pulses. Experiments involving lasers are done in this laboratory. The third harmonic of a Nd: YAG laser and a nitrogen laser are used. Sample analysis is performed in Hearst's laboratory.

The degree of crosslinking is characterized by the ratio ds/(ds + ss) plotted as a function of time delay in Fig. 5. A distinct rise in the level of crosslinking is seen at a delay of about 1 μs. A plot of log (0.423 - ds/(ds + ss)) vs time delay, where 0.423 is the plateau level of ds/(ds + ss) for long time delays and gives a straight line, indicating a first-order process. The slope of this line yields a rate constant of $(7.9 \pm 2.2) \times 10^5\ s^{-1}$, or a 1/e lifetime of 1.3 ± 0.3 μs.

It is most likely that this delay is caused by a conformational change in the DNA in the region of the monoadduct. After formation of the initial cyclobutane bridge, some movement could be required to achieve the alignment of bonds

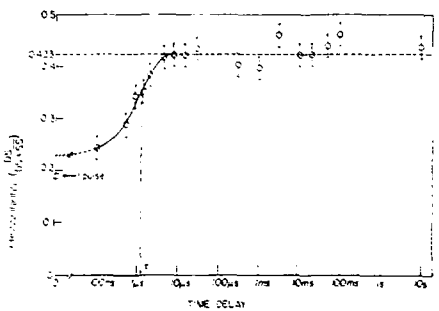

Fig. 5. Crosslinking as a function of time delay between the two laser pulses, corrected for fluctuations in Nd-YAG laser intensity using calibration curves showing the dependence of solution transmittance and quantum yield of monoaddition on intensity. Crosslinking is measured as the ratio ds/(ds + ss), where ds and ss are the peak heights of double- and single-stranded DNA peaks in the ultracentrifuge tracing. The dotted extension between 0 and 100 ns is an extrapolation based on first order kinetics. (XBL 813-8417)

between the unreacted end of the psoralen and the second pyrimidine base needed for completion of the crosslink. The time measured is of the order required for formation of a base pair or for the single-strand helix-to-coil transition. Similar motions may be taking place following formation of a monoadduct. It is known that the formation of a cyclobutane bridge introduces extra angle strain as long as the psoralen and pyrimidine moieties remain parallel. This conformational change involving some unstacking probably occurs in the region of the psoralen immediately after photoreaction to relieve angle strain.

As can be seen in Fig. 5, not all of the psoralen molecules capable of crosslinking require the 1 μs time delay. The crosslinking resulting from a single laser pulse can be ascribed to intercalation complexes which, because of their nucleotide sequence or other special condition, do not require a large conformational change before crosslinking can occur. This phenomenon is discussed separately by Johnston and Hearst.[3]

* * *

†This work was partially supported by the American Cancer Society, the National Institute of Health, and a National Science Foundation Grant for Chemical Instrumentation.

1. B. H. Johnston, M. A. Johnson, C. B. Moore, and J. E. Hearst, Science 197, 906 (1977).
2. B. H. Johnston, A. H. Kung, C. B. Moore, and J. E. Hearst, In press: Biochemistry (1980).
3. B. H. Johnston and J. E. Hearst, In press: Biochemistry (1980).

RESEARCH PLANS FOR CALENDAR YEAR 1981

The primary emphasis of research plans for 1981 is to understand the possibilities for and limitations of selective photochemical processes. Part of the efforts are devoted to the study of relaxation of selectively excited states to thermally heated states, part to chemical dynamics of the unrelaxed states, and part to the chemistry of the comparable thermal systems.

Research will include:

Spectroscopy and Kinetics of High Vibrational States. High overtone spectra of the C-H stretching motions of simple molecules in the visible region will continue to be studied. These spectra reveal the nature of coupling among vibrational modes and of collisionless intramolecular energy transfer for high vibrational states. The chemistry of these highly excited molecules will be observed. Bond selective vibrational photochemistry will be attempted, following single photon absorption into specific quantum states of these and more complex molecules in both gases and liquids.

Energy Transfer of Molecules on Surfaces. Initial experiments show that the vibrational relaxation of CO adsorbed on silica gel is orders of magnitude faster than for CO in matrices or pure liquid. Experiments are being extended to shorter time scales (a few nsec) and to alumina and metal surfaces. The ir laser-excited vibrational fluorescence technique is used.

Radical-Radical Reactions and Combustion Chemistry. Accurate values of the rate constants for radical-radical reactions are essential for the modeling of combustion processes. The use of laser flash kinetic spectroscopy for quantitative measurements of these combustion rates has recently been demonstrated in this laboratory. Accurate absolute radical concentration measurements are made simply by measurement of the laser power absorbed when radicals are produced by laser photodissociation. Approximate rate constants for H + HCO and HCO + HCO have been determined by monitoring HCO absorption following formaldehyde photolysis. The measured rates are one order of magnitude larger than those previously predicted and used for combustion modeling. It is proposed to refine the experimental system to produce rate constants as a function of temperature with better than 20% accuracy. The potential surface for the H + HCO reaction is being investigated by H. F. Schaefer's group. The combined results should produce an excellent model for this unusually fast reaction and should make possible accurate estimation of rate constants for experimentally inaccessible conditions.

Many radicals may be produced in high concentration by photolysis with uv excimer laser lines. It is also possible to study reactions between two molecular excited species. New types of reaction products may be expected for the same reasons that photochemically accessed reaction paths lead to different products than do thermal reaction paths.

1980 PUBLICATIONS AND REPORTS

Refereed Journals

†1. P. Hess and C. B. Moore, "Study of Energy Transfer in Methane by Excitation of Fundamental, Overtone, and Combination Bands," in Laser-Induced Processes in Molecules, eds. K. L. Kompa and S. D. Smith, Proceedings of the European Physical Society Divisional Conference, Edinburgh, Scotland, 1978, p. 33[illegible]. (1980).

‡2. C. B. Moore and I. W. M. Smith, "Vibrational Rotational Excitation - Chemical Reactions of Vibrationally Excited Molecules," Faraday Dis. Chem. Soc. 67, 146 (1980).

†3. F. E. Hovis and C. B. Moore, "Temperature Dependence of Vibrational Energy Transfer in NH_3 and $H_2{}^{18}O$," J. Chem. Phys. 72, [illegible]397 (1980).

§4. C. J. Dasch and C. B. Moore, "Single Quantum Vibrational Energy Transfer from HCl(v = 2) and HBr(v = 2)," J. Chem. Phys. 72, 4117 (1980).

§5. C. J. Dasch and C. B. Moore, "Experimental V → V Energy Transfer from Directly Excited

CO(v = 2) and DCl(v = 2)," J. Chem. Phys. 72, 5219 (1980).

6. J. S. Wong, "Pressure Broadening of Single Vibrational-Rotational Transitions of Acetylene at v = 5," J. Mol. Spectrosc. 82, 449 (1980).

‖7. P. Hess, A. H. Kung, and C. B. Moore, "Vibration → Vibration Energy Transfer in Methane," J. Chem. Phys. 72, 5525 (1980).

¶8. S. S. Miljanic and C. B. Moore, "Vibrational Relaxation of $D_2O(\nu_2)$," J. Chem. Phys. 73, 226 (1980).

LBL Reports

‡1. B. H. Johnston, A. H. Kung, C. B. Moore, and J. E. Hearst, "Kinetics of Formation of DNA Crosslinks by 4'-Amino-methyl-4,5', 8-Trimethyl-psoralen, Biochemistry," LBL-12164 (1980).

Other Publications

1. C. B. Moore, ed., Chemical and Biochemical Applications of Lasers, Vol. V, Academic Press, Inc., New York (1980).

Invited Talks

1. C. Bradley Moore, "Vibrational Chemistry," Avco Everett Research Laboratories. Everett, MA, December 20, 1979.

2. C. Bradley Moore, "Laser-induced Chemistry," University of British Columbia, Vancouver, B.C., March 4, 1980.

3. C. Bradley Moore, "Laser-induced Chemistry," University of Nebraska, NE, March 7, 1980.

4. C. Bradley Moore, "Bond Selective Excitation of Molecules," Sergio Porto Memorial Conference, Rio de Janeiro, Brazil, June 29 - July 3, 1980.

5. C. Bradley Moore, "Vibrational Photochemistry," Allied Chemical, Morristown, NJ, September 28, 1980.

6. C. Bradley Moore, "Bond Selectivity (?) Vibrational Photochemistry," Avco Everett Research Laboratories, Everett, MA, September 30, 1980.

7. Chi-ke Cheng, Hai-Lung Dai, C. Bradley Moore, and James S. Wong, "Overtone Spectroscopy in the Transition Region From Discrete to Quasicontinuous Levels," Second Chemical Conference of the North American Continent, Las Vegas, NV, August 24 - 29, 1980.

* * *

†Partially supported by the U. S. Air Force Office of Scientific Research and the U. S. Army Research Office, Triangle Park, NC.

‡Partially supported by the National Science Foundation.

§Solely supported by the U. S. Army Research Office, Triangle Park, NC.

‖Partially supported by the U. S. Air Force Office of Scientific Research.

¶Partially supported by the U. S. Army Research Office, Triangle Park, N.C. and the National Science Foundation.

d. Physical Chemistry with Emphasis on Thermodynamic Properties*

Kenneth S. Pitzer, Investigator

1. RELATIVISTIC EFFECTS ON COVALENT BONDING FOR HEAVY ATOMS AS EXEMPLIFIED IN TlH

Phillip A. Christiansen and Kenneth S. Pitzer

In recent years several relativistic effective-potential formalisms have been proposed.[1-5] In most of these, relativistic contributions, except for spin-orbit, are introduced into the molecular calculations via the effective potentials (EP). The spin-orbit effects are added later as some sort of perturbation. However, for molecules containing some of the sixth row elements such as Tl or Pb the spin-orbit contributions may be substantially larger than correlation effects and perturbation methods may be inadequate. For such cases it seems preferable to include the spin-orbit effects in the SCF step of the calculation. This is the procedure employed in the two-component molecular spinor formulation of Lee, Ermler, and Pitzer.[1] In this procedure, the molecular SCF computations are done directly in ω-ω coupling.

In the present work, we have extended the molecular spinor formalism of Lee, et al. in two important ways. First, we have generalized the ω-ω SCF procedure to include a multiconfiguration SCF treatment (MCSCF). This permits one to include the major effects of electron correlation and to obtain proper dissociation in all cases. In addition, we have replaced the previously used Phillips-Kleinman type EP formalism[6] with the much more accurate EP formalism developed by Christiansen, Lee, and Pitzer.[7]

For a first test of our procedure, we chose the thallium hydride molecule, for which good spectroscopic data are available.[8] TlH is particularly interesting due to the large $P_{1/2}$ - $P_{3/2}$ spin-orbit splitting for the single 6p electron. Since the lower energy (by nearly 1 eV) $p_{1/2}$ spinor is dominated by π character, partial promotion to $p_{3/2}$ is presumably required to form a strong bond with hydrogen which forms only sigma bonds.

In our molecular calculations we treat explicitly only the outermost 13 electrons of thallium (the 5d, 6s electrons and the single $6p_{1/2}$ electron). The relativistic contraction of the 6s atomic spinor causes a substantial energy gap between the 6s and 6p atomic spinor energies; hence, the bonding in TlH is somewhat similar to that in LiH, NaH, etc. Previous calculations for the ground states of the light alkali metal dimers and hydrides[9] indicate that one obtains a good approximation to the experimental bond energies by correlating only the two valence electrons using a relatively small MCSCF wavefunction.

We computed total molecular energies for the ground state of TlH using, (a) single determinant (essentially closed-shell Dirac-Fock), (b) two determinant (to obtain proper dissociation), and (c) five determinant MCSCF wavefunctions formed from two-component spinors. In the five-determinant calculation, various plausible configurations were introduced into exploratory calculations and the five most important were used in the final calculations. The internuclear separation was varied from 3 to 15 atomic units (a.u.). The mathematical details of our calculations are given in Refs. 10 and 11. Spectroscopic constants for the single determinant and MCSCF wavefunctions are listed in Table 1 along with single determinant values from previous calculations and the experimental values. Plots of our dissociation curves are given in Fig. 1.

With our five determinant MCSCF wavefunction we were able to obtain more than 85% of the experimental dissociation energy. Although similar calculations[12] for the light alkali metal dimers frequently obtain 90% or more of the bond energy, we believe that the combination of a somewhat poorer basis set and the smaller energy difference between the Tl 6s and 6p spinors (compared to that between the alkali metal valence s and inner-shell p electrons) could easily explain the difference. It is the large s-p separation which allows us to treat correlation in TlH as though there were only two valence electrons.

In the principal bonding spinor from our five configuration calculations, the $6p_{3/2}$ to $6p_{1/2}$ population ratio is approximately 0.6. However, this ratio shows a marked radial dependence relative to the Tl origin, varying from about 0.5 at the Tl nucleus to about 3.5 at infinity. (The ratio corresponding to a non-relativistic sigma orbital is 2.0). In the region near the H nucleus, the ratio is such that the Tl contribution to the

Table 1. Spectroscopic constants for TlH.

	Present				
	MCSCF	Single Conf.	Single Conf.[a]	Single Conf.[b]	Exp[c]
R_e (A)	1.96	1.93	1.84	1.87	1.87
D_e (eV)	1.66	0.93	1.55	--	1.97
ω_e (cm^{-1})	1330	1450	1450	1500	1391

[a]13 electron calculations employing Phillips-Kleinman type relativistic EPs from Ref. 1.
[b]One-center Dirac-Fock, Ref. 13.
[c]Reference 8.

*This work was supported by the Director, Office of Energy Research, Office of Basic Energy Sciences, Chemical Sciences Division of the U.S. Department of Energy under Contract No. W-7405-ENG-48.

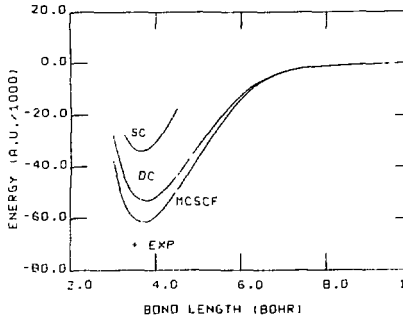

Fig. 1. Dissociation curves for single configuration (SC), double configuration (DC), and five configuration (MCSCF) calculations for the ground state of TlH. The minimum in the experimental curve is also indicated (+). (XBL 814-8977))

spinor is more than three-quarters sigma. Since the contribution from the hydrogen is almost exclusively 1s the bond appears to be principally sigma in character. Also, our results indicate some ionic character (Tl^+H^-) with about 0.3 extra electron population on the hydrogen, in close agreement with the earlier calculation.[1]

Very recently, Pyper[9] has claimed that the π component of the $p_{1/2}$ spinor will have a significant bonding interaction with the hydrogen atom; he calls this an "orthogonal triplet bond." We tested this proposal by making another two-configuration calculation excluding the $p_{3/2}$ spinor, but with no other change. The resulting energy is almost exactly that expected from the fractional sigma bond allowed by the $p_{1/2}$ spinor. Thus, the orthogonal triplet interaction makes no significant contribution to the bonding in TlH. Other evidence is cited in Ref. 11 which independently leads to the conclusion that the orthogonal triplet interaction is not important in molecules such as GaH, InH, or TlH.

* * *

1. Y. S. Lee, W. C. Ermler, and K. S. Pitzer, J. Chem. Phys. 73, 360 (1980). See also references cited therein.
2. P. Hafner and W. H. E. Schwarz, Chem. Phys. Lett. 65, 537 (1979).
3. G. Das and A. C. Wahl, J. Chem. Phys. 69, 53 (1978).
4. W. R. Wadt, P. J. Hay, and L. R. Kahn, J. Chem. Phys. 68, 1752 (1978).
5. S. N. Datta, C. S. Weig, and J. R. Van Wazer, Chem. Phys. Lett. 57, 83 (1978).
6. J. C. Phillips and L. Kleinman, Phys. Rev. 116, 287 (1959).
7. P. A. Christiansen, Y. S. Lee, and K. S. Pitzer, J. Chem. Phys. 71, 4445 (1979).
8. These studies are summarized by K. P. Huber and G. Herzberg, Molecular Spectra and Molecular Structure, IV. Constants of Diatomic Molecules, Van Nostrand Reinhold Co., New York, (1979).
9. N. C. Pyper, Chem. Phys. Lett. 73, 385 (1980).
10. P. A. Christiansen and K. S. Pitzer, J. Chem. Phys. 73, 5160 (1980).
11. K. S. Pitzer and P. A. Christiansen, Chem. Phys. Lett. 77, 589 (1981).
12. H. F. Schaefer III, The Electronic Structure of Atoms and Molecules, Addison-Wesley, Reading, MA, (1972).
13. P. Pyykkö and J. P. Desclaux, Chem. Phys. Lett. 42, 545 (1976).

2. ELECTRONIC STRUCTURE AND DISSOCIATION CURVES FOR THE GROUND STATES OF Tl_2 AND Tl_2^+ FROM RELATIVISTIC EFFECTIVE POTENTIAL CALCULATIONS

Phillip A. Christiansen and Kenneth S. Pitzer

Although dissociation energies and other spectroscopic parameters for the ground states of most of the group III homonuclear diatomic molecules have been determined experimentally,[1] to our knowledge this is not the case for Tl_2. Based on the failure to observe any Tl_2 signal in Tl vapor at approximately 900 K Drowart and Honig,[2] suggest an upper limit to the bond energy of Tl_2 of 0.9 eV. The only positive experimental data concerning Tl_2 appear to be the spectra of Ginter et al.,[3] which include emission bands in the range 15,300 to 16,000 cm^{-1} and absorption bands in the range 23,000 to 23,500 cm^{-1} for Tl vapor at about 1600 K. Unfortunately, for the present, a detailed interpretation of the spectra appears unfeasible; and there is no assurance that any of these bands involve the ground state of Tl_2. There is considerable interest in the properties of Tl_2 in relation to recent experiments on parity nonconservation in transitions in atomic thallium.[4]

Since, for many purposes, it can be considered to have only a single valence electron (due to the relativistic contraction, the 6s shell is substantially lower in energy), and because of the large spin-orbit splitting, almost 1 eV between the $6p_{1/2}$ and $6p_{3/2}$ spinors, Tl is a particularly interesting subject for heavy element bonding studies. Bonding between heavy atoms must be described in terms of spinors which are usually combinations of spin-orbitals of differing angular symmetry. This mixing of sigma, pi, etc., spin-orbitals is the result of the spin-orbit coupling as given by the Dirac equation. The thallium $6p_{1/2}$ spinor is composed essentially of 6p sigma and pi type spin-orbitals with coefficients of $\sqrt{1/3}$ and $\sqrt{2/3}$ respectively. One can show that a molecular spinor formed as a sum or difference of two such atomic spinors on different centers, retaining the overall g or u symmetry, must be either sigma-bonding and pi-antibonding or else sigma-antibonding and pi-bonding. For this reason, one would not expect the $p_{1/2}$ spinors alone to form substantial molecular bonds in Tl_2. Furthermore, in contrast to simple molecular orbital theory, this mixture

of bonding and antibonding character in our molecular spinor model for $p_{1/2}$ bonds makes a prediction of the relative stabilities of the bonds in the corresponding ions difficult. Thus, it is not obvious whether Tl_2^+ should be more or less strongly bonded than Tl_2.

Using the relativistic effective potentials and basis sets, generated for our TlH studies (the mathematical details are given in Refs. 5 and 6), potential energy curves were computed for the lowest 0_g^+, 0_u^-, and 1_u states of Tl_2 which dissociate to ground state atoms. For the 0_u^- and 1_u states, these were single configuration calculations. For the 0_g^+ state, this requires two configurations, the difference being a double excitation from a $1/2_g$ to $1/2_u$ spinor. Plots of the dissociation curves for these three states are shown in Fig. 2. As can be seen these curves show very little bonding character, and in fact the 1_u curve shows no minimum in this approximation.

Although there is no clear experimental evidence that the Tl_2 ground state is substantially bound, there is evidence that Tl_2^+ is stable.[7] For further comparison, we have computed curves for the lowest $1/2_g$ and $1/2_u$ states of Tl_2^+ using single configuration wavefunctions. Since no electron pairs are formed during bonding, we expect that correlation corrections for Tl_2^+ will be relatively small. Plots of these two curves are given in Fig. 3. The D_e and R_e values are 0.58 eV and 3.84 Å for $1/2_g$ and 0.06 eV and 3.50 Å for $1/2_u$, respectively.

Although further correlation corrections will certainly increase the well depths for the 0_g^+, 0_u^-, and 1_u states of Tl_2 we expect the corrections will be fairly small because of the relatively large bond lengths and because the molecular spinors are distorted only slightly from primitive combinations of atomic spinors. (Indeed, further calculations on the 0_g^+ state using an eight configuration MSCSF wavefunction lowered the potential minimum by only about 0.01 eV.) Nevertheless, the shallowness of the wells and the minimal separation between the three curves make impossible for the present any detailed conclusions regarding the dissociation energies, the locations of the minima, and even the relative order of these three states.

The underlying cause for such weak bonding is illustrated in Fig. 4 where we have plotted the potential curves for 0_g^+, 0_u^- and 1_u states of Tl_2 along with curves for the corresponding $^1\Sigma_g^+$, $^3\Sigma_g^-$ and $^3\Pi_u$ terms without spin-orbit coupling. These latter curves were computed as before but with the individual $p_{1/2}$ and $p_{3/2}$, etc. components averaged to eliminate the spin-orbit effect. Thus, other relativistic effects were retained. The

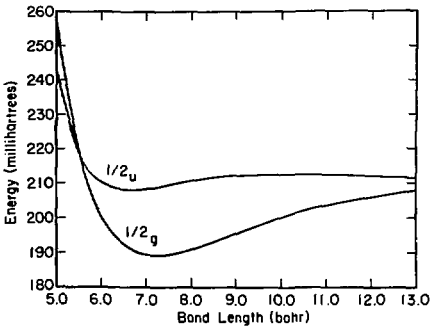

Fig. 3. Dissociation curves for the lowest $1/2_g$ and $1/2_u$ states of Tl_2^+. (XBL 814-8974)

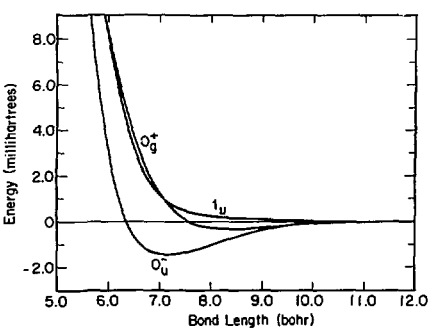

Fig. 2. Dissociation curves for the 0_g^+, 0_g^-, and 1_u states of Tl_2 which dissociate to ground-state atoms. (XBL 814-8975)

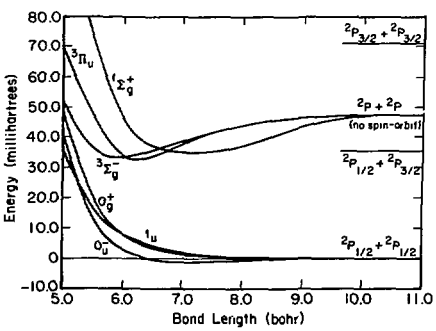

Fig. 4. Potential curves for the 0_g^+, 0_u^-, and 1_u states of Tl_2 with $^3\Sigma_g^-$, $^3\Pi_u$ and $^1\Sigma_g^+$ curves (computed without spin-orbit coupling for comparison. (XBL 814-8976)

$^1\Sigma_g^+$, $^3\Sigma_g^-$ and $^3\Pi_u$ curves have been placed at the proper energies with reference to the true $^2P_{1/2}$ and $^2P_{3/2}$ atoms and our calculated curves for the 0_u^-, 0_g^+ and 1_u molecular states. It is evident that in the absence of the spin-orbit effect, Tl_2 is a well-bound molecule in any of the $^1\Sigma_g^+$, $^3\Sigma_g^-$ or $^3\Pi_u$ states. However, the potential minima for these states are well above the energy for a pair of $^2P_{1/2}$ atoms. Hence, the absence of strong bonding in Tl_2 appears to arise from the spin-orbit term and is a purely relativistic effect.

With the introduction of the spin-orbit term, the $^1\Sigma^+$, $^3\Sigma^-$ and $^3\Pi_u$ states yield 1_g, 0_u^+, and 2_u relativistic states in addition to the 0_u^+, 0_u^-, and 1_u states which dissociate to ground state atoms. Although we did not compute full potential curves for these additional states, single configuration calculations in the bonding region indicated that the respective energies were well above those for the lowest three states. However, in view of the higher energies for their dissociated atoms, the 1_g, 0_u^+, and 2_u states may be more strongly bound with smaller R_e and larger D_e and ω_e values than for the lower energy states. The tentative R_e values are 3.02, 3.26, and 3.30 Å for the 1_g, 0_u^+, and 2_u states, respectively.

While we see possible assignments and, therefore, no conflict with the experimental spectra attributed t Tl_2, it is not worthwhile to suggest definite [illegible]ents until our calculations for excited [illegible] completed. At that time, we expect to disc[illegible] the spectral interpretation and various aspects of the bonding in these species.

* * *

1. K. P. Huber and G. Herzberg, Molecular Spectra and Molecular Structure IV. Constants of Diatomic Molecules, Van Nostrand Reinhold Co., New York, (1979).
2. J. Drowart and R. E. Honig, J. Phys. Chem. 61, 980 (1957).
3. D. S. Ginter, M. L. Ginter, and K. K. Innes, J. Phys. Chem. 69, 2480 (1965).
4. E. D. Commins, P. Buckshaun, L. Hunter, and P. Drell, Phys. Res. Lett. 42, 343 (1979); also Phys. Lett. 60A, 96 (1978).
5. P. A. Christiansen and K. S. Pitzer, J. Chem. Phys. 73, 5160 (1980).
6. P. A. Christiansen and K. S. Pitzer, J. Chem. Phys. 74, 1162 (1981).
7. J. Berkowitz and T. A. Walter, J. Chem. Phys. 49, 1184 (1968).

3. PHASE EQUILIBRIA FOR HIGHLY UNSYMMETRICAL PLASMAS AND ELECTROLYTES

Kenneth S. Pitzer

The classical Debye-Hückel equation indicates separation into two phases for a plasma or electrolyte with a highly unsymmetrical charge pattern, such as the solar plasma including highly ionized iron. Pollock and Alder[1] showed that the Debye-Hückel equation gave this result for solar conditions and discussed its implications for the solar neutrino dilemma. They also noted that Debye-Hückel theory was not valid for the iron-rich phase; thus a better theory is needed for reliable prediction of the phase behavior of solar plasma.

While the extension of Debye-Hückel theory to be presented below is approximate, it identifies the major correction needed and shows that the indication of phase separation was false. The present theory is based on classical (rather than quantum) mechanics for the translational motion of the ions (including dissociated electrons); in that domain, no phase separation is expected.

In a two-component system the possibility of phase separation is determined by the sign of the second derivative of the Gibbs energy with respect to the fraction of one component. Thus we wish to obtain for a mixture with a fixed total of N particles

$$\frac{\partial^2 G}{\partial x^2} = \frac{\partial^2 G^{id}}{\partial x^2} + \frac{\partial^2 G^{ex}}{\partial x^2} \qquad (1)$$

where G^{id} is the Gibbs energy on an ideal gas (or ideal solution) basis and G^{ex} is the excess Gibbs energy. The ideal term is always positive, and if it dominates, no phase separation is possible. But if the second derivative of the excess Gibbs energy becomes sufficiently negative, it may exceed the positive value of the ideal term and separation into two phases may occur.

It proves easier to discuss initially the excess internal energy E^{ex}. One then calculates the excess Helmholz energy by integrating the thermodynamic relationship $[\partial(A/T)/\partial(1/T)]_V = E$ from zero in 1/T to the final value and thereafter one adds the term $VP = -V(\partial A/\partial V)_T$ to obtain G.

The radial distribution functions provide the basis for understanding the present problem. The excess internal energy of the system is given by the equation

$$E^{ex} = 2\pi V \sum_i \sum_j c_i c_j \int_0^\infty u_{ij} g_{ij} r^2 dr \qquad (2)$$

where c_i, c_j are the concentrations of the particular species and V is the total volume for N particles. Also u_{ij} is the interparticle potential, in this case the coulombic potential $z_i z_j e^2/r_{ij}$. While Debye and Hückel developed their theory in other terms, it may be restated in this form with the results

$$g_{ij} = 1 - (z_i z_j e^2/kT)(e^{-\kappa r}/r) \qquad (3)$$

$$\kappa^2 = (4\pi e^2/kT) \sum z_i^2 c_i \qquad (4)$$

$$E^{ex} = G^{ex} = kTV\kappa^3/8\pi \ .$$

This expression for g_{ij} is a linear approximation of a Boltzmann exponential in which the exponent

is the last term in Eq. (3). Thus, the simple Debye-Hückel treatment fails if this exponent becomes larger than one for any appreciable range in r.

For the solar plasma, it is reasonable to assume that the iron is +24, i.e., retaining only the pair of 1s electrons undissociated, but the exact degree of ionization is not important. We also assume $T = 1.7 \times 10^7$ K (1.5 keV) and $P = 10^5$ Mbar. The radial distribution functions on a Debye-Hückel basis are shown on Fig. 5. The H^+-e^-, H^+-H^+, and e^--e^- functions depart only slightly from unity and are omitted. The Fe^{+24}-e^- and Fe^{+24}-H^+ functions exceed 2 and drop below zero, respectively, only at small r; hence, the error in these cases is moderate. However, the Fe^{+24}-Fe^{+24} function becomes large and negative over a major range in r, and this leads to a large and spuriously negative value of the integral in Eq. (2) for this term. A negative value of g_{ij} is, of course, physically impossible, and it arises only from the linear approximation in Eq. (3).

At very low concentration of iron, the factors c_{Fe} in Eq. (4) and c_{Fe}^2 in Eq. (2) are so small that little error is contributed by the Fe-Fe terms to the reciprocal length κ or the total excess energy in Eq. (5). However, the second derivative with respect to the fraction iron essentially removes the c_{Fe}^2 factor, and that term assumes full importance in comparison with the other terms in Eq. (2). A greatly improved approximation is obtained by a simple substitution of zero for the false negative value of g. Thus, if g_{ij} is zero at r'_{ij}, the corrected excess internal energy becomes

$$E^{ex} = -\frac{kTV\kappa^3}{8\pi} - 2\pi V \sum_i \sum_j c_i c_j \int_0^{r'} g_{ij} u_{ij}\, r^2 dr \qquad (6)$$

where the integral covers only that region where $g_{ij} < 0$.

In view of the approximate nature of this basic procedure, approximations were made in the expression for r' and in the conversion from E^{ex} to G^{ex}, but it was verified that these approximations would not significantly affect the final results. While the curve D-H on Fig. 6 for the simple Debye-Hückel equation shows a negative curvature from small x up to about 0.4 or 0.5, the "corrected" curve shows a substantial positive curvature across the entire composition range. Thus no phase separation is expected. Certain other approximations were explored and are discussed in the report of this work[2] but do not affect the over all conclusion.

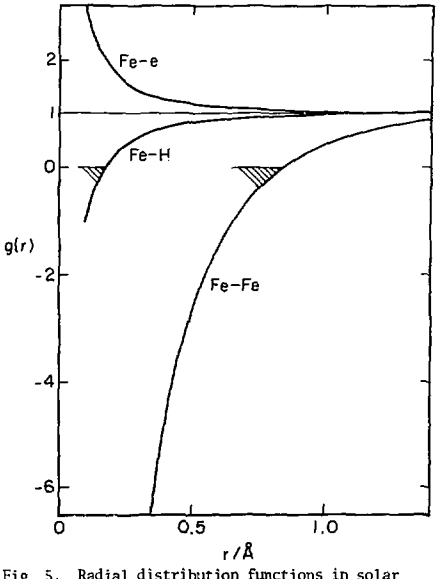

Fig. 5. Radial distribution functions in solar plasma according to classical Debye-Hückel theory. The negative regions are physically impossible and are removed in the corrected calculation. (XBL 814-8973)

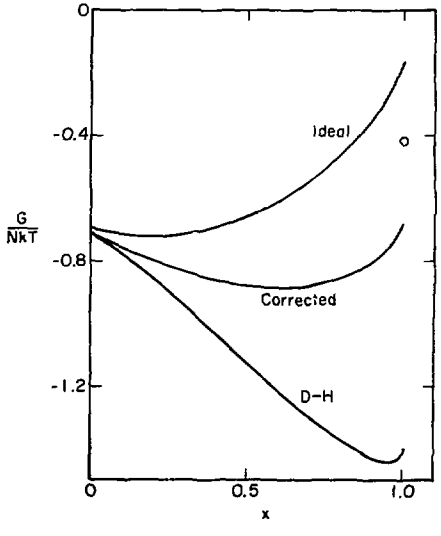

Fig. 6. The Gibbs energy for iron-hydrogen plasma under solar conditions. The curves are explained in the text. (XBL 814-8978)

* * *

1. E. L. Pollock and B. J. Alder, Nature 275, 41-43 (1978).
2. K. S. Pitzer, Proc. Nat. Acad. Sci. 77, 3103 (1980), LBL-10590.

4. DISSOCIATION ENERGIES OF MOLECULES WITH VERY HEAVY ATOMS FROM MASS SPECTROMETRY

Kenneth S. Pitzer

The dissociation energies of many molecules including heavy atoms have been measured by mass-spectrometric methods. In the "third law" method of treating the data, the partition functions are required. Thus, the electronic partition function of the molecule is needed. For molecules with very heavy atoms, relativistic effects yield large spin-orbit splittings and in some cases this reduced the electronic partition function by a significant factor. This is illustrated below for the two cases Pb_2[1] and BiLi[2].

In each of these cases, lighter analogs Si_2 and SbH have $^3\Sigma^-$ ground states; hence, the assumption made[1,2] of an electronic multiplicity of 3 was reasonable, prima facie. However, for BiH, it is known[3] that the J = 1 component of $^3\Sigma^-$ is 4917 cm^{-1} higher in energy than the J = 0 component. Thus, the case c or relativistic notation 1 and 0^+ is more appropriate, and there is a single 0^+ ground state. Even at the temperature of experiment, 1100 K, the population of the doubly degenerate 1 state is less than 1%. This spin-orbit splitting is essentially a property of the bismuth atom, and it should not be much different in BiLi. Thus the electronic partition function should be reduced from 3 to 1 and the function $-(G_T - H_0^\circ)/T$ reduced by R ln 3. The effect of this change is shown in Table 2 which includes both the original and revised values of ΔH_0° of dissociation from the third law. In addition, the temperature dependence of the equilibrium constant yields a less precise value of ΔH at the temperature of the experiment, and this can be converted to zero Kelvin. This is called the second law result and is not affected by this change in molecular parameters. While the 2nd law value for BiLi still differs from the more precise 3rd law value by more than the apparent uncertainty, the deviation is reduced by 10 kJ mol^{-1} by the use of the correct electronic multiplicity.

In the case of Pb_2, there are recent spectroscopic data from Bondybey and English[4] which confirms the ground state as 0_g^+, a single state. While there is no explicit value for the energy of excitation to the 1_g state (the other component of $^3\Sigma_g^-$), it is expected to be comparable to the spin-orbit splitting ($^3P_1$ - $^3P_0$) in the atomic spectrum, 7819 cm^{-1}. Thus, it is expected that the 1_g population at 1000 K will be negligible. For Pb_2, there is also a small revision[4] in the vibration frequency, 110 instead of 119 cm^{-1}. These two changes yield the results shown in Table 2. The third law result for Pb_2 now agrees very well with the second law value and gives much greater assurance of the correctness of the new selected value of 83 ± 1 kJ/mole (0.86 ± 0.01 eV).

Similarly large spin-orbit splittings may be expected for other molecules with very heavy atoms; thus, one should be cautious in adopting the electronic partition function of a lighter analog.

* * *

1. K. A. Gingerich, D. L. Cooke, and F. Miller, J. Chem. Phys. 64, 4027 (1976).
2. A. Neubert, H. R. Ihle, and K. A. Gingerich, J. Chem. Phys. 73, 1406 (1980).
3. K. P. Huber and G. Herzberg, "Molecular Spectra and Molecular Structure IV. Constants of Diatomic Molecules," Van Nostrand Reinhold, New York (1979).
4. V. E. Bondybey and J. H. English, J. Chem. Phys. 67, 3405 (1977).

Table 2. Revision of the dissociation energies of Pb_2 and BiLi.

	Pb_2	BiLi
Approximation temperature	1000	1100 K
Original ΔH_0° of diss. (3rd law)	74 ± 1	135.7 ± 1.1 kJ mol^{-1}
Revised ΔH_0° of dissoc. (3rd law)	82.5 ± 1	145.7 ± ? kJ mol^{-1}
ΔH_0° of diss. (2nd law) unchanged	84 ± 2	160 + 7 kJ mol^{-1}
Selected value	83 ± 1	150 ± 5 kJ mol^{-1}
Selected value in eV	0.86 ± .01	1.55 ± 0.05 eV

RESEARCH PLANS FOR CALENDAR YEAR 1981

The relativistic quantum chemistry program for molecules including very heavy atoms will be extended from diatomic molecules to polyatomic molecules with non-linear structures. This will allow more meaningful models of catalytic behavior to be explored in addition to stable molecules. While this extension of calculational methods will be the most important objective for next year, further calculations will be carried out for diatomic molecules of particular interest. Relativistic effects were shown to greatly reduce the bonding between atoms of Tl, but further work is needed to yield firm predictions of the excited-state as well as ground-state properties of Tl_2. The diatomic molecules Pb_2 and Pt_2 are also of great interest and calculations for one or both of them are planned. There is now a great interest in the relatively small relativistic effect in the energy difference between singlet and triplet methylene. We hope to handle this problem by more approximate methods of sufficient accuracy where no heavy atoms are involved.

An experimental program was initiated in 1980 for measurement of the thermodynamic properties of extremely concentrated aqueous electrolytes, including systems continuously miscible to the fused salt. The apparatus, now nearing completion, will be tested and probably modified to overcome unexpected problems. Measurements on systems of particular interest will then proceed, hopefully in the latter part of 1981 and continue into 1982. Exploratory studies for improved theoretical methods for these systems will also be carried forward as time allows. These extremely concentrated systems have received very little attention, hence their exploration is of considerable scientific interest. They are relevant to the behavior of concentrated brines of geological or industrial significance. Related aqueous electrolyte research for systems of more moderate concentration will continue with support from the geoscience program in the Earth Sciences Division at LBL.

1980 PUBLICATIONS AND REPORTS

Refereed Journals

1. Kenneth S. Pitzer, Electrolytes: "From Dilute Solutions to Fused Salts," J. Am. Chem. Soc. 102, 2902-6 (1980), LBL-9708.

2. Yoon S. Lee, Walter C. Ermler, and Kenneth S. Pitzer, "Ab Initio Effective Core Potentials Including Relativistic Effects: V. SCF Calculations with ω-ω coupling including results for Au_2^+, TlH, PbS, and PbSe," J. Chem. Phys. 73, 360-6 (1980), LBL-10101.

3. Kenneth S. Pitzer and J. Christopher Peiper, "Activity Coefficient of Aqueous $NaHCO_3$," J. Phys. Chem. 84, 2396-8 (1980), LBL-10298.

4. Kenneth S. Pitzer, "Phase Equilibria for Highly Unsymmetrical Plasmas and Electrolytes," in Proceedings of the Nat'l Academy of Sciences of the USA, 77, 3103-4 (1980), LBL-10590.

Other Publications

1. K. S. Pitzer, "Thermodynamics of Aqueous Electrolytes at Various Temperatures, Pressures, and Compositions," Chapter 23 in Thermodynamics of Aqueous Systems with Industrial Applications, edited by S. A. Newman, ACS Symposium Series [illegible], American Chemical Society, Washington, DC (1980).

2. K. S. Pitzer, "Theory: Ion Interaction Approach," Chapter 7 in Activity Coefficients in Electrolyte Solutions, edited by R. M. Pytkowicz, CRC Press, Inc., Boca Raton, FL (1979).

LBL Reports

1. Phillip A. Christiansen and Kenneth S. Pitzer, "Electronic Structure for the Ground State of TlH from Relativistic Multiconfiguration SCF Calculations," LBL-11210, submitted to J. Chem. Phys.

2. Phillip A. Christiansen and Kenneth S. Pitzer, "Electronic Structure and Dissociation Curves for the Ground States of [illegible] and Hg_2^+ from Relativistic Effective Potential Calculations," LBL-11512, submitted to J. Chem. Phys.

3. Kenneth S. Pitzer and Phillip A. Christiansen, "Relativistic Modifications of Covalent Bonding in Heavy Elements: Calculations for TlH," LBL-11611, submitted to Chem. Phys. Lett.

4. Kenneth S. Pitzer, "Dissociation Energies of Molecules with Very Heavy Atoms from Mass Spectrometry," LBL-11765, submitted to J. Chem. Phys.

e. Chemical Dynamics Studies*

Bruce H. Mahan, Yuan T. Lee, and John S. Winn, Investigators

1. OPTICAL SPECTRUM AND RADIATIVE LIFETIME OF SINGLET CH^+

Bruce H. Mahan and Anthony O'Keefe

Highly reactive, small organic cations are of great significance in both astrophysical processes and combustion chemistry. Such species are extremely difficult to study under controlled laboratory conditions, and information about them is fragmentary and often contradictory. Our recently completed studies of CH^+ and CD^+, using laser induced fluorescence (LIF), have produced a significant amount of unambiguous information about these ions.

The apparatus used in these studies has been described in detail elsewhere.[1] The ions were produced through the electron impact ionization and dissociation of CH_4 and CD_4. The $CH^+(CD^+)$ produced in this fashion constitutes ~ 3% of the total ion product, necessitating high mass selectivity in our studies. The $A^1\Pi \leftarrow X^1\Sigma^+$ system of the ion was studied under collision-free conditions using a pulsed dye laser with a short (~ 10 nsec) pulse duration. Although this system has been seen in optical emission studies, only the lowest few rotational levels have been observed. The LIF studies discussed here detected many rotational components and have resulted in an accurate determination of electronic term values for this system. Representative portions of the (0,0) bands for both CH^+ and CD^+ are shown in Figs. 1 and 2 respectively. The lines have been marked according to their position in the P, Q, or R branch of the band. Molecular constants were obtained from these data for both CH^+ and CD^+.

The short duration of the pumping laser pulse permits an unambiguous determination of the radiative lifetime of the $A^1\Pi$ state of the ion. We have measured the radiative lifetime of the v = 0 level of the $A^1\Pi$ state for both CH^+ and CD^+. The results for the CH^+ bandhead shown in Fig. 3 are significantly larger than those obtained by less reliable experimental techniques[4] but are in good agreement with ab initio calculations.[5]

* * *

1. F. J. Grieman, B. H. Mahan, A. O'Keefe, and J. Winn, "Discussions of the Faraday Society," No. 71 (1981).

*This work was supported by the Director, Office of Energy Research, Office of Basic Energy Sciences, Chemical Sciences Division of the U. S. Department of Energy under Contract No. W-7405-ENG-48.

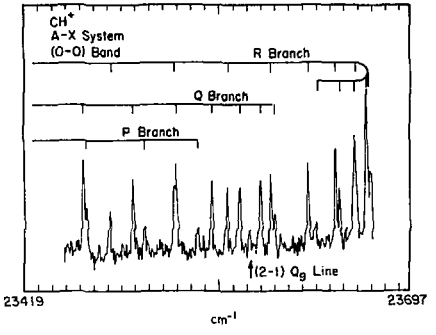

Fig. 1. LIF spectrum of the (0,0) band of the A-X system of CH^+. (XBL 808-11411)

2. A. E. Douglas and G. Herzberg, Can. J. Res. 20, 71 (1942).
3. A. Antić-Jovanović, W. Bojović, D. S. Pešić, and S. Weniger, J. Mol. Spec. 75, 197 (1979).
4. P. Erman, Ap. J. 213, L89 (1977).
5. M. Yoshimine, S. Green, and P. Thaddeus, Ap. J. 183, 899 (1973).

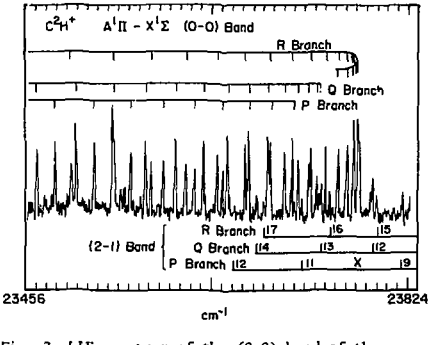

Fig. 2. LIF spectrum of the (0,0) band of the A-X system of CD^+. (XBL 808-11413)

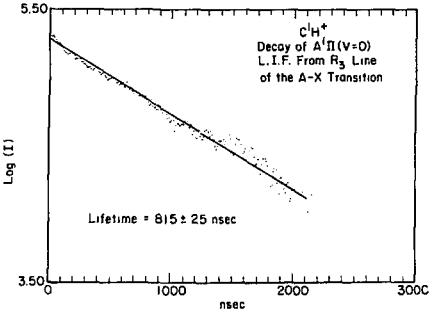

Fig. 3. Semilogarithmic plot of the fluorescence intensity vs time for CH^+ $A^1\Pi$ v = 0.
(XBL 808-11410)

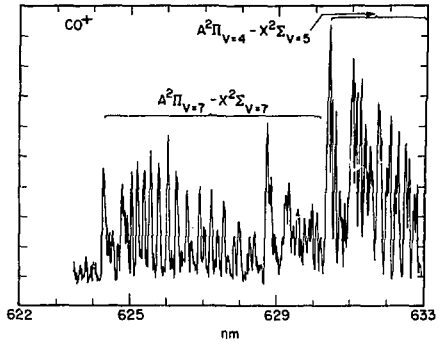

Fig. 4. Portions of the (7,7) and (4,5) bands of CO^+.
(XBL 808-11412)

2. INTERNAL STATE DISTRIBUTION OF ELECTRON IMPACT IONIZED CO^+

Bruce H. Mahan and Anthony O'Keefe

Within energy constraints, the direct electron impact ionization of a molecule will populate many vibrational and electronic levels of the resulting ion. For most ion-molecule reaction studies, the excited electronic state populations of the reactant ion can be easily monitored, but excited vibrational state populations are much more difficult to ascertain. The use of laser-induced fluorescence to probe population distributions of ground or metastable electronic states presents a convenient approach to this problem.

We have measured the relative populations for several vibrational levels of CO^+ produced by electron impact ionization. Most vibrational population of the $X^2\Sigma^+$ state results directly from the ionization and follows a regular Franck-Condon profile. A significant fraction of the ionization leaves the CO^+ in the first excited electronic state, $^2\Pi$. This population is spread out over several vibrational levels and quickly fluoresces to the $X^2\Sigma^+$ state. The distribution resulting from this cascading should be rather broad, based upon calculations of branching ratios for the fluorescence.[1]

We have used our ion trap to confine CO^+ under collision free conditions and have studied the vibrational state distribution using laser induced fluorescence.[2] We have found a substantial population residing in high vibrations of the $X^2\Sigma^+$ state. The relative intensities of the observed bands can be used to map out the entire population distribution if they are scaled by known or calculated Franck-Condon factors. Portions of two bands observed, the (7,7) and (4,5) bands, are presented in Fig. 4. Neither of these bands has been observed in previous emission studies indicating that much of the population in these levels results from the direct ionization process.

* * *

1. R. F. Holland and W. B. Maier II, J. Chem. Phys. 56, 5229 (1972).
2. J. S. Winn, In press: "Molecular Ions: Electronic and Geometric Structure," Proceedings of the NATO Advanced Study Institute (1981).

3. COLLISIONAL HEATING OF ROTATIONAL STATES OF N_2^+

Bruce H. Mahan and Anthony O'Keefe

Conventional high pressure ion sources and flow tube systems make use of the many collisions an ion or radical experiences to help relax any excited electronic, vibrational, and rotational states the ion may possess. Active ion storage devices, such as an rf trap, have been shown to drive the motion of the contained ion . Recent studies of ions in a trap of the type used in our lab revealed a velocity distribution consistent with a translational temperature of several thousand degrees Kelvin.[1] We have utilized this driven motion to internally excite molecular ions by inducing collisions with an inert buffer gas. To monitor the effect of collisions on the rotational and vibrational distributions, we record laser-induced fluorescence spectra of an ion as a function of buffer gas pressure.

A convenient system to study this effect with is the N_2^+ ion, using the $B^2\Sigma$ - $X^2\Sigma$ transition as a monitor. This electronic transition has been studied previously;[2] and, under collision-free conditions, the rotational temperature of the trapped ions is essentially room temperature (300 K). The vibrational temperature is apparently much higher, reflecting the Franck-Condon overlap

of the ion with the ground state neutral molecule. The effect of collisions of the N_2^+ with Ar is seen in Fig. 5, where a, b, c, and d correspond to 0, 5, 25, and 50 collisions, respectively. Because the ions possess a large amount of translational energy, the usual estimates of ion-molecule collision rates are not accurate, and the collision numbers cited above provide only upper bounds to the true value.

The presence of a long sought $^4\Sigma^+$ state of N_2^+ has been recently cited as the cause of a reported perturbation in several high rotational levels (N' = 30, 31) of the $B^2\Sigma$ state.[3] Using the collisional heating effect, we have been able to pump substantial population into the levels in quation. Our studies[4] demonstrate that there is, in fact, no significant perturbation present which cannot be attributed to other causes.

Work is in progress to study this heating effect in other molecular ions, especially CO^+ which, while isoelectronic, is not homonuclear.

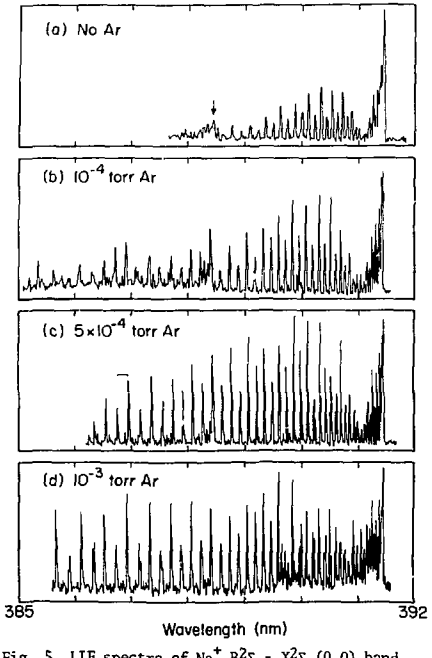

Fig. 5. LIF spectra of N_2^+ $B^2\Sigma$ - $X^2\Sigma$ (0,0) band. Figures a, b, c, and d show the rotational distribution of N_2^+ after 0, 5, 25 and 50 collisions respectively. (XBL 8011-7450)

* * *

1. R. D. Knight and M. H. Prior, J. Appl. Phys. 50, 3044 (1979).
2. F. J. Grieman, "Laser Induced Fluorescence of Trapped Molecular Ions," Ph.D. thesis, LBL-10021 (1979).
3. J. Dufayard, thesis, L'Universite Scientifique et Medicale de Grenoble (1977).
4. B. H. Mahan and A. O'Keefe, LBL-12026.

4. *ELECTRONIC STATE COMPOSITION OF ION BEAMS*

Bruce H. Mahan and Steven G. Hansen

Open shell atomic and molecular ions are often produced under ionizing conditions that lead to excited electronic states, many of which are optically metastable. Collision studies that use ion beams produced by such conditions cannot be properly interpreted without knowledge of the extent of such electronic excitations. As described in previous reports from this group, we have used beam attenuation measurements to analyze ion state compositions. This technique relys on the differences in charge transfer cross sections between different electronic states.

We have recently[1] extended these analyses by measuring, not only attenuations, but also the total luminescence produced by an ion beam traversing a scattering gas. An example of the type of data obtained in these experiments, is shown in Fig. 6. This figure shows plots of total luminescence (normalized to the total beam current) versus lab energy for O^+ ions traversing a scattering cell of, respectively, CO, N_2O, and H_2S. The O^+ was produced either by electron impact on CO_2(X) or by a microwave discharge through O_2 (circles). The relevant states of O^+ are the 4S ground state and the ^2D metastable state. With CO and N_2O, the charge transfer reaction from $O^+(^2D)$ to low-lying vibrational levels of the excited ions CO^+ ($A^2\pi$) and N_2O^+(A). For H_2S, charge exchange from the ground state of O^+ to the excited state of H_2S^+ is more favorable. Attenuation measurements had shown previously that the microwave discharge source produces ground state O^+ almost exclusively, while the electron impact source produces a significant amount of $O^+(^2D)$. The data in Fig. 6 are consistent with our expectations as to the relative amounts of these states.

This method was used in a similar fashion to probe the electronic state composition of F^+ beams. Ground state F^+, ^3P, is separated by 2.5 eV from a metastable ^1D state and by 5 eV from a metastable ^1S state. Total luminescence studies from various gases, summarized in Table 1, indicate indicate that all sources produce ground state F^+ almost exclusively.

* * *

1. S. G. Hansen, Ph.D. thesis, LBL-11208.

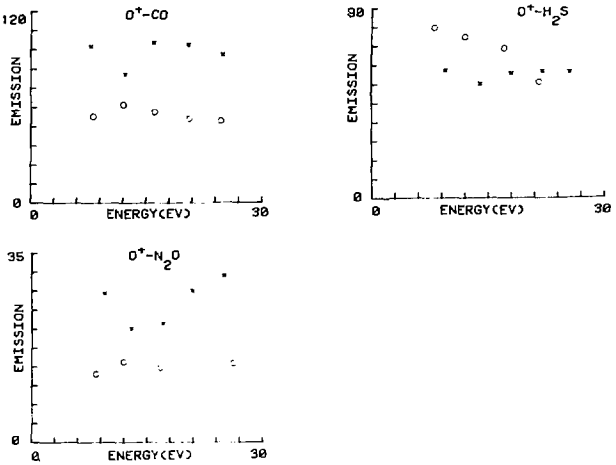

Fig. 6. Plot of total luminescence in thousands of photons/sec/nA of beam current vs lab kinetic energy for O^+ produced by electron impact on CO_2(x) and microwave discharge (circles) through O_2 using CO, N_2O, and H_2S as collision partners. (XBL 807-10772)

Table 1. Total luminescence intensity measured for the indicated ions colliding with the indicated collision partners at 25 eV. The values are normalized.

	F^+					
	160 Electron Impact On			μ Wave Discharge	Ne^+ 160 eV Elec. Impact	Ar^+ 160 ev Elec. Impact
Gas	CF_4	NF_3	SF_6	CF_4:NO 2:1		
N_2	9.4	9.6	8.6	10.7	6.0	0.9
CO_2	96	98	98	92	9.7	0.2
CO	63	64	65	64	1.2	5.2
C_2H_2	4.1	4.9	3.8	–	–	–

RESEARCH PLANS FOR CALENDAR YEAR 1981

We have begun studies of the fragmentation processes important in the production of CH^+. Using isotope enriched reactant molecules, we plan to investigate the energy disposal pathways that play important roles in the formation of this ion. In addition, we will attempt to monitor the residence lifetime of ions in our trap as a function of vibrational level. Such data will provide information on both the natural lifetime of excited vibrations in molecular ions and on the variation in reactivity of the ion with vibrational excitation.

Work has begun in the reaction dynamics of S^+ with D_2. The reaction $S^+(D_2,D)\ SD^+$ is 0.9 eV endothermic but should have dynamical features in common with the well studied $O^+(H_2,H)OH^+$ system. Preliminary results show a direct mechanism producing SD^+ but with a lower cross-section than that seen in the O^+ system. The relative velocity or centerline distribution of SD^+ shows a maximum near the spectator stripping velocity. Non-reactive S^+ scattering by D_2 appears to be very elastic in nature. These and other aspects of this system will be investigated further.

1980 PUBLICATIONS AND REPORTS

Refereed Journals

1. S. G. Hansen and B. H. Mahan, J. Chem. Phys. 73, 2200 (1980), LBL-9806.

2. F. J. Grieman, B. H. Mahan, and A. O'Keefe, J. Chem. Phys. 72, 4246 (1980), LBL-10297.

3. S. G. Hansen, J. M. Farrar, and B. H. Mahan, J. Chem. Phys. 73, 3750 (1980), LBL-10965.

LBL Reports

1. F. J. Grieman, B. H. Mahan, A. O'Keefe, and J. S. Winn, "Laser Induced Fluorescence of Trapped Molecular Ions: The CH^+ $A^1\Pi \rightarrow X^1\Sigma^+$ System," In press: Discussions of the Faraday Society No. 71, LBL-11534.

2. B. H. Mahan and A. O'Keefe, "Rotational Excitation and Radiative Lifetimes of N_2^+," LBL-12026.

3. F. J. Grieman, B. H. Mahan, and A. O'Keefe, "The Laser Induced Fluorescence Spectrum of Trapped BrCN Cations," In press: J. Chem. Phys., LBL-11208.

4. Steven George Hansen, "Ion-Molecule Interactions in Crossed Beams," Ph.D. thesis, LBL-11208.

Invited Talks

1. F. J. Grieman, B. H. Mahan, A. O'Keefe and J. S. Winn, "Laser Induced Fluorescence Studies of Mass Selected Molecular Ions," Thirty-fifth Symposium on Molecular Spectroscopy, Ohio State University, Columbus, OH, June 16-20, 1980.

2. B. J. Mahan, A. O'Keefe, and J. S. Winn, "Laser Induced Fluorescence Studies of CH^+ (CD^+) $A^1\Pi \rightarrow X^1\Sigma^+$," Thirty-fifth Symposium on Molecular Spectroscopy, Ohio State University, Columbus, OH, June 16-20, 1980.

f. Theory of Low-Energy Atomic and Molecular Collision Processes*

William H. Miller, Investigator

1. COLLISION INDUCED ABSORPTION SPECTRA FOR GAS PHASE CHEMICAL REACTIONS IN A HIGH POWER IR LASER FIELD†

Ann E. Orel and William H. Miller

Our earlier work[1] has shown how high power infrared lasers can affect the mechanics of reactive collisions, for example, of the type A + BC → AB + C. This work investigates another aspect of this collision induced absorption (CIA) process, namely, the absorption spectrum of the laser which results from the collisional system. For systems which absorb only during the reactive collision process, observation of this CIA is essentially an "infrared spectroscopy of the transition state," the observation and analysis of which would provide direct information about the reaction mechanics in the transition state region of the potential energy surface.

Calculations were carried out using a previously developed classical model[2] for treating the molecular and the laser systems in a dynamically consistent way. Examples of direct and of complex-forming reactions were studied, and the collision-induced absorption spectra show significant differences between the two reactions. All calculations were carried out on a Harris Slash Four minicomputer funded by a National Science Foundation Grant CHE79-20181.

* * *

†Brief version of J. Chem. Phys. 72, 5139 (1980).
1. A. E. Orel and W. H. Miller, Chem. Phys. Lett. 47, 362 (1978); J. Chem. Phys. 70, 4393 (1979).
2. See, for example, E. Bar-Ziv, and S. Weiss, J. Chem. Phys. 64, 241, 247 (1976).

2. CLASSICAL MODEL FOR LASER-INDUCED ELECTRONICALLY NON-ADIABATIC COLLISION PROCESSES†

Ann E. Orel and William H. Miller

The classical model we have developed[1] (and applied[2]) for treating the interaction of IR lasers with the heavy particle mechanics of molecular systems has been generalized to incorporate electronically non-adiabatic processes induced by visible lasers. This is a "completely classical" model because, not only are the heavy particle degrees of freedom (i.e., translation, rotation, and vibration) modeled classically, but so are the electronic degrees of freedom of the molecular system and those of the laser itself. This makes numerical calculations relatively easy within a classical trajectory approach.

The specific system investigated is a collinear model of the following laser-induced reaction

$$LiF + H + h\nu \rightarrow Li^{*} + HF .$$

Figure 1 shows the reaction probability calculated for this reaction as a function of initial translational energy. The dotted line is the result with no laser present, and one sees that the reaction has a classical threshold of ~3.8 eV. The other curves are the results obtained with a laser, and one sees that the reaction is affected dramatically. The structure in the laser-induced cross section can be explained in terms of a simple Franck-Condon argument. All calculations were carried out on a Harris Slash Four minicomputer funded by a National Science Foundation Grant CHE79-20181.

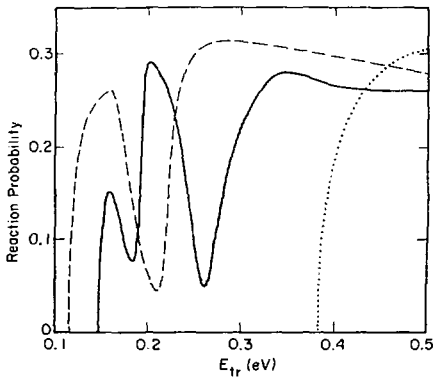

Fig. 1. Total reaction probability for H + LiF → HF + Li as a function of the initial translational energy E_{tr}, from a quasiclassical trajectory calculation. LiF is initially in its ground vibrational state. The dotted curve is the laser-free result. The other two curves are for a laser frequency $\hbar\omega$ = 6.2 eV, the laser power being such that $\mu_{01}E_0$ = 0.01 eV (solid curve) and 0.008 eV (dashed curve). (XBL 802-8045)

*This work was supported by the Director, Office of Energy Research, Office of Basic Energy Sciences, Chemical Sciences Division of the U.S. Department of Energy under Contract No. W-7405-ENG-48.

* * *

†Brief version of J. Chem. Phys. 73, 241 (1980).
1. W. H. Miller, J. Chem. Phys. 69, 2188 (1978).
2. A. E. Orel and W. H. Miller, Chem. Phys. Lett. 57, 362 (1978); J. Chem. Phys. 70, 4393 (1979); Ibid. (to be published).

3. REACTION PATH MODEL FOR TUNNELING IN THE HNC → HCN UNIMOLECULAR ISOMERIZATION†

Stephen K. Gray, William H. Miller, Yukio Yamaguchi and Henry F. Schaefer III

The recently developed reaction path Hamiltonian model[1] is applied to the unimolecular isomerization

$$HNC \rightarrow NCN \ .$$

The reaction path, and the energy and force constant matrix along it, are calculated at the SCF level with a large ("double zeta plus polarization") basis set. The microcanonical rate constant k(E) for the reaction is computed within the "RRKM plus tunneling" model[2] in the energy region near and below the classical threshold.

Figure 2 shows k(E) as a function of energy E relative to the classical barrier height V_{sp}. The arrow on the energy scale indicates the classical threshold of the reaction, i.e., the "zero point energy corrected" barrier height.

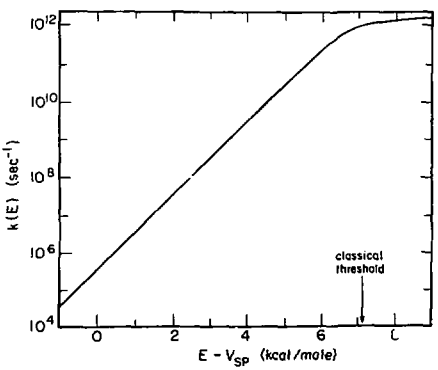

Fig. 2. Microcanonical rate constant for zero total angular momentum for the reaction HNC → HCN, as a function of total energy relative to the barrier height. The classical threshold, which is indicated, includes the effect of zero point energy of the transition state; i.e., it is the value $E = V_{sp} + 1/2\,[\hbar\omega_1(0) + \hbar\omega_2(0)]$. (XBL 806-9866)

One sees that unimolecular rates as fast as 10^5 sec^{-1} can occur at energies ~8 kcal/mole below the classical threshold. All calculations were carried out on a Harris Slash Four minicomputer funded by a National Science Foundation Grant CHE79-20181.

* * *

†Brief version of J. Chem. Phys. 73, 2733 (1980).
1. W. H. Miller, N. C. Handy, and J. E. Adams, J. Chem. Phys. 72, 99 (1980).
2. W. H. Miller, J. Am. Chem. Soc. 101, 6180 (1979).

4. MODEL STUDIES OF MODE-SPECIFICITY IN UNIMOLECULAR REACTION DYNAMICS†

Boyd A. Waite and William H. Miller

Essentially exact quantum mechanical calculations are carried out to determine the energies and lifetimes of the quasi-bound states for a system of two (non-linearly) coupled oscillators, one of which is harmonic, the other being able to dissociate. For weak coupling the system displays mode-specificity, i.e., the unimolecular rate constants are not a monotonic function of the total energy. However, increased coupling and frequency degeneracy tends to destroy mode-specificity. A somewhat surprising result is that, for a given coupling, the degree of mode-specificity is roughly independent of the energy. This in marked contrast to the fact that there is an energetic threshold for the onset of "stochastic trajectories" of the corresponding classical system; i.e., there seems to be no relation between statistical/mode-specific behavior of the unimolecular rate constants and stochastic/regular classical trajectories. In order to be able to treat more physically relevant models--i.e., those with more than two degrees of freedom, a semiclassical model is constructed and seen to be able to reproduce the accurate quantum mechanical rates reasonably well.

Figure 3 shows the unimolecular decay rates (i.e., inverse lifetimes) of the quasibound states versus their energy for the uncoupled case. This shows complete mode specificity; i.e., the rate depends not only on the total energy but on how the energy is partitioned between the two modes. Figure 4 shows a case for which there is efficient coupling between the two modes, and here the rate constants are approximately a function only of the total energy of the system. One interesting aspect of these results is, as noted above, that the degree of mode-specificity does not appear to be a sensitive function of energy. All calculations were carried out on a Harris Slash Four minicomputer funded by a National Science Foundation Grant CHE79-20181.

* * *

†Brief version of J. Chem. Phys. 73, 3713 (1980).

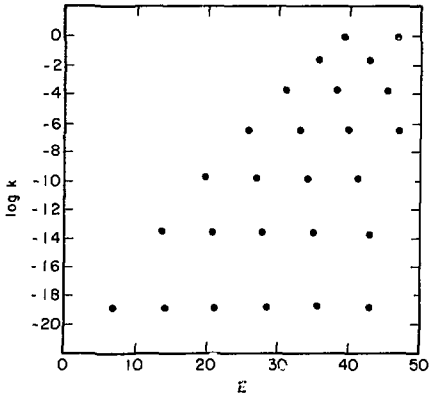

Fig. 3. Rate constants, $k \equiv \Gamma/\hbar$, for unimolecular decay versus total energy E, for the quasi-bound states of the two-oscillator system. This case is for no coupling between the two modes.
(XBL 806-10267)

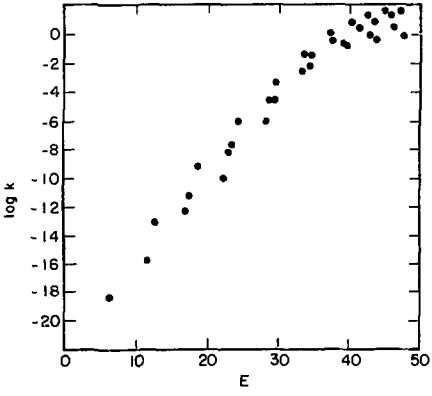

Fig. 4. Same as Figure 3, except for coupling between the two modes. (XBL 806-10273)

5. *FURTHER DEVELOPMENT OF THE REACTION PATH FORMULATION OF POLYATOMIC REACTION DYNAMICS*†

William H. Miller

Several developments and new applications of the recently developed reaction path Hamiltonian model[1] for polyatomic reaction dynamics are described: (1) The original form of the Hamiltonian is transformed so that the coupling between vibrational modes normal to the reaction path appears in the *potential rather than in the kinetic energy* of the Hamiltonian. This is easier to deal with in some applications. (2) It is shown that the unified statistical model[2] takes an extremely simple form within the reaction path Hamiltonian model. Also, a generalized version of the unified statistical model is derived that permits an arbitrary number of "bottlenecks" (flux minima) along the reaction path. (3) A generalized Langevin equation[3] is derived for motion along the reaction path. This is an equation of motion for only one degree of *freedom, the reaction coordinate*, but it experiences "friction" and "random" forces that are due to coupling with the vibrational modes normal to the reaction path.

* * *

†Abstracted from ACS Symp. Series.

1. W. H. Miller, N. C. Handy, and J. E. Adams, J. Chem. Phys. 72, 99 (1980).
2. W. H. Miller, J. Chem. Phys. 65, 2216 (1976).
3. See, for example, S. A. Adelman and J. D. Doll, J. Chem. Phys. 61, 4242 (1974); J. Chem. Phys. 64, 2375 (1976).

RESEARCH PLANS FOR CALENDAR YEAR 1981

Polyatomic Reaction Dynamics. The approach based on the reaction path Hamiltonian offers the possibility of an *ab initio* treatment of many aspects of reaction dynamics in small polyatomic systems. More accurate treatments of the tunneling dynamics in the unimolecular dissociation of *formaldehyde*,

$$H_2CO \rightarrow H_2 + CO \ ,$$

and some other similar examples are planned. This work is in collaboration with quantum chemical calculations by H. F. Schaefer's group for the potential energy surfaces.

Plans are also to pursue and develop the generalized Langevin model mentioned in article 5 above. This should make it possible to model a complex reaction by treating a small sub-system fully dynamically and the remainder of the system as a statistical "bath."

Mode-Specific Chemistry. Further studies are planned on the features responsible for mode-specificity in chemical reactions. An interesting example would be the formaldehyde dissociation above, i.e., to see if the dissociate rate depends on whether the vibrational energy in H_2CO is initially in a C-H stretch, C-O stretch, the out-of-plane bend, etc.

Semiempirical Valence Bond Model. The diatomics-in-molecules (DIM) model for constructing electronic potential energy surfaces has been quite useful in some interesting cases: H_3, FH_2, CH_2, etc; but this approach bogs down when applied to much more complicated systems. Plans are underway to develop a semiempirical valence bond model, also based on diatomic input, which is similar in many ways to the DIM model but capable of much more general and fascile application.

1980 PUBLICATIONS AND REPORTS

Refereed Journals

1. W. H. Miller, N. C. Handy, and J. E. Adams, "Reaction Path Hamiltonian for Polyatomic Molecules," J. Chem. Phys. 72, 99 (1980), LBL-9275.

2. W. H. Miller, "Reply to a Comment on 'A Classical/Semiclassical Theory for the Interaction of Infrared Radiation with Molecular Systems,'" J. Chem. Phys. 72, 788 (1980), LBL-9765.

3. H.-D. Meyer and W. H. Miller, "Analysis and Extension of Some Recently Proposed Classical Models for Electronic Degrees of Freedom," J. Chem. Phys. 72, 2272 (1980), LBL-9910.

4. A. E. Orel and W. H. Miller, "Collision Induced Absorption Spectra for Gas Phase Chemical Reactions in a High Power IR Laser Field," J. Chem. Phys. 72, 5139 (1980), LBL-9999.

5. A. E. Orel and W. H. Miller, "Classical Model for Laser-Induced Non-Adiabatic Collision Processes," J. Chem. Phys. 73, 241 (1980), LBL-10445.

6. S. K. Gray, W. H. Miller, Y. Yamaguchi and H. F. Schaefer, "Reaction Path Hamiltonian: Tunneling Effects in the Unimolecular Isomerization HNC → HNC," J. Chem. Phys. 73, 2733 (1980), LBL-10953.

7. C. W. McCurdy and W. H. Miller, "Progress in the Application of Classical S-Matrix Theory to Inelastic Collision S-Matrix Theory to Inelastic Collision Processes," J. Chem. Phys. 73, 3191 (1980), LBL-11003.

8. B. A. Waite and W. H. Miller, "Model Studies of Mode-Specificity in Unimolecular Reaction Dynamics," J. Chem. Phys. 73, 3713 (1980), LBL-11038.

Other Publications

1. W. H. Miller, "Chemical Dynamics," in McGraw-Hill Encyclopedia of Science and Technology, 5th Edition.

2. W. H. Miller, "Reaction Path Hamiltonian for Polyatomic Systems: Further Developments and Applications," in ACS Symp. Series.

LBL Reports

1. S. K. Gray, W. H. Miller, Y. Yamaguchi, and H. F. Schaefer, "Tunneling in the Unimolecular Decomposition of Formaldehyde, a More Quantitative Study," in press: J. Am. Chem. Soc., LBL-11361.

2. Y. Osamura, H. F. Schaefer, S. K. Gray, and W. H. Miller, "Vinylidene, a Shallow Minimum on the C_2H_2 Potential Energy Surface: Static and Dynamical Considerations," In press: J. Am. Chem. Soc., LBL-11625.

Invited Talks

1. W. H. Miller, "Reaction Path Hamiltonian for Polyatomic Molecules," International Symposium on Atomic, Molecular, and Solid-State Theory, Collision Phenomena, and Computational Quantum Chemistry, in honor of Professor E. Bright Wilson, Daytona Beach, March 10-15, 1980.

2. W. H. Miller, "A New Classical Model for Electronically Non-Adiabatic Collision Processes," Frontiers in Chemistry Lecture, Wayne State University, Detroit, April 21, 1980.

3. W. H. Miller, "Reaction Path Hamiltonian for Polyatomic Molecules," Symposium honoring Henry Eyring in his 80th year, Northwest Rocky Mountain Meeting of the American Chemical Society, Salt Lake City, June 12-14, 1980.

4. W. H. Miller, "Model Studies of Mode-Specificity in Unimolecular Rate Constants," Bielefeld Workshop on Energy Scrambling in Molecules, Bielefeld, Germany, July 3-12, 1980.

5. W. H. Miller, "Reaction Path Hamiltonian and its Application to Unimolecular Reaction Dynamics," Symposium on Potential Energy Surfaces and Dynamics Calculations, American Chemical Society National Meeting, Las Vegas, August 24-29, 1980.

g. Photoelectron Spectroscopy*

David A. Shirley, Investigator

Introduction. The main research theme in this program is electron spectroscopy, with emphasis on spectroscopic studies based on synchrotron radiation research in the 6-4000 eV range, supported by research with laboratory sources. Emphasis is given to new types of experiments, based on new effects. The projects completed in 1980 divide naturally into two groups: (a) surface science research and (b) gas-phase research. These are discussed separately below.

Overview of Surface Science Research

Photoelectron diffraction provided the main focus of our 1980 surface-science research (articles 1-4). A new method of analysis--Fourier transformation photoelectron diffraction (FTPD)--was conceived and tested on theoretical scattering curves, yielding peaks at perpendicular interlayer distances (article 1) and establishing an analogy with EXAFS. FTPD was applied to data from adsorbate chalcogenides on nickel (article 2). The analogy of photoelectron diffraction with surface EXAFS was also pursued through temperature-dependence studies (article 3). Finally, the first two applications of photoelectron diffraction to molecular adsorbates were completed and analyzed (article 4).

Near-edge studies of the C(1s) photoelectron current from adsorbed CO yielded the first observation of a core-level "shape resonance" and established a substrate dependence (article 5). Another absorption edge-EXAFS study was initiated, this one on the sulfur K-edge, newly accessible to study on a new beam line at SSRL (article 6). Finally, XPS and UPS studies of samarium metal clusters showed the first unambiguous evidence for size-dependent valency changes (article 7).

1. FOURIER-TRANSFORM ANALYSIS OF NORMAL PHOTOELECTRON DIFFRACTION DATA FOR SURFACE-STRUCTURE DETERMINATION†

Z. Hussain, D. A. Shirley, C. H. Li,‡ and S. Y. Tong§

Following the prediction by Liebsch[1] that diffraction effects are present in photoemission from adsorbate-atom core levels, such effects have been observed in several experimental configurations. In each case, comparison of experimental results with curves derived from microscopic theory based on certain surface structures showed good agreement, thereby establishing photoelectron diffraction (PD) as a technique for structure determination. In this article, we propose a direct and explicit method for analysis of normal photoelectron diffraction (NPD) data which is independent of model calculations.

First, we note some similarities between NPD and EXAFS, in which both differ from LEED. The intensity-versus-energy (I/E) curve in NPD is similar in appearance to either a LEED I/V curve or an EXAFS absorption curve. However, like the latter, NPD is atom-specific. Just as in EXAFS, where multiple scattering effects are unimportant and/or average out and single-scattering theory prevails,[2] the modulation pattern in NPD at higher kinetic energies depends largely on single backscattering. Finally, in NPD, as in EXAFS, the periodicity in k space of the sinusoidal modulation increases with decreasing $d_\perp$ where the theoretical curves are calculated over a small range of $d_\perp$. These similarities suggest that Fourier transformation of NPD I/E curve might yield distances directly, as in EXAFS.

Figure 1(a) shows the theoretically calculated normalized NPD intensity, $\chi(k)$, plotted against k for $(\sqrt{3} \times \sqrt{3})$ R30° Se(3d)-Ni(001) system. Figure 1(b) shows F(r), the magnitude of Fourier transform of the $\chi(k)$ shown in Fig. 1(a). Four prominent peaks occur in F(r), at 2.83 Å, 4.49 Å, 6.66 Å and 8.66 Å. The last three peaks fall within 0.08 Å, of distances corresponding to $d_\perp + b$, $d_\perp + 2b$, and $d_\perp + 3b$, where $d_\perp = 2.51$ Å is the perpendicular distance from Se to the first Ni(111) surface layer, used for calculating $\chi(k)$ in Fig. 1(a); and b = 2.033 Å is the interlayer spacing in Ni(111). Figure 2 shows the distances Z_F, derived from F(r), plotted against the input "structural" distances Z_S for all three $d_\perp$ values. We conclude from this plot that:

1. The agreement between Z_F and Z_S is excellent for the 2nd, 3rd, and 4th interplanar distances; i.e., $d_\perp + nb$, with n = 1, 2, 3.

2. The first interplanar distance, $d_\perp$, is high by about 0.3 Å in all three cases. Among the possible reasons for this discrepancy are a different effective potential for electrons in the overlayer-substrate region, effects of multiple scattering, and the choice of g(k).

3. Of most importance, the derivatives of Z_F with respect to Z_S are near unity, and the dominant peaks in Z_F arise only from normal interplanar distances. Thus, Z_F faithfully yields these distances and no others.

*This work was supported by the Director, Office of Energy Research, Office of Basic Energy Sciences, Chemical Sciences Division of the U.S. Department of Energy under Contract No. W-7405-ENG-48. All projects except 1, 6, 9, and 11 were performed at the Stanford Synchrotron Radiation Laboratory, which is supported by the NSF Grant No. DMR 77-27489, in cooperation with the Stanford Linear Accelerator Center. One of us (J.G.T.) acknowledges support from an NSF predoctoral fellowship.

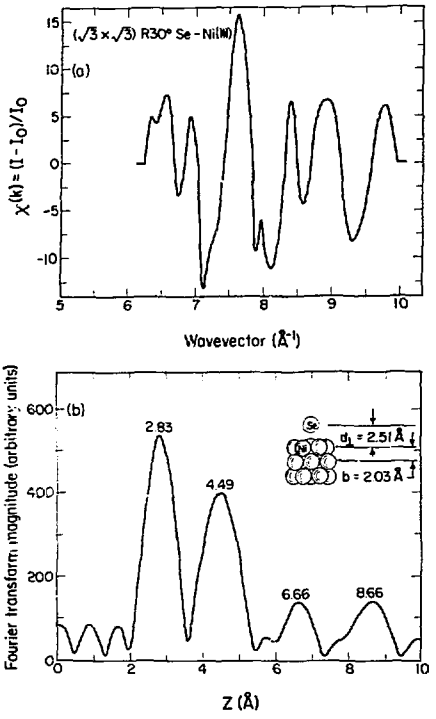

Fig. 1. (a) Theoretically calculated normalized NPD intensity versus k for ($\sqrt{3} \times \sqrt{3}$) R30° Se(3d) Ni(111) with $d_\perp$ = 2.51 Å and inner potential V_0 = 0 eV. (b) Magnitude of the Fourier transform $|F(r)|$ according to Eq. (1) of the data in (a). Schematic representation of the adsorption geometry is shown in the inset. (XBL 8011-2362)

A parallel analysis for the p(2 × 2) Se/Ni (001) system, which is not shown here, also yields similar results. These results suggest that it is probably possible--given good data and careful analysis--to derive $d_\perp$ values (probably from the 2nd, 3rd and 4th peaks) accurate to ~2% by Fourier transformation of NPD data.

In comparing Fourier-transform NPD with surface EXAFS, a complementarity is obvious: the determination of both $d_\perp$ from NPD and the nearest-neighbor distance from surface EXAFS would be especially desirable. NPD has the advantages over surface EXAFS that $\chi(k)$ is about an order of magnitude larger and that there is no contribution to

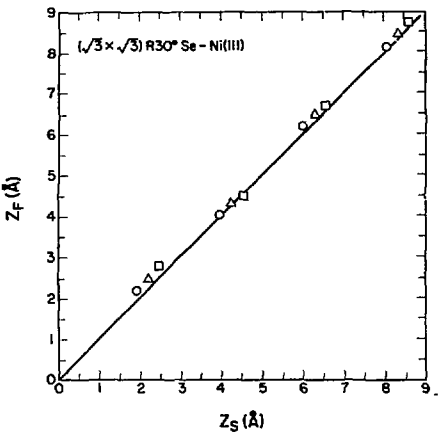

Fig. 2. Fourier-transform derived distances Z_F plotted against input structural distances Z_S for three $d_\perp$ values of 1.93 Å (circles), 2.22 Å (triangles), and 2.51 Å (squares) (see inset in Fig. 1(b)). A linear curve with slope = 1.0 is drawn to facilitate comparison between Z_F and Z_S. (XBL 8011-2364)

the interference term from the source atom phase shift, which cancels in the direct and scattered waves.[3]

In seems clear that Fourier transformation of NPD I/E curves will yield normal interplanar spacings. In seeking a qualitative explanation, we note that scattering of photoelectrons from a state propagating normally into the substrate into one propagating normally outward is favored. Therefore, the magnitude of photoelectron diffraction modulations is greater by a factor of 3 - 5 for normal emission as compared to non-normal emission.[4] Further tests are needed, including experimental data sets extending to high kinetic energies.

* * *

†Brief version of LBL-11686; to be submitted to Physical Review Letters.

‡Permanent address: Department of Physics, National Tsing Hua University, Hsinchu, Taiwan, Republic of China.

§Permanent address: Surface Studies Laboratory and Department of Physics, University of Wisconsin, Milwaukee, Wisconsin 53201.

1. A. Liebsch, Phys. Rev. Lett. 32, 1203 (1974); Phys. Rev. B 13, 544 (1976).
2. E. A. Stern, Phys. Rev. B 10, 3027 (1974).
3. P. A. Lee, Phys. Rev. B 15, 5261 (1976).
4. S. D. Kevan et al., Phys. Rev. B 20, 4133 (1979).

2. NORMAL PHOTOELECTRON DIFFRACTION OF c(2×2)O(1s)-Ni(001) AND c(2×2)S(2p)-Ni(001), WITH FOURIER TRANSFORM ANALYSIS†

D. H. Rosenblatt, J. G. Tobin, M. G. Mason,‡ R. F. Davis, S. D. Kevan,§ D. A. Shirley, C. H. Li,‖ and S. Y. Tong¶

Normal photoelectron diffraction (NPD), which has produced accurate structural determinations of ordered atomic[1] and molecular[2] overlayers on metal surfaces, was utilized to study the c(2×2) oxygen and sulfur overlayers on Ni(001). In an NPD experiment, the photoemission intensity of an adsorbate core level is measured normal to the surface as a function of photon and, consequently, photoelectron energy. The intensity-kinetic energy curve thus generated is compared to theoretical calculations to make the structure determination. The important structural parameter in NPD is $d_\perp$, the perpendicular spacing between the adsorbate layer and the top substrate layer.

Angle-resolved photoemission spectra of the O(1s) level were taken at photon energy intervals of 3 eV over the range 550 eV $\leq h\nu \leq$ 740 eV. In Fig. 3, the experimental NPD curve derived for the O(1s) level from the c(2×2)O overlayer on Ni(001) is shown, along with two theoretical curves for oxygen in a fourfold hollow site above the nickel surface at $d_\perp$ = 0.90 Å and 1.76 Å. These curves show the closest agreement with our data of all $d_\perp$ spacings tested, and of the two, the lower curve ($d_\perp$ = 0.90 Å) clearly gives the better fit, because three peaks match almost exactly while two others differ only by 3 eV. Thus, the oxygen is found to be situated above the fourfold hollow site with $d_\perp$ = 0.90 ± 0.04 Å (with a Ni-O bond length of 1.98 Å). Figure 4 shows the experimental NPD curve for the S(2p) level in c(2×2)S - Ni(001), derived from photoemission spectra taken over the range 200 eV $\leq h\nu \leq$ 370 eV. The theoretical calculations shown are for the fourfold hollow site ($d_\perp$ = 1.30 Å), the twofold bridge site ($d_\perp$ = 1.80 Å), and the atop site ($d_\perp$ = 2.19 Å). The best agreement between theory and experiment is found for the fourfold hollow site, with the sulfur atoms situated 1.30 ± 0.04 Å above the nickel surface.

The calculations shown in Figs. 3 and 4 are quite involved, due to the importance of multiple scattering of the final state photoelectron wave in the energy region studied. These complications have motivated us to apply a Fourier transform analysis to the experimental data to isolate the single scattering effects. A Fourier transform of NPD experimental data might be sensitive to the one-dimensional structure normal to the crystal face.[3] Recently, our group has applied the Fourier transform technique to calculated NPD curves with much success.[5] This work represents the first attempt to use Fourier transform analysis on experimental NPD data. The function $\chi(k) = (I-I_0)/I_0$, where I is the NPD intensity and I_0 is the estimated atomic background, was determined for the O(1s) and S(2p) levels, and then Fourier transformed. The result for the S(2p) level is shown in Fig. 5, where the magnitude of the Fourier transform for the sulfur system is shown to yield

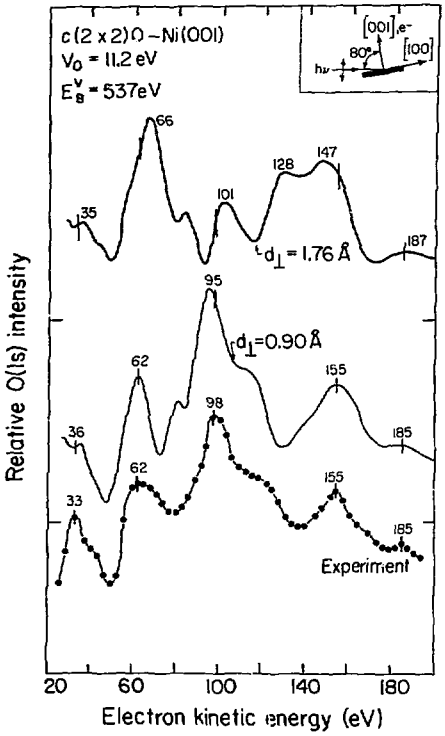

Fig. 3. NPD curve for O(1s) electrons from c(2×2)S - Ni(001), compared with theoretical curves for $d_\perp$ = 0.90 and 1.76 Å for the experimental geometry shown. (XBL 8010-2112)

two major peaks at 3.02 and 4.83 Å. NPD and LEED analyses yielded $d_\perp$ = 1.30 Å, and the interlayer spacing for Ni(001) is b = 1.76 Å. These two peaks can therefore be attributed to the distances $d_\perp$ + b = 3.06 Å and $d_\perp$ + 2b = 4.82 Å. There is no peak in the real-space distribution function for $d_\perp$ = 1.30 Å, probably because our NPD data do not extend to high enough kinetic energy. The agreement for the two main peaks is very good considering the limited data range. The O(1s) data also yielded good results; the Fourier transform yielded peaks at 2.70 and 4.33 Å, in good agreement with the NPD and LEED results of $d_\perp$ + b = 2.66 Å and $d_\perp$ + 2b = 4.42 Å.

* * *

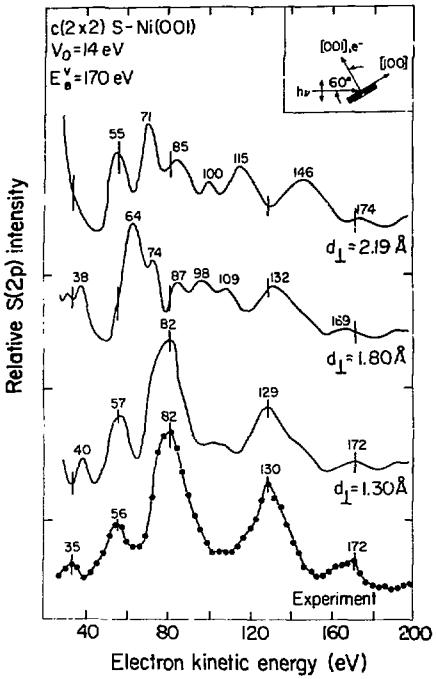

Fig. 4. NPD curve for S(2p) electrons from c(2×2)S - Ni(001), compared with theoretical curves for $d_\perp$ = 1.30, 1.80, and 2.19 Å for the experimental geometry shown. (XBL 8010-2113)

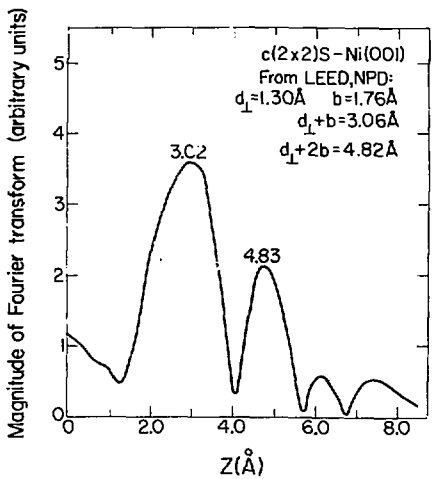

Fig. 5. Magnitude of the Fourier transform of the function $X(k) = (I - I_0)/I_0$ for S(2p) NPD data from c(2×2)S - Ni(001). (XBL 8010-2116)

[†]Brief version of LBL-11447; submitted to Physical Review B.

[‡]Permanent address: Research Laboratory, Eastman Kodak, Rochester, NY 14650.

[§]Permanent address: Bell Laboratories, Murray Hill, NJ 07974.

[‖]Permanent address: Department of Physics, National Tsing Hua University, Hsinchu, Taiwan, Republic of China.

[¶]Permanent address: Department of Physics and Surface Studies Laboratory, University of Wisconsin-Milwaukee, Milwaukee, WI 53201.

1. S. D. Kevan, et al., Phys. Rev. Lett. 41, 1565 (1978), Phys. Rev. B 20, 4133 (1979).
2. S. D. Kevan et al., to be published.
3. Z. Hussain et al., to be published.

3. TEMPERATURE DEPENDENCE OF NORMAL EMISSION PHOTOELECTRON DIFFRACTION AND ANALOGIES WITH EXAFS[†]

S. D. Kevan,[‡] J. G. Tobin, D. H. Rosenblatt, R. F. Davis, and D. A. Shirley

Our group has addressed the characterization of normal emission photoelectron diffraction (NPD), in which the photoemission intensity of an adsorbate core level is measured normal to the surface as a function of photon (and thus kinetic) energy.[1] In NPD, an intensity-energy curve similar to a low energy electron diffraction (LEED) I-V curve is generated which, when compared to theoretical curves, may yield a surface structure. Given its genesis, photoelectron diffraction is usually conceptualized by its relation to LEED, and the same general accuracies and limitations are usually perceived to be associated with the two methods.

In this study, we take the view that while this comparison to LEED is valuable, an equally enlightening comparison of normal photoelectron diffraction to extended x-ray absorption fine structure[2,3] (EXAFS) can be made. We note that, while the NPD intensity-energy curves resemble LEED-I-V curves, their calculated behavior actually mimics EXAFS data, with $d_\perp$, the interplanar spacing between the overlayer and the outermost substrate layer, being the important structural parameter,

rather than the nearest neighbor distance, R_{nn}. This result, first observed by Li and Tong[4] and emphasized elsewhere,[1,5] is illustrated in Fig. 6. In the top three curves, the calculated selenium 3d normal emission angle resolved photoemission (ARP) intensity for the p(2×2) Se-Ni(001) system is plotted for three different values of $d_\perp$. The oscillation frequency is seen to increase monotonically with $d_\perp$ in much the same way as EXAFS oscillation frequencies increase with nearest-neighbor distances. The lower curve in Fig. 6 shows our experimental data. The match to the $d_\perp$ = 1.55 Å calculation reported previously[1] is evident. The registry of the selenium layer with the nickel surface was found to be relatively unimportant in determining the calculated result:[4] nearly the same curve was obtained for different local site geometries, if they were compared at the same $d_\perp$.

Empirically, NPD data thus behave similarly to EXAFS data with the important difference that the structural sensitivity is to $d_\perp$ rather than R_{nn}. In the context of investigating this analogy further, we report in this article new temperature-dependence results on the Se-Ni(001) model system. Taken at face value, these data are of interest in further characterizing the system. Of more general interest, however, is their value in characterizing the NPD phenomenon; in fact they constitute more evidence for the NPD-EXAFS analogy.

Figure 7 shows two different NPD data sets accumulated at T = 120 K for the p(2×2) Se-Ni(001) system. The upper curve was accumulated using an unannealed overlayer prepared by exposing to H_2Se at 120 K, while the lower curve was accumulated after an anneal at 450 K. Both surfaces yielded p(2×2) LEED patterns, though that of the annealed surface was sharper. While the same general structure is observed in the curves, a systematic and monotonically increasing shift of peak positions to lower energy is evident in the upper curve. The amplitude of oscillation is also larger in the lower curve. The data in that curve are in good agreement with our previous data,[1] and are best fitted as before by a calculated curve with $d_\perp$ = 1.55 Å, corresponding to the accepted four-coordinated hollow site adsorption geometry. The most likely explanation for the shifts observed in

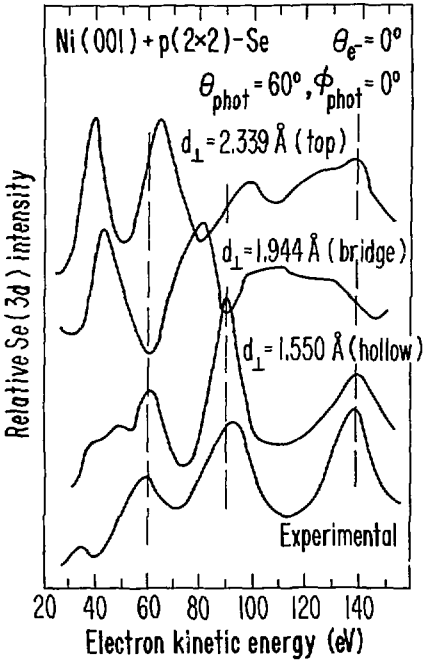

Fig. 6. Top three curves: calculated selenium 3d intensity as a function of electron kinetic energy for p(2×2) Se-Ni(001) at three different values of $d_\perp$ as defined in the text, after Tong and Li. Bottom curve: experimental result.
(XBL 7911-13241)

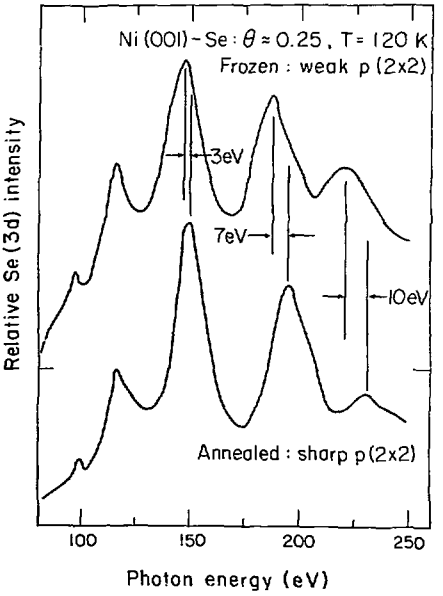

Fig. 7. Comparison of NPD curves for frozen and annealed p(2×2) Se-Ni(001). Note the systematic shift of peak energies. (XBL 805-1071)

the upper curve is that $d_\perp$ has increased slightly, leading to slightly more rapid oscillations. Since the higher-energy peaks disperse more rapidly with $d_\perp$, the higher energy regions are further out of phase. Indeed, if we had limited our study to $h\nu \leq 160$ eV, the pronounced shift seen in Fig. 7 would have been difficult to discern. The lesson is the same as in EXAFS:[6,7] an extended data range permits more accurate and higher resolution NPD studies. From two independent methods, we estimate the shift in $d_\perp$ to be approximately 0.06 - 0.10 Å.

To investigate the temperature dependence of the cross section modulations, we studied the NPD of c(2×2) Se(3d)-Ni(001) at a series of temperatures.

Most thermal diffuse scattering mechanisms are interpreted in terms of a Debye-Waller factor:[8,9]

$$I \approx \exp - \langle (\Delta\vec{k} \cdot \Delta\vec{r})^2 \rangle$$

which diminishes the fraction of coherently scattered particles. Assuming a Debye model for vibrational frequencies and amplitudes, and also that the vibrations are isotropic, this equation is reduced to the form familiar from x-ray diffraction studies:[8,9]

$$I \approx \exp - \left(\frac{3|\Delta\vec{k}|^2 T}{m k_B \theta^2} \right) \qquad (1)$$

with m = the atomic mass, k_B = Boltzmann's constant, T = the absolute temperature, and θ = the Debye temperature.

It is necessary to isolate the scattering contribution by subtracting the smooth atomic background, I_o, from the intensity, I.

In Fig. 8, we show the dependence of $\ln[(I - I_o)/I_o]$ on temperature for the two photon energies corresponding to the two peaks in the c(2×2) Se-Ni(001) cross section. Aside from substantial random scatter, an approximately linear plot is obtained. The functional form of Eq. (1) is therefore obeyed, although the Debye model per se is inappropriate. It is instructive to replace θ in Eq. (1) by an effective temperature θ_{eff}, then use it to fit the data. If effective temperatures are derived from the slopes of linear least squares fits to the data at the two peak energies, the results are θ_{eff} = 135 K and 133 K for photon energies of 149 and 192 eV, respectively. A consistent, but probably less accurate, value of θ_{eff} = 125 K was derived from the amplitude of the minimum at hν = 174 eV.

* * *

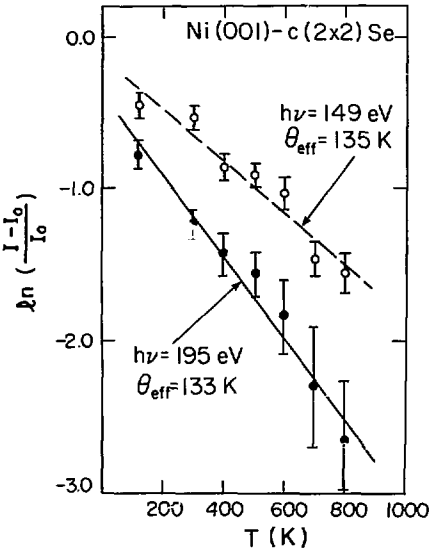

Fig. 8. Plots of $\ln[(I - I_o)/I_o]$ vs. absolute temperature for 149 and 192 eV photon energy. (XBL 805-1073)

†Brief version of LBL-11199, In press: Physical Review.

‡Present address: Bell Laboratories, Murray Hill, NJ 07974.

1. S. D. Kevan et al., Phys. Rev. Lett. 41, 1565 (1978); Phys. Rev. B 20, 4133 (1979).
2. E. A. Stern, Phys. Rev. B 10, 3027 (1974).
3. P. A. Lee and J. B. Pendry, Phys. Rev. B 11, 2795 (1975).
4. C. H. Li and S. Y. Tong, Phys. Rev. B 19, 1769 (1979).
5. G. P. Williams et al., Sol. State Commun. 31, 15 (1979).
6. E. A. Stern, D. E. Sayers, and F. W. Lytle, Phys. Rev. Lett. 27, 1204 (1971); Phys. Rev. B 11, 4836 (1975).
7. T. M. Hayes, P. N. Sen, and S. H. Hunter, J. Phys. C 9, 4357 (1976).
8. B. E. Warren, X-Ray Diffraction, Addison-Wesley, Reading, MA. (1969).
9. J. B. Pendry, Low Energy Electron Diffraction, Academic Press, New York (1974).

4. STRUCTURAL DETERMINATION OF MOLECULAR OVERLAYER SYSTEMS WITH NORMAL EMISSION PHOTOELECTRON DIFFRACTION: c(2×2)CO-Ni(001) AND (√3×√3)R30° CO-Ni(111)†

S. D. Kevan,‡ R. F. Davis, D. H. Rosenblatt, J. G. Tobin, M. G. Mason,§ D. A. Shirley, C. H. Li,‖¶ and S. Y. Tong¶

Recent results[1] indicate that an angle-resolved photoemission technique, called normal emission photoelectron diffraction (NPD), can be applied to

precise surface structural determination of atomic overlayer systems in a way analogous to low energy electron diffraction (LEED). In this report, measurements of c(2×2)CO-Ni(001) and $(\sqrt{3} \times \sqrt{3})R30°$ CO-Ni(111) provide the first experimental evidence that NPD can be used for structural determinations of molecular adsorbates. As a consequence, the NPD technique may be readily applied to systems subject to primary LEED beam damage or to those which exhibit poor or no lateral ordering--systems which have been problematical for LEED intensity analysis in the past. Most importantly, NPD greatly simplifies the structural problem relative to LEED by offering the possibility of locating the position of each atomic species in the adsorbate independently, allowing determination of atomic positions at smaller $d^{\perp}$ (the perpendicular spacing from the top substrate layer) first in an "inside-out" manner. As a result, the magnitude of the structural search for an n-atomic adsorbate molecule is reduced from I^n, as in LEED, to nI, where I is the number of structural possibilities considered for each atom.

Experiments were performed with synchrotron radiation in the range 300 eV ≤ hν ≤ 650 eV, and calculations used a multiple scattering algorithm[2] with inner potentials of 11.2 and 10.5 eV for Ni(001) and Ni(111), respectively. The calculations were done for CO with the generally accepted orientation[3] (C-end down and the bond axis parallel to the surface normal), in the top, bridge, and hollow sites, with the C-Ni interplanar distance ($d^{\perp}_{CNi}$) and the CO bond distance ($d^{\perp}_{CO}$) varied at steps of 0.1 Å in a systematic search for the best fit to the experimental results (hereafter referred to as the NPD fit). The calculations show[2] that the C(1s) NPD curve peak energy positions disperse with $d^{\perp}_{CNi}$ but not with $d^{\perp}_{CO}$, whereas the reverse is observed for O(1s). These theoretical results imply that each $d^{\perp}$ value can be determined in a separate NPD measurement (i.e., C(1s) for $d^{\perp}_{CNi}$ and O(1s) for $d^{\perp}_{CO}$), an expectation that is verified in CO by this experimental study, and which may be expected to carry over analogously to other molecular systems. The reason for this "structural separability" lies in the localized nature and phase coherence of the NPD process. For example, in CO, the phase difference between direct and O-atom forward-scattered C(1s) photoelectron waves is nearly independent of $d^{\perp}_{CO}$, whereas the substrate back-scattered C(1s) wave picks up phase in traversing the distance $2d_{CNi}$ yielding substantial sensitivity.[2]

The results of the above discussion are manifested in the experimental results. For C(1s) NPD in the CO-Ni(001) system (Fig. 9), the best NPD fit is obtained by fixing $d^{\perp}_{CO}$ = 1.13 Å (the free-molecule value) and varying $d^{\perp}_{CNi}$, yielding $d^{\perp}_{CNi}$ = 1.8 Å (the LEED-derived value[4]). Experimental and theoretical curves for this structure are compared in Fig. 9 (inset), and the plot of ΔE = E(theor.) - E(exper.) versus NPD peak number (E values are NPD peak energies), for various values of $d^{\perp}_{CNi}$, shows quantitatively that only $d^{\perp}_{CNi}$ = 1.8 Å is fully consistent with both theory and experiment. Moreover, O(1s) studies (Fig. 10) in the same

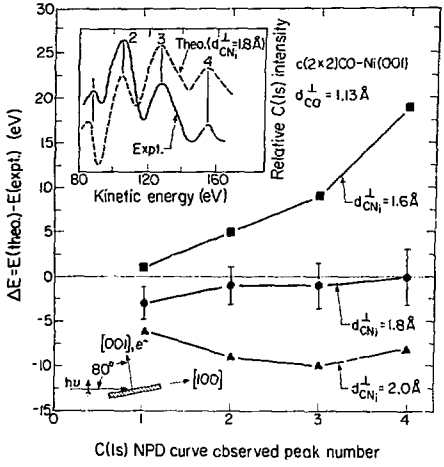

Fig. 9. Plot of ΔE = E(theory)-E(experiment) versus NPD curve peak number for the C(1s) level in c(2×2) CO-Ni(001) with fixed CO bond length and various carbon-nickel spacings. A comparison of calculated ($d^{\perp}_{CNi}$ = 1.8 Å, $d^{\perp}_{CO}$ = 1.13 Å) and experimental NPD curves is shown in the inset. (XBL 8012-2435)

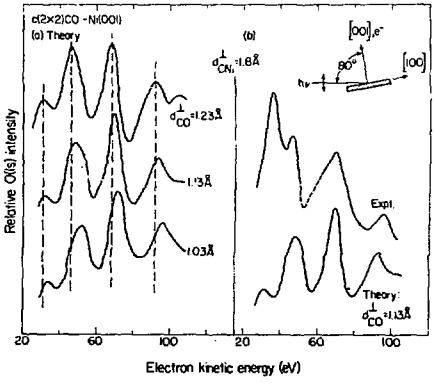

Fig. 10. a) Calculated NPD curves for the O(1s) level in c(2×2) CO-Ni(001) for fixed carbon-nickel spacing and various CO bond lengths. b) Comparison of the experimental result to the best-fit calculation from (a). (XBL 8012-2436)

CO-Ni(001) system show not only $d^{\perp}_{CO}$ dispersion in the calculated curves (Fig. 10a), but that the best NPD fit is obtained by fixing $d^{\perp}_{CNi}$ = 1.8 Å and varying $d^{\perp}_{CO}$, yielding $d^{\perp}_{CO}$ = 1.13 Å (Fig. 10b). As shown by the experimental curve in Fig. 10b, however, our measurements were limited to E_k < 100 eV because of generally poor radiation flux and resolution above the O(K) - edge. Thus, although consistent with the LEED result,[4] our $d^{\perp}_{CO}$ results would be greatly improved by an O(1s) study over a wider kinetic energy range.

Figure 11 summarizes the extension of these CO-Ni studies to ($\sqrt{3} \times \sqrt{3}$)R30° CO-Ni(111). The C(1s) NPD results confirm previous indications that the CO adsorbate molecule is bonded in the twofold bridge position on Ni(111).[5] Aside from the region near E_k = 90 eV, an excellent NPD fit is obtained for $d^{\perp}_{CNi}$ = 1.27 Å, corresponding to the bridge-bonded site, while poor fits are obtained for other values of $d^{\perp}_{CNi}$. Limited energy range O(1s) results are also shown. As with CO-Ni(001), a reasonable fit is obtained for the isolated molecule value of $d^{\perp}_{CO}$ = 1.13 Å. It should be emphasized that, based upon the poor quality of the LEED superstructure spots, a precise LEED analysis of the system would have been impossible.

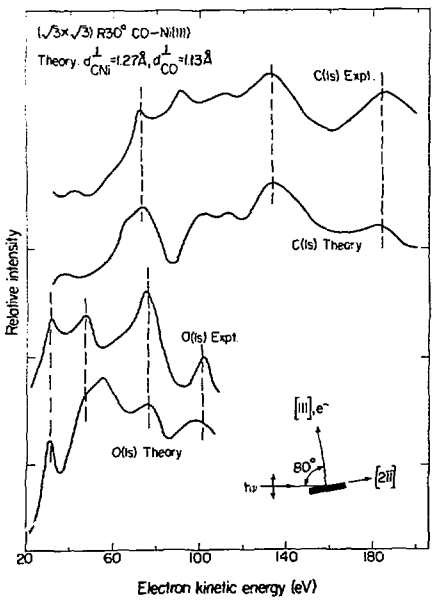

Fig. 11. Comparison of the best-fit calculation to experiment for both C(1s) and O(1s) levels in ($\sqrt{3} \times \sqrt{3}$)R30° CO-Ni(111). (XBL 8012-2437)

* * *

†Brief version of LBL-10024; to be submitted for publication in Physical Review Letters.
‡Present address: Bell Laboratories, Murray Hill, NJ 07974.
§Permanent address: Research Laboratories, Eastman Kodak Company, Rochester, NY 14650.
‖Department of Physics and Surface Studies Laboratory, University of Wisconsin-Milwaukee, WI 53201.
¶Present address: Department of Physics, National Tsing Hua University, Hsinchu, Taiwan, Republic of China.

1. S. D. Kevan et al., Phys. Rev. Lett. 41, 1565 (1978); Phys. Rev. B 20, 4133 (1979).
2. C. H. Li and S. Y. Tong, Phys. Rev. Lett. 43, 526 (1979).
3. C. L. Allyn, T. Gustafsson, and E. W. Plummer, Solid State Commun. 28, 85 (1978); and G. Apai et al., Phys. Rev. Lett. 37, 1497 (1976).
4. M. Passler et al., Phys. Rev. Lett. 43, 360 (1979).
5. W. Erley, H. Wagner, and H. Ibach, Surf. Sci. 80, 612 (1979).

5. SUBSTRATE-DEPENDENT C(1s) SHAPE RESONANCE IN CO OVERLAYERS ON Ni(111) AND Ni(001)†

R. F. Davis, S. D. Kevan,‡ D. H. Rosenblatt, M. G. Mason,§ J. G. Tobin, and D. A. Shirley

In the c(2×2)CO-Ni(001) molecular adsorbate system, an intensity resonance in the angle-resolved photoemission (ARP) overlayer level derived from the 4σ molecular orbital has been assigned to the adsorbed-molecule analogue of the well-known gaseous CO valence-shell shape resonance (SR).[1] The angular peaking of photoelectrons along the molecular axis (M) at the SR energy can serve as a direct "beacon" identifying molecular adsorbate orientation if adsorbed molecules possess resonances similar to those predicted for free molecules. In this connection, adsorbate core levels are distinctly advantageous for orientation studies because their spatial localization eliminates ambiguities due to initial-state substrate effects. We report the first observation of adsorbate core-level ARP resonances, for the C(1s) level in c(2×2)CO-Ni(001) and ($\sqrt{3} \times \sqrt{3}$)R30° CO-Ni(111). Although these resonances are similar to the predicted oriented-molecule core-level SR,[2] there is strong evidence for both substrate perturbations and substrate specificity.

The experimental geometry and crystal orientations are summarized in Figs. 12(a) and 12(b), respectively. Synchrotron radiation in the range 300 eV ≤ hν ≤ 360 eV was employed in conjunction with our rotating hemispherical-analyzer spectrometer. The C(1s) resonance is clearly seen in Fig. 12(c) for normal emission from CO-Ni(111), where some normalized photoemission energy distribution curves (EDCs) are plotted for a range of photon energies, sweeping through the resonance maximum at hν = 311 eV. In Fig. 13, we show a region of the energy-dependent C(1s) cross-section curve for both systems, obtained from EDC peak areas. Although the resonances are peaked at

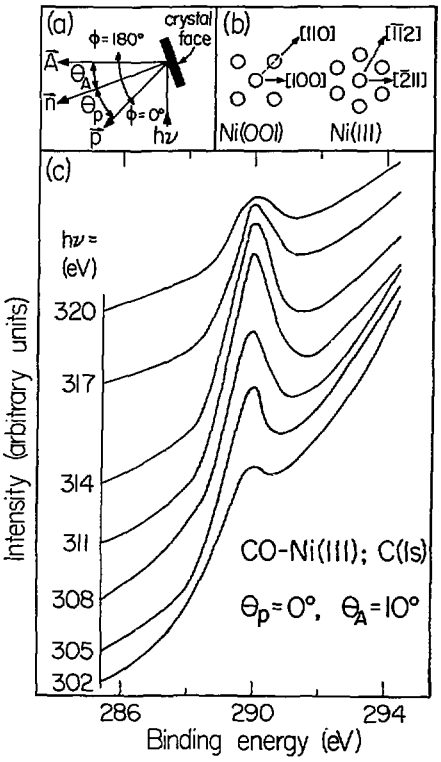

Fig. 12. (a) Experimental arrangement, showing typical orientations of the vector potential $\vec{A}$, the outgoing photoelectron direction $\vec{p}$, the crystal normal $\vec{n}$, and the incident photon beam direction hν. All three vectors were confined to the plane of incidence ($\phi = 0°$ or $180°$), with $\theta_p = \angle(\vec{n},\vec{p})$ and $\theta_A = \angle(\vec{n},\vec{A})$. (b) Experimental orientation of the crystals. The [100] and [$\bar{2}$11] directions are in the $\phi = 0°$ azimuth. (c) C(1s) photoemission EDCs for Ni(111) + 2L CO. (XBL 808-11120)

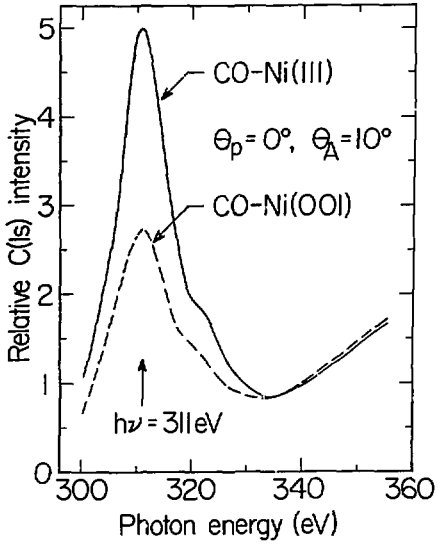

Fig. 13. Relative C(1s) photoemission cross-section for CO-Ni(111) and CO-Ni(001). (XBL 808-11129)

hν = 311 eV for both systems, the intensity maximum relative to the "atomic-like" background near hν = 335 eV (where the curves are normalized) is attenuated by a factor of two for CO-Ni(001) relative to CO-Ni(111).

The characterization of this resonant behavior is aided by previous orientation studies, which yielded $\vec{M} \parallel \vec{n}$ for CO overlayers on both substrates.[1,3] Consequently, we have determined that the resonance has properties very similar to those for the SR predicted in the C(1s) cross-section in gaseous CO. For an oriented CO molecule, the SR photoemission intensity should be sharply maximized in θ when the three vectors $\vec{A}$, $\vec{p}$, and $\vec{M}$ (or $\vec{n}$ in the present case) are aligned.[4] Figures 14a and 14b show that the adsorbate resonance has this property. In Fig. 14a, the θ_A-dependence of the near-resonance cross-section for CO-Ni(111) is shown to yield the maximum intensity when $\vec{A}$ is in closest alignment with fixed $\vec{p}$ and $\vec{n}$. The θ_p-dependence of the C(1s) intensity at hν = 311 eV is shown in Fig. 14b for both systems, indicating that as $\vec{p}$ is brought to near alignment with fixed $\vec{n}$ and $\vec{A}$, the intensity reaches a maximum.

However, comparison of the resonant behavior for CO-Ni(111) and CO-Ni(001) allows us to identify important differences between the predicted gas-phase and observed adsorbed-molecule SRs. These constitute substrate or condensed-phase effects, two of which are summarized below:

(1) The resonance intensity difference of a factor of two between the two nickel faces obviously cannot be accounted for by any isolated molecule theory and must indicate a strong differential substrate effect, very likely resulting from the known difference in CO adsorption site geometries, i.e., atop site for Ni(001) and two-fold bridge site for Ni(111).

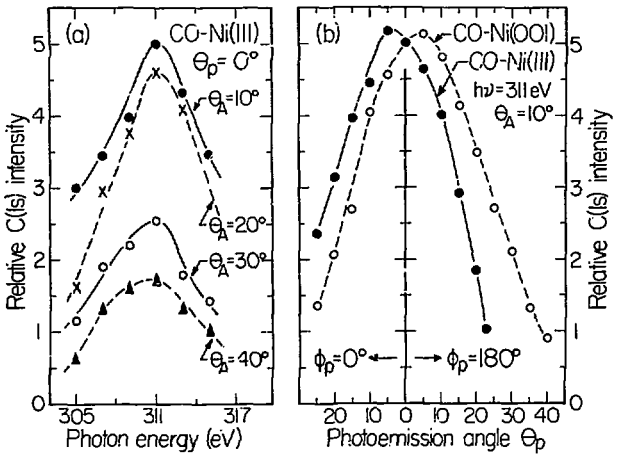

Fig. 14. Relative C(1s) cross-section: (a) θ_A-dependence near the resonance maximum energy for CO-Ni(111), (b) θ_p-dependence at hν = 311 eV for CO-Ni(111) and CO-Ni(001), with θ_p varied in both azimuths. For comparison, the two curves are normalized at θ_p = 0°. (XBL 808-11118)

(2) For CO-Ni(001), the θ_p angular distribution shown in Fig. 14b is peaked in intensity when $\vec{p}$ is exactly between $\vec{A}$ and $\vec{M}$, but for Ni(111) the entire curve is shifted 10° away from Ni(001) and the peak is on the other side of $\vec{n}$. This unexpected result for CO-Ni(111) is consistent with a substrate-induced shift of the ARP intensity maximum away from the molecular axis $\vec{M}$ (and thus from $\vec{n}$), a shift which could be symmetry masked for Ni(001) but not for the three-fold symmetric [111] axis on Ni(111).

The adsorbate shape resonance is highly sensitive to molecular orientation and photon energy. However, the unanticipated substrate effects observed imply that future theoretical treatments of adsorbate SR phenomena must take into account the position of substrate atoms to facilitate a meaningful comparison with theory.

* * *

†Brief version of LBL-11116; to be published in *Physical Review Letters*.
‡Present address: Bell Laboratories, Murray Hill, NJ 07974.
§Permanent address: Research Laboratories, Eastman Kodak Company, Rochester, NY 14650.

1. C. L. Allyn, T. Gustafsson, and E. W. Plummer, Solid State Commun. 28, 85 (1978), and references therein.
2. J. L. Dehmer and Dan Dill, Phys. Rev. Lett. 35, 213 (1975).
3. G. Apai et al., Phys. Rev. Lett. 37, 1497 (1976).
4. Scott Wallace, Dan Dill, and J. L. Dehmer, Phys. Rev. B 17, 2004 (1978).

6. K-EDGE STRUCTURE AND EXAFS ON SULFUR IN VARIOUS COALS†

Z. Hussain, J. J. Barton, E. Umbach, and D. A. Shirley

Sulfur is an important contaminant in fossil fuels. Although present only in low concentrations (typically 4% by weight or less), sulfur causes problems in essentially every process that uses coal. Catalysts are poisoned, and thus deactivated, by sulfur. Containers are corroded, and even simple combustion is complicated by the conversion of sulfur in coal to pollutant SO_2. Any process for coal conversion or combustion must contain a strategy for dealing with the constituent sulfur. On the other hand, very little is understood about the chemical structure of coal. This is particularly true of properties and structure measured in situ; i.e., non-destructively. In the case of sulfur, an absence of viable in situ methods of analysis obviates development of an optimum strategy for sulfur removal with any real confidence.

Among the in-situ methods that have not been applicable to sulfur in the past is near-edge x-ray absorption and extended x-ray absorption fine structure (EXAFS) because the sulfur K-edge lies at 2470 eV. Radiation at this energy is unavailable at the conventional synchrotron radiation beam lines because it is not adequately transmitted through a window thick enough to support 1 atm pressure. During the past year, Z. Hussain has been involved in helping to commission a double-crystal ultrahigh-vacuum monochromator at the Stanford Synchrotron Radiation Laboratory (SSRL)

to provide monochromatic radiation in the 800-4000 eV energy range--a heretofore inaccessible region of the electromagnetic spectrum. The monochromator is now operational and the sulfur K-edge is accessible for the first time. In this article, we describe a preliminary set of results on the photoelectric K-edge excitation of sulfur in iron sulfides and in a variety of standard coals.[1] The samples were studied as single chunks by detecting total electron yield as a function of incident photon energy.

The iron sulfide edge-structure spectra are shown in Fig. 15. These compounds were studied because a large fraction of the sulfur in coal is typically present in pyritic form. Systematic variations in the near-edge structure are clearly present. There appears to be adequate spectral sensitivity to facilitate characterization of the particular form of iron sulfide under study, although more work is needed to confirm this tentative conclusion.

Figure 16 shows EXAFS structure, on an expanded energy scale, for the same compounds. A good spectral contrast ratio is apparent, and enough oscillations are visible to indicate that a Fourier transform would yield reliable iron-sulfur and perhaps sulfur-sulfur distances.

The near-edge absorption spectra of sulfur in coal are shown in Fig. 17. The first surprise in these spectra, in light of the low-abundances of sulfur, is that the "edge jump ratio" above background is so large. The explanation lies in the fact that, except for iron and trace impurities, sulfur is by far the heaviest element present in coal. At 2470 eV the oscillator strengths of absorbing K-edges of carbon, nitrogen, and oxygen are very low. There is enough variation in the

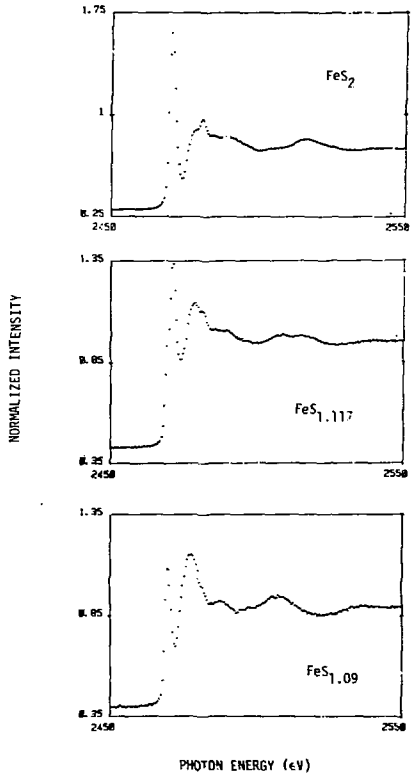

Fig. 15. Sulfur K-edge absorption spectra, showing near-edge structure, in three iron sulfide samples. (XBL 812-8059)

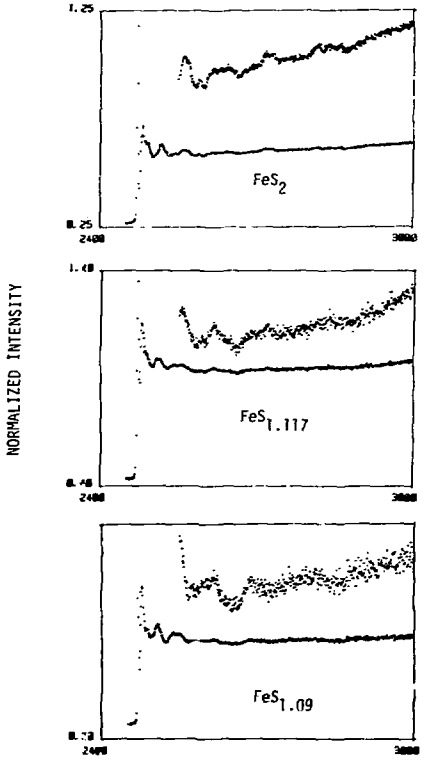

Fig. 16. Extended x-ray absorption fine structure (EXAFS) above the sulfur K-edge in three iron sulfide samples. (XBL 812-7906)

SULFUR IN COAL

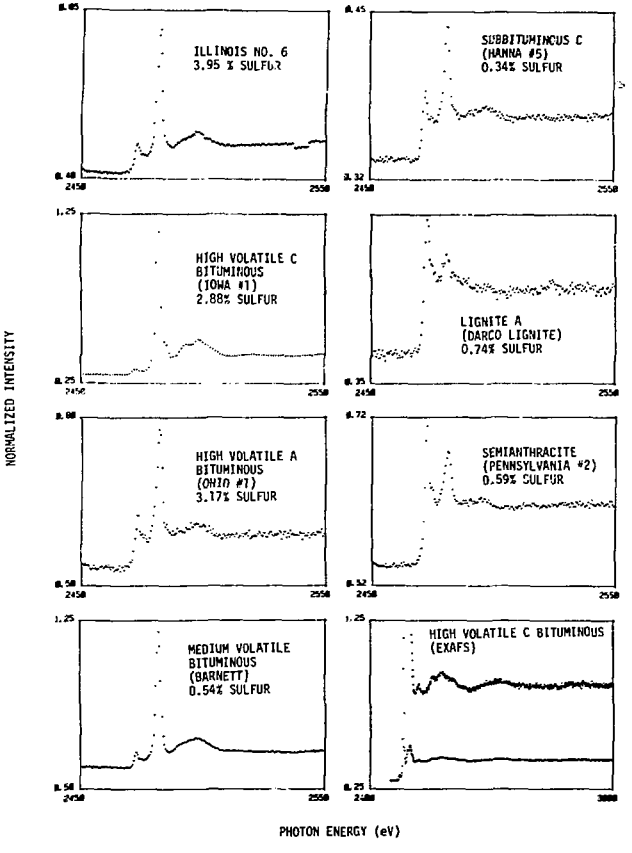

Fig. 17. *Near-edge structure of sulfur K-edge in seven coals, and extended x-ray absorption fine structure (EXAFS) in one coal type.* (XBL 812-7907)

spectra to show that sulfur K-edge structure is a promising technique for "fingerprinting" the chemical structure of sulfur in coal in situ. In one case EXAFS structure is already visible.

In conclusion, sulfur K-edge absorption spectra in coal provide both sensitivity and a good range of dependence on chemical structure. It appears that we have the basis of a useful spectroscopic method for in situ characterization of sulfur in fossil material.

* * *

†Brief version of LBL-11811; to be submitted to *Phys. Rev. B.*

1. We are indebted to H. Heinemann, MMRD, for the sample of Illinois No. 6 coal; and to A. Davis, P. L. Walker, Jr. and J. M. Lambert, Jr of the Pennsylvania State University College of Earth and Mineral Sciences, for the other coal and iron sulfide samples.

7. PARTICLE SIZE INDUCED VALENCE CHANGES IN SAMARIUM CLUSTERS†

M. G. Mason,‡ S. T. Lee,‡ G. Apai,‡ R. F. Davis, D. A. Shirley, A. Franciose,§ and J. H. Weaver§

We report the first example of an unambiguous change in electronic configuration with particle size. This finding has been accomplished by measuring both core and valence level photoemission from samarium clusters on carbon substrates. Several characteristics make Sm uniquely suited for this study. The free Sm atom ground state is divalent [(Xe)$4f^6 6s^2$], in contrast to the trivalent [$4f^5(6s5d)^3$] ground state of the bulk metal. These states are separated by 2.2 eV in the atom, but the predicted separation is only ~ 0.2 eV in metallic Sm.[1] At the surface of the metal, the change in local symmetry and reduced coordination number generates a perturbation of the Fermi level and the valence bands large enough so that both divalent (2+) and trivalent (3+) signals are observed in condensed-phase photoelectron spectra of Sm.[2] Furthermore, because of the localized nature of the 4f electrons, the core-level spectra show a large (2+) - (3+) separation of 7.6 eV (Ref. 2) and the $4f^5$ and $4f^4$ multiplet structures of the 4f photoemission final state are very diagnostic of the initial $4f^6$ and $4f^5$ configurations,[3] respectively.

The clusters were prepared by vapor deposition of Sm on the carbon substrates. Coverages were monitored by a quartz crystal oscillator and checked by neutron activation. In separate measurements, it was shown that this procedure gives rise to nucleation and growth processes very similar to those observed in the transition and noble metals.[4] Core-level photoemission spectra were measured with monochromatic Al Kα radiation and the valence region was investigated using hν = 60 eV synchrotron radiation.

Because of their large photoemission cross-section, the Sm($3d_{3/2}$), ($3d_{5/2}$) lines are relatively easy to measure with good statistics at low Sm concentrations. Figure 18 shows these spectra for various coverages, including the bulk metal. The predominance of the 2+ species at low coverages remains almost constant to a coverage of 3-4 × 10^{15} atoms/cm^2 (the break point), where there is a sharp rise in the 3+ intensity with increasing coverage. Figure 19 shows a plot of the $3d_{5/2}$ (3+)/(2+) intensity ratio as a function of coverage, showing quantitatively that Sm exists primarily in the divalent ground state at coverages below the sharp break point (and thus at small cluster size). A mean particle size estimation at the break point coverage is 25 ± 10 A, which also corresponds to the coverage range where photoemission spectra of noble and platinum group metals begin to show "bulk-like" characteristics.[5] At higher coverages (~ 10^{-16} atoms/cm^2), the clusters are no longer discrete but have coalesced to form a semi-continuous film with a very high ratio of surface to volume. The stabilizing effect of a surface for the divalent species[2] causes the (3+)/(2+) ratio to remain below that of the bulk metal even at these high coverages where the transition and noble metals have achieved most of their bulk-like properties. The approximate surface/bulk atom ratio is shown

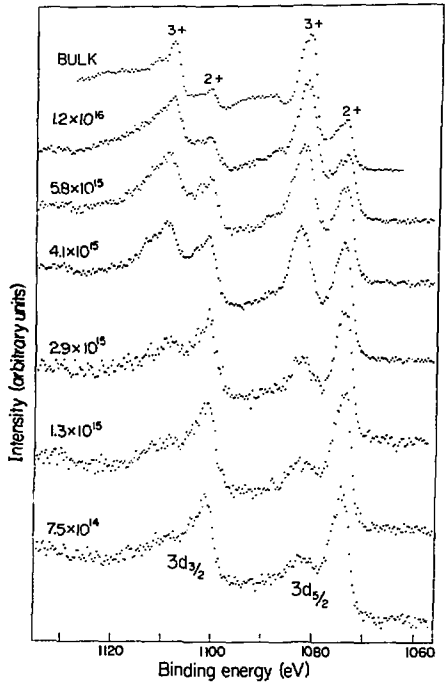

Fig. 18. Al Kα photoemission spectra of the 3d region of carbon supported samarium clusters at various coverages (atoms/cm^2), showing divalent (2+) and trivalent (3+) signals for each 3d line. (XBL 811-7773)

along the top of Fig. 19 for comparison with the data; however, the break in the curve is too sharp to be due to this ratio alone.

For these clusters, valence region photoemission intensity was too weak to be measured accurately with Al Kα radiation. However, the spectra shown in Fig. 20 for hν = 60 eV clearly identify the same trends in the 4f levels as in the 3d core levels, thereby constituting direct evidence of a cluster size dependence in the electronic configuration. In these valence spectra, peaks C, D, and E are due to the $4f^4$ final-state multiplets produced by ionization of $4f^5$ in trivalent Sm. Peaks A and B are primarily due to the $4f^5$ multiplets from divalent Sm, with some contribution to A from the sd valence bands. At low coverages, the 3+ photoemission signal is observed to be weak, becoming significant for coverages in the mid 10^{15} atoms/cm^2 region.

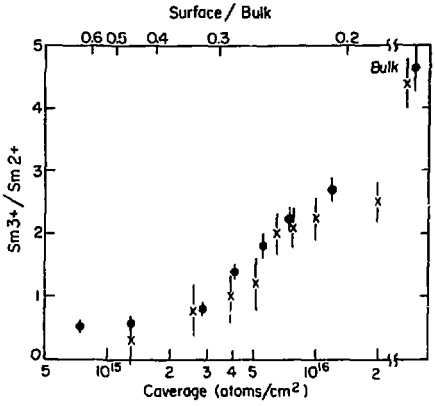

Fig. 19. $3d_{5/2}$ intensity ratio of Sm(3+) to Sm(2+) as a function of coverage and estimated surface to bulk atom ratio. (XBL 811-7772)

In summary, both core-level and valence region spectra show a predominance of the atomic-like divalent state at small particle size; and, with increasing size, the bulk-like 3+ state is formed but a large divalent contribution from the surface remains. Depending on the magnitude of the energy required to induce changes in the 4f level occupancy, many of the other rare-earth metals should exhibit analogous size dependence phenomena.

* * *

†Brief version of LBL-11810; to be submitted for publication.

‡Permanent address: Research Laboratories, Eastman Kodak Company, Rochester, NY 14650

§Permanent address: Synchrotron Radiation Center, Physical Sciences Laboratory, University of Wisconsin, Stoughton, WI 53589.

1. J. F. Herbst, R. E. Watson, and J. W. Wilkins, Phys. Rev. B 17, 3089 (1978).
2. G. K. Wertheim and G. Crecelius, Phys. Rev. Lett. 40, 813 (1978).
3. J. W. Allen et al., Phys. Rev. B 21, 1335 (1980), and references therein.
4. J. F. Hamilton and P. C. Logel, Thin Solid Films 23, 89 (1974).
5. M. G. Mason, L. J. Gerenser, and S. T. Lee, Phys. Rev. Lett. 39, 288 (1977).

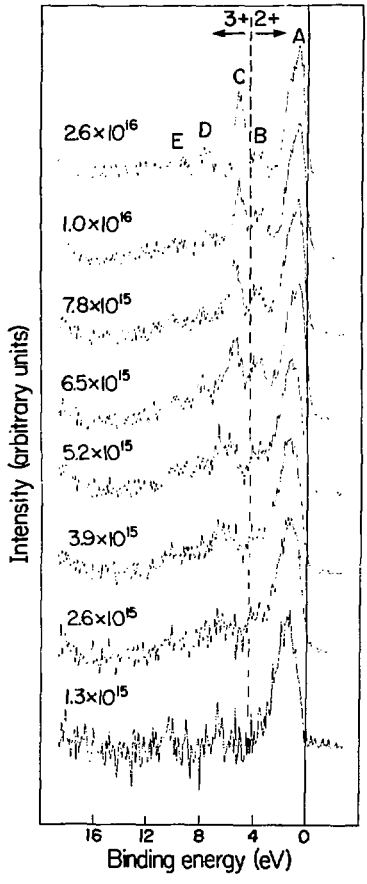

Fig. 20. hν = 60 eV photoemission spectra of the 4f and valence band region of carbon supported samarium clusters at various coverages (atoms/cm²), after the carbon valence band background has been subtracted. (XBL 811-7774)

8. DEVELOPMENT OF A MONOCHROMATIC LIGHT SOURCE IN THE 800-1500 eV RANGE

Z. Hussain, E. Umbach, J. Barton, and D. A. Shirley

A serious constraint on experimental spectroscopy is the limited energy range over which suitable light sources are available. Before the advent of high energy accelerators, intense tunable light sources were available only for energies up into the ultraviolet range. During the 1970s, synchrotron radiation with appropriate monochromators has extended this range considerably.

In the United States, there are now several synchrotron radiation sources. The most complete energy range is covered at Stanford Synchrotron Radiation Laboratory (SSRL); the hard ultraviolet is covered from about 5 eV to 800 eV; and the x-ray range from 3200 eV to 40,000 eV. A new double crystal monochromator has been developed by J. Stöhr at SSRL, and the range 1950 eV to 4200 eV is covered with a pair of germanium crystals. The work on the sulfur K-edge reported in article 6 was carried out on this instrument.

With the explicit goal of closing the gap in available photon energies, a crystal of beryl--a naturally occurring mineral--was carefully selected by one of us (Z.H.) and cut to provide a pair of monochromator crystals. With these crystals, the monochromator should provide highly monochromatic light of good intensity from 805 eV (the d spacing of 15.92 Å in beryl corresponds to 775 eV) to 2100 eV, with the intensity at higher energies being attenuated by the Al K-edge at ~ 1540 eV from natural aluminum in the beryl. At this writing, (December, 1980), the instrument has been tested and found to perform extremely well.

To assess the inherent resolution capabilities of the beryl crystals, rocking curves were measured at several photon energies. Table 1 shows the results. Clearly, line widths below 1 eV can be expected throughout this whole energy range.

The first example of an extended x-ray absorption fine structure (EXAFS) curve in this range is shown in Fig. 21, which depicts the electron yield curve above the sodium K-edge in crystalline sodium chloride. We conclude that the beryl crystal monochromator provides an excellent light source in the new energy range 800-1500 eV.

Table 1. Rocking curve results for beryl crystals.

Photon energy (eV)	Line width (eV)[a]
810	0.34
1000	0.55
1250	0.65
1500	0.85

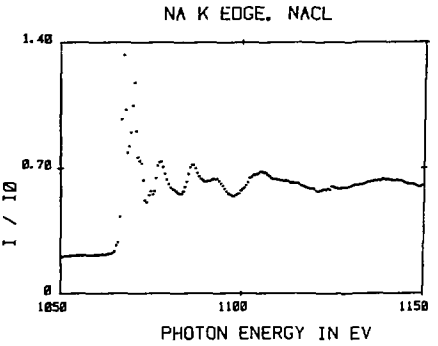

Fig. 21. Electron yield curve from crystalline NaCl, using the beryl crystal monochromator at SSRL. (XBL 812-8058)

Overview of Gas-Phase Research

Using the time-of-flight photoelectron analyzer, photoelectron angular distributions have been carried out on many species and are in the process of analysis. In a benchmark experiment, electron asymmetries were observed following excitation of the Xe 4d shell. This is the first such study at high photon energies (up to hν = 340 eV), the first comprehensive study on an inner shell, and the first case in which radiation-induced Auger electron intensities were observed (article 9). In addition, photoelectron asymmetries from molecular orbitals of many small molecules have been observed as functions of photon energy (article 12).

Molecular beam-synchrotron radiation photoionization studies were carried out on Ne_2 and He clusters (article 10, with Y. T. Lee). Finally, the molecular beam photoelectron spectrometer was completed, and it has yielded the highest-resolution molecular photoelectron spectra ever observed (article 11, with Y. T. Lee).

9. PHOTOELECTRON AND AUGER ELECTRON ANGULAR DISTRIBUTIONS: ALIGNMENT OF $Xe^+(^2D_{5/2})^+$

S. H. Southworth, P. Kobrin, C. M. Truesdale, D. Lindle, S. Owaki, and D. A. Shirley

It has been shown[1] theoretically that photoionization of an atomic subshell with angular momentum $j > 1/2$ can produce an alignment in the ion state, i.e., the magnetic sublevels are populated unequally with the result that Auger electrons are ejected with anisotropic angular distributions. In the two-step model of the Auger process, the decay of the excited ion state is separated from the excitation step. Alignment of the ion state is described by the alignment tensor,[2]

which is determined by the photoionization (electric dipole) matrix elements. The photoionization matrix elements also determine the angular distribution of the photoelectron. The angular distributions of the Auger electrons depend on the alignment tensor (the excitation step) and also, in general, on transition matrix elements of the Coulomb operator (the decay step). Thus, measurements of photoelectron and Auger electron angular distributions are sensitive to atomic electron structure and dynamics. We have used synchrotron radiation to measure angular distributions of Xe 4d subshell photoelectrons and the resulting Auger electrons and find them consistent with the predictions of theoretical calculations.

The measurements were made on the soft x-ray branch line at the Stanford Synchrotron Radiation Laboratory using a time-of-flight (TOF) electron spectrometer.[3] Two TOF detectors are operated simultaneously, one positioned to accept electrons ejected at 0° relative to the photon polarization vector and the other at 54.7°. Comparison of the intensities of electrons ejected at the two angles determines the asymmetry parameter β, which completely characterizes the angular distribution. Figure 22 shows the TOF spectra of Xe recorded at 70.9 eV photon energy. A major advantage of the TOF technique is that all of the ejected electron peaks are recorded simultaneously, giving β values for all of the accessible photoelectrons and Auger electrons.

Figure 23 shows the measured β values for the Xe 4d subshell, the measurements of Torop et al.,[4] the theoretical results of Kennedy and Manson[5] using Hartree Fock wavefunctions, the relativistic Dirac Fock calculations of Ong and Manson,[6] and the relativistic, many-electron RRPA theory of Johnson and Huang.[7] The measurements confirm the oscillatory nature of the angular distribution profile. This oscillation is primarily a nonrelativistic, one-electron effect,[5] due to a centrifugal barrier and a Cooper minimum in the 4d → εf channel. However, the DF and RRPA theories more accurately predict the position of the Cooper minimum near 200 eV.

Figure 24 shows the β values measured for the Auger transition[8]

$$Xe^{+}(4d^{9}5s^{2}5p^{6},\ ^{2}D_{5/2}) \rightarrow Xe^{2+}(4d^{10}5s5p^{5},\ ^{1}P_{1}) + e^{-}\ .$$

Also shown in the Fig. 24 is a theoretical β curve for an Auger transition of the type

$$Xe^{+}(4d^{9}5s^{2}5p^{6},\ ^{2}D_{5/2}) \rightarrow Xe^{2+}(^{1}S_{0}) + e^{-}\ .$$

The theory is based on a calculation[2] of the alignment tensor for $Xe^{+}(^{2}D_{5/2})$ using Hartree Fock wavefunctions. The strong asymmetry ($\beta \neq 0$) near the ionization threshold is due to the centrifugal barrier in the 4d → εf channel, while the asymmetry at high energy occurs near the Cooper minimum.

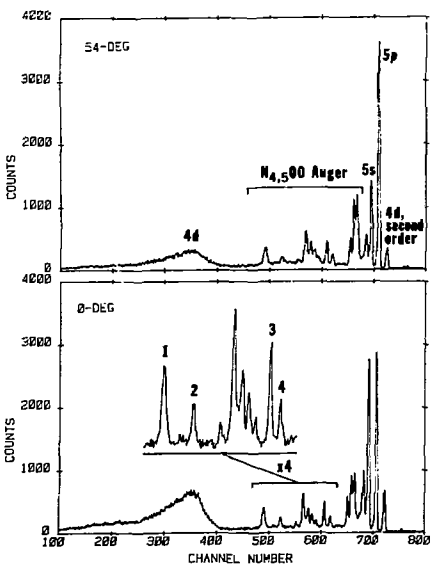

Fig. 22. Time-of-flight photoelectron and Auger electron spectra of xenon recorded at 70.9 eV photon energy. (XBL 808-11201)

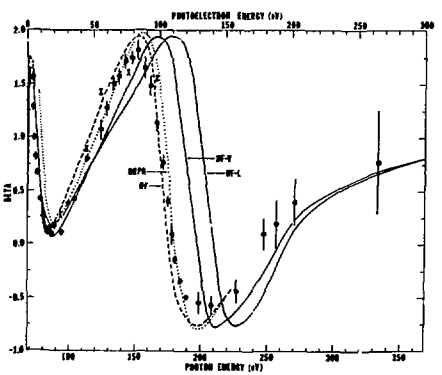

Fig. 23. Experimental and theoretical[5,6,7] photoelectron angular distributions of Xe4d subshell. Circles, this work; X's reference 4. (XBL 8012-12852)

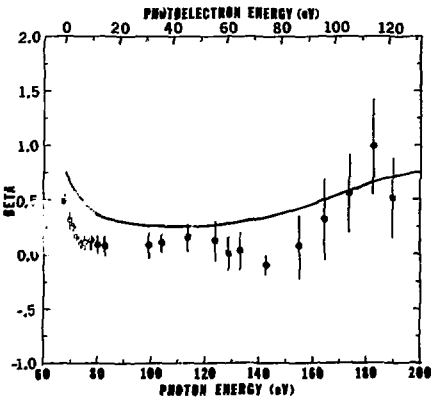

Fig. 24. Experimental and theoretical[2] Auger electron angular distributions from Xe^+ ($^2D_{5/2}$). (XBL 8011-12729)

* * *

†Brief version of LBL-11483; to be submitted to Phys. Rev. Lett.

1. S. Flügge, W. Mehlhorn, and V. Schmidt, Phys. Rev. Lett. 29, 7 (1972).
2. E. G. Berezhko, N. M. Kabachnik, and V. S. Rostovsky, J. Phys. B: Atm. Molec. Phys. 11, 1749 (1978).
3. M. G. White et.al., Rev. Sci. Instrum. 50, 1268 (1979).
4. L. Torop, J. Morton, and J. B. West, J. Phys. B: Atom. Molec. Phys. 9, 2035 (1976).
5. D. J. Kennedy and S. T. Manson, Phys. Rev. A 5, 227 (1972).
6. W. Ong and S. T. Manson, to be published.
7. W. R. Johnson and K.-N. Huang, to be published.
8. L. O. Werme, T. Bergmark, and K. Siegbahn, Phys. Scripta 6, 141 (1972).

10. PHOTOIONIZATION MASS SPECTROMETRY OF Ne_2 AND OF He CLUSTERS†

D. J. Trevor, J. E. Pollard, W. D. Brewer,‡
S. H. Southworth, C. M. Truesdale, Y. T. Lee,§
and D. A. Shirley

We present the first measurements of the photoionization yield of Ne_2^+ and He_2^+ from Ne_2 and He clusters, respectively. Structure observed in the photoionization efficiency of Ne_2 indicates the importance of spin-orbit interactions in autoionization at large internuclear distances. A lower bound to Ne_2^+ dissociation energy was obtained from the energy of its observed threshold. The existence of the simplest van der Waals molecule, He_2, has been the subject of much work in recent years. The very small direct ionization of He clusters produced in our beam made it impossible to prove whether the supposed molecule, He_2, exists.

The photoionization experiments on Ne_2 and He clusters were performed at SSRL with our recently developed supersonic molecular beam photoionization mass spectrometer. The measurements were made by crossing the monochromatized photon beam with a differentially pumped supersonic molecular beam. The resulting ions were extracted, mass analyzed, and detected with a quadrupole mass spectrometer. The vacuum of this apparatus was isolated from that of the rest of the beam line by an ultra thin (1500 Å) Al/Si window.

The photoionization yield of Ne_2^+ recorded at a resolution of 0.8 Å FWHM is shown in Fig. 25. Ne_2 was prepared by expanding Ne gas at 77 K and 2000 torr through a 20 μm aperture. The threshold of Ne_2^+ production was taken to be the energy at which its signal rose above background in a scan at 2.5 Å FWHM (insert, Fig. 25). The observed appearance potential was 20.21 ± 0.05 eV, which serves as an upper bound to the adiabatic ionization potential of Ne_2. Combining this value with the atomic ionization potential (21.565 eV)[1] and the van der Waals well depth (0.004 eV),[2] 1.36 ± 0.05 eV is obtained for a lower bound to the Ne_2^+ dissociation energy. This value is in excellent agreement with previous spectral line shape studies by Connor and Biondi[5] (1.35 eV). However, it is significantly larger than the electron impact value of 0.69 ± 0.2 eV.[4]

The photoionization efficiency of Ne_2^+ increases very slowly above threshold due to an unfavorable Frank-Condon factor. This results from the large difference in equilibrium internuclear distance between the neutral molecule and the ion. The dominant mechanism for production of Ne_2^+ is autoionization. The large internuclear distance in the vertical transition region samples the autoionizing molecular Rydberg states close to their atomic limit. The energies of the atomic $^2P_{3/2}$ ns, nd and $^2P_{1/2}$ ns, nd states are indicated in the upper part of Fig. 25. The observed autoionizing molecular states are only slightly shifted from their atomic dissociation limit. The molecular states associated with the indicated atomic levels account for the majority of the observed signal. Figure 26 shows schematic potential energy curves for the state with $^2P_{3/2}$ 6s + $^1S_0$ and $^2P_{1/2}$ 6s + $^1S_0$ atomic limits. The lowest O_u^+ and 1u Rydberg states have the core configuration of the ground ionic state and similar potential energy curves. Therefore, only high vibrational levels which should vibrationally autoionize can be excited. However, vibrational autoionization is efficient for only small changes in vibrational quanta, severely limiting its effectiveness near the molecular threshold. Consequently, autoionization of molecular Rydberg states, with $^2P_{3/2}$ ns atomic limits is not expected to be competitive with fluorescence or dissociation. This is demonstrated in our data by the very weak intensity observed in the regions of the $^2P_{3/2}$ 5s and 6s states.

The O_u^+ state with $^2P_{1/2}$ 6s + $^1S_0$ atomic dissociation products has an ionic core configuration similar to the $B^2\Pi_g$ excited ionic state. The long

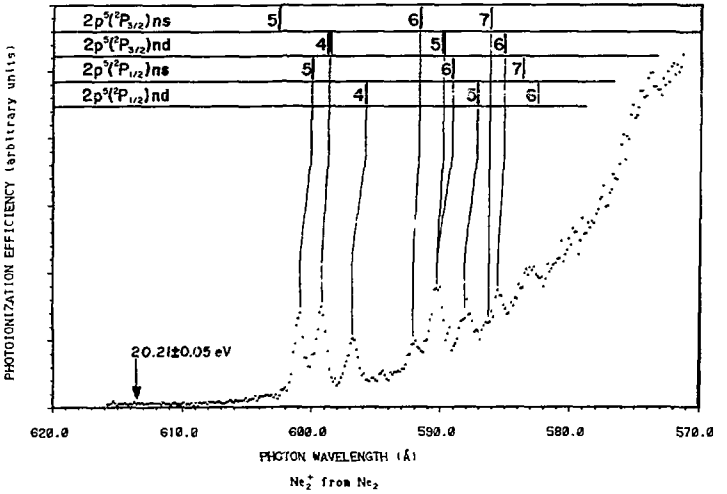

Fig. 25. Photoionization efficiency of Ne_2 measured with a resolution of 0.8 Å FWHM. Plotted, in the upper portion, are the energies of the dipole allowed atomic transitions for Ne. The insert shows a scan near threshold with 2.5 Å FWHM resolution. (XBL 802-8338)

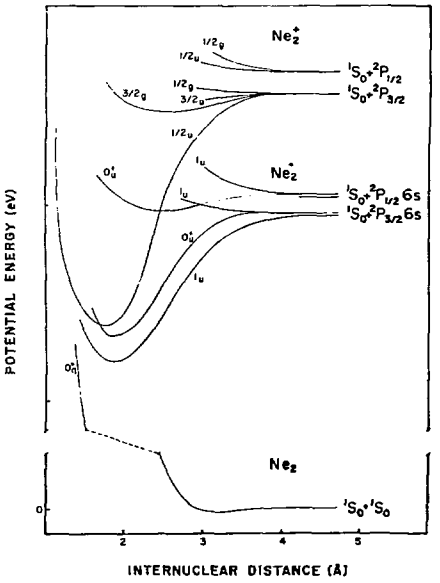

Fig. 26. Schematic molecular potential energy curves of Ne_2, Ne_2^* (in the region of the 6s Rydberg states) and Ne_2^+. (XBL 809-11810)

range minimum and the different ionic core configuration, coupled to the ground ionic core by spin orbit interactions, greatly enhance this state's autoionization rate. The states of this type appear as intense peaks in the photoionization efficiency.

There are several molecular Rydberg states with $B^2\Pi_g$ core and $^2P_{1/2}$ nd dissociation limits. As in the case of the $^2P_{1/2}$ ns, these states efficiently autoionize and appear as intense features in the photoionization efficiency. However, in contrast to the $^2P_{3/2}$ ns states, some of the $^2P_{3/2}$ nd molecular Rydberg states also have $B^2\Pi_g$ cores and thus competitively autoionize.

The photoionization yield of He_2^+ from our helium beam between 545 Å and 495 Å at 0.8 Å resolution is shown in Fig. 27. The beam conditions were 700 torr of He gas at 4.2 K expanded through 20 μm aperture. The spectrum is dominated by sharp autoionization structure from molecular Rydberg states with atomic limits of $1s(^2S_{1/2})np$ with $n \geq 3$. The signal arising from direct ionization was less than 1% of that observed at the resonances. This very small direct ionization cross-section made it impossible

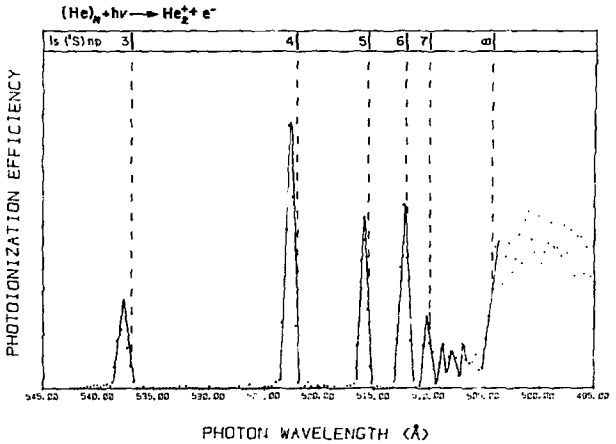

Fig. 27. The photoion yield of He_2^+ from a 700 torr, 4.2 K He beam, measured with a photon resolution of 0.8 Å FWHM. Also plotted are the energies of the dipole allowed atomic transitions for He. (XBL 809-11805)

to prove whether the He_2^+ originated from the supposed molecule He_2 or from dissociative ionization of larger cluster. No signal for He_3^+ could be detected above our background of about 0.1 counts sec^{-1}. By comparison, the He_2^+ signal was about 4 counts sec^{-1} at the resonances, and the He^+ signal was typically 3000 counts sec^{-1} beyond threshold. The background pressure in the ionization region was estimated to be 6×10^{-7} torr. This low number density excludes the possibility of He_2^+ being produced solely by chemi-ionization. Additional experiments at 77 K and higher background pressures confirmed these estimates. The most likely source of the observed He_2^+ signal was dissociative photoionization c larger clusters.

The positions of the autoionization resonances are observed to be slightly red shifted from the atomic states. These shifts indicate that the autoionizing states are attractive at large internuclear distances. The wavelength offset for this scan was determined by aligning the atomic ionization potential with the onset indicated in the figure. The accuracy of this procedure is estimated to be ± 0.3 Å, indicating the shifts are not experimental artifacts.

* * *

†Brief version of LBL-11249.
‡Permanent address: Institut fur Atom- and Festkorperphysik Freie Universitat Berlin, 1 Berlin 33, West Germany.
§Work performed in collaboration with Professor Yuan T. Lee's research group.

1. C. E. Moore, Atomic Energy Levels, Circular of the National Bureau of Standards 467, Vol. I, pp. 76-81 (1949).
2. P. E. Siska et al., J. Chem. Phys. 55, 5762 (1971).
3. T. R. Conner and M. A. Biondi, Phys. Rev. 140, 4778 (1965).
4. M. S. B. Munson, J. L. Franklin and F. H. Field, J. Phys. Chem. 67, 1542 (1963).

11. NEW HIGH RESOLUTION PHOTOELECTRON SPECTROMETER†

James E. Pollard, Dennis J. Trevor, Yuan T. Lee, and David A. Shirley

We have developed a new instrument which significantly advances the state-of-the-art in molecular photoelectron spectroscopy. By introducing the sample gas in the form of a supersonic molecular beam, we have found that the Doppler and rotational broadenings observed in conventional spectrometers are largely eliminated. This makes possible the study of spectral features such as spin-orbit splittings, Jahn-Teller effects, and rotational transitions which would be obscured in a room temperature sample. To take advantage of this potential for high resolution, it was necessary to design an energy analyzer having a theoretical resolution better than 10 meV (FWHM), as well as good sensitivity and a high signal-to-noise ratio. Ours is an optimized double monochromator, consisting of a 180° hemispherical deflector (10.2 cm mean radius), a 90° spherical sector pre-analyzer, and a system of electrostatic lenses. The detector consists of a 40 mm microchannel plate with a resistive anode position encoder for multichannel data collection. When used in conjunction with a

rare-gas resonance lamp and a differentially pumped supersonic beam source, this analyzer allows high resolution data to be recorded in a reasonable length of time. In the tests performed thus far, we have been operating in a single channel mode; but, with the installation of the nearly completed multichannel detection system, a gain in collection efficiency by a factor of 10 to 15 should be realized.

The He Iα photoelectron spectrum of Ar shown in Fig. 28 demonstrates the attainable resolution and characteristically low background of this apparatus. The design resolution is 0.004 eV FWHM in the absence of contributions from the linewidth of the photon source. Higher count rates are obtained by increasing the pressure in the lamp, although the resolution degrades to 0.010 eV FWHM for Ar. The spectrum of O_2 shown in Fig. 29 was taken under these conditions, and the observed resolution is 0.011 eV, only 10% larger than that seen for Ar. Due to the rotational cooling the two spin-orbit components of each vibrational level are much better separated than can be achieved with a sample at room temperature. Figure 30 shows the v' = 1 transition in the spectrum of H_2 with rotational structure partly resolved. The Doppler broadening which amounts to 0.020 eV at room temperature is nearly absent here.

* * *

+Brief version of LBL-11250.

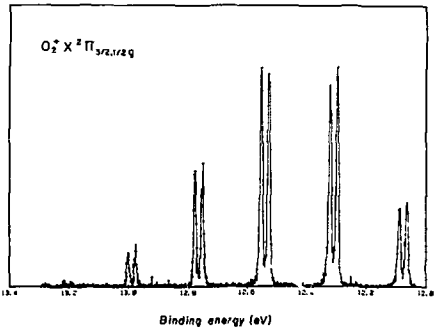

Fig. 29. Photoelectron spectrum of the first band ($X^2\Pi g$) of O_2^+ taken at 0.5 eV pass energy using He Iα (584 Å) radiation. Pure O_2 was expanded from 1000 torr through a 70 μm-diameter nozzle. (XBL 809-11855)

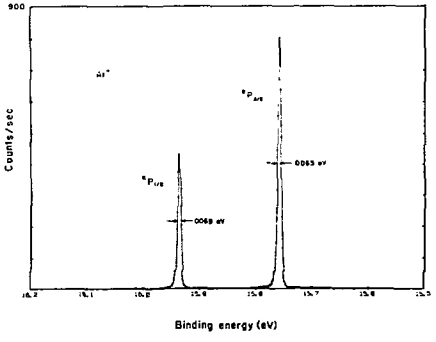

Fig. 28. Photoelectron spectrum of Ar^+ taken at 0.5 eV pass energy using He Iα (584 Å) radiation. (XBL 809-11856)

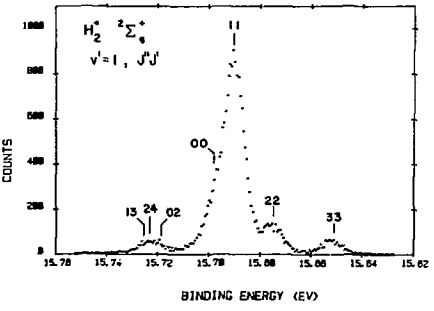

Fig. 30. Photoelectron spectrum of the v' = 1 level of H_2^+ taken at 0.5 eV pass energy using He Iα (584 Å) radiation. Pure H_2 was expanded from 1200 torr through a 70 μm-diameter nozzle. (XBL 8011-12798)

12. PHOTOELECTRON ANGULAR DISTRIBUTIONS OF SMALL MOLECULES†

C. M. Truesdale, S. H. Southworth, P. H. Kobrin, D. W. Lindle, and D. A. Shirley

We have made a survey of photoelectron angular distributions for the ionic states of H_2, deuterium (D_2), NO, N_2O, CO_2, CS_2, OCS, and H_2O at photon energies of 18-30 eV using the VUV continuum radiation available from the 8° beam line located at the Stanford Synchrotron Radiation Laboratory (SSRL). The highly polarized (97%) source with a time structure (0.3 nsec pulse width, 780 nsec repetition period) is used to obtain photoelectron spectra of small molecules by the time of flight (TOF) method. A detailed description of the apparatus is given in Ref. 1. Two detectors simultaneously measure the intensity of the ejected electrons. The detectors are placed at 0° and 54.7° (magic angle) to the polarization vector of the photon beam, and a comparison of their intensities determines the asymmetry parameter β. The transition amplitudes to the final continuum channels and their interference determines the β parameter which completely characterizes the photoelectron angular distribution. A schematic of the geometry used in the experiments is shown in Fig. 31.

In the dipole approximation when 100% polarized light is used, the equation that describes the angular distribution is given by the equation

$$\frac{d\sigma}{d\Omega}(\varepsilon,\alpha) = \frac{\sigma(\varepsilon)}{4\pi}\left[1+\beta(\varepsilon)\frac{(3\cos^2\alpha-1)}{2}\right]$$

where $\sigma(\varepsilon)$ is the total photoionization cross-section, α is the angle between the observation and polarization vector, and $d\sigma/d\Omega\ (\varepsilon,\alpha)$ is the differential cross-section. Our $\beta(\varepsilon)$ calculations must be corrected for the 3% unpolarized component of the radiation and the efficiencies of the two detectors in measuring photoelectrons with various kinetic energies.

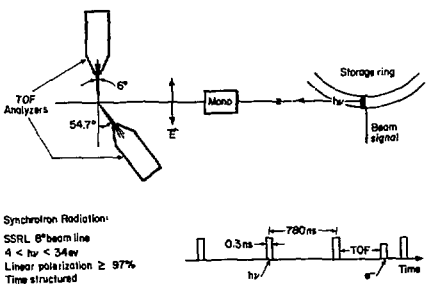

Fig. 31. Schematic of experimental setup. (XBL 7910-4225)

Examples of the variation of β and the cross-section σ with photon energy are shown for three ionic states of H_2O in Figs. 32-37. The water molecule has the electronic ground state valence configuration $2a_1^2\ 1b_2^2\ 3a_1^2\ 1b_1^2$. The $2a_1$ orbital derives most of its character from the O 2s with some contribution from the 1s orbitals of hydrogen. The $1b_2$ orbital arises from the bonding of the O 2p to the H 1s orbitals. The $3a_1$ orbital is essentially described by the bonding of the O 2p to the H 1s orbitals. Most of the character of the $1b_1$ orbital is described by the non-bonding orbitals of the O 2p. Roche and Salahub have used a multiple scattering theoretical model[3,4] to describe the β parameter and the cross-section for the H_2O molecule and the O atom.[5] There is very good agreement with their calculations. This gives strong evidence for the orbital picture described above.

For the other molecules studied, the theoretical calculations show only qualitative agreement with experiment. The principal value of these early measurements will probably be the calibration of the accuracy of several early theoretical estimates.

* * *

†Brief version of LBL-11822; to be submitted for publication.

1. M. G. White et al., Rev. Sci. Instrum. 50, 1268 (1979).
2. C. N. Yang, Phys. Rev. 74, 764 (1948).
3. D. Dill and J. L. Dehmer, J. Chem. Phys. 61, 692 (1974).
4. J. Siegel, D. Dill, and J. L. Dehmer, J. Chem. Phys. 64, 3204 (1976).
5. M. Roche and D. Salahub, J. Electron Spectrosc. Rel. Phen. 19, 273 (1980).

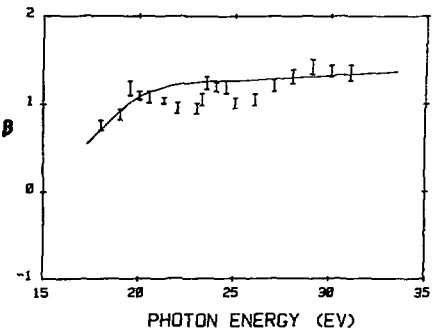

Fig. 32. Asymmetry parameter for the $^2B_1(1b_1)^{-1}$ state of H_2O versus photon energy (B.E. = 12.6 eV). The solid curves in Figs. 32-37 were calculated by Roche and Salahub. (XBL 8012-12879)

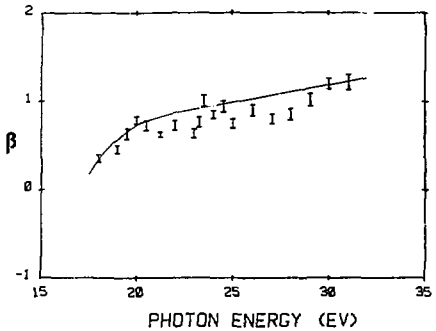

Fig. 33. Asymmetry parameter for the $^2A_1(3a_1)^{-1}$ state of H_2O versus photon energy (B.E. = 14.7 eV). (XBL 8012-12880)

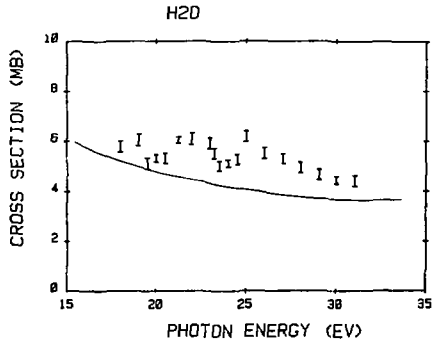

Fig. 35. Cross-section for the $^2B_1$ state of H_2O versus photon energy. (XBL 8012-12882)

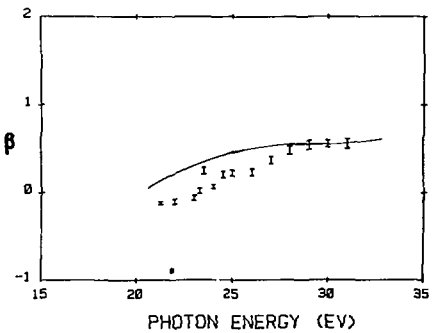

Fig. 34. Asymmetry parameter for the $^2B_2(1b_2)^{-1}$ state of H_2O versus photon energy (B.E.-18.5 eV). (XBL 8012-12881)

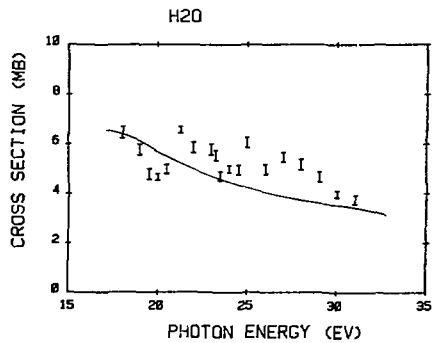

Fig. 36. Cross-section for the $^2A_1$ state of H_2O versus photon energy. (XBL 8012-12883)

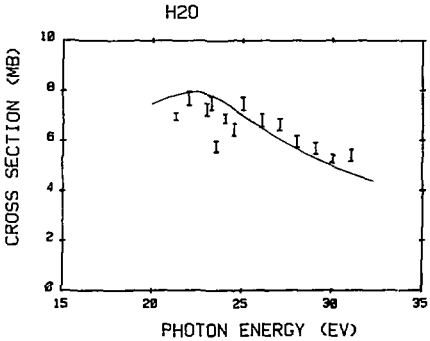

Fig. 37. Cross-section for the $^2B_2$ state of H_2O versus photon energy. (XBL 8012-12884)

RESEARCH PLANS FOR CALENDAR YEAR 1981

Photoelectron diffraction will be further studied and will be compared with surface EXAFS for elucidation of surface structures. Sulfur and other elements with K edges in the 800-4000 eV range, recently made accessible at SSRL, will be studied as adsorbates. Angle-resolved photoemission will be applied further to valence bands of noble-metal systems. Electron energy loss measurements on surfaces will be initiated.

Gas-phase studies will include photoelectron asymmetry measurements in atoms and molecules and Auger-electron asymmetry measurements in atoms. High-resolution molecular-beam photoelectron spectroscopy will be applied to several atomic and molecular systems.

1980 PUBLICATIONS AND REPORTS

Refereed Journals

1. R. S. Williams, D. Denley, D. A. Shirley, and J. Stöhr, "Soft X-ray Absorption Spectroscopy. Electronic and Morphological Structure of Poly(vinylidene fluoride)," J. Am. Chem. Soc. 102, 5717 (1980), LBL-8681.

2. R. A. Rosenberg, S.-T. Lee, and D. A. Shirley, "Observation of a Collective Excitation in the Ejected-Electron Spectra of Yb and Ba," Phys. Rev. A 21, 132 (1980), LBL-9120.

3. R. F. Davis, S. D. Kevan, B.-C. Lu, J. G. Tobin, and D. A. Shirley, "Condensed Phase Photoelectron Asymmetry," Chem. Phys. Lett. 71, 448 (1980), LBL-9384.

4. K. A. Mills, R. F. Davis, S. D. Kevan, G. Thornton, and D. A. Shirley, "Angle-Resolved Photoemission Determination of A-Line Valence Bands in Pt and Au Using Synchrotron Radiation," Phys. Rev. B 22, 581 (1980), LBL-9430.

5. D. Denley, P. Perfetti, R. S. Williams, and D. A. Shirley, "Carbon K-edge Fine Structure in Graphite Foils and in Thin-Film Contaminants on Metal Surfaces," Phys. Rev. B 21, 2267 (1980), LBL-9431.

6. E. D. Poliakoff, S. H. Southworth, M. G. White, G. Thornton, R. A. Rosenberg, and D. A. Shirley, "Decay Dynamics of the CN*($B^2\Sigma^+$) and XeF*($B^2\Sigma^+$ and $C^2\Pi_{3/2}$) States," J. Chem. Phys. 72, 1786 (1980), LBL-9491.

7. G. Thornton, R. F. Davis, K. A. Mills, and D. A. Shirley, "An Angle-Resolved Photoemission Determination of the Band-Structure of Platinum between Γ and X," Solid State Commun. 34, 87 (1980), LBL-9790.

8. M. G. White, S. H. Southworth, P. Kobrin, and D. A. Shirley, "The Photoelectron Angular Distributions of HBr and HI at hν = 21.2 eV," J. Elect. Spectros. and Rel. Phen. 19, 115 (1980), LBL-9807.

9. S. D. Kevan and D. A. Shirley, "High-Resolution Angle-Resolved-Photoemission Studies of the M-Point Surface State on Cu(001)," Phys. Rev. B 22, 542 (1980), LBL-10025.

10. R. F. Davis, S. D. Kevan, D. H. Rosenblatt, M. G. Mason, J. G. Tobin, and D. A. Shirley, "Substrate-Dependent C(1s) Shape Resonance in CO Overlayers on Ni(111) and Ni(001)," Phys. Rev. Lett. 45, 1877 (1980), LBL-11116.

LBL Reports

1. S. D. Kevan, R. F. Davis, D. H. Rosenblatt, J. G. Tobin, M. G. Mason, D. A. Shirley, C. H. Li, and S. Y. Tong, "Structural Determination of Molecular Overlayer Systems with Normal Emission Photoelectron Diffraction: c(2×2)CO-Ni(001) and ($\sqrt{3} \times \sqrt{3}$)R30° CO-Ni(111)," LBL-10024, to be submitted to Phys. Rev. Lett.

2. S. D. Kevan, "Normal Emission Photoelectron Diffraction Studies at SSRL," LBL-10963, to be published in Applied Optics.

3. S. D. Kevan, "Normal Emission Photoelectron Diffraction: A New Technique for Determining Surface Structure," Ph.D. thesis, LBL-11017.

4. S. D. Kevan, J. G. Tobin, D. H. Rosenblatt, R. F. Davis, and D. A. Shirley, "Temperature Dependence of Normal Emission Photoelectron Diffraction and Analogies with EXAFS," LBL-11199, accepted for publication, Phys. Rev. B.

5. R. F. Davis, K. A. Mills, G. Thornton, S. D. Kevan, and D. A. Shirley, "Angle-Resolved Photoemission Studies of Ag, Au, and Pt," LBL-11247.

6. D. J. Trevor, J. E. Pollard, W. D. Brewer S. H. Southworth, C. Truesdale, D. A. Shirley Y. T. Lee, "Photoionization Mass Spectrometry N_2 and of He Clusters," LBL-11249.

7. J. E. Pollard, D. J. Trevor, Y. T. Lee, and D. A. Shirley, "Photoelectron Spectroscopy of Supersonic Molecular Beams," LBL-11250.

8. D. J. Trevor, "Photoelectron Photoion Molecular Beam Spectroscopy," Ph.D. thesis, LBL-11434.

9. D. H. Rosenblatt, J. G. Tobin, M. G. Mason, R. F. Davis, S. D. Kevan, D. A. Shirley, C. H. Li, and S. Y. Tong, "Normal Photoelectron Diffraction of c(2×2)O(1s)-Ni(001) and c(2×2)S(2p)-Ni(001), with Fourier Transform Analysis," LBL-11447, submitted to Phys. Rev. B.

10. S. H. Southworth, P. H. Kobrin, C. M. Truesdale, D. W. Lindle, S. Owaki, and D. A. Shirley, "Photoelectron and Auger Electron Asymmetries: Alignment of $Xe^+(^2D_{5/2})$ by Photoionization," LBL-11483, to be submitted to Phys. Rev. Lett.

11. S. D. Kevan, R. F. Davis, D. H. Rosenblatt, J. G. Tobin, M. G. Mason, and D. A. Shirley, "Core Level Photoemission Cross-section Modulations and Resonances of Chalcogens and Carbon Monoxide Adsorbed on Low Miller Index Surfaces of Nickel," LBL-11484.

12. Z. Hussain, D. A. Shirley, C. H. Li, and S. Y. Tong, "Fourier-Transform Analysis of Normal Photoelectron Diffraction Data for Surface-Structure Determination," LBL-11686, to be submitted to Phys. Rev. Lett.

13. M. G. Mason, S. T. Lee, G. Apai, R. F. Davis, D. A. Shirley, A. Franciose, and J. H. Weaver, "Particle Size Induced Valence Changes in Samarium Clusters," LBL-11810, to be submitted to Phys. Rev. Lett.

14. Z. Hussain, J. J. Barton, E. Umbach, and D. A. Shirley, "Near Edge and EXAFS Studies of Sulfur in Various Coal Samples," LBL-11811, to be submitted to Phys. Rev. Lett.

15. C. M. Truesdale, S. H. Southworth, P. H. Kobrin, D. W. Lindle, and D. A. Shirley, "Photoelectron Angular Distributions of Small Molecules," LBL-11822, to be submitted for publication.

Invited Talks

1. D. A. Shirley, "Photoelectron Diffraction in Adsorbates," Science Meeting on Low-Temperature Physics and Surface Chemical Physics, Mexican Petroleum Institute, Oaxtapec, Mexico, January 2, 1980.

2. D. A. Shirley, "U.V. Spectroscopy-Chemistry," National Science Foundation Meeting, Washington, D.C., January 21, 1980.

3. D. A. Shirley, "Angular Distribution Effects in Photoemission from Solids," American Chemical Society National Meeting, Houston, Texas, March 24, 1980.

4. D. A. Shirley, "Relativity and Correlation Effects in Tunable-Energy Photoemission from Atomic Xe and Ba," 1980 March Meeting of The American Physical Society, New York, New York, March 27, 1980.

5. D. A. Shirley, "Adsorbate Structure from Photoelectron Diffraction" and "Angular Distributions of Photoelectrons from Solids and Gases," Department of Physics, Freie University, Berlin, West Germany, August 18, 1980.

6. D. A. Shirley, "Photoemission from Solids: The Transition from Solid-State to Atomic Physics," International Conference on X-ray Processes and Inner-Shell Ionization, Stirling University, Glasgow, Scotland, United Kingdom, August 25, 1980.

7. D. J. Trevor, "Photoionization and Photoelectron Spectroscopy of Supersonic Molecular Beams," Physical Chemistry Seminar, Illinois Institute of Technology, Chicago, Illinois, June 11, 1980.

8. S. D. Kevan, "Photoelectron Diffraction," Midwinter Gordon Conference on Solid State, University of California, Irvine, California, January 14, 1980.

9. S. D. Kevan, "Normal Photoelectron Diffraction Studies of Adsorbed Atoms and Molecules," Conference on Trends in Studies of Electronic Properties of Metals by Photoemission, Centre de Physique des Houches, Les Houches, France, March 3, 1980.

10. S. D. Kevan, "Normal Emission Photoelectron Diffraction Studies at SSRL," VIth International Conference on Vacuum-UV Radiation Physics, University of Virginia, Charlottesville, Virginia, June 2, 1980.

11. D. H. Rosenblatt, "A Critique of the 4° Beam Lines at SSRL," Seventh Annual Stanford Synchrotron Radiation Laboratory Users Meeting, Stanford, California, October 23, 1980.

h. Crossed Molecular Beams*

Y. T. Lee, Investigator

1. PRIMARY PRODUCT IDENTIFICATION AND DYNAMICS OF O + C_2H_4

R. J. Baseman, R. J. Buss, and Y. T. Lee

A major effort in chemistry research in recent years has been directed toward clarification of the complex reaction mechanisms occurring in combustion systems because a thorough understanding of these chemical processes should enable the development of fuel efficient and nonpolluting energy sources. Accurate information on the elementary reactions that occur in flames has often proven elusive because the species of interest are exceedingly reactive and cannot be isolated without secondary reactions. Investigation of these reactions under single collision conditions in crossed molecular beams can permit unequivocal observation of the primary reaction products and, at the same time, provide valuable dynamical information about the reactive encounter.

The reaction of oxygen atoms with ethylene is particularly interesting as a prototype of oxygen/olefin systems. The more recent studies[1] of this system have identified two major channels, the products being CH_3 + HCO, and H_2 + C_2H_2O. We have undertaken the study of O + C_2H_4 in order to clarify our understanding of the reaction mechanism and dynamics.

The apparatus was our crossed beam machine with rotatable quadrupole mass spectrometer, in which we intersected supersonic beams of O atoms and ethylene. The oxygen atoms were generated[2] in an rf plasma and were measured to have a peak velocity of 2.37×10^5 cm/sec and a velocity spread of about 25% FWHM. The olefin beam, which was produced by expansion of C_2H_4 from a 0.1 mm orifice in a quartz tube, had a peak velocity of 8.1×10^4 cm/sec with a velocity spread of 20% FWHM. Laboratory angular distributions were obtained for reactive product signal at m/e 43, 42, and 29. These distributions were found to be exactly superimposable within the errors of the experiment. Thus, we can conclude that the H atom elimination channel giving C_2H_5O (mass 43) is the primary product and that m/e 42 and 29 are merely fragments produced in the electron bombardment ionizer. The intensity of the m/e 42 signal which was the greatest of the three was used for the analysis. In the laboratory angular distribution of m/e 42 shown in Fig. 1, it can be seen that the product peaks near the center of mass as expected when the very light H atom has been ejected. Velocity distributions of the product were obtained at 10 angles by the cross correlation time of flight method, and the direct convolution method[3]

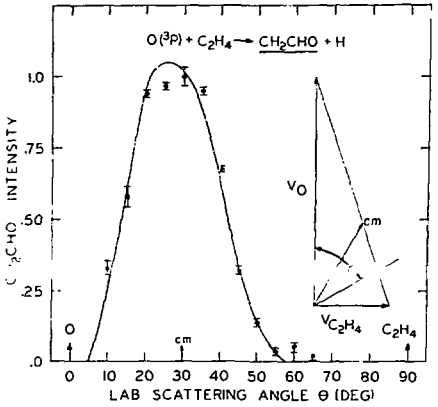

Fig. 1. Laboratory angular distribution of m/e 42 signal from O + C_2H_4. Solid line is a calculated best fit. Error bars are one standard deviation. (XBL 802-8221)

was used to analyze the data with the assumption that the product translational energy and the center of mass angular distributions were separable. The contour map of product flux which produced a best fit to the data (Fig. 2) shows that the product is not distributed symmetrically about 90° in the center of mass reference frame. The reaction must, therefore, occur extremely rapidly, the mean lifetime of the initial adduct being less than a rotational period.

The initial approach of O(^{3}P) to C_2H_4 occurs on a triplet surface and it is reasonable to postulate that the intermediate will be the triplet biradical CH_2CH_2O. This intermediate is expected to be very weakly bound (0 to 10 kcal/mole) with respect to loss of H atom. The major channel which has been previously reported, formation of HCO + CH_3, requires a hydrogen migration that is expected to have a very large barrier on a triplet surface. The formation of H_2 + ketene, previously reported to be a minor channel, involves a three- or four-centered elimination which should also require the surmounting of an impressive energy barrier. It is quite reasonable, then, that the H atom elimination is the dominant channel, and it is expected that this behavior will be typical of the family of oxygen atom/olefin reactions; simple bond rupture will tend to prevail over hydrogen migrations or multicenter elimination.

*This work was supported by the Director, Office of Energy Research, Office of Basic Energy Sciences, Chemical Sciences Division of the U. S. Department of Energy under Contract No. W-7405-ENG-48.

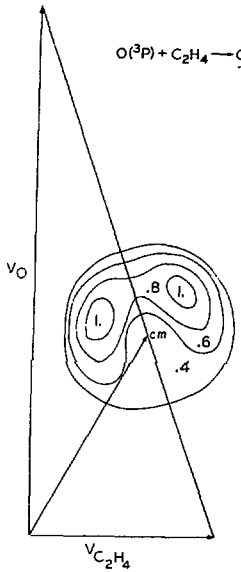

Fig. 2. Contour map of m/e 42 product flux shown on the canonical Newton diagram. (XBL 802-8219)

* * *

1. J. R. Kanofsky and D. Gutman, Chem. Phys. Lett. 15, 236 (1972); and B. Blumenberg, K. Hoyermann, and R. Sievert, Sixteenth Symposium on Combustion, p. 841, The Combustion Institute, 1976.
2. S. J. Sibener, R. J. Buss and Y. T. Lee, Rev. Sci. Instr. 51, 167 (1980).

2. REACTION DYNAMICS OF O + ACETYLENE

R. J. Baseman, R. J. Buss, P. Casavecchia, and Y. T. Lee

Acetylene molecules show a great affinity for oxygen atoms, the thermal rate constant being $k = 6.7 \times 10^{13} \exp(-4000/RT)$ cc $mol^{-1}s^{-1}$. While there remains some disagreement concerning the relative cross sections for different reactive channels, various researchers[1] have converged on a single qualitative description of the reaction. The major product is believed to be $CO + CH_2$ and a second channel, that of the hydrogen atom elimination to form C_2HO, is thought to occur. We have begun our investigation of the reaction $O + C_2H_2$ by measuring the relative cross section for the two channels and by examining the dynamics of the H-atom channel.

The crossed molecular beams apparatus has been previously described. The oxygen beam was a supersonic jet produced by expansion of a 5% O_2/He mixture in which was maintained an rf plasma discharge. The acetylene beam was a supersonic expansion of pure C_2H_2 that was delivered through a dry ice acetone bath to remove acetone contaminant. The mean collision energy was 7.9 kcal/mole with an energy spread of 40 FWHM. The angular distribution of m/e 41 signal is shown in Fig. 3. The product is seen to peak at the nominal center of mass angle; its intensity here was 3000 counts per second. Angular scans of m/e 28, which can arise from ionization of CO product or from fragmentation of C_2HO product in the ionizer, reveal that the H atom elimination channel is much more important than has previously been thought. The cross section for CO production is less than that of the H atom channel under these reaction conditions.

Velocity distributions of the m/e 41 signal were obtained at 9 angles using the cross correlation time of flight method. Deconvolution of the angular and velocity data using the method of Siska generated the contour map shown in Fig. 4. The product is seen to be sideways scattered in the center of mass reference frame. If the reaction proceeds with attack by oxygen perpendicular

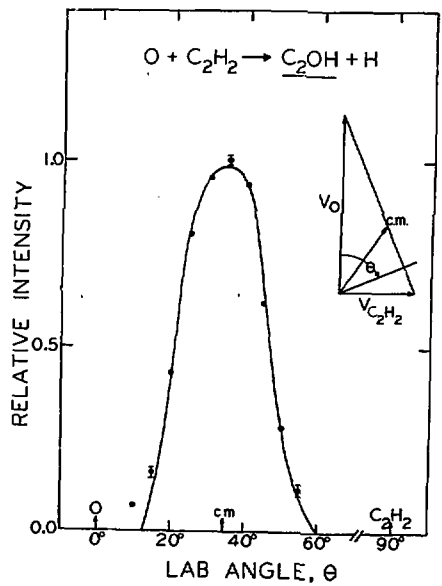

Fig. 3. Angular distribution of m/e 41 from the reaction $O + C_2H_2$. The solid line shows best fit. Error bars are one standard deviation of the mean. (XBL 7912-13561)

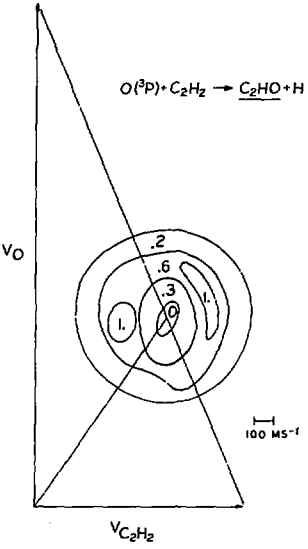

Fig. 4. Contour map of mass 41 product flux shown with the canonical Newton diagram. (XBL 802-8222)

to the C-C bond and hydrogen loss is rapid, the resulting angular distribution would be predominantly sideways peaked.

The product translational energy distribution peaks at 8 kcal/mole with about 30% of the available energy appearing in translation. The centrifugal barrier to H atom elimination is expected to be low because the hydrogen mass is small; thus, the large fraction of the energy in product translation suggests the presence of a potential energy barrier in the exit channel.

The $O(^3P)$ approaches C_2H_2 on a triplet surface and might be expected to form a triplet biradical adduct. Recent calculations by Harding[2] show that the barrier to hydrogen migration in this triplet species should be large, about 53 kcal/mole, and that loss of hydrogen atom should be the dominant process. Our experimental finding that C_2HO is a major product is in qualitative agreement with these calculations.

* * *

1. J. R. Kanofsky, D. Lucas, F. Pruss, and D. Gutman, J. Phys. Chem. 78, 311 (1974); B. Blumenberg, K. Hoyermann, and R. Sievert, Symp. (Int.) Combust., 16th, 841 (1977).
2. L. D. Harding, to be published.

3. VIBRATIONAL EFFECTS IN PROTON AND CHARGE TRANSFER IN THE H_2^+ + Ar SYSTEM

F. A. Houle, S. L. Anderson, and Y. T. Lee

Theoretical studies of charge transfer and proton transfer processes in the $(Ar\text{-}H_2)^+$ system, reactions (1)-(4) below,

$$H_2 + Ar^+ \rightarrow H_2^+ + Ar \qquad \Delta E = -0.15 \text{ eV} \qquad (1)$$

$$H_2 + Ar^+ \rightarrow ArH^+ + H \qquad \Delta E = -1.45 \text{ eV} \qquad (2)$$

$$H_2^+ + Ar \rightarrow Ar^+ + H_2 \qquad \Delta E = +0.15 \text{ eV} \qquad (3)$$

$$H_2^+ + Ar \rightarrow ArH^+ + H \qquad \Delta E = -1.30 \text{ eV} \qquad (4)$$

indicate that, although these reactions are direct, they involve several potential surfaces which are very close in energy. Transitions between these surfaces during the course of a collision are found to be very important, especially in reaction (2) where the reagents do not correlate to ground state products. The probability of undergoing such transitions depends strongly on vibrational motion of H_2 or H_2^+ as the system moves through an avoided crossing region. The transitions, or lack of them, will dictate the observable branching ratios between reactions (1) and (2) or (3) and (4). Experimental testing of the theory by measurement of integral and differential cross sections has been frustrated by the difficulty of producing reagents in known internal energy states, so much of the published work is restricted to Ar^+ ($^2P_{3/4}$, $^2P_{1/2}$) + $H_2(V = 0)$.[1] In this report, we describe the results of the first experiments in which the effects of both vibration and kinetic energy on Ar^+ and ArH^+ formation from H_2^+ + Ar have been examined.

The experimental technique used in this work was developed in this laboratory.[2] Briefly, it uses a He discharge lamp (Hopfield continuum), a vacuum ultraviolet monochromator, radiofrequency ion guides (15 MHz), a scattering cell, a quadrupole mass spectrometer, and a Daly detector. Ions are formed within the ion guides by photoionization of a supersonic neutral beam. Photoionization permits generation of an ion beam having a well-characterized distribution of vibrational states. The ions are then guided through a differentially pumped region, accelerated to the desired collision energy, and passed through a scattering cell. All reactant and product ions are subsequently collected, mass analyzed, and detected. Variation of ionizing wavelength and collision energy allows determination of integral reaction cross sections as a function of vibrational state and kinetic energy.

Figure 5 compares relative cross sections for v = 0-4 at several center-of-mass energies. Preliminary determinations of absolute values indicate that at low kinetic energies (< 1 eV) the charge transfer and proton transfer cross sections are similar in magnitude, in agreement with previous work on both H_2 + Ar^+ and Ar + H_2^+. The most important features to note are: (1) the very small charge transfer cross section for v = 0 compared to v > 0, and (2) the strong resemblance

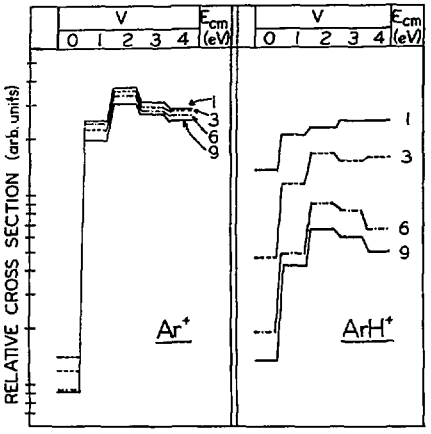

Fig. 5. Vibrational state dependence of proton and charge transfer cross sections at several kinetic energies: 1V(——), 3V(—·—), 6V(—— · ——) and 9V(——). (XBL 880-12891)

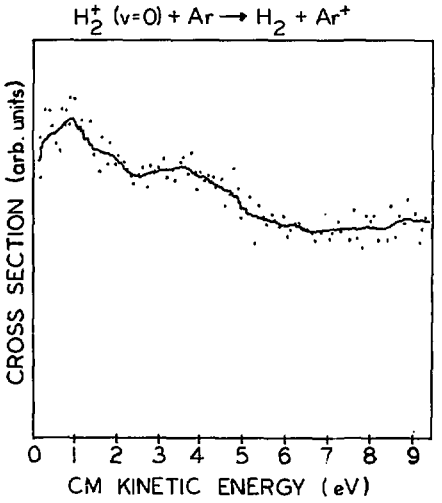

Fig. 6. Kinetic energy dependence of charge transfer between H_2^+(v = 0) and Ar. The points are the experimental data, and the solid line is the result of a 3-point smooth of the points. The maximum of the cross section is approximately 1.5 $Å^2$. (XBL 8012-12890)

between the vibrational dependence of both reactions at kinetic energies > 3 eV.

Theoretical treatments of long range charge transfer have shown that both energy resonance and favorable Franck-Condon overlaps enhance the process. The vibrational dependence shown in Fig. 5 is entirely consistent with this, except that energy resonance seems to be the controlling factor: the H_2^+ (v = 0) + Ar reaction is the only one that is non-resonant. Its cross section is very low despite reasonable Franck-Condon factors and the availability of up to 9 eV of kinetic energy, as shown in Figs. 5 and 6. These results seem to argue against the importance of translational-to-internal energy conversion in promoting charge transfer. In fact, the cross section for v = 0 falls with increasing kinetic energy.

The undulations in the cross section for H_2^+ (v = 0) charge transfer are very interesting. The mass combination is such that the effective width increases from 0.1 to 0.3 eV are not artificially wide although the dips at ~2.5 and 5 eV may be much sharper. Similar structure has been observed in our laboratory for D_2^+ (v = 0) + Ar → Ar^+ + D_2, but not for any other vibrational states of H_2^+ or D_2^+. The origin of the variation in cross section with kinetic energy, which has not been predicted theoretically, is not known, but may reflect aspects of an intimate collision process.

Theoretical treatments of the proton transfer channel have shown that only H_2^+ + Ar correlated to ArH^+. Since H_2^+ (v = 0) has little probability of undergoing charge transfer (a transition to an unreactive surface), it might be expected that direct proton transfer would be more facile for this state than for the higher vibrational states. In fact, at all energies vibration enhances proton transfer. Furthermore, the strong resemblance between the vibrational dependences for charge and proton transfer suggests that above ~ 3 eV, both channels involve passage through a common region of the potential energy surfaces available to the system. Failure to do so may result in largely nonreactive scattering. Regardless of the details of the collisions, it is not likely that proton transfer results from simple motion on the H_2^+ + Ar surface.

* * *

1. K. Tanaka, J. Durup, T. Kato and I. Koyano, J. Chem. Phys. 73, 586 (1980); W. A. Chupka and M. E. Russell, J. Chem. Phys. 49, 5426 (1968).
2. S. L. Anderson et al., to be published.

4. COMPARISON OF VIBRATIONAL ENERGY EFFECTS ON THE REACTIONS OF D_2^+ WITH H_2 AND H_2^+ WITH D_2

S. L. Anderson, F. A. Houle, D. Gerlich and Y. T. Lee

The reaction $H_2^+ + H_2 \rightarrow H_3^+ + H$ with its isotopic variants has been extensively studied. It is exoergic and has been shown to occur by a direct mechanism, with no evidence for a barrier.[1] The reaction cross section is large (ca. 100 Å^2) at thermal energies and falls rapidly with increasing collision energy.[1] This system is quite complex due to the existence of a number of low lying potential energy surfaces (PES). Particularly important is an avoided crossing parallel to the reaction coordinate in the entrance channel. This splits the entrance channel into two regions, each corresponding to one charge state of the reactants; say $H_2^+ + D_2$ and $H_2 + D_2^+$. There is a barrier between the two regions, which rapidly decreases as the reagents approach, allowing the possibility of mixing of the two charge states. Unfortunately, nearly all the experimental work to date has utilized H_2^+ prepared by electron bombardment, which populates a broad distribution of H_2^+ vibrational states. Since the charge state mixing and surface hopping behavior in $H_2^+ + H_2$ are expected to be strongly influenced by reagent vibration, the broad distribution of initial states largely obscures the detailed reaction dynamics.

We have carried out a series of experiments in which we measure the dependence of the various reaction cross sections on reagent charge state, isotopic composition, vibrational state, and collision energy. The experimental method has been described previously.[2] Photoionization is used to select the reagent ion vibrational state. The ions are allowed to react with the neutral reagent ion vibrational state. The ions are allowed to react with the neutral reagent in a scattering cell. The use of guided beam ion optics allows all the product ions to be collected and counted by a mass spectrometer detector.

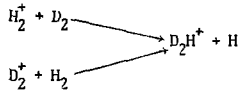

We have measured D_2H^+ production cross sections from both the $H_2^+ + D_2$ and $D_2^+ + H_2$ charge state. Figure 7 compares the cross sections as a function of reagent ion vibrational state for a number of cm collision energies. For $H_2^+ + D_2$, nominally a proton transfer reaction, vibrational excitation inhibits the reaction at low collision energies, but enhances it at energies above ~1.4 eV. The $D_2^+ + H_2$ (atom transfer) channel shows no vibrational effect at low collision energies. At energies from ~1 to 3 eV there is substantial vibrational enhancement, followed by a sharp vibrationally enhanced fall-off at energies greater than 3 eV. Earlier observations[3] of vibrational inhibition of the reaction $H_2^+ + H_2 \rightarrow H_3^+ + H$ at

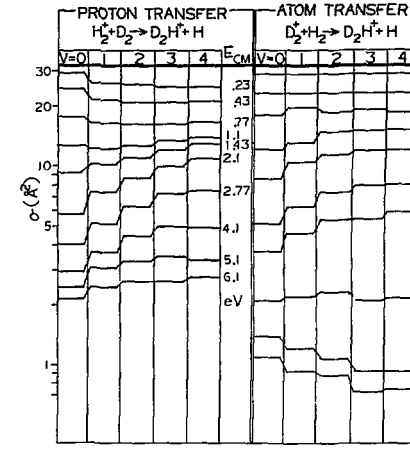

Fig. 7. Comparison of D_2H^+ production from $H_2^+ + D_2$ and $D_2^+ + H_2$. (XBL 808-10864)

low energies are seen to result from a combination of the "proton" and "atom" transfer.

At low and intermediate energies, the production of D_2H^+ from the $H_2^+ + D_2$ and $D_2^+ + H_2$ charge states occurs with similar cross sections and, at intermediate energies, the cross sections have comparable vibrational enhancement, suggesting similar dynamics. This observation is consistent with suggestion of facile charge state mixing in the entrance channel to the reaction[3,4] and suggests that mixing is nearly complete even for vibrationless reagents. Measurement of the energy dependence of the cross section for charge exchange of D_2^+ with H_2 supports the idea of a long range charge transfer process. The cross section is quite large and relatively independent of energy, as is expected for a long range interaction. A drop in cross section at low collision energy is probably due to competition with the reactive channel.

The fact that considerable differences are observed in the reaction of the $H_2^+ + D_2$ and $D_2^+ + H_2$ charge states at high collision energies shows that, at least for the collisions with small impact parameter which lead to reaction, charge transfer no longer mixes the charge states efficiently.

Collision Induced Dissociation. We have measured cross sections for H^+ and D^+ production in collisions of D_2^+ and HD. The cross sections show considerable vibrational enhancement as well as reduction in threshold with ion vibrational excitation. The cross sections increase from threshold to above 5 eV, where there is a leveling

off. The thresholds are consistent with the D_2^+ dissociation energy of 2.69 eV, when consideration is taken of the resolution broadening of our data. Ratios of the D^+ to the H^+ production channel for several D_2^+ vibrational states were obtained. At energies above ~ 5 eV the ratio is 3 within experimental error. This suggests that CID is occurring through statistical decay of intermediate complexes, which are most likely to be D_3^+ and D_2H^+. This is consistent with the results of Durup and Durup[8] who studied CID of $D_2^+ + D_2$ by crossed beam techniques. Below 5 eV, the ratios show evidence of non-statistical behavior.

Finally, it is observed that the shape, magnitude, and vibrational enhancement of the falloff of the $D_2^+ + H_2 \rightarrow D_2H^+ + H$ (atom transfer) cross section at energies >3 eV is very similar to the observed CID cross sections. This suggests that the falloff is due to competition between CID and D_2H^+ production. The fact that little, if any, competition is observed between CID and D_2H^+ production from $H_2^+ + D_2$ (proton transfer) further supports the idea that there is little mixing between the two reagent charge states at energies > 3 eV.

* * *

1. S. L. Anderson et al., In press: J. Chem. Phys.
2. S. L. Anderson, D. Gerlich, F. A. Houle and Y. T. Lee, LBL-10000 (1979), p. 341.
3. W. A. Chupka, M. E. Russell, K. Refaey, J. Chem. Phys. 48, 1518 (1968); I. Koyono, K. Tanaka, J. Chem. Phys. 72, 4858 (1980).

5. INTERACTION POTENTIALS FOR $Br(^2P + Ar, Kr, Xe(^1S)$

Piergiorgio Casavecchia, Guo-zhong He, Randal K. Spark, and Yuan T. Lee

This study is a continuation of a previous investigation from this laboratory on elastic scattering of F-Ne, Ar, Kr, Xe, and Cl-Xe. A newly designed higher resolution version[1] of the original universal crossed molecular beams machine is used. The collision energy was varied by adjusting the Br velocity by changing the bromine atom rare gas carrier, employing the seeded beam technique, and keeping the Br source nozzle temperature at ~1800 K. The beam was collimated in a differential pumping region to an angular spread of 1.0°. The target rare gas is a pure beam at room temperature, defined to an angular divergence of 1.9°. Under our geometrical arrangement, the collision volume is always contained in the viewing angle of the detector, which has an angular resolution of 1.0°. The velocity distributions of the beams are characterized by conventional "single shot" time-of-flight (TOF) measurements. Table 1 gives the beam characteristics and center-of-mass collision energies. As an example, one experimental result $I(\Theta)$ of Br scattered off Xe is presented in Fig. 8. Comparison of calculated $I(\Theta)$ with experimental $I(\Theta)$ provides the basis for evaluation of the interaction potentials. The results were obtained for Br-Xe, Kr, Ar system and plotted in Fig. 9 for the Br-Xe system. While the Br-Xe $X^{1/2}$ potential (ε = 0.645 kcal/mole, r_m = 380 Å) shows a stronger interaction than the 1 + potential of Kr-Xe, the Br-Kr (ε = 0.460 kcal/mole, r_m = 3.90 Å) and Br-Ar (ε = 0.380 kcal/mole, r_m = 3.73 Å) $X^{1/2}$ potentials are closer to the corresponding rare gas pair. The $I^{3/2}$ potential for all three systems is found to have a more shallow ε, a slightly larger r_m, and a more repulsive wall than the $^1\Sigma^+$ potential of the corresponding rare gas pair.

It should be noted that there exists quite a good agreement between the slope of the repulsive inner wall of the ground state curves estimated from diffuse spectra[1,2] and derived from the experiments described in this article. What our study adds is the absolute scale of the internuclear distance.

* * *

1. R. K. Spark, Ph.D. thesis, University of California, Berkeley (1979); M. F. Golde and A. Kvaran, J. Chem. Phys. 72, 434 (1980); J. Chem. Phys. 72, 442 (1980).
2. J. Tellinghuisen et al., J. Chem. Phys. 65, 4475 (1976).

Table 1. Beam characteristics and center-of-mass collision energies.

Br beam Seeded Mixture	T/K	Stagnation Pressure (torr)	Mach Number	Peak $v/10^4$ cm/s	(FWHM) $\Delta v/v$	Br-Xe	Br-Kr	Br-Ar
9% Br_2 + 91% Xe	1206	700	8.1	7.86	17	4.2	3.8	2.9
7.7% Br_2 + 92.3% Ar	3017	820	10.5	12.42	15	9.8	8.4	–
6.3% Br_2 + 93% He	8505	1000	9.1	20.86	17	26.4	–	14.8
Xe	298	200	17.3	3.08	10			
Kr	296	300	17.6	3.81	10			
Ar	296	300	17.3	5.55	10			

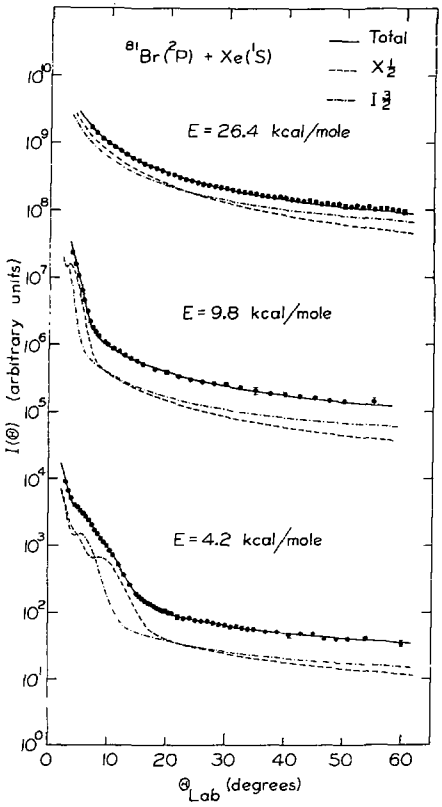

Fig. 8. Laboratory angular distributions of scattered Br for the $Br(^2P) + Xe(^1S)$ system at three collision energies. Solid circles are data points, and the solid curves are calculated from the best fit potentials, averaging over angular and velocity distributions of experimental conditions. Dashed and dashed-dotted curves represent the relative contribution to I(Θ) of the $X^{1/2}$ and $I^{3/2}$ potentials according to Eq. (1). Typical error bars are ± 2 standard deviations of the mean. (XBL 804-9352)

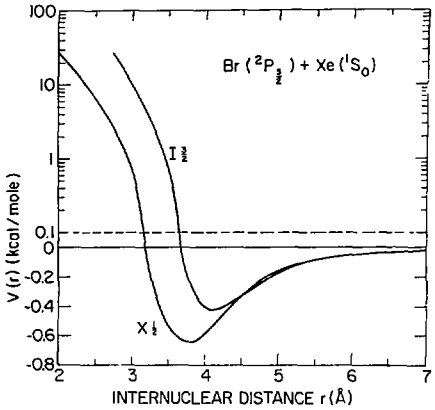

Fig. 9. Interaction potentials of $Br(^2P_{3/2}) + Xe(^1S_0)$. Note the scale change at V(r) higher than 0.1 kcal/mole. (XBL 804-6977)

6. ON THE PHOTODISSOCIATION OF NITROMETHANE AT 266 nm†

H. S. Kwok, G.-Z. He, R. K. Sparks, and Y. T. Lee

Nitromethane is one of the high yield clean liquid fuels; its detonation characteristics have been studied quite extensively. Recently, there has also been some interest in the photodissociation of nitromethane because of the possibly important role played in atmospheric chemistry. The absorption spectrum of nitromethane in the UV region consists of a main band peaking at 190 nm with a relatively large cross section of $\sim 2 \times 10^{-17}$ cm^2 and a much weaker band at around 270 nm with almost a 600 times smaller cross section. The transition is believed to be a $n \rightarrow \pi^*$ transition into a NO_2 π orbital. A quantum yield of unity was often assumed for dissociation over the entire absorption wavelengths in view of the continuous nature of the absorption spectrum.

However, in an earlier study of the photodissociation of nitromethane in liquid using 266 nm picosecond pulses, it was found that the product of NO_2 seemed to increase linearly in time after an induction period of several nanoseconds after

the laser pulsed.[1] This apparent abnormal behavior was in line with the suggestion that the photodissociation of CH_3NO_2 at 266 nm is indirect[2] and raised the question of quantum yield and primary dissociation mechanism at a weaker absorption band around 270 nm.

We performed a study of the photodissociation of nitromethane and nitromethane clusters in a crossed laser molecular beam apparatus. Our purpose was to clarify whether the previously reported photodissociation of nitromethane at 266 nm can actually take place under collision-free conditions. If the excitation of isolated nitromethane is not a direct photodissociation transition and does not dissociate appreciably under collision free conditions, it will be interesting to answer the question of whether the dissociation will be facilitated by exciting CH_3NO_2 in small molecular clusters of CH_3NO_2, or whether the vibronically excited clusters will only dissociate into molecular products by breaking van der Waal's bond through a vibrational predissociation process.

After an intensive search for the most likely photodissociation products, CH_3 and NO_2 at masses 15 (CH_3^+), 46 (NO_2^+), no signal was observed even after accumulating for over 40,000 laser shots. Signals were also checked for less likely dissociation channels at masses 30 (NO^+), 31 (HNO^+), and 45 (CH_3NO^+); but, again, no evidence of dissociation was found at any of these mass numbers. Detector angles were set at 20° and 30° from the molecular beam in our search for signal. According to a velocity diagram using the molecular beam velocity and the c.m. translational recoil velocity of the fragment for a given product translational energy, dissociation products should reach these laboratory detector angles even if a large fraction of excess energy of 45 kcal/mole appears as internal excitation of products. For CH_3 and NO_2, the required product translational energies are only 0.1, 0.2, and 0.9, 2.0 kcal/mole respectively.

According to an estimate of the sensitivity of our detection system, commensurate with the integration time and the intensity of the molecular beam, the minimum detectable dissociation cross section is approximately 10^{-21} cm^2 if the molecule dissociates with a lifetime shorter than 10^{-5} second, which is the transit time of the molecules passing through the viewing zone of the detector. This estimate is also in agreement with the results of ozone and ketene photofragmentations experiment which have been successfully performed using this apparatus. The published absorption cross section for nitromethane is around 3×10^{-20} cm^2 at 266 nm. Therefore, the apparent conclusion is that nitromethane excited at 266 nm does not photodissociate directly. Namely, the dissociation lifetime must be much longer than 10^{-5} seconds under collision free conditions.

Crossing the laser (266 nm) with the molecular beam containing small fractions of dimers and trimers of nitromethane, signals due to laser excitation were observed at mass 61 ($(CH_3NO_2)_2^+$) and 122 ($(CH_3NO_2)_3^+$). These signals were due to the following vibrational predissociation processes of vibronically excited molecular clusters:

$$(CH_3NO_2)_2 + h\nu \rightarrow (CH_3NO_2)_2^* \rightarrow 2CH_3NO_2$$

$$(CH_3NO_2)_3 + h\nu \rightarrow (CH_3NO_2)_3^* \rightarrow (CH_3NO_2)_2 + CH_3NO_2.$$

This predissociation occurs because the excitation energy in the vibrational degrees of freedom in the cluster is larger than the binding energy between components of the cluster. Similar predissociations have been observed via infrared vibrational excitation in clusters of benzene, ammonia, methanol, water, and hydrogen fluoride. Figures 10 and 11 show the angular and velocity distributions of the product detected as $(CH_3NO_2)_2^+$. By comparison with the velocity distribution of the CH_3NO_2 trimers before dissociation, we can see that the extra translational energy in the fragments broadens the velocity distribution considerably.

From Fig. 12 it is clearly seen that the maximum translational energy in the predissociation product is about 1 kcal/mole. However, most of the product fragments have no excess kinetic energy. This observation is almost identical to the results on the predissociation of benzene clusters.

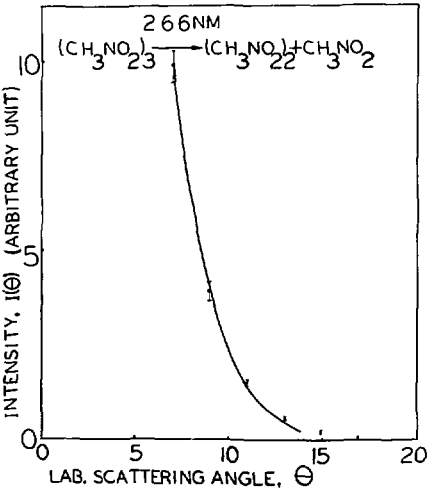

Fig. 10. Laboratory angular distributions of $(CH_3NO_2)_2$ from vibrational predissociation of vibronically excited $(CH_3NO_2)_3$ at 266 nm excitation. Dots are experimental results. The solid curve is the calculated angular distribution using the energy distribution of Fig. 12.
(XBL 8010-12360)

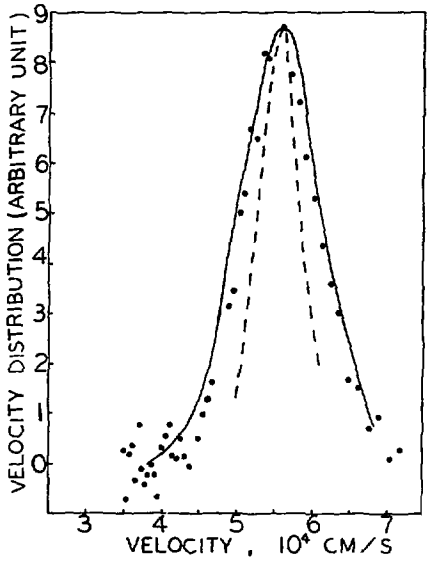

Fig. 11. Laboratory velocity distributions of $(CH_3NO_2)_2$ from $(CH_3NO_2)_3$. Symbols are the same as indicated in Fig. 10. Dashed curve is the velocity distribution of $(CH_3NO_2)_3$. (XBL 8010-12362)

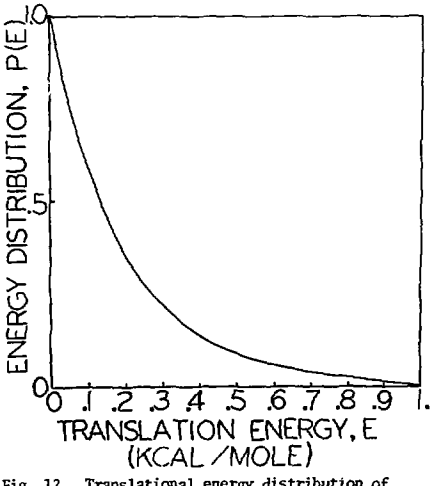

Fig. 12. Translational energy distribution of the process $(CH_3NO_2)_3 \xrightarrow{266\ nm} (CH_3NO_2)_2 + CH_3NO_2$ which gives the best fit to the data shown in Figs. 10 and 11. (XBL 8010-12361)

The observation of strong predissociation signal from the clusters also points to the conclusion that the lack of signal from the photodissociation of CH_3NO_2 experiment is indeed a real indication that CH_3NO_2 excited by 266 nm does not dissociate directly. As mentioned above, it implies an upper limits of 10^{-22} cm^2 for the direct photodissociation cross section of CH_3NO_2. Since the corresponding absorption cross section is 3×10^{-20} cm^2, this absorption must be due to a bound-bound transition. The observation of NO_2 fragments in all previous bulk experiments on nitromethane must be due to collisional dissociation of the excitation molecules. At atmospheric pressure, collision relaxation should compete with collisional dissociation, and the assumption of quantum yield of unity at weaker absorption band peaking at 270 nm is clearly not justified.

* * *

†This work was partially supported by the Office of Naval Research under Contract No. N00014-75-C-0671.

1. W. L. Faust, et al., in Chemical Physics 4: Picosecond Phenomena, Springer-Verlag, New York (1978).
2. K. Spear, Chem. Phys. Lett. 54, 373 (1978).

7. MEASUREMENT OF SINGLET-TRIPLET SPLITTING OF CH_2†

C. C. Hayden, D. M. Neumark and Y. T. Lee

The first two electronic states of methylene, CH_2, have been frequently studied, but the energy splitting between the ground ($^3B_1$) and lowest excited ($^1A_1$) state has not been unambiguously determined. Methods, based on observation of the photochemical threshold for production of the two states and on equilibration between them, have given a value of about 8-10 kcal/mole. However, the most direct previous experiment was a laser photoelectron detachment study of the CH_2^- ion; and, from it, a value of 19.5 kcal/mole was assigned to the splitting.1

We recently performed a photofragmentation study of ketene (CH_2CO) to provide another direct measurement of the methylene singlet-triplet splitting. A supersonic beam of ketene seeded in helium was crossed at right angles with the beam from a lumonics excimer laser borrowed from the San Francisco Laser Center. The photolysis products, CH_2 and CO, were detected by an electron impact ionization quadrupole mass spectrometer and were velocity analyzed by the time of flight technique. A product was detected at several laboratory angles from photodissociation with light at 350 nm and 308 nm.

At 350 nm, we observed a single peak in our time of flight spectra in which the fastest product corresponds to 4.0 ± 0.5 kcal/mole of translational energy. The signal at this wavelength is due entirely to triplet product, as the photon energy of 81.7 kcal/mole is insufficient to produce singlet CH_2. Thus the process

$$CH_2CO \rightarrow CH_2(^3B_1) + CO$$

is endoergic by 77.1 ± 0.5 kcal/mole. The experiments at 308 nm (92.8 kcal/mole) also yielded a single peak, with the fastest fragments corresponding to 6.7 ± 0.5 kcal/mole of product translational energy. This must be due to singlet CH_2 therefore requires 86.1 kcal/mole. Combining this with the data at 350 nm yields a splitting of 8.4 kcal/mole, with an estimated accuracy of ± 0.5 kcal/mole.

In summary, we have determined the CH_2 singlet-triplet splitting by measuring fragment energy distributions from the photofragmentation of ketene at two different wavelengths. Our results agree with several previous experiments and theoretical predictions but do not support the interpretation of photoelectron detachment experiments, which gives a value of 19.5 kcal/mole for this quantity. In addition, we have found that photolysis of ketene at 308 nm produces entirely singlet methylene, contrary to earlier work where it was concluded that there was significant triplet production.[2]

The rare gas halide laser used in this research was a loan from the San Francisco Laser Center Supported by the National Science Foundation under Grant No. CHE79-16250 awarded to the University of California at Berkeley in collaboration with Stanford University.

* * *

†This work is partially supported by the Office of Naval Research under Contract No. N00014-75-C-0671.

1. P. F. Zittel et al., J. Am. Chem. Soc. 98, 3731 (1976).
2. V. P. Zabransky and R. W. Carr, Jr., J. Am. Chem. Soc. 98, 1130 (1976).

8. DYNAMICS OF ENDOTHERMIC REACTIONS $X + YR \rightarrow XY + R$

D. Krajnovich, Z. Zhang, F. Huisken, and Y. T. Lee

We have used the crossed molecular beams method to study the following endothermic reactions:

Reaction	ΔH (kcal/mole)	
$I + CH_3Br \rightarrow CH_3 + IBr$	27	(1)
$I + CF_3Br \rightarrow CF_3 + IBr$	25	(2)
$Br + CH_3I \rightarrow CH_3 + IBr$	14	(3)
$Br + CF_3I \rightarrow CF_3 + IBr$	11	(4)

Relative collision energies greater than 80 kcal/mole were obtainable by the seeded beam technique. For each reaction, laboratory angular and time-of-flight distributions of the IBr product were measured at two or more collision energies. Detailed contour maps of the product flux as a function of center-of-mass angle and velocity may be extracted from the data. These contour maps illustrate the important role of angular momentum conservation in determining the product translational energy distribution in endothermic reactions.

The qualitative features of all four reactions are similar and are summarized below:

a. The IBr product peaks strongly backwards with respect to the velocity of the attacking halogen atom.

b. On the average, more than half of the excess energy (relative collision energy minus the endothermicity), appears as translational energy of the products.

c. Essentially, no products are formed with very low translational energy, indicating that the initial orbital angular momentum is mainly converted into product orbital angular momentum ($L \rightarrow L'$). This effect is less pronounced for reactions (1) and (3), since the leaving group is a light CH_3.

d. The reaction cross-sections all increase very steeply with increasing collision energy, due to the increased density of available product states as well as to increase in the actual "state-to-state" cross-section at higher collision energies.

e. No evidence was observed for the substitution reactions $X + YR \rightarrow Y + XR$ at any collision energy, even though these reactions are favored energetically.

9. STATE DISTRIBUTION OF PHOTODISSOCIATION PRODUCTS OF O_3

Guo-zhong He, R. J. Sparks, H. S. Kwok, and Y. T. Lee

The purpose of this work was to investigate the laser-frequency dependence of product state distributions of the ozone photolysis. Important questions which need to be answered about the photodissociation of ozone are the variation of branching ratio between $O_2(^3\Sigma_g^-)$ and $O_2(^1\Delta_g)$ and the vibrational state distributions of $O_2(^1\Delta_g)$ as a function of photon energy.

High resolution molecular beam measurements of the translational velocity distribution of the primary photolysis products of ozone were carried out at 279 nm, 276 nm, 266 nm, 259 nm, and 248 nm. Identification of product quantum states and their population distributions are obtained from the analysis of time-of-flight velocity spectra.

The molecular beam machine used for this experiment and the method for data processing and analysis have been described in detail.[1,2] Experiments were carried out by crossing a supersonic molecular beam of ozone seeded in argon at

a right angle with the laser beam of various frequencies; a frequency quadrupled pulsed Nd:YAG laser for 266 nm; a frequency doubled pulsed dye laser for 279 nm, 276 nm, and 259 nm; and an excimer laser for 248 nm.

The energy diagram of $O + O_2$ and photon energies of the five laser wavelengths used are shown in Fig. 13. Product state distributions obtained for these laser wavelengths are shown in Table 2.

From the experimental results, we concluded:

a. $O_2(^3\Sigma_g^-)$ production was found to be around 10% in the frequency range covered. It increased slightly (~1-2%) as the laser wavelength decreased from 279 nm to 248 nm.

b. The vibrational state distribution of $O_2(^1\Delta_g)$ obeys approximately the Boltzmann distribution, and the vibrational temperature of $O_2(^1\Delta_g)$ increases. Approximate vibrational temperatures are 2700 K and 3500 K at 266 nm and 259 nm, respectively.

* * *

1. R. K. Sparks et al., J. Chem. Phys. 72, 15 (1980).
2. R. K. Sparks, Ph.D. thesis, University of California, Berkeley (1979).

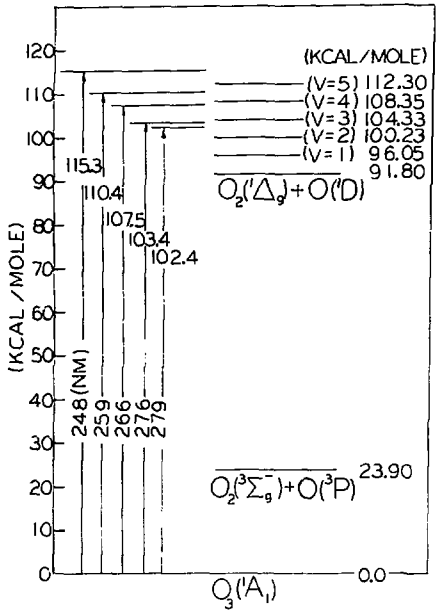

Fig. 13. The energy diagram of $O + O_2$ and the photon energies. (XBL 8012-12949)

Table 2. Product state distributions (%) for the five laser wavelengths

Laser Wavelength / State	279 (nm)	276 (nm)	266 (nm)	259 (nm)	248 (nm)
$O_2(^1\Sigma_g^-)$	12.2	12.2	11.6	11.5	10.4
$O_2(^1\Delta_g)$ v = 0	57.6	53.1	50.3	42.1	37.9
v = 1	25.2	25.5	23.9	23.0	28.3
v = 2	5.0	9.2	9.7	11.5	10.4
v = 3			4.5	7.7	5.2
v = 4				4.2	4.8
v = 5					3.0

10. MOLECULAR BEAM STUDIES OF THE F + HD REACTION

D. M. Neumark, C. C. Hayden and Y. T. Lee

We have investigated the reactive scattering of atomic fluorine with H_2 and its isotopic variants in our high resolution crossed molecular beams apparatus. The F + H_2 and F + D_2 reactions have been extensively examined and reported elsewhere.[1] We have also undertaken preliminary studies of the F + HD reaction, and our results thus far are summarized in this article.

This group of reactions is particularly interesting to study in a crossed beams experiment because the large vibrational spacing in the HF(DF) product, along with the small amount of product rotational energy, permit one to obtain center-of-mass angular and energy distributions for each product vibrational state. One can therefore learn a great deal about the detailed reaction dynamics of these systems, and the comparison of the results with theoretical predictions can be quite fruitful. For example, the F + H_2 reaction was studied at collision energies of 2.00 and 3.17 kcal/mole. At the lower energy, all the HF product vibrational states (v = 1-3) were strongly backward-scattered with respect to the incoming fluorine beam. This is the expected result if the reaction is most likely to occur for a zero impact parameter collision in which all three atoms are collinear. At the higher energy, the v = 1 and v = 3 products were still backward-peaked, but the v = 2 product shifted to a much broader distribution. This indicated that higher impact parameter collisions were contributing significantly to HF v = 2 formation, whereas the contribution from zero impact parameter collisions was depleted.

The results were consistent with a three-dimensional quantal calculation by Redmon and Wyatt.[2] They predicted a maximum in the HF v = 2 reaction probability, which occurred at zero impact parameter for low energy collisions but moved out to nonzero impact parameters for collision energies above 2.5 kcal/mole. Our results may therefore represent the first observation of such a resonance effect in a reactive system.

We hoped to find similar effects in the F + HD reaction. Angular scans of the HF and DF products were taken at collision energies of 2.38 and 4.55 kcal/mole, and these are shown in Figs. 14 and 15. Because we have no velocity distribution data as yet, we have not determined the center-of-mass product angular and energy distributions. However, several noteworthy features are apparent in the angular scans.

The DF angular distributions show that the product is predominantly backward-scattered at both energies. The HF angular distributions are markedly different from the DF distributions. At both energies, the HF back-scattered product is considerably less intense, and the most intense signal comes from forward-scattered product. This is at variance with a recent classical trajectory calculation by Muckerman who calculated the angular distribution at 3.0 kcal/mole and found both products to be strongly back-scattered. Up to now no

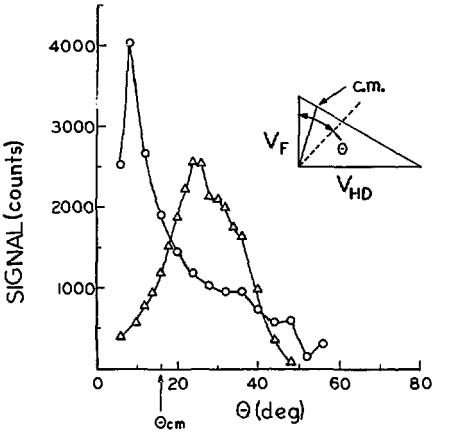

Fig. 14. Laboratory angular distribution of products for F + HD collision energy of 2.38 kcal/mole. O = HF, Δ = DF. (XBL 8012-12951)

3-dimensional quantal calculations have been performed on the F + HD system. These would be most interesting because the classical description of the reaction dynamics appears inadequate.

Thus far, the features observed in the F + HD reaction clearly warrant further investigation. We plan to take time-of-flight measurements of

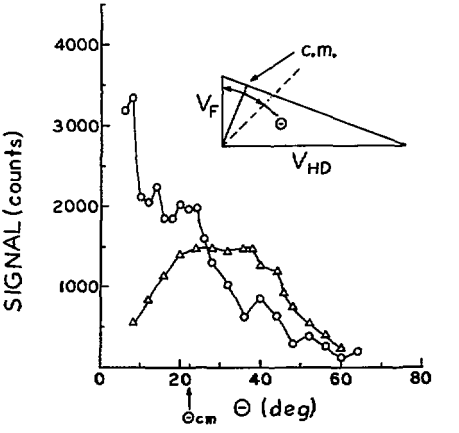

Fig. 15. Same as Fig. 14 at collision energy of 4.55 kcal/mole. (XBL 8012-12950)

the products at several energies to obtain energy and angular distributions for all observed vibrational states. We are especially interested in doing the experiment with a liquid nitrogen-cooled HD beam, which will allow the collision energy to be lowered continuously down to 1.0 kcal/mole. In a one-dimensional (1-D) quantal calculation on the F + HD reaction, a sharp resonance was predicted in the HF reaction probability at low collision energy.[3] Although it is risky to predict an experimental result from a 1-D calculation, one might expect the calculation to approximate a zero-impact parameter collision in which all three atoms are collinear. The products from such a collision will be sharply backward-peaked. Therefore, a resonance in the 1-D reaction probability should correspond to enhanced backward-scattered product. The observed forward-scattered HF may result from this zero-impact parameter resonance moving out to higher impact parameters at the energies we studied. If this is true, the HF distribution should become more backward-peaked as the energy is lowered. We hope to observe this shift by doing the experiment at the low energies accessible with the cooled HD beam.

* * *

1. R. K. Sparks et al., "Molecular Beam Studies of Reaction Dynamics of F + H_2, D_2," Horizons of Quantum Chemistry, D. Reidel Publishing Company, pp. 91-105 (1980).
2. M. J. Redmon and R. E. Wyatt, Chem. Phys. Lett. 63, 209 (1979).
3. G. C. Schatz, J. M. Berman, and A. Kuppermann, J. Chem. Phys. 63, 685 (1975).

RESEARCH PLANS FOR CALENDAR YEAR 1981

In the area of state-to-state chemistry, heavy particle quantum mechanical dynamical resonance phenomena, the vibrational state selected ion-molecule reactions, and the reaction of electronically excited atoms and molecules will be pursued. The investigation of dynamic resonance phenomena will focus on the translational energy dependence of the product branching ratio and angular distributions of individual vibrational states in the reaction of F + HD. In ion-molecule reactions, the excitation of vibrational degrees of freedoms in reagents often causes a more drastic change in the reaction dynamics than that found in the reactions of neutral molecules. A systematic study will be carried out to investigate the degree to which these effects are the result of the vibrational state dependent non-adiabatic coupling or charge transfer in the entrance channel of the reactants.

Molecular beam studies of combustion related elementary chemical reactions will remain one of our major research subjects. Determination of reaction mechanisms of oxygen atoms with olefins and halogenated olefins will be continued. New projects which will be initiated in the coming year include the development of an OH radical beam source, the comparison of the detection and identification of quantum states of OH radicals by the multiphoton ionization process and laser induced fluorescence method, and the reaction of alkyl radicals with O atoms.

A new molecular beam apparatus, which has been under construction during the past year, will be put into operation. This apparatus, equipped with a photoionization mass spectrometer, is designed for the investigation of infrared absorption spectra and the heat of formation of polyatomic radicals using various IR laser excitation, photoionization schemes.

The interaction of reaction intermediates, especially chemically activated polyatomic radical molecules of known excitation energy formed by single collision conditions in crossed molecular beams with high power CO_2 laser, will be investigated. Of particular interest in this interaction is the laser stabilization of chemically activated complexes due to stimulated emission of IR photons. Since the efficiency of laser stabilization processes depends on the lifetime of the reaction complexes and the intensity of the laser, the observed results will provide valuable information on the nature of molecular quantum states in the continuum and the dynamics of intramolecular energy transfer.

1980 PUBLICATIONS AND REPORTS

Refereed Journals

1. S. J. Sibener and Y. T. Lee, "Internal Energy Dependence of Molecular Condensation Coefficients Determined from Molecular Beam Surface Scattering Experiments," in Rarefied Gas Dynamics, Eleventh International Symposium on Rarefied Gas Dynamics, Vol. 2, p. 1417, Commissariat A L'Energie Atomique, Paris, France, edited by R. Campargue, (1979).

2. S. J. Sibener, R. J. Buss, and Y. T. Lee, "Development of a High Pressure Atomic Oxygen Beam Source," in Rarefied Gas Dynamics, Eleventh International Symposium on Rarefied Gas Dynamics, Vol. 2, p. 981, Commissariat A L'Energie Atomique, Paris, France, edited by R. Campargue, (1979).

3. R. J. Buss, M. J. Coggiola, and Y. T. Lee, "Molecular Beam Studies of Unimolecular Reactions, Cl, F + C_2H_3Br," Farad. Disc. Chem. Soc. 67, 162 (1979).

4. R. K. Sparks, L. R. Carlson, K. Shobatake, M. L. Kowalczyk, and Y. T. Lee, "Ozone Photolysis: A Determination of the Electronic and Vibrational State Distributions of Primary Products," J. Chem. Phys. 72, 1401 (1980).

5. S. J. Sibener, R. J. Buss, C. Y. Ng, and Y. T. Lee, "Development of a Supersonic $O(^3P_J)$, $O(^1D_2)$ Atomic Oxygen Nozzle Beam Source," Rev. Sci. Instrum. 51, 167 (1980).

6. S. J. Sibener, R. J. Buss, P. Casavecchia, T. Hirooka, and Y. T. Lee, "A Crossed Molecular Beams Investigation of the Reactions $O(^3P)$ + C_6H_6, C_6D_6," J. Chem. Phys. 72, 4341 (1980).

7. C. H. Becker, P. Casavecchia, P. W. Tiedemann, J. J. Valentini, and Y. T. Lee, "Study of the Reaction Dynamics of Li + HF, HCl by the Crossed Molecular Beams Method," J. Chem. Phys. 73, 2833 (1980).

8. F. P. Tully, N. N. Cheung, H. Haberland, and Y. T. Lee, "Mass and Orientation Effects in Dissociative Collisions Between Rare Gas Atoms and Alkali Halide Molecules," J. Chem. Phys. 73, 4460 (1980).

LBL Reports

1. C. C. Kahler, "Crossed Molecular Beam Studies of Chemiluminescent Reactions," Ph.D. thesis, LBL-10545.

2. C. C. Kahler and Y. T. Lee, "Crossed Molecular Beam Studies of Chemiluminescent Reactions: F_2 + I_2, Br_2 and ICl," submitted to J. Chem. Phys. May 1980, LBL-11005.

3. S. L. Anderson, T. Hirooka, P. W. Tiedemann, B. H. Mahan, and Y. T. Lee, "Photoionization of $(H_2)_2$ and the Clusters of O_2 Molecules," submitted to J. Chem. Phys. June 1980, LBL-11033.

4. Yuan T. Lee and Y. Ron Shen, "Molecular Beam Studies of IR Laser Induced Multiphoton Dissociation and Vibrational Predissociation," submitted to Physics Today, June 1980, LBL-11105.

Invited Talks

1. Y. T. Lee, "Reaction of Oxygen Atoms with Unsaturated Hydrocarbons," Harvard-MIT Joint Physical Chemistry Seminar, Cambridge, Massachusetts, March 13, 1980.

2. Y. T. Lee, "Dynamics of Photodissociation of O_3," XI Informal Conference on Photochemistry, Newport Beach, California, March 30-April 3, 1980.

3. D. J. Krajnovich, "Competing Dissociation Channels in Multiphoton Dissociation of Polyatomic Molecules, Photochemistry Conference, Newport Beach, California, March 30-April 3, 1980, LBL-10492 Abs.

4. Y. T. Lee, "Reaction of Oxygen Atoms with Unsaturated Hydrocarbons," Department of Chemistry, Columbia University (Falk-Plaut Lectures) April 16, 1980.

5. Y. T. Lee, "Dynamical Resonances in State-to-State Chemical Reactions," Department of Chemistry, Columbia University (Falk-Plaut Lectures) April 17, 1980.

6. Y. T. Lee, "Dynamics of the Reaction of Oxygen Atoms with Unsaturated Hydrocarbons," Naval Research Laboratory, Washington, D. C., April 24, 1980.

7. Y. T. Lee, "Infrared Multiphoton Dissociation of Polyatomic Molecules," Department of Chemistry, University of Nevada, Reno, Nevada, May 9, 1980.

8. Y. T. Lee, "Reaction of Oxygen Atoms with Unsaturated Hydrocarbons," Department of Chemistry, California Institute of Technology, Pasadena, California, May 21, 1980.

9. D. J. Trevor, "Photoionization Mass Spectrometry of Ne_2 and of He Clusters," VI International Conference on Vacuum Ultraviolet Radiation Physics, Charlottesville, Virginia, June 2-6, 1980, LBL-11249.

10. Y. T. Lee, "Photodissociation of Molecules by High Power Lasers," Eyring Symposium, University of Utah, Salt Lake City, Utah, June 13, 1980.

11. Y. T. Lee, "Lecture series on Chemical Kinetics and Reaction Dynamics," Institute of Chemistry, Beijing, China, June 23-July 12, 1980.

12. Y. T. Lee, "Lecture series on Molecular Beam Chemical Kinetics," Institute of Chemical Physics, Dalien, China, July 16-20, 1980.

13. R. K. Sparks, "Molecular Beam Studies of Reaction Dynamics of F + H_2, D_2," Gordon Conference on Atomic and Molecular Interactions, Wolfeboro, New Hampshire, July 21-25, 1980.

14. Y. T. Lee, "Photofragmentation Translational Spectroscopy of Ozone and Methyl Iodide," Institute of Optics, Shanghai, China, July 22, 1980.

15. Y. T. Lee, "Dynamics of Infrared Multiphoton Dissociation of Polyatomic Molecules," Shanghai Science Association, Shanghai, China, July 23, 1980.

16. Y. T. Lee, "Reaction of Oxygen Atoms with Unsaturated Hydrocarbons," Fudan University, July 24, 1980.

17. Y. T. Lee, "Reaction Mechanism of Oxygen Atoms with Unsaturated Hydrocarbons," Chinese University of Hong Kong, July 30, 1980.

18. C. C. Hayden, "Molecular Beam Studies of the F + H_2, D_2 Reaction," Second Chemical Congress of the North American Continent, Las Vegas, Nevada, August 24-29, 1980, LBL-11129 Abs.

19. F. A. Houle, "Bimolecular Reactions of State-Selected Molecular Ions," Second Chemical Congress of the North American Continent, Las Vegas, Nevada, August 24-29, 1980, LBL-11130 Abs.

20. S. L. Anderson, "The Effect of H_2^+ Vibration on the H_2^+ + H_2 Reaction," Second Chemical Congress of the North American Continent, Las Vegas, Nevada, August 24-29, 1980, LBL-11131 Abs.

21. Y. T. Lee, "Energy Splitting Between Singlet and Triplet Methylene," Department of Chemistry, University of California, Berkeley, California, September 30, 1980.

22. D. J. Trevor, "Photoionization Mass Spectrometry of Ne_2 and of He Clusters," Stanford Synchrotron Radiation Laboratory Users Group Meeting, Stanford, California, October 23-24, 1980, LBL-11485 Abs.

23. Y. T. Lee, "Determination of the Energy Splitting Between Singlet and Triplet Methylene by Photodissociation of Ketene," Joint Physics and Chemistry Department Colloquium, University of Oregon, Eugene, Oregon, November 6, 1980.

I. Potential Energy Surfaces for Chemical Reactions*

Henry F. Schaefer III, Investigator

1. THE PROTOTYPE ALUMINUM-CARBON SINGLE, DOUBLE AND TRIPLE BONDS: $Al\text{-}CH_3$, $Al{=}CH_2$, AND $Al{\equiv}CH$†

Douglas J. Fox, Douglas Ray, Philip C. Rubesin, and Henry F. Schaefer III

Organoaluminum compounds are used on an industrial scale as components of the Ziegler-Natta catalysts for olefin polymerization. In the form of $LiAlH_4$, aluminum also plays a key role in synthetic organic and inorganic chemistry. Although aluminum has a notable chemistry, this is primarily restricted to single bonded and/or electron-deficient species. A very useful example of the latter is the $Al_2(CH_3)_6$ molecule, which has the diborane structure.

Perhaps the most common single-bonded organoaluminum species is the monomeric trimethyl aluminum, $Al(CH_3)_3$, the molecular structure of which has been determined by electron diffraction. Since aluminum alkyls often appear in complexes with ethers, it is noteworthy that the structure of the dimethyl ether complex

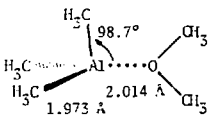

(1)

has also been determined recently.

Comparison with the above cited monomer structure demonstrates that complexation has only a mild effect (e.g., 0.016 Å in the Al-C distance) on the free $Al(CH_3)$ geometry.

No aluminum-carbon multiple bond has yet been prepared in the laboratory. This is usually thought not to be due to the inability of molecules such as

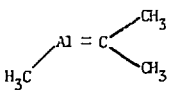

(2)

to exist as isolated species. Rather, it seems likely that such molecules do represent relative minima on their respective potential energy surfaces, but are extremely reactive. Theoretical studies shed light on the possibility of observing such molecules in the laboratory. Trenary, Casida, Brooks, and Schaefer already demonstrated the relevance of theoretical structures of the aluminum-carbon double bond to experimental investigations. In the present research are reported theoretical studies of the prototype single, double, and triple bonds

$$: Al\text{-}CH_3 \ , \qquad (6)$$

$$\cdot\ Al{=}CH_2 \ , \qquad (7)$$

and

$$Al{\equiv}CH \ . \qquad (8)$$

Nonempirical quantum mechanical methods have been used to investigate the $AlCH_3$, $AlCH_2$, and AlCH molecules, which may be considered to represent the simplest aluminum-carbon single, double, and triple bonds. Equilibrium geometries (see Fig. 1) and

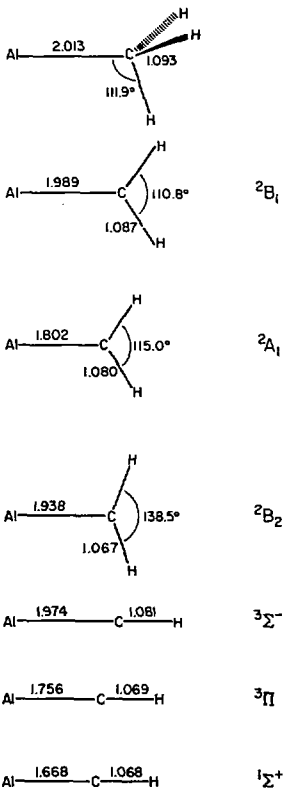

Fig. 1. Predicted equilibrium geometries of several electronic states of AlCH, $AlCH_2$, and $AlCH_3$. Bond distances are in Å. (XBL 803-8745)

*This work was supported by the Director, Office of Energy Research, Office of Basic Energy Sciences, Chemical Sciences Division of the U.S. Department of Energy under Contract No. W-7405-ENG-48.

vibrational frequencies were determined at the self-consistent-field level of theory using a double zeta basis set: Al(11s7p/6s4p), c(9s5p/4s2p), H(4s/2s). The $^1A_1$ ground state of $AlCH_3$ has a reasonably conventional Al-C single bond of length 2.013 Å, compared to 1.96 Å in the known molecule $Al(CH_3)_3$. The CH equilibrium distance is 1.093 Å and the Al-C-H angle 111.9°. The structures of three electronic states each of $AlCH_2$ and AlCH were similarly predicted. The interesting result is that the ground state of $AlCH_2$ does not contain an Al-C double bond, and the ground state of AlCH is not characterized by an Al≡C bond. The multiply bonded electronic states do exist, but they lie 21 kcal ($AlCH_2$) and 86 kcal (AlCH) above the respective ground states. The dissociation energies of the three ground electronic states are predicted to be 68 kcal ($AlCH_3$), 77 kcal ($AlCH_2$), and 88 kcal (AlCH). Vibrational frequencies (see Table 1) are also predicted for the three molecules, and their electronic structures are discussed with reference to Mulliken populations and dipole moments.

* * *

†Brief version of LBL-10871.

Table 1. Predicted harmonic vibrational frequencies (in cm^{-1}) for the ground electronic states of $AlCH_3$, $AlCH_2$, and AlCH.

$AlCH_3$		$AlCH_2$		$^3\Sigma^-$ AlCH	
3200	C-H stretch	3290	C-H stretch	3350	C-H stretch
3200		3140		670	Al-C stretch
3120		1070	$C-H_2$ scissor	380	Bend
1580	CH_3 deformation	660	Al-C bend	380	
1400		640	Al-C stretch		
1400		630	Al-C bend		
630	CH_3-Al bending				
630					
600	C-Al stretch				

2. A POSSIBLE ROLE FOR TRIPLET H_2CN^+ ISOMERS IN THE FORMATION OF HCN AND HNC IN INTERSTELLAR CLOUDS†

Thomas L. Allen,‡ John D. Goddard, and Henry F. Schaefer III

The structures and energies of the lowest triplet states of four isomers of H_2CN^+ have been determined by self-consistent-field and configuration interaction calculations. When both hydrogen atoms are attached to the nitrogen atom, H_2NC^+, the molecule has its lowest triplet state energy, which is 97.2 kcal mol^{-1} above the energy of the linear singlet ground state. The structure has C_{2v} symmetry, with an HNH bond angle of 116.8° and bond lengths of 1.009 Å (H-N) and 1.268 Å (N-C). Other isomers investigated include the H_2CN^+ isomer at 104.7, the cis-$HCNH^+$ isomer at 105.3, and the trans-$HCNH^+$ isomer at 113.6 kcal mol^{-1}. The H_2CN^+ isomer has an unusual "carbonium nitrene" structure, with a C-N bond length of 1.398 Å. All four geometrical structures are illustrated in Fig. 2. It is suggested that the triplet H_2NC^+ isomer may play a role in determining the relative yields of HCN and HNC from the reaction of C^+ and NH_3. Specifically, a triplet path is postulated in which C^+ and NH_3 yield the triplet H_2NC^+ isomer, which then yields the singlet H_2NC^+ isomer by phosphorescent emission. Because this emission removes a large amount of energy, the singlet H_2NC^+ isomer has insufficient energy to isomerize to the linear singlet ground state. Reaction with an electron then yields a hydrogen atom and the HNC isomer. The energetics of the various processes are illustrated in Fig. 3.

* * *

†Brief version of LBL-11923.

‡Department of Chemistry, University of California, Davis, California 95616.

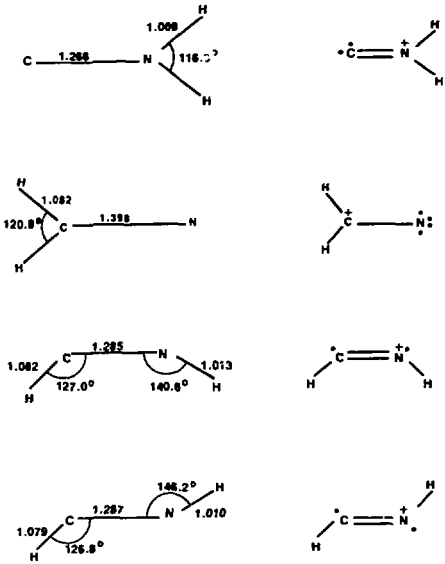

Fig. 2. Bond lengths and bond angles of the lowest triplet states for four isomers of H_2CN^+, from DZ SCF calculations, and the corresponding Lewis structures. Bond lengths are in Å. (XBL 813-8365)

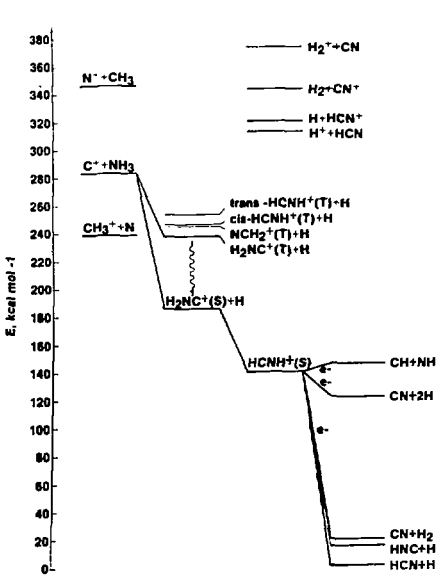

Fig. 3. Relative energies (in kcal mol^{-1}) of the H_2CN^+ system and related molecules. (XBL 813-8368)

3. ELECTRONIC STRUCTURE OF THE N_4^+ MOLECULAR ION†

Sandra C. de Castro, Russell M. Pitzer,‡ and Henry F. Schaefer III

The N_4^+ ion is an important species in the chemistry of the atmosphere. Here, N_4^+ has been studied theoretically using the methods of *ab initio* molecular quantum mechanics. There is considerable complexity involved in the theoretical study of N_4^+ due to: (a) the fact that N_2^+ has two low-lying electronic states, X $^2\Sigma_g^+$ and A $^2\Pi_u$ and the order of these is reversed within the Hartree-Fock approximation; and (b) there are six low-lying electronic states of N_4^+. Results are first presented at the self-consistent-field (SCF) level of theory using a double zeta (DZ) basis set N(9s 5p/4s 2p). Koopmans' Theorem and direct positive ion calculations in both D_{2h} (rectangle) and C_{2v} (regular trapezoid) symmetry suggest only a single (out of six) substantially bound electronic state, the $^2B_{2u}(D_{2h})$ or $^2A_1(C_{2v})$ state. Because the D_{2h} SCF wave function necessitates a compromise description of the $N_2 + N_2^+$ asymptote, the predicted dissociation energy is artificially large, although in reasonable agreement with experiment. Polarization functions were added to the basis set, and all three geometrical parameters examined to locate the C_{2v} equilibrium structure, which lies 19.9 kcal below the dissociation limit $N_2 + N_2^+(^2\Sigma_g^+)$. Similar theoretical methods were applied to the T-shaped geometry with the constrained equilibrium bound by 24.2 kcal. The linear conformation represents the absolute minimum on the N_4^+ potential energy surface, lying 30.4 kcal below $N_2 + N_2^+$. The latter dissociation energy agrees well with the experimental value of ~ 26 kcal. In studying the linear $^2\Sigma^+$ state, the surprising result was found that the $^2\Sigma_g^+$ restricted Hartree-Fock wave function is unstable with respect to the removal of the g/u element of symmetry. The $^2\Pi$ state is stable in this respect; and as a result, the $^2\Sigma_g^+$ state of N_2^+ falls closer to the $^2\Pi_u$ state in this mildly unrestricted form of Hartree-Fock theory. The trapezoidal, T-shaped, and collinear equilibrium geometries are seen in Fig. 4.

* * *

†Brief version of LBL-11267.

‡Department of Chemistry, Ohio State University, Columbus, Ohio.

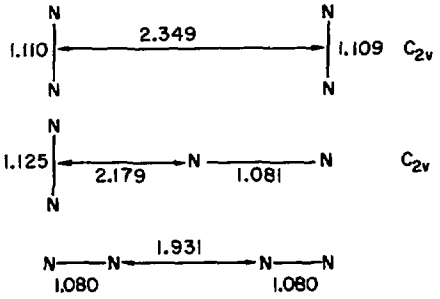

Fig. 4. Constrained equilibrium geometries for the trapezoid, T-shaped, and collinear arrangements of N_4^+. All three structures were optimized at the double zeta plus polarization direct SCF level of theory. (XBL 807-3452)

4. GEOMETRY AND ELECTRONIC STRUCTURE OF $(CO)_3NiCH_2$, A MODEL TRANSITION METAL CARBENE†

Dale Spangler,‡ John J. Wendoloski,‡ Michel Dupuis,‡ Maynard M. L. Chen, and Henry F. Schaefer III

A critical ingredient in the flowering of organometallic chemistry over the past decade has been the synthesis and characterization of transition metal carbene complexes. This research began with the report in 1964 by Fischer and Maasböl of methoxymethyl carbene (pentacarbonyl) tungsten. Although the notion of a double bond between transition metals and carbon was initially unorthodox, it is now well entrenched and is indeed an integral part of the thought patterns of organometallic reseachers. In fact, metal carbene concepts borrowed from organometallic chemists are now being used in attempts to understand surface chemistry and heterogeneous catalysis.

A primary motivation for the construction of such an analogy has been the growing consensus that transition metal carbenes are homogeneous catalysts in the olefin metathesis reaction

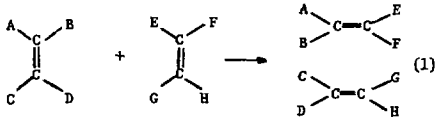

Of the two mechanisms often considered for the olefin metathesis reactions, one involves the pairwise exchange between two olefins in the coordination sphere of a metal, while the other is the "carbene chain reaction" in which a carbene metal complex is the active catalyst. Experimentally, isomerization patterns and isotope scrambling ratios are utilized to decide between alternative mechanisms.

From a theoretical perspective, the simplest realistic transition metal carbene might involve only CO ligands and the primitive CH_2 or methylene itself. In the present paper, we report a detailed theoretical study of the simplest of the three prototypes $(CO)_3Ni{=}CH_2$. Not only is this the first ab initio investigation of a realistic metal carbene complex, it is also one of the very few studies [see, for example, our recent work on $Ni(C_2H_4)_3$] of any organometallic species using a large and flexibly contracted basis set. The research was carried out at the self-consistent-field (SCF) level.

A large and flexibly contracted basis set was chosen, labeled Ni(15s 11p 6d/11s 8p 3d); C,O(9s 5p/4s 2p); H(5s/3s). In addition, the importance of methylene carbon d functions was investigated. The critical predicted equilibrium geometrical parameters were R[Ni-C(methylene)] = 1.83 Å, θ(HCH) = 108°, as seen in the Fig. 5. The sixfold barrier to rotation about the Ni-C (methylene) axis is small, ~ 0.2 kcal. The electronic structure of $(CO)_3NiCH_2$ is discussed and compared with those of the "naked" complex $NiCH_2$ and the stable $Ni(CO)_4$ molecule. Orbital energies for these three species are given in Table 2.

* * *

†Brief version of LBL-10650.

‡National Resource for Computation in Chemistry, LBL.

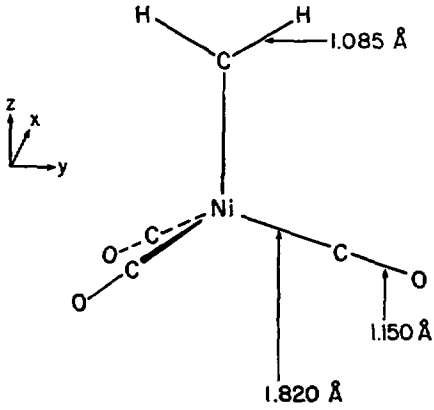

Fig. 5. Structural assumptions for the prototype nickel carbene complex. The three CO ligands are assumed to be tetrahedrally coordinated about the nickel atom. (XBL 803-8756)

Table 2. Valence orbital energies (in Hartree atomic units) of $NiCH_2$, $(CO)_3NiCH_2$ and $Ni(CO)_4$.

$NiCH_2$		$(CO)_3NiCH_2$		$Ni(CO)_4$	
	--	13a'	-1.5528	$6a_1$	-1.5622
	--	14a'	-1.5493		-1.5620
	--	5a"	-1.5491	$5t_2$	-1.5620
	--		--		-1.5620
$7a_1$	-0.8245	15a'	-0.9012	$7a_1$	-0.8240
		16a'	-0.8233		-0.8092
		17a'	-0.8085	$6t_2$	-0.8092
		6a"	-0.8075		-0.8092
$8a_1$	-0.8038	18a'	-0.6927	$8a_1$	-0.6883
$3b_2$	-0.7200	7a"	-0.6604	1e	0.6623
		19a'	-0.6597		-0.6623
$9a_1$	-0.6657	8a"	-0.6593		-0.6598
		20a'	-0.6555	$7t_2$	-0.6598
		21a'	-0.6491		-0.6598
		9a"	-0.6484		-0.6517
		22a'	-0.6432	$1t_1$	-0.6517
		10a"	-0.6430		-0.6517
		11a"	-0.5873		-0.6334
		23a'	-0.5432	$8t_2$	-0.6334
		12a"	-0.5199		-0.6334
		24a'	-0.4822	2e	-0.4444
$4b_2$	-0.5236	13a"	-0.4241		-0.4444
$10a_1$	-0.3544	25a'	-0.3604		-0.3785
$4b_1$	-0.2356	26a'	-0.3214	$9t_2$	-0.3785
					-0.3785

5. MECHANISM OF THE H + O_3 REACTION†

Maynard M. L. Chen, Ross W. Wetmore, and Henry F. Schaefer III

Studies of the near infrared spectra of night-day radiation led Bates, Nicolet, Meinel, and Herzberg to attribute their origin to the radiation of vibrationally excited hydroxyl radicals in the $^2\Pi$ ground state. Herzberg suggested that these radicals were a product of the reaction of atomic hydrogen with ozone.

$$H + O_3 \rightarrow OH^{\dagger} + O_2 \qquad \Delta G = -77 \text{ kcal/mole} \quad (1)$$

This explanation was verified when McKinely, Garvin, and Boudart were able to reproduce these Meinel bands in the laboratory by mixing H atoms with ozone. Since then, reaction (1) has been carefully studied by kineticists. There have been several determinations of its rate constant and various estimates of the energy partitioning in the products. The most recent experimental value for the rate constant was 2.79 (± 0.18) $\times 10^{-11}$ cm^{-3} $molecule^{-1}$ sec^{-1}, and the Arrhenius activation energy was found to be approximately 1 kcal/mole.

From the mechanistic perspective, the research of Polanyi and co-workers, using the "arrested relaxation" variant of the infrared chemiluminescence method, is the most informative. They found that the large exothermicity of reaction (1) was primarily channeled (90%) into vibrational activation of the OH product, only ~ 3% into OH rotation, and 7% into translation and internal energy of O_2. Due to the extreme inversion of the vibrational distribution in the $OH^{\dagger}$ product, only the highest accessible state (v' = 9) showed sufficient emission intensity for reliable analysis. In essence, this means that for the H + O_3 reaction, energy release is converted into vibration in the new bond with a higher efficiency than for any other reaction analyzed in this manner to date.

Polanyi and Sloan then compared their H + O_3 experimental results with classical trajectory studies on a London-Eyring-Polanyi-Sato (LEPS) potential surface for model triatomic systems of the type light-atom plus heavy-diatom (abbreviated $L + H\,H$). The underlying assumption behind this tetra-atomic/triatomic analogy was that since the fraction of internal energy taken up by O_2 (f_I'') was very small (< 7%), it could be reasonably approximated by a single heavy atom. They concluded that the potential energy hypersurface of this reaction was a strongly attractive one. Moreover, they also discovered that the

ratios of rotational energy (f'_R) to vibrational energy (f'_V) in OH was much smaller than the usual ratios found in the products of their LEPS model surfaces. This led them to suggest that the potential energy surface favors collinearity of the HOO approach and that it is restricted to a narrow range of impact parameters. Lee, Michael, Payne, and Stief have also studied this reaction and were in agreement with that conclusion, adding that the collinear approach should be even more enhanced if their measured activation energy (0.892 ± 0.115 kcal/mole) could be associated with a barrier on the surface.

Here, certain aspects of the HO_3 potential energy hypersurface have been investigated using nonempirical molecular electronic structure theory. For the qualitative purposes of the present study, most wave functions were of the self-consistent-field (SCF) variety, constructed from a double zeta basis set of contracted Gaussian functions. Two low energy pathways were established for the reaction. The first involves a coplanar transition state with a nearly *linear H-O-O arrangement. The second possible* mechanism allows the hydrogen atom to descend perpendicularly upon the ozone molecule. The two mechanisms are evaluated in light of the above-discussed experimental understanding of the $H + O_3$ reaction. Qualitative molecular orbital theory, as illustrated in Fig. 6, is helpful in explaining the quantum mechanical predictions.

* * *

+Brief version of LBL-11922.

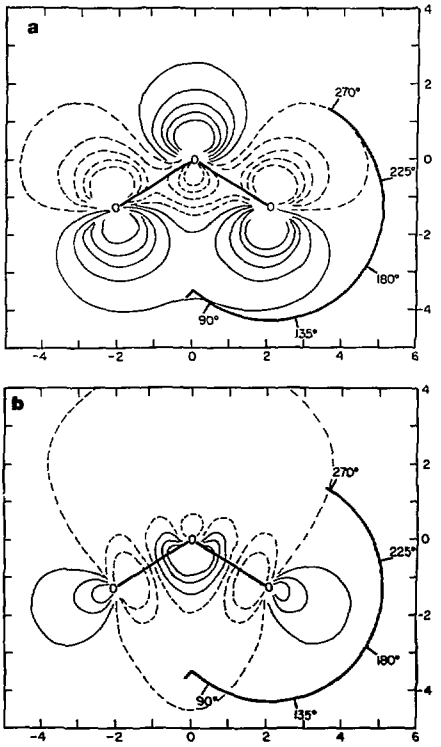

Fig. 6. (a) Contour map of the in-plane ozone HOMO. Scales on sides are in angstroms and the superimposed angular scale at r(OH) = 1.6 Å shows the variation of the hydrogen position as a function of θ. (b) Contour map of the in-plane LUMO. [(a) XBL 802-8268; (b) XBL 813-8366]

6. LARGE MULTICONFIGURATION SELF-CONSISTENT-FIELD WAVEFUNCTIONS FOR THE OZONE MOLECULE†

William D. Laidig and Henry F. Schaefer III

The electronic structure of the ozone molecule is of particular interest in light of Goddard's characterization of the ground state as a biradical. Rigorously optimized multiconfiguration self-consistent-field (MCSCF) wavefunctions of varying size have been determined here for ozone via newly developed techniques utilizing the unitary group approach. The largest of these ab initio MCSCF wavefunctions includes 13,413 configurations, i.e., all singly- and doubly-excited configurations relative to the two reference configurations required for the biradical description of ozone. The convergence of the MCSCF procedures is discussed, as well as the structure of the MCSCF wavefunctions, and the effectiveness of different orbital transformations. There is a significant energy difference (0.034 hartrees) between the MCSCF wavefunctions involving one and two reference configurations. This gives emphasis to the fact that orbital optimization alone cannot compensate for the exclusion from the wavefunction of important classes of configurations. A simple test for the determination of the fraction biradical character of systems such as ozone suggests 23% biradical character for O_3 at its equilibrium geometry. The results are summarized in Table 3.

* * *

†Brief version of LBL-11507.

7. THEORETICAL CHALLENGE TO THE EXPERIMENTALLY DETERMINED GEOMETRICAL STRUCTURE OF DIMETHYLSILAETHYLENE†

Yasunori Yoshioka, John D. Goddard, and Henry F. Schaefer III

In a recent communication (1980), Mahaffy, Gutowsky and Montgomery[1] (MGM) presented an experimental molecular structure for 1,1 dimethylsilaethylene (DMSE), based on their electron diffraction data. Their work was of particular interest, inasmuch as it represented the first experimental structural study of any molecule containing a carbon-silicon double bond.[2] The most significant finding of MGM was an extremely long Si=C double bond, namely 1.83 ± 0.04 Å, or only 0.08 Å shorter than their observed Si—C single bond, 1.91 ± 0.02 Å. For comparison, the typical C=C double bond (1.35 Å) is 0.19 Å shorter than the typical C—C single bond (1.54 Å). If this long Si=C distance of 1.83 Å is correct, one would likely infer that the π bond in DMSE is exceptionally weak.

MGM noted an apparent discrepancy between theory and experiment. For the parent unsubstituted silaethylene $H_2Si{=}CH_2$, MGM cited about a dozen quantum mechanical predictions of the Si=C bond distance, and these vary from 1.63 Å to 1.75 Å. Of these the most complete study[3] was carried out at the self-consistent-field (SCF) level of theory and employed a double zeta (DZ) basis set of contracted gaussian functions. Since the predicted Si=C bond distance of 1.715 Å is so much less than the experimental DMSE value of

Table 3. Summary of large MCSCF results for the $^1A_1$ ground state of ozone near its equilibrium geometry.

Number of configurations	Description of configurations	Type of wavefunction	Energy (hartrees)	Coefficients of two most important configurations C_1	C_2
1	(1) in text	SCF	-224.207 656	1.0000	--
2	(1) and (2) in text	TCSCF	-224.310 437	0.8765	-0.4815
6,825	All S + D excitations relative to (1)	CI[a]	-224.613 929	0.9331	-0.1493
6,825	" "	MCSCF	-224.615 493	0.9343	-0.1620
13,413	All S + D excitations relative to (1) and (2)	CI[a]	-224.640 183	0.8935	-0.2957
13,413	" "	CI[b]	-224.647 645	0.8762	-0.3553
13,413	" "	MCSCF	-224.649 326	0.8870	-0.3371

[a]CI used one-configuration SCF orbitals.
[b]CI used two-configuration SCF orbitals.

1.83 Å, one is logically left with three alternatives or some combination of them:

(a) the two methyl substituents greatly increase the Si=C distance in DMSE relative to the parent $H_2Si{=}CH_2$

(b) the theoretical predictions for the Si=C bond distance in $H_2Si{=}CH_2$ are all incorrect.

(c) the experimental Si=C distance in DMSE is in error.

In the present communication, we report theoretical results which drastically reduce the possibility that points (a) or (b) above could be responsible for the discrepancy between theory and experiment. First, an explicit optimization of the geometrical structure of DMSE has been completed. Furthermore, this equilibrium geometry was determined at a level of theory higher than any previous structural optimization of even the parent $H_2Si{=}CH_2$. A set of d functions on each heavy atom was added to the double zeta (DZ) basis used by Hood and Schaefer.[3] These polarization functions were assigned orbital exponents $\alpha = 0.75$ (carbon) and $\alpha = 0.60$ (silicon). The designation of this DZ+d basis set is then Si(11s7p1d/6s4p1d), C(9s5p1d/4s2p1d), H(4s/2s).

The predicted theoretical structure for DMSE is seen in Fig. 7. The relative orientations of the two methyl groups was arbitrarily chosen to maintain point group C_{2v}, but the barriers to rotation about these Si–C single bonds should be quite small. Figure 7 shows that the predicted Si=C bond distance, 1.692 Å, falls far outside the range 1.83 ± 0.04 Å provided by the experimental electron diffraction study.[1] The predicted Si–C single bond distance, 1.873 Å, is also shorter than experiment, 1.91 ± 0.02 Å, but in this case the disagreement is much less severe. None of the other geometrical parameters of DMSE were determined by MGM,[1] but the predicted theoretical values are all quite consistent with chemical intuition. Furthermore, a steadily increasing body of comparisons between theory and experiment would suggest a typical reliability of ± 0.01 Å for bond distances predicted at the DZ + d SCF level of theory.

To assess the relationship between the structures of DMSE and the parent silaethylene, the latter equilibrium geometry was theoretically determined in a manner precisely the same as that described above for DMSE. This DZ + d SCF structure for the parent is illustrated in the middle of Fig. 7, which shows that, at the DZ + d SCF level of theory, the Si=C bond distances of $H_2Si{=}CH_2$ and $(CH_3)_2Si{=}CH_2$ are identical (1.692 Å) to within one-thousandth of an angstrom. This would certainly appear to dispense with the possibility, suggested by MGM,[1] that the Si=C distance is significantly longer in DMSE.

The only remaining satisfactory explanation of the experimental DMSE geometry is that the DZ + d SCF level of theory systematically predicts Si=C distances much too short. The possibility has been examined by explicitly determining the structure of $H_2Si{=}CH_2$ using highly correlated wave functions. Using the DZ + d basis

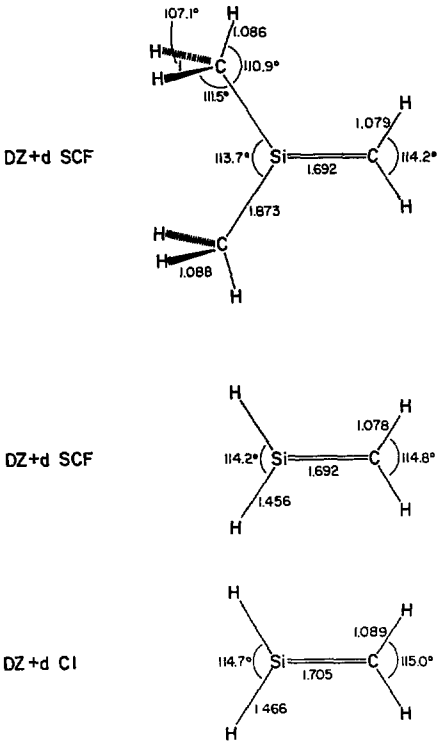

Fig. 7. Theoretical equilibrium geometries for 1,1 dimethylsilaethylene (DMSE) and the parent unsubstituted silaethylene. (XBL 813-8367)

set, configuration interaction (CI) was carried out including all single and double excitations relative to the Hartree-Fock reference configuration. With the six core orbitals (C 1s, Si 1s, 2s, $2p_x$, $2p_y$, $2p_z$) constrained to be doubly occupied in all configurations, this approach yields a total of 6,920 $^1A_1$ configurations.

The DZ + d CI structure of silaethylene shown at the bottom of the Fig. 7 demonstrates clearly that electron correlation has little effect on the predicted Si=C bond distance. The theoretical distance is 1.705 Å, or only 0.013 Å longer than the analogous SCF result. For the above-discussed comparison of the silaethylene and DMSE structures, one anticipates that the DMSE Si=C bond distance will also be ~ 1.70 Å. Based on previous experience, we suggest that the exact (unknown) Si=C bond distance, r_e, for the unsubstituted silaethylene is 1.705 ± 0.03 Å. To

our thinking, this prediction casts serious doubt upon the assumptions made by MGM in extracting the Si=C distance in DMSE from the reported electron diffraction data.[1]

* * *

†Brief version of LBL-11633.

1. P. G. Mahaffy, R. Gutowsky, and L. K. Montgomery, J. Amer. Chem. Soc. 102, 2854 (1980).
2. L. E. Gusel'nikov and N. S. Nametkin, Chem. Rev. 79, 529 (1979).
3. D. M. Hood and H. F. Schaefer, J. Chem. Phys. 68, 2985 (1978).

RESEARCH PLANS FOR CALENDAR YEAR 1981

A primary goal of our research is to construct models that probe the relationships between surface chemistry, heterogeneous catalysis, and organometallic chemistry. Particular emphasis in calendar year 1981 will be placed on the interaction between small aluminum clusters and organic fragments. Research on the prototype mononuclear species Al_3-CH_3, $Al=CH_2$, and $Al\equiv CH$ has been completed and a study of the Al_2-CH_2 system is well underway. The prototype trinuclear carbyne system Al_3-CH will be examined in the very near future. In a more direct assault on the organometallic field, the molecule $Ni(C_4H_4)_2$, a realistic model for the recently synthesized octaphenyl compound, will be examined in detail via quantum theoretical techniques. The simple but realistic carbyne $F(CO)_2Ni\equiv CH$ will be subjected to a complete structural determination. Collaboration with the MMRD experimental group of Y. T. Lee is expected to continue in the form of studies of the H_n^+ ions and the hydrogen fluoride trimer. A unique interdisciplinary project to be carried out in collaboration with R. N. Cahn, an LBL physicist, will explore the importance of molecular quantum mechanics for the determination of the mass of the neutrino.

1980 PUBLICATIONS AND REPORTS

Refereed Journals

1. W. C. Swope, Y.-P. Lee, and H. F. Schaefer, "Sulfur Oxide: Low-Lying Bound Molecular Electronic States of SO," J. Chem. Phys. 71, 3761 (1979), LBL-9142.

2. M. E. Casida, M. M. L. Chen, R. D. Mac Gregor, and H. F. Schaefer, "Walsh's Rules and the Small Bond Angle States of Triatomic Dihydride Molecules," Israel J. Chem. 19, 127 (1980).

3. R. M. Pitzer and H. F. Schaefer, "Conformational Preferences and Electron Structures of $Ni(C_2H_4)_2$ and $Ni(C_2H_4)_3$," J. Amer. Chem. Soc. 101, 7176 (1979).

4. W. D. Laidig and H. F. Schaefer," 1,1 Dilithioethylene: A Ground State Triplet Olefin with Nearly Free Rotation about the Double Bond," J. Amer. Chem. Soc. 101, 7184 (1979).

5. B. R. Brooks, W. D. Laidig, P. Saxe, N. C. Handy, and H. F. Schaefer, "The Loop-Driven Graphical Unitary Group Approach: A Powerful Method for the Variational Description of Electron Correlation," Physica Scripta 21, 312 (1980).

6. J. Demuynck and H. F. Schaefer, "The Gas Phase Structure of Transition Metal Dihydrides," J. Chem. Phys. 72, 311 (1980), LBL-9509.

7. A. Komornicki, J. D. Goddard, and H. F. Schaefer," The Reaction of Acetylene with Fulminic Acid. The Prototype 1,3 Dipolar Cycloaddition," J. Amer. Chem. Soc. 102, 1763 (1980).

8. R. W. Wetmore, H. F. Schaefer, P. C. Hiberty, and J. I. Brauman, "Dipole-Supported States: A Very Low-Lying Excited State of the Acetaldehyde Enolate Anion," J. Amer. Chem. Soc. 102, 5470 (1980).

9. M. M. L. Chen and H. F. Schaefer, "Potential Energy Surface for the Li + HF → LiF + H Reaction," J. Chem. Phys. 72, 4376 (1980), LBL-10111.

10. L. Radom, H. F. Schaefer, and M. A. Vincent, "The C_7H_6 Isomers: Cycloheptatrienylidene and Phenylcarbene," Nouvaeu Journal De Chimie 4, 411 (1980).

11. B. R. Brooks, W. D. Laidig, P. Saxe, and H. F. Schaefer," A Multiconfiguration Self-Consistent-Field Formalism Utilizing the Two-Particle Density Matrix and the Unitary Group Approach," J. Chem. Phys. 72, 3837 (1980).

12. P. Saxe, Y. Yamaguchi, P. Pulay, and H. F. Schaefer, "Transition State Vibrational Analysis for the Methyl Isocyanide Rearrangement $CH_3NC \rightarrow CH_3CN$," J. Amer. Chem. Soc. 102, 3718 (1980).

13. B. R. Brooks, W. D. Laidig, P. Saxe, J. D. Goddard, Y. Yamaguchi, and H. F. Schaefer, "Analytic Gradients from Correlated Wave Functions via the Two-Particle Density Matrix and the Unitary Group Approach," J. Chem. Phys. 72, 4652 (1980).

14. W. C. Swope and H. F. Schaefer, "A Genealogical Electronic Coupling Procedure Incorporating The Hartree-Fock Interacting Space and Suitable for Degenerate Point Groups. Application to Excited States of BH_3," J. Chem. Phys. 73, 407 (1980), LBL-9580.

15. P. Saxe and H. F. Schaefer, "Can Cyclopropyne Really Be Made?," J. Amer. Chem. Soc. 102, 3239 (1980).

16. W. D. Laidig and H. F. Schaefer, "Some Characteristics of the Intravalence Triplet-Triplet Electronic Transition in HCN," J. Chem. Phys. 73, 1470 (1980).

17. W. D. Laidig, P. Saxe, and H. F. Schaefer, "Multiconfiguration Self-Consistent-Field Study of the Importance of Triply and Quadruply Excited Electronic Configurations in the Water Molecule," J. Chem. Phys. 73, 1765 (1980).

18. Y. Yamaguchi and H. F. Schaefer, "A Systematic Theoretical Study of Harmonic Vibrational Frequencies: The Ammonium Ion NH_4^+ and Other Simple Molecules," J. Chem. Phys. 73, 2310 (1980).

19. K. Kim and H. F. Schaefer, "Geometric Isomerism in Triplet Carbenes: Carbohydroxycarbene," J. Amer. Chem. Soc. 102, 5389 (1980).

20. D. J. Fox, D. Ray, P. C. Rubesin, and H. F. Schaefer, "The Prototype Aluminum-Carbon Single, Double, and Triple Bonds: $Al—CH_3$, $Al=CH_2$, and $Al\equiv CH$," J. Chem. Phys. 73, 3246 (1980), LBL-10871.

21. T. L. Allen, J. D. Goddard, and H. F. Schaefer, "A Possible Role for Triplet H_2CN^+ Isomers in the Formation of HCN and HNC in Interstellar Clouds," J. Chem. Phys. 73, 3255 (1980).

22. S. K. Gray, W. H. Miller, Y. Yamaguchi, and H. F. Schaefer, "Reaction Path Hamiltonian: Tunneling Effects in the Unimolecular Isomerization HNC → HCN," J. Chem. Phys. 73, 2733 (1980), LBL-10953.

23. J. Demuynck, D. J. Fox, Y. Yamaguchi, and H. F. Schaefer," Triplet Methylnitrene: An Indefinitely Stable Species in the Absence of Collisions," J. Amer. Chem. Soc. 102, 6204 (1980).

Other Publications

1. C. D. Dykstra and H. F. Schaefer, "Theoretical Methods and Their Application to Ketenes and Allenes," Chapter 1 of The Chemistry of Ketenes and Allenes, Saul Patai ed. Wiley/Interscience, London, (1979), pgs. 1-44.

LBL Reports

1. S. P. So, R. W. Wetmore, and H. F. Schaefer, "Excited Singlet Electronic States of Acetylene: cis and trans Structures and Energetics," J. Chem. Phys., LBL-10818.

2. S. C. de Castro and H. F. Schaefer, "Electronic Structure of the N_4^+ Molecular Ion," J. Chem. Phys., LBL-11267.

3. Y. Osamura, J. D. Goddard, H. F. Schaefer and K. S. Kim, "Near Degenerate Rearrangement Between the Radical Cations of Formaldehyde and Hydroxymethylene," J. Chem. Phys., LBL-11174.

4. H. F. Schaefer, "Approaching the Hartree-Fock Limit for Organotransition Metal Complexes," J. Molec. Structure, LBL-11973.

5. Y. Osamura, H. F. Schaefer, S. K. Gray, and W. H. Miller, "Vinylidene: A Shallow Minimum on the C_2H_2 Potential Energy Surface. Static and Dynamical Considerations," J. Amer. Chem. Soc., LBL-11625.

6. M. M. L. Chen, R. W. Wetmore, and H. F. Schaefer, "Mechanism of the $H + O_3$ Reaction," J. Chem. Phys., LBL-11922.

7. D. Spangler, J. J. Wendoloski, M. Dupuis, M. M. L. Chen, and H. F. Schaefer, "Geometry and Electronic Structure of $(CO)_3NiCH_2$. A Model Transition Metal Carbene," LBL-10650.

8. W. D. Laidig and H. F. Schaefer, "Large Multiconfiguration Self-Consistent-Field Wavefunctions for the Ozone Molecule," J. Chem. Phys., LBL-11507.

9. Y. Yoshioka, J. D. Goddard, and H. F. Schaefer, "Theoretical Challenge to the Experimentally Determined Geometrical Structure of Dimethylsilaethylene," J. Amer. Chem. Soc., LBL-11633.

10. P. Saxe, H. F. Schaefer, and N. C. Handy, "Exact Solution (Within a Double Zeta Basis Set) of Schrödinger's Electronic Equation for Water," Chem. Phys. Lett., LBL-11634.

11. P. Saxe, H. F. Schaefer, and N. C. Handy, "Methylene Singlet-Triplet Separation: An Explicit Variational Treatment of Many-Body Correlation Effects," J. Chem. Phys., LBL-11624.

12. S. K. Gray, W. H. Miller, Y. Yamaguchi, and H. F. Schaefer, "Tunneling in the Unimolecular Decomposition of Formaldehyde, a More Quantitative Study," J. Amer. Chem. Soc., LBL-11361.

Invited Lectures

National and International Conferences:

1. H. F. Schaefer, "Australian Conference on Molecular Physics and Quantum Chemistry," The Science Centre, Sydney, Australia, February 17-20, 1980.

2. H. F. Schaefer, "New Quantum Methods in Inorganic Chemistry and Catalysis," American Chemical Society, Houston, March 24-28, 1980.

3. H. F. Schaefer, "Seventh Canadian Symposium on Theoretical Chemistry," Banff, Alberta, Canada, June 15-21, 1980.

4. H. F. Schaefer, "Theoretical Organic Chemistry," NATO Advanced Study Institute, Menton, France, June 29-July 13, 1980.

5. H. F. Schaefer, "Symposium on Potential Energy Surfaces and Dynamics Calculations," American Chemical Society, San Francisco, California, August 27-29, 1980.

University Colloquia:

1. H. F. Schaefer, Research School of Chemistry, Australian National University, March, 1980.

2. H. F. Schaefer, New Mexico State University, Las Cruces, New Mexico, April, 1980.

3. H. F. Schaefer, Louisiana State University, Baton Rouge, Louisiana, May, 1980.

J. Picosecond Laser Excitation of Chemical Reactions*

John H. Clark, Investigator

Introduction. The emphasis of this program is the *systematic study of the mechanism and* kinetics of ultrafast chemical reactions in solution. This research is centered around the use and development of picosecond laser spectroscopic techniques for the direct observation of such reactions. Because this program was established midway through 1980, and since progress in the field is contingent upon the development of sophisticated instrumentation, a primary focus of this effort has been the construction of a picosecond, time-resolved emission spectroscopy apparatus. Nevertheless, initial investigations into the dynamics of excited-state proton-transfer reactions have been carried out in 1980. These studies have produced the first direct measurements of the effect of intramolecular hydrogen bonding on intermolecular proton transfer rates, as well as the first direct observation of the kinetics of quenching of electronically excited states by solvated protons. In addition, the program has demonstrated that subtle changes in the geometric and electronic structure of a molecule can lead to exceedingly large changes in excited-state proton-transfer rates.

1. A SYSTEMATIC STUDY OF EXCITED-STATE PROTON TRANSFER IN NAPHTHOLS AND SULFONATED NAPHTHOLS

Stanley L. Shapiro,† Margaret A. Tolbert, Kenneth R. Winn,† and John H. Clark

It is now well established that the acid-base properties observed for many organic and inorganic compounds in electronically excited states differ markedly from those observed in the ground state.[1] Quantitative aspects of this effect, such as excited-state pK values and proton-transfer rates, were first obtained by applying a Forster cycle calculation to results obtained from steady-state, fluorescence titration measurements. Such a calculation involves a number of assumptions which, in general, may not be justified. For this reason, nanosecond fluorimetry has more recently been used to study excited-state proton-transfer reactions.[2,3] Often, however, these reactions are so rapid that even nanosecond time resolution is not sufficient to permit them to be directly studied.[4] Thus the techniques of picosecond spectroscopy have been applied as a general method for the direct study of excited-state proton-transfer reactions and have been used to determine previously unmeasureable excited-state proton-transfer kinetics.[4]

The naphthols and substituted naphthols provide convenient systems for the study of excited-state proton-transfer reactions. Their absorption spectra lie in a region of the ultraviolet easily accessible with the third (355 nm) and fourth (266 nm) harmonics of a Nd:YAG laser. When electronically excited, naphthols become from 7 to 11 orders of magnitude more acidic and can adiabatically transfer a proton to surrounding solvent molecules. In aqueous solution, the transfer occurs on a time-scale comparable to or shorter than the excited-state lifetime. The reaction scheme which typifies this excited-state proton transfer is shown in Fig. 1. Electronically excited states of the protonated species, ROH^*, and the anion, RO^{-*}, may either fluoresce or be quenched nonradiatively back to their respective ground states. For the naphthols and their anions, typical fluorescence lifetimes are ~10 ns. ROH^* may also transfer a proton to H_2O, while RO^{-*} may be protonated in the bimolecular reaction $RO^{-*} + H_3O^+$. As shown in Fig. 2 for the case of 2-naphthol, the electronically excited anion formed by the proton transfer has an emission spectrum which is substantially red-shifted from the emission of the protonated species. Thus, the time history of the excited-state populations for both the acid and anion can be conveniently monitored by temporal and spectral resolution of the emission.

A schematic diagram of the apparatus used for carrying out such measurements is shown in Fig. 3. A passively mode-locked Nd:YAG oscillator is used to generate a train of 25-picosecond duration pulses at 1060 nm. A Pockels cell selects a single pulse from the train for subsequent amplification to ~10 mJ. The amplified pulse is frequency multiplied in suitable nonlinear optical crystals to produce the excitation wavelength

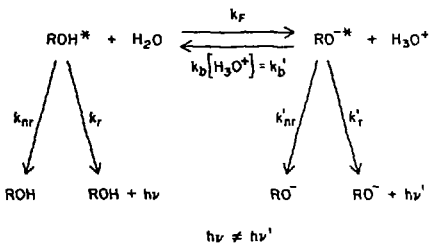

Fig. 1. Generalized reaction scheme for an excited-state proton-transfer reaction.
(XBL 814-9101)

*This work was supported by the Lawrence Berkeley Laboratory Director's Office under Contract No. W-7405-ENG-48 with the U. S. Department of Energy.

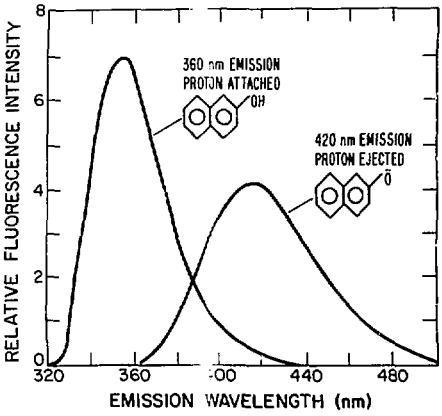

Fig. 2. Emission spectra of electronically excited 2-naphthol and 2-naphtholate.
(XBL 814-9100)

(typically 355 or 266 nm) desired in a particular experiment. The output of the harmonic generating crystals is spectrally filtered to remove all frequencies other than that desired for excitation of the sample and is imaged onto the sample. The emission from the sample is imaged through the entrance slit of an ultrafast streak camera (Hadland Photonics 675-II). Spectral filters placed between the sample and the streak camera slit are used to isolate the spectral regions of interest. The image at the output of the streak camera is detected and digitized using an optical multichannel analyzer (OMA). The output signal from the OMA is fed directly into a signal averager for further signal processing.

A small fraction of the incident laser pulse is split off and imaged onto the entrance slit of the streak camera. The arrival time of this precursor pulse is adjusted by means of an optical delay so that it preceeds the arrival of the emission from the sample. This precursor pulse serves as a relative time reference and ensures that the ± 50-ps time jitter of the streak camera will not prohibit accurate signal averaging.

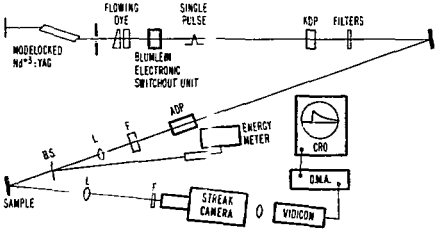

Fig. 3. Schematic diagram of picosecond, time-resolved emission spectroscopy apparatus.
(XBL 814-9099)

With this apparatus, it has become possible to carry out systematic studies of the kinetics of excited-state proton transfer in a series of naphthols and sulfonated naphthols. Such systematic investigations are the key to elucidating the essential details of the dynamics of excited-state proton-transfer processes. The experimental results for the relaxation of the excited protonated species in 1-naphthol, 1-naphthol-2-sulfonate, and 1-naphthol-5-sulfonate are presented in Fig. 4 and summarized in Fig. 5. Similar results for 2-naphthol and 2-naphthol-6-sulfonate have been previously reported.[5] It is interesting to note that with picosecond time-resolved emission spectroscopy, the emission from the neutral form of 1-naphthol is easily observed. This contrasts with previous descriptions of this emission as "completely extinguished"[6] and "hardly noticeable"[7] reported from non-time-resolved studies. It can be seen that 1-naphthol and the two 1-naphthol derivatives dissociate extremely rapidly. The kinetics of the rapid proton transfer indicate that the excited-state pH value (pK^*) for all three derivatives is in the vicinity of zero. This estimate is confirmed by a Forster-cycle calculation based on the absorption and emission spectra of the pure compounds. Notice also that the dissociation rate for 1-naphthol-2-sulfonate is slower than for the other two derivatives. Evidently, the intramolecular hydrogen bond formed between the adjacent hydroxy and sulfonate groups leads to a slowdown in the proton ejection rate for this compound. These observations represent the first confirmation of this previously postulated effect.[8]

Crucial to the success of these experiments and to their interpretation are sample preparation and purification. All samples are prepared under oxygen-free conditions via preparative liquid chromatography. The samples were determined to be greater than 99.9% pure by analytical liquid chromatography using a fluorescence detector. Samples were prepared in a nitrogen filled glove-box, and all solvents were thoroughly degassed by undergoing successive freeze-pump-thaw cycles. As discussed below, such careful sample handling and analysis is another feature of our work which sets it apart from earlier work in the field.

The results presented here for 1-naphthol-2-sulfonate differ strikingly from those of Zaitsev et al. who, using nanosecond techniques, reported that the dissociation rate for this compound is 5.4×10^8 sec^{-1} (1.85 ns).[9] Our experiments indicate that this long decay time may be due to impurities. For example, a sample of 1-naphthol-2-sulfonate obtained from Eastman Kodak and used without further purification yields only a long-lived decay, also a few ns in duration.

Further confirmation for the 55-ps lifetime reported here is obtained from the emission spectrum of purified, oxygen-free 1-naphthol-2-sul-

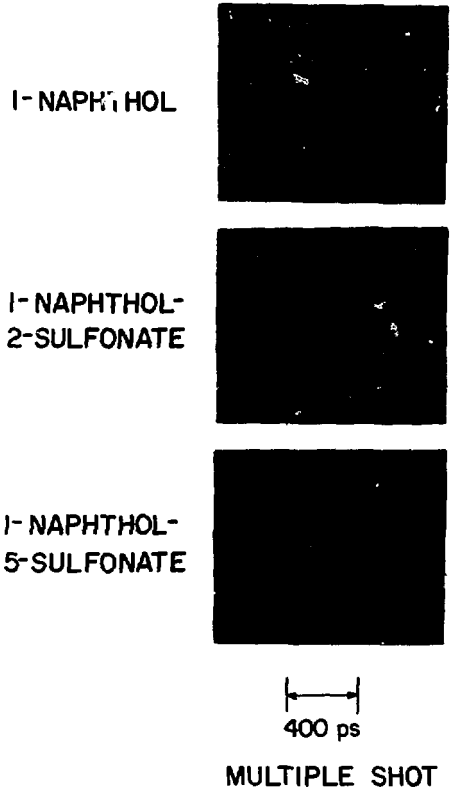

Fig. 4. Intensity versus time traces for the fluorescence decay of (a) 1-naphthol, (b) 1-naphthol-2-sulfonate, and (c) 1-naphthol-5-sulfonate. The symmetric peak on the right of each streak camera trace is a precursor pulse from the laser, and serves as a relative time marker between different laser pulses. The tailing seen at long times in (c) is caused by incomplete blocking of the emission from electronically excited 1-napthol-ate-5-sulfonate anions.

(XBB 813-3059)

fonate excited at 313 nm, which is completely dominated by the emission from the deprotonated species. This is in contrast to the spectrum obtained by Zaitsev et al.,[9] in which the ratio of the emission intensities of the deprotonated species to that of the protonated form is only 2 to 1.

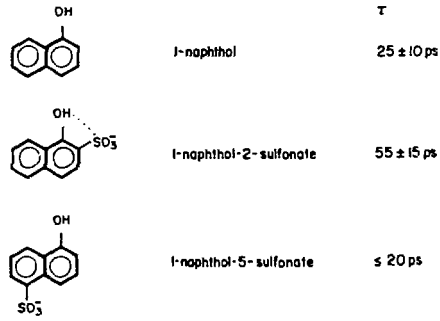

Fig. 5. Decay time (τ) for emission from electronically excited 1-naphthol, 1-naphthol-2-sulfonate, and 1-naphthol-5-sulfonate.

(XBL 814-9102)

For the case of 1-naphthol, Martynov, et al.[10] estimated a dissociation rate of $>3 \times 10^9$ sec^{-1}. The present measurement of 25 ± 10 ps is in accord with this estimate. What is most striking about these results is the remarkable difference between the proton transfer rates in 1-naphthol ($k_f \sim 4 \times 10^{10}$ sec^{-1}) and 2-naphthol ($k_f \sim 5 \times 10^7$ sec^{-1})[8], given the rather minor differences in electronic and geometrical structure between these two molecules.

Previously, we suggested that by using intense laser pulses, the pH of a solution could be changed in a manner analogous to the temperature change in a T-jump experiment. This laser pH jump technique[5] might permit the study of rapid acid-base reactions. The rapid deprotonation of the 1-naphthol compounds demonstrates that the pH of a solution may be manipulated on a time scale of less than 20 ps. This rapid rate, the fastest intermolecular proton transfer process observed to date, offers the possibility of producing very large and rapid pH jumps for studying rapid chemical reactions.

* * *

†Permanent Address: Los Alamos Scientific Laboratory, Los Alamos, New Mexico 87545.

1. J. F. Ireland and P. A. H. Wyatt, Adv. Phys. Org. Chem. 12, 131 (1976).
2. M. Ofran and J. Feitelson, Chem. Phys. Lett. 19, 427 (1973).
3. A. B. Demyaschkevitch, N. K. Zaitsev, and M. G. Kuz'min, J. Chem. Phys. 80, 898 (1976).
4. M. R. Loken, J. W. Hayes, J. R. Gohlke, and L. Brand, Biochemistry 11, 4779 (1972).
5. J. H. Clark et al., J. Am. Chem. Soc. 101, 746 (1979).
6. A. Weller, Z. Elektrochem. 56, 662 (1952).
7. L. D. Derkacheva, Opt. Spectrosk. 9, 209 (1960) [Eng. Trans. p. 110].

8. R. M. C. Henson and P. A. H. Wyatt, JCS Faraday II 71, 669 (1975).
9. N. K. Zaitsev, A. B. Demyashkevich, and M. G. Kuz'min, Khimiya Vysokikh Energii 12, 436 (1978) [Eng. Trans. p. 365].
10. I. Yu. Martynov et al., Zhurnal Prikladnoi Spektroskopii 28, 1075 (1978) [Eng. Trans. p. 732].

2. THE KINETICS OF QUENCHING OF ELECTRONICALLY EXCITED STATES BY SOLVATED PROTONS.

Stanley L. Shapiro,[†] Margaret A. Tolbert, Kenneth R. Winn,[†] and John H. Clark

The classic investigations of Forster[1] and Weller[2] on excited-state proton-transfer reactions established a field of research that has remained vigorous for nearly 30 years. At the same time, these early studies produced an unsettling paradox. Although electronically excited 1-naphthol was found to live long enough to produce excited 1-naphtholate anions via proton transfer, it was found that excited 1-naphthol itself did not fluoresce in aqueous solution. This result stood in marked contrast to the results obtained when 2-naphthol was excited under identical experimental conditions and evoked a considerable number of explanations for the substantial difference in behavior between two such similar compounds. The results presented in the preceeding article--namely, that the excited-state proton-transfer rate in 1-naphthol is nearly 10^3 times faster than the corresponding rate in 2-naphthol--completely resolves this paradox.

There remains, however, a second, more complex paradox in the early work. From the reaction scheme of Fig. 1 in Article 1, it can be seen that a decrease in solution pH would be expected to increase the rate of reprotonation of electronically excited naphtholate anions (RO^{-*}), and hence to increase the fluorescence quantum yield from the excited naphthol (ROH^*). In 2-naphthol, this is indeed the case; and this fact forms the theoretical basis for the literally hundreds of investigations in which excited-state pK values are deduced from steady-state fluorometric titrations.[3] The behavior of 2-naphthol again stands in marked contrast to that of 1-naphthol, for which a decrease in solution pH indeed leads to a decrease in the fluorescence quantum yield from the excited naphtholate anion but without any concomitant increase in fluorescence from the excited 1-naphthol. This surprising result has over the years evoked a number of different interpretations. One recent hypothesis is that both electronically excited 1-naphthol and 1-naphtolate could undergo diabatic quenching by H_3O^+.[4]

This program approaches the study of chemical dynamics in solution from the standpoint that direct, real-time observation of reactant, intermediate, and product species is of the utmost importance in understanding complex chemical phenomena. The investigation of the kinetics of the interaction between electronically excited 1-naphtholate anions and solvated protons provides an interesting test of this philosophy.

Using the apparatus of Fig. 3, Article 1, the fluorescence lifetime of excited 1-naptholate was measured as a function of solution pH. The experimental results are shown in Fig. 6. From the time-dependent data alone, the increasingly rapid decay of the excited 1-naphtholate molecules is obvious and compelling evidence for diabatic quenching by solvated protons. In Fig. 7 the fluorescence decay times from the data of Fig. 6, are shown plotted versus solution pH. For comparison, the original 30 year-old data of Weller[2] for fluorescence quantum yield (ϕ) as a function of solution pH is also plotted in Fig. 7. The lifetime data is normalized to Weller's limiting value for ϕ of 0.64 at pH = 10. Emission spectroscopy has been carried out to confirm that the quenching is due to solvated protons rather than any counter ion present from the acid used to vary the pH.

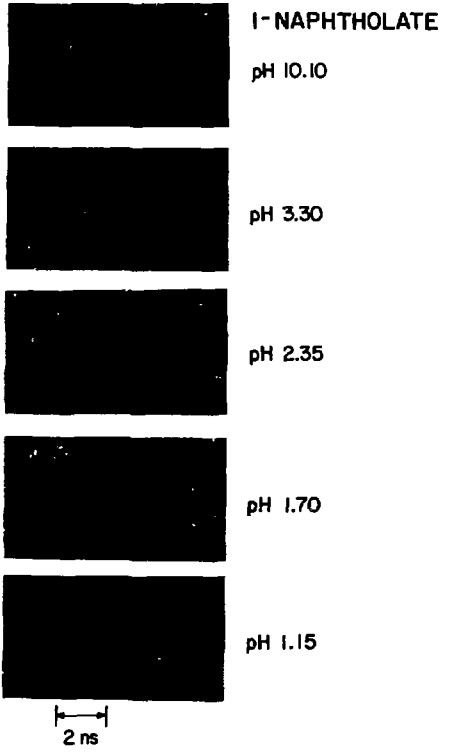

Fig. 6. Intensity versus time traces for the emission from electronically excited 1-naphtholate at various values of solution pH. (XBB 813-3060)

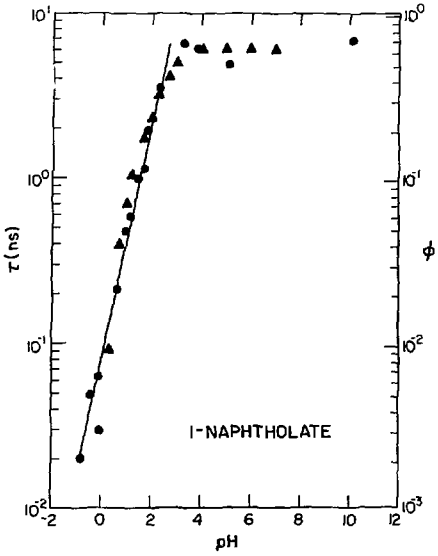

Fig. 7. Decay time (τ) for emission from electronically excited 1-naphtholate (left, solid dot), and fluorescence quantum yields (φ) for emission from excited 1-naphtholate (right, solid triangle) as a function of solution pH. (XBL 814-9098)

Although the results reported here establish that diabatic quenching of excited 1-naphtholate by H_3O^+ is indeed the mechanism whereby the paradoxical behavior of 1-naphthol can be explained, the reasons why this process should dominate in 1-naphthol and be absent in 2-naphthol are not yet clear. A substantial effort to establish the nature of the nonradiative pathways which are opened by interaction with solvated protons is currently underway.

* * *

†Permanent Address: Los Alamos Scientific Laboratory, Los Alamos, New Mexico 87545

1. Th. Forster, Z. Elektrochem. 54, 531 (1950).
2. A. Weller, Z. Elektrochem. 56, 662 (1952).
3. J. F. Ireland and P. A. H. Wyatt, Adv. Phys. Org. Chem. 12, 131 (1976).
4. C. M. Harris and B. K. Selinger, J. Phys. Chem. 84, 1366 (1980).

RESEARCH PLANS FOR CALENDAR YEAR 1981

Picosecond time-resolved emission work will be extended to include systematic study of the di- and tri-sulfonated naphthols. Detailed investigation of the effects of hydrogen-bonding on excited-state proton transfer will be carried out on naphthol sulfonates with varying strengths of and geometries for the interaction between sulfonate and hydroxyl groups. Picosecond laser studies of excited-state electron transfer reactions will begin with the goal of clarifying the role of geometric and electronic structure on those processes. The laser pH jump technique will be developed to the point where it can be used to initiate acid-base catalyzed reactions.

1980 PUBLICATIONS AND REPORTS

Refereed Journals

1. A. Hartford, Jr., E. J. Huber, J. L. Lyman, and J. H. Clark, "Laser Purification of Silane: Impurity Reduction to the Sub-Part-per-Million Level," J. Appl. Phys. 51, 4471 (1980).

Other Publications

1. S. L. Shapiro, K. R. Winn, and J. H. Clark, "Excited-State Proton-Transfer Kinetics in 1-Naphthol, 1-Naphthol-Sulfonates, and Organometallic Complexes," Picosecond Phenomena II, W. Kaiser and R. Hochstrasser, eds., Springer, New York, p. 227.

2. A. Hartford, Jr., and J. H. Clark, "Laser *Purification of Materials," in Chemical and Biochemical Applications of Lasers, Vol. V*, C. B. Moore, ed., Academic Press, New York, p. 217.

Invited Talks

1. John H. Clark, "Laser-Induced Chemical Processes," Dow Chemical U.S.A., Midland, Michigan.

3. Atomic Physics

a. Atomic Physics

Richard Marrus, Investigator

1. ELECTRON CAPTURE BY TRAPPED Ne^{10+} AT VERY LOW ENERGIES

C. R. Vane, M. H. Prior, and Richard Marrus

Electron capture by low-energy multiply charged ions on neutral gases has been a subject of considerable recent interest in connection with fusion research[1] and astrophysical problems.[2] A considerable number of calculations have resulted based on a variety of models.[3] Experimental progress has been achieved mainly using beam-gas techniques[4] but, for multicharged heavy ions, has been almost entirely confined to the kinetic energy range above ∿1 keV and charge states less than fully stripped.

A new technique has been developed that uses the low-energy multicharged recoil ions produced in a gas traversed by a fast heavy-ion beam.[5] These ions are then trapped in an electrostatic trap where they undergo electron capture from the atoms in the residual gas. By sampling the ion population in time after their creation, the decay rates associated with electron capture are directly measured. Varying the trap potential allows determination of these rates as a function of ion kinetic energy. From this information, it is possible to infer values for the total cross section for electron capture and the velocity dependence. As a demonstration, a measurement of the total capture cross section of Ne^{10+} (fully stripped) on neutral neon gas in the range of mean kinetic energies 7 eV - 45 eV is described. However, the method has application to very low-energy, high-charge states of a wide variety of ions and target gases.

Pulsed 3.5 MeV/u Xe^{27+} beams from the LBL Super HILAC were collimated to ∿1.25 cm diameter and passed through an isolated ultra-high vacuum target chamber. The base chamber pressure was typically 1×10^{-8} torr. The ion beam was collected in a deep, well-shielded Faraday cup several meters downstream of the chamber. The collected charge was used for data normalization, and a beam arrival pulse was generated for timing synchronization. An electrostatic ion trap[6] was constructed as shown schematically in Fig. 1. It consists of a ∿15 cm diameter copper cylinder ∿ 18 cm in length coaxially mounted with an electrically isolated thin tungsten wire (diam. = 0.08 mm). A potential difference (ΔV) maintained between these elements produced a nearly logarithmic potential well in which slow positive ions were radially confined. Isolated end caps, held at an appropriate potential with respect to the central wire, restricted ion motion parallel to the axis so that a three-dimensional trapping configuration could be achieved without seriously disturbing the logarithmic potential near trap center. The ion trap was mounted in the target chamber so that the projectile beam was transmitted axially through the trap parallel with the central wire at a separation of 1.25 cm.

Neon-22 target gas was admitted into the trap region from a clean glass reservoir through a variable leak valve. Target Ne ions created during the 3.3 msec Xe^{38+} beam pulse recoil at nearly 90° with respect to the incident beam, i.e., in a plane perpendicular to the trap axis. The trapped Ne^{q+} ions interact with neutrals in

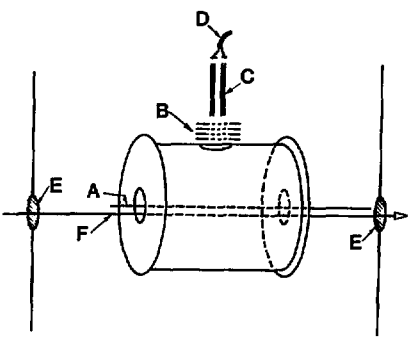

Fig. 1. Electrostatic ion trap. (A) central wire, (B) accel/decel grids, (C) quadrupole m/q analyzer, (D) channel electron multiplier, (E) vacuum isolation foils, (F) beam axis. (XBL 809-11947)

*This work was supported by the Director, Office of Energy Research, Office of Basic Energy Sciences, Chemical Sciences Division of the U. S. Department of Energy under Contract No. W-7405-ENG-48.

the thin background gas while orbiting the central wire. Both elastic and inelastic collisions can occur, but impact energies are usually too low for ionization of neutrals except through electron capture; and, for the trap geometry chosen, very few elastic collisions can lead to loss of the ions from the trap (only those which reduce the ion angular momentum to essentially zero). Therefore, decay of a Ne^{q+} population through interactions with neutral target gas is due primarily to electron capture collisions.

The bare ion decay rate was measured by emptying the ion trap at progressive delay times after detection of the projectile beam pulse and by storing the number of Ne^{10+} ions released into the detection system as a function of time. Ions were dumped from the trap by switching the central wire potential from its negative trapping value to the positive potential of the outer cylinder. A geometric fraction of the released ions passed through grid-covered hole in the trap outer cylinder. Transmitted ions were filtered according to their mass-to-charge ratio (m/q) by a commercial quadrupole residual gas analyzer (RGA) and detected by a channel electron multiplier, as shown in Fig. 1. Isotopically pure ^{22}Ne target gas was used in these experiments. The RGA resolution is sufficient to separate all charge states of $^{22}Ne^{q+}$ and in particular to fully resolve m/q = 2.20 ($^{22}Ne^{10+}$) ions from m/q = 2.00 ions (e.g., H_2^+). The RGA can be remotely scanned at fixed delay times to provide m/q spectra for calibration and to ensure negligible background signal from other gases. To preclude the possibility of substantial levels of contaminants being introduced with the target gas, m/q scans were taken at widely varied target densities and the spectra searched for pressure dependent non-$^{22}Ne^{q+}$ peaks. None were found.

In measurements of the decay rates of Ne^{10+}, the RGA was programmed to transmit only m/q = 2.20 ions. The time interval from production to release of the ions from the trap (trapping time t_i) was then scanned in a stepwise fashion. The trapping time was held fixed at each value t_i for many beam pulses until a prescribed beam charge had been accumulated at the Faraday cup. The trapping time was then incremented and the process repeated until the period between beam pulses had been scanned. The analyzed ion count data was collected by a minicomputer in multi-channel scaling mode, each channel corresponding to a particular t_i.

The resulting decay curves are well described by a single exponential, $N = N_0 e^{-\gamma t}$, as shown by the semilog plots of Fig. 2. The decay rate, γ can be expressed as $\gamma = \langle\sigma v\rangle n + \gamma_0$, where γ_0 is the net decay rate associated with trap leakage and collisions with background gases other than neon; $\langle\sigma v\rangle n$ is the decay rate of $^{22}Ne^{10+}$ due to electron capture to all lower charge states from neutral ^{22}Ne at density n. The rates γ vs n were obtained from least-squares fits to series of data such as shown in Fig. 2. Plots of γ vs n for several trap potentials are shown in Fig. 3. The slopes of straight line fits to these data provide $\langle\sigma v\rangle$, the capture collision rate constant averaged over the Ne^{10+} velocities at each trap potential. The ex-

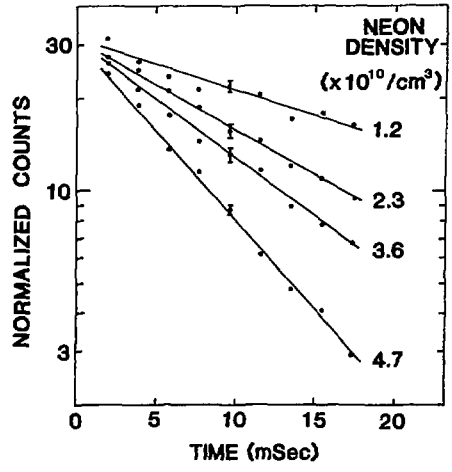

Fig. 2. Decay of trapped Ne^{10+} at trap potential of 20.7 V for various neon densities. Each curve has been normalized at t = 0, corresponding to the trailing edge of the beam pulse. Error bars indicate statistical uncertainties of the data.
(XBL 809-11944)

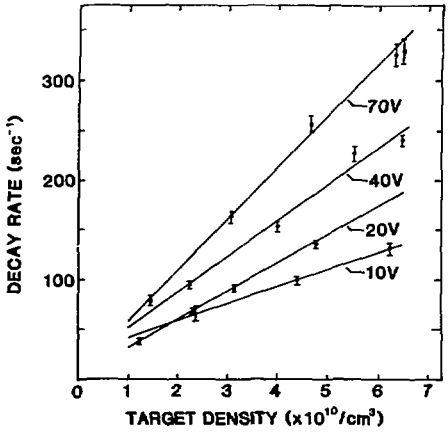

Fig. 3. Ne^{10+} decay rates as a function of target density for trap potentials shown. Slopes give $\langle\sigma v\rangle$ for electron capture from neon.
(XBL 809-11946)

trapolated decay rate for Ne^{10+} ions at zero neon density was approximately 3 sec^{-1}, consistent with ion loss due to electron capture from the N_2 and H_2O dominated background density of about 6×10^8 cm^{-3}.

The virial theorem applied to ion motion in the plane perpendicular to the trap axis near trap mid length shows that the rms ion velocity v_{rms} is independent of initial conditions and depends only on the trapping potential as $v_{rms} = C(q\Delta V)^{1/2}$, where $C = 7.6 \times 10^4$ cm/sec-$(eV)^{1/2}$ is determined by the geometry of the trap and ion mass. This has been compared with the mean ion velocities found from the TOF and retardation data, and found to be consistent with those results to within 10%. To study the velocity dependence of the capture cross section, the trap potential was varied from 10 V to 70.7 V. Assuming a power dependence of $\langle\sigma v\rangle$ on the trap potential $\langle\sigma v\rangle = A(q\Delta V)^p$, a least-squares fit to the data yields $p = 0.54 \pm 0.05$. Figure 4 demonstrates the constancy of $\langle\sigma v\rangle/(\Delta V)^{1/2}$ with $(\Delta V)^{1/2}$, implying that in the range of impact energies studied here, the cross section is velocity independent. A forced fit of $\langle\sigma v\rangle = \sigma_{e.c.} v_{rms}$ to the data yields $\sigma_{e.c} = 2.4(0.2) \times 10^{-15}$ cm^2. This error is the statistical error in the least-squares fit. The absolute error is estimated to be 30 percent primarily due to uncertainty in the neon density.

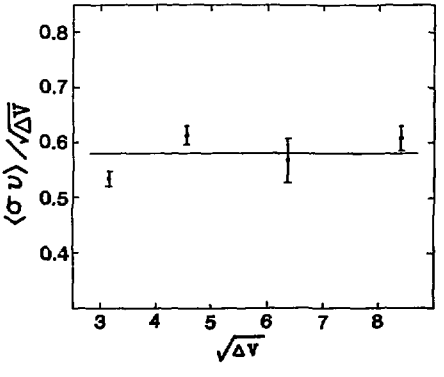

Fig. 4. Decay rate constant $\langle\sigma v\rangle$ scaled by $(\Delta V)^{-1/2}$ versus $(\Delta V)^{1/2}$. Units of vertical and horizontal axes are 10^{-9} cm^3/sec-$V^{1/2}$ and $V^{1/2}$, respectively. Error bars indicate only the statistical errors in least-squares fits to the data.

(XBL 809-11945)

* * *

1. H. B. Gilbody, in Advances in Atomic and Mol. Physics (Vol. 15), D. R. Bates, ed., Academic Press, New York (1979), p. 293.
2. A. Dalgarno, in Advances in Atomic and Mol. Physics (Vol. 15), D. R. Bates, ed, Academic Press, New York (1979) p. 37.
3. For a summary of many relevant references, see R. E. Olson, in Electronic and Atomic Collisions, N. Oda and K. Takayanagi, eds., North-Holland Publishing Co., Amsterdam (1980) p. 391.
4. D. H. Crandall, R. A. Phaneuf, and F. W. Meyer, Phys. Rev. A22, 379 (1980), and refs. therein; E. Salzborn and A. Muller, in Electronic and Atomic Collisions, N. Oda and K. Takayanagi, eds., North-Holland Publishing Co., Amsterdam (1980), p. 407.
5. I. A. Sellin et al., Z. Physik A283, 320 (1977); C. L. Cocke, Phys. Rev. A20, 749 (1979); T. J. Gray, C. L. Cocke, and E. Justiniano, Phys. Rev. A22, 849 (1980).
6. K. H. Kingdon, Phys. Rev. 21, 408 (1923). Ion trajectories in the logarithmic potential have been calculated by R. H. Hooverman, J. Appl. Phys. 34, 3505 (1963).

2. NEW OBSERVATION OF PARITY NONCONSERVATION IN ATOMIC THALLIUM†

P. Bucksbaum, E. Commins, and L. Hunter

We report new observations of parity nonconservation (PNC) in the $6^2P_{1/2} - 7^2P_{1/2}$ transition in atomic thallium. The transition amplitude is forbidden M1 with measured amplitude $M = (-2.1 \pm 0.3) \times 10^{-5}\ |e\hbar/2m_ec|$.[1] Parity nonconservation causes the $6^2P_{1/2}$ and $7^2P_{1/2}$ states to be admixed with $2S_{1/2}$ states; thus the transition amplitude contains an additional E1 component $\mathcal{E}_p$. This results in circular dichroism, defined by:

$$\delta = \frac{\sigma_+ - \sigma_-}{\sigma_+ + \sigma_0} = \frac{2\mathrm{Im}(\mathcal{E}_p M^*)}{|M|^2 + |\mathcal{E}_p|^2} \simeq \frac{2\mathrm{Im}\,\mathcal{E}_p}{M} \qquad (1)$$

where $\sigma_\pm$ are the cross sections for absorption of 293 nm photons, with $\pm$ helicity, respectively. Theoretical estimates of $\mathcal{E}_p$ based on the Weinberg-Salam (W-S) model[2] yield[3-5]

$$\delta_{theo} = \frac{2\mathrm{Im}(\mathcal{E}_{p,theo})}{M_{expt}} = (2.1 \pm 0.7) \times 10^{-3} \qquad (2)$$

for $\sin^2\theta_W = 0.23$, where θ_W is the Weinberg angle.

The aim of this experiment is to measure δ. The dipole amplitude $\mathcal{E}_p$ and M are observed by their interference with a Stark E1 amplitude $\mathcal{E}E$ caused by a 215 V/cm electric field E, in the $6P_{1/2}$, $F = 0 - 7^2P_{1/2}$, $F = 1$ transition. This causes a polarization $\Delta = 2M/\mathcal{E}E\ (1 \pm \delta/2)$ in the $7^2P_{1/2}$,

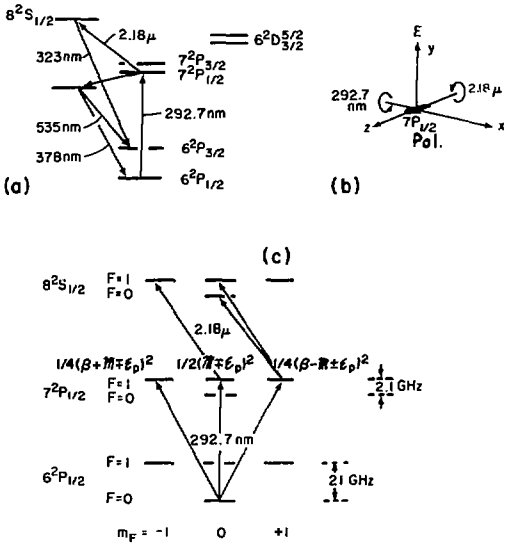

Fig. 5. (a) Low-lying energy levels of Tl (not to scale). (b) Coordinate system, orientation of photon beams, and electric field direction. (c) Schematic diagram indicating production and analysis of $7^2P_{1/2}$ polarization in the 0-1 transition. The transition amplitudes to the $m_F = \pm 1$ levels of $7^2P_{1/2}$ are indicated. The polarization is analyzed by circularly polarized 2.18-μm radiation ($7^2P_{1/2}$ - $8^2S_{1/2}$ transition). The $8^2S_{1/2}$ hfs is not resolved. (XBL 7811-6652)

F = 1 state. The latter is analyzed by selective excitation of $m_F = +1$ or -1 substates to the $8^2S_{1/2}$ state with circularly polarized 2.18μ light, followed by observation of $8^2S_{1/2}$ - $6^2P_{3/2}$ fluorescence at 323 nm. (See Fig. 5.) In a preliminary version of the experiment[6] we obtained the result $\delta = +(5.2 \pm 2.4) \times 10^{-3}$. Although the basic method has remained unchanged, numerous improvements in the apparatus have been made, and we have also carried out a thorough investigation of possible sources of systematic error.

Apparatus improvements include use of a new thallium cell with better geometry, yielding higher signal and lower background; better detection efficiency; better laser stability and higher laser output power; use of a Pockels cell instead of a rotating quarter-wave plate to produce circularly polarized 293 nm light; automatic laser frequency control for 293 nm light; use of a faster on-line computer with a more sophisticated interface and running program; use of a mirror to reflect the 293 nm beam back through the main cell, which does not affect the genuine parity asymmetry but reduces the M1 asymmetry; and other miscellaneous improvements.

The main sources of possible systematic error (false parity asymmetry) are (a) imperfect UV circular polarization, and (b) stray electric fields in the interaction regions which do not reverse exactly in proportion to the main component of electric field employed for the Stark effect.[7] By means of a combination of auxiliary experiments carried out during each parity experimental run, we have measured precisely the contribution of these effects to the parity asymmetry, and have corrected for them with very small uncertainty. The auxiliary experiments involve asymmetry measurements with linearly polarized 293 nm light and with circularly polarized 293 nm light and a magnetic field of ± 5 gauss along the 293 nm beam direction, each with and without the mirror.

We observe a parity asymmetry in the $6^2P_{1/2}$ (F = 0) → $7^2P_{1/2}$ (F = 1) transition:

$$\Delta_p(0\text{-}1) = (1.51 \pm 0.36 \pm 0.09) \times 10^{-5} \qquad (3)$$

where the first uncertainty is statistical and the second is systematic. Comparing with the observed M1 asymmetry we obtain:

$$\delta = + (2.9 \pm 0.7 \pm {}^{0.3}_{0.2}) \times 10^{-3} \qquad (4)$$

which is consistent with δ_{theo} (see Eq. (2)).

* * *

†Submitted to Phys. Rev. Lett. November 1980.
1. S. Chu, E. Commins, and R. Conti, Phys. Lett. 60A, 96 (1977).
2. S. Weiberg, Phys. Rev. Lett. 19, 1264 (1967) and 27, 1688 (1971); and Phys. Rev. D 5, 1412 (1972). A. Salam in Elementary Particle Theory, edited by N. Svartholm, Almquist Forlag, Stockholm (1968).
3. D. V. Neuffer and E. Commins, Phys. Rev. A 16, 844 (1977).
4. O. P. Sushkov, V. V. Flambaum, and I. B. Khriplovich, Pis' ma Zh. Eksp. Teor. Fiz. 24, 461 (1976) [JETP Lett. 24, 502, 1976].
5. T. P. Das, private communication.
6. R. Conte, et al., Phys. Rev. Lett. 42, 343 (1979).
7. M. A. Bouchiat, J. Guená, and L. Pottier, J. Phys. Lett. (Paris) 41, L-299 (1980).

3. VACUUM SPARK SOURCE FOR TRAPPED METAL IONS

M. H. Prior and Peter Latham

A simple technique has been implemented that will produce ions of virtually any metal, and probably other solids, for injection into an electrostatic ion trap. Once inside the trap, a number of spectroscopic and collision studies can be carried out during the long confinement times available (several seconds being easily achieved).

The method uses a vacuum spark between a tantalum electrode raised to approximately 20 kilovolts and a solid sample of the metal of interest. A schematic of the source, trap and ion detector is shown in Fig. 6. The gap between the sample and the high voltage electrode can be varied by an x-y motion vacuum feed-through and is typically 0.5-1.0 mm. The energy stored in capacitor C is dumped through the vacuum gap on command of the system controller (a DEC PDP 11/10) via the triggered spark gap. The discharge lasts a few microseconds and transfers about 1 joule of energy to the sample. A transient plasma is produced which expands across the stainless steel ultrahigh vacuum chamber containing the ion trap. As long as the ion density is high enough, ions inside the expanding plasma are shielded from the electrostatic field of the ion trap. However, it is possible for a portion of the plasma to enter the trap volume largely shielded but lose this shielding as it expands across the trap. Ions in this portion of the plasma thus see the trap field switched on while they are inside and hence can be captured. This critical density is of the order of 10^6 cm^{-3}.

For analysis, the ions captured by the trap are dumped radially by raising the wire potential up to that of the cylindrical outer trap electrode. A fraction of these dumped ions enter a commercial

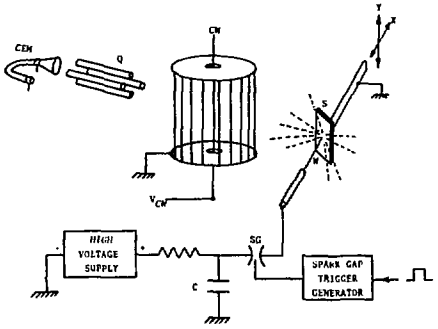

Fig. 6. Spark source and electrostatic ion trap system. Discharge of 0.005 μF capacitor C through the vacuum gap between the tantalum wire W and sample S is initiated by the triggered spark gap SG when commanded by the system controller. Some of the expanding ion cloud is captured by the electrostatic field surrounding the trap central wire CW. For capture and storage, the wire voltage, V_{CW}, is typically -300 V with respect to the surrounding cage at ground potential. To dump the ions for analysis by the quadrupole mass analyzer, Q, V_{CW} is switched to a few volts above ground potential. Electron multiplier, CEM, provides amplified ion pulses for accumulation by a multichannel collection system. (XBL 8012-12998)

quadrupole mass analyzer. Counts received from an electron multiplier at the exit of the analyzer are accumulated by the data collection system in channels which are scanned in synchronism with the voltage which sets the mass to charge ratio (m/q) transmitted by the quadrupole. A portion of such a scan, showing Ti^+ ions dumped after storage for 0.29 seconds, is shown in Fig. 7. Besides the main peak at m/q = 48, one can see four smaller peaks at 46, 47 and 49, 50. This pattern approximates the abundances of the stable Ti isotopes 46(7.9%), 47(7.3%), 48(74.0%) and 50(5.3%). Similar results were obtained for lithium and aluminum ions.

Ions containing an unfilled d-shell (e.g., Ti^+) offer a rich area for the study of forbidden radiative decay because they invariably contain a large number of low lying states of the same parity. In the case of Ti^+, there are about 40 forbidden lines (magnetic dipole and electric quadrupole) among these states with wavelengths less than 6000 A. Initial optical observations indicate that the spark source produces significant populations of the long lived excited states involved in these transitions.

The low duty cycle, pulsed nature of the vacuum spark source is well suited to ion trap studies of metastable ionic states. Very little source

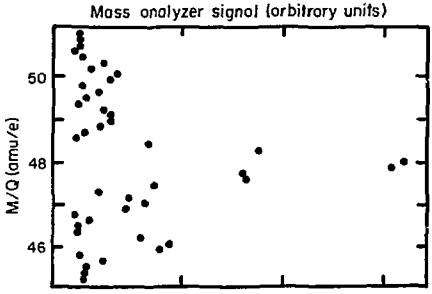

Fig. 7. Mass spectrum of Ti^+ ions from the vacuum spark source after storage in the ion trap for 0.29 seconds. The trap potential was -350 V. The small peaks at M = 46, 47 and 49, 50 are the less abundant stable isotopes of Ti whose main constituent is M = 48 (74%). (XBL 8012-12999)

material is consumed (especially important if a separated isotope is required), and the transient discharge does not perturb seriously the required ultrahigh vacuum. The spark source and ion trap combination offer the possibility of studying the forbidden spectra and metastable lifetimes of a wide variety of ions in an environment free of allowed electric dipole transitions which often mask the weak forbidden lines in a continuous source.

4. INITIAL TESTS OF POSSIBLE SECOND BORN-INDUCED ASYMMETRY IN FORWARD ELECTRON EJECTION BY FAST BARE NUCLEI

M. Breinig,† S. B. Elston,† I. A. Sellin,† L. Liljeby,† R. S. Thoe,† C. R. Vane, Harvey Gould, Richard Marrus, and Roman Laubert‡

To date, no unambiguous experimental tests of the relative importance of second and higher Born amplitudes compared to first Born amplitudes exist for any charge transfer process, even at asymptotically high (though nonrelativistic) ion velocities v. An excellent review of theoretical research on the high velocity charge transfer problem has recently appeared.[1] It has often been suggested that the Born series diverges for an exchange amplitude that includes charge transfer. What is less clear is the significance of this result for a calculation which stops at the second Born term. Because the Born series may be an asymptotic series, the question of which term(s) are dominant at high velocities becomes important. For radiationless electron capture by protons in hydrogen, for example, the Born series is dominated at high velocities (≳ 20 a.u.) by the second Born term[1,2] (which scales as ~ v^{-11}) as opposed to the first Born term (~ v^{-12}). It is far from clear to what extent the second Born term improves the first Born calculation, or even that either provides a good approximation, especially since alternative scattering calculations (e.g., approximate Faddeev-Watson scattering theory approaches yield somewhat different predictions[3] for the asymptotic velocity dependence).

A potentially important step forward was made recently by Shakeshaft and Spruch.[4] They observed that measurements[5] of strong asymmetry found in the velocity spectrum of electron capture to continuum states by bare ions traversing gases (ECC) might be the first experimental indication of the importance of the second Born term, even though the impact velocities were appreciably below that required to assure dominance in total cross section. Theoretically, the asymmetry arises entirely[4] from second Born terms, for which the differential cross section $d\sigma/dv_e$ is asymmetric under the transformation $(\vec{v}_e - \vec{v}) \to -(\vec{v}_e - \vec{v})$.

A counter conjecture concerning the origin of the observed asymmetry is provided by Chan and Eichler,[6] who note that retention of terms linear in $\Delta v_e = (|\vec{v}_e - \vec{v}|)/v$ beyond those incorporated in the first Born-Brinkmann-Kramers (BK) approach originally used by Dettmann et al.,[6] produces a similar asymmetry when compared[4,6] to earlier Ar target data at v = 9 a.u.[5] However, predictions of Refs. 4 and 6, concerning the projectile Z and v dependence of both shape and yield, are very different, as is the predicted shape of the corresponding cusps. The results of the first tests of the predicted second Born asymmetry conjecture for Ar^{18+} on He is the principal subject of this report.

Briefly, 15 and 18 a.u. beams of bare Ar ions obtained from LBL SuperHILAC accelerator pass through a ~2 cm long gas cell containing He, Ne, or Ar at pressures well within single collision conditions.[5] The cell is situated at the entrance focus of a double focusing, 90-deg magnetic sector analyzer set to record electron spectra for ejection within a cone of half-angle $\theta_0 = 1.7°$, centered on the forward direction. The momentum resolution is 1.7% FWHM.

Typical data for Ar^{18+} on He are displayed in Fig. 8, overlaid with the best fits to the data obtained with a convoluted Shakeshaft-Spruch (SS) line shape (curve A), and a convoluted Chan-Eichler (CE) line shape (curve D). Data were acquired over a wider velocity range, but since detailed line shape predictions apply only very near $v = v_e$, only the corresponding region is displayed. Convolution of parameterized theoretical line shapes (curves B and E) with the 1.7% FWHM, nearly triangular apparatus function shown in curve H (from electron gun calibration data) yielded the best fits (curves A and D). That the asymmetries observed are valid is demonstrated in curve G, which depicts the narrower, much more symmetric line shape (with Auger structure superposed) obtained for forward electron loss from 8.5 MeV/u Ar^{13+} on Ar.

Because the theoretical curves B and E apply to Z = 6 at 9 a.u. in a hydrogenic target,[7] our comparisons are only partially appropriate. However, these comparisons are sufficiently successful that a calculation for v = 15-20 a.u. in He is

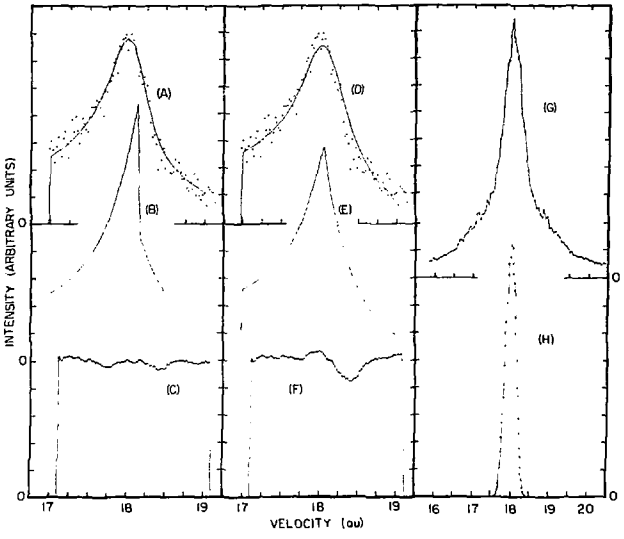

Fig. 8. Comparison of the central portion of ECC cusps obtained for 18.1 a.u. Ar^{18+} on He with the overlaid convoluted line shapes read from Ref. 4(A) and Ref. 6(D). The respective best fit theoretical shapes (B) and (E), when convoluted with the measured apparatus function (curve H), produce fits (A) and (D). A narrower more symmetric ELC spectrum for 18.1 a.u. Ar^{18+} on He is shown in (G). Curves (C) and (F) display 10 channel moving averages of the corresponding deviation spectra ($y_i - y_{FIT}$ vs i) as discussed in the text.
(XBL 812-8086)

strongly indicated. The characteristic feature of the SS shape is the sheer drop on the high velocity side of the peak. When convoluted with the instrument function, a drop is expected whose slope and width are essentially determined by the analyzer resolution function, a feature displayed by every ECC cusp we have ever observed for C^{6+}, O^{8+}, Si^{14+}, and Ar^{18+} in He, Ne, and Ar at all velocities (5-18 a.u.).[8] This property is not shared by the CE shape. Second, the CE shape is predicted to become symmetric at high v as ~ 1/v. There is no evidence in our data for any decline in asymmetry. On the contrary, for He, the asymmetry (as defined below) is found to rise very slightly in the range 15 to 18 a.u. (consistent with v independence within errors). For C^{6+}, O^{8+}, and Si^{14+} on Ne, the asymmetry is a strongly increasing function of v in the range 7-18 a.u., rising sharply as the neon K-velocity matching condition is reached.[8] Third, the ECC asymptotic velocity dependence of $d\sigma/dv_e$ predicted by Dettmann et al.,[6] when integrated over an appropriately scaled velocity region [e.g., $(1-\alpha)v$ to $(1+\alpha)v$ with $\alpha = 0.04$] is ~ v^{-10}. This dependence coincides with our experimental results for Ar^{18+} in He, which (over the range v = 15 → 18 a.u.) scale as ~ $v^{-9.9}$, suggesting that the anticipated asymptotic dependence has been reached (not so for either Ne or Ar targets, which scale as ~ v^{-7} over the same range).

Standard χ^2 per degree of freedom tests, in addition to a deviation test to be described, exhibit a marked preference for the SS as opposed to the CE shapes. For the data of Fig. 8, the fitted SS line shape yields $\chi^2 = 1/2 \pm 0.2$, whereas the CE shape yields 1.8 ± 0.4. Curves C and F are derived from the deviation spectrum ($y_i - y_{FIT}$, vs i) corresponding to A and B.

Curves C and F represent ten-channel moving averages, smaller than, but of the same order as, the analyzer resolution (16 channels). The clear preference for the SS vs the CE fit is exhibited by the large dip in curve F, which shows that the CE shape simply lacks the drop-off characterizing both the SS line shape and, by this test, the data.

A direct experimental measure of the asymmetry is the ratio $(\Gamma_\ell - \Gamma_r)/(\Gamma_r + \Gamma_\ell)$, where Γ_ℓ and Γ_r are the half widths (half maximum) of the cusp to the left and right of the peak. At 15 a.u. the measured values in He, Ne, and Ar are 0.28, 0.45, and 0.35, respectively. At 18 a.u., they are 0.35, 0.39, and 0.44, respectively. The range errors are ± 0.07 in each case. The Ne

asymmetry results are dominated by ECC of the Ne-1s electrons[8] (v is appreciably greater than the Ne K-shell electron velocity). A measurable increase in observed asymmetry for Ar targets is ascribed to the approach to K-shell velocity matching taking place in the velocity region 15-18 a.u.

Though the present shape and velocity dependence data are much better in accord with Ref. 4 than with Ref. 6, other predictions of Ref. 4 are not observed. For example, the asymmetries observed in Ne, Ar are very similar for all bare projectiles ranging from Z = 6-18, a finding not in accord with a predicted strongly Z-dependent asymmetry. Also, the yields scale at ~1:200:500 for 18 a.u. Ar^{18+} on He, Ne, and Ar, respectively, a dependence much weaker than a simple Z_{ARG}^{5} dependence.[4] Here, the theoretical restriction to the case of asymptotic velocities in hydrogen may be limiting.

Confirmation of a drop-off at $v \sim v_e$ at least as steep as the analyzer resolution function permits is thus the strongest evidence in favor of the SS asymmetry conjecture provided by our data.

* * *

1. R. Shakeshaft and L. Spruch, Rev. Mod. Phys. 51, 369 (1979), and many references therein; R. Drisko, unpublished thesis, Carnegie Institute of Technology (1955).
2. L. H. Thomas, Proc. R. Soc. 114, 561 (1927).
3. J. C. Y. Chen and P. J. Kramer, Phys. Rev. A 5, 1207 (1972); C. S. Shastry, A. K. Rajgopal, and J. Callaway, Phys. Rev. A 6, 268 (1972).
4. R. Shakeshaft and L. Spruch, Phys. Rev. Lett. 41, 1037 (1978).
5. C. R. Vane, IEEE Transactions on Nuclear Science NS-26, No. 1, 1078 (1979).
6. F. T. Chan and J. Eichler, Phys. Rev. A 20, 367 (1979); R. Shakeshaft and L. Spruch, Phys. Rev. A 20, 376 (1979); K. Dettmann, K. G. Harrison, and M. W. Lucas, J. Phys. B 7, 269 (1974); and K. C. R. Chiu, et al., J. Phys. B 12, L-147 (1979).
7. R. Shakeshaft, private communication.
8. C. R. Vane, et al., Book of Abstracts, 11th International Conference on the Physics of Electronic and Atomic Collisions, K. Takayanagi and N. Oda, eds., The Society for Atomic Collision Research, Japan (1979), p. 752; see Ref. 5.

RESEARCH PLANS FOR CALENDAR YEAR 1981

Electron Capture by Trapped Neon Ions at Very Low Energies. We plan to measure electron capture cross sections for all the neon charge states (Ne^{1+} through Ne^{10+}) over an energy range encompassing almost two orders of magnitude (10V ≤ trapping potential ≤ 1 kV). Several target gases will be used. These studies should provide a very stringest test for theoretical models.

Ion Trap Research Program. It is planned to measure the lifetimes of several metastable states of fourth period metal ions, such as Ti^{+}, Fe^{+}, and Cu^{+} utilizing the vacuum spark source/electrostatic ion trap combination. In favorable cases, laser excitation and subsequent fluorescence of the trapped ions may be utilized to probe the metastable populations. A high collection efficiency optical system will be developed to allow moderate resolution spectroscopy of the spontaneous forbidden spectra of these ions in the visible and near ultraviolet region.

Precision Measurements of Parity Nonconservation in Atomic Thallium. We will continue to pursue the investigation and verification of the Weiberg-Salam model in atomic thallium. The presence of parity non-conservation (PNC), as predicted by the WS theory, has been verified. We wish to improve the precision of the previous measurement in an experiment that will take advantage of a new and more powerful laser (Drell and Chu, Optics Communications 28, 343, 1979) and a simplified experimental set up that will result in higher counting statistics and fewer systematic effects. The improvements result from the fact that the entire experiment takes place in a 5 kG magnetic field, provided by a large electromagnet, so that the infrared laser and complicated optical pumping scheme for the original measurements are not needed. The same transition in thallium is used (6P → 7P) though now several hyperfine components can be resolved, each with a different size and sign of PNC. This experiment will enable us to investigate the PNC as a function of several parameters (frequency, magnetic field, electric field), thus permitting us to look for a clear and distinctive signature of the effect and separating it from possible systematics. It is planned to start taking data with the experiment in spring 1981.

1980 PUBLICATIONS AND REPORTS

Refereed Journals

1. R. D. Knight and M. H. Prior, "Radiative Lifetime of Metastable 2^3S, Li^{+}," Phys. Rev. A 21, 179 (1980).

2. Mark Hillery and Peter J. Mohr, "Radiative Decay of Hydrogenlike Atoms in an Electric Field," Phys. Rev. A 21, 24 (1980).

3. D. D. Dietrich, J. A. Levitt, H. Gould, and R. Marrus, "Radiative Decay of the 2p $^2P_{3/2,1/2}$ States of Li-like Krypton (Z = 36) and the 2S 2p $^3P_1$ State of Be-like Krypton," Phys. Rev. A 22, 1109 (1980).

4. M. H. Prior and R. D. Knight, "Fluorescence of Optically Pumped Trapped Ions," Optics Communications 35, 54 (1980).

5. M. Breinig, S. B. Elston, I. A. Sellin, L. Liljeby, R. S. Thoe, C. R. Vane, Harvey Gould, Richard Marrus, and Roman Laubert, "Initial Tests of Possible Second Born-Induced Asymmetry in Forward Electron Ejection by Fast Bare Nuclei," Phys. Rev. Lett. 45, 1689 (1980).

B. Processes and Techniques

1. Chemical Energy

a. Formation of Oxides of Sulfur from SO_2*

Robert E. Connick, Investigator

Introduction. The purpose of this project is to study the basic chemistry of sulfur dioxide in solution and the species formed from it by acid-base reactions, polymerization, and oxidation-reduction. This chemistry is fundamental to the understanding of wet processes for flue gas desulfurization at power plants and the chemical fate of atmospheric sulfur dioxide. The research is not directed towards the solution of immediate process problems.

1. OXIDATION OF BISULFITE ION BY OXYGEN

Robert E. Connick and Thomas G. Braga

Work on this problem has been transferred to the Solution Thermodynamics of Sulfites and Sulfite Oxidation Mechanisms program of this Annual Report because of the strong current interest of Morgantown in trying to control the reaction in flue gas desulphurization processes.

2. THE OXIDATION OF BISULFITE ION BY OXYGEN

Robert E. Connick and Thomas G. Braga

The solution reaction $2HSO_3^- + O_2 \rightleftharpoons 2SO_4^{2-} + 2H^+$ is of importance in flue gas desulphurization processes carried out in aqueous solutions or slurries. Depending on the process, it may be desirable either to enhance or restrict oxidation of bisulfite. In addition, the reaction is of concern in air pollution by SO_2 because oxidation of the SO_2 in water droplets or films is believed to be the primary way in which acid rain is formed. To control the reaction, a thorough understanding of the rate and mechanism is desirable.

The kinetics of the reaction has been studied by many investigators[1] with little agreement as to rate, rate law, or mechanism. This interesting and surprising result stems from the fact that the reaction is a chain reaction that is very susceptible to effects of impurities, with the consequence that the rate is highly irreproducible.

Instead of attempting to eliminate impurities as others have done, our approach has been to try to eliminate impurity effects by deliberately adding species that will control the chain initiation, chain termination, and chain propagation.

Initially, the reaction was followed by measuring the rate of O_2 gas absorption in solutions of Na_2SO_3 at pH ∿ 9. It was discovered that the observed rate was limited by the mass transfer rate of the O_2 gas into the solution, even though extremely vigorous agitation of the liquid with the gas was used. This finding casts doubt on the interpretations of results of a number of studies reported in the literature where a similar experimental method was used.

At pH ∿ 4 to 5, the region of greatest interest in FGD processes, the reaction is slowed enough so that mass transfer is not limiting. Experiments, conducted with equimolar sodium acetate-acetic acid buffer solutions, yielded an apparent 3/2 order dependence on bisulfite concentration and an inverse first power dependence on hydrogen ion concentration. Although the rates were not perfectly reproducible, changing the buffer concentration or using different sources of water seemed to have little effect.

To eliminate mass transfer completely, the reaction was studied by measuring the oxygen concentration with an oxygen meter in a closed container having no gas phase. This technique permitted data to be obtained more easily and more rapidly. The rate was determined at 25°C and was somewhat less than zero order in O_2 and presumably 3/2 and -1 order in HSO_3^- and H^+ from the shaking experiments.

Ethyl alcohol was added to control the termination step because Bäckström's work strongly indicates that the inhibitory effect of alcohol arises from its ability to terminate chains. Ethanol decreased the rate by the factor $1(k + k'[ETOH])$ at low ethanol concentration; but at ethanol concentrations > 0.1 M, the rate approached zero order dependence on ethanol, presumably because of a separate reaction path. This new term was roughly 100-fold smaller than the rate with no ethanol and had a 3/2 power dependence on the oxygen concentration. It was also dependent on the buffer concentration.

The catalyst manganous ion greatly speeded up the rate with an apparent linear dependence on manganous concentration.

To avoid complications with buffers, experiments are being run without buffer but controlling

*This work was supported by the Director, Office of Energy Research, Office of Basic Energy Sciences, Chemical Sciences Division of the U. S. Department of Energy under Contract No. W-7405-ENG-48.

the pH by manual addition of base. With no additives, the rate is roughly 3 fold slower than in a 0.25 M acetic acid-sodium acetate buffer of the same pH. A solution of sodium bicarbonate has been found suitable for maintaining constant pH. Again, the rate appears to be somewhat less than zero order in $[O_2]$; alcohol enters as before in the denominator to the first power.

Since there was evidence that the catalytic effect of manganous ion did not arise from the presence of a new initiation step, it was desirable to find a new initiator. Ultra-violet light was chosen because a photochemical path for the reaction is well known and it seemed likely that light would be initiating the chain. When the solution was illuminated by a General Electric 100A4/T bulb, the rate increased about 25-fold and the oxygen dependence became zero order. Further, the rate appeared to be independent of hydrogen ion concentration around pH 4.5. The dependence on bisulfite concentration was to the 3/2 power.

The rate of a chain reaction of long chain length may be represented symbolically by a chain initiating Step I, a chain propagating step P, and a chain terminating step T:

$$\text{Rate} = P\left(\frac{I}{T}\right)^{1/n} ,$$

where n is a small integer, usually 1 or 2. The rates of initiation and termination are equal, i.e., I = T. The factor I/T is introduced to cancel from the rate law the concentration(s) of chain carrier(s) which appear in P and T. If the termination involves one chain carrier, n will be unity; if it involves two chain carriers, n will be two.

While the catalytic effect of manganous ion could most simply be attributed to the introduction of either a new initiation path or a new chain propagation step, there is evidence that the latter possibility is correct. The evidence comes from the reactions in which ultra-violet light was used and apparently initiated the reaction. The factor increase in rate, produced by a given concentration of Mn^{2+}, appeared to be about the same with and without light, even though with light the rate was 25 fold greater. This result is understandable if the role of manganous ion is to provide a new propagation step rather than to create a new initiation step.

The results so far demonstrate the sensitivity of the rate to impurities and added reagents. It appears that the initiation can be controlled by UV irradiation, the propagation by addition of Mn^{2+}, and the termination by addition of ethanol. Using these "controls" it should be possible to determine whether any catalyst or inhibitor is acting in the initiation, propagation, and/or termination steps of the reaction, as was done for Mn^{2+}.

* * *

1. Gmelin's Handbüch der Anorganischen Chemie, Eighth ed., Sulfur System No. 9, Part B, Lieferung 3, pp. 1293-1519, (1963).
2. H. Bäckström, J. Am. Chem. Soc. 49, 1460 (1927); H. Alyea and H. Bäckström, ibid 51, 90 (1929).

RESEARCH PLANS FOR CALENDAR YEAR 1981

Research is currently underway to detect directly whether the isomer of bisulfite ion exists which has the proton attached to an oxygen. Raman measurements will be made in non-aqueous solvents in the O-H stretch region. It is expected that the solid $Na_2S_2O_5$ can be made sufficiently soluble by addition of one water per $S_2O_5^{2-}$ and the use of crown ethers to encapsulate the Na^+. Hopefully, the NMR study of oxygen exchange between solvent water, HSO_3^-, $SO_2(aq)$, SO_3^{2-} and $S_2O_5^{2-}$ will be resumed. The fitting of the bisulfite dimerization equilibrium quotient to Pitzer's activity coefficient equations will be completed. Computer modeling of exchange reactions of solvent molecules coordinated to metal ions will be continued as well as some experimental work on these reactions.

1980 PUBLICATIONS AND REPORTS

LBL Reports

1. R. E. Connick and T. G. Braga, "The Rate of Oxidation of Bisulfite Ion by Oxygen," Quarterly Reports to Morgantown Energy Technology Center, (Sept. 1979, March 1980, and Sept. 1980).

2. Mary Thompson and Robert E. Connick, "Hydrolytic Polymerization of Chromium(III). I. The Two Dimeric Species," LBL-11336 (Aug. 1980).

Invited Talks

1. Leo Brewer, "Thermodynamics of Compounds of Interest to the SO_2 Removal Program," Flue Gas Desulfurization Symposium, Morgantown, West Virginia, November 7, 1980.

2. Robert E. Connick and Thomas G. Braga, "The Kinetics of the Oxidation of Bisulfite Ion by Oxygen," Flue Gas Desulfurization Symposium, Morgantown, West Virginia, November 6, 1980.

b. Conversion of Coal to Clean Liquid and Gaseous Fuels*

Gabor A. Somorjai and Alexis T. Bell, Investigators

1. HYDROGENATION OF CO OVER RHODIUM OXIDE CATALYSTS

P. R. Watson and G. A. Somorjai

Hydrogenation of CO at 6 atm in the temperature range of 250-360°C has been carried out over a catalyst of $Rh_2O_3 \cdot 5H_2O$ deposited on small area (~ 1 cm^2) Au or Pt foils. The reaction was investigated in an apparatus which allowed determination of the surface composition by Auger electron spectroscopy before and after reaction.

This catalyst leads to a suppression of methane formation and greatly increased proportions of oxygenated hydrocarbon products compared to rhodium metal even when the metal was preoxidized. At 250°C and 1:1 H_2/CO ratios, up to 30 wt% of oxygen containing hydrocarbons are produced, mainly acetaldehyde with some propionaldehyde and small amounts of methanol. Increasing the temperature lowers the total yield of oxygenated products while increasing the H_2/CO ratio leads to a predominance of methanol over acetaldehyde in the product distribution.

The oxide catalyst surface appears to be oxygen deficient and may consist of a partially reduced metallic rhodium layer on top of the bulk rhodium oxide. After the reaction, the catalyst is covered by a carbonaceous layer that can be hydrogenated to methane. Kinetic measurements indicate that the activation energy for both methane and acetaldehyde formation are about 15 kcal/mole.

2. THE CONSTRUCTION OF A HIGH PRESSURE HREELS APPARATUS FOR STUDIES OF REACTION INTERMEDIATES

P. Davies and G. A. Somorjai

The system, presently under construction, will enable the structure and surface compositions of single crystal or other model, small area catalyst surfaces to be examined by the high resolution electron energy loss spectroscopy (HREELS) technique as well as by other techniques of surface science. These studies can be carried out both before and after exposure to reactant gases at pressures up to 7 atm. The catalyst surfaces are enclosed in an isolation cell during high pressure exposure, rapid pumping being employed to maintain base pressures of $\sim 10^{-10}$ torr in the main system. The HREELS equipment is similar to one presently in use in this laboratory; but, through a modification of lens design and an improvement in control electronics, the resolution and data acquisition rate will be substantially improved.

Using this system, we plan to examine the vibrational spectra of organic fragments present on metal catalyst surfaces during the catalyzed hydrogenation of CO and during hydrocarbon conversion reactions to understand their role in determining catalyst specificity and selectivity.

3. EFFECTS OF METAL-SUPPORT INTERACTIONS ON THE SYNTHESIS OF METHANOL OVER PALLADIUM‡

R. F. Hicks, Yu. A. Ryndin, and A. T. Bell

The synthesis of methanol and other products from CO and H_2 was studied over Pd catalysts prepared by adsorption of $Pd(\pi\text{-}C_3H_5)_2$ on MgO, ZnO, La_2O_3, $\gamma\text{-}Al_2O_3$, SiO_2, TiO_2, and ZrO_2 as well as over a SiO_2-supported Pd catalyst prepared from $PdCl_2$ and Pd black.

Reactions were carried out at 10 atm over the temperature range of 150 to 300°C. Both the activity and selectivity of Pd were found to be affected strongly by the nature of the support and the composition of the Pd precursor. The specific activity for methanol synthesis decreased in the order Pd/La_2O_3 >> Pd/SiO_2 [derived from $PdCl_2$] > Pd/ZrO_2 > $PdZnO_2$ ≈ Pd/MgO > $PdTiO_2$ > Pd/Al_2O_3 ≈ Pd/SiO_2 [derived from $Pd(\pi\text{-}C_3H_5)_2$] >> Pd black, while the specific activity for hydrocarbon synthesis decreased in the order Pd/TiO_2 ≳ Pd/ZrO_2 > Pd/La_2O_3 > Pd/Al_2O_3 ≈ Pd/SiO_2 [derived from $PdCl_2$] ≳ Pd/SiO_2 [derived from $Pd(\pi\text{-}C_3H_5)_2$] ≈ Pd black >> Pd/MgO ≳ Pd/ZnO. Compared at a fixed set of reaction conditions, the highest specific activity for methanol synthesis was a factor of 165-fold greater than the lowest, and the highest specific activity for hydrocarbon synthesis was a factor of 250-fold greater than the lowest. Dimethyl ether production was observed over four of the catalysts, and the activity for formation of this product decreased in the order Pd/Al_2O_3 >> Pd/TiO_2 >> Pd/MgO ≈ Pd/ZrO_2. Product selectivity was also affected by support composition. Basic metal oxide supports, such as MgO, ZnO, and La_2O_3, were found to favor the formation of methanol, the selectivity to this product exceeding 98%. A methanol selectivity of 98% was also observed for Pd supported on SiO_2, a neutral oxide. When acidic metal oxides such as Al_2O_3, TiO_2, or ZrO_2 were used as the support, the methanol selectivity was suppressed at the expense of forming hydrocarbons. Acidic sites on the support also appear to be responsible for converting a part of the methanol formed to dimethyl ether.

*This work was supported by the Director, Office of Energy Research, Office of Basic Energy Sciences, Chemical Sciences Division of the U. S. Department of Energy under Contract No. W-7405-ENG-48.

The manner in which the acid/base properties of the support express their influence on the catalytic properties of Pd is not understood at present. An electronic interaction between the metal and the support is suggested but it appears that this interaction is not of the SMSI-type discussed in the literature.[1,2] XPS investigations have been initiated to characterize the oxidation states of supported Pd and the metallic component of the oxide. It is anticipated that these studies will shed light on the nature of the metal-support interaction and the influence of catalyst preparation and pretreatment on the strength of this interaction.

* * *

†Brief version of LBL-11603.

‡Supported in part by NSF.

1. S. J. Tauster, S. C. Fung, and R. L. Garten, J. Am. Chem. Soc. 100, 170 (1978).
2. S. J. Tauster, and S. C. Fung, J. Catal. 55, 29 (1978).

4. THE MECHANISM AND KINETICS OF HYDROCARBON SYNTHESIS OVER RUTHENIUM

C. S. Kellner and A. T. Bell

The synthesis of methane and higher molecular weight hydrocarbons over Ru catalysts can be represented by the mechanism shown in Table 1. Isotopic substitution experiments conducted with ^{12}CO and ^{13}CO in the presence of H_2 indicate that reaction (1) is at equilibrium under reaction conditions. Moreover, in-situ infrared observations show that the surface coverage of CO is given by a Langmuir isotherm, for which the equilibrium constant is $K_1 = 1.1 \times 10^{-9} \exp(25{,}500/RT)$ atm^{-1}. The dissociation of molecularly adsorbed CO occurs at temperatures above 150°C and recent isotope scrambling studies conducted with $^{12}C^{18}O$ and $^{13}C^{16}O$ (Ref. 1) suggest that this process is reversible and near equilibrium. Hydrogen chemisorption is also at equilibrium, as supported by H_2/D_2 scrambling studies. The observation of a strong inverse H_2/D_2 isotope effect on the synthesis of methane strongly supports the hypothesis that one or more equilibrium steps involving carbon hydrogenation, precede the rate limiting step.[2]

Under the assumption that reaction (8) is the rate limiting step for methane formation and that atomic oxygen is released from the surface solely by reaction (4), the rate of methanation can be expressed

$$N_{C_1} = k_e P_{H_2}^{1.5}/P_{CO} \qquad (1)$$

$$k_e = \frac{K_3}{K_1}(k_4 k_8 K_2 K_5 K_6 K_7)^{0.5} \qquad (2)$$

Table 1. Proposed mechanism of CO hydrogenation over Ru.

Reaction No.	Reaction	
1.	$CO + S \rightleftarrows CO_s$	K_1
2.	$CO_s + S \rightleftarrows C_s + O_s$	K_2
3.	$H_2 + 2S \rightleftarrows 2H_s$	K_3
4.	$H_2 + O_s \rightarrow H_2O + S$	k_4
5.	$C_s + H_s \rightleftarrows CH_s + S$	K_5
6.	$CH_s + H_s \rightleftarrows CH_{2_s} + S$	K_6
7.	$CH_{2_s} + H_s \rightleftarrows CH_{3_s} + S$	K_7
8.	$CH_{3_s} + H_s \rightarrow CH_4 + 2S$	k_8
9.	$CH_{3_s} + CH_{2_s} \rightarrow C_2H_{5_s} + S$	k_9
10.	$C_2H_{5_s} + S \rightarrow C_2H_4 + H_5 + S$	k_{10}
11.	$C_2H_{5_s} + H_s \rightarrow C_2H_6 + 2S$	k_{11}
12.	$C_2H_{5_s} + CH_{2_s} \rightarrow C_2H_{7_s} + S$	k_{12}
	etc.	

The form of Eq. (1) is in excellent agreement with experimental observations of methanation kinetics obtained at pressures between 1 and 10 atm, H_2/CO ratios between 1 and 3, and temperature between 175 and 275°C.

Chain growth is postulated to begin via methylene addition to surface methyl groups [reaction (9)], and then continues by addition of methylene groups to surface alkyl species [reaction (12)]. Olefins are produced by hydrogen elimination from the β-carbon of the surface alkyls [reaction (10)] and alkanes are produced by hydrogen to the α-carbon of the alkyl structure [reaction (11)]. Based on this view of hydrocarbon chain propagation and termination, it has been demonstrated that the rate of formation of hydrocarbons containing n atoms is given by

$$N_{C_n} = (1 + \beta/P_{H_2}^{0.5})\, N_{C_1} \qquad (3)$$

and that the olefin to paraffin ratio is given by

$$\frac{N_{C_n}^{=}}{N_{C_n}^{-}} = \beta/P_{H_2}^{0.5} \qquad (4)$$

where

$$\beta = k_{to}/(k_{tp}k_3^{0.5}) \quad (5)$$

The chain propagation probability, α, is given by

$$\alpha = [1 + \gamma P_{CO}^{-0.67}(1 + \beta P_{H_2}^{-0.5})]^{-1} \quad (6)$$

where

$$\gamma = [K_3/(k_p^2 k_4 K_1^2 K_2 K_5 K_6)]^{0.33} \quad (7)$$

Equations (3), (4), and (6) are found to provide an excellent description of the kinetics for forming C_2 through C_{10} olefins and paraffins. Deviations of the experimental data from the predicted kinetics are ascribable to the occurrence of secondary reactions, principally olefin hydrogenation and paraffin hydrogenolysis.

* * *

1. A. Bossi, et al. J. Catal. 65, 16 (1980).
2. C. S. Kellner, LBL-10786 (In press: J. Catal.)

5. THE INFLUENCE OF POTASSIUM PROMOTION ON FISCHER-TROPSCH SYNTHESIS OVER IRON

H. Arakawa and A. T. Bell

In the field of Fischer-Tropsch synthesis, it has long been known that the addition of a small amount of potassium to iron influences its adsorptive as well as catalytic properties. The purpose of this study was to establish the effects of K/Fe ratio on the specific activity of the catalyst, the methane selectivity, the olefin/paraffin ratio of the products, CO_2/H_2O ratio in the products, and the specific activity for carbon deposition via CO disproportionation. Catalysts were prepared by impregnation of Al_2O_3 with aqueous solutions of $Fe(NO_3)$, and KNO_3. The catalysts all contained 20 wt% Fe and had K/Fe ratios between 0.0 and 0.4. Testing was carried out in glass microreactors at 1 atm using H_2/CO ratios of 1 to 3 and temperatures of 200 to 300°C.

Progressive addition of potassium caused a twofold decline in Fe dispersion. The ratio of H_2 to CO chemisorbed at saturation equaled unity and was independent of K/Fe, indicating that CO is bridge-bonded. Increasing the K/Fe ratio does not affect the strength of H_2 adsorption but does increase the strength of CO adsorption. For K/Fe = 0.0 to 0.07, the specific activity of the catalyst is unaffected by potassium promotion; but, at higher K/Fe ratios, the activity declines rapidly with increasing promotion. Potassium promotion strongly affects the product distribution. Over the range of K/Fe ratios examined, the methane selectivity declines by threefold, and the product switched from principally parafinic to totally olefinic as the K/Fe ratio increased. Concurrently, the CO_2/H_2O increased from ~ 1.0 to greater than 30. Investigation of the effects of changing space velocity, H_2/CO ratio, and temperature revealed that C_{2+} olefins and methane are the primary hydrocarbons formed over iron and that oxygen is released primarily as water. The production of paraffins occurs primarily via olefin hydrogenation; and the production of CO_2, by the water gas shift reaction. Potassium promotion inhibits the first of these processes and enhances the second.

In a separate series of tests, it was established that potassium promotion greatly enhances CO disporportionation. Hydrogenation of the carbon thus formed is also affected by the presence of potassium, higher yields of olefins being observed with than without potassium. Examination of the catalyst by powder x-ray diffraction following reaction reveals than the iron is converted to the hexagonally close-packed carbide, and that this structure is supported by elemental analysis. It is also established that the carbide deposited during reaction in H_2/CO mixtures contains a considerable amount of hydrogen. This observation could explain the greater reactivity of the carbon deposited under reaction conditions than that formed via CO disproportionation.

6. PARTICIPATION OF MOLECULAR H_2 IN THE HYDROGENOLYSIS OF COAL-RELATED MODEL COMPOUNDS BY ZINC CHLORIDE

T. J. Fredrick and A. T. Bell

The hydrogenolysis of benzylic ether linkages and short aliphatic linkages present in coal can be catalyzed by zinc halides. The objective of the present studies was to investigate the degree to which molecular hydrogen enters into these reactions and the influence of $ZnCl_2$, $ZnBr_2$, and ZnI_2 on the activation of H_2. Reactions were carried out in a high pressure autoclave, using selected model compounds to represent the desired linkages between aromatic nuclei.

An investigation was performed of the effects of hydrogen partial pressure and catalyst composition on the hydrogenolysis of dibenzyl ether in benzene solution. In the presence of $ZnCl_2$, diphenylmethane was the principal product formed, and the extent of reaction was unaffected by the presence of absence of molecular H_2. These results indicate that the overall reaction can be written as

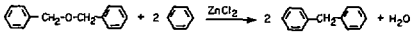

and that the hydrogen required for the formation of water derives from the benzene.

$ZnBr_2$ and ZnI_2 also catalyze the hydrogenolysis of dibenzyl ether but are less active

than $ZnCl_2$, the activity decreasing in the order $ZnCl_2 > ZnBr_2 > ZnI_2$. In the presence of $ZnBr_2$ and, in particular, ZnI_2, toluene is produced in addition to diphenylmethane. It is observed that while the extent of ether hydrogenolysis is unaffected by H_2 pressure, the selectivity to toluene using these catalysts is directly proportional to the H_2 pressure. These results indicate that $ZnBr_2$ and, in particular, ZnI_2 are more effective in activating H_2 than $ZnCl_2$ but that, even in an activated state, hydrogen does not affect the rate of consumption of dibenzyl ether.

The hydrogenolysis of 4-hydroxydiphenyl methane (4HDM) and 1-benzylnaphthalene (1BN) in benzene solution were studied to establish the effects of hydrogen partial pressure and catalyst composition on the cleavage of aliphatic linkages between aromatic nuclei. In the presence of zinc halide catalyst, 4HDM reacts to form phenol, diphenyl methane, and toluene. As shown in Table 2, the hydrogen partial pressure has no effect on the conversion of 4HDM, but the selectivity to toluene increases with the hydrogen partial pressure. The catalytic activity in this instance decreases in the order $ZnBr_2 > ZnCl_2 > ZnI_2$ and the selectivity to toluene increases in the order $ZnBr_2 > ZnCl_2 > ZnI_2$. The reaction of 1BN produces naphthalene, diphenyl methane, and toluene. The effects of hydrogen partial pressure and catalyst composition on the reactions of this compound are similar to those for 4HDM.

The reaction products obtained from 4HDM and 1BN and the kinetics by which these reactants are converted to products (2) can be explained on the basis of the following mechanism:

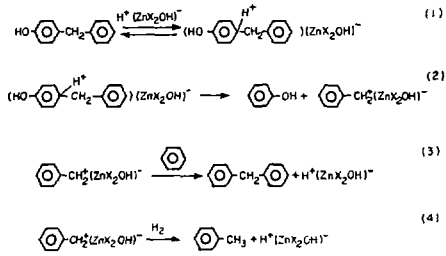

Studies in which the ratio of H_2O to ZnX_2 were varied clearly demonstrate that the active form of the catalyst is a Brönsted acid, $H^+(ZnX_2OH)^-$ Cleavage of the alkyl linkage is initiated by

Table 2. Effects of H_2 pressure and catalyst composition on the reactions of 4HDM and 1BN.

Reactant	Catalyst	H_2 Press. (atm)[a]	Reactant Conversion (%)[b]	Product Yield[c] (%) Toluene	Diphenyl methane
4HDM	$ZnCl_2$	37	27.1	5.4	38.2
4HDM	$ZnCl_2$	71	27.9	10.5	30.0
4HDM	$ZnBr_2$	44	62.2	3.4	42.0
4HDM	ZnI_2	37	12.6	27.9	20.2
4HDM	ZnI_2	68	13.7	49.9	13.7
1BN	$ZnCl_2$	44	16.8	12.9	35.2
1BN	$ZnCl_2$	68	17.4	20.3	31.7
1BN	$ZnBr_2$	81	22.7	6.9	51.8
1BN	ZnI_2	51	13.4	37.3	26.7

Reaction conditions: T = 325°C; benzene = 80 cm^3; $4HDM/ZnX_2$ = 40 mole/mole; $1BN/ZnX_2$ = 1.0 mole/mole

[a]At reaction temperature.

[b]Following 2 hr of reaction.

[c]Based on moles of dibenzyl ether reacted.

protonation. Both the equilibrium constant associated with this step and the rate coefficient for the subsequent step are affected by catalyst composition. The nature of the final products is dictated by reactions (3) and (4) and the ratio of the rate coefficients associated with these reactions is also affected by catalyst composition.

7. EFFECTS OF LEWIS ACID CATALYSTS ON THE HYDROGENATION AND CRACKING OF AROMATIC AND HYDROAROMATIC STRUCTURES RELATED TO COAL†

S. S. Salim and A. T. Bell

The hydrogenation and cracking of fused-ring aromatic and hydroaromatic structures is one of the processes which occurs during the liquefaction of coal by Lewis acid catalysts. In an effort to understand the mechanisms by which these reactions proceed and the influence of organic structure on reactivity, we have investigated the hydrogenation and cracking of naphthalene, anthracene, and phenanthrene, as well as derivative compounds under the influence of $ZnCl_2$ and $AlCl_3$.

Comparison of the reactivities of naphthalene, 1-methylnaphthalene, and 1-naphthol indicate that nucleophilic substitution strongly influences the rates of hydrogenation and cracking. The presence of a hydroxyl group at the 1-position of naphthalene greatly increases the rate of hydrogenation of the substituted ring and, to a lesser degree, the neighboring ring. Substitution of a methyl group at the 1-position causes a somewhat smaller increase in the rate of hydrogenation of naphthalene; but, in this case, both rings are affected to nearly an equivalent extent. Cracking of the saturated ring in tetralin is also enhanced by substitution of either a methyl or a hydroxyl group on the unsaturated ring.

The hydrogenation of two-ring aromatic compounds and the trends in reactant reactivity can be explained on the basis of a carbonium ion mechanism. In this scheme the active catalyst is a Brönsted acid represented by $H^+(MX_nY)^-$ [M = Zn,Al; X = Cl; Y = OH,Cl]. Hydrogenation is proposed to occur via sequential protonation and hydride acceptance. The first of the steps involves the transfer of a proton from the active catalyst to the substrate, a process which is enhanced by the presence of a nucleophilic substituent on the aromatic portion of the reactant. The second step proceeds by transfer of a hydride ion from one of the products of Scholl condensation or from molecular hydrogen. The first of these two sources is predominant when $AlCl_3$ is used as the catalyst, and the second when $ZnCl_2$ is used. The cracking of hydroaromatic rings is initiated by either protonation or hydride abstraction and then progresses through a complex series of ionic reactions.

The hydrogenation of anthracene and phenanthrene proceed via a mechanism similar to that proposed for naphthalene. In this instance, hydrogenation occurs first at the 9-, 10-positions of the central ring and then proceeds to the outer rings. Cracking of the central ring of either 9-, 10-dihydroanthracene or 9-, 10-dihydrophenanthrene does not take place in the presence of either $ZnCl_2$ or $AlCl_3$. It was observed, though, that cracking of the central ring could be accomplished if the number of carbon atoms in this ring was either decreased or increased. Thus, fluorene was cracked in the presence of $AlCl_3$, and dihydrobibenzocycloheptene was cracked in the presence of both $ZnCl_2$ and $AlCl_3$.

* * *

†Brief version of LBL-11512 and LBL-11855.

RESEARCH PLANS FOR CALENDAR 1981

Iron nitride surfaces will be characterized and tested for the catalyzed hydrogenation of CO. The influence of additives such as chlorine and potassium on the catalytic activity of rhodium oxide will be explored. Rhodium compounds containing various oxidation states of the metal will be investigated for their ability to catalyze the $CO-H_2$ reaction.

The influence of metal-support interactions and metal dispersion on the synthesis of oxygenated products will be investigated using palladium and rhodium catalysts. In-situ infrared spectroscopy and XPS will be used to identify the effects of metal-support interactions on the oxidation state of the metal and its ability to chemisorb CO.

Transient response experiments will be carried out to differentiate the relative rates of CO adsorption/desorption, dissociation/association, and reaction with H_2 on ruthenium and other Group VIII metals. These studies will be complemented by the use of reactive scavenging techniques to identify reaction intermediates.

The effects of reactant structure on the reactivity of aliphatic bridges between aromatic nuclei will be investigated using zinc halide catalysts. The effects of water, alcohols, and other promoters on the catalytic properties of zinc halides will be examined.

1980 PUBLICATIONS AND REPORTS

Refereed Journals

1. L. H. Dubois and G. A. Somorjai, "The Chemisorption of CO and CO_2 on Rh(111) Studied by High Resolution Electron Energy Loss Spectroscopy," Surface Sci. 91, 514 (1980).

2. J. G. Ekerdt and A. T. Bell, "Evidence for Intermediates Involved in Fischer-Tropsch Synthesis Over Ru," J. Catal. 62, 19 (1980).

3. D. P. Mobley and A. T. Bell, "Hydrogenolysis of Dibenzyl Ether Using Zinc Chloride - Metal Catalyst Systems," J. Catal. 64, 494 (1980).

†4. V. L. Kuznetsov, A. T. Bell, and Yu. I. Yermakov, "An Infrared Study of Alumina- and Silica-Supported Ruthenium Cluster Carbonyls," J. Catal. 65, 374 (1980).

5. N. D. Taylor and A. T. Bell, "Effects of Lewis Acids Catalysts on the Cleavage of Aliphatic and Aryl-Aryl Linkages in Coal-Related Structures," Fuel 59, 499 (1980).

6. D. P. Mobley and A. T. Bell, "Effects of Zinc Chloride on Sulfur Removal from Coal-Related Structures," Fuel 59, 507 (1980).

7. A. T. Bell, "Applications of Fourier-Transform Infrared Spectroscopy to Studies of Adsorbed Species," in Vibrational Spectroscopies for Adsorbed Species, edited by A. T. Bell and M. L. Hair, ACS Symposium Series Vol. 137, American Chemical Society, Washington, D. C. (1980).

LBL Reports

1. D. G. Castner and G. A. Somorjai, "LEED, AES, and Thermal Desorption Studies of the Oxidation of the Rh(111) Surface," LBL-9288.

2. D. G. Castner, R. L. Blackadar, and G. A. Somorjai, "CO Hydrogenation Over Clean and Oxidized Rhodium Foil and Single Crystal Catalysts," LBL-10018.

3. L. H. Dubois, P. K. Hansma, and G. A. Somorjai, "The Application of High Resolution Electron Energy Loss Spectroscopy to the Study of Model Supported Metal Catalysts," LBL-10733.

4. D. G. Castner, L. H. Dubois, B. A. Sexton, and G. A. Somorjai, "Evidence for Dissociation on Rhodium Surfaces," LBL-11205.

5. G. A. Somorjai, "The Catalytic Hydrogenation of CO. The Formation of C_1 Hydrocarbons," LBL-11354.

6. C. S. Kellner and A. T. Bell, "Evidence for H_2/D_2 Isotope Effects on Fischer-Tropsch Synthesis Over Supported Ruthenium Catalysts," LBL-10786.

7. D. P. Mobley, "Zinc Chloride-Catalyzed Reactions of Oxygen and Sulfur-Containing Compounds Which Model Structures in Coal," Ph.D. Thesis, LBL-11026.

8. A. T. Bell, "Catalytic Synthesis of Hydrocarbons Over Group VIII Metals. A Discussion of the Reaction Mechanism," LBL-11339.

9. S. S. Salim, "Hydrogenation and Cracking of Coal Related Fused-Ring Structures Using $ZnCl_2$ and $AlCl_3$ Catalysts," Ph.D. thesis, LBL-11512.

†10. Yu. A. Ryndin, R. F. Hicks, and A. T. Bell, "Effects of Metal-Support Interactions on the Synthesis of Methanol Over Palladium," LBL-11603.

11. S. S. Salim, "Effects of Lewis Acid Catalysts on the Hydrogenation and Cracking of Two-Ring Aromatic and Hydroaromatic Structures Related to Coal," LBL-1185.

Invited Talks

1. G. A. Somorjai, "High Resolution Electron Loss Spectroscopy and LEED Studies of CO, H_2 and Organic Adsorbates on Pt and Rh Surfaces," Oblad Symposium, Salt Lake City, Utah, October 3, 1979.

2. G. A. Somorjai, "Catalytic Hydrogenation of CO," U. C. Berkeley, Physical Chemistry Seminar, October 9, 1979.

3. G. A. Somorjai, "The Catalyzed Hydrogenation of CO on Transition Metal Surfaces," Université Louis Pasteur, Strasbourg, France, July 3, 1980.

4. G. A. Somorjai, "The Catalyzed Hydrogenation of CO on Transition Metal Surfaces," ETH, Zurich, Switzerland, May 12, 1980.

5. A. T. Bell, "Chemical Changes Produced in Coal Through the Action of Lewis Acid Catalysts," Mobil Research & Development Corp., Central Research Div., Princeton, NJ, December 1979.

6. A. T. Bell, "Chemical Changes Produced in Coal Through the Action of Lewis Acid Catalysts," Philadelphia Catalysis Club, Philadelphia, PA, December 1979.

7. A. T. Bell, "The Effects of Potassium Promotion on the Characteristics of Iron Fischer-Tropsch Catalysts," 179th National ACS Meeting, Houston, Texas, March 1980.

8. A. T. Bell, "Fischer-Tropsch Synthesis Over Alumina-Supported Ru Clusters," 179th National ACS Meeting, Houston, Texas, March 1980.

9. A. T. Bell, "H_2/D_2 Isotope Effects Observed During the Fischer-Tropsch Synthesis Over Ruthenium Catalysts," The California Catalysis Society, Berkeley, CA, March 1980.

10. A. T. Bell, "Studies of Catalytic Reactions Using Transient Response Techniques," Materials and Molecular Research Division, Lawrence Berkeley Laboratory, May 1980.

11. A. T. Bell, "Studies of Catalytic Reactions Using Transient Response Techniques," Materials and Molecular Research Division, Lawrence Berkeley Laboratory, May 1980.

12. A. T. Bell, "Investigations of the Mechanism of Fischer-Tropsch Synthesis Over Ruthenium Catalysts," Chiyoda Chemical Co., Yokohama, Japan, June 1980.

13. A. T. Bell, "Applications of Catalysis to the Production of Liquid Fuels from Coal," Department of Chemistry, Ibaraki University, Mito, Japan, June 1980.

14. A. T. Bell, "Recent Investigations of Fischer-Tropsch Synthesis Over Ruthenium,"

Post-Congress Symposium: Catalysis - From Fundamentals to Design, Nagoysa, Japan, July 1980.

15. A. T. Bell, "Fischer-Tropsch Synthesis of Hydrocarbons Over Group VIII Metals," First Berkeley Catalysis and Surface Science Conference, Lawrence Berkeley Laboratory, Berkeley, CA, July 1980.

16. A. T. Bell, "Chemical Interactions of Ru Clusters with γ-Al_2O_3," Solid State Science Division, Argonne National Laboratory, Argonne, IL, July 1980.

17. A. T. Bell, "The Mechanism and Kinetics of Fischer-Tropsch Synthesis Over Ruthenium Catalysts," Solid State Science Division, Argonne National Laboratory, Argonne, IL, July 1980.

18. A. T. Bell, "Effects of Metal-Support Interactions on the Synthesis of Methanol Over Palladium," The California Catalysis Society, Irvine, CA, October 1980.

19. A. T. Bell, "Transient Response Studies of Carbon Monoxide Hydrogenation Over Ruthenium," The California Catalysis Society, Irvine, CA, October 1980.

* * *

†Supported in part by the National Science Foundation.

c. Organometallic Chemistry of Coal Conversion*

K. Peter Vollhardt, Investigator

1. BISCARBYNE COBALT CLUSTERS AS HOMOGENEOUS ANALOGS OF FISCHER-TROPSCH INTERMEDIATES ON SURFACES

Neil T. Allison and K. Peter C. Vollhardt

Alkynes may be cleaved by $CpCo(CO)_2$ to give biscarbyne trinuclear cobalt clusters (see MMRD Annual Report 1979). It has now been found that alkynes can be regenerated intact by their gas phase thermolysis (e.g., 1→2). Since this carbon-carbon bond forming step might mechanistically mimick Fischer-Tropsch carbon chain

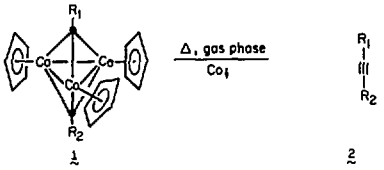

1 2

build-up on surfaces the mechanism of its (presumed microscopic) reverse, the synthesis of the clusters, was investigated by isolation of possible intermediates from reaction mixtures generated under a variety of conditions. Particularly interesting is the reaction of trimethylsilylacetylene with $CpCo(CO)_2$ in which, in addition to 1 (R_1 = Me_3Si; R_2 = H), three other trinuclear cobalt clusters could be isolated. Structures 3-5 have been assigned based on spectroscopic characteristics. On heating, 3 and 4 appear to equilibrate, but eventually decarbonylate to give 1. Compound 5 is a proto-

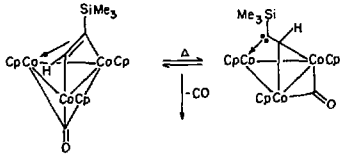

3 4

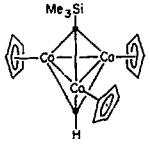

1

desilylated analog of 3 and an x-ray structural analysis is in progress. A fourth complex isolated appears to have structure 6 and formally constitutes a good model for a surface bound C_2H_2-fragment.

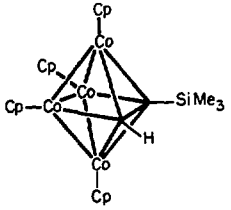

2. SYNTHESIS AND REACTIVITY OF HOMOGENEOUS ANALOGS OF POLYSTYRENE-BOUND CYCLOPENTADIENYL COBALT DICARBONYL†

Linda S. Benner and K. Peter C. Vollhardt

In an effort to identify the structural features responsible for the catalytic Fischer-Tropsch activity of polystyrene supported $CpCo(CO)_2$ (MMRD Annual Report 1979), several soluble analogs were designed and synthesized according to Scheme I. Since substitution of the Cp-ligand in $CpCo(CO)_2$ by the polystyrene chain appeared to be the origin of the special stability to the CpCo-moiety in the presence of hydrogen, it was reasoned that similar substitution by phenyl group carrying alkyl chains might have the same effect. Should these models undergo oxidative addition to benzylic or phenylic C-H bonds, this might be readily ascertainable by structural of H-D exchange studies.

The phenyl substituted alkyl halides are available by literature procedures. Complexation to cobalt occurred most efficiently in the presence of a slight excess of $Co_2(CO)_8$ and cyclohexene. The latter

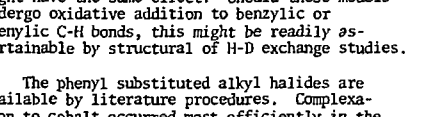

+ 1,3-$R_2CpCo(CO)_2$.
~ 20%

R = $C_6H_5(CH_2)_m$ or R = $C_6H_5CHCH_3(CH_2)_n$

m = 3-5 n = 2,4

Scheme I

*This work was supported by the Director, Office of Energy Research, Office of Basic Energy Sciences, Chemical Sciences Division of the U. S. Department of Energy under Contract No. W-7405-ENG-48.

alkene evidently serves to quench any intermediate $HCo(CO)_4$, protecting the valuable cyclopentadiene ligand from reduction. Both mono- and bisalkylated cyclopentadienyl complexes were isolated in an approximate ratio of 6:1 by column chromatography as red-brown oils. Both sets of compounds proved to be considerably more air and thermally sensitive than the parent system. Whereas irradiation in sealed tubes did not result in any observable change, simple heating produced insoluble clusters. In an effort to suppress bimolecular reactions two of the complexes [R = $C_6H_5(CH_2)_3$, $C_6H_5CHCH_3(CH_2)_2$] were subjected to flash vacuum pyrolysis at low contact times (300-450°C, 2×10^{-4} torr). The resulting product mixtures contained starting material, free protonated ligand RCpH, and cobaltocenes $(RCp)_2Co$. The pyrolysis tube was covered by a cobalt mirror. Several of the model compounds were then exposed to Fischer-Tropsch conditions. No activity was found until decomposition set in, producing traces of methane. Pressurization with CO/D_2, however, furnished some deuterated RCpH and recovered deuterated complex. Extensive deuteration of the latter was achieved under conditions which left the structure of the complex relatively intact (200°C, 4d, D_2/CO = 10/1, 130 psig). In the case of $RCpCo(CO)_2$ [R = $(CH_2)_4CH(CH_3)C_6H_5$], the incorporation of up to 10 deuterium atoms could be ascertained by mass spectrometry. Surprisingly, as indicated by the fragmentation pattern, very little (if any) of the deuterium label is found on the aromatic ring. The proton NMR spectrum reveals that most of the H-D exchange has occurred on the Cp ligand, its ordinarily complex AA'BB' pattern having been simplified to two broad singlet absorptions of relative combined intensity of 0.5. The aryl (5H) and aliphatic (12H) regions appear unchanged. That deuterium uptake is preferred on the RCp ligand is also suggested by the relative intensity of the $RCp\text{-}d_4Co(CO)_2$ molecular ion peak, which is the signal of maximum height in the peak envelope of deuterated parent ion. It is possible that H-D exchange occurs through a cobalt hydride intermediate in an intramolecular manner. Further exchange along the alkyl chain might occur via insertion of cobalt into ligand C-H bonds. The instability of the model compounds again highlights the special stability associated with the polymer supported system. Perhaps choice of differently substituted homogeneous analogs will provide a structure endowed with the catalytic capabilities of the resin-bound system. This is the subject of continuing work.

* * *

†Brief version of LBL-11710.

RESEARCH PLANS FOR CALENDAR YEAR 1981

The ligand mobility of trinuclear biscarbyne clusters will be explored, with particular emphasis on carbon-carbon bond breaking and bond forming processes.

Activation of biscarbyne clusters by electron transfer reactions will be attempted in order to observe potential catalytic activity.

Ongoing work will be continued and aimed at removing sulfur from coal and coal derived liquids and from model compounds.

New homogeneous model systems based on the phenylcyclopentadienyl unit as a ligand will be constructed in an attempt to mimick the structural environment of polymer supported $CpCo(CO)_2$, a Fischer-Tropsch catalyst.

1980 PUBLICATIONS AND REPORTS

Refereed Journals

†‡1. K. P. C. Vollhardt, "The Cobalt Way to Estrone," Ann. N. Y. Acad. Sci. 333, 241 (1980).

†2. A. J. Barkovich, E. S. Strauss, and K. P. C. Vollhardt, "Unusual Rearrangements in the $C_{12}H_{12}$-Manifold: 1,5,9-Cyclododecatriyne, 1,2:3,4:5,6-Tricyclobutabenzene, Hexaradialene," Isr. J. Chem. 20, 225 (1980).

†‡3. R. L. Funk and K. P. C. Vollhardt, "Thermal, Photochemical, and Transition Metal Mediated Routes to Steroids by Intramolecular Diels-Alder Reaction of o-Xylylenes," Chem. Soc. Rev. 9, 41 (1980).

†‡4. K. P. C. Vollhardt, "Physical, Chemical, and Some Biological Properties of Strained Ring Hydrocarbons," Pure Appl. Chem. 52, 1645 (1980).

‡5. R. L. Funk and K. P. C. Vollhardt, "2-Methyl-2-cyclopenten-1-one From 2-Methylcyclopenta-1,3-dione," Synthesis 118 (1980).

‡6. R. H. Hillard III and K. P. C. Vollhardt, "Potential Routes to Cyclobuta[1,2-c] cyclopropabenzene," Tetrahedron 36, 2435 (1980).

7. J. R. Fritch and K. P. C. Vollhardt, "Bis carbyne Clusters by Alkyne Cleavage: a General Reaction," Angew. Chem., 92, 570 (1980); Angew. Chem., Int. Ed. Engl. 19, 559 (1980).

†‡8. R. L. Funk and K. P. C. Vollhardt, "Cooligomerizations of 3-Substituted 1,5-Hexadiynes With Bis(trimethylsilyl)acetylene Catalyzed by Cobalt. A General Synthesis of Tricyclic Ring Systems From Acyclic Precursors," J. Am. Chem. Soc. 102, 5245 (1980).

†‡9. R. L. Funk and K. P. C. Vollhardt, "Transition Metal Catalyzed Alkyne Cyclizations. A Cobalt Mediated Total Synthesis of d,l-Estrone," J. Am. Chem. Soc. 102, 5253 (1980).

‡10. E. R. F. Gesing, J. A. Sinclair, and K. P. C. Vollhardt, "1,3-Bis(trimethylsilyl)

propyne and Alkyltrimethylsilylalkynes As Efficient Co-oligomerisation Partners in Cobalt Catalysed Alkyne Cyclisations," J. Chem. Soc., Chem. Commun. 286 (1980).

††11. E. D. Sternberg and K. P. C. Vollhardt, "Cobalt Mediated Cyclizations of Linear Achiral Diyneenes. A One Step Construction of Complexed Chiral Polycycles," J. Am. Chem. Soc. 102, 4839 (1980).

Other Publications

1. J. M. Huggins, J. A. King, Jr., K. P. C. Vollhardt, and M. J. Winter, "Preparative Separation of Organometallic Diastereomers, Structural Isomers, and Homologs on Ultrasphere ODS," Altex Chromatogram, 3(4), 2 (1980).

LBL Reports

1. J. M. Huggins, J. A. King, Jr., K. P. C. Vollhardt, and M. J. Winter, "Separation of Diastereomers, Structural Isomers, and Homologs of η^5-Cyclopentadienyl Cobalt and Dinuclear Molybdenum Complexes by Reverse Phase High Performance Liquid Chromatography Using Deoxygenated Solvents," LBL-11801.

2. L. S. Benner, P. Perkins, and K. P. C. Vollhardt, "Hydrocarbon Formation on Polymer-Supported η^5-Cyclopentadienyl Cobalt," LBL-11710.

Invited Talks

1. K. P. C. Vollhardt, "Transition Metal Mediated Carbon-Carbon Bond Forming and Bond Breaking Reactions," Searle Research and Development, Chicago, Illinois, February 1980.

2. K. P. C. Vollhardt, "Cobalt Mediated Carbon-Carbon Bond Formation," 3M Company, St. Paul, Minnesota, February 1980.

3. K. P. C. Vollhardt, "Reactions Catalyzed by Polystyrene Bound η^5-$CpCo(CO)_2$," Plenary Lecture, 179th ACS National Meeting, Symposium on Heterophase Attached Homogeneous Catalysis, Houston, Texas, March 1980.

4. K. P. C. Vollhardt, "Cobalt Mediated Carbon-Carbon Bond Forming and Bond Breaking Reactions," Dow Chemical Corporation, Midland, Michigan, April 1980.

5. K. P. C. Vollhardt, "Cobalt Mediated Carbon-Carbon and Carbon-Heteroatom Bond Formation," American Cyanamide Company, Lederle Labs, Pearl River, New York, May 1980.

6. K. P. C. Vollhardt, "Cobalt Mediated Carbon-Carbon Bond Forming and Bond Breaking Reactions," IBM, Yorktown Heights, New York, May 1980.

7. K. P. C. Vollhardt, "Cobalt Catalyzed Carbon-Carbon Bond Formations En Route to Natural Products," University of Santiago de Compostela, Spain, May 1980.

8. K. P. C. Vollhardt, "Remarkable Transformations in the Coordination Sphere of Cobalt," Consejo Superior de Investigaciones Cientificas, Madrid, Spain, May 1980.

9. K. P. C. Vollhardt, "The Cobalt Way to Natural Products," University of Madrid, Spain, May 1980.

10. K. P. C. Vollhardt, "Transition Metal Catalyzed Routes to Natural Products," University of Barcelona, Spain, May 1980.

11. K. P. C. Vollhardt, "Transition Metal Catalyzed Carbon-Carbon Bond Formations," Plenary Lecture, Third IUPAC Symposium on Organic Synthesis, Madison, Wisconsin, June 1980.

12. K. P. C. Vollhardt, "The Cobalt Way to Estrone," Tennessee Eastman Kodak, Kingsport, Tennessee, June 1980.

13. K. P. C. Vollhardt, "Cobalt Mediated [2+2+2] Cycloadditions: A Better Version of the Diels-Alder Reaction?", Plenary Lecture, Symposium on Catalytic Reactions in Chemical Synthesis, Massachusetts Institute of Technology, Boston, Massachusetts, June 1980.

14. K. P. C. Vollhardt, "Hydrocarbon Formation on Polymer Supported Cobalt," Plenary Lecture, Symposium on Catalytic Activation of Carbon Monoxide, 2nd Chemical Conference of North America, Las Vegas, Nevada, August 1980.

15. K. P. C. Vollhardt, "Transition Metal Mediated Carbon-Carbon Bond Formation," Plenary Lecture, 2nd International Symposium on Homogeneous Catalysis, Düsseldorf, West Germany, September 1980.

16. K. P. C. Vollhardt, "Remarkable Transformations in the Coordination Sphere of Cobalt," University of Lund, Lund, Sweden, September 1980.

17. K. P. C. Vollhardt, "Transition Metal Mediated [2+2+2]-Cycloadditions: A Better Version of the Diels-Alder Reaction?" University of Konstanz, Konstanz, West Germany, September 1980.

18. K. P. C. Vollhardt, "Transition Metal Mediated [2+2+2]-Cycloadditions: A Better Version of the Diels-Alder Reactions?" Georgia Institute of Technology, Atlanta, Georgia, October 1980.

19. K. P. C. Vollhardt, "Transition Metal Mediated [2+2+2]-Cycloadditions: A Better Version of the Diels-Alder Reaction?" Emory University, Atlanta, Georgia, October 1980.

20. K. P. C. Vollhardt, "Transition Metal Mediated [2+2+2]-Cycloadditions: A Better Version of the Diels-Alder Reaction?" Atlantic Richfield Company, Philadelphia, Pennsylvania, October 1980.

21. K. P. C. Vollhardt, "Transition Metal Mediated [2+2+2]-Cycloadditions: A Better Version of the Diels-Alder Reaction?" University of California, Santa Cruz, California, October 1980.

22. K. P. C. Vollhardt, "Transition Metal Catalyzed Approaches to the Total Synthesis of Natural Products," "Aspects of Cobalt Catalyzed Hydrocarbon Synthesis," 2 lectures, PPG Industries, Barberton, Ohio, November 1980.

23. K. P. C. Vollhardt, "Transition Metal Mediated [2+2+2] Cycloadditions in Organic Synthesis," Plenary Lecture, 16th Midwest Regional ACS Meeting, Symposium on Organometallic Chemistry, Lincoln, Nebraska, November 1980.

24. K. P. C. Vollhardt, "Excessively Unhappy Hydrocarbons," Ehime University, Matsuyama, Japan, November 1980.

25. K. P. C. Vollhardt, "Transition Metal Catalyzed Approaches to the Total Synthesis of Natural Products," Hiroshima University, Japan, November 1980.

26. K. P. C. Vollhardt, "Excessively Unhappy Hydrocarbons," Osaka University, Japan, November 1980.

27. K. P. C. Vollhardt, "Transition Metal Mediated Carbon-Carbon Bond Formation," Kyoto Institute of Technology, Japan, November 1980.

28. K. P. C. Vollhardt, "Transition Metal Catalyzed Approaches to the Total Synthesis of Natural Products," Kyoto University, Japan, November 1980.

29. K. P. C. Vollhardt, "Transition Metal Catalyzed Approaches to the Total Synthesis of Natural Products," Nagoya University, Japan, November 1980.

30. K. P. C. Vollhardt, "Cobalt Mediated Carbon-Carbon Bond Formation," Rikagaku Kenkyusho Saitama, Japan, November 1980.

31. K. P. C. Vollhardt, "Transition Metal Catalyzed Approaches to the Total Synthesis of Natural Products," University of Tokyo, Japan, November 1980.

32. K. P. C. Vollhardt, "Transition Metal Catalyzed Approaches to the Total Synthesis of Natural Products," Sagami Chemical Research Center, Sagamihara, Japan, November 1980.

33. K. P. C. Vollhardt, "Transition Metal Catalyzed Approaches to the Total Synthesis of Natural Products," Tohoku University, Sendai, Japan, December 1980.

34. K. P. C. Vollhardt, "Cobalt Mediated Carbon-Carbon Bond Formations," Tokyo Metropolitan University, Tokyo, Japan, December 1980.

35. K. P. C. Vollhardt, "Transition Metal Catalyzed Approaches to the Total Synthesis of Natural Products," Yokohama National University, Yokohama, Japan, December 1980.

* * *

†This work was supported in part by the National Science Foundation.

‡This work was supported in part by the National Institute of Health.

d. Synthetic and Physical Chemistry*

William L. Jolly, Investigator

1. ON CORRELATING PHOSPHORUS CORE BINDING ENERGIES, PHOSPHORUS LONE PAIR IONIZATION POTENTIALS, AND PROTON AFFINITIES OF TERVALENT PHOSPHORUS COMPOUNDS†‡

T. H. Lee, W. L. Jolly, A. A. Bakke, R. Weiss, and J. G. Verkade

For certain compounds of oxygen, nitrogen, and phosphorus with nonbonding "lone-pair" electrons on these atoms, the oxygen, nitrogen, and phosphorus core electron binding energies are linearly correlated with the corresponding proton affinities. Indeed, it has been claimed that core binding energy shifts can be used to predict proton affinities. However, there is evidence that such correlation only holds when considering compounds which are very closely related, such as those in a homologous series of compounds. On the other hand, correlations have been observed between "lone pair" ionization potentials and proton affinities which appear to be more general than those between core binding energies and proton affinities. In this paper, we discuss the factors that determine the magnitudes of core binding energies, ionization potentials, and proton affinities, emphasizing the differences between these three types of energy. For illustrative purposes we use data for tervalent phosphorus compounds. However, the principles discussed are applicable to all compounds containing lone-pair electrons.

To widen the variety of tervalent phosphorus compounds for which core binding energies are known, we have measured the phosphorus $2p_{3/2}$ binding energies of 13 phosphorus compounds. By combining these values with values previously measured in our laboratory and with a few other values from the literature, we obtained phosphorus binding energies for 22 compounds containing phosphorus atoms with valence-shell lone-pair electrons. These values were compared with literature values of the corresponding lone pair ionization potentials and proton affinities. No single correlation was found between all the core binding energies and the corresponding lone pair ionization potentials (Fig. 1) or proton affinities (Fig. 2), but the lone pair ionization potentials are linearly correlated with the proton affinities

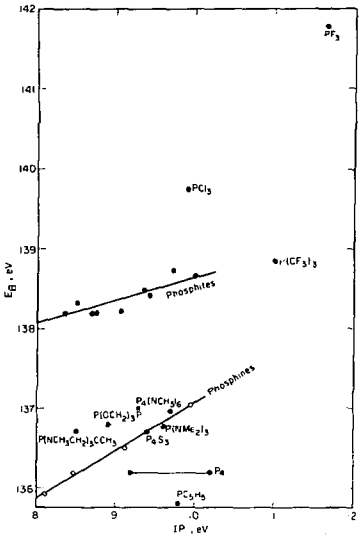

Fig. 1. Plot of phosphorus $2p_{3/2}$ binding energy vs. phosphorus lone pair ionization potential for tervalent phosphorus compounds. The open circles correspond to the phosphines, PH_3-$P(CH_3)_3$. (XBL 794-3398)

(Fig. 3). It is concluded that the electronic relaxations accompanying lone-pair ionization and proton attachment are similar in character and energy, whereas the electronic relaxation accompanying core ionization is of a somewhat different type, in which atomic orbital rehybridization plays a relatively unimportant role.

* * *

*This work was supported by the Director, Office of Energy Research, Office of Basic Energy Sciences, Chemical Sciences Division of the U. S. Department of Energy under Contract No. W-7405-ENG-48.

†Brief version of J. Am. Chem. Soc. 102, 2631 (1980).

‡This work was partially supported by the National Science Foundation.

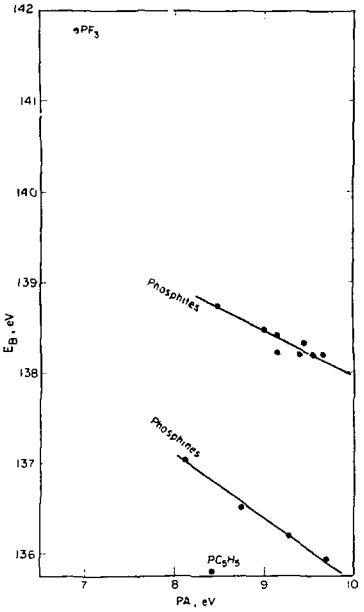

Fig. 2. Plot of phosphorus $2p_{3/2}$ binding energy vs proton affinity for tervalent phosphorus compounds. (XBL 794-3397)

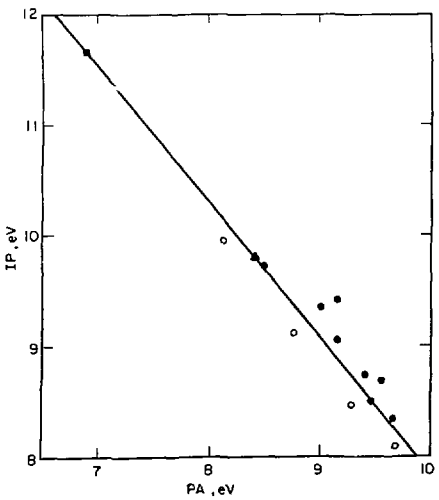

Fig. 3. Plot of phosphorus lone pair ionization potential vs proton affinity for tervalent phosphorus compounds. The solid points correspond to the phosphite esters, the open circles to the phosphines, the triangle to phosphabenzene, and the square to PF_3. (XBL 794-3396)

2. ELECTRONIC INTERACTION OF LIGANDS WITH CARBONYL GROUPS IN TRANSITION-METAL COMPLEXES OF THE TYPES $LMn(CO)_5$ and $LMo(CO)_5$†

S. C. Avanzino, H.-W. Chen, C. J. Donahue, and W. L. Jolly

In recent years much attention has been given to the electronic interaction of various ligands, L, with carbonyl groups in transition-metal complexes of the type $L_xM(CO)_y$. No general consensus has been reached regarding the nature of the interaction. Thus, the influence of the group L on the C-O stretching force constants has been variously explained: entirely in terms of the π-acceptor character of L, entirely in terms of the σ-donor character of L, and in terms of both the π-acceptor and σ-donor characters of L.

We have used x-ray photoelectron spectroscopy to study the problem because this technique yields information not readily obtained by any other method, that is, information about the charges of individual atoms in compounds. We restricted this study to volatile $LM(CO)_5$ compounds of manganese and molybdenum and determined gas-phase core binding energies of the metal, carbon, and oxygen atoms, as well as of the atoms in the ligands L.

The Mn $2p_{3/2}$, C 1s, and O 1s binding energies of $LMn(CO)_5$ compounds are linearly related to each other and to the inductive constant σ_I and the Pauling electronegativity x_P of the group L. The binding energies show little correlation with the mesomeric constant σ_R^o. Apparently only the σ-donor ability of L is important in determining the degree of back-bonding to the CO groups in $LMn(CO)_5$. The Mo $3d_{5/2}$, C 1s, and O 1s binding energies of $LMo(CO)_5$ compounds (L = PX_3 or CO) are linearly related to each other and to the phosphorus lone-pair ionization potential of the free PX_3. The data indicate that both the σ-donor and π-acceptor abilities of PX_3 are important in determining the degree of back-bonding to the CO groups in $X_3PMo(CO)_5$. The π-acceptor ability of PF_3 appears to be slightly greater than that of CO.

* * *

†Brief version of Inorg. Chem. 19, 2201 (1980).

3. A TABLE OF ABSOLUTE CORE-ELECTRON BINDING-ENERGIES FOR GASEOUS ATOMS AND MOLECULES†

A. A. Bakke, H.-W. Chen, and W. L. Jolly

During the last twelve years, gas-phase x-ray photoelectron spectroscopy has been carried out in at least ten different laboratories in North America and Europe. More than 1800 core binding

energies have been measured for about 800 different compounds. These data are of interest, not only to photoelectron spectroscopists, but also to many chemists and physicists who wish to correlate core binding energies with outer physical/chemical properties. Therefore, we have prepared a table that contains all the gas-phase core binding-energy data that we know of. The binding energies are grouped according to core level (C 1s, Mn $2p_{3/2}$, etc.), with the various groups arranged alphabetically according to elemental chemical symbol. Because of the length of this table, it is not reproduced in this article.

* * *

†Brief version of J. Electron Spectrosc. Rel. Phenom. 20, 333 (1980).

RESEARCH PLANS FOR CALENDAR YEAR 1981

We plan to study the bonding in organometallic clusters of the type $RCCo_3(CO)_9$, where R = H, Me, Me_3Si, MeO, Cl, and Br. The results will be of interest because the bonding in these molecules between the RC group and the metal atoms is similar to that involved in various metal surface-catalyzed organic reactions. In a similar vein, we shall continue our study of CH_2-bridged metal atoms and the allyl-metal bond, and we hope to study transition-metal olefin complexes.

Current XPS studies of the competitive back-bonding in the nitrosyls $CpM(NO)_2Cl$ (M = Cr, Mo, W) are giving us insight into the differences in π-donor ability between first-, second-, and third-row transition metals. Studies of compounds such as $W(CO)_5CS$, $Cr(CO)_5CS$, $C_6H_6Cr(CO)_2CS$, etc., indicate that the CS group is a stronger σ-donor and a stronger π-acceptor than the analogous CO group. Both of these studies are nearing completion.

We hope to use XPS in a study of the bonding and electronic structure of unstable molecules and radicals in the gas phase. We have devised a low-pressure flow system for studying such species and plan initially to look at some simple species such as S_2O, SiF_2, and perhaps atomic species.

1980 PUBLICATIONS AND REPORTS

Refereed Journals

†1. T. H. Lee, W. L. Jolly, A. A. Bakke, R. Weiss, and J. G. Verkade, "On Correlating Phosphorus Core Binding Energies, Phosphorus Lone Pair Ionization Potentials, and Proton Affinities of Tervalent Phosphorus Compounds," J. Am. Chem. Soc. 102, 2631 (1980), LBL-11936.

2. S. C. Avanzino, A. A. Bakke, H.-W. Chen, C. J. Donahue, W. L. Jolly, T. H. Lee, and A. J. Ricco, "Study of Charge Transfer in Back-Bonding to Carbonyl and Nitrosyl Groups," Inorg. Chem. 19, 1931 (1980), LBL-10121.

3. S. C. Avanzino, H.-W. Chen, C. J. Donahue, and W. L. Jolly, "Electronic Interaction of Ligands with Carbonyl Groups in Transition-Metal Complexes of the Types $LMn(CO)_5$ and $LMo(CO)_5$," Inorg. Chem. 19, 2201 (1980), LBL-11937.

4. A. A. Bakke, H.-W. Chen, and W. L. Jolly, "A Table of Absolute Core Electron Binding Energies for Gaseous Atoms and Compounds," J. Electron Spectrosc. Rel. Phenom. 20, 333 (1980), LBL-11938.

LBL Reports

1. Thomas Stafford Briggs, "Kinetic and Synthetic Studies on Boron-Nitrogen Hydrides," Ph.D. thesis, LBL-11494 (October 1980).

2. W. L. Jolly, "The Use of Core Electron Binding Energies as Bench Marks for the Comparison of Valence Shell Ionization Potentials," LBL-11396 (September, 1980).

3. H.-W. Chen, W. L. Jolly, S.-F. Xiang, I. S. Butler, and J. Sedman, "An X-Ray Photoelectron Spectroscopic Study of Transition Metal Thiocarbonyl and Thionitrosyl Complexes," LBL-11443 (September 1980).

4. H.-W. Chen, W. L. Jolly, S.-F. Xiang, and P. Legzdins, "An X-Ray Photoelectron Spectroscopic Study of Organometallic Nitrosyl Compounds of Chromium, Molybdenum and Tungsten," LBL-11444.

Invited Talks

1. W. L. Jolly, "The Study of Bonding in Organometallic Compounds," Chemistry Dept., McGill University, Montreal, Canada, May 27, 1980.

2. W. L. Jolly, "The Study of Bonding in Organometallic Compounds," Chemistry Dept., University of Western Ontario, London, Ontario, May 28, 1980.

3. W. L. Jolly, "The Study of Bonding in Organometallic Compounds," Chemistry Dept., McMaster University, Hamilton, Ontario, May 29, 1980.

4. W. L. Jolly, "Competitive Ligand-Metal Interactions as Studied by X-Ray Photoelectron Spectroscopy," Gordon Research Conference on Organometallic Chemistry, Andover, New Hampshire, August 11, 1980.

5. W. L. Jolly, "XPS Studies of the Bonding in Organometallic Compounds," Chemistry Dept., Stanford University, Stanford, California, November 25, 1980.

* * *

†Partly supported by the National Science Foundation

e. Chemistry and Morphology of Coal Liquefaction

Alexis T. Bell, Robert G. Bergman, James W. Evans, Heinz Heinemann, Alan V. Levy, Gabor A. Somorjai, and K. Peter Vollhardt, Investigators

See Fossil Energy section.

f. Electrochemical Systems*

John Newman, Investigator

1. MASS TRANSFER TO ROTATING DISKS AND ROTATING RINGS IN LAMINAR, TRANSITION, AND FULLY DEVELOPED TURBULENT FLOW+

Clarence G. Law, Peter Pierini, and John Newman

On rotating disks and rotating rings, the flow regime may vary from laminar near the center to fully developed turbulent near the periphery. The fundamentals of fluid flow and mass transfer are well characterized in laminar flow. However, transition flow, existing between laminar and fully developed turbulent flow, and the turbulent flow regime have not been described to the same extent. Correlations of experimental results form the basis of most of the available information concerning the mass transfer rates for these systems.

A complete understanding of mass transfer phenomena in turbulent flow is necessary to predict the rates of corrosion for systems in turbulent flow. Full knowledge of the mechanism of corrosion is the first step from which techniques can be developed to lead to corrosion prevention. Understanding the corrosion mechanism is therefore important whether electrochemical (anodic or cathodic protection) or materials improvements (alloys) are chosen to reduce corrosion rates.

To model accurately mass-transfer processes on a rotating disk (as in corrosion), reliable local mass-transfer rates are required. Average mass transfer rate data must be differentiated to obtain information on local mass transfer rates. Differentiation of data with considerable scatter may not give reliable information. Therefore, a model was developed from which local mass transfer rates can be calculated. These local rates can then be integrated for comparison with measured average mass transfer rates.

In the study of corrosion on a rotating disk, local mass-transfer rates are needed when the mass-transfer commences at an arbitrary radial position on the surface. This is analogous to rotating rings with different thicknesses. Data taken by Delouis and Keddam[1] on thick rings indicate that the Sherwood number is proportional to the Reynolds number raised to the 0.9 power, similar to disk correlations. However, for thin rings the data give rise to an exponent of 0.6. It was found that measured values of the limiting current for thin rings in transition and turbulent flow were below the Levich[2] relationship for thin rings.

The model developed here is based on the boundary layer form of the time-averaged convective diffusion equation. Due to the large Schmidt numbers which are encountered for most electrochemical systems, the velocity components may be adequately represented by the first term in a Taylor series expansion. Introduction of the Lighthill[3] variable allows the equation to be expressed in a form which, subject to further development, is amenable to analytical treatment.

The results of the model depend strongly on the values of the shear stress at a given Reynolds number. The Reynolds number dependence of the radial shear stress is shown in Fig. 1.

To provide data with which to compare predictions, limiting currents were measured on thin rotating ring electrodes. Rotation rates were varied to investigate the laminar, transitional, and as much of the turbulent region as possible. The electrochemical system used was the potassium ferricyanide-potassium ferrocyanide redox couple (approximately 0.005 molar) with an excess of potassium hydroxide (2 molar) supporting electrolyte.

Figure 2 shows the results for average mass-transfer rates on a rotating disk compared to data given by Mohr and Newman[4] and Daguenet.[5] Agreement between the two is obtained over a considerable range of Reynolds numbers. The line marked $f(R) = 0$ corresponds to no eddy diffusivity, while $f(R) = 1$ allows for the full eddy diffusivity contribution. Note that absence of the eddy diffusivity term, $f(R) = 0$, may result in an average flux below the corresponding laminar flow value.

The data from our experiments with rotating ring electrodes are given in Fig. 3. The current

*This work was supported by the Director, Office of Energy Research, Office of Basic Energy Sciences, Chemical Sciences Division of the U.S. Department of Energy under Contract No. W-7405-ENG-48.

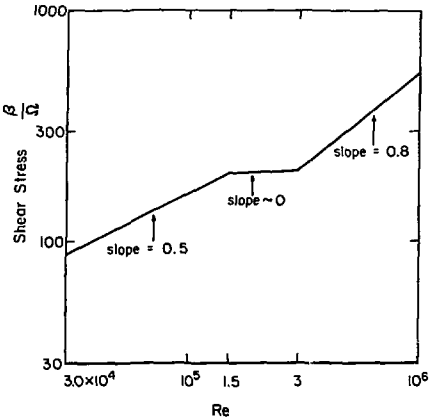

Fig. 1. The Reynolds number dependence of the radial shear stress. (XBL 805-9566A)

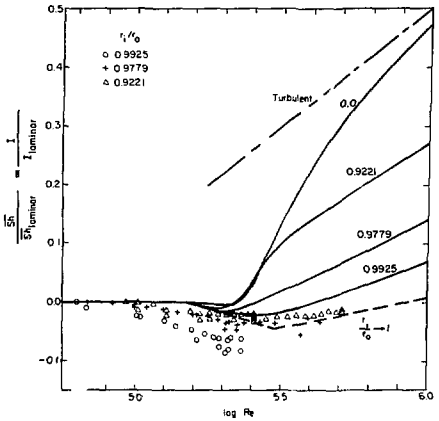

Fig. 3. The results of our mass-transfer experiments on rotating rings compared to calculations. (XBL 805-9569A)

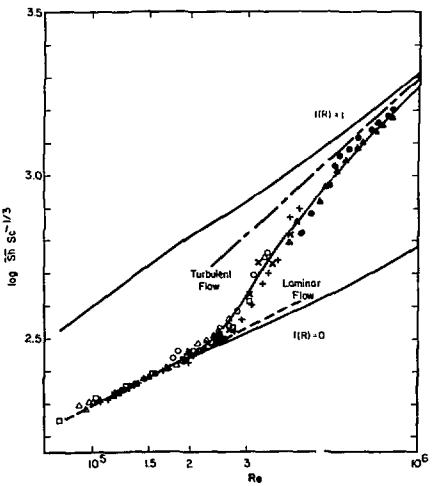

Fig. 2. Overall mass-transfer rate vs Reynolds number for laminar, transition, and turbulent regimes. The Schmidt number for the data of Mohr and Newman □ 1192, △ 1377, + 1636, ○1760, × 2465; for the data of Daguenet ● 1212, ▲ 1980. ——— calculated results. (XBL 805-9570A)

is made dimensionless with the current calculated as though laminar flow conditions existed. Agreement of the data with the calculations is adequate at low Reynolds numbers; however, at higher values the calculated results exceed the measurements.

From the data presented in Fig. 3 and from the lines representing thin rings, it is clear that mass-transfer in transition and turbulent flow can be less than that given by the laminar-flow expression. The results of the analysis show that the mass-transfer rate normalized with the laminar rate depends only upon the shear stress value.

Local mass-transfer rates representative of a number of different conditions are presented in Fig. 4. The curves show the local mass-transfer rates on rotating rings to be high at the beginning of the mass-transfer region and to approach the rotating disk results down-stream of the inner radius. This is true whether the diffusion boundary layer begins in laminar, transition, or fully developed turbulent flow.

The model compares well to rotating disk data and to data for relatively thick rotating rings. For the data given herein on thin rotating rings, the calculated results may exceed the measured mass-transfer rate in the transition and fully developed turbulent flow regimes. The contribution of the eddy diffusivity term to the overall mass-transfer is too high, even for these thin rings. A cubic form for the eddy diffusivity is used. However, no improvement in the comparison with the thin ring data was obtained for a combined cubic-fourth power form.

* * *

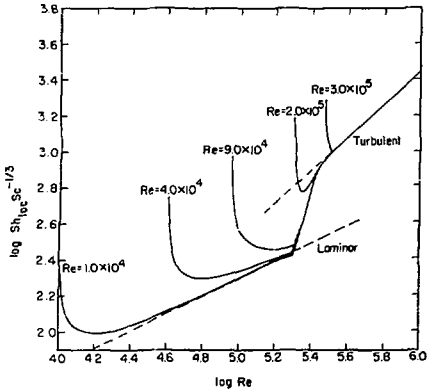

Fig. 4. Local mass-transfer rate for rotating rings of various dimensions. The Reynolds number designation on the respective curves denotes the point at which mass transfer begins. (XBL 805-9568A)

†Brief version of LBL-11241.

1. C. Delouis and M. Keddam, International Journal of Heat and Mass Transfer 16, 1763 (1973).
2. B. Levich, Physicochemical Hydrodynamics, section 18, Prentice-Hall, Inc., Englewood Cliffs, N.J. (1962).
3. M. J. Lighthill, Proceedings of the Royal Society A202, 359 (1950).
4. Charles M. Mohr, Jr. and John Newman, Journal of the Electrochemical Society 123, 1687 (1967).
5. M. Daguenet, International Journal of Heat and Mass Transfer 11, 1581 (1968).

2. THEORETICAL ANALYSIS OF LIQUID-JUNCTION PHOTOVOLTAIC CELLS†

Mark E. Orazem and John Newman

Liquid-junction photovoltaic cells utilize semiconductors as one or both electrodes to drive electrochemical reactions in the presence of light. These devices produce an electrical current while converting solar energy to chemical energy, which can be stored.

A one-dimensional model was developed for the liquid-junction photovoltaic cell with a thin-film semiconducting anode. The relationships governing the anode were Poisson's Equation and macroscopic material balances of the charge-carrying species. The effect of the semiconductor-electrolyte interface was modeled with a fixed surface charge concentration and set rates of production of electrons and holes.

A limiting current of -41.16 mA/cm^2 was predicted for a thin-film n-type GaAs anode under AM-2 solar illumination, and a limiting current of 0 mA/cm^2 was predicted for the anode in the dark. This prediction was based on a limiting concentration of holes. Incomplete utilization of incident radiation, due to reflection and scattering losses, and recombination of electrons and holes at the interface will decrease the magnitude of the limiting current.

An extension of this model is under development that includes adsorption, desorption, and charge transfer reactions at the semiconductor-electrolyte interface.

* * *

†Brief version of "Electrochemical Systems," presented by Mark E. Orazem at Kansas State University, December 22, 1980.

RESEARCH PLANS FOR 1981

Modeling of the liquid-junction photovoltaic cell will be extended to include adsorption, desorption and charge-transfer reactions of the semiconductor-electrolyte interface. A mathematical model of the iron/chromium flow redox battery will be developed. An experimental program will begin to study the electrochemical removal of mercury from brine and wastewater.

1980 PUBLICATIONS AND REPORTS

LBL Reports

1. Clarence G. Law, Jr., Peter Pierini, and John Newman, "Mass Transfer to Rotating Disks and Rotating Rings in Laminar, Transition and Fully Developed Turbulent Flow," LBL-11241 (July 1980).

2. Clarence G. Law, Jr., Richard Pollard, and John Newman, "Characteristics of the Dropping-Mercury Electrode Below Limiting Current," LBL-10079 (July 1980).

Invited Talks

1. D. Ullman and J. Newman, (presented by David Ullman), "A Possible Mechanism of Electron Exchange at the Semiconductor-Electrolyte Interface," Houston Meeting of the American Chemical Society, March 26, 1980.

2. D. Ullman, "Some Aspects of the Potential Distribution at the Semiconductor-Electrolyte Interface," Houston Meeting of the American Chemical Society, March 26, 1980.

3. M. E. Orazem, "Electrochemical Systems," Invited address before the Department of Chemical Engineering, Kansas State University, Manhattan, Kansas, December 22, 1980.

g. Metal-Cluster, Metal-Surface Analogy*

Earl L. Muetterties, Investigator

1. CHEMICAL AND STRUCTURAL FEATURES OF CHEMISORBED SPECIES ON METALLIC SURFACES

Cynthia Friend, Min-Chi Tsai, and Earl L. Muetterties

The geometric features that elicit carbon-hydrogen bond scission reactions have been incisively characterized from a chemisorption study of hydrocarbons and their derivatives on nickel and platinum surfaces, wherein the chemistry was defined as a function of surface crystallography and surface composition. Basically, these studies show that if the initial chemisorption state is so structured that hydrogen atoms bound to carbon can closely approach a metal surface atom, then carbon-hydrogen bond scission becomes a probable event even at relatively low temperatures. Such stereochemistry is more common to irregular surfaces and much less so to atomically flat surfaces like Ni(111), Ni(100), and Pt(111).

In establishing these features of surface-mediated carbon-hydrogen bond breaking reactions, the benzene and toluene systems have been most illuminating. On the atomically flat and clean nickel and platinum surfaces, benzene chemisorbs in a plane parallel to the crystal surface plane. No C-H bonds are cleaved below temperatures of ~100°C and 150°C for Ni(111) and Ni(100), respectively. In contrast, some C-H bonds are cleaved at 25°C on stepped and stepped-kinked nickel surfaces. No reversible C-H bond breaking for benzene was observed on any of the nickel surfaces--as established in studies with C_6H_6-C_6D_6 mixtures--under the conditions of the ultra high vacuum experiments. Platinum surfaces behaved in an analogous fashion but a stepped platinum surface, Pt 6(111)x(111), effected reversible C-H bond breaking as shown with C_6H_6-C_6D_6 and with C_6H_6-D_2 mixtures. In contrast, Pt(111) did not detectably effect reversible C-H bond breaking reactions.

Toluene was irreversibly chemisorbed on all the nickel surfaces. Attempted thermal desorption led to no detectable toluene desorption; only hydrogen was evolved from such surfaces. Studies of nickel surfaces with (111) or (100) terrace sections showed that the aliphatic carbon-hydrogen bonds are completely cleaved before any aromatic carbon-hydrogen atoms are cleaved, as established in thermal decomposition studies of the labelled toluene molecules, $C_6D_5CH_3$ and $C_6H_5CD_3$. On Ni(111), all aliphatic C-H bonds are cleaved below 150°C; and the aromatic C-H bonds are cleaved at ~185°C. These studies establish the surface crystallographic features that can provide a selective introduction of deuterium into the methyl group of toluene in the presence of D_2. Hydrogen-deuterium exchange is selective to the aliphatic sites in toluene for D_2-$C_6H_5CH_3$ mixtures with nickel films but is not selective with irregular nickel catalysts like Raney nickel. On the atomically flat surfaces, toluene is believed to be chemisorbed as the benzyl radical with the seven carbon atoms in a plane more or less parallel to the surface plane.

Much of the benzene surface studies have been informative because of the finding that an intact benzene molecule chemisorbed on nickel or platinum surfaces can be displaced by trimethylphosphine. This discovery has now been utilized to define the surface chemistry of cyclohexane, cyclohexene and cyclohexadiene. All three of these hydrocarbons have been shown to chemisorb on a stepped platinum surface with dehydrogenation to give chemisorbed benzene molecules and hydrogen atoms--trimethylphosphine displaced benzene molecules from these surface states. A similar behavior was established for the Ni(111) surface, except for cyclohexane which did not react with this nickel surface at 20-80°C.

Trimethylphosphine is very strongly chemisorbed on all the nickel surfaces. On the Ni(111) surface, thermal decomposition occurs readily, and CH_4 and H_2 are desorbed as decomposition products with desorption maxima at 90 and 98°C, respectively. Chemisorption of this phosphine initially must involve a donor-acceptor interaction centered at the phosphorus atom. Models show that the methyl hydrogen atoms can then closely approach the surface metal atoms. Cleavage of C-H bonds probably occurs at or near 25°C, and P-C-Ni bonds are then irreversibly formed. This surface chemistry qualitatively mirrors that of trimethylphosphine in the coordinately unsaturated complex $Fe[P(CH_3)_3]_4$, which is primarily $HFe[\eta^2\text{-}\underline{C}H_2\underline{P}(CH_3)_2][P(CH_3)_3]_3$ in the solution state.

On the Ni(100) and Pt(111) surface, pyridine is irreversibly chemisorbed; and three hydrogen thermal desorption maxima of relative intensities 1:2:2 were observed. These data suggest that pyridine initially chemisorbs in a plane normal to the surface by bonding through the nitrogen atom. This places the α - CH hydrogen atoms close to surface metal atoms and C-H bond cleavage should occur very readily (at 20°C or slightly higher temperatures) to form a pyridyl species. Ring tipping, so as to ultimately lie in a plane parallel to the surface, may then occur in two stages at high temperatures.

RESEARCH PLANS FOR CALENDAR YEAR 1981

The surface crystallographic and electronic features that affect the C-H bond breaking (and bond making) reactions in hydrocarbons and hydrocarbon reactions will be defined for nickel and

*This work was supported by the Director, Office of Energy Research, Office of Basic Energy Sciences, Chemical Sciences Division of the U. S. Department of Energy under Contract No. W-7405-ENG-48.

platinum surfaces: chemisorption of intact saturated hydrocarbons is believed to involve two electron multicenter C-H surface metal atom bonds. Characterization of these bonds will be attempted through studies of chemisorption heats and through vibrational studies of these surface states using a series of linear, cyclic, and branched-chain hydrocarbons. A study of ethylene and acetylene surface chemistry modeled on the benzene-toluene investigations will be completed to define the geometric and electronic surface factors that affect C-H bond breaking and bond making processes. In addition to these parent olefinic and acetylenic molecules, methyl derivatives such as propylene, the butene isomers, propyne, and the butyne isomers will be studied to assess the steric and electronic factors in this surface chemistry of unsaturated hydrocarbons.

1980 PUBLICATIONS AND REPORTS

Refereed Journals

†1. E. L. Muetterties, A. J. Sivak, R. K. Brown, J. W. Williams, M. F. Fredrich, and V. W. Day, "Metal Clusters 22. The Polynuclear Rhodium Hydride Set $\{HRhL_2\}$," in Fundamental Research in Homoge[illegible] Catalysis, Vol. 3, M. Tsutsui, ed., Plenum [illegible]ng Corp., p. 487.

‡2. E. L. Mu[illegible]es and Judith Stein, "Mechanistic Featu.es of Catalytic Carbon Monoxide Hydrogenation Reactions," Chem. Revs., p. 479 (1980).

‡3. Henry W. Choi, Robert M. Gavin, and Earl L. Muetterties, "Zerovalent Metal Phosphite Chemistry: Photochemistry of $W[P(OCH_3)_3]_6$," J. Chem. Soc., Chem. Comm., p. 1085 (1980).

‡4. Richard K. Brown, Jack M. Williams, Andrew J. Sivak, and Earl L. Muetterties, "Coordinately Unsaturated Metal Clusters. A Neutron Diffraction Study of the Crystal and Molecular Structure of the Trimeric Rhodium Complex $\{HRh[P(OCH_3)_3]_2\}_3$," Inorg. Chem. 19, 370 (1980).

5. E. L. Muetterties, "Stereochemistry in the Coordination Chemistry of Metal Surfaces," Israel J. Chem. 20, 84 (1980).

†6. M. Tachikawa and E. L. Muetterties, "Metal Clusters 25. A Uniquely Bonded C. H. Group and Reactivity of a Low-Coordinate Carbidic Carbon Atom," J. Am. Chem. Soc. 102, 4541 (1980).

‡7. M. Beno, J. M. Williams, M. Tachikawa, and E. L. Muetterties, Fischer-Tropsch Chemistry: Structure of a Seminal η^2-CH Cluster Derivative, J. Am. Chem. Soc. 102, 4524 (1980).

‡8. E. L. Muetterties, E. Band, A. Kokorin, W. R. Pretzer, and M. G. Thomas, "Metal Clusters 23. Tetranuclear Nickel Alkyl Isocyanide Clusters," Inorg. Chem. 19, 1552 (1980).

‡9. M. R. Thompson, C. S. Day, V. W. Day, R. I. Mink, and E. L. Muetterties, "Transition Metal Arene Chemistry 4," J. Am. Chem. Soc. 102, 2979 (1980).

‡10. S. S. Wreford, J. K. Kouba, J. F. Kirner, E. L. Muetterties, I. Tavanaiepour, and V. W. Day, "A Study of Structure and Dynamic Stereochemistry in Seven Coordination," J. Am. Chem. Soc. 102, 1558 (1980).

11. C. M. Friend, R. M. Gavin, E. L. Muetterties, and M.-C. Tsai, "Coordination Chemistry of Metal Surfaces 1," J. Am. Chem. Soc. 102, 1725 (1980).

†12. M. Tachikawa, A. C. Sievert, E. L. Muetterties, M. R. Thompson, C. S. Day, and V. W. Day, "Metal Clusters 24," J. Am. Chem. Soc. 102, 1725 (1980).

‡13. E. L. Muetterties, Coordination Chemistry of Metal Surfaces and Metal Complexes, Pure and Applied Chem. 52, 2061 (1980).

†14. E. Band, E. L. Muetterties, "The Olefin Metathesis Reaction--Characterization of An Active Metathesis Catalyst Precursor from the $WOCl_4$-$(CH_3)_2Mg$ Reaction," J. Am. Chem. Soc. 102, 6572 (1980).

‡15. M. Tachikawa, J. Stein, E. L. Muetterties, R. G. Teller, M. A. Beno, E. Gebert, and J. M. Williams, "Metal Clusters with Exposed and Low Coordinate Nitride Nitrogen Atoms," J. Am. Chem. Soc. 102, 6648 (1980).

---

†Supported by the National Science Foundation.

‡Partially supported by the National Science Foundation.

h. High-Energy Oxidizers and Delocalized-Electron Solids*

Neil Bartlett, Investigator

Introduction. The projects described below all deal with aspects of novel synthetic metals made by oxidizing graphite. The first project sprang from the persistent reluctance of some[1,2] to accept the earlier conclusion[3] from these laboratories that intercalation of graphite by arsenic pentafluoride is accompanied by oxidation of the graphite according to the equation:

$$2e^-(\text{from graphite}) + 3AsF_5 \rightarrow 2AsF_6^- + AsF_3. \quad (1)$$

Further impetus came from the observation that the conductivity of graphite that had been intercalated fully with AsF_6^- alone was almost an order of magnitude less than that intercaled fully by AsF_5.

The second project bears on the nature and stability of the fluoro-germanium species that are present in the graphite salts $C_{12}GeF_5$ and $C_{12}GeF_6$. Earlier studies[4] in these laboratories had indicated that these materials are in equilibrium with elemental fluorine at ordinary temperatures and pressures, according to the equation:

$$C_{12}GeF_5 + 1/2\ F_{2(g)} \rightleftharpoons C_{12}GeF_6. \quad (2)$$

The prime aim has been to find fluorogermanate salts that might serve as fluoride ion conductors; but, as aspects of that broad study, the nature of the bonding in "GeF_5^{-1}" salts has been explored and some thermodynamic measurements have been made with the intent of assessing the first and second fluoride-ion affinities of the GeF_4 molecule.

The third project reports on the relationship of C_xSO_3F to its protonated relative $C_x(SO_3F)_y(HSO_3F)_{1-y}$. These materials are each metallic and their interconversion merely involves transfer of electrons and protons.

Perhaps the most exciting project (Work in Progress) is still incomplete. It deals with the observation that the intercalation of graphite, by arsenic pentafluoride in the presence of fluorine, consumes half a mole of fluorine more than that required to prepare merely AsF_6^-.

* * *

1. L. Ebert, H. Selig, Mat. Sci. Eng. 31, 177 (1977).
2. M. J. Moran, J. E. Fischer, and W. R. Salaneck, J. Chem. Phys. 73 (2), 629 (1980).
3. N. Bartlett et al., J. Chem. Soc., Chem. Commun. 200, 1978; N. Bartlett, B. W. McQuillan, and A. S. Robertson, Mat. Res. Bull. 13, 1259 (1978).
4. E. M. McCarron, Y. Jean Grannec, and N. Bartlett, J. Chem. Soc., Chem. Commun. 1980, in press.

*This work was supported by the Director, Office of Energy Research, Office of Basic Energy Sciences, Chemical Sciences Division of the U. S. Department of Energy under Contract No. W-7405-ENG-48.

1. THE ELECTRICAL CONDUCTANCE OF GRAPHITE-AsF_5 INTERCALATION COMPOUNDS AND THEIR RELATIONSHIP TO OTHER GRAPHITE-MF_6 SALT CONDUCTANCES

T. E. Thompson, E. M. McCarron, and Neil Bartlett

Recently McCarron and Bartlett[1] have shown that salts containing AsF_6^- as the sole intercalant have a staging formula $C_{12n}AsF_6$ for all stages, n, except the first. The first stage ranges in composition from $C_{12}AsF_6$ to C_8AsF_6. They have also established that the addition of AsF_3 converts the $C_{12n}{}^+AsF_6^-$ salts to materials that appear to be identical to the intercalation compounds made directly from graphite and arsenic pentafluoride and which obey a staging formula $C_{8n}AsF_5$. All of their observations are in accord with AsF_5 intercalating graphite as represented in Eq. (1) of the Introduction. As the oxidation of the graphite proceeds, the increase in positive charge in the graphite layers will tend to make the conversion of AsF_5 into AsF_6^- and AsF_3 less complete. Therefore, first stage "C_8AsF_5" must contain more unconverted AsF_5 than second stage, $C_{16}AsF_5$, and so on. Even in the second stage, however, the conversion of AsF_5 to AsF_6^- and AsF_3 appears to be nearly total.

In this study, the emphasis has been placed on conductivity/composition correlations. Pieces of highly oriented pyrolytic graphite (HOPG) typically 5 × 5 mm^2, with a pristine thickness of 0.5 mm, have been used for the conductance measurements. Compositions have been followed gravimetrically, and changes in stage have been monitored by x-ray diffraction and by micrometry. In all cases, the preparations involving the pieces of HOPG were paralleled by more massive powder samples to check on the validity of the less precise HOPG gravimetries.

The graphite/AsF_5 samples were made directly from graphite and AsF_5 (clean by IR spectroscopy). Graphite $^+AsF_6^-$ salts were prepared either by treating graphite with $O_2{}^+AsF_6^-$:

$$O_2{}^+AsF_6^- + xC \rightarrow C_xAsF_6 + O_2$$

or by controlled fluorination of the graphite AsF_5 compound:

$$C_xAsF_5 + 1/2\ F_2 \rightarrow C_xAsF_6.$$

Room temperature, basal-plane conductivity measurements were made in situ, as AsF_5 intercalation of the HOPG pieces proceeded, using a commercial contactless-conductivity apparatus.[2] Table 1 gives the gravimetric composition, thickness ratios, oscillator voltage ratio, and the ratio of conductivity of the intercalated graphite compound, C_xAsF_5, to that of the starting graphite. The findings indicate (Fig. 1) that the earlier report, by others, of a conductivity closer to that of copper, is in error.

From the data in Table 2 for AsF_6^- salt prepared from $O_2^+AsF_6^-$, the sample of composition $C_{14.6}AsF_6$, which was nearly a first-stage material (homogeneous $C_{12}AsF_6$ is the first stage), is seen to be an inferior conductor, compared to AsF_5 materials of comparable composition. Table 2, for the AsF_6^- salts made by fluorinating AsF_5 compounds, also shows that the first-stage salts ($C_{12}AsF_6$ through to C_8AsF_6) must be poor conductors in comparison with AsF_5 compounds of comparable composition. This is not so for the second and higher stages.

The removal of volatiles from $C_{8n}AsF_5$ ($n \geq 2$) (Table 3) results largely in the removal of AsF_3, and neither the thickness (which correlates with stage) nor the conductivity, changes significantly. Similarly, the introduction of AsF_3 to $C_{12n}AsF_6$ to form $C_{8n}AsF_5$ does not produce significant changes in thickness or conductivity. These last observations are in accord with the description of $C_{8n}AsF_5$ ($n \geq 2$) as $C_{12n}(AsF_6^-)_{2/3}(AsF_3)_{1/3}$. Indeed, it is appropriate to view the galleries of the $n \geq 2$ stages as the same as in the $C_{12n}AsF_6$ salts but with the vacant sites of those galleries now occupied by AsF_3 molecules. Since the number of vacancies in a gallery of $C_{12n}AsF_6$ is equal to half the number of anions, it is tempting to assume that the anions are packed as indicated in Fig. 2. This arrangement means that each anion has only three nearest neighbors in contrast to six in a close packed array, such as occurs in C_8AsF_6.

The important difference between the conductivities of the $C_{8n}AsF_5$ compounds and their $C_{12n}^+AsF_6^-$ salt relatives is in the first-stage behavior. Unfortunately, there is no reliable structural information available for $C_{12}AsF_6$ or C_8AsF_5. Earlier work in these laboratories has indicated,[3] however, that the first stage AsF_6^- salts appear to undergo a structural change. In that change, the graphite layers may lose their high symmetry. Certainly, the first stage C_xAsF_6 salts, made from graphite single crystals diffract well and show hexagonal symmetry, when freshly prepared and held at low temperature. This is lost within a few hours at room temperature. Similar effects have been noted[3] for C_8OsF_6 and C_8IrF_6. In contrast, crystals of C_8AsF_5 diffract well over many weeks at room temperature. Therefore, it seems likely that the chaotic mix of AsF_6^-, AsF_3, and even some AsF_5 in the C_8AsF_5 may contribute to the preservation of the hexagonal symmetry of the graphite layers.

Table 1. Composition, thickness, oscillator voltage, conductivity of the HOPG-AsF_5 compounds C_xAsF_5.

Sample	Gravimetric composition,[a] x	t/t_0[b,c]	V/V_0[a]	σ/σ_G[e]
1	16	1.71	20.8	12.2
	7.9	2.45	29.6	12.1
2	16	1.72	20.0	11.6
	12.7	1.96	22.1	11.3
3	8.3	2.8	30.0	12.4[f]
4	9.4	2.32	25.3	10.9
5	16.0	1.76	22.3	12.7
6	16.4	1.82	22.1	12.1
7	18.6	1.68	17.1	10.2
8	20	1.65	16.7	10.1
9	22.9	1.53	18.3	12.0
10	24.8	1.48	18.3	12.4
11	34	1.39	16.9	12.2
12	35.9	1.38	13.0	9.4
13	39.7	1.35	15.9	11.8

[a] x is the C/As ratio, C_xAsF_5.

[b] Systematically 5% too large, perhaps because of microscopic cracking. There is also a 3-5% measurement uncertainty.

[c] $8 \leq x \leq 16$: t/t_0 (x) = (1-x-8/8) t/t_0 [1st stage] + (x-8/8) t/t_0 [2nd stage]. $16 \leq x \leq 24$: t/t_0 (x) = (1 - x-16/8) t/t_0 [2nd stage] + (x-16/8) t/t_0 [3rd stage]. Pure stage t/t_0 values are based on a measured c-spacing of 8.05(3) Å for C_8AsF_5 and a parent-graphite gallery height of 3.35 Å.

t/t_0 [1st stage] = 8.05 Å/3.35 Å = 2.40.

t/t_0 [2nd stage] = 8.05 Å + 3.35 Å/2(3.35 Å) = 1.70.

t/t_0 [3rd stage] = 8.05 Å + 2(3.35 Å)/2(3.35 Å) = 1.47.

[d] The voltage measurements have a 5% estimated uncertainty.

[e] $\sigma/\sigma_G = (V/V_0) \times (t/t_0)^{-1}$ has an estimated 10% uncertainty.

[f] Calculated using the theoretical t/t_0 = 2.40.

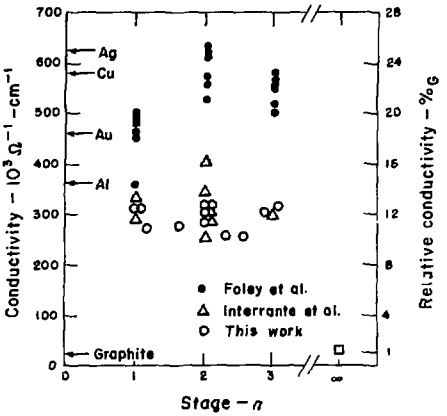

Fig. 1. Electrical conductivity of graphite-arsenic pentafluoride intercalation compounds.[4] (XBL 813-2204)

Table 2. Composition, stage, relative thickness and relative conductivity of HOPG$^+$ AsF_6^- salts.

Preparation	Gravimetric Composition	Stage[a] n	t/t_0[b]	σ/σ_G[b]
from $O_2^+AsF_6^-$	$C_{14.6}AsF_6$	~first	2.24	4 to 6
	$C_{30.9}AsF_6$	mixture second and third	1.59	11.1
from C_xAsF_5 plus F_2	$C_{11}AsF_6$	first	2.34	2.2
	C_8AsF_6	first	2.48	1.5[c]

[a]The stages present in the sample were determined by x-ray diffraction by mounting each sample, under Mylar, on a diffractometer.

[b]See Table 1 for definitions.

[c]*Because of slight exfoliation*, the σ/σ_G value was calculated using the ideal t/t_0 value of 2.40.

Table 3. The effect of alternately pumping and adding AsF_5 on the composition, relative thickness, and relative meter voltage ($=R/R_G$) for four different HOPG-AsF_5 samples.

Sample and description	A $\xrightarrow{\text{Pump}}$	B $\xrightarrow{\text{Add } AsF_5}$	A' $\xrightarrow{\text{Pump}}$	B' $\xrightarrow{\text{Add } AsF_5}$	A'' $\xrightarrow{\text{Pump}}$	B''
1. Gravimetric composition	$C_{16.0}AsF_5$	$C_{23.9}AsF_6$	$C_{18.1}AsF_5$			
t/t_0	1.76	1.67	1.71			
V/V_0	22.3	19.0	19.7			
2. Gravimetric composition	$C_{22.9}AsF_5$	$C_{30.7}AsF_6$	$C_{24.4}AsF_5$	$C_{39.2}AsF_6$	$C_{26.4}AsF_5$	$C_{38.3}AsF_6$
t/t_0	1.53	1.49	1.51	1.44	1.48	1.39
V/V_0	18.3	18.7	18.7	17.8	16.7	15.5
3. Gravimetric composition	$C_{24.8}AsF_5$	$C_{32.3}AsF_6$	$C_{25.4}AsF_5$	$C_{37.2}AsF_6$	$C_{25.0}AsF_5$	$C_{33.7}AsF_6$
t/t_0	1.48	1.46	1.48	1.45	1.48	1.43
V/V_0	18.3	17.5	17.9	17.2	16.3	16.2
4. Gravimetric composition	$C_{16.4}AsF_5$	$C_{22.6}AsF_6$				
t/t_0	1.82	1.68				
V/V_0	22.1	21.3				

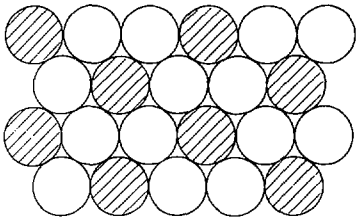

Fig. 2. A model for the disposition of AsF_6^- (open circles); ions in $C_{12n}AsF_6$ and $C_{12n}AsF_6 \cdot 1/2AsF_3$ (shaded circles). (XBL 813-2208)

In $C_{12}^+AsF_6^-$, all of the intercalant species are anions. Their cooperative interaction (one on each side of a carbon layer) will concentrate positive charges at certain sites much more than is likely in C_8AsF_5. In these highly charged positive-carbon systems this may result in a change in the graphite-layer bonding, with consequent band gap development.

* * *

1. E. M. McCarron and Neil Bartlett, J. Chem. Soc., Chem. Commun., 404 (1980).
2. C. Zeller, A Demenstein, and G. M. T. Foley, Rev. Sci. Instrum. 50, 602 (1979).
3. N. Bartlett et al., Synthetic Metals 1, 221 (1979).
4. G. M. T. Foley et al., Solid State Comm., 24, 371 (1977); L. V. Interramte, R. S. Markiewicz, and D. W. McKee, Synthetic Metals 1, 290 (1980).

2 THERMODYNAMIC AND STRUCTURAL STUDIES OF $(GeF_5)_n^{n-}$ AND GeF_6^{2-} SALTS

T. Mallouk and N. Bartlett

Several new compounds of general formula, A GeF_5, have been prepared (A = NO, NO_2, SF_3, and ClO_2). Vibrational spectra of these and of the previously known XeF_5GeF_5, O_2GeF_5, and NF_4GeF_5 show that the anion must be similar in all. Since, however, there has not been a full structure determination on any A GeF_5 compound, a prime concern has been to obtain such a structure.

Single crystals of both ClO_2GeF_5 (data in Table 4) and XeF_5GeF_5 prove to be relatively easy to grow, but the greater volatility of the former compound has imposed problems in data gathering. The structure of the latter is complete (Fig. 3). There are no discrete GeF_5^- species. Instead, we see that the anion is an endless chain of elongated GeF_6 octahedra, which share trans apices. That is, trans F-ligands of the octahedra are bridging; and those bridging Ge-F distances, as is usual for such bridge bonds, are 0.15 Å longer than equatorial Ge-F bonds. The approximately C_{4v} symmetry XeF_5^+ cations each make weak bridging contacts with four equatorial F-ligands of two GeF_6 groups. It may be that this interaction of two adjacent GeF_6 groups with each XeF_5^+ is the factor that determines the size of the bridging Ge-F-Ge angle. The interaction of the four F-ligands of the $(GeF_4)(F_{1/2})_2^-$ chain, with each XeF_5^+, completes a capped Archimedean antiprism arrangement of F-ligands about each Xe atom. The XeF_5^+ size and shape are almost identical to XeF_5^+ + XeF_5^+ PtF_6^-.

Table 4. Single crystal data for ClO_2GeF_5 and NO_2GeF_5.

Compound	Space Group	Unit Cell a	b	c	Cell Volume	Z
NO_2GeF_5	$Cmc2_1$ or Cmcm or Ama2	19.52	11.37	31.8	7.058	48(?)
ClO_2GeF_5	C_{222_1}	14.65	7.52	8.87	977	8

Since the vibrational data of the other A GeF_5 salts mentioned are so similar to that of XeF_5GeF_5, it seems likely that nearly octahedral coordination of the germanium occurs in all. The NO_2GeF_5 salt infrared and Raman data are so close to those for XeF_5GeF_5 that it even seems likely that trans bridging of the GeF_6 units occurs there also.

It does appear that previous assumptions of GeF_5^- ions in A GeF_5 salts are likely to be erroneous. It also seems probable that the species in $C_{12}GeF_5$ is a fluorine bridged polymer.

Thermodynamic data for ClO_2GeF_5 and $(SF_3)_2GeF_6$ are given in Table 5. On the basis of an estimate of the lattice energy of $ClO_2^+GeF_5^-$ of -142 (± 8) kcal mole^{-1} and from established values for other terms in the Born Haber cycle, the enthalpy for the fluoride-ion addition to GeF_4 to make the polymeric anion, i.e.,

$$\Delta H^\circ [F_{(g)}^- + GeF_{4(g)} \longrightarrow GeF_4(F_{1/2})_{2(g)}^-]$$

≈ - 114 (± 10) kcal mole^{-1}. This is significantly more exothermic than the fluoride-ion enthalpy for BF_3, the value of ΔH° $[F_{(g)}^- + BF_{3(g)} \longrightarrow BF_{4(g)}^-]$, but comparable with estimates for the strong Lewis acid AsF_5, for which $\Delta H^\circ [F_{(g)}^- + AsF_{5(g)} \longrightarrow AsF_{6(g)}^-]$ ≈ - 110 (± 5) kcal mole^{-1}.

The estimate for the double fluoride-ion enthalpy of GeF_4, ΔH° $[2F_{(g)}^- + GeF_{4(g)} \rightarrow GeF_{6(g)}^{2-}]$ is much less reliable since the lattice energy evaluation, $U(SF_3)_2GeF_6$ = - 405 (± 30) kcal

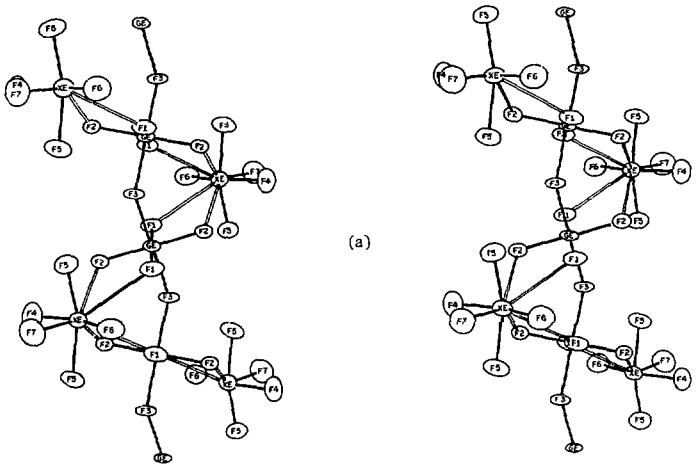

(a)

(b)

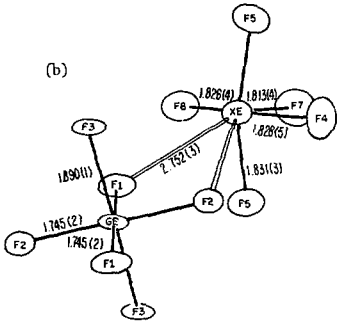

(c) Positional and thermal parameters and their estimated standard deviations.

Atom	X	Y	Z	B(1,1)	B(2,2)	B(3,3)	B(1,2)	B(1,3)	B(2,3)
XE	0,13903(3)	0.2500(0)	0.36600(5)	0,00386(2)	0,00810(5)	0,01067(7)	0.0000(0)	-0,00363(7)	0.0000(0)
GE	0,0000(0)	0.0000(0)	0.0000(0)	0,00318(3)	0,00243(8)	0,00818(9)	-0,00007(8)	-0.0007(1)	-0.0006(2)
F1	-0,0289(1)	0,0587(2)	0,2242(3)	0,0054(1)	0,0059(3)	0,0094(4)	0,0035(4)	0,0014(5)	-0.0013(6)
F2	0,1283(1)	0,0567(2)	0,0423(3)	0.0032(1)	0,0070(3)	0,0160(4)	0,0014(4)	-0.0008(5)	-0.0001(7)
F3	-0,0289(2)	0,2500(0)	-0.0706(4)	0.0040(2)	0,0026(4)	0,0100(6)	0,0000(0)	-0.0048(7)	0.0000(0)
F4	0,2688(2)	0,2500(0)	0,2898(5)	0.0040(2)	0,0208(7)	0,0249(8)	0.0000(0)	-0,0034(10)	0.0000(0)
F5	0,1530(2)	0,5030(2)	0,4067(3)	0,0062(1)	0,0094(4)	0,0198(5)	-0.0029(4)	-0.0061(6)	-0.0053(8)
F6	0,0342(2)	0,2500(0)	0,5314(5)	0,0064(2)	0,0150(6)	0,0118(6)	0,0000(0)	0.0024(8)	0.0000(0)
F7	0,2135(3)	0,2500(0)	0,5741(5)	0,0084(3)	0,0194(7)	0,0186(7)	0,0000(0)	-0,0157(9)	0.0000(0)

The form of the anisotropic thermal parameter is:

Exp[-(B(1,1)*H*H + B(2,2)*K*K + B(3,3)*L*L + B(1,2)*H*K + B(1,3)*H*L + B(2,3)*K*L)].

Fig. 3. The crystal and molecular structure of XeF_5GeF_5. (a) Stereo view of the structure. (b) The structural unit dimensions. (c) Crystal data: S. G.: P n m a, orthorhombic, a = 12.986(4), b = 7.119(2), c = 7.398(1), Z = 4. [(a) XBL 813-2205, XBL 813-2206; (b) XBL 813-2207]

Table 5. Some thermodynamic data for $(SF_3^+)_2GeF_6^{2-}$ and $(ClO_2^+)_n(GeF_5)_n^{n-}$.

Compound (equation for dissociation)	Temp. range (°C)	$\Delta H°$ kcal mole^{-1}	$\Delta S°$ cal deg^{-1} mole^{-1}	$\Delta G°_{298}$ kcal mole^{-1}
$(SF_3)_2GeF_{6(c)}$ ⇌ $2SF_{4(g)}^+ + GeF_{4(g)}$	0.0 to 36.8	44.2(8)	130(3)	+5.5
$ClO_2GeF_{5(c)}$ ⇌ $ClO_2F_{(g)}^+ + GeF_{4(g)}$	0.2 to 33.4	29.1(4)	90(1)	+2.4

mole^{-1} is very uncertain. This uncertainty arises because the cation is rather unsymmetrical (C_{3v}) and there is no reliable basis presently for assigning fractional charges on each of the species in the complex ion. The lattice energy evaluation has therefore followed the relatively crude formula devised by Kapustinskii.[1] A variety of thermodynamic information for SF_3^+ salts indicates that $\Delta H°[SF_{4(g)} \rightarrow SF_{3(g)}^+ + F_{(g)}^-]$ = + 210 (± 6) kcal mole^{-1}. Consequently, from the enthalpy of reaction given in Table 4, $\Delta H°[GeF_{4(g)} + 2F_{(g)}^- \rightarrow GeF_6^{2-}]$ = - 59 (± 36).

* * *

1. A. F. Kapustinskii, Quarterly Revs. Chem. Soc. 10, 284 (1956).

3. THE RELATIONSHIP OF GRAPHITE FLUOROSULFATES TO RELATIVES CONTAINING FLUOROSULFURIC ACID

R. N. Biagioni and Neil Bartlett

The discovery[1] that peroxydisulfuryl difluoride, $S_2O_6F_2$, would oxidize graphite spontaneously to yield fluorosulfates C_xSO_3F indicated that such materials should be reducible to the previously known salts, which were believed to be approximately of composition $C_{24}2HSO_3F{\cdot}SO_3F$. The latter had been made by electrochemical oxidation[2] in fluorosulfuric acid. The limiting value of x in C_xSO_3F is close to 7.5. For a sample of C_xSO_3F, with x = 8, it is clear that the relationship of $C_{24}2HSO_3F{\cdot}SO_3F$ would be as expressed in the reduction:

$$C_{24}3SO_3F + 2H^+ + 2e^- \rightarrow C_{24}2HSO_3F{\cdot}SO_3F.$$

This requires that merely H^+ and electrons need be exchanged to convert one material into the other.

The blue first-stage C_xSO_3F ($x \approx 7.5$) is characterized by a gallery height of 7.6 to 7.7 A. This is equivalent to the c spacing, since the diffraction data gives no evidence of a super lattice ordering along c. Such syntheses, even at 80°C, often yielded some second-stage material. The latter is characterized by a c axis repeat dimension of ~11.0 A. This is the value anticipated on the basis of the sum of a graphite sheet thickness (3.35 A) and an occupied-gallery height of ~ 7.6 to 7.7 A. Mainly, second-stage material was obtained by bringing the $S_2O_6F_2$ into interaction with the HOPG at -78° initially, then slowly bringing the mixture to ambient temperatures. Such material, slightly contaminated by first-stage material, had a composition $C_{13.6}SO_3F$. This implies a gallery occupancy comparable with that of the first stage.

Treatment of C_xSO_3F with HSO_3F always resulted in a first-stage material of composition $C_{\sim 7.5}SO_3F_x{\cdot}HSO_3F_{(1-x)}$. Thus for an HOPG C_xSO_3F of composition $C_{8.8}SO_3F$, which x-ray dirfraction data showed to be a mixture of first and second stages, a first-stage salt of composition $C_{\sim 7.8}SO_3F_xHSO_3F_{(1-x)}$ was formed. This, like all of these mixed intercalate materials, showed an appreciable expansion of the occupied-gallery height over that for the pure fluorosulfate.

Experiments with graphite possessing less order than HOPG yielded first-stage materials in which two-thirds of the intercalent was HSO_3F and the composition approximately $C_{7.6}SO_3F_{1/3}{\cdot}2HSO_3F_{2/3}$. Such materials rapidly interacted with acid-free graphite fluorosulfate, made from the same lower-grade graphite, to yield homogeneous material (as characterized by x-ray diffraction). Figure 4 shows the c spacing for the homogeneous product of mixing (in various ratios) an acid-free material, A (of composition $C_{7.0}SO_3F$), with an acid-containing material, B [of composition $C_{7.0}(0.4SO_3F, 0.6HSO_3F)$]. Pure A was characterized by a c spacing of 7.70 A and B by c = 7.88 A. The variation of c with composition is essentially

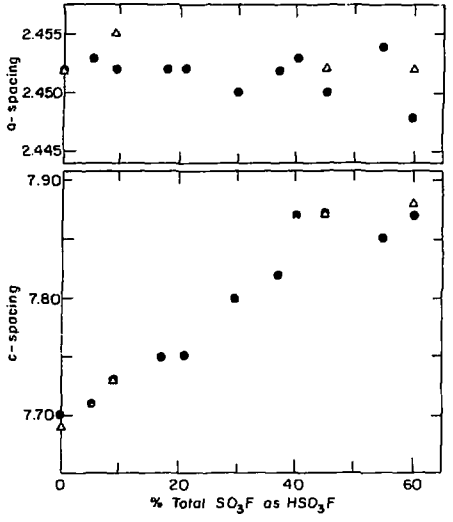

Fig. 4. Lattice parameters vs. composition for $C_x(SO_3F,HSO_3F)$. Triangles indicate duplication run of a given composition. (XBL 8010-6009A)

linear and indicative of a redox interaction, involving H^+ and electron transfer, between metal A and metal B.

The acid containing graphite fluorosulfates give sharper diffraction patterns than do their non-acid containing relatives. This may mean that, because of hydrogen bonding between intercalents within the galleries of the acid containing salts, there is less thermal motion than in the C_xSO_3F cases. But it may also mean that, in the more highly charged C_xSO_3F salts, a distortion of the graphite layers has been produced, which has no registry on neighboring layers. Certainly, the first-stage C_xSO_3F is an inferior electrical conductor (a b plane) to the acid containing materials, and this low conductivity is most simply explained by assuming a change in the graphite structure.

Although it has not been possible to obtain single crystals of either the graphite fluorosulfates or their acid relatives, an analysis of the disposition of the intercalents, relative to the graphite layers, in an acid containing material has been attempted on the basis of 00ℓ data from an HOPG sample. The analysis of the $\bar{0}0\ell$ data indicates that the SO_3F species are present in two orientations (roughly equal): one with the c axis parallel to a pseudo two-fold axis (z parameters: S = 1/2; 3O, 1F = 3/8) and the other with its pseudo three-fold axis approximately parallel to the a b plane (z parameters: S = 0.7; 3O(F) at 3/8; 1O(F) at 1/2). The former orientation requires less separation of the carbon layers than the latter, but the difference is not great. Certainly an orientation of the SO_3F, with its three-fold or pseudo-three-fold axes parallel to c, requires a greater separation of the carbon layers, and it is presumbly for that reason that this orientation does not occur.

* * *

1. N. Bartlett et al. J. Chem. Soc., Chem. Commun., 200 (1978); N. Bartlett, B. W. McQuillan, and A. S. Robertson, Mat. Res. Bull. 13, 1259 (1978).
2. M. J. Bottomley et al., J. Chem. Soc. 5674 (1963).

4. WORK IN PROGRESS

E. M. McCarron, T. Mallouk, and N. Bartlett

In the preparation of AsF_6^- salts by addition of elemental fluorine to $C_{8n}AsF_5$ compounds, it has been found that more fluorine is consumed than is necessary to make AsF_6^-. Indeed, it is now established, at least for the second and higher stage materials, that one mole of fluorine is taken up for each mole of AsF_5 in the $C_{8n}AsF_5$ compound:

$$C_xAsF_5 + F_2 \rightarrow C_xAsF_6 \cdot F \ (x \geq 24) \ .$$

This extra fluorine cannot be removed under dynamic vacuum at ordinary temperatures, and magnetic susceptibility measurements fail to show any evidence for species such as F_2^- or other odd electron systems. However, upon adding one-third of a mole of AsF_3 for each mole of $C_xAsF_6 \cdot F$, the extra fluorine is consumed according to the equation:

$$3C_{4y}AsF_6 \cdot F + AsF_3 \rightarrow 4C_{3y}AsF_6 .$$

Typically of $C_x^+AsF_6^-$ salts, this material is vacuum stable at room temperature. Treatment of the fluorine-rich $C_xAsF_6 \cdot F$ materials with excess AsF_3 leads to consumption of one mole of AsF_3 per mole of $C_xAsF_6 \cdot F$ according to the equation:

$$C_xAsF_6 \cdot F + AsF_3 \rightarrow 2_2C_{x/2}AsF_5 .$$

This last material appears to be identical to $C_{x/2}AsF_5$ made directly from graphite and AsF_5.

Experiments with pieces of HOPG have established that the staging--composition relationship, for the fluorine-rich systems, obeys the formula $C_{12n}AsF_6 \cdot F$. Since this is a similar relationship to that which occurs for the $C_{12n}^+AsF_6^-$, it is probable that the extra fluorine occupies the holes which occur in the $C_{12n}AsF_6$ gallery and which are illustrated in Fig. 2 (in Article 1 above). Each of these holes is large enough to accept a hexafluoro-species as in the C_8MF_6 compounds, hence there is no difficulty in locating two fluorine atoms in such a hole. (Such an occupancy is required by there being only one hole for two MF_6 in $C_{12}MF_6$, but the formula $C_{12}NF_6 \cdot F$ requires one

extra fluorine atom for each MF_6. Since the fluorine is not lost from the graphite under vacuum but is consumable by AsF_3, it is probable that it is present in the galleries as F^- ion. Thus, each hole in the loosely packed AsF_6^- arrangement in the gallery of $C_{12}AsF_6$ appears to be capable of taking up two F^- ions. This, of course, means that the appropriate formulation for the fluorine-rich materials would be $C_{12n}^{2+}AsF_6^-F^-$. Thus, in $C_{24}^{2+}AsF_6^-F^-$, the average charge on the graphite layers is equivalent to $C_{12}^{+}AsF_6^-$. Clearly, $C_{24}^{2+}AsF_6^-F^-$ should be a far more potent oxidizer than $C_{24}^{+}AsF_6^-$. Moreover, the interconversion

$$C_{24}^{+}AsF_6^- + F^- \rightleftarrows C_{24}^{2+}AsF_6^{+}F^- + e^-$$

should be manageable electrochemically, since both graphite salts are electrical conductors. An attractive extra feature is that the interconversion involves no change in stage; therefore, there is unlikely to be a large change in the dimensions of the graphite.

An interesting point about the take up of extra fluorine by $C_{12}AsF_6$ is that graphite alone will not intercalate fluorine. Indeed, in the second and higher stages, the fluorine only enters the galleries which are already occupied by AsF_6^-. The unoccupied galleries remain unoccupied. This means that elemental fluorine can intercalate oxidatively into graphite (probably making F^-) but, in order to do so, it appears to need a large intercalate ion in place. Perhaps the role of the AsF_6^- is to promote the penetration of the small, highly charged F^- ion. In the absence of the AsF_6^-, the F^- ion is likely to become strongly attracted to a somewhat positive carbon atom at the mouth of the gallery and to be rendered incapable of moving to another carbon of the layer for a progression through the gallery. It may be that, with the AsF_6^- in attendance, a fleeting AsF_7^{2-} species could form, then slough off a different F^- ion, and thus provide for a leap-frogging of F^- through the gallery.

RESEARCH PLANS FOR CALENDAR YEAR 1981

The extent of fluorine consumption by $C_{12n}AsF_6$ salts will be studied as a function of stage, n. Since the extra fluorine incorporated into the occupied galleries of the $C_{12n}AsF_6$ salts appears to be F^-, the $C_{12n}AsF_6.F$ compounds should have much higher oxidation potential than their $C_{12n}AsF_6$ relatives. Attempts will be made to measure these potential differences. The reversibility of the process, $C_{12n}AsF_6 + 1/2F_2 \rightleftharpoons C_{12n}AsF_6 \cdot F$, will also be explored with appropriate electrochemical cells. The addition of fluorine to $C_{12n}AsF_6$, although not changing the stage, should change the gallery spacing. Gallery spacing (from x-ray diffraction) may be a convenient diagnostic way of following the extent of conversion to $C_{12}AsF_6 \cdot F$.

Chlorine will not form a stable compound with graphite alone. It remains to be seen whether or not $C_{12n}AsF_6$ will incorporate chlorine. It is unlikely that two chloride ions could be accommodated into a vacancy in an occupied gallery of $C_{12n}AsF_6$, but one Cl^- per vacancy could occur. Thus, one might anticipate $C_{12n}AsF_6 \cdot 1/2Cl$ as a limiting composition.

Direct synthetic methods involving SnF_4, F_2 and graphite have failed to bring about intercalation, but oxidation by salts A_2SnF_6 containing strongly oxidizing cations may be effective. A salt such as $C_{12}SnF_6$ should be excellent for electrochemical redox studies of such salts, since SnF_2 and its solid solutions with the trifluorides, SbF_3 or BiF_3, are excellent F^- conductors. Thus, the cell $Sn|SnF_2(BiF_3)|C_{12}SnF_6$ looks most promising. An added feature of interest is the planar nature of SnF_4, which is a sheet polymer.

The incorporation of PF_5 into graphite, in the presence of fluorine, (see Ref. 4 of Article 1), to make PF_6^-, raises the possibility that the perfluorophenyl compound, $C_6F_5PF_4$ may similarly intercalate because of graphite oxidation according to: $C_6F_5PF_4 + 1/2F_2 + e^- \rightarrow C_6F_5PF_5^-$. The benzene ring orbitals of this anion may well provide the means for this anion to back donate to the positively charged graphite layers. Such electron synergism would reduce the tendency to localize positive charge in the graphite layers. Thus, such salts as $C_y^{+}PF_5C_6F_5^-$, if they can be made, may behave more like $C_{8n}AsF_5$ than $C_{12n}AsF_6$, and be superior electronic conductors.

The search for excellent fluoride-ion and proton conductors will continue. The prime means of detecting such conductors is to make complex impedance measurements on the solids. Since the fluoride-ion conductors are to be compatible with powerful oxidizers, the major problem is one of suitable cell construction for such measurements. Suitable solids appear to be salts of anions containing large fluxional anions, e.g., ZrF_7^{3-} and TaF_8^{3-}, but salts in which both anion and cation have ill-defined or fluxional geometries are also of interest. The possibility of tautomerism between the compound $(XeF_5^{+})_2GeF_6^{2-}$ and $Xe_2F_{11}^{+}GeF_5^-$ and the stability of Xe(VI) towards further oxidation, marks this system for early study.

1980 PUBLICATIONS AND REPORTS

Refereed Journals

1. E. M. McCarron and Neil Bartlett, "Composition and Staging in the Graphite-AsF_6 System and Its Relationship to Graphite-AsF_5," J. Chem. Soc., Chem. Commun, 404 (1980), LBL-10190.

2. E. M. McCarron, Y. Jean Grannec, and Neil Bartlett, "Fluorogermanium(IV) Salts of Graphite--A System in Equilibrium with Elemental Fluorine," J. Chem. Soc., Chem. Commun, 890 (1980), LBL-10228.

3. K. Züchner, T. J. Richardson, O. Glemser, and Neil Bartlett, "The Pentafluoropyridine Cation, $C_5F_5N^+$," Augewandte Chemie 19, 944 (1980), LBL-11293.

LBL Reports

1. T. E. Thompson, E. M. McCarron, and Neil Bartlett, "The Electrical Conductivity of Graphite-AsF_5 Intercalation Compounds and Their Relationship to Other Graphite-MF_6 Salts, LBL-1211.

2. F. L. Tanzella, "Electron Oxidation of Aromatic Molecules and Related Delocalized-Electron Solids," Ph.D. thesis, January 1980, LBL-10478.

3. E. M. McCarron, "Novel Graphite Salts of High Oxidizing Potential," Ph.D. thesis, August 1980, LBL-11272.

Invited Talks

1. Neil Bartlett, Jeremy Musher Memorial Lecture: "Chemistry of the Noble Gases--Discovery and Significance," The Hebrew University of Jerusalem, Israel, March 12, 1980.

2. Neil Bartlett, "New Synthetic Metals," Ben-Gurion University of the Negev, Israel, March 13, 1980.

3. Neil Bartlett, "Electron-Oxidation of Aromatic Molecules, Boron Nitride and Graphite and New Synthetic Metals," Central Research E. I. de Pont de Nemours and Company, May 19, 1980.

4. Neil Bartlett, "Possible Electrode and Solid Electrolyte Materials," International Workshop on Advanced Materials Problems, University of Bordeaux, France, June 23-26, 1980.

5. Neil Bartlett, "New Synthetic Metals for Graphite," Josef Stefan Institute, Ljubljiana, Yugoslavia, July 2, 1980.

6. Neil Bartlett, "Graphite Salts and Other Synthetic Metals--Their Constitution and Properties," Gordon Research Conference on Electron-Donor-Acceptor Interactions, Wolfeboro, New Hampshire (Gordon Conference), August 11-15, 1980.

7. Neil Bartlett, "New Fluoroanion Graphite Salts, Including a System in Equilibrium with Elemental Fluorine at Ordinary Temperatures," Fluorine Award Symposium, Second Chemical Congress of the North American Continent, Las Vegas, Nevada, August 28, 1980.

8. Neil Bartlett, "Some New Synthetic Metals from Graphite," Distinguished Speaker Lecture, University of Utah, Salt Lake City, Utah, October 16, 1980.

9. Neil Bartlett, "Some New Synthetic Metals from Graphite," Minnesota American Chemical Society Inorganic Topical Group Seminar, University of Minnesota, Minneapolis, October 29, 1980.

10. Neil Bartlett "Electron Oxidation of Aromatic Molecules and other Delocalized-Electron Systems," at Ames Laboratory, Iowa State University, Ames, Iowa, October 30, 1980.

11. Neil Bartlett, "Some New Synthetic Metals from Graphite," State University of Iowa, Iowa City, October 31, 1980.

12. Neil Bartlet·, "New Synthetic Metals from Graphite and Boron Nitride," California State Los Angeles, November 5, 1980.

13. Neil Bartlett, "Noble-Gas Chemistry and its Significance," and "From Super-Oxidizers to Synthetic Metals," California State Sacramento, November 17, 1980.

I. Analysis of Transplutonium Elements in Dilute Solution*

Steven D. Brown, Investigator

1. SEPARATION OF OVERLAPPED VOLTAMMETRIC PEAKS BY RECURSIVE DIGITAL FILTERING

Teri F. Brown and Steven D. Brown

A major limitation in the electrochemical analysis of materials in dilute solution is the overlap of current versus potential peaks of either different substances in solution or different oxidation states in solution; this is especially true for the transplutonium elements. Accurate analysis requires the deconvolution of the overlapped peaks. We have developed a new method of peak deconvolution based on the Kalman Filter, a recursive digital filtering algorithm which can be used for linear parameter estimation.

The Kalman Filter combines estimates of variables based on a model of linear system noise with measurements at equally spaced times to produce optimal estimates of the variables and their covariance. For peak separation, the most common variables are peak height, peak width, and various peak shape parameters. By using the measurement function and single component voltammograms to define the peak position and shape, it is possible to reduce the dimensionality of the problem until only the peak heights need be estimated. In voltammetry, peak height is a direct measure of concentration.

The method has been tested using both synthetic data and selected metal systems which show overlapped peaks. Figure 1 shows the quantitative resolution of a three component system which is not separable using other techniques. Quantitative resolution was possible on data containing random noise with peaks as close as 2.5 mV. The method is applicable to any voltammetric waveform. Additionally, because the algorithm is small, rapid, and recursive, on-line analysis time is considerably reduced.

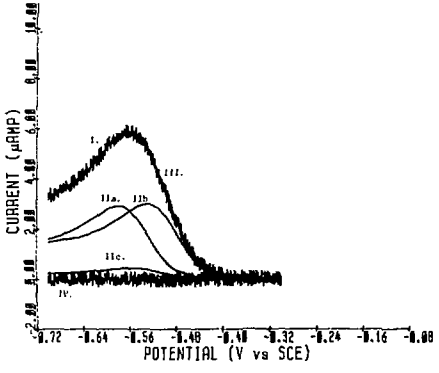

Fig. 1. Peak separation of a three-component mixture: I. the original data with S/N=15.; IIa., IIb., IIc., the peaks of the individual components with relative heights of 1:1:1/10 and with 25 mV separation; III. the sum of the component peaks; and IV. the residual of the fit. (XBL 811-7704)

2. NOISE PROCESSES IN ELECTROCHEMISTRY

Teri F. Brown and Steven D. Brown

The use of computers in electrochemical analysis has increased the application of numerical techniques for data manipulation. Some of these techniques, such as least squares fitting and digital filtering, require the assumption that the noise contained in the data is random and remains random throughout any data transformations.

We have developed analysis procedures using the Fourier power spectrum and lag models, based on auto- and cross-correlation techniques, which make it possible to determine the distribution of the noise when the data is taken and subsequently numerically processed. The power spectra in Fig. 2

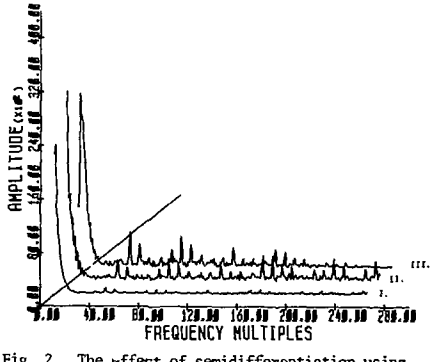

Fig. 2. The effect of semidifferentiation using different algorithms on the noise distribution of a voltammogram: I. the Fourier power spectrum of the original voltammogram; II. the power spectrum of the voltammogram after semidifferentiation by the Gl algorithm; and III. the power spectrum of the voltammogram after semidifferentiation by the Huber algorithm. (XBL 811-7705)

*This work was supported by the Director, Office of Energy Research, Office of Basic Energy Sciences, Chemical Sciences Division of the U. S. Department of Energy under Contract No. W-7405-ENG-48.

show the changes that occur in the frequency distribution of the data when it is semidifferentiated[1] to produce narrow peaks in the time domain. In this example, one algorithm increased the noise (the high frequency components) but left the overall noise structure unchanged, while the other algorithm not only increased the noise, but also introduced a lag-2 component and changed the frequency distribution, making the noise nonrandom. This type of analysis allows one to choose algorithms for data handling that both transform the data in the desired manner and satisfy the noise assumptions needed for rigorous statistical analysis.

* * *

1. J. J. Toman, R. M. Corn, and S. D. Brown, Anal. Chim. Acta 123, 187 (1981).

3. WORK IN PROGRESS

We are currently developing photoacoustic spectroscopic techniques for ultra-trace analysis. Laser-induced photoacoustic analysis of trace Nd^{+3} and Pr^{+3}, using piezoelectric detection, has shown excellent detection limits, and appears to be a promising alternative to electrochemical approaches.

RESEARCH PLANS FOR CALENDAR YEAR 1981

During 1981, studies will continue on the application of numerical techniques to electrochemistry and to photoacoustic spectroscopy. Applications of the Kalman Filter to sorption modified electrochemical responses are planned, as are studies of poorly complexed metals. Applications to U and Pu analysis are anticipated.

1980 PUBLICATIONS AND REPORTS

Refereed Journals

[+]1. S. D. Brown, R. K. Skogerboe, and B. R. Kowalski, "Assessment of the Impact of Coal Mining on Water Quality," Chemosphere 9, 265 (1980).

[‡]2. J. J. Toman, R. M. Corn, and S. D. Brown, "Convolution Voltammetry of Metal Complexes," Anal. Chim. Acta 123, 187 (1981), LBL-10820.

LBL Reports

1. J. J. Toman and S. D. Brown, "Peak Resolution by Semiderivative Voltammetry," LBL-11738, submitted to Analytical Chemistry.

2. T. F. Brown and S. D. Brown, "Resolution of Overlapped Peaks Using the Kalman Filter," LBL-11917, submitted to Analytical Chemistry.

Invited Talks

1. S. D. Brown, "Metal Speciation and Partitioning," Dept. of Public Health, University of California, April 1980.

2. S. D. Brown, "Analytical Methods for Metal Speciation," West Coast Water Chemistry Winter Conference, January 1980.

3. S. D. Brown, "Convolution Voltammetry of Metal Complexes," General Chemistry Division, Lawrence Livermore Laboratory, April 1980.

4. S. D. Brown, "Novel Applications of Computers in Electrochemistry," Analytical Chemistry Division, Dow Chemical Company, August 1980.

5. S. D. Brown, "Metal Speciation by Computer-Controlled Electrochemistry," Dept. of Chemistry, Oregon State University, November 1980.

6. S. D. Brown, "Peak Deconvolution in Electrochemistry: Three New Methods," Dept. of Chemistry, Cornell University, December 1980.

* * *

[+]Work supported at the University of Washington by the Office of Naval Research.
[‡]Work supported, in part, by the Office of Nuclear Waste Isolation, Department of Energy.

I. Transition Metal Catalyzed Conversion of CO, NO, H_2, and Organic Molecules to Fuels and Petrochemicals*

Robert G. Bergman, Investigator

1. THE MECHANISM OF ALDEHYDE FORMATION IN THE REACTION OF A MOLYBDENUM HYDRIDE WITH MOLYBDENUM ALKYLS†

William D. Jones, Michael J. Wax, John M. Huggins, and Robert G. Bergman

Recent evidence indicates that the terminal C-H bond-forming step in hydroformylation (the oxo process) involves two, rather than one, metal complex.[1] We have uncovered a similar binuclear reaction in the molybdenum series[2] (see Scheme I and 1979 Annual Report) and are now examining the mechanism of this reaction.

Scheme I

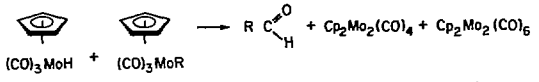

a, R = CH_3

b, R = C_2H_5

c, R = $CH_2C_6H_5$

d, R = CD_3

Several mechanistic possibilities have now been rigorously excluded. No exchange of methyl groups was observed when 2a was heated with the methylcyclopentadienyl derivative of 2d under the C-H bond-forming reaction conditions, both in the presence and absence of 1. In addition, reaction of $MeCpMo(CO)_3H$ with 2b gives only mixed dimers, $(MeCp)(Cp)Mo_2(CO)_4$ and $(MeCp)(Cp)Mo_2(CO)_6$, and very little of the corresponding Cp/Cp or MeCp/MeCp dimers. Along with the lack of detected alkane products, these observations provide convincing evidence against the intermediacy of both free methyl radicals and free $CpMo(CO)_3$ radicals. That $CpMo(CO)_3^-$ does not lie on the reaction coordinate was demonstrated by showing that 2a is not produced when 1 is heated with either 2b or CH_3I. The fact that 1 reacts with 2b at about the same rate as does the less acidic derivative $CpMo(CO)_2(PPh_3)H$ also suggests the hydride is not acting as a proton donor in this system. The failure of added LiCl to form $CpMo(CO)_3Cl$ militates against the existence of $CpMo(CO)_3^+$ as an intermediate.

The mechanism most consistent with our observations involves initial reversible carbonyl insertion in 1, followed by attack of metal hydride on the 16-electron acyl, 5 (Scheme II), in analogy to a mechanism proposed for hydroformylation.[3] We do not yet know very much about the true structure or chemical properties of bridging hydride intermediate 6. However, we have found that when 2a is heated with $CpW(CO)_3H$, which has a stronger metal-hydrogen bond than does 1,[4] aldehyde production is retarded (see Table 1). This indicates that some influence of the monomer's M-H bond strength is "remembered" in the bridging hydride dimer, and this property

Scheme II

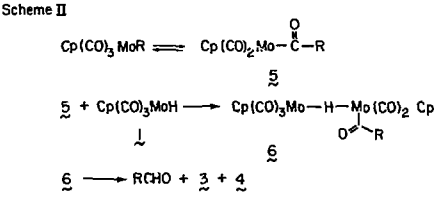

Table 1. Rate constants for reaction between $Cp(CO)_3MH$ $Cp(CO)_3MoR$ in THF-d_8 at 50°C.[a]

M in Hydride	R in Alkyl	k ($M^{-1}sec^{-1}$)
Mo	CH_3	2.5×10^{-4}
Mo	C_2H_5	4.0×10^{-3}
Mo	$CH_2C_6H_5$	8.5×10^{-4}
W	CH_3	1.4×10^{-5}

[a]Rates measured by disappearance of starting alkyl resonances in the NMR spectrum.

*This work was supported by the Director, Office of Energy Research, Office of Basic Energy Sciences, Chemical Sciences Division of the U. S. Department of Energy under Contract No. W-7405-ENG-48.

influences its propensity for reductive elimination of aldehyde.

* * *

†Brief version of LBL-11697.

1. N. H. Alemdaroglu, J. L. M. Penninger, and E. Ottay, Monatsch. Chem. 107, 1153 (1976).
2. W. D. Jones and R. G. Bergman, J. Am. Chem. Soc. 101, 5447 (1979).
3. J. R. Norton, Accounts Chem. Res. 12, 139 (1979).
4. A. P. Humphries and H. D. Kaesz, Prog. Inorg. Chem. 25, 145 (1979).

2. OBSERVATION OF CHEMICALLY INDUCED DYNAMIC NUCLEAR POLARIZATION DURING HYDROGENOLYSIS OF A COBALT ALKYLIDYNE CLUSTER COMPLEX

Henry E. Bryndza, Jane E. Fromner, Louis H. Stuhl, and Robert G. Bergman

The terminal step in the heterogeneous Fischer-Tropsch hydrocarbon synthesis is postulated to involve reaction between hydrogen gas and a surface-bound alkyl fragment. In an effort to understand this process, we have studied a related homogeneous model reaction, the interaction of tricobalt nonacarbonylalkylidyne complexes (1) with H_2 gas.

A new synthetic route to the alkylidyne complexes 1 has been developed.[1] This synthesis relies on the interaction of mononuclear metal hydrides with binuclear terminal alkyne complexes, as shown in Scheme I. This method reproducibly generates trinuclear alkylidyne complexes in high yields, in contrast to other existing methods which are characterized by more tedious procedures and poorer yields.

Hydrogenation of the neopentyl alkylidyne complex 1 (R = t-butyl) results in the production of 3,3-dimethyl-1-butene as major product in addition to minor amounts of 2,2-dimethylbutene and 4,4-dimethylpentenal as shown in Scheme I. Relative yields of the three products depend on the reaction conditions.

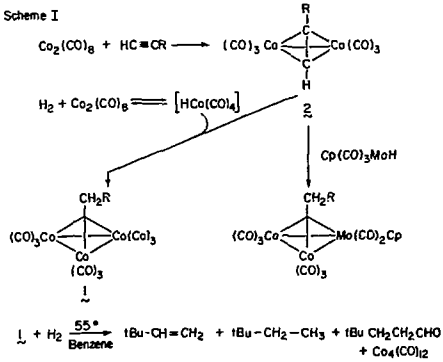

When trace amounts of dicobalt alkyne complexes (2) are present in hydrogenation solutions, strong chemically induced dynamic nuclear polarization (CIDNP) is observed in the olefin product upon hydrogenation of 1 in the heated probe of an NMR spectrometer (Fig. 1). Labeling studies indicate that the multiple effect CIDNP signals arise from the starting tricobalt alkylidyne complex and not from the alkyne added to the reaction solution. Furthermore, the dimethylbutene produced in those studies shows specific deuterium labeling when labelled 1 is hydrogenated; the CIDNP signals also show the specific labeling results suggesting that all the olefin is generated from the CIDNP enhanced pathway.

After its discovery about ten years ago, CIDNP was observed in a number of organic reactions and has been shown to be expressly diagnostic of radical intermediates.[2] However, CIDNP has been observed in only a very few organotransition metal transformations.[3] Furthermore, the example summarized here appears to be the first case of the appearance of CIDNP in a process involving interaction of two clusters. Further studies are now under way aimed at delineating the mechanism of this cluster-cluster reaction, and identifying the specific radical intermediates produced as a result of this interaction.

* * *

1. D. Seyferth, Advan. Organomet. Chem. 14, 97 (1976).

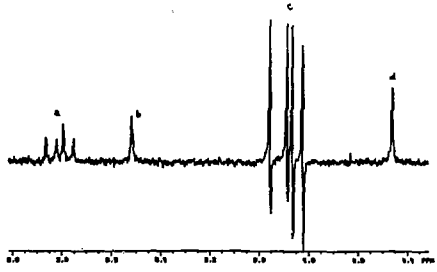

Fig. 1. NMR spectrum taken during reaction of cobalt cluster 1 with H_2 (benzene-d_6, 55°C) in presence of cluster 2. Resonance pattern (a) internal vinyl hydrogen in t-butylethylene (enhanced CIDNP absorption); (b) carbon-bound hydrogen in 2; (c) terminal vinyl hydrogens in t-butylethylene (enhanced CIDNP absorption and emission); and (d) dissolved H_2. (XBL 812-7939)

2. A. R. Lepley and G. L. Closs "Chemically Induced Dynamic Nuclear Polarization," Wiley, N. Y. (1973).
3. See, for example, (a) A. V. Kramer and J. A. Osborn, J. Am. Chem. Soc. 96, 7832 (1974); (b) R. L. Sweany and J. Halpern, ibid. 99, 8335 (1977).

3. PHOSPHINE SUBSTITUTION IN η^5-CYCLOPENTADIENYL-BIS-TRIPHENYLPHOSPHINECOBALT. EVIDENCE FOR A DISSOCIATIVE MECHANISM[†]

Andrew H. Janowicz, Henry E. Bryndza, and Robert G. Bergman

It has been known for almost 20 years that rapid CO exchange in $CpCo(CO)_2$ and $CpRh(CO)_2$ occurs by an associative (S_N2) mechanism[1,2] rather than by dissociation of a carbonyl group to give a (possibly linear) CpMCO intermediate. The apparent difficulty[3] of generating d^8 complexes having CpML structures, especially in thermal reactions, might possibly be due to the fact that such complexes, in their linear geometry, are forced by symmetry to have open-shell electronic configurations.[5] However, not many detailed studies of substitution lability in d^8 $CpML_2$ complexes (where $L \neq CO$) have been carried out. We decided to test the generality of the open shell/slow substitution hypothesis by examining the mechanism of ligand replacement in $CpCo(PPh_3)_2$ (1).

Complex 1 reacts cleanly with PMe_3 in toluene-d_8 to form the mixed complex (2) and PPh_3 (Scheme I). The substitution reaction was followed by NMR at -60°C. A first order plot of ln [1] vs. time yielded a linear plot, indicating that the reaction is first order in 1 and zero order in PMe_3. As shown in Fig. 2, the reaction rate is also strongly inhibited by added PPh_3.

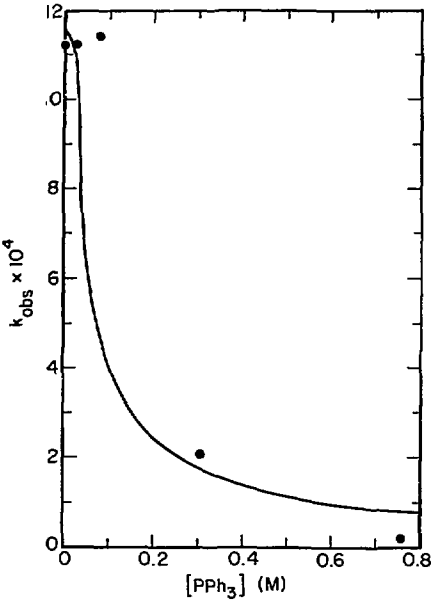

Fig. 2. Dependence of the pseudo-first order rate constants for reaction of 1 with excess PMe_3 upon the concentration of added excess PPh_3. (XBL 812-7938)

Scheme I

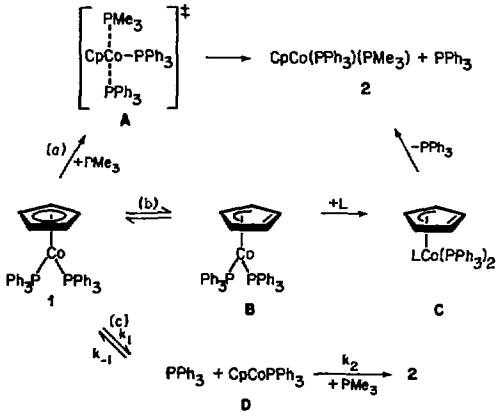

Three possible mechanisms for this reaction are shown in Scheme I. Mechanism (a) is associative (S_N2), would exhibit bimolecular kinetics under all conditions, and therefore cannot be operating. Mechanism (b) would give a rate law which could, under some conditions, be first order in 1 and zero order in PMe_3. However, inhibition by PPh_3 could be produced only by buildup of significant quantities of a complex such as C ($L = PPh_3$). No evidence for such a complex was detected.[6] The simple dissociative mechanism (c) gives the rate law shown in Eq. (1). At low $[PPh_3]$, $k_2[PMe_3] >> k_{-1}[PPh_3]$, and this equation reduces to a first order rate law. As $[PPh_3]$ increases, and the first term in the denominator becomes important, inhibition should set in, as is observed.

$$\text{Rate} = \frac{k_1 k_2 [1][PMe_3]}{k_{-1}[PPh_3] + k_2[PMe_3]} \quad . \qquad (1)$$

Using eq. (1), the best fit curve gives $k_1 = 1.15 \times 10^{-3}\ sec^{-1}$ and $k_2/k_{-1} = 4$. This value for k_1 corresponds to an activation free energy ($\Delta G^{\ddagger}$) of 15.2 kcal/mole at -60°C. (Calculations suggest an activation energy of 12-13 kcal/mole.[7])

The precise structure for the intermediate involved, $CpCoPPh_3$, is not yet clear. The symmetry and d-orbital configuration of $CpCoPPh_3$ is such that the lowest singlet state of the simple linear complex has an open-shell structure.[4] The presence of an open-shell electronic structure in the transition state of a concerted pericyclic organic reaction indicates that a level crossing is encountered in the MO correlation diagram for the process; this normally is manifested in a high activation energy barrier.[8] Whether such correlations necessarily exist in organotransition metal reactions, where filled and unfilled d-orbitals normally lie much closer together in energy, is not yet clear. Therefore, either a) $CpCoPPh_3$ is linear, but its open-shell electronic structure does not destabilize it appreciably, or b) $CoCoPPh_3$ avoids reaching a linear configuration as phosphine dissociation proceeds. In any case, our study demonstrates that dissociation substitution is an especially facile, rather than unusually slow, process in $CpCo(PPh_3)_2$.

* * *

†Brief version of LBL-11160.

1. A. Wojcicki and F. Basolo, J. Inorg. Nuclear Chem. 17, 77 (1961).
2. H. G. Schuster-Woldan and F. Basolo, J. Chem. Soc. 88, 1657 (1966).
3. We are grateful to Prof. J. Collman for bringing this prediction to our attention: cf. (a) J. P. Collman and L. S. Hegedus, "Principles and Applications of Organotransition Metal Chemistry," University Books, Inc., 1980; (b) J. Berg and J. P. Collman, manuscript in preparation.
4. (a) M. Elian et al., Inorg. Chem. 15, 1148 (1976); (b) A. R. Pinhas and R. Hoffmann, Inorg. Chem. 18, 654 (1979); (c) H. Berke and R. Hoffmann, J. Am. Chem. Soc. 100, 7224 (1978).
5. J. P. Lauher and R. Hoffmann, J. Am. Chem. Soc. 98, 1729 (1976).
6. If the concentration of C were to build up, but C were in rapid equilibrium with 1 on the NMR time scale, one would expect a dramatic change in the chemical shifts of the resonances due to 1. No such change is observed.
7. We are grateful to Dr. R. McKinney for sharing the results of his calculations prior to publication. For related work, see R. J McKinney and D. A. Pensak, Inorg. Chem. 18, 3413 (1979).
8. R. B. Woodward and R. Hoffmann, The Conservation of Orbital Symmetry, Verlag Chemie, Germany (1970).

4. MECHANISM OF HYDROGENOLYSIS OF DIALKYLCOBALT COMPLEXES: EVIDENCE FOR AN AUTOCATALYTIC MECHANISM INVOLVING A METAL HYDRIDE/METAL ALKYL REACTION AS A CRITICAL STEP†

Andrew H. Janowicz and Robert G. Bergman

The cleavage of organotransition metal-carbon bonds by H_2 is an important step in many catalytic processes, including the final step in hydroformylation,[1] homogeneous hydrogenation,[2] and the Fischer-Tropsch reaction.[3] It has commonly been assumed that M-R hydrogenolysis occurs by oxidative addition of H_2 to the metal center carrying the carbon fragment, followed by formation of a new C-H bond by reductive elimination of alkane.[4]

Recent evidence indicates that, in hydroformylation, the final C-H forming step is a binuclear process,[5a] and we have discovered analogous binuclear C-H bond forming mechanisms in reactions between molybdenum hydrides and alkyls.[5b] In the present project, we are studying the mechanism of hydrogenolysis of cyclopentadienyldimethyl cobalt derivatives. Reaction of $CpCo(PPh_3)Me_2$ (1) with H_2 in benzene-d_6 at 45°C yields two equivalents of CH_4 and 0.5 equivalents of $CpCo(PPh_3)_2$ (2). In the presence of an added equivalent of PPh_3, the reaction rate is slower but in this case almost a full equivalent of 2 is formed. Treatment of 1 with D_2 yields exclusively CH_3D as the organic product.

Monitoring the reaction of 1 with H_2 in the presence of added phosphine revealed the presence of an induction period, whose length was dependent on the phosphine concentration (Fig. 3). Since an induction period sometimes accompanies a radical chain mechanism, the hydrogenolysis of $CpCo(PPh_3)(CD_3)_2$ was carried out with D_2 in the presence of a good radical trap, 1,4-cyclohexadiene.[6] The methane produced was exclusively CD_4, thus eliminating a radical chain process as responsible for the induction period. A second explanation for the induction period is that the hydrogenolysis is autocatalytic. In agreement with this hypothesis, adding both PPh_3 and the $CpCo(PPh_3)_2$ to the initial reaction mixture

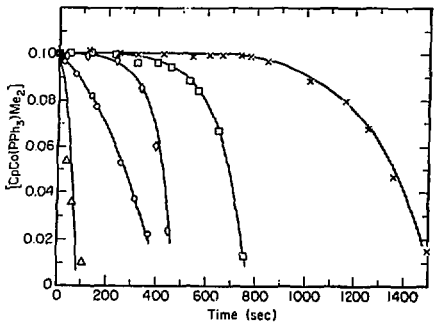

Fig. 3. Concentration vs. time plots showing the disappearance of 1 (initial concentration = 0.10 M) when exposed to H_2 gas in benzene-d_6 at 45°C, with the following additives: Δ no additives; ◇ 0.025 M PPh_3; □ 0.05 M PPh_3; X 0.10 M PPh_3; ○ 0.10 M PPh_3 and 0.017 M $CpCo(PPh_3)_2$.
(XBL 812-7940)

makes the induction period disappear, although the overall rate still exhibits phosphine inhibition (Fig. 3).

An autocatalytic mechanism consistent with the observations reported above is outlined in Scheme I. We sought additional support for this mechanism by attempting to prepare the dihydride 5, but were unsuccessful. As an alternative, we prepared 6,[7] the pentamethylcyclopentadienyl analog of 1. When 6 and excess H_2 were allowed to react in benzene-d_6 at 45°C, CH_4 was again produced, as was a new material: $Me_5CpCo(PPh_3)H_2$ (7). Dihydride 7 could not be isolated as a pure solid but solutions are stable for relatively long periods of time under H_2.

Dialkyl 6 and dihydride 7 react readily at 45°C to give CH_4 and unidentified metal-containing products. In the presence of excess 7 and PPh_3, the rate of disappearance of 6 shows good pseudo-first-order kinetics. Steady state

Scheme I

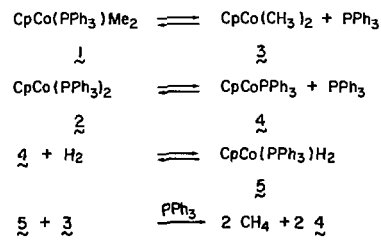

analysis of the mechanism in Scheme II predicts that k_{obs} should depend on 7 and PPh_3 concentrations in such a way that a plot of k_{obs}^{-1} vs. $[PPh_3]/[7]$ should give a straight line. In fact, the plot did yield a straight line giving $k_1 = 1.83 \times 10^{-4}$ sec and $k_{-1}/k_2 = 1.44$.

In summary, even though the inaccessibility of the formal Co(V) oxidation state prevents oxidative addition of H_2 to cyclopentadienylcobalt(III) derivatives, they still undergo facile hydrogenolysis. However, this hydrogenolysis involves a metal alkyl/metal hydride reaction as a critical step. It appears that M-H/M-R reactions are relatively facile and should be given serious consideration as alternatives to mononuclear steps in homogeneous catalytic processes involving C-H bond formation.

* * *

†Brief version of LBL-11932.

1. M. Orchin and W. Rupilius, Cat. Rev. 6, 85 (1972).
2. G. Dolcetti and N. W. Hoffman, Inorg. Chim. Acta 9, 269 (1974).
3. C. Masters, Adv. Organomet. Chem. 17, 61 (1979).
4. R. R. Schrock and G. W. Parshall, Chem. Rev. 76, 243 (1976).

Scheme II

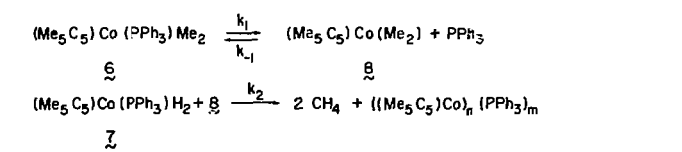

$$\frac{-d[6]}{dt} = \frac{k_1 k_2 [6][7]}{k_2 [6] + k_1 [PPh_3]}$$

5. (a) N. H. Alemdaroglu, J. L. M. Penninger, and E. Oltay, Monatsch. Chem. 107, 1153, (1976); (b) W. D. Jones and R. G. Bergman, J. Am. Chem. Soc. 101, 5447 (1979).
6. L. Kaplan, "Free Radicals," in Reactive Intermediates, Vol. 1, M. Jones and R. A. Moss (eds.), John Wiley and Sons, New York (1978).

5. INTERMOLECULAR CYCLOPENTADIENYL LIGAND EXCHANGE BETWEEN METAL ATOMS IN ORGANOCOBALT COMPLEXES†

Henry E. Bryndza and Robert G. Bergman

Cyclopentadienyl ligand exchange has been observed in electronically unsatisfied metallocenes and has been implicated in the degradation of polymer bound organometallic catalysts. However, no clear examples of such an exchange have been discovered for the large class of coordinatively satisfied (saturated) transition metal complexes.[1] We have identified such an exchange reaction between two cobalt complexes in different oxidation states.

In addition, the reactions of numerous catalytic species have been postulated to involve coordinatively unsaturated complexes. We have investigated two such unsaturated species with special attention to their electrophilicity. We have obtained evidence which shows that both iron tetracarbonyl and cyclopentadienyldimethylcobalt(III) remove two electron ligands from other coordinatively saturated species.

Specifically, methyl cyclopentadienyl(trimethylphosphine)dimethylcobalt(III) and cyclopentadienylbistriphenylphosphinecobalt(I) undergo the equilibration shown in Scheme I. The specificity of the trimethylphosphine label in the products suggests a cyclopentadienyl exchange [path (a)] because trimethylphosphine does not dissociate from either the starting material or the product of the reaction. In order to rule out the other possible route to products [stepwise methyl exchange followed by phosphine exchange; reaction (b) in Scheme I], we combined the intermediates one would obtain after methyl exchange and found that no products were produced under the reaction conditions. This indicates that cyclopentadienyl ligand exchange is taking place in this reaction. Unfortunately, side reactions in this system preclude gathering more information on the nature of the transition state for exchange.[2]

The reaction of cyclopentadienyl(triphenylphosphine)dimethylcobalt(III) with iron pentacarbonyl produces acetone, diiron nonacarbonyl, and cyclopentadienyl dicarbonylcobalt(I).[3] Triphenylphosphine dissociates rapidly from the cobalt(III) dialkyl; substitution of that labile ligand with the non-dissociating trimethylphosphine yields a dialkyl which does not react with the iron carbonyl. This evidence suggests that an unsaturated cobalt fragment removes CO from the iron carbonyl. The cyclopentadienyl trimethylphosphine dimethylcobalt(III) does lose its phosphine ligand to iron tetracarbonyl, an unsaturated species, which electrophilically removes the two-electron donor from the cobalt dialkyl. The series of reactions leading to the observed products is shown in Scheme II. It is interesting to note that unsaturated species are electrophilic enough to remove donor ligands from complexes which do not easily dissociate them. It seems likely that the extreme electrophilicity of these easily generated species may be more general than heretofore believed. Further studies will be required to probe the generality of this reactivity.

* * *

†Brief version of LBL-11826.

1. For leading references on the Cp ring interchanges observed for some of the electronically unsatisfied metallocenes see (a) C. P. Boekel, et al., J. Organometal. Chem. 136, 211 (1977); (b) G. E. Coates, M. L. H. Green, and K. Wade, Organometallic Compounds, Vol. 2, Chapman and Hall, London, pp. 90-164 (1972).
2. Perhaps the intermediate involves bridging cyclopentadienyl ligands as seen in stable Pd complexes; cf. (a) H. Werner and H. J. Kraus, J. Chem. Soc., Chem. Commun., 814 (1979);

Scheme I

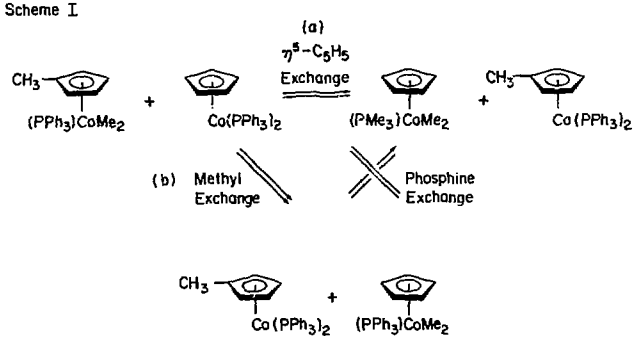

Scheme II

a) $Fe_2(CO)_9 \longrightarrow Fe(CO)_4 + Fe(CO)_5$

b) $CpCoLMe_2 \longrightarrow CpCo(Me_2) + L$

c) $CoCoMe_2 + Fe(CO)_5 \longrightarrow CpCo(CO)Me_2 + Fe(CO)_4$

d) $CpCo(CO)Me_2 + 2Fe(CO)_5 \longrightarrow CpCo(CO)_2 + 2Fe(CO)_4 + CH_3COCH_3$

e) $Fe(CO)_4 + L \longrightarrow LFe(CO)_4$

f) $3Fe(CO)_4 \longrightarrow Fe_3(CO)_{12}$

c') $CpCoLMe_2 + Fe(CO)_4 \longrightarrow CpCoMe_2 + LFe(CO)_4$

(b) H. Werner and A. Kuhn, Angew, Chem. 89, 427 (1977); (c) A. Kuhn and H. Werner, J. Organometa. Chem. 179, 421 (1979).
3. A cyclopentadienyl carbonyldimethylcobalt(III) intermediate is observed which easily generates acetone at room temperature. This intermediate suggests that CO ligands are removed from iron pentacarbonyl by unsaturated cobalt species as $Fe(CO)_5$ does not dissociate CO at these (25°C) temperatures.

RESEARCH PLANS FOR CALENDAR YEAR 1981

During the past year we have established that carbon-hydrogen bond-forming reactions between organotransition metal alkyls and hydrides are quite general. Direct reactions of this type proceed surprisingly easily, and we have found in one case that reaction between a metal alkyl and H_2 gas (hydrogenolysis) also proceeds via a mechanism involving a M-R/M-H reaction as a critical step. As one part of our work for the upcoming year, we plan to study hydrogenolysis reactions of metal alkyl complexes, other than the single one we have so far investigated, to determine how many of these related reactions also involve "disguised" reactions between metal hydrides and metal alkyls. In addition, we will begin a systematic study of direct M-H/M-R reactions to determine the effect of changing structure on the rates of these processes.

The most significant new research begun during the present year has been the investigation of hydrogenolysis of cluster complexes containing metal-carbon bonds, as models for catalytic processes such as the Fischer-Tropsch reaction, in which the terminating step involves hydrogen-induced extrusion of a carbon fragment from a multi-metal catalytic site (e.g., a metal surface). This work has also given us our most dramatic result: the detection of chemically induced dynamic nuclear polarization (CIDNP) during NMR observation of the reaction between nonacarbonyltricobalt alkylidyne complexes and H_2, when they are carried out in the presence of binuclear cobalt alkyne complexes. The results clearly implicate cluster-cluster reaction steps, as well as organic free radicals, in the mechanisms of such processes. One of our highest priorities during calendar year 1981, therefore, will be to try to understand the exact mechanism by which the CIDNP phenomena are produced in the cobalt cluster system. In addition, we will be investigating the generality of this striking CIDNP observation by (a) examining related tricobalt clusters containing modified alkyl groups, (b) determining which binuclear cobalt cluster partners are required in order to produce CIDNP, and (c) looking for similar CIDNP phenomena in alkylidyne clusters containing metals other than cobalt.

1980 PUBLICATIONS AND REPORTS

Refereed Journals

†1. M. A. White and R. G. Bergman, "Identification of Binuclear Acyl Complexes as Intermediates in the CO-Induced Conversion of $[\eta^5C_5H_5Co(CO)(CH_3)]_2$ to acetone and $[\eta^5C_5H_5Co(CO)(CH_3)]_2$ to 3-pentanone," Chem. Commun. 1056 (1979).

2. R. G. Bergman, "The Use of Isotope Crossover Experiments in Investigating Carbon-Carbon Bond Forming Reactions of Binuclear Dialkyl Cobalt Complexes," Acc. Chem. Res. 13, 113 (1980), LBL-10212.

3. H. E. Bryndza, E. R. Evitt, and R. G. Bergman, "Reversible Metal-to-Metal Methyl Transfer in η^5-cyclopentadienyl(triphenylphosphine)dimethylcobalt(III)," J. Am. Chem. Soc. 102, 4948 (1980), LBL-10213.

‡4. P. L. Watson and R. G. Bergman, "Reactivity of Alkyne Tungsten and Molybdenum Complexes. Heterolytic C-H Bond Activation in Coordinated Alkynes," J. Am. Chem. Soc. 102, 2698 (1980).

†5. E. R. Evitt and R. G. Bergman, "Substitution, Alkyl Transfer and Thermal Decomposition Reactions of η^5-cyclopentadienyl(trimethylphosphine)dimethylcobalt(III)," J. Am. Chem. Soc. 102, 7003 (1980).

‡6. J. E. Frommer and R. G. Bergman, "The Effect of Polymer Attachment on the Equilibrium Acidity of an Organotransition Metal Hydride and an

Organic Carboxylic Acid. Synthesis and Properties of a Polymer-Supported Metal Anion," J. Am. Chem. Soc. 102, 5227 (1980).

7. M. R. Berman, P. B. Comita, C. B. Moore, and R. G. Bergman, "Flow Pyrolysis and Direct and SiF_4-Sensitized Laser-Induced Decomposition of Tetralin. Identification of Retro-[2+4] Cleavage as the Primary Homogeneous Thermal Decomposition Channel," J. Am. Chem. Soc. 102, 5692 (1980), LBL-10731.

‡
8. P. N. Becker, M. A. White, and R. G. Bergman, "A New Method for 1,2-Diamination of Alkenes Using Cyclopentadienylnitrosylcobalt Dimer/$NOLiAlH_4$," J. Am. Chem. Soc. 102, 5675 (1980).

†9. K. H. Theopold and R. G. Bergman, "Synthesis of Metallacycles Containing Two Metals in the Ring. Thermal Decomposition to Cyclopropane and Ligand-Induced Conversion to Stable Mononuclear Metallacyclopentanones," J. Am. Chem. Soc. 102, 5694 (1980).

10. T. P. Lockhart, C. B. Mallon, and R. G. Bergman, "2,3-di-n-propyl-1,4-dehydrobenzene," J. Am. Chem. Soc. 102, 5976 (1980) LBL-10828.

LBL Reports

1. A. H. Janowicz, H. E. Bryndza, and R. G. Bergman, "Phosphine Substitution in η^5-Cyclopentadienyl-Bis-Triphenylophosphinecobalt(I): Evidence for a Dissociative Mechanism," LBL-11160.

2. T. P. Lockhart and R. G. Bergman, "Determination of the Reactive Spin State of 1,4-Dehydrobenzenes," LBL-11695.

3. T. P. Lockhart, P. B. Comita, and R. G. Bergman, "Kinetic Evidence for the Formation of Discrete 1,4-Dehydrobenzene Intermediates. Trapping by Inter- and Intra-molecular Hydrogen Atom Transfer and Observation of High-Temperature CIDNP," LBL-11696.

4. J. M. Huggins, "A Study of Fundamental Reaction Pathways for Transition Metal Alkyl Complexes," Ph.D. Thesis, LBL-11697.

5. J. E. Frommer, "Syntheses and Reactions of Polymer-Bound Molybdenum Complexes and Hydrogenolyses of an Alkynyl Cobalt Carbonyl Cluster," Ph.D. Thesis, LBL-11698.

6. T. P. Lockhart, "The Chemistry of 1,4-Dehydrobenzenes," Ph.D. Thesis, LBL-11699.

7. H. E. Bryndza and R. G. Bergman, "Reactions of η^5-Cyclopentadienylcobalt(III) alkyls with Cobalt(I) phosphines and iron carbonyls. Evidence for Direct η^5-Cyclopentadienyl and Trimethylophosphine Group Transfer Between Metal Centers," LBL-11826.

8. R. G. Bergman, "Physical Organic Studies of Organometallic Reactions," LBL-11827.

Invited Talks

Lectures Presented by Robert G. Bergman. These were presented during the past year at the places and times listed below. Unless indicated otherwise, titles of talks given were, "Carbon-carbon Bond Forming Reactions Mediated by Binuclear Organotransition Metal Complexes," "Transformations of Organic Compounds Mediated by Binuclear Organotransition Metal Complexes," "Hydrogenolysis of Metal-Carbon Bonds: Models for C-H Bond-forming Steps in the Oxo and Fischer-Tropsch Processes," and "Mechanisms of Metal-Induced Transformations Involving Multinuclear Reaction Sites."

1. Stanford University, Stanford, California, February 28, 1980.

2. Symposium on Formation and Cleavage of Metal-Carbon Bonds, American Chemical Society National Meeting, Houston, Texas, March 24, 1980.

3. University of Minnesota, Minneapolis, Minnesota, May 28, 1980.

4. Exxon Corporation, Linden, New Jersey, June 17, 1980.

5. ARCO Research, Glenolden, Pennsylvania, June 18, 1980.

6. Synthetic and Catalytic Reactions Symposium, Massachusetts Institute of Technology, Cambridge, Massachusetts, June 24, 1980.

7. General Electric Research Corporation, Schenectady, New York, June 25, 1980.

8. Gordon Conference on Organometallic Chemistry, Proctor Academy, Andover, New Hampshire, August 15, 1980.

9. "Physical Organic Studies of Organometallic Reactions," Plenary Lecture, Sixth International Union of Pure and Applied Chemistry (IUPAC) Symposium on Physical Organic Chemistry, Santa Cruz, California, August 26, 1980.

10. Five Lectures in Organometallic Chemistry, Suisse Romande Summer Organic Chemistry Workshop, Les Diablerets, Switzerland, September 1-5, 1980.

11. Union Carbide Company, Bound Brook, New Jersey, November 17, 1980.

12. American Chemical Society Cleveland Section Meeting, Cleveland, Ohio, November 19, 1980.

13. Emory University, Atlanta, Georgia, November 20, 1980.

14. University of Florida, Gainesville, Florida, November 21, 1980.

15. Exxon Corporation, Baton Rouge, Louisiana, December 10, 1980.

16. Symposium on the Chemistry of Binuclear Complexes, American Chemical Society Joint

Southeast/Southwest Regional Meeting, December 11-12, 1980.

Lectures Presented by Coworkers. Lectures entitled, "Syntheses and Reactions of Polymer-Bound Molybdenum Complexes and Hydrogenolyses of an Alkynyl Cobalt Carbonyl Cluster," were presented during the past year by Ms. Jane E. Frommer at the following places and times:

1. Union Carbide Company, Bound Brook, New Jersey, January 9, 1980.

2. Oxirane International, Princeton, New Jersey, January 10, 1980.

3. Western Electric Company, Princeton, New Jersey, January 11, 1980.

4. Union Carbide Company, Tarrytown, New York, January 30, 1980.

5. Mobil Research and Development, Princeton, New Jersey, February 1, 1980.

6. Fabric Research Laboratory, Dedham, Massachusetts, February 4, 1980.

7. Rohm and Haas, Spring House, Pennsylvania, February 20, 1980.

8. ARCO Research, Glenolden, Pennsylvania, February 21, 1980.

9. Allied Chemical Company, Morristown, New Jersey, February 25, 1980.

10. Merck Sharp and Dohme, Rahway, New Jersey, February 26, 1980.

11. Bell Laboratories, Murray Hill, New Jersey, February 29, 1980.

12. Exxon Research, Linden, New Jersey, March 4, 1980.

Lectures entitled, "Chemistry of 1,4-Dehydrobenzenes," were presented during the past year by Mr. Thomas Lockhart at the following places and times:

1. E. I. DuPont de Nemours and Company, Experimental Station, Wilmington, Delaware, January 30, 1980.

2. Rohm and Haas Corporation, Spring House, Pennsylvania, February 1, 1980.

3. Western Electric Company, Princeton, New Jersey, February 4, 1980.

4. Monsanto Company, St. Louis, Missouri, February 6, 1980.

5. IBM Corporation, East Fishkill, New York, February 20, 1980.

6. Union Carbide Corporation, Bound Brook, New Jersey, February 22, 1980.

7. General Electric Company, Schenectady, New York, February 25, 1980.

8. Eastman Kodak Company, Rochester, New York, February 28, 1980.

9. Union Carbide Corporation, Tarrytown, New York, March 3, 1980.

10. California Institute of Technology, Pasadena, California, August 22, 1980.

* * *

†Supported by the National Science Foundation.

‡Supported by the National Institutes of Health.

2. Chemical Engineering Sciences

a. High-Pressure Phase Equilibria in Hydrocarbon-Water (Brine) Systems

John M. Prausnitz, Investigator

1. HIGH-PRESSURE PHASE EQUILIBRIA FOR METHANE-WATER (BRINE)

Wallace B. Whiting, Eldon R. Larsen, and John M. Prausnitz

Geological studies[1] indicate that there are very large deposits of natural gas in deep geopressured reservoirs in the coastal regions of Louisiana and Texas. This natural gas (mostly methane) is in contact with water or brine at pressures near 100 MPa and temperatures to 200°C. At present, it is not economical to mine these reservoirs; but, in view of the very large deposits, there is much incentive to make such mining economically feasible. This project is concerned with obtaining some of the fundamental physico-chemical information required to do so.

We seek a molecular-thermodynamic method for calculating the high-pressure phase equilibria of aqueous systems containing methane, small amounts of other light hydrocarbons, nitrogen, and carbon dioxide. Toward that end, we have initiated experimental and theoretical research. The latter is to supply a suitable model for interpreting and correlating previously published and new experimental data.

Experimental. We are using a high-pressure static-equilibrium apparatus similar in concept to those described by Schneider.[2] We have constructed a high-pressure cell of Inconel (a nickel-chromium alloy) with a 25 mm inside diameter and an inside height of 330 mm. All surfaces within the system exposed to the methane-water (brine) mixture are of Inconel or type 316 stainless steel.

The cell is charged with a mixture of methane and water (brine). The temperature of the cell is raised by an external, electrical-resistance heating mantle, and the pressure is increased by a hand-operated piston pump. For various temperature-pressure conditions, small (less than 0.1 ml each) samples of both phases (vapor and liquid) are removed after equilibrium is attained. We determine the concentration of salt by either titration or atomic absorption spectrophotometry (depending on the salt concentration).

Equilibrium between the liquid and vapor phases can not be reached unless the contents of the cell are first thoroughly mixed. For this reason, we have constructed a gold-plated, cylindrical mixing magnet that can be periodically driven vertically through the cell contents by external electromagnets.

Our apparatus is designed for temperatures between ambient and 400°C and pressures to 200 MPa. Working within these ranges, we expect to observe the critical region of the methane-water and methane-brine systems. Very little reliable experimental information is available for the former system in this region; none is available for the latter.

Molecular-Thermodynamic Model. We have developed three models for the methane-water system. For each model, we have derived a partition function from which we can calculate the fluid-phase equilibria.

(1) The perturbed-hard-chain theory of Beret, Donohue, and Prausnitz[3,4] for fluid mixtures of nonpolar compounds has been extended to include water by splitting the potential-energy parameter for water into a nonpolar part (from the spherically-symmetric portion of the potential) and a polar part (from the orientation-dependent portion of the potential). The latter is approximately proportional to the inverse of the absolute temperature.

(2) By superimposing a chemical dimerization hypothesis on the perturbed-hard-chain theory, Gmehling et al.[5] developed a model that is reasonably accurate for calculating the phase equilibria of polar fluids. In this model, the strong orientational forces between polar molecules are accounted for by postulating the existence of dimers in equilibrium with the monomers. Whiting and Prausnitz[6] extended this idea to water by considering not only water dimers but trimers, tetramers, and all higher-order j-mers. We have extended the dimerization model to methane-water mixtures.

(3) By considering the nonrandomness of polar fluids, we have developed a local-composition theory, which we are applying to the methane-water system. This theory is more fully explained in article 2 below.

Methods 1 and 2 above show semi-quantitative agreement with the limited experimental data now available for methane-water. Method 3, the

*This work was supported by the Director, Office of Energy Research, Office of Basic Energy Sciences, Chemical Sciences Division of the U. S. Department of Energy under Contract No. W-7405-ENG-48.

local-composition theory, shows better quantitative agreement; we expect to develop it more fully.

Once we have a satisfactory model for methane-water, we expect to allow for salt effects by incorporating some of the work of Pitzer[8] on aqueous salt solutions.

* * *

1. R. H. Wallace, Jr., T. F. Kraemer, R. E. Taylor, and J. B. Wesselman, "Assessment of Geopressured Resources in the Northern Gulf of Mexico Basin," in U. S. Geological Survey Circular 790, 1978.
2. G. M. Schneider, Chapter 16, Part 2, in Experimental Thermodynamics, Volume II, edited by B. Le Neidre and B. Vodar, Butterworths, London, 1975.
3. S. Beret and J. M. Prausnitz, AIChE J. 21, 1123 (1975).
4. M. D. Donohue and J. M. Prausnitz, AIChE J. 24, 849 (1978).
5. J. Gmehling, D. D. Liu, and J. M. Prausnitz, Chem. Eng. Sci. 34, 951 (1979).
6. W. B. Whiting and J. M. Prausnitz, Proc. Int. Conf. Prop. Steam, 9th, Munich, 83 (1979), LBL-9571.
7. W. B. Whiting and J. M. Prausnitz, paper presented at the Sixth West Coast Statistical Mechanics Conference, San Jose, California, June 1980.
8. K. S. Pitzer, Accounts of Chem. Res. 10, 371 (1977).

2. MODIFICATIONS OF GENERALIZED VAN DER WAALS THEORY FOR MIXTURES

Wallace B. Whiting, Eldon R. Larsen, and John M. Prausnitz

The generalized van der Waals theory has been the most useful theory of fluids for engineering purposes. The simplicity of the resulting partition function far outweighs, in most cases, the inaccuracies caused by the assumption that the intermolecular potential can be separated into a hard-sphere repulsive part and a simple attractive part. However, in three regions the generalized van der Waals theory, as presently used, becomes significantly inaccurate. We have focused our attention on these three regions.

Low-Density Region. In the low-density region, the common assumption of random mixing, or uniform density, is not valid. Because almost all equations of state are based on the random-mixing assumption, they predict second-virial coefficients that are consistently too positive. We have used this observation to develop an empirical correction[1,2] to the partition function that enables reproduction of the experimental second-virial-coefficient data but does not affect properties far from the zero-density limit. This correction can be applied to any partition function of the van der Waals form for pure components and for mixtures.

Another approach to the low-density-region problem is to improve the attractive part of the partition function directly. We have recently[3] started using the discrete distribution approximation of Barker and Henderson[4] to close the standard perturbation expansion of Zwanzig[5] after the first two terms. Previously (as in the perturbed-hard-chain theory,[6,7] we truncated the perturbation expansion after the first four terms given by Alder et al.[8] We have found, however, that the two-term closed series is essentially equal to the four-term expansion at high densities and far superior to it in the low-density, second-virial-coefficient region. This theoretical technique is preferred to the empirical method above but cannot be applied to equations of state other than those based on perturbation theory.

Critical Region. No generalized van der Waals equation of state fits pure-component vapor-liquid-equilibria data near the critical point if the adjustable parameters are evaluated from data away from the critical region. We have examined this problem using several equations of state and have decided to proceed with the closed-series perturbation-theory equation described above. Our approach is to correct the Helmholtz energy predicted by the equation of state in the critical region to reproduce the known values for methane. We determined such a correction function and are now studying the relationship between the values of the adjustable parameters in the equation of state and the size of the necessary critical-region correction. Once we have determined the optimum correction function, we hope to be able to apply it to any equation of state of the van der Waals form for pure components and for mixtures.

Asymmetric Mixtures. The poor (although common) assumption of random mixing is particularly bad for asymmetric mixtures, in which the molecules of the two (or more) components vary greatly in size and/or intermolecular potential. For such mixtures, homogeneity is not attained; local concentrations differ from overall concentrations. For a binary mixture, we propose a two-fluid theory[3] in which the local compositions are related to the overall compositions with Boltzmann factors of the intermolecular energies of the local configurations. This idea was first proposed by Guggenheim[9] for liquids but has never before been applied to fluids of all densities. By using local surface fractions (rather than local mole fractions), we take into account differences in molecular size, and, by using the Boltzmann factors, we take into account differences in intermolecular potentials. Our initial success with the local-composition theory (for the methane-water system) is promising.

Our local-composition theory can be used in any generalized van-der-Waals equation of state and can be applied to multicomponent mixtures in a straight-forward manner.

* * *

1. W. B. Whiting and J. M. Prausnitz, Proc. Int. Conf. Prop. Steam, 9th, Munich, 83 (1979), LBL-9571.
2. A. I. El-Twaty, Ph.D. thesis, University of California, Berkeley, 1979.

3. W. B. Whiting and J. M. Prausnitz, paper presented at the Sixth West Coast Statistical Mechanics Conference, San Jose, California, June 1980.
4. J. A. Barker and D. Henderson, Rev. Mod. Phys. 48, 587 (1976).
5. R. W. Zwanzig, J. Chem. Phys. 22, 1420 (1954).
6. S. Beret and J. M. Prausnitz, AIChE J. 21, 1123 (1976).
7. M. D. Donohue and J. M. Prausnitz, AIChE J. 24, 849 (1978).
8. B. J. Alder, D. A. Young, and M. A. Mark, J. Chem. Phys. 56, 3013 (1972).
9. E. A. Guggenheim, Proc. Roy. Soc. A 148, 304 (1935).

3. CALCULATION OF FLUID-PHASE EQUILIBRIA FROM EQUATIONS OF STATE

Wallace B. Whiting, Robert J. Topliss, and John M. Prausnitz

The vital connection between molecular-thermodynamic research and the industrial use of that research is the computer program. Without an efficient and robust algorithm for calculation of fluid-phase equilibria from any equation of state, technology transfer to the industrial sector is nearly impossible. We are developing two different types of algorithms for calculation of fluid-phase equilibria.

Free-Energy Minimization. At equilibrium, the chemical potential of each species must be the same in all phases. The direct use of this fact in phase-equilibrium calculation is known as free-energy minimization. If the true, global minimum of the free energy is found, the phase-equilibrium problem is, by definition, solved. In this calculation, material balance is assumed.

One of the best algorithms we have found is that of Michelsen.[1] This free-energy minimization technique alleviates the two most common problems with phase-equilibria algorithms: slow convergence, or no convergence, (1) for poor initial guesses and (2) in the critical region. We have used the techniques of Michelsen to devise computer programs that can be used for any equation of state and for any combination of thermodynamic constraints.

Material Balance. Conservation of mass is the concept behind material-balance algorithms. In this calculation, phase equilibrium is assumed (equal chemical potentials in all phases), and the compositions of all components in each phase are calculated. There are multiple criteria for convergence: for each phase the sum of the mole fractions of the species must be unity. The algorithm varies a thermodynamic variable (e.g., temperature or pressure) until these criteria are achieved.

The free-energy-minimization approach differs from the material-balance approach because, in the former, mass conservation is assumed and the equality of chemical potentials is to be achieved.

We are developing a material-balance algorithm that can be used with any equation of state to calculate the three-phase (vapor-liquid-liquid) equilibria of asymmetric mixtures. Reliable heuristics for calculating initial guesses and reliable methods for detecting degenerate three-phase (e.g., two-phase) equilibria have been developed and incorporated into our computer programs.

* * *

1. M. L. Michelsen, Fluid Phase Equil. 4, 1 (1980).

RESEARCH PLANS FOR CALENDAR YEAR 1981

During 1981, we expect to obtain experimental data for methane-water and methane-brine phase equilibria using our high-pressure apparatus. We also expect to develop further our local-composition theory for asymmetric mixtures, our critical-region and low-density region corrections to the generalized van der Waals partition function, and our computer algorithms for calculating multiphase, multicomponent fluid-phase equilibria from equations of state.

1980 PUBLICATIONS AND REPORTS

Refereed Journals

1. C. G. Van de Rostyne and J. M. Prausnitz, "Vapor Pressures of Some Nitrogen-Containing, Coal-Derived Liquids," J. Chem. Eng. Data 25, 1 (1980).

†2. G. Miller, C. J. Radke, and J. M. Prausnitz, "Adsorption of Weak Organic Electrolytes from Aqueous Solution on Activated Carbon," J. Phys. Chem. 84, 369 (1980).

‡3. A. Landauer, R. N. Lichtenthaler, and J. M. Prausnitz, "Mutual Solubilities of Alkanes and Methyl Cellosolve," J. Chem. Eng. Data 25, 152 (1980).

§4. T. F. Anderson and J. M. Prausnitz, "Computational Methods for High-Pressure Phase Equilibria and Other Fluid-Phase Properties Using a Partition Function. 1. Pure Fluids," Ind. Eng. Chem. Proc. Des. Develop. 19, 1 (1980).

§5. T. F. Anderson and J. M. Prausnitz, "Computational Methods for High-Pressure Phase Equilibria and Other Fluid-Phase Properties Using a Partition Function. 2. Mixtures," Ind. Eng. Chem. Proc. Des. Develop. 19, 9 (1980).

§6. D. D. Liu and J. M. Prausnitz, "Calculation of Phase Equilibria for Mixtures of Ethylene and Low-Density Polyethylene at High Pressures," Ind. Eng. Chem. Proc. Des. Develop. 19, 205 (1980).

†7. H. Lazalde-Crabtree, G. J. F. Breedveld, and J. M. Prausnitz, "Solvent Losses in Gas Absorption. Solubility of Methanol in Compressed Natural and Synthetic Gases," AIChE J. 26, 462 (1980).

‖8. B. K. Kaul, M. D. Donohue, and J. M. Prausnitz, "Henry's Constants and Second Virial Coefficients from Perturbed-Hard-Chain Theory," Fluid Phase Equil. 4, 171 (1980).

†9. W. Merk, R. N. Lichtenthaler, and J. M. Prausnitz, "Solubilities of Fifteen Solvents in Copolymers of Poly(vinyl acetate) and Poly(vinyl chloride) from Gas-Liquid Chromatography. Estimation of Polymer Solubility Parameters," J. Phys. Chem. 84, 1694 (1980).

¶10. A. I. El-Twaty and J. M. Prausnitz, "Correlation of K-Factors for Mixtures of Hydrogen and Heavy Hydrocarbons," Chem. Eng. Sci. 35, 1765 (1980).

Other Publications

‡1. J. M. Prausnitz, T. F. Anderson, E. A. Grens, C. A. Eckert, R. Hsieh, and J. P. O'Connell, Computer Calculations for Multicomponent Vapor-Liquid and Liquid-Liquid Equilibria, Prentice-Hall, Englewood Cliffs, NJ (1980).

†2. P. J. Hicks, Jr., "The Solubility of Acetone and Isopropyl Ether in Compressed Nitrogen, Methane, and Carbon Dioxide," M. S. thesis, Department of Chemical Engineering, University of California, Berkeley (1980).

3. D. R. Edwards, "Vapor Pressures of Coal-Related Liquids," M. S. thesis, Department of Chemical Engineering, University of California, Berkeley (1980).

4. C. R. Gonzalez-Yradier, "Vapor-Liquid Equilibrium of High-Boiling Petroleum Fractions," M. S. thesis, Department of Chemical Engineering, University of California, Berkeley (1980).

**5. G. Lobien, "Activity Coefficients at Infinite Dilution for Partially Miscible Liquid Systems," Ph.D. thesis, Department of Chemical Engineering, University of California, Berkeley (1980).

Invited Talks

1. J. M. Prausnitz, "State-of-the-Art Review of Phase Equilibria," Keynote Lecturer, Second International Conference on Phase Equilibria and Physical Properties for the Chemical Industry, West Berlin, Germany, March 1980, LBL-10767.

2. J. M. Prausnitz, Wilhelm Lecturer, Chemical Engineering Department, Princeton University, Princeton, NJ, April 1980.

3. W. B. Whiting and J. M. Prausnitz, "A Perturbed-Hard-Sphere, Local-Composition Model for Liquid Mixtures," Sixth West Coast Statistical Mechanics Conference, San Jose, CA, June 1980.

4. D. Edwards, C. G. Van de Rostyne, J. Winnick, and J. M. Prausnitz, "Estimation of Vapor Pressures of High-Boiling Fractions in Liquefied Fossil Fuels Containing Heteroatoms Nitrogen or Sulfur," Second Chemical Congress of the North American Continent, Las Vegas, NV, August 1980.

5. J. M. Prausnitz, Phillips Petroleum Company Research Laboratories, Bartlesville, OK, October 1980.

6. J. M. Prausnitz, Centennial Lecturer, Chemical Engineering Department, Louisiana State University, Baton Rouge, LA, November 1980.

* * *

†Supported in part by the Deutsche Forschungsgemeinschaft (administered by the Technical University of Berlin).

‡Supported in part by the Department of Chemical Engineering, University of California, Berkeley.

§Supported in part by the Petroleum Research Fund (administered by the American Chemical Society).

‖Supported in part by the Gas Processors Association.

¶Supported in part by a fellowship from the government of the Libyan Arab Republic.

**Supported in part by the National Science Foundation.

A. Low-Energy Nuclear Sciences

1. Heavy Element Chemistry

a. Actinide Chemistry*

Norman M. Edelstein, Richard A. Andersen, Neil Bartlett, John G. Conway, Kenneth N. Raymond, Glenn T. Seaborg, Andrew Strietwieser, Jr., David H. Templeton, and Alan Zalkin, Investigators

Specific Sequestering Agents for the Actinides

1. SYNTHESIS OF AND ^{238}Pu(IV) REMOVAL FROM MICE BY CARBOXYLATE CATECHOYL AMIDES

F. L. Weitl, K. N. Raymond and P. W. Durbin

Generation of electricity in nuclear reactors and application of actinide elements as heat, power, ion, and radiation sources make the actinides important industrially. The biological hazard of nuclear fuels and their actinide byproducts and wastes is a major concern of the nuclear industry. In general, inhaled soluble actinide compounds may be transported into the body, and inhaled insoluble actinide compounds tend to be retained in the lung. Excretion of actinides deposited in all those sites is ordinarily slow; and promotion of excretion from the body is, therefore, essential treatment for actinide contamination.

The search for ways to remove actinides from the body began soon after the first reactor-produced plutonium was separated. Diethylenetriaminepentaacetic acid (DTPA) was synthesized and tested in 1957. DTPA is not an ideal ligand for tetravalent actinides; it does not form a complete 1:1 chelate with Pu(IV) at pH 7; and it forms stable chelates with several biologically essential metals [Ni(II), Zn(II), and Fe(III)]. There is a strong chemical and biochemical similarity between Pu(*IV*) and Fe(*III*); 2,3-Dihydroxybenzoic acid (DHBA, Fig. 1) is a low toxicity monomer, and when given orally or parenterally, DHBA enhances excretion of iron from chronically transfused animals. Those observations suggested that CAM ligands containing carboxyl ($-CO_2H$) groups might be as effective for Pu(IV) binding as the sulfonated analogues and less toxic. Several CAMC ligands (Figs. 2,3) have been designed and synthesized. The functional group of these derivatives of terephthalic acid is p-substituted DHBA; and, in our abbreviated nomenclature, they are designated CAMC compounds. They are otherwise identical to the prototype CAM ligands, and the DHBA units are connected by amide linkages to linear or cyclic alkane backbones.

Several synthetic macromolecular CAMC ligands, some structurally related monomers, and four sulfonated CAM ligands (CAMS) have been tested for their ability to promote Pu(IV) excretion in mice. The structures of the compounds are shown in Figs. 2-7, and the results of the 24-hr Pu(IV) excretion tests are collected in Table 1. Overall, the CAMC ligands promote more Pu(IV) excretion than their sulfonated analogues. The linear tetramer, 3,4,3-LICAMC, elicits excretion of 70% of newly injected Pu(IV). The effectiveness of the cyclic ligands, 3,3,3,3-CYCAMC, is much greater than its sulfonated analogue. The trimer, 3,4-LICAMC, which cannot fully coordinate with Pu(IV), still is capable of promoting about 50% excretion of Pu(IV). A sample of 3,4,3-LICAMC was sent to the University of Utah. The experimental conditions were the same as for the test of 3,4,3-LICAMS. In two dogs, retention of Pu(IV) at seven days was 11.8%, somewhat less than after treatment with the sulfonated compound.

There is a major qualitative difference in the biological actions of the carboxylated and sulfonated CAM ligands. No CAMS ligand appeared to be capable of removing Pu from the liver or improving biliary excretion of Pu. In marked contrast, 3,4,3-LICAMC appears to be capable of accelerating elimination of Pu(IV) from the mouse liver, via biliary excretion, to a greater degree than an equimolar amount of $CaNa_3DTPA$. (Compare the amounts of Pu in liver, GI tract, and feces for DTPA and the two CAM ligands shown in Table 2.) The degree of acceleration by 3,4,3-LICAMC of biliary elimination of Pu from the liver of the mouse, and promotion of elimination of Pu from the liver of an animal that ordinarily retains it remain to be investigated.

The dosage-effectiveness of 3,4,3-LICAMC was studied, and the results are shown in Fig. 8, compared to curves for 3,4,3-LICAMS and $CaNa_3DTPA$. The stoichiometry of the Pu(IV)-LICAMC chelate is believed to be 1:1, and although the curve for 3,4,3-LICAMC lies close to the 3,4,3-LICAMS curve, 3,4,3-LICAMC is more concentration dependent, in agreement with the expectation that some 3,4,3-LICAMC may be lost to competition with other metals.

Two preliminary tests have been made of the toxicity of 3,4,3-LICAMC: (a) A 5-day acute toxicity test was extended to 20 injections of 30 μmole/kg/injection in 28 days. The treated mice gained weight at the same rate as controls, and no tissue changes were visible at autopsy. Histological preparations have not been examined.

*This work was supported by the Director, Office of Energy Research, Office of Basic Energy Sciences, Nuclear Sciences Division of the U. S. Department of Energy under Contract No. W-7405-ENG-48

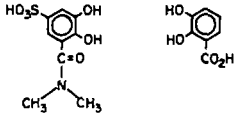

Fig. 1. Abbreviation	Molecular formula (weight)	IUPAC name
DiMCAMS	$C_9H_{11}NO_5S \cdot 2.5H_2O$ (305.3)	N,N-dimethyl-2,3-dihydroxy-5-sulfobenzamide
2,3-DHB	$C_7H_6O_4$ (154.1)	2,3-dihydroxybenzoic acid (XBL 8012-13611)

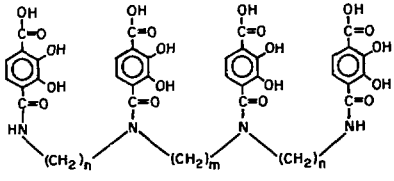

Fig. 2. Abbreviation	m,n	Molecular formula	Weight	IUPAC name
3,4,3-LICAMC	3,4	$C_{42}H_{42}N_4O_{20} \cdot 3H_2O$	980	N^1,N^5,N^{10},N^{14}-tetra(2,3-dihydroxy-4-carboxybenzoyl)-tetraazatetradecane (XBL 8012-13615)

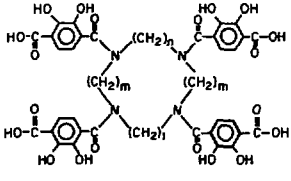

Fig. 3. Abbreviation	l,m,n	Molecular formula	Weight	IUPAC name
3,3,3,3-CYCAMC	3,3,3	$C_{44}H_{44}N_4O_{20} \cdot 2.5H_2O$	994	N^1,N^5,N^9,N^{13}-tetra(2,3-dihydroxy-4-carboxybenzoyl)-tetraazacyclohexadecane (XBL 8012-13616)

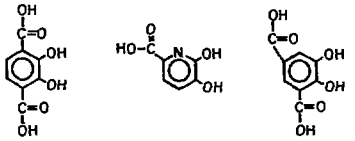

DHTA DHPA DHIPA

Fig. 4.

Abbreviation	Molecular formula	Weight	IUPAC name
DHTA	$C_8H_4O_6Na_2$	242	Disodium-2,3-dihydroxyterephthlate
DHPA	$C_6H_4NO_4Na$	177	Sodium-2,3-dihydroxy-6-pyridine carboxylate
DHIPA	$C_8H_6O_6 \cdot H_2O$	216	2,3-dihydroxyisophthalic acid

(XBL 8012-13612)

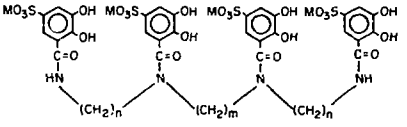

Fig. 5.

Abbreviation	M	n	m	Molecular formula	IUPAC name
2,3,2-LICAMS	K	2	3	$C_{37}H_{42}N_4O_{24}S_4K_4 \cdot 3H_2O$	N^1,N^4,N^8,N^{11}-tetrat(2,3-dihydroxy-5-sulfobenzoyl)-tetraazaundecane
3,3,3-LICAMS	Na	3	3	$C_{37}H_{46}N_4O_{24}S_4Na_4 \cdot 2H_2O \cdot {}^1/_4Na_2SO_4$	N^1,N^5,N^9,N^{13}-tetrat(2,3-dihydroxy-5-sulfobenzoyl)-tetraazatridecane
4,4,4-LICAMS	Na	4	4	$C_{40}H_{52}N_4O_{24}S_4Na_4 \cdot 4H_2O \cdot {}^1/_2Na_2SO_4$	N^1,N^6,N^{11},N^{16}-tetrat(2,3-dihydroxy-5-sulfobenzoyl)-tetraazahexadecane
4,3,4-LICAMS	K	4	3	$C_{39}H_{46}N_4O_{24}S_4K_4 \cdot 6H_2O$	N^1,N^6,N^{10},N^{15}-tetrat(2,3-dihydroxy-5-sulfobenzoyl)-tetraazapentadecane
3,4,3-LICAMS	Na	3	4	$C_{38}H_{38}N_4O_{20}S_4Na_4 \cdot 6.5H_2O$	N^1,N^5,N^{10},N^{14}-tetrat(2,3-dihydroxy-5-sulfobenzoyl)-tetraazatetradecane

(XBL 8012-13609)

(b) The test at the University of Utah of efficiency of Pu removal in dogs was accompanied by clinical tests of renal function, a gross autopsy, and preparation of sections for histology. The clinical tests yielded normal values, there were no grossly visible tissue lesions at autopsy, and the microscopic anatomy of the kidneys was normal.

The CAMC ligands appear to have achieved both major design goals - they are as effective for in vivo chelation and promotion of Pu(IV) excretion as the sulfonated analogues, and they are significantly less toxic.

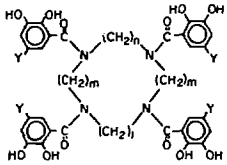

Fig. 6.

Abbreviation (Y)	l,m,n	Molecular formula	IUPAC name
3,3,3,3-CYCAM(H)	3,3,3	$C_{30}H_{30}N_4O_{12}\cdot 2H_2O$	N^1,N^5,N^9,N^{13}-tetra(2,3-dihydroxybenzoyl)-tetraazacyclohexadecane
2,3,3,3-CYCAM(SO_3Na)	2,3,3	$C_{30}H_{29}N_4O_{24}S_4Na_4\cdot 2H_2O$	N^1,N^4,N^8,N^{12}-tetra(2,3-dihydroxy-5-sulfobenzoyl)tetraazacyclopentadecane
3,3,3,3-CYCAM(SO_3Na)	3,3,3	$C_{30}H_{28}N_4O_{24}S_4Na\cdot 5H_2O$	N^1,N^5,N^9,N^{13}-tetra(2,3-dihydroxy-5-sulfobenzoyl)tetraazacyclohexadecane
2,3,2,3-CYCAM(NO_2)	2,3,2	$C_{28}H_{26}N_8O_{20}\cdot 2H_2O$	N^1,N^4,N^8,N^{11}-tetra(2,3-dihydroxy-5-nitrobenzoyl)-tetraazacyclotetradecane (XBL 8012-13610)

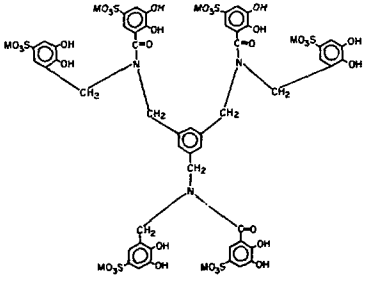

DiMECAMS

Fig. 7.

Abbreviation	Molecular formula	Weight	IUPAC name
DiMECAMS	$C_{51}H_{39}N_3O_{33}S_6Na_6\cdot 6H_2O$	1660	N,N',N''-tris(2,3-dihydroxy-5-sulfbenzyl)-N,N',N''-tris(2,3-dihydroxy-5-sulfobenzoyl)-1,3,5-triamiomethylbenzene

(XBL 8012-13615)

Table 1. Effect of catechoylamide sulfonates and carboxylates and related compounds on retention of $^{238}Pu(IV)$ in the mouse.[a,b]

	^{238}Pu excreted (% of dose)	Figure No.
Sulfonated CAM compounds		
3,4,3-LICAMS	65	5
Diisopropyl, 3,4,3-LICAMS	44	5
3,3,3,3-CYCAMS	35	6
DMECAMS	17	7
3,4,3-LISAMS	6.2	
Carboxyl CAM compounds		
3,4,3-LICAMC	69	2
3,3,3,3-CYCAMC	59	3
3,4-LICAMC	54	2
Poly-LICAMC	37	2
DHBA[b]	3.5	1
DHTA[b]	9.7	4
DHPA[b]	9.0	4
DHIPA[b]	5.3	4

[a]Ligands were administered (i.p.) 1 hr and mice were killed 24 hr after injection (i.v.) of ^{238}Pu citrate.

[b]Ligand dosage was 30 μmole/kg except for the monomers, DHTA, DHPA, and DHIPA, for which the dosage was 480 μmole/kg, and DHBA, for which the dosage was 78 μmole/kg.

Table 2. Retention of $^{238}Pu(IV)$ in tissues of mice treated with various chelating agents.[a] Results are expressed as percent of injected dose ± S.D. normalized to 100% recovery.

	Control	$CaNa_3DTPA$	3,4,3-LICAMS	3,4,3-LICAMC	Poly-LICAMC
No. of mice	34	5	5	10	
Tissue					
Liver	51 ± 7.0	17.7 ± 4.4	23.8 ± 7.9	8.7 ± 3.0	29.5 ± 10.7
Skeleton	31 ± 6.3	10 ± 1.4	6.6 ± 1.0	9.7 ± 2.0	10.0 ± 1.0
Soft tissues	5.1 ± 0.8	3.3 ± 1.4	1.9 ± 0.4	2.7 ± 0.9	9.1 ± 1.8
GI(full)	4.6 ± 1.1	5.2 –	2.5 –	8.0 –	11.5 –
Kidneys	2.6 ± 2.6	0.5 –	1.3 –	2.0 –	2.5 –
Excreta	6.1 ± 2.0[c]	63.0[e] –	64.1 –	69.0[b] –	37.1[d] –

[a]Ligands (30 μmole/kg) were injected (i.p.) 1 hr and mice sacrificed 24 hr after $^{238}Pu(IV)$ citrate (i.v.).

[b]For 5 mice urine, 50.2%; feces, 14.1%.

[c]Mean ± S.D. for 7 groups of mice. For 10 of those mice urine, 1.0%; feces, 1.9%.

[d]Urine, 30.5%; feces 7.0%.

[e]Feces, approximately 4% (78).

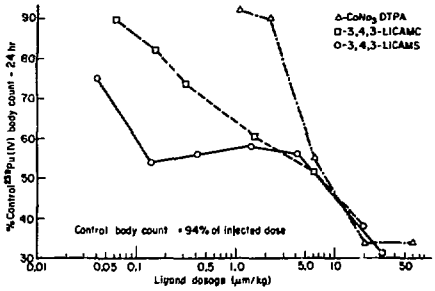

Fig. 8. Effectivensss in adult mouse of a single i.p. injection of test ligand in promoting excretion of ^{238}Pu. Test ligands were injected at 1 hr and excreta collected and body contents measured at 24 hr after i.v. injection of $^{238}Pu(IV)$ citrate. (XBL 8012-13618)

2. THE OXIDATION OF URANIUM(IV) BY N-PHENYLBENZOHYDROXAMIC ACID AND THE STRUCTURE OF THE REACTION PRODUCT: CHLORODIOXO-N-PHENYLBENZO-HYDROXAMATO-BIS(TETRAHYDROFURAN)URANIUM(IV)†

W. L. Smith and K. N. Raymond

Hydroxamic acids have been widely used in the analysis of metal ions because of their powerful coordination as bidentate ligands. The formation constants of hydroxamic acids with actinide ions suggest that these ligands may serve as functional groups in synthetic sequestering agents designed specifically for the tetravalent actinides. Although several actinide(IV) hydroxamates have been formed during solvent extraction or precipitated in gravimetric analyses, the few complexes which have been isolated involve Th(IV). In order to explore the feasibility of benzohydroxamic acids as sequestering agents for Pu(IV) and U(IV), the coordination properties of N-phenylbenzohydroxamic acid (PBHA) with U(IV) have been investigated. Instead of simple coordination, the hydroxamic acid oxidizes U(IV) to UO_2^{2+} forming the title compound and benzanilide.

The addition of a 4:1 mole excess of PBHA anion with U(IV) led to the formation of $UO_2Cl(PBHA)(THF)_2$, 1, via the reaction:

$$U(IV) + 3PhC(O)N(O)Ph^- + Cl^- + 2THF + 2H^+ \rightarrow UO_2Cl[PhC(O)N(O)Ph](THF)_2 + 2PhC(O)NHPh \quad (1)$$

The uranyl complex has been identified by elemental analysis, electronic and vibrational spectra and x-ray diffraction. The molecular structure of 1 is shown in Figs. 9 and 10.

The oxidation of uranium(IV) to uranyl occurred under anhydrous, anaerobic conditions. The isolation of benzanilide established that PBHA was reduced to its corresponding amide, to complete

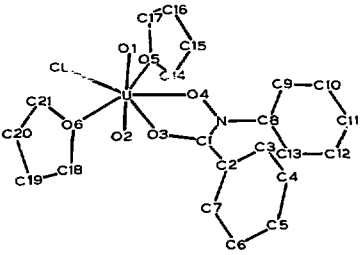

Fig. 9. Molecular geometry of $UO_2Cl(PBHA)(THF)_2$. (XBL 783-7435)

the redox couple. No other reductions of hydroxamic acids by metal ions have been characterized. Lutwick and Ryan observed the oxidation of V(II) to V(IV), Ti(III) to Ti(IV) and Sn(II) to Sn(IV) by several hydroxamic acids in dilute aqueous solution. However, they did not take special precautions against oxygen and it was later shown that oxygen was responsible for the oxidation of Sn(II) and not the hydroxamic acids. Considering the following aqueous reduction potentials:

$$UO_2^{2+} + 4H^+ + 2e^- \rightarrow U^{4+} + 2H_2O; \quad \varepsilon° = 0.32\ V$$

$$VO^{2+} + 2H^+ + e^- \rightarrow V^{3+} + H_2O; \quad \varepsilon° = 0.34\ V$$

$$TiO^{2+} + 2H^+ + e^- \rightarrow Ti^{3+} + H_2O; \quad \varepsilon° = 0.1\ V$$

and the fact that all metal ions are oxidized to oxo-cations, it seems likely that Ti(III) and V(III) would also reduce PBHA anion in THF via an oxygen transfer reaction.

* * *

†Brief version of LBL-8281; published in J. Inorg. Nucl. Chem. 41, 1431 (1979).

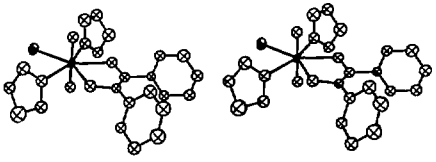

Fig. 10. Stereopair of $UO_2Cl(PBHA)(THF)_2$ with thermal ellipsoids at the 30% probability level. (XBL 782-7191)

3. SULFONATED CATECHOLAMIDE ANALOGUES OF *ENTEROBACTIN*†

F. L. Weitl, W. R. Harris and K. N. Raymond

The treatment of certain genetic diseases, such as β-*thalassemia major* (*Cooley's anemia*), requires chronic transfusion therapy. This produces a secondary hemochromatosis, which eventually results in the failure of vital organs due to buildup of iron in the tissues, and the death of most patients by early adulthood. Since there is no physiological mechanism in man for the removal of iron, the treatment of iron overload must rely on chelating agents which can effect iron excretion, the development of which is now the goal of a major program.[1] We have shown that the siderophore (microbial iron-transport agent) enterobactin (1) is the most powerful ion(*III*) chelating agent known to date. While enterobactin is itself not a suitable candidate for removal of iron from humans, other 2,3-dihydroxybenzoylamides are good possibilities, and we have previously reported the preparation of 1,5,9-N,N',N''-tris(2,3-dihydroxybenzoyl) cyclotriazatridecane (2) and 1,3,5-N,N',N''-tris (2,3-dihydroxybenzoyl)triaminomethylbenzene (3) (Fig. 11). Thermodynamic and biochemical studies of these compounds have shown them to be very powerful chelating agents for ferric ion. Since we have shown that there is a close resemblance of the coordination chemistry of Fe(*III*) and Pu(*IV*), these iron complexing agents are prototypes for Pu(IV) complexing agents.

Sulfonation increases the acidity, resistance to air oxidation, and aqueous solubility of catechols. For these reasons, we expected that sulfonated catecholamide ligands and related catechols would have chelating properties superior to those of the parent compounds. We report here the synthesis (Figs. 12-14) and preliminary evaluation of several sulfonated catechol chelating agents.

The sulfonated tricatecholamides react with ferric ion at pH 7-8 to give deep-red solutions with λ_{max} ~ 480-490 and ε 5000-6000. These values strongly suggest that the ferric ion is coordinated to all six phenoli oxygens of the three dihydroxybenzoyl side groups. As the pH is lowered, the ferric complexes are protonated in discrete one-proton steps to form FeHL, FeH_2L, and FeH_3L complexes. Each successive protonation shifts λ_{max} to longer wavelengths and decreases ε. Similar results have been observed with 3 and 4 and with enterobactin (1).

Proton-dependent metal ligand formation constants have been determined spectrophotometrically by competition with ethylenediaminetetra-acetic acid (Eq. 1). At neutral or basic pH, complexation by the

$$Fe(EDTA)^- + H_6L^{3-} \rightleftharpoons Fe(L)^{6-} + EDTA^{4-} + 6H^+ \qquad (1)$$

catecholamides is strong enough to remove essentially all the iron from $Fe(EDTA)^-$. Thus, it was necessary to measure this equilibrium at pH ~ 5, in order to ensure a detectible distribution of iron between the two ligands.

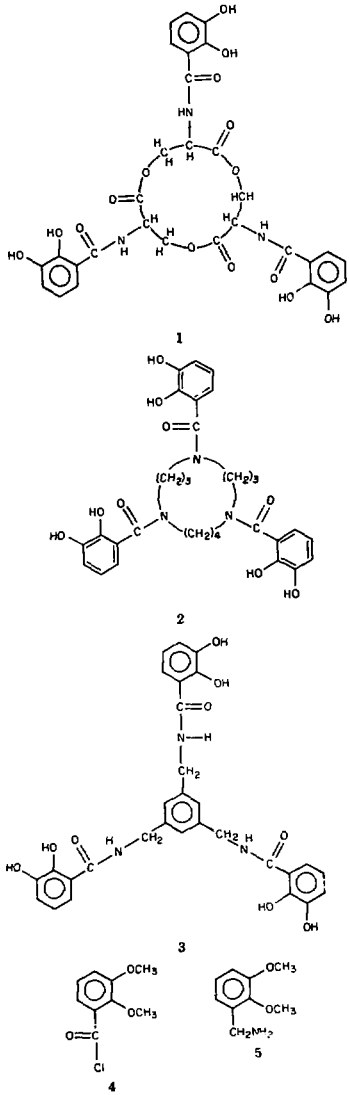

Fig. 11. Previous tricatechol ligands and precursor compounds. (XBL 812-8089)

The proton-dependent formation constants are not the best indicator of the ability of a ligand

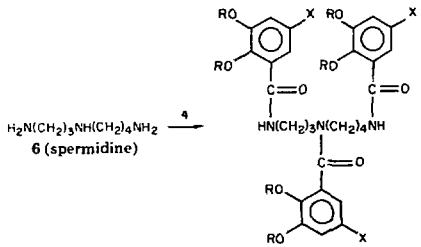

Fig. 12. Synthesis of a linear trimeric sulfocatecholate ligand. (XBL 812-8093)

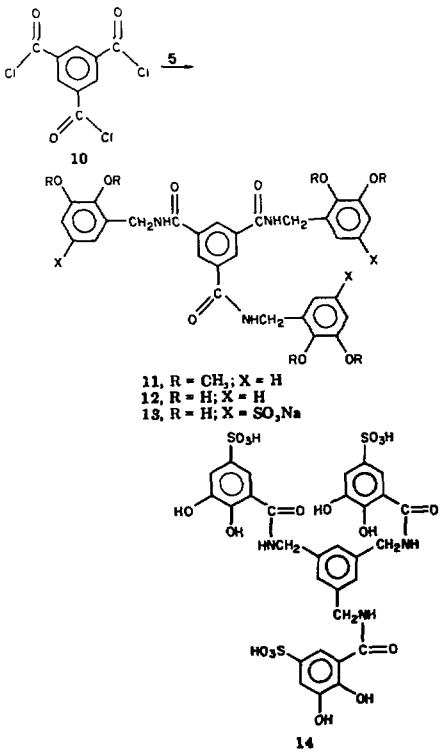

Fig. 13. Synthesis of trimeric sulfocatecholate platform ligands. (XBL 812-8097)

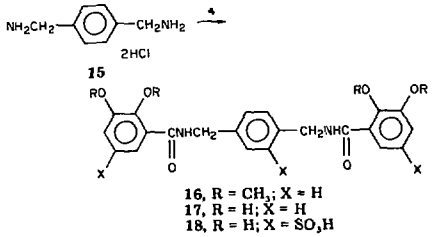

Fig. 14. Synthesis of a dimeric linear sulfocatecholate platform ligand. (XBL 812-8090)

to sequester ferric ion at physiological pH, since these constants do not reflect the competition from hydrogen ion for the very basic phenolic ligating groups. Therefore, we have calculated the equilibrium concentration of $[Fe(H_2O)_6]^{3+}$ in a solution which is 1 μM total iron and 10 μM total ligand at pH 7.4. The results, expressed as pM (pM = -log $[Fe(H_2O)_6]^{3+}$), are shown in Table 3. A comparison of various ligands is now straightforward; i.e., a larger pM denotes a more effective ligand. The pM values of all the tricatecholamides exceed the transferrin pM, indicating that these ligands are thermodynamically capable of removing iron from transferrin. Furthermore, the pM values of 9 and 14 indicate that ligands are several hundred times more effective at sequestering ferric ion than is desferrioxamine B, the current drug of choice for therapeutic iron removal in man.

Thus, we have prepared a new class of ligands which combine several properties needed for an effective iron-removal agent. Like enterobactin, they have an exceptionally high affinity for iron, much higher than transferrin or desferrioxamine B. Unlike enterobactin, they are hydrolytically stable over a wide range of pH. In addition, sulfonation greatly increases the water solubility of

Table 3. pM[a] Values for synthetic catecholamides and pertinent biological iron chelators

Compound	pM
Enterobactin(1)	35.5
14	29.4
3	29.1
9	28.5
Desferrioxamine B	26.6
13	25.1
Transferrin	23.6
N,N-dimethyl-2,3-dihydroxy-5-sulfobenzamide	19.2

[a]Total Fe concentration = 10^{-6} M; total ligand concentration = 10^{-5} M; pH 7.4.

these ligands and stabilizes their dihydroxybenzoyl groups toward air oxidation. Finally, recent studies in this laboratory have shown that, while the hydroxamate ligands such as desferrioxamine B are kinetically unable by themselves to remove iron from transferrin, the catecholate ligands reported here readily remove the iron from this iron-transport protein of human serum.

* * *

†This work was supported in part by the National Institutes of Health under Grant No. HL-24775.

1. W. F. Anderson and M. C. Hiller, Eds., abstracted from J. Med. Chem. 22, 1281 (1979).

Synthetic and Structural Studies of Actinides and Other Compounds

4. PENTAMETHYLCYCLOPENTADIENYL DERIVATIVES OF THE TRIVALENT LANTHANIDE ELEMENTS (NEODYMIUM, SAMARIUM, AND YTTERBIUM)†

T. D. Tilley and R. A. Andersen

The anionic Me_5C_5-derivatives of the trivalent lanthanide elements (Nd, Sm, Yb) have been prepared, as have the neutral trivalent species. The anionic or neutral species are

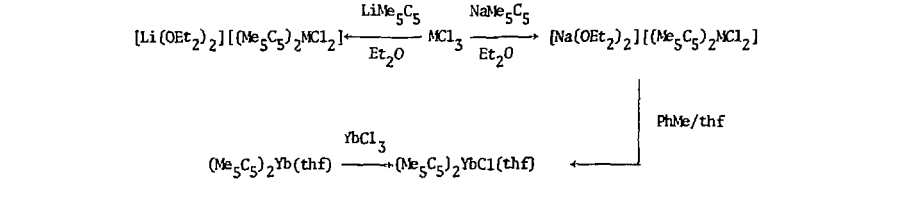

useful starting materials for synthesis of compounds with other functional groups, for example the silylamides:

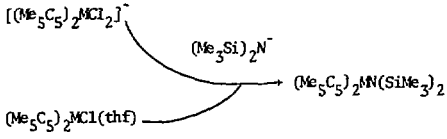

* * *

†Brief version of LBL-11189, submitted to Inorganic Chemistry.

5. ALKYL AND HYDRIDE BIS(TRIMETHYLSILYL)AMIDO DERIVATIVES OF THE ACTINIDE ELEMENTS; PREPRATION AND HYDROGEN-DEUTERIUM EXCHANGE†

S. J. Simpson, H. W. Turner, and R. A. Andersen

Reaction of hydrogen with metal-carbon bonds is an elementary reaction that is fundamental to some catalytic processes, viz., hydrogenation and hydrocarbon activation. This investigation was initiated with the aim of establishing the potential of f-element organometallic compounds in these processes.

The hydride and methyl derivatives of the actinide metals of the type $[(Me_3Si)_2N]_3MR$, where M is thorium or uranium and R is hydride or methyl, undergo γ-elimination of either hydrogen or methane, a hydrocarbon activation process, giving metallocycle I. The mechanism of

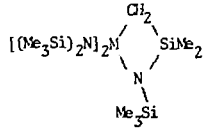

I, M = Th, U

this process can be regarded as a concerted oxidative-addition of the γ-hydrogen atom from a Me_3SiN-group followed by reductive-elimination of hydrogen or methane.

The elimination of hydrogen, but not methyl, is reversible, i.e., addition of hydrogen to I generates the hydride. When deuterium is used in place of hydrogen, the perdeuterodeuteride is formed. The latter reaction is a novel activation

process in which 55 hydrogen atoms are exchanged for deuterium, a reaction with no precedent. The mechanism of this process is shown in the scheme shown below.

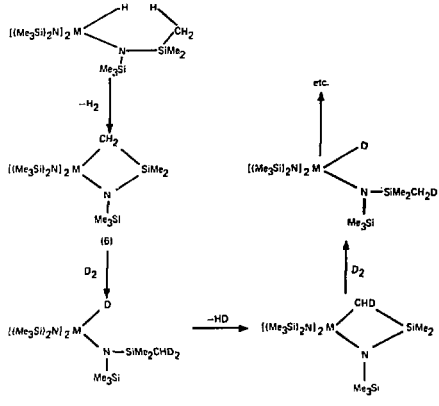

* * *

†Brief version of LBL-11609; submited to J. Am. Chem. Soc.

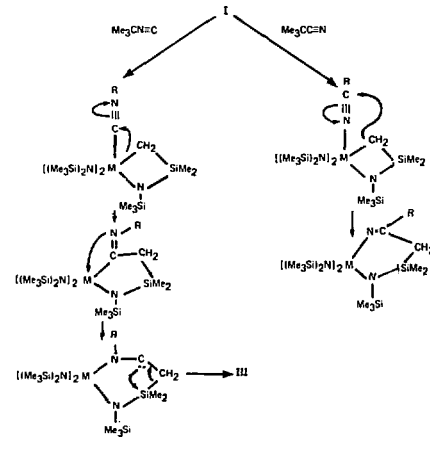

The mechanism of these insertion reactions can be generalized as shown in the scheme below, using $Me_3CC{\equiv}N$ and $Me_3CN{\equiv}C$ as examples.

6. ACTINIDE-CARBON BONDS: INSERTION REACTIONS OF CARBON MONOXIDE, TERT-BUTYLISOCYANIDE, AND TERT-BUTYLCYANIDE INTO $[(Me_3Si)_2N]_2\overline{MCH_2Si(Me)_2NSiMe_3}$†

S. J. Simpson and R. A. Andersen

Insertion of small organic molecules (CO) into metal-carbon bonds is an elementary reaction that is essential to many catalytic processes, i.e., Fischer-Tropsch. This investigation was initiated with the aim of establishing the potential of f-element organometallic compounds in these reactions.

The actinide metallocycles (I) undergo reaction at room temperature with carbon monoxide (20 atm), tert-butylisocyanide, tert-butylcyanide, and trimethylsilylazide to give II, III, IV, and V, respectively, where M is thorium or uranium. Thus, carbon monoxide and tert-butylisocyanide yield products formally derived from insertion of these isoelectronic, 1,2-dipolar molecules into the carbon-silicon bond of metallocycle I. In contrast, tert-butylcyanide yields a product derived from insertion into the actinide-carbon bond of I. The 1,3-dipolar species, Me_3SiN_3, yields a simple coordination complex.

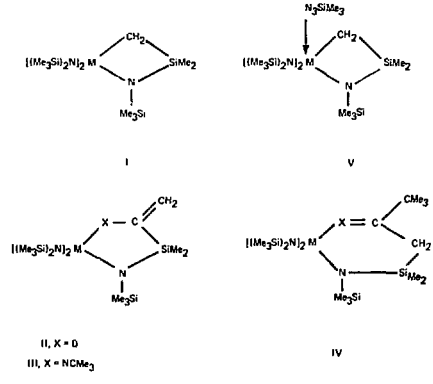

* * *

†Brief version of LBL-11730; submitted to Journal of American Chemical Society.

7. DIVALENT LANTHANIDE CHEMISTRY; BIS(PENTAMETHYLCYCLOPENTADIENYL) EUROPIUM(II) AND YTTERBIUM(II) DERIVATIVES: CRYSTAL STRUCTURE OF BIS(PENTAMETHYLCYCLOPENTADIENYL)YTTERBIUM(II) TETRAHYDROFURAN HEMI (TOLUENE) AT 176 K†

T. Don Tilley, Richard A., Andersen, Brock Spencer, Helena Ruben, Allan Zalkin and David H. Templeton

In contrast to the reasonably extensive literature associated with trivalent lanthanide organometallic compounds, the divalent oxidation state of these metals has largely been ignored, except for complexes with the cyclopentadienyl ion.[1-5] We have now prepared some coordination complexes of europium(II) and ytterbium(II) with pentamethylcyclopentadienyl and have determined the crystal structure of one of them.

Addition of three molar equivalents of sodium pentamethylcyclopentadienide to europium trichloride in refluxing tetrahydrofuran yields the divalent species, $(Me_5C_5)_2Eu(THF)(OEt_2)$ upon crystallization from diethyl ether. In contrast, the mono-tetrahydrofuran complex, $(Me_5C_5)_2Eu(THF)$, is obtained when toluene is used as a solvent of crystallization. These two compounds can be interconverted, e.g., crystallization of the mono-tetrahydrofuran complex from diethyl ether yields $(Me_5C_5)_2Eu(THF)(Et_2O)$, whereas crystallization of the latter complex from toluene yields $(Me_5C_5)_2Eu(THF)$.

The magnetic moment of $(Me_5C_5)_2Eu(THF)(OEt_2)$, $\mu_B = 7.99$ B.M., follows Curie behavior from 5 to 50 K. This behavior is consistent with the $^8S_{7/2}$ ground state expected for a europous (f^7) ion.

The divalent ytterbium derivative, $(Me_5C_5)_2Yb(THF)$, is most readily prepared from sodium pentamethylcyclopentadienide and ytterbium dichloride in refluxing tetrahydrofuran. If diethyl ether is used as crystallization solvent, green $(Me_5C_5)_2Yb(OEt_2)$ and red $(Me_5C_5)_2Yb(THF)$ are isolated by fractional crystallization. If toluene is used for crystallization, $(Me_5C_5)_2Yb(THF) \cdot 1/2\ PhMe$ is isolated.

The divalent ytterbium(II) species (f^{14}) is vigorously diamagnetic (from 5 K to 50 K), as expected for a $^1S_0$ ground state ytterbous ion, and normal, diamagnetic ^1H and $^{13}C\{^1H\}$ nuclear magnetic resonance parameters are observed. However, the proton chemical shift of the methyl resonance of the Me_5C_5 group is temperature dependent, ranging from δ 1.98 at 80°C to δ 2.19 at -50°C. The tetrahydrofuran resonances are also temperature dependent; between 80° and -50°C the α-protons range from δ 4.02 to δ 3.30 and the β-protons range from δ 1.81 to δ 1.32.

Crystals of bis(pentamethylcyclopentadienyl) ytterbium(II) (tetrahydrofuran) (hemi-toluene) are monoclinic, space group $P2_1/n$ with cell dimensions $a = 11.358(8)$ Å, $b = 21.756(19)$ Å, $c = 10.691(7)$ Å, $\beta = 101.84(5)°$, and $V = 2585.6$ Å^3 at 176(5) K. With $Z = 4$ and a molecular weight of 533.62 g mol^{-1}, the calculated density is 1.37 g cm^{-3}.

The molecular structure was determined by single crystal x-ray diffraction methods. The three-fold coordination of the Yb(II) ion is planar with the ytterbium Cp(centroid) average distance of 2.37 Å and an angle between the centroids of the two Cp-rings of 144°. In addition, the average Cp-Yb-O angle is 108°, giving approximate C_2 symmetry about the Yb-O axis, as can be seen in Fig. 15. The approximate C_2 symmetry is carried further in the THF molecule and in the staggered conformation of the C_5Me_5 groups (see Fig. 16). The Cp-rings are planar and normal to the Yb-Cp axis in both cases as indicated by the lack of significant systematic variation in Yb-C (ring) distances. The methyl groups, however, are bent out of the plane of each Cp-ring away from the Yb(II) ion with the largest deviation in each ring (0.18 Å for C(9) and 0.21 Å for C(17)) occurring for those methyl groups with the closest intramolecular contacts. Otherwise, the C_5Me_5-groups have normal geometry. The THF molecule is probably disordered since the rms amplitudes of displacement for C(22) and C(23) are much larger than for other carbon atoms and are highly anisotropic. Such disorder is normal for THF molecules.[6] The toluene molecule is not coordinated to the Yb atom and resides in this structure in a disordered fashion as shown in Fig. 17.

* * *

†Brief version of LBL-10490; Inorg. Chem. 19, 2999 (1980).

1. T. J. Marks, Prog. Inorg. Chem. 24, 51 (1978).
2. E. O. Fischer, H. Fischer, J. Organomet. Chem. 3, 181 (1965).
3. R. G. Hayes, J. L. Thomas, Inorg. Chem. 8, 2521 (1969).
4. F. Calderazzo, R. Pappalardo, S. Losi, J. Inorg. Nucl. Chem. 28, 987 (1966).
5. G. W. Watt, E. W. Gillon, J. Am. Chem. Soc. 91, 775 (1969).
6. R. R. Rietz, et al., Inorg. Chem. 17, 658 (1978) and references therein.

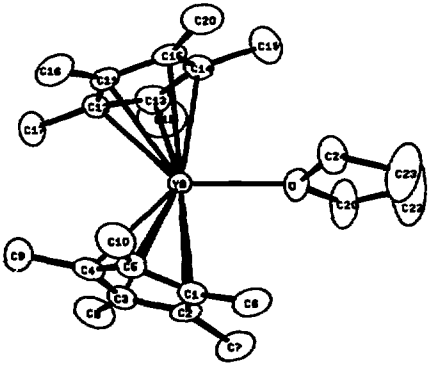

Fig. 15. ORTEP diagram showing atom numbering. (XBL 799-11775)

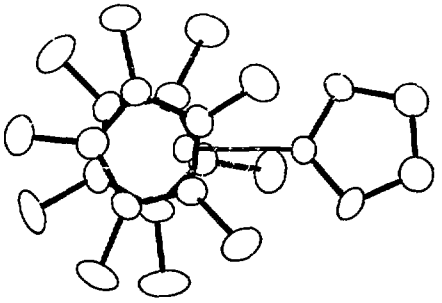

Fig. 16. ORTEP diagram showing the staggered configurations of the Cp rings. (XBL 799-11777)

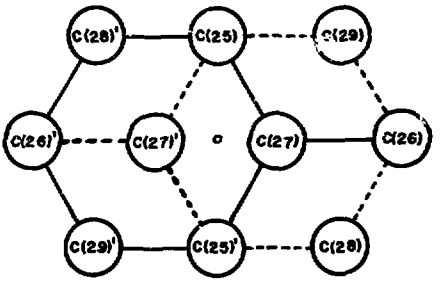

Fig. 17. Disordered model for the toluene molecule. Carbons C(25) and C(26) were given full occupancy and C(27), C(28), and C(29) were given half occupancy, corresponding to two toluene molecules per unit cell containing four ytterbium ions. (XBL 803-8701)

8. CRYSTAL AND MOLECULAR STRUCTURE OF HYDRIDOTRIS[BIS(TRIMETHYLSILYL)AMIDO]URANIUM(IV)†

Richard A. Andersen, Allan Zalkin, and David H. Templeton

We have determined the crystal structure of the title compound, a hydride derivative of uranium (IV), and have shown that the analogous thorium compound is isostructural. The related uranium(III) compound, which lacks only the hydride ion, also crystallizes in the same structure. Since this compound is the first monomeric, monohydride derivative of the f-block elements to be prepared, it was essential to establish its geometry unequivocally by x-ray studies.

Hydridotris[bis(trimethylsily)amido]thorium (IV), hydridotris(bis(trimethylsily)amido]uranium (IV), and tris[bis(trimethylsily)amido]uranium (III) were prepared as previously described.[1,2] The crystals used in the x-ray analysis were grown from pentane (-10°C). The brown, hexagonal-shaped crystals of the uranium hydride crystallize in the trigonal space group $P\bar{3}1c$, and have cell parameters a = 16.402(8) Å and c = 8.501(4) Å, and $\bar{V}$ = 1980.6 Å.[3] There are two molecules in the unit cell.

The molecular structure was determined by single crystal x-ray techniques. An ORTEP drawing of the structure and a packing diagram are shown in Figs. 18 and 19. The uranium atom is on a crystallographic 3-fold axis and bonded to three nitrogen atoms. Uranium is disordered in the z direction at locations 0.51 Å above and below the plane at z = 1/4. The electron density in the channel, that runs parallel to c at the origin, is attributed to pentane solvent molecules in highly disordered arrangements.

Although $[(Me_3Si)_2N]_3UH$ is isostructural with the binary silylamides of those lanthanide derivatives which have been structurally characterized (Nd, Eu, and Yb), the uranium species is tetravalent. The uranium-nitrogen bond length of 2.24 Å is very close to those previously found for terminal, tetravalent uranium-nitrogen bond lengths in $[U(NEt_2)_4]_2$, $[U(MeNCH_2CH_2NMe)_2]_3$, $[U(MeNCH_2CH_2NMe)_2]_4$, and $[U(NPh_2)_4]$, which are 2.22, 2.21, 2.27, and 2.24 Å, respectively. The thorium (IV)-nitrogen bond length in the six-coordinate tetrahydroborate derivative, $Th[N(SiMe_3)_2]_3BH_4$, is 2.32 Å. The ionic radius of thorium(IV) is estimated to be about 0.05 Å larger than that of uranium(IV).[4] Hence, a uranium(IV)-nitrogen bond length of about 2.27 Å

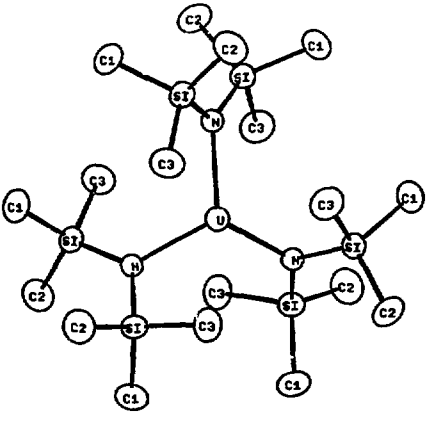

Fig. 18. ORTEP view down, but slightly off, the c axis. (XBL 802-8029)

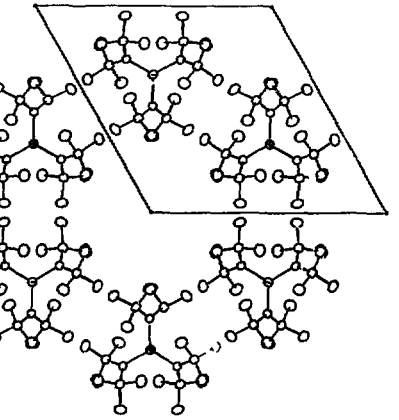

Fig. 19. Packing diagram as seen down the c axis. (XBL 802-80[illegible])

can be estimated, in good agreement with the observed value. Since the ionic radius of uranium(III) is about 0.08 Å longer than that of thorium(IV), a uranium(III)-nitrogen bond length can be estimated to be about 2.4 Å, much longer than that observed. Thus, the U-N bond length in $[(Me_2Si)_2N]_3UH$ supports the identification as a compound of tetravalent uranium.

Unfortunately, a crystal of $U[N(SiMe_3)_2]_3$ suitable for a full structure determination could not be obtained, but it was found to be isostructural with the hydride, $HU[N(SiMe_3)_2]_3$. The larger cell dimensions and volume (Table 4) of the trivalent species are consistent with the fact that uranium(III) is larger than uranium(IV).

Table 4. Cell dimensions (Å) of the tris(bis(trimethylsilyl)amido complexes of U(III), U(IV) and Th(IV)

	U(III)	U(IV)	Th(IV)
Color	Dark red	Brown	White
a	16.56(5)	16.402(8) Å	16.47(3) Å
c	8.43(4)	8.501(4) Å	8.53(3)
V	2002 $Å^3$	1981 $Å^3$	2004 $Å^3$

* * *

†Brief version of LBL-10489.

1. H. W. Turner, S. J. Simpson, R. A. Andersen, J. Am. Chem. Soc. 101, 2782 (1979).
2. R. A. Andersen, Inorg. Chem. 18, 1507 (1979).
3. R. A. Andersen, D. H. Templeton, A. Zalkin, Inorg. Chem. 17, 2317 (1978).
4. R. D. Shannon, Acta Crystallogr. A 32, 751 (1976).

9. DIVALENT LANTHANIDE CHEMISTRY; PREPARATION OF SOME FOUR AND SIX COORDINATE BIS(TRIMETHYLSILYLAMIDO) COMPLEXES OF EUROPIUM(II). THE CRYSTAL STRUCTURE OF BIS[DI(TRIMETHYLSILYL)AMIDO]BIS(1,2-DIMETHOXYETHANE)EUROPIUM(II)†

T. Don Tilley, Allan Zalkin, Richard A. Andersen, and David H. Templeton

As part of a study of divalent lanthanide compounds, we have prepared some coordination complexes of bis[di(trimethylsilyl)amido] europium(II) and determined the crystal structure of one of them.

The best synthesis of the tetrahydrofuran complex is:

$$2Eu[N(SiMe_3)_2]_3 + EuCl_3 \xrightarrow{thf} 3ClEu[N(SiMe_3)_2]_2$$

$$ClEu[N(SiMe_3)_2]_2 +$$

$$Na\text{-}Naphthalene \xrightarrow{thf} [(Me_3Si)_2N]_2Eu(thf)_2$$

All attempts to isolate an intermediate chloroamide have failed. However, addition of sodium naphthalene to the chloro-amide, prepared in situ, yields a yellow solution from which yellow $Eu[N(SiMe_3)_2]_2(thf)_2$ may be isolated by crystallization from pentane.

The tetrahydrofuran in $Eu[N(SiMe_3)_2]_2(thf)_2$ can be displaced by 1,2-dimethoxyethane or bipyridine yielding yellow $[(Me_3Si)_2N]_2Eu(MeOCH_2CH_2OMe)$ or $[(Me_3Si)_2N]_2Eu(Bipy)$, respectively. Both coordination complexes are soluble in hydrocarbon solvents from which they may be crystallized. The 1,2-dimethoxyethane complex follows Curie behavior, $\chi_M = C_M(T)^{-1}$, from 5 to 45 K with $C_M = 8.82$ and $\mu_{eff} = 8.43$ B.M. The magnetic moment, like that of gadolinium(III), is consistent with a $^8S_{7/2}$ ground state. In contrast the base-free europium(III) silylamide, $Eu[N(SiMe_3)_2]_3$, is a temperature-independent paramagnet (T.I.P.); the temperature-independent susceptibility is about 0.4 B.M. and is consistent with a $^7F_0$ ground state. In addition, the ytterbium(III) derivative, $Yb[N(SiMe_3)_2]_3$, follows Curie behavior (5-45 K) with $\mu_{eff} = 3.10$ B.M.

Isolation of well-developed crystals of $Eu[N(SiMe_3)_2]_2(dme)_2$ enabled us to carry out this first single crystal x-ray analysis of a molecular complex of europium(II).

Yellow crystals of bis[di(trimethylsilyl) amido]europium(II) bis(1,2-dimethoxyethane) crystallize in the monoclinic space group C2/c with cell parameters: a = 13.398(4) Å, b = 17.454(6) Å, c = 15.013(5) Å, β = 92.91(3)° and V = 3506 Å^3. For Z = 4 and a molecular weight of 652.98, the calculated density is 1.24 g/cm^3.

Figures 20a and 20b illustrate the two conformations of the 1,2-dimethoxyethane ligands that give rise to disorder in the C(9) and C(10) atoms. Disorder in the rest of the 1,2-dimethoxyethane ligand is probably present but is small enough to be treated as an anisotropic thermal motion.

Figure 21 is a view of the coordination geometry about the six-coordinate europium(II) ion. The two bulky silylamide groups are surprisingly close to one another, resulting in an N-Eu-N angle of only 134.5°. Kepert has shown, from points-on-a-sphere repulsion energy calculations, that, for six-coordinate complexes of the type $M(bidentate)_2(unidentate)_2$, the unidentate ligands are pulled together when the bidentate ligands have small normalized bites, where the normalized bite of a chelating ligand is the distance between donor atoms in the chelate group, divided by the metal-donor atom distance.[1] It is the bidentate nature of the 1,2-dimethoxyethane ligands that prevents the two silylamide groups from repelling each other to a greater extent.

The EU(III)-N bond distance is 2.53 Å, the first such bond length determined, whereas the Eu(III)-N bond length in $Eu[N(SiMe_3)_2]_3$ is 2.26 Å. The difference of 0.27 Å is due mostly to the change in bond length with oxidation state, estimated as 0.23 Å from the ionic radii listed by Shannon.[2]

* * *

†Brief version of LBL-10858.

1. D. L. Kepert, Prog. Inorg. Chem. 23, 1 (1977).
2. R. D. Shannon, Acta Crystallogr. Sec. A 32, 751 (1976).

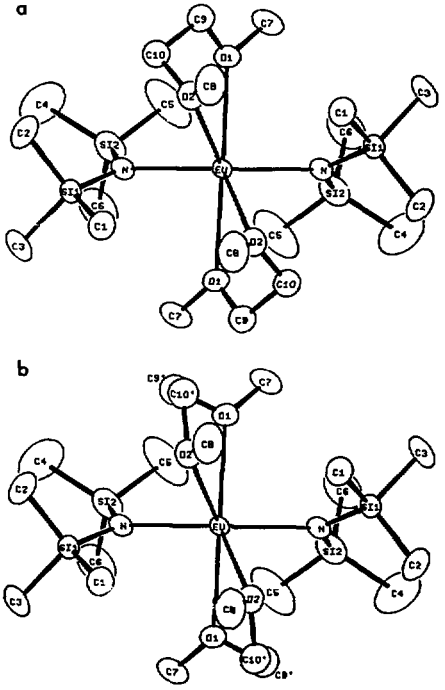

Fig. 20. (a) ORTEP drawing as viewed down the 2-fold axis. (b) ORTEP drawing showing the molecule in the other configuration due to the disorder in C(9) and C(10). (a) (XBL 7911-12675) (b) (XBL 7911-12676)

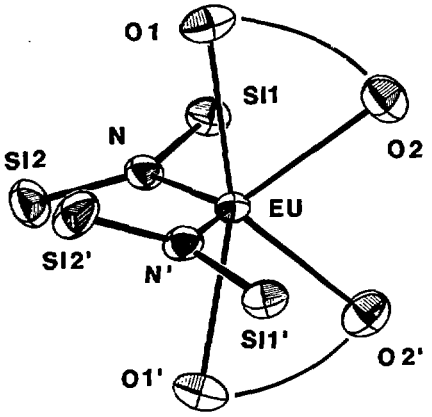

Fig. 21. ORTEP view of the coordination sphere about Eu(III). (XBL 803-8765)

10. PREPARATION AND CRYSTAL STRUCTURE OF THE 1,2-DIMETHOXYETHANE COMPLEX OF BIS[DI(TRIMETHYLSILYL) AMIDO]DICHLOROURANIUM(IV)†

Laughlin G. McCullough, Howard W. Turner, Richard A. Andersen, Allan Zalkin, and David H. Templeton

As part of a study of the comparative chemistry of organometallic compounds of the transition metal Group 4B series and the actinide series, we have prepared bis[di(trimethylsilyl)amido] dichlorouranium(IV) and determined the crystal structure of its 1,2-dimethoxyethane complex. Addition of two molar equivalents of sodium bis(trimethylsilyl)amide to a tetrahydrofuran solution of uranium tetrachloride, followed by crystallization from pentane, yields microcrystals of $[(Me_3Si)_2N_2]_2UCl_2$. Addition of 1,2-dimethoxyethane to the dichloro species yields $[(Me_3Si)_2N]_2UCl_2$ (dimethoxyethane) as green prisms from pentane. The complex may also be prepared directly from sodium bis(trimethylsilyl) amide and uranium tetrachloride in 1,2-dimethoxyethane.

The crystals are orthorhombic, space group Pbca, with cell parameters: (a) = 15.207(4) Å, (b) = 12.021(3) Å, (c) = 33.427(9) Å. For Z = 8, V = 6110.6 Å^3, and a molecular weight of 719.84, the calculated density is 1.565 g cm^{-3}. The molecular structure was determined by single crystal x-ray diffraction methods.

The uranium atom in this structure has approximate C_2 symmetry (Fig. 22) and is hexacoordinated to the two oxygen atoms of the dimethoxyethane (DME) ligand, to two nitrogen atoms of the bis(trimethylsilylamide) ligands, and to two chloride ions.

The geometry of the complex was initially surprising since our intuition suggested that the two sterically large $(Me_3Si)_2N$ groups would occupy trans-positions rather than cis ones in a cis-octahedral arrangement. The observed geometry can be rationalized by reference to Kepert's point-on-a-sphere model.[1] In a molecule of the type M(bidentate)A_2B_2 the location of

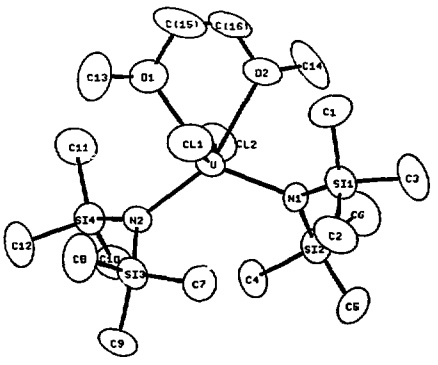

Fig. 22. ORTEP view of the structure of the dimethoxyethane complex. (XBL 803-8700)

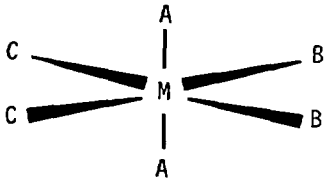

C = oxygen atoms of 1,2-dimethoxyethane
A = Cl
B = $N(SiMe_3)_2$
M = uranium

The A atoms relative to the B atoms is dictated by the M-A and M-B bond distances. Monodentate ligands that have the shortest metal-ligand bond lengths will occupy the less sterically crowded B sites in complexes where the normalized bite of the chelating ligand is small. The average uranium-nitrogen bond length in $[(Me_3Si)_2N]_2UCl_2$ (1,2-dimethyoxyethane) (2.34 Å) is shorter than the uranium-chloride bond length (2.63 Å), and the normalized bite (the distance between donor atoms in the chelate group divided by the metal-donor atom distance) of 1,2-dimethoxyethane is 1.06. Thus, the observed geometry is in accord with Kepert's model.

* * *

†Brief version of LBL-11042.

1. D. L. Kepert, Prog. Inorg. Chem. 23, 1 (1977).

11. BONDING IN METAL-BOROHYDRIDE COMPLEXES†

N. Edelstein

The borohydride ligand has been shown in various structural studies to bond to a wide variety of metal ions via bidentate, tridentate, and, in one instance, monodentate hydrogen bridges. Vibrational spectroscopy also provides data which can be used to determine the metal-borohydride coordination geometry in a large number of compounds. Bernstein et al.,[1] in their discussion of the neutron diffraction structure of $U(BH_4)_4$, which has both double and triple hydrogen-bridged metal boron bonds, proposed using the metal-boron bond length as a criterion for determining whether the metal ion is bonded by two or three bridging hydrogen atoms to the boron atom. This idea implies that one can assign an ionic radius to the borohydride ion. Bernstein et al. determined the values ~ 1.3 Å and ~ 1.6 Å for the ionic radii of a triple hydrogen bridge group and a double hydrogen bridge BH_4^- group, respectively.

Raymond et al.,[2,3] have recently systematized the structural criteria for ionic bonding

in $(C_5H_5)^-$, $(C_8H_8)^{2-}$ and $N[Si(CH_3)_3]_2^-$ metal complexes and have used Pauling's approach to calculate corrections for differences in coordination number for a particular ion. Following Raymond's criteria, we have correlated the structural data for doubly and triply hydrogen-bridged metal-boron bonds with ionic radii for the metal ions obtained from Shannon's table.[4] Plots of ionic radius vs. metal-boron distance are shown in Figs. 23 and 24.

The correlation between ionic radius and the metal-boron bond length is remarkably good, considering the uncertainties in the metal ion-boron bond lengths, the different methods, temperatures, and phases for which structures were determined, the large range of coordination number and of the periodic table covered, plus the variety of other ligands attached to the metal atom. For most molecules the metal-boron bond distance can be calculated with reasonable accuracy using the ionic bonding model. Clearly, it is not possible to draw conclusions about covalent bonding between the metal atom and the borohydride group solely from structural considerations based on the metal-boron distance.

The one compound which does not fit this correlation is $[((CH_3)_3Si)_2N]_3ThBH_4$.[5] The Th ion is formally six coordinate in this molecule, and the ionic radius obtained for the triple-hydrogen bridged BH_4^- group (unambiguously assigned from the infra-red spectrum) is much too large (Fig. 24). The bistrimethylsilylamide group is an extremely bulky ligand which is known to form low coordination number complexes with metal ions of large ionic radii such as the lanthanides. Although this ligand acts in a monodentate manner, it appears to have a much larger effective coordination number due to its steric bulk. From Fig. 24 one can extrapolate an effective coordination number $\geq$ 12 for the Th ion in $[((CH_3)_3Si)_2N]_3ThBH_4$.

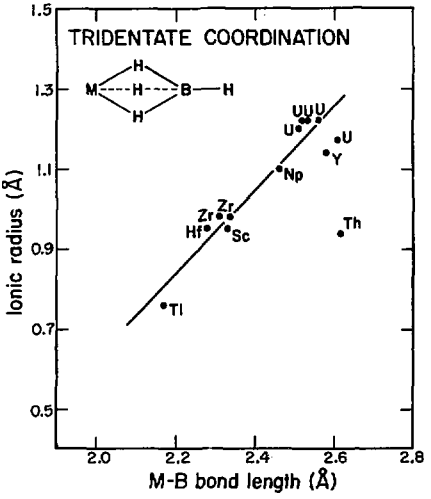

Fig. 24. Metal ionic radius vs. M-B bond length for compounds with metal-boron tridentate hydrogen bridges. (XBL 804-645)

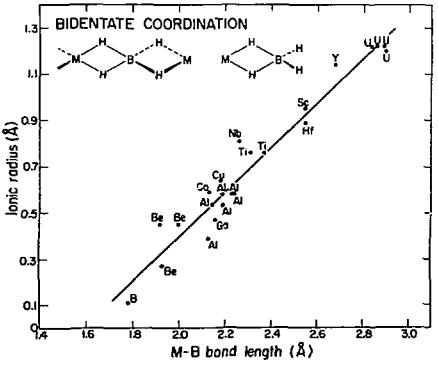

Fig. 23. Metal ionic radius vs. M-B bond length for compounds with metal-boron bidentate hydrogen bridges. (XBL 804-646)

* * *

†Brief version of LBL-10855; to be published in Inorganic Chemistry.

1. E. R. Bernstein et al., Inorg. Chem. 11, 3009 (1972).
2. K. N. Raymond, In Organometallics of the f Elements, T. J. Marks, R. D. Fischer, Eds., D Reidel Publishing Co.: Boston (1979) p. 249.
3. K. N. Raymond and C. W. Eigenbrot, Jr., Accts. Chem. Res. 13, 276 (1980).
4. R. D. Shannon, Acta Crys. A 32, 751 (1976).
5. R. A. Andersen, D. H. Templeton, and A. Zalkin, Inorg. Chem. 17, 2317 (1978).

12. 1,4- AND 1,6-DI-TERT-BUTYLCYCLOOCTATETRAENES†

Matthew H. Lyttle, Robert W. Kluttz, and
A. Streitwieser, Jr.

As part of our search for volatile and air-stable organoactinide compounds, we had previously prepared cyclooctatetraenes (COT) highly substituted by tert-butyl groups.[1] Our earlier preparation of 1,4-di-tert-butylCOT was a specific synthesis; we have now developed an alternative synthesis from COT oxide as outlined in Fig. 25 that can readily be generalized to other substituents. In the process we discovered some unusual properties of this hydrocarbon.

Deprotonation of the di-tert-butylcyclooctatriene shown with potassium amide in a mixture of liquid ammonia and tetrahydrofuran gave 1,4-di-tert-butylcyclooctatetraene dianion, which, on oxidation with iodine, gave a product whose nmr spectrum indicated a mixture of 1,4- (1) and 1,6-di-tert-butyl-cyclooctatetraene (2). Treatment of the mixture with $AgNO_3$ in boiling alcohol gave the silver nitrate complex only of 2 as a crystalline material having a satisfactory analysis. Treatment of this silver complex with ammonia regenerated the hydrocarbon having the nmr spectrum only of 2. The spectrum changed gradually to that of the equilibrium mixture of 1 and 2. The vinyl proton region of the nmr spectrum of the mixture is shown in Fig. 26 with the assignments.

A solution of the mixture of 1 and 2 was allowed to equilibrate at temperatures from 25°C to 50°C with the results in Table 5. A plot of lnK vs 1/T was linear and gave the thermodynamic data: $\Delta H° = 0.48$ Kcal mol^{-1} and $\Delta S° = 0.92$ e.u. What is most surprising in these results is that 2 is significantly more stable than 1 despite the proximity of the bulky tert-butyl groups to each other in 2. Our interpretation is that the tert-butyl groups are held in such a position that

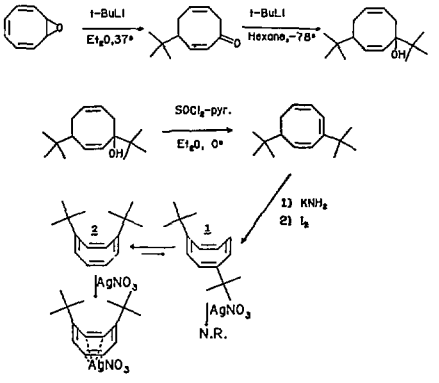

Fig. 25. Preparation of 1,4- and 1,6-di-tert-butylcyclooctatetraenes. (XBL 812-8091)

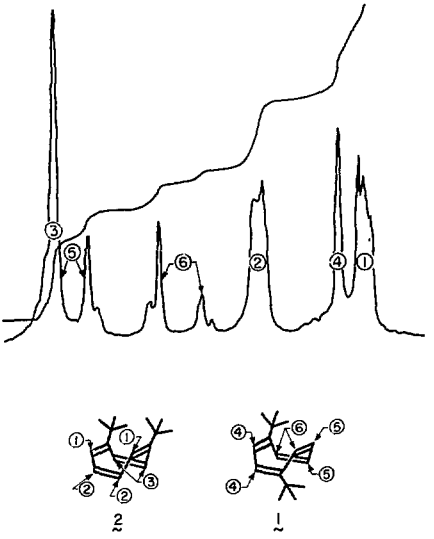

Fig. 26. Proton nmr spectrum in the vinyl region of a mixture of 1 and 2. (XBL 813-508)

steric repulsion is actually small but that Van der Waals attraction is significant.

Solutions of the $AgNO_3$ complex were treated with ammonia and immediately held at constant temperature in an nmr probe. The ratio of 1 and 2 was determined as a function of time and gave the kinetic results summarized in Table 6. These results lead to the activation parameters, $\Delta H^{\ddagger} = 14.7$ Kcal mol^{-1}, $\Delta S^{\ddagger} = -26.3$ e.u. The enthalpy of activation is not too different from that of some reported mono-substituted cyclooctatetraenes (COT): COT-COOEt,[2] 12.8 Kcal mol^{-1}; COT-CMe_2OH,[2] 15.4 Kcal mol^{-1}; COT-OCH_3,[3] 16 Kcal mol^{-1}, COT-$OC(CH_3)_3$,[3] 13 Kcal mol^{-1}. However,

Table 5. Equilibrium constants for the interconversion of 1 and 2; K = [1]/[2].

Temp, °C	K
25	0.702
30	0.714
40	0.728
45	0.739
50	0.75

Table 6. First order rate constants for the conversion of 2 to 1 as a function of temperature.

Temp. °C	k_1, 10^5 sec^{-1}
25	7.8
30	12
40	23
45	41

the entropy of activation is far more negative than those of the other systems. Apparently, many motions of the tert-butyl group are frozen out in the planar octagonal transition state in our reaction.

* * *

†This research was supported in part by a National Science Foundation grant.

1. M. J. Miller, and A. Streitwieser Jr., LBL-7355 (1977) p. 463; M. J. Miller, M. H. Lyttle, and A. Streitwieser Jr., submitted to J. Org. Chem.
2. F. A. L. Anet, A. J. R. Bourn, Y. S. Lin, J. Am. Chem. Soc. 86, 3576 (1964).
3. J. F. M. Oth, R. Merenyi, Th. Martini, G. Schröder, Tet. Lett. 3087 (1966).

13. BIS-π-(CYCLOBUTENOCYCLOOCTATETRAENE) URANIUM(IV)†

Wayne D. Luke, Stuart R. Berryhill, and Andrew Streitwieser, Jr.

The title compound 3 has special interest in organoactinide chemistry because of the highly strained and fused 4-member ring. Interesting questions involve the induced distortion of the 8-membered ring and the consequent effects on bonding. Moreover, the relatively rigid structure permits a detailed analysis of the nmr spectrum into contact and pseudo-contact contributions.

Cyclobutenocyclooctatetraene dianion, 1, was prepared by deprotonation of the triene 2 with KNH_2 in liquid ammonia as described by Staley.[1] Reaction with UCl_4 in THF gave the dark green crystalline uranocene, 3. The visible spectrum shows the expected bathochromic shift of an alkyl-substituted uranocene with λ_{max} at 623 nm (ϵ = 610). The crystal structure was reported previously;[2] this structure determination showed only slight distortion of the 8-membered rings from a regular octagon and the uranium remained accurately along the centers of these rings (Figs. 27a and 27b).

The magnetic susceptibility of 3 was measured via the vibrating magnetometer method over the

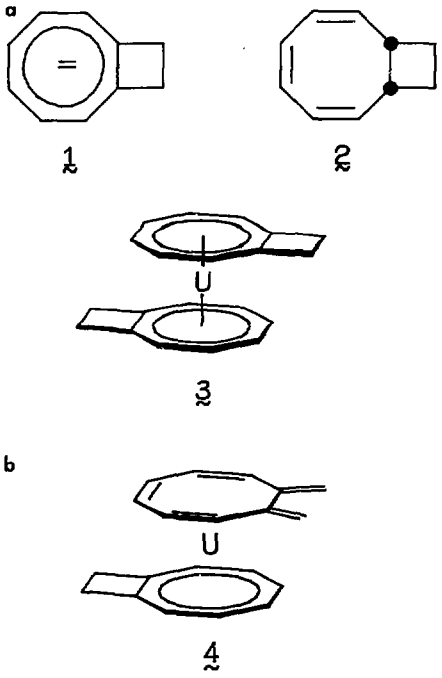

Fig. 27. (a) and (b): Structures of various uranocenes and their precursors.
(a) (XBL 8011-12103)
(b) (XBL 8011-12104)

range of 4.2 K to 100 K to provide the data plotted in Fig. 28. The magnetic susceptibility displays Curie-Weiss behavior from 15 K to 100 K with μ_{eff} = 2.36 B.M.; θ = 8.5 K and is essentially temperature independent below 15 K. Susceptibility measurements at 30°C by the Evans method[3] gave a value of $\chi_{AVE} = 2.34 \times 10^3$, emu mol^{-1}. This number is in excellent agreement with that extrapolated from the low temperature data, 2.23×10^{-3} emu mol^{-1}. This temperature dependence behavior corresponds well with that of uranocene and several of its derivatives.

The nmr spectrum was particularly significant. The ^1H nmr spectrum as a function of temperature is summarized in Fig. 29. Two of the ring protons, like the ring proton resonances in uranocene and substituted uranocenes, are linear in T^{-1}. In contrast, the low-field ring proton resonance and both of the methylene proton resonances are nonlinear, indicative of temperature-dependent conformational mobility. Using the known crystal

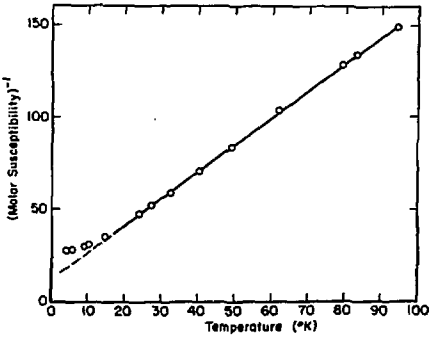

Fig. 28. The reciprocal of the molar magnetic susceptibility as a function of temperature (Curie-Weiss plot). The least squares line based as indicated on the points shown yields the Curie constant = 0.690 emu °K mol^{-1}, θ = 8.5 K, μ_{eff} = 2.36 B.M. (XBL 812-8092)

structure of 3 (Ref. 2) in conjunction with some reasonable assumptions, we could calculate the geometry factors[4] for the exo and endo protons to be -0.709 × 10^{21} cm^{-3} and -16.97 × 10^{21} cm^{-3}, respectively.

The resonances of 3 referenced to 1 as a diagmagnetic standard give the following isotropic shifts at 30°C: δ 16.35 ppm (exo), -30.05 ppm (endo), -33.28 ppm, -41.48 ppm, -49.38 ppm (ring). The approximate conformational equivalence of the exo and endo hydrogens implies that they should have equal contact shifts. Equation (1) can be derived for such a case to relate the observed isotropic shift (δ) differences directly to the geometry factors (G) that determine the pseudo-contact shift:

$$\frac{(\mu_{\parallel}^2 - \mu_{\perp}^2)}{3} \quad \frac{\beta^2}{3kT} = \frac{\delta_{exo} - \delta_{endo}}{G_{exo} - G_{endo}} . \qquad (1)$$

This analysis yields a value of 12.5 B.M.[2] for $\mu_{\parallel}^2 - \mu_{\perp}^2$, with corresponding pseudocontact shifts of -2.03 ppm (exo) and -48.5 ppm (endo) and a contact shift of 18.4 ppm. These calculated values show that the difference in the sign of the observed isotropic shifts of the methylene protons results from the fact that the isotropic shift for the exo protons is principally contact in nature whereas the endo isotropic shift is dominated by the pseudocontact component; the "magic angle" lies close to the exo-hydrogen. There is some uncertainty, but our estimate supports the conclusion of Fischer et al.[5,6] that $\mu_{\perp} \neq 0$.

Finally, we searched for possible ring-opening reactions of 3 to form 4; but heating with potential dienophiles such as dimethyl acetylenedicarboxylate, bis-trimethylsilylacetylene, and maleic anhydride gave no evidence for Diels-Alder products. These results show that electrocyclic

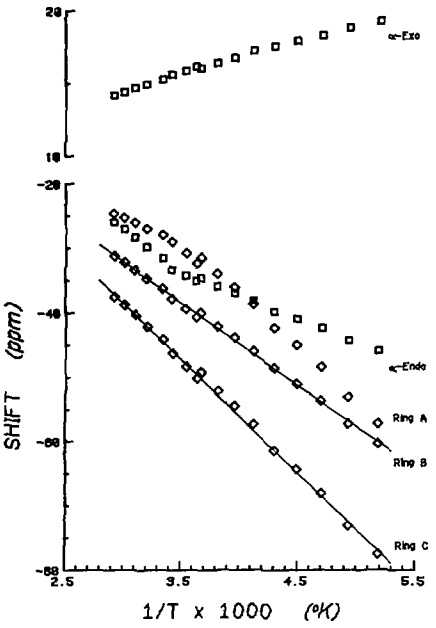

Fig. 29. Isotropic shifts of 3 relative to the dianion as a function of reciprocal temperature. The protons on the 8-membered ring are not assigned and the resonances are labeled A,B,C in order of increasing field. Linear relations for the chemical shifts of B and C are given by:
$\delta(B) = 6.25 \pm 0.48 - (12809 \pm 123)/T$;
$\delta(C) = 14.05 \pm 0.77 - (17582 \pm 197)/T$.
(XBL 8011-12102)

ring opening of the type 3 → 4 is not more facile than for benzocyclobutene itself.

*We conclude that despite the strain of the 4-*membered ring, compound 3 behaves as a rather normal uranocene with little change in bonding. The structure did, as hoped, provide important results as regards the nmr spectrum which could be generalized to other uranocenes.

* * *

†This research was supported in part by grants from the National Science Foundation.

1. S. W. Staley, G. M. Cramer, and A. W. Orvedal, J. Am. Chem. Soc. (1974) 96, 7433 (1974).
2. A Zalkin, et al., Inorg. Chem. 18, 2287 (1979).
3. D. F. Evans, J. Chem. Soc. 2003 (1959).
4. W. D. Luke and A. Streitwieser, Jr. in Lanthanide and Actinide Chemistry and Spectroscopy, N. M. Edelstein, ed., ACS Symposium Series 131, Washington, D. C. (1980), p. 93.

5. R. D. Fischer, in Organometallics of the f-Elements, T. J. Marks and R. D. Fischer, eds., D. Reidel, Boston (1979), p. 337.
6. R. D. Fischer, A. W. Spiegl, and F. Dickert, In press: Chem. Ber.

Physical and Spectroscopy Studies

14. OPTICAL SPECTRA AND ZEEMAN EFFECT FOR Er^{3+} IN $LuPO_4$ AND $HfSiO_4$†

T. Hayhurst, G. Shalimoff, N. Edelstein, L. A. Boatner, and M. M. Abraham

One of the most important problems in radioactive waste isolation is the choice of material to be used as a container. It has been suggested that the mineral monazite and its synthetic analogs have chemical and physical properties which make them attractive candidates as host materials for long-lived actinide ions.[1] It is important to characterize the possible sites where impurity ions could be incorporated into these materials and to determine the oxidation states of the actinide ions after incorporation.

Monazite is a mixed orthophosphate containing $(La,Ce,Y,\cdots)PO_4$. Pure lanthanide orthophosphates are structurally divided into two classes: the first half of the series ($LaPO_4$ to $GdPO_4$) has the monoclinic monazite structure while the second half of the series ($TbPO_4$ to $LuPO_4$, YPO_4, and $ScPO_4$) has the tetragonal zircon structure. Previous studies have shown by electron paramagnetic resonance (EPR) techniques that Gd^{3+} occupies identical substitutional sites in both single crystal and powder samples of the tetragonal orthophosphates.[2]

The electronic states resulting from an f^n configuration restricted to D_{2d} symmetry can be described with an effective Hamiltonian of the form

$$H = H_1 + H_2 + H_3 + H_4,$$

where H_1 is the electrostatic interaction, H_2 is the spin-orbit interaction, H_3 is the crystalline field interaction, and H_4 contains configuration interaction terms, three-body interactions, and additional magnetic terms.[3]

Preparation and characterization of the $Er^{3+}:LuPO_4$ crystals by EPR was very similar to the previously reported work on $Er^{3+}:HfSiO_4$.[4] The ground state g values for $Er^{3+}:LuPO_4$ were found to be $g_{\parallel} = 6.386$ and $g_{\perp} = 4.970$,[5] compared to $g_{\parallel} = 4.316$ and $g_{\perp} = 6.682$ for $Er^{3+}:HfSiO_4$. The absorption lines of both crystals were observed by detecting the transmitted light from a 100-W tungsten-halogen lamp. Transitions between 12,000 and 28,000 cm^{-1} were photographed on a spectrograph with a dispersion of about 5.2 A/mm while the transitions between 6,000 and 12,000 cm^{-1} were observed using a scanning monochromator with a PbS detector.

Fifty-five transitions were assigned to $Er^{3+}:LuPO_4$ and 46 transitions to $Er^{3+}:HfSiO_4$. The free ion and crystal field parameters associated with H_1, H_2, and H_3 were then varied via least squares optimization of the agreement between the calculated and assigned transitions. The additional free ion parameters associated with H_4 were fixed at the $Er^{3+}:LaCl_3$ values. Some assignments were then confirmed by comparing calculated and measured g values where it was possible to observe magnetic field splittings of the absorption lines.

Satisfactory fits were obtained in both cases, with a residual (σ) of 13.2 cm^{-1} for $Er^{3+}:LuPO_4$ and 14.5 cm^{-1} for $Er^{3+}:HfSiO_4$. In addition, the model was tested on $Er^{3+}YPO_4$ by fitting to previously reported data.[6,7] The calculated g values for the ground states in each case agree well with the EPR measurements. The fitted parameters for Er^{3+} in all three crystals, $LuPO_4$, YPO_4, and $HfSiO_4$, can be compared in Table 7. The crystal field parameters reported here will provide a good starting point for future work on tetrapositive actinide ions in this type of host crystal.

* * *

† Brief version of LBL-11943, submitted for publication to the Journal of Chemical Physics.

1. M. M. Abraham, et al., to be published.
2. L. A. Boatner, et al., J. Chem. Phys. 73, 1095 (1980).
3. W. T. Carnall, H. C. Crosswhite, and H. M. Crosswhite, "Energy Level Structure and Transition Probabilities in the Spectra of the Trivalent Lanthanides in LaF_3," Argonne National Laboratory report (unpublished).
4. R. W. Reynolds, et al., J. Chem. Phys. 56, 5607 (1972).
5. M. M. Abraham, L. A. Boatner, and M. Rappaz, to be published.
6. M. Dzionara, H. G. Kahle, and F. Schedewie, Phys. Stat. Sol. (b) 47, 135 (1971).
7. D. Kuse, Z. Physik 203, 49 (1967).

Table 7. Crystal field parameters for Er^{3+} (cm^{-1}).

Parameter	$LuPO_4$	YPO_4	$HfSiO_4$
F^2	97015	97058	97530
F^4	69141	69142	68589
F^6	48232	48232	49022
ζ	2366	2368	2368
B_0^2	146	279	-520
B_0^4	68	155	427
B_4^4	-760	-756	-884
B_0^6	-643	-537	-467
B_4^6	-89	-141	-4
F^0	44051	44062	44137
α [a]	15.9	15.9	15.9
β [a]	632.0	632.0	632.0
γ [a]	2017.	2017.	2017.
T^2 [a]	157.5	157.5	157.5
T^3 [a]	48.0	48.0	48.0
T^4 [a]	18.0	18.0	18.0
T^6 [a]	-342.0	-342.0	-342.0
T^7 [a]	214.0	214.0	214.0
T^8 [a]	449.0	449.0	449.0
M^0 [a]	4.5	4.5	4.5
M^2 [a]	2.52	2.52	2.52
M^4 [a]	1.71	1.71	1.71
P^2 [a]	667.0	667.0	667.0
P^4 [a]	500.3	500.3	500.3
P^6 [a]	333.5	333.5	333.5
σ	13.2	14.7	14.5

[a] From Ref. 3.

15. VIBRATIONAL SPECTRA AND NORMAL COORDINATE ANALYSIS OF NEPTUNIUM (IV) BOROHYDRIDE AND NEPTUNIUM (IV) BORODEUTERIDE†

R. H. Banks‡ and N. Edelstein

Uranium borohydride, $U(BH_4)_4$, the first tetrakis-borohydride known, was synthesized during the Manhattan Project. $Hf(BH_4)_4$, $Zr(BH_4)_4$, and $Th(BH_4)_4$ like $U(BH_4)_4$ are solids at room temperature, but $Hf(BH_4)_4$ and $Zr(BH_4)_4$ are appreciably more volatile than their actinide analogs. We have recently reported the syntheses of $Pa(BH_4)_4$, $Np(BH_4)_4$ and $Pu(BH_4)_4$. As expected, $Pa(BH_4)_4$ has physical properties (melting point, sublimation temperature) intermediate to those of Th and U borohydrides. However, $Np(BH_4)_4$ and $Pu(BH_4)_4$ are liquids at room temperature with vapor pressures like those of $Hf(BH_4)_4$ and $Zr(BH_4)_4$ rather than like $U(BH_4)_4$ and $Th(BH_4)_4$.

The seven known metal tetrakis-borohydrides are all of the same symmetry in the gas phase but, in the solid state, exhibit three types of crystal structures. Analyses of the vibrational spectra have been reported for the tegragonal, polymeric structure displayed by Th, Pa, and U borohydrides and for the cubic monomeric structure shown by $Zr(BH_4)_4$ and $Hf(BH_4)_4$. Those studies revealed that the vibrational spectra are highly dependent on solid-state structure, and very noticeable spectral differences were observed for the two structure types. However, in certain regions of the spectra, it was not clear whether molecular geometry or other factors were primarily responsible for dissimilarities. In addition, the assignments of some spectral features remained doubtful and need further examination.

We report in this paper an analysis of the IR and Raman spectra of $Np(BH_4)_4$ and $Np(BD_4)_4$ which, like the analogous Pu compounds, display the third structure type, tetragonal and monomeric. An attempt was made to elucidate some of the uncertainties in earlier analyses and to explain the origin of the nonfundamental bands seen in the IR spectra from 25 to 7400 cm^{-1} for $Np(BH_4)_4$ and in the near IR region for $Zr(BH_4)_4$. It was found that the unobserved T_1 fundamentals and modes involving the less abundant ^{10}B atoms were very important and required a heavy reliance on the normal coordinate calculations using the derived force field.

Solid state spectra for $Np(BH_4)_4$ and $Np(BD_4)_4$ are shown in Fig. 30. The program NORCRD was used to calculate frequencies and normal coordinates. It sets up the normal coordinate problem in terms of mass-weighted Cartesian coordinates in which the kinetic energy matrix is a unit matrix and the potential energy matrix contains the force constants in terms of bond distances and angles. In diagonalizing the V matrix the frequencies and normal modes are obtained. Since there are fewer observed spectral data than independent force constants, an approximate general valence force field was derived using a limited number of the more important constants.

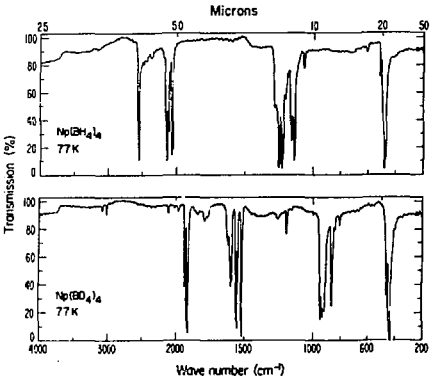

Fig. 30. Solid state - IR spectra of $Np(BH_4)_4$ and $Np(BD_4)_4$ at 77 K. (XBL 794-9123A)

The optimum force field is given in Table 8 and the calculated frequencies it produces are listed in Table 9. The standard deviation is 10 cm^{-1} for 32 of the 36 allowed fundamentals.

The solid state structure of $Np(BH_4)_4$ has a vibrational spectrum which is basically similar to those of Zr and Hf borohydrides. A few differences are seen, mostly in the lower energy spectral region. These differences persist in the gas phase where all $M(BH_4)_4$ molecules are isostructural.

Although the two force fields found for $Np(BH_4)_4$ and $Hf(BH_4)_4$ cannot be compared in fine detail, the values of the force constants are very similar, especially those related to the BH_4 group. Similarity is to be expected since the BH_4 modes prove to be not strongly dependent on metal size or mass. Greater differences are found in the force constants involving the MH_3B structures; but, in general, these constants follow the same trend where the MB constant is higher than the MH_b constant. As was also noted in the vibrational analyses of Hf and Zr borohydrides, MB bonding may be significant in these molecules.

* * *

†Brief version of LBL-10901; accepted for publication in J. Chem. Phys.

‡Permanent address: Chemistry Department, Argonne National Laboratory, Argonne, IL 60439.

Table 8. Best-fit force constants for neptunium borohydride at 77 K

Primary Force Constants Internal Coordinates	Value	Interaction Force Constants Internal Coordinates	Value
νBH_t	3.51 md/A	$\nu BH_b : \nu BH_b$ [b]	0.04 md/A
νBH_b	2.36	$\nu MH_b : \nu MH_b$	0.02
νMH_b	0.37	$\nu MB : \delta H_bMH_b$	-0.09 md
νMB	1.28	$\nu BH_b : \delta H_bBH_b$ [b]	0.04
δH_tBH_b	0.28 md/A	$\nu MH_b : \delta H_bMH_b$	0.04
δH_bBH_b	0.36		
δH_bMH_b (C_3)	0.26		
εH_bBMB	0.18[a]		

[a]The torsion force constant is essentially undetermined since the A_2 mode is not observed. It was set at 0.18 and kept constant during all fits.

[b]Internal coordinates in this constant interact only with other like coordinates in the same BH_4 group.

Table 9. Fundamental vibrations (cm^{-1}) of $Np(BH_4)_4$ and $NP(BD_4)_4$.

Normal Mode	$Np(BH_4)_4$ Observed	$Np(BH_4)_4$ Calculated	$Np(BD_4)_4$ Observed	$Np(BD_4)_4$ Calculated
$\nu_1 T_2$	2551	2557	1912	1911
$\nu_2 T_2$	2143	2144	1548[a]	1603
$\nu_3 T_2$	2069	2078	1516	1485
$\nu_4 T_2$	1247	1266	926	897
$\nu_5 T_2$	1225	1223	917	895
$\nu_6 T_2$	1138	1104	860	824
$\nu_7 T_2$	——	575	437	447
$\nu_8 T_2$	475	488	——	415
$\nu_9 T_2$	130	156	112	139
$\nu_1 A_1$	2557	2554	1913	1905
$\nu_2 A_1$	2149	2147	1517	1523
$\nu_3 A_1$	1283	1284	955	953
$\nu_4 A_1$	517	517	475	466
$\nu_1 E$	2123	2117	1619	1589
$\nu_2 E$	1260	1270	905	899
$\nu_3 E$	1053	1089	795	807
$\nu_4 E$	——	571	——	413
$\nu_5 E$	168	142	154	125
$\nu_1 T_1$	——	2116	——	1587
$\nu_2 T_1$	——	1256	——	889
$\nu_3 T_1$	——	1084	——	810
$\nu_4 T_1$	——	565	——	405
$\nu_5 T_1$	——	405	——	288
νA_2	——	288	——	204

[a]This mode is in Fermi resonance with $2\nu_3 T_2(D)$.

16. ELECTRONIC SOLUTION SPECTRA FOR URANIUM AND NEPTUNIUM IN OXIDATION STATES (III) TO (VI) IN ANHYDROUS HYDROGEN FLUORIDE†

M. Baluka,‡ N. Edelstein, and T. A. O'Donnell§

Spectra have been recorded for solutions in anhydrous hydrogen fluoride (AHF) of uranium and neptunium in oxidation states (III) to (VI), Figs. 31

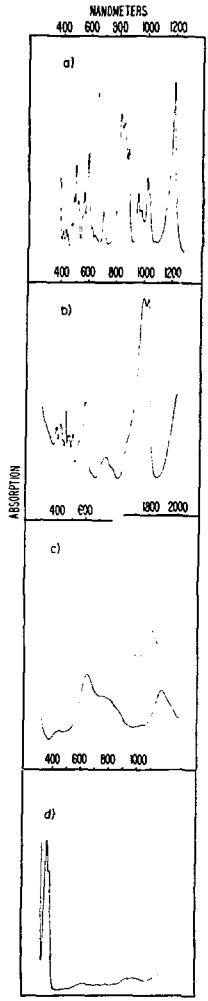

Fig. 31. Optical spectra of (a) U(III)/AHF and AsF_5 (2 atm); (b) U(IV)/AHF and AsF_5 (2 atm); (c) UF_5/AHF and AsF_5 (1.5 atm); (d) UF_6/AHF and AsF_5 (1.5 atm). (XBL 809-2021)

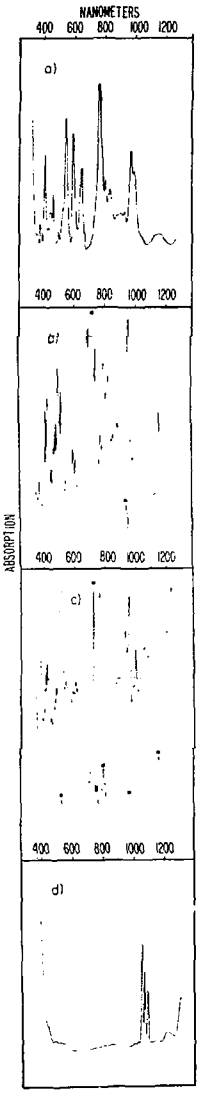

Fig. 32. Optical spectra of (a) Np(III)/AHF and AsF_5 (2 atm); (b) Np(IV)/AHF and AsF_5 (2 atm); (c) NpF_5/AHF and AsF_5 (2 atm); (d) NpF_6/AHF and BF_3 (2 atm). The * above certain peaks represents absorption occuring on the second absorption scale (OD between 1 and 2) of the Cary 17.
(XBL 809-2022)

and 32. The fluorides of these elements can be made soluble in AHF by the application of BF_3 or AsF_5 at approximately two atmospheres pressure to a suspension of the metal fluoride. U(III) or NP(III) can be obtained easily by the treatment of U or Np metal with AHF - AsF_5.

The optical spectra for U(III), Np(III), and NP(IV) in AHF are very similar to those in acidified aqueous solution, but that for U(IV) suggests that the cationic species is UF_2^{2+}. The AHF spectra for the elements in oxidation states (V) and (VI) are not comparable with those of the formally analogous aqueous solutions, where the elements exist as well-defined dioxo-cations. However, these AHF spectra can be related to spectra in the gas phase, in the solid state or in nonaqueous solvents for each element in its appropriate oxidation state.

* * *

†Brief version of LBL-11618; submitted to Inorganic Chemistry.

‡Present address: Institute for Low Temperature Research, Polish Academy of Sciences, Wroclaw, Poland.

§Present address: University of Melbourne, Victoria, Australia.

17. ELECTRON PARAMAGNETIC RESONANCE SPECTRA OF Er(III), Dy(III), AND Gd(III) IN YTTRIUM AND LANTHANUM HYDRIDES†

B. Spencer‡ and N. Edelstein

Many lanthanide, actinide, and transition elements form binary hydrides that look metallic, have metallic conductivities, and show other metallic properties such as ordering at low temperature.[1] Substantial regions of nonstoichiometry and transition to semimetallic behavior, as the trihydride composition is approached, also characterize these materials. Yttrium and lanthanum typify lanthanide behavior by combining with hydrogen at moderate temperatures and low hydrogen pressures to approach a cubic fluorite structure for the dihydride with the hydrogen atoms occupying tetrahedral sites in the cubic, metal lattice.

The present study was undertaken to confirm the oxidation state of the metal and the hydridic nature of the hydrogen by obtaining electron paramagnetic resonance (EPR) parameters sensitive to the oxidation state of the metal and to the sign of the charge on the hydrogen for representative lanthanides (Er, Dy, and Gd) diluted in the nonmagnetic host materials YH_x and LaH_x. For hydride compositions near x = 2.0, the environment of the dopant metal ion should be cubic for the majority of the ions present, thus providing a convenient situation for determining the oxidation state and electronic ground state of the ion in question so as to distinguish between protonic and hydridic crystalline electric fields.

X-band EPR spectra, which were recorded with the samples in flowing helium gas at a temperature of ~10 K, are shown in Table 10. Samples of YH_2 and YH_3 doped with Yb, Sm, Eu, and Ce did not give observable signals. However, the cerium samples were particularly sensitive to air oxidation and formed some oxide prior to arc melting so the hydride samples may not have contained significant amounts of Ce.

The EPR spectra summarized in Table 1 are characteristic of the trivalent ions of Er, Dy, and Gd, thus confirming the +3 oxidation state for the metal ions with three electrons presumably donoted to the conduction band in the dihydrides. Sm^{3+}, with a Γ_8 ground state in a cubic hydridic crystal field, should have an anisotropic EPR transition so that failure to observe spectra for samarium is consistent with the +3 state. Europium might be expected to remain Eu^{2+} with an easily observable isotropic $^8S_{7/2}$ ground state since pure EuH_2 cannot be converted to a higher hydride,[1] so failure to observe spectra for samples doped with europium is consistent with Eu^{3+} in YH_x. Ytterbium, which could be expected to exhibit an isotropic Γ_7 ground state if present as Yb^{3+}, apparently remains in the diamagnetic +2 state as it does in pure orthorhombic YbH_2, since spectra are not observed for Yb in this cubic host. Preliminary studies of pure YbH_2, however, did give EPR transitions at g = 4.7 and 3.9, perhaps indicating some Yb^{3+} in this lower symmetry environment, as has been suggested[1] to explain the slight room temperature paramagnetism of YbH_2.

Gd^{3+} gives a single isotropic line at g = 1.996 in YH_2 and g = 1.96 in $LaH_{2.0}$ as expected for an S-state ion, although the zero-field splitting expected even in a cubic environment is absent. Such collapse of a zero-field multiplet into a single line is characteristic of exchange narrowing through coupling via conduction electrons, as is found for Gd in gold[2] and for Gd in d-band intermetallic compounds.[3] The broadening of the Gd^{3+} resonance line in LaH_x, as x increases from 2.0 to 2.6, could reflect either the decrease in conductivity or the decrease in site symmetry or both, as hydrogen occupies additional octahedral sites. The complex spectra obtained for Gd^{3+} in YH_3 show that exchange narrowing by coupling through conduction band electrons is no longer effective as the hydride loses its metallic character.

* * *

†Brief version of LBL-11935; to be submitted to Inorganic Chemistry.

‡Permanent address: Department of Chemistry, Beloit College, Beloit, WI 53511.

1. K. M. McKay, in Comprehensive Inorganic Chemistry, Vol. 1., J. C. Bailar et al. eds.; Pergamon, New York, (1973), p. 38.
2. K. Baberschke and Y. V. Spalden, Phys. Rev. B 19, 5933 (1979).
3. G. E. Barberis, et al., Phys. Rev. B 19, 5495 (1979).

Table 10. Summary of EPR observations at ~10 K.

Ion	Mol. %	Host	Observations
Er^{3+}	0.6	YH_2	Single line, g = 6.60 ± 0.05, ΔH = 125 gauss
	0.6	YH_3	Complex spectrum, principal lines at g = 10.9, 5.0, 3.7
	5	LaH_{2-3}	No spectra observed
Dy^{3+}	1	YH_2	Single line, g = 6.9 ± 0.2, ΔH = 287 gauss
	1	YH_3	Weak lines at g = 6.1 ± 0.5 and g = 14 ± 1
	4	LaH_{2-3}	No spectra observed
Gd^{3+}	2	YJ_2	Single line, g = 2.00 ± 0.02, ΔH = 305 gauss
	2	YH_3	Complex spectrum from g = 19 to 1.0
	5	$LaH_{2.0}$	Single line, g = 1.96 ± 0.04, ΔH = 195 gauss
	5	$LaH_{2.4}$	Single line, g = 1.96 ± 0.04, ΔH = 300 gauss
	5	$LaH_{2.6}$	Single line, g = 2.00 ± 0.05 ΔH = 433 gauss

18. SPECTRUM AND ENERGY LEVELS OF Pr^{3+} IN $ThBr_4$ †

J. G. Conway, J.-C, Krupa,‡ P. Delamoye,‡ and M. Genet‡

The strong features in the absorption spectrum and the laser excited fluorescence spectrum of Pr^{3+} diluted in $ThBr_4$ have been interpreted as arising from levels of Pr^{3+} in a D_{2d} symmetry site. Forty-three levels have been fitted to the usual parameters with an rms deviation of 61 cm^{-1}. The parameters are listed in Table 11. There are many processes going on in this crystal, as can be seen from Fig. 33, which shows the structure of the $^3P_0$ absorption. In pure D_{2d} symmetry, this should be a single sharp line assigned to the transition $\Gamma_5 - \Gamma_1$. The structure indicates many vibronic frequencies and also the possibility of another site. However, the strong features of the spectrum belong to the D_{2d} symmetry site.

* * *

†Brief version of LBL-11601; to be published in J. Chem. Phys.

Table 11. Parameters obtained from fitting Pr^{3+} in $ThBr_4$ in cm^{-1}.

F^2	68354
F^4	50310
F^6	33799
F^0	11558
ζ	738.8
α	21.26 fixed [a]
$\beta/12$	-66.67 fixed [a]
γ	1342.9 fixed [a]
B^2_0	260.0
B^4_0	-644.2
B^4_4	929.2
B^6_0	1089.0
B^6_4	240.6

Notes: Final fit had 42 levels and 6 parameters B^K's, F^0.
RMS = 61 cm^{-1}, where RMS = $[\Sigma(E_c-E_o)^2/L-P]^{1/2}$, in which L = number of levels, and P = number of parameters.
[a]Fixed at the aqueous values, Ref. 1.

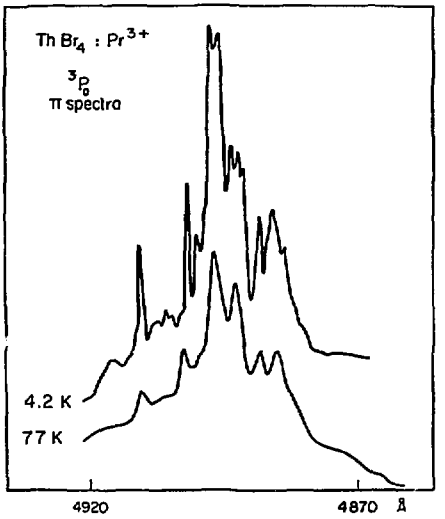

Fig. 33. Structure of the $^3P_0$ absorption line. (XBL 8011-12051)

‡Institut de Physique Nucléaire, Orsay, France.

1. W. T. Carnall, P. R. Fields, and K. Rajnak, J. Chem. Phys. 49, 4424 (1968).

RESEARCH PLANS FOR CALENDAR YEAR 1981

The basic purpose of the project in heavy element chemistry is to study lanthanide and actinide materials in order to provide the basic knowledge necessary for their safe and economic utilization in present and future technology. This work encompasses related problems of an applied nature in actinide chemistry.

The program includes the preparation of new gaseous, liquid, and solid phases and studies of their physical and chemical properties. Techniques for characterization include x-ray diffraction, optical and vibrational spectroscopy, magnetic resonance, and magnetic susceptibility. Equilibrium and kinetic data for complex formation will be measured. From these complementary studies, new insights into the structural and chemical principles of actinide compounds will be obtained with which to design new synthetic schemes to produce new materials.

A major aspect of our program is the design and testing of sequestering agents for actinide ions that can engulf the ion and generate neutral or negatively charged complexes. Synthesis and

evaluation of actinide-specific sequestering agents will continue. The testing of the carboxylated catecholyl amides such as 3,4,3-LiCAMC will continue and new modifications will be examined. Entirely new ligand structures which incorporate monoprotic ligand groups isosteric with catechol will be examined. These include 2-hydroxypyridine-N-oxide and its isomers and derivatives.

The thermodynamics of actinide binding by our sequestering agents will be studied by solution equilibrium competition studies and potentiometric techniques.

The mode of bonding of the actinides and similar ions by the human iron transport protein transferrin will be studied, since this is the major mechanism of Pu(IV) transport in mammals. The kinetics of the release of actinide ions from transferrin to the actinide sequestering agents will be examined.

Further studies of organoactinides are planned. Our new synthesis of 1,4-disubstituted cyclooctatetraenes starting with cyclooctatetraene oxide lends itself to various substituents. The synthesis also provides routes to deuterated t-butylcyclooctatetraenes required to confirm the assignment of ring proton chemical shifts in uranocenes; the preparations now in progress will be completed. The 1,5-di-t-butylcyclooctatetraene, recently synthesized, will be converted to the corresponding uranocene. The discovery by dynamic NMR studies of intramolecular attraction between the aryl rings in 1,1'-dimesityluranocene will be confirmed by preparation and study of the monosubstituted uranocene. The synthesis of cyclohexyluranocenes will be completed, and we expect to start synthetic studies of silyluranocenes. We will continue efforts to prepare stable allylic uranium compounds. Our NMR studies of uranocenes will continue with emphasis next on ^{13}C NMR.

We will continue collaboration with Dr. J. Green of Oxford in the determination of PES spectra by sending substituted thorocenes. We will also continue the collaboration with Dr. N. Rösch of Munich in relativistic Xα-SW calculations of uranocene structures. Our own extended Hückel calculations will be extended to relativistic calculations.

The 1-cyclooctatetraenyl-2-cyclopentadienylethane which we prepared recently will be used to study its various anions and for conversion to a uranium derivative. We will continue our attempts to prepare bridged uranocenes.

If the availability of suitable personnel permits, we will continue our studies of transuranium organometallic chemistry, particularly with the preparation and chemistry of neptunium and plutonium compounds.

Studies on the preparation and physical properties of new actinide amides, alkoxides, alkyls, and borohydrides will continue. The reaction chemistry on compounds of the type $XM[N(SiMe_3)_2]_3$ where X is H, BH_4, or Me and M is Th or U will be pursued. Reactions with unsaturated and other organic molecules with the intent of developing new chemistry is of particular interest. Studies will continue on the low-valent (i.e., divalent oxidation) state of Sm, Eu, and Yb with the bulky ligands $(Me_3Si)_2N$ and C_5Me_5. Our principal objective is to understand the chemistry and reactivity of these low-valent materials.

The spectroscopic program will emphasize the crystal spectra of lanthanide and actinide ions in a variety of host crystals. Optical studies (in collaboration with the Solid State Division of ORNL) were initiated this year on lanthanide ions diluted in $LuPO_4$. This synthetic material is closely related to the mineral monozite which has chemical and physical properties that make its synthetic analogues attractive candidates as host materials for long-lived actinide ions for radioactive waste isolation. This work will be expanded to include radioactive actinide ions and related host materials, such as YPO_4 and $ScPO_4$. Work will continue on magnetic and optical studies of the actinide borohydrides. A major effort is underway to classify the free-ion spectra of U, obtained this year as a function of current and time after excitation, and the higher Z actinides such as Am and Cm.

1980 PUBLICATIONS AND REPORTS

Refereed Journals

1. D. L. Perry, H. Ruben, D. H. Templeton, and A. Zalkin, "Structure of Di-μ-Aquo-Bis[Dioxobisnitratouranium(VI)-Diimidazole, $[UO_2(NO_3)_2(H_2O)\cdot C_3H_4N_2]_2$, A Water Bridged Dimer of Uranyl Nitrate," Inorg. Chem. 19, 1066 (1980), LBL-9973.

2. A. Zalkin, D. H. Templeton, C. LeVanda, and A. Streitwieser, Jr., "Synthesis and Structure of Two Crystalline Forms of Cyclooctatetraenethorium(IV) Dichloride Bistetrahydrofuran," Inorg. Chem. 19, 2560 (1980), LBL-10537.

3. R. H. Banks, N. M. Edelstein, B. Spencer, D. H. Templeton, and A. Zalkin, "Volatility and Molecular Structure of Neptunium(IV) Borohydride," J. Am. Chem. Soc. 102, 620 (1980), LBL-9229.

4. H. Ruben, B. Spencer, D. H. Templeton, and A. Zalkin, "Structure of Tris(urea)dioxouranium(VI) Sulfate, $UO_2(OC(NH_2)_2)_3SO_4$," Inorg. Chem. 19, 776 (1980), LBL-9478.

5. T. D. Tilley, R. A. Andersen, B. Spencer, H. Ruben, A. Zalkin, and D. H. Templeton, "Divalent Lanthanide Chemistry; Bis(pentamethylcyclopentadienyl)europium(II) and Ytterbium(II) Derivatives: Crystal Structure of Bis(pentamethylcyclopentadienyl)ytterbium(II) Tetrahydrofuran Hemi(toluene) at 176K," Inorg. Chem. 19, 2999 (1980), LBL-10490.

6. D. L. Perry, D. P. Freyberg, and A. Zalkin, "Imidazolium Tetrachlorodioxouranate(VI), $(C_5H_5N_2)_2UO_2Cl_4$," J. Inorg. Nucl. Chem. 42, 243 (1980), LBL-8687.

†7. L. K. Templeton, D. H. Templeton, and R. P. Phizackerley, "L_3-Edge Anomalous Scattering of X-rays by Praseodymium and Samarium" J. Am. Chem. Soc. 102, 1185 (1980), LBL-9865.

†8. D. H. Templeton and L. K. Templeton, "Polarized X-ray Absorption and Double Refraction in Vanadyl Bisacetylacetonate," Acta Cryst. A36, 237 (1980), LBL-9530.

†9. D. H. Templeton, L. K. Templeton, J. C. Phillips, and K. O. Hodgson, "Anomalous Scattering of X-rays by Cesium and Cobalt Measured with Synchrotron Radiation," Acta Cryst. A36, 436 (1980), LBL-9880.

10. C. LeVanda, J. P. Solar and A. Streitwieser, Jr., "Half-Sandwich Cyclooctatetraenethorium Compounds," J. Am. Chem. Soc. 102, 2128 (1980).

11. J. P. Solar, H. Burghard, R. Banks, A. Streitwieser, Jr. and D. Brown, "Bis-η_8-(1,3,5,7-tetramethylcyclooctatetraene) Compounds of Protactinium, Neptunium and Plutonium," Inorg. Chem. 19, 2186 (1980).

12. W. L. Smith and K. N. Raymond, "The Oxidation of Uranium(IV) by N-Phenylbenzohydroxamic Acid and the Structure of the Reaction Product: Chlorodioxo-N-Phenylbenzohydroxamato-Bis(Tetrahydrofuran)Uranium(VI)," J. Inorg. Nucl. Chem. 41, 1431 (1979).

13. W. L. Smith and K. N. Raymond, "Synthesis of Aliphatic Dimeric N-Isopropylhydroxamic Acids and the Crystal and Molecular Structure of N,N'-Dihydroxy-N,N'-Diisopropylhexanediamide: A Hydroxamic Acid in the Trans Conformation," J. Am. Chem. Soc. 102, 1252 (1980).

14. F. L. Weitl and K. N. Raymond, "Specific Sequestering Agents for the Actinides. 3. Polycatecholate Ligands Derived from 2,3-Dihydroxy-5-Sulfobenzoyl Conjugates of Diaza- and Tetraazaalkanes," J. Am. Chem. Soc. 102, 2289 (1980).

15. P. W. Durbin, E. S. Jones, K. N. Raymond and F. L. Weitl, "Specific Sequestering Agents for the Actinides. 4. Removal of $^{238}Pu(IV)$ from Mice by Sulfonated Tetraneric Catechoyl Amides," Rad. Res. 81, 170 (1980).

16. K. N. Raymond and C. W. Eigenbrot, Jr., "Structural Criteria for the Mode of Bonding of Organoactinides and -Lanthanides and Related Compounds," Acc. Chem. Res. 13, 276 (1980).

17. G. Thornton, N. Rösch, and N. Edelstein, "A Quasi-Relativistic SCF X-α Study of Octahedral $5f^1$ Complexes," Inorg. Chem. 19, 1304 (1980), LBL-9693.

18. M. Baluka, S. Yeh, R. Banks, and N. Edelstein, "Preparation and Structural Characterization of α-NpF_5," Inorg. Nucl. Chem. Letters 16, 75 (1980), LBL-10123.

19. N. Edelstein, W. Kolbe, and J. E. Bray, "Electron Paramagnetic Resonance Spectrum of the Γ_8 Ground State of Np^{4+} Diluted in Cs_2ZrCl_6," Phys. Rev. B 21, 338 (1980), LBL-8787.

20. J. P. Hessler, W. T. Carnall, H. M. Crosswhite, H. Crosswhite, N. Edelstein, J. G. Conway, and R. Sarup, "Energy Level Analysis of Np^{3+}:$LaCl_3$ and Np^{3+}:$LaBr_3$," J. Chem. Phys. 72, 5089 (1980).

21. R. H. Banks, N. M. Edelstein, B. Spencer, D. H. Templeton, and A. Zalkin, "Volatility and Molecular Structure of Neptunium (IV) Borohydride," J. Am. Chem. Soc. 102, 620 (1980), LBL-9229.

22. R. H. Banks and N. M. Edelstein, "Vibrational Spectra and Normal Coordinate Analysis of Neptunium (IV) Borohydride and Neptunium (IV) Borodeuteride," J. Chem. Phys. 73, 3589 (1980), LBL-10901.

23. J. O. Berg, T. E. Christensen, P. W. Kidd, G. R. Neil, and J. G. Conway, "Identification of U III and U IV Lines," J. Opt. Soc. Am. 70, 716 (1980).

24. J. Blaise, F.-F. Wyart, J. G. Conway, and E. F. Worden, "Generalized Parametric Study of $5f^N$ and $5f^N7s$ Configurations," Physica Scripta. 22, 224 (1980).

25. K. N. Raymond and C. W. Eigenbrot, Jr., "Structural Criteria for the Mode of Bonding of Organoactinides and Lanthanides and Related Compounds," Acc. of Chem. Res. 8, 276 (1980), LBL-10467.

Other Publications

1. N. M. Edelstein, Ed. "Lanthanide and Actinide Chemistry and Spectroscopy," ACS Symposium Series 131, Washington, D. C. (1980).

2. R. A. Andersen "Bis-trimethylamide Derivatives of the f-block Elements," in Lanthanide and Actinide Chemistry and Spectroscopy, N. M. Edelstein, Ed., ACS Symposium Series 131, Washington, D. C. (1980) pp. 31-44.

3. J. P. Solar, A. Streitwieser, Jr., and N. M. Edelstein, "Cyclooctatetraeneactinide(IV) Bis-borohydrides," in Lanthanide and Actinide Chemistry and Spectroscopy, ibid, p. 81-91.

4. W. D. Luke and A. Streitwieser, Jr., "Nuclear Magnetic Resonance Studies of Uranocenes", ibid., p. 93-140.

5. K. N. Raymond et al., "Specific Sequestering Agents for the Actinides," ibid., pp. 143-172.

6. R. H. Banks and N. M. Edelstein, "Synthesis and Characterization of Protactinium(IV), Neptunium(IV) and Plutonium(IV) Borohydrides," ibid., pp. 331-348.

7. E. F. Worden and J. G. Conway, "Multistep Laser Photoionization of the Lanthanides and Actinides," ibid., pp. 381-426.

8. Wayne Luke, "I. Synthesis and Characterization of Annulated Uranocenes. II. The Variable

Temperature ^{1}H NMR of Uranocenes," Ph.D. thesis, LBL-10497.

9. Thomas Hayhurst, "The Application of Some Hartree-Fock Model Calculations to the Analysis of Atomic and Free-Ion Optical Spectra," Ph.D. thesis, LBL-10978.

10. Bruce Lulu, "The Zeeman Spectrum of Scandium," Ph. D. thesis, LBL-11407.

Reports

1. R. A. Andersen, A. Zalkin, and D. H. Templeton, "Crystal and Molecular Structure of Hydridotris[bis-(trimethylsilyl)amido] uranium(IV)," LBL-10489, In press: Inorg. Chem.

2. T. D. Tilley, A. Zalkin, R. A. Andersen, and D. H. Templeton, "Divalent Lanthanide Chemistry; Preparation of Some Four and Six Coordinate Bis(trimethylsilylamide) Complexes of Europium(II). The Crystal Structure of bis[di(trimethylsilyl)amido]bis(1,2-dimethoxyethane)europium(II)," LBL-10858, In press: Inorg. Chem.

3. L. G. McCullough, H. W. Turner, R. A. Andersen, A. Zalkin and D. H. Templeton, "Preparation and Crystal Structure of 1,2-dimethoxyethane Complex of Bis[di(trimethylsilyl)amido]dichlorouranium(IV)," LBL-11047, In press: Inorg. Chem.

4. F. L. Weitl, K. N. Raymond, and P. W. Durbin, "Synthetic Enterobactin Analogs. Carboxamido-2,3-Dihydroxyterephthalate Conjugates of Spermine and Spermidine," LBL-11412, In press: J. Med. Chem.

5. W. L. Smith and K. N. Raymond, "Actinide-Specific Sequestering Agents and Decontamination Applications," Springer-Verlag, LBL-11533, In press.

6. V. L. Pecoraro, W. R. Harris, C. J. Carrano and K. N. Raymond, "Siderophilin Metal Coordination. 2. Difference Ultraviolet Spectroscopy of Di-, Tri-, and Tetravalent Metal Ions with Transferrin and Ethylene-bis(o-hydroxyphenylglycine)," LBL-11657, Submitted to: J. Am. Chem. Soc.

7. V. P. Pecoraro, F. L. Weitl, and K. N. Raymond, "Ferric Ion-Specific Sequestering Agents. 7. Synthesis, Iron Exchange Kinetics, and Stability Constants of N-Substituted, Sulfonated Catechoylamide Analogues of Enterobactin," LBL-11807, Submitted to: J. Am. Chem. Soc.

8. C. W. Eigenbrot, Jr. and K. N. Raymond, "The Synthesis and Crystal Structure of $UCp_3(C_3H_3N_2)$. A New Model of Pyrazolate Bonding," LBL-11877, Submitted to: Inorg. Chem.

9. W. R. Harris, C. J. Carrano, V. L. Pecoraro, and K. N. Raymond, "Sierophilin Metal Coordination. 1. Complexation of Thorium by Transferrin: Structure-Function Implications," LBL-11878, Submitted to: J. Am. Chem. Soc.

10. T. Hayhurst, G. Shalimoff, N. Edelstein, L. A. Boatner, M. M. Abraham, "Optical Spectra and Zeeman Effect of Er^{3+} in $LuPO_4$ and $HfSiO_4$," LBL-11943, To be submitted to: J. Chem. Phys.

11. N. Edelstein, "Bonding in Metal-Borohydride Complexes," LBL-10855, In press: Inorg. Chem.

12. M. Baluka, N. Edelstein, and T. A. O'Donnell, "Electronic Solution Spectra for Uranium and Neptunium in Oxidation States (III) to (VI) in Anhydrous Hydrogen Fluoride," LBL-11618, Submitted to: Inorg. Chem.

13. W. D. Luke and A. Streitwieser, Jr., "The Barriers to Ring Rotation in 1,1',4,4'-tetra-t-Butyluranocene and 1,1',3,3'-tetra-t-Butylferrocene," LBL-11722, Submitted to: J. Am. Chem. Soc.

14. B. Spencer and N. M. Edelstein, "Electron Paramagnetic Resonance Spectra of Er(III), Dy(III), and Gd(III) in Yttrium and Lanthanum Hydrides," LBL-11935, Submitted to: Inorg. Chem.

15. J. G. Conway, J. C. Krupa, P. Delamoye and M. Genet, "Spectrum and Energy Levels of Pr^{3+} in $ThBr_4$," LBL-11601, In press: J. Chem. Phys.

Invited Talks

1. A. Streitwieser, Jr., "Chemistry of Uranocene," Institute of General Chemistry, University of Pisa, Italy, May 30, 1980.

2. A. Streitwieser, Jr., "Chemistry of Uranocene," Institute of Organic Chemistry, University of Köln, West Germany, June 30, 1980.

3. A. Streitwieser, Jr., "Chemistry of Uranocene," School of Inorganic Chemistry, Technical University, Munich, West Germany, July 11, 1980.

4. A. Streitwieser, Jr., "Chemistry of Uranocene," Department of Inorganic Chemistry, Oxford University, England, July 24, 1980.

5. R. A. Andersen, "Alkyl and Hydride Derivatives of the Actinide Metals," Columbia University, New York, New York, May 1, 1980.

6. R. A. Andersen, "Alkyl and Hydride Derivatives of the Actinide Metals," Exxon Corporation, Linden, New Jersey, May 5, 1980.

7. R. A. Andersen, "Alkyl and Hydride Derivatives of the Actinide Metals," DuPont Company, Wilmington, Delaware, May 6, 1980.

8. R. A. Andersen, "Alkyl and Hydride Derivatives of the Actinide Metals," University of Oxford, Oxford, England, June 28, 1980.

9. D. H. Templeton, "X-ray Birefringence," University of California, San Francisco, January 31, 1980.

10. D. H. Templeton, L. K. Templeton, R. P. Phizackerley, and K. O. Hodgson, "L_3-Edge Anomalous Scattering Measured with Synchrotron Radiation," American Crystallographic Assoc., Calgary, Alberta, August 17, 1980.

11. K. N. Raymond, K. Abu-Dari, W. R. Harris, W. Pecoraro, and T. Tufano, "Siderophore Complexes," 4th Senior Technical Meeting, American Chemistry Society Puerto Rico Section, San Juan, Puerto Rico, December 7, 1979.

12. K. N. Raymond, "Coordination Chemistry of Microbial Iron Transport and Metal-Ion Specific Sequestering Agents," Smith, Kline and French Laboratories, Philadelphia, Pennsylvania, December 18, 1979.

13. K. N. Raymond, "Coordination Chemistry of Microbial Iron Transport and Metal-Ion Specific Sequestering Agents," Brigham Young University, Provo, Utah, February 26, 1980.

14. K. N. Raymond, "Coordination Chemistry of Microbial Iron Transport and Metal-Ion Specific Sequestering Agents," University of Utah, Salt Lake City, Utah, February 27, 1980.

15. K. N. Raymond, "Coordination Chemistry of Microbial Iron Transport and Metal-Ion Specific Sequestering Agents," Utah State University, Logan, Utah, February 28, 1980.

16. K. N. Raymond, "Biological Iron Transport: Microbial and Synthetic," University of California, Santa Cruz, California, June 4, 1980.

17. K. N. Raymond, "Design of Ligands for the Chelation of Trivalent Metals," Third International Symposium on Radiopharmaceutical Chemistry, Washington University, St. Louis, Missouri, June 16, 1980.

18. K. N. Raymond, "Macrocyclic Ligands Specific For: A) Fe(III), B) Actinide(IV) Ions," Fourth Symposium on Macrocyclic Compounds, Brigham Young University, Provo, Utah, August 11, 1980.

19. K. N. Raymond, "Design of New Chelating Agents," Second Symposium on Development of Iron Chelators for Clinical Use, Sir Francis Drake Hotel, San Francisco, California, August 23, 1980.

20. N. Edelstein, "Actinide Borohydrides, Synthesis, Physical and Electronic Properties," 10 eme Journees des Actinides, Stockholm, Sweden, May 7, 1980.

21. J. G. Conway, "Laser Spectroscopy of Lanthanide and Actinides," Institut de Physique Nucleaire, Orsay, France, January 15, 1980.

22. J. G. Conway, "Atomic Spectroscopy of the Actinide Elements," Centre d'Etudes Nucleaires de Saclay, France, March 27, 1980.

23. J. G. Conway, "Review of the Spectroscopy of the Actinides," Institute of Chemistry, University of Wroclaw, Wroclaw, Poland, June 19, 1980.

24. J. G. Conway, "Laser Spectroscopy of Rare Earth and Actinide Atoms," Institut de Physique Nucleaire de Lyon, Lyon, France, July 11, 1980.

* * *

†Partially supported by the National Science Foundation

Fossil Energy

a. Electrode Surface Chemistry*

Philip N. Ross, Investigator

Introduction. Commercialization of phosphoric acid fuel cell technology requires a capital cost reduction and an extension of power plant life compared to currently available technology. Significant capital cost reduction can be achieved if an oxygen reduction catalyst that is catalytically more active than platinum can be developed. The objective of the present research is to develop the physical and chemical understanding of the oxygen-platinum surface interactions necessary for the rational selection of alloying ligands that modify the basic catalyst properties of platinum. It is felt that the platinum-oxygen bond energy, which we can measure directly, will be changed when ligands are bonded to the surface platinum atoms and that, by the use of appropriate ligands, an optimal bond energy will result in enhanced catalytic activity relative to the pure platinum surface.

The molten carbonate fuel cell is undergoing extensive research and development as an advanced fuel cell system for converting synthesis gas to electric power. Current operating schemes involve passage of the fuel gas, following contaminant removal, past a porous nickel anode which contacts an electrolyte. The hydrogen and carbon monoxide are electrochemically oxidized in the fuel cell anode via

$$H_2 + CO_3^{2-} \rightleftharpoons H_2O + CO_2 + 2e^-$$

$$CO + CO_3^{2-} \rightleftharpoons 2CO_2 + 2e^-$$

The carbon dioxide produced is recycled to the air intake for the cathode to form the gas mixture that is electrochemically reduced via

$$CO_2 + 1/2O_2 + 2e \rightleftharpoons CO_3^{2-}$$

Commercial fuel cell development programs have concentrated their work on performance characteristics and materials evaluation in subscale hardware. Kinetic studies in alkali metal carbonate electrolytes have been done only with noble metal electrodes, e.g., Au. Little is known about the reaction kinetics or mechanism on materials used in practice, e.g., nickel oxide.

*This work was supported by the Assistant Secretary for Fossil Energy, Office of Fuel Cells, Advanced Concepts Division of the U. S. Department of Energy under contract No. W-7405-ENG-48 through the Fuel Cell Project Office, NASA Lewis Research Center, Cleveland, OH.

The objectives of our research are to study the kinetics and mechanism of oxygen reduction on electrode materials of practical interest.

1. OXYGEN ADSORPTION ON Pt INTERMETALLIC SURFACES†

P. N. Ross and G. Derry

Many theoretical descriptions of catalytic reactions at metal surfaces attribute the remarkable catalytic properties of Pt to the unique d-electron configuration in this atom. The Engel-Brewer bonding rules suggest the enormous thermodynamic stability of intermetallics like Pt_3Ti is due to strong metal-metal d-orbital bonding which is absent in the pure metals. The Engel-Brewer bonding picture for this class of intermetallics has not yet been confirmed by probes of the electronic structure. It is the objective of our initial study of Pt-Group IV intermetallic surfaces to determine the nature of the metal-metal bonding by photoelectron spectroscopy. An electron energy analyzer of the hemispherical type,[1] developed specifically for angle-resolved photoemission here at LBL, has been built. The analyzer has been integrated into UHV system with both x-ray and helium gas discharge photon sources. Photoemission studies of Pt_3Ti are in progress.

* * *

†Supported by the National Aeronautics and Space Administration under Contract No. NSE-2193 and by the Lawrence Berkeley Laboratory Director's Office under Contract No. W-7405-ENG-48 with the U. S. Department of Energy.

1. This apparatus is described in LBL-10025 by S. D. Kevan and D. A. Shirley.

2. THE KINETICS OF THE O_2/CO_2 REACTION IN MOLTEN CARBONATE: REACTION ORDERS FOR O_2 and CO_2 ON NiO†,‡

P. N. Ross and J. Winnick§

Kinetic studies were initiated in the oxygen reduction reaction on nickel electrodes in a carbonate eutectic of a composition used in the commercial fuel cell programs. Kinetic rates free of mass transport effects in the electrolyte were obtained using a potentiostatic transient method with a nonporous (lithiated) nickel oxide electrode. Six different CO_2 partial pressures (0.5-5%) and three O_2 partial pressures (10, 19, 33%) were used to obtain the orders of the reaction

in CO_2 and O_2. Transport free polarization curves were used to derive the kinetic symmetry factor (Bronsted coefficient) and Tafel slope.

The reaction orders were obtained from the partial pressure dependence of the exchange current density (I_o) and from the values of the Bronsted Coefficient (α). Let

$$\left(\frac{\partial \log I_o}{\partial \log P_{CO_2}}\right)_T = m$$

$$\left(\frac{\partial \log I_o}{\partial \log P_{O_2}}\right)_T = n$$

then the reaction orders for the anodic (I_+) and cathodic (I_-) partial currents are:

$$\left(\frac{\partial \log I_\pm}{\partial \log P_{CO_2}}\right)_{E,T} = \begin{cases} m - 1 + (\alpha/2) & \text{anodic} \\ m + (\alpha/2) & \text{cathodic} \end{cases}$$

$$\left(\frac{\partial \log I_\pm}{\partial \log P_{O_2}}\right)_{E,T} = \begin{cases} n - 2/1 + (\alpha/2) & \text{anodic} \\ n + (\alpha/4) & \text{cathodic} \end{cases}$$

The exchange current density was found to follow the relation

$$I_o = 0.75\ P_{CO_2}^{0}\ P_{O_2}^{0.4}\ \exp[-6 \times 10^3/(T + 273)] \quad ,$$

where I_o is in A/cm^2 for T = 550 - 750° and partial pressure of 0.1-0.5 atm. Thus, m = 0 and n = 0.4. The Bronsted Coefficient was found to be 0.65. Therefore, we find:

$$\left(\frac{\partial \log I}{\partial \log P_{CO_2}}\right)_{E,T} \approx \begin{cases} -0.63 & \text{anodic} \\ +0.32 & \text{cathodic} \end{cases}$$

$$\left(\frac{\partial \log I}{\partial \log P_{O_2}}\right)_{E,T} \approx \begin{cases} +0.23 & \text{anodic} \\ -0.66 & \text{cathodic} \end{cases}$$

It is interesting to note that none of the reaction mechanisms yet proposed for the CO_2/O_2 reaction in alkali carbonate melts are consistent with the reaction orders we report here. They are also very different from the values reported by Appleby and Nicholson[1] for Au, which is indicative of differences in kinetics between Au and NiO electrodes. It is also possible that the NiO electrode surface chemistry changes as a function of the CO_2/O_2 ratio by virtue of the Lux-Flood acid-base properties of the carbonate electrolyte, i.e., the equilibrium concentration of oxide ion in the melt. Future mechanistic studies of the CO_2/O_2 reaction should consider the use of (specific) oxide ion electrodes to monitor possible changes in melt basicity with gas composition.

* * *

†Co-sponsored by NASA Research Contract NSG-2193 and the Office of the Director, Lawrence Berkeley Laboratory.

‡Brief version of LBL-10937; accepted for publication in Journal of the Electrochemical Society.

§Permanent address: Department of Chemical Engineering, Georgia Institute of Technology, Atlanta, GA 30332.

1. A. J. Appleby and S. B. Nicholson, J. Electroanal. Chem. 53, 105 (1974); J. Electroanal. Chem. 83, 309 (1977).

RESEARCH PLANS FOR CALENDAR YEAR 1981

No further work with molten carbonate electrolytes is planned. The study of intermetallic bonding in the Pt-Group IV compounds using photoelectron spectroscopy will continue. Studies on the chemisorption of oxygen on Pt-Group IV intermetallic compound surfaces will be initiated.

1980 PUBLICATIONS AND REPORTS

Refereed Journals

1. P. N. Ross. "Hydrogen Chemisorption on Pt Single Crystal Surfaces in Acidic Solutions," Surface Science 101, 1 (1980).

LBL Reports

1. P. N. Ross and J. Winnick, "The Kinetics of the CO_2/O_2 Reaction in Molten Carbonate: Reaction Orders for O_2 and CO_2 on NiO," LBL-10937; accepted for publication in J. Electrochem. Soc.

Invited Talks

1. P. N. Ross and J. Winnick, "The Kinetics of the CO_2/O_2 Reaction in Molten Carbonate: Reaction Orders for O_2 and CO_2 on NiO," 158th Meeting of the Electrochemical Society, October 5-10, 1980.

b. Deuterium Analysis of Coal by NMR*

Alexander Pines, Investigator

1. CYLINDRICAL SAMPLE TURBINE FOR MAGIC ANGLE NMR†

R. Eckman and A. Pines

Measurement of isotropic chemical shift spectra in NMR of solids by magic angle sample spinning requires a high speed sample turbine, as is well known from recent novel studies of ^{13}C and ^{2}D in solids. For high resolution deuterium NMR in solids, these requirements are particularly stringent since: (a) the axis must be stable to within 0.001°, and (b) the spectral bandwidth is limited to the spinner frequency due to the need for synchronous sampling. Mechanical design improvements in the sample turbine NMR probe now allow easily reproducible frequencies of rotation in excess of 300,000 rpm with previously used polymer turbines. Figure 1 shows the high resolution isotropic chemical shift spectrum of deuterated solid dimethoxybenzene indicating that the turbine axis is stable to within 0.001°. Thus, the mechanical system exceeds the requirements for high resolution deuterium NMR in solids. A number of resolved ^{2}D spectra in solids have been obtained for the first time in this way. Construction of new sample turbines from boron nitride and glass ceramic materials is in progress. These should allow significantly higher frequencies of rotation which can make isotropic spectra of carbon-13 at high field ($\omega_L(^{13}C)$ = 90 MHz readily available. Further improvements in the NMR probe rf design to give greater efficiency and increased power capability are also under way.

* * *

†Based in part on LBL-10864; J. Mag. Res. 41, 440 (1980).

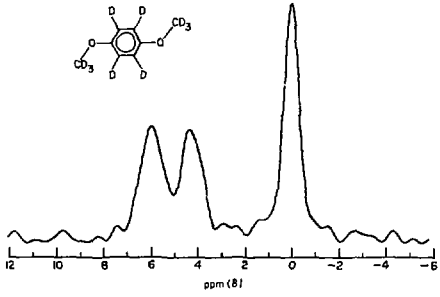

Fig. 1. Resolved ^{2}D NMR spectrum in solid deuterated dimethoxybenzene obtained by magic angle spinning with synchronized sampling. The aromatic peak is split into two lines, indicating inequivalent aromatic deuteron sites in the solid, in contrast to the liquid where the methoxy groups rotate freely. (XBL 8010-12563)

2. DEUTERIUM SPIN-LATTICE RELAXATION IN MAGIC ANGLE SPINNING†

R. Eckman and A. Pines

The spin-lattice relaxation time, T_1, for deuterium in non-rotating solids can be extremely long. This makes the analysis for many chemically distinct types difficult, if not impossible. The T_1's measured selectively for several model compounds in magic angle NMR, given in Table 1, indicate a trend for which a simple model has been proposed. Molecular motion of one deuterium type, for example the rotating methyl group, provides spin-lattice relaxation via the quadrupole mechanism. Cross relaxation with other deuterium types is brought about by the sample rotation about the magic angle which causes the resonances of distinct types to overlap for a fraction of the cycle. Preliminary results, showing no dependence of $-\phi D_4$ T_1's on temperature or frequency of sample rotation, agree with this model. Further detailed temperature dependence studies in addition to NMR high field measurements are under way to confirm the model. In addition, T_1 measurements in oriented single crystals are in progress which can be conclusive to understanding this model, as well as higher order cross relaxation mechanisms.

*This work was supported by the Assistant Secretary for Fossil Energy, Office of Coal Research, Liquefaction Division of the U. S. Department of Energy under Contract No. W-7405-ENG-48 through the Pittsburgh Energy Center, Pittsburgh, PA.

Table 1. Deuterium solid state T_1 (T = 290 K).

Compound	Deuterium type $-CD_3$	$-CD_2$	$-\phi D_4$
perdeutero-para-di-t-butylbenzene $\{(CD_3)_3\phi D_4(CD_3)_3\}$	0.01	-	7
perdeutero-terephthalic acid diethylester $[D_5C_2O_2C\phi D_4CO_2C_2D_5]$	0.14	8	22
perdeutero-hexamethylbenzene $[C_{12}D_{18}]$	0.04	-	-
perdeutero-dimethylnaphthalene $[C_{12}D_{12}]$	0.09	-	1.1
perdeutero-terephthalic acid dimethylester $[D_3CO_2C\phi D_4CO_2CD_3]$	0.86	-	28
terephthalic acid dimethyl ester $[H_3CO_2C\phi D_4CO_2CH_3]$	-	-	640
perdeutero-para-di-methoxybenzene $[D_3CO\phi D_4OCD_3]$	0.26	-	5
para-dimethoxybenzene $[H_3CO\phi D_4OCH_3]$	-	-	400

* * *

†Based in part on LBL-9948; Chem. Phys. Lett. 71, 376 (1980).

3. PROTON-DEUTERIUM CROSS POLARIZATION IN ROTATING SOLIDS†

R. Eckman, L. Müller, and A. Pines

The NMR of rare isotopes is typically difficult to detect (e.g., small amounts of deuterium in solids). We recently demonstrated that sensitivity of magic angle deuterium NMR in solids can be considerably increased by application of proton-enhanced NMR in which spin polarization is transferred from an abundant (proton) spin system to the rare (deuterium) system. This was possible because the sample rotation modulates the quadrupole coupling so that all dueterons can undergo Hartmann-Hahn matching with the proton system for some fraction of the spinner cycle. Our goal was to apply this result to double-quantum magic angle NMR as well as to maximize the sensitivity gain in ^1H-^2H cross polarization. Proton-enhanced deuterium spectra magic angle spinning solids have been obtained with good signal enhancement. Cross polarized signals show considerable gain over the unenhanced signals. Maximum enhancement factors for some polycrystalline model compounds are given in Table 2. Cross polarization was performed

Table 2. Deuterium signal proton-enhancement factors in magic angle spinning solids.

Compound	Theoretical S^{CP}/S^0	Experimental S^{CP}/S^0	$\omega_Q/2\pi$ (kHz)
30% random-deutero hexamethylbenzene	3.0	3.2	14
4.9% random-deutero durene	5.7	4.4	34
dimethoxybenzene $DH_2CO-\phi D_4-OCH_2D$			
(1) (2) Total	2.1	2.2	--
(1)	-	2.7	33
(2)	-	1.4	130

both by single and multiple contact sequences. Theoretical and experimental investigation of the dynamics of ^1H-^2H cross polarization is in progress in order to maximize gain in sensitivity. This also includes measurement of the dependence on the frequency of sample rotation, ω_r, over a wide range and the effect of off-resonant rf fields. Preliminary evidence was found to suggest that cross relaxation in the proton-enhanced experiment can occur via an effective field deuterium double-quantum spin flip accompanied by multiple spin slips in the proton system. High resolution deuterium magic angle NMR can now be applied to a variety of systems of chemical interest as well as basic coal research, to study the evolution of hydrogen during processing.

* * *

†Based in part on LBL-10245, Chem. Phys. Lett. 76, 149 (1980); and LBL-10338, Phys. Rev. A. 22, 638 (1980).

4. DOUBLE QUANTUM NMR IN SOLIDS†

R. Eckman, L. Müller, J. B. Murdoch, and A. Pines

Two aspects of double quantum NMR have been pursued in solid state deuterium studies: (a) as we showed previously, the double quantum deuterium spectrum is independent of quadrupole broadening to first order and thus gives the chemical shielding powder pattern directly. Our new contribution is to study the orientation of the deuterium shielding tensor by analyzing the shape of the double quantum transfer function. As shown in Fig. 2, the powder lineshapes are sensitive to these details. (b) By observing the double quantum signal the sensitivity of magic angle deuterium experiments to spinner stability can be eliminated. Sharp double quantum lines and echo spectra were obtained with magic angle spinning, even though the normal deuterium signal was broadened beyond detection levels. Such deuterium NMR experiments should provide useful tools for observing the nature and evolution of deuterium (or hydrogen) sites in solids.

* * *

†Based in part on LBL-10331, Chem. Phys. Lett. 74, 376 (1980); and LBL-11360.

5. CARBON-13 NMR OF WHOLE AND PROCESSED COALS†

D. Wemmer,‡ D. D. Whitehurst,§ G. Drobny, and A. Pines

We have continued our studies of coal and coal processing by carbon-13 NMR, in collaboration with Mobil Research and Development. Four types of carbon (aliphatic, oxygen-bonded aliphatic, aromatic and condensed aromatic) can be distinguished directly in the solid state. This has permitted a correlation of carbon type distribution with the source of coal, the type of coal and with changes which occur during processing. An example of evolution of aromatic carbon content during solvent refining in Fig. 3 shows a change only at ~ 80% conversion. The solvent refined coal (SRC) and the residue both exhibit an increase in aromatic carbon content. A number of our results are contrary to those obtained by indirect techniques, such as solution infrared spectroscopy, which until recently have not been able to study the solid samples directly.

* * *

†Based in part on LBL-10533; Proc. Roy. Soc., in press.

‡Current address: Department of Chemistry, Stanford University, Stanford, California.

§Mobil Research and Development.

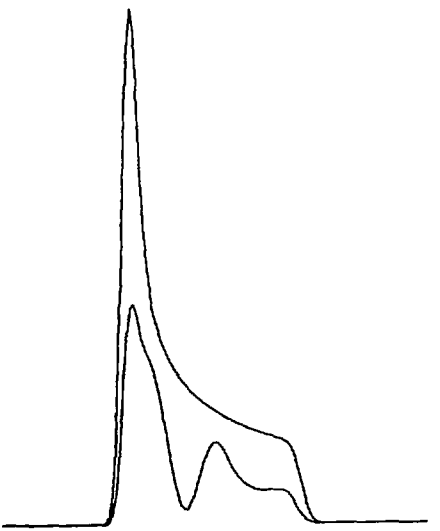

Fig. 2. The top is an undistorted chemical shielding powder pattern with axial symmetry. This is normally unobservable since the quadrupolar broadening for deuterium is typically one hundred or more times greater than the above linewidth. The lower curve is that obtained by double quantum NMR in which quadrupolar broadening is eliminated. It provides a value for the shielding anisotropy and an analysis of the wavy lineshapes allows a determination of orientations for the principal axes of the shielding tensor. (XBL 811-7666)

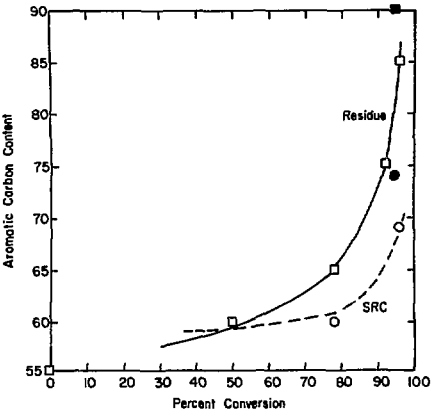

Fig. 3. Change in aromatic carbon content for solvent refined coal (SRC) and residue as a function of conversion in the solvent refining process. These numbers were obtained by proton enhanced ^{13}C NMR directly in the solid samples. (XBL 806-10552)

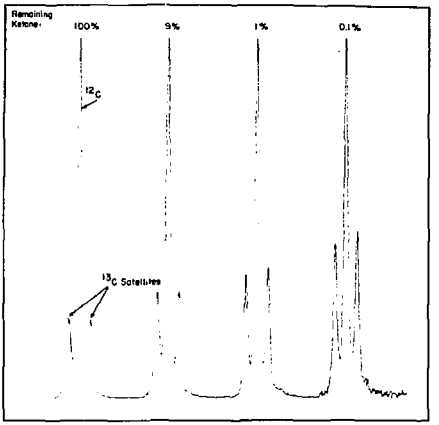

Fig. 4. Carbon-13 enrichment of the carbonyl position in dibenzyl ketone allowed an accurate study of the increase in $^{13}C/^{12}C$ ratio during photochemical irradiation due to the nuclear magnetic isotope effect. (XBL 806-9851)

6. SYNTHESIS OF ISOTOPICALLY LABELED MOLECULES AND LIQUID AND SOLID CRYSTALS†

S. Wolfe and A. Pines

A number of our experiments require the use of isotopically labeled photochemical precursors, liquid crystals, or large single crystals. Synthetic work involves the preparation of isotopically-enriched starting materials, their incorporation into liquid crystal molecules, preparation of single domain samples, orientation with polarized microscope techniques, Bridgeman preparation of single crystals, orientation with x-ray techniques, measurement of isotope content by mass spectrometry, etc. For example, ^{13}C enrichment of the carbonyl position of dibenzyl ketone allowed us to easily follow the nuclear magnetic isotope effect during photochemical decomposition as shown in Fig. 4. Other examples are a ten-step synthesis of a specifically labeled ^{2}D and ^{13}C molecule for chain configuration studies. In exploring new methods for catalytic exchange of protons by deuterium, we have found 10% Pt on carbon to be a suitable catalyst when mixed with the material and D_2O at 150-170° in a glass bomb. This catalyst is more active and less susceptible to poisoning than the reduced PtO_2 used previously.

* * *

†Brief version of article in J. Chem. Phys., in press.

7. SYMMETRY OF MOTIONAL MOLECULAR JUMPS IN SOLIDS†

D. E. Wemmer‡ and A. Pines

The symmetry and energy barriers for molecular reorientation in a number of solids have been studied using high resolution solid state ^{13}C-^{1}H double resonance. A dynamical application of group theory shows that similarities in the powder pattern for the slow jump region are extremely sensitive to the point group of the molecular potential. The symmetry places constraints on the number and types of motional parameters which may be obtained by NMR. For example, in solid permethylferrocene motional jumps of $2\pi/5$ are more than four times more probable than those of $4\pi/5$. The activation energy in the jump process is 13.5 k joules/mole. Furthermore, from the change in lineshape due to motion, the orientation of the principal axes of the chemical shielding tensor were determined. This is shown in Fig. 5.

* * *

†Based in part on LBL-10563, J. Am. Chem. Soc., in press.

‡Current address: Department of Chemistry, Stanford University.

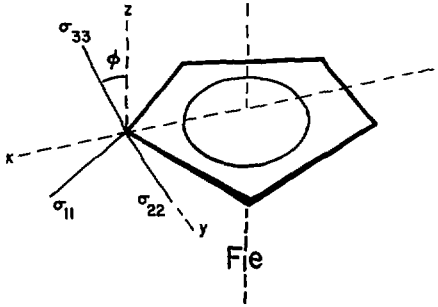

Fig. 5. Top half of ferrocene ring showing orientation of ring carbon-13 chemical shielding tensor. The twist in principal axes by angle ϕ has been measured at ~ 20° by motional lineshape studies. (XBL 811-7667)

RESEARCH PLANS FOR CALENDAR YEAR 1981

Research will continue in the following areas:

1. Development of deuterium magic angle spinning NMR and application to model complex molecules with partial deuteration as basis for study of hydrogen evolution during coal processing.

2. Application of double quantum NMR with magic angle spinning to deuterium as well as other isotopes including nitrogen-14. The double quantum double resonance should allow studies of rare isotopes with high resolution and with high sensitivity.

3. Spin diffusion and spin relaxation of quadrupolar nuclei in solids, to study local structure and dynamics.

4. Collaboration on coal research using carbon-13 and extension to other nuclei such as deuterium, nitrogen-14, and sulphur-33.

1980 PUBLICATIONS AND REPORTS†

Refereed Journals

1. M. Alla, R. Eckman, and A. Pines, "Spin Diffusion and Spin-Lattice Relaxation of Deuterium in Rotating Solids," Chem. Phys. Lett. 71, 148 (1980), LBL-9948.

2. L. Müller, R. Eckman, and A. Pines, "Deuterium Double Quantum NMR with Magic Angle Spinning," Chem. Phys. Lett. 74, 376 (1980), LBL-10331.

3. J. Tang, L. Sterna, and A. Pines, "Anisotropic Spin-Lattice Relaxation of Deuterated Hexamethylbenzene," J. Mag. Res. 41, 389 (1980).

4. R. Eckman, M. Alla, and A. Pines, "Deuterium NMR in Solids with a Cylindrical Magic Angle Sample Spinner," J. Mag. Res. 41, 440 (1980), LBL-10864.

LBL Reports

1. D. Wemmer, A. Pines, and D. D. Whitehurst, "NMR Studies of Coal and Coal Abstracts," LBL-10533, in press: Proc. Roy. Soc.

2. Luciano Müller, "Double Quantum Deuterium Echoes in Magic Angle Spinning Polycrystalline Solids," LBL-11360, submitted to Chem. Phys.

Invited Talks

1. A. Pines, Symposium on Chemistry and Physics of Coal, American Physics Society, New York, N.Y., March 1980, invited lecture.

2. A. Pines, Chemistry Department, University of California, Riverside, California, April 1980.

3. A. Pines, Royal Society Discussion Meeting on New Coal Chemistry, London, England, May 1980, invited lecture.

4. A. Pines, Royal Society Discussion Meeting on NMR in Solids, London, England, June 1980, invited lecture.

5. A. Pines, Shell Research Laboratories, Amsterdam, The Netherlands, June 1980, invited lecture.

6. A. Pines, Physics Department, University of Delft, The Netherlands, Seminar.

7. A. Pines, "Selectivity in Multiple Quantum Spectroscopy," Rocky Mountain Conference on Analytical Chemistry of Spectroscopy, Denver, Colorado, August 1980, Plenary Lecture.

8. A. Pines, "Selective Absorption of Groups of Photons in Spectroscopy," 12th International Meeting on Spectroscopy, Sydney, Australia, August 1980, Plenary Lecture.

9. A. Pines, Chemistry Department, University of Sydney, Sydney, Australia, August 1980, Seminar.

10. A. Pines, Advanced NATO Workshop on High Resolution NMR in Solids, Sardinia, Italy, September 1980, invited lectures.

11. A. Pines, "New Vistas in Chemical Instrumentation," Dedication of New Facility, California Institute of Technology, October 1980, invited lecture.

12. A. Pines, Chemistry Department, University of Brisbane, Brisbane, Australia, August 1980.

13. A. Pines, Physics Department, University of Pennsylvania, Philadelphia, March 1980, Seminar.

14. A. Pines, Purdue University, Lafayette, Indiana, March 1980, Seminar.

15. A. Pines, Department of Chemistry, UCLA, Los Angeles, February 1980, Seminar.

16. A. Pines, Physics Department, University of California, Berkeley, February 1980, Seminar.

* * *

†For additional listings, see section on "Nuclear Magnetic Resonance."

c. Oil Shale Retort Components*

Alan V. Levy, Investigator

Introduction. An oil-shale-containing crucible in an argon-filled laboratory furnace was used to expose specimens of mild and stainless steels to shale retorting products at temperature-time combinations representative of modified in-situ retorts. These exposures, at temperatures near the 1000°C that actually occur in underground retorts and for the durations that will occur in full scale retorts, can now be used to test materials. Shale in various stages of pyrolysis, combustion, and cooling are being used to better define the conditions where corrosive attack of metals is most destructive. The promise of protective aluminide coatings on mild steel to prevent harmful corrosion is being pursued along several avenues to determine what variables affect the performance of the coatings and what processing variables will produce superior coating systems.

1. CORROSION IN SIMULATED IN-SITU OIL SHALE RETORTS†

G. Nguyen and A. Levy

The corrosion behavior of carbon and stainless steels was determined in above ground, simulated in-situ oil shale retorts by exposing 1 in. x 3 in. x 0.25 in. specimens directly in shale beds that were retorted at the Laramie Energy Technology Center (LETC) and the Lawrence Livermore National Laboratory (LLNL). Underground retort exposures were also studied in thermowell performance in a horizontally oriented retort operated by the Geokinetics Corp.

The differences were determined between 300 and 400 series stainless steels exposed to Green River shale in a 10-ton retort at LLNL. The temperatures in the run spiked to 900°C, but exceeded 825°C for only 4 hr. Figure 1 shows the scales formed on 316SS and 410SS, the former having 18% chromium (Cr) content, the latter only 12% Cr. The difference in Cr content was a major factor in the large difference in corrosion, but not the only difference. Other factors, such as the crystallographic structure and the presence of nickel and molybdenum, also contributed to the markedly less corrosion of the 316SS.

The multi-layer, porous scale that formed on the 410SS is typical of heavy scale formations on any alloy in an oil shale retorting environment. It is composed of a gradation of chromium sulfides to iron-chromium sulfide spinels. The thin, primarily Cr_2O_3 scale on the 316SS, should be compared to the scale layers on the 410SS, considering the great difference in magnification of the two pictures.

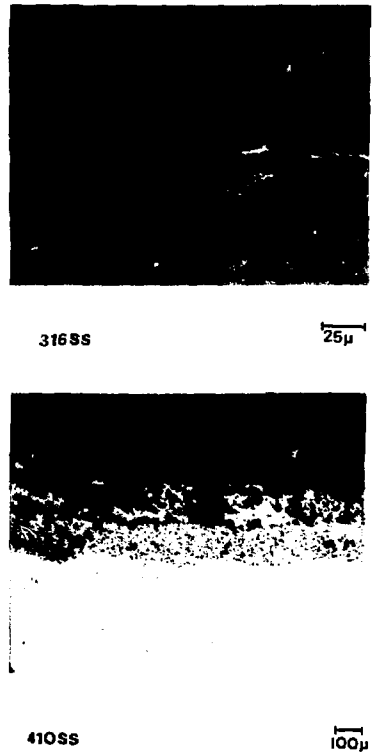

Fig. 1. Scales formed on 316SS and 410SS L-2 retort. (XBB 801-159)

Corrosion is a chemical reaction and is affected by temperature. Figure 2 shows the amount of scale formed on 1018 mild steel placed in two different locations in the 10 ton retort at LETC, test S-60. The test was conducted with Green River shale and air and saturated steam, with a total retorting time of 64 hr, 50 hr on air and steam. The amount of scale formed at the 600° and 875°C areas of the retort is markedly different; note the difference in magnification of the pictures. This test indicates that A53 mild steel piping does have a limited, but possibly acceptable life, at temperatures no more than 550-650°C in retorts. The scaling rate at the lower temperatures could be planned for.

*This work was supported by the Assistant Secretary for Fossil Energy, Office of Coal Research, Materials Components Division of the U. S. Department of Energy under Contract No. W-7405-ENG-48.

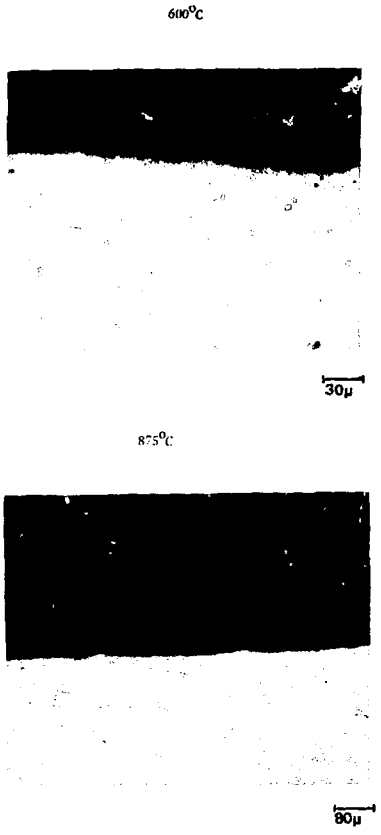

Fig. 2. Scales formed on 1018 mild steel at 600° and 875°C in S-60 retort. (XBB 801-157A)

* * *

†Brief version of LBL-12019.

2. CORROSION IN LABORATORY CRUCIBLE TESTS

William Goward

Studies are being conducted in a laboratory furnace crucible containing oil shale at various stages of retorting to determine the oxidation and sulfidation behavior of different alloys that are candidates for use in full scale retorting operations.

304SS and 1018 steel have been exposed in a laboratory crucible containing unreacted Anvil Points (24 gal/ton) shale and spent Colony Mines Colorado shale (35 gal/ton) at 1000°C for 50 hr. The system was flushed with argon at the start of the test. The specimens were submerged in the shale, which was ground to an appropriate particle size for the laboratory crucible. The exposure of 304SS to spent shale resulted in the formation of a scale consisting of a top layer of chromium sulfide that has small particles of iron oxide in it and an underlayer whose matrix is predominantly chromium oxide with particles of iron oxide distributed in it. Some internal oxidation and sulfidation occurred at the grain boundaries. There is also a chromium depleted zone just underneath the scale due to the diffusion of chromium out to the surface of the metal where the scale growth occurs. Figure 3(a) shows the cross section of the exposed sample. The EDAX

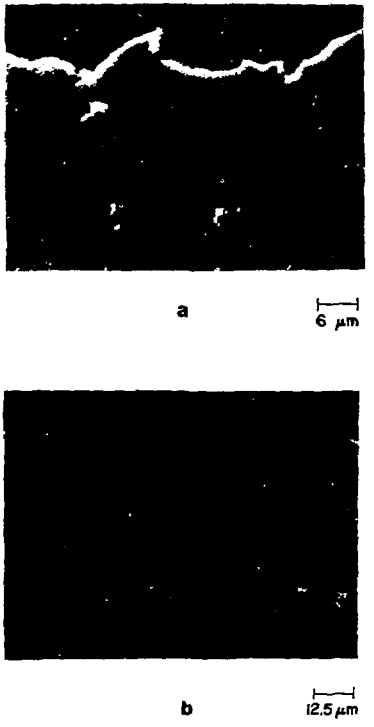

Fig. 3. (a) Scale and internal oxidation/sulfidation on a 304SS specimen from crucible test. (b) Scale and internal oxidation/sulfidation on 1018 exposed in crucible tests. (XBB 813-2347)

analyzer on the scanning electron microscope was used to verify the constituents of the scale and the internal oxidation and sulfidation products.

The exposure of 1018 to the fresh oil shale resulted in the formation of an iron sulfide and manganese sulfide scale. There was more material loss of the 1018 than the 304SS. More internal oxidation/sulfidation occurred in the 1018 than in the 304SS. Figure 3(b) shows the cross section of exposed 1018.

The data indicates that the corrosive attack which occurs on steels in an oil shale environment is related to the type and condition of the shale with which the metals are in contact, as well as the composition of the steel and the test temperature and time. The exposure of 304SS caused it to form a somewhat protective Cr_2O_3 scale, which resulted in less internal corrosion occurring. The 1018 had essentially a non-protective scale, consisting primarily of iron sulfide, and, hence, more external as well as internal corrosion resulted.

The laboratory furnace crucible tests showed the same corrosion behavior as the actual retort tests except that 1018 was observed to have more internal attack in the laboratory tests.

3. ALUMINIDE COATINGS FOR FERROUS ALLOYS

W. Goward and D. Boone

The ability to use inexpensive aluminide coating processes to upgrade the corrosion resistance of low cost steels in oil shale retorting environments has been further demonstrated by additional testing during the last year. Aluminized 1018 mild steel showed greater resistance to corrosion at 1500°F in a simulated in-situ retort exposure than some uncoated higher alloyed steels.

Examination of the initial coating structures and degradation modes revealed a range of coating structures depending on alloy composition and structure and coating application variations. Figure 4 shows some of the varying structures which result from the same aluminizing cycle on several 300 series stainless steels.

A review of the literature indicated that much less information is available for the potentially useful iron aluminide systems than for the nickel and cobalt base aluminides. Examination of the structures of the as-formed iron aluminides revealed that many coatings were formed by an outward diffusion mechanism (a low activity out-

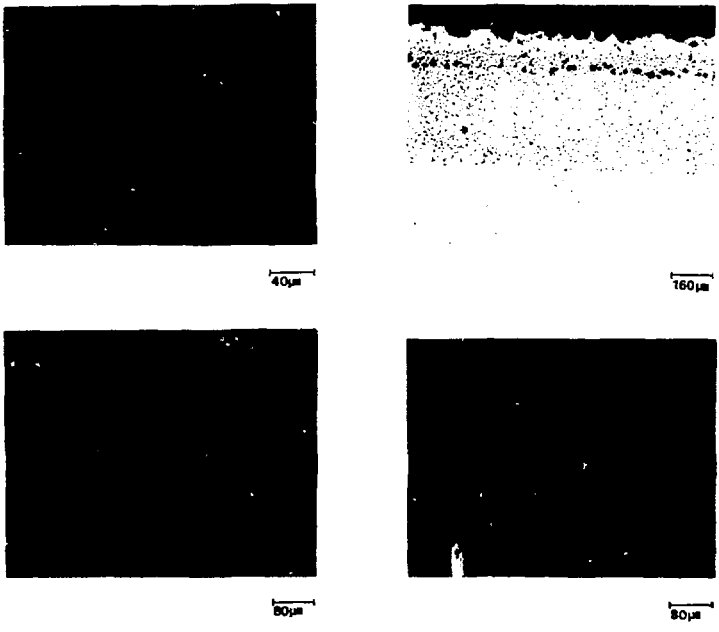

Fig. 4. Varying structures from same aluminizing cycle on several 300 series stainless steels.
(XBB 809-11381)

ward type coating) and resulted in excessive and potentially detrimental entrapment of pack mix in the outer zone of the coating (Fig. 5). Such occurrences can be controlled by changes in pack cementation aluminum activity and the use of separately generated aluminum sources, so called out-of-the-pack techniques. Specimens have been coated under a variety of controlled aluminizing techniques to better understand the growth mechanisms and resulting structures obtainable.

Potential problems in the pack cementation aluminizing of large structures could be overcome by the use of slurry and wire spray techniques that are being evaluated. An additional advantage of these processes over the chemical vapor deposition technique which has been demonstrated in oil shale retort service is the potential for incorporation of additional beneficial elements such as silicon into the coatings. In other studies, coatings containing silicon have been shown to be extremely resistant to contaminated fuel environments. Specimens of slurry-applied aluminide coatings are being evaluated for structural and compositional features as a function of processing parameters prior to testing in an oil shale retort.

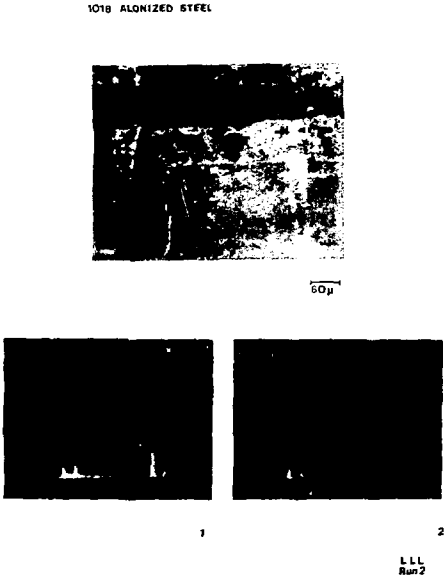

Fig. 5. Microstructure of an iron aluminide coating on 1018 mild steel. (XBB 801-160)

4. LASER MODIFICATION OF COATINGS AND ALLOYS†

W. Goward and D. Boone

Studies of the mechanisms of protection provided by the in-situ formation of oxide barrier scales on metals have identified the importance of substrate structure as well as composition on the nature of the barrier scale. Grain size, phase distribution, and active element type, form, and distribution all are found to influence the nature and adherence of the barrier oxide layer.

Surface thermal modification treatments such as laser fusion have been shown to have a large effect on the microstructure of both substrates and applied coatings. The principle effects of these treatments on coatings have been to promote the densification, adherence, and grain size refinement of the coating applied by a slurry or thermal spray process. In this treatment considerable intermixing of substrate and coating materials can occur. These effects combine to modify the formation of the oxide barrier scale forming on the surface of the coating. However, little information is available on the effects of process variations in these high energy fusion treatments on the structure and protectiveness of the resulting oxide. A study is being conducted to examine the effects of laser surface treatment and selected pretreatments on the fully dense, MCrAlY electron beam, physical vapor deposition (EBPVD) applied coatings systems.

Results of laser treatments showed that a controlled surface layer, 10-100 μm thick, could be processed with no detrimental substrate interactions. Examination of the laser treated coating revealed an essentially structureless affected zone with a dispersion of very fine second phase particles ~1000 Å in diameter (Fig. 6). Later examination, using SAM, indicated

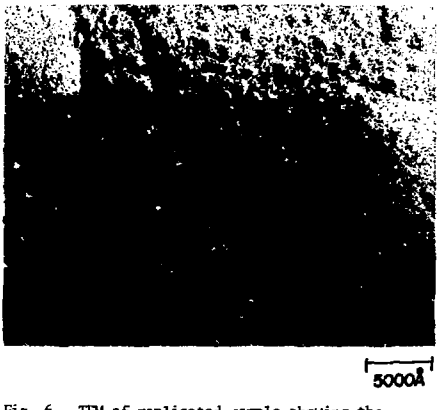

Fig. 6. TEM of replicated sample showing the fine dispersion of particles present in the lased area. (XBB 813-2344)

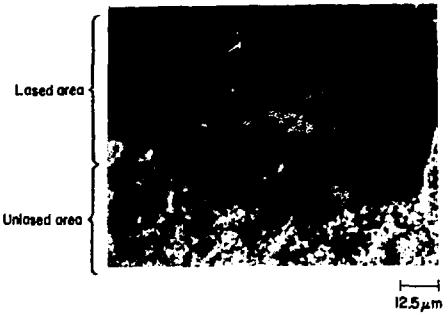

Fig. 7. Difference in surface morphology between lased and unlased areas upon subsequent oxidation exposure. (XBB 813-2345)

the fine dispersed particles to be aluminum, yttrium, and oxygen rich (Al_2O_3-Y_2O_3). Subsequent oxidation exposure resulted in the formation of a more adherent, smooth Al_2O_3 layer over the laser treated area (Fig. 7). The protectiveness and durability of this oxide is predicted to be greatly increased over that of the small crystallite surface area of the unlased portion of the oxide.

In attempts to further improve this effect, postulated to result in part from the presence of the finely dispersed active element containing oxides, pre-laser treatments were investigated including pre-oxidation of leader growth structure to promote greater density of dispersed oxides and surface doping with yttrium and hafnium. The laser-treated structure of the pre-oxidized CoCrAlY is shown in Fig. 8. Again, improvements

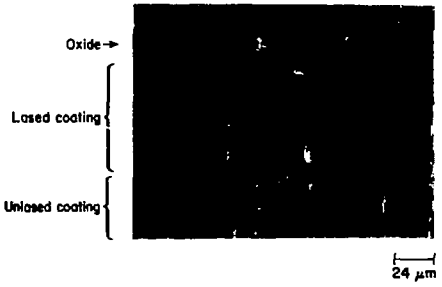

Fig. 8. Cross section of a lased area after deep etching with a methyl bromine solution. (XBB 813-2346)

in protective oxide structure were observed. The pre-oxidized leader structure is shown, as well as the laser treated zone with the distribution of fine oxides (unresolvable at this magnification).

The deep etched microstructure shows the heavily oxidized leaders in the un-laser affected coating and the uniform fine structure of the laser affected coating. Structural details of this zone are now being studied. An additional feature of this deep etched microstructure is the detail of the underside of the protective oxide formed in-situ on the laser treated coating. Structural and growth morphologies of these oxides are being studied by this technique because they are affected by processing variables.

* * *

*Brief version of LBL-12020.

RESEARCH PLANS FOR CALENDAR YEAR 1981

Exposures of coated and uncoated metal specimens to underground retort combustion conditions and product collection environments will be carried out as availability occurs in underground retorts. The corrosion problems in above ground retorting operations will be defined and specimens will be exposed in retort operations. Laboratory crucible testing will concentrate on determining the relative corrosion behavior of candidate low alloy and stainless steels, uncoated and coated. Shales at various states of pyrolysis, combustion, and spent conditions will be used to determine at what stage in the in-situ process corrosion is most severe.

Above ground retorting conditions will be used in laboratory tests to determine the behavior of metals and refractories that are candidates for use in retorts. The combined effects of abrasive-corrosive environments on materials will be assessed. Liquid products from retorting operations will be obtained and specimens exposed in them to determine the corrosive potential of the fluids. Refinements in coating composition and processing to improve protection levels, primarily of aluminides on carbon and low alloy steels, will be made.

1980 PUBLICATIONS AND REPORTS

LBL Reports

1. A. Levy and R. Bellman, Jr., "Corrosion of Metals in Oil Shale Environments," LBL-12019.

2. D. H. Boone, W. D. Goward, and P. G. Moore, "Structure of Laser Treated MCrAlY Coatings," LBL-12020.

Other Publications

1. A. Levy, "Corrosion of Metals in Oil Shale Retorting Operations," in Proceedings of NACE Materials and Corrosion Problems in Energy Systems Conference, New Orleans, Louisiana, February 1980.

2. A. Levy and D. Whittle, "Corrosion of Steels in In-Situ Oil Shale Retorting Environments," NACE Corrosion '80 National Meeting, Chicago, Illinois, March 1980.

Invited Talks

1. A. Levy, "Corrosion of Metals in In-Situ Oil Shale Retorts," DOE-LETC 3rd Annual Oil Shale Conference, Denver, Colorado, January 1980.

2. A. Levy, "Materials Behavior in Oil Shale Retorting," AIME-TMS Bay Area Chapter Meeting, Stanford University, January 1980.

3. D. Boone, "Laser Surface Treatment of NiCrAlY Coating," International Conference on Metallurgical Coatings, San Diego, California, April 1980.

4. A. Levy and D. Boone, "Corrosion of Aluminized Steel in Oil Shale Retorts," AIME-TMS Annual Meeting, Pittsburgh, Pennsylvania, October 1980.

5. W. Goward and D. Boone, "Effects of Laser Surface Treatments of MCrAlY Coatings," AIME-TMS Annual Meeting, Pittsburgh, Pennsylvania, October 1980.

d. Chemistry and Morphology of Coal Liquefaction*

Alexis T. Bell, Robert G. Bergman, James W. Evans, Heinz Heineman, Alan V. Levy, Gabor A. Somorjai, and K. Peter Vollhardt, Investigators

Introduction. The first year of this project has been completed, and much of the time and effort has been concentrated on equipment building, assembling, testing, and staffing. This, of course, has been more true in the areas of work with spectroscopic and high pressure equipment than in organic chemical reactions. More experimental results are therefore reported in the areas of hydrogen transfer mechanisms and catalysis and organo-metallic chemistry.

This project has brought together a team of organic, physical, and organometallic chemists, chemical engineers, and material scientists, some of whom have had extensive industrial experience. The advantages of an interdisciplinary approach have become apparent in regular meetings, numerous discussions, and suggestions, often coming from analogies in other areas. Finally, the project provides an excellent training ground for future workers in synthetic fuels research and development, because all work is carried out by graduate students and post-docs under the leadership of experts in a variety of fields.

1. SELECTIVE SYNTHESIS OF GASOLINE RANGE COMPONENTS FROM CO AND H_2

A. T. Bell

The design and construction of the experimental apparatus have occupied a major portion of the time during the past year. Two catalyst testing units were designed and constructed. The first utilizes a fixed bed of catalyst and is intended for screening of new catalyst preparations. The second unit uses a high pressure stirred autoclave. This reactor can be used to study mass transfer effects with either catalysts in oil suspensions or larger catalyst particles contained in a rotating basket.

A schematic of the apparatus used in conjunction with the autoclave reactor is shown in Fig. 1. Reactants are purified and then fed to the autoclave via mass flow controllers. The use of such controllers makes it possible to maintain a constant supply of H_2 and CO over long durations. The reactor is a 450 cm^3 Parr autoclave and is fitted with a thermocouple well and an impeller that can be rotated at speeds of up to 1000 rpm. The autoclave can be maintained at elevated temperatures by means of a furnace connected to a temperature controller.

Both gases flow out of the autoclave and the liquids contained within them are analyzed by gas chromatography. The gaseous products are sampled from a heat-traced line maintained at reaction pressure. The hydrocarbons present in the gas phase are analyzed on a 50 m glass capillary column coated with OV-101 and contained within a Varian Aerograph Model 3700 gas chromatograph. The products leaving the capillary are detected by a flame ionization detector. The contents of CO, H_2, and C_1 through C_5 hydrocarbons in the product gas are analyzed using a 3-in. column packed with Chromsorb 106. The effluents from this column are detected by a thermal conductivity detector. An analysis of the liquid in the autoclave is achieved using the capillary column. The data generated by the chromatograph are stored on-line using a Commodore PET microprocessor connected to a floppy disc. Following acquisition, the data are analyzed to determine peak areas and a table of product composition is generated by the microprocessor. It is anticipated that by using such a sophisticated product analysis scheme, it will be possible to obtain a complete mass balance around the reactor.

The flow manifold used in conjunction with the fixed bed reactor is similar to that shown in Fig. 1. The reactor in this case is a stainless steel tube that is heated in a temperature-regulated sand bath. The gaseous reaction products from this reactor are analyzed using the procedures described above. Thus, the chromatograph and data acquisition system serve both reactor systems.

*This work was jointly supported by the Director, Office of Energy Research, Office of Basic Energy Sciences, Chemical Sciences Division, and Assistant Secretary for Fossil Energy, Office of Coal Research, Liquefaction Division of the U. S. Department of Energy under Contract No. W-7405-ENG-48 through the Pittsburgh Energy Technology Center, Pittsburgh, PA.

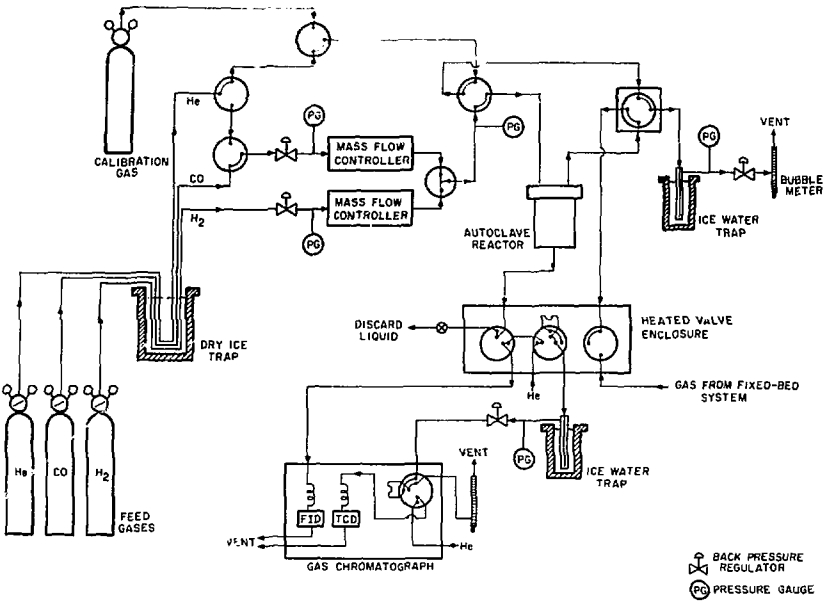

Fig. 1. Autoclave apparatus schematic. (XBL 811-7592)

2. ELECTRON MICROSCOPE STUDIES OF COAL DURING HYDROGENATION

J. W. Evans, J. A. Little, and M. I. Perez

This project will concentrate on characterization of coal microstructures and observation of in situ gasification reactions in an environmental cell. So far this study has concentrated on the initial characterization of coal microstructures using a Phillips 400 TEM/STEM microscope, but it will be broadened to include the use of a small environmental cell in a Hitachi 650-kV microscope so that both the temperature and pressure of different gases can be simultaneously controlled over the specimen while it is being viewed directly in electron transmission. A residual gas analyzer has also been purchased from Anacon Ltd. to monitor the gases leaving the environmental cell so that the course of the conversion reaction can be followed kinetically.

Figure 2 shows a high-ash anthracite which was found to contain many particles containing only titanium as seen in the x-ray display (Fig. 2, at A). By using a finely focused electron beam with a probe diameter of approximately 100 Å, micro-micro diffraction patterns could be obtained and the mineral particle identified as anatase, a form of TiO_2. The detection of titanium bearing particles is important because titanium has a detrimental effect on the Co-Mo catalyst used in liquefaction processes. Figure 2 (B and C) shows

Fig. 2. Transmission electron micrograph of high-ash anthracite showing a titanium bearing particle at A and a partially degraded clay particle (B and C). (XBL 803-3120)

a large grain of clay, the extensive streaking of the diffraction spots indicating that the grain is composed of very many thin clay platelets. Although the mineral underwent rapid degradation under the electron beam (e.g., at C), it was tentatively labeled as sericite, a form of muscovite.

Figure 3 is a montage of micrographs indicating the sequence of events from identification of the macerals in a high volatile class A bituminous coal by optical methods to examination in the electron microscope. Figure 4 shows micrographs of the two different areas "A" and "C" shown in Fig. 3. Figure 3a is from a fusinite band and shows particles tentatively identified as kaolinite from the x-ray and diffraction data. Figure 4b is from the vitrinite region of the specimen (C) and Fig. 4c shows an electron micrograph from the Telocollinite region with very small regularly shaped particles containing mainly aluminum with a small amount of calcium.

Figure 5 shows an example of a Western subbituminous coal. The high moisture content of this coal together with its high volatile content may make it susceptible to partial charring in the ion-beam thinner. The catalytic effect of certain minerals within coals is often ascribed to their ability to "wet" the surface of the coal and provide additional reaction sites. As a possible semi-char this coal will already have "gasified" to some extent and therefore it is instructive to compare the elemental distribution in the coal. This is seen in Fig. 5. Elemental mapping of the silicon and titanium expose the silica and titania particles, which appear as essentially discrete particles against a background of random 'noise' from the x-ray detector. The sulphur scan shows a general level of sulphur throughout the sample, as might be expected from the organic sulphur in the coal grains. However, the calcium scan shows no localization of calcium-containing particles but, instead, a high level of calcium spread evenly over the coal grains of this particular area. Thus, it would appear that calcium does have a good ability to 'wet' the surface of the coal.

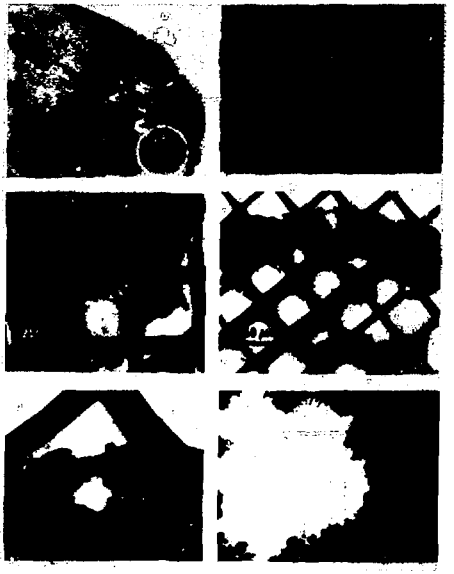

Fig. 3. Montage of optical and electron micrographs showing the preparation method used to accurately characterize the coals and correlate both optical and electron-optical micrographs. (a) Optical micrograph showing vitrinite (c) and fusinite (A) bands. (b) The same areas as (a) mounted in a folding grid. (c) The same area as (a) and (b) viewed in transmitted light. (d) The area after ion beam thinning. (e) Low magnification electron micrograph of the sample. (f) Higher magnification electron and micrograph showing more image detail. (CBB 807-8897)

Fig. 4. Electron micrographs showing microstructures and particles associated with the different macerals in the coal. (a) Particles of kaolinite in the fusinite band. (b) Microstructure of the vitrinite band. (c) Microstructure and particles from a tellocollinite region. (CBB 807-8895)

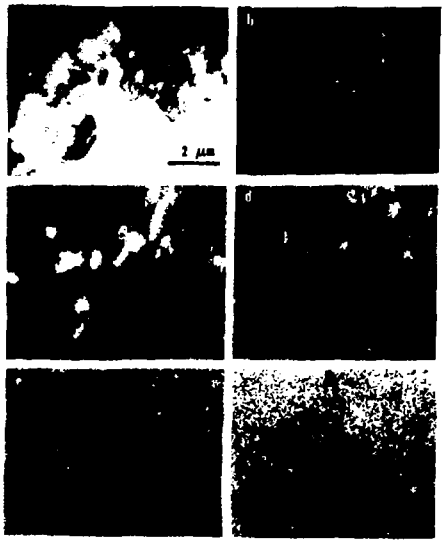

Fig. 5. Elemental distribution in the sub-bituminous coal specimen. (a) STEM micrograph of area. (b) X-ray analysis of the whole area. (c) Silicon map. (d) Titanium map. (e) Sulphur map. (f) Calcium map. (XBB 807-8747)

3. CATALYZED LOW TEMPERATURE HYDROGENATION OF COAL

G. A. Somorjai and A. Cabrera

With the advancement of surface analysis techniques, it is now possible to characterize the structure, composition, and oxidation states of surface atoms and molecules on the atomic scale. Progress made in this field once again encouraged the study of catalyzed coal conversion for the purpose of gathering more information on the basic steps of the process.

There are several recent papers on the hydrogenation and oxidation of graphite catalyzed by metal particles (transition metals and alloys of transition metals). Surface characterization in these studies was by electron-microscopy. Instrumentation developed by surface science is capable of combining both studies of the actual kinetics at high pressures and studies of surface analysis in ultrahigh vacuum with the sample in situ. We have developed and built an ultra high vacuum system that enables studying catalytic reactions at high pressures and characterizing the surface by several techniques in the same chamber. We are presently applying the system to the studies of the catalyzed, low temperature hydrogenation of graphite.

4. SELECTIVE HYDROGENATION, HYDROGENOLYSIS, AND ALKYLATION OF COAL AND COAL DERIVED LIQUIDS BY ORGANOMETALLIC SYSTEMS

K. P. C. Vollhardt

Nucleophilic Additions to Cationic Transition Metal Arene Complexes (Wilson Tam and K. P. C. Vollhardt).

In an effort to delineate the potential of using organometallic catalysts and reagents for the nucleophillic depolymerization and lipophilization of coal models, double nucleophillic additions to $CpCoC_6H_6^{2+}$ were studied. Such additions had been attempted in rhodium and iridium compounds previously by others but had, when successful, only led to single adducts. It was found that nucleophiles of moderate basicity, e.g., methoxide, malonate, and cyclopentadienide anion, furnish disubstituted complexed cyclohexadienes. Addition occurs vicinally, stereospecifically exo, and to the benzene ring only, in accord with theoretical expectations. Other nucleophiles lead to ligand displacements and decomposition. The bisadducts are exceedingly thermally and air sensitive precluding further chemistry. Nevertheless, the basic feasibility of this approach to benzene

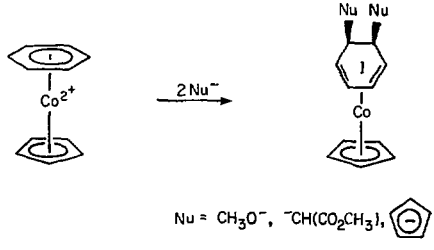

ring substitution has been demonstrated. Several other systems were investigated, particularly complexes based on iron and manganese as shown below:

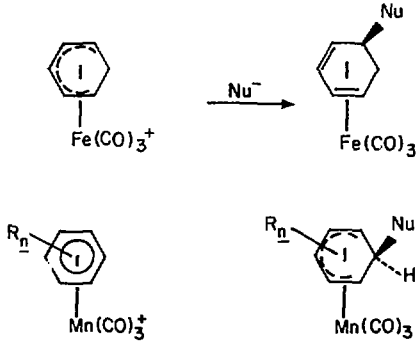

New compounds have been fully characterized and analyzed. Some of the complexes obtained show mobility of the hydrogens located endo. Hydrogen shifts occur stereospecifically, presumably via metal hydride intermediates, but neither ring carbonylation nor carbon monoxide reduction were observed.

Preparative Separation of Organometallic Diastereomers, Structural Isomers, and Homologs on Ultrasphere ODS.† (John M. Huggins, Joseph A. King, Jr., K. Peter C. Vollhardt, and Mark J. Winter).

Successful separations of complex mixtures of organometallic compounds by chromatography are rare. However, high performance reversed phase liquid chromatography (RPLC) of isomeric n^5-cyclopentadienyl-n^4-cyclobutadiene cobalt complexes and of structurally analogous dinuclear molybdenum derivatives has been achieved. Although some of these compounds are moderately to strongly air-sensitive, quantitative isolation on a preparative scale is possible by using deoxygenated and argon saturated mobile phases. Among the organometallic complexes resolved are diastereomers and structural isomers; their separation demonstrates both the versatility and high resolving power of RPLC (Figs. 6-9). All separations were accomplished using 10 mm × 250 mm ULTRASPHERE ODS columns (sample loop 1ml). Conditions are specified in the figure captions. Initial gravity elution chromatography of the compounds shown gave inseparable mixtures.

* * *

†Supported in part by NSF and NIH.

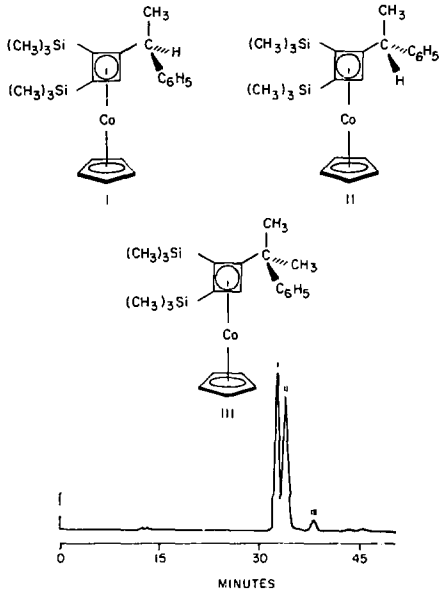

Fig. 6. Chromatogram of 5 to 10 mg of a mixture of (I)-(III) in 1.0 ml; flow 1.3 ml/min; CH_3CN-H_2O, 9:1. (XBL 814-2216)

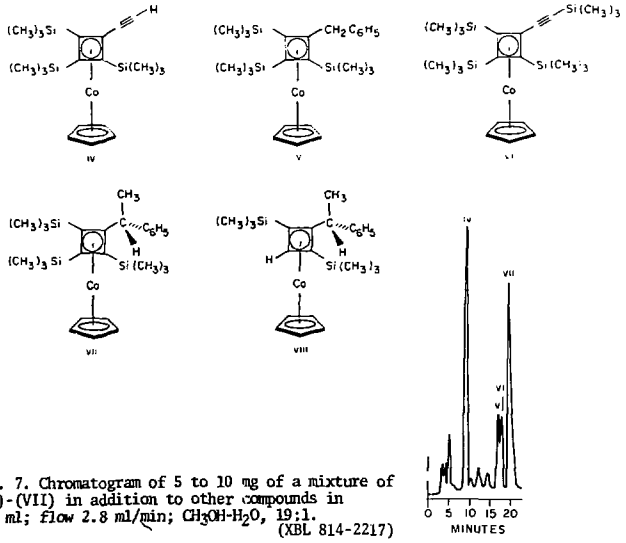

Fig. 7. Chromatogram of 5 to 10 mg of a mixture of (IV)-(VII) in addition to other compounds in 1.0 ml; flow 2.8 ml/min; CH_3OH-H_2O, 19:1. (XBL 814-2217)

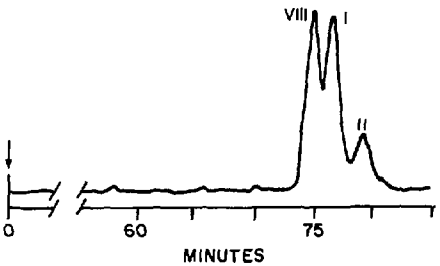

Fig. 8. Chromatogram of 5 to 10 mg of a mixture of (I), (II), and (VIII) in 1.0 ml; flow 3 ml/min; CH_3OH-H_2O, 9:1. This separation necessitated the coupling of two preparative columns in series.
(XBL 815-785)

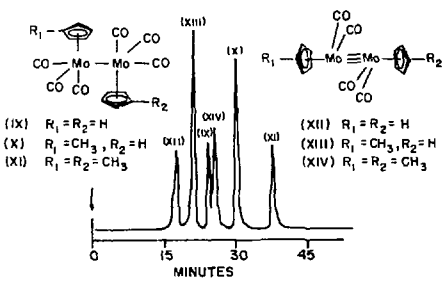

Fig. 9. Chromatogram of 5 to 10 mg of (IX)-(XIV) in 1.0 ml; flow 0.5 ml/min; CH_3CH-H_2O, 5:1.
(XBL 814-2218)

5. CHEMISTRY OF COAL SOLUBILIZATION AND LIQUEFACTION PYROLYSIS STUDIES

R. G. Bergman

The Thermal Chemistry of Tetralin (Paul B. Comita and Robert G. Bergman)

The thermal chemistry of tetralin (1) has been under intense investigation recently,[1-5] due to interest in the fate of hydrogen donors that are used as recycle liquids in the solvent refining of coal. The reactivity of tetralin appears to be dependent on the presence of hydrogen, hydrogen acceptor molecules, different types of reactor surfaces, and surface history. This has resulted in conflicting data in the literature and confusion as to what the thermal reactivity is in the absence of any catalytic effects. In an effort to resolve this situation, we have examined the reactivity of tetralin resulting from several different methods of activation.

Three methods for energization of 1 were investigated: conventional flow pyrolysis, infrared multiphoton excitation, and sensitized infrared laser thermal activation. All three give rise to six major products: benzocyclobutene (2), styrene (3), o-allyltoluene (4), indene (5), 1,2-dihydronaphthalene (6), and naphthalene (7), (see Scheme I), and several minor products. The primary concern of this work is to delineate the energetics of the ethylene-loss channel (giving rise to 2 and 3) versus the hydrogen-loss channel (giving rise to 6 and 7) without interference from catalytic effects.

A number of parameters affected the product distribution for the decomposition in a flow reactor, including the composition of the surface, the history of the surface, and the pressure of the system (see Table 1). However, dehydrogenation was always the predominant decomposition mode. Unconditioned surfaces, higher pressures, and longer contact times in the reactor led to more dehydrogenation of 1.

Multiphoton excitation of 1 in the gas phase was accomplished with a pulsed CO_2 TEA laser tuned to 945.99 cm^{-1}. All six major products found from the pyrolysis also resulted from photolysis of tetralin, including one additional product, phenylacetylene. The distribution of these products, however, was at variance with the distribution from the pyrolysis (see Table 1); the major reaction channel for the multiphoton dissociation of tetralin involved ethylene loss.

In the third method of activation, 1 and varying pressures of SiF_4, an inert sensitizer which absorbs strongly in the infrared, were irradiated with an unfocused, pulsed CO_2 TEA laser tuned to 1027.36 cm^{-1}. Pure tetralin does not decompose under unfocused conditions; thus, all chemistry is due to sensitization by SiF_4. All six major products were again found.

The number of pulses and the maximum temperature of SiF_4 both had pronounced effects on the product distribution. The variation in the number of pulses had a number of effects. With increasing number of pulses the percentage of 2 and 6 decreased, and the percentage of 3, 5, and 7 increased. This is consistent with 2 and 6 being primary products, and at least some fraction of 3, 5, and 7 being derived from them. Sensitized photolysis of 2 gave rise to a clean isomerization to 3, the sole product of the reaction (70% conversion). Sensitized photolysis of 6 (20% conversion) gave rise to two major products, 7 (68% of product) and 5 (11%). Temperature variation was achieved by changing the beam intensity and by varying the sensitizer pressure. Less secondary decomposition took place at lower temperatures. Dehydrogenation is predominantly a result of 1,2-elimination of H_2 (see Table 2).

We draw the following conclusions from the above experiments: (1) A significant fraction of the dehydrogenation reaction in the flow reactor is surface catalyzed. This leads to an anomalously large amount of 1,2-dihydronaphthalene and naphthalene in the reaction products in these flow pyrolysis studies and very likely in all previous in-

Table 1. Product distribution for thermal reaction of 1.

Conditions	Products (%) 2	3	4	5	6	7	other	% conversion of 1
Flow pyrolysis, 1 atm N_2, quartz reactor, 750°C.	2.4[a,b]	18.3	0.5	17.5	10.7	45.8	4.2	74.8
Vacuum flash pyrolysis, 0.05 torr, quartz reactor, 750°C.	34.7	9.9	7.9	4.1	31.8	8.2	3.4	3.7
Multiphoton excitation, 0.325 torr 1, energy/pulse 0.4 joules, 13,020 pulses.	72.6	11.7[c]	3.4	4.2	6.2	0.0	2.0	0.5
Multiphoton excitation,[d] 0.325 torr 1, energy/pulse 0.8 joules, 2790 pulses	54.8	19.7[c]	2.6	5.5	9.0	trace	8.4	0.8
SiF_4 sensitization,[11] T_{max}= 650°C, 5 torr SiF_4, 0.325 torr 1, 4960 pulses.	58.5	8.3	20.8	2.2	10.3	0.0	0.0	1.5
SiF_4 sensitization,[11] T_{max}= 1490°C, 6 torr SiF_4, 0.325 torr 1, 180 pulses.	38.2	20.1	8.4	9.4	15.5	5.6	2.8	7.7

[a]Numbers are percent of total product found. [b]All data have been corrected for FID response. [c]Includes phenylacetylene response. [d]Visible emission in the focal region was observed in this experiment.

Table 2. Deuterium labeling in products from photolysis of 1-d_4.[a]

Product	% of total mixture	Isotopomer (%) d_4	d_3	d_2	d_1
2	57.8	100[b,c]	0	0	0
3	10.6	32	8	29	31
4	8.2	100	0	0	0
5	4.2	0	42	43	15
6	12.8	10	83	7	0
7	2.3	0	1	95	4

[a]Photolysis conditions: 1-d_4 (0.325 torr) was irradiated with 300 pulses, 0.27 joules per pulse, with 5 torr SiF_4. T_{max} was 1240°C. [b]The numbers are the percent of product with the indicated number of deuterium atoms as determined by GC-MS analysis.16 [c]The data are corrected for ^{13}C natural abundance and 98.7% deuterium incorporation in 1-d_4.

vestigations. (2) The lowest energy homogeneous reaction channel for tetralin is the retro-[2+4] channel giving rise to benzocyclobutene. This fact is borne out in both the multiphoton and SiF_4 sensitized experiments where surface chemistry does not appear to be important. (3) The low energy dehydrogenation channel of tetralin is almost exclusively 1,2-dehydrogenation. This process, if concerted, is symmetry forbidden and without precedent as the lowest energy dehydrogenation channel in cyclic olefins.

Brief version of LBL-10731; J. Am. Chem. Soc. 102, 5692 (1980). This research was carried out in collaboration with C. Bradley Moore and Michael R. Berman.

1. A. G. Loudon, A. Maccoll, and S. K. Wong, J. Chem. Soc.(B), 1733 (1970).
2. R. J. Hooper, H. A. J. Battaerd, and D. G. Evans, Fuel 58, 132 (1979).
3. P. Bredael and T. H. Vinh, Fuel 58, 211 (1979).
4. B. M. Benjamin, E. W. Hagaman, V. F. Raaen, and C. J. Collins, Fuel 58, 386 (1979).
5. T. Gangwer, D. MacKenzie, and S. Casano, J. Phys. Chem. 83, 2013 (1979).

The Reactivity of 1,4-Dehydrobenzenes†

(Thomas P. Lockhart and Robert G. Bergman)

Important focuses in fossil fuel research include the study of solvents that serve as hydrogen transfer agents in coal liquifaction and the characterization of the reactivity of aromatic radicals which may serve as models for coal "edge" sites.[1] We have examined the reactivity of alkyl substituted 1,4-dehydrobenzenes (aromatic biradicals) with regard to unimolecular and bimolecular hydrogen transfer processes.

Substituted 1,4-dehydrobenzenes are generated by the thermal reaction of 2,3-dialkyl-hexa-1,5-diyn-3-enes.[2] Our results with octa-4,5-diethynyl-4-ene (1) are summarized in Scheme I. Ring closure produces 2,3-dipropyl-1,4-dehydrobenzene (2) which undergoes several interesting unimolecular reactions. Ring opening to produce isomeric diyne 3, which is stable to the conditions of reaction of 1, occurs in competition with unimolecular [1,5] hydrogen transfer which produces biradical 4. The [1,5] transfer is exothermic by about 12 kcal/mole because a more stable primary alkyl radical is produced.[3] Intramolecular transfer of a second hydrogen atom may take place to produce biradical 5. This biradical may undergo both unimolecular combination and disproportionation reactions, yielding 6 and 7, respectively. When 1 is pyrolyzed in the gas phase a quantitative yield of the three unimolecular products is obtained (Table 3). When pyrolyzed in inert solvent (such as chlorobenzene or diphenyl ether) at 200°C, the same unimolecular products are obtained in good yield.

In the presence of an effective trapping agent such as 1,3-cyclohexadiene, the reduced product (o-di-n-propylbenzene, 8) is obtained in good yield (Table 1). By employing 2,2,5,5-tetradeutero-1,4-cyclohexadiene as trapping agent, 8 containing 2 deuteria/molecule was obtained. By selectively exchanging the aromatic deuteria with protons (by heating with HCl in H_2O), it was possible to determine the position of trapping in 8 (VPC-MS was used to analyze for the relative amounts of d_0, d_1 and d_2 8 after exchange; these correspond to trapping of biradicals 5, 4, and 3, respectively). The results are summarized in Scheme II, which shows that biradicals 3 and 4 are most efficiently trapped.

It is interesting to compare the experiments with 1 with those obtained in the pyrolysis of the lower homologue 9. When this compound was heated in the gas phase, formation of the diyne isomer 11 was observed. Only at much higher temperatures (ca. 400°C) did products derived from trapping of the 1,4-dehydroaromatic intermediate (10) appear (Table 4). These products, in particular tetralin (14) and o-ethylstyrene (15), suggest that [1,4] hydrogen transfer takes place to generate biradicals 12 and 13. When 9 is heated to 190°C in solution (benzene), a high yield of 11 is obtained but products due to intramolecular [1,4] hydrogen abstraction are not observed. When 1,4-cyclohexadiene was added to the reaction solution, a good yield of o-diethylbenzene was produced; this is consistent with the formation of biradical 2 as expected in this reaction. These results suggest that [1,4] hydrogen transfer occurs more slowly than either intramolecular ring opening or bimolecular trapping reactions of the biradical 10. The high temperatures required to produce appreciable amounts of intramolecular trapping products in the gas phase suggest that, only when 10 is generated repeatedly by the cyclization of 9 and 11, does intramolecular trapping begin to appear. This result stands in contrast to the relative rates of [1,5] hydrogen transfer and ring opening and trapping with 1,4-cyclohexadiene for biradical 2.

In summary, 2,3-dialkyl-1,4-dehydrobenzene biradicals may undergo several different reactions depending on the presence of labile hydrogen atoms on alkyl side chains. Competitive with

Table 3. Product yields in the thermal reaction of 1.

Phase	T (°C)	1,4-cyclohexadiene (M)	Absolute yield (%)[a] 3	6	7	8	Total (3-8)
Gas[b]	37°	---	32	19	25	0	76
Solution[c]	196	0.0	20.3	20.8	36.9	0	78
Solution[c]	196	0.4	10.1	5.4	8.9	48	71

[a]Yields were determined by digital integration of FID VPC trace and reference to an internal standard.

[b]N_2 flow (1 atm), through quartz tube.

[c]Chlorobenzene solvent, [1] = 0.01 M.

Table 4. Product yields in the reaction of 9.

Phase	T (°C)	Absolute yields (%)[a] 11(c+t)	14	15	16	other
Gas[a]	400	100	0	0	0	0
Gas[a]	500	76.8	1.6	8.8	0	9.1
Benzene solution[b]	195	51	0	0	5	0
Benzene solution[b] + 1,4-cyclohexadiene (1.1 M)	195	6	0	0	75	0

[a]See Table 3.

[b][9] = 0.01 M.

fast intermolecular and intramolecular hydrogen abstraction pathways is opening of the aromatic ring to generate diethynyl olefins.

* * *

†Brief version of LBL-10828, J. Am. Chem. 102, 5976 (1980).

1. J. W. Larsen, ed., "The Organic Chemistry of Coal," ACS Symposium Series No. 71 (1978).
2. R. R. Jones, and R. G. Bergman, J. Am. Chem. Soc. 94, 660 (1974); R. G. Bergman, Acc. Chem. Res. 6, 25 (1973).
3. S. W. Benson, "Thermochemical Kinetics," Wiley-Interscience, N. Y., (1976).

RESEARCH PLANS FOR CALENDAR YEAR 1981

Selective Synthesis of Gasoline Range Components. It is proposed to investigate first the performance of alumina-supported iron and ruthenium catalysts with different levels of potassium promotion. Three objectives have been set for these studies. The first will be to establish empirically the influence of conversion on the distribution of organic products formed. Preliminary studies suggest that low molecular weight olefins formed via primary reactions are reincorporated during the latter stages of reaction, thereby suppressing the formation of methane and very high molecular weight products. The implications of these initial results will be examined to determine whether secondary reactions can be used to control significantly the ultimate distribution of hydrocarbons formed. The second objective will be to determine the extent to which the oxygen released during Fischer-Tropsch synthesis can be rejected as CO_2 rather than water. The influence of gas space velocity on the extent of conversion will be examined as well as the effect of potassium loading. Here again, initial studies have shown that the extent of CO_2 formation relative to H_2O increases as an iron catalyst is promoted with potassium. The extent to which a ruthenium catalyst might be similarly affected is little known and worthy of investigation.

Following this work, experiments will be conducted using iron and ruthenium supported on ZSM-5 and related zeolites. The purpose of this work will be to establish the role of the zeolite in controlling the molecular weight distribution of the products formed. In addition, efforts will be made to establish whether the metallic component substituted into the zeolite is stable or whether the metal migrates to the outer surface of the zeolite particles.

Detailed studies of the effects of mass transport and olefin reincorporation will be conducted using the autoclave apparatus. Several objectives will be pursued. The first will be to establish the extent to which catalysts suspended in an oil phase produce product distributions similar to those obtained in the fixed bed reactor.

Electron Microscope-Studies of Coal. The environmental cell within the 650kV Hitachi electron microscope, together with the mass spectrometer (attached to the gas exit of the environmental cell) will be used to examine various samples during the course of gasification reactions and simultaneously measure reaction rates. Initial work will be with carbonaceous materials that are relatively free of volatiles, e.g., graphite and coal char.

The work on the characterization of mineral matter in coal will be continued.

Catalyzed Low Temperature Hydrogenation of Coal. We intend to study the catalytic effects of transition metals evaporated over highly oriented graphite and the catalytic effects of potassium carbonate (K_2CO_3). The plan is to obtain a better characterization of the surface, both the graphite and the deposited catalyst, before studying its interaction with hydrogen, water, oxygen, and carbon monoxide. Then the surface will be characterized again after the reaction. Next we plan to add promoters to the catalysts to study their role in these interactions.

Selective Hydrogenation, Hydrogenolysis, and Alkylation of Coal and Coal Derived Liquids by Organometallic Systems. The preported Fischer-Tropsch alkylation of aromatic rings under Lewis acid and transition metal catalyzed conditions will be subjected to synthetic and mechanistic scrutiny. The potential for transition metal mediated rearrangements of coal models by hydrogen shifts will be investigated. Novel methods in cleavage and hydrogenolysis of sp^2-sp^2 hybridized (aromatic) bonds are being developed.

Chemistry of Coal Solubilization and Liquefaction Pyrolysis Studies. During the next fiscal year we plan to complete our work on the thermal hydrogen-transfer and carbon-extrusion reactions of tetralin. We will continue our study of direct and SiF_4-sensitized multiphoton vibrational excitation of tetralin, using a CO_2 laser, to carefully distinguish the truly homogeneous and wall-catalyzed decomposition processes. In addition, we plan to make use of the chemical activation technique to generate tetralin at vibrational levels much higher than those available by laser-induced decomposition; the results of these studies will be compared with the multiphoton decompositions.

Having developed a technique that we are confident provides information about the truly homogeneous (uncatalyzed) decomposition of molecules used as hydrogen donors in coal liquefaction, we plan to expand our studies to catalyzed decomposition and hydrogen transer. One line of approach will involve an investigation of common metal carbonyl complexes that catalyze hydrogenation of coal-related aromatic hydrocarbons, using both H_2 and water as a source of hydrogen. We will also be searching for clean, well-behaved reactions in which coordinatively unsaturated organotransition metal complexes abstract H_2 from partially saturated hydrocarbons, and then this hydrogen to acceptor molecules. When such processes are found, intensive studies of their mechanisms will be carried out.

Experiments will be designed to define the role of transition metal hydrides as hydrogen transfer agents in coal liquefaction. Model acceptor compounds will test the reaction. Recently, work by Pettit et al. have shown that the water gas shift (WGS) reaction can be used with a wide variety of transition carbonyl compounds to generate transition metal hydrides catalytically. This is done by reaction of the transition metal carbonyl with a weak base in the presence of carbon monoxide. We will be utilizing the WGS reaction to generate various transition metal hydrides in the presence of appropriate model acceptor molecules.

1980 PUBLICATIONS AND REPORTS

Refereed Journals

1. J. A. Little, J. W. Evans and K. H. Westmacott, "Early Stages of the Reduction of Nickel Oxide Single Crystals: An Investigation by Transmission Electron Microscopy," Met. Trans. 11B, 519 (1980), (LBL-10176).

†2. M. Ranade and J. W. Evans, "The Reaction Between a Gas and a Solid in a Non-isothermal Packed Bed: Simulation and Experiments," I. and E. C. Process Design and Development 19, 118 (1980).

†3. A. Malazgirt and J. W. Evans, "Production of Aluminum and Aluminum Coatings by Thermal Decomposition of Aluminum Alkyls," Met. Trans. 11B, 225 (1980).

†4. J. W. Evans and M. Ranade, "The Grain Model for Reaction Between a Gas and a Porous Solid--A refined Approximate Solution to the Equations," Chem. Eng. Sci. 35, 1261 (1980).

‡5. J. W. Evans, M. H. Abbasi and A. Sarin, "A Monte Carlo Simulation of the Diffusion of Gases in Porous Solids," J. Chem. Phys. 72, 2967 (1980).

6. J. M. Huggins, J. A. King, Jr., K. P. C. Vollhardt, and M. J. Winter, "Preparative Separation of Organometallic Diastereomers, Structural Isomers, and Homologs on Ultrasphere ODS," Altex Chromatogram 3, (4), 2 (1980).

7. M. R. Berman, P. B. Comita, C. B. Moore and R. G. Bergman, "Flow Pyrolysis and Direct and SiF_4-sensitized Laser-Induced Decomposition of Tetralin," J. Am. Chem. Soc. 102, 5692 (1980).

8. T. P. Lockhart, C. B. Mallon, and R. G. Bergman, "2,3-Di-n-propyl-1,4-dehydrobenzene," J. Am. Chem. Soc. 102, 5976 (1980).

LBL Reports

1. J. A. Little, M. I. Perez and J. W. Evans, "Transmission Electron Microscopy Studies of Coals," LBL-11473.

2. J. W. Evans, Y. Zundelevich and D. Sharma, "A Mathematical Model for Prediction of Currents, Magnetic Fields, Melt Velocities, Melt Topography and Current Efficiency in Hall-Héroult Cells," LBL-11675.

3. J. M. Huggins, J. A. King, Jr., K. P. C. Vollhardt, and M. J. Winter, "Separation of Diastereomers, Structural Isomers, and Homologs of n^5-Cyclopentadienyl Cobalt and Dinuclear Molybdenum Complexes by Reverse Phase High Performance Liquid Chromatography Using Deoxygenated Solvents," LBL-11801.

Invited Talks

1. K. P. C. Vollhardt, "Cobalt Mediated Carbon-Carbon Bond Formation," 3M Company, St. Paul, Minnesota, February 1980.

2. K. P. C. Vollhardt, "Reactions Catalyzed by Polystyrene Bound n^5-$CpCo(CO)_2$, "Plenary Lecture, 179th ACS National Meeting, Symposium on Heterophase Attached Homogeneous Catalysis, Houston, Texas, March 1980.

3. K. P. C. Vollhardt, "Cobalt Mediated Carbon-Carbon Bond Forming and Bond Breaking Reactions," Dow Chemical Corporation, Midland, Michigan, April 1980.

4. K. P. C. Vollhardt. "Cobalt Mediated Carbon-Carbon Bond Forming and Bond Breaking Reactions," IBM, Yorktown Heights, New York, May 1980.

5. K. P. C. Vollhardt, "Remarkable Transformations in the Coordination Sphere of Cobalt," Consejo Superior de Investigaciones Cientificas, Madrid, Spain, May 1980.

6. K. P. C. Vollhardt, "Hydrocarbon Formation on Polymer Supported Cobalt," Plenary Lecture, Symposium on Catalytic Activation of Carbon Monoxide, 2nd Chemical Conference of North America, Las Vegas, Nevada, August 1980.

7. K. P. C. Vollhardt, "Transition Metal Mediated Carbon-Carbon Bond Formation," Plenary Lecture, 2nd International Symposium on Homogeneous Catalysis, Düsseldorf, West Germany, September 1980.

8. K. P. C. Vollhardt, "Remarkable Transformations in the Coordination Sphere of Cobalt," University of Lund, Lund, Sweden, September 1980.

9. K. P. C. Vollhardt, "Aspects of Cobalt Catalyzed Hydrocarbon Synthesis," PPG Industries, Barberton, Ohio, November 1980.

§10. D. Ziegler, M. Dubrovsky, and J. W. Evans, (presented by D. Ziegler), "The use of Novel Anodes in the Electrowinning of Metals by Fluidized Bed Cathodes," Annual Meeting of the American Institute of Metallurgical Engineers, Las Vegas, Nevada, 24-28 February 1980.

†11. I. Masterson, M. Dubrovsky, and J. W. Evans, (presented by J. W. Evans), "Fluidized Bed Electrowinning of Cobalt from Sulfate Solutions," Ibid.

12. J. A. Little, J. W. Evans, and K. Westmacott, (presented by J. W. Evans), "Ex-situ and In-situ Studies of the Reduction of Nickel Oxide Single Crystals Using Transmission Electron Microscopy," Ibid.

‡13. M. Abbasi and J. W. Evans, (presented by J. W. Evans), "A Monte Carlo Simulation of the Diffusion of Gases in Porous Solids," Ibid.

* * *

†National Science Foundation.

‡Intra-mural funding.

§Office of Surface Mining, Dept. of Interior.

e. Coal Liquefaction Alloys Test Program*

Alan V. Levy, Investigator

Introduction. A group of a candidate steels for service in coal liquefaction systems was tested in a 30 wt.% coal-kerosene slurry. It was determined that performance varied over a difference range of 100% for alloys of similar hardness. Mild steel and austenitic stainless steels had higher erosion rates than higher carbon steels, low and medium Cr containing steels and ferritic chromium stainless steel.

Jet impingement tests, using coal-kerosene and abrasive-water slurries, have shown that the erosion of ductile metals in liquid-solid particle abrasive streams is considerably different than their erosion in gas-solid particle streams. Maximum erosion occurs at 90° impingement angle for liquid slurries compared to 20° for gas-solid particle flows. A minimum in the erosion curve vs. impingement angle occurs in liquid slurry erosion while none occurs in gas-solid particle erosion.

1. EROSION BEHAVIOR OF ALLOYS IN COAL SLURRY POT TESTS†

R. Indig and A. Levy

A number of candidate materials for service in coal liquefaction components that are subjected to slurry erosion were tested in the 2 liter pot test. Their relative resistance to erosion and the effects of metallurgical and hardness differences between them on their erosion behavior were determined. A 30 wt.%, -200 mesh Illinois #6 coal was used in a kerosene liquid for the slurry. The effective velocity was 40 fps and the tests were performed at 25°C.

Figure 1 shows the cumulative erosion of three non-stainless steels of varying hardness. In the 120-minutes exposure, the difference in cumulative erosion among the 3 alloys was 100%. The lowest hardness material, 2-1/4Cr 1Mo steel, had an intermediate amount of erosion, indicating that hardness was not a factor in the erosion resistance of the 3 alloys. The reason for the large variation is still under investigation.

The possible effect of chromium content on erosion behavior is shown in Fig. 2. For the 3 alloys tested, the eriosion decreased with increased Cr content while the hardness of the 3 alloys was comparable. A 67% difference in erosion between the A53 mild steel and the 410 ferritic stainless steel after 120 minutes of exposure is significant.

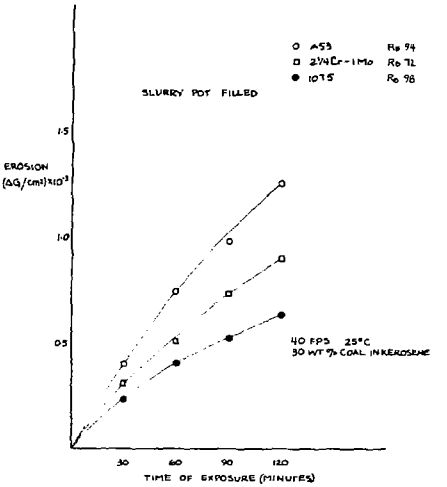

Fig. 1. Cumulative erosion of three non-stainless steels of varying hardness. (XBL 809-11985)

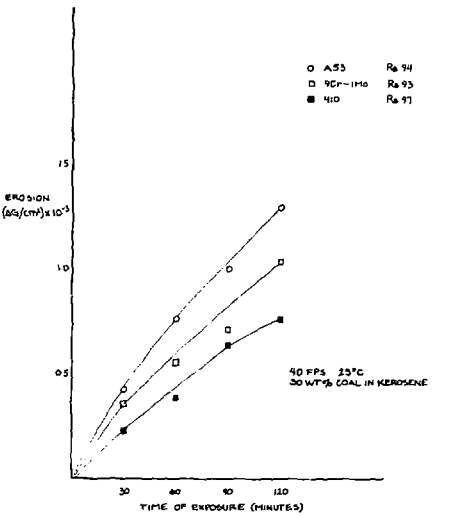

Fig. 2. Cumulative erosion of three alloys with increasing Cr content. (XBL 809-11986)

*This work was supported by the Assistant Secretary for Fossil Energy, Office of Coal Research, Materials and Components Division of the U. S. Department of Energy under Contract No. W-7405-ENG-48 through the Fossil Energy Materials Program, Oak Ridge National Laboratory, Oak Ridge, TN.

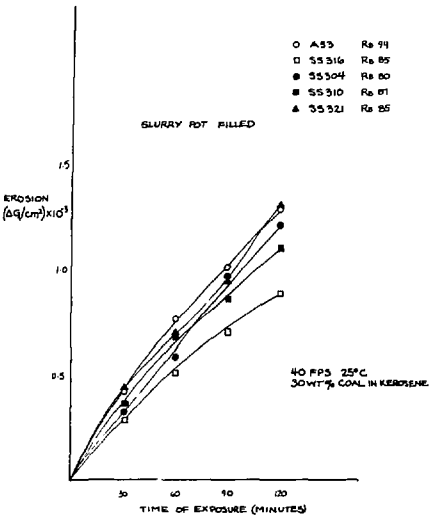

Fig. 3. Cumulative erosion of A53 mild steel compared to 4 stainless steels. (XBL 809-11981)

Figure 3 shows the relative similarity of A53 mild steel and several austenitic stainless steels. Again, it is seen that hardness has no effect on the relative erosion behavior of the alloys. The comparatively high rates of erosion of the stainless steels, comparable to that of the A53 carbon steel, indicate that corrosion was not active in slurry pot erosion tests. The 300 series austenitic stainless steels eroded at a significantly higher rate than the 410 ferritic stainless steel, as can be seen by comparing their curves in Figs. 2 and 3. The lower amount of erosion of the 316SS as compared to the other steels may be due to the molybdenum content of the 316SS. It was observed that the 2-1/4Cr-1Mo steel also had a low amount of erosion in this type of test.

Selection of steels for slurry erosion service does not have to be related to hardness, as was previously thought. The effects of composition, ductility or toughness, crystallographic structure, and other metallurgical factors govern the erosion resistance of steels in slurry flow environments.

* * *

†Brief version of LBL-10044.

2. JET IMPINGEMENT TESTER†

S. Li

The purpose of this research is to evaluate under controlled laboratory conditions the quantitative rate of erosive wear of various flat metal samples caused by the impact of a particle-laden liquid jet of variable velocity and impingement angle. The effects on erosion behavior of the following parameters were determined: jet velocity, slurry concentration, metal and particle hardness characteristics, relative densities of fluid and solid phase, fluid viscosity, particle composition of slurry, and orientation angle of the impinging jet.

The erosion that occurred on 6061-T6 aluminum in a 20 wt.% coal-kerosene slurry is shown in Fig. 4. Maximum erosion occurs at a 90° impingement angle. This behavior of solid particles in a liquid slurry differs markedly from that which occurs in gas-solid particle erosion, which is shown by the dashed curve in the figure. The differences between the two carrier fluids that affect erosion behavior of metals is being determined. Figure 5 compares the erosion rates of 1018 mild steel and 6061-T6 aluminum in a coal slurry erosive environment. The lower erosion rate and slope of the mild steel as a function of velocity reflects the fact that the steel is both stronger and more ductile than the aluminum alloy. Both properties contribute to the erosion behavior of ductile metals.

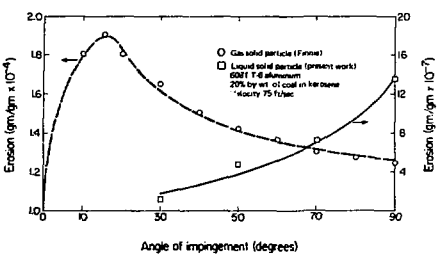

Fig. 4. Erosion of 6061-T6 Al at various impingement angles in 20 wt.% coal-kerosene slurry. (XBL 8012-2451)

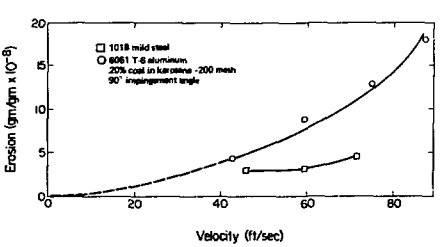

Fig. 5. Erosion of 6061-T6 Al and 1018 mild steel at various velocities in 20 wt.% coal-kerosene slurry. (XBL 8012-2450)

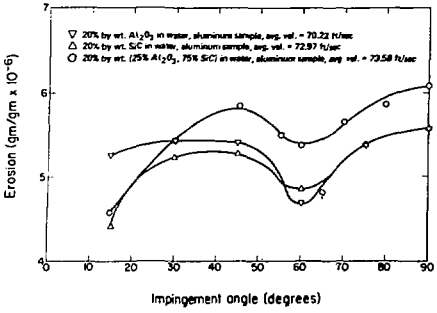

Fig. 6. Erosion of 6061-T6 Al in various Al_2O_3, SiC-water slurries. (XBL 8012-2456)

Figure 6 shows the dimensionless rate of wear as a function of jet impingement angle for 6061-T6 aluminum alloy, using mixtures of SiC and Al_2O_3 abrasive particles in water. It is seen that maximum erosion occurs for a jet impinging normal to the metal sample surface ($\alpha = 90°$). The occurrence of a minimum in the erosion curve at $\alpha = 60°$ also differs from gas-solid particle erosion behavior. The SiC containing slurry generally caused more erosion than the Al_2O_3 or mixed particle slurries. This difference is not usually observed in gas-solid particle erosion.

The major differences in resultant erosion behavior that are observed between the liquid-solid particle erosive streams used in this project and the gas-solid particle streams used in other work are indicative of several major differences in the erosive environments. The fluid mechanics of each type of flow differs, and this difference is being studied and defined as a function of Reynolds number and other variables. Further, the lubricity of the liquids change the mechanical nature of the erosive particles striking the target surface. Fluids with the same viscosity and major differences in lubricity have been procured for erosion testing.

* * *

†Brief version of LBL-11959.

RESEARCH PLANS FOR CALENDAR YEAR 1981

The effects of larger coal particles and other liquids, including those with different lubricity for the same viscosity, on erosion of metals and hard protective coatings will be determined. Viscosity of different slurries than those used to date will be determined at elevated temperatures. Elevated temperature testing to 200°C will be carried out. New pumps will be installed in the slurry loop and evaluated along with piping materials other than the A53 mild steel and 300 series stainless steels tested to date. Data presenting performance levels of various tested materials will be compiled for design used.

1980 PUBLICATIONS AND REPORTS

Other Publications

1. A. Levy, "Erosion-Corrosion Behavior of Piping Materials in Coal Liquefaction System Slurries," NACE Corrosion '80 National Meeting, Chicago, Illinois, March 1980.

LBL Reports

1. S. Li, J. A. C. Humphrey, and A. Levy, "Erosive Wear of Ductile Metals by a Particle Laden, High Velocity Liquid Jet," LBL-11959.

Invited Talks

1. A. Levy, "Erosion in Coal Liquefaction Systems," Fifth Annual Conference on Materials for Coal Conversion and Utilization--DOE, Gaithersburg, Maryland, October 1980.

2. A. Levy, "Erosion of Metals by Non-Aqueous Slurries," AIME-TMS Annual Meeting, Pittsburgh, Pennsylvania, October 1980.

f. Materials Characterization in Fossil Fuel Combustion Products*

David P. Whittle, Donald H. Boone and Alan V. Levy, Investigators

Introduction. The use of protective coatings on structural components to provide corrosion and erosion protection, and thermal insulation in some applications, is an effective way to extend the performance range of alloys in high temperature service. The ability of the coatings to provide the protection required is a function of their composition, morphology, thickness, method of application, and the substrate upon which they are formed. The effect of increased aluminum content of the substrate alloy on increasing the formation of a more discrete inner coating zone with resultant improved performance of an aluminized coating was determined.

The effects of surface preparation and component geometry on desireable leader growth of a yttria stabilized zirconia thermal barrier ceramic coating was determined. Marked differences in the morphology of oxide scales formed on aluminide coatings deposited on nickel and cobalt super alloys were found to be due to differences in the application techniques for the same basic aluminide coating. Raman and IR spectroscopy techniques were developed to identify some of the complex phases and structures that form in the oxide scales as a result of variations in processing techniques for the application of ceramic thermal barrier coatings.

1. SUBSTRATE EFFECTS ON COATING PROTECTION†

D. Crane and D. Boone

The use of protective coatings has, in large part, been successful in providing the required surface stability of structural components in high temperature service without compromising the load carrying ability of the substrate. However, as use temperatures increase, the interaction between coating and substrate increases, and the independence of the coating from the substrate is greatly reduced.

Considerable promise for strengthening the substrate alloys at elevated temperatures has been shown by the use of fine oxide dispersion strengthening (ODS), often obtained by mechanical alloying (MA) techniques. However, the ability to use these ODS alloys at very high temperatures, > 0.8 Tm, is often limited by the increasing reactivity between the alloy and its protective coating. This has been observed for diffusion type coatings such as the aluminides and, to a lesser extent, for the overlay type coatings. Little is understood about the nature of this interaction or the potential for designing some coatability into these high strength substrates to retard or prevent the interaction. The reported high diffusion rates in the ODS materials are clearly one of the problems, but there may be other factors.

Studies are being conducted to develop an understanding of the factors affecting coating stability and protectiveness, using MA alloys with varying substrate aluminum levels, and simple inward and outward type diffusion aluminum coatings. Experimental techniques involve isothermal exposures and careful metallographic analysis.

It was found that the aluminum content of the substrate had a large effect on the structure of the resulting coating; increasing aluminum level promoted the formation of a more discrete and desirable inner coating zone. Figure 1 shows the structures of an outward type coating on two ODS alloys, one with 0.6% Al (MA754) and the other with 4.5% Al (MA6000E). Significant differences in inner coating zone structure is observed. The thicker, less continuous inner coating zone on the ODS alloy with higher aluminum content is expected to show greater resistance to interdiffusion and coating separation.

Isothermal exposures of a MA6000E coating sample with an outward type coating at 1000°C for varying times showed rapid formation of voids in the coating inner diffusion zone and aluminum diffusion into the substrate. Use of deep etching techniques and fractography were helpful in determining the size and location of voids often obscured or exaggerated by normal metallographical procedures. Figure 2, a fracture surface of a specimen exposed for 24 h at 1000°C, shows the porosity concentrated in the inner coating zone with failure at the coating substrate interface. These results indicate that while substrate aluminum content has a large effect on inner coating structure and apparent stability, inter-diffusion still results with rapid loss of coating integrity. The kinetics of void precipitation and location are being determined.

* * *

*This work was supported by the Assistant Secretary for Fossil Energy, Office of Coal Research, Heat Engines and Heat Recovery Division of the U. S. Department of Energy under Contract No. W-7405-ENG-48 through the Battelle Memorial Institute, Pacific Northwest Laboratories, Richland, WA.

†Brief version of LBL-12021.

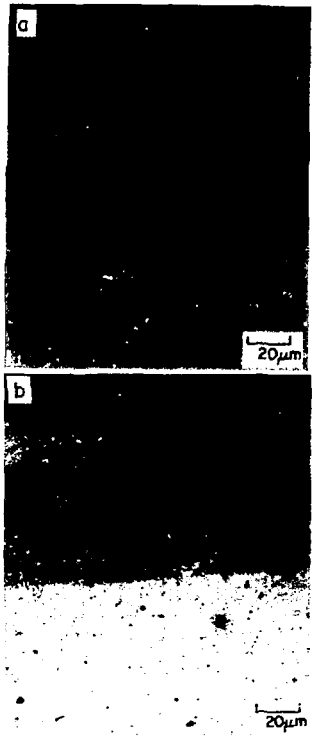

Fig. 1. Microstructures of aluminide coatings applied to ODS alloys with different aluminum contents: (a) MA754, 0.6% Al, (b) MA 6000E, 4.5% Al. (XBB 814-3236)

Fig. 2. Fracture cross section of aluminide coating on MA6000E alloy. (XBB 814-3235)

2. CHARACTERIZATION OF THERMAL BARRIER CERAMIC COATINGS†

D. Boone

The use of ceramic-oxide, thermal-barrier coatings to protect metal in combustion zone environments has accelerated with the demonstration of the ability of ceramic coating layers to survive on a variety of critical components in gas turbine and diesel engines. Ceramic coatings serve the function of a thermal barrier, greatly increasing the allowable surface temperature of the load carrying component, thereby increasing operating efficiency of the engines. The ceramic also has the potential for greater surface durability against corrosion in synfuel and lower quality fuel combustion products.

This project has as its primary objective the characterization of the as-deposited coating structures and their resultant performance as influenced by starting materials, methods of deposition (e.g., plasma spray and physical vapor deposition), substrate preparation, and inner layers used. Precise definition of the mechanisms of degradation and failure of the coatings is important in optimizing their composition and application procedures.

Suitable test components were selected for existing turbine and diesel engines, and application variations defined for preparing initial specimens. Evaluation of test results on incompletely characterized samples was conducted. Results of diesel piston and valve tests[1] of plasma-spray-applied, partially-stabilized zirconium coatings were encouraging, as were reported results of gas turbine exposures.

Examination of the structure of electron beam physical vapor deposition (EB-PVD) yttria stabilized zirconia (YSZ) applied to turbine airfoils with differing surface pretreatments indicated the nature of the range of structural variables that occur. The fracture surface of the coating (Fig. 3) shows the desirable leader growth struc-

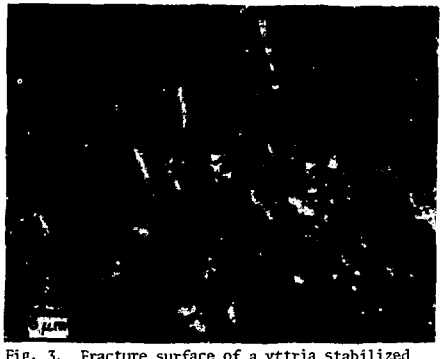

Fig. 3. Fracture surface of a yttria stabilized zirconia coating applied to a turbine airfoil. (XBB 807-9196A)

ture which is deemed necessary to provide the required thermal strain tolerance necessary for a brittle ceramic coating to survive on a more ductile metallic substrate. Size, aspect ratio, and amount of porosity of the coatings as a function of substrate and processing variables are being investigated.

On these airfoils, initial surface roughness of the substrate was found to have little effect on resulting ceramic growth morphology. The radius of curvature at leading and trailing edges and between pressure (concave) and suction (convex) surfaces had a much greater effect on the density of leader growth. Determination of the effect of a wider range of surface conditions, geometry, and deposition variables on coating performance than was initially considered, was indicated by these tests.

The contrast between the highly oriented (a [220] growth direction was found) EB-PVD zirconia coating and a plasma spray (PS) applied zirconia coating presently undergoing tests on diesel engine valves is seen in the structure of the PS coating in Fig. 4. A controlled level of porosity in the PS coating was found to be important as well as the composition and degree of stability of the ceramic, and the orientation of the plasma applied deposits. Inner layer roughness for improved mechanical adherence also appears to be a factor in the performance of the coating.

Fig. 4. Plasma sprayed applied zirconia coating diesel valve head test in an engine for 1000 hr: (a) surface, (b) cross section. (XBB 814-5809)

* * *

†Brief version of *LBL-10520*.

1. I. Kvernes, "Characterization of Microstructures and Measurements of Thermal Effects of Ceramic Coatings in Diesel Engines in Service," in Thin Solid Films (1979).

3. EFFECT OF COATING PROCESSING AND STRUCTURE ON OXIDE FORMATION AND PROTECTIVENESS†

D. Crane and D. Boone

Much attention is being given to the effect of protective coating composition, processing techniques, and structure on the resulting oxide formed on the coating's surface and its behavior in a variety of conditions and environments. Systems being investigated are often the Al_2O_3 forming MCrAlY's produced by EB-PVD, sputtering, and plasma spray techniques. A promising research technique is the examination of the protective oxide structure by removal of the coating material from the substrate.

Much less attention has been given to understanding the effects of composition and processing on the structure and performance of the simple aluminides applied to nickel and cobalt base superalloys. These systems are still the most widely used protective coatings in gas turbine and other combustion environments. Several inward and outward type aluminide coatings, applied to nickel and cobalt based superalloys, showed large differences in surface structure for the various systems.

Figure 5 shows examples of the as-coated surface of these aluminides and the results of their oxidation in air for 50 hr at 1000°C. Significant differences exist in the structures and oxidation behavior for the different coating processes and substrate alloys coated. Increased coating thickness and the possible presence of a lower melting-point, low-ductility phase prior to coating diffusion may account for the extreme surface roughness observed in the surface of some thick aluminides, as seen in Fig. 6. Pre-coating surface treatments such as pack cementation, application of chromium, or electrolytic application of chromium or a precious metal, such as platinum, also were found to influence the surface of the as-aluminized sample. The causes of these differences and their effect upon protectiveness in oxidizing and hot corrosion environments are being investigated.

* * *

†Brief version of LBL-10522.

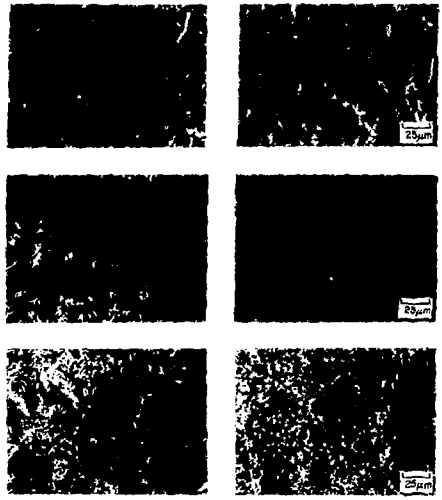

Fig. 5. Surface structure of aluminide coatings on nickel and cobalt base alloys: (a), (b), and (c) are as received; (b), (d), and (f) are after 50 hr at 1000°C in air. (a) and (b) are cobalt base aluminide on WI-52, inward type aluminide. (b) and (c) are nickel base aluminide on IN738, inward type aluminide. (e) and (f) are nickel base aluminide on IN738, outward type aluminide, showing pack mix entrapment.
(XBB 815-4029)

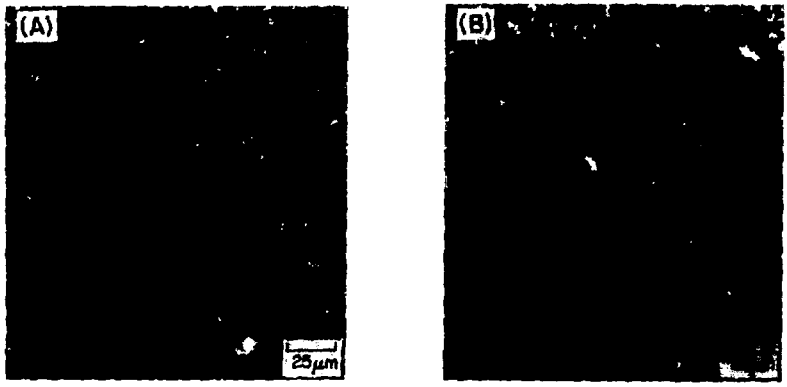

Fig. 6. Comparison of surface roughness of thick and thin aluminide coatings. (XBB 814-3810)

4. RAMAN AND IR SPECTROSCOPY CHARACTERIZATION OF OXIDE COATINGS

D. Boone

In studies of the structures of ceramic thermal barrier coatings, the phase composition and degree of stoichiometry are known to play a key role in the mechanical and thermal performance of the systems. Considerable work is currently underway at LBL and elsewhere to improve the performance of these coatings by structural control involving both composition and processing variables. The direction and success of this work involves the ability to identify the often complex phases that occur as the result of processing parameters, high service temperatures, and phase transformation temperatures. Stoichiometry of the as-applied coating, and changes during exposure, can be very critical for the ceramic's adherence and resistance to thermal shock. Also, the performance of protective oxides, which form on metallic coatings and alloys during exposure, depend on the structure and composition of the oxide as well as its interaction with active element oxide phases used to promote pegging and adherence.

Laser Raman spectroscopy and infrared spectroscopy studies for this project that are being carried out at the Sandia National Laboratories, Livermore, have shown the potential of this diagnostic technique to identify some of the complex phases and structures in the oxide scales.

Thermal barrier coatings, deposited by several techniques including EB-PVD, sputtering and plasma thermal spraying with compositions of varying ZrO_2/Y_2O_3 ratios and varying degrees of stoichiometry, have been examined metallographically and analyzed by Raman and IR spectroscopy.

Results show that the transition from tetragonal to monoclinic structure is easily resolved as distinct peaks using the Raman Technique with the potential for analysis of rare earth impurities by strong fluorescence.[1,2] Figure 7 shows the Raman spectra of a yttria stabilized ZrO_2 (YSZ) for a source material and for the EB-PVD deposited coating. Differences in peak heights and location indicate that the coating process results in variations in the coating structure from that of the standard source material. The effects of such variations as a function of processing and service variables are being related to coating performance. Figure 8 presents the results of a study of infrared peak shift for EB-PVD deposited YSZ with varying levels of oxygen bleed. This demonstrates that this technique may possibly be used to characterize the stoichiometry of ceramic coatings deposited by reactive evaporation and sputtering techniques where complete reaction with oxygen may not occur. Subsequent oxidation of the off-stoichiometric ceramic can change coating structure and density and, hence, adherence. The results are being correlated with behavior of these coatings in engine and rig tests.

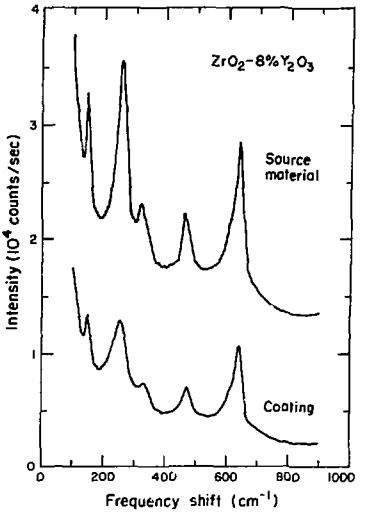

Fig. 7. Raman spectra for source material and EB-PVD deposited yttria stabilized zirconia coating. (XBL 813-2203)

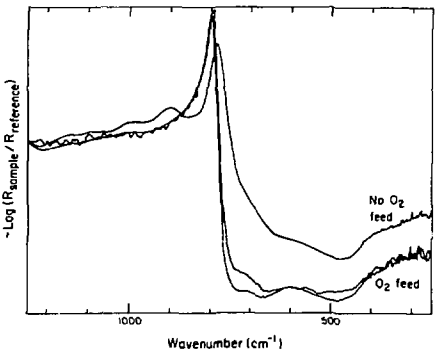

Fig. 8. Infrared spectrum for EB-PVD deposited yttria stabilized zirconia coating. (XBL 813-2210)

* * *

1. R. E. Benner and A. S. Nagelberg, "Characterization of ZrO_2-Y_2O_3 Thermal Barrier Coatings by Raman Scattering," Accepted for Presentation at the 8th International Conference on Metallic Coatings, San Francisco, April 1981.
2. R. L. Farrow, et al., "Characterization of Metallic Corrosion," presented at the 7th International Conference on Metallic Coatings and accepted for publication in Thin Solid Films, SAND 79-8782.

RESEARCH PLANS FOR CALENDAR YEAR 1981

The structural features and phase equilibria of partially stabilized zirconia will be more completely established for several deposition techniques and starting materials and correlated with degradation modes observed in gas turbine, diesel engine, and rig testing. Additional ceramic compositions will be investigated.

Coating processing effects, such as type of CVD aluminizing, high or low aluminum activity process, effect of additions such as chromium, manganese, and silicon, will be studied further and related to the nature and performance of the protective oxide formed. Cyclic oxidation and hot corrosion testing are planned. Substrate alloy compositional and structural effects on the performance of the coatings will be investigated.

1980 PUBLICATIONS AND REPORTS

Publications

1. D. Boone and J. Fairbanks, "Advanced Electron Beam Techniques for Metallic and Ceramic Protective Coatings," presented at the ASM/SAMPE Conference on Specialized Cleaning, Finishing and Coating Processes, Los Angeles, February 1980 and to be published in the proceedings.

2. D. Boone and J. Fairbanks, "The Turbojet: A Perpetual Search for Better Materials," Materials Engineering (Sept. 1980), p. 78.

LBL Reports

1. D. Boone, D. Crane, and D. Whittle, "The Structure and Interdiffusional Degradation of Aluminide Coatings on Oxide Dispersion Strengthened Alloys," LBL-12021.

2. D. Boone and J. Fairbanks, "Advanced Electron Beam Techniques for Metallic and Ceramic Protective Coatings," LBL-10520.

3. D. Boone, D. Crane, D. Whittle, "Oxide Structures on Aluminide Coatings," LBL-12022.

g. Solution Thermodynamics of Sulfites and Sulfite Oxidation Mechanisms*

Leo Brewer and Robert E. Connick, Investigators

1. THERMODYNAMIC DATA FOR FLUE-GAS DESULFURIZATION PROCESSES

Leo Brewer, Gerd Rosenblatt, Bea-Jane Lin and Michael Cima

The chemistry of tetravalent sulfur is complicated by the thermodynamic instability of many of the phases containing tetravalent sulfur. Many of the phases and aqueous species, which play an important role in the limestone scrubbing process for removal of sulfur dioxide from coal combustion flue gas, are metastable phases. Some of these metastable phases can equilibrate with one another without reaching equilibrium in a reasonable time with respect to the ultimately stable products. The calcium sulfate system can be cited as an example. There are only two thermodynamically stable phases, $CaSO_4$, anhydrite, and $CaSO_4 \cdot 2H_2O$, but these phases can not be equilibrated with one another. Instead, $CaSO_4 \cdot 2H_2O$ dehydrates to two different metastable $CaSO_4 \cdot 1/2H_2O$ phases depending upon the conditions. These hemihydrate phases equilibrate with two different metastable $CaSO_4$ phases. In the $CaSO_3$ system, which results from the reaction of SO_2 with limestone, this problem of metastability is enhanced by the thermodynamic instability with respect to disproportionation to higher and lower oxidations states of sulfur. With varying impurities in coal ash, the catalysis of various possible reactions may take place unexpectedly and it is important to unravel the possibilities.

In an effort to provide the thermodynamic information that might be needed for understanding the possible reactions that can take place in limestone scrubbers, a critical review of the literature has been carried out and a compilation of the data at 298.15 K has been prepared. The application of the Pitzer model for the thermodynamics of aqueous solutions was carried out last year by Gerd Rosenblatt. This is being combined with the data for the solid phases to provide a complete description of the thermodynamics of the limestone scrubbing process.

2. THE OXIDATION OF BISULFITE ION BY OXYGEN

Robert E. Connick and Thomas G. Braga

The solution reaction $2HSO_3^- + O_2 = 2SO_4^{2-} + 2H^+$ is of importance in flue gas desulfurization processes carried out in aqueous solutions or slurries. Depending on the process, it may be desirable either to enhance or restrict oxidation of bisulfite. In addition, the reaction is of concern in air pollution by sulfur dioxide because oxidation of the SO_2 in water droplets or films is believed to be the primary way in which acid rain is formed. To control the reaction, a thorough understanding of the rate and mechanisms is desirable.

The kinetics of the reaction has been studied by many investigators[1] with little agreement as to rate, rate law, or mechanism. This interesting and surprising result stems from the fact that the reaction is a chain reaction that is very susceptible to effects of impurities, with the consequence that the rate is highly irreproducible.

Rather than tackle the impurity problem head-on, as others have done, our approach has been to try to eliminate impurity effects by deliberately adding species that will control the chain initiation, chain termination, and chain propagation.

Initially, the reaction was followed by measuring the rate of oxygen gas absorption in solutions of Na_2SO_3 at pH ~ 9. It was discovered that the observed rate was limited by the mass transfer rate of the O_2 gas into the solution, even though extremely vigorous agitation of the liquid with the gas was used. This finding casts doubt on the interpretations of results of a number of studies reported in the literature where a similar experimental method was used.

By going to pH ~ 4 to 5, the region of greatest interest in FGD processes, the reaction is slowed enough so that mass transfer is not limiting. Experiments conducted with equimolar sodium acetate-acetic acid buffer solutions, yielded an apparent 3/2 order dependence on bisulfite concentration. Variation of the buffer gave an inverse first power dependence on hydrogen ion concentration. The oxygen dependence was not determined. The rates were not perfectly reproducible, but changing the buffer concentration or using different sources of water seemed to have little effect.

To eliminate mass transfer completely, the reaction was studied by measuring the oxygen concentration with an oxygen meter in a closed container having no gas phase. This technique permitted data to be obtained more easily and more rapidly. The rate was determined at 25°C under a wide variety of conditions in acetic acid-sodium acetate buffer solutions. Ethyl alcohol was added in many of the experiments to control the termination step as Bäckström's[2] work strongly indicates that the inhibitory effect of alcohol arises from its ability to terminate chains. The powerful catalyst manganous ion was also present in many of the experiments. Its role could be either that of an initiator or chain propagator.

The results of these studies indicated that, without addition of alcohol or manganous ion, the reaction was somewhat less than zero order in

*This work was supported by the Assistant Secretary for Fossil Energy, Office of Coal Research, Advanced Environmental Control Division of the U. S. Department of Energy under Contract No. W-7405-ENG-48 through the Morgantown Energy Technology Center, Morgantown, WV.

oxygen concentration and presumably 3/2 order in $[HSO_3^-]$ and -1 order in hydrogen ion concentration from the mixing experiments.

Addition of ethanol decreased the rate by the factor $1/(k + k' [ETOH])$ at low ethanol concentration; but, when the ethanol became sufficiently concentrated, the rate approached zero order dependence on ethanol, presumably because of a separate reaction path. This new term was roughly 100-fold smaller than the rate with no ethanol. At this high alcohol concentration, the rate depended on the 3/2 power of the oxygen concentration.

Manganous ion greatly speeded up the rate in the absence of alcohol with an apparent linear dependence on manganous concentration. When both manganous ion and alcohol were present, the results were more complex. At constant $[Mn^{2+}]$, the rate decreased slowly with increasing alcohol concentration, then decreased very rapidly, and suddenly became independent of alcohol. The behavior could best be explained by the formation of a complex between the manganous ion, presently at about 4×10^{-4} M, and an impurity in the alcohol. Distillation of the alcohol and different sources yielded changes in rate but never seemed to eliminate the impurity. Further, it was found that the rate depended on the buffer concentration.

To avoid complications with buffers, experiments are currently being run without buffer but controlling the pH by manual addition of base. With no additives, the rate is roughly 3-fold slower than in 0.25 M acetic acid-sodium acetate buffer of the same pH. Sodium hydroxide solution was abandoned as the added base when it was found to contain some catalyst that increased the rate with each addition. A solution of sodium bicarbonate has been found suitable for maintaining constant pH. Again, the rate appears to be somewhat less than zero order in $[O_2]$. Alcohol enters as before in the denominator to the first power.

Since there was evidence that the catalytic effect of manganous ion did not arise from the presence of a new initiation step, it was desirable to find a new initiator. Ultra-violet light was chosen because a photochemical path for the reaction is well known and it seemed very likely that light would be initiating the chain. The solution was illuminated by a General Electric 100A4/T bulb. The rate increased about 25-fold and the oxygen dependence became zero order. Further, the rate appeared to be independent of hydrogen ion concentration around pH 4.5. The dependence on bisulfite concentration was to the 3/2 power.

The rate of a chain reaction of long chain length may be represented symbolically by a chain initiating step I, a chain propagating step P, and a chain terminating step T:

$$\text{Rate} = P\left(\frac{I}{T}\right)^{1/n} ,$$

where n is a small integer, usually 1 or 2. The rates of initiation and termination are equal, i.e., I = T. The factor I/T is introduced to cancel from the rate law the concentration(s) of chain carrier(s) which appear in P and T. If the termination involves one chain carrier, n will be unity; if it involves two chain carriers, n will be two.

While the catalytic effect of manganous ion could most simply be attributed to the introduction of either a new initiation path or a new chain propagation step, there is evidence that the latter possibility is correct. The evidence comes from the reactions in which ultra-violet light was used, presumably to initiate the reaction. The factor increase in rate produced by a given concentration of Mn^{2+} appeared to be about the same with and without light, even though in the former case the rate was 25-fold greater. This result is understandable if the role of manganous ion is to provide a new propagation step rather than to create a new initiation step.

* * *

1. Gmelin's Handbuch der Anorganischen Chemie, Eighth ed., Sulfur System No. 9, Part B, Lieferung 3, pp. 1293-1519 (1963).
2. H. Backstrom, J. Am. Chem. Soc. 49, 1460 (1927); H. Alyae and H. Backstrom, ibid 51, 90 (1929).

RESEARCH PLANS FOR CALENDAR YEAR 1981

Studies of the rate, rate law, and mechanism of the oxidation of bisulfite ion by oxygen will be continued. Attention will be directed to the control of the initiation step by the use of ultraviolet illumination. It will be necessary to measure the effect as a function of light intensity, wavelength, and concentrations of absorbing species. The identity of the active absorber will be sought. With both the initiation and termination steps controlled, it is hoped that the rate will be more reproducible. Quantitative studies of the effect on the rate of a particular additive, in conjunction with variations of light intensity, manganous concentration, and alcohol concentration, should make it possible to deduce whether the additive is affecting the initiation, propagation, or termination step(s) of the chain reaction. Mechanisms can then be deduced and reasonable postulates made for the chain carriers of the reaction.

Work will continue on the characterization of the $CaSO_3$ and $CaSO_3 \cdot 2H_2O$ phases and their solid solutions with $CaSO_4$. The compilation of thermodynamic data at 298.15 K will be extended to higher temperatures and the standard state data will be combined with the program for activity coefficients in the aqueous phase to provide a complete thermodynamic characterization of the limestone scrubbing system.

1980 PUBLICATIONS AND REPORTS

Other Publications

1. R. E. Connick and T. G. Braga, "The Rate of Oxidation of Bisulfite Ion by Oxygen," Quarterly Reports to Morgantown Energy Technology Center, (Sept. 1979, March 1980, and Sept. 1980).

Invited Talks

1. Leo Brewer, "Thermodynamics of Compounds of Interest to the SO_2 Removal Program," Flue Gas Desulfurization Symposium, Morgantown, West Virginia, November 7, 1980.

2. Robert E. Connick and Thomas G. Braga, "The Kinetics of the Oxidation of Bisulfite Ion by Oxygen," Flue Gas Desulfurization Symposium, Morgantown, West Virginia, November 6, 1980.

h. Process Chemical Parameters in Aqueous Sulfur Dioxide Removal by Lime/Limestone Scrubbers*

Robert E. Connick, Investigator

1. RAMAN SPECTROSCOPIC DETERMINATION OF AQUEOUS SULFUR OXYANIONS

M. Ospina,† K. Ward,† K. Koshlap, and B. Meyer

The Raman spectra of standard solutions of sulfite, disulfite, bisulfite, sulfate, bisulfate, dithionate, thiosulfate, and polythionate solutions were used to interpret spectra of a sulfur dioxide/limestone slurry which contains mixtures of unknown compositions. This procedure makes it possible to conduct a comprehensive analysis of all sulfur species in these solutions. Since the water band at 1,650 cm^{-1} remains reasonably constant in solutions containing oxyacid species, this method can also be used to compare the concentration of all species. However, concentration of the species must be greater than 0.1 M to be identified reliably.

We are currently installing a Nicolet computer system which will make the analysis quicker and more reliable. This will make it possible to store spectra on disc and to conduct rapid comparison of mixtures on a TV monitor while spectra are being scanned. It will also make it possible to compile multiple scans of spectra, thus increasing the sensitivity appreciably.

A major breakthrough has been the identification of tri- and tetrathionate (Fig. 1), which participate in a complex equilibrium reaction that provides the link in the sulfite degradation reaction. A description of the method has been published this year.[1]

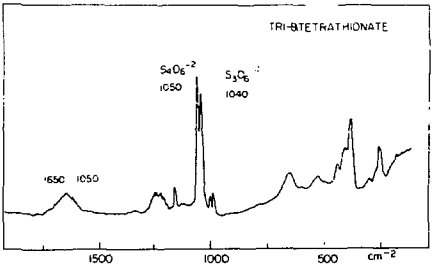

Fig. 1. Spectra of tri- and tetrathionate ions. (XBL 808-11335)

*This work was supported by the Assistant Secretary for Fossil Energy, Office of Coal Research, Advanced Environmental Control Division on the U. S. Department of Energy under Contract No. W-7405-ENG-48 through the Morgantown Energy Technology Center, Morgantown, WV.

* * *

†Chemistry Department, University of Washington, Seattle, WA.

1. B. Meyer, M. Ospina, and L. Peter, Anal. Chim. Acta 117, 301 (1980).

2. THE DECOMPOSITION OF AMMONIA-SULFUR DIOXIDE SOLUTIONS

K. Koshlap and B. Meyer

Aqueous ammonia saturated with sulfur dioxide gas yields yellow solutions which rapidly decompose at elevated temperature. At 70°C, the decomposition is visible after 36-60 hr by the appearance of crystals on the walls of tubes containing the solutions; and, after about 70 hrs, the decomposition is essentially complete, yielding elemental sulfur, which appears as transparent supercooled drops, and sulfate, which crystallizes in long needles. The solutions are saturated with sulfate and contain only a small amount of residual sulfite. The reaction also proceeds at room temperature, but takes up to a year for completion. The reaction is concentration dependent and pH dependent.

Earlier work is reported in Refs. 1 and 2.

* * *

1. B. Meyer, B. Mulliken, and H. Weeks, Phosphorus and Sulfur 8, 291 (1980).
2. B. Meyer, B. Mulliken, and H. Weeks, Phosphorus and Sulfur 8, 291 (1980).

3. THERMAL DECOMPOSITION OF SULFITE†

B. Meyer, M. Rigdon‡ and T. Bruner

The thermal decomposition of 1 M and saturated sodium, potassium sulfite, and bisulfite solutions was studied as a function of temperature and transition metal catalysts. The reaction yields elemental sulfur and sulfate as end products. The concentration of intermediates and end products was monitored. Oxygen-free 1 M and saturated solutions decompose with a half-life between 1 hr and 1 wk at 160°C, depending on the additive. Concentrated solutions are more stable. The decomposition rate depends also on the pH; sulfite solutions are more stable than bisulfite. Iron, copper, manganese, and other multivalent transition metal ions catalyze the reaction of different degrees as do elemental sulfur and selenium, yielding half-lives between 1 hr and 100 hr at 100°C. Sulfate seems to inhibit completion of the conversion. At low temperature, thiosulfate can occur as intermediate, as well as tri- and tetrathionate. With manganese ion, dithionate occurs under narrowly defined conditions. All reaction rates are sensitive to impurities.

* * *

†Brief version of LBL-11969.

‡Chemistry Department, University of Washington, Seattle, WA.

4. THERMAL DECOMPOSITION OF THIOSULFATE†

M. Ospina,‡ A. Tini,‡ and B. Meyer

The decomposition of 1 M and saturated sodium thiosulfate solution was studied at 20°C and 55°C. The intermediates and reaction products comprise elemental sulfur, sulfur dioxide, hydrogen sulfide, trithionate, tetrathionate, and sulfate. Above pH 3, thiosulfate solutions are stable over long periods of time. Oxygen-free solutions are stable for several weeks. In the pH range 2 to 3, the solution reacts noticeably within a few hours. At the onset of the reaction, after an incubation period, hydrogen sulfide odor can be noted. The main products are trithionate and elemental sulfur, depending on temperature. In the pH range 1 to 2, sulfur dioxide evolves and trithionate is the main product, with tetrathionate and elemental sulfur occurring as side products. Below pH 1, tetrathionate can be made the predominant product, and trithionate converts slowly into tetrathionate. All reactions involve complex mechanisms and equilibria. The transition from a reductive to an oxidative environment below pH 2 indicates that the reaction mechanism involves sulfane-sulfonic acids as intermediates. This work suggests that it is most likely the mechanism proposed by Davis that occurs; this mechanism calls for stepwise catenation similar to a reversal of the well-known sulfite degradation of elemental sulfur.

* * *

†Brief version of LBL-11969.

‡Chemistry Department, University of Washington, Seattle, WA.

5. THE REACTION OF SULFITE WITH FORMALDEHYDE†

M. Rigdon,‡ R. Munlist, and B. Meyer

The reaction products and intermediates in the reaction of sulfite, disulfite, bisulfite, and sulfur dioxide with aqueous solutions of 37%, 10%, 3.7%, 1%, 0.3% and 0.1 wt% paraformaldehyde and formalin were observed with ^{13}C NMR as a function of concentration, reagent molar ratio, pH, temperature, and time. At a high field of 4.3T, corresponding to 45 MHz carbon frequency, peaks corresponding to methylene glycol and polyoxymethylene glycol appear well resolved. Upon addition to sulfur (IV) oxyacids, new peaks appear, which, on the basis of concentration and mole ratio behavior, can be assigned to monomeric and polymeric sulfoxide derivatives. At low concentration of methylene glycol, only $CH_2(OH)SO_3^-$ monomer appears. The pK of this compound is estimated to be 11.6. At a pH above 12.5, the spectra change significantly, indicating that only monomeric $CH_2(OH)SO_3^-$ exists. Raman spectra of sulfur-34 isotopes were used to characterize the compound. The C-S band at 777 cm^{-1} shifts as expected. Shifts of other bands make possible the potential assignments to the various C-S-O modes. At intermediate and high concentrations, the CH_2-O-CH_2 band at 921 cm^{-1} dominates the spectrum. D_2O and methanol were used to identify other vibrational motions.

* * *

†Supported by the U. S. Consumer Product Safety Commission.

‡Chemistry Department, University of Washington, Seattle.

6. *CHEMISTRY OF WASTE SULFUR UTILIZATION*†

B. Meyer and R. Munlist

Addition to sulfite to urea-formaldehyde adhesives has been studied, with the help of Carbon 13 NMR, to identify the reaction products of formaldehyde with formaldehyde derivatives. The formaldehyde-sulfite complex has been identified in the formaldehyde spectrum at 86.5 ppm. The sulfur-carbon bond is strong enough to compete with the polymerization process and thus degrades both polymeric formaldehyde and urea-formaldehyde resin polymers.

This work constitutes a continuation of earlier work reported in Ref. 1.

* * *

†Brief version of LBL-11762.

1. B. Meyer, W. S. Johns, and J. K. Woo, Forest Products Journal 30 (11), 24 (1980).

RESEARCH PLANS FOR CALENDAR YEAR 1981

The computer-aided laser Raman spectrometric determination method for in-situ analysis of aqueous sulfur oxyacids will be used to study the decomposition mechanism of ammonia/sulfur-dioxide-saturated solutions; it will be applied to limestone saturated with sulfur dioxide, as supplied from the laboratory pilot plant of EPA/RTP, and to other homogenous and heterogenous systems in which basic aqueous solutions have been saturated with sulfur dioxide. This method will also be used to identify intermediates and to investigate the kinetics of decomposition of calcium sulfite and calcium bisulfite solutions and slurries. Exploratory work on metal-ligand interactions of sulfite will be continued, and the exploration of the sulfur dioxide-formaldehyde reaction will be concluded. This work will remain in close contact with the complementary work conducted by Prof L. Brewer and R. E. Connick.

1980 PUBLICATIONS AND REPORTS

Refereed Journals

1. B. Meyer, M. Ospina, and L. Peter, "Absolute Raman Intensities of Aqueous Oxyanions of

Sulfur," Anal. Chim. Acta 117, 301 (1980).

2. B. Meyer, B. Mulliken, and H. Weeks, "The Reaction of Ammonia with Excess Sulfur Dioxide," Phosphorus and Sulfur 8, 291 (1980).

3. B. Meyer, B. Mulliken, and H. Weeks, "The Reaction of Sulfur Dioxide with Excess Ammonia," Phosphorus and Sulfur 8, 301 (1980).

4. B. Meyer, W. S. Johns, and J. K. Woo, "Formaldehyde Release from Sulfur Modified Urea-Formaldehyde Resins," Forest Products Journal 30 (III), 24 (1980).

LBL Reports

1. B. Meyer and R. Nunlist, "C-13 NMR Identification of Urea-Formaldehyde Resins," LBL-11762.

2. B. Meyer, M. Rigdon, T. Burner, and A. Tini, "Thermal Decomposition of Sulfur (IV) Oxyacids," LBL-11969.

Invited Talks

1. Beat Meyer, "Thermal Decomposition of Sulfite, Bisulfite and Disulfite," Department of Energy Workshop in Morgantown, West Virginia, November 6-7, 1980.

2. Beat Meyer, "Indoor Air Quality Research Needs," U. S. Government Interagency Regulatory Liaison Group Meeting, July 31, 1980, at EPA in Washington, D. C.

3. Beat Meyer, "Formaldehyde Release from Urea-Formaldehyde Bonded Products," California Legislature, Joint Legislative Audit Committee, Investigative Subcommittee Hearing, Westminster, California, September 17, 1980.

4. Beat Meyer, Chairman, Technical Workshop on Formaldehyde, sponsored by the U. S. Consumer Product Safety Commission, at the National Bureau of Standards, held April 9-11, 1980.

5. Beat Meyer, "Monitoring and Instrumentation for Measuring Air Quality," Federal Interagency Workshop, Leesburg, Virginia, December 3-5, 1980.

6. Beat Meyer, "The National Research Program for Indoor Air Quality," Formaldehyde Seminar, organized by the Formaldehyde Institute, L'Enfant Center, Washington, D. C., December 15, 1980.

7. B. Meyer, M. Rigdon and T. Burner, "Decomposition of Aqueous Sulfite, Bisulfite and Disulfite," ACS National Meeting, Las Vegas, Nevada, August 27, 1980, Paper #253, Inorganic Chemistry Division.

8. B. Meyer, M. Ospina, and A. Tini, "Decomposition of Aqueous Thiosulfate Solutions," ACS National Meeting, Las Vegas, Nevada, August 27, 1980, Paper #254, Inorganic Division.

9. B. Meyer and R. Nunlist, "Chemical Composition and Stability of Urea-Formaldehyde Resins," ACS National Meeting, Las Vegas, Nevada, August 29, 1980, Paper #146, Cellulose Chemistry Division.

I. Coal Liquefaction Research*

Heinz Heinemann, Investigator

1. FIXED BED AND SUSPENSION BED FISCHER-TROPSCH REACTION

W. McKee, D. Stern, A. T. Bell, and H. Heinemann

The literature reports that suspension bed Fischer-Tropsch reactors can tolerate higher CO/H_2 ratios than fixed or fluid bed reactors. This result is important because omission of a water gas shift step represents capital and energy savings. Reasons for this difference in reactor behavior are not well understood. Two major hypotheses are proposed and under investigation: (a) There is greater isothermicity in a liquid medium, such as in a suspension bed reactor, thus avoiding hot spots during the exothermic reaction and a possible catalyst deactivation by coking; or, (b) there are different diffusion rates of hydrogen and carbon monoxide from the gas phase through the liquid to the catalyst surface and, therefore, different reactant concentrations on the surface.

Experimentation with two fixed bed reactors of 1/4 in. and 1 in. diameter, respectively, in a fluidized sand bath has shown that there appears to be less tendency to plugging with the smaller reactor, which has a higher surface-to-volume ratio and better isothermicity. It was found that there is a very sensitive temperature range at 300-325°C in which coking (and reactor plugging proceed rapidly, possibly by graphitization of reactive carbon on the catalyst surface. The effects of temperature and H_2/CO ratio on coking are inverse, and higher temperatures can be tolerated at higher H_2/CO ratios. Although additional work remains to be done, it is tentatively concluded that catalyst coking and reactor plugging occur at lower temperatures at higher CO/H_2 ratios than at lower ratios and that there is a critical temperature range for each H_2/CO ratio. Hot spots, which inevitably occur in fixed bed reactors, are therefore the likely cause for limitations on practical H_2/CO ratios in fixed bed reactors. This suggests that operation of fixed bed reactors at low H_2/CO ratios is possible if a heat exchange type reactor is used with a multitude of small diameter (e.g. 1 in.) catalyst tubes in a heat exchange medium.

Work has started on the mass transfer hypothesis described under (b) above. A slurry-type reactor, shown in Fig. 1, has been built, taken into operation, and tested.

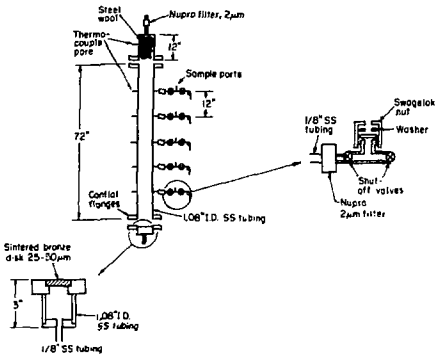

Fig. 1. Slurry reactor. (XBL 8012-3897)

RESEARCH PLANS FOR CALENDAR YEAR 1981

The objective of the present phase of the investigation is to see if mass transfer limits catalyst deactivation, to determine the extent to which recombination occurs in the slurry, and to assess, through modeling, whether the well-mixed slurry could result in product distributions that differ significantly from those observed with fixed bed reactors.

To answer these questions, three sets of experiments are being undertaken. In the first, the rate of reaction will be measured at varying amounts of catalyst per reactor volume, with constant gas flow rate and concentration. The second set of experiments is aimed at examining the role of product recombinations in shifting product distributions; it involves the addition of ethylene to reactant gases. If recombination occurs, increased amounts of heavier hydrocarbons will be seen in the reaction products. Runs at higher conversion will also be made; and, if recombination occurs, the product distribution at higher conversion will be slanted towards heavier products. In the third set of experiments, a series of runs at conditions known to be reaction-limited will be made to examine intrinsic kinetics and look at the effect of H_2/CO ratio on deactivation.

1980 PUBLICATIONS AND REPORTS

Refereed Journals

1. A. T. Bell, H. Heinemann and W. McKee: "An Anomaly in the Case of Catalytic Cracking," J. Catalysis 66, 463 (1980).

*This work was supported by the Assistant Secretary of Fossil Energy, Office of Coal Research, Liquefaction Division of the U. S. Department of Energy under Contract No. W-7405-ENG-48 through the Pittsburgh Energy Center, Pittsburgh, PA.

LBL Reports

1. Heinz Heinemann: "A Brief History of Industrial Catalysis," LBL-10278.

2. Heinz Heinemann: "Zeolite Catalysis--Technology," LBL-11662.

Invited Talks

1. Heinz Heinemann, "Shape-Selective Catalysis," Catalysis Institute of the Consejo Superior, Madrid, Spain, October 1980; also, Royal Spanish Chemical Society, Madrid, October 1980.

2. Heinz Heinemann, "Coal Liquefaction," A.C.S., National Meeting, Las Vegas, NE, fall, 1980; also, Catalysis Institute of the Consejo Superior, Madrid, Spain, October 1980.

3. Heinz Heinemann, "Conversion of Coal, Heavy Oil and Tar Sands to Liquid Hydrocarbon Fuels," Conference on Heavy Fuels, sponsored by INTEVEP, Caracas, Venezuela, October 1980.

4. Heinz Heinemann, "Zeolite Catalysis--Technology" First Berkeley Catalysis and Surface Science Conference, Berkeley, CA., July 1980.

Advanced Isotope Separation Technology

a. Isotope Separation by Laser Photochemistry*

C. Bradley Moore, Investigator

1. LASER PYROLYSIS OF TETRALIN

Michael R. Berman

The energy thresholds of the reaction channels available in unimolecular decomposition and their variation with temperature are manifested in the reaction activation energy, E_a, and A-factor. They determine what conditions are needed to favor the production of a given set of products. The identification of the lowest energy reaction channel in unimolecular decompositions can often be complicated by heterogeneous surface reactions at high temperatures. Surface-catalyzed reactions can often mask the true low-energy homogeneous gas phase pathway. We have used CO_2 laser excitation to energize reactant molecules, while keeping the reaction vessel cool. Thus homogeneous unimolecular reactions occur in the absence of wall reactions. IR multiphoton dissociation (MPD) and SiF_4-sensitized decomposition of the organic molecule tetralin (1) have been used to identify which of the observed dissociation channels, ethylene loss or H_2 loss, is the lowest energy channel.

MPD was achieved with a focused TEA CO_2 laser tuned to 946.0 cm^{-1}. In the sensitized photolyses, a cell containing tetralin (0.3 torr) and SiF_4 (5 - 10 torr) was irradiated at 1027.4 cm^{-1} with an unfocused beam. Tetralin does not absorb in this region, and the strong Si-F bond (~130 kcal/mole) insures that SiF_4 *remains inert*. All chemistry is caused by the high temperature achieved following the thermal equilibration of the energy deposited in the SiF_4. The temperature decay, as observed from the ir fluorescence from SiF_4, indicates that most of the reaction in the heated column occurs in the first few tens of microseconds. Temperatures were varied in different experiments by attenuating the laser beam or changing the SiF_4 pressure. Since the 6-mm diameter beam is 2 cm from the cell walls, hot molecules will not reach the walls, which are themselves cool, and experience catalytic effects. The maximum temperature achieved in the gas is calculated from the measured absorbed energy, assuming a statistical distribution into all available degrees of freedom.

Six major reaction products (Fig. 1)--benzocyclobutene (2), styrene (3), o-allyltoluene (4), indene (5), 1,2-dihydronaphthalene (6), and naphthalene (7)--were seen for each excitation method as well as for conventional flow pyrolysis (Table 1). The major reaction channel for both laser-initiated decompositions is ethylene loss. This result is at variance with the product distribution from flow pyrolysis. We conclude that, in the flow pyrolysis experiments, some fraction of the dehydrogenation reaction is surface catalyzed. Another major reaction channel is observed at low temperatures, C-C bond cleavage to form the isomer 4. Secondary decompositions of 2, 4, and 6 have been separately observed, especially, at higher temperatures.

The detailed mechanism of these reactions was investigated by SiF_4-sensitized photolysis of selected deuterated isotopes of 1. Photolysis of 1,1,4,4 tetradeuteriotetralin (1-d_4) produces predominantly 6-d_3 indicating a 1,2 hydrogen loss. Photolysis of a 1:2 mixture of 1-h_{12} and 1-d_{12} yielded H_2, HD, and D_2, in a 1:2:1 ratio. The scrambled HD product indicates that free H and D *atoms are present; thus, dehydrogenation is a* stepwise, radical process rather than a concerted H_2 loss. This conclusion was confirmed by the observation of 6-d_9 from the photolysis of 1-d_{10} in which the 2 H's were in the cis-1,2 positions. All 2 and 4 produced from photolysis of 1-d_4 retained all 4 D atoms. The mixture of isotopes found in 3 and 5 were consistent with production from secondary decomposition of 2 and 4.

The techniques of MPD and SiF_4 sensitized photolysis have proved to be valuable tools for investigating competing reaction channels in unimolecular decompositions. In the case of 1, C_2H_4 loss has been established as the low energy reaction path; dehydrogenation was determined to be

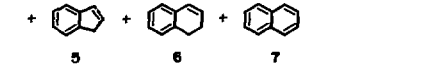

Fig. 1. Reaction scheme for the pyrolysis of tetralin (1) to form the six major products, benzocyclobutene (2), styrene (3), o-allyltoluene (4), indene (5), 1,2-dihydronaphthalene (6), and naphthalene (7). (XBL 812-8087)

*This work was supported by the Assistant Secretary for Nuclear Energy, Office of Advanced Isotope Separation Technology, Advanced Isotope Separation Technology Division of the U. S. Department of Energy under Contract No. W-7405-ENG-48.

Table 1. Product distribution for thermal reaction of 1.

Conditions	Products (%)							% Conversion of 1
	2	3	4	5	6	7	other	
Flow pyrolysis, 1 atm N_2, quartz reactor, 750°C.	2.4[a,b]	18.3	0.5	17.5	10.7	45.8	4.2	74.8
Vacuum flash pyrolysis, 0.05 torr, quartz reactor, 750°C.	34.7	9.9	7.9	4.1	31.8	8.2	3.4	3.7
Multiphoton excitation, 0.325 torr 1, energy/pulse 0.4 joules, ~13,020 pulses.	72.6	11.7[c]	3.4	4.2	6.2	0.0	2.0	0.5
Multiphoton excitation,[d] 0.325 torr 1, energy/pulse 0.8 joules, ~2790 pulses	54.8	19.7	2.6	5.5	9.0	trace	8.4	0.8
SiF_4 sensitization, T_{max}= 650°C, 5 torr SiF_4, 0.325 torr 1, 4950 pulses	58.5	8.3	20.8	2.2	10.3	0.0	0.0	1.5
SiF_4 sensitization, T_{max}= 1490°C, 6 torr SiF_4, 0.325 torr 1, 180 pulses.	38.2	20.1	8.4	9.4	15.5	5.6	2.8	7.7

[a]Numbers are percent of total product found.

[b]All data have been corrected for FID response.

[c]Includes phenylacetylene response.

[d]Visible emission in the focal region was observed in this experiment.

stepwise rather than concerted; and a new primary reaction channel 4 has been identified. Work is in progress to make the SiF_4 technique more quantitative.

This work was done in collaboration with Paul Comita and Robert Bergman.

2. QUENCHING, ELECTRONIC ENERGY TRANSFER AND ROTATIONAL RELAXATION OF S_1 FORMALDEHYDE†

D. Bamford, J. C. Weisshaar, and E. Specht

The mechanisms by which the first excited singlet state (S_1) of formaldehyde decays are only partially understood. Previous work in our laboratory has shown that the collision-free decay is quite different from the collision-induced one. In the absence of collisions, it appears that S_1 decays to H_2 and CO via dissociatively broadened levels of the ground electronic state (S_0) of formaldehyde.[1-3] However, under the influence of collisions, decay occurs through a set of discrete (long-lived) states, and an intermediate S_1 is observed to decay at least an order of magnitude more rapidly than the dissociation product CO is formed.[4] A complete understanding of the collision-induced decay requires knowledge of the rates of many competing processes. Among these are rotational and vibrational relaxation within S_1, perhaps to states with very different lifetimes; electronic energy transfer to an identical collision partner, which may be indistinguishable from relaxation with S_1; electronic quenching to the intermediate states; and quenching directly to dissociative states. We have carried out three kinds of S_1 fluorescence decay measurements to begin to sort out these collision-induced decay processes.

To understand the possible role of E → E (electronic → electronic) relaxation, an attempt was made to observe D_2CO emission following selective excitation of H_2CO (S_1) in mixtures. The D_2CO emission was distinguished on the basis of time scale; at several torr, D_2CO lifetimes are about five times longer than H_2CO lifetimes. A simplified kinetic scheme shows that the rate constant for the reaction H_2CO (S_1) + D_2CO (S_0) $\xrightarrow{k_{HD}}$ H_2CO (S_0) + D_2CO (S_1) can be derived by measuring the lifetimes and relative amplitude of the fast (H_2CO) and slow (D_2CO) emission after excitation of a specific rovibronic state of H_2CO (S_1). This was done in a mixture of 1 torr H_2CO and 3.7 torr D_2CO. The rate constant k_{HD} was observed to be 0.17 ± 0.13 μsec^{-1} $torr^{-1}$.

This is about 2% of the gas kinetic collision rate of 10.6 μsec^{-1} $torr^{-1}$. The rate for the reaction H_2CO (S_1) + H_2CO (S_0) → H_2CO (S_0) + H_2CO (S_1) should be similar, since the isotope effect is expected to be small. Thus, E → E energy transfer does not appear to play a significant role in the collisional decay of S_1 H_2CO.

The second type of fluorescence decay measurement involved excitation of single rotational levels of S_1 formaldehyde in the pressure range 10^{-3} - 5 torr. Since collision-free lifetimes vary greatly with rotational quantum number, collision-induced rotational quantum number changes drastically affect observed lifetimes. If rotational equilibration is not complete on the time scale of the fluorescence decay, nonexponential fluorescence decay curves may result as collisions take the initially excited SRL to other SRL's with different lifetimes. In such cases, an average lifetime $\langle\tau\rangle$ can be obtained by measuring the area under a fluorescence intensity vs. time curve and dividing by the t = 0 fluorescence intensity. Plots of $\langle\tau\rangle^{-1}$ versus H_2CO pressure for several H_2CO SRL's are shown in Fig. 2. These Stern-Volmer plots show considerable curvature. An attempt to model the shape of these curves was made by assuming that all of their curvature is caused by rotational relaxation to states of different lifetimes from those of the initially excited states. The results are shown in the dashed lines in Fig. 3. The agreement with the experimental curves (solid lines) is less than satisfactory, perhaps because the electronic quenching rate itself may show some curvature as a function of pressure.

Because rotational relaxation in formaldehyde should produce a Boltzmann distribution of rotational levels at pressures above 5 torr, it should be possible to measure true electronic relaxation rates for S_1 H_2CO and D_2CO by excitation of a small group of rotational states at sufficient quenching gas pressures. We have done this using Ar, CO_2, CH_3F, O_2, and NO as the quenchers, Figs. 4 and 5. The standard quenching kinetics for a rotationally relaxed system gives straight line Stern-Volmer curves. The striking curves of Figs. 4 and 5 are predicted by the mixed state model of Gelbart and Freed.[5] Their theory suggests that a linear high-pressure portion of the Stern-Volmer curves should extrapolate back to a common intercept at zero pressure. The data of Figs. 3 and 4 are not sufficiently linear in the 250 - 700 torr region to define an intercept accurately. Thus, we need to extend this experiment to higher pressures to test the Gelbart-Freed model quantitatively. The effect of deuteration on rate is in the expected direction for NO and O_2 but in the opposite direction for Ar, CO_2, and CH_3F quenching.

While these experiments have not provided us with a complete picture of the collisional decay mechanism of S_1 formaldehyde, the data yielded do provide some difficult tests for any photochemical mechanism proposed.

* * *

†This work was partially supported by the National Science Foundation.

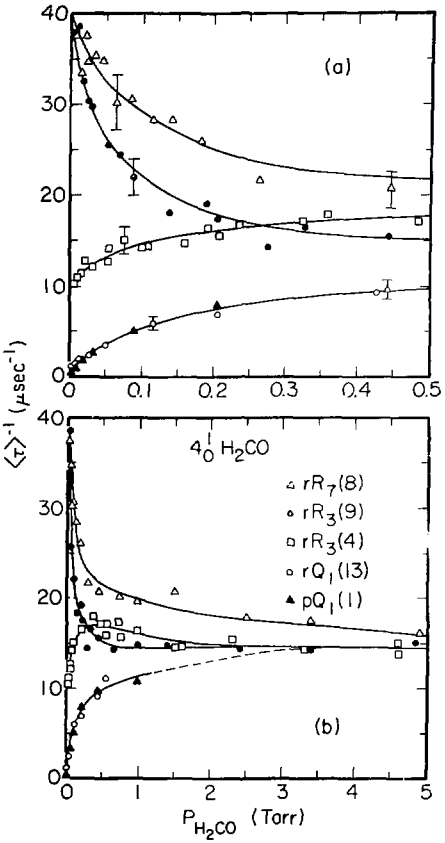

Fig. 2. Plots of $\langle\tau\rangle^{-1}$ vs. pressure in pure H_2CO after excitation of various single rotational transitions. (XBL 7911-12719)

1. J. C. Weisshaar and C. B. Moore, J. Chem. Phys. 70, 5135 (1979).
2. J. C. Weisshaar and C. B. Moore, J. Chem. Phys. 72, 2875 (1980).
3. J. C. Weisshaar and C. B. Moore, J. Chem. Phys. 72, 5415 (1980).
4. P. L. Houston and C. B. Moore, J. Chem. Phys. 65, 757 (1976).
5. W. M. Gelbart and K. F. Freed, Chem. Phys. Lett. 18, 470 (1973); K. F. Freed, J. Chem. Phys. 64, 1604 (1976).

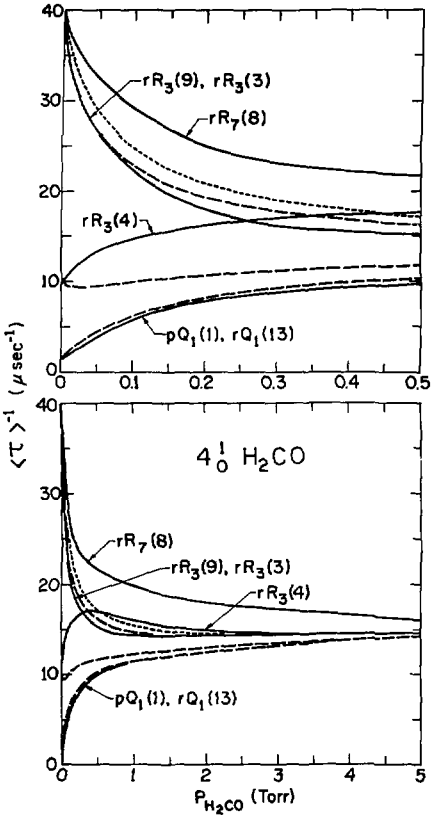

Fig. 3. Stern-Volmer plots of $\langle\tau\rangle^{-1}$ vs. pressure for excitation of various SRL's in pure H_2CO. The solid lines are smooth curves drawn through the experimental data of Fig. 2. The dashed lines are calculated curves using a simple rotational relaxation model. (XBL 7911-14553)

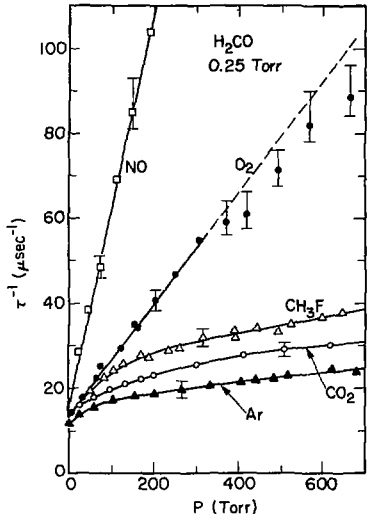

Fig. 4. Quenching of 0.25 torr of H_2CO by various collision partners. (XBL 7911-12717)

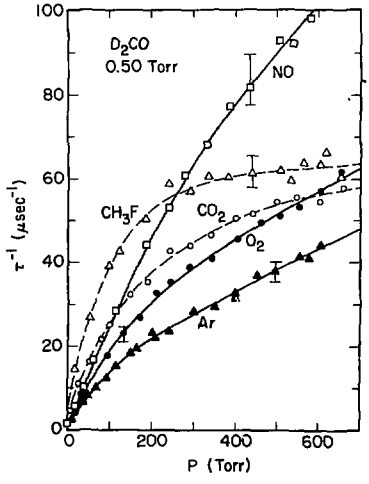

Fig. 5. Quenching of 0.5 torr of D_2CO by various collision partners. (XBL 7911-12716)

RESEARCH PLANS FOR CALENDAR YEAR 1981

Several types of experiments will be pursued to elucidate the nature of multiphoton excitation and dissociation processes. The small molecule limit, in which excitation through the discrete levels limits yield, is being studied using CO_2 laser excitation of d_2-formaldehyde. An accurate determination will be made of thermal dissociation rate parameters using the SiF_4-

sensitized decomposition method, which was applied in a qualitative way above to tetralin decomposition. Only when these parameters are well known is it possible to identify any mode-selective photochemical processes. An apparatus will be built for flash kinetic infrared absorption spectroscopy. The time resolution will initially be limited to a few nsec by the photolysis source. Wavelength resolution should be limited only by the Doppler width of the species studied. This system will allow the dynamics of multiphoton ir excitation to be studied in detail.

1980 PUBLICATIONS AND REPORTS

Refereed Journals

†1. D. J. Douglas and C. B. Moore, "Vibrational Relaxation of HF(v = 3,4) by HF, H_2, D_2, and CO_2, and Isobutene, Laser-Induced Processes in Molecules," K. L. Kompa and S. D. Smith, eds. in Proceedings of the European Physical Society Divisional Conference, Edinburgh, Scotland, (1978), p. 336.

‡§2. P. Ho and C. B. Moore, "Laser Separation of Isotopes by Photopredissociation," in Proceedings of the First National School "Laser Application in Atomic, Molecular and Nuclear Physics," Vilnius, U.S.S.R., August 1978. (Published 1980).

‡§3. F. E. Hovis and C. B. Moore, "Energy Transfer and Laser Photochemistry," in Proceedings of the First National School "Laser Application in Atomic, Molecular and Nuclear Physics," Vilnius, U.S.S.R., August 1978. (Published 1980).

§4. H.-L. Dai, A. H. Kung, and C. B. Moore, "Resonant Multiphoton Dissociation Mechanism of Excitation for Ethyl Chloride," Phys. Rev. Lett. 43, 761 (1979).

†5. J. C. Weisshaar and C. B. Moore, "Electric Field Dependence of Collisionless, Single Rotational Level Lifetimes of S_1 H_2CO," J. Chem. Phys. 72, 2875 (1980).

†6. J. C. Weisshaar and C. B. Moore, "Isotope, Electric Field, and Vibrational State Dependence of Single Rotational Level Lifetimes of S_1 Formaldehyde," J. Chem. Phys. 72, 5415 (1980).

†7. R. G. Macdonald and C. B. Moore, "Reaction and Deactivation of HCl(V = 1,2) by Cl, Br, and H atoms," J. Chem. Phys. 73, 1681 (1980).

8. M. R. Berman, P. B. Comita, C. B. Moore, and R. G. Bergman, "Flow Pyrolysis and Direct and SiF_4-Sensitized Laser-Induced Decomposition of Tetralin. Identification of Retro-[2 + 4] Cleavage as the Primary Homogeneous Thermal Decomposition Channel," J. Am. Chem. Soc. 102, 5692 (1980).

‖9. R. E. M. Hedges, P. Ho, and C. B. Moore, "Enrichment of ^{14}C by Selective Laser Photolysis of Formaldehyde," Appl. Phys. 22, 1699 (1980).

10. H.-L. Dai, A. H. Kung, and C. B. Moore, "Multiphoton Dissociation of Ethyl Chloride at 3.3 μm: Excitation Mechanism and Rate Equations Analysis," J. Chem. Phys. V.73, 6124 (1980).

LBL Report

§1. J. C. Weisshaar, D. J. Bamford, E. Specht, and C. B. Moore, "Quenching, Electronic Energy Transfer and Rotational Relaxation of S_1 Formaldehyde," LBL-11453 (1980). In press: J. Chem. Phys.

Other Publications

†1. J. S. Wong and C. B. Moore, "Bond Selective Excitation of Molecules," in Proceedings of the Sergio Porto Memorial Conference, July 1980, Rio de Janeiro, Brazil.

Invited Talks

1. C. Bradley Moore, "Laser-Induced Chemistry," Simon Fraser University, Vancouver, B. C., March 5, 1980.

2. C. Bradley Moore, "Photophysics and Photochemistry of Formaldehyde," 14th Informal Conference on Photochemistry, Newport Beach, CA, March 30-April 4, 1980.

3. C. Bradley Moore, "Photochemistry of Formaldehyde," I.B.M. Symposium on Laser Photochemistry in Large Molecules, San Jose, CA, August 20-22, 1980.

4. C. Bradley Moore, "Electric Field Tuning and Rotational Effects on Formaldehyde Predissociation," Avco Everett Research Laboratories, Everett, MA, September 30, 1980.

5. C. Bradley Moore, "High Resolution Laser Photophysics and Photochemistry of Formaldehyde," Lippincott Medal Symposium, 7th Annual Meeting of the Federation of Analytical Chemistry and Spectroscopy Societies, Philadelphia, PA, October 1, 1980.

6. Hai-Lung Dai, Andrew H. Kung, and C. Bradley Moore, "Multiphoton Dissociation at 3.3 micron: Excitation Mechanism and Rate Equations Analysis," Second Chemical Conference of the North American Continent, Las Vegas, NV, August 24-29, 1980.

* * *

†Partially supported by the U. S. Army Research Office, Triangle Park, N.C. and the National Science Foundation.

‡Partially supported by the U. S. Air Force Office of Scientific Research and the U. S. Army Research Office, Triangle Park, N.C.

§Partially supported by the National Science Foundation.

‖Supported by the National Science Foundation and the University of California.

b. Molecular Beam Laser Isotope Separation*

Yuan T. Lee and Y. Ron Shen, Investigators

1. PHOTOFRAGMENTATION TRANSLATIONAL SPECTROSCOPY OF Br_2

Z. Zhang, M. Sigrist, F. Huisken, D. Krajnovich, Y. R. Shen, and Y. T. Lee

We used a Nd:YAG laser to investigate the photodissociation of bromine. The second harmonic wavelength of the Nd:YAG laser produces only ground state bromine atoms either by absorption into the continuum of the A $1_u(^3\pi)$ state and subsequent dissociation or by absorption into a discrete level of the B $0_u^+(^3\pi)$ state followed by predissociation. By changing the polarization of the laser beam these two processes can be distinguished. In 1975, Wilson and his coworkers did a similar experiment on bromine photodissociation,[1] using a neodyminum glass laser. They were surprised that they did not observe predissociation. Under our experimental conditions, predissociation is clearly observed.

The experiments were performed with a universal molecular beam machine.[2] The bromine molecular beam was produced by bubbling argon through a bromine reservoir and expanding the mixture through a heated quartz nozzle. We then measured the Br product at 10° from the molecular beam as a function of laser polarization.

The A → X transition is a perpendicular transition. The polarization dependence of recoiling Br atoms in the center of mass coordinate system has the form:

$$W(\theta) \propto \sin^2\theta$$

where θ is the center-of-mass angle of recoil with respect to the electric vector of the light. In our setup, the relation between θ and α, the polarization of the laser beam in lab coordinates has a simple form, i.e., $\cos\theta = \cos\alpha \cos 18.5°$ (see Fig. 1). Therefore, the polarization dependence should coincide with curve A in Fig. 2 if there is no predissociation via the B state. The deviation of the experimental result from the theoretical curve is evidence of predissociation.

We also checked the possibility of predissociation from the vibrational and rotational levels of the bromine molecule.[2,3] The vibrational and rotational energy levels are different for different bromine isotopic species and so the probability of predissociation will be different for $^{79\text{-}79}Br_2$, $^{81\text{-}81}Br_2$ and $^{79\text{-}81}Br_2$. Assuming the

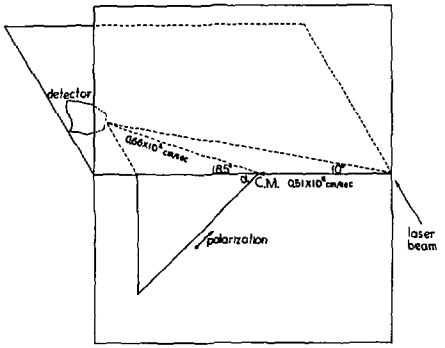

Fig. 1. Relation between angle α (laser polarization) and angle θ (the c.m. angle of recoil with respect to the electric vector of the laser beam). (XBL 8012-12943)

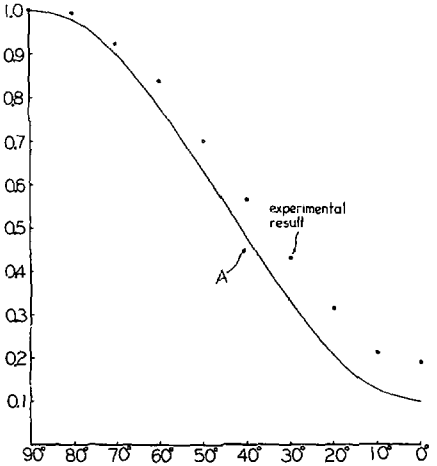

Fig. 2. Polarization dependence of Br* measured at 10° from the bromine molecular beam. Solid curve A is the theoretical curve for perpendicular transition only [$A1_u(^3\ ) \leftarrow X\ 0_g^+(^1)$]. Circles represent the experimental result. (XBL 8012-12952)

*This work was supported by the Assistant Secretary for Nuclear Energy, Office of Advanced Systems and Nuclear Projects, Advanced Isotope Separation Division of the U. S. Department of Energy under Contract No. W-7405-ENG-48.

rotational temperature of the bromine beam is 20K, the most probable predissociation is for $^{81,81}Br_2$. The transition is from v'' = 0, J'' = 15 to v' = 23, J' = 14 or from v'' = 0, J'' = 17 to v' = 23, J' = 18. The populations of the states J'' = 15 and J'' = 17 are 4.5 and 3.5 respectively. For $^{79-81}Br_2$, two possible transitions start from J'' = 26 and J'' = 28 of v'' = 0, but the probability of predissociation for this species is low since the populations for J'' = 26 and J'' = 28 are less than 0.5. Predissociation of $^{79,79}Br_2$ seems impossible at this wavelength.

* * *

1. R. J. Oldman, R. K. Sander, and K. R. Wilson, J. Chem. Phys. 63, 4252 (1975).
2. J. A. Horsley and R. F. Barrow, Trans. Faraday Soc. 63, 32 (1967).
3. J. A. Coxon, J. Quant. Spectrosc. Radiat. Transfer, 11, 443 (1971).

2. PHOTODISSOCIATION OF BROMINE DIMERS

Z. Zhang, M. Sigrist, F. Huisken, D. Krajnovich, Y. R. Shen, and Y. T. Lee

We have used the second harmonic wavelength of the Nd:YAG laser to investigate the photodissociation of bromine dimers by the crossed laser-molecular beams method. We have detected Br_3^* and Br_3^+ products in our mass spectrometer detector. Since these species have different velocity distributions, we conclude two different dissociation channels occur for the dimer, namely:

$$(Br_2)_2 \longrightarrow Br_3 + Br^* \qquad (1)$$

and

$$(Br_2)_2 \longrightarrow Br_3^* + Br \longrightarrow Br_2 + Br + Br. \qquad (2)$$

These processes can be explained with the aid of Fig. 3. The primary step in both processes is the absorption of a 18783 cm^{-1} photon by the dimer and the ejection of a Br atom from the cluster. If a $Br^*(^2P_{1/2})$ atom is ejected [process (1)], the Br_3 cluster which is left behind cannot dissociate, and hence may be detected as Br_3^+ in the ionizer. However, if a ground state $Br(^2P_{3/2})$ atom is ejected [process (2)], the remaining Br_3 cluster is not bound, and must eventually dissociate into a bromine molecule and another ground state bromine atom. The bromine molecule will be detected as Br_2^+ in the ionizer.

That process (1) occurs at all means that the bottom of the Br_3 potential well must be lower than the photon energy of 18783 cm^{-1}. If the molecule dissociates just at the bottom of the potential well, there will be no internal energy in the Br_3 fragment, and all of the excess energy will appear as translational energy of the Br_3 + Br^* products. Therefore, by determining the maximum center-of-mass translational energy of the Br_3 + Br^* pair, we can obtain a minimum value for the Br_3 binding energy. Our analysis yields a

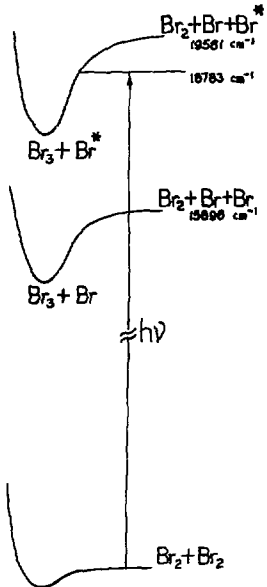

Fig. 3. Energy diagram for bromine dimer photodissociation. (XBL 8012-12941)

maximum center-of-mass translational energy of ~ 3 kcal/mole for Br_3 + Br^*. We must add to this the difference between the Br_2 + Br + Br* energy (19581 cm^{-1}) and the photon energy (18783 cm^{-1}), which brings the value up to 5.2 kcal/mole. Finally, we should take into account the binding energy of $(Br_2)_2$, which effectively lowers the photon energy. This energy is not known, but is probably ~ 1 kcal/mole. Therefore, we conclude that the binding energy of Br_3 is > 6 kcal/mole.

3. VIBRATIONAL PREDISSOCIATION SPECTRA OF MOLECULAR DIMERS

J. M. Lisy,† M. F. Vernon, R. Page, Y. R. Shen, and Y. T. Lee

In the past year we have initiated experiments on a molecular beam apparatus using a co-linear configuration with the optical parametric oscillator. The new experimental system is shown in Fig. 4. The interaction region where the laser and molecular beams overlap is approximately 10 cm, a 50-fold increase over the crossed laser-molecular beam arrangement used in previous in-

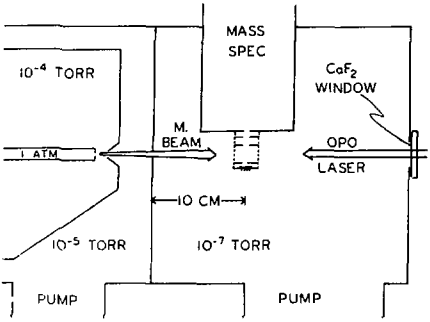

Fig. 4. Experimental arrangement for vibrational predissociation spectra utilizing the co-linear configuration. (XBL 8012-12953)

vestigations.[1] Typical signal levels of 40 cts/laser shot are readily obtained, greatly reducing the time required for data collection. Using the co-linear configuration, the vibrational predissociation spectra of all cluster sizes, including dimers, can be obtained by tuning the mass spectrometer to the mass of the particular cluster of interest and monitoring the decrease in signal when the laser fires. A second modification for this study has involved the use of seeded molecular beams, using Ar and He as carrier gases, as opposed to the use of neat HF and H_2O in earlier work.[2]

The spectrum of $(C_2H_4)_2$ is displayed in Fig. 5. The most intense features in the spectrum correspond to the infrared active modes of the monomer. The frequency shifts from the ν_3 (2989.5 cm^{-1}) and ν_9 (3105.5) monomer transitions are very small and cannot be precisely determined at this time. A new infrared monochrometer on order will improve the accuracy of our frequency measurements to within 1 cm^{-1}. Note that red-shifted 25 cm^{-1} from the band near 3100 cm^{-1} is a small peak with a linear dependence. We tentatively assign this feature as a van der Waals hot band, i.e., a transition from a state with one vibrational quantum in a van der Waals stretch or bend between the two C_2H_4 units to a final state with one vibrational quantum in a C-H stretch. Thus the vibrational frequency for this van der Waals mode is approximately 25 cm^{-1}.

The spectra of $(H_2O)_2$ and previously measured[1] $(H_2O)_3$ are displayed in Fig. 6. The two sharp bands at 3716 and 3594 cm^{-1} for $(H_2O)_2$ are shifted to lower energy by 40 and 58 cm^{-1} respectively from the ν_3 and ν_1 fundamentals[3] of H_2O. There are no low-frequency (<3475 cm^{-1}) components to the dimer system. Isotopic substitution is planned to help assign the experimental frequencies to specific vibrational motion in the dimer. It does seem apparent that the bands at lower frequency in the trimer must arise from a substantially different configuration, which we believe to be cyclic. Further analysis of the H_2O systems is in progress with the partially deuterated dimer.

* * *

†National Science Foundation Postdoctoral Fellow, 1979-80.

1. H. S. Kwok, et al., MMRD Annual Report, LBL-10000, (1979), pp. 338-341.
2. D. J. Krajnovich, et al., MMRD Annual Report, LBL-10000, (1979), pp. 505-506.
3. G. Herzberg, Infrared and Raman Spectra of Polyatomic Molecules, Van Nostrand Reinhold, New York (1945).

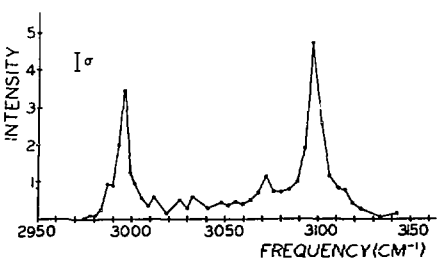

Fig. 5. Vibrational predissociation spectrum of $(C_2H_2)_2$. (XBL 8012-12944)

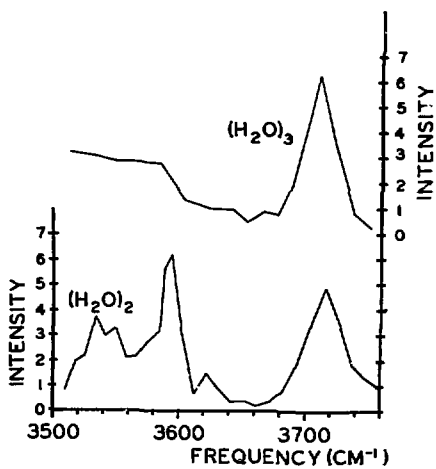

Fig. 6. Vibrational predissociation spectra of $(H_2O)_2$ and $(H_2O)_3$. (XBL 8012-12946)

4. REACTIVE SCATTERING OF CF_3I + Br, VIBRATIONAL EFFECTS

D. Krajnovich, Z. Zhang, F. Huisken, Y. R. Shen, and Y. T. Lee

The reaction $CF_3I + Br \rightarrow CF_3 + IBr$ has been studied in crossed molecular beams. This reaction is endothermic by 11 kcal/mole. We performed the experiment in two ways. First, we crossed the Br beam with a room temperature (vibrationally cold) CF_3I beam at a relative collision energy of 29 kcal/mole and measured the laboratory angular distribution of the IBr product. The result is shown by the dashed curve in Fig. 7. The IBr product is strongly backward-peaked relative to the incident bromine direction. Second, we used a CO_2 TEA laser to vibrationally excite part of the CF_3I beam to near the dissociation threshold and then detected the laser-correlated IBr signal as a function of laboratory angle. As shown in Fig. 7, there is appreciably more forward-scattered IBr product when Br reacts with vibrationally hot CF_3I than when it reacts with vibrationally cold CF_3I. Presumably, the greater extension of the C-I bond in the multiphoton excited CF_3I molecules enables larger impact parameters to react, with a consequent shift of the product intensity toward the forward direction.

In addition, we hoped to compare the relative efficiency of translational versus vibrational energy in promoting this endothermic reaction. Classical trajectory[1] results on endothermic hydrogen transfer reactions have suggested that vibrational energy is vastly superior to translational energy in promoting reaction. Although analysis of our results is difficult (mainly due to uncertainty in the degree of vibrational excitation produced by the CO_2 laser pulse), it is nevertheless clear that vibrational energy is not orders of magnitude more effective than an equivalent amount of translational energy in promoting this endothermic reaction.

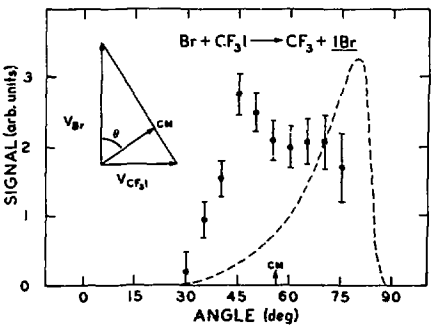

Fig. 7. Dashed line represents angular distribution of IBr obtained with vibrationally cold CF_3I at a relative collision energy of 29 kcal/mole; arrow denotes the center-of-mass direction. Filled circles show angular distribution of IBr obtained with vibrationally hot CF_3I molecules. (Hot CF_3I molecules were produced by multiphoton excitation.) (XBL 8012-12942)

* * *

1. J. C. Polanyi and W. H. Wong, J. Chem. Phys. 51, 1439 (1969); M. H. Mok and J. C. Polanyi, J. Chem. Phys. 51, 1451 (1969).

5. DYNAMICS OF VIBRATIONAL PREDISSOCIATION OF VAN DER WAALS MOLECULES

M. F. Vernon, J. Lisy, H. S. Kwok, and Y. T. Lee

Over the past year we have made additional measurements on the vibration predissociation process in small benzene polymers. The goal of these studies was to elucidate the features of the predissociation process defined by

$$(C_6H_6)_n + h\nu \xrightarrow{\tau} (C_6H_6)_m + (C_6H_6)_p + \Delta E_{trans}$$

where τ is the dissociation time, $3000\ cm^{-1} < h\nu < 3100\ cm^{-1}$, and $m + p = n$. In particular, we posed four questions.

1. What are the limits which can be placed on τ?

2. Is there a propensity for $p = 1$ in the dissociation?

3. How is the excess energy distributed between translation (ΔE_{trans}) and internal energy?

4. Is the internal energy concentrated in either of the fragments?

The new information is shown in Fig. 8, which shows the angular distributions of two fragment masses measured under the best nozzle conditions where the polymerization was minimal. At these conditions, the ratio of the mass 156 (ϕ_2^2) and 234 (ϕ_4^4) signal in the molecular beam was 30/1. The angular distributions of the two fragments are similar, and extend only to ~ 10° from the benzene beam. By measuring the beam velocity (v_b) of the initial polymers, the transverse velocity of the dissociation fragments is computed from the laboratory angle (θ). From this and momentum balance, the total kinetic energy of the fragments can be shown to be

$$E_{trans} = \frac{M_1 p^2}{2} \left(\frac{1}{m} + \frac{1}{p}\right) (v_b \sin\theta)^2 \qquad (1)$$

where M_1 is the mass of the monomer. From energy conservation the internal energy of the fragments is

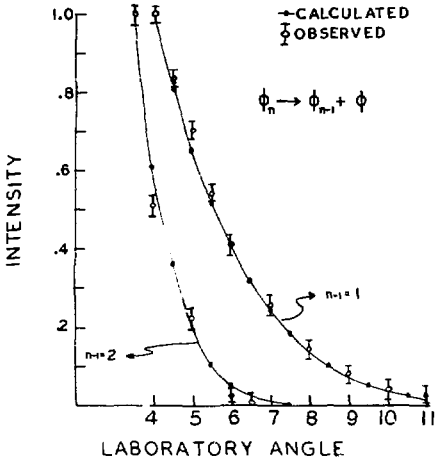

Fig. 8. Laboratory angular distribution of benzene polymer photofragments. (XBL 8012-13531)

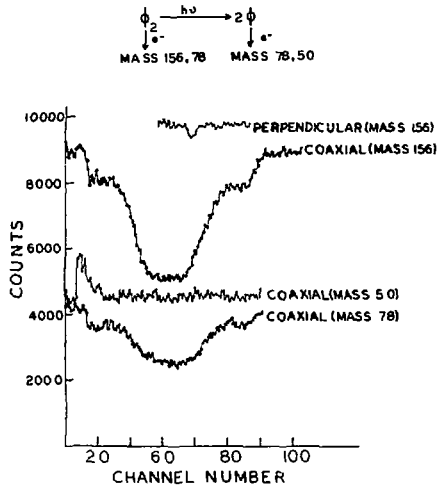

Fig. 9. Comparison of signals observed with coaxial and perpendicular laser-molecular beam geometries. (XBL 8012-13533)

$$E^{final}_{internal} = E_{photon} + E^{initial}_{internal} - E_{bond} - E_{trans}. \quad (2)$$

We assume $E^{initial}_{internal}$ to be negligible and the bond energy/monomer unit to be ~ 800 cm^{-1} (Ref. 1). The minimum amount of internal energy (ΔE_{int}) is then 2088 cm^{-1}. The monotonic increase of the dissociation signal with decreasing lab angle can be fit only with a translational energy distribution which also has a similar increase with decreasing translational energy, peaking at zero translational energy. The minimum lab angle measured of 4° shows less than 25 cm^{-1} in translational energy. The beam composition at 0° would imply that only benzene dimers and trimers will contribute to the photodissociation signal. Measurements of polymer fragmentation patterns indicate that there is substantial fragmentation, with only 1/10 of the dimers appearing at the parent mass 156 (Ref. 2). Consequently, the assignment of the laser-induced off-axis signal to a parent polymer is not trivial. However, by measuring the signal at mass 50, we can safely assign the observed signal at mass 78 to fragments from dimer dissociations. The signals from a coaxial laser-molecular beam experiment show that mass 50 correlates only to monomer fragments. Figure 9 shows the detector signal observed in this arrangement. The initial time delay after the laser pulse is a result of the finite flight time of ions from the ionization region to the detector. The subsequent increase in signal is due to an increase in the number density of benzene monomer from dissociations of polymers in or near the ionizer at the time of the laser pulse. The decrease of the monomer signal is a result of the dissociation of polymers by the laser upstream from the ionizer which otherwise would have cracked in the ionization process to mass 78. These dissociation products are scattered out of the molecular beam, hence a net decrease in signal. The comparison of the two mass signals provides a check for the polymer origin of the signals.

The monotonic increase of the angular signals for both masses 78 and 156 suggests that the dissociation mechanism favors concentrating the energy in the monomer fragment, and that p = 1 in Eq. (1) for the polymers measured here. If the internal energy was placed in the dimer fragment, this would be in excess of the bond energy. Because there is no observable break in the shape of the angular scan, we assume no change in the dissociation mechanism; therefore, the internal energy must be in the departing monomer fragment. There are many low-frequency monomer vibrations which are nearly resonant with the excess energy remaining after breaking the intermolecular bond. The similarity of the angular scans is a result of the near-resonant energy transfer characteristics of the monomer benzene molecule, not of the cluster.

The transit time of the molecules through the detector viewing zone is ~2 μsecs. To place a lower bound on τ, we changed the polarization of the laser from linear to circular. If the complexes dissociate faster than the rotational frequency of the excited complex in space, the

orientation of the transition dipole with respect to the dissociation axis will result in an anisotropic laboratory angular distribution. No effect was observed. This would be reasonable if the lifetime is longer than the rotational period or if the transition dipole is not oriented parallel to the intermolecular bond. The T-shaped structure of the dimer[2] would also smear out some of the anisotropy of the dipole with respect to the intermolecular bond in this case.

In conclusion, our current understanding of the dissociation process is:

$$(C_6H_6)_n + h\nu \xrightarrow{\tau < 10^{-6}\ \text{secs}} (C_6H_6)_{n-1} + C_6H_6^{\ddagger} + E_{trans}(0),$$

where $C_6H_6^{\ddagger}$ indicates vibrationally excited benzene.

* * *

1. T. B. MacRury, W. A. Steele, and Bruce J. Berne, J. Chem. Phys. 64, 1288 (1976).
2. Kenneth C. Janda et al., J. Chem. Phys. 63, 1419 (1975).

RESEARCH PLANS FOR CALENDAR YEAR 1981

Dynamics of IR multiphoton dissociation processes will be further investigated for selected polyatomic molecules containing H, F, and Cl atoms, using the combination of two IR lasers with vastly different frequencies. Selective dissociation will be attempted by using the output of the optical parametric oscillator to excite the molecule to the quasicontinuum through the CH stretching vibrational ladder, followed by a high-power CO_2 laser pulse. This process will be compared with the direct multiphoton dissociation, using either an optical parametric oscillator or a CO_2 laser alone.

Chemical behavior of multiphoton excited molecules will be carefully investigated. The reaction of highly vibrationally excited CF_3I with Br did not show a drastic vibrational enhancement. This endothermic reaction is likely to have a barrier in the entrance channel which would tend to make translational energy more effective. Endothermic substitution reaction of unsaturated halocarbons with halogen atoms will have a barrier in the exit channel. This type of reaction will be investigated in the coming year.

Vibrational predissociation of van der waals molecules and hydrogen-bonded molecular clusters will be studied at higher wavelength resolution. In all the systems studied thus far, a very small fraction of the excess energy appears to be translational. This is exactly what one would predict from momentum-gap law. For larger polyatomic molecules, the partitioning of the excess energy between the vibrational and rotational degrees of freedom is not clear. Laser-induced fluorescence will be used to investigate this question.

1980 PUBLICATIONS AND REPORTS

Refereed Journals

1. Aa. S. Sudbo, P. A. Schulz, D. J. Krajnovich, Y. R. Shen, and Y. T. Lee, "Photoionization Study of Multiphoton Excited SF_6 in a Molecular Beam," Opt. Lett. 4, 219 (1979).

2. P. A. Schulz, Aa. S. Sudbo, D. J. Krajnovich, H. S. Kwok, Y. R. Shen, and Y. T. Lee, "Multiphoton Dissociation of Polyatomic Molecules," Ann. Rev. Phys. Chem. 30, 379 (1979).

3. P. A. Schulz, Aa. S. Sudbo, E. R. Grant, Y. R. Shen, and Y. T. Lee, "Multiphoton Dissociation of SF_6 by a Molecular Beam Method," J. Chem. Phys. 72, 4985 (1980).

LBL Reports

1. Yuan T. Lee and Y. Ron Shen, "Molecular Beam Studies of IR Laser Induced Multiphoton Dissociation and Vibrational Predissociation," submitted to Physics Today, June 1980, LBL-11105.

2. M. W. Sigrist, D. J. Krajnovich, F. Huisken, Z. J. Zhang, Y. T. Lee, and Y. R. Shen, "Laser-Induced Dissociation of Monomers and Dimers of Bromine," submitted to Helv. Phys. Acta, June 1980, LBL-10991.

Invited Talks

1. M. F. Vernon, "Infra-red Vibrational Photodissociation Spectra of Molecular Beams of Small, Hydrogen Bounded Clusters," 35th Annual Symposium on Molecular Spectroscopy, Ohio State University, Columbus, Ohio, June 16-20, 1980, LBL-10566 Abs.

2. Y. R. Shen, "Two-Channel Multiphoton Dissociation of Polyatomic Molecules," XI International Quantum Electronics Conference, Boston, Massachusetts, June 23-26, 1980, LBL-10316 Abs.

3. H. S. Kwok, "Vibrational Predissociation Spectra of Small Clusters of H_2O, HF, NH_3, CH_3OH, C_6H_6 and C_6H_{12}," International Quantum Electronics Conference, Boston, Massachusetts, June 23-26, 1980, LBL-10288 Abs.

4. Y. T. Lee, "Molecular Beam Studies on Laser Chemistry," Zhonshan University, Guanzhou, China, July 28, 1980.

5. Y. T. Lee, "I.R. Multiphoton Dissociation and Vibrational Predissociation of Molecular Clusters," Gordon Conference on Vibrational Spectroscopy, Brewster Academy, Andover, New Hampshire, August 18-22, 1980.

6. F. Huisken, "Two-Channel Multiphoton Dissociation of CF_2Cl_2 and Ethyl Vinyl Ether, Third European Study Conference on Low Energy Molecular Collisions (MOLEC III), Oxford, United Kingdom, September 2-6, 2980, LBL-11132 Abs.

VI Energy Storage

Energy Storage

a. Development of Electrochemical Synthesis and Energy Storage

James W. Evans, Rolf H. Muller, John Newman, Philip N. Ross, and Charles W. Tobias, Investigators

Introduction. The overall aim of this program is to improve the energy efficiency, lower the capital cost, and increase the materials yield of electrochemical processes employed in the direct conversion of chemical to electrical energy in galvanic cells and in the production of materials by electrolysis.

Anodic Surface Layers on Battery Materials

The purpose of this work is to provide direct experimental information about formation and properties of surface layers on battery-electrode materials. A more broadly-based, fundamental research program, supported by the Division of Materials Sciences, Office of Basic Energy Sciences, is described under "Electrochemical Phase Boundaries," R. H. Muller, Investigator.

1. ELLIPSOMETRIC STUDIES OF LITHIUM IN PROPYLENE CARBONATE SOLUTIONS†

Felix Schwager and Rolf H. Muller

The use of lithium in ambient-temperature batteries, which employ nonaqueous solvents, is made possible largely by the formation of surface layers which inhibit thermodynamically favored spontaneous reactions. These surface layers may, however, hinder the delivery of electric power upon discharge, when the metal is dissolved; and they are generally considered responsible for the poor performance of lithium electrodes upon recharging, when metal is redeposited from the solution. This work is undertaken to determine structure, composition, and mode of formation of surface layers in some representative battery environments in order to identify possible approaches to improve electrode behavior.

Film formation on lithium, immersed in pure propylene carbonate solvent and its 1 M $LiClO_4$ and 1 M $LiAsF_6$ solutions, has been observed in situ by ellipsometry and ex situ by Auger electron spectroscopy, ion etching, and secondary-ion mass spectroscopy.

The following conclusions are drawn from ellipsometer measurements under open-circuit conditions:

(1) Ellipsometer measurements are possible even though refractive indices of some potential film materials are close to that of the solution (Table 1).

(2) Film growth continues throughout the 15-day period of observation.

(3) Film growth rates strongly depend on electrolyte composition. They decrease in the order; pure solvent, 1 M $LiAsF_6$, 1 M $LiClO_4$.

(4) Film growth is not greatly affected by the addition of small amounts (1000 ppm) of water to $LiClO_4$ solutions.

(5) Interpretation of ellipsometer measurements requires the use of inhomogeneous film models with refractive index decreasing from the metal substrate to the solution side, indicative of increased porosity in that direction (Fig. 1).

(6) A high real part of the refractive index of the film material near the metal substrate is essential for a satisfactory interpretation of measurements and indicates the presence of Li_2O or possibly LiCl (Table 1).

The inhomogeneous porous film model has been confirmed by changing the immersion medium of the film from solution to vacuum. The evaporation of solvent from the pores results

Table 1. Refractive indices of potential film material, solution, and substrate.

LiOH	1.466
Li_2CO_3	1.50
Li_2O	1.644
LiCl	1.662
PC, 1 M $LiClO_4$	1.429
Li	0.25-2.3i

*This work was supported by the Assistant Secretary for Conservation and Solar Energy, Office of Advanced Conservation Technology, Electrochemical Systems Research Division of the U. S. Department of Energy under Contract No. W-7405-ENG-48.

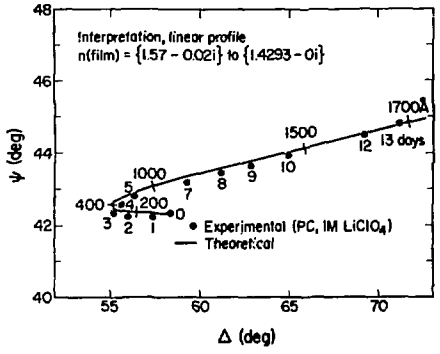

Fig. 1. Ellipsometer parameters Δ and ψ for film formation on Li in 1 M $LiClO_4$ under open circuit. Measurements and interpretation for an inhomogeneous film with refractive index 1.57-0.02 i at the substrate side, decreasing linearly with distance to 1.429 (refractive index of solution) on the solution side. (XBL 809-2047)

in a considerable change in effective film refractive index. The same film thickness was derived.

Depth profiling by argon-ion etching and Auger spectroscopy confirmed the film thicknesses derived by ellipsometry and was consistent with the presence of Li_2O rather than LiCl near the substrate. The presence of carbon throughout the film may indicate a partial content of Li_2CO_3. Chlorine content was also uniform but small. Secondary-ion mass spectroscopy only partially agreed with Li_2CO_3 calibration results.

* * *

†Brief version of LBL-11846.

2. TRANSIENT ELECTROCHEMICAL MEASUREMENTS ON LITHIUM IN PROPYLENE CARBONATE SOLUTIONS†

Yordan Geronov and Rolf H. Müller

Galvanostatic pulse measurements have been conducted to determine thickness, conductivity, and kinetics of formation of surface layers formed on lithium with solutions of 1 M $LiClO_4$ and 0.5 M $LiAsF_6$ in propylene carbonate solvent. The electrode capacitance was derived from the rate of initial potential increase with short (5 to 10 μs) current pulses. IR-free overpotential values were obtained from the response to long (20 ms) pulses.

The film thickness was computed from the capacitance measurements for a plane-parallel film geometry under the assumption of a film dielectric constant, with the series-connected, double-layer capacitance being neglected. Exchange current densities were determined from micropolarization measurements. Film resistivity was derived from current flow at steady-state overpotential.

Film thickness derived from capacitance measurements is typically about 5 times lower than that obtained by ellipsometry. The difference supports the concept of an inner, compact film section that controls capacitance adjacent to electrolyte-filled porous sections facing the solution. The thickness of the compact section reaches a steady state (Fig. 2) in contrast to the ellipsometer measurements, which show a continuing overall film growth. The continued increase in film thickness therefore appears to be due to growth of the porous sections. Higher water content results in faster film growth but unchanged steady-state thickness with perchlorate and hexafluoroarsenate solutions.

Film conductivities of $2.7 \times 10^{-9}\ \Omega^{-1}\ cm^{-1}$ and $5.1 \times 10^{-9}\ \Omega^{-1}\ cm^{-1}$ have been determined for immersion in solutions of $LiClO_4$ and $LiAsF_6$ respectively. An increase in the water content of $LiClO_4$ solutions to 1000 ppm resulted in lower film conductivity but did not affect film conductivity with pure propylene carbonate or $LiAsF_6$ solutions.

* * *

†Brief version of LBL-11126.

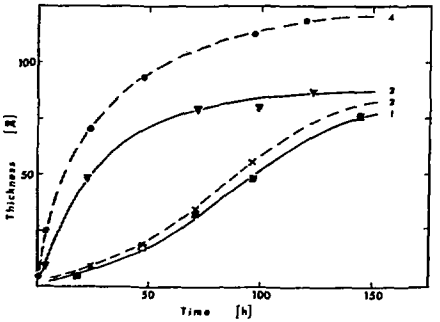

Fig. 2. Growth of compact surface layer on lithium in different propylene carbonate solutions. Film thickness derived from capacitance measurements under the assumption of dielectric constant = 4.9. (1) 1 M $LiClO_4$; (2) same with 1000 ppm H_2O added; (3) 0.5 M $LiAsF_6$; (4) same with 1000 ppm H_2O added. (XBL 8012-12965)

Surface Morphology of Metals in Electrodeposition

The objective of this project is to develop a pragmatic understanding of the partial processes governing the macrocrystallization of metals. This understanding is necessary for the design and optimization of metal deposition processes, including those in rechargeable galvanic cells. Current projects included: (a) The effect of hydrodynamic flow on the surface morphology of copper and of zinc, and (b) Dynamic modeling of surface profiles in electrodeposition and dissolution.

3. MICROSTRUCTURAL DEVELOPMENT DURING MASS TRANSFER CONTROLLED DEPOSITION

Andrew Kindler and Charles W. Tobias

The formation of powdery deposits during electrodeposition at the limiting current is a phenomenon familiar to all electroplaters. In the case of copper electrodeposition from solutions of $CuSO_4$ - H_2SO_4 in channel flow, the powder particles are nodular in appearance when the electrode is viewed from the top under a scanning electron microscope (Fig. 3, top two photos). None of the many attempts made to explain this phenomenonl is satisfactory. Our copper deposition experiment, conducted under carefully controlled hydrodynamic conditions, supports the hypothesis that mass transfer overpotential is a requirement for dendritic growth.

The nodules are dendritic structures that undergo morphological transformation during growth. As shown in Fig. 4, this results in the coverage of the dendrite tip by a mushroom cap. The transformation occurs because the growing dendrite disturbs the thin mass transfer boundary layer (approximately 30 microns thick in the experiment of Fig. 3). Therefore, the dendrite is no longer growing at the limiting current. Below the limiting current, solid coherent deposits similar to the mushroom cap are known to be formed. Three lines of evidence support this explanation.

First, the overpotential in galvanostatic copper deposition at the limiting current declines. It can be shown that a surface-area increase cannot account for a decrease of this magnitude (see Fig. 5). The drop in overpotential must be caused by the decrease of concentration overpotential resulting from mass transfer boundary layer disruption.

A second line of evidence was developed by performing copper electrodeposition under approximately potentiostatic conditions and at limiting current. Under such conditions, the dendrite tip is always near limiting current because potentiostatic operation causes the current density to increase as the boundary layer is disrupted. This keeps the overpotential fairly constant. The resulting deposit was clearly dendritic and lacked any appearance of the beginning of morphological transformation (see Fig. 6, top left photo). Figure 6, top

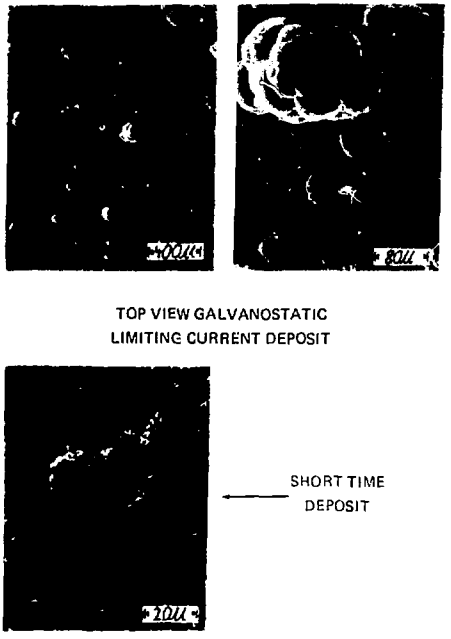

Fig. 3. 0.228 M $CuSO_4$, 0.95 M H_2SO_4, limiting current: 83.6 mA/cm^2 Re = 23,000, galvanostatic. Top two photos: same experiment. 58.9 coulombs/cm^2 passed. Bottom: Same experimental conditions but 10.78 coulombs/cm^2 passed. (XBB 805-5761)

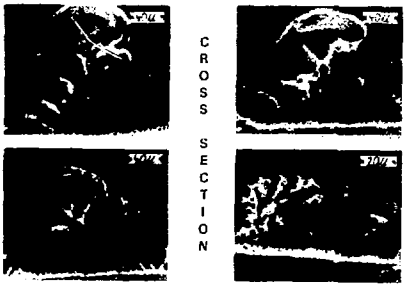

Fig. 4. Cross sections of photos in Fig. 3. Top two and lower left: same experiment, 58.9 coulombs/cm^2 passed. Lower right: 10.78 coulombs/cm^2 passed. (XBB 805-5762)

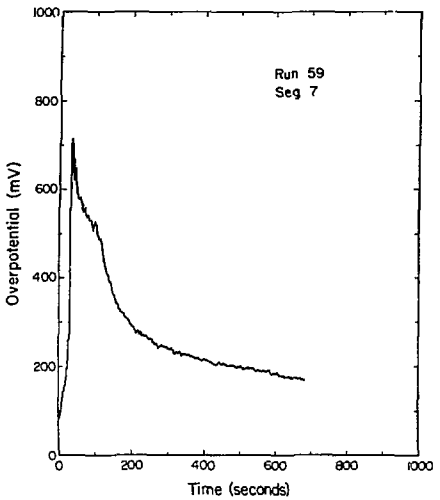

Fig. 5. Decline of total overpotential with time during a galvanostatic run set at limiting current. Conditions: same as in Fig. 3. (XBL 813-455)

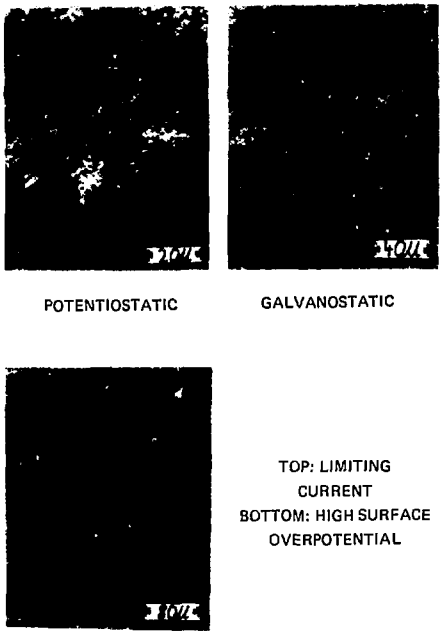

Fig. 6. Top: 0.228 M $CuSO_4$, 0.932 M H_2SO_4, Re = 23,000 9.9 coulombs/cm^2. Top left: potentiostatic -0.600 volt, Top right: galvanostatic at limiting current, 83.6 mA/cm^2. Bottom: 0.4 $CuSO_4$, 0.925 M H_2SO_4, Re = 185,000, 50.75 coulombs/cm^2, 273 mA/cm^2: 95% of limiting current density. (XBB 805-5764)

right also shows a galvanostatic deposit formed by passing the same number of coulombs. The galvanostatic deposit does not show signs of mushroom capping; rather, grape-like clusters are visible, which will eventually fuse as deposition continues. To prove that lack of mushroom capping is due to the shortness of the deposition time, compare bottom photo in Fig. 3 to the two top photos. Both deposits were produced under identical deposition conditions except that the bottom photo shows a short-time deposit. The same sort of comparison can be made between the photographs in Fig. 4, which are simply of cross sections of the deposits shown in Fig. 3. The top two and bottom left photos are different views of the same sample. The lower right is a view from a short-time experiment, again without the mushroom cap.

The third line of evidence is the observation[2] that dendrites grow on copper deposited from solutions of H_2SO_4-$CuSO_4$ when hydrogen is evolved. In this special case, copper is deposited at constant mass-transfer overpotential, η_c, near the limiting current. These are, of course, the previously stated conditions for dendrite formation. The η_c stays constant in this special case because any disturbance of the mass-transfer boundary layer will make copper deposition easier, thus diverting current from the hydrogen evolution reaction, which by comparison becomes energetically less favored.

These three lines of evidence reduce the phenomena of dendrites and nodules at limiting current to just one: dendrites. These dendrites form at the limiting current probably as a result of an instability phenomenon.[3] At limiting current, the supply of copper ions at the metal electrolyte interface approaches zero. Any projection from the electrode penetrating into the mass-transfer boundary layer will find itself in an environment relatively more rich in copper ions. It will therefore tend to grow faster than flat regions of the electrode. Some evidence supporting a mass-transfer explanation rather than a kinetic one is provided by Fig. 6, bottom photo. Here, a copper deposit performed on a rotating cylinder is shown. The fraction of the limiting current was only 54% so that η_c is negligible. The charge-transfer overpotential, η_s, however, was 0.26 volt or about the same as in a powder-producing experiment run at 95% of limiting current. If η_s were responsible for producing dendrites, these should have formed on the rotating cylinder. Instead a

smooth surface was obtained. Clearly, a large mass-transfer overpotential (close to limiting current) is required for the growth of dendrites.

* * *

1. N. Ibl, "Applications of Mass Transfer Theory: The Formation of Powdered Metal Deposits," Advances in Electrochemistry and Electrochemical Engineering 2, 49 (1962).
2. C. L. Mantell, Electrochemical Engineering, McGraw-Hill Book Co., Inc., New York (1960), p. 124.
3. A. R. Despic and K. I. Popov, "Transport Controlled Deposition and Dissolution of Metals," Modern Aspects of Electrochemistry, 7, 223 (1972).

4. EFFECTS OF HYDRODYNAMIC FLOW ON THE ELECTROCRYSTALLIZATION OF ZINC FROM ACID ELECTROLYTES

James L. Faltemier, Vladimir Kommenic, Tetsuaki Tsuda, and Charles W. Tobias

The influence of current density, hydrodynamic conditions, time of metal deposition, nature of zinc salt, and substrate conditions on the quality of zinc deposits has been studied galvanostatically in a rotating-disk system containing a platinum cathode and a zinc anode.

A current-density interval well below limiting current has been identified in which spiral-like striations form, reflecting the fluid motion over the surface of the electrode. Within this interval, increasing current density increases the number of spirals and decreases the time for their formation. Above some critical value, a more uniform nucleation density occurs, and a smooth deposit is produced. Spirals where observed in 1 M $ZnCl_2$ solutions below 80 to 100 mA/cm^2, while in 1 M $ZnSO_4$ solutions spirals where observed below 10 mA/cm^2. The occurrence of spirals in both the highly-complexing $ZnCl_2$ and the noncomplexing, less conductive, $ZnSO_4$ solutions confirms that the spiral phenomenon is not dependent upon complex-ion formation or mass transfer. Short-time experiments showed a nonhomogeneity on the electrode substrate at the lower current densities with zinc preferentially deposited along the scratch lines and more uniform nucleation density at the higher current densities.

Variable-current step and AC pulse techniques were used to detect the influence of the original substrate surface and of preferential sites on the formation of spirals. By prolonging, or eliminating, spiral formation altogether, these methods showed the close relationship between surface defects, nucleation density, and spiral formation.

Rotating-ring electrodes were employed to examine the leading-edge effect in a rotating system. Experiments were conducted at a current density of 5 mA/cm^2 and at rotating speeds of 200, 400, 800, and 1,600 rpm in 1 M zinc sulfate solution (pH 2). The results may be summarized as follows:

(1) Spiral ridges originally appear from the outer edge of a ring electrode propagating inwards along the spiral pattern. Then, after about a three-minute deposition, spirals appear at the inner edge propagating outwards. Spiral formation is much more pronounced at the outer edge. Finally, many protrusions in the intermediate region are connected to each other to form complete spiral ridges.

(2) At 200 rpm, spiral formation at the inner edge did not occur. This might suggest that spirals are not formed below a certain rotational velocity.

(3) The number of spirals increases with an increase of rotation speed.

(4) Melding of spirals after prolonged deposition is more pronounced at higher rotation speeds.

(5) The formation time of spiral grooves does not diminish with increasing rotation speed.

(6) Shapes of spirals closely resemble (but don't exactly correspond to) logarithmic spirals [i.e., $r = a^{\theta}$ or $\theta - \theta_0 = 1/(\ln a) \cdot \ln r/r_0$]. The characteristic constant $[1/(\ln a)]$ seems to be nearly independent of the rotation speed.

5. DYNAMIC MODELING OF SURFACE PROFILES IN ELECTRODEPOSITION AND DISSOLUTION

Geoffrey A. Prentice and Charles W. Tobias

A model for simulating the transient behavior of electrodes undergoing deposition or dissolution has been developed. The model accounts for ohmic drop, charge-transfer overpotential, and mass-transport effects. Finite-difference techniques were used in the computer simulations. A procedure to overcome the instabilities inherent in the calculation of secondary and tertiary current distributions has been developed.[1] With this procedure, convergence has been attained for all reasonable values of the physical parameters. General guidelines for determining the computational parameters (convergence criteria, mesh size, time-step interval) have been established and error limits estimated.

Carefully controlled electrodeposition experiments were performed in a contoured, rotating-cyclinder electrode system. Two sinusoidal profiles were machined on different stainless steel cylinders. The amplitude-to-wavelength (A_0/λ) ratio was 0.1 in both cases, but the actual dimensions were greater by a factor of 7 for the larger profile. Experiments were performed with these two cylinders where the Wagner number was varied between 2 and 20.

In previous work[2] rough deposits were obtained at relatively high current densities

(80 mA/cm^2) in an acid-copper bath. Because smoother matte deposits were obtained at lower current densities, all subsequent experiments were conducted near 25 mA/cm^2. The original stainless steel cylinder with an amplitude of 2 mm and a wavelength of 2 cm is depicted in Fig. 7. The resulting deposit after 46 h at 800 rpm is shown in Fig. 8. The deposit, obtained under similar conditions, on the smaller wavelength profile appears in Fig. 9.

When the Wagner number is low (high wavelength case), the current density variation on the profile is greatest. In these cases, a shoulder tends to form near the peak, where the current density and curvature variations are relatively high. As the shoulder grows, the increased curvature in that area causes current to be diverted from the peak, where a depression forms. When the Wagner number is high (low wavelength case), the current density is more uniform, and no depression at the peak occurs.

The kinetic parameters were determined from overpotential behavior determined on smooth copper rotating cylinders. These parameters, along with other physical property and geometric data, were incorporated in simulations of the growing sinusoidal profiles. Based on the deposit thickness, the simulated and experimental profiles generally agreed to within 10% (Fig. 10). The depression at the peak for the low Wagner number runs was predicted by the simulations.

The effects of mass transport on growing sinusoidal profiles were considered. The depletion of reactant concentration that accompanies the passage of cathodic current reduces the exchange current density. When this dependence is taken into account, a more uniform current distribution results. As the limiting current density is approached, the concentration overpotential becomes significant. The functional dependence of the concentration overpotential and surface overpotential on the current density is markedly different. Because the concentration overpotential increases rapidly at high fractions of limiting current, a broad flattening of the peak results when the current density at the peak approaches the limiting current density. The surface overpotential increases logarithmically in the high-current-density range. This slower increase in

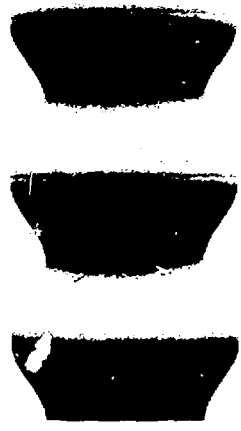

Fig. 8. Copper deposit after 46 h, 800 rpm, and an average current density of 25 mA/cm^2. W = 2.7. (CBB 805-6273)

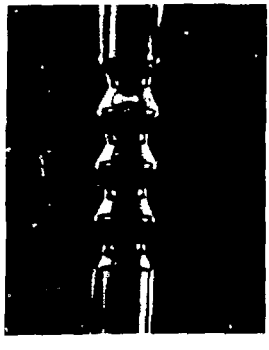

Fig. 7. Original rotating stainless steel electrode. Amplitude is 2 mm and wavelength is 2 cm. (CBB 798-11056)

Fig. 9. Copper deposit on small scale sinusoidal electrode. 20 h, 800 rpm, average current density of 25 mA/cm^2. W = 18. (CBB 807-8913)

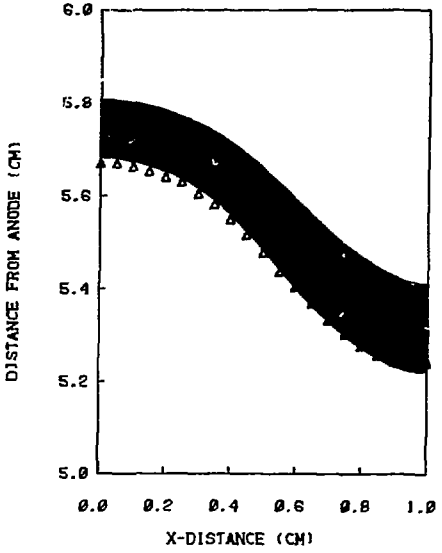

Fig. 10. Half wavelength of simulated and experimental profiles from Fig. 8. The upper curve depicts the original profile, and the lowest curve is the simulated final profile. The experimentally obtained profile is denoted by triangles.
(XBL 808-10851)

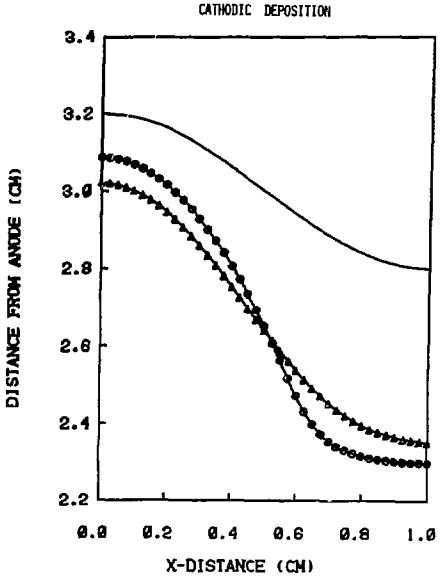

Fig. 11. Simulated deposition on a sinusoidal profile. (o) W = 0.5, 99% of limiting current, (Δ) W = 1.3. (XBL 808-10957A)

surface overpotential causes the resulting profiles to be more uniform. This contrasting behavior is shown in Fig. 11.

Simulations of sinusoidal profiles undergoing anodic dissolution were also performed. These simulations were compared with Wagner's analytical results.[3] Because of the assumptions that Wagner invoked in order to obtain a solution, his prediction of the time-dependent decrease in amplitude is accurate to within a few percent for an initial amplitude-to-wavelength (A_0/λ) ratio of less than 0.05. Numerical results were obtained for A_0/λ up to 0.3 The simulations performed at high A_0/λ showed that the initial rate of change of amplitude, computed by Wagner, was in error by at least 20%.

* * *

1. G. A. Prentice and C. W. Tobias, "Finite Difference Calculation of Current Distributions at Polarized Electrodes," Paper No. 96d, AIChE Annual Meeting, 1980.
2. G. A. Prentice and C. W. Tobias, MMRD Annual Report 1979, LBL-10000, pg. 511.
3. C. Wagner, J. Electrochem. Soc. 101, 225 (1954).

Bifunctional Air Electrodes for Metal-Air Batteries

The objective of this program is to conduct supporting research in air-electrode technology for DOE metal-air battery projects. Two metal-air systems are currently in active development, the mechanically recharged Al-air system and the electrically recharged Fe-air system. It is expected that two new projects will be started in FY 81, the mechanically recharged Zn-air and a hydrogen-air fuel cell optimized for vehicle use. Both projects will require low-cost, efficient, unifunctional, air-electrode technology, as does the Al-air system. Metal-air systems are, in principle, high-energy and high-power-density systems (> 100 W-hr/kg, > 100 W/kg) because one of the electroactive species need not be contained within the battery or vehicle. However, practical development of this technology has historically been slow due to problems in finding a suitable air-electrode technology. This search has been particularly difficult for the electrically recharged systems, where the positive electrode must be bifunctional, both evolving and consuming oxygen. Materials stability is also a question at the potentials required for oxygen evolution. These problems, combined with the catalytic properties required of the electrode, greatly limited the number of suitable materials, and these materials were too

costly in electrodes using then-existing technology, e.g., Pt-black electrodes. The intrinsic difficulties in the electrically rechargeable electrode have caused emphasis to shift to mechanically recharged metal-air batteries, where only a unifunctional air electrode is required. Recent advances in gas-fed electrode technology in numerous fuel-cell projects indicate that efficient, low-cost, unifunctional electrodes can be developed. The bifunctional air electrode, however, appears to require a major breakthrough in both catalytic and materials technology.

6. *OXYGEN REDUCTION WITH CARBON-SUPPORTED METALLIC CLUSTER CATALYSTS IN ALKALINE ELECTROLYTE*†

Philip N. Ross and Lee R. Johnson

Renewed interest in metal-air batteries and hydrogen-air fuel cells for vehicle application stems, at least in part, from the tremendous improvements in air-electrode technology that have occurred during the development of the phosphoric-acid fuel cell. Since a mechanically recharged battery requires only a unifunctional electrode, it seems reasonable to investigate the phosphoric-acid fuel cell electrode for use in alkaline electrolytes. In this concept, a high-surface-area carbon is used both as the support for maintaining dispersion of the active catalyst and as the current collector. The active catalyst can, in principle, be any highly dispersed (< 100 A crystallite) material of interest. In the first phase of the program, we have examined selected Group VIII transition metals dispersed as metallic clusters on a turbostratic carbon-black (Vulcan XC-72, Cabot) material, e.g., Ni, Ru, Rh, Pd, Ag, Ir, and Pt, and in ongoing work. We are examining certain Pt and Ag intermetallic clusters, e.g., Pt_3Ti, or Ag_3Ti, dispersed on the same carbon support.

The metallic clusters were prepared by a combination of impregnation and ion-exchange techniques[1] with hydrogen reduction at 473 K. The metallic phase was confirmed by x-ray diffraction, and the metal dispersion was determined using transmission electron microscopy (TEM). Figure 12 shows a TEM micrograph of the Pt cluster catalyst, from which the cluster size was observed to be 20-30 A. For Ni, Ru, Rh, Ir, and Pt, the metal loading was adjusted to give a close grouping of crystallite sizes in the 20-30 A range. Pd and Ag clusters could not be prepared in the same size range with reasonable metal loading (> 5 w/o). Instead, Ag cluster sizes in the 100-200 A range were utilized with 2.5 w/o metal loading, and Pd clusters in the 20-30 A range were prepared at 1.3 w/o. Effective metal surface areas were calculated from the TEM measured "surface average diameter," using procedures developed in previous work.[1]

Specific catalytic activity was defined as the current per unit weight of metal at an electrode potential of 0.85 V (vs. a reversible hydrogen electrode) using pure oxygen as the oxidant gas. The specific activities for oxygen reduction in 20% NaOH at 343 K are summarized in Table 2. The

Fig. 12. Transmission electron micrograph of Pt clusters dispersed on Vulcan XC-72 carbon black. (XBB 813-2265)

specific activity of the Ni catalyst was improved by using KOH-LiOH electrolyte rather than NaOH; the other catalysts were relatively indifferent to the alkali-metal cation. The nickel catalyst was oxidized in situ, and the LiOH presumably resulted in lithium doping and improved activity.

The activity measure of interest for development purposes is the catalyst cost to achieve the required performance characteristics, i.e., the

Table 2. Activity of metal clusters for oxygen reduction in alkaline 20% NaOH 345 K.

Metal	Crystallite size (A)	mA/mg at 0.85 V (RHE)	Tafel slope (mV)
Pt	20-30	600	50
Ru	20-30	60	60
Ir	20-30	18	50
Rh	20-30	30	50
Pd	15-25	12	60
Ni	30-50	7	60
Ag	100-200	36	100

product of specific activity, required catalyst loading, and catalyst cost. In terms of cost effectiveness, Pt and Ag are the metals of choice. However, the polarization characteristics of the two electrocatalysts are very different, as shown by the curves in Fig. 13, due to differences in reaction mechanism. For operation at high current density (> 100 mA/cm^2), the Pt catalyst is the most cost-effective catalyst of all the materials examined in this study. Actual testing of subscale (1 cm^2) H_2-air fuel cells (35% KOH, 70°C) have indicated the total (anode plus cathode) Pt cost would be only $60 per m^2 cell area for a vehicle fuel cell with sustained power density of 240 mW/cm^2 at 40% thermal efficiency. For operation at low current density (> 50 mA/cm^2) and/or high (> 55%) faradaic efficiency, the Ag cluster catalyst appears to be the more cost effective, although there are problems with Ag dissolution under certain conditions of use.

The intermetallic cluster catalysts Pt_3Ti and Ag_3Ti have both shown improved polarization behavior relative to the pure metallic clusters. The improvement was particularly dramatic for Ag_3Ti, where the catalytic activity per unit weight of Ag increased nearly an order of magnitude. The reasons for the improved activity appear twofold: an improved dispersion of the metal on the carbon support and a basic alteration of the catalytic properties of the noble metal via a ligand effect. Ti is often used as a catalyst support in alkaline electrolyte, particularly for electrolysis. Based on our results with the Ti intermetallic compounds, we would expect to see a strong metal-support interaction (SMSI) for Pt or Ag dispersed on Ti. We are currently looking for these SMSI effects.

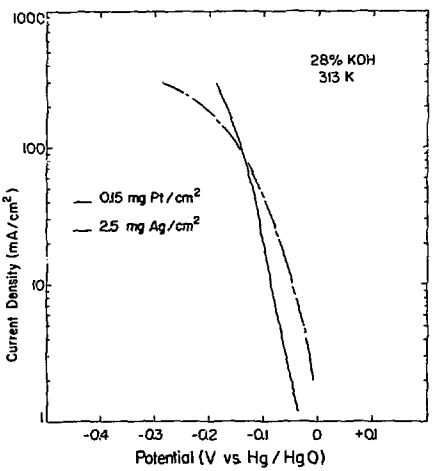

Fig. 13. Polarization curves for oxygen reduction with Teflon-bonded gas diffusion electrodes using Pt and Ag cluster catalysts. 20% O_2 180% N_2 ambient pressure. (XBL 811-59)

* * *

†*Brief version of LBL-11891.*

1 . P. N. Ross, LBL-10799 and Electric Power Research Institute Report EM-1553.

7. *ROTATING RING-DISC STUDIES OF OXYGEN REDUCTION ON Pt AND Ag IN ALKALINE ELECTROLYTE*†

Philip N. Ross and Daniel A. Scherson

Previous studies in this laboratory have shown that Pt and Ag are the most important pure metals for use as catalysts of the metal cluster type in alkaline electrolyte. The characteristic polarization curves for these two catalysts are, however, dramatically different, suggesting that different reaction mechanisms are operative. The mechanism of oxygen reduction on a wide variety of electrode materials may be analyzed in terms of a reaction pathway involving a direct 4-electron reduction of oxygen in parallel with a pathway involving the 2-electron intermediate hydrogen peroxide. The most general description of the reaction pathways is shown in Fig. 14. The 4-electron path is distinguished by the absence of O_2H^- as an intermediate. The rotating ring-disc electrode (RRDE) is useful in distinguishing between paths involving free O_2H^- (in equilibrium with H_2O_2) as an intermediate. Peroxide desorbing from the disc electrode is transported to the ring electrode by convection where it is oxidized; the ring current is equal to the rate of peroxide desorption times the collection efficiency of the ring. The general scheme in Fig. 14 takes into account recycling of the oxygen produced by heterogeneous catalytic (non-electrochemical) decomposition of peroxide. The quantitative evaluation of rate constants k_1, k_2, and k_3 from RRDE data is simplified if the rate of the heterogeneous process,

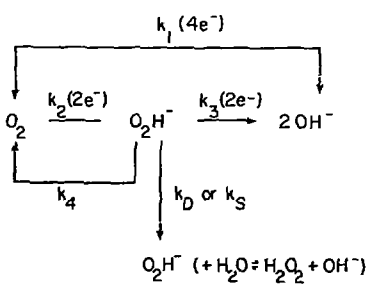

Fig. 14. General reaction sequence for oxygen reduction pathways in alkaline electrolyte. (XBL 811-58)

k_4, can be measured independently, and by making separate kinetic measurements on oxygen and peroxide-containing solutions. The catalytic decomposition of peroxide on both the Pt and Ag surfaces is extremely rapid, so measurement of k_4 is not a simple matter.

We have developed a new chronopotentiometric technique for the independent measurement of k_4 which makes no assumptions as to the order of reaction or the relative magnitude of the kinetics. An exact solution was found for the problem of convective diffusion to a rotating disc with a prescribed initial concentration profile and a current step at the disc surface. The steady-state (initial) surface concentration can be determined from the transition time τ by use of the parametric plots in Figs. 15 and 16. The surface concentration, C_o is related to the rate constant, k_4, reaction order, n, and the rotation rate, Ω, by the expression

$$\ln C_o = \frac{1}{1+n} \ln \Omega^{1/2} + \frac{1}{1+n} \ln \frac{K}{k_4},$$

where K is a known constant. A plot of $\ln C_o$ vs. $\ln \Omega^{1/2}$ yields a straight line from which both the reaction order and rate constant can be determined from the slope, m, and intercept, b. as

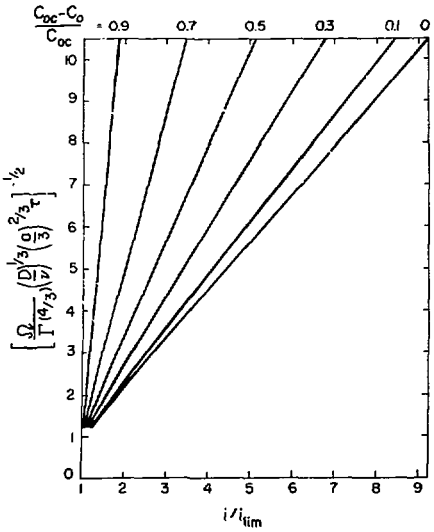

Fig. 15. Theoretical relationship of the transition time, τ, to the current step, i, for selected values of $(C_\alpha - C_o)/C_\alpha$. (XBL 811-61)

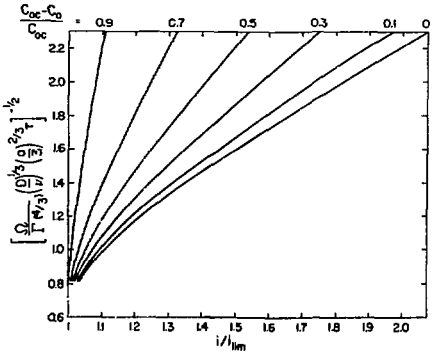

Fig. 16. Expanded region of Fig. 15. (XBL 811-60)

$$n = \frac{1-m}{m} \quad \text{and} \quad k_4 = K \exp[(1-n)b].$$

A particularly attractive feature of this method is that the reaction order can be obtained in a single experiment.

Experiments on the Pt and Ag disc electrodes are in progress. In preliminary experiments, it is clear that the direct 4-electron path is predominant on Pt, whereas for Ag the reaction proceeds exclusively via the 2-electron pathway. Recycling via peroxide decomposition is thus very important for Ag, and, in porous electrodes with Ag catalysts, the steady-state level for peroxide is probably quite high. Free peroxide would be expected to lower electrode life by accelerating corrosion of cell components and by loss of hydrophobicity of the electrode structure.

* * *

†Brief version of LBL-10700; accepted for publication in J. Electroanal. Chem.

Improvements in Efficiency of Aluminum Reduction Cells

In the U. S., approximately 100 billion kWh of electrical energy are consumed each year in the electrolytic production of aluminum in Hall-Héroult cells. There is, therefore, considerable incentive to improve the performance of such cells and reduce the energy consumed per unit of metal produced.

Part of a cell is shown in cross section in Fig. 17. The molten "cryolite" electrolyte, at about 950°C, serves as a solvent for aluminum oxide. Passage of current from the carbon anode

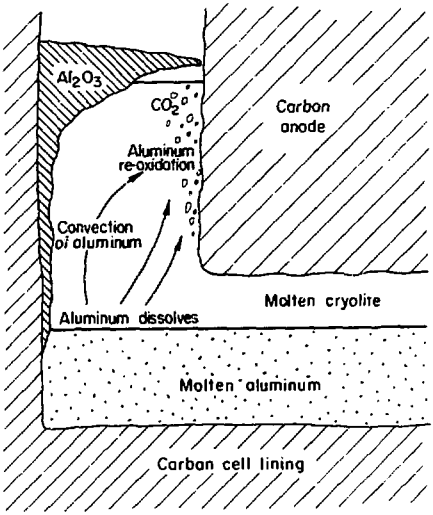

Fig. 17. Sketch of part of the cross section of a Hall-Héroult cell showing the transport of part of the aluminum product to the anode region where it is re-oxidized with consequent current efficiency loss. (XBL 784-8016)

through this electrolyte to a pool of molten aluminum at the bottom of the cell causes the reduction of the aluminum oxide, aluminum metal being generated at the surface of the aluminum pool and carbon dioxide gas bubbles at the surface of the anode. Unfortunately, a portion of the aluminum generated is lost by a mechanism which consists of the dissolution of aluminum into the cryolite and its turbulent convection to the anode where it is re-oxidized by carbon dioxide bubbles. This loss of product, or loss of current efficiency, should be reduced if means can be found to reduce the turbulent convection in the electrolyte. Motion of the electrolyte and the resulting turbulence are mainly due to electromagnetic stirring forces within the cell. A typical Hall-Héroult cell has a current of 100-200 kA; such currents generate strong magnetic fields. The interaction of the currents and the fields yields electromagnetic forces that stir both the molten cryolite and molten aluminum, creating velocities of the order of 10 cm/sec.

The electromagnetic forces have a second effect. These forces result in a distortion, or bowing, of the interface between the metal and cryolite. Parasitic energy consumption (i.e., resistive heating of the electrolyte) can be reduced by bringing the anodes as close as possible to the metal surface without contacting it. This is difficult to achieve if the surface is significantly bowed. The magnetic field within the cell, and consequently the electromagnetic forces, is a function of the arrangement of electrical conductors ("bus-bars") in the vicinity of the cell. It is therefore evident that some bus-bar arrangements will yield more or less bowing of the interface and current efficiency loss than others. The objective of the present investigation is to determine by means of mathematical models, what changes in cell design (e.g., bus-bar arrangements) result in cells with high current efficiency and little distortion of metal-cryolite interface.

8. CURRENT INEFFICIENCIES IN ALUMINUM REDUCTION CELLS

Stephen Lympany and James W. Evans

The mathematical computations required to improve bus-bar arrangements in these cells entail the solution of Laplace's equation, which determines the current density distribution in the cell. Knowing the currents within the cell and external bus-bars, the magnetic field within the cell can be computed and, subsequently, the electromagnetic forces acting on metal and cryolite. With these forces as input, the turbulent fluid flow equations for the cryolite and the metal are then solved to yield velocities and turbulence levels in both liquids, together with the shape of the metal-cryolite interface. Knowing the turbulence level within the cryolite, the rate of mass transfer of dissolved aluminum can be calculated, yielding the cell current efficiency.

Two common bus-bar arrangements for Hall-Héroult cells in the U. S. are "end riser" arrangements and "quarter riser" arrangements; they differ in the way current is brought from one cell to an adjacent cell. The computed cryolite velocities for end riser and quarter riser cells are depicted in Fig. 18. The cell is shown from above, the motion of the cryolite being predominantly in a horizontal plane. Also shown are velocity vectors for a riser that represents a first attempt at a bus-bar arrangement giving a better cell performance. The velocities are seen to be significantly different for the three arrangements; there are four circulation loops for the end riser arrangement, as opposed to two for the other arrangements; and the more complex circulation pattern results in higher turbulence levels in the molten cryolite and, consequently, lower computed current efficiency, as indicated in Table 3. Aluminum cells are typically equipped with aluminum covers to prevent escape of cell gases. It can be conjectured that replacement of these covers by steel covers could be managed at little expense and would have the effect of shielding the inside of the cell from magnetic fields generated by the bus bars, thus reducing electromagnetic forces and improving cell performance. Table 3 reveals that such replacement improves the current efficiency of end riser cells, but not of quarter riser cells. The reasons for this are are discussed in a full-length report of this project (LBL-11675).

Figure 19 compares the computed contours of the metal-cryolite interface for the three designs. The end riser design is seen to be somewhat

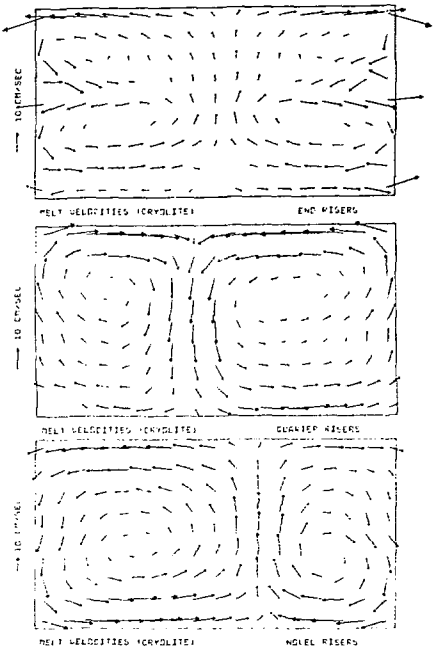

Fig. 18. Computed velocities in the molten cryolite electrolyte for three arrangements of the "riser" bus-bar bringing current to the cell. (XBL 809-11704)

inferior to the quarter riser design in that the interface is more bowed. The new design, which appeared superior to the end riser in current efficiency, is seen to be inferior in interface topography. This new riser arrangement is only a first attempt at improving cell design, other schemes will be studied to find arrangements that are superior in both current efficiency and cell topography.

Table 3. Computed current efficiencies for various designs of Hall-Héroult cell.

	Cell with usual Aluminum covers	Steel cell covers
End riser	93.8	92.9
Quarter riser	88.6	90.3
Novel riser	93.4	93.4

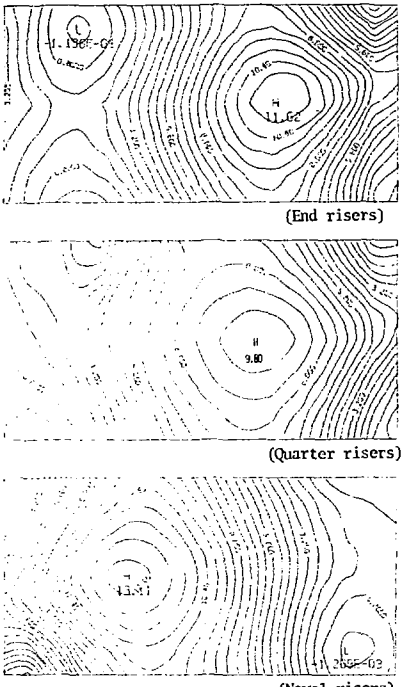

Fig. 19. Computed contours of the metal-cryolite interface for the three riser designs; the least amount of bowing is shown for the quarter riser arrangement. (Aluminum-cryolite interfaces, heights in cm.) (XBL 809-11703)

Electrochemical Properties of NASICON

One of the more attractive systems for load load leveling or for vehicle propulsion is based on the sodium/sulfur electrochemical couple with a ceramic electrolyte. To date, sodium-beta" alumina is the most developed ceramic electrolyte, but alternatives to it are being provided by the search for fast ion conductors. One of these is the three-dimensional sodium ion conductor Nasicon, ($Na_{1+x}Zr_2\ Si_x\ P_{3-x}\ O_{12}$). Nasicon possesses some advantage, especially in the fabrication stage, over beta" alumina. Its resistivity is potentially lower at 300°C than that of sodium-beta" alumina polycrystalline electrolyte, This research intends to examine the properties of Nasicon so that they can be critically compared with sodium-beta" alumina solid electrolytes.

9. PROPERTIES OF NASICON

David C. Hitchcock, Craig P. Cameron, Herbert K. Schmid, and Lutgard C. De Jonghe

Nasicon, $Na_{1+x}Zr_2 Si_xP_{3-x}O_{12}$ has been prepared in different compositions by the sol gel process. Two compositions were prepared and tested, x = 2 and x = 2.3. The samples were either sintered or hot pressed. The best results were obtained by the hot pressing of Nasicon in which the graphite mold had been coated with hexagonal boron nitride powder. After preparation, the specimens were immersed in molten sodium held at 300°C for times up to two weeks. In all cases, there was a chemical attack of the Nasicon by the molten sodium. The most pronounced degradation was found for Nasicon compositions with x = 2; the least degradation was observed for Nasicon speciments with x = 2.3. A crack pattern usually could be observed on the immersed samples as shown in Fig. 20. The mechanical strength of the samples was severely decreased by the formation of the cracks. X-ray analysis before and after immersion showed that an unidentified compound, possibly a phosphate, with the most prominent reflection at 4.3 on A, was severely attacked by the molten sodium. Additionally, it was found that the lattice parameter of the Nasicon was increased by approximately 2% due to the immersion in the sodium. The stresses that are generated due to this lattice expansion, as well as a dissolving of the second phase, could account for the severe degradation of the Nasicons prepared in contact with molten sodium.

Some Nasicons were also examined in the transmission electron microscope. Electron beam radiation was found to destroy the crystal structure very rapidly, although this destruction was slower at 500 keV than 100 keV. The microstructure of the polycrystalline Nasicon before and after destruction by the electron beam in the high voltage electron microscope is shown in Fig. 21.

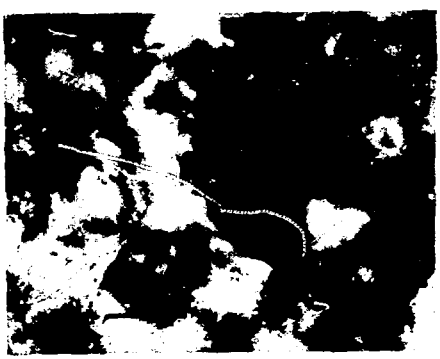

Fig. 20. Cracks due to chemical attack of Nasicon by Na at 350°C for 1 week. (XBB 807-8654)

Fig. 21. Relic formation after irradiation at 500 kV in the Transmission Electron Microscope. (XBB 807-8749)

Interestingly, the amorphous Nasicon formed a relic of the original crystalline structure in which the grain boundaries apparently formed an amorphous structure of different density or of different composition. The ionic resistivity of the samples was determined by AC admittance measurements over the range of frequencies up to 5 MHz and for a range of temperatures between 50°C and 425°C. The immersion of Nasicon with x = 2 in sodium for about 90 hours increased the resistivity by two orders of magnitude. This could be attributed to the formation of cracks and to the reaction of the Nasicon with the sodium.

The lowest ionic resistivity at 300°C, determined thus far for Nasicon prepared in this laboratory, was 2.5 Ω-cm, with an activation energy of approximately 4 kcal/mol.

Analysis and Simulation of Electrochemical Systems

This work supports the development of energy-storage systems by means of mathematical models and by experiments designed to test the accuracy and completeness of the models. A one-dimensional model has been developed for the Li(Al) - FeS_x battery in conjunction with a major experimental program at Argonne National Laboratory. This model can be used to identify system limitations and to describe the actual phenomena associated with the Li(Al)- FeS_x battery during relaxation and charging.

10. MATHEMATICAL MODELING OF THE LITHIUM-ALUMINUM, IRON SULFIDE BATTERY†

Richard Pollard and John Newman

The lithium-aluminum, iron sulfide battery is under development for use in electric-vehicle propulsion. A mathematical model of the LiAl/LiCl, KCl/FeS cell has been used to study the behavior of the system during relaxation and charging. The changes that take place in the

cell during relaxation and charging conditions could influence the dependence of cell performance on the number of completed cycles. Therefore, it is important to identify the factors that can limit the system during these modes of operation. The governing differential equations used to study the cell discharge behavior[1] can be used directly in this analysis, and it is only necessary to replace the initial composition and porosity with the appropriate distributions and to modify the model for negative electrode kinetics.

Figure 22 shows composition profiles across the cell sandwich for several times after interruption of the current at the end of a discharge. In the negative electrode, the back becomes cathodic with respect to the front portions, and local concentration cells, with the reaction

$$LiAl \rightleftarrows Li^+ + Al + e^-, \qquad (1)$$

are established. Although these concentration cells promote uniform electrolyte composition, they accentuate the nonuniform utilization of reactants since there is no mechanism for equalization of local state of charge within the alloy. In the positive electrode, the possibility of simultaneous reactions exists. Adjacent to the current collector, FeS reacts with lithium ions according to the reaction

$$2FeS + 2Li^+ + 2e^- \rightleftarrows Li_2FeS_2 + Fe \qquad (2)$$

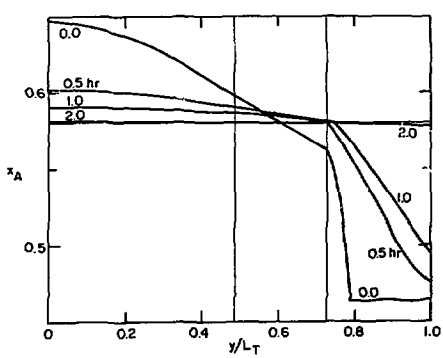

Fig. 22. Position dependence of mole fraction of LiCl at different times after current interruption. Simulation parameters: $Q_- = 2800$ C/cm^3, $Q_+ = 4630$ C/cm^3, $L_- = 0.32$ cm, $L_S = 0.16$ cm, $L_+ = 0.18$ cm, $N = 5.5 \times 10^7$ cm^{-3}, $h_0 = 8.25 \times 10^{-2}$ W/m^2 K, $R_g = 1.55\ \Omega$ cm^2, h = 0.004 cm, w = 0, $-c^{-\beta}_{Li}/(c^{\beta}_{Li})_{sat} = 1.0$, $D_\beta = 4 \times 10^{-8}$ cm^2/s. Parameters at start of previous discharge: $\varepsilon^0 = 0.39$, $\varepsilon_S = 0.75$, $\varepsilon^0_I = 0.555$, $T_0 = 470°C$, $I = 41.6$ mA/cm^2, $x^0_A = 0.58$. Initial stage of charge, $\lambda(t = 0) = 47.9\%$. Additional parameters specified in Tables 1 and 3 of Ref. 1.
(XBL 7912-14569)

whereas, near the front of the electrode, Li_2S reacts anodically with iron according to the reaction

$$2Li_2S + Fe \rightleftarrows Li_2FeS_2 + 2Li^+ + 2e^-. \qquad (3)$$

Heat is not generated in the cell during relaxation, and the temperature falls in accordance with the specified rate of heat transfer to the surroundings. As a result, precipitation of the electrolyte may also occur.

After the current is switched off, an initial rise in cell voltage occurs. The magnitude of this step change can, in principle, be used as a basis for the estimation of cell resistance. However, the influence of double-layer capacity is not included in this model, and the final total cell voltage predicted by the discharge model prior to interruption may be much lower than expected in practice. Therefore, separate calculations are necessary to estimate the interruptor resistance. Double-layer effects are not included since they are not generally regarded as being significant during normal cell operation.

Following the initial rise, the voltage gradually approaches the equilibrium open-circuit cell potential. The shape of the voltage relaxation time curve is determined by the reactions that occur in the individual electrodes.

Figure 23 shows simulated composition profiles at different stages of a constant-current charge. The parameter λ represents the overall state of charge. The composition profiles represent the combined effects of diffusion, migration, and electrochemical reaction. A relaxation time of

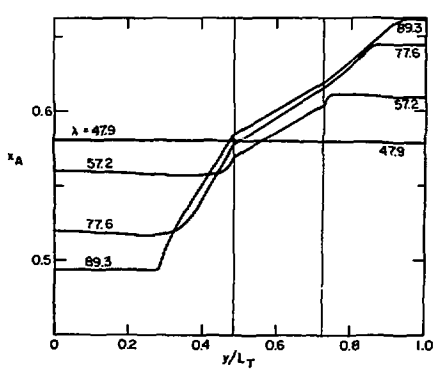

Fig. 23. Position dependence of mole fraction of LiCl at different states of charge for a constant current charge of -41.6 mA/cm^2. A relaxation time of 2 hours is included between the end of the previous discharge and the beginning of the charging process. Simulation parameters: T(t = 0) = 480.4°C, see also Fig. 22.
(XBL 7912-14567)

two hours was included between the initial discharge and the start of the charging process. Without relaxation, the profiles are very similar, and there is little trace of the starting composition profile after the charge is completed.

The average cell temperature in Fig. 23 falls from 753.5 to 740.0 K during the charge as a result of reversible heat effects and heat transfer to the surroundings. This drop in temperature causes the saturation limit for KCl to rise, and precipitation begins at the reaction front in the negative electrode when $\lambda = 85.9$. If the cell is not relaxed before charging, the temperature falls over a higher range (769.4 to 751.6 K), and precipitation is delayed until $\lambda = 91.1$ The difference in charging behavior caused by the temperature drop during relaxation emphasizes the need for careful thermal management of battery modules.

Figure 24 shows the fraction of active material utilized within the negative electrode, for the example in Fig. 23. The region closest to the electrode/separator interface is recharged first, and the reaction front moves back through the electrode as the alloy is completely reconverted to β-LiAl. Relaxation of the electrolyte composition results in an increase in nonuniform utilization of reactants compared to the unrelaxed examples.

The complementary reaction distribution for the positive electrode is shown in Fig. 25. A

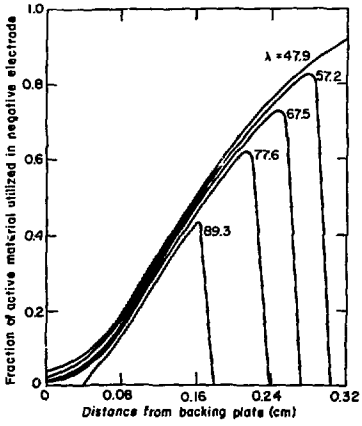

Fig. 24. Fraction of active material utilized in negative electrode at different overall states of charge during a constant current charge of -41.6 mA/cm^2. A relaxation time of 2 hours is included between the end of the previous discharge and the beginning of the charging process. Simulation parameters are as in Fig. 22.
(XBL 7912-14565)

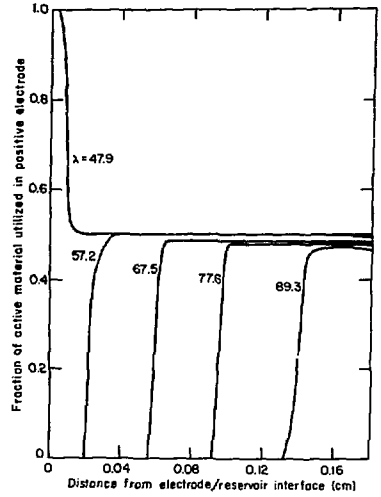

Fig. 25. Fraction of active material utilized in positive electrode at different overall states of charge during a constant current charge of -41.6 mA/cm^2. A relaxation time of 2 hours is included between the end of the previous discharge and the beginning of the charging process. Simulation parameters as in Fig. 22.
(XBL 7912-14561)

sharp reaction front moves through the electrode as Li_2FeS_2 is consumed. This mechanism also predominates is the unrelaxed case, but the final distribution of unreacted material is shifted from the back of the electrode.

In summary, the analysis indicates that composition variations become less pronounced during relaxation, but the local state of charge within the electrodes can become more nonuniform. The results obtained are sensitive to the details of the heat balance used in the calculation, and this reflects a need for precise thermal management of LiAl/FeS battery modules.

* * *

†Brief version of LBL-10421.

1. R. Pollard and J. Newman, LBL-10420 (January 1980).

11. METAL COUPLES IN NON-AQUEOUS SOLVENTS

Charles W. Tobias

The objective of this project is to develop practical alternatives to aqueous or high-temperature molten salt systems for the efficient

electrochemical reduction and oxidation of reactive metals. Past accomplishments include the efficient reduction of potassium metal from $KAlCl_4$ dissolved in propylene carbonate. Current work concerns the determination of the thickness and chemical nature of surface films on lithium in propylene carbonate electrolytes. This project is carried out under the direction of Dr. R. H. Muller.

RESEARCH PLANS FOR CALENDAR YEAR 1981

Anodic Surface Layers on Battery Materials. Further evidence for the inhomogeneous porosity of surface layers will be sought and means investigated to increase the ionic conductivity of the innermost nonporous part which seems to provide the protective function. A study of film behavior under anodic and cathodic polarization, where surface roughness is greatly increased, will benefit from use of a new laser light source and digital data acquisition system.

Surface Morphology of Metals in Electro-Deposition. Our differential nucleation theory, tentatively attributed to be the cause for the generation of regular macroscopic deposition patterns in the deposition of zinc from acid solutions, will be subjected to critical experimental evaluation. According to this hypothesis, uneven growths of different crystal facets lead to protrusions, which generate secondary flows (e.g., roll cells) in the presence of free or forced convection past the surface. This secondary flow causes small, periodic variations of concentration, and hence of potential, in a direction normal to the flow. Since nucleation density is potential dependent, the rate of growth of metal deposit tends to follow the spatial periodicity of potential produced by the secondary flow. The effect of electrolyte composition, including that of lightly absorbed surface active agents on the propagation and persistence of surface patterns, will be systematically investigated and interpreted. Simulation of advancing or receding electrode profiles, under mixed mass transfer/charge transfer control, will include a number of models of practical significance.

Bifunctional Air Electrodes for Metal-Air Batteries. Studies of Pt and Ag intermetallic catalysts for oxygen reduction will continue. Rotating ring-disc methods will be applied to the study of intermetallic catalysts found to be of interest in the study of bimetallic cluster catalysts. Carbon corrosion studies will begin to develop carbon support materials that are more resistant to oxidation than Vulcan XC-72. Studies of gas evolution in porous, hydrophobic, polymer-bonded type structures will be initiated. The objective of the latter studies is to determine how the electrolyte wetting in the catalyst layer changes during gas evolution, and what material properties are important in controlling electrolyte displacement.

Improvements in Efficiency of Aluminum Reduction Cells. Computations will be carried out for many alternative cell designs in an attempt to find designs that have superior current efficiency and freedom from distortion of the metal-electrolyte interface. Research will be initiated to test the results of the predictions. Research will be started on motion of the cryolite-metal interface (motion detrimental to cell performance).

Electrochemical Properties of Nasicon. Continued efforts are planned in the preparation of Nasicons of slightly varying compositions, in which certain elements may be added to improve sintering and resistance to chemical reaction with sodium. Once such composition has been clearly defined, the electrochemical stability of the Nasicon will be tested.

Electrochemical measurements will be made on the Nasicon/molten sodium interface for pure and impure sodium. Potential static and galvanostatic techniques will be used to identify the important electrode reactions.

Analysis and Simulation of Electrochemical Systems. Experimental work will continue on the electrochemical removal of lead from wastewater. The model of the lithium/iron sulfide battery will be extended. A mathematical model will be developed to describe the concentration profiles and current distribution in a thin-gap flow cell containing a redox couple.

Metal Couples in Non-Aqueous Solvents. This project will be directed toward the exploration of criteria for the efficient recovery, refining, and galvanic cycling of certain of the group II and III metals, notably magnesium, calcium, and aluminum. In addition to the propylene carbonate family of solvents, other solvent options will also be considered. Progress in this project will depend on the availability of graduate research assistants.

1980 PUBLICATIONS AND REPORTS†

Refereed Journals

‡1. Daniel A. Scherson and John Newman, "The Warburg Impedance in the Presence of Convective Flow," J. Electrochem. Soc. 127, 110 (1980).

2. Richard Pollard and John Newman, "Silicon Deposition on a Rotating Disk," J. Electrochem. Soc. 127, 744 (1980), (LBL-9154).

3. Richard Pollard and John Newman, "Transient Behaviour of Porous Electrodes with High Exchange Current Densities," Electrochim. Acta 25, 315 (1980).

§4. M. Ranade and J. W. Evans, "The Reaction Between a Gas and a Solid in a Non-Isothermal Packed Bed: Simulation and Experiments," I. and E. C. Process Design and Development 19, 118 (1980).

§5. A. Malazgirt and J. W. Evans, "Production of Aluminum and Aluminum Coatings by Thermal Decomposition of Aluminum Alkyls," Met. Trans. 11B, 225 (1980).

§6. J. W. Evans and M. Ranade, "The Grain Model for Reaction Between a Gas and a Porous Solid--A Refined Approximate Solution to the Equations," Chem. Eng. Sci. 35, 1261 (1980).

‖7. J. W. Evans, M. H. Abbasi and A. Sarin, "A Monte Carlo Simulation of the Diffusion of Gases in Porous Solids," J. Chem. Phys. 72, 2967 (1980).

8. D. A. Scherson and P. N. Ross, "Theory of Transition Times: Catalysis at Rotating Disc Electrodes," J. Electroanal. Chem. 132, 523 (19[illegible]). LBL-10700.

Other Publications

1. John Newman and Richard Pollard, "Micro-Modeling Studies" in High Performance Batteries for Electric-Vehicle Propulsion and Stationary Energy Storage, ANL-79-74, Argonne National Laboratory, Argonne, Illinois (March 1980).

LBL Reports

1. Wing Cheong Hui (with Charles W. Tobias), "Electrolytic Gas Evolution in Forced Flow," M. S. thesis, University of California, Berkeley (1980), LBL-11945.

2. Y. Geronov, F. Schwager, and R. H. Muller, "Film Formation on Lithium in Propylene Carbonate Solutions under Open Circuit Conditions," LBL-11126.

3. Richard Pollard and John Newman, "Mathematical Modeling of the Lithium-Aluminum, Iron Sulfide Battery. I. Galvanostatic Discharge Behavior," LBL-10420 (January, 1980).

4. Richard Pollard and John Newman, "Mathematical Modeling of the Lithium-Aluminum, Iron Sulfide Battery. II. The Influence of Relaxation Time on the Charging Characteristics," LBL-10421 (January, 1980).

5. Richard Pollard, "Mathematical Modeling of the Lithium-Aluminum Iron Sulfide Battery," Ph.D. thesis LBL-10197 (December, 1979).

6. J. W. Evans, Y. Zundelevich, and D. Sharma, "A Mathematical Model for Prediction of Currents, Magnetic Fields, Melt Velocities, Melt Topography and Current Efficiency in Hall-Héroult Cells," LBL-11675.

7. P. N. Ross, "Oxygen Reduction with Carbon Supported Metallic Cluster Catalysts in Alkaline Electrolyte," LBL-11891.

Invited Talks

1. Karrie J. Hanson, Rolf H. Muller, and Charles W. Tobias, (presented by Karrie J. Hanson), "Mass Transfer Enhancement by Turbulence Promoters," Extended Abstracts, vol. 80-1, No. 388, pp. 963-965 (based on LBL-9038), presented at 157th Meeting of the Electrochemical Society, St. Louis, MO, May 11-16, 1980.

2. Milan M. Jaksic, and Charles W. Tobias, (presented by Milan M. Jaksic), "Hydrodynamic Flow Visualization by the Electrochemical Method," presented at the International Symposium on Flow Visualization, Ruhr-University Bochum, Germany, September 9-12, 1980.

3. Henry H. Law and Charles W. Tobias, (Presented by Henry H. Law), "The Kinetic Stability of Potassium in Propylene Carbonate Electrolytes," Extended Abstracts, vol. 80-2, No. 39, pp. 106-108, 1980 (based on LBL-11487), presented at the 158th Meeting of The Electrochemical Society, Hollywood, FL, October 5-10, 1980.

4. Henry H. Law and Charles W. Tobias, (presented by Henry H. Law), "The Morphology of Potassium Deposited from Propylene Carbonate Electrolyte," Extended Abstracts, vol. 2, No. 392, pp. 991-992 (based on LBL-11253), presented at the 158th Meeting of The Electrochemical Society, Hollywood, FL, October 5-10, 1980.

5. Geoffrey A. Prentice and Charles W. Tobias, (presented by Geoffrey A. Prentice), "Finite Difference Calculations of Current Distributions at Polarized Electrodes," (based on LBL-11058), presented at the 73rd Annual Meeting of the American Institute of Chemical Engineers, Chicago, IL, November 16-20, 1980.

6. F. Schwager, Y. Geronov, and R. H. Muller, "Ellipsometric Studies of Surface Layers on Lithium." Extended Abstract No. 37, No. 37, vol. 80-2 (LBL-11846), presented at the 158th Meeting of The Electrochemical Society, Hollywood, FL, October 5-10, 1980.

7. Y. Geronov, F. Schwager, and R. H. Muller, "The Film Formation on Lithium in Propylene Carbonate Solutions Under Open Circuit Conditions," Workshop on Lithium Nonaqueous Battery Electrochemistry, June 4-6, 1980, Case Western Reserve University, Cleveland, OH.

8. Y. Geronov, "The Film Formation on Lithium in Propylene Carbonate Solutions Under Open Circuit Conditions," Abstract No. 708 RNP, presented to the 158th Meeting of The Electrochemical Society, Hollywood, FL. October 5-10, 1980.

9. Rolf H. Muller, "Electrochemical Synthesis and Energy Storage, LBL In-House Research Program," Review of the Applied Battery and Electrochemical Research Program Managed by LBL, Washington D.C., March 7, 1980.

10. Rolf H. Muller, "Lithium Surface Layers," Applied Battery and Electrochemical Research Program Review, Berkeley, CA, August 14-15, 1980.

¶11. John Newman, "Modeling of Lead-Acid Batteries," Department of Energy Battery & Electrochemical Contractors' Conference, Arlington, VA, December 10, 1979.

12. John Newman, "Modeling of Li-Al/FeS Batteries," Department of Energy Battery & Electrochemical Contractors' Conference, Arlington, VA, December 11, 1979.

13. John Newman, "Engineering of Electrochemical Storage Batteries," Invited address before the Department of Chemical Engineering, Texas A&M University, College Station, TX, March 21, 1980.

14. John Newman, On-site review for the Department of Energy of the Ford Motor Company program on sodium-sulfur batteries, Newport Beach, CA, April 22, 1980.

15. John Newman, On-site review for the Department of Energy of the Argonne National Laboratory program on lithium-iron sulfide batteries, Argonne, IL, June 25-26, 1980.

16. John Newman, "Electrochemical Modeling," Address at the review of the lithium-iron sulfide battery program, Argonne National Laboratory, Argonne, IL, June 26, 1980.

17. John Newman, "Li/FeS Modeling," Review of the Applied Battery and Electrochemical Research Program, Lawrence Berkeley Laboratory, Berkeley, CA, August 14, 1980.

18. Pier Filippo Marconi and John Newman, "Mathematical Modeling of Hybrid-Redox Flow-Through Porous Electrode Cells for Energy Storage, the $Fe/Fe^{2+}/Fe^{3+}$ System." Presented at the 31st Meeting of the International Society of Electrochemistry, Venice, Italy, September 22-26, 1980.

**19. D. Ziegler, M. Dubrovsky, and J. W. Evans, (presented by D. Ziegler), "The Use of Novel Anodes in the Electrowinning of Metals by Fluidized Bed Cathodes," Annual Meeting of the American Institute of Metallurgical Engineers, Las Vegas, NV, February 24-28, 1980.

§20. I. Masterson, M. Dubrovsky, and J. W. Evans, (presented by J. W. Evans), "Fluidized Bed Electrowinning of Cobalt from Sulfate Solutions," ibid.

‖21. M. Abbasi and J. W. Evans, (presented by J. W. Evans), "A Monte Carlo Simulation of the Diffusion of Gases in Porous Solids," ibid.

22. L. C. De Jonghe, "Degradation of Solid Electrolytes," Third International Symposium on Solid Electrolytes, Tokyo, Japan, September 1980.

23. L. C. De Jonghe, "Solid Electrolyte Batteries," National Defense Academy, Yokosuka, Japan, September 1980.

* * *

†Other publications by the above authors, supported by other sources, are listed under the following headings in this Annual Report:

"Improved Beta-Alumina Electrolytes for Advanced Storage Batteries," Lutgard C. De Jonghe, Investigator.

"In-Situ Investigations of Gas-Solid Reactions by Electron Microscopy," James W. Evans, Investigator.

"Electrochemical Phase Boundaries," Rolf H. Muller, Investigator.

"Electrochemical Systems," John Newman, Investigator.

"Investigation of New Fuel-Cell Electrolyte and Electrode Concepts," Phillip N. Ross, Investigator

"Electrochemical Processes," and "Engineering Analysis of Gas Evolution in Electrolysis," Charles W. Tobias, Investigator.

‡Work supported by Sandia Laboratories.

§Work supported by the National Science Foundation.

‖Work supported by Intramural funding.

¶Work supported by Johnson Controls, Inc.

b. Engineering Analysis of Gas Evolution in Electrolysis*

Charles W. Tobias, Investigator

Introduction. Gas evolution by electrolysis is one of the most common reaction types in electrosynthesis. As of late, electrically rechargeable batteries are under development which also develop gases on charge. This project is directed toward the physical description and correlation of the behavior of electrochemically generated gas-electrolyte emulsions, including the effect bubble streams have on mass transport at electrode surfaces. Liberation of hydrogen or oxygen from various metallic surfaces, situated in a flow channel, is observed under intense illumination over broad ranges of current densities and flow rates. The ohmic component of overpotential is measured and correlated to process conditions. Understanding the behavior of bubble streams should lead to improvements in the energy efficiency of gas-generating processes.

1. GAS EVOLUTION IN FORCED FLOW†

Wing C. Hui and Charles W. Tobias

The effects of forced flow and cathode surface morphology on the nature of hydrogen bubble evolution in 5M KOH solution have been investigated in a flow system; a special flow channel (Fig. 1) allowed both optical observation and electrical measurement to be carried out simultaneously. Optical observation was made with regular- and high-speed cameras. Both the overpotential and the incremental ohmic drop caused by bubbles were determined over the current density range of 0.4 - 2,000 mA/cm^2 for purposes of engineering analysis.

The principal conclusions of this work can be summarized as follows:

(1) Hydrogen bubble evolution strongly depends on the surface morphology of the cathode. (See Figs. 2,3.)

(2) The dominant factors affecting bubble evolution are the density and the distribution of the nucleation sites.

(3) The polarization behavior is heavily influenced by the surface morphology of the electrode. Among the electrodes studied, the sanded electrodes demonstrate the lowest overpotentials.

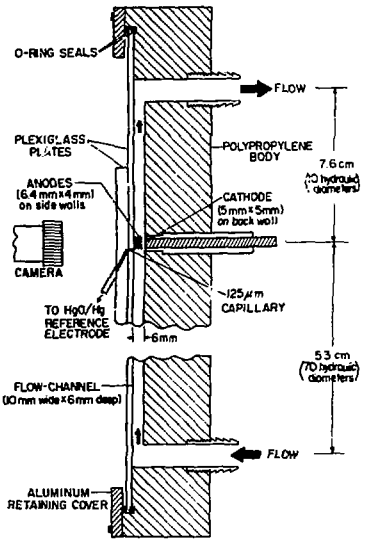

Fig. 1. Longitudinal cross-section of the flow channel used for electrical measurements, and for simultaneous preparation of motion pictures. (XBL 804-5050)

(4) The orientation of the surface morphology to the flow has no significant effect on the mass transfer and charge transfer overpotentials.

(5) Forced flow can reduce the mass transfer overpotential only at low current densities (< 10 mA/cm^2). The reduction increases with increasing flow rate and decreasing current density. Within our experimental range, the reduction is around a few mV to 14 mV. It is the highest for the parallel sanded electrode.

(6) Incremental resistance caused by bubbles increases with the average bubble size at separation.

(7) For the sanded and the polished electrodes, both the incremental resistance and the bubble size increase as the current density is increased. The incremental ohmic drop becomes significant only at current density higher than 40 mA/cm^2. Usually, the incremental resistances are about a few tenths of an ohm. The corresponding incremental ohmic drops then range from a few mV (at 40 mA/cm^2) to ~200-300 mV (at 2 A/cm^2).

*This work was supported by the Assistant Secretary for Conservation and Solar Energy, Office of Energy Storage Systems, Electrochemical Systems Support Division of the U.S. Department of Energy under Contract No. W-7405-ENG-48 through the Chicago Operations Office, Technical Management Division of the Argonne National Laboratory, Argonne, IL.

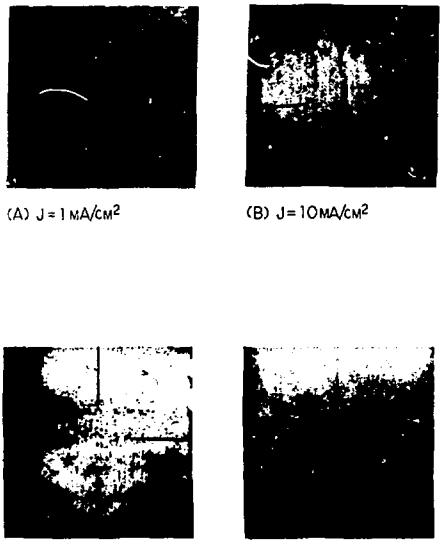

Fig. 2. Bubble formation on an electrode sanded parallel to the direction of electrolyte flow. 5 × 5 mm electrode surface. (XBB 800-12461)

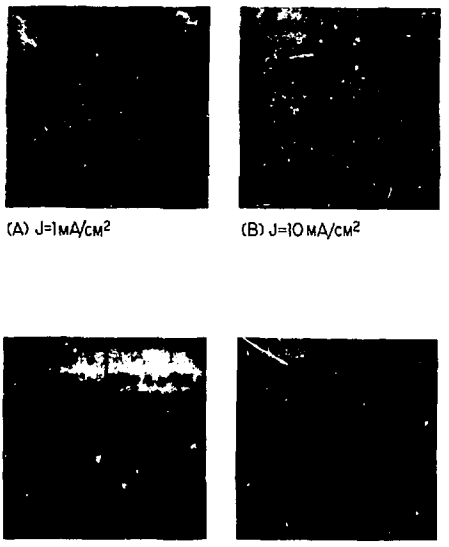

Fig. 3. Bubble formation on an electrode grooved crosswise to the direction of electrolyte flow. 5 × 5 mm electrode surface. (XBB 800-12066)

(8) Both incremental resistance and bubble size are reduced by forced flow. The degree of reduction of the incremental resistance decreases as the flow rate is increased to high values. Therefore, depending on the current density, the forced flow can reduce the incremental resistance effectively only up to certain flow velocity. For the sanded and the polished electrodes, the reduction ranges from 30-55%, (Fig. 4).

(9) The incremental resistance is found to be dependent on the dimensionless ratio of the specific rate of bubble evolution and the velocity of the forced flow, (r_g/U_0).

(10) Incremental resistance and bubble size is strongly affected by the surface morphology of the electrode. In this study, the lowest incremental resistance and bubble size was found on electrodes which were sanded parallel to the direction of flow.

(11) The number of nucleation sites activated increases as current density is increased; it levels off at around a few hundred mA/cm².

(12) The effect of forced flow on cell voltage varies with current density. Forced flow reduces the mass transfer overpotential noticeably only at low current densities (< 10 mA/cm²), and decreases the incremental ohmic drop only at high current densities. It is much less effective in reducing the cell voltage in the transition current density range (~ 10-40 mA/cm²).

* * *

†Brief version of LBL-11945.

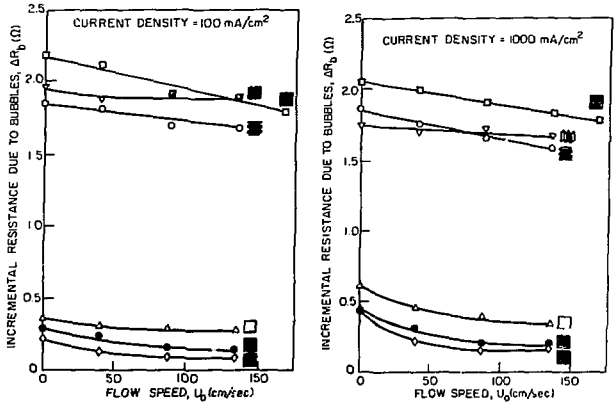

Fig. 4. The influence of surface texture on the incremental resistance caused by H_2 bubbles on the electrode surface. ∇ grooved parallel to flow; O grooved sidewise; □ grooved in both directions (pyramidal); Δ polished; ◇ sanded parallel to flow; ● sanded crosswide.
(XBL 804-5045A)

2. MASS TRANSFER STUDIES WITH A MICRO-SEGMENTED ELECTRODE

Dennis Dees and Charles W. Tobias

Electrochemical gas evolution enhances the rate of mass transfer to and from the electrode. As the gas molecules are produced at the electrode, bubbles are nucleated, which grow and coalesce until they disengage from the surface. Each of these phenomena causes a microscopic flow of electrolyte near the occurrence. The flow replensishes reactants at the surface and thus contributes to an enhancement in the mass transfer rate.

A special electrochemical cell was used to measure the enhancement of mass transfer caused by a single occurrence of a bubble event on a horizontal electrode facing upward. The measuring electrode was composed of a coplanar matrix of circular, (125 μm diameter) platinum micro-electrodes imbedded into epoxy resin, set on approximately 250 μm centers [Fig. 5]. The counter-electrode was placed at a distance of approximately 100 cathode diameters from the cathode. All electrodes in the matrix were polarized cathodically in the mass transfer limiting region to reduce ferric- to ferrous-ion, just above the potential for hydrogen evolution. By reducing the potential of an individual electrode in the matrix to 100 - 200 mV below the potential of the other electrodes, a single hydrogen bubble was nucleated. The mass transfer enhancement was

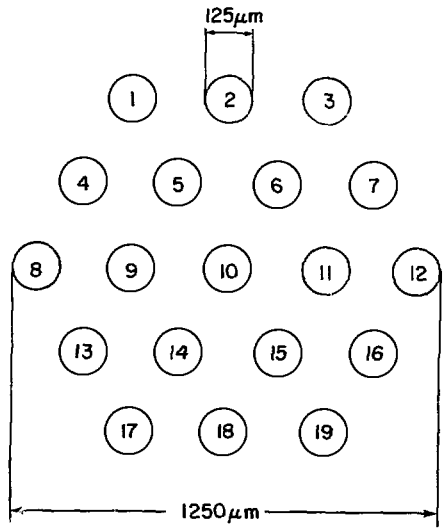

Fig. 5. Geometry of the micro-segmented electrode. Circles denote polished platinum surfaces imbedded into epoxy resin. (XBL 814-4554)

Table 1. Maximum enhancement of mass transport observed in the vicinity of two coalescing bubbles on the surface.

Bubble diameter at time of coalescence	Electrode at which bubbles were generated	% Change in current	Electrode at which current was monitored
200 μm 150 μm	4 5	13.2	6
200 μm 150 μm	4 5	3.2	1
500 μm 500 μm	4 6	32.0	5

Table 2. Maximum enhancement of mass transport observed in the vicinity of a bubble disengaging from the surface.

Bubble diameter at time of separation	Electrode at which bubbles were generated	% Change in current	Electrode at which current was monitored
1.2 mm	10	38.3	19
1.2 mm	1	12.2	19

measured by monitoring the change in the current to the electrodes where only ferric ion reduction occurred.

The effects of both bubble coalescence and disengagement from the surface were studied. It was found that the mass transfer enhancement was of the same order of magnitude for both phenomena. Increases of >35% in currents to individual micro-electrodes were observed. (See Tables 1 and 2.) The enhancement vanished at distances greater than two bubble diameters. The maximum current was reached in approximately 40 milliseconds and decayed to zero within a few seconds.

These experiments form the basis for future, more exacting investigations on mass transfer at gas-evolving electrodes. The results were used to design a more sophisticated experimental apparatus: a micro-mosaic electrode, prepared on a silicon chip by integrated circuit manufacturing techniques.

RESEARCH PLANS FOR CALENDAR YEAR 1981

Quantitative information about the processes controlling the mass transport characteristics at gas-evolving electrodes will be obtained using the mosaic-electrode, which was conceived and developed in this Laboratory, and built for us by Hewlett-Packard Co. We can measure and control the current and/or potential for each 100 × 100 μm surface element. The precise location of nucleation events and the rate of growth of bubbles at any and all mosaic elements will be predetermined. Certain mosaic elements will be used only for reference electrode purposes or for measuring the limiting current density of the indicator ion. This electrode offers the possibility of measuring the mass transfer overpotential as it depends on neighboring bubble coalescence and separation events. A theoretical model will be developed to quantitatively describe the influence of convection due to gas bubbles. A systematic study will be initiated on the effects of surface morphology, and of surface active agents, on bubble separation, and on bubble propagation in the electrolyte.

1980 PUBLICATIONS AND REPORTS†

LBL Reports

1. Wing Cheong Hui with Charles W. Tobias, "Electrolytic Gas Evolution in Forced Flow," M. S. thesis, University of California, Berkeley (1980), LBL-11945.

Invited Talks

1. Charles W. Tobias, "Prospects and Problems in

Electrochemical Engineering," invited address delivered in the frame of the International Symposium on Electrochemistry in Industry -- New Directions, celebrating the centennial of Case Institute of Technology, Cleveland, OH. October 20-22, 1980.

2. Charles W. Tobias, "The Coming of Age of Electrochemical Engineering," opening address at the Symposium on Energy Savings in the Electrolytic Industries," 89th National Meeting of the American Institute of Chemical Engineers, Portland, OR, August 17-20, 1980.

* * *

†A complete listing of publications, reports, and papers presented by Charles W. Tobias and Associates is provided under "Electrochemical Processes" in the Materials Sciences section of this Report.

VII Magnetic Fusion Energy

Magnetic Fusion Energy

a. Materials and Weldments for High Field Superconducting Magnets*

John W. Morris, Jr., Investigator

The project reported here is intended to identify and develop improved materials for structural use in high field superconducting magnets. The principal focus of the research work has been on the continued development of ferritic structural steels which promise substantial advantages in mechanical properties and cost in structural applications at 4 K. Since magnet cases are field-welded structures, materials development requires the identification of appropriate welding methods, as well as the development of suitable heat treatment for the base plate.

1. ALLOYING ELEMENT EFFECT ON THE CRYOGENIC MECHANICAL PROPERTIES OF 12Ni-0.25Ti STEEL

Chol K. Syn

The interstitial-free ferritic 12Ni-0.25Ti steel developed by this group several years ago is recognized as a potential cryogenic structural material for its superior strength (200 ksi yield strength) and fracture toughness (230 ksi) at liquid helium temperature. This combination of strength and toughness was achieved by microstructure refinement through a unique heat treatment technique known as the 2B treatment. The microstructure refining mechanism in the 2B treatment is not completely understood and is the subject of a fundamental research task. Anticipating the commercialization of this steel, however, it is important to establish tolerance limits for common impurity elements such as Mn, Si, C, and others. As an initial step, steels of 12%Ni - 0.25%Ti - 0.25%Mo, 12%Ni - 0.25%Ti - 1.0%Mo, and 12%Ni - 0.25%Ti - 0.5%Al - 2.0% Cu with and without 0.5%Mn, as shown in Table 1, were tested and compared with the base composition of 12%Ni - 0.25% Ti. After the same 2B treatment, the microstructures of these steels refined to a degree comparable to 12Ni - 0.25Ti steel. The fracture toughness, as measured in three-point bending at liquid nitrogen temperature, revealed a rather dramatic deleterious effect of Mn on both the fracture toughness level and the fracture crack propagation characteristics. This effect was eliminated through the addition of 1%Mo, which is known to suppress embrittlement in many steel systems. However, in the case of 12Ni - 0.25Ti - 0.5Al - 2.0Cu steel, a 0.25%Mo addition seemed to promote unstable crack propagation. The effect of variations in heat treatment and in the content of other impurity elements, such as Si and C, is under investigation.

Table 1. Nominal compositions of 12Ni steels and fracture toughness at liquid nitrogen temperature.

No.	Nominal Composition (wt.%)	Fracture Toughness K_{Ic}^{J} [a] (ksi $\sqrt{in}$)	Fracture Crack Propagation[b]
1	12Ni-0.25Ti	257	Stable
2	#1 + 0.25Mo	280	Stable
3	#1 + 0.25Mo + 0.5Mn	162	Unstable
4	#1 + 1.0Mo	200	Stable
5	#1 + 1.0Mo + 0.5Mn	256	Stable
6	#1 + 0.5Al + 2.0Cu	259	Stable
7	#6 + 0.5Mn	249	Unstable
8	#6 + 0.5Mn + 1.0Mo	250	Unstable

[a] K_{Ic}^{J}: estimated K_{Ic} from J value up to the maximum load level.

[b] Stable: Stable crack propagation until the load level was reduced to one-third of the peak load. Unstable: The load level dropped discontinuously before peaking.

2. MICROSTRUCTURAL REFINEMENT MECHANISMS DURING THE 2B TREATMENT OF Fe-12Ni-0.25Ti STEEL

Hur-Ion Lin and Chol K. Syn

A systematic effort to ascertain the microstructural refinement mechanism and microstructural evolution during the 2B treatment (Fig. 1) of 12Ni-0.25Ti steel was initiated this year in the light of the potential importance of the steel as a cryogenic structural material. Time-sequenced optical microscopy was performed for each step of the 2B treatment during an initial slow-rate heating period and subsequent holding period of two hours. Figure 2 shows the final microstructures obtained after each step of the treatment and the gradual refinement of microstructure as the heat treatment goes from the 1A to the 2B steps.

*This work was supported by the Director, Office of Energy Research, Office of Development and Technology, Magnetic Systems Division of the U.S. Department of Energy under Contract No. W-7405-ENG-48.

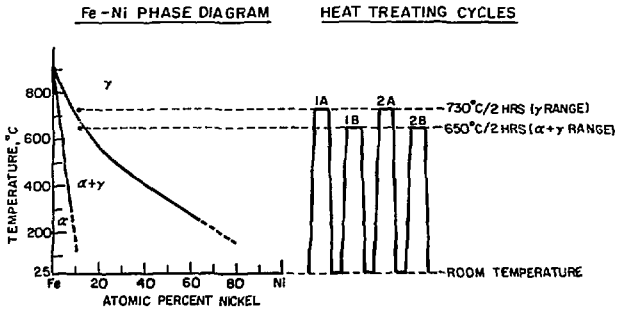

Fig. 1. 2B heat treatment with Fe-Ni equilibrium phase diagram.
(XBL 739-1884)

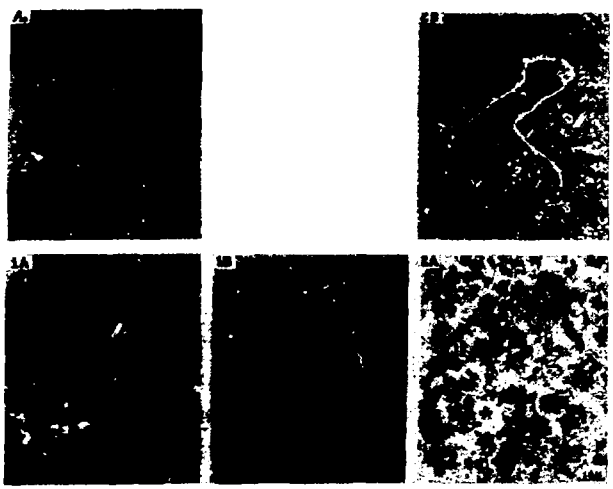

Fig. 2. Microstructure evolution in 12Ni steel.
(XBL 800-13592)

The actual microstructural refinement process can be summarized from the optical microscopy as follows: during the 1A step, a duplex-like substructure develops within the packets of martensite and a γ phase develops along the packet and prior-γ grain boundaries at the expense of the earlier formed duplex-like substructure. The new γ phase (white regions in 1A of Fig. 2) breaks into martensite packets on cooling after the 1A treatment. In the 1B step, new γ regions form so that the entire microstructure is duplex (1B of Fig. 2) and appears similar to the pearlite structure of carbon steels. The average grain size is not changed by the duplex formation during the 1B step. During the 2A and 2B steps, reactions occur which repeat those of 1A and 1B, but on a much finer scale. Thus, the superior strength and toughness of the 12Ni-0.25Ti steel after the 2B treatment seems to be due to the fine grain size and duplex structure developed along with the fine grain size.

3. A STUDY ON THE WELDABILITY OF GRAIN-REFINED Fe-12Ni-0.25Ti STEEL WITH MATCHING FERRITIC FILLER METAL

Hee-Jin Kim

Grain-refined Fe-12Ni-0.25Ti steel has been processed with a fracture toughness greater than 200 ksi $\sqrt{in}$ at the 200 ksi yield strength level in liquid helium. Since most applications at cryogenic temperatures require the use of welded structures, the absence of a currently available combination of weld wire and a welding process suitable for this alloy limits its potential use. The main purpose of the present research was to develop a combination of weld wire and a process to provide strength and toughness levels in multipass weldments matching those of the base plate.

Previous LBL welding research on these alloys has demonstrated that combinations of the GMAW process with Inconel 92 or the EBW process without filler metal addition were not appropriate. However, detailed investigations of EB welding data and weld heat cycle simulation studies showed that even one subsequent weld thermal cycle can completely destroy the coarsened HAZ grains and large columnar grains in weld metal. The low temperature impact toughness was dramatically improved for a wide range of peak temperatures as shown in Fig. 3. It is interesting to note that the useful peak temperature range in weld thermal cycling is much broader than that for conventional base metal processing treatments. Although the ferritic grades of filler metals were previously rejected from consideration for liquid helium use, it seems reasonable to infer from these preliminary studies that matching ferritic weld metal can establish superior toughness at cryogenic temperature in the as-welded condition.

Plates 0.7 in. thick were heat treated by the 2B process and welded manually by the GTAW process using a 14%Ni ferritic filler metal. The weldments were radiographed and sectioned for mechanical testing at cryogenic temperatures. Charpy impact test results are shown in Fig. 4.

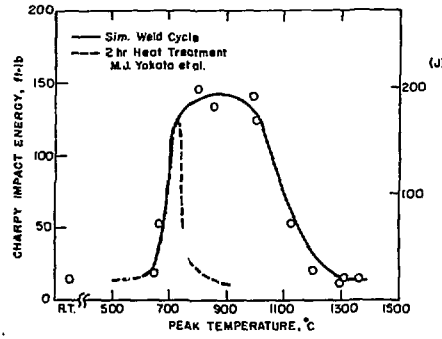

Fig. 3. Variation of Charpy impact energy at 77 K with peak temperature for rapidly and slowly heated Fe - 12Ni - 0.25Ti. (XBL 809-5979)

Weldments made with either of two levels of heat input do not show any ductile-brittle transition in impact testing down to liquid helium temperature. The fracture toughness of the weld metal tested in three-point bending at 77 K was about 300 ksi $\sqrt{in}$, which is almost equal to that of the base plate. These results offer considerable encouragement for the combination of ferritic filler metals and GTAW process to permit the use of ferritic cryogenic steels in as-welded structures at liquid helium temperature.

RESEARCH PLANS FOR CALENDAR YEAR 1981

During calendar year 1981 we propose to carry out the following research under this project:

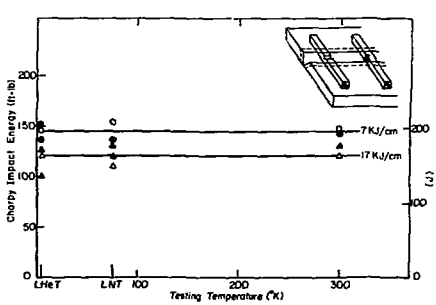

Fig. 4. Variation of weld Charpy impact energy with testing temperature, heat input and orientation. (XBL 808-5753)

1. We plan to continue investigation of the heat treatment of 12Ni cryogenic steels for 4 K use. These investigations will focus on the role of chemical impurities and on the use of heat treatments resembling the potential commercial treatment of thick plates.

2. We plan to continue research into the controlled welding of 12Ni cryogenic steels to characterize welding response and establish welding practice to achieve reproducible toughness at 4 K.

3. We plan to extend studies of both heat treatment and welding to commercial 9Ni steel as this alloy is likely to prove more attractive for short-term commercialization.

4. We plan to continue to monitor developments in other classes of alloys which show promise for structural service at 4 K, including in particular the high manganese austenitic steels now under intensive development in several commercial laboratories.

1980 PUBLICATIONS AND REPORTS

Invited Talks

1. J. W. Morris, Jr., "Structural Materials and Weldments for High Field Superconducting Magnets," NBS-DOE Workshop on Materials for Low Temperature Service, Vail, Colorado, October, 1980.

2. J. W. Morris, Jr., "Materials and Weldments for High Field Superconducting Magnets," Central Research Laboratories, Nippon Kokan K. K., Kawasaki, Japan, December 1980.

3. J. W. Morris, Jr., "Materials and Weldments for High Field Superconducting Magnets," Japan Atomic Research Institute, December 1980.

Nuclear Waste Management

a. Thermodynamic Properties of Chemical Species in Nuclear Waste*

Norman M. Edelstein, Investigator

1. DETERMINATION OF TRACE METAL COMPLEXATION BY CONVOLUTION VOLTAMMETRY†

J. J. Toman and S. D. Brown

In an effort to extend our studies of metal complexation at stationary electrodes, we have examined metal systems using linear scan anodic stripping voltammetry (ASV). This technique is applicable to dilute solutions (10^{-7}-10^{-10}M), as might be expected for solutions of actinides containing naturally significant complexing agents, such as carbonate.

As with our work in linear scan voltammetry, solution of the Fick equations, with appropriate boundary conditions,[1] gives:

$$E = E^R_{1/2} + \frac{RT}{nF} \ln\left(\frac{m^*-m(E)}{m(E)}\right), \qquad (1)$$

where E is the potential, $E^R_{1/2}$ is the reversible half-wave potential, m* is a constant, and m(E) is the semiintegral:

$$m(E) = \int_{E_i}^{E} \frac{i(\gamma)d\gamma}{\sqrt{E-\gamma}}. \qquad (2)$$

Equation 2 is a convolution integral of i with $E_{1/2}$. By differentiating Eq. (1), the semiderivative[2] is obtained, namely:

$$e(E) = \frac{dm(E)}{dE} = \frac{n^2F^2A\nu^{1/2}Do^{1/2}}{4RT} \operatorname{sech}^2 \frac{nF}{RT}(E-E^R_{1/2}). \qquad (3)$$

For systems in rapid equilibrium with complexing ligands, Eq. (3) becomes:

$$e(E) = \frac{dm(E)}{dE} = \frac{n^2F^2A\ ^{1/2}Do^{1/2}}{4RT} \operatorname{sech}^2 \frac{nF}{RT}(E-E^R_{1/2}-\ln Fo), \qquad (4)$$

where

$$Fo(L) = 1 + \beta_1[L] + \beta_2[L]^2 + \cdots + \beta_n[L]^n \qquad (5)$$

and where [L] is the ligand concentration.

We have tested this equation on the Pb-Cl system, where Pb concentrations were held at 10^{-7} M. The Pb-Cl system is known to have several small constants; such a system provides an excellent test of the reproducibility of the measurements. A second problem associated with ASV is capacitative current, which is not included in the theory. This current component can be effectively removed by subtraction of a blank,[3] leaving a background-corrected ASV scan that can then be convoluted with $E^{-1/2}$ and subsequently differentiated to yield the semiderivative, as shown in Fig. 1.

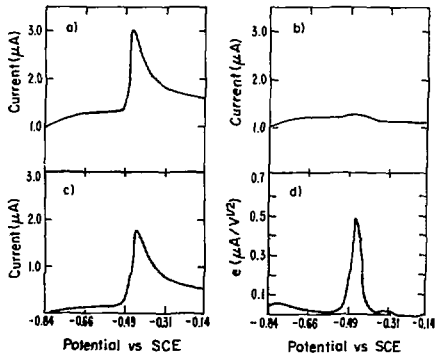

Fig. 1. (a) ASV wave; (b) background scan; (c) background-subtracted wave; (d) resulting semiderivative wave. (XBL 804-714)

*This work was supported by the Assistant Secretary of Nuclear Energy, Office of Commercial Nuclear Waste Management, Commercial Waste Management Program Division of the U. S. Department of Energy under Contract No. W-7405-ENG-48 through the Battelle Memorial Institute, Office of Nuclear Waste Isolation (ONWI), Columbus, Ohio.

Studies of Pb^{+2} complexation with chloride in 2.2 M ionic strength solutions (controlled with $NaClO_4$) gave the results listed in Table 1. Only three complexes have been observed. The small experimental errors observed and the agreement with literature values indicate that the technique is well suited to measurement of stability constants.

Table 1. Results of Pb^{+2} complexation with chloride in solution

Method	Temp.(K)	Medium	$\log\beta_n$	Ref.
potentiometry	25	3 M $NaClO_4$	1.16 1.7 1.97 0.7	4
polarography	25	3 M $NaClO_4$	1.17±.03 1.7±.1 1.4±.2 1.2±.2	5
convolution potential voltammetry	20	2.22 M $NaClO_4$	1.09±.18 1.02±.10 1.59±.01	This work

* * *

†Brief version of LBL-10820, Anal. Chim. Acta 125, 187 (1981).

1. M. Grenness and K. B. Oldham, Anal. Chem. 44, 1121 (1972).
2. M. Goto and D. Ishii, J. Electroanal. Chem. 61, 361 (1975).
3. S. D. Brown and B. R. Kowalski, Anal. Chem. Acta 107, 13 (1979).
4. Special Publication No. 25, Supplement No. 1, part 1, The Chemical Society, London (1971).
5. R. M. Smith and A. Martell, Critical Stability Constants, Vol. 4, Plenum Press, New York, (1976).

2. STUDIES OF COPPER AND NEODYMIUM HYDROLYSIS

Y.-T. Wu and S. D. Brown

Studies of the complexation of Cu^{+2} and Nd^{+3} by OH^- were performed by potentiometry. The Nd^{+3} system was examined as a model for Am^{+3} because the two metals are expected to behave similarly. Kinetic effects complicated the Nd^{+3} study. Table 2 reports the various models used for the Nd^{+3} systems, the stability constant calculated, and the fit parameters. The simple Nd^{+3}-OH^- model seems to represent the data best, although other models, such as $NdOH^{2+}$, $Nd(OH)^+$, or $NdOH^{2+}$, $Nd_2(OH)_2^{4+}$ cannot be ruled out.

Table 2. Comparison of Nd hydrolysis.

Model[a]	-log β	Std. Deviation	Goodness of Fit
1. 1,1	- 9.21	0.0196	45.87
2. 2,2	-13.85	0.061	74.26
3. 1,1	- 9.21	---	47.59
2,2	-15.36	0.1592	
4. 1,1	- 9.21	---	46.64
1,2	-17.58	0.315	
5. 1,1	- 9.21	---	
2,2	-15.36	---	110.58
3,5	-30.99	0.312	
6. 1,1	- 9.21	---	
1,3	-20.399	0.304	190.23
2,2	-13.85	---	
7. 1,2	-16.84	1.19	
2,2	-13.85	---	74.85

[a]Numbers x,y indicate values for $Nd_x(OH)_4$.

3. SEPARATION OF OVERLAPPED PEAKS BY SEMIDIFFERENTIAL ELECTROANALYSIS†

J. J. Toman and S. D. Brown

One limitation of dynamic electrochemistry, when used for studies of metal complexation or for measurements of trace metals, is the resolution of overlapped peaks. Previous approaches have either used time-intensive methods with many blanks or relied upon guesses of peak shapes. We have appled convolution voltammetry (see Article 1) to this problem and have developed two techniques based entirely upon theoretical parameters.

Both approaches fit theoretically defined semiderivative peak shapes to the data sets generated by semidifferentiating the data containing the overlapping peaks. One is based on an iterative, sequential stripping algorithm similar to to that used in x-ray spectrometry.[1] The other fits all peaks simultaneously, using the simplex algorithm, a multi-dimensional, linear programming method.[2] These approaches were characterized by deconvolution of synthetic overlapped peak systems and subsequently applied to semidifferentiated linear scan voltammograms (LSV) of Cd^{+2}, Pb^{+2}, and In^{3+}, as well as to semidifferentiated linear scan anodic stripping voltammograms of Cd^{+2}, In^{3+}, and Tl^+.

For synthetic data, both approaches worked well, failing only when the difference between peak potentials is less than 20 mV for two peaks of 40 mV half-width. Each approach has strengths and weaknesses, with the iterative stripping routine working best when peak heights are quite different for the overlapped peaks, while the simplex routine worked best when the peak widths of

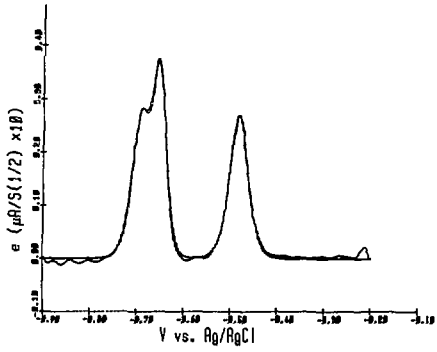

Fig. 2. Semidifferentiated LSV scan for Cd^{+2}, Pb^{+2}, and In^{+3}, with fitted result.
(XBL 8011-3937)

the overlapped peaks differ greatly. In both cases, the algorithms are best able to provide peak potentials, doing better here than the peak heights or with peak half-widths, the other fitting parameters used in this study.

A typical fit obtained for a real data set is shown in Fig. 2, where Cd, Pb and In are successfully deconvoluted. The efficiency of separation of real systems was investigated by adding aliquots of each of the overlapped components. Figure 3 shows the results of such a study for ASV scans of Cd^{+2}, In^{+3}, and Tl^{+}. The constancy of the slopes and the size of the intercepts

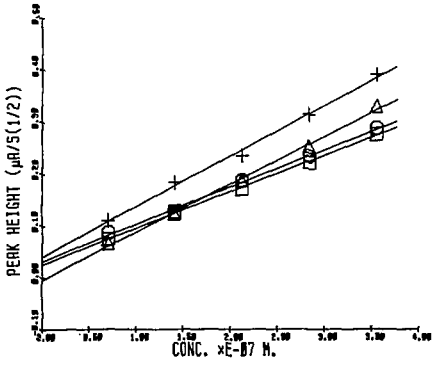

Fig. 3. Peak height vs. concentration plots with corresponding straight line fits for the Tl^{+} ASV single and overlapped peak systems. Symbols: squares, Tl^{+} only; octagons, Tl^{+} and Cd^{+2}; triangles, Tl^{+} and In^{+3}; and crosses, Tl^{+}, In^{+3} and Cd^{+2}. (XBL 8011-3935)

(ideally zero) indicate the ability of the algorithm in separating peaks. The output of physically significant peak parameters allows study of electrode processes, even in systems containing overlapping peaks.

* * *

†Brief version of LBL-11738.

1. P. J. Statham, Anal. Chem. 49, 2149 (1977).
2. S. N. Deming and S. L. Morgan, Anal. Chem. 45, 278A (1973).

4. SOLUBILITY OF AMERICIUM HYDROXIDE IN NEUTRAL AND BASIC SOLUTIONS†

R. J. Silva

Initial experiments were aimed at determining the solution concentration of Am as a function of hydroxyl ion concentration in aqueous solutions from which CO_2 was excluded. From previous experiments, it had been determined that for initial concentrations less than 10^{-6} M, most of the Am tends to be adsorbed on the polyethylene container walls. In an attempt to saturate the sorption sites (both in solution and on the walls) with other cations and thus stabilize the Am in solution, the use of supporting electrolytes was investigated. However, in all the solutions, most of the Am ended up on the walls of the container.

In the next set of experiments, 10 ml solutions of purified $^{243}Am^{3+}$ were prepared with concentrations of 1.62×10^{-6} M and 1.13×10^{-8} M and with 0.1 M $NaClO_4$ as supporting electrolyte. The pH of the solutions was adjusted to pH ~ 7, 8.5 or 10. The solutions were agitated periodically for three days, and any needed pH adjustment was made. After this period, 2 ml of the unfiltered solutions were placed in plastic counting vials. Also, about 3.5 ml of each solution was passed through 0.2 μm Gelman filters, and 2 ml of the last 2.5 ml through the filter also was placed in plastic counting vials. The Am concentration was assayed by gamma counting.

These experiments indicated that Am was reasonably stable for initial concentrations of 10^{-6} M or greater using 0.1 M $NaClO_4$ as supporting electrolyte. Therefore, we set out to measure the solubility of americium as a function of pH using 0.1 M $NaClO_4$ as supporting electrolyte.

Duplicate samples (labeled Am I and Am II) of 100 ml volumes, $1.023 \pm 0.031 \times 10^{-5}$ M in purified $^{243}Am^{3+}$ and 0.1 M in $NaClO_4$, were prepared. The pH of these solutions was initially adjusted to 5 with dilute NaOH. The pH was then increased in steps of ~1 pH unit to pH 10. At each new pH value, the solutions were allowed to sit for several days to reach equilibrium. The pH was checked nearly daily and readjustments made as necessary. In the range 6-9, the pH tended to drift slowly, even after four days, usually to lower values. Therefore, waiting times were extended to longer periods to allow the pH to more or less stabilize. However, even after the longer periods, some drift was observed at pH 7, 8, and 9.

At the end of the waiting periods, samples of the two solutions were taken and centrifuged. One ml of the centrifuged solutions was taken directly for analysis for ^{243}Am content. Two mls of the centrifuged solutions were passed through 0.4 micron Gelman disposable filters. Since any precipitated Am could be in a finely divided form, at pH 8, 9, and 10, portions of the centrifuged solutions were also passed through 0.015 micron Nucleopore filters to determine if there might be an effect due to filter pore size. All aliquots of the centrifuged and filtered solutions were acidified to 0.1 M in HCl before removal from the inert box for analyses. ^{243}Am concentrations were determined by gross alpha counting using a liquid scintillation counter. The concentrations determined for ^{243}Am as a function of pH are given in Table 3.

There was essentially no observed loss in Am from solution for both Am I and Am II at pH values of ~ 5, 6 and 7. Both the centrifuged and 0.4 micron filtered samples gave nearly the same results. At pH ~ 8, Am began to be lost from solution, and the centrifuged and filtered samples began to give slightly different results. At pH values of 9 and 10, the centrifuged samples contained considerably more Am in solution than the filtered samples. These higher values, compared to the filtered solutions, could have resulted from finely divided $Am(OH)_3$, from Am sorbed on very small contaminant particles, or from sampling problems. However, the values obtained for the centrifuged samples do represent an upper limit to the solubility of Am under these conditions. At pH 9, the 0.4 micron and 0.015 micron filtered samples gave similar results, but at pH 10, the 0.4 micron samples contained approximately a factor of three less Am than the 0.015 micron samples for both Am I and Am II. Perhaps the filtration process removed Am from solution. The 0.4 micron Gelman filters are more massive and probably present a larger possible sorption area to the solutions than the 0.015 micron Nucleopore filters. The averaged results for the Am concentrations at various pH are shown in Fig. 4. We assume these data represents the solubility of $Am(OH)_3$.

Allard has reported estimates for the hydrolysis constants for Am^{3+} in aqueous solution as well as for the solubility product of $Am(OH)_3$.[1] Using a computer program, which includes corrections for ionic strength by the Davies equation, we have calculated the solubility limit for Am in a 0.1 N $NaClO_4$ solution as a function of pH from Allard's estimates. The results of the calculation are shown in Fig. 4 as curve A.

Baes and Mesmer[2] have also estimated the solubility product for $Am(OH)_3$ from a comparison with a lanthanide ion of nearly the same ionic radius, i.e. Nd^{3+}. Using this value and measured or estimated values of the hydrolysis constants of Nd as estimates for Am, solubility limits for $Am(OH)_3$ in 0.1 N $NaClO_4$ were calculated and are shown in Fig. 4 as curve B. Clearly, our experimental data favor the solubility limits calculated from the Baes and Mesmer estimates. In fact, if the solubility of $Am(OH)_3$ estimated by Baes and Mesmer is decreased about a factor of 10, i.e., changing log K = - 18.7 to log K = - 17.5, the calculated curve C results.

Table 3. Concentration of americium in solution as a function of pH.

		Am I (M)			Am II (M)		
pH	(days)	1[a]	2[b]	3[c]	1[a]	2[b]	3[c]
4.95 ± 0.05	4	0.954×10^{-5}	0.964×10^{-5}		0.9451×10^{-5}	0.913×10^{-5}	
5.90 ± 0.15	5	1.020×10^{-5}	1.048×10^{-5}		1.059×10^{-5}	1.042×10^{-5}	
6.85 ± 0.20	7	0.873×10^{-5}	0.912×10^{-5}		0.921×10^{-5}	0.936×10^{-5}	
7.90 ± 0.15	23	0.757×10^{-6}	3.393×10^{-6}	2.131×10^{-6}	5.715×10^{-6}	5.322×10^{-6}	3.975×10^{-6}
8.95 ± 0.10	21	1.699×10^{-7}	1.140×10^{-8}	2.362×10^{-8}	7.700×10^{-8}	1.288×10^{-8}	1.297×10^{-8}
10.00 ± 0.05	12	1.595×10^{-7}	1.750×10^{-9}	5.040×10^{-9}	7.716×10^{-8}	1.698×10^{-9}	4.394×10^{-9}

Initial Am concentration = $1.023 \pm 0.031 \times 10^{-5}$ M.

[a]1 = contrifugation

[b]2 = centrifugation plus 0.40 micron filtration

[c]3 = centrifugation plus 0.015 micron filtration.

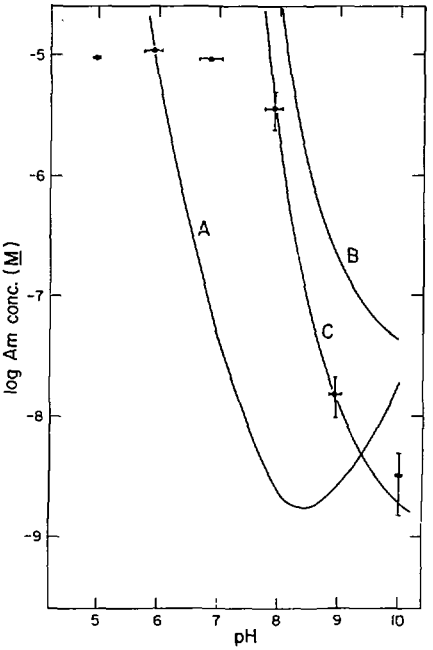

Fig. 4. (XBL 8011-2630)

* * *

†Brief version of Final Report-FY 80 Work--Subtask III, Battelle/ONWI Identification MPO No. 511-05100.

1. B. Allard and G. W. Beall, "Predictions of Actinide Species in Groundwater," Workshop on Environmental Chemistry of the Actinide Elements, Warrington, VA., October 9-12, 1978.
2. C. F. Baes, Jr. and R. E. Mesmer, "The Hydrolysis of Cations," John Wiley & Sons, New York, (1976).

RESEARCH PLANS FOR CALENDAR YEAR 1981

The purpose of this program is to investigate the thermodynamic properties of anticipated actinide and fission product ions and the compounds they may form in geologic environments so that their chemical behavior and potential migration in a nuclear waste setting can be assessed with improved capability.

A number of laboratory studies will be undertaken to obtain data concerning species, oxidation states, effect of complexing ligands, and other related information. Such data will contribute to a better understanding of the chemical systems that may be involved in various geologic media and will furnish more reliable parameters for radionuclide migration modeling studies.

During 1981, the techniques developed during the past year will be applied to studies of actinide complexation. A survey of electrochemical properties will be undertaken in order to identify especially convenient systems for study, such as Np(V). Other systems that will receive attention are Pu(IV) and U(VI). Initial studies will focus on hydrolysis of actinide ions and on complexation of actinide ions with CO_3^{2-} because these two reactions are expected to be the predominant ones in groundwaters. We will also examine the photoacoustic spectra of such lanthanides as Nd^{+3} and Pr^{+3}, with and without complexing ligands, in order to evaluate the stability constants in these systems. Photoacoustic spectroscopy will also be applied to the Am^{+3} - CO_3^{2-} system and to the Pu(V) - Pu(IV) system.

1980 PUBLICATIONS AND REPORTS

Refereed Journals

†J. J. Toman, R. M. Corn, and S. D. Brown, "Convolution Voltammetry of Metal Complexes," Anal. Chim. Acta 123, 187 (1980), LBL-10820.

LBL Reports

†J. J. Toman and S. D. Brown, "Peak Resolution by Semiderivative Voltammetry," LBL-11738, submitted to Analytical Chemistry.

†Supported in part by the Director, Office of Energy Research, Office of Basic Energy Sciences, Chemical Sciences Division, Office of Basic Energy Sciences, U. S. Department of Energy.

IX Other Projects

Other Projects

a. Solubilities of Heavy Hydrocarbons in Water*

John M. Prausnitz, Investigator

1. LIQUID-LIQUID PHASE EQUILIBRIA FOR HEAVY HYDROCARBON-WATER SYSTEM

Frank E. Anderson, Michael M. Gibson, and John M. Prausnitz

In coal gasification operations, a complex mixture of high-molecular-weight compounds, primarily aromatic, called coal tar, is in the effluent gases. Many molecules in coal tar contain heteroatoms; oxygen is most common, but some sulfur and nitrogen are also present. Roughly 85% of the compounds in coal tar have normal boiling points in the range: 220 to 420°C.[1] In normal gasifier operation, the hot effluent gases are quenched at about 259°C with water. This quenching removes the high-boiling coal tar and results in clean, transportable gases plus a three- or four-phase mixture of water and coal tar.

Reliable methods are not available for calculation of this complex multiphase, multicomponent equilibrium and for calculating the equilibria occurring in subsequent operations for the separation of the organic compounds from the water. We have initiated experimental and theoretical research to provide for such calculations.

Experimental. We have designed and constructed an apparatus with which to measure the mutual solubilities of representative aqueous mixtures at temperatures and pressures found in commercial quenching operations. Our equilibrium cell is machined from a single crystal of quartz to allow for visual observation of the contents. It has an inside diameter of 32 mm and an outside diameter of 108 mm. The cell is sealed with MONEL (a nickel-copper alloy) flanges through which a motorized stirrer is attached.

After the cell is charged, it is heated in an oven, and samples of the coexisting phases are withdrawn for analysis in a gas chromatograph.

Theoretical. Coal tar is a very complex, multicomponent mixture. We cannot hope to obtain experimental phase-equilibrium data for all possible combinations of the coal-tar constituents and water. Therefore, we must develop a method for extrapolating the limited data we obtain from our experiments on representative mixtures.

We are pursuing the two approaches described below. It is not yet possible to predict which approach will be more useful.

The equation-of-state method for calculation of phase equilibria requires an equation of state for mixtures at densities from zero to the liquid density and over the entire temperature range of interest. For simple (i.e., nonpolar) compounds, the Perturbed-Hard-Chain Theory (PHCT)[2,3] can be used. However, for the complex molecules found in coal tar, extensions to the PCHT are necessary, and new extrapolation techniques are required to determine parameter values for compounds and tar cuts for which experimental data are not available.

The activity-coefficient method is the second approach. With this method, an equation of state is used for the vapor phase, but a separate model is developed for the liquid phase. An engineering-oriented model is UNIFAC,[4] a group-contribution method that would be readily applicable to mixtures of constituents of coal tar and water. Unfortunately, UNIFAC is inadequate, in its present form, for mixtures containing large organic solutes. We are working on improvements to the UNIFAC method.

* * *

1. A. B. Macknick, Ph.D. thesis, University of California, Berkeley (1979).
2. S. Beret and J. M. Prausnitz, AIChE J. 21, 1123 (1975).
3. M. D. Donohue and J. M. Prausnitz, AIChE J. 24, 849 (1978).
4. Aa. Fredenslund, R. L. Jones, and J. M. Prausnitz, AIChE J. 21, 1086 (1975).

RESEARCH PLANS FOR CALENDAR YEAR 1981

During 1981, we expect to assemble and test our experimental apparatus and to obtain liquid-liquid equilibrium data for several aqueous mixtures of aromatic hydrocarbons containing nitrogen, sulfur, or oxygen at conditions representative of those in a coal-gasification quench operation. We also expect to develop further both our equation-of-state and our activity-coefficient models for calculation on these complex multiphase, multicomponent equilibria.

1980 PUBLICATIONS AND REPORTS

Refereed Journals

†1. C. G. Van de Rostyne and J. M. Prausnitz, "Vapor Pressures of Some Nitrogen-Containing,

*This work was supported by the Electric Power Research Institute (EPRI) under Contract No. RP 1901-1 through an agreement with the Director, Office of Energy Research, U.S. Department of Energy under Contract No. W-7405-ENG-48.

Coal-Derived Liquids," J. Chem. Eng. Data 25, 1 (1980).

‡2. G. Müller, C. J. Radke, and J. M. Prausnitz, "Adsorption of Weak Organic Electrolytes from Aqueous Solution on Activated Carbon," J. Phys. Chem. 84, 369 (1980).

§3. A. Landauer, R. N. Lichtenthaler, and J. M. Prausnitz, "Mutual Solubilities of Alkanes and Methyl Cellosolve," J. Chem. Eng. Data 25, 152 (1980).

‖4. T. F. Anderson and J. M. Prausnitz, "Computational Methods for High-Pressure Phase Equilibria and Other Fluid-Phase Properties Using a Partition Function. 1. Pure Fluids," Ind. Eng. Chem. Proc. Des. Develop. 19, 1 (1980).

‖5. T. F. Anderson and J. M. Prausnitz, Computational Methods for High-Pressure Phase Equilibria and Other Fluid-Phase Properties Using a Partition Function. 2. Mixtures," Ind. Eng. Chem. Proc. Des. Develop. 19, 9 (1980).

‖6. D. D. Lui and J. M. Prausnitz, "Calculation of Phase Equilibria for Mixtures of Ethylene and Low-Density Polyethylene at High Pressures," Ind. Eng. Chem. Proc. Des. Develop. 19, 205 (1980).

‡7. H. Lazalde-Crabtree, G. J. F. Breedveld, and J. M. Prausnitz, "Solvent Losses in Gas Absorption. Solubility of Methanol in Compressed Natural and Synthetic Gas," AIChE J. 26, 462 (1980).

¶8. B. K. Kaul, M. D. Donohue, and J. M. Prausnitz, "Henry's Constants and Second Virial Coefficients from Perturbed-Hard-Chain Theory," Fluid Phase Equil. 4, 171 (1980).

‡9. W. Merk, R. N. Lichtenthaler, and J. M. Prausnitz, "Solubilities of Fifteen Solvents in Copolymers of Poly(vinyl acetate) and Poly(vinyl chloride) from Gas-Liquid Chromatography. Estimation of Polymer Solubility Parameters," J. Phys. Chem. 84, 1694 (1980).

**10. A. I. El-Twaty and J. M. Prausnitz, "Correlation of K-Factors of Mixtures of Hydrogen and Heavy Hydrocarbons," Chem. Eng. Sci. 35, 1765 (1980).

Other Publications

§1. J. M. Prausnitz, T. F. Anderson, E. A. Grens, C. A. Eckert, R. Hsieh, and J. P. O'Connell, Computer Calculations for Multicomponent Vapor-Liquid and Liquid-Liquid Equilibria, Prentice-Hall, Englewood Cliffs, New Jersey (1980).

‡2. P. J. Hicks, Jr., "The Solubility of Acetone and Isopropyl Ether in Compressed Nitrogen, Methane, and Carbon Dioxide," M. S. thesis, Department of Chemical Engineering, University of California, Berkeley (1980).

†3. D. R. Edwards, "Vapor Pressures of Coal-Related Liquids," M. S. thesis, Department of Chemical Engineering, University of California, Berkeley (1980).

†4. C. R. Gonzalez-Yradier, "Vapor-Liquid Equilibrium of High-Boiling Petroleum Fractions," M. S. thesis. Department of Chemical Engineering, University of California, Berkeley (1980).

††5. G. Lobien, "Activity Coefficients at Infinite Dilution for Partially Miscible Liquid Systems," Ph.D. thesis, Department of Chemical Engineering, University of California, Berkeley (1980).

Invited Talks

†1. J. M. Prausnitz, "State-of-the-Art Review of Phase Equilibria," Keynote Lecturer, Second International Conference on Phase Equilibria and Physical Properties for the Chemical Industry, West Berlin, Germany, March 1980 (LBL-10767).

2. J. M. Prausnitz, Wilhelm Lecturer, Chemical Engineering Department, Princeton University, Princeton, New Jersey, April 1980.

†3. W. B. Whiting and J. M. Prausnitz (presented by W.B. Whiting) "A Perturbed-Hard-Sphere, Local-Composition Model for Liquid Mixtures," Sixth West Coast Statistical Mechanics Conference, San Jose, California, June 1980.

†4. D. Edwards, C. G. Van de Rostyne, J. Winnick, and J. M. Prausnitz (presented by D. Edwards), "Estimation of Vapor Pressures of High-Boiling Fractions in Liquefied Fossil Fuels Containing Heteroatoms Nitrogen or Sulfur," Second Chemical Congress of the North American Continent, Las Vegas, August 1980.

5. J. M. Prausnitz, Phillips Petroleum Company Research Laboratories, Bartlesville, Oklahoma, October 1980.

6. J. M. Prausnitz, Centennial Lecturer, Chemical Engineering Department, Louisiana State University, Baton Rouge, Louisiana, November 1980.

†Supported in part by the U.S. Department of Energy.

‡Supported in part by the Deutsche Forschungsgemeinschaft (administered by the Technical University of Berlin).

§Supported in part by the Department of Chemical Engineering, University of California, Berkeley.

‖Supported in part by the Petroleum Research Fund (administered by the American Chemical Society).

¶Supported in part by the Gas Processors Association.

**Supported in part by a fellowship from the government of the Libyan Arab Republic.

††Supported in part by the National Science Foundation.

b. High Strength Austenitic Alloys for Generator Retaining Rings*

John W. Morris, Jr., Investigator

Introduction. This research project involved the development of new ultra high strength austenitic alloys that are intended for such applications as the retaining rings of large electrical generators.

1. ULTRA HIGH STRENGTH PRECIPITATION-HARDENED AUSTENITIC STEELS

Keh-Minn Chang and Hyun K. Shin

Previous research under this project led to the development of a Ta-modified iron-based superalloy, designated EPRI-T, which has nominal composition Fe-34.5Ni-5Cr-3Ti-0.5Al-3Ta-1Mo-0.3V-0.01B. This alloy can be heat treated to yield strength in excess of 200 ksi if it is processed from the as-forged condition, and it retains high toughness and good resistance to stress corrosion cracking in the high strength condition. It is currently under study for possible commercialization in a separate contract funded by EPRI.

The continuation of research reported here involved two tasks, both of which were intended to accomplish further improvements in the properties of Alloy T. The first involved the use of thermomechanical treatment prior to aging to improve the strength-toughness combination of the alloy. The second involved the use of chemical modifications to change the precipitating species from cubic γ' to tetragonal γ". This modification increases the efficiency of hardening and creates the possibility of achieving a 200 ksi strength level without thermomechanical processing.

The results of experiments on thermomechanical treatment are shown in Fig. 1. The thermomechanical treatments utilized three controlled rolling schedules:

Re: 1150°C/1 hr - 25% reduction

→ 1000°C/10 min - W.Q.

Hf: 1150°C/1 hr - 25% reduction

→ 1000°C/10 min - 13% reduction → w.d.

Lf: 1150°C/1 hr - 25% reduction

→ 1000°C/10 min - 13% reduction

→ 85°C - 14% reduction → W.Q.

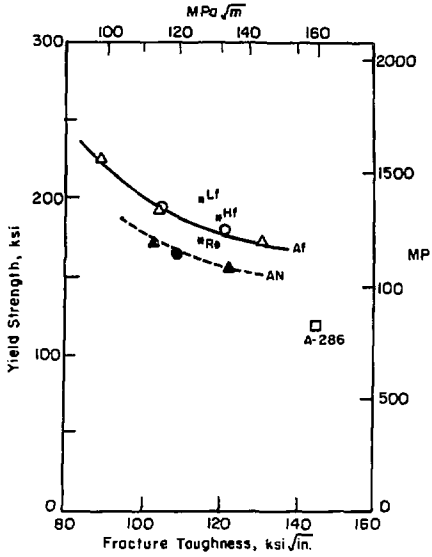

Fig. 1. Improvement of strength-toughness relation by thermomechanical processing. (XBL 804-5034)

After controlled rolling, the specimens were given a double-aging heat treatment at 750°C, 16 hr + 650°C, 16 hr. The figure documents that substantial improvements in the strength-toughness combination can be obtained with appropriate thermomechanical processing schedules.

The alloys studied in the second task are listed in Table 1. These alloys all contain substantial tantalum additions, which previous research has shown to cause a change in precipitate structure from the cubic γ' to the tetragonal γ". The alloys were annealed to remove forging damage

Table 1. The compositions of Ta-bearing superalloys.

Alloy No.	Fe	Ni	Cr	Ti	Al	Ta	Mo	V	B
A	bal	34.5	5	2.5	-	5.5	1	0.3	0.01
B	bal	34	5	2.5	-	6.5	1	0.3	0.01
C	bal	34	5	2.5	0.3	6.5	1	0.3	0.01

*This work was supported by the Electric Power Research Institute (EPRI) under Contract Nos. RP 1061 and RP 1266-12 through an agreement with the Director, Office of Energy Research, U.S. Department of Energy under Contract No. W-7405-ENG-48.

and were then given the thermal treatments listed in Table 2. The results show that yield strengths very close to 200 ksi can be achieved in these alloys after thermal treatment alone. The results also document the beneficial effect of the tantalum increase and suggest that the addition of aluminum has a deleterious influence on attainable strength.

Table 2. The strength properties of alloys after various heat treatments (ksi).

	Alloy A[a]	Alloy B[b]	Alloy C[b]
750°C/8 hr	163	159	170
750°C/16 hr	166	178	175
750°C/8 hr + 650°C/16 hr	189	198	191
725°C/16 hr	173	179	170
725°C/32 hr	179	192	186
725°C/16 hr + 640°C/32 hr	189	195	191

[a]Annealed at 1000°C/1 hr.
[b]Annealed at 1100°C/1 hr.

1980 PUBLICATIONS AND REPORTS

Invited Talks

1. Keh-Minn Chang, "The Effect of Controlled Rolling on Properties and Structures in Age-Hardening Fe-Ni Based Alloys," TMA/AIME Annual Meeting, Law Vegas, February 24-28, 1980.

2. H. J. Lee, "Annealing Embrittlement in Age-Hardened Fe-Ni Based Austenitic Alloys," TMA/AIME Annual Meeting, Las Vegas, February 24-28, 1980.

3. J. W. Morris, Jr., "Controlling the Hydrogen Resistance of High Strength Austenitic Alloys," TMA/AIME Annual Meeting, Las Vegas, February 24-28, 1980.

4. J. W. Morris, Jr., "Development of High Strength Hydrogen-Resistant Austenitic Alloys," TMS-AIME Conference in Hydrogen Effects in Metals, Jackson Hole, Wyoming, August 1980.

5. J. W. Morris, Jr., "Development of High Strength Austenitic Alloys for Generator Retaining Rings, Materials for Fossil Energy Conversion, NBS, Gaithersburg, Virginia, October 1980.

c. Investigation of New Fuel Cell Electrolyte and Electrode Concepts*

Philip N. Ross, Investigator

Introduction. In contemporary theories of catalysis by metal alloys, the result of alloying metal B with an active metal A can generally be classed in the following ways: (1) a dilution effect, where B is an inactive metal which serves only to dilute the AB surface of the active metal A without affecting the intrinsic activity of A; (2) a configuration effect, where B does chemisorb the reactant, and the unique nearest neighbor configuration around the active metal A produces unique adsorbate configurations with unique reaction rates; (3) a ligand effect, where the AB chemical bonding is such that the adsorptive properties of A are changed. In heterogeneous hydrocarbon catalysis, the most widely observed effect is dilution, occurring when Group VIII transition metals are diluted with the Group Ib metals. Ligand effects were also widely postulated in the early studies of alloy catalysis, where they were frequently referred to in the context of d-band filling, particularly with Group VIII-Ib alloys, but contemporary studies on these alloys have shown the ligand effect to be minor. The well-known property of the transition metals to chemisorb oxygen and hydrogen at room temperature, in contrast to only physical adsorption on sp-metals (Group Ib), has long been attributed to the unfilled d-orbitals. Metal-ligand bonding that involves d-orbital overlap and thus changes the d-orbital occupancy of the active metal atoms might be expected to produce dramatic catalytic effects. According to the Engel-Brewer valence bond model, the enormous thermodynamic stability of the Pt intermetallics like Pt_3Ti or Pt_3Zr, where the free energy of formation is about -420 kJ/mol, is due to donation of unpaired electrons from Zr (ground state d^3s) to the Pt (excited state) to form 5 bonding d-orbitals. It is anticipated, therefore, that the class of metal ligands forming the extremely stable intermetallics may produce electronic configurations which result in heats of adsorption of oxygen both above and below that for the pure metal. One objective of the present project is to study oxygen reduction on carbon-supported Pt intermetallic clusters in phosphoric acid, and to determine the general applicability of the concept to other transition metals, e.g., Pb and Ru.

The kinetics of oxygen reduction at any given metal electrode surface will, in principle, always depend on the nature of the electrolyte. The polarization curve observed using practical gas diffusion electrodes will show an even greater dependence on the nature of the electrolyte because of the combined effect of the electrolyte on kinetics and transport properties. One might, therefore, anticipate that several material properties that relate either to the kinetics of electrode reactions or to the rates of transport in electrolytes may cause significantly different polarization characteristics for gas diffusion electrodes in different electrolytes. Kinetic effects that might be anticipated are, for example, the effect of the proton solvation shell on the kinetics of electron transfer for the elementary step

$$O_2 + HS^+ + 1e^- = O_2H + S \quad ,$$

where S denotes the solvation shell in nearly anhydrous acid and the effect of specific anion adsorption on site availability or on activation energy. Transport effects might occur due to changes in solubility and diffusivity of molecular oxygen, or to the HS^+ mobility in very concentrated (nearly anhydrous) acid. The objectives of the present study are to evaluate strong perfluoroalkyl acids as electrolytes for air electrodes in acid fuel cell and to determine how the oxygen kinetics and/or oxygen transport are different in these acids.

1. OXYGEN REDUCTION ON CARBON-SUPPORTED Pt and Pd INTERMETALLIC CLUSTER CATALYSTS IN ACID ELECTROLYTE†

P. N. Ross and L. Johnson

A procedure was developed for preparing small (3-5 nm) bimetallic clusters dispersed on a conductive carbon substrate. Vulcan XC-72 R (Cabot Corp.) carbon black was impregnated with platinum to 10 w/o by use of a colloidal method. The alloy metal of interest was deposited (as hydrated oxide) onto the carbon by precipitation from chloride solution with ammonium hydroxide. The binary alloy was formed by heat treating; the most probable reaction sequence is:

$$MO_x + C \rightarrow x/2\ CO_2 + MC + 3Pt \rightarrow MPt_3 + C$$

That dispersed intermetallic clusters were indeed formed on the carbon surface was confirmed by detailed structure analysis using x-ray diffraction (XRD) and transmission electron microscopy (TEM). Lattice imaging by TEM confirmed the existence of metallic clusters (mean diameter 3-5 nm) of a single phase. Lattice parameters were measured using standard x-ray powder diffraction methods. The structure and composition of the most interesting intermetallics studied so far are summarized in Table 1.

Oxygen reduction kinetics were studied using a thin porous layer technique[1] in which the effects of molecular oxygen transport in the liquid film are analyzed with the same accuracy as achieved in the rotating disc electrode technique.[2] The results of these kinetic studies are shown in

*This work was supported by the Electric Power Research Institute (EPRI) under Contracts RP 1200-5 and RP 1676-02 through an agreement with the Assistant Secretary for Conservation and Renewable Energy, U. S. Department of Energy under Contract No. W-7405-ENG-48.

Table 1. Characterization of supported Pt-group IVb and Group Vb alloys and intermetallics by x-ray diffraction.

Alloy	Phases	Lattice Parameter	Est. Composition	Crystallite Size
Pt-Ti	fcc Ti Pt_3	3.906Å	25 a/o Ti	6 nm
Pt-Zr	fcc "Zr Pt_4"	3.958	20 a/o Zr	4
Pt-Hf	fcc "Hf Pt_4"	3.955	20 a/o Hf	4
Pt-V	fcc γ-V Pt_3	3.888	20 a/o V	3.5
Pt-Nb	fcc "Nb Pt_5"	3.963	20 a/o Nb	5-6
Pt-Ta	fcc "Ta Pb_5"	3.965	20 a/o Ta	7

Table 2. Because of the potentially complex interaction between the intermetallic clusters and the electrolyte, no mechanistic interpretation of the kinetics of oxygen reduction on these catalysts is possible at this time. There is merit, however, to a phenomenological description of changes in kinetics brought about by intermetallic bonding. The kinetic parameters for the Pt intermetallic clusters VPt_3, $ZrPt_4$, and $TaPt_5$ differed significantly from the parameters for pure Pt clusters of the same cluster size dispersed on the same support. These parameters showed:

(1) an order of magnitude higher activity for oxygen reduction at potentials where anodic film formation starts on Pt clusters;

(2) a slightly higher activation energy in the oxide-free potential region, but also a higher apparent pre-exponential factor;

(3) an essentially temperature-independent Tafel slope above 400 K of 120 ± 5 mV per decade on the intermetallic catalyst versus 110 ± 5 mV for the Pt catalyst.

The cyclic voltammetry of these intermetallic cluster compounds revealed that the large difference in kinetics at potentials where the anodic layer forms on Pt clusters is probably due to a less exothermic free energy of formation of oxide on the intermetallic clusters. If it is assumed that changes in the heat of adsorption of the rate-determining intermediate (generally $-O_2H$) are reflected in changes in the heat of adsorption of the like-spacies that constitute the anodic film,[3] it is easily shown that the reduced heat of adsorption leads simultaneously to higher activation energy and a higher pre-exponential factor. The change in pre-exponential factor reflects a large change in total coverage of intermediates (at constant potential) rather than a significant change in activation entropy. The kinetic parameters found in this work are consistent with the interpretation of elementary processes that lead to "volcano" relations between reaction rate and adsorption energy.[4] This volcano relation suggests further gains in catalysis can be obtained by finding materials for which the heat of adsorption of oxygenated species is even less exothermic than those found here. From a practical standpoint, in 0.5 mg/cm^2 electrodes of optimized structure, the expected performance gain for ambient

Table 2. Kinetic parameters for oxygen reduction on Pt and Pt intermetallics in H_3PO_4.

Catalyst	Cluster size (A)	Surface area (m^2/g)	Specific Activity[a] (mA/mg)	Specific Activity[a] (μA/cm^2 Pt)	Tafel slope (mV)	E_{act}[b] (kJ/mol)	Air performance[c] (mV at 200 ASF)
Colloidal Pt	18	100	21	20	105	34.3	688
Heat-treated Pt	25	75	36	52	110	42.5	702
$HfPt_4$, $ZrPt_4$	40	50	55	110	120	48	722
VPt_3	30	65	50	75	115	~48	725
$TaPt_5$, $NbPt_5$	40	50	40	100	120	~48	715

[a]Defined as normalized current density at 0.9 V in 97 wt% H_3PO_4 at 450 K, pure oxygen at ambient pressure.

[b]In oxide-free potential region.

[c]In optimized PTFE-bonded electrode with 0.5 mgPt/cm^2, 97 wt% H_2PO_4, 450 K, ambient pressure.

air consumption using the intermetallic catalysts developed in this work should be 20-40 mV at 200 ASF over the conventional Pt catalyst.

* * *

*Brief version of LBL-10799.
1. P. N. Ross and P. Stonehart, Electrochim. Acta 21, 441 (1976).
2. J. Newman, J. Phys. Chem. 70, 1327 (1966).
3. A. Damjanovic and V. Brusic, Electrochim. Acta 12, 615 (1967).
4. A. J. Appleby, Catal. Rev. 4, 221 (1970).

2. OXYGEN REDUCTION KINETICS ON Pt IN PERFLUOROALKYL ACID ELECTROLYTES

P. N. Ross and L. Johnson

The kinetics of oxygen reduction on Pt in the usual inorganic acids ($HClO_4$, H_2SO_4, H_3PO_4) are being compared to the perfluoroalkyl acids listed in Table 3, using rotating ring-disc electrode (RRDE) techniques. The electrolytes appearing there are selected to determine the effect of acid functional group (-COOH, -SO_3H, -PO_3H), and the effect of anion symmetry (e.g., $^-OOC\ CF_2\ COO^-$ vs. CF_3COO^-). Trifluoroacetic (TFA) perfluorosuccinic (PFSA) and trifluoromethanesulfonic (TFMSA) are standard commercial items. Difluoromethanedisulfonic (DFMDSA), tetrafluoroethanedisulfonic (TFEDSA), and difluoromethanediphosphonic (DFMDPA) are being synthesized. During the past year, we have completed room temperature Pt RRDE studies of H_2SO_4, $HClO_4$, H_3PO_4, TFA, and TFMSA, all at pH = 1. With the exception of TFA, oxygen reduction on Pt RRDE in these electrolytes has been studied before. Our purpose, however, is to pull all the known data together with new data in a consistent manner so as to make a quantitative comparison of all electrolytes. Further, while the data for a Pt RRDE in dilute $HClO_4$ and H_2SO_4 are consistent and have been reproduced in many laboratories, the results for dilute TFMSA reported by O'Grady et al.[1] differ substantially from those of Appleby and Baker.[2] Dilute H_3PO_4 has not been thoroughly investigated.

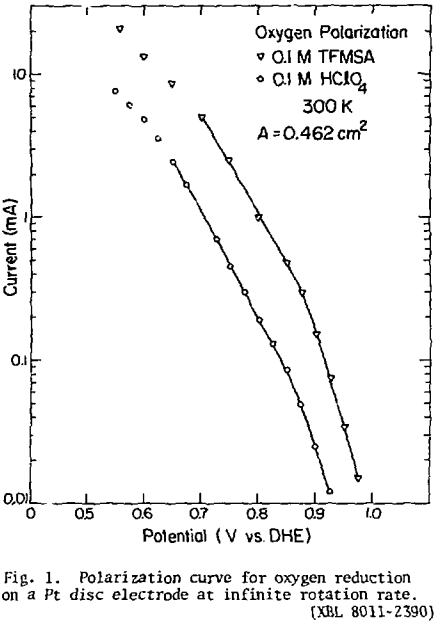

Fig. 1. Polarization curve for oxygen reduction on a Pt disc electrode at infinite rotation rate. (XBL 8011-2390)

Figure 1 shows the polarization curve for a smooth Pt disc at infinite rotation rate, produced by extrapolation using the relation,

$$\frac{1}{i} = \frac{1}{i_k} + \frac{1}{B\omega^{1/2}} \quad ,$$

where

Table 3. Acid electrolytes for fuel cells.

Carboxylic	Sulfonic	Phosphonic
trifluroacetic	trifluoromethane sulfonic	N.A.
$CF_3\ CO_2H$	$CF_3\ SO_3H$	
N.A.	difluoromethane disulfonic	difluoromethane diphosphonic
	$SO_3H\ CF_2\ SO_3H$	$PO_3H\ CF_2\ PO_3H$
perfluorosuccinic	tetrafluoroethane disulfonic	N.A.
$CO_2H\ CF_2\ CF_2\ CO_2H$	$SO_3H\ CF_2\ CF_2\ SO_3H$	

N.A. = not available in this study.

$$B = (2\pi/60)^{1/2}\, nAF\, \nu^{1/2}\, Co$$

$$\times\, [0.621\, S^{-2/3}/(1 + 0.3\, S^{-1/3} + 0.145\, S^{-2/3})] \quad ,$$

where n is the number of electrons transferred per mole of O_2 consumed, ν the kinetic viscosity, S the Schmidt number, and Co the solubility of oxygen. In all three electrolytes, the B coefficient was found to be 0.064 ± 0.004, exactly the value expected for n = 4 in these solutions. The ring currents indicated that < 5% of the oxygen leaves the electrode surface as peroxide. The results for H_2SO_4 and $HClO_4$ are essentially identical to reported values,[3] and the TFMSA results are very close to those reported by O'Grady et al.[1] However, we find no evidence for any enhancement of oxygen solubility in 0.1 N TFMSA as suggested by O'Grady et al., since the B coefficient was exactly the same as in 0.1 N $HClO_4$ and the limiting currents were within ± 10% (Fig. 2). Since anion specific adsorption in 0.1 N $HClO_4$ is already minimal, the enhanced reaction rate must be purely catalytic, i.e., higher rate per Pt surface atom.

The results obtained with dilute H_3PO_4 were surprising. The concentration of solution for which the measured pH is 1 was 0.7 M. Cyclic voltammetry of a clean Pt electrode in 0.7 M H_3PO_4 indicated characteristic changes in the underpotential hydrogen features that are usually attributed to specific adsorption of phosphate anions. The extent of specific anion adsorption is generally felt to increase in the order

$$HF < HClO_4 < H_2SO_4 < H_3PO_4 \quad .$$

TFMSA appears to fall between HF and $HClO_4$ in this ranking. Yet, the RRDE results for oxygen reduction in H_3PO_4 are almost indistinguishable from those obtained in $HClO_4$. Any active site blocking by specific anion adsorption must be minimal, or the anions are easily displaced from the Pt surface by chemisorbed oxygen or both.

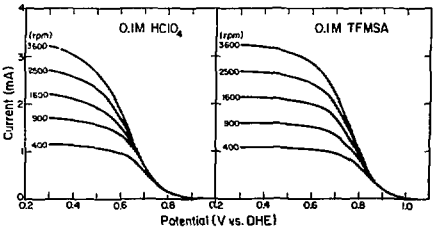

Fig. 2. Potentiodynamic polarization curves for oxygen reduction on a Pt disc electrode (10 mV/sec). (XBL 809-2000)

The kinetics in 0.1 N TFA were similar to those in 0.1 N TFMSA, showing a catalytic enhancement of a factor of at least 5 over the inorganic acids. The accelerated kinetics in perfluoroalkyl acids appears, therefore, to be associated with the perfluoroalkyl group rather than with the acid functional group.

* * *

1. W. E. O'Grady, E. J. Taylor and S. Srinivasan, to be published in J. Electroanal. Chem.
2. A. J. Appleby and B. S. Baker, J. Electrochem. Soc. 125, 404 (1978).
3. A. Damjanovic and V. Brusic, Electrochim. Acta 12, 615 (1967).

RESEARCH PLANS FOR CALENDAR YEAR 1981

The program will concentrate on the study of the kinetics of oxygen reduction on Pt in perfluoroalkyl acids using rotating ring-disk methods. Further exploratory studies on the use of Pd and Pd intermetallic cluster catalysts in both phosphoric and perfluoroalkyl sulfonic acids are planned.

1980 PUBLICATIONS AND REPORTS

LBL Reports

1. P. N. Ross. "Oxygen Reduction on Supported Pt Alloys and Intermetallic Compounds in Phosphoric Acid," LBL-10799.

Other Publications

1. P. N. Ross, "Oxygen Reduction on Supported Pt Alloys and Intermetallic Compounds in Phosphoric Acid," Final Report, EPRI Project 1200-5, Report EM-1553, September 1980.

Invited Talks

1. P. N. Ross, "Oxygen Reduction on Carbon Supported Pt Intermetallic Catalysts," National Fuel Cell Seminar, San Diego, CA, July 14-16, 1980.

2. P. N. Ross, "Electrocatalytic Properties of the Pt-Group IVb and Vb Intermetallic Compounds," ACS National Meeting, Houston, Texas, April 15-20, 1980.

3. P. N. Ross, "The Reduction of Oxygen on the Pt-Group IVb and Vb Intermetallics in Acidic Electrolytes," 158th Meeting of the Electrochemical Society, Hollywood, Florida, October 5-10, 1980.

4. P. N. Ross, "Anomalous Current Ratios in Teflon Bonded Electrodes in Very Concentrated H_3PO_4," 158th Meeting of the Electrochemical Society, Hollywood, Florida, October 5-10, 1980.

d. Improved Beta-Alumina Electrolytes for Advanced Storage Batteries*

Lutgard C. De Jonghe, Investigator

1. LOCAL ELECTRODE CURRENT DENSITY AND FLAW DECORATION OF SODIUM-BETA" ALUMINA†

Lutgard C. De Jonghe and Leslie Feldman

When ionic currents are passed through sodium-beta alumina, metal filled cracks may propagate from the cathodic to the anodic interface. Several authors have modeled the progression of this type of electrolyte failure.

The initiation stage of this phenomenon is the most important one. The lateral dimensions of the flaws from which the degradation initiates are thought to be very small, on the order of the grain size or smaller. Local electrode current densities are thus expected to be of significance in the very early stages of degradation. Both local electrode current densities and small sodium-filled flaws are not readily observable. Two simple decoration methods have been developed that can qualitatively reveal local electrode current densities and permit decoration of small sodium-filled cracks: an electrolytic decoration and a chemical decoration.

The electrolytic decoration of the anolyte/beta aluminum interface was described in the previous annual report. It clearly demonstrated the heterogeneous nature of the beta" alumina electrode interface.

When the sodium crack network has propagated through a degraded sample, it appears optically very diffuse because the polycrystalline electrolytes are translucent rather than transparent, and light scattering prevents a clear examination of the metal-filled cracks. Where the cracks intersect the surface, reaction with the atmosphere depletes the sodium so that optical surface detection of the cracks is difficult.

Crack openings are quite small, as a result, regular dye penetrants seem to be ineffective. In our chemical decoration methods, the polished and degraded samples are submerged for about 5 to 20 minutes in an aqueous, one molar solution of silver nitrate kept at about 80°C. The cracks are then decorated with a dark deposit. Presumably, Ag^+ reacts with the NaOH that has formed in the fine cracks. When viewed with crossed polarizers that reduce surface reflection, the details of the cracks network show up clearly. Figure 1 is an example of a decorated crack network in a section parallel to the direction of crack propagation. A multitude of fine cracks intersect the surface, again indicating crack branching. Denser crack clusters can also be observed in the same samples as shown in Figs. 2(a) and 2(b). Figure 2(a) shows a combination of single cracks and crack clusters as they emerge at the anodic interface.

Fig. 1. Silver decorated cracks in degraded sodium-beta" alumina sample. (XBB 801-45)

The appearance of crack clusters can vary, as is evident from Fig. 3. At this anodic interface, the crack clusters were mainly along grain boundaries. Interestingly, degradation emerged in this case in a high porosity area. While there are some indications that the cracks prefer paths of high porosity, clear relationship between pore distribution and degradation path was not found.

* * *

†Brief version of Mat. Res. Bull. 15, 777 (1980).

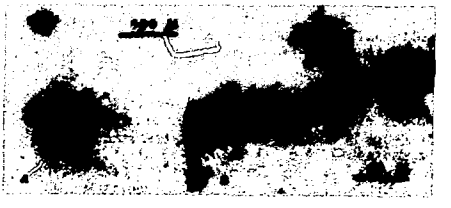

Fig. 2. Silver decorated cracks and crack clusters on anodic surface of a degraded electrolyte specimen. (XBB 801-44)

*This work was supported by the Electric Power Research Institute (EPRI) under Contract No. RP 252-3 through an agreement with the Assistant Secretary for Conservation and Renewable Energy, U.S. Department of Energy under Contract No. W-7405-ENG-48.

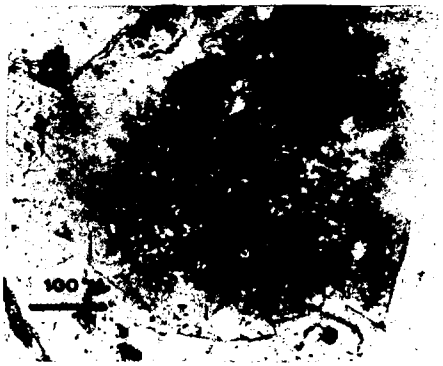

Fig. 3. Silver decorated crack cluster. The degradation has emerged in a high porosity area. Extensive cracking along grain boundaries is evident. (XBB 801-46)

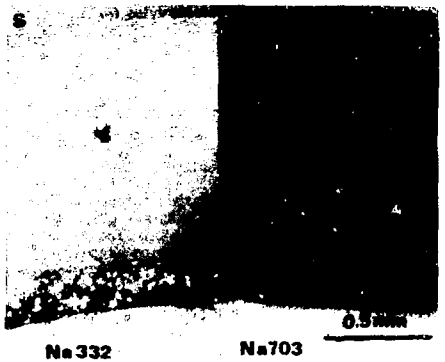

Fig. 4. Damage layer progressing from Na side of the electrolyte after charge transfer of 332 and 703 A·hr cm^{-2}. For the lower cycle life, the damage layer is uneven. (XBB 804-4119)

2. SLOW DEGRADATION AND ELECTRON CONDUCTION IN SODIUM-β ALUMINAS†

Lutgard C. De Jonghe, Leslie Feldman, and Andrew C. Buechele

Sodium-beta aluminas used as solid electrolytes in sodium-sulfur batteries degrade during cell cycling. This type of degradation, which was first discussed by Armstrong et al.,[1] has been examined in more detail by a number of authors. This degradation, called Mode I here, involves the propagation of a sodium-filled crack driven by a cathodic deposition mechanism. In general, a significant threshold current density must be exceeded before the rapid Mode I fracture degradation is initiated.

From our examinations of a number of sodium-beta alumina electrolytes that were used in Na/S cells, it appeared that a second type of degradation was active. This mode of degradation, called Mode II here, manifests itself as a damage layer developing from the sodium side of the electrolyte. Degradation was also found to develop from the sulfur side of the electrolyte. Additionally, the usual chemical coloration propagating from the sodium electrode was also present.

Used electrolytes were obtained from the General Electric Research and Development Center. They were beta alumina electrolytes with a composition of 9.6 wt% Na_2O, 0.25 wt% Li_2O, balance Al_2O_3. The electrolytes had been cycled in sodium/sulfur cells at current densities of approximately 100 mA·cm^{-2}, around 300°C.

Important observations on the used electrolytes are shown in Fig. 4. In these polished and stained cross-sections it is clearly shown that significant electrolyte damage has occurred in a layer-like fashion from the sodium/electrolyte interface. At 703 A·hr cm^{-2} of total ionic charge transfer, this layer of degradation has progressed through about one-third of the tube wall. The white, spotty reflections were subsurface. It is proposed that they are microfractures caused by internal sodium deposition. Supporting evidence is presented in Figs. 5 and 6. Figure 5a is a high-voltage transmission electron micrograph of a thick foil prepared by ion milling from the degraded region of an electrolyte subjected to 332 A·hr cm^{-2} of charge transfer. The arrows indicate where sodium metal appears to have deposited. The deposition occurred at some grain boundaries, as well as at some grain triple junctions. The degraded triple junctions contained silicon as well (Fig. 5b). It therefore appears that grain boundaries, as well as intergranular phases, are active in the Mode II degradation. Figure 6 shows a microfracture area, where excess sodium as well as silicon was detected with the analytical scanning transmission electron microscope.

This slow Mode II sodium penetration cannot be accounted for by Poiseuille pressure arguments. Indeed, Mode I degradation leads invariably to rapid crack propagation. Instead, it involves some electron conduction from the sodium/beta alumina interface, followed by electron-Na^+ recombination in the electrolyte.

Mode I flaws were also observed in cycled electrolytes. An example is shown in Fig. 7. Possibly, the microcracking associated with the Mode I failure might actually have initiated the Mode I failure. It is interesting to note that the Mode I crack shown in Fig. 7 did not remain

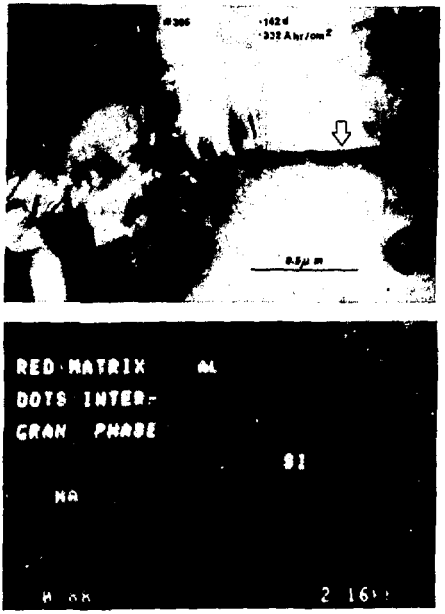

Fig. 5. (a) Sodium deposits in damage layer of electrolyte after charge transfer of 332 A cm^{-2}. Arrows indicate sodium deposits. Both grain boundaries and grain triple junctions appear involved. Thick foil observed in high-voltage transmission electron microscope to minimize loss of Na. (b) Analytical microscopy shows that Si is present in the triple grain junction, where extra Na has deposited.
[(a) (XBB 803-3889); (b) (XBB 803-3568)]

perpendicular to the tube walls. We attribute this deflection to a basic instability in the Mode I geometry: a deflected crack is more effectively current-fed. This deflection can clearly lead to spalling of the electrolyte surfaces. Similar crack deflections have been observed by us in accelerated sodium/sodium testing of electrolyte tubes at 300°C.

Degradation was observed on the sulfur side of the used electrolytes as well. At short cycling times, the sulfur/electrolyte surface is virtually unaffected. At long cycling times, a significant degradation occurs, as shown in Fig. 8. Figure 8 clearly shows the "imprinting effect" that has been reported by other workers as well. Surface cracks are also present, as shown in Fig. 7. The light and dark regions in the electrolyte surface reflect the macrostructure of the graphite filler that was used to facilitate current extraction from the positive sulfur electrode. A cross-section of the electrolyte

Fig. 6. Thick foil prepared from damage region of electrolyte subjected to 703 A·hr cm^{-2} of charge transfer. Microcracks associated with sodium deposition are arrowed. Care must be taken to distinguish these cracks from cracks introduced in foil preparation. Thick foils are necessary to avoid interference from foil artifacts.
(XBB 806-7055)

at the positive electrode is shown in Fig. 9. Again, a band of degradation is observed after extensive charge transfer. This layer appears quite nonuniform at low-charge transfer, but is is fully established after 703 A·hr cm^{-2}. The indications are that again a sodium deposition has occurred. This highly unusual situation would require the positive interface to act as a pseudo-cathode during part of the charge cycle.

* * *

†Brief version of LBL-10946.

1. R. D. Armstrong, T. Dickinson, and J. Turner, Electrochim. Acta 19, 187 (1974).

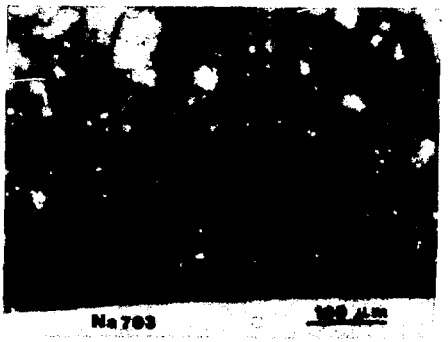

Fig. 7. Mode I flaw, arrowed, in electrolyte after 703 A·hr cm^{-2} of charge transfer. These flaws, when present, always emanate from the Na side.
(XBB 804-4120)

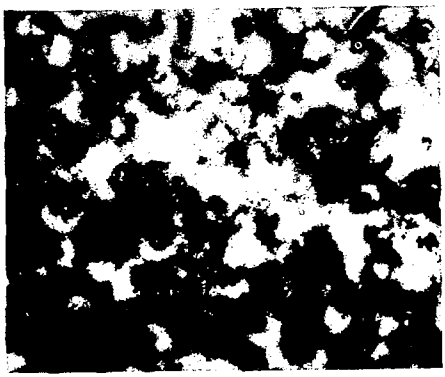

Fig. 8. "Imprinting" effect of graphite fiber filler on S side of electrolyte. (XBB 804-4125)

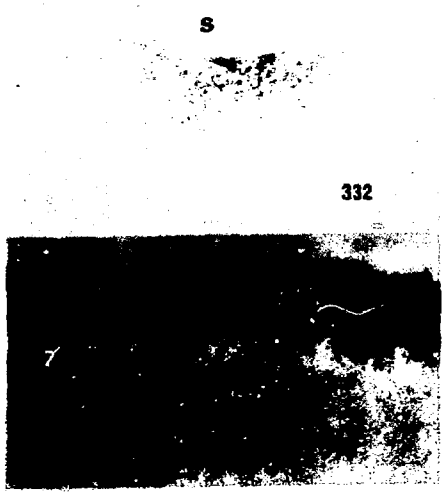

Fig. 9. Degradation, after silver staining, of sulfur side of electrolyte after 332 and 703 A·hr cm^{-2}. The degradation layer becomes more uniform after prolonged electrolysis. (XBB 804-4128)

3. INITIATION OF DEGRADATION IN POLYCRYSTALLINE SODIUM-BETA ALUMINA ELECTROLYTES†

Lutgard C. De Jonghe, Lester Feldman, and Andrew C. Buechele

The initiation stage of Mode I degradation in β and β" solid electrolytes is the most important one since cracks propagate rapidly once they are formed.[1,2] Here, the significance of the local microstructure on the Mode I initiation is discussed. It appears that grain boundaries can be favorable sites for Mode I failure initiation.

The Mode I failure initiation presupposes the existence of small surface flaws, typically between 1 to 20 μ long, with a crack opening less than 1000Å. Once such flaws are filled with sodium by electrolysis, the critical stress intensity factor, K_{IC}, can be exceeded at the crack tip at sufficiently high macroscopic current densities. Current focusing on the small intruding crack is essential for the operation of the Mode I failure. The usual calculations of the critical current densities at which the Mode I failure initiates involves the solution of Laplace's equation to describe the detailed electric field and the resulting primary current distribution on the crack phases. Approximate solutions for the secondary current distributions were recently obtained by Brennan.[2] All treatments consider only solutions for isotropic solids. Beta alumina is, however, an extremely anisotropic solid, and frequently blocking grain boundaries can be found.[3] The microstructure will therefore strongly alter the current flow into cracks, especially when these are of the order of the grain size. Geometrical considerations show that cracks are most effectively fed when they are oriented perpendicular to the conduction planes, as shown in Fig. 10a. However, β-alumina cleaves most readily parallel to the conduction planes. The next most favorable crack-feeding geometry is shown in Fig. 10b. This shows a blocking grain boundary that is faceted along the conduction planes. Evidence of failure initiation at grain boundaries such as those in Fig. 10, at 300°C, above the melting point of sodium, is found in Fig. 11. The micrographs clearly indicate the importance of local geometry in failure initiation.

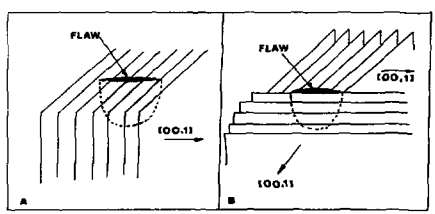

Fig. 10. (a) Local geometry for most effective current focusing; (b) local geometry for next best current focusing, involving a 00.1 faceted grain boundary. (XBL 805-9786)

Fig. 11. Degradation initiation at 300°C, after a charge passage of 20 A·hr cm^{-2}. Grain boundaries are again involved. (XBL 804-4117)

* * *

†Brief version of LBL-11000.

1. R. D. Armstrong, T. Dickinson, and J. Turner, Electrochim. Acta 19, 187 (1974).
2. M. P. J. Brennan, In press: Electrochim. Acta (1980).
3. L. C. De Jonghe, L. Feldman, A. Buechele, LBL-10946 (May 1980).

RESEARCH PLANS FOR CALENDAR YEAR 1981

Galvanostatic and potentiostatic measurements will be carried out to determine polarization phenomena occurring at the Na/electrolyte interface with pure and impure electrodes. A relation will be sought between electrode overvoltages and the onset of degradation. The onset of Mode I degradation will be detected by acoustic emission monitoring during electrolysis.

The electronic conductivity of partly reduced electrolytes will be measured by the asymmetrical polarization method. The nature of the chemical coloration of the electrolyte when in contact with molten Na will be studied.

1980 PUBLICATIONS AND REPORTS

Refereed Journals

1. L. C. De Jonghe and L. Feldman, "Local Electrode Current Densities and Flaw Decoration of Sodium-Beta Alumina," Mat. Res. Bull. 15, 777 (1980).
2. L. C. De Jonghe, "High Resolution Images of β" Aluminas," Acta Cryst. A36, 831 (1980).

LBL Reports

1. L. C. De Jonghe, L. Feldman, and A. Buechele, "Slow Degradation and Electron Injection in Sodium-β Aluminas," LBL-10946 (May 1980).

2. L. C. De Jonghe, L. Feldman, and A. Buechele, "Initiation of Degradation in Polycrystalline Sodium-Beta Aluminum Electrolytes," LBL-11000 (May 1980).

Invited Talks

1. L. C. De Jonghe, "Microstructures, Defects, and Sodium Transport in Sodium-Beta Alumina Solid Electrolytes," U. S. Japan Conference in Defects and Transport in Solids," October 1979, Honolulu, Hawaii.

2. L. C. De Jonghe, "Chemical Coloration of Sodium-Beta Alumina Solid Electrolytes," Cornell University, April 1980, Ithaca, New York.

3. L. C. De Jonghe, "In-Cell Degradation of Sodium-Beta Aluminas," General Electric Co., April 1980, Schenectady, New York.

4. L. C. De Jonghe, "Breakdown Phenomena in Beta Alumina Solid Electrolytes," Ford Motor Co., Aeronautics Division, August 1980, Redondo Beach, California.

5. L. C. De Jonghe, "Degradation Mechanisms in Solid Electrolysis," Tokyo Institute of Technology, September 1980, Yokohama, Japan.

X Appendices

Appendix A

PERSONNEL

MATERIALS AND MOLECULAR RESEARCH DIVISION

SCIENTIFIC STAFF

Investigators	Postdoctoral and Other Scientists	Graduate Students
Neil Bartlett	G. Beindorf B. Desbat F. Dove T. Richardson	R. Biagioni T. Mallouk E. McCarron B. McQuillan F. Okino F. Tanzella S. Yeh
Alexis Bell	H. Arakawa W. Cant A. Daneshrad	J. Baker W. Canella R. Dictor T. Frederick R. Hicks C. Kellner W. McKee A. Salhi S. Salim D. Stern P. Winslow
Robert Bergman		P. Becker J. Bonfiglio H. Bryndza P. Comita J. Frommer J. Huggins A. Janowicz T. Lockart V. Mainz M. Seidler P. Seidler K. Theopold M. Wax S. Webb G. Yang
Robert Bragg	S. Rao	D. Baker L. Henry J. Hoyt J. Johnson B. Mehrotra A. Pearson
Leo Brewer	K. Krushwitz R. Lamoreaux C-B. Meyer G. Rosenblatt	D. Davis J. Gibson D. Goodman B. Lin
John Clark	H. Sokol	H. Nathel L. Phillips M. Tolbert S. Webb
John Clarke	T. Lemberger G. Schon D. Van Harlingen	R. Koch R. Lee H. Mamin J. Martinis R. Miracky D. Seligson

Investigators	Postdoctoral and Other Scientists	Graduate Students
Marvin Cohen	S. Froyen S. Louie	J. Ihm P. Lam Z. Levine J. Northrup M. Yin
Robert Connick	T. Braga	D. Horner
Lutgard De Jonghe	H. Schmid	A. Buechele C. Cameron M. Chang L. Feldman D. Hitchcock S-C. Hu R. McClelland
Didier de Fontaine		H. Tsai
Norman Edelstein N. Bartlett J. Conway K. Raymond G. Seaborg A. Streitwieser D. Templeton A. Zalkin	K. Abu-Dari R. Andersen J. Bucher C. Carrano G. Chapuis S. Davis P. Edwards T. Hayhurst F. Hollander S. Hubert S. Jones R. Kluttz H. Nitsche H. Ruben B. Schilling G. Shalimoff S. Simpson J. Solar L. Templeton C-H. Van Deurzen H-K. Wang F. Weitl G. Wong Y-T. Wu	J. Arenivar S. Barclay C. Carriere D. Caster R. Corn C. Eigenbrot G. Freeman B. Gilbert G. Girolami D. Grimmett M. Halpern D. Kagan M. Kappel S. Kingsley B. Lulu M. Lyttle V. Mainz V. Pecoraro R. Petro G. Phillips R. Planalp B. Raine S. Rutan R. Shinomoto K. Smith W. Smith R. Tatz T. Tilley J. Toman S. Un
Anthony Evans	W. Kriven D. Marshall M. Nisenholz J. Porter H. Ruf	W. Blumenthal W. Burlingame S. Chiang G. Crumley K. Faber Y. Fu C-H. Hsueh M. Huang A. Rana M. Sakarcan M. Spears
James Evans	D. Coates J. Little S. Lympany Y. Zundelevich	M. Abbasi M-F. Rau
Ron Gronsky	J. Penisson P. Rez L. Tanner	L. Andersen J. Briceno-Valero S. Cheruvu P. De Roo

Investigators	Postdoctoral and Other Scientists	Graduate Students
Ron Gronsky (cont'd)		E. Kamenetzky R. Kilaas J. Mazur J. Rose G. Tamayo E. Thomann
Charles Harris	H. Auweter	M. Berg C. Bergman J. Chao P. Cornelius G. Erdheim S. George G. Goncher A. Harris S. Marks H. Robota P. Whitmore
Heinz Heinemann	J. Sinclair	
Dennis Hess		C. Blair A. Wakita L. Williams
Carson Jeffries	J. Furneaux	J. Culbertson E. Pakulis J. Perez J. Weiner
William Jolly	K. Bomben H. Chen A. Gin	M. Ajmani A. Bakke
Harold Johnston		M. Kowalczyk D. Littlejohn W. Marinelli H. Nelson J. Podolske S. Solomon
Yuan Lee	R. Buss P. Casavecchia M. Coggiola G. He J. Hepburn F. Houle F. Huisken H. Kwok J. Lisy J. Peel R. Sparks R. Tse Z-J. Zhang	S. Anderson R. Baseman S. Bustamente C. Hayden C. Kahler D. Krajnovich T. Minton D. Neumark M. Okumura P. Schulz D. Trevor M. Vernon P. Weiss
Alan Levy	D. Boone W. Coons I. Cornet I. Finnie R. Glardon M. Holt J. Humphrey I. Hutchings S. Jahanmir J. Laitone M. Landkof A. Modavi E. Peterson	P-K. Chen M. Des Jardin M. Khatibloo S. Li F. Pourahmadi W. Tsai P. Turi M. West R-J. Yang W. Yeung

Investigators	Postdoctoral and Other Scientists	Graduate Students
Alan Levy (cont'd)	J. Sabnis J. Stringer R. Varma W. Worrell W. Yeung	
Bruce Mahan		S. Hansen A. O'Keefe T. Turner
Richard Marrus	P. Bucksbaum E. Commins H. Gould J. Leavitt M. Prior H. Shugart C. Vane	P. Bucksbaum P. Drell L. Hunter P. Latham
William Miller	C. Cerjan G. Herling S. Shi	D. Ali P. Dardi S. Gray A. Orel B. Waite
. Bradley Moore	C. Chi-Ke M. Diegelmann J. Jasinski A. Kung Z. Sabet-Imani	A. Abbate D. Bamford M. Berman H. Dai J. Frisoli P. Ho F. Hovis A. Langford W. Natzle E. Specht J. Wong L. Young
John W. Morris, Jr.	K-M. Chang D. de Fontaine M. Hong G-X. Hu J. Kim K. Mahin R. Powell J. M. Sanchez C. Syn H. Yamauchi	C-M. Chang D. Dietderich G. Fior-Zurlo B. Fultz M. Hong H. Kim H-J. Kim Y-H. Kim H. Lee H-L. Lin P. Ling K. Mahin T. Mohri K. Sakai J. Sanchez Y-C. Shih H-K. Shih M. Strum L. Summers D. Wedge I-W. Wu
Earl Muetterties	J. Kouba J. Stein M. Tachikawa	J. Bleeke R. Burch H. Choi W. Cwirla C. Friend T. M. Gentle G. Schmidt K. Shanahan S. Slater

Investigators	Postdoctoral and Other Scientists	Graduate Students
Earl Muetterties (cont'd)		M. Tsai R. Wexler
Rolf Muller	F. Schwager	C. Coughanowr J. Farmer R. Gyory
John Newman	P. Marconi R. Pollard	D. Bernardi V. Edwards D. Law M. Matlosz M. Orazem P. Pierini T. Risch G. Trost
Donald Olander	M. Balooch A. Machiels S. Zhou	D. Dooley M. Farnaam K. Kim S. Kim S. Shann D. Sherman F. Tehranian C. Tsai S. Yagnik R. Yang
Joseph Pask	R. Langston P. Spencer A. Tomsia F. Zhang	S. Chandratreya S. Chiang P. Flaitz S. Johnson D. Miller V. Nagesh M. Sacks K. Wada
John Prausnitz		F. Anderson M. Gibson E. Larsen W. Whiting
Norman Phillips	G. Brodale E. Hornung K. Matho	J. Boyer W. Fogle M. Mayberry J. Van Curen
Alexander Pines	L. Mueller U. Nitsan J-F. Wang S. Wolfe	G. Drobney R. Eckman J. Garbow J. Murdoch S. Sinton L. Sterna J. Tang W. Warren D. Weitekamp G. Wolf Y-S. Yen D. Zax
Kenneth Pitzer	K. Balasubramanian P. Christiansen	J. Simonson
Paul Richards	R. Bailey E. Kreysa T-M. Shen A. Smith T. Timusk J. Tucker	R. Bloemhof J. Bonomo R. Britt W. Challener S. Chiang C. Collins

Investigators	Postdoctoral and Other Scientists	Graduate Students
Paul Richards (cont'd)	H. Van Kempen	M. Hueschen C. Markley S. McBride W. McGrath T. Shen G. Tobin
Moshe Rosen	M. Pickus J. Wang	
Philip Ross	U. Bardi G. Derry D. Scherson	F. Wagner
Alan Searcy	D. Beruto A. Buchler D. Meschi Z. Munir G. Spinolo	T. Dai J. Farnsworth N. Jacobson M. G. Kim T. Reis S. Roche
Y. Ron Shen	S. Arakelian K-C. Chu A. DeCastro P. Motisuke D. Ricard S. Shen M. Sigrist H. Zhu	G. Boyd C. Chen S. Durbin T. Heinz J. Hunt R. Hsu R. Page R. Pecyner R. Smith H. Tom
David Shirley	U. Becker W. Brewer O. Dabbousi W. Heppler Z. Hussain G. Mason D. Trevor E. Umbach	A. Baca J. Barton C. Bahr R. Davis S. Kevan L. Klebanoff P. Kobrin D. Lindle C. Parks J. Pollard D. Rosenblatt S. Southworth J. Tobin D. Trevor C. Truesdale A. Uyanik
Henry F. Schaefer	J. Goddard R. Pitzer S. So M. Vincent Y. Yamaguchi Y. Yoshioka	D. Fox M. Hueschen K. Kim W. Laidig G. Pittman P. Saxe
Gabor Somorjai	W. Brennen A. Cabrera P. Davies S. Ferrer J. Frost M. Jazzar M. Langell W. McLean C. Minot J. Sachtler M. Salmeron N. Spencer	R. Blackadar R. Carr J. Crowell S. Davis L. Dubois C. Galik E. Garfunkel W. Gillespie W. Guthrie R. Koestner T-H. Lin M. Quinlan

Investigators	Postdoctoral and Other Scientists	Graduate Students
Gabor Somorjai (cont'd)	M. Van Hove P. Watson	F. Zaera
Gareth Thomas	R. Hoel J. Koo O. Krivanek C. Kung R. Mishra J. Rayment J. Steeds A-J. Yang	C. Ahn J. Ahn J-S. Gau E. Goo A. Jhingan N. Kim K. Krishnan C. Kwok I-N. Lin J. Mazur A. Nakagawa S. Ong T. Rabe L. Rabenberg W. Salesky M. Sarikaya T. Shaw M. Sung H. Tokushige J. Wasynczuk C. Wu L. K. Wu X-F. Wu Y. S. Yoon
Charles Tobias	P. Cettou Y. Geronov T. Hryniewicz V. Komnenic	D. Dees J. Dukovic J. Faltemier K. Hanson W. Hui A. Kindler G. Prentice D. Roha P. Sides T. Tsuda S. Yu
K. Peter Vollhardt	N. Allison L. Benner Y-H. Lai W. Tam D. Van Horn M. Winter	R. Colborn J. Drage J. Fritch J. Tane E. Walborsky
Jack Washburn	U. Dahmen G. Hirsch C. Lampert D. Sadana	B. Chin R. Drosd C. Jou H. Ling P. Ling W-L. Lo T. Mowles T. Sands N-R. Wu T. Zee
David Whittle	I. Allam M. El Dahshan F. Gesmundo O. Goncel H. Hindam A. Malik H. Schmid F. Viani	H. Akuezue S-H. Choi L. Kingsley A. Misra R. Pendse P. Risse S. Shaffer F. Yang M. Yee

Investigators	Postdoctoral and Other Scientists	Graduate Students
John Winn	M. Maier	J. Goble B. Hale W. Hollingsworth D. Horak H. Luftman S. Sherrow

SUPPORT STAFF

MATERIALS AND MOLECULAR RESEARCH DIVISION

C. Peterson - Division Administrator
K. McArthur - Assistant Division Administrator

Administrative Staff

M. Janzen - Staff Assistant, Administration
*J. Knight - Technical Editor
E. Skrydlinski - Staff Assistant, Personnel
S. Stewart - Staff Assistant, Purchasing

Clerical and Secretarial Staff

J. Amoroso
M. Barsony
K. Becky
M. Besser
K. Brusse
M. Bowman
B. Burt
B. Carter
J. Denney
S. Ewing
V. Farr
R. Fletcher
L. Franson
P. Gassler
C. Hacker
A. Harrington
S. Harris
J. Hayes
L. Irvin
H. Johnson
R. Jones
T. Judson
B. Komatsu
K. Krushwitz
S. Lasarte
V. Lovejoy
E. McClelland
R. McCollough
D. Merrill
M. Moore
V. Narasimhan
A. Ozturkmen
I. Pelletreau
S. Quarello
M. Rector
I. Rochell
J. Shull
J. Smith
C. Sterling
A. Weightman
C. Yoder
S. Young

Technical Staff

W. Toutolmin - Technical Coordinator

D. Ackland
G. Baum
T. Bakker
J. Barrett
D. Bazell
R. Bellman
T. Britt
*M. Brown
R. Brusasco
E. Carter
S. Carter
C. Carvalho
P. Chik
M. Cima
M. Clement
C. Coulman
J. Cox
D. Crane
M. Des Jardin
D. Dietderich
*K. Frank
R. Friedman
L. Galovich
K. Gaugler
W. Giba
C. Gibson
J. Glanville
C. Gosnell
A. Gronsky
W. Goward
H. Harrell
G. Hickey
G. Hirsch
J. Holthuis
H-Y. Hu
R. Indig
J. Jacobsen
M. Jayko
*L. Johnson
M. Johnson
D. Jurica
K. Koshlap
E. Kostlan
*D. Krieger
C. Lam
W. Lau
M. Lutz
J. Lince
*R. Lindberg
J. Maasberg
D. MacDonald
R. Mackey
V. Manty
C. Markley
J. Martinis
*B. McAllister
L. McCullough
C. Morley
M. Mulvehill
W. Murrell
B. Neilson
*D. Newhart
Q. Nguyen
A. Pentecost
M. Perez
J. Peterson
*B. Pope
*H. Riebe
M. Rigdon
D. Rosenberg
P. Ruegg
K. Sakai
E. Scherr
C. Scolari
S. Shaffer
*J. Severns
D. N. Shirley
L. Sindelar
M. Snow
H. Sokol
B. Steakley
V. Stumpf
C. Thom
P. Tom
M. Trask
P. Trevor
P. Turi
K. Wada
J. Wafer
R. Wagner
J. Wallace
H. Weeks
*J. Wodei
W. Wong
P. Yarnold
N. Yates
M. Yee
C. Yu
*M. Zbinden

---

* Assigned to MMRD from LBL support divisions.

Appendix B

MATERIALS AND MOLECULAR RESEARCH DIVISION COMMITTEES

DIVISIONAL COUNCIL

M. Cohen
N. Edelstein
H. Heinemann
H. Johnston*
J. Morris, Jr.

BUILDING AND SPACE COMMITTEE

(Includes Buildings 62, 70A, 72, and the Chemical and Materials Sciences Laboratory)

J. Clark
R. Gronsky
D. Meschi
R. Muller*

DIVISIONAL STAFF COMMITTEE

N. Edelstein
R. Muller*
L. Falicov
K. Westmacott

EQUIPMENT REVIEW COMMITTEE
(Chemical and Materials Sciences)

J. Clarke
A. Evans
C. B. Moore
R. Muller*

SAFETY AND LABORATORY STANDARDS COMMITTEE

(Buildings 62 and 72)

G. Baum
T. Britt
D. Davis
B. Fultz
W. Giba
W. Hemphill
H. Hindam
J. Holthuis
L. Irvin
L. Johnson
D. Krieger
K. McArthur
D. Meschi*
R. Muller
C. Peterson
J. Severns
W. Toutolmin
W. Wong

TECHNICAL STAFF AND SHARED FACILITIES COMMITTEE

L. DeJonghe*
R. Gronsky
J. Morris, Jr.
P. Ross
G. Somorjai
D. Whittle

MMRD Building 62 Building Manager: D. Meschi
(Alternate: C. Peterson)

MMRD Building 72 Building Manager: K. Westmacott

*Chairman

Appendix C

LIST OF SEMINARS

MATERIALS AND MOLECULAR RESEARCH DIVISION

Surface and Catalysis Science

Date	Speaker and Affiliation	Seminar Title
1-9-80	M. Boudart Stanford University	Recent Work on Oxidation of Dihydrogen and Carbon Monoxide by Metals and Alloys
1-16-80	F. R. Gamble Exxon Research and Engineering	Superconductivity Electrochemistry and Catalysis in the Layered Transition Metal Sulfides
1-22-80	T. Engle IBM, Zurich	The Scattering of Beams of Small Molecules from Palladium Crystal Surfaces
1-23-80	R. P. Merrill Cornell University	Concentration Profiles in the Impregnation of Porous Catalysts
1-24-80	A. M. Bradshaw Fritz-Haber-Institut, Berlin	Angle-Resolved Photoemission from Molecules Adsorbed in Metal Surfaces
1-30-80	J. Schwartz Princeton University	Development of Catalytically Active Zirconium Species: The Naked Truth
2-6-80	L. C. De Jonghe Lawrence Berkeley Laboratory/ Materials and Molecular Research Division	Reduction Reactions
2-13-80	J. Yates U.S. Bureau of Standards	Spectroscopic and Other Structural Studies of Chemisorbed Species on Metal Single Crystals and on Dispersed Metal Substrates
2-15-80	R. Pettit University of Texas	Bridging Methylene Metal Groups and Their Possible Role in Fischer-Tropsch Reactions
2-20-80	S. Overbury Oak Ridge National Laboratory	Low Energy in Ion Scattering for Structure Analysis: The Reconstructed Au (110) Surface
2-27-80	R. L. Schwoebel Sandia Laboratories	Surface and Near Surface Research at Sandia Labs
2-29-80	S. Bernasek Princeton University	Internal Energy of Heterogenous Reaction Products: Nitrogen Atom Recombination on Iron
3-5-80	M. White University of Texas	Chemisorption on Copper Covered Ru (001)
3-5-80	A. Joshi Physical Electronics Industries	Metallurgical Applications of Electron Spectroscopy
3-11-80	P. Stair Northwestern University	The Acidic Character of Oxidized Metal Surfaces and the Decomposition of Trimethylamine
3-12-80	W. W. Kaeding Mobil Chemical Company	New Organic Reactions Over Synthetic Zeolites
4-9-80	E. Kugler Exxon	Selective Fischer-Tropsch Catalysis
4-11-80	W. Ellis Los Alamos Scientific Laboratory	LEED/ISS Studies of Crystalline Compound Surfaces
4-16-80	C. H. Bartholomew Bringham Young University	Crystallite Size and Support Effects in CO Hydrogenation on Supported Nickel

LIST OF SEMINARS (continued)

Surface and Catalysis Science (continued)

Date	Speaker and Affiliation	Seminar Title
4-17-80	H. S. Jarrett Du Pont	Decomposition of Water by Use of the Photovoltaic Effect
4-22-80	S. Ittel Du Pont	The Activation of C-H Bonds by Iron
4-30-80	G. W. Keulks University of Wisconsin	Selective Catalytic Oxidation of Propylene
5-9-80	B. Gate: University of Delaware	A Hierarchy of Supported Metal Catalysts, Complexes, Clusters, and Crystallites
5-14-80	A. T. Bell Department of Chemistry University of California, Berkeley Lawrence Berkeley Laboratory/ Materials and Molecular Research Division	Application of Transient Response Techniques for the Study of Catalytic Reactions
5-21-80	M. Farcasiu Mobil Research and Development Corporation	Coal Conversions and Chemical Structure
5-28-80	M. A. Vannice Penn State University	Carbon Monoxide Hydrogenation Over Carbon Supported Iron
9-2-80	M. Kobayashi Kitami Institute of Technology	Characterization of Mechanisms in Heterogeneous Catalysis by a Transient Response Method
9-24-80	J. G. Dash University of Washington	Monolayer Films, 2-D or Not 2-D
10-1-80	R. Brundel IBM, San Jose, CA	Kinetics and Mechanisms of the Interaction of Oxygen with Nickel and Iron and Ni/Fe (100) Surfaces
10-6-80	J. Melrose Mobil Research and Development	Thermodynamics of Micellization
10-15-80	A. Kam Mobil Research and Development Corporation	Gasoline from Coal Natural Gas via Methanol
10-22-80	D. Ollis UC Davis	Heterogeneous Photo Assisted Catalysis
10-23-80	J. Rojo University of Madrid	Effects of Ion Bombardment on Surface Reactivity
10-29-80	A. Kaldor Exxon Research and Engineering Company	Surface Science Measurements on Iron and Iron Oxide
11-5-80	N. Y. Chen Mobil Research and Development Corporation	Recent Developments in Shape Selective Catalysis
11-6-80	M. Grunze Fritz-Haber-Institut der Max-Planck- Gesellschaft, Berlin	Molecular and Dissociative Nitrogen Adsorption on Transition Metal Surfaces
11-12-80	J. G. Ferry Virginia Polytechnic Institute	Metanogenic Microbial Food Chains--A Unique Biological Group
11-19-80	T. R. Hughes Chevron Research Corporation	Improved Aromatic Selectivity of Naptha Reforming Catalysts by Carbonaceous Deposits from Reactant Hydrocarbons

LIST OF SEMINARS (continued)

Surface and Catalysis Science (continued)

Date	Speaker and Affiliation	Seminar Title
12-3-80	J. Hemminger University of California, Irvine	Raman Scattering Cross-Section of Adsorbed Pyridine Molecules on a Smooth Silver Surface
12-8-80	G. Comsa KFA Julich; West Germany	Molecular Processes on Stepped Surfaces

Reaction Dynamics

1-23-80	J. Beauchamp Department of Chemistry, California Institute of Technology, Pasadena, CA	New Approaches to the Study of Reactions Intermediates in Organometallic Chemistry
2-25-80	H. Rabits Department of Chemistry, Princeton University, Princeton, NJ	Sensitivity Analysis in Molecular Dynamics and Chemical Kinetics
3-5-80	J. A. Beswick Laboratory for Molecular Photophysics, University of Paris, Orsay, France	Dissociation Van der Waals Molecules
3-27-80	M. Bowers Department of Chemistry, University of California, Santa Barbara, CA 93106	Multiple Transition States in Chemical Reactions: A Unified Statistical Theory Approach. Application to C_4H_8
4-7-80	S. R. Leone JILA, National Bureau of Standards, University of Colorado, Boulder, CO 80309	IR Chemiluminescence Studies of Reactive Dynamics
4-11-80	J. Hepburn Lash Miller Chemical Laboratories, 80 St., George St., Toronto, Canada	Vacuum UV Laser Induced Fluorescence Studies in Chemical Dynamics
5-21-80	H. Pritchard Department of Chemistry, York University, Ontario, Canada	New Approach to Unimolecular Reaction Theory
6-29-80	R. Miller Department of Physics, University of Waterloo, Waterloo, Ontario, Canada	Infrared Laser Molecular Beam Spectroscopy
10-24-80	D. L. Thompson Department of Chemistry Oklahoma State University, Stillwater, OK 74074	Formation and Decay of Quasi-Bound Clusters of Ar Atoms
10-27-80	J. Farrar Department of Chemistry, University of Rochester, Rochester, NY 14627	Crossed Beam Studies of Proton Transfer Reactions at Low Energy
11-17-80	J. P. Toennies Max-Planck-Institut Bottingerstr. 4-8, 3400 Gottingen, West Germany	Beam Scattering Experiments on Rotational and Vibrational Excitation

LIST OF SEMINARS (continued)

Electron Microscopy of Materials

Date	Speaker and Affiliation	Seminar Title
1-14-80	O. L. Krivanek Lawrence Berkeley Laboratory/ Materials and Molecular Research Division	Electron Energy Loss Spectroscopy: Towards Single Atom Analysis
1-28-80	L. E. Thomas Hanford Energy Development Laboratory, Richmond, WA	Microanalysis of Neutron - Irradiated Super - Alloys
2-22-80	D. B. Wiliams Department of Metallurgy and Materials Engineering, Lehigh University, Bethlehem, PA 18015	Applications and Limitations of the Analytical Electron Microscope
2-22-80	C. Colliex Laboratoire de Physique des Solides, Universite de Paris-Sud, 91405, Orsay, France	Energy Loss Spectrometry
2-29-80	P. R. Okamoto Materials Science Division, Argonne National Laboratory Argonne, Illinois	Nonequilibrium Segregation Phenomenon in Irradiated Alloys
3-17-80	Y. Bando National Institute for Research in Inorganic Materials, Sakura-mura, Niihari-gun, Ibaraki 305, Japan. Present address; Center for Solid State Science, Arizona State University, Tempe, AZ	Structure Analysis by 1 MV High-Resolution Electron Microscopy
4-25-80	R. M. Fisher Basic Research, U.S. Steel Corp., Research Laboratory, Monroeville, PA 15146	Catalytic Gasification on Graphite
5-5-80	M. Ruhle Max-Planck-Institut fur Metallforschung Stuttgart	Electron Energy Loss Spectrometry at Grain Boundaries in Ceramics

Appendix D

INDEX OF INVESTIGATORS

Andersen, Richard A. 381

Bartlett, Neil 355, 381
Bell, Alexis T. 336, 427
Bergman, Robert C. 366, 427
Boone, Donald H. 441
Bragg, Robert H. 100
Brewer, Leo 192, 447
Brown, Steven D. 364

Clark, John H. 321
Clarke, John 165
Cohen, Marvin L. 178
Cornick, Robert E. 334, 447, 450
Conway, John G. 381

De Jonghe, Lutgard, C. 93, 519

Edelstein, Norman M. 381, 503
Evans, Anthony G. 54
Evans, James W. 136, 427, 471

Falicov, Leo 174

Gronsky, Ronald 3

Harris, Charles B. 238
Heineman, Heinz 427, 453
Hess, Dennis W. 203

Jeffries, Carson D. 158
Jolly, William L. 347

Lee, Yuan T. 262, 295, 462
Levy, Alan V. 121, 421, 427, 438, 441

Mahan, Bruce, H. 262
Marrus, Richard 326
Miller, William H. 267

Moore, C. Bradley 248, 457
Morris, J.W., Jr. 35, 497, 513
Muetterties, Earl L. 353
Muller, Rolf H. 205, 471

Newman, John 350, 471

Olander, Donald R. 195

Pask, Joseph 75
Phillips, Norman E. 183
Pines, Alexander 217, 415
Pitzer, Kenneth S. 255
Prausnitz, John M. 375, 511

Raymond, Kenneth N. 381
Richards, Paul L. 139
Rosen, Moshe 73
Ross, Philip N. 413, 471, 515

Schaefer, Henry F., III 310
Seaborg, Glenn T. 381
Searcy, Alan W. 87
Shen, Y. Ron 146, 462
Shirley, David A. 271
Somorjai, Gabor A. 208, 336, 427
Streitwieser, Andrew, Jr. 381

Templeton, David H. 381
Thomas, Gareth 3, 11
Tobias, Charles W. 187, 471, 489

Vollhardt, K. Peter 343, 427

Washburn, Jack 45
Westmacott, Kenneth H. 29
Whittle, David P. 107, 441
Winn, John S. 244, 262

Zalkin, Alan 381

GPO 788-120/1